

Monday

1:15PM - 2:50PM

Washington Marriott Wardman Park, Maryland A/B/C 4E

- Excerpta - I

E-01

1:15PM - 1:20PM

The temporal appearances of intracranial aspergillosis

D Saunders¹, B Adams¹, H Cliffe¹, S Currie¹, J Macmullen-Price¹, D Warren¹, I Craven¹

¹Leeds Teaching Hospitals Trust, Leeds, West Yorkshire

Purpose

Aspergillosis is an uncommon infection which predominantly affects immunocompromised subjects. Intracranial infection is rare but carries significant morbidity and mortality. Early diagnosis is key to prompt initiation of appropriate, potentially lifesaving treatment; yet the clinical presentation is often non-specific and the reporting radiologist may be the first to suspect a fungal aetiology. We present the temporal imaging changes in a case of successfully treated intracranial aspergillosis.

Materials and Methods

A five year old male who was undergoing chemotherapy for acute lymphocytic leukaemia and who was being investigated for febrile neutropenia developed flaccid right arm weakness. Initial imaging demonstrated multiple non-specific intracranial lesions but none to account for his symptoms. Aspergillus was the only positive blood culture. Despite high dose antibiotic / antifungal therapy there was an initial, significant deterioration in imaging and clinical symptoms with progression to quadriplegia and associated respiratory compromise. Following a protracted admission there was almost complete neurological recovery with only minor residual weakness, mirrored by on-going radiological improvement.

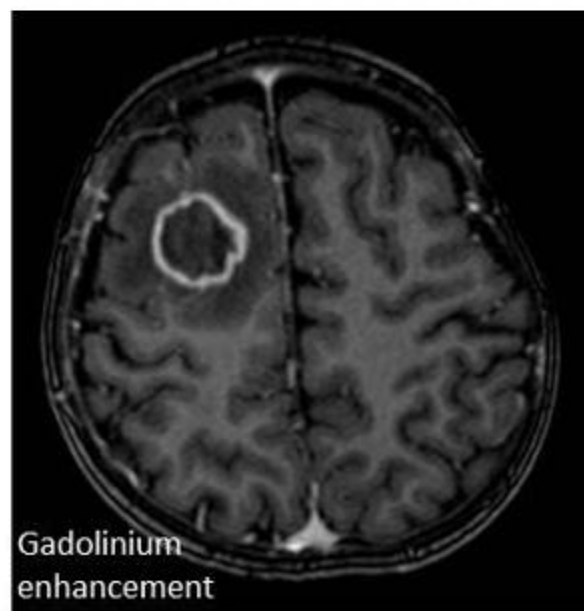
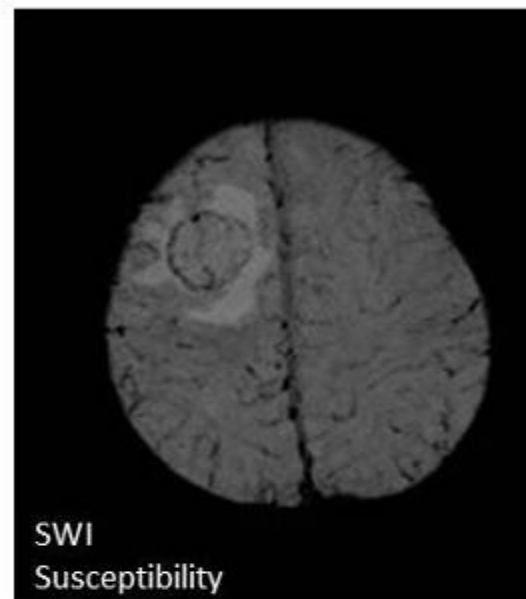
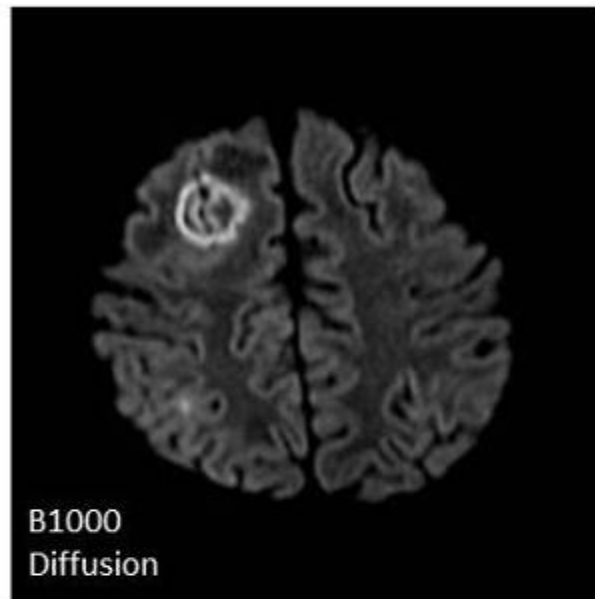
Results

Initial cross sectional imaging demonstrated multiple poorly-enhancing intracranial and intramedullary lesions which showed avid diffusion restriction. Repeat studies performed at 8 and 27 days demonstrated evolution with ring enhancement and a double rim sign of restriction and susceptibility. Several of the lesions contained a central, non-enhancing crenation highly suspicious for atypical infection. Following 2 months of high dose antifungal therapy repeat imaging demonstrated interval improvement with abscess maturation including thickening of the capsule, decreased diffusion restriction and increased peripheral T1 signal.

Conclusions

The incidence of intracranial aspergillosis is increasing, carrying significant morbidity and mortality. Awareness of the suggestive imaging findings is an important adjunct

to maintaining a high index of suspicion which is essential to optimise the chance of successful management. This case serves as an extremely useful illustrative example.



(Filename: TCT_E-01_intracranialaspergillosis.jpg)

E-02

1:20PM - 1:25PM

**Microarteriovenous Malformations of Hereditary Hemorrhagic Telangiectasia:
Utility of Arterial Spin Labeling Perfusion MRI**

N Lall¹, J Leach¹, L Linscott¹, E Alvarado¹, T Abruzzo¹, A Hamill¹
¹*Cincinnati Children's Hospital Medical Center, Cincinnati, OH*

Purpose

Cerebral microarteriovenous malformations (micro-AVMs) are defined as AVMs less than 1 cm in size. Though seen in less than 10% of patients with sporadic AVMs, micro-AVMs may occur in up to 50% of patients with intracranial AVMs associated with Hereditary Hemorrhagic Telangiectasia (HHT). The small size of these lesions contributes to their classic description as occult on CT and MRI and their frequent initial presentation with intracranial hemorrhage. While prior studies have confirmed the value of pCASL (pseudo-continuous arterial spin labeling) perfusion MRI in screening and surveillance of AVMs, none have specifically evaluated its ability in detecting these potentially "occult" micro-AVMs. This case series highlights our initial experience with pCASL as an enhancement to traditional non-invasive imaging evaluation of micro-AVMs in HHT.

Materials and Methods

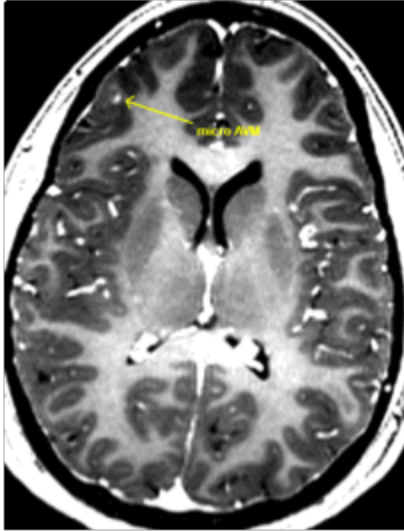
Four patients with known HHT underwent MRI/MRA of the brain to screen for intracranial AVMs, with addition of pCASL perfusion sequence. The patients later underwent conventional angiography, which was correlated with the findings on MRI.

Results

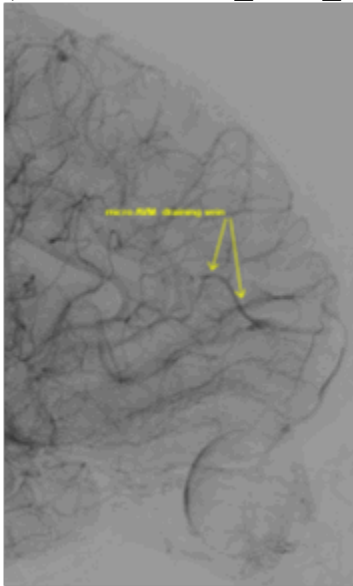
Angiographically proven or suspected micro-AVMs demonstrated focally increased perfusion on the pCASL images, with high conspicuity compared to the normal background parenchymal perfusion. On post-contrast 3D T1-weighted images, these lesions were often inconspicuous if not completely occult; millimetric foci of enhancement were present in association with these lesions, though in some instances were only identifiable retrospectively. Attached images demonstrate a right frontal micro-AVM on pCASL MRI, post-contrast T1 MRI, and arterial and parenchymal phase DSA. Larger left perisylvian AVM is also shown on the MRI images.

Conclusions

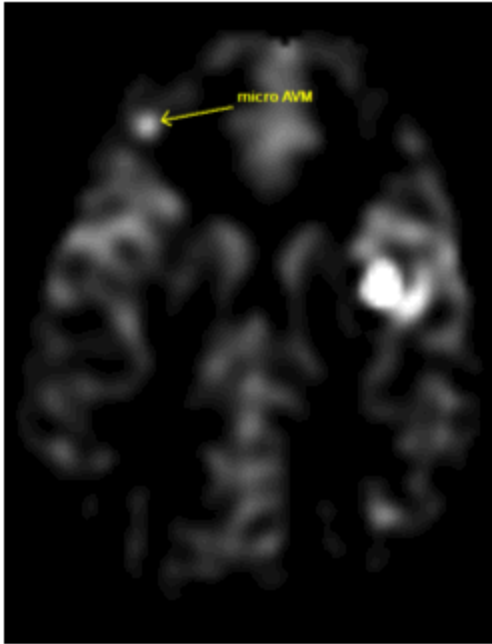
Given the frequency of micro-AVMs in patients with HHT and their near occult appearance on non-invasive imaging techniques, pCASL may serve as a useful adjunct to conventional MR sequences in screening and surveillance of such patients.



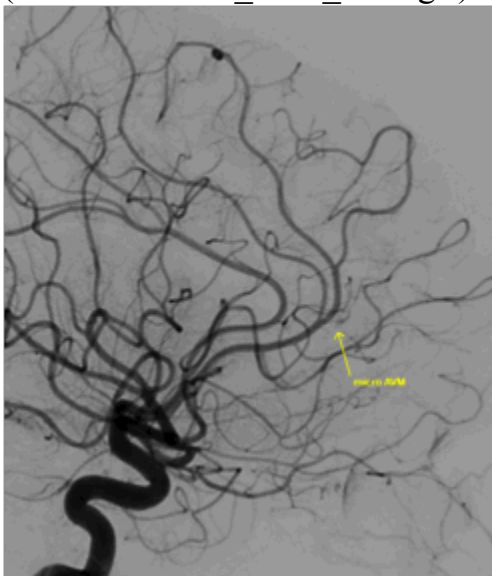
(Filename: TCT_E-02_Post.gif)



(Filename: TCT_E-02_Parenchymal.gif)



(Filename: TCT_E-02_AS�.gif)



(Filename: TCT_E-02_Arterial.gif)

E-03

1:25PM - 1:30PM

Developmental Venous Anomalies (DVAs) Mimicking Neoplasm on 11C-Methionine PET and DSC Perfusion MRI.

J Harreld¹, J Angel¹, B Shulkin¹, M Doubrovin¹

¹St. Jude Children's Research Hospital, Memphis, TN

Purpose

Sensitivity and specificity of ^{18}F FDG-PET CT for brain tumor assessment are limited by high background activity of normal brain. Radiolabeled amino acids such as ^{11}C -methionine, a marker for elevated amino acid transport and metabolism in proliferative cells, may be more sensitive and specific. However, we have noticed increased uptake on ^{11}C -methionine-PET (Met-PET) associated with developmental venous anomalies (DVAs), which could mimic tumor and misdirect biopsy. DVAs also show increased relative cerebral blood volume (rCBV) on dynamic susceptibility contrast (DSC) perfusion MRI, also frequently associated with higher-grade tumors. We illustrate the Met-PET, DSC perfusion and MR imaging features of DVAs in three children imaged for brain tumors at our institution.

Materials and Methods

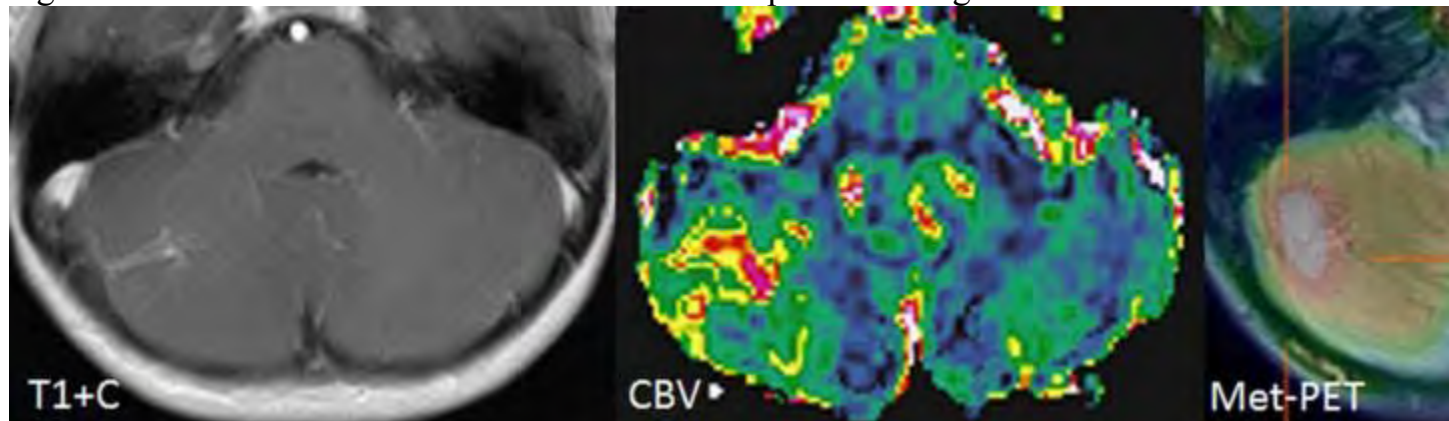
Three patients with developmental venous anomalies incidentally noted on MRI -- a 16-year-old female with residual posterior fossa low-grade glioma, a 19-year-old male with right frontal high-grade glioma, and a 9-year-old female with multifocal low-grade gliomas -- underwent both Met-PET and brain MRI with DSC perfusion. ROIs were placed in areas of increased signal on Met-PET and CBV maps associated with DVAs and in contralateral normal brain; width of anomalous veins were measured on post-contrast T1WI. Ratios of DVA:normal brain ^{11}C -methionine uptake (rSUV), rCBV and DVA width were compared (Pearson correlation).

Results

^{11}C -methionine uptake was elevated in cortex overlying the DVAs (mean rSUV=1.31, range 1.11-1.63) and increased with size of DVA ($r=0.926$) and rCBV ($r=0.949$); correlation of DVA size with rCBV was less consistent ($r=0.760$). All DVAs were visible on post-contrast T1WI; one was visible on non-contrast T1WI; and none were visible on non-contrast CTs accompanying Met-PET.

Conclusions

Because DVAs are not readily visible on CT, prevention of misdirected biopsy in patients with focally elevated ^{11}C -methionine and rCBV relies on analysis and registration to MRI with contrast to exclude non-neoplastic etiologies.



(Filename: TCT_E-03_ASNRFig.jpg)

Primary Leptomeningeal Atypical Teratoid/Rhabdoid Tumor: Case Report

A Mamere¹, C Cavalcante¹, M Matsushita¹, G Almeida¹, E Silva¹

¹*Barretos Cancer Hospital, Barretos, SP*

Purpose

To report a rare pathology-proven case and to show the imaging findings of a primary leptomeningeal atypical teratoid/rhabdoid tumor.

Materials and Methods

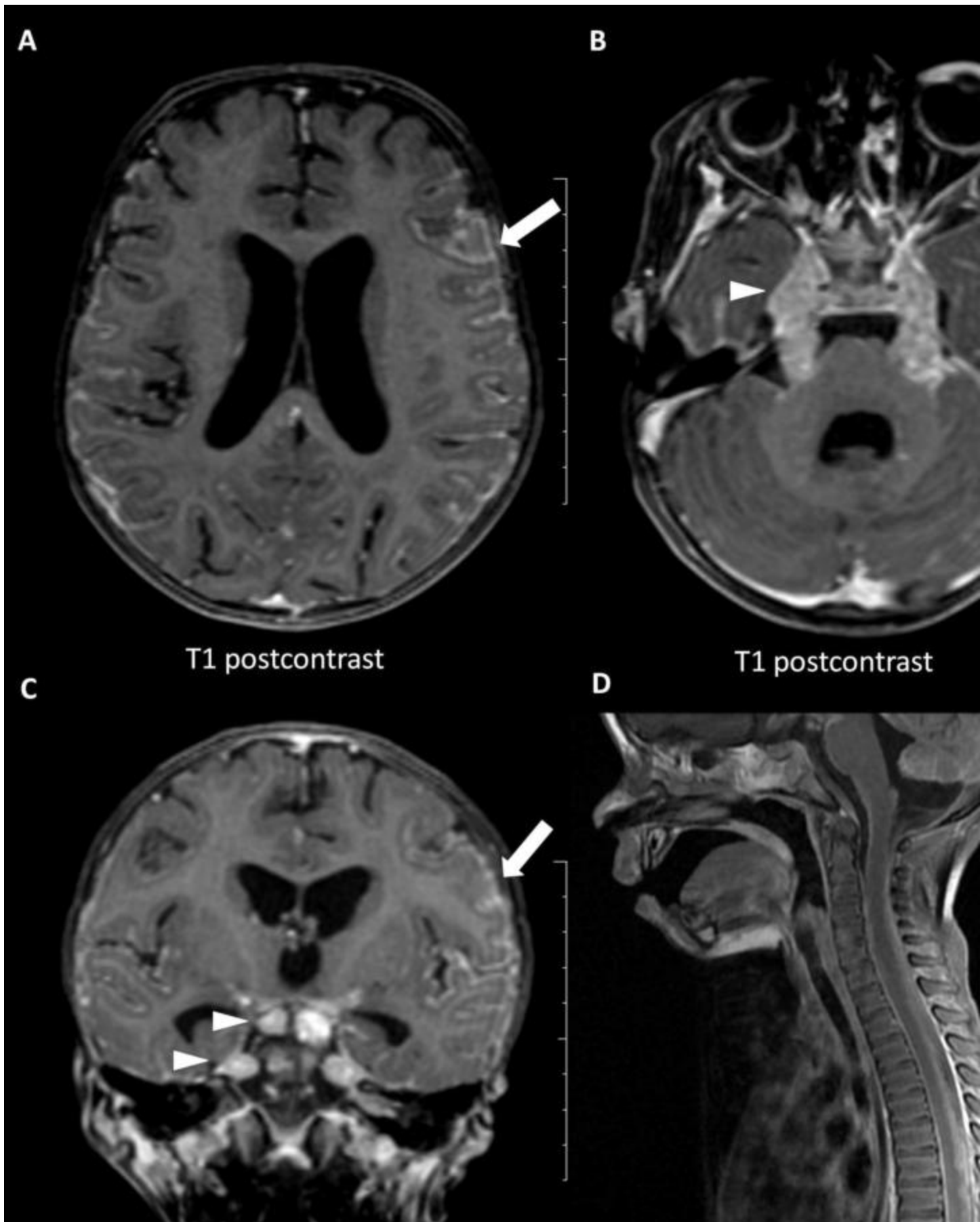
A 20-month-old girl presented with a 1-month history of unilateral ptosis and quadriparesis. Magnetic resonance imaging (MRI) showed diffuse leptomeningeal disease. Cerebrospinal fluid analysis was not performed. Serological tests for infectious diseases were all negative. Surgical meningeal biopsy in the lumbar region was performed and the pathological findings were consistent with atypical teratoid/rhabdoid tumor.

Results

MRI of the neural axis showed diffuse leptomeningeal thickening and enhancement in the whole brain (white arrows in A and C), circumferential enhancement in the spinal cord (white arrow in D), nerves roots and cauda equina. Diffuse cranial nerve thickening and enhancement (specially the trigeminal nerves and the optic chiasm) were also observed (white arrow heads in B and C). No focal primary mass was present. The subarachnoid space and the cerebral ventricles were slightly enlarged.

Conclusions

In the absence of a primary mass, leptomeningeal thickening and enhancement are most commonly due to infectious or inflammatory disorder and in cases where the primary neoplasm is known, leptomeningeal carcinomatosis is the principal diagnosis. Atypical teratoid/rhabdoid tumor is a rare aggressive malignant tumor (WHO grade 4) occurring most often in young children (usually younger than 3 years old). Typically, it presents as an intra-axial mass, which can be infra or supratentorial, with heterogeneous contrast enhancement. Leptomeningeal dissemination may occur and is associated with poorer prognosis. Primary leptomeningeal atypical teratoid/rhabdoid tumor, without a focal mass, is even rarer. The first case was described in 2010. In our literature review, we have found only four cases previously reported. Despite its extreme rarity, this tumor should be included in the differential diagnosis in young children with leptomeningeal disorder.



(Filename: TCT_E-04_Teratoid300dpi.jpg)

E-05

1:35PM - 1:40PM

Central Nervous System Imaging Findings in Bannayan-Riley-Ruvalcaba syndrome (BRRS)

D Johnson¹, V Lehman¹, J Morris¹

¹*Mayo Clinic, Rochester, MN*

Purpose

Bannayan-Riley-Ruvalcaba syndrome (BRRS) is a rare autosomal dominant syndrome that represents part of the PTEN Hamartoma Tumor Syndrome (PHTS) spectrum, along with Cowden syndrome (CS), Proteus syndrome, and Proteus-like syndrome. BRRS and the far more common CS may represent variable manifestations of the same mutation, as they can co-occur in the same family. No formal diagnostic criteria for BRRS have been set, but cardinal features suggesting the diagnosis include macrocephaly, hamartomatous intestinal polyposis, lipomas, and pigmented macules of the glans penis. The full scope of neuroradiological findings in BRRS has yet to be defined.

Materials and Methods

A 3-year-old boy with a family history of BRRS due to known PTEN mutation presented with global developmental delay and stereotyped episodes concerning for seizure activity. Physical examination demonstrated macrocephaly.

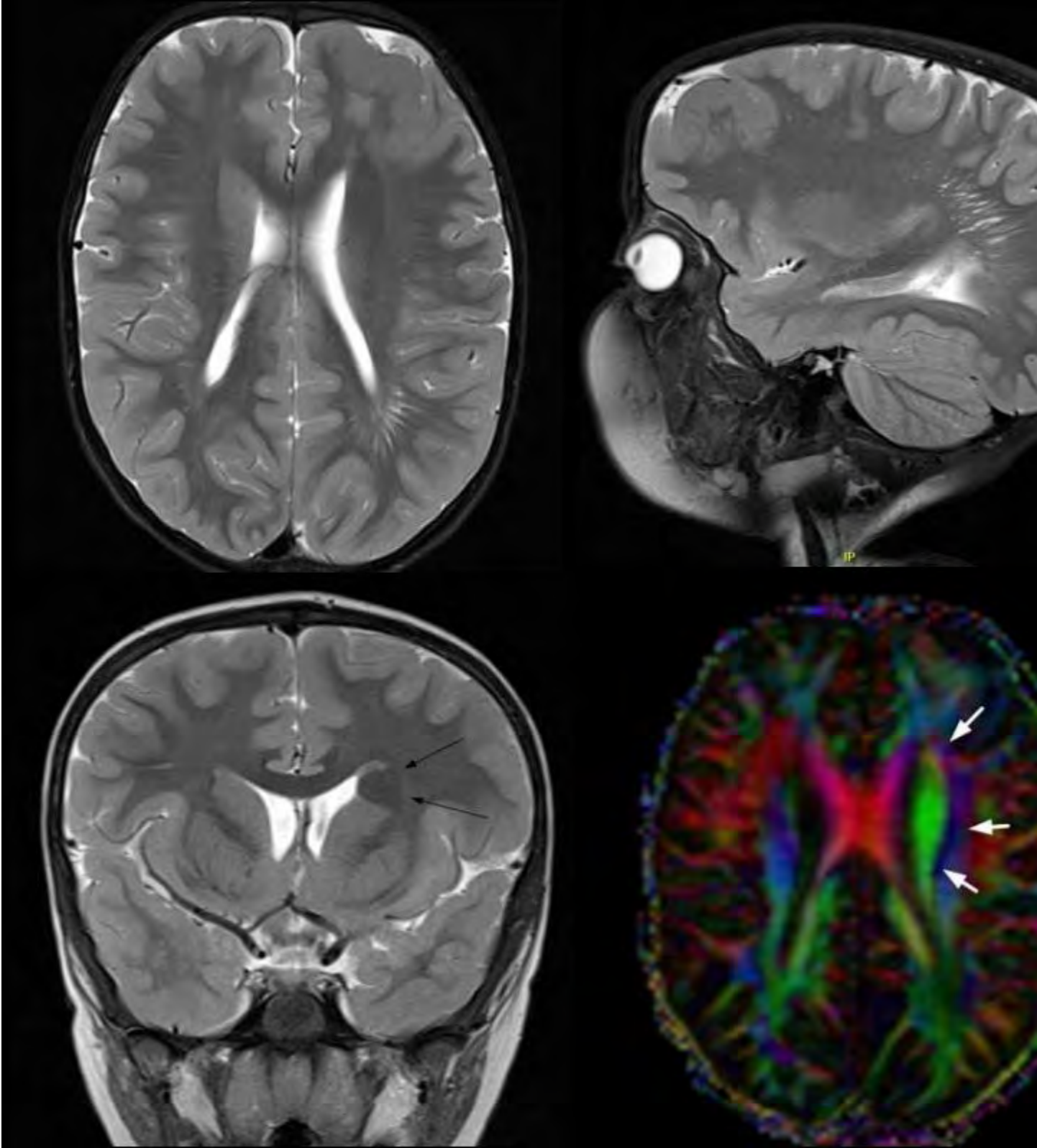
Results

Brain MRI revealed a left anterior frontal lobe cortical migration anomaly with prominent cerebral veins overlying the anomaly, as well as several tiny abnormal veins running through the involved cortex. A markedly enlarged abnormal white matter tract running along the expected course of the superior fronto-occipital fasciculus (SFOF) which blunted the left caudate head superiorly was visible on anatomic images and confirmed with diffusion tensor imaging (DTI). Prominent perivascular spaces were noted in the parietal lobes bilaterally.

Conclusions

Cystic-appearing dilated parietal perivascular spaces, as seen in our patient, have been previously reported to occur in 100% of a series of seven patients with BRRS, and represent the most common focal intracranial abnormality associated with this condition. This finding should prompt consideration of BRRS in a pediatric patient with unexplained macrocephaly. The additional findings seen in our patient, including cortical dysplasia which has been previously described in a single case report and the markedly enlarged white matter tract, which to our knowledge has not been

previously reported, represent a portion of the expanded spectrum of BRRS-associated intracranial abnormalities.



(Filename: TCT_E-05_composite_14468281884696.jpg)

Positional CSF Leakage Into the Lumbar Subdural Space

B Salehi¹, D Park², B Yoo¹

¹*UCLA, Los Angeles, CA*, ²*UCLA, Los Angeles,, CA*

Purpose

To report a unique case of a positional CSF leak into the subdural space.

Materials and Methods

A 36-year-old woman underwent an L4-5 and L5-S1 microdiscectomy that was complicated by epidural hematoma requiring subsequent surgical evacuation. 10 days after surgery, the patient began to experience postural headaches suggestive of intracranial hypotension. An MRI of the lumbar spine was performed to evaluate for a potential CSF leak, which revealed a small subdural fluid collection in the lower lumbar spinal canal. A subsequent MRI one week later demonstrated near resolution of the subdural fluid collection. A lumbar myelogram and post-myelogram CT of the lumbar spine was then performed to confirm and localize the presence of a CSF leak. Surprisingly, the myelogram demonstrated a large, ventral and dorsal subdural fluid collection extending from L2 to S1, resulting in significant effacement of the thecal sac and crowding of the lumbar nerve roots. The fluid collection was slightly hyperdense relative to CSF, suggesting diluted myelographic contrast within the collection. The patient did not report new symptoms of lower back pain or nerve root compression at the time of the myelogram. An MRI of the lumbar spine was performed the next day, which demonstrated near resolution of the subdural fluid collection, and slightly increased epidural fluid. The patient then underwent a revision laminectomy at L4-5 and L5-S1 for repair of a dural tear. Intraoperatively, it was noted there were 2, 1-2 mm dorsal dural tears with associated subarachnoid blebs that ruptured under the epidural fat, with intact lamina directly dorsal. The leak was intermittent and positional and would tamponade as the dura expanded against the lamina. The dural tears were surgically repaired; postoperatively, the patient's postural headaches resolved.

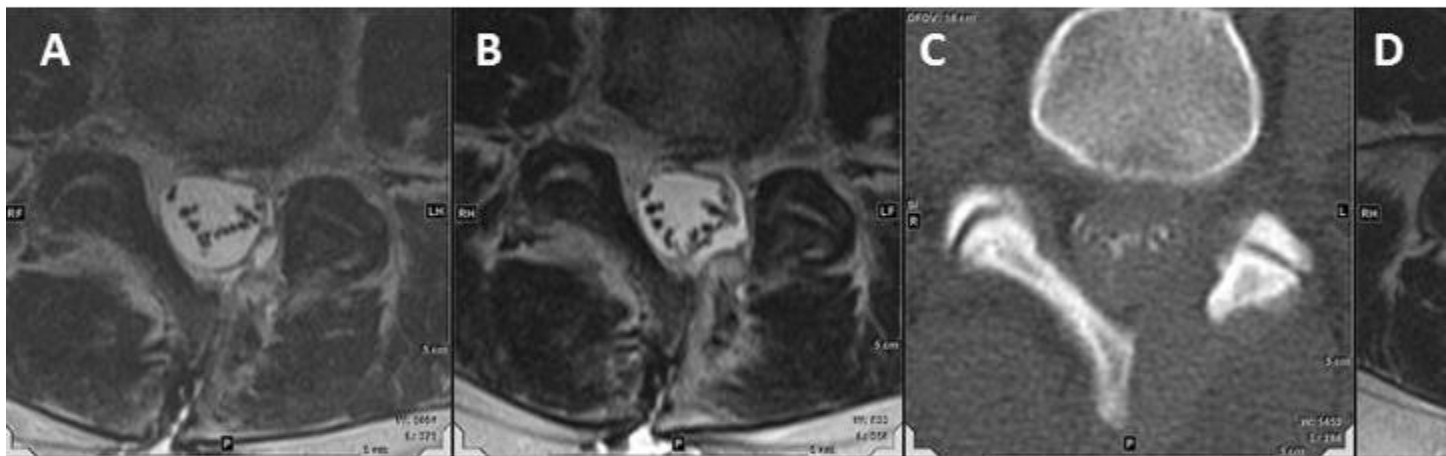
Results

A. MRI of the lumbar spine demonstrates a small dorsal subdural fluid collection. B. MRI performed one week later demonstrates near resolution of the subdural fluid collection. C. CT myelogram of the lumbar spine demonstrates marked increase in the subdural collection, resulting in significant effacement of the thecal sac. D. Subsequent MRI demonstrates resolution of the subdural fluid collection.

Conclusions

We report a unique case of a positional CSF leak into the subdural space from

incidental durotomy from spinal surgery. The dynamic nature of the subdural leak is likely related to the position of the dural tears in relation to the lamina; we hypothesize, based on the patient's position, the dural tears would tamponade against the adjacent lamina, preventing leakage of CSF into the epidural space and forcing CSF to dissect into the subdural space, resulting in transient subdural fluid collections as demonstrated by serial imaging. In conclusion, while CSF leakage from spinal dural tears most commonly present as extra-dural CSF collections, it is important to be aware that leakage into the subdural space can occur.



(Filename: TCT_E-06_subdural.jpg)

Lateral Meningocele Syndrome: Imaging Findings of a Rare Disorder

S Lin¹, J Dorr¹, Y Guo¹, R Pandit¹, M Patel¹

¹*Santa Clara Valley Medical Center, San Jose, CA*

Purpose

Lateral Meningocele Syndrome (LMS), also referred to as Lehman Syndrome, is a rare genetic disorder with only approximately 10 reported cases in the literature. It is characterized by multiple lateral meningoceles, dural ectasia, skeletal abnormalities, and facial dysmorphism. In this report, imaging of a mother and daughter with findings compatible with LMS is presented. A review of the 3 layers of the meningeal membranes within the thecal sac is also accomplished.

Materials and Methods

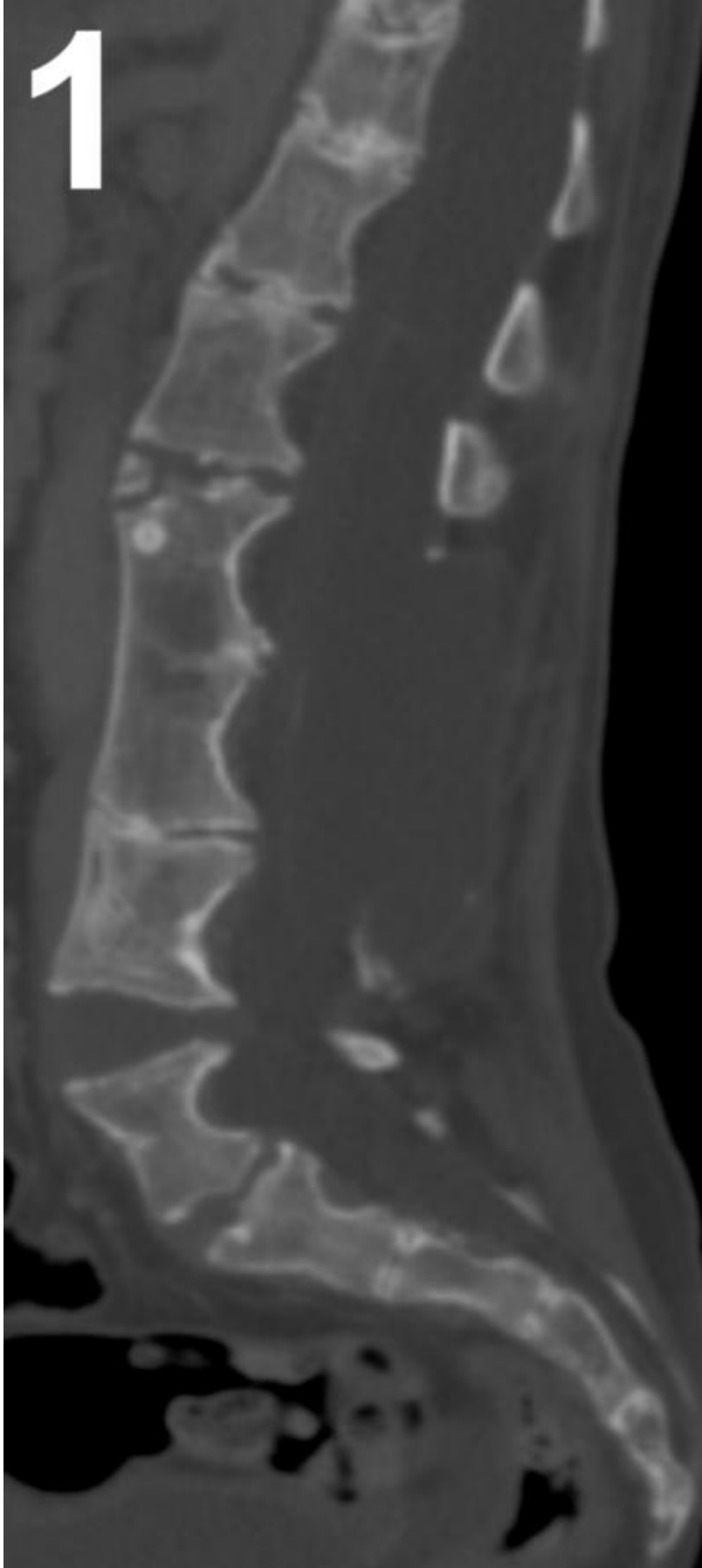
A case of LMS in a female diagnosed in her early teens is presented. She had already undergone surgical excision of an inferior lumbar arachnoid cyst due to lower extremity weakness. She has levoscoliosis of the thoracolumbar spine, and exhibits many craniofacial, skeletal, and auditory findings associated with LMS. Due to her diagnosis, the patient's mother was subsequently imaged and noted to have similar imaging findings, also compatible with LMS. This suggests a genetic etiology for this syndrome.

Results

Figures 1-2 are of the daughter; Figures 3-4 are of the mother. - Figure 1: Sagittal CT image of the lumbosacral spine demonstrating prominent posterior scalloping, widening of the spinal canal, and elongated and partially fused vertebrae. - Figure 2: Sagittal T2-weighted MR image of the lumbar spine with inset axial T2-weighted slice. Dural ectasia and large lateral T2 hyperintense collections compatible with meningoceles are seen. The spinal cord is displaced anteriorly. - Figure 3: Axial T2-weighted MR image at the L2-3 level demonstrating large lateral meningoceles. - Figure 4: Coronal (left) and sagittal (right) T2-weighted MR images of the inferior thoracolumbar spine depicts multi-level lateral meningoceles and foraminal expansion.

Conclusions

Although originally described by Lehman et al. as "familial otosclerosis," the lateral meningoceles identified in subsequent patients in the literature resulted in a shift in the syndrome label. The imaging and clinical features of Lateral Meningocele Syndrome affecting a daughter and mother are presented. An autosomal dominant or X-linked dominant inheritance pattern is suggested.



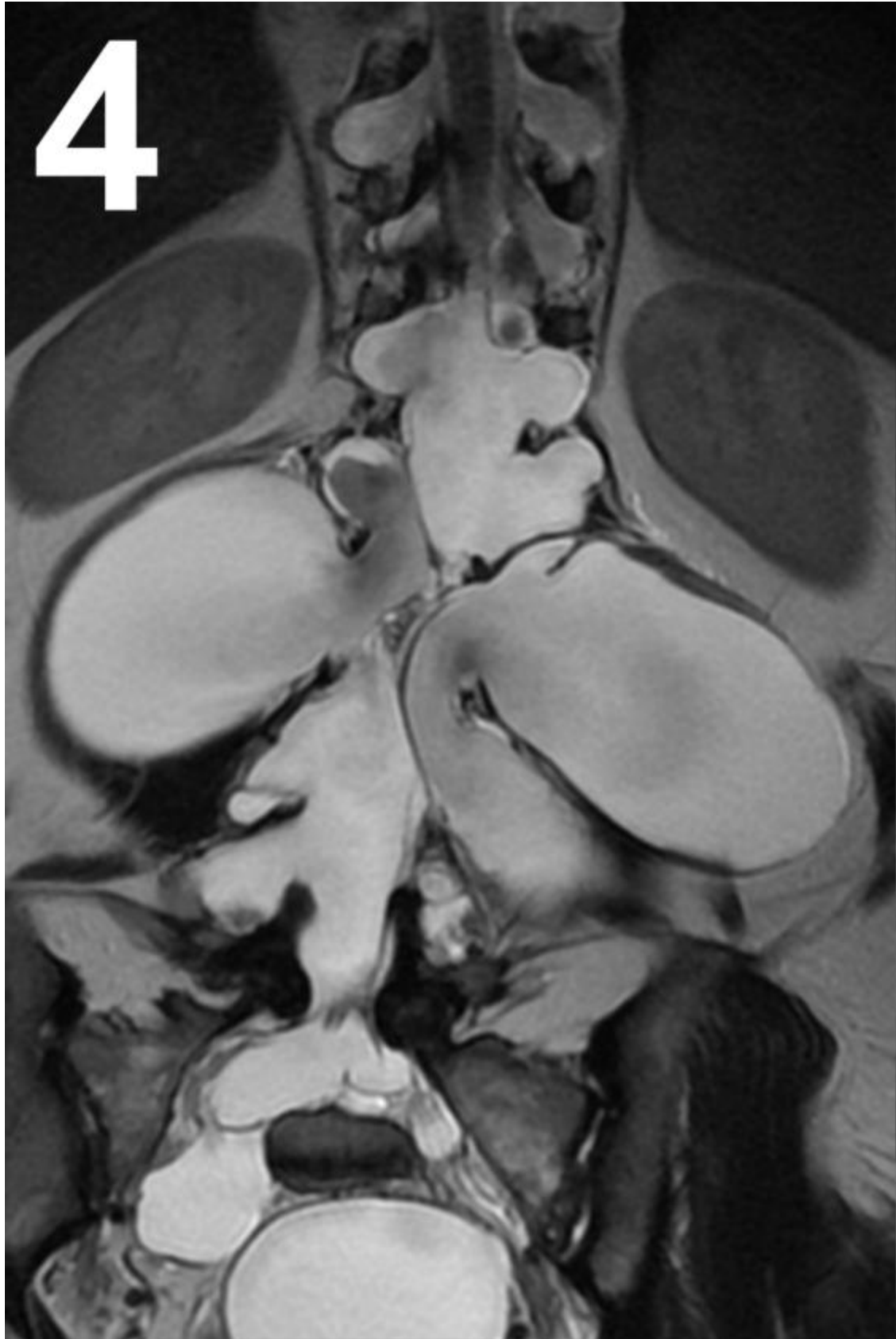
(Filename: TCT_E-07_Fig1.jpg)



(Filename: TCT_E-07_Fig2.jpg)



(Filename: TCT_E-07_Fig3.jpg)



(Filename: TCT_E-07_Fig4.jpg)

E-08

1:50PM - 1:55PM

Close your windows at night! An unusual cause of cauda equina enhancement

R Lobo¹, D McCorquodale¹, D Wynn¹, S McNally², S Ansari¹

¹University of Utah, Salt Lake City, UT, ²university of Utah, Salt Lake City, UT

Purpose

This case presents a rare cause of cauda equina enhancement from rabies. It has rarely been extensively imaged. Our case report presents the imaging and pathological findings along with a fascinating clinical history.

Materials and Methods

A 77 year old woman with several days of muscle pain, stiffness and weakness who presented to an outside hospital with a "flu like" illness after a fall. She had dysarthria and dysphagia with aspiration of water in the emergency department. She was transferred to our hospital for a more complete work up with suspicion of Guillain Barre Syndrome. She was intubated for respiratory distress. Clinical history that came to light later shortly after admission revealed a prior history of waking up at night (5 weeks prior to admission) with a bat on her face. There was no bite mark identifiable, and the bat was not captured. Rabies became the most likely diagnosis and additional lumbar punctures, skin biopsy and serum samples were all sent to CDC confirming rabies virus in all compartments. Despite IVIG administration, the patient's condition worsened. Care was withdrawn and the patient expired shortly thereafter.

Results

Mild cauda equina enhancement without additional abnormality in the spine. Diffuse dural enhancement and moderate enhancement of the right greater than left preganglionic trigeminal nerves.

Conclusions

This excerpta presents and unusual cause of nerve enhancement. The clinical history eventually revealed rabies as a cause, with positive samples from skin, CSF and serum all confirmed within 2 hours of arriving at CDC (Atlanta, GA).

E-09

1:55PM - 2:00PM

Blastomycosis of Lumbar Spine with Iliopsoas Abscess: TB or not TB.

S Emamian¹, D Boatman¹, F Allard¹, M Fox¹

¹University of Virginia Medical Center, Charlottesville, VA

Purpose

To present a case report and illustrate blastomycosis as a differential diagnosis for tuberculosis (TB). Endemic to Southeast and Midwest North America, *Blastomyces dermatitidis* is a fungus that can cause skin and lung infection. If disseminated, blastomycosis can involve the lumbar spine and present with abscess along the iliopsoas muscle. The distinguishing features between TB and blastomycosis in our case will be discussed.

Materials and Methods

We present a 43 year old white male with lumbar spine blastomycosis. In December 2013, the patient had a chest CT, following an abnormal chest x-ray, which revealed a right upper lobe infiltrate and hilar lymphadenopathy. Due to concern for malignancy, a PET-CT was performed which demonstrated a focal hypermetabolic area at L5-S1. The patient was lost to follow-up. The patient then presented to our institution in June 2015 with a right groin and thigh mass, back pain and subjective fever, but normal lab results to include WBC and ESR. CT demonstrated destructive change of the right L1-L5 vertebral bodies, the sacrum bilaterally, and enlargement of the right iliopsoas muscle. MRI revealed a rim enhancing collection in the right iliopsoas extending inferiorly into the presacral space bilaterally and into the right inguinal region. Due to the constellation of a lung lesion, hilar lymphadenopathy, multiple lumbar vertebral body lesions and an iliopsoas collection, the diagnosis of tuberculosis was entertained. CT guided biopsy of the iliopsoas was performed with appropriate precautions for tuberculosis utilized, including a performing the biopsy in a negative pressure room. Histologic evaluation demonstrated numerous intracellular yeast forms within histiocytes. The three main differential diagnoses for intracellular yeast forms are cryptococcus, blastomyces and histoplasma. The size of the yeast forms, patterns of budding, lack of a mucicarmine-positive capsule, PCR sequencing and fungal culture were all confirmative of *Blastomyces dermatitidis*. The collection was percutaneously drained and the patient was started on IV amphotericin for 6 weeks followed by oral itraconazole.

Results

PET-CT (1a) from December 2013 demonstrated hypermetabolic lesion on the right side of L5 and S1. CT and MRI (1b, 1c and 1d) from June/July 2015 demonstrated destruction of right side of L1-L5 vertebral bodies with abscess along the right iliopsoas muscle presenting as a protruding mass in the right groin. There was also involvement of the sacrum with bilateral presacral abscesses. It is difficult to distinguish between TB spondylitis and Blastomycosis based on imaging alone, since vertebral body destruction and iliopsoas abscess are common between the two entities. However, the lack of significant disc space involvement and a normal ESR in our patient is somewhat unusual for TB.

Conclusions

Blastomycosis can present with spinal bony destruction and an iliopsoas abscess.

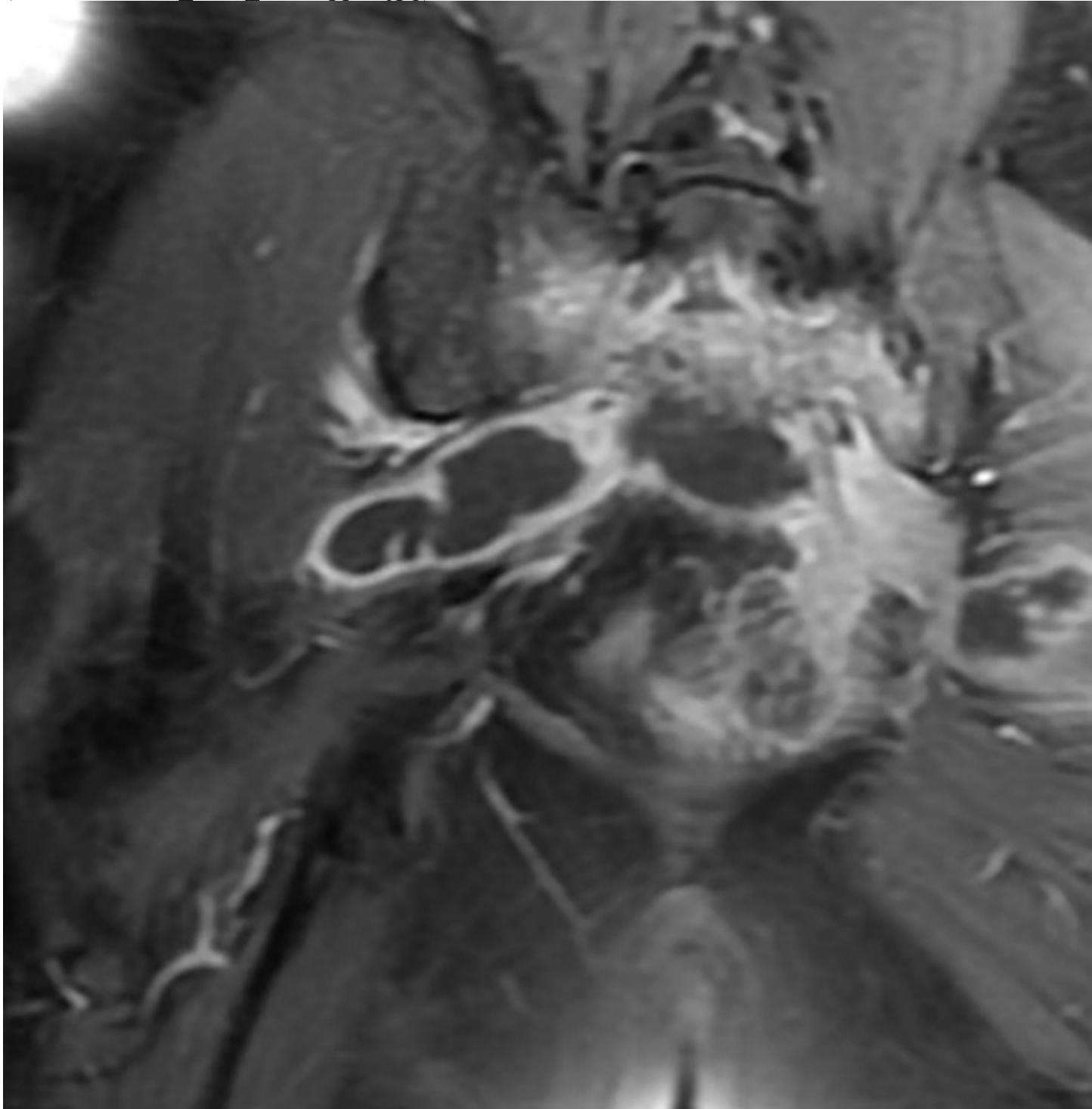
Overlap between the imaging features of blastomycosis and TB can occur and, in endemic areas, blastomycosis should be considered in the differential diagnosis of suspected spinal tuberculosis.



(Filename: TCT_E-09_PETcropped.jpg)



(Filename: TCT_E-09_CTcropped.jpg)



(Filename: TCT_E-09_MR3cropped.jpg)



(Filename: TCT_E-09_MR2cropped.jpg)

E-10

2:00PM - 2:05PM

Idiopathic Hypertrophic Pachymeningitis of the Cervical Spine

R Sharma¹, S Ali¹, E Stein¹

¹*Maimonides Medical Center, Brooklyn, NY*

Purpose

To outline a case of idiopathic hypertrophic spinal pachymeningitis (IHSP) involving the cervical spine and the radiographic findings.

Materials and Methods

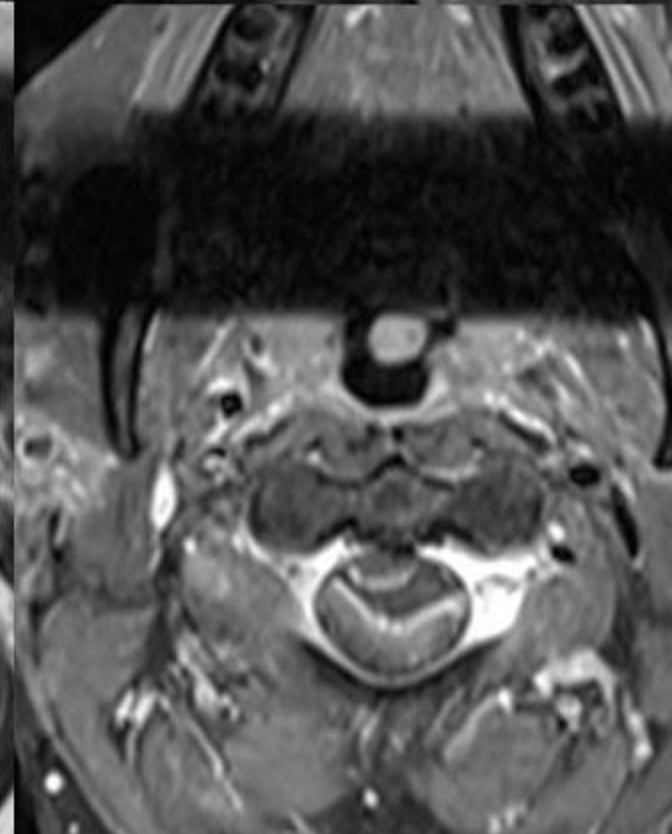
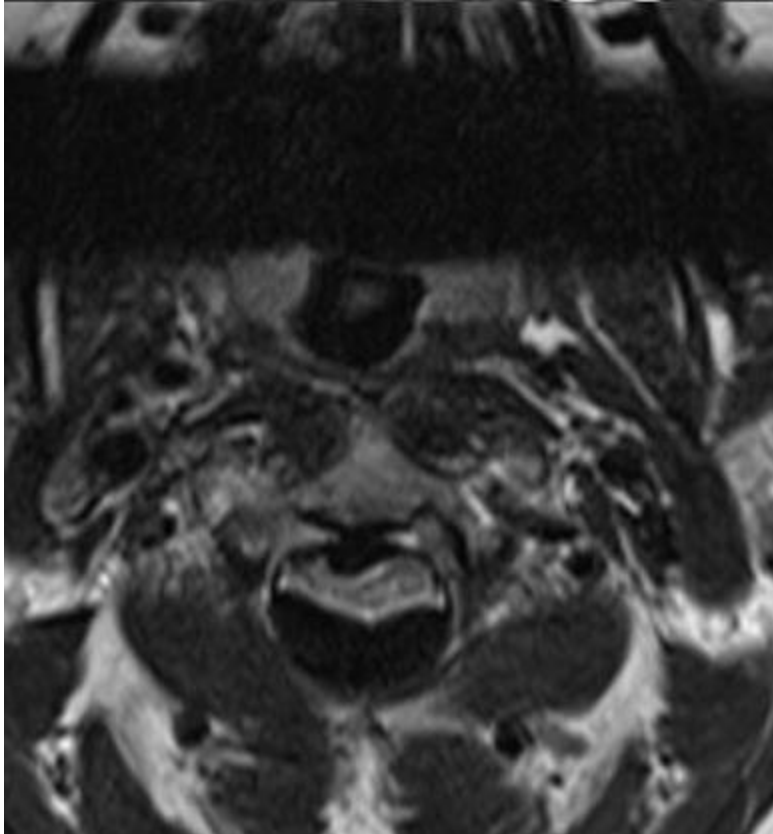
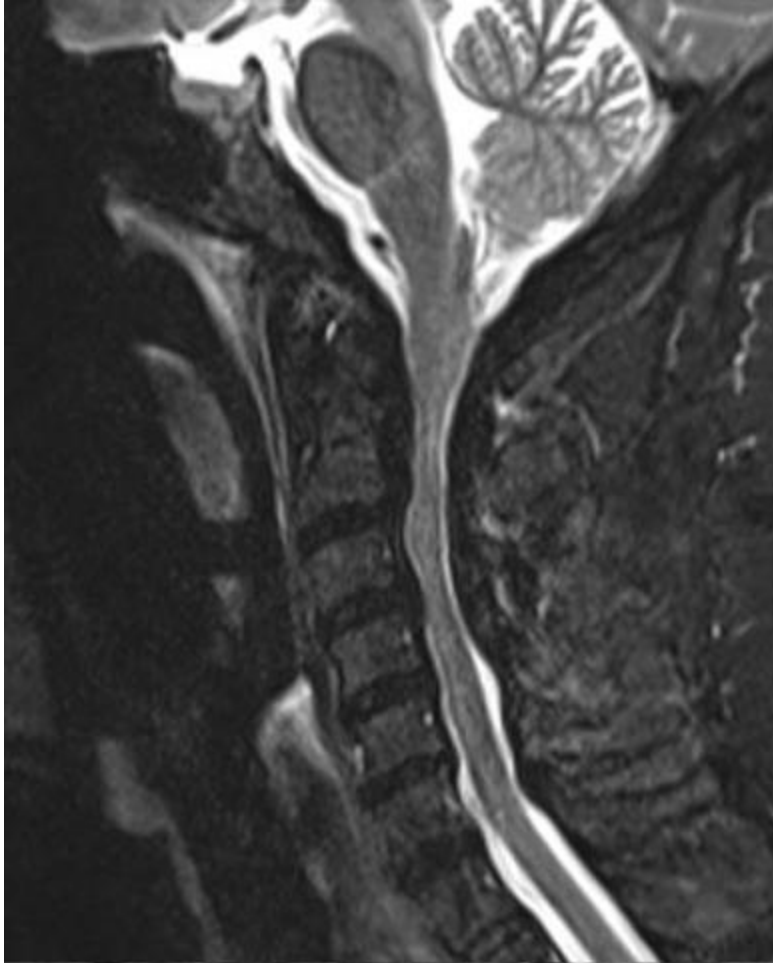
A 55-year old female with multiple comorbidities presents with dizziness and progressive right-sided extremity weakness and myelopathy. The patient had decreased right-sided sensation to light touch with positive Hoffman sign and clonus. Further work-up revealed an extradural posterior fossa and cervical spine mass extending to C6/7 with marked spinal canal stenosis and cord compression from C1 to C4. The patient underwent C4 laminectomy and biopsy of the extradural mass.

Results

MRI of the brain and cervical spine with intravenous gadolinium contrast revealed nodular thickened enhancement of the dura overlying the occipital bone to the level of the transverse sinus and over the clivus to the level of the sella. The enhancement extended into the cervical spinal canal to the level of C6/7 with severe cord compression from C1 to C4. This mass was very low in signal intensity on T1/T2-weighted imaging as well as FLAIR. There was diffuse enhancement with more intense enhancement peripherally. Additionally, there was high signal within the cord compatible with myelomalacia. These imaging findings were suggestive of a fibrous process like IHSP. Other possibilities included meningioma, lymphoma, tuberculosis, sarcoidosis, and amyloidosis.

Conclusions

This case highlights a patient presenting with progressive right-sided myelopathy with a dural-based nodular mass extending into the cervical spine with cord compression. Surgical biopsy and decompressive laminectomy was performed and the patient clinically improved. Pathology revealed IgG4-negative fibrous tissue showing chronic inflammation with mixed inflammatory infiltrate. IHSP is a chronic progressive inflammatory fibrosis of the dura that can cause similar symptoms of compression of neural structures as IgG4-related sclerosing spinal pachymeningitis. IHSP is a diagnosis of exclusion after infectious and malignant etiologies have been ruled out.



(Filename: TCT_E-10_EEIHSP.jpg)

E-11

2:05PM - 2:10PM

Chondroblastic Osteosarcoma of the Pelvis: A Rare Variant with Cartilaginous Imaging Features

J Morris¹, J Williams¹

¹*Mayo Clinic, Rochester, Minnesota*

Purpose

To review the imaging findings of a sacral chondroblastic osteosarcoma, a rare variant whose imaging features are not well described in the literature. To demonstrate that this rare subtype of osteosarcoma has imaging features similar to a chondrosarcoma, but is typically seen in a younger patient population.

Materials and Methods

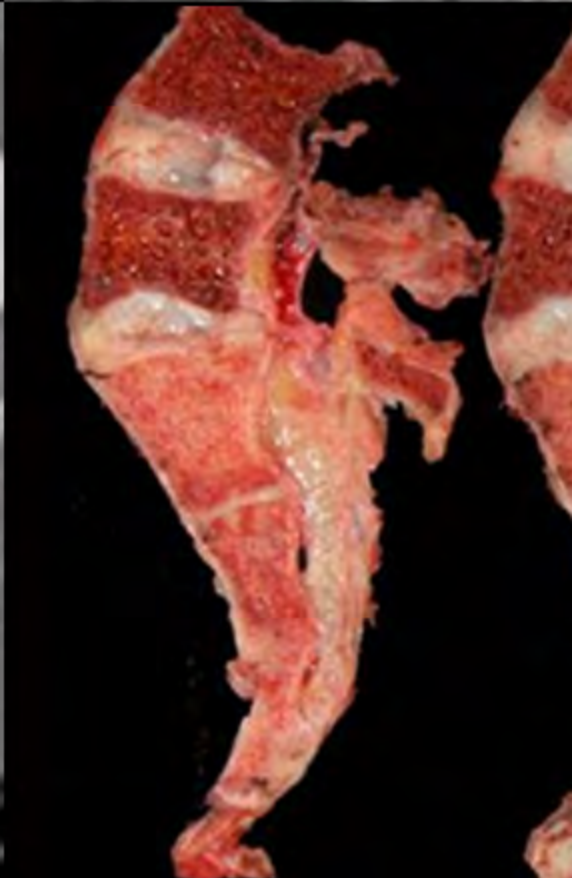
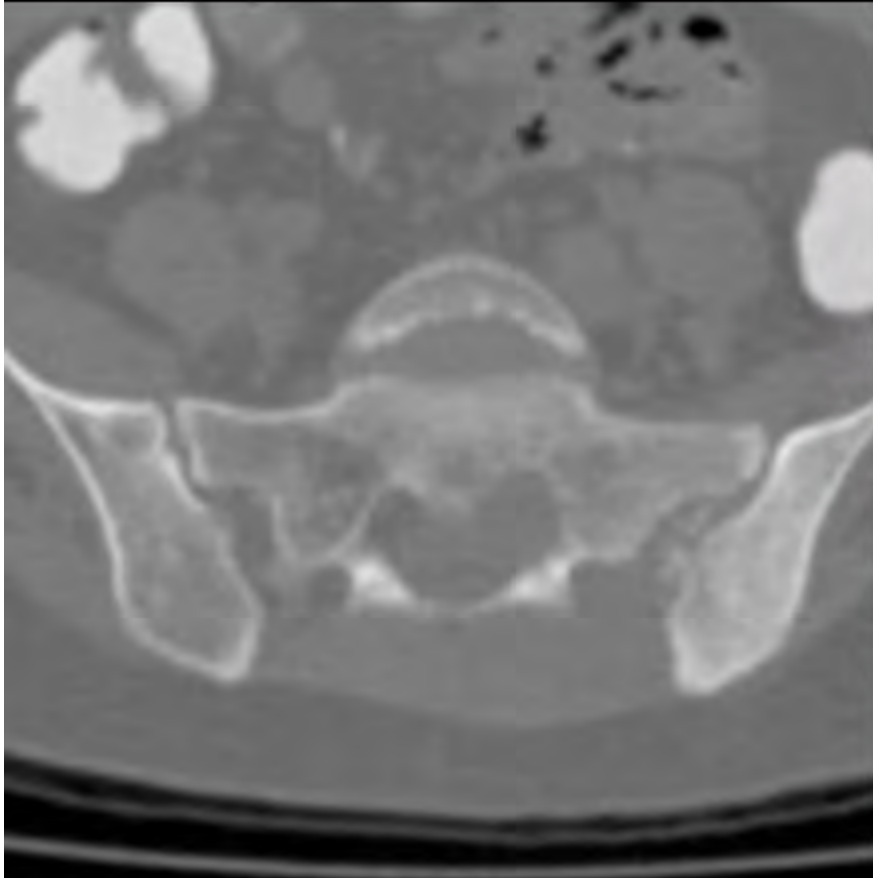
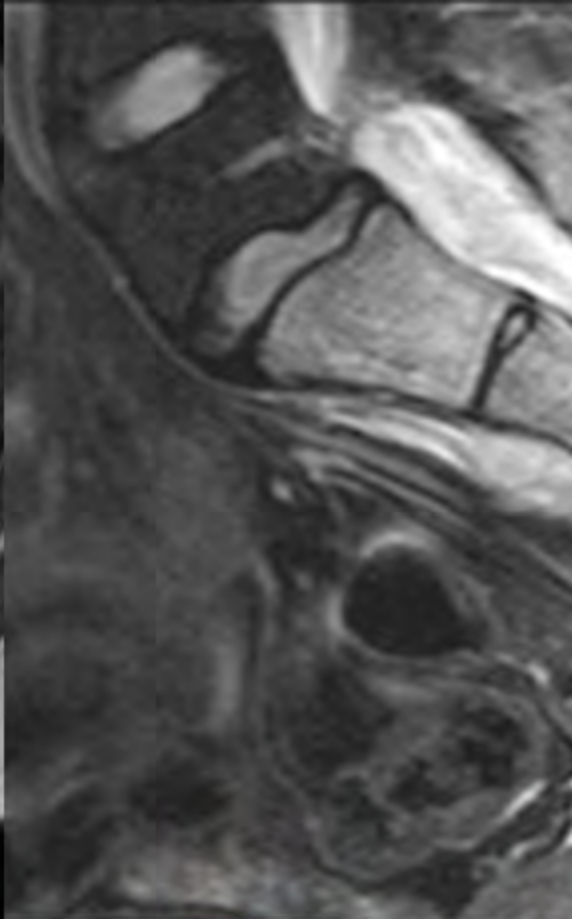
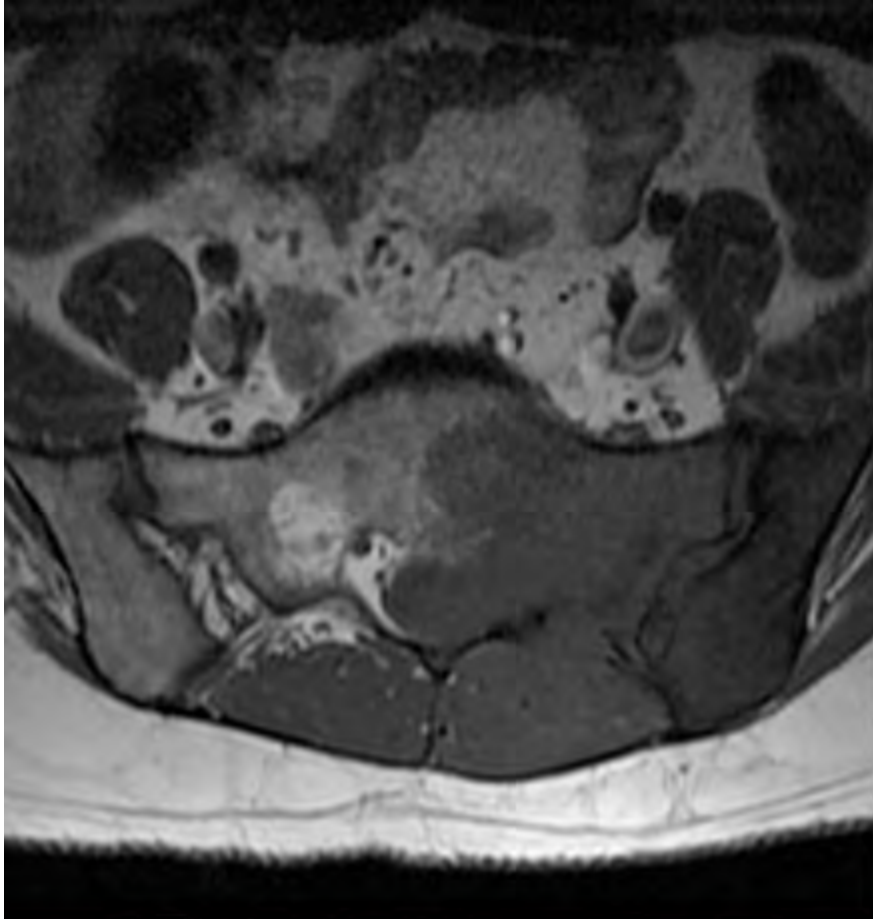
A 22 year-old female with past medical history of acute lymphoblastic leukemia diagnosed at age 4, treated with radiation and autologous bone marrow transplantation, presented with pain and numbness in the left lower extremity. After a failed trial of conservative therapy, an MRI was obtained which demonstrated a large infiltrative sacral mass extending into the epidural space and across the SI joint into the ilium. Biopsy demonstrated a grade III chondroblastic osteosarcoma.

Results

MRI demonstrated a T1 hypointense, T2 hyperintense, infiltrative sacral mass with speckled enhancement pattern which crossed the left sacroiliac joint into the ilium. An associated soft tissue component extended into the parasacral region and epidural space. CT demonstrated a sclerotic nondestructive lesion, with associated chondroid matrix adjacent to the left sacroiliac joint (Figure 1).

Conclusions

The markedly hyperintense T2 signal, avid speckled enhancement pattern, and chondroid matrix of this tumor make its imaging appearance similar to a chondrosarcoma. However, a chondrosarcoma at this patient's age would be atypical. Despite its rarity as a subtype, higher grade osteosarcomas in the pelvis are more likely to be the chondroblastic variant than those in the extremities (Saab et al. 2005), particularly in patients with a history of radiation exposure as a child. The neuroradiologist should be aware of the chondroblastic subtype of osteosarcoma, which should be included in the differential diagnosis of an aggressive-appearing cartilaginous tumor in a younger patient.



(Filename: TCT_E-11_ChondroblasticOsteosarcoma.jpg)

E-12

2:10PM - 2:15PM

A Case of Multiple Intra-spinal Melanocytic Tumours Mimicking Radiological Features of Neurofibromatosis Type II

N Saleem¹, S Currie¹, C Derham², A Chakrabarty²

¹*Leeds General Infirmary, Leeds, West Yorkshire, United Kingdom*, ²*Leeds General Infirmary, Leeds, West Yorkshire*

Purpose

Illustrate the key imaging features of multiple spinal melanocytic tumours of uncertain malignant potential (MelTUMP), so as to allow radiological differentiation from multiple meningiomata and schwannomas.

Materials and Methods

A 37-year old female presented with gradual deteriorating lower limb weakness and bowel and bladder dysfunction. MRI demonstrated multiple intraspinal extramedullary lesions, which were initially considered to represent multiple meningiomata and schwannomas. There was no clinical suspicion of malignant disease and a staging CT of the thorax, abdomen and pelvis was negative for malignancy. There were no clinical parameters to indicate an underlying diagnosis or family history of neurofibromatosis type 2. At the time of surgery for a large compressive lesion at T12, dark brown/ black pigmentation of the spinal dura was observed and histology of the resected lesion was consistent with MelTUMP.

Results

Magnetic resonance imaging demonstrated multiple (six) discrete durally-based extramedullary lesions of varying sizes in the thoracolumbar spine. Some of the lesions occupied the neural exit foramina while others were sited within the spinal canal. The lesions were iso- to slightly hyperintense on T1 and isointense to hypointense on T2 weighted sequences relative to the spinal cord and demonstrated homogenous contrast enhancement. The enhancement pattern was identical to that of meningioma/schwannoma however slight T1 hyperintensity and T2 hypointensity indicated the presence of melanin in the lesions.

Conclusions

Spinal MelTUMPs are rare; to our knowledge only a few cases (< 100) of spinal melanocytomas are reported in the literature; but no case of multiple spinal MelTUMP has been reported to date. Our case demonstrated multiple intra-spinal melanocytomas which mimicked multiple spinal meningiomata on standard structural imaging. This case also highlights that reporting radiologists should consider MelTUMP in the

differential diagnosis of multiple spinal lesions, particularly if these lesions exhibit T1 hyperintensity and T2 hypointensity relative to the spinal cord.

E-13

2:15PM - 2:20PM

A Case of Chronic Lymphocytic Inflammation with Pontine Perivascular Enhancement Responsive to Steroids (CLIPPERS) with Diffuse CNS Involvement

S Lee¹, R Kumar², T Ebbert²

¹*University of Wisconsin School of Medicine and Public Health, Madison, WI,* ²*Gundersen Lutheran Hospital, La Crosse, WI*

Purpose

To present an unusual case of chronic lymphocytic inflammation with pontine perivascular enhancement responsive to steroids (CLIPPERS) with diffuse involvement of the spinal cord, brainstem, cerebellum and supratentorial brain including basal ganglia, periventricular and subcortical white matter.

Materials and Methods

A 74 year-old Caucasian male presented with a two-month history of progressive bilateral lower extremity weakness, gait ataxia, diplopia, dysphagia, dysarthria, urinary incontinence, and mild cognitive impairment. The patient was diagnosed with CLIPPERS based on MRI findings, brain biopsy and response to a trial dose of IV methylprednisolone. He was then started on prednisone oral 60 mg once daily and methotrexate 10 mg once weekly. After discharge, the patient struggled with medication compliance and was re-hospitalized three months later for bilateral lower extremity weakness and gait ataxia.

Results

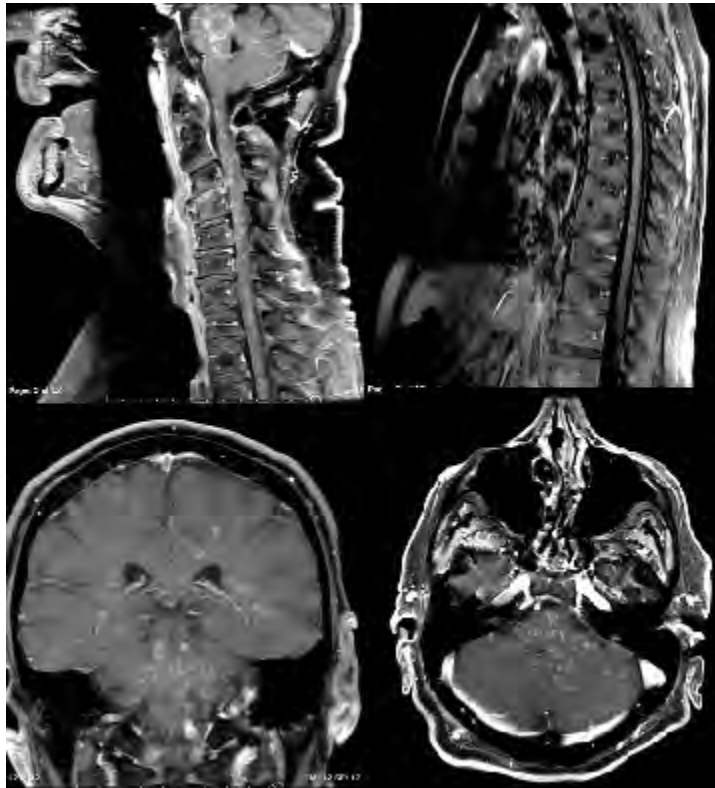
MRI of head, cervical spine, and thoracic spine revealed punctate and curvilinear enhancement with associated high T2 signal diffusely involving the spinal cord, brainstem, basal ganglia and white matter, including cerebellar and supratentorial white matter. The enhancement was most densely concentrated within the pons and cerebellum. The enhancement improved after treatment with IV steroids.

Approximately one month later, repeat MRI showed progression of abnormal enhancement throughout the brain and spine in the setting of medication non-compliance.

Conclusions

CLIPPERS is an inflammatory central nervous system disorder that was first defined in 2010. It is a challenging diagnosis and imaging plays a key role in confirming it. Early recognition of CLIPPERS along with initiation of long-term steroid therapy is important because it results in significant clinical improvement. Therefore, awareness

of this entity by the radiologist is important in expediting diagnosis and treatment. Our case demonstrates MRI findings that are atypical in their extent when compared to other cases described in the literature.



(Filename: TCT_E-13_Clippersimagefile1.jpg)

E-14

2:20PM - 2:25PM

Chemotherapy-Induced Myelopathy after Intrathecal Chemotherapy; Magnetic Resonance Imaging Findings.

N Zakhari¹, C Torres²

¹The Ottawa Hospital, Ottawa , Ontario, ²The Ottawa Hospital, Ottawa, Ontario

Purpose

Intrathecal (IT) chemotherapy is used for prophylaxis and treatment of the central nervous system (CNS) in patients with hematological malignancies. Myelopathy following IT chemotherapy is a rare complication. Differentiation of this condition from neoplastic infiltration of the CNS significantly impacts patients' management given the different treatment strategies for each entity. We describe the distinctive imaging pattern of myelopathy following IT chemotherapy on serial MR examinations.

Materials and Methods

82 year-old man diagnosed with testicular Diffuse Large B-Cell Lymphoma, completed a course of R-CHOP and intrathecal cytarabine with methotrexate chemotherapy in January, 2015. In February 2015, he presented with gradually progressive inability to walk, legs incoordination, urinary retention and bowel incontinence. A lumbar puncture was negative for infectious or lymphomatous involvement and cord/cauda equina compression was excluded on imaging. He was started on corticosteroids and high-dose folinic acid with some improvement of motor function.

Results

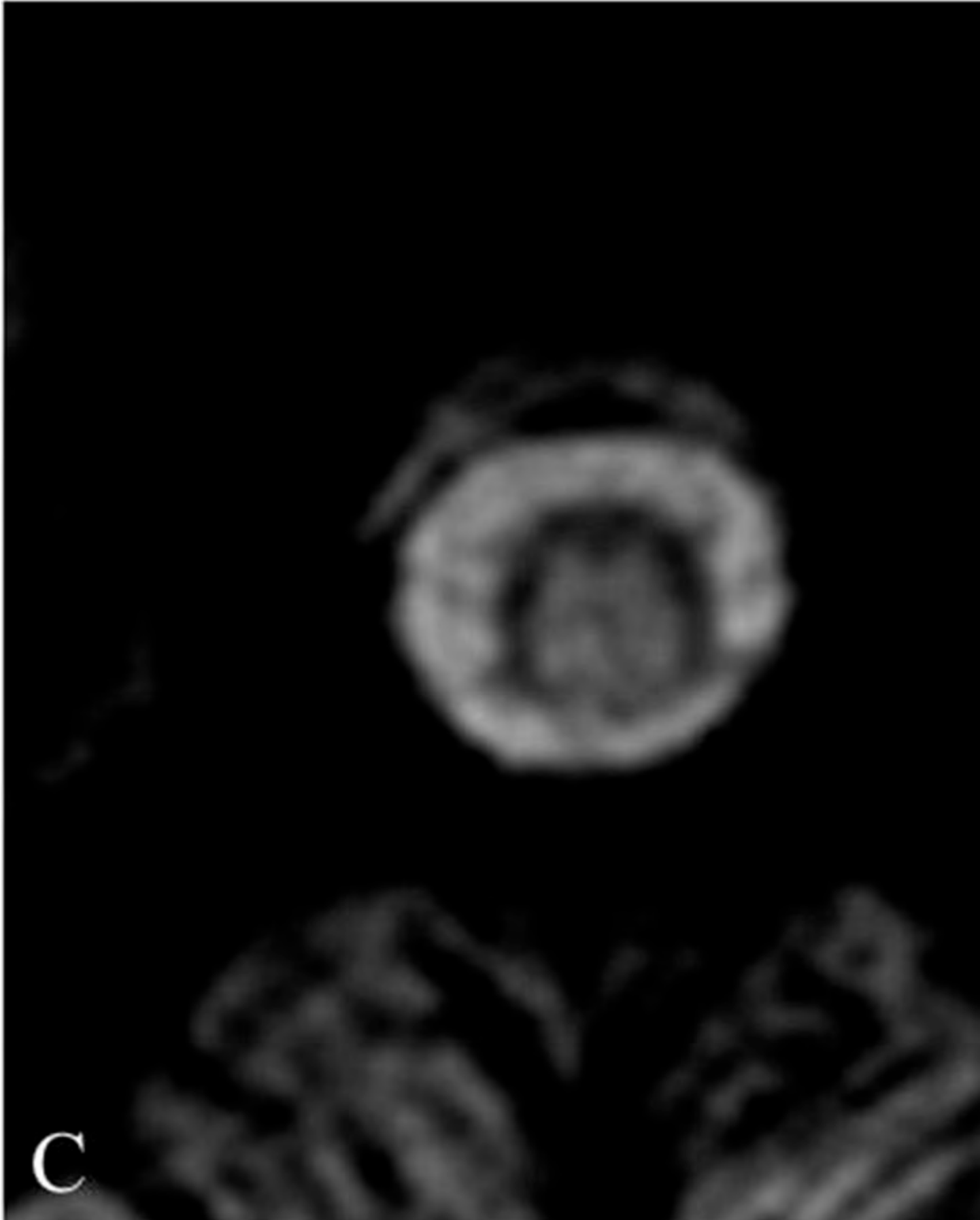
At presentation, two MRIs -three weeks apart- were unremarkable. Abnormalities manifested on MR at 6 weeks (Fig. A) and worsened at 8 weeks (Fig. B-D) despite treatment initiation. Long segment T2 hyperintensity was seen centrally and involving the posterior columns with mild cord expansion (Fig. A-C) and subtle enhancement (Fig. D) extending from the mid thoracic cord at T5-T6 level to the conus.

Conclusions

Chemotherapy-induced myelopathy after IT chemotherapy is a rare complication of unclear underlying pathophysiology that develops over variable time range after exposure to chemotherapy. MRI is the best modality for assessment in this situation with a characteristic involvement of the posterior columns. However, the MRI findings may lag behind the clinical presentation and MRI cannot exclude the diagnosis. Awareness of the typical imaging findings is crucial to avoid misinterpretation as neoplastic infiltration in this clinical context. The findings remain nonspecific and other etiologies of posterior spinal columns signal change needs to be excluded.



(Filename: TCT_E-14_D.jpg)



(Filename: TCT_E-14_C.jpg)



(Filename: TCT_E-14_B.jpg)



(Filename: TCT_E-14_A.jpg)

E-15

2:25PM - 2:30PM

A Case of Hirayama Disease.

R Yu¹, H Kale²

¹University of Pittsburgh Medical Center, Pittsburgh, PA, ²University of Pittsburgh Medical center, Pittsburgh, PA

Purpose

Hirayama disease, also known as juvenile muscular atrophy of the distal upper extremity, is a rare condition mainly in young males between the ages of 15 and 25 years, characterized by progressive asymmetric muscle weakness and atrophy in the upper extremities, followed by spontaneous arrest within several years. We present a case of Hirayama disease and describe the imaging features on both neutral and flexion magnetic resonance images.

Materials and Methods

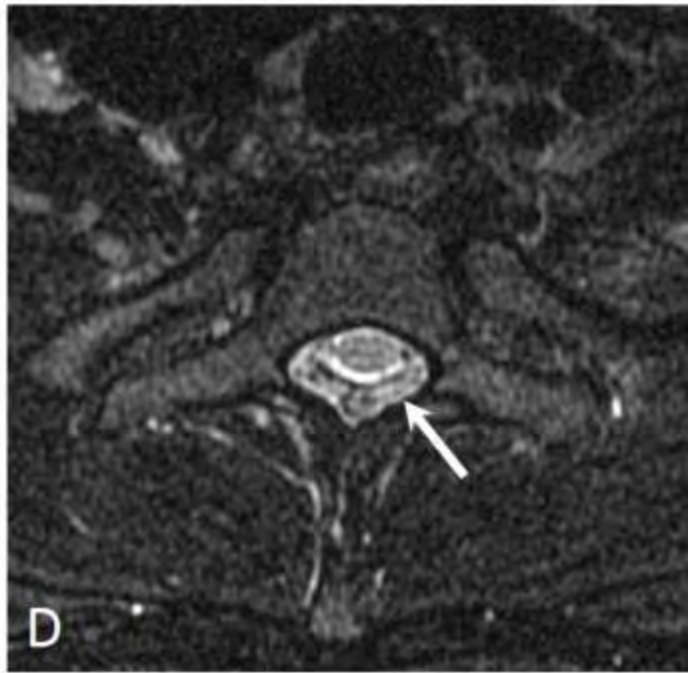
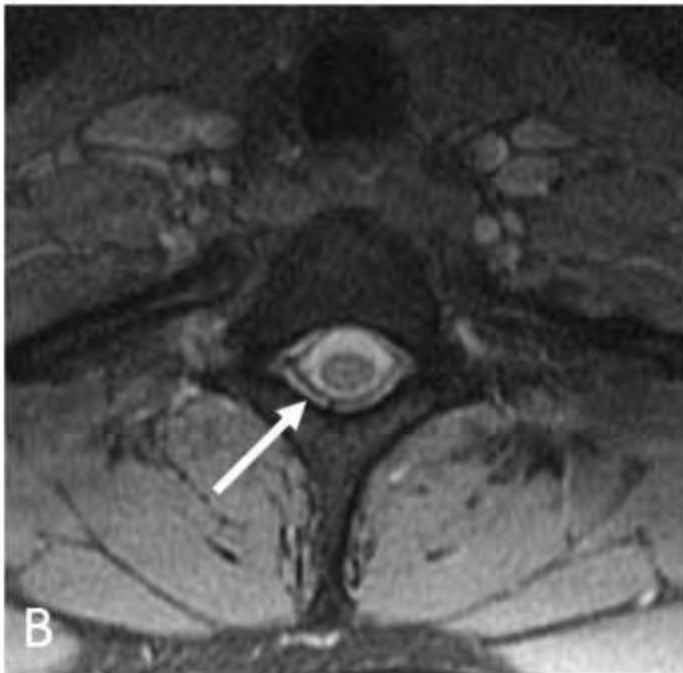
A previously healthy 18-year-old male baseball player presented with a one year history of progressive weakness in his left grip without associated sensory deficit. There was no history of trauma or family history of neurologic disease. The clinical examination revealed atrophy of the left first dorsal interosseous muscle. Fasciculation was not seen. Electromyography showed borderline low normal amplitude of the ulnar nerve and normal amplitude of the median nerve, without conduction abnormalities or sensory impairment. MRI of the cervical spine including neck-flexion images revealed findings compatible with Hirayama disease.

Results

(A) Neutral position sagittal T2-weighted image of the cervical spine show a cervical cord normal in signal and morphology, within a patent central canal. (B) Neutral position axial gradient-echo image at the level of C7-T1 shows loss of attachment of the dorsal dura with the lamina (arrow). (C, D) Sagittal and axial T2-weighted images in flexion shows forward displacement of the dura with associated multiple prominent curvilinear flow voids within the dorsal epidural space (arrows). The neural foramen were patent.

Conclusions

Although Hirayama disease is a self-limiting disease, early diagnosis is needed as early intervention can stop disease progression. The diagnosis of Hirayama disease should be considered in young patients with a clinical history of asymmetric upper extremity weakness and atrophy. Careful attention for suspicious findings on neutral-position MR imaging is necessary, and additional neck-flexion MR imaging should be performed to confirm the diagnosis.



(Filename: TCT_E-15_Figure-Hirayama.jpg)

E-16

2:30PM - 2:35PM

Paralysis in Morquio Syndrome: Catastrophic Consequence of Untreated Cervical Instability

J Dorr¹, M Patel¹, R Pandit¹

¹*Santa Clara Valley Medical Center, San Jose, CA*

Purpose

Morquio Syndrome, also known as Mucopolysaccharidosis (MPS) type IV, is a lysosomal storage disorder due to an enzymatic deficiency with an autosomal recessive inheritance. Although it affects multiple organs, abnormalities of the bones, ligaments, and connective tissue are most prominent. Of particular concern is instability at C1-2 and thoracolumbar kyphosis that predisposes patients to spinal cord compression. In this report, characteristic imaging findings in a young male with MPS IV is presented.

Materials and Methods

A 19 year-old male with a history of MPS IV presented after mechanical fall resulting in lower extremity weakness that was increased from baseline. Plain film, CT, and MR imaging revealed characteristic findings of dysostosis multiplex. Although severe spinal stenosis, cord compression, and likely myelomalacia were also identified, the patient refused surgical decompression. Six months later he again presented after repeat fall, this time resulting in tetraplegia.

Results

Figure 1: Sagittal CT (left) and subsequent sagittal T2-weighted MR (right) images through the cervical spine after the patient's initial fall demonstrating odontoid hypoplasia, platyspondyly, and severe stenosis with cord compression (arrows) at the craniocervical junction with suggestion of increased cord signal. Figure 2: Sagittal T2-weighted MR image through the cervical spine after the second fall, when the patient presented with tetraplegia, demonstrates increased T2 hyperintensity (arrow) in the cord at the level of stenosis, compatible with myelomalacia. Figure 3: Companion sagittal STIR MR image with abnormal signal suggesting ligamentous injury. Figure 4: Frontal chest (top) and abdomen (bottom) plain film images demonstrating characteristic dysostosis multiplex.

Conclusions

MPS IV is an autosomal recessive lysosomal storage disorder with certain characteristic image findings. Some of the spinal abnormalities, including cervical instability, predispose to paralysis as highlighted in this case report. Recognition of

the pattern of imaging findings can assist with guidance of proper management and preventative treatment.



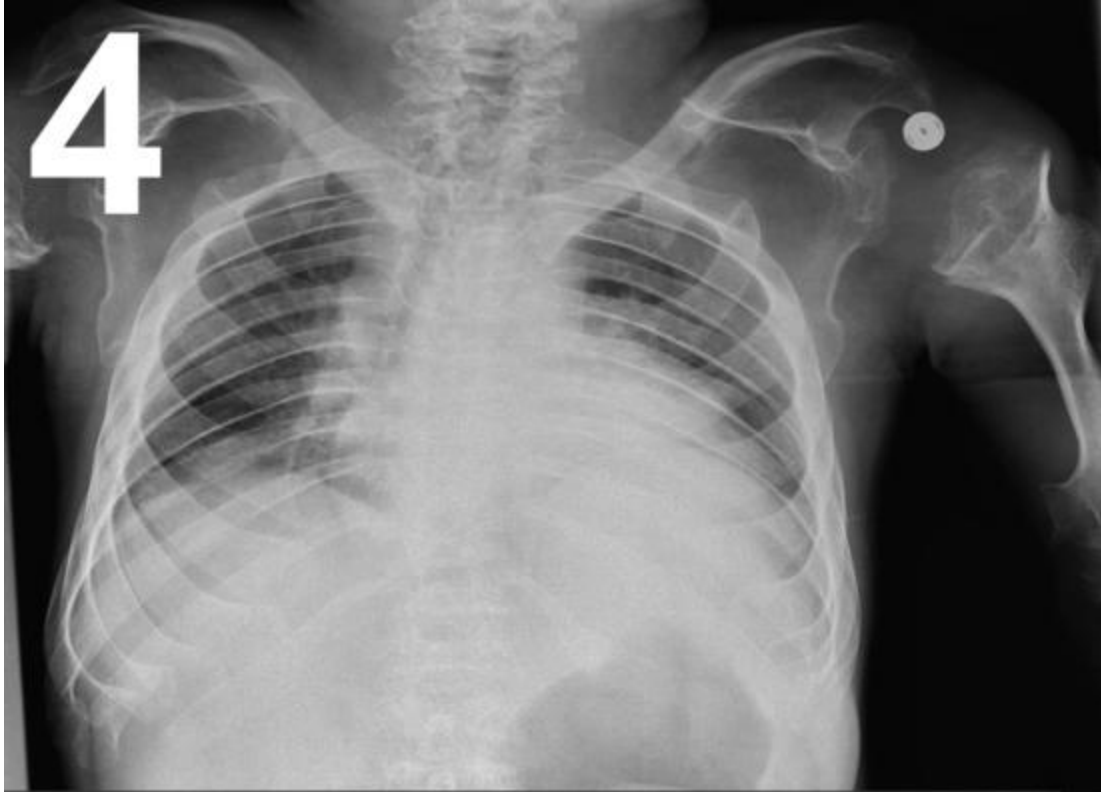
(Filename: TCT_E-16_Fig1.jpg)



(Filename: TCT_E-16_Fig2.jpg)



(Filename: TCT_E-16_Fig3.jpg)



(Filename: TCT_E-16_Fig4.jpg)

E-17

2:35PM - 2:40PM

Non-traumatic Cervical Spinal Subarachnoid Hemorrhage from a Radiculomedullary Artery Pseudoaneurysm

P SHAH¹, M Potts², T Hijaz³, S Ansari², B Liu⁴

¹*Northwestern University Feinberg School of Medicine, CHICAGO,*

IL, ²Northwestern University, Feinberg School of Medicine, Chicago, IL, ³Feinberg School Of Med., Northwestern Univ., Chicago, IL, ⁴Northwestern University Feinberg School of Medicine, Chicago, IL

Purpose

1. Describe a case of non-traumatic subarachnoid hemorrhage in the cervical spine secondary to rupture of a partially thrombosed radiculomedullary artery pseudoaneurysm. 2. Discuss the causes of non-traumatic cervical spinal subarachnoid hemorrhage.

Materials and Methods

A 48-year-old woman with rheumatoid arthritis and two prior episodes of right knee hemarthrosis of undetermined etiology presented with new onset neck pain and right upper extremity weakness. The patient was on prophylactic warfarin anticoagulation with an INR of 1.8 for a recent total left knee arthroplasty. MRI of the cervical spine demonstrated extensive subarachnoid hemorrhage. A focal area of enhancement within the hemorrhage raised concerns for a vascular lesion. Subsequent conventional spinal angiography confirmed the presence of a 2-3 mm fusiform aneurysm involving the C5 radiculomedullary branch of the right vertebral artery associated with a vertebral artery dissection. On a repeat cervical spine MRI performed two days later, the majority of the pseudoaneurysm had thrombosed spontaneously, and the patient was managed conservatively.

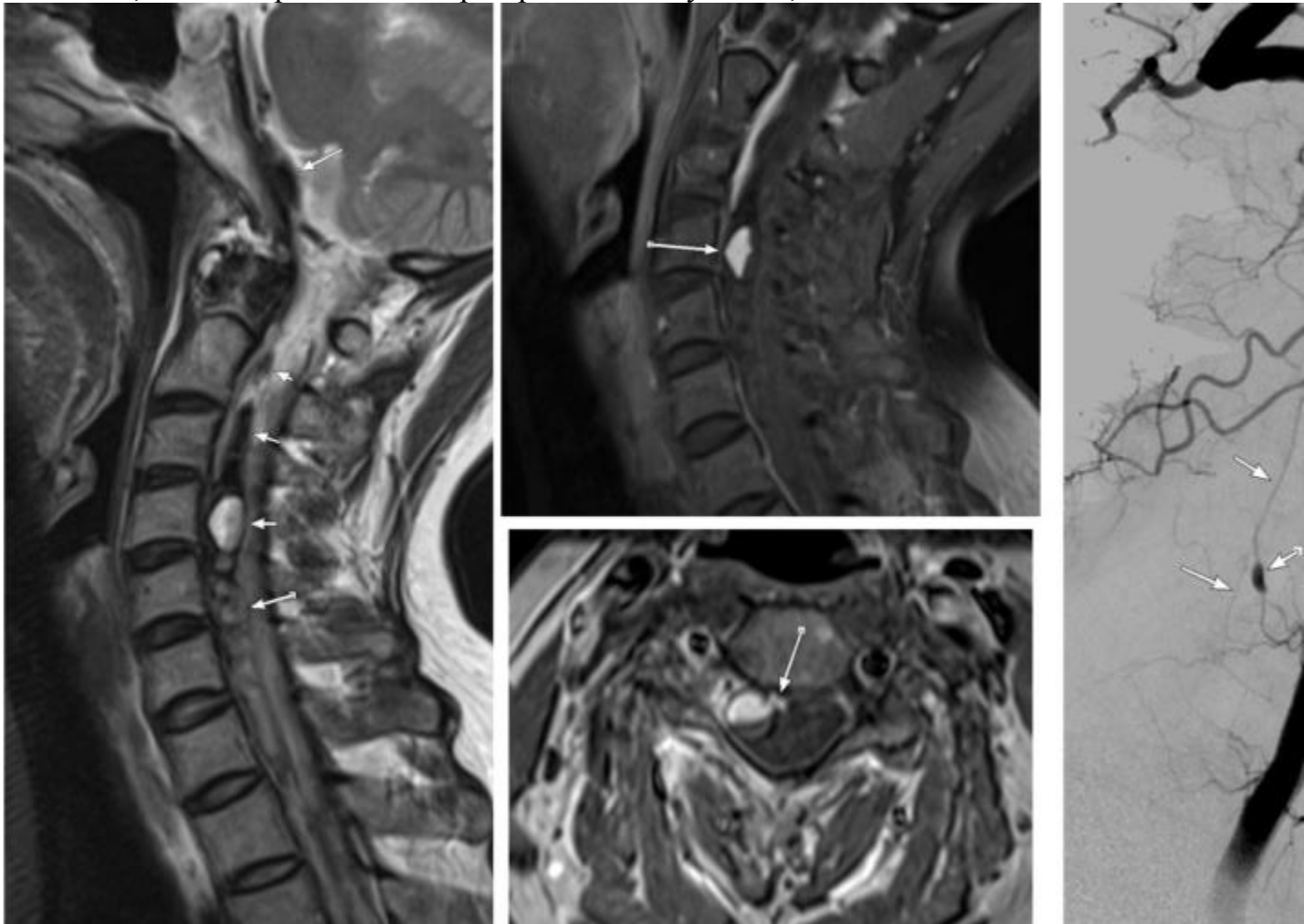
Results

1. Extensive ventral intradural subarachnoid hemorrhage of the cervical spine (Figure 1). 2. Fluid-debris or fluid-fluid level (Figure 1) with the nondependent compartment exhibiting avid contrast enhancement (Figure 2) and an associated linear tail of enhancement (Figure 3) suggestive of vascular etiology. 3. Small fusiform aneurysm of the C5 radiculomedullary artery arising from the right vertebral artery (Figure 4), subsequently supplying the anterior spinal artery.

Conclusions

Non-traumatic cervical spinal subarachnoid hemorrhage secondary to a pseudoaneurysm of a cervical radiculomedullary artery is an exceedingly rare presentation of a rare entity. Auto-thrombosis of the radiculomedullary pseudoaneurysm

is rare. We present MR and conventional spinal angiographic imaging to demonstrate the imaging appearance of this diagnosis and discuss various other causes of non-traumatic cervical spinal subdural hemorrhage, including radiculomedullary artery dissections, cervical spinal dural or pial/perimedullary AVFs, and AVMs.



(Filename: TCT_E-17_finalimagesforradiculomedullaryarterypseudoaneurysmcase report.jpg)

E-18

2:40PM - 2:45PM

Supratentorial Intracerebral Schwannoma: Very Rare Variant Location of an Otherwise Common Tumor

J Chua-Tuan¹, C Li¹, J Chen², S Imbesi¹, D Amaro³

¹University of California, San Diego, San Diego, CA, ²San Diego VA / UCSD Med. Center, La Jolla, CA, ³University of California, San Diego, San Diego, CA, San Diego, CA

Purpose

To describe a rare presentation of supratentorial intracerebral schwannoma: a common tumor found in an unusual location.

Materials and Methods

Patient is a 34-year-old male in his usual state of health who presented after falling while playing basketball and hitting the back of his head, without loss of consciousness. He experienced immediate headache associated with seeing bright lights and blurry vision that resolved in a few minutes, though his headache persisted. The patient was otherwise asymptomatic prior to this episode. Thus, he presented to the emergency room for clinical and imaging workup.

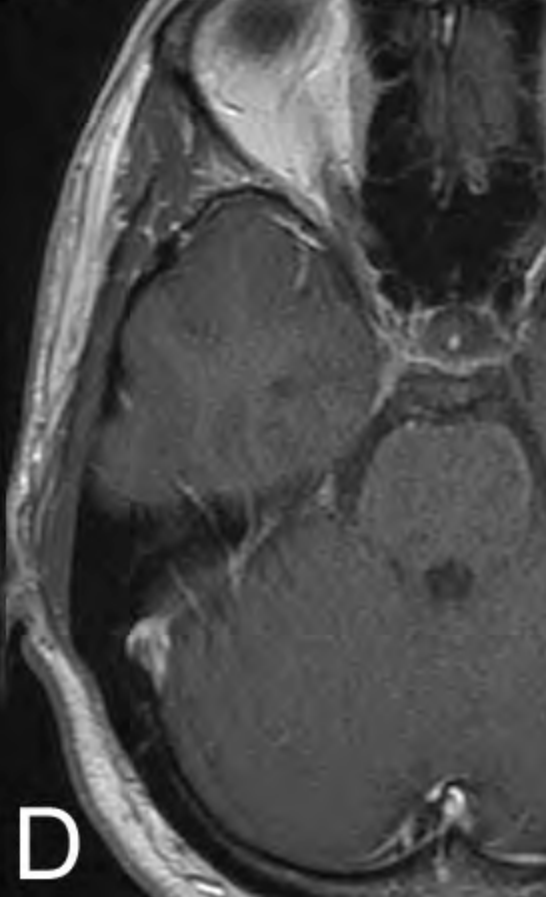
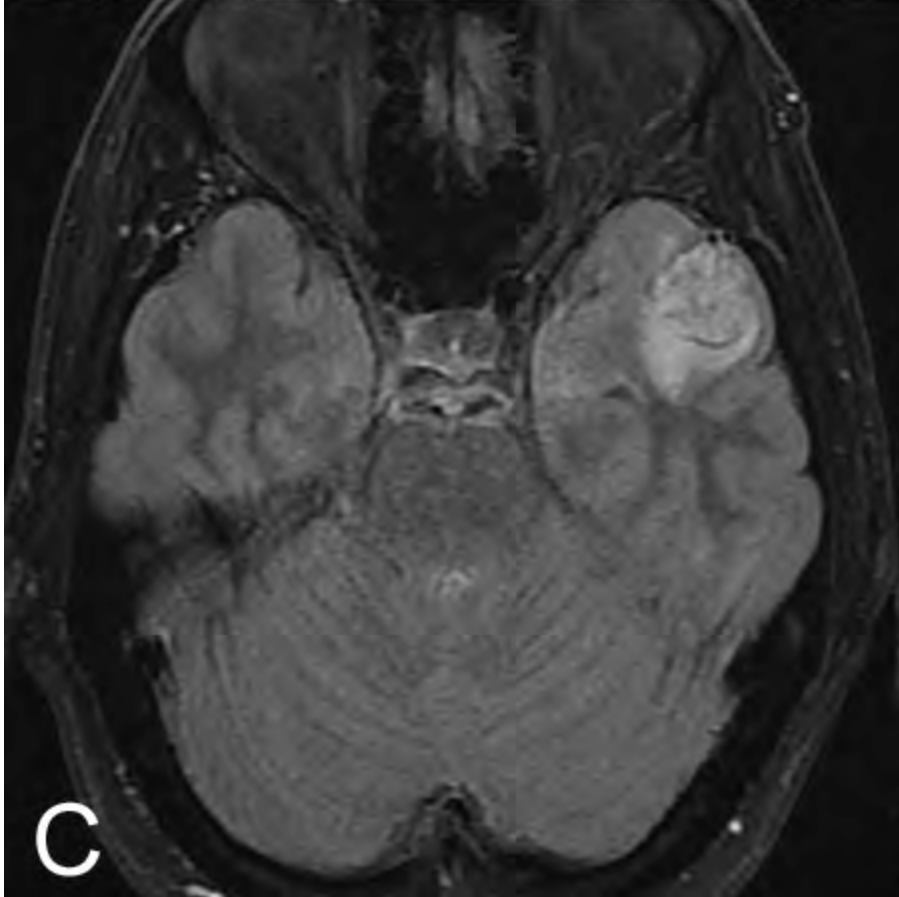
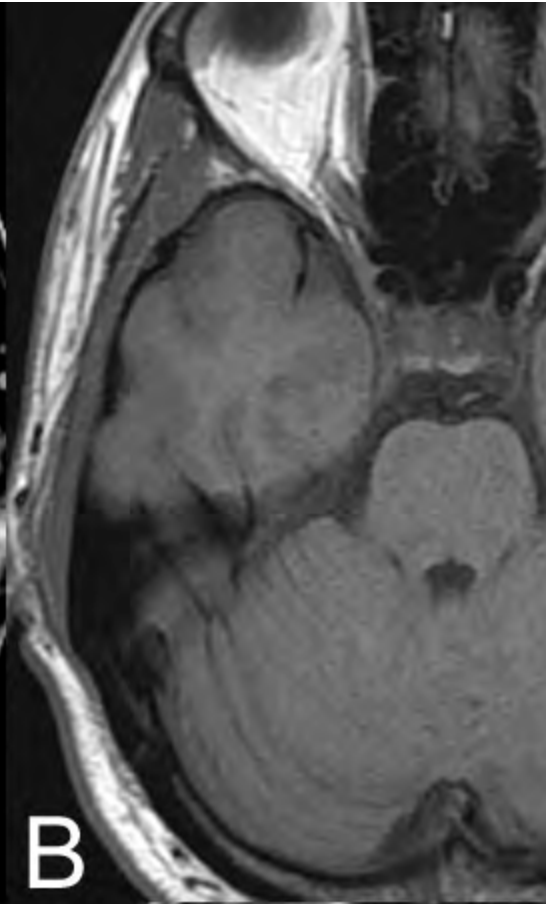
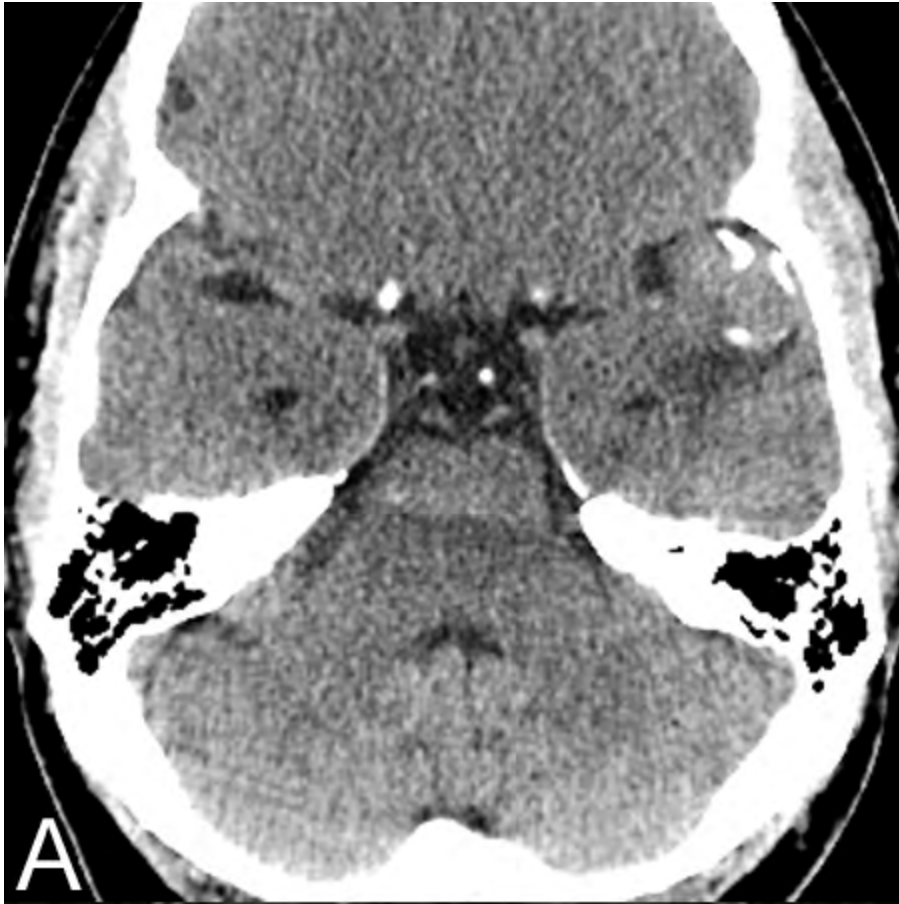
Results

Noncontrast head CT (Figure, A) demonstrated a mass lesion within the anterior pole of the left temporal lobe with rim calcification and mild peritumoral edema.

Subsequent MRI examination (Figure, B-D) demonstrated apparent intra-axial location of the mass with well-defined and mildly lobulated margins and rim of magnetic susceptibility due to calcification. The lesion was slightly low signal intensity on T1-weighted images and high signal intensity on T2/FLAIR. There was also peripheral hyperintensity on T2-weighted images representing peritumoral edema or gliosis. Postcontrast sequences demonstrated homogenous avid enhancement of the mass. Quantitative cerebral blood flow with arterial spin labeling technique was markedly elevated, consistent with neoplasm.

Conclusions

Our case represents a rare presentation of pathologically proven supratentorial intracerebral schwannoma, a benign tumor that is diagnosed predominantly in children and young adults. On surgical and pathological report, the tumor was actually extra-axial in location, either within a perivascular space or deep within a sulcus. The histogenesis of these lesions remains unclear, as Schwann cells are not normally present within the supratentorial brain parenchyma to a significant degree. Multiple theories of their origin have been proposed including presence of Schwann cells within perivascular vasa nervorum within the subarachnoid spaces, displaced neural crest cells forming foci of intraparenchymal Schwann cells, and differentiation of pial cells to Schwann cells. Imaging features are nonspecific, though commonly described characteristics include cyst formation, calcification, and peritumoral edema or gliosis, findings common to many low-grade neoplasms. Though rare, it is important to recognize intracerebral schwannoma in the differential diagnosis of supratentorial benign tumors in young adults, as surgical resection is essentially curative.



(Filename: TCT_E-18_FigureSchwannoma.jpg)

E-19

2:45PM - 2:50PM

Ecchordosis Physaliphora: Imaging Characteristics of a Benign Retroclival Embryologic Notocord Remnant

J Dorr¹, R Pandit¹, M Patel¹

¹*Santa Clara Valley Medical Center, San Jose, CA*

Purpose

Ecchordosis physaliphora (EP) is a benign remnant of notochord cells that is typically discovered as an asymptomatic incidental finding. It is most commonly located in the prepontine cistern, although can be seen anywhere along the craniospinal axis. The lesion typically has a midline intradural component that is connected via stalk or pedicle to the dorsum of the clivus. The purpose of this report is to describe the imaging characteristics of this benign lesion to facilitate differentiation from other retroclival lesions such as chordoma, arachnoid cyst, and dermoid and epidermoid cysts.

Materials and Methods

A 62 year-old female presented for MR imaging to evaluate symptoms of vertigo. A non-enhancing round lesion was noted anterior to the medulla, with imaging characteristics compatible with EP. A pituitary microadenoma was also seen, which permitted subsequent longitudinal monitoring of the EP lesion over four years.

Results

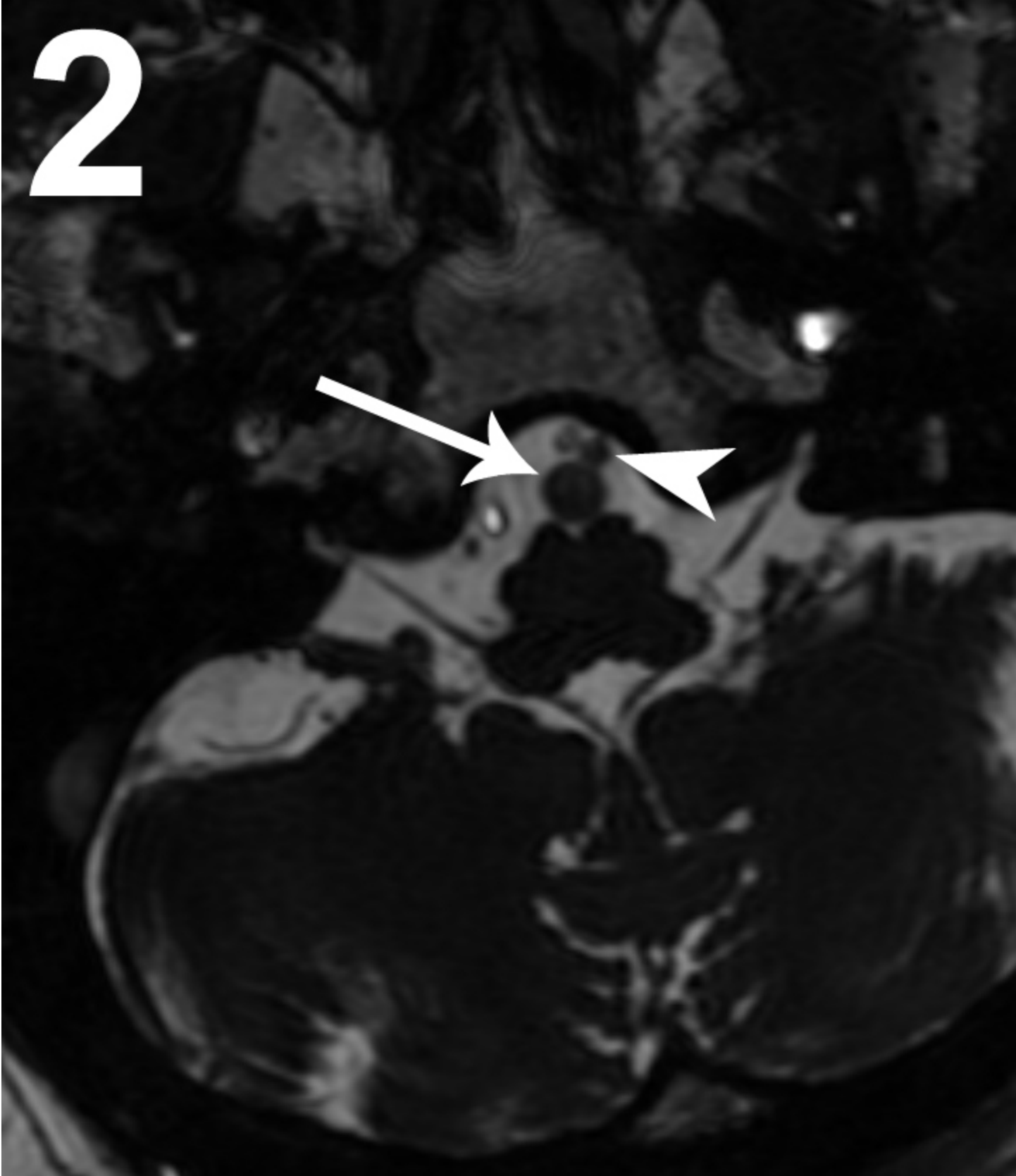
Figure 1: Axial CT (left) and MR FIESTA (right) images at the level of the Dorello canal (arrowheads) demonstrate a well-defined lesion of the dorsal clivus (arrows). Figure 2: Axial MR FIESTA image which shows a tiny stalk (arrowhead) which connects the clival lesion to the round intradural lesion (arrow) anterior to the medulla. Figure 3: Axial T2-weighted FLAIR MR image showing typical T2 hyperintensity of the intradural component of EP (arrow). Figure 4: Sagittal T1 pre-contrast (left) and post-contrast (right) MR images through the brainstem demonstrating lack of enhancement of the pre-medullary lesion (arrows), compatible with EP.

Conclusions

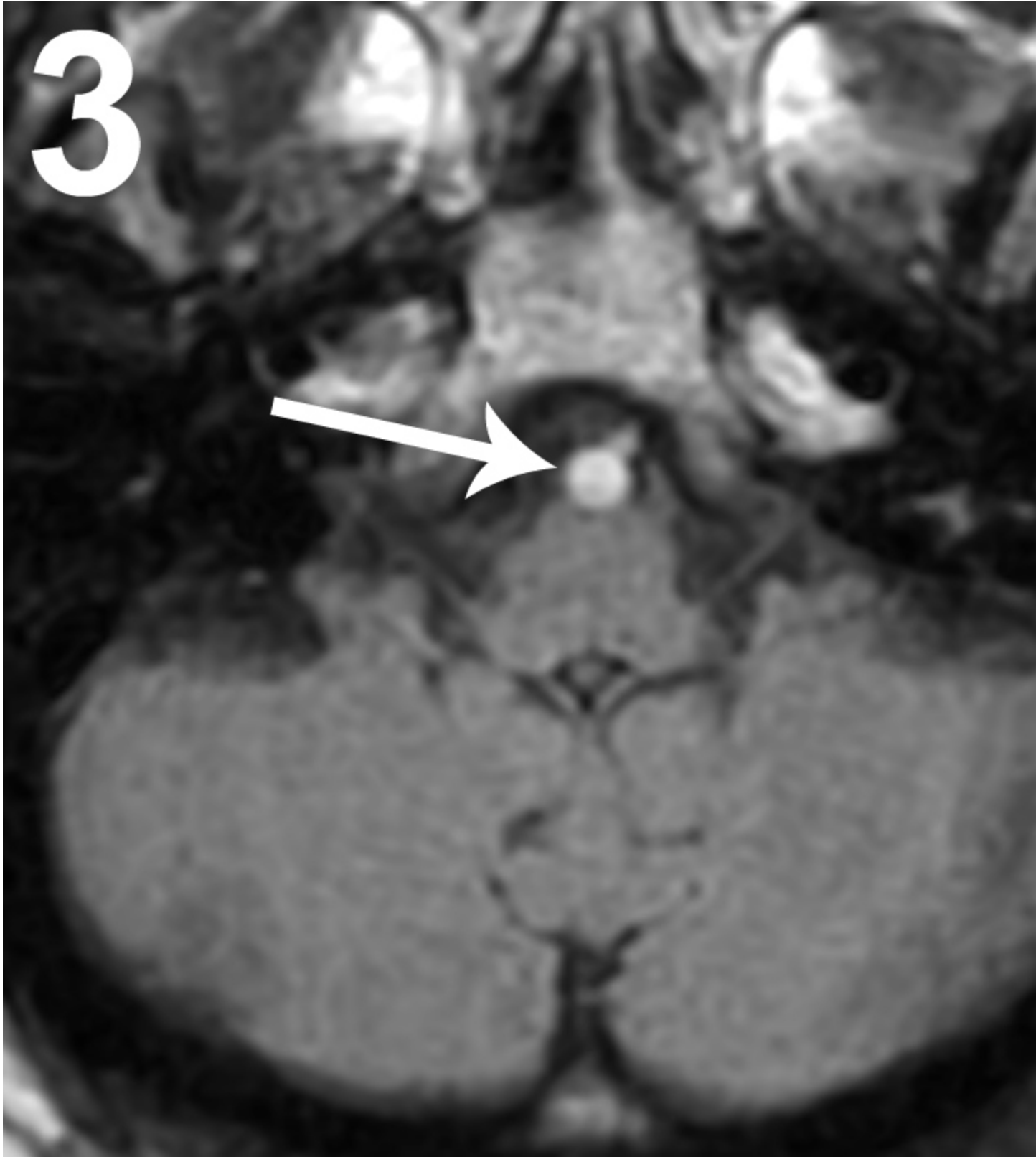
Ecchordosis physaliphora is a benign uncommon retroclival lesion which may be distinguished from other lesions such as chordoma, also of notochordal origin, by location and imaging characteristics. In this report, the differential of retroclival lesions is discussed and specific imaging findings of EP are presented. Balanced steady-state free precession sequences such as FIESTA, can assist with identifying the unique features of EP.



(Filename: TCT_E-19_Fig1.jpg)



(Filename: TCT_E-19_Fig2.jpg)



(Filename: TCT_E-19_Fig3.jpg)



(Filename: TCT_E-19_Fig4.jpg)

Monday

1:15PM - 2:45PM

Washington Marriott Wardman Park, Roosevelt 4

**4F-PARALLEL PAPER SESSION: Interventional Management of CNS Aneurysms
O-93**

1:15PM - 1:23PM

**Distinct Morphological Changes Found in Longitudinal Comparison of Growing
vs. Stable Aneurysms**

A Chien¹, Q Yu¹, V Lau¹

¹*David Geffen School of Medicine at UCLA, Los Angeles, CA*

Purpose

Aneurysm growth is a key factor influencing aneurysm rupture risk. Properly predicting aneurysm growth can have positive contributions to treatment planning and rupture prevention. This study investigates and compares morphological characteristics between growing and nongrowing stable aneurysms.

Materials and Methods

Internal carotid artery (ICA) aneurysm CTA images were segmented using the threshold method to generate 3D models. A total of 37 ICA aneurysm cases: seven ophthalmic aneurysms, six superior hypophyseal aneurysms, and 24 posterior communicating artery (Pcom) aneurysms were analyzed. Each aneurysm case was analyzed using images collected at three distinct time points, with average separation time of 1.2 ± 0.5 year. Aneurysm neck size ranged from 1.8 to 12.1 mm, with an average of 4.6 ± 2.0 mm. Eleven out of 37 total cases were identified as showing growth: two ophthalmic aneurysms, two superior hypophyseal aneurysms and seven Pcom aneurysms. Mean follow-up time after each exam time point for the growing group was 1.3 ± 0.6 year, and 1.2 ± 0.5 year for the stable group. Several morphological parameters such as aneurysm volume, surface area, aspect ratio, and size ratio were investigated. Because a nominally stable aneurysm's shape may change while the maximum dimension remains the same, we studied additional shape indices which describe the irregularity of aneurysm shapes (nonsphericity index, NSI), volume ratio (AVSV), and surface ratio (AASA).

Results

For the group of growing aneurysms, the average rate of increase for aneurysm volume was $31.4 \pm 27.8\%$ per year, and $4.8 \pm 4.2\%$ per year for neck diameter. To assess the consistency of measurements, aneurysm neck size was compared for each case in the stable group and found to not significantly differ between the and last time points ($p = 0.705$). In general, growing aneurysms showed 16.0% and 28.6% increases in aspect ratio and size ratio, respectively, and a 6.5% decrease in NSI over the three time points. Stable aneurysms showed 4.0% and 10.6% increases in NSI and AASA, respectively, over the three time points. The changing rates of AASA versus volume for growing aneurysms and stable aneurysms, on average -0.0011 and 0.038, respectively, are significantly different ($p = 0.0485$).

Conclusions

Results suggest that growing aneurysms have a higher tendency to develop a spherical shape over time.

O-94

1:23PM - 1:31PM

Association of Aneurismal Rupture with the Lunar Cycle

J Banfield¹, J Shankar²

¹Nova Scotia Health Authority, Halifax, Nova Scotia, ²Dalhousie University, Halifax, Nova Scotia

Purpose

Popular conception supposes that the risk of intracranial aneurysm rupture varies across phases of the moon. One study found an increased risk of rupture during new moon (1). Larger studies, however, found no association (2, 3). These studies analyzed the eight qualitative moon phases and none were conducted in North America. The purpose of this study was to review cases from our Canadian institution to assess any association between aneurysm rupture and the lunar cycle.

Materials and Methods

We retrospectively reviewed all cases of subarachnoid hemorrhage secondary to ruptured aneurysm treated with endovascular coiling in our institution from October 2005 to October 2015. We included only cases with a known rupture date. We used degree of illumination of the moon to quantitatively code the lunar cycle. We grouped together patients whose aneurysms ruptured when the moon was illuminated by: 1) .0-.20, 2) .21-.40, 3) .41-.60, 4) .61-.80, and 5) .81-1.0. We used 0.41-0.60 as baseline. Odds of aneurysmal rupture in other periods were calculated using likelihood ratio and Wald test. 95% confidence interval and p values were calculated.

Results

A total of 213 cases were included in our analyses. Results are presented in the table below.

Conclusions

Odds of aneurysm rupture were greater when the moon was least (new moon) and most (full moon) illuminated, compared to the middle of the lunar cycle. However, we did not include ruptured aneurysms that were not treated with endovascular coiling, which may not be distributed equally across the lunar cycle. Regardless, our findings could help optimize hospital staffing decisions.

| Amount of illumination | n | Odds of rupture (95% CI) | p |
|-------------------------------|----------|---------------------------------|----------|
| .00-.20 | 58 | 2.76 (1.69-4.45) | <.001 |
| .21-.40 | 33 | 2.05 (1.21-3.48) | <.001 |
| .41-.60 | 22 | | |
| .61-.80 | 27 | 1.24 (0.70-2.19) | 0.35 |
| .81-1.0 | 73 | 3.48 (2.13-5.67) | <0.001 |

(Filename: TCT_O-94_table.jpg)

Canadian Registry of LVIS Jr for Treatment of Intracranial Aneurysms (CaRLA)

J Shankar¹, D Iancu², A Quateen³, S Patro², R Fahed⁴, Z Kaderali⁵, M Cortes⁶, D Tampieri⁷, C Lum², A Weill⁸

¹Dalhousie University, Halifax, Nova Scotia, ²The Ottawa Hospital, Ottawa, Ontario, ³Dalhousie University, Halifax, Halifax, Nova Scotia, ⁴CHUM, Montreal, AR, ⁵Health Sciences Centre Winnipeg, Winnipeg, Manitoba, ⁶McGill University, montreal, Quebec, ⁷Radiology Department, Montreal Neurological Institute, McGill University, Montreal, Quebec, ⁸CHUM Montreal QC, Montreal, QC

Purpose

Stents confer a statistically significant decrease in the rate of angiographic recurrence. The newest stent for intracranial use is Low Profile Visible Intraluminal Support Device (LVIS Jr). The purpose of this study was to assess the efficacy of the new stent in a multicenter retrospective registry.

Materials and Methods

Centers across Canada utilizing LVIS Jr were contacted to participate in a retrospective registry of patients treated with LVIS Jr for intracranial aneurysms between January 2013 and July 2015.

Results

A total of 89 patients (65 females; Age-56.43 ± 10.66 years) were treated with LVIS Jr stent in five centers in Canada. Mean maximum diameter of dome and neck of the aneurysm and dome to neck ratios were 7.08±4.03 mm, 4.24±1.78 mm and 1.72±0.79 respectively. The stent was used as a bail out situation in 22 (25%) cases. A "Y" stent construction was used in 10 (11.5%) cases. Angiographic complications were noted in 22 (26%) patients but clinical complications were noted only in 10 (16%) patients. On follow up, the mortality and morbidity were 2.6% and 9.2%. Angiographic and clinical complications were higher in patients with ruptured aneurysm (odds ratio- 5.98 and 3.06) and when LVIS Jr was used as a bail out scenario (odds ratio- 3.34 and 2.87). Clinical complications were higher when a dyna CT was not used to confirm the opening of the stent (odds ratio- 3.23). Class 1, 2 and 3 results were respectively seen in 50.57%, 36.78% and 12.64% immediately after coiling and 57.97%, 26.09% and 15.94% on the last follow up.

Conclusions

The LVIS Jr stent is a promising device for stent-assisted coiling but continues to be technically challenging. Higher complications were associated with use in ruptured aneurysm; in bailout situation and when opening was not confirmed with dynaCT.

Initial experience with a low profile-microcatheter and small flow diverter device, Fred Jr.

J CHUDYK¹, C Bleise², E Scrivano³, R Ceratto², J Chudyk⁴, P Lylyk⁵

¹*Instituto Médico ENERI - Clínica Sagrada Familia, BUENOS AIRES, Buenos Aires,* ²*Instituto Médico ENERI - Clínica Sagrada Familia, Buenos Aires, CABA,* ³*Instituto Médico ENERI - Clínica Sagrada Familia, Buenos AIRES, Buenos Aires,* ⁴*Instituto Médico ENERI - Clínica Sagrada Familia, Buenos Aires, Buenos Aires,* ⁵*Clinica ENERI, Buenos Aires, Buenos Aires*

Purpose

Flow diversion is a well-recognized technique for the treatment of wide neck and complex proximal aneurysms, especially for large and giant aneurysms. Recently, the indications have been expanded to include distal and small aneurysms. Most flow diverted devices use large microcatheters, which can make treatment difficult in small arteries. Fred Jr. represents the first flow diverter (FD) available for smaller microcatheters, specifically the headway 21. We report our initial experience using Fred Jr for the treatment of aneurysms and dissections in small arteries.

Materials and Methods

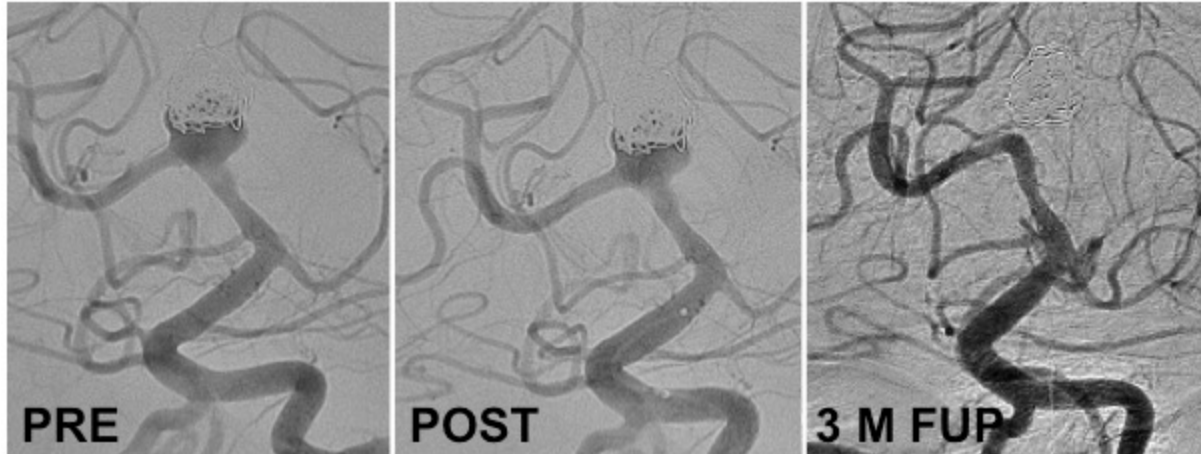
Since June 2015 to October 2015, four patients with three aneurysms and one symptomatic ICA dissection were treated with Fred Jr. Two aneurysms were previously treated with coils. Two aneurysms were small in size. Clinical and angiographic follow up was performed at 24 hours and 3 months after treatment.

Results

All patients were treated successfully with Fred Jr. One device was required for each aneurysm. For the ICA dissection, three devices were used because of the extension of the lesion. All patients were treated with dual antiplatelet drugs. No ischemic or hemorrhagic complications were observed during treatment or the follow up stage. Occlusion rate at 3 months was 66%. Morbidity and mortality rate was 0%.

Conclusions

In this small series of patients, Fred Jr. showed promising results. It seems to be a reasonable strategy for lesions located in small arteries. More cases and longer follow up are needed to prove its safety and efficacy.



(Filename: TCT_O-97_fredjrasnr.jpg)

O-98

1:55PM - 2:03PM

Computation of the Change in Length of a Flow Diverter when Deployed in Realistic Vessel Models

J Blasco Andaluz¹, L San Roman², H Fernández³, R Kale⁴, I Larrabide⁵, L Serra⁶, N Macias², O Chirife⁷, F Zarco⁸, W Mailaender⁹, J Macho²

¹*Interventional Neuroradiology, BARCELONA, -- SELECT --*, ²*Hospital Clinic of Barcelona, Barcelona, Barcelona*, ³*Galgo Medical, barcelona, barcelona*, ⁴*Galgo Medical, Barcelona, Barcelona*, ⁵*Galgo Medical / Pladema-CONICET, barcelona, barcelona*, ⁶*Galgo Medical, barcelona, Barcelona*, ⁷*hospital Clinic of Barcelona, Barcelona, Barcelona*, ⁸*Hospital Clinic of Barcelona, Barcelona, barcelona*, ⁹*Acandis GmbH, Pforzheim, Mannheim*

Purpose

The Derivo® Embolization Device (Acandis GmbH) is a nitinol-based braided flow diverter (FD) which allows intracranial aneurysm treatment by redirecting the flow and subsequent thrombosis of the aneurysm sac. Based on two individual cases in which a 3D silicon model was created based on the 3DRA images acquired some weeks before the treatment, we analyzed the behavior of the FD in terms of final length and positioning of: 1) a virtually deployed FD, 2) the FD deployed inside the silicon model and 3) the FD position after the real procedure. The main purpose of the study was to evaluate the accuracy prediction of the virtual deployment of the FD and the one on the silicon model.

Materials and Methods

Three dimensional RA images of aneurysmatic patients were segmented and virtual deployment of a FD was performed with the Fast Virtual Endovascular Treatment (FVET®) software. Landing zone and final length of the real deployment of the

device after the procedure were compared with virtual deployment and with the 3DRA images acquired after the deployment of the same device in a 3D silicon model from a 3D printer, in order to evaluate the accuracy prediction of both methods.

Results

The length of the simulated stent was accurately consistent with the deployed stent during the patient intervention, being the accuracy prediction of the software about 97% on average in the two cases analyzed. In the first case, Derivo1(P2), A higher distance was observed between the length of the FD deployed in the patient and the length of the stent deployed in the silicon model: being the FD inside the silicon model about 6 millimeters longer. The diameter of the silicon model was 400 micrometers lower than the vessel diameter of the patient, thus exhibiting a larger FD length. On the other hand, in the second model, both vessel geometries presented a similar diameter; therefore, the FD lengths were almost equal between them. Despite the fact that silicon models are printed from 3DRA images of patient anatomy, these models could present deviations in the vessel diameter, which may affect the FD deployment. In the cases studied, a difference of 400 microns in vessel diameter led to 6 millimeters difference in the final stent length. The computational method seems to overcome this limitation as long the vessel geometry is accurately extracted from the 3DRA images, leading to a better estimation of the FD length and therefore final positioning.

Conclusions

Silicon models provide a realistic environment for the planning and training of FD intervention, which faces the interventionist with the actual difficulties (geometry, navigation, etc.) to be found in the patient. Nevertheless, an accurate prediction of the final FD position can be hampered by the accuracy of the reconstructed vessel geometry (modeling, fabrication and 3D printing). Alternatively, the algorithm of FD deployment software has a time cost in the order of few seconds and showed an accuracy of 97%, which makes it a promising technique for the support of clinical decisions in real time.

O-99

2:03PM - 2:11PM

Intra-Operative Rupture with Balloon-Assisted Coiling is Associated with a High Rate of Good Clinical Outcome

Y Kayan¹, J Delgado Almandoz¹, J Fease¹, J Scholz¹, A Milner¹, M Mulder¹

¹*Abbott Northwestern Hospital, Minneapolis, MN*

Purpose

Intra-operative rupture of an intracranial aneurysm during coil embolization is a potentially devastating event. Historically, large series of intracranial aneurysm

embolizations have reported poor outcomes after intra-operative rupture. We hypothesize that intra-operative rupture in the setting of balloon-assisted coiling (BAC) is not associated with poor outcomes.

Materials and Methods

A retrospective review of our prospectively acquired database of endovascular intracranial aneurysm treatments was completed for embolizations performed between December 20, 2007 and December 9, 2015. The pre-operative rupture status, treatment modality, presence of intra-operative aneurysm rupture, discharge disposition and 6-month follow up modified Rankin Scale (mRS) were recorded. Clinical outcomes of intra-operative aneurysm rupture were compared between BAC and non-BAC coil embolization procedures using Fisher's exact test with $p < 0.05$ accepted as statistically significant.

Results

A total of 36 intra-operative ruptures occurred among 962 coil embolizations (3.7%). Of these, 34 were aneurysm ruptures (3.1%) and two were vessel ruptures. Among the 669 BAC's (70% of treatments), there were 26 aneurysm ruptures (3.9%), 14 in the setting of subarachnoid hemorrhage (SAH) and 12 in non-SAH patients. Among the 293 non-BAC coil embolizations (30% of treatments), there were eight aneurysm ruptures (2.7%), two in the setting of SAH and six in non-SAH patients. Clinical outcomes of BAC and non-BAC procedures are compared in the Table. Among non-SAH patients, there was a 37% increased rate of good clinical outcome after intra-operative aneurysm rupture with BAC compared to non-BAC, though this did not achieve statistical significance ($p = 0.245$).

Conclusions

While intra-operative rupture of intracranial aneurysms during endovascular treatment has the potential to be a devastating event, control of bleeding with balloon tamponade, regardless of pre-operative rupture status, is effective at maximizing the rate of a good clinical outcome.

Table. Comparison of clinical outcomes of intra-operative aneurysm occlusion during coil embolization with and without balloon-assistance

| | BAC (n = 669) | Non-BAC (n = 293) |
|--|--------------------------|------------------------------|
| Intra-operative aneurysm ruptures | 26 (3.9%) | 8 (2.7%) |
| SAH patients | 14 | 2 |
| Discharge disposition | | |
| • Death | 2 | 0 |
| • Skilled nursing facility | 1 | 0 |
| • Rehabilitation center | 2 | 1 |
| • Home | 9 | 1 |
| 6-month mRS 0, 1 or 2 | 10 (71%) | 2 (100%) |
| Non-SAH patients | 12 | 6 |
| Discharge disposition | | |
| • Death | 1 | 1 |
| • Skilled nursing facility | 0 | 0 |
| • Rehabilitation center | 2 | 1 |
| • Home | 9 | 4 |
| 6-month mRS 0 or 1 | 11 (92%) | 4 (67%) |

(Filename: TCT_O-99_intra-oprupturetable.jpg)

O-100

2:11PM - 2:19PM

Patient Outcomes, Aneurysm Occlusion, and Cerebral Infarction Following Endovascular Treatment of Dissecting Vertebral Artery Aneurysms

J Heit¹, R Dodd¹, H Do¹, G Steinberg¹, S Chang¹, M Marks¹

¹Stanford University, Stanford, CA

Purpose

Subarachnoid hemorrhage (SAH) secondary to rupture of an intradural dissecting vertebral artery aneurysm (DVAA) results in significant morbidity and mortality. Prior studies have suggested favorable outcomes following endovascular treatment of ruptured DVAA most commonly by parent vessel occlusion or stent-assisted coil embolization, but postprocedural cerebral infarction related to endovascular treatment is less well characterized. We determined patient outcomes and cerebral infarction following endovascular treatment of ruptured DVAA.

Materials and Methods

We retrospectively reviewed all consecutively patients presenting to our neurovascular referral center over a 10-year period with with SAH due to a ruptured DVAA. Patient demographic, treatment, and outcome data were determined from the medical record. Digital subtraction angiography (DSA), CT, and MRI studies were reviewed for DVAA characteristics and cerebral infarction. Statistical analysis was performed using XLSTAT; p-value of 0.05 was considered significant.

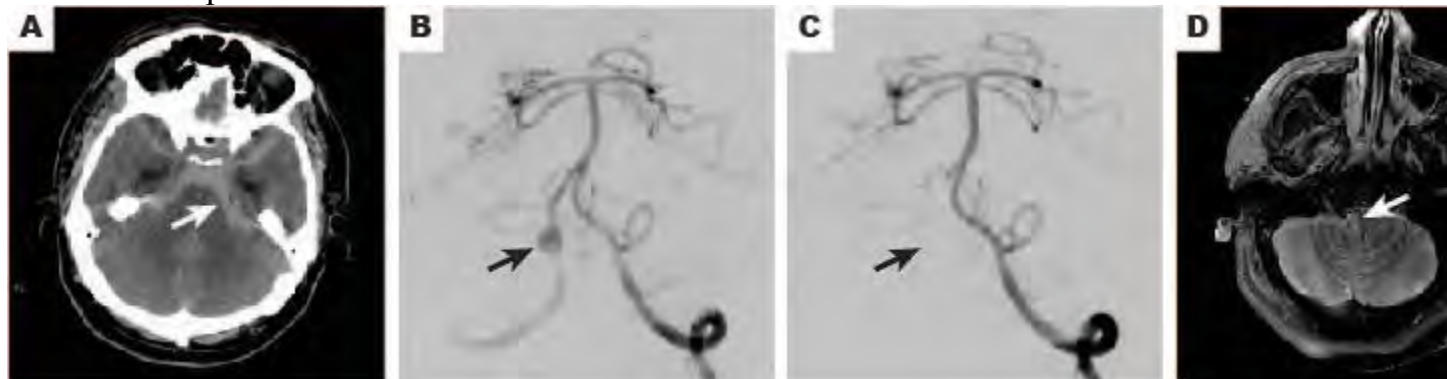
Results

Ruptured DVAA were identified in 30 patients (11 males and 19 females; p=0.3) with an average age of 56 years (range 35-86 years). Dissecting vertebral artery aneurysm affected the right vertebral artery in 20 patients (67%; p=0.2), the nondominant vertebral artery in 18 patients (60%; p=0.4). Parent vessel occlusion was performed in 25 patients, stent-assisted coiling in four patients, and flow diversion in one patient. Aneurysm occlusion was achieved in 27 patients (90%). Symptomatic vasospasm requiring endovascular treatment occurred in 12 patients (35%). Cerebral infarction occurred in nine patients (30%) following endovascular treatment, which were secondary to vasospasm in five patients (56%), parent vessel occlusion in two patients (22%), and a combination of vasospasm and parent vessel occlusion in two patients (22%). No other complications were identified. Eight patients (27%) had a good clinical outcome (mRS 2) at discharge, which increased to 18 patients (60%) at 3-months of follow up. Five patients (17%) died as a result of their ruptured DVAA. Presenting Hunt and Hess scale greater than 3 (p=0.003) was associated with a poor clinical outcome (mRS >2 or death). Patient sex, age, hypertension, hyperlipidemia, diabetes, coronary artery disease, smoking, illicit drug use, alcohol abuse, a family history of aneurysms, presenting Fisher grade, and the development of vasospasm requiring endovascular treatment did not correlate with clinical outcome.

Conclusions

Endovascular DVVA treatment results in a high rate of aneurysm occlusion and good clinical outcome in a majority of patients. The rate of cerebral infarction related to

endovascular parent vessel occlusion is high. Further studies are warranted to determine if ruptured DVVA treatment by flow diversion results in acceptable rates of aneurysm occlusion and lower rates of post-treatment cerebral infarction compared to endovascular parent vessel occlusion.



(Filename: TCT_O-100_ASNRVerAneurFigure.jpg)

O-101

2:19PM - 2:27PM

Real-time Fluoroscopic Evaluation of Ommaya Reservoir Integrity

J Heit¹, M Hayden¹, L Shuer¹, A Moraff¹

¹Stanford University, Stanford, CA

Purpose

Ommaya reservoirs are surgically implanted catheter systems that allow for repeated access to the cerebrospinal fluid (CSF) and intrathecal chemotherapy administration. Ommaya reservoirs may develop blockage or leakage due to damage of the reservoir or catheter components, which may result in nontarget delivery of chemotherapy or the development of an extra-axial fluid collection. Surgical replacement of the Ommaya may be required in the setting of Ommaya reservoir compromise, and there is an increased risk of infection and bleeding complications in this patient population that frequently is neutropenic and thrombocytopenic. Neuroimaging of Ommaya reservoir integrity is challenging given the need for high temporal and spatial resolution when interrogating the system. Computed tomography (CT) or magnetic resonance imaging (MRI) may determine the location of the Ommaya catheter tip and identify extra-axial collections following placement. However, these techniques do not evaluate the dynamic flow of fluid through the Ommaya reservoir, which limits its ability to detect tubing blockage or the site of leakage. Radioisotopes may be introduced through the Ommaya to assess for CSF flow blockage or Ommaya leakage, but this technique has poor spatial and temporal resolution. To prevent unnecessary Ommaya replacement when compromise of the reservoir or tubing is incorrectly suspected, better minimally invasive dynamic diagnostic testing of

Ommaya system integrity is needed. We describe real-time fluoroscopic interrogation of Ommaya reservoir integrity in a patient with a symptomatic enlarging extra-axial collection.

Materials and Methods

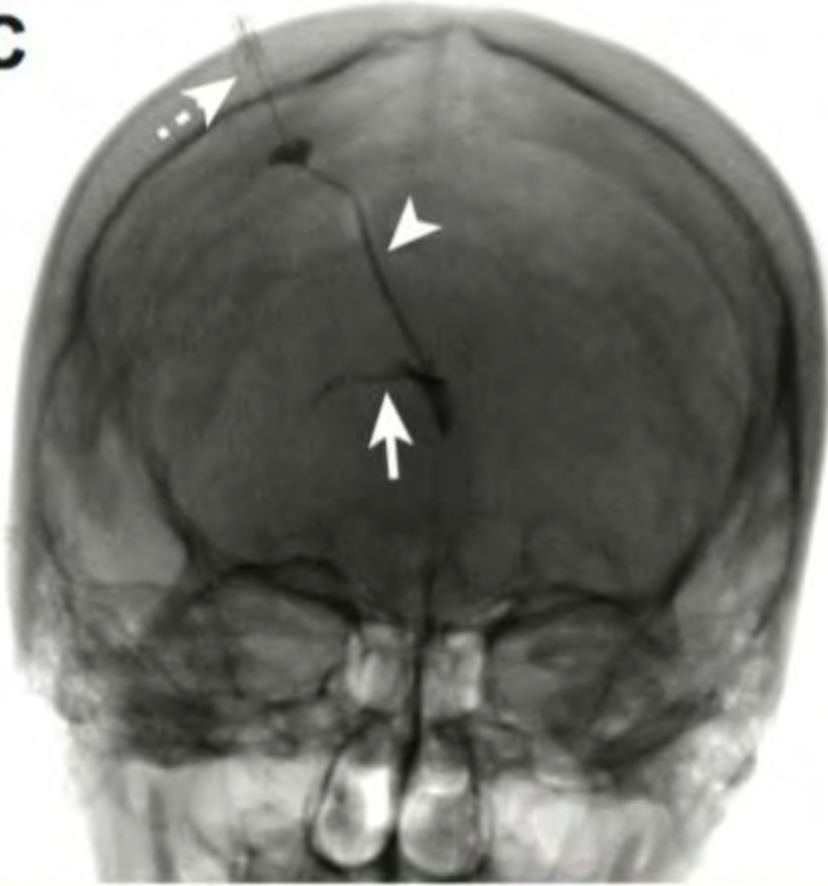
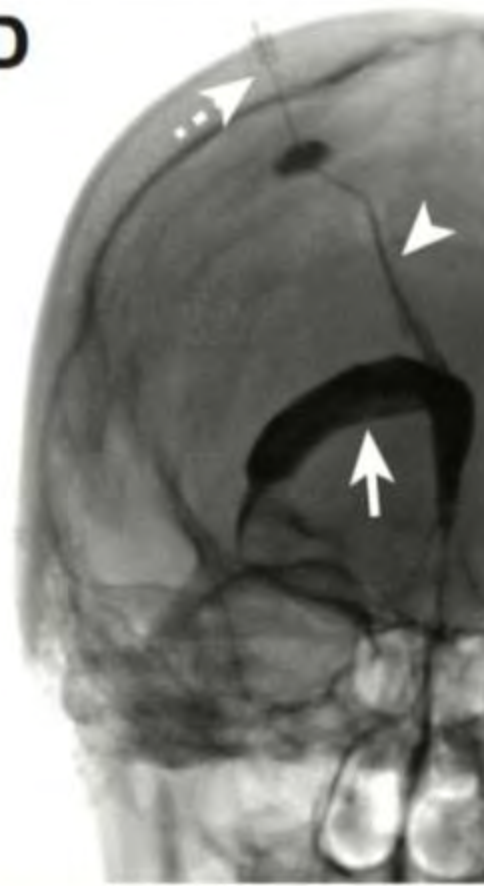
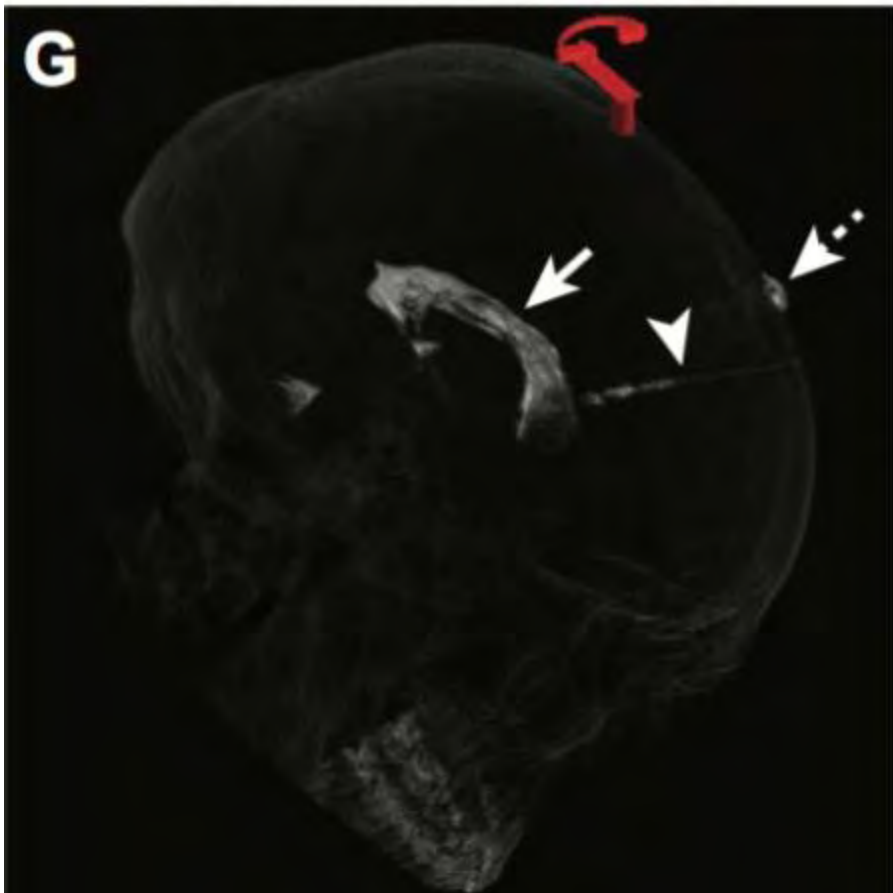
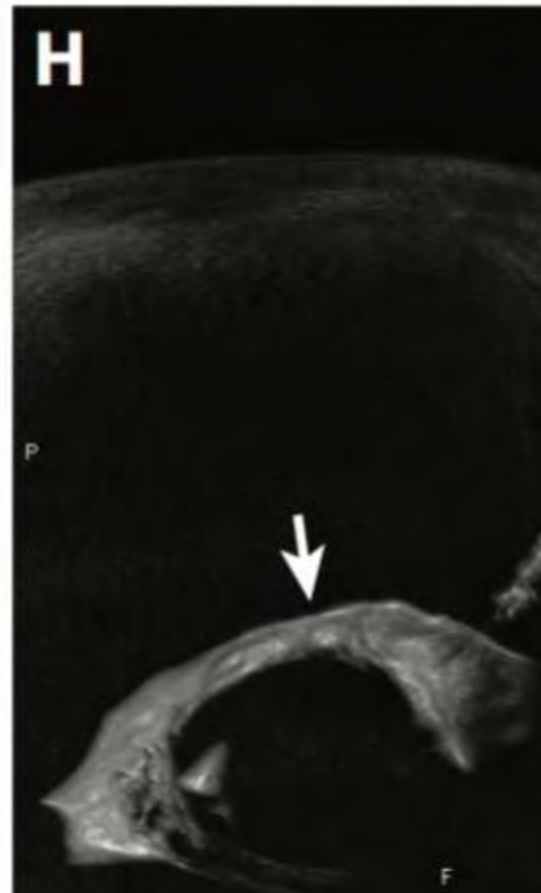
The Ommaya reservoir was accessed with a needle in a neuroendovascular suite with biplane fluoroscopy. Five ml of Omnipaque-300 was injected into the Ommaya reservoir. Contrast transit was monitored with continuous low dose fluoroscopy. There was progressive filling of the Ommaya reservoir, catheter, and ventricle system. No contrast leakage was identified. Dyna CT demonstrated no evidence of contrast leakage into the subdural space or other location outside of the Ommaya reservoir or normal CSF space.

Results

Real-time fluoroscopic evaluation of contrast transit through the Ommaya system demonstrated integrity of the Ommaya reservoir without evidence of blockage or leakage of the system. A Dyna CT performed after contrast injection demonstrated opacification of the Ommaya tubing and ventricles without evidence of contrast extension into the subdural space. These findings were consistent with normal function of the Ommaya system. Given the results of this study, the patient underwent uncomplicated evacuation of the subdural collection without replacement of the Ommaya reservoir and made an excellent recovery.

Conclusions

Real-time fluoroscopic evaluation of Ommaya reservoir integrity by iodinated contrast injection may be performed safely to evaluate integrity of the catheter system. This technique may offer superior evaluation of Ommaya integrity relative to CT and MRI studies in the setting of presumed blockage, and future studies may evaluate this possibility.

C**D****G****H**

(Filename: TCT_O-101_Figure.jpg)

O-102

2:27PM - 2:35PM

Anatomy of the basilar artery tip in the presence of a persistent trigeminal artery. What can we learn about the origin of posterior cerebral, superior cerebellar and basilar tip perforating arteries.

A Galinato¹, H Marin¹, B Griffith¹, M Kole¹

¹*Henry Ford Health System, Detroit, MI*

Purpose

There is considerable individual variability in the appearance of the basilar tip bifurcation, posterior cerebral arteries, and origin of the superior cerebellar arteries and basilar tip perforating arteries. Development of these vessels is intricately linked to fusion of the posterior longitudinal arteries, the timing of the involution of persistent trigeminal arteries, and posterior communicating arteries. Our hypothesis is that if there is a persistent trigeminal artery, there is either symmetrical or asymmetrical ipsilateral caudal fusion pattern of the posterior longitudinal arteries. We also hypothesize that the superior cerebellar artery arises as a single vessel in the cranial fusion pattern and as duplicated vessel in the caudal pattern. In case of asymmetrical fusion, the basilar tip perforators arise asymmetrically from the cranial fusion side.

Materials and Methods

We reviewed our 12-year radiology angiography archive to identify all cases where there was a persistent trigeminal artery. Each case was reviewed carefully for side and size of the PTA, configuration of the basilar tip, superior cerebellar and posterior cerebral arteries, and appearance of the basilar tip perforating vessels. We classify the basilar tip bifurcation in the two posterior cerebral arteries as 'symmetrical fusion' if the P1 segments are similar in size and configuration, and "asymmetrical fusion" if there is difference in caliber or morphology between the P1 segments. We also classify basilar tip bifurcation as "cranial fusion" configuration if there is a 'T' shape of the tip of the basilar artery with SCA arising from the distal basilar and as "caudal fusion" configuration if there is a 'V' shape of the tip of the basilar artery with the SCA arising from the proximal P1 segment.

Results

Thirty cases with PTA were identified in which basilar tip bifurcation configuration could be classified. Symmetrical cranial fusion was seen in 17 cases and symmetrical caudal fusion was seen in one case. Asymmetrical fusion with caudal type ipsilateral to the PTA was seen in one case. Our hypothesis that a duplicated SCA arises from the caudal fusion side was confirmed in one case.

Conclusions

Our study confirms the hypothesis that the side of a PTA influences the origin and appearance of the superior cerebellar arteries. These findings are likely valid also in cases where there is no PTA. The careful analysis of the appearance of the BA can predict the side of dominant origin of the basilar tip perforators in cases with an asymmetrical appearance allowing assessment of endovascular or surgical treatment risks in cases of basilar tip aneurysms.

O-463

2:35PM - 2:43PM

Automated and Quantitative Angiographically Based Assessment of Pial Collaterals during Acute Ischemic Stroke

C Haddad¹, G Christoforidis¹, M Giger¹, T Carroll²

¹University of Chicago, Chicago, IL, ²Northwestern University, Chicago, IL

Purpose

This work aims to develop a novel, automated, and quantitative angiographic-based method for evaluating leptomeningeal collaterals in acute ischemic stroke.

Materials and Methods

Digital angiographic images (Philips AlluraXper System) from six patients with acute ischemic stroke due to MCA occlusion acquired at six frames/sec were analyzed using an in-house computerized quantitative image analysis program. Contrast-time curves were generated for each pixel in the image and filtered using smoothing splines. Quantitative features were extracted automatically from the filtered contrast-time curves and included: arterial arrival time (AAT), time-to-peak (TTP), and the maximum value of the first derivative of each curve [Contrast Uptake Rate (CUR)]. Color-coded angiographic parameter maps were generated, yielding AAT-map images, TTP-map images, and CUR-map images (Fig.). Using these three parameters with unsupervised fuzzy C-means (FCM) cluster analysis, summary metrics were determined within five circular regions of interest (ROIs) that spanned the ischemic vascular territory, yielding information on major vessels, pial collateral blush, and background.

Results

Computer-extracted angiographic CUR, AAT and TTP parameters appear to correspond to pial collateral scores derived from patients (Fig.). Fuzzy C-means was able to distinguish capillary blush from vessels within the ROIs (Fig.). During the development of the algorithm for this analysis, pitfalls were identified and will be discussed. Among the three features, CUR and TTP appeared least susceptible to these pitfalls compared to AAT.

Conclusions

Preliminary work indicates that an automated, quantitative angiographic-based computerized method for evaluating leptomeningeal collaterals in acute ischemic stroke is feasible and appears to compare favorably to semiquantitative pial collateral assessment methods.

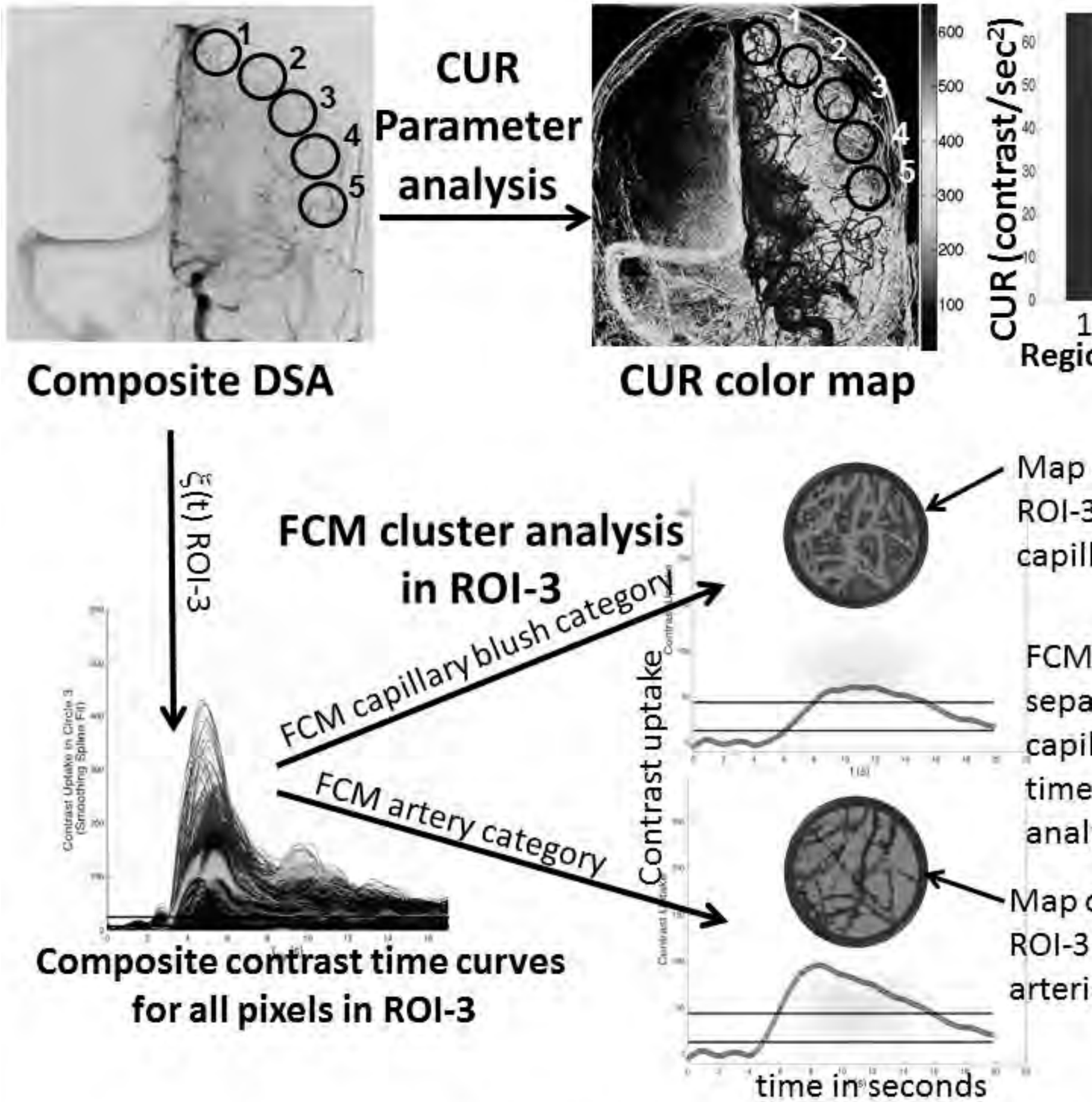


Figure: Example parametric & FCM DSA analyses in a patient with occlusion. Other parameters studied included AAT & TTP. Specific analysis for arteries & capillaries is possible following FCM cluster

(Filename: TCT_O-463_HaddadASNR2016.jpg)

Monday

3:00PM - 4:30PM

Washington Marriott Wardman Park, Marriott Ballroom

5A-ASPNR Programming: Pediatric Epilepsy 2016

5A-1

3:00PM - 3:20PM

Brain Malformations and Epilepsy: New Concepts Using Molecular Pathways as a Guide

Barkovich, A.

UCSF Benioff Children's Hospital

San Francisco, CA

5A-2

3:20PM - 3:40PM

Advanced Imaging in Pediatric Epilepsy

Grant, P.

Children's Hospital Boston

Boston, MA

5A-3

3:40PM - 4:00PM

Advances in Clinical Epilepsy Management

Dlugos, D.

The Children's Hospital of Philadelphia

Philadelphia, PA

5A-4

4:00PM - 4:20PM

Advances in Surgical Epilepsy Management

Madsen, J.

Children's Hospital Boston

Boston, MA

5A-5

4:20PM - 4:30PM

Discussion

Monday

3:00PM - 4:30PM

Washington Marriott Wardman Park, Washington 4/5/6

5B-AOSNHNR Programming: Advances in Vascular Imaging: Diagnosis and Treatment Implication

5B

3:00PM - 3:10PM

Introduction

5B-1

3:10PM - 3:30PM

Advances in the Imaging of Moyamoya Disease

Yun, T.

Seoul National University Hospital

Seoul

5B-2

3:30PM - 3:50PM

Current Clinical Applications of Intracranial Vessel Wall Imaging

Tsuchiya, K.

Tokyo Teishin Hospital

Tokyo

5B-3

3:50PM - 4:10PM

Clinical Application of 3D T1-Weighted Black-Blood MRI in Head and Neck Arterial Lesions

Maeda, M.
Mie University School of Medicine
Tsu, Mie

5B-4

4:10PM - 4:30PM

Intracranial Arterial Stenosis: MR Patterns and Outcomes of Management

Chang, F.
Taipei Veterans General Hospital & National Yang Ming University
Taipei, Taiwan

Monday

3:00PM - 4:30PM

Washington Marriott Wardman Park, Washington 1/2/3

5C-Evidence Based Medicine Programming: Speed Journal Club to Review New Evidence in the Literature on Hot Topics in Neuroradiology

5C-1

3:00PM - 3:25PM

Brain

Sanelli, P. · Gupta, A.
Northwell Health · New York-Presbyterian Hosp/Weill Cornell Med Ctr
New York, NY

5C-2

3:25PM - 3:45PM

Spine

Jarvik, J.
Univ of Washington
Seattle, WA

5C-3

3:45PM - 4:00PM

Head and Neck

Anzai, Y.
University of Utah
Salt Lake City, UT

5C-4

4:00PM - 4:15PM

Pediatric

Medina, L.
Miami Children's Hospital
Miami, FL

5C-5

4:15PM - 4:30PM

NIR

Hirsch, J.
Massachusetts General Hospital
Boston, MA

Monday

3:00PM - 4:30PM

Washington Marriott Wardman Park, Roosevelt 1-3

**5D-PARALLEL PAPER SESSION: Turbo Talks - CNS Tumors: Biomarkers,
Genomics, and Radiomimics**

O-103

3:00PM - 3:03PM

Preclinical Validation of Radiogenomics in Glioblastoma

R Colen¹, F Zandi¹, A Kotrotsou¹, M Hatami¹, S Singh¹, M Luedi¹, G Thomas², A Elakkad¹, E Sulam¹, F Lang¹, D Piwnica Worms¹, P Zinn¹

¹MD Anderson Cancer Center, Houston, TX, ²The University of Texas MD Anderson Cancer Center, Houston, TX

Purpose

A plethora of magnetic resonance imaging (MRI) features have been correlated to cancer genomics to date; however, none have established causality. Here, we present an in vivo xenograft RNA interference validated, potentially clinically applicable test method termed "magnetic resonance radiomic sequencing" (MRRS) for the noninvasive detection of cancer genomics in glioblastoma. Magnetic resonance radiomic sequencing comprehensively assesses the entire tumor mass using imaging texture based algorithms that generate thousands of variables (features) inherent to the tumor.

Materials and Methods

Two independent glioblastoma stem cells (GSC1 and GSC3) harboring doxycycline inducible short hairpin RNA against Periostin (POSTN), a gene previously identified in our radiogenomic screen, were implanted at orthotopic location in nude mouse brain (n=30). The T2 and T1 post MRI texture features, in edema/tumor invasion and contrast enhancement phenotype features were compared between doxycycline (POSTN knockdown) and sucrose (control) group of mice using T test statistics. The significant features were included in a Stepwise Forward Logistic Regression analysis to build the final predictive model. The accuracy of the model was tested using ROC curve analysis.

Results

In vivo knockdown of >90% and ~60% POSTN gene was achieved in GSC3 and GSC1 respectively. In GSC3 mice cohort, 117 features were significantly (p-value<0.05) different between the doxycycline and sucrose groups. The significant features were included in a Stepwise Forward Logistic Regression analysis, 2 textures features (#234 of edema T1 edema/tumor-invasion and #251 of edema/tumor-invasion T2) were selected to be included in the final predictive model. The AUC of the model for prediction of high POSTN group with leave one out cross validation method was 100%.

Conclusions

Our results therefore describe the first mouse model derived MRRS signature to describe a causal link of gene alteration to MRRS. This novel test method may open an avenue for human mouse matched co-clinical trials and noninvasive Radiogenomic diagnostics.

O-104

3:03PM - 3:06PM

Association of angiogenesis microstructure characteristics with molecular genomic biomarkers and their survival predictive value in patients with glioblastoma - A study using ROI-based measurement and voxel-based histogram analysis of MR dynamic susceptibility contrast perfusion weighted imaging

X Liu¹, W Tian¹

¹*University of Rochester Medical Center, Rochester, NY*

Purpose

Glioblastoma is the most common malignant primary brain tumor in adults. Angiogenesis is one of the key pathology features in glioblastomas, and plays an important role in tumor proliferation and invasion, which is associated with poor survival outcome. Magnetic resonance (MR) dynamic susceptibility contrast perfusion-weighted imaging (DSC-PWI) is a major imaging tool investigating hemodynamic changes of glioblastomas in vivo. The purpose of this study is to evaluate association between molecular genomic biomarkers and multiple MR-DSC-PWI parameters, and their performance of predicting survival outcome in patients with glioblastomas.

Materials and Methods

Forty-one cases (mean age is 62.32±12.09 years) with new pathology confirmed glioblastomas were enrolled in this study. Region of interest (ROI)-based approach and voxel-based histogram analysis were used to measure mean and maximal rCBV ratio of the enhancing tumor (rCBV_{mean} and rCBV_{max}), and maximal rCBV ratio of peri-enhancing tumor area (rCBV_{peri-tumor}) as well as 15%, 25%, 50%, 75%, 85% quantiles and the interquartile range (IQR) in the enhancing tumor. The association between MR-PWI parameters and Ki-67 labelling index, isocitrate dehydrogenase (IDH), mammalian target of rapamycin (mTOR), and epidermal growth factor receptor (EGFR) was assessed, the Cox regression was used to evaluate their implication on overall survival time (OS). The difference of clinical and imaging parameters, and molecular genomic biomarkers between the patients who survived less than 14 months and more than 14 months was compared.

Results

The rCBV_{max}, and 50%, 75%, 85% quantiles and IQR had significant association with mTOR, (p =0.047). The rCBV_{peri-tumor} showed significant difference in the group comparison between patients survived less or longer than 14 months (p =0.002), the age and 15% quantiles showed the trend of significant difference (Fig.1). The Cox regression analysis showed that rCBV_{peri-tumor} and age were the two strongest predictors of OS (hazard ratio= 1.29 and 1.063; p =0.003 and 0.005 separately). The combination of rCBV_{peri-tumor} and age improved the prediction of OS with specificity of 78.9% and sensitivity of 81.8% (Fig. 2).

Conclusions

The quantitative rCBV parameters are associated with mTOR-EGFR pathway biomarkers, which may suggest that mTOR-EGFR pathway moderates angiogenesis process in the tumor proliferation and vasculature infiltration in glioblastomas. And rCBV_{peri-tumor} had better prognostic value than molecular genomic biomarkers alone. Combination of ROI-based measurement and voxel-based histogram analysis is useful for better understand of angiogenesis characteristics in glioblastomas.

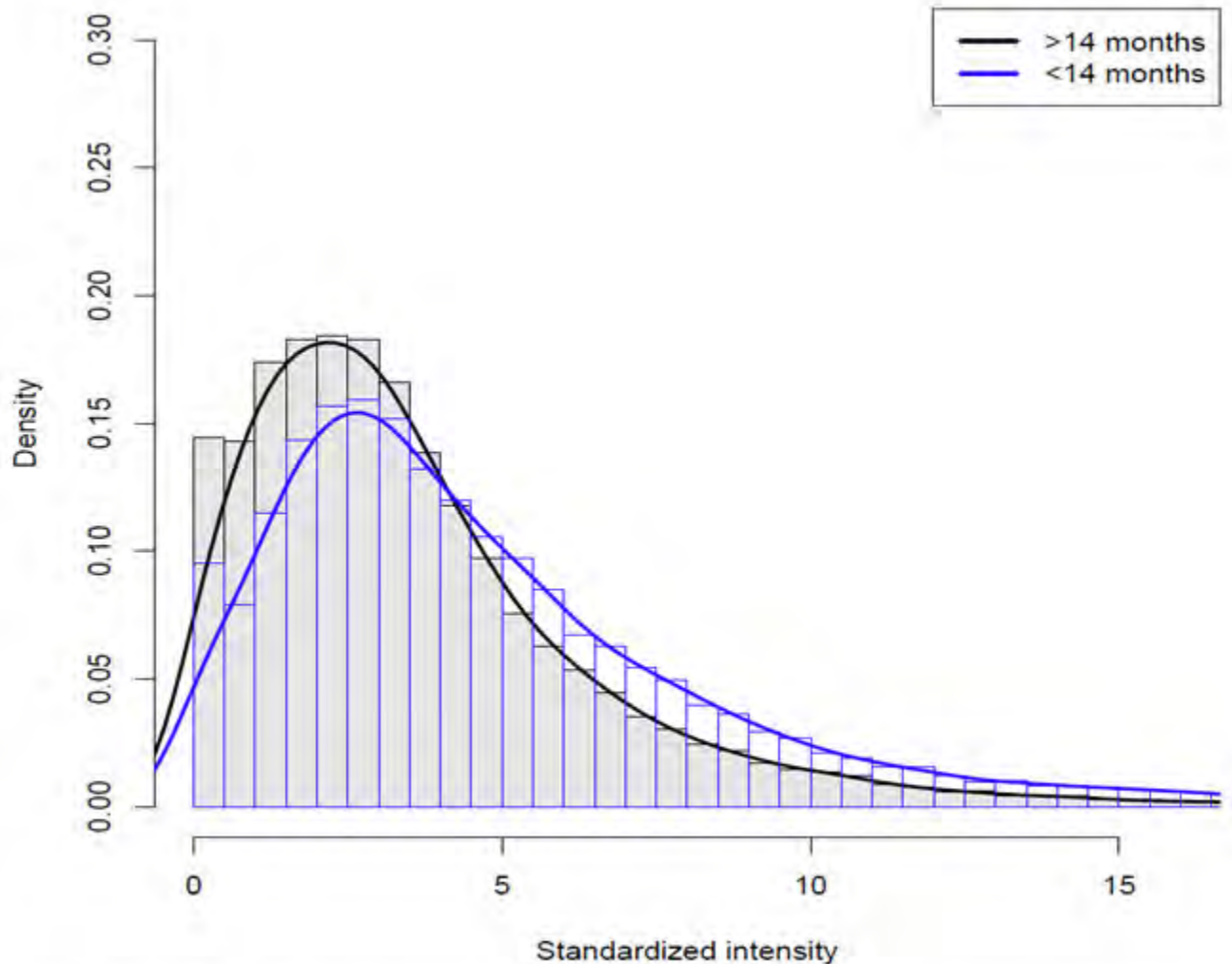


Figure 1: Histogram group comparison between glioblastoma patients (Filename: TCT_O-104_Figure1---ASNR2015---Glioblastoma--mTORhistogramcomparison.jpg)

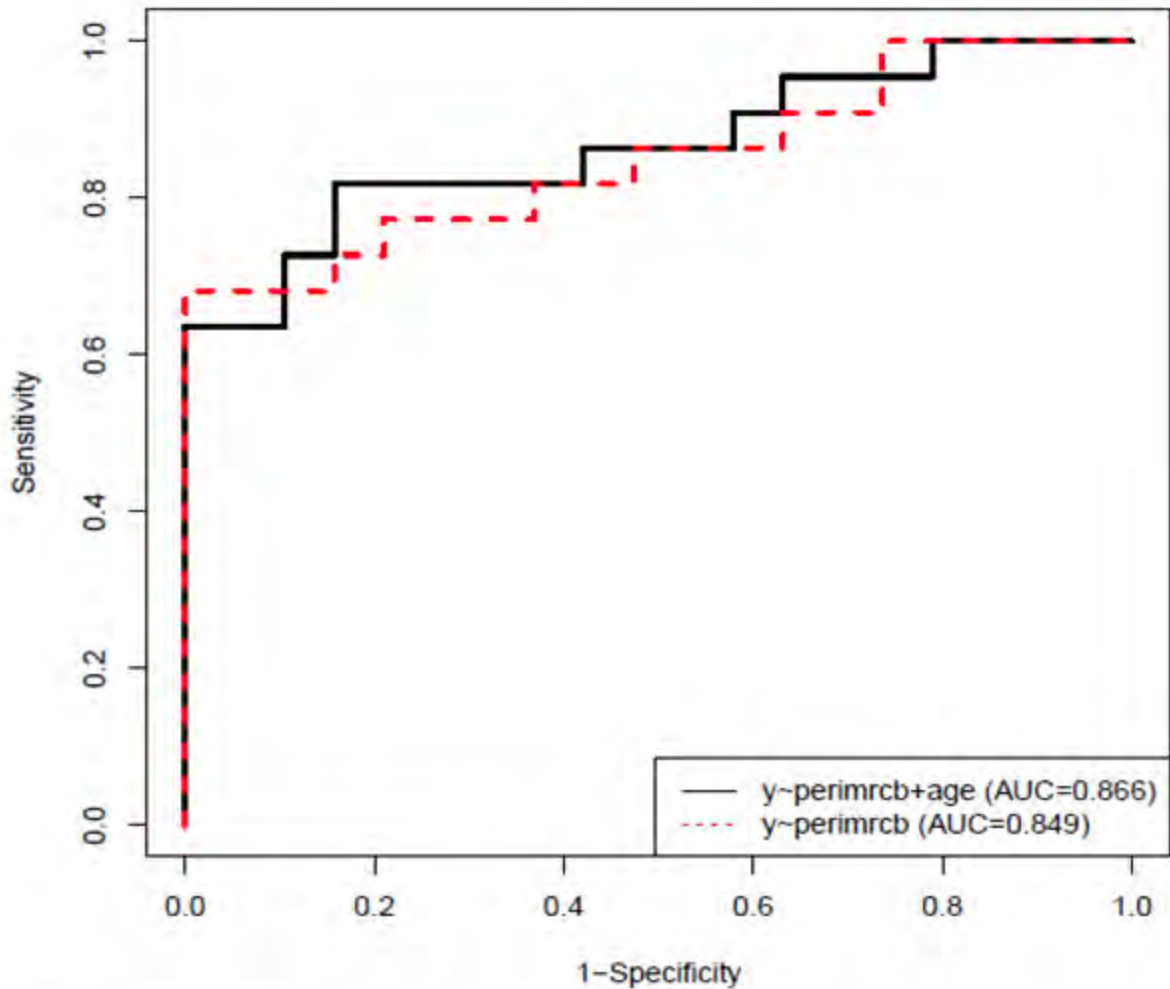


Figure 2: combination of $rCBV_{\text{peri-tumor}}$ and age had better area under the curve in the ROC analysis compared single biomarker alone

(Filename: TCT_O-104_Figure2--ASNR2015---mTOR--glioblastoma---ROCresult.jpg)

O-105

3:06PM - 3:09PM

Radiogenomic Mapping in Enhancing Volume Phenotype Identifies Novel Drivers in Glioblastoma Proliferation: Comprehensive Genomic, Proteomic, MicroRNA and Pathway Analysis

G Thomas¹, Y Abu Eleneen¹, H Abouhatab¹, S Abrol², A Kotrotsou², S Singh³, P Zinn⁴, R Colen²

¹The University of Texas MD Anderson Cancer Center, Houston, TX, ²MD Anderson Cancer Center, Houston, TX, ³MD Anderson Cancer Center Houston, TX, Houston, TX, ⁴Baylor College of Medicine, Houston, TX

Purpose

Glioblastoma (GBM) is the most common and most aggressive primary malignant brain tumor in adults. It accounts for 20% of all the intracranial malignancies. Currently, the survival of patients diagnosed with GBM remains less than 2 years despite extensive therapy. So time has arrived to look into newer, more focused methods of biomarker discovery and target identification that would help to develop molecular-targeted therapies and address the issue of tumor heterogeneity. We have been successful in harnessing magnetic resonance imaging (MRI) to identify different imaging phenotypes and assessing the genotypic background responsible for these phenotypes in the newly emerging field of imaging genomics. In this study, we identify the novel genes, pathways and networks relating to the contrast enhancement volume phenotype.

Materials and Methods

We retrospectively analyzed 106 patients from the TCGA (The Cancer Genome Atlas) with imaging obtained from the Cancer Imaging Archive (TCIA). Over 13,000 genes and over 500 microRNA were analyzed in each patient and patients were stratified on the basis of their contrast enhancement volume phenotype by grouping them based on survival using Kaplan –Meier statistics. Contrast enhancement volumetrics were obtained using 3D Slicer software. Discovery and Validation were employed to reduce false discovery. Differentially expressed genes, miRNAs and proteomics were analyzed using gene pattern software (MIT Broad institute) and ingenuity pathway analysis.

Results

Pathways and networks associated with a high contrast enhancing volume phenotype versus a low contrast enhancing volume phenotype were identified. The top proliferative genes were identified as novel molecules involved in driving tumor proliferation in glioblastoma. The upstream regulators previously not described in relation to GBM were found. Further in vitro studies will be ongoing to validate our in silico finding.

Conclusions

Radiogenomic discovery of potential molecules describing physiologic imaging phenotypes were identified; similar to our published paper (Zinn et al PLOS One 2011), we can expect our in vitro and in vivo validation to confirm our findings and open the door to personalized medicine and therapeutics.

O-106

3:09PM - 3:12PM

Fast whole brain multispectral pH-weighted molecular MRI in human gliomas using multi-echo amine CEST EPI

B Ellingson¹, R Harris¹, K Leu¹, W Pope¹, T Cloughesy¹

¹University of California Los Angeles, Los Angeles, CA

Purpose

Decreased extracellular pH within the tumor microenvironment has been shown to result in increased tumor proliferation, increased genetic alterations, immune privilege, and resistance to antineoplastic therapies. We recently have demonstrated that amine chemical exchange saturation transfer (CEST) imaging can be used to identify and characterize acidic tumor tissue by targeting amine protons on neutral amino acids including glutamine (1). In the current study we have dramatically improved this technique to obtain whole brain coverage and a multi-echo echoplanar readout (2-gradient echoes, 1-asymmetric spin echo, and 1-spin echo), allowing interrogation of different water populations and correction of CEST data with respect to transverse relaxation effects.

Materials and Methods

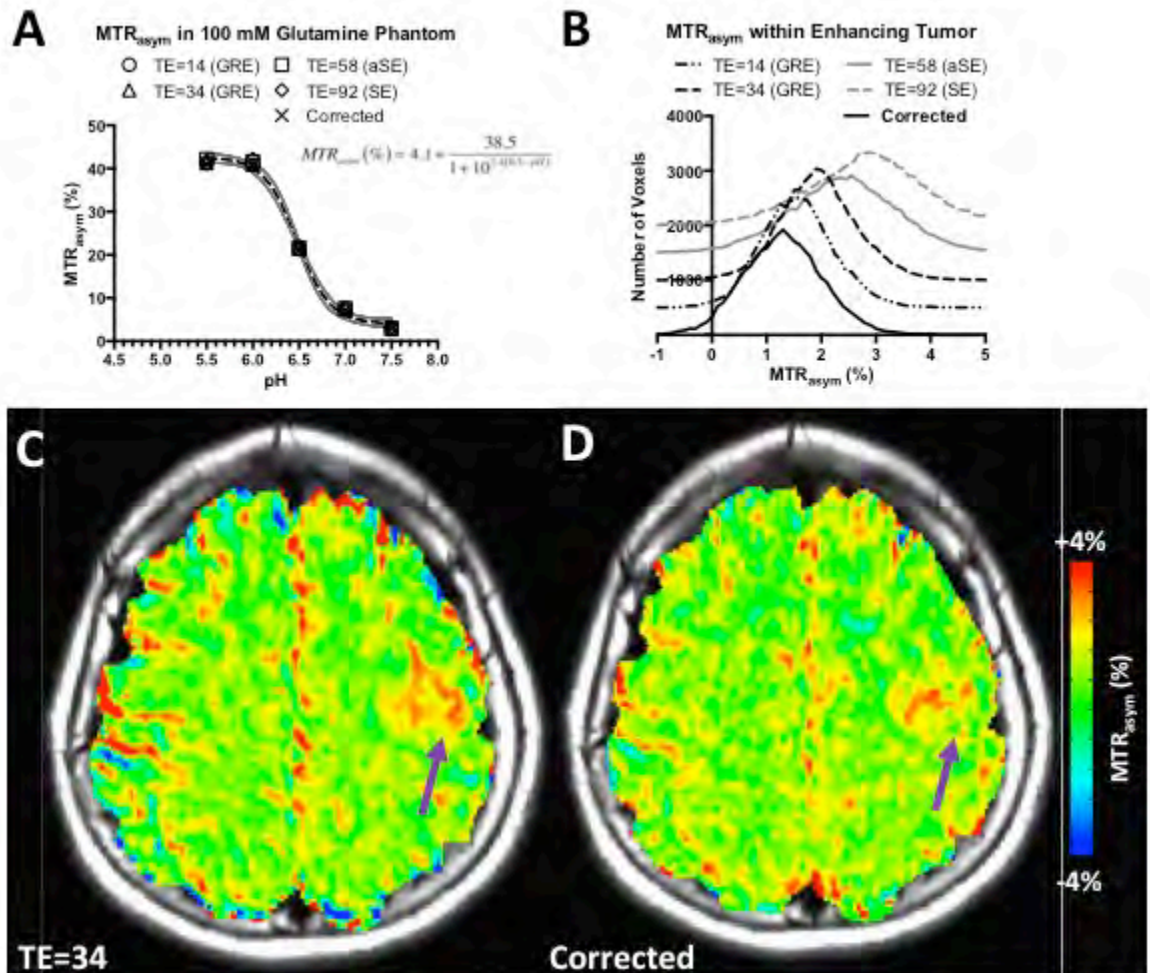
The multi-echo CEST sequence was first applied in phantoms of 100 mM glutamine at varying pH to verify its pH sensitivity. Five glioma patients then underwent multi-echo pH-weighted CEST magnetic resonance imaging (MRI) using a pulse train of three 100 ms, 6 μ T saturation pulse with 29 spectral points centered around \pm 3 ppm and 0 ppm. An image with identical parameters but no saturation pulse (S_0) was acquired for normalization. The readout consisted of two gradient echo (GRE) measurements at 14.0 and 34.1 ms, an asymmetric spin echo (aSE) measurement at 58.0 ms, and a spin echo (SE) measurement at 92.4 ms. Following B_0 inhomogeneity correction, the asymmetry at 3.0 ppm was calculated for each voxel by $MTR_{asym} = [S(-3\text{ppm}) - S(+3\text{ppm})]/S_0$. An image corrected for T2 and T2* decay was calculated using T2 and T2* maps obtained from fitting the SE and GRE echoes, respectively. Maps of MTR_{asym} for each contrast (four echoes and one corrected image) were observed qualitatively and the distribution of MTR_{asym} then was pulled from the tumor region for each patient and contrast.

Results

The multi-echo sequence had equivalent sensitivity to pH due to a single water pool present in the phantoms, with the different contrasts providing similar values of MTR_{asym} in water (Fig. 1A). Histograms from a patient with a glioma showed different CEST characteristics for different echo readouts, suggesting proton exchange was different for different water pools within the tissue (Fig. 1B). The CEST data corrected for transverse relaxation provided different localization of acidic regions within the tumor (Figs. 1C and D). Histopathological data from stereotactic biopsies also were compared with corrected and noncorrected CEST data.

Conclusions

Multi-echo CEST EPI is a novel technique to acquire fast, whole brain, high density pH information in brain tumors and neuropathologies.



(Filename: TCT_O-106_Slide1.jpg)

O-107

3:12PM - 3:15PM

Relationship of Subventricular Zone with Tumor Genomics and Survival in Gliomas: A TCGA/TCIA Project

B Griffith¹, L Poisson¹, J Chen², R Jain³

¹Henry Ford Health System, Detroit, MI, ²San Diego VA / UCSD Med. Center, La Jolla, CA, ³NYU School of Medicine, New York, NY

Purpose

Prior studies have shown glioblastoma (GBM) location relative to the subventricular zone (SVZ) to be associated with worse prognosis. The purpose of this study was to determine whether this difference in prognosis is seen in all glioma grades. We also assessed whether SVZ-related survival differences correlated with IDH mutation and chromosome 1p/19q co-deletion status in lower grade gliomas (LGG) given their distinct prognosis paths.

Materials and Methods

Three hundred fifty-six patients with untreated LGGs (WHO Grade 2 and 3) and GBMs, molecular information assayed by the TCGA, and presurgical imaging collected by the TCIA were included (LGG, n=153; GBM, n=203). Tumor location (T2/FLAIR for LGGs; contrast-enhancing lesion for GBMs) was classified as follows: involving both SVZ and cortex (Group I), SVZ only (Group II), cortex only (Group III), neither SVZ nor cortex (Group IV). Overall survival (OS) trajectories were determined using Kaplan-Meier estimates. Group differences were assessed by log-rank test.

Results

There was a statistically significant difference in OS for GBMs with SVZ involvement compared to those with only cortex involvement (median 0.81 versus 1.28 years, $p=0.004$) (Fig. 1B). There was suggestion of shorter OS in LGGs (median 5.3 versus 11.1 years, $p=0.079$) (Fig. 1A) with a more apparent difference for Grade II gliomas (no deaths observed versus median 7.3 years, ($p=0.108$)) (Fig. 1B). For LGGs, there was no evidence that T2/FLAIR location is associated with IDH mutation ($p=0.839$) or 1p/19q co-deletion status ($p=0.178$).

Conclusions

Involvement of the SVZ is associated with worse overall survival in both low and high grade gliomas, most notably Grade II and IV. This difference is not driven by molecular profiles associated with LGG evolution paths delineated by IDH mutation or 1p/19q loss, nor are definite molecular markers seen in GBMs. Subventricular zone involvement may represent a prognostic imaging biomarker independent of tumor grade or molecular classification.

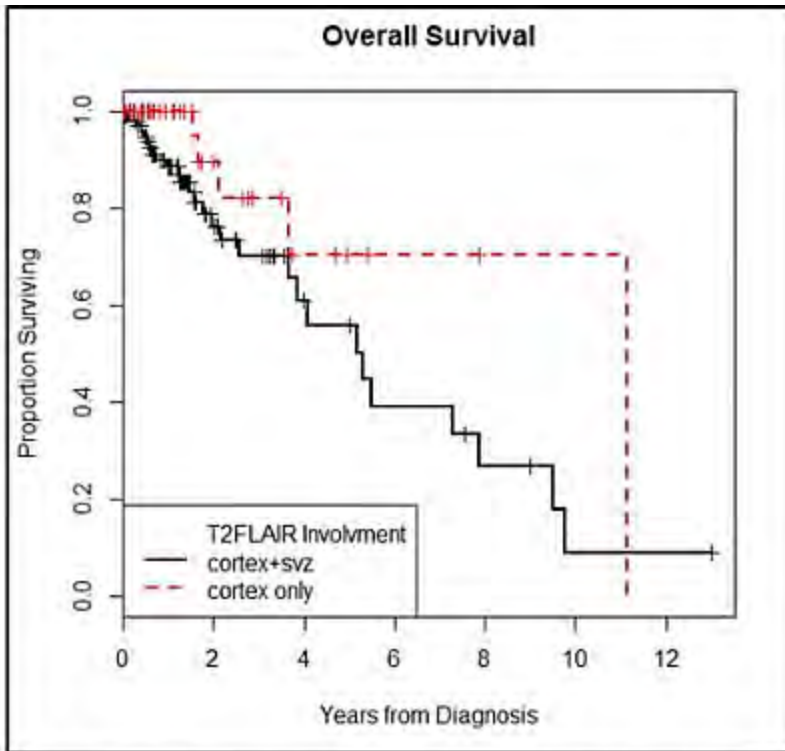


FIG 1A. Overall survival for Grade II/III disease

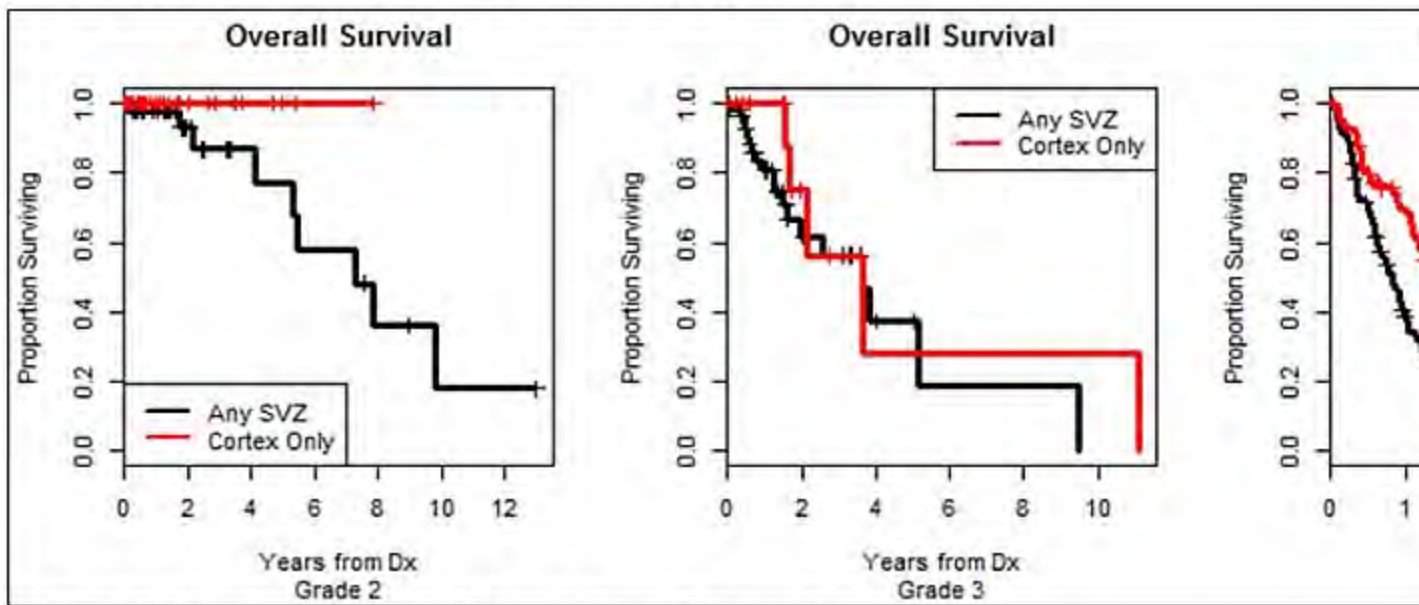


FIG 1B. Overall survival for glioma by grade.

(Filename: TCT_O-107_LGGSVZFigure.jpg)

O-108

3:15PM - 3:18PM

Prognostic Imaging Markers in Triple Negative Lower Grade Gliomas: A TCGA/TCIA Project

B Griffith¹, L Poisson¹, J Chen², R Jain³

¹Henry Ford Health System, Detroit, MI, ²San Diego VA / UCSD Med. Center, La Jolla, CA, ³NYU School of Medicine, New York, NY

Purpose

Triple-negative lower grade gliomas (TN-LGGs) demonstrate clinical behavior similar to glioblastoma and are associated with poor overall survival. The purpose of this study was to determine whether MR imaging characteristics could prospectively identify this subset of LGGs and provide prognostic information.

Materials and Methods

Patients with untreated LGGs, molecular information assayed by The Cancer Genome Atlas, and presurgical imaging collected by The Cancer Imaging Archive were included (n=150). IDH 1/2 mutation, chromosome 1p/19q deletion, P53 mutation, and clinical data were available from prior publication. Pre-operative MR images were scored with determination of T2/FLAIR location, subventricular zone (SVZ) and cortex involvement, enhancement, and multifocality. Categorical variable association was assessed by Fisher's exact test. Overall survival (OS) and progression-free survival (PFS) curves were constructed by Kaplan-Meier estimation. Log-rank tests compared survival curves between groups. Cox regression, with likelihood ratio test, was used for multivariable survival models.

Results

Histologic tumor diagnoses were 48 astrocytoma, 36 oligoastrocytoma, and 66 oligodendroglioma. IDH 1/2 mutation was found in 116 (77.3%), 1p19q co-deletion in 41 (27.3%), and P53 mutation in 79 (52.7%). Twenty-six tumors (17.3%) had none of these (TN-LGGs). Triple negative lower grade gliomas were neither more likely to enhance ($p>0.99$) nor to be multifocal (38% versus 34%, $p=0.656$). Triple negative lower grade gliomas were less likely to occur in the frontal lobe compared to other classes (23% versus 76% IDHmut/codel, Forty-three percent IDHmut/noncodel, $p=0.009$). Triple negative lower grade gliomas without SVZ involvement demonstrated better OS (median 11.1 years versus 1.22 years, $p=0.030$) and PFS also trended towards improvement (median 1.43 years versus 0.55 years; $p=0.086$) (Fig. 1). Subventricular zone involvement remained a significant predictor of OS even after adjusting for grade ($p=0.018$).

Conclusions

Triple negative lower grade gliomas demonstrate clinical behavior and molecular characteristics similar to GBM. However, those tumors without SVZ involvement demonstrated improved OS indicating that this feature may represent an important prognostic imaging biomarker for this aggressive subset of LGGs.

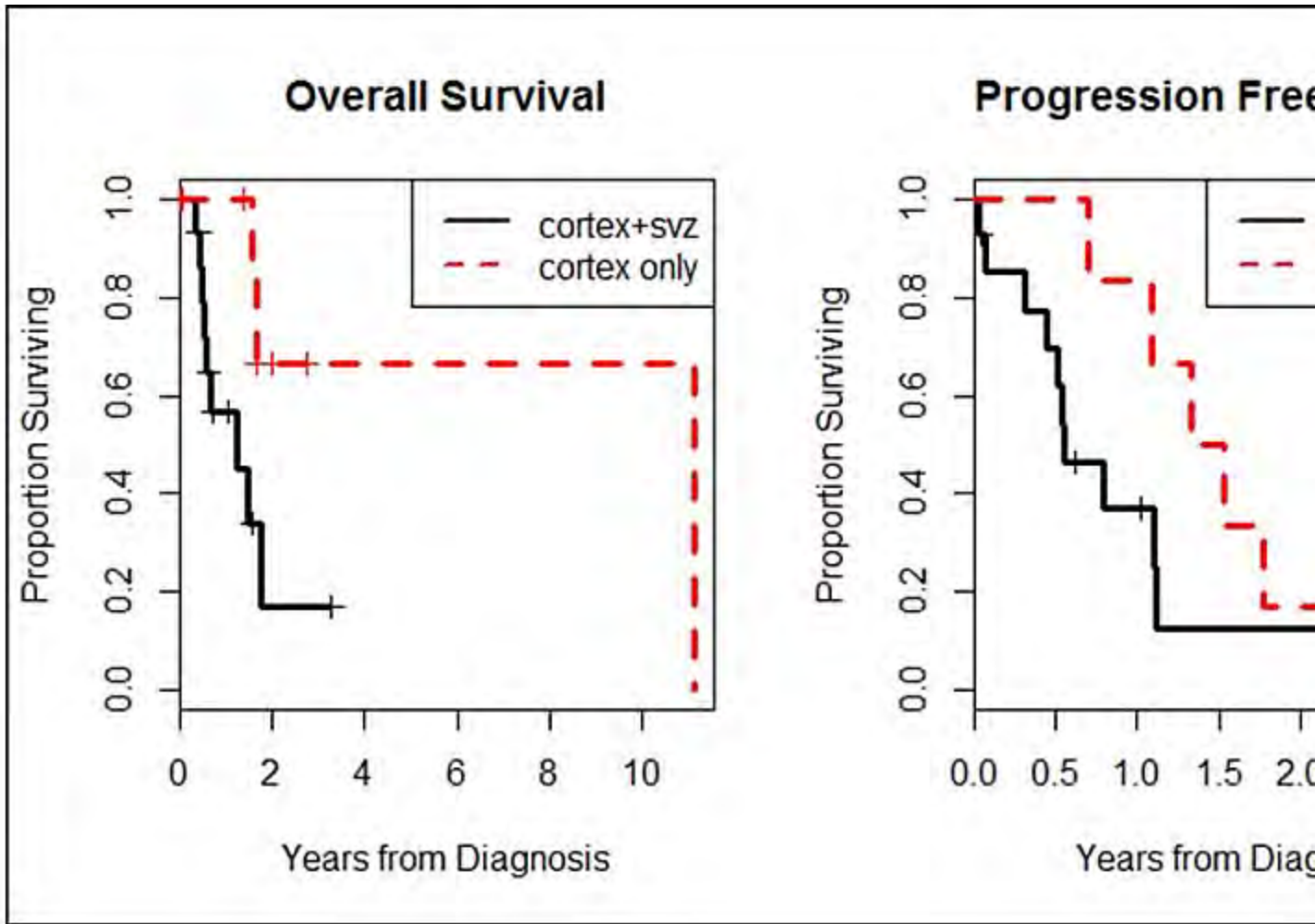


FIG 1. Overall survival and progression free survival for TN-LGGs according to S

(Filename: TCT_O-108_TNLGGFigure.jpg)

O-109

3:18PM - 3:21PM

T2-FLAIR Mismatch, a Potential Imaging Biomarker for IDH Mutant Status in Lower Grade Gliomas: A TCGA/TCIA Project

S Patel¹, L Poisson², A Franceschi³, B Griffith², R Jain⁴

¹NYU Langone Medical Center, New York, NY, ²Henry Ford Health System, Detroit, MI, ³NYU Medical Center, New York, NY, ⁴NYU School of Medicine, New York, NY

Purpose

Lower grade gliomas (LGGs) comprise a genetically heterogenous group of tumors. Relative signal suppression of FLAIR compared to T2-WI is a little reported imaging feature described in low grade brain neoplasms (1). The purpose was to assess

whether this "T2-FLAIR mismatch" sign represents a distinct imaging biomarker for a subset of lower grade gliomas.

Materials and Methods

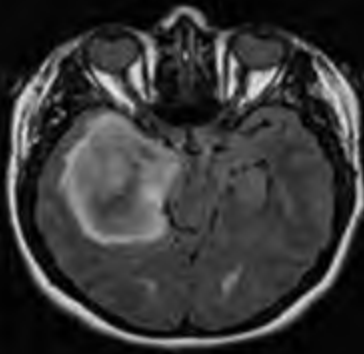
Patients with untreated LGGs, molecular information assayed by The Cancer Genome Atlas, and presurgical imaging (including FLAIR imaging and/or double echo T2-WI) collected by The Cancer Imaging Archive were eligible for inclusion (n=117). IDH 1/2 mutation, chromosome 1p/19q deletion, P53 mutation, and clinical data were available from prior publication (2). Pre-operative MR images were scored with determination of T2-FLAIR mismatch sign (yes/no). The T2-FLAIR mismatch sign was present if a lesion showed predominantly hyperintense signal on T2-WI, and large area of central signal loss with peripheral hyperintense rim on the FLAIR sequence. Categorical variable association was assessed by Fisher's exact test. Overall survival (OS) and progression-free survival (PFS) curves were constructed by Kaplan-Meier estimation. Log-rank tests compared survival curves between groups.

Results

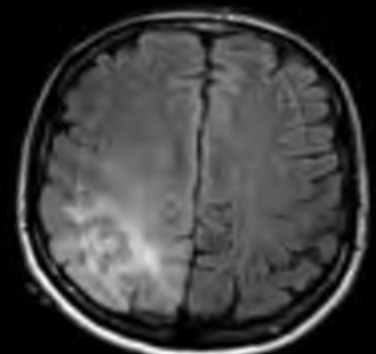
Of the 117 cases, 30 (25.6%) were IDH mutated/1p19q co-deleted, 63 (53.8%) were IDH mutated/1p19q nonco-deleted, and 24 (20.5%) were IDH wild type. The T2-FLAIR mismatch sign was found in 17 (14.5%) cases. All cases with T2-FLAIR mismatch sign (17/17, 100%) were IDH mutated/1p19q nonco-deleted. Fisher's exact test indicated an association between T2-FLAIR mismatch sign and IDH mutated/1p19q nonco-deleted genotype ($p < 0.0001$). There was no statistically significant difference in OS or PFS between glioma patients without and with the T2-FLAIR mismatch sign.

Conclusions

Amongst LGGs, the T2-FLAIR mismatch sign appears to represent a specific imaging biomarker for a subset of IDH mutant/1p19q nonco-deleted gliomas.



Subject TCGA-DU-6407 with a right temporal lobe oligodendroglioma demonstrating T2-FLAIR mismatch. Genotype was IDH mutated/1p19q non-co-deleted.



Subject TCGA-CS-6665 with a right parietal lobe oligodendroglioma demonstrating no T2-FLAIR mismatch. Genotype was IDH mutated/1p19q non-co-deleted.

| | IDH mutated/ 1p19q co-deleted | IDH mutated/ 1p19q non-co-deleted | IDH wild type |
|-----------------------|----------------------------------|--------------------------------------|---------------|
| No T2-FLAIR mismatch | 30 | 46 | 24 |
| Yes T2-FLAIR mismatch | 0 | 17 | 0 |

Cases distributed by IDH/1p19q status and T2-FLAIR mismatch sign.

(Filename: TCT_O-109_LGGASNRT2-FLAIR.jpg)

O-110

3:21PM - 3:24PM

Predilection of Genomic Markers and Contrast-Enhancement of Lower Grade Gliomas by Anatomic Lobe: A TCGA/TCIA Project

J Chen¹, L Poisson², B Griffith², R Jain³

¹San Diego VA / UCSD Med. Center, La Jolla, CA, ²Henry Ford Health System, Detroit, MI, ³NYU School of Medicine, New York, NY

Purpose

Lower grade (WHO grades 2 and 3) gliomas (LGG) have known lobar predilections, but the WHO plans tumor reclassification based on gene expression instead of histology. This study's purpose was to determine the lobar predilection of lower grade tumors based on genomic markers and contrast enhancement.

Materials and Methods

Patients with untreated LGGs, molecular information assayed by The Cancer Genome Atlas, and presurgical imaging collected by The Cancer Imaging Archive were included (n=150). IDH 1/2 mutation and chromosome 1p/19q deletion were available from prior publication (1). Pre-operative MR images were scored by consensus for lobe of tumor center and presence of contrast enhancement. Survival differences were assessed by log-rank test. Categorical contrast-enhancement associations were assessed by Fisher's exact test.

Results

Tumor genetics were 41 IDHmutant 1p19q co-deleted (27.3%), 75 IDHmutant noncodeleted (50%), 34 IDH wild-type (22.7%). Seventy-two (47%) tumors were centered in the frontal lobe, 24 (16%) parietal, 43 (28%) temporal, two (1%) occipital, and 12 (8%) insular. Tumors originating in the frontal lobe were more likely IDHmutant regardless of 1p19q status (89%) than IDHwt (11%). IDHmutant 1p19q co-deleted tumors preferred the frontal lobe (78%) to the temporal (12%) or parietal (12%) lobes; none occurred in the occipital or insular lobes. Rare LGGs originating in the occipital lobe (1.3%) were divided evenly between IDHmutant non-1p19q codeleted and IDHwt; none were 1p19q codeleted. IDHwt tumors showed no lobar preference. Contrast enhancement was associated with primary location (p=0.0094), least likely in the insula (27%), more likely in the frontal (75%), parietal (82%), temporal (62%) and occipital lobes (100%).

Conclusions

Lobar location may provide useful information regarding IDH mutation status and enhancement in LGGs. LGGs rarely occur in occipital lobe, whereas IDHwt LGGs may arise anywhere. Insular tumors are the least likely LGGs to demonstrate contrast enhancement and were more likely to be non-1p19q co-deleted.

O-112

3:27PM - 3:30PM

Reliability of Noncontrast-Enhancing Tumor as a Biomarker of IDH1 Mutation Status in Glioblastoma

A Lasocki¹, A Tsui², F Gaillard², M Tacey², K Drummond², S Stuckey³

¹Peter MacCallum Cancer Centre, East Melbourne, Victoria, ²The Royal Melbourne Hospital, Parkville, Victoria, ³Monash Health, Clayton, Victoria

Purpose

Glioblastomas with IDH1 (isocitrate dehydrogenase-1) mutations are associated with a better prognosis. The literature suggests that these mutations may be associated with frontal lobe tumors with significant nCET (noncontrast-enhancing tumor)(1), but the results are mixed. Our purpose was to examine the imaging features of IDH1-mutated tumors, concentrating on the predictive value of nCET.

Materials and Methods

Consecutive patients with a new diagnosis of glioblastoma from September 2007 to March 2011 were identified. Only patients with at least T2 FLAIR and postcontrast imaging and sufficient histological material for IDH1 mutation analysis were included. Pre-operative magnetic resonance images (MRIs) were reviewed, primarily based on the VASARI feature set (2), focusing on nCET.

Results

One hundred fifty-three patients met the inclusion criteria. Tumors frequently demonstrated >5% nCET (89 patients, or 59%), with 34 patients having >33% nCET. Five patients had IDH1 mutations (3%). Three patients with IDH1 mutations also had >33% nCET, but the association between nCET and IDH1 mutation status was not statistically significant ($p=0.209$). Two of the five patients with IDH1 mutations had a frontal lobe tumor, not significantly different to the incidence of 36% for IDH1-wild type tumors ($p=0.848$). Of note, the 12 frontal lobe tumors with >33% nCET all had wild type IDH1.

Conclusions

Our results suggest that the association between frontal lobe glioblastomas with significant nCET with IDH1 mutations is not as strong as previously believed. IDH1-mutated glioblastomas frequently have substantial nCET, but this feature is also present in many IDH1-wild type glioblastomas, thus nCET is not sufficiently predictive of IDH1 mutation status given the low incidence of the mutation.

O-113

3:30PM - 3:33PM

FLAIR Imaging Pattern can Predict IDH Status in Lower Grade Gliomas.

R Delfanti¹, C McDonald², K Leyden², A Krishnan², D Piccioni³, N Farid²

¹University of California, San Diego, San Diego, CA, ²Multimodal Imaging Laboratory, La Jolla, CA, ³University of California, San Diego, La Jolla, CA

Purpose

Tumor genotyping in neuro-oncology holds tremendous promise in helping to

differentiate otherwise histologically similar tumors and in providing key prognostic information. This is of particular relevance given the recent discovery that isocitrate dehydrogenase (IDH) status is highly correlated to tumor behavior and prognosis in lower grade gliomas, with the wildtype (WT) tumors behaving clinically analogous to glioblastoma. Therefore, we aim to determine if there are distinct imaging features which can predict IDH status in lower grade gliomas.

Materials and Methods

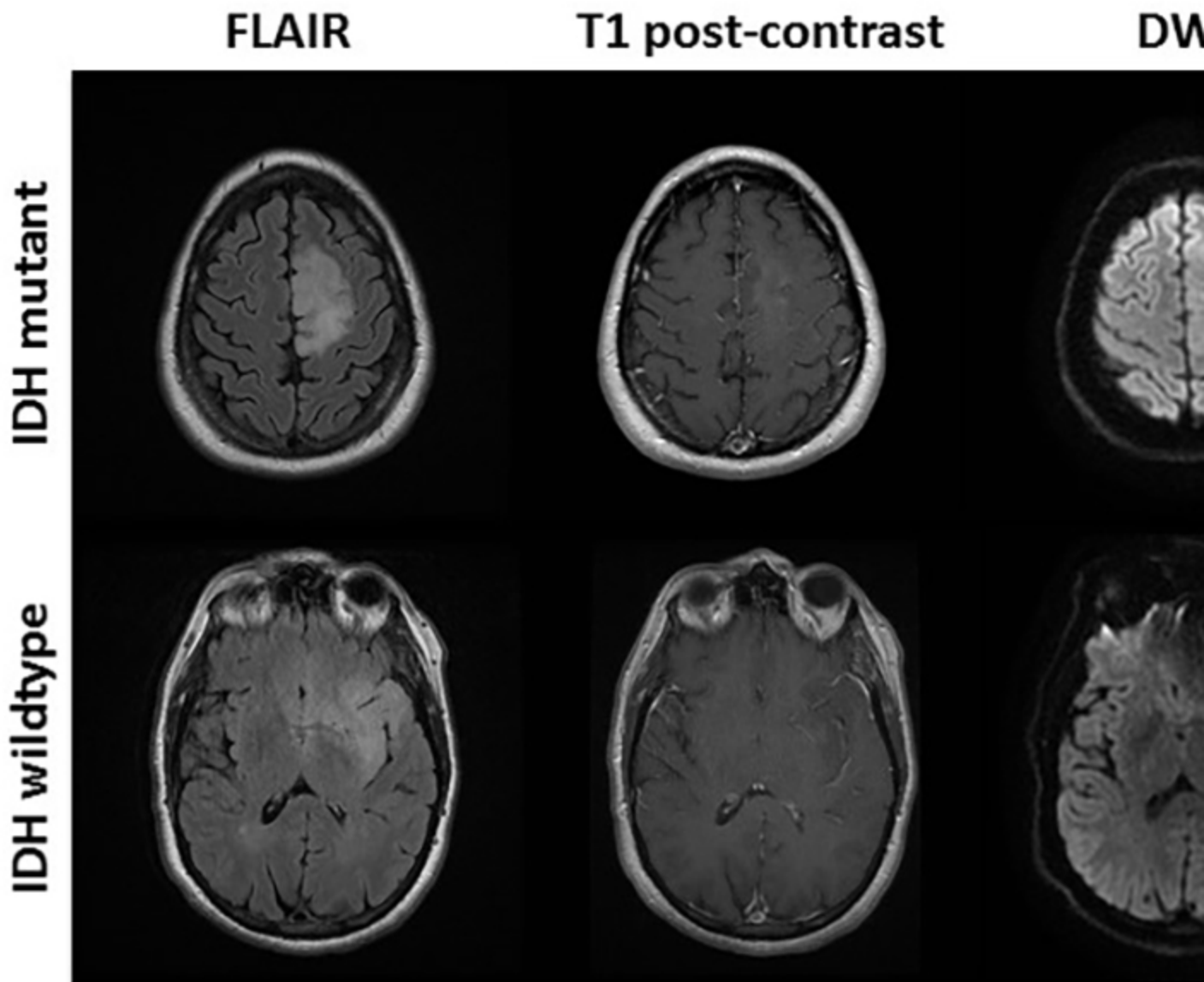
Pretreatment brain magnetic resonance images (MRIs) were analyzed for 44 patients with pathologically proven lower grade gliomas (WHO grade II or III). A board-certified neuroradiologist (with 6 years of experience) who was blinded to the pathologic diagnosis and IDH status of the patients performed qualitative evaluation of the FLAIR, postcontrast, and diffusion-weighted sequences, assigning each a numerical value based on a predesignated scale. The Fisher exact test was used to evaluate the relationship of these parameters as well as tumor location with respect to IDH status.

Results

An infiltrative pattern on FLAIR was associated significantly with IDH WT tumors, whereas the IDH mutant tumors demonstrated either well defined or ill defined borders on FLAIR ($p < 0.001$). Degree of contrast enhancement and presence of diffusion restriction were not associated with IDH status. Among the 26 unilobar tumors, IDH mutant tumors were more likely to be located in the frontal lobe ($p < 0.05$).

Conclusions

IDH WT lower grade gliomas are more likely to demonstrate an infiltrative pattern on FLAIR compared to IDH mutants. Furthermore, IDH mutant gliomas had a predilection for the frontal lobes. Given the aggressive clinical course of these tumors, this finding has the potential to provide essential prognostic information at initial imaging diagnosis and to possibly influence treatment making decisions prior to patients undergoing surgery and chemoradiation.



The top panel demonstrates axial FLAIR, T1 post-contrast, and diffusion weighted imaging (DWI) from a patient with a left superior anaplastic astrocytoma (WHO grade III) which was IDH mutant. The bottom panel demonstrates axial FLAIR, T1 post-contrast, and DWI from a patient with a left insular/frontotemporal lobe tumor, also an anaplastic astrocytoma (WHO grade III) which was IDH wildtype. Both patients demonstrate mild contrast enhancement and lack of restricted diffusion. However, they demonstrate discrete imaging patterns on FLAIR with the IDH mutant showing relatively well-defined borders in contrast to the wildtype tumor's ill-defined and infiltrative borders.

(Filename: TCT_O-113_ASNRIDHAbstract_Final.jpg)

O-114

3:33PM - 3:36PM

Correlation Between MR Imaging Features and IDH Mutational Status in Lower Grade Gliomas

J Villanueva-Meyer¹, S Cha²

¹University of California - San Francisco, San Francisco, CA, ²University of California San Francisco, San Francisco, CA

Purpose

Lower grade gliomas (LGGs) are a heterogeneous group of tumors with unpredictable clinical behavior and prognosis. Upcoming WHO classification will include molecular markers such as IDH to better characterize LGGs. The purpose of our study was to determine qualitative and quantitative MR imaging parameters that can discriminate an aggressive subtype of LGG that is characterized by IDH-wildtype status.

Materials and Methods

We evaluated 99 adult cases of pathologically confirmed LGG with molecular testing for IDH mutation. Presurgical magnetic resonance images (MRIs) were analyzed for qualitative imaging characteristics including tumor location, volume, cortical involvement, hemorrhage or mineralization, and contrast enhancement. Quantitative diffusion and perfusion MRI also were assessed. Logistic regression and receiver operating characteristic analyses were used to assess MRI metrics to distinguish IDH mutational status. Clinical data including patient sex, age, treatment, performance status, and outcomes were collected. Kaplan-Meier curves were used to evaluate the association between IDH mutational status and clinical outcomes.

Results

Of the evaluated tumors, 32 were IDH-wildtype and 67 were IDH-mutated. Lower grade gliomas with IDH-wildtype status showed a significantly lower incidence of cortical involvement ($p < 0.005$) and lower apparent diffusion coefficient (ADC) values ($p < 0.005$). No significant difference was observed in other qualitative characteristics or in quantitative perfusion measures. Multiple logistic regression analysis showed cortical involvement and minimum ADC values as independent predictors of IDH-wildtype LGG. Receiver operating characteristic showed a minimum ADC threshold value of 1.0×10^{-3} mm²/s provided a sensitivity of 94% and a specificity of 64% in classifying IDH mutation status. IDH-wildtype LGGs were associated with significantly decreased time to progression and overall survival relative to IDH-mutated LGGs.

Conclusions

IDH-wildtype LGGs are associated with lower ADC values and lack of cortical

involvement on MR examination and with a clinically aggressive phenotype.
Minimum ADC values with a threshold of less than or equal to $1.0 \times 10^{-3} \text{ mm}^2/\text{s}$ may be predictive of IDH-wildtype LGGs.

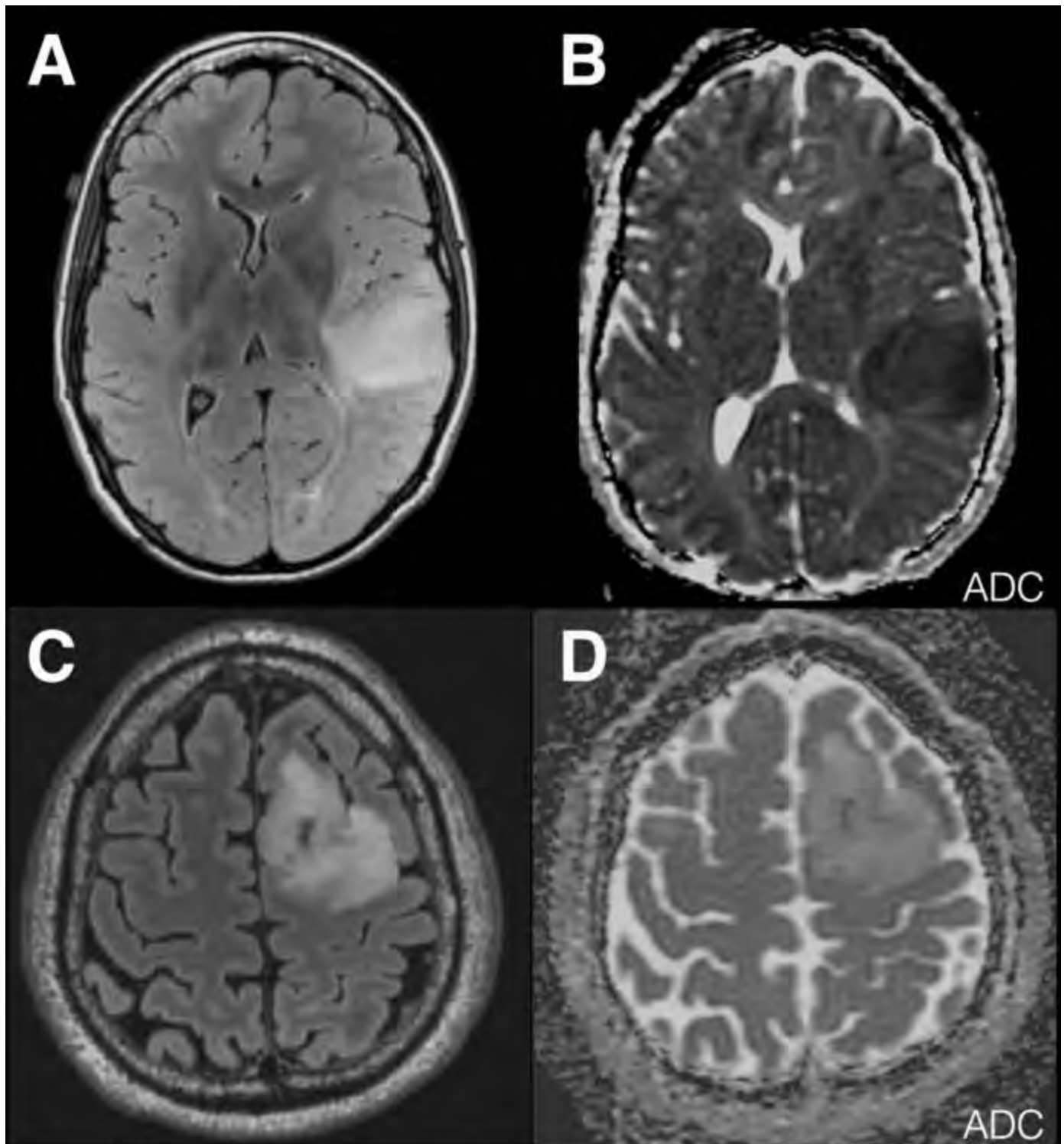


Figure 1. 19-year-old woman presenting with stroke symptoms (A, B). Axial FLAIR (A) and ADC map (B) MR images demonstrate an infiltrative left temporal mass with low signal on ADC map. At pathology this represents an IDH-wildtype lower grade glioma.

55-year-old man presenting with seizures (C, D). Axial FLAIR (C) and ADC map (D) MR images demonstrate an infiltrative left frontal mass with high signal on ADC map. At pathology this represents an IDH-mutant lower grade glioma.

(Filename: TCT_O-114_ASNR_2016_Abstract_Image.jpg)

O-115

3:36PM - 3:39PM

Radiomics differentiate between true progression and pseudoprogression in GBM patients.

S Abrol¹, G Thomas², A Hassan³, A Kotrotsou¹, P Zinn⁴, R Colen¹

¹MD Anderson Cancer Center, Houston, TX, ²The University of Texas MD Anderson Cancer Center, Houston, TX, ³MD Anderson cancer center, HOUSTON, TX, ⁴Baylor College of Medicine, Houston, TX

Purpose

The benign imaging changes that occur as a result of radiation therapy often are difficult to distinguish from true progression of the tumor. Pseudoprogression (PsP) can potentially complicate the management of the patients if mistaken for treatment failure. This study was conducted to assess the potential of radiomics to differentiate PsP from true progression (PD) of brain tumors with histopathological evidence.

Materials and Methods

We evaluated 100 brain tumor patients retrospectively, with new or increased enhancement after surgical resection of primary tumor followed by radiation therapy uncertain for PsP versus true progression. All patients had undergone biopsy or resection with histopathological evidence of PsP or recurrent tumor. Volumetrics and texture analysis were performed of the enhancing lesion(s) in question. Demographics were collected. Gene expression was determined and relationship to enhancement pattern was studied.

Results

Eighty patients had histopathological evidence of PD and 20 evidence of PsP. There were five texture features that predicted whether a patient had Psp or PD. The ability to discriminate between the two was 97%. The sensitivity and specificity was 90% and 86%, respectively. Patients with PsP had higher methylation of MGMT

Conclusions

Radiomic analysis has the ability to discriminate between those patients with Psp versus recurrent tumor in those patients with increase or new enhancing lesions.

O-116

3:39PM - 3:42PM

Radiographic patterns of progression with associated outcomes after bevacizumab therapy in glioblastoma patients

N Elshafeey¹, D Cachia², M Hatami¹, C Kamiya Matsuoka¹, K Alfaro-Munoz¹, J Mandel³, J de Groot,¹ R Colen¹

¹MD Anderson Cancer Center, HOUSTON, TX, ²Medical University of South Carolina, Charleston, SC, ³Baylor College Medicine, HOUSTON, TX

Purpose

To determine the radiographic patterns of progression and their association with outcome. Patterns of progression following bevacizumab (bev) treatment and associated outcomes remain poorly characterized in patients with glioblastoma (GB).

Materials and Methods

Sixty-four patients treated at MD Anderson matched the predetermined inclusion criteria. Tumor progression after bev treatment was assessed according to the RANO criteria and patients categorized into groups based on previously published data: Group 1: exclusively T2-diffuse hyperintense tumor (T2-diffuse), Group 2: initial decrease and subsequent flare-up of contrast enhancement (CE) at progression (cT1 Flare-up), Group 3: no decrease in CE or development of new lesions at first follow-up imaging (nonresponders), Group 4: exclusively T2-circumscribed hyperintense tumor progression (T2-circumscribed). In addition, we screened for new diffusion-restricted lesions or precontrast T1-hyperintense lesions or both (double-positive).

Results

Patients were categorized into Group 1: 11%, Group 2: 33%, Group 3: 45%, Group 4: 11%. Sixteen patients had T1-hyperintense lesions and 37 had restricted diffusion; 10 patients had double-positive lesions. There was no significant difference in time-to-initiation of Bev treatment in the four groups. After starting Bev, median OS and PFS (months) was Group 1: 8.6, 4.2; Group 2: 12.3, 3.9; Group 3: 5.6, 1.4; Group 4: 7.0, 3.2 respectively. Comparing nonresponders versus the rest of the groups (responders), OS from initiation of Bev was 5.6 versus 10 months ($p < 0.001$). OS from diagnosis of GB was not significantly different between the four groups. Postprogression on Bev, OS was: Group 1: 3.9; Group 2: 6.4; Group 3: 3.8 and Group 4: 3.0. Patients with restricted diffusion had worse OS (23.4 versus 7.4 months). There was no difference in survival based on presence/absence of T1-hyperintense or double-positive lesions.

Conclusions

Compared to nonresponders, cT1 Flare-up have better PFS/OS after Bev initiation. Postprogression on Bev, cT1 Flare patients lived significantly longer than T2-diffuse and nonresponders. Though T2-diffuse and T2-circumscribed have a better PFS after Bev initiation compared to nonresponders, no OS benefit was seen. Restricted diffusion was a radiographic marker of worse outcomes.

O-118

3:45PM - 3:48PM

Quantitative Features of High-grade Gliomas Predictive of Treatment Response to Anti-PD-1 Immunotherapy

P Chang¹, A Dubey¹, F Iwamoto¹, A Lassman¹, A Lignelli¹

¹*Columbia University Medical Center, New York City, NY*

Purpose

Anti-PD-1 immunotherapy agents represent a promising new drug class in treatment of high-grade gliomas (HGG) (1-3). Given recent introduction of these agents into clinical trials, there are, to date, no known quantitative magnetic resonance (MR) tumor features associated with treatment success. Such prognostic features may be used as imaging criteria to guide future patient selection.

Materials and Methods

As part of an IRB-protocol, HGG patients receiving an anti-PD-1 monoclonal antibody (Nivolumab or Pembrolizumab) for at least two treatment sessions were identified. Treatment response was determined by new immunotherapy-RANO guidelines (4), including a minimum 3-month confirmatory exam in cases of disease progression. Based on iRANO criteria, patients were labeled as nonresponders (progression) and responders (stable or response for minimum of 3 months). A fully automated software algorithm was used to quantify absolute volume of contrast-enhanced tumor (CET), relative volume of CET with respect to FLAIR abnormality, necrosis and peritumoral FLAIR abnormality, as well as enhancement avidity and margin irregularity. Significance was assessed with a two-tailed t-test. All segmentation masks were inspected for accuracy by a board-certified neuroradiologist blinded to results.

Results

A total of 13 patients met inclusion criteria: six nonresponders and seven responders to PD1-immunotherapy. Prior to immunotherapy, PD1-responders demonstrated larger absolute (58.3 versus 21.8 cm³, p=0.021) and relative (31% versus 20%, p=0.0054) volumes of CET. A trend towards significance was seen for larger initial total tumor volume (165 versus 118 cm³, p=0.089) and greater initial enhancement avidity (2.5 versus 1.9, p=0.25) of PD1-responders in this small sample size. Necrosis, peritumoral FLAIR and margin irregularity were insignificant predictors of treatment response.

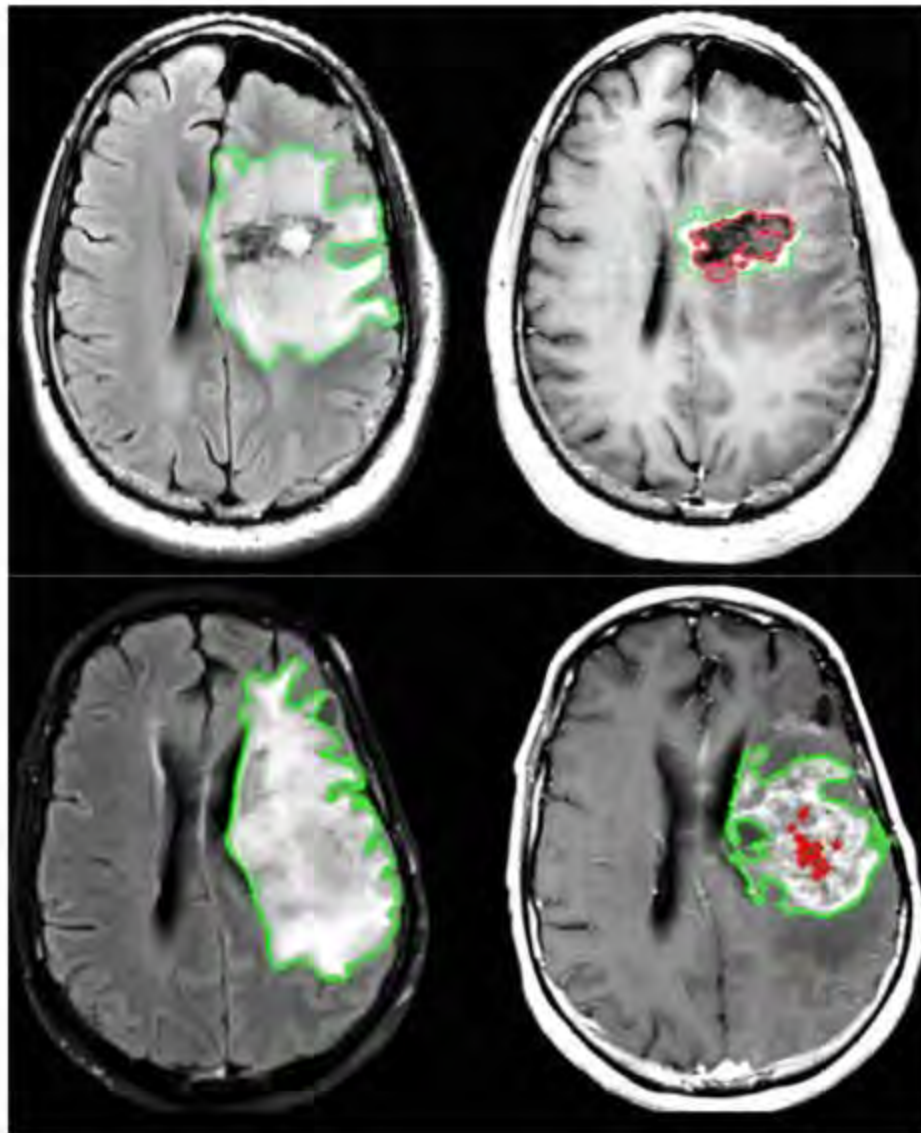
Conclusions

Preliminary data suggests that absolute and relative proportion of enhancing tumor prior to initiation of anti-PD-1 immunotherapy were predictors of good response, with a threshold of >25% CET associated with 86% sensitivity and 100% specificity in this small sample size. These findings may suggest an association between programmed-death (PD-1) ligand expression and contrast enhancement. One hypothesis for this finding may be found in studies showing lower PD-1 expression with proneural GBM

(1), a molecular subtype associated with lower CET (5). Currently we have not included clinical response criteria in our analysis, nor have we accounted for concomitant therapies and their effects. Further analysis of clinical response criteria and effects of concomitant therapies will follow.

Figure 1. Imaging Appearance of Anti-PD-1 Therapy Non-Responders and Responders

Axial FLAIR (left) and post-contrast (right) images in two representative patients: one anti-PD-1 therapy non-responder (top; minimal contrast enhancement) and one responder (bottom; significant contrast enhancement). On the left, FLAIR masks are outlined in green. On the right, contrast-enhancing margins (green) and necrosis (red) masks are outlined.



(Filename: TCT_O-118_Figure.jpg)

Monday

3:00PM - 4:36PM

Washington Marriott Wardman Park, Maryland A/B/C

**5E-PARALLEL PAPER SESSION: Head & Neck: Skull Base and Temporal Bone
O-119**

3:00PM - 3:08PM

**Application of Iterative Reconstruction Algorithms to Perform Sub-millisievert
CT of the Facial Bones and Paranasal Sinuses**

A Tabari¹, S Singh¹, s Rincon², P Caruso², d singh², M Gee¹

¹Massachusetts General Hospital, Boston, MA, ²MGH, Boston, MA

Purpose

Computed tomography (CT) radiation dose optimization is crucial for children. Several dose reduction strategies are available, including tube current modulation, lowering of tube potential based on body size as well as newer iterative reconstruction (IT) algorithms. Since the 1970s, filtered back projection (FBP) algorithm has been used in all commercial CT scanners for reconstructing CT images. For the past several years, newer IR algorithms have been introduced to lower CT dose with cautious selection of settings to fine tune image quality. The purpose of this study was to evaluate pediatric para-nasal CT image quality and dose reduction with IR, as compared to FBP.

Materials and Methods

Our study was HIPPA compliant and written informed consent was waived by the IRB. All consecutive pediatric para-nasal sinus CT performed on IR capable scanner [Discovery 750 HD with Adaptive Statistical Iterative Reconstruction (ASIR), GE Healthcare] were included in the study cohort; the control group was comprised of FBP images. Effective dose was calculated as per the ICRP103 guidelines. Detailed subjective image quality including image noise, sharpness of bony edges, and visibility of nasal septum, middle turbinate, lamina papyracea, cribriform plate, optic nerve, inferior rectus muscle, and ocular globe were defined on a scale from 1 (unacceptable noise, nondiagnostic) to 5 (excellent image quality, best diagnostic value). In addition, objective image noise (standard deviation of HU values) and contrast to noise ratio (CNR) was measured in the axial plane for the right globe (vitreous), right masseter muscle, and in air within the center of the right maxillary sinus. Statistical analysis was performed with the Student's t-test.

Results

The study cohort, included 97 para-nasal CT examinations performed on 60 children

(average age, 12.0 ± 4.0 years; F:M 28:32) with IR capable scanner (ASIR), whereas the control group included 13 para-nasal CT examinations (average age 10.7 ± 5.0 , M:F 2:8) with standard FBP reconstruction. There was no significant difference between ASIR and FBP for age and facial diameter (14.2 ± 2 cm compared to 14.5 ± 2 cm) ($p = 0.05$, $p = 0.05$, respectively). Clinical indications for para-nasal sinus or facial CT included; lump or mass ($n=39$), difficulty opening mouth ($n=12$), developmental jaw deformity ($n=11$), and osteosarcoma ($n=7$). ASIR algorithm was set at 90% settings (available from 10-100% with 10% increments). ASIR90 resulted in 73% reduction in CT radiation dose (CTDIvol 5.5 ± 7.2 mGy, DLP 91.6 ± 120.0 mGy.cm, 0.2 mSv), as compared to FBP (20.2 ± 13.1 mGy, 320.1 ± 170.6 mGy.cm, 1 mSv, respectively) ($p < 0.001$). Objective image noise measured at the masseter and maxillary sinus air on ASIR90 images was found to be similar as FBP ($p = 0.5-0.6$). In addition, contrast to noise ratio (CNR) was not affected with ASIR90%, when compared to FBP ($p = 0.67$).

Conclusions

Para-nasal sinus CT can be performed with 70% reduced radiation dose with iterative reconstruction algorithms without affecting image quality.



Figure 1:

Axial and Coronal face CT images acquired at low-dose reconstructed with ASIR 90% technique (A1, A2) and Standard-dose with FBP (B1, B2) in a 5 year-old boy with right intraorbital subperiosteal abscess (yellow arrows).

Low-dose scan was performed at a radiation dose of 0.51 mSv (CTDI_{vol}: 8.2 mGy) as compared to the effective dose of 0.78 in Standard-dose scan (CTDI_{vol}: 14.6) mGy.

(Filename: TCT_O-119_Face-CT.jpg)

O-120

3:08PM - 3:16PM

**Cracking the Code of Temporal Bone and Skull Base Anatomy with 3D Printing:
A Conceptual Approach**

R Javan¹, A Abdelazim²

¹George Washington University Hospital, Washington, DC, ²The George Washington University Hospital, Washington, DC

Purpose

The purpose of this exhibit is to utilize 3D printing to conceptually simplify understanding the complex three-dimensional anatomy and neurovascular contents of the temporal bone and skull base as they pertain to neuroradiologists.

Materials and Methods

The temporal bone and skull base along with their subsections and their contents, including the middle ear, pterygopalatine fossa, petrous apex, middle cranial fossa, Meckel's cave and cavernous sinus are represented as cube-shaped rooms and their communications as hallways, doors and windows. A 3D printed model then is created with its 'rooms' having been de-roofed. This approach simplifies the three-dimensional understanding, by providing an alternative method of visualization from within the cavity itself and identifying structures as isolated objects. Initially, simple computer enhanced hand-drawn illustrations were created with proper perspective view to provide the 'big picture'. Subsequently, graphics design software, Autodesk 3D Studio Max 9.0, was used to create volumetric meshes of the conceptualized structures. The middle ear structures include the ossicles, scutum, chorda tympani nerve, facial canal, tensor tympani, cochlear promontory, round and oval windows, tympanic membrane, tympanic canaliculus, aditus ad antrum, facial recess, sinus tympani and pyramidal eminence surrounded by internal carotid artery, internal jugular vein, facial nerve and inner ear elements. The petrous apex, Meckel's cave and cavernous sinus contents emphasize the relative location of the cranial nerves with respect to anatomical landmarks such as the petroclinoid ligament and cavernous ICA. The pterygopalatine fossa has the surrounding connections of pterygomaxillary and superior orbital fissure, sphenopalatine foramen and the palatine canals which connect via the foramen of rotundum and vidian canal to the middle cranial fossa containing the foramina of ovale and spinosum as well as the petrous portion of the carotid canal.

Results

An enlarged physical model of the temporal bone and skull base was created with individual structures portrayed conceptually for the specific use of teaching complex anatomy. The incredible customizability that 3D printing technologies afford the radiologist in designing educational tools is discussed.

Conclusions

An alternative approach to learning the intricate three-dimensional anatomy of temporal bone and skull base was designed as a bridge between anatomy books and cross-sectional imaging. A detailed understanding of the specific anatomical spaces and structures is a crucial first step in identifying and distinguishing pathologic conditions by neuroradiologists. The necessary software and the available options for acquiring 3D models also are discussed.



(Filename: TCT_O-120_IMG_0240.JPG)

O-121

3:16PM - 3:24PM

In Pediatric Patients with Hypoplastic Internal Auditory Canals, What is the Utility of Thin-Section T2-Weighted Imaging to Determine the Contents of the IAC?

N Emmanuel¹, E Kari², J Go³

¹University of Southern California, Los Angeles, CA, ²Keck USC School of Medicine, Los Angeles, CA, ³LAC/USC Medical Center, Los Angeles, CA

Purpose

Hypoplastic internal auditory canals (IACs) may be found in a subset of pediatric patients being evaluated for cochlear implant (CI). Both computed tomography (CT) and magnetic resonance (MR) imaging have become routinely used to evaluate CI as a viable option. For assessment with high resolution T2-weighted images, there should be sufficient CSF in the IAC to evaluate the VIIth/VIIIth nerve complex. To date, it has not been reported if CT and MR are both necessary for assessment of hypoplastic internal auditory canals. The focus of this abstract is to determine if there is a numeric threshold of the internal auditory canal diameter that may be obtained on imaging below which MR will not be able to yield diagnostic information.

Materials and Methods

Twelve patients with hypoplastic IACs were reviewed retrospectively. The maximal measurement of the IAC midpoint was obtained. Magnetic resonance was used to determine if there was sufficient CSF within the IAC to assess the VIIth/VIIIth nerve complex.

Results

If the maximal measurement of the IAC midpoint is 2.18 mm or less, the VIIth/VIIIth nerve complex cannot be assessed on MR.

Conclusions

Based on a retrospective review of children with hypoplastic IACs for cochlear implant, there is a numeric threshold (2.18 mm) below which the VIIth/VIIIth cranial nerve complex cannot be assessed on MR, and MR should not be obtained. This data may result in reduced costs, optimal resource utilization and not subjecting pediatric patients to risks associated with sedation for these imaging examinations. Further research should be employed to optimize MR pulse sequences to obtain clinically useful information in the shortest time possible.

O-122

3:24PM - 3:32PM

Detecting Meniere's disease in conventional MRI scans using radiomics

E Burg vd¹, M Hoof¹, A Postma², M Janssen³, R Stokroos⁴, H Kingma⁴
¹MUMC+, Maastricht, none, ²MUMC+, Maastricht, Netherlands, ³Maastricht University, Maastricht, none, ⁴MUMC+, maastricht, none

Purpose

Meniere's disease is a disorder of the inner ear, which is characterized by recurrent attacks of vertigo. Currently it remains difficult to differentiate between different causes of dizziness. Cone beam computed tomography (CT) or magnetic resonance imaging (MRI) enhanced by invasive contrast agents such as gadolinium nowadays are investigated as a possible diagnosis for Meniere's disease. Here, an alternative approach is taken using readily available and conventional MRI scans. Lately, the evidence is increasing that with new imaging processing and analysis techniques, more information can be gathered from standard imaging modalities. This so-called radiomics approach does not necessarily rely on features perceptually visible by the (neuro)radiologist, but it instead relies on the extraction and analysis of quantitative image features. The main objective of this pilot study was to investigate whether a quantitative image analysis of the labyrinth in conventional MRI scans using a radiomics approach showed differences between patients with Meniere's disease and the control group.

Materials and Methods

Magnetic resonance imaging scans of the affected labyrinths of 24 patients with Meniere's disease were compared to the MRI scans of labyrinths of 29 patients with an asymmetrical sensorineural hearing loss (best hearing side). The 1,5T and 3T MRI scans previously had been made in a clinical setting, without contrast enhancement. 3D Slicer 4.4 (<http://slicer.org>) was used to extract several substructures of the labyrinth from the original MRI scans. A quantitative analysis of the normalized radiomic image features was performed in Mathematica 10 (Wolfram Research). The image features of the two groups were compared statistically.

Results

In numerous image features, there was a statistically significant difference between the Meniere's disease group and the control group. These differences were localized in all substructures of the labyrinth (the cochlea, the area containing the reuniting duct and the semicircular canals).

Conclusions

A quantitative analysis of the labyrinth on conventional MRI scans shows statistically significant differences between patients with Meniere's disease and the control group. This demonstrates that there is a difference between the two groups in the distribution of the intensities on MRI.

O-123

3:32PM - 3:40PM

Detection of Endolymphatic Hydrops in Meniere's Disease Using Traditional MR Imaging Sequences

J Keller¹, B Branstetter¹

¹University of Pittsburgh Medical Center, Pittsburgh, PA

Purpose

To determine whether Meniere's disease (MD) is detectable using unenhanced T2-weighted MR sequences by comparing endolymphatic and perilymphatic spaces in the inner ear.

Materials and Methods

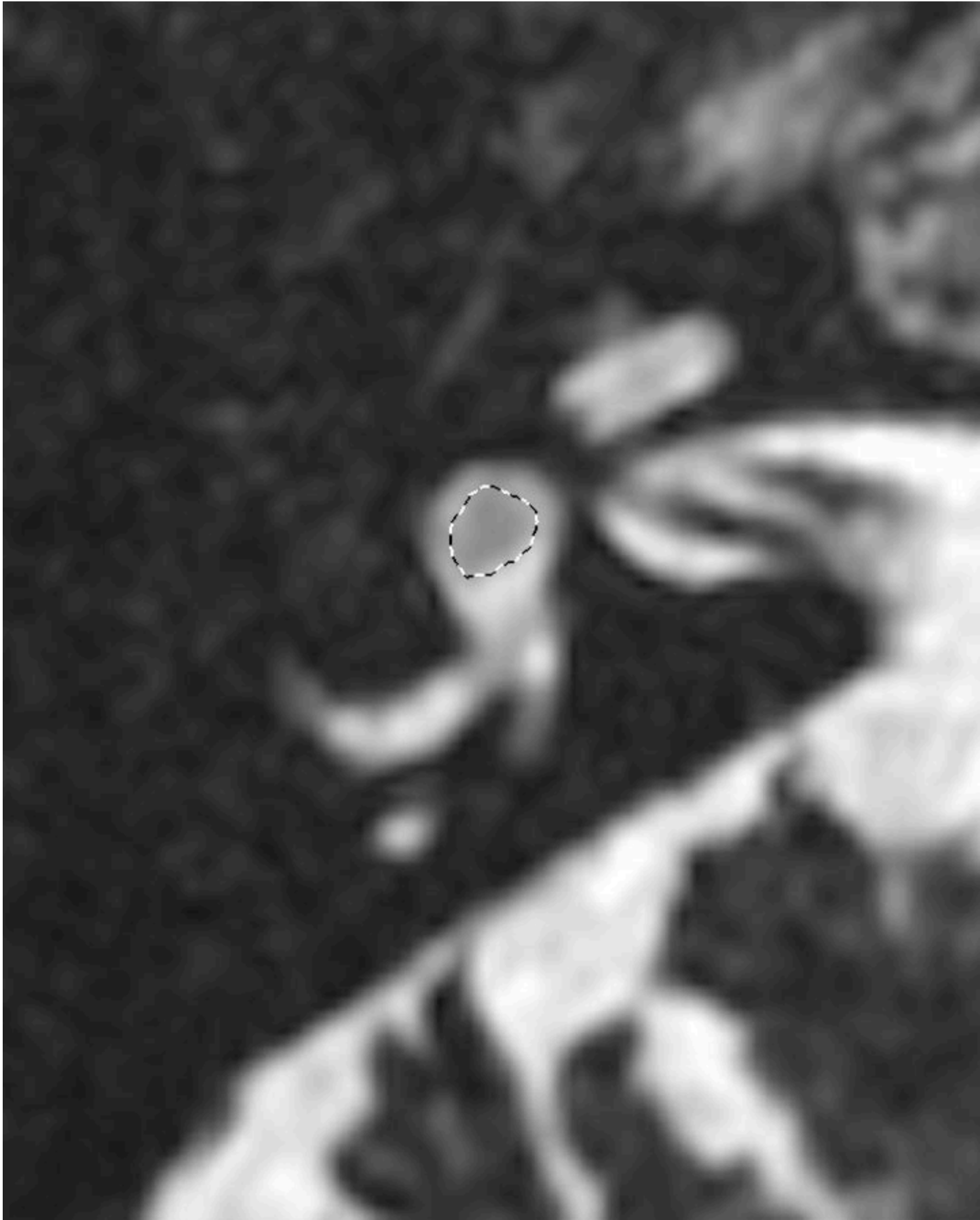
We identified patients with documented MD who had a high-resolution T2-weighted or SSFP MRI of the temporal bones within 1 month of diagnosis. Patients were compared to age- and sex-matched controls. Cross-sectional area, maximum length, and maximum width of the bony vestibule and utricle were measured in all imaged ears along with the width of the basal turn of the cochlea and its contained endolymphatic space. Absolute values and ratios of endolymph to perilymph size were compared across affected, contralateral, and control ears using analysis of variance and post-hoc pairwise comparisons.

Results

Eighty-five case-control pairs were enrolled in this study. Mean utricle areas for affected, contralateral, and control ears were 0.038 +/- 0.012 cm², 0.037 +/- 0.11 cm², and 0.033 +/- 0.009 cm², respectively. Mean utricle-to-vestibule area ratios for affected, contralateral, and control ears were 0.32 +/- 0.07, 0.32 +/- 0.08, and 0.29 +/- 0.07, respectively. There was a statistically significant difference between groups as determined by one-way ANOVA: for utricle area, $F(2, 337) = 9.44$, $p = 0.0001$, and for utricle-to-vestibule ratio, $F(2, 337) = 11.2$, $p = 0.00002$. Post-hoc comparisons revealed no difference between affected and contralateral ears in Meniere's patients, while control ears were different from both affected and contralateral ears in the patients with MD. All other measurements failed to show a significant difference between groups.

Conclusions

Increases in utricle area and utricle-to-vestibule area ratios in MD can be detected using conventional high-resolution T2-weighted MR sequences. This data support the use of MRI as a diagnostic tool in the evaluation of suspected MD and suggests that the use of intratympanic contrast may be unnecessary.



(Filename: TCT_O-123_Utriclelasso.jpg)

O-124

3:40PM - 3:48PM

Skull Base Hemangioma Masquerading as Vascular Tumors

D Landry¹, C Glastonbury²

¹*University of Montreal, Montreal, Quebec,* ²*University Of California, San Francisco, San Francisco, CA*

Purpose

Vertebral body "hemangiomas" are common benign bone lesions which, in most cases, are incidental and require no follow up or intervention. When they occur in the skull base, they can be readily confused with vascular bone tumors including jugular paraganglioma. We present the imaging findings of six patients with these vascular lesions.

Materials and Methods

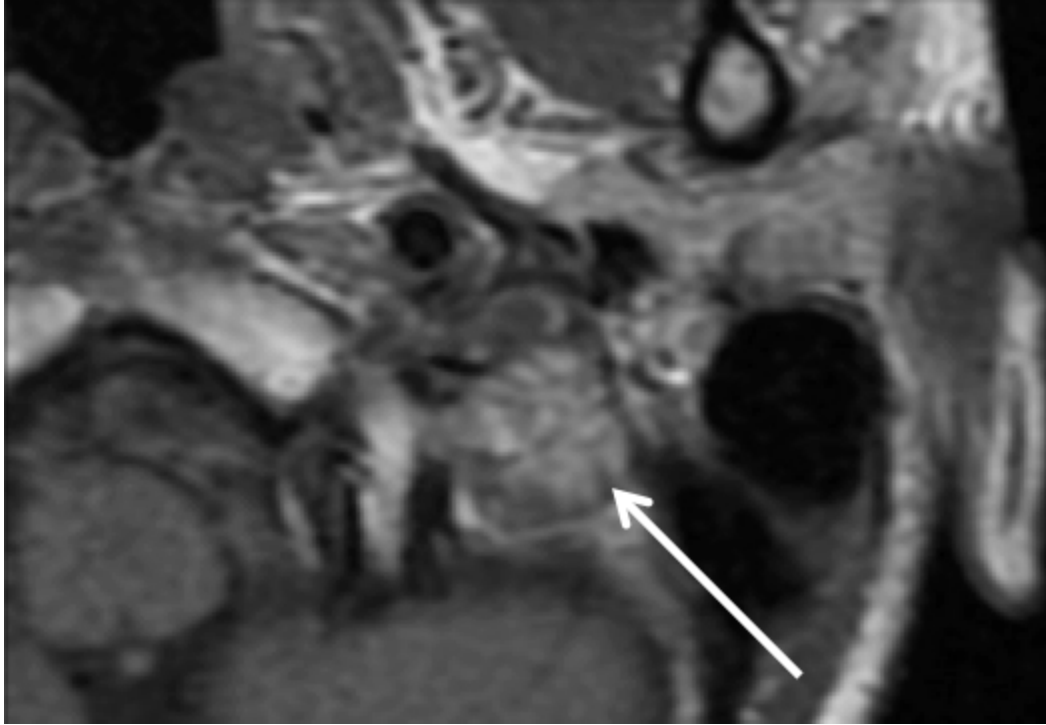
We report six cases, collected between June 2014 and November 2015, at two institutions where these skull base lesions caused diagnostic consternation.

Results

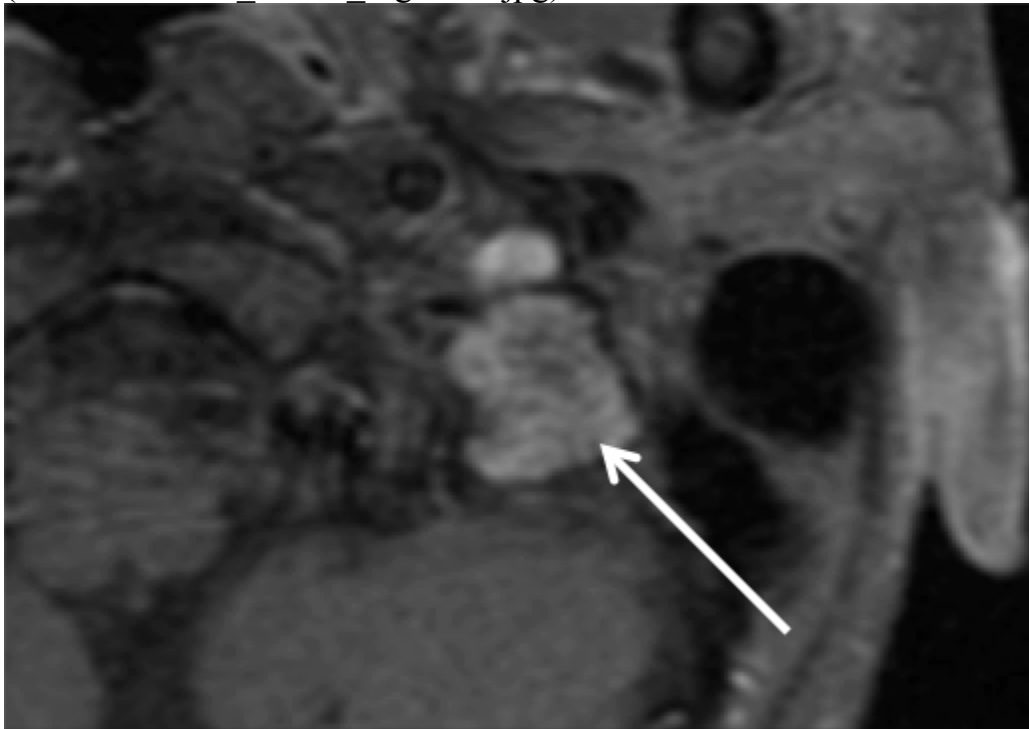
Intra-osseous hemangiomas are benign vascular malformations and are recognized most frequently in the vertebral bodies and calvaria (1). These cavernous hemangiomas typically have a "polka-dot" appearance on high-resolution computed tomography (CT) due to trabeculae and show T2 hyperintensity and avid enhancement on magnetic resonance imaging (MRI). Jugular paraganglioma, or glomus tumors, usually are confined to the jugular foramen but erode adjacent bone, producing a moth-eaten appearance. Because of their increased vascularity and propensity to bleed, they often have a salt-and-pepper appearance on T1 MRI. Differentiation between hemangioma and vascular masses such as paraganglioma on MRI can be challenging, however, high-resolution CT can clarify the intraosseous location and the absence of bone destruction (2, 3) (Figs. 1a-d).

Conclusions

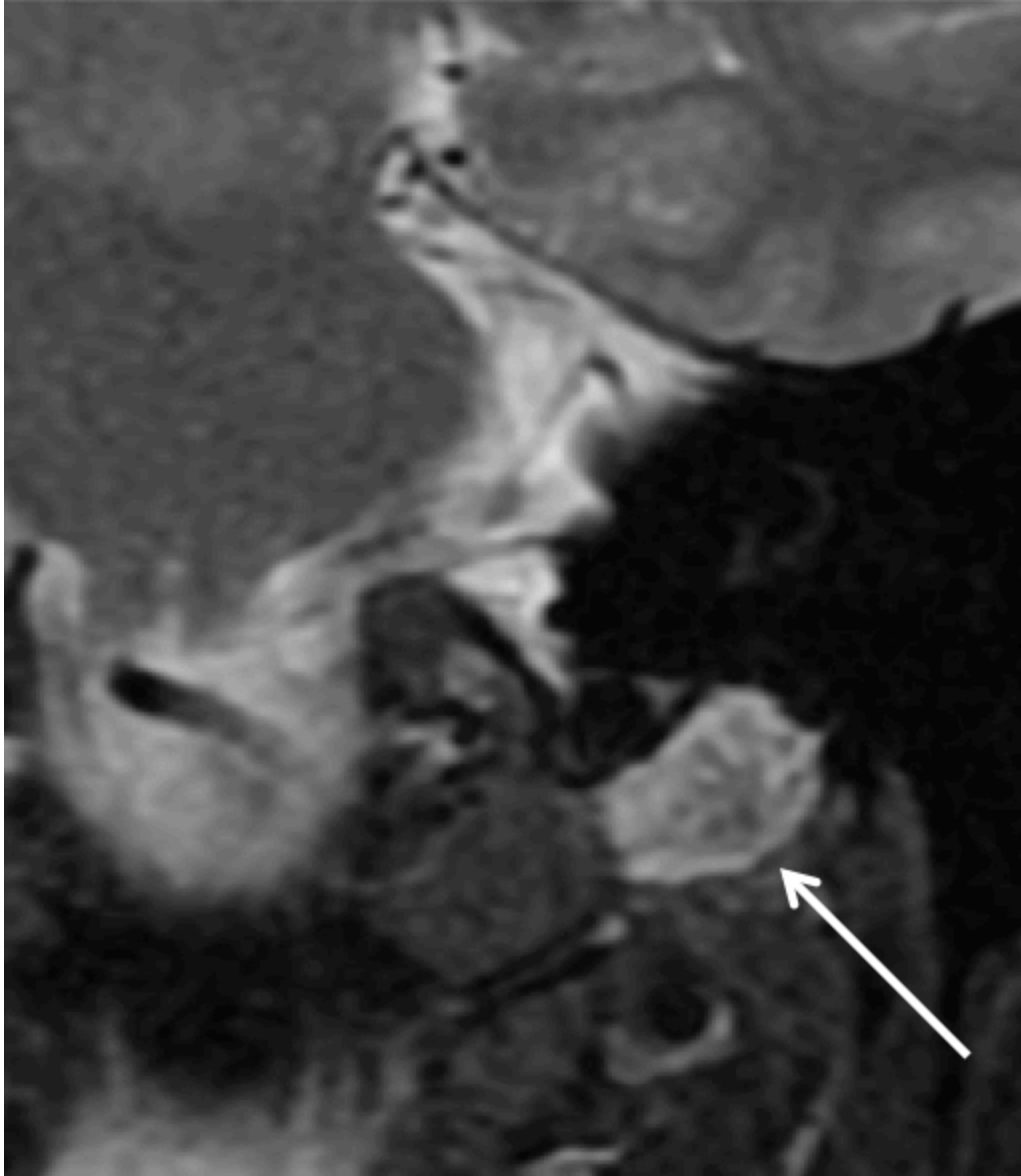
Hemangiomas can occur in the skull base bone as well as the well recognized calvarial and vertebral body locations and, on MRI, may mimic vascular tumors including jugular paraganglioma. Skull base CT scan is a valuable tool to differentiate a benign vascular lesion from an erosive tumor.



(Filename: TCT_O-124_Figure1d.jpg)



(Filename: TCT_O-124_Figure1c.jpg)



(Filename: TCT_O-124_Figure1b.jpg)



(Filename: TCT_O-124_Figure1a.jpg)

O-125

3:48PM - 3:56PM

Dural Metastases: A Form of Recurrence in Uncommon Sinonasal Malignancies

R Valenzuela¹, L Ginsberg², R Riascos³, M Ramirez⁴, D Ruiz⁵, D Shatzkes⁶, C Sitton⁵, M Michel⁷, L Loevner⁸, E Hanna⁹

¹The University of Texas, Houston, TX, ²MD Anderson Cancer Center, Houston, TX, ³UTHSC-Houston, Houston, TX, ⁴The University of Texas Health Science Center at Houston. Department of diagnostic and intervention, Houston, TX, ⁵The University of Texas Health Science Center at Houston UTHealth, Houston, TX, ⁶Lenox Hill Hospital, New York, NY, ⁷Medical College Of Wisconsin/Froedtert Hosp., Milwaukee,

WI, ⁸University of Pennsylvania, Philadelphia , PA, ⁹UT MD Anderson Cancer Center, Houston, TX

Purpose

Demonstrate dural metastases (DM) as an unusual form of tumoral spread, from treated sinonasal malignancies. Show the different imaging presentations of DM arising from primary sinonasal malignancies.

Materials and Methods

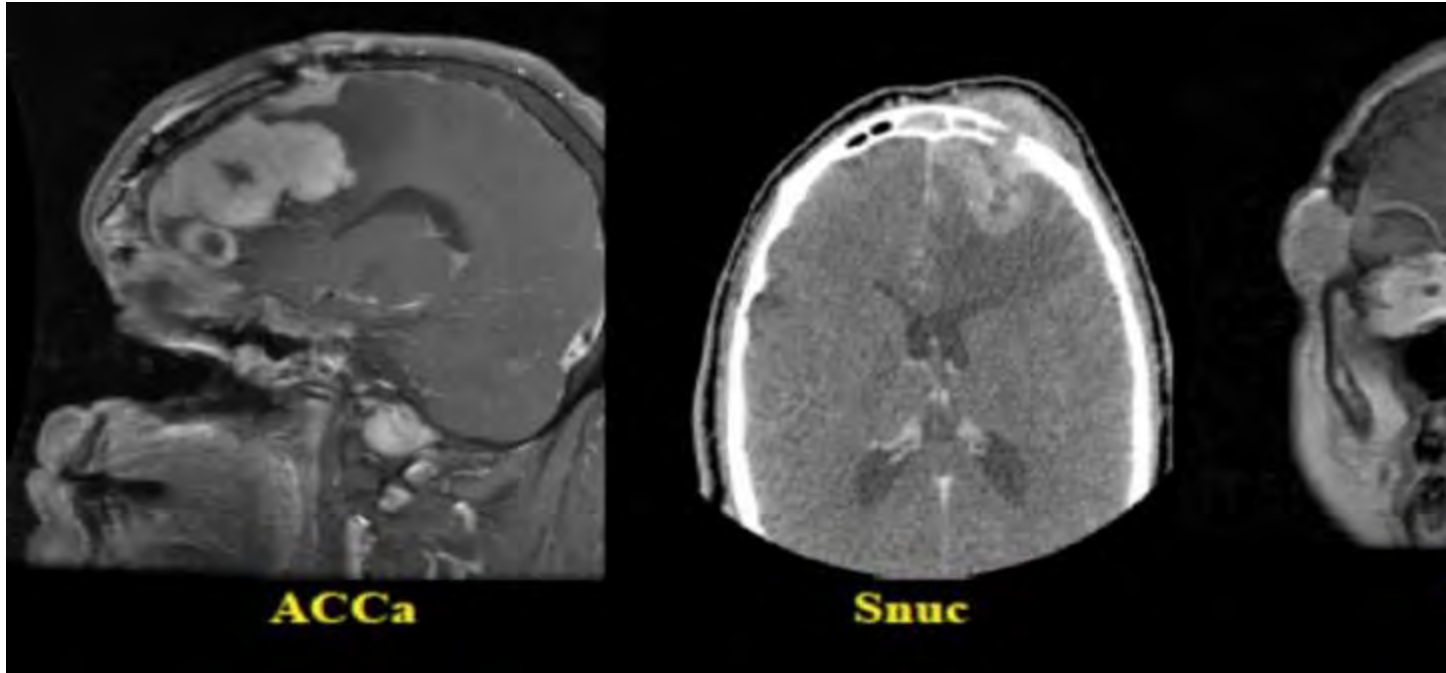
A review of 20 DM cases diagnosed during routine postoperative follow-up imaging is presented, occurring on a group of sinonasal malignancies, treated by anterior craniofacial resection (CFR).

Results

Dural metastases was observed in 12 cases of sinonasal undifferentiated carcinoma (SNUC), seven olfactory neuroblastoma (ONB) and one adenoid cystic carcinoma (ACCa). Dural metastases appeared on an average 7.3 years after treatment on ONB. The maximum DM size was 4.3 cm on SNUC and 2.5 cm on ONB. The maximum distance from primary tumor to DM was 7.9 cm for ONB and 4.3 cm for SNUC. Dural metastases was observed at the Burr Hole on 50% of SNUC and 29% ONB. Dural metastases presented as nodular, multinodular, cystic or plaque pattern, 75% presented nodular form and 43% the cystic form.

Conclusions

Dural metastases may arise from direct extension or hematogenous spread. With the exception of one case published of dural metastases related to ONB, reported by Bogucki, et al. we are not aware of any sinonasal malignancies DM-related series. Sinonasal malignancies represent a small proportion of head and neck tumors, in which 80% accounts for squamous cell carcinoma (SCC) and 10% for ACCa. Less common malignancies includes SNUC and ONB. The presence of a cystic DM was observed only in relation to ONB. A local mechanism could be considered in the DM development, involving the dural venous plexus as a pathway of tumor spread, when surgical or tumoral ACF breach is present. Dural metastases is an unusual form of sinonasal malignancies spread. There are different forms of DM spread, shown on MR imaging. Dural metastases is associated with unusual malignancies other than SCC, in which brain MR could be necessary as complement in the follow up.



(Filename: TCT_O-125_DMSinonsalTU.jpg)

O-126

3:56PM - 4:04PM

Radiographic Findings in Primary Intraosseous Meningiomas: 9 Patients with Operative and Pathologic Confirmation

B Iorgulescu¹, J Tung², R Crotty³, S Sood⁴, T Smith¹

¹*Brigham and Women's Hospital, Harvard Medical School, Boston, MA*, ²*Harvard Medical School, Boston, MA*, ³*Massachusetts General Hospital, Harvard Medical School, Boston, MA*, ⁴*Boston Children's Hospital, Harvard Medical School, Boston, MA*

Purpose

Primary intraosseous meningiomas represent an exceedingly rare subtype of both primary extradural meningiomas and osseous lesions, with unclear radiographic features and outcomes.

Materials and Methods

Radiographic details and clinical course were examined for all patients with a diagnosis of intraosseous meningioma from Partners Healthcare hospitals, confirmed by pathologic and operative findings. Patients with dural-based lesions that demonstrated intraosseous involvement were excluded.

Results

Nine patients had a diagnosis of primary intraosseous meningioma, as confirmed by radiographic, pathologic, and operative findings. Five presented with neurologic

deficits, two presented with asymptomatic physical changes, and two were diagnosed incidentally; at a median lesion size of 3.0 cm in greatest dimension (range 1.8 - 6.0 cm). Primary intraosseous meningioma demonstrated a predilection for calvarium and sphenoid wing, and often manifested radiographically as homogenous expansile ground-glass calcific densities with well marginated bony excrescences into neighboring soft tissues and irregular cortical margins. Approximately half of lesions demonstrated sclerotic features on computed tomography (CT), whereas the remainder displayed lytic changes; with isointense to mildly-hypointense T1 sequence features on magnetic resonance imaging (MRI). In most cases initial CT impressions often favored metastasis, although integration with MRI findings highlighted meningiomas in the differential.

Conclusions

Primary intraosseous meningiomas represent a rare benign skull lesion with mixed CT features, whose diagnosis markedly benefits from the integration of CT and MRI findings and should be remembered in the differential for slow-growing expansile intraosseous lesions of the skull.

O-127

4:04PM - 4:12PM

Unusual Extramedullary Plasmacytoma of the Head and Neck: A Case Series

M Labib¹, P Som¹

¹*Icahn School of Medicine at Mount Sinai, New York, NY*

Purpose

Extramedullary plasmacytomas are immunoglobulin-secreting neoplasms that arise from a monoclonal proliferation of plasma cells. Nearly 80% of these tumors arise in the head and neck and the risk of developing multiple myeloma in these patients is between 33.3%-50% (1, 2). These tumors also may occur in an intramedullary location and they can develop as isolated lesions or as part of multiple myeloma.

Overall, plasmacytomas are uncommon tumors, with extramedullary plasmacytoma (EP) representing less than 1% of all malignancies of the head and neck (3).

Additionally, these tumors tend to occur in unusual locations and demonstrate a varied appearance on imaging (4). As such, plasmacytomas tend to pose a diagnostic challenge. The successful head and neck radiologist should be familiar with their typical imaging characteristics in order to successfully identify these lesions should they arise.

Materials and Methods

A retrospective review of the magnetic resonance imaging (MRI) and computed tomography (CT) examinations of the head and neck performed at our institution was conducted over the past 5 years. Attention was given to patients with a known

diagnosis of multiple myeloma and to those with imaging findings suggestive of the diagnosis.

Results

Six patients were identified with both a histological diagnosis of multiple myeloma and the presence of plasmacytoma in the head and neck. Among these cases, extramedullary plasmacytomas were identified localizing to the parapharyngeal space, the masticator space, the orbit, the antrum, and the larynx. An intramedullary plasmacytoma also was identified at the mandible. The imaging appearance of each of these lesions was reviewed in turn.

Conclusions

Given their infrequency and varied imaging appearance, plasmacytomas of the head and neck pose a diagnostic challenge. We describe six cases of plasmacytoma of the head and neck, reviewing the imaging characteristics of each lesion in turn. Through this review we highlight some of the common locations and imaging characteristics of this uncommon disease.

O-128

4:12PM - 4:20PM

Migration of Bone Wax into the Dural Venous Sinuses Following Posterior Fossa Surgery

K Byrns¹, A Khasgiwala¹, S Patel¹

¹NYU Langone Medical Center, New York, NY

Purpose

Bone wax is a biologically inert mixture of beeswax, paraffin, and a wax-softening agent that commonly is used during surgery of the posterior fossa for achieving hemostasis or packing violated mastoid air cells (1). A rare complication of its use is migration into the dural venous sinuses via emissary vein channels (2, 3). On imaging, migrated bone wax appears as a computed tomography (CT) hypodense (attenuation between fat and simple fluid) or magnetic resonance (MR) hypointense (owing to its semicrystalline solid nature) filling defect. Our goal was to review retrospectively imaging studies performed for patients who had undergone posterior fossa surgery to identify instances of this complication.

Materials and Methods

A query of our radiology report database identified reports containing the terms "suboccipital," "retrosigmoid," or "mastoideotomy" generated over a 6-month period. Scans of the 451 resultant patients then were reviewed to identify cases that had in fact undergone surgery and for which contrast-enhanced CT or MR imaging was performed. This yielded 212 patients. The morphology of the filling defect, the ability to trace it to an emissary vein channel or the surgical bed, and the signal/attenuation

characteristics were used to identify likely instances of migrated bone wax and a chart review was performed for each.

Results

Of the 212 patients reviewed, we identified eight cases that met criteria for bone wax migration into the transverse or sigmoid sinuses (Table 1). For six cases, both MR and CT imaging was available (Table 2). Patient age ranged from 30 to 78 years and indications for surgery included three cranial nerve schwannomas, three meningiomas, a cerebellar hemangioblastoma, and a cerebrospinal fluid (CSF) leak repair. The interval between the initial operation and the MR study varied from immediately postop to over 6 years. The operative note specifically mentioned the use of bone wax in six cases. In no instance was a negative clinical outcome attributed to bone wax migration or re-operation performed for this reason.

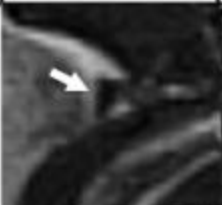
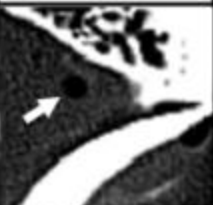
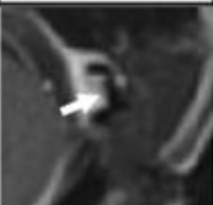
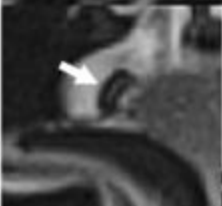




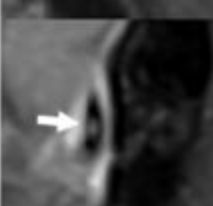

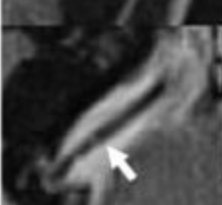
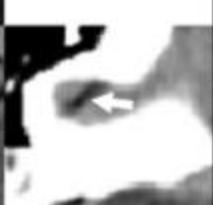


Conclusions

Migration of bone wax into the dural venous sinuses is a rare complication of posterior fossa surgery that radiologists should recognize and be prepared to differentiate from more serious complications, such as venous sinus thrombosis. The finding may persist for many years postoperatively and, as in our series, may not have any associated negative clinical outcome.

Table 1

| Case | Age | Gender | Bone wax mentioned in operative note? | Interval between operation and most recent scan (days) | Surgical approach | Lesion tre |
|------|-----|--------|---------------------------------------|--|--------------------|------------|
| 1 | 60 | M | Yes | 1213 | Left suboccipital | Vestibula |
| 2 | 78 | F | Yes | 1134 | Right suboccipital | Clival men |
| 3 | 39 | F | Yes | 246 | Left suboccipital | Trigemina |
| 4 | 30 | F | Yes | 58 | Right suboccipital | Jugular fo |
| 5 | 30 | F | No | 0 | Left retrosigmoid | CPA meni |
| 6 | 45 | F | Yes | 3 | Right retrosigmoid | Petrous a |
| 7 | 61 | M | Yes | 2273 | Left suboccipital | CSF leak r |
| 8 | 36 | F | No | 63 | Right suboccipital | Hemangi |

Table 2

| Case | MR | CT | Case | MR | CT |
|------|---|--|------|---|---|
| 1 |  |  | 5 |  | N/A |
| 2 |  |  | 6 |  |  |
| 3 |  | N/A | 7 |  |  |
| 4 |  |  | 8 |  |  |

(Filename: TCT_O-128_Tablescopy.jpg)

O-129

4:20PM - 4:28PM

The CT Prevalence of Arrested Pneumatization of the Sphenoid Sinus in Patients with Sickle Cell Disease

A Prabhu¹, B Branstetter¹

¹*University of Pittsburgh Medical Center, Pittsburgh, PA*

Purpose

Arrested sphenoid pneumatization is an incidental radiologic finding on computed tomography (CT) and magnetic resonance imaging (MRI) that may be confused with more aggressive pathologic conditions. No definite etiology for arrested sphenoid pneumatization has been established, although changes in regional blood flow during childhood, as is seen with sickle cell disease (SCD), have been proposed. The purpose of our study was to compare the prevalence of arrested pneumatization of the sphenoid sinus in patients with and without SCD.

Materials and Methods

We retrospectively identified 146 patients with SCD who had undergone CT scans of the skullbase between January 1990 and May 2015. We then identified 292 control patients without SCD, matched for age and sex in a 2-to-1 ratio. We tabulated the prevalence of arrested pneumatization along with the location and size of the lesions. We used Fisher's exact test to correlate SCD with arrested pneumatization of the sphenoid sinus and Student's t test to correlate SCD with lesion size.

Results

Of the 146 patients with SCD, 14 (9.6%) had arrested pneumatization of the sphenoid sinus. In the 292 control patients, six (2.1%) had arrested pneumatization. Patients with SCD had a statistically significantly higher rate of arrested pneumatization compared to patients without SCD ($p < 0.001$). There was no statistically significant correlation between lesion size and diagnosis of SCD.

Conclusions

Patients with SCD have a greater prevalence of arrested pneumatization of the sphenoid sinus than patients without SCD. This supports the theory that regional blood flow anomalies cause arrested sinus pneumatization.

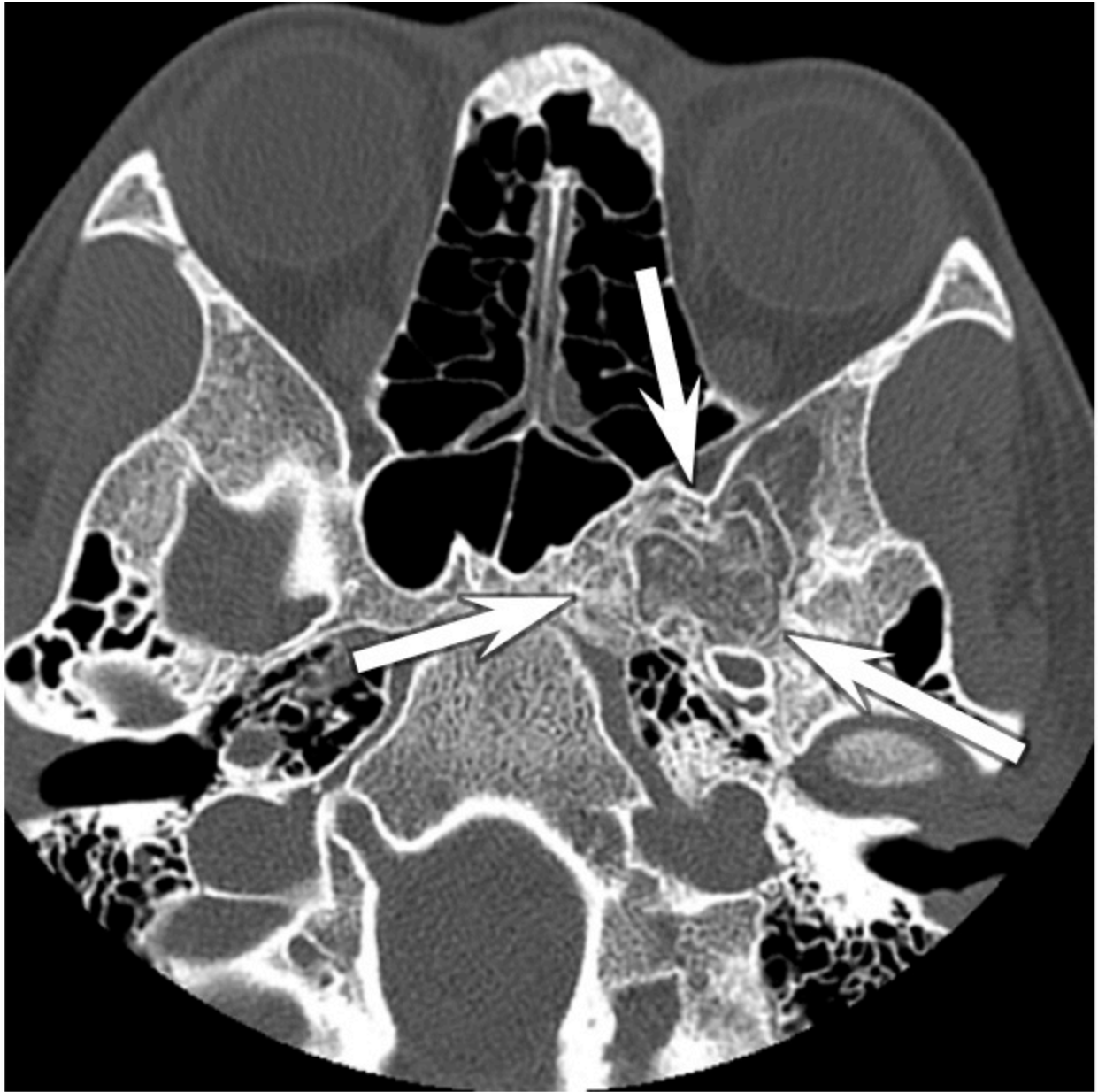


Figure. Axial contrast-enhanced CT image shows a nonexpansile lesion (arrows) located at a normal left sphenoid sinus pneumatization site with a thin cortical margin, internal fatty content, and curvilinear internal calcifications. This is the characteristic appearance and location for arrested pneumatization of the sphenoid sinus.

(Filename: TCT_O-129_Figure.jpg)

O-129a

4:28PM - 4:36PM

Dynamic contrast enhanced MRI derived intracellular water lifetime (τ_{wi}): a prognostic marker for patients with squamous cell carcinomas of head and neck.

S Chawla¹, L Loevner², S Wang¹, S Mohan³, H Poptani⁴

¹Hospital of the University of Pennsylvania, Philadelphia, PA, ²University of Pennsylvania, Philadelphia, PA, ³University of Pennsylvania, Philadelphia, PA, ⁴University of Liverpool, Liverpool, UK

Purpose

Shutter-speed pharmacokinetic analysis of dynamic-contrast-enhanced (DCE)-MRI allows estimation of volume transfer constant (K_{trans})¹ of contrast agent exchange between intravascular plasma and tumor interstitium compartments as well as transcytolemmal water exchange characterized by intracellular water molecule lifetime (τ_i).² While K_{trans} reflects tumor perfusion and permeability¹, τ_i reflects cell membrane permeability.² K_{trans} has shown great potential in predicting local treatment response³ and short-term survival⁴ in patients with head and neck squamous cell carcinomas (HNSCC). Some studies have demonstrated that τ_i may be used as a prognostic imaging biomarker in hepatocellular carcinomas, and breast cancers. Prognostic significance of τ_i in HNSCC has not been explored. In this study, we sought to investigate the prognostic value of K_{trans} and τ_i , in predicting short (< 5 years), and long-term (>10 years) survival in HNSCC patients.

Materials and Methods

Seventy-two patients with HNSCC were recruited. Three patients were excluded because they underwent upfront neck dissection, and 9 patients were excluded either due to suboptimal DCE-MRI data or being lost to follow-up. Survival was evaluated in remaining 60 patients from the end date of chemo-radiation therapy. The date of death, or the date of last clinical follow-up was used as end point. Pretreatment K_{trans} , τ_i , and volume were computed from the largest metastatic node, and median values of these indices were used to divide patients into 2 groups (at or above the threshold value [group I] and below the threshold value [group II]). Overall survival was analyzed by Kaplan-Meier method, and the results were compared by using a log rank test. A P value < .05 was considered significant.

Results

For short-term analysis, 15 of 60 patients had died by the last follow-up period. Patients with higher K_{trans} ($p=0.03$) and τ_i ($p=0.01$) had prolonged survival compared to those with lower K_{trans} and τ_i . For long-term analysis, 18 of 60 patients had died by the last follow-up period. Patients with higher τ_i had prolonged survival compared to patients with lower τ_i ($p=0.03$). A trend towards prolonged survival was observed for patients with high K_{trans} ($p=0.06$). No significant differences in nodal volume ($p>0.05$) were observed in predicting survival.

Conclusions

Though both K_{trans} and τ_i predicted short-term survival, τ_i was the most effective prognostic biomarker in predicting long term survival in patients with HNSCC. Using rat 9L-epigastric tumors, Koch et al.⁵ suggested an inverse correlation between τ_i and

EF5, a marker of hypoxia. They also observed that elevated τ_i regions were associated with high blood flow. Earlier studies⁶ support the notion that tumors with relatively higher blood flow are associated with increased oxygenation resulting in better access to chemotherapeutic drugs and radio-sensitivity. Since τ_i is affected by sodium-potassium channels as well as mitochondrial metabolism² and inhibition of mitochondrial metabolism by lonidamine results in reduced cellular ATP and increased τ_i . Taken together, these studies and our observations provide evidence that the higher degree of hypoxia, probably due to a combination of reduced mitochondrial metabolism and blood flow, results in low τ_i which indicates an adverse tumor microenvironment affecting overall survival. Conclusion: Patients harboring higher pretreatment τ_i had prolonged survival compared to those with lower τ_i .

Monday

3:00PM - 4:30PM

Washington Marriott Wardman Park, Roosevelt 4

5F-PARALLEL PAPER SESSION: Spine: Trauma & Techniques

O-130

3:00PM - 3:08PM

Cervical Spine Clearance After Blunt Traumatic Injury: A Meta-Analysis

X Wu¹, V Kalra¹, D Durand¹, R Liu¹, R Bronen¹, K Abbed¹, H Forman¹, A Malhotra¹
¹*Yale University School of Medicine, New Haven, CT*

Purpose

Magnetic resonance imaging (MRI) frequently is performed for clearance of cervical spine (CS) injury in blunt trauma patients. Several meta-analyses have been done in the past assessing the utility of MRI, with interestingly opposing conclusions (1-4). The purpose of this meta-analysis is to quantify the rate of unstable injuries detected by MRI missed on computed tomography (CT), and assess the utility of MRI in CS clearance in blunt trauma patients.

Materials and Methods

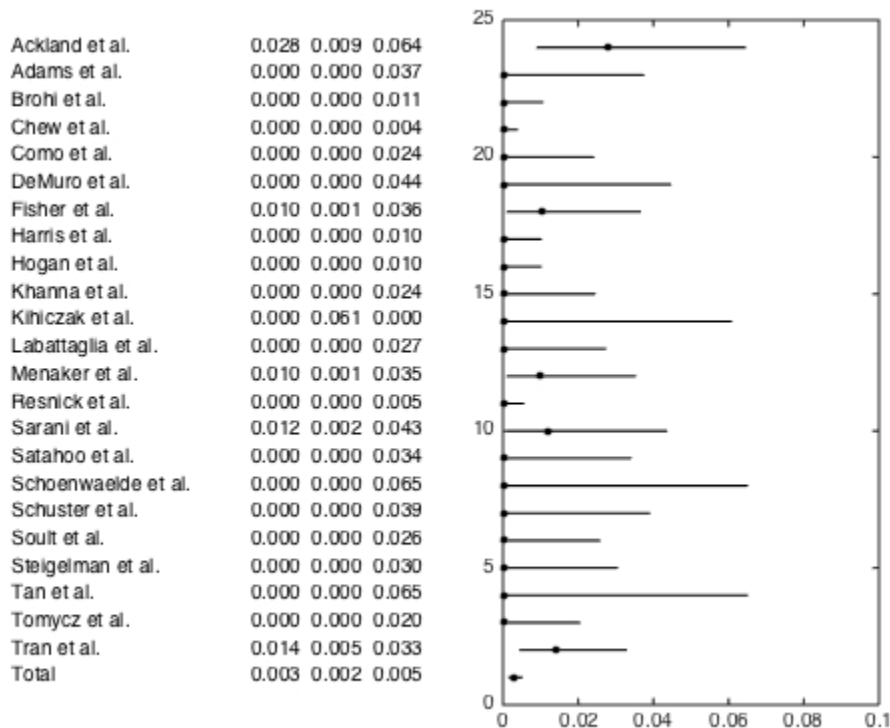
We undertook a systematic review and meta-analysis of the worldwide evidence across five major medical databases produced since 2000, including studies with obtunded patients and those with alert patients. Studies were included if they reported the number of unstable injuries or enough details for the instability to be inferred. Variables assessed included severity of injury, CT/MRI specifications, timing of imaging and outcome/follow up. Pooled incidence of unstable injury detected on follow up weighted by inverse of variance among all included as well as among obtunded or alert patient subgroups was reported. Heterogeneity of the literature was assessed.

Results

Of 407 unique citations, 23 studies proved eligible, with 5,286 patients found, and 16 unstable injuries reported in five different studies. The overall pooled incidence is 0.0029%. Among studies that only reported obtunded patients, the pooled incidence is 0.017%. In alert patients the incidence is 0.011%. All positive findings were critically reviewed, and only 11 could be considered as truly unstable. The I2 statistics demonstrate significant heterogeneity.

Conclusions

The overall positive finding rate is extremely low in both obtunded and alert patients. There is significant heterogeneity in the literature regarding the use of further imaging after a negative CT in patients with blunt injury. The use and role of "confirmatory" tests to detect unstable injury shows wide variations. Although MRI frequently is performed, its utility and cost-effectiveness needs further study.



(Filename: TCT_O-130_figure2.jpg)

O-131

3:08PM - 3:16PM

CSF Pulsations in the Spinal Canal in Acute Traumatic Spinal Stenosis Patients: Evidence of Interstitial Movement of Fluid and Spinal Cord Sources and Sinks

N Settipalle¹, M Boakye¹, A Amini¹, M Negahdar¹, R Bert¹

¹*University of Louisville, Louisville, KY*

Purpose

We have used cardiac-gated magnetic resonance imaging (MRI) phase contrast cine to study cerebrospinal fluid (CSF) pulsations in patients with acute traumatic spinal stenosis and compared the CSF and spinal cord time-flow curves at, above and below the level of spinal cord injury.

Materials and Methods

After IRB approval, nine patients with acute cervical spine injury aged 18-57 years and of both genders were scanned with prospective cardiac gating:

1.5T/TE/TR=6/60ms, flip angle=70, slice thickness=6mm, FOV=160mm, 5+phases.

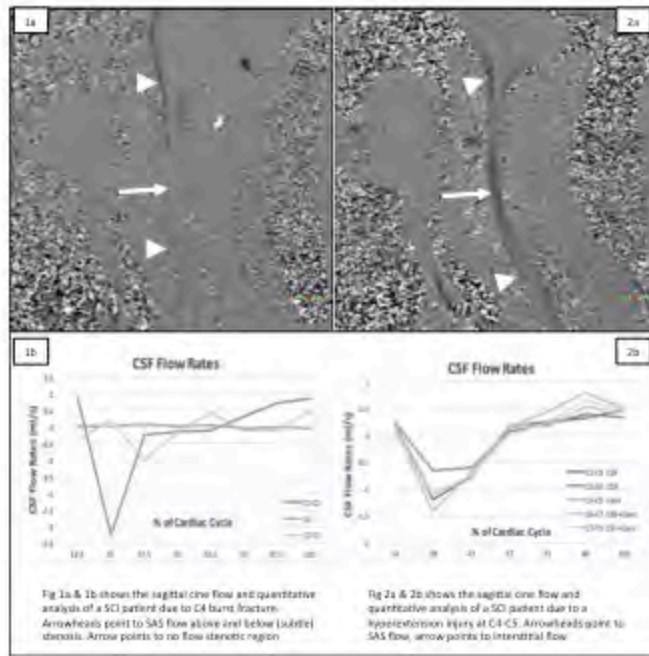
VENCs were customized to 5, 10, 15 or 20cm/s to avoid aliasing. Transverse scans were above, below and at the level of maximal spinal canal stenosis. Cine flow images analysis used custom software based on Matlab. Mean flow, velocity, ROI area were measured at each cine timepoint for the CSF and cord interstitial flow, with delta and net flow calculated.

Results

Flow waveforms both above and below stenoses were affected by the presence and degree of the stenosis. Flow caudal to the stenosis fell into three types: normal same phase if stenosis was incomplete, normal same phase if stenosis was complete and cord interstitial flow present, phase change and present if stenosis incomplete and no vertebral artery dissection. In cases of complete stenosis and no arterial dissection, instantaneous flow exceeded the continuity equation.

Conclusions

Cerebrospinal fluid flow pulsations are affected by the presence of an acute spinal stenosis. Flow pulsations can persist below the level of even when CSF effacement is complete, either by transmittance of flow through cord interstitial spaces or by regeneration from arterial pulsations within the distal cord. We currently are evaluating prognostic implications of high versus no interstitial flow with complete stenosis and the impact of vertebral arterial dissection on pulsations.



(Filename: TCT_O-131_Slide1.jpg)

O-132

3:16PM - 3:24PM

Isolated Increased STIR signal of the Posterior Atlanto-occipital and Atlanto-axial Membranes: A Reliable Indicator of Acute C1-C2 Fractures on MRI

Y Chang¹, N Peri², G Kim², E Papavassiliou², R Rojas², R Bhadelia³

¹Beth Israel Deaconess Medical Center, Newton, MA, ²Beth Israel Deaconess Medical Center, Boston, MA, ³Beth Israel Deaconess Medical Center, Boston, MA

Purpose

Diagnosis of acute C1 and/or C2 (C1-C2) fractures on magnetic resonance imaging (MRI) may be challenging secondary to a lack of associated elevated STIR marrow signal (1, 2). The purpose of this study was to determine the value of increased STIR signal in the posterior atlanto-occipital and/or atlanto-axial membranes (PAOM/PAAM) in predicting acute C1-C2 fractures on MRI.

Materials and Methods

Our institutional imaging database was reviewed from 2008-2015 to identify patients with C1-C2 fractures that had both computed tomography (CT) and MRI performed within a 24-hour span. Presence of acute C1-C2 fractures was determined by CT and clinical examination. Two control groups were selected: (1) No fracture (NF) group

with trauma history but negative CT, and (2) Other fracture (OF) group with acute cervical spine fractures other than C1-2. Elevated PAOM/PAAM signal on midline sagittal STIR images was assessed by consensus between two neuroradiologists. Patients with abnormal ligamentous signal at other levels (with or without PAOM/PAAM signal) and those without signal abnormality were considered negative. Sensitivity, specificity and positive predictive value (PPV) of increased signal isolated to the PAOM /PAAM was determined for acute C1-C2 fracture versus patients in NF and OF groups.

Results

Isolated increased PAOM/PAAM signal was seen in 23/36 (64%) of C1-C2, 1/37(3%) of NF, and 1/19 (5%) of OF patients. Isolated increased PAOM/PAAM signal at C1-2 had 64% sensitivity, 97% specificity and 96% PPV versus NF, and 64% sensitivity, 95% specificity and 96% PPV versus OF.

Conclusions

The presence of isolated increased PAOM/PAAM signal on STIR images is a reliable indicator of an acute C1-C2 fracture on MRI. This may be a useful imaging sign for occult acute C1-C2 fractures on MRI in patients without prior CT for comparison.

O-133

3:24PM - 3:32PM

Comparative diagnostic evaluation of CT vs MR with management/outcomes in cervical spine trauma based on age and injury appearance pattern

D Durand¹, V Kalra¹, X Wu¹, A Malhotra²

¹*Yale University School of Medicine, New Haven, CT*, ²*Yale New Haven Hospital, New Haven, CT*

Purpose

Advances in computed tomography (CT) and magnetic resonance imaging (MRI) necessitate reevaluation of these modalities presumed complimentary roles in blunt cervical trauma. Radiation dose, cost, and throughput considerations weigh against performing both CT and MRI if management/outcomes are not changed significantly. We perform subgroup analysis based on age and injury appearance pattern.

Materials and Methods

Seven hundred seventy-eight patients who underwent both CT and MR for blunt cervical spinal trauma from late 2013 to late 2015 were included. Magnetic resonance imaging was performed within 24 hours of the CT. Most common indications were fall, MVC, and assault. Injury patterns were subgrouped into increased anterior angulation, increased posterior angulation, AP translation, lateral translation, unilateral facet perching, unilateral facet dislocation, bilateral facet perching, bilateral facet dislocation, and avulsion.

Results

Of the total of 778 patients, 260 had positive CT findings. Sixty-four of these (24.6% of the CT positive group and 8.2% overall) had negative MR findings, while 196 (75.4% of the CT positive group and 25.2% overall) had positive MR findings. Five hundred eighteen of the 778 total patients had negative CT findings. Of these, 405 also had negative MR (78.2% of the negative CT group and 52.1% overall) and 113 had positive MR findings (21.8% of the negative CT group and 14.5% overall). Using either modality positive as a reference, CT showed sensitivity of 69.7% and negative predictive value of 78.2% and MR demonstrated sensitivity of 82.8% and negative predictive value of 86.4%.

Conclusions

Computed tomography and MR demonstrate varying diagnostic sensitivities and specificities based on patient and injury appearance pattern. Using either modality positive as a reference, CT showed sensitivity of 69.7% and negative predictive value of 78.2% and MR demonstrated sensitivity of 82.8% and negative predictive value of 86.4%.

MR findings in relation to CT findings

| | |
|---|-----|
| Total positive cervical spine CTs | 260 |
| Total positive cervical spine CTs with negative cervical spine MRIs | 64 |
| Total positive cervical spine CTs with positive cervical spine MRIs | 196 |
| | |
| Total negative cervical spine CTs | 518 |
| Total negative cervical spine CTs with negative cervical spine MRIs | 405 |
| Total negative cervical spine CTs with positive cervical spine MRIs | 113 |

(Filename: TCT_O-133_asnrabstracttable.gif)

O-134

3:32PM - 3:40PM

Atlas-based quantitative analysis of T2 signal abnormality in the spinal cord predicts outcome in acute flaccid paralysis.

D McCoy¹, J Talbott¹, M Mamlouk², J Cohen-Adad³, J Narvid¹

¹UCSF, San Francisco, CA, ²Kaiser Permanente, Santa Clara, CA, ³Polytechnique Montreal, Montréal, Quebec

Purpose

To investigate the use of a T2-weighted anatomical template and probabilistic atlas of the spinal cord (SC) to quantitatively evaluate the percentage of gray matter (GM) and white matter (WM) affected by lesion in acute flaccid paralysis (AFP).

Materials and Methods

Spinal cord imaging for nine patients presenting with AFP were analyzed using the Spinal Cord Toolbox MRI processing tool. A semi-automated pipeline was developed to identify and segment the spinal cord, register each patient image to the anatomical template, warp the patient image with the template and extract data on lesion involvement in GM and WM.

Results

Percent GM and WM affected by lesion, calculated as the weighted average of lesion involved in probabilistic GM and WM voxel space, was calculated for each patient at three regions of interest i). center axial slice of lesion ii). lesion segment area, and iii.) full spinal cord. Gray matter metrics extracted at the lesion center significantly associated with both clinical outcomes and the Medical Research Council (MRC) Scale for Muscle Strength Scores.

Conclusions

Recent advances in quantitative imaging have led to the development of a robust anatomical template and probabilistic atlas of the spinal cord. With these new tools, spinal cords now can be registered to a common reference and morphological differences quantified at both a group and individual level for comparison. This is the first research study to quantify spinal cord lesions with the Spinal Cord Toolbox and correlate metrics with clinical outcomes.

O-135

3:40PM - 3:48PM

Paraspinal Edema on Unenhanced MRI is Highly Sensitive for the Detection of Lumbar Spinal Epidural Abscess

A Shifrin¹, Q Lu², M Lev³, T Meehan⁴, R Hu⁴

¹Mount Auburn Hospital, Cambridge, MA, ²Zhongda Hospital, Southeast University, Jiangsu, China, ³Massachusetts Gen'l Hosp./Harvard Med. Schl., Boston, MA, ⁴Massachusetts General Hospital, Boston, MA

Purpose

Spinal epidural abscess (SEA) is a neurosurgical emergency. Although contrast-enhanced spine magnetic resonance imaging (MRI) is the mainstay for diagnosis of

SEA, unenhanced MRI typically is obtained in patients with nonspecific symptoms or insufficient clinical information. We evaluated the sensitivity/specificity of imaging features suggestive of SEA on unenhanced spine MRI.

Materials and Methods

Our study was IRB approved. We searched for contrast-enhanced lumbar spine MRI exams from 01/01/2000-08/01/2014 with "epidural abscess" in the report. We included 68 patients >18 years with an enhancing epidural collection on MRI and surgical (62%), microbiologic (19%) or clinical (19%) confirmation of SEA. Sixty-eight age/sex-matched controls without SEA also were selected. Three readers scored unenhanced MRI images on the degree of psoas/paraspinal muscle edema, extent of bone marrow edema, and abnormal disk signal. Location/dimensions of SEA on contrast MRI also were recorded.

Results

Paraspinal edema was highly sensitive (97%) for SEA, with lower sensitivities for psoas, bone marrow, and disk edema (54, 65, and 66%, respectively). Each of these markers was highly significant in univariate analysis ($p < 0.001$). A multivariate logistic regression model adjusting for age and gender found that paraspinal ($p < 0.001$) and bone marrow edema ($p = 0.006$) were significant independent predictors of SEA, with a trend toward significance for psoas edema ($p = 0.07$) and abnormal disk signal ($p = 0.07$). Psoas muscle edema was the most specific (96%) for presence of SEA.

Conclusions

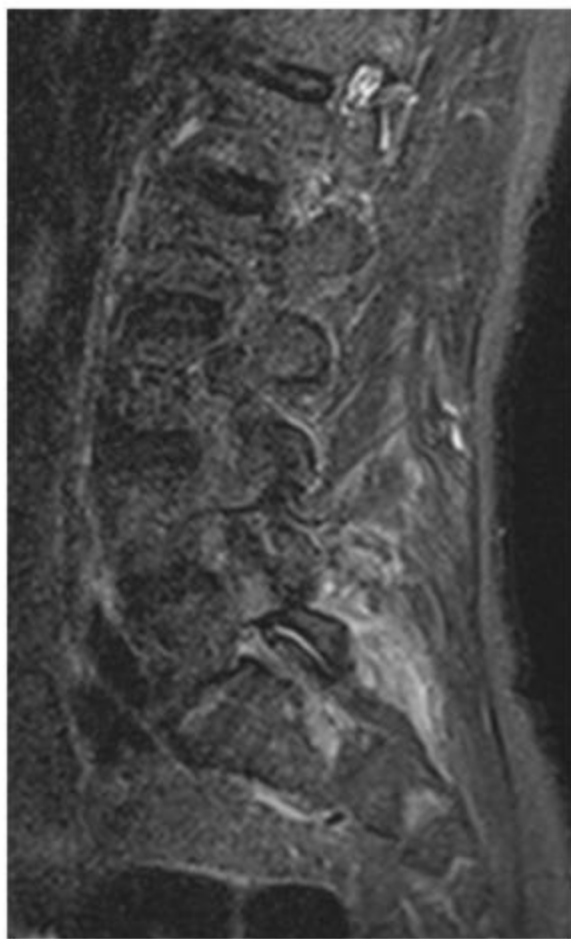
Paraspinal edema is highly sensitive for SEA. Familiarity with the unenhanced MRI findings of SEA could help expedite further, definitive evaluation when contrast is not administered.

Figure 1A. 58-year-old female with no significant past medical history with 5 days of severe low back pain and fevers. Sagittal T2WI demonstrates nonspecific prominence of the ventral epidural space and possibly dilated epidural venous plexus, with T2 hypointense material posterior to the vertebral space that has the appearance of a disc extrusion. There is no significant endplate irregularity or abnormal disc signal.



(Filename: TCT_O-135_Figure1A.jpg)

Figure 1B. Right parasagittal STIR image demonstrates extensive paraspinal edema in the lumbosacral region.



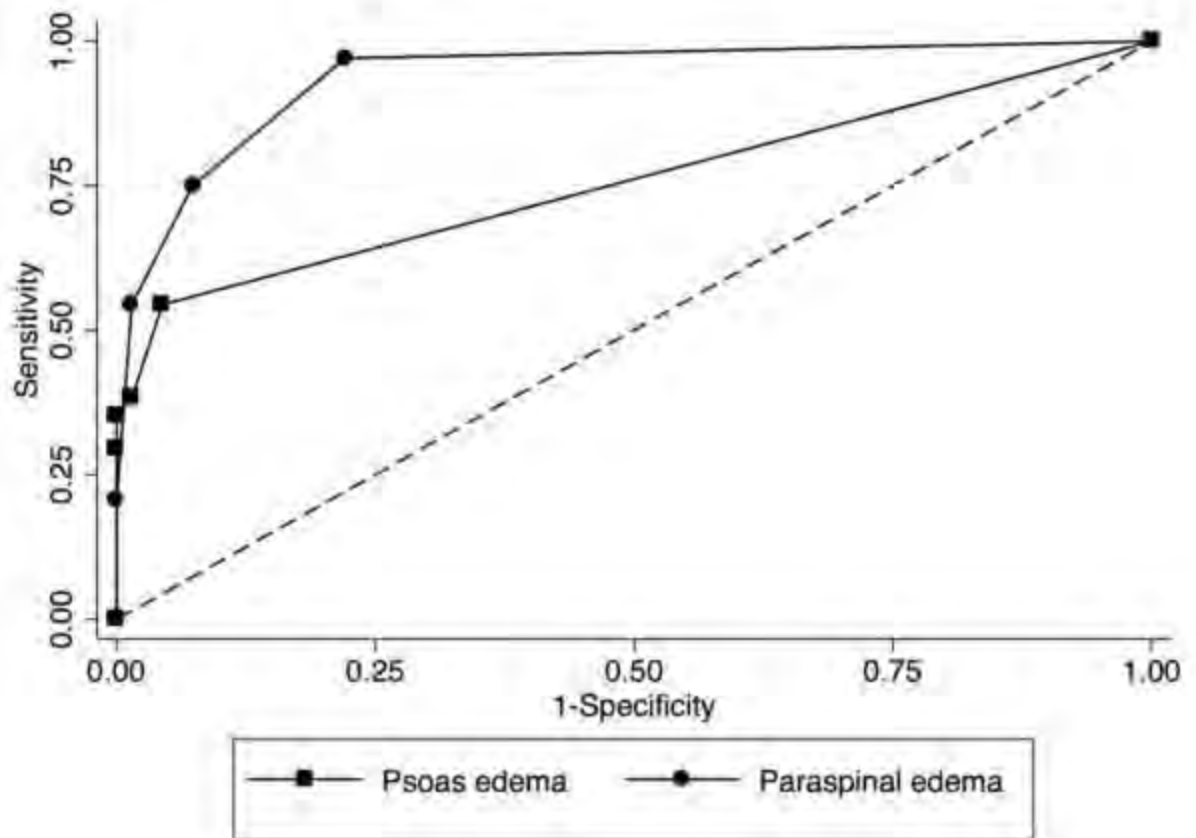
(Filename: TCT_O-135_Figure1B.jpg)

Figure 1C. Sagittal T1WI post-gadolinium image demonstrates an epidural collection in the ventral epidural space extending contiguously on axial imaging (not shown) from the L3-4 to L5-S1 interspace. Blood culture positive for staphylococcus aureus, and the patient was treated with antibiotics with subsequent clinical and imaging improvement.



(Filename: TCT_O-135_Figure1C.jpg)

Receiver operating curve analysis depicting sensitivity and specificity point severity scale for paraspinal muscle edema and psoas muscle unenhanced MRI for the detection of SEA.



(Filename: TCT_O-135_Table1.jpg)

O-136

3:48PM - 3:56PM

Bone texture analysis of lumbar spine on CT to detect early finding of multiple myeloma: Comparison of control subjects with normal bone density, patients with osteoporosis, and patients with multiple myeloma

T Kakigi¹, K Hassan², M Qureshi², M Chapman², B Li², O Sakai²

¹Boston Medical Center, Boston University/Kyoto University Graduate School, Boston, MA, ²Boston Medical Center, Boston University School of Medicine, Boston, MA

Purpose

To evaluate the difference in control subjects with normal bone density, patients with osteoporosis, and patients with multiple myeloma using texture analysis, and to identify possible early lesions of multiple myeloma before a "punched out" lesion is seen.

Materials and Methods

This study was IRB-approved and HIPAA-compliant with a waiver of the need for informed consent. Fifteen control subjects (8 males and 7 females; mean age 68.9 years old, ranged from 53 to 88 years old), 13 osteoporotic patients (1 male and 12 females; mean age 66.5 years old, ranged from 55 to 91 years old), and 10 myeloma patients (6 males and 4 females; mean age 69 years old, ranged from 56 to 86 years old) were enrolled. The L3 vertebral body on contrast-enhanced CT examinations was evaluated by texture analysis. Differences in 42 texture parameters including 13 histogram features, 5 gray-level co-occurrence matrix (GLCM) features, 11 gray-level run length (GLRL) features, 4 gray-level gradient matrix (GLGM) features, and 9 Law's features were examined in each two groups (control subjects and osteoporotic patients, control subjects and myeloma patients, and osteoporotic patients and myeloma patients) using Student's t-test and a false discovery rate (FDR) correction.

Results

Twenty-nine, 26, and 31 out of 42 parameters demonstrated statistically significant differences in each two groups ($P < .05$). After using FDR correction, 24, 26, and 29 parameters were significant in differentiating between each two groups ($Q < .05$).

Conclusions

Bone texture analysis may enable us to differentiate control subjects from osteoporotic patients. Some parameters in texture analysis also showed significant differences between osteoporotic patients and myeloma patients. This means that it is possible to differentiate normal osteoporosis from osteoporosis due to myeloma. Bone texture analysis could be useful as one of the imaging markers of multiple myeloma without visible bone lesions.

O-137

3:56PM - 4:04PM

Spinal Osseous Involvement of Sarcoidosis

A Hendrickson¹, J Morris², P Luetmer²

¹Mayo Clinic, Rochester, MN, ²Mayo Clinic, Rochester, MN

Purpose

To determine the prevalence and neuroimaging appearance of spinal and sacral osseous involvement in patients diagnosed with sarcoidosis at a single quaternary referral center.

Materials and Methods

After IRB approval the medical record, pathology and radiology databases were searched for patients carrying the diagnosis of sarcoidosis or related sarcoid terms over the last 15 years. This list was cross referenced with patients who had a magnetic resonance imaging (MRI) or computed tomography (CT) dedicated to or containing the spine/sacrum. Five hundred thirty-five patients were identified. Patients without a definitive diagnosis of sarcoid were excluded leaving 396 patients. The neuroimaging of these patients was reviewed.

Results

Forty-six of the 396 were found to have osseous abnormalities involving the spine and sacrum. Forty-five out of 46 patients had a MRI and 44 had CT scans. Twenty-six cases had radiographic abnormalities on CT. Nineteen were lytic, five were sclerotic, one had a diffuse mottled appearance, and one was mixed lytic and sclerotic. Thirty-two patients had multilevel well circumscribed lesions in the vertebral bodies. On CT three of these were sclerotic, 12 were occult, and 15 were lytic. Three patients had diffuse marrow replacement of multiple levels. Two patients had diffuse involvement of one level. Nine patients had multilevel patchy, less well defined areas of involvement (Fig. 1). Thirteen patients initially presented with neuroradiographic abnormalities in the spine/sacrum which ultimately led to the diagnosis of sarcoid. Four patients had osseous spinal involvement as their only finding of sarcoidosis. Nineteen of 46 (41%) patients underwent spine/sacral biopsies of involved areas. Twelve of 19 (63%) of the biopsies were positive, and six (33%) were negative.

Conclusions

While most patients have other supportive findings of sarcoidosis some may present with intraosseous involvement of the spine. Neuroradiologists should be aware of the varied appearance of sarcoid in the axial skeleton which may avoid unnecessary biopsies or help solidify the diagnosis of sarcoidosis.

O-138

4:04PM - 4:12PM

The effect of lytic lesions on the kinematic response of human thoracolumbar spines

R Alkalay¹, D Hackney²

¹Beth Israel Deaconess medical Center, Boston, MA, ²Beth Israel Deaconess Medical Center, Boston, MA

Purpose

This study investigated the effect of simulated lytic metastases (LM) in the vertebral body and the posterior elements on the kinematic response of thoracic and lumbar cadaveric human spines in response to flexion and extension loading. The results may guide vertebral augmentation strategies to reduce the risk of pathologic fracture.

Materials and Methods

Twenty-three three-level thoracic and lumbar spinal motion units were instrumented with optical markers for measurement of inter-segmental motion. Using a six degree of freedom test frame, each segment was exposed to axial compression (200N) and increasing magnitudes of either flexion or extension moment. Angular rotations and axial displacement were measured throughout each test. Large defects were created in the vertebral body with or without ipsilateral destruction of the pedicle and facet joint. Kinematic testing was repeated. Repeated measure ANOVA (V 11. JMP, SAS, NC) was used to test the effect of lytic defects and spine region (thoracic versus lumbar) on the response of the motion segments.

Results

Response to flexion moments the LM spines showed higher angular motion (θ_X : flexion-extension, Fig. 1) at lower moment values whilst exhibiting lower angular motion at higher moment values, these differences being significant in comparison to the intact spine ($p < 0.01$). This pattern was mirrored for the axial displacement along the spine's axial (ΔZ : $p < 0.01$, Fig. 1) and sagittal (Y axis, $p < 0.05$, respectively) anatomical axes as well as the pattern of coupled rotational angular motions (Extension: $p < 0.01$ and Flexion: $p < 0.05$).

Conclusions

Lytic metastases defect significantly affected both primary (flexion-extension) and coupled (axial torsion) motions with the spine showing significant changes in intervertebral displacements. These observed increases, and the observed regional specific changes in this pattern may form an important part of fracture risk in patients with vertebral metastatic disease.

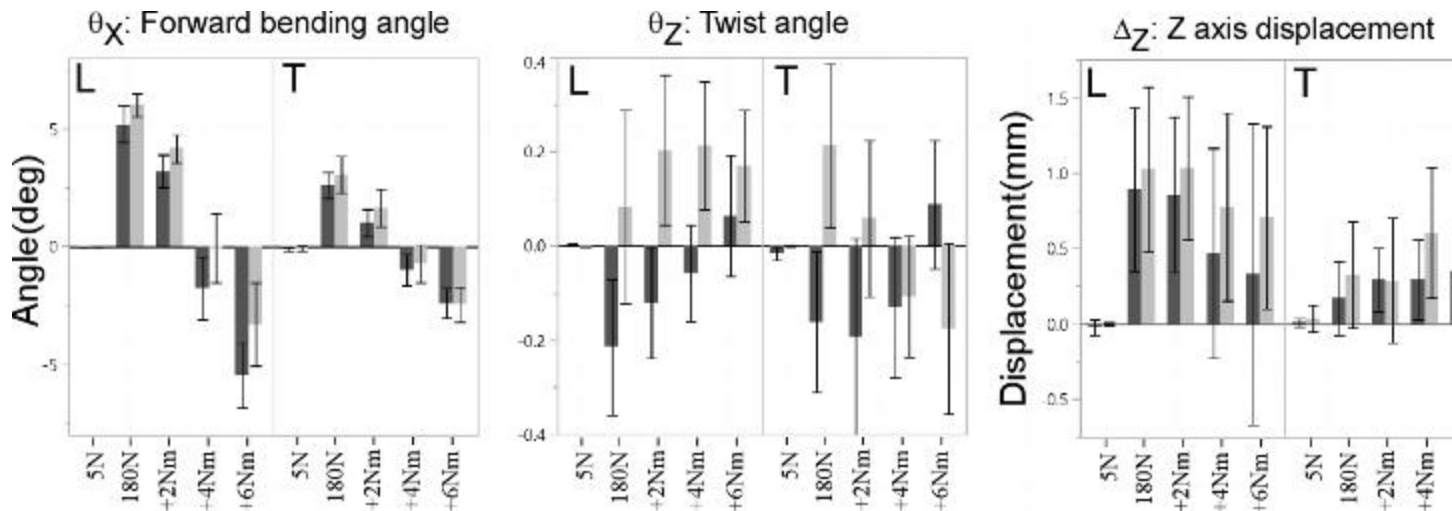


Fig. 1 Effect lytic defects on the kinematical response of thoracic and lumbar h
 (Filename: TCT_O-138_metsfigure.jpg)

O-139

4:12PM - 4:20PM

Diagnostic Quality of 3D T2-SPACE Compared to T2 2D-FSE in Evaluating Cervical Spine MRI Anatomy

F Chokshi¹, G Sadigh¹, W Carpenter¹, J Allen¹
¹Emory University School of Medicine, Atlanta, GA

Purpose

To compare the diagnostic quality of 3D T2-SPACE with 2D T2-FSE sequences in visualization of cervical spine (C-spine) anatomy. We predict 3D T2-SPACE will be equivalent or superior to T2-FSE for visibility of cervical spine anatomy.

Materials and Methods

Consecutive patients undergoing noncontrast C-spine MRI with T2-FSE and T2-SPACE sequences for radiculopathy or myelopathy between September 2014 and February 2015 were included. Two blinded, subspecialty-trained radiologists [musculoskeletal (R1) and neuroradiology (R2)] independently assessed visibility of 12 anatomical structures using a 5-point scale (0 = not visible and 4 = excellent visibility) and CSF flow artifact using a 4-point scale (0 = severe artifact and 3 = no artifact) on sagittal view and 6 axial levels from C2-T1 on T2-FSE; 2 weeks later and after randomization, T2-SPACE was evaluated. Diagnostic quality for each structure and cerebrospinal fluid (CSF) flow visibility in both sequences was compared using t-test. Inter-observer agreement was calculated (kappa).

Results

Forty-five patients included (mean age, 57; 40% male); 8,190 visibility scores per reviewer. Per Table 1, average scores for intervertebral disk signal, neural foramina,

ligamentum flavum, ventral rootlets and dorsal rootlets were higher for T2-SPACE compared to T2-FSE for both reviewers ($p < 0.001$). Average scores for remaining anatomical structures were either not statistically different or superiority of one sequence was discordant between both reviewers. T2-SPACE showed less degree of CSF flow artifact ($p < 0.001$). Interobserver variability ranged between -0.02 to 0.20 for T2-SPACE and -0.02 to 0.30 for T2-FSE consistent with slight to fair agreement.

Conclusions

1. T2-SPACE may be superior to T2-FSE for evaluation of some, but not all, evaluated c-spine anatomical structures and shows less degree of CSF flow artifact.
2. Slight to fair interobserver agreement may be related to a learning curve in acclimating to this sequence.

Table 1. Average visibility score for anatomic structures and CSF flow artifact of FSE vs. T2-SPACE sequences. FSE, Fast Spin Echo; SPACE, Sample Perfection in Application-optimized Contrasts using different flip-angle Evolution

| | Reviewer 1 (MSK) | | | Reviewer 2 (Neuro) | |
|--|------------------|----------|------------------|--------------------|----------|
| | T2-FSE | T2-SPACE | P-Value | T2-FSE | T2-SPACE |
| Bone marrow signal | 2.10 | 2.00 | <0.001 | 2.94 | 2.96 |
| Intervertebral Disc | 2.00 | 2.50 | <0.001 | 2.85 | 2.95 |
| Facet Joints | 1.95 | 1.95 | 0.85 | 2.90 | 3.07 |
| Neural Foramina | 1.90 | 1.97 | <0.001 | 2.87 | 3.29 |
| Anterior Longitudinal Ligament | 0.23 | 0.16 | 0.004 | 2.83 | 2.92 |
| Posterior Longitudinal Ligament | 0.69 | 0.50 | <0.001 | 2.91 | 3.00 |
| Ligamentum Flavum | 1.41 | 1.78 | <0.001 | 2.90 | 2.99 |
| Interspinous Ligament | 1.15 | 1.36 | <0.001 | 1.99 | 2.00 |
| Spinal Cord Signal | 1.93 | 1.98 | 0.01 | 2.80 | 2.40 |
| Ventral Rootlets | 0.39 | 1.43 | <0.001 | 0.41 | 1.67 |
| Dorsal Rootlets | 0.50 | 1.87 | <0.001 | 0.55 | 2.35 |
| Dorsal Root Ganglia | 1.38 | 1.88 | <0.001 | 1.11 | 2.64 |
| CSF Flow Artifact** | 1.65 | 2.93 | <0.001 | 1.69 | 2.8 |

**** Please note higher scores of CSF flow artifact corresponds to less degree of**

(Filename: TCT_O-139_Table_1-ASNR-2016-SPACE.jpg)

Monday

4:45PM - 6:15PM

Washington Marriott Wardman Park, Marriott Ballroom

6A-Advanced Imaging Programming: Demystifying Advanced Imaging

6A-1

4:45PM - 5:15PM

Demystifying Diffusion

Berman, J.

Children's Hospital of Philadelphia

Philadelphia, PA

6A-2

5:15PM - 5:45PM

Demystifying Perfusion

Field, A.

Univ. Of Wisconsin Hospital

Madison, WI

6A-3

5:45PM - 6:15PM

Demystifying MR Spectroscopy

Shungu, D.

Weill Cornell Medical College

New York, NY

Monday

4:45PM - 6:15PM

Washington Marriott Wardman Park, Washington 4/5/6

6B-CSI Programming: Electronic Meetings and Publishing: Putting It All Together

6B-1

4:45PM - 5:05PM

Gathering Data: Polls

Gibbs, W.
University of Southern California, Keck School of Medicine
Los Angeles, CA

6B-2

5:05PM - 5:25PM

Conducting A Meeting: Ways to Do This Over the Internet (Video Conferencing)

Quigley, E.
University Of Utah
Salt Lake City, UT

6B-3

5:25PM - 5:45PM

Planning a Meeting or Research Project? Using Google Spreadsheets

Go, J.
LAC/USC Medical Center
Los Angeles, CA

6B-4

5:45PM - 6:05PM

E Publishing

Takhtani, D.
University of Massachusetts Medical School
Worcester, MA

6B-5

6:05PM - 6:15PM

Questions

Monday

4:45PM - 6:15PM

Washington Marriott Wardman Park, Washington 1/2/3

6C-Evidence Based Medicine Programming: Appropriateness of Neuroimaging and Clinical Decision Support in the Emergency Department

6C-1

4:45PM - 5:05PM

Impact of Clinical Decision Support on the Volume and Appropriateness in the Emergency Department

Mukundan, S.

Brigham & Women's Hospital

Boston, MA

6C-2

5:05PM - 5:25PM

Emergency Medicine Physician Perspective on Using Clinical Decision Support

Raja, A.

Massachusetts General Hospital

Boston, MA

6C-3

5:25PM - 5:45PM

Value Based ER Radiology

Seidenwurm, D.

Sutter Health

Sacramento, CA

6C-4

5:45PM - 6:05PM

Legal Implications of Clinical Decision Support Tools

Bello, J.

Montefiore Medical Center

Bronx, NY

6C-5

6:05PM - 6:15PM

Panel Discussion

Monday

4:45PM - 6:15PM

Washington Marriott Wardman Park, Roosevelt 1-3

**6D-PARALLEL PAPER SESSION: Turbo Talks - Advanced Pediatric MRI /
Gadolinium Deposition
O-141**

4:45PM - 4:48PM

**An Investigation of Visualization Improvement Algorithms Using Color
Transformation Techniques for Clinical Pediatric Spinal Cord MRI Images in
Healthy Subjects and Patients with Spinal Cord Injury**

M Alizadeh¹, P Shah¹, D Middleton¹, C Conklin², S Faro³, M Mulcahey², F
Mohamed²

¹Temple University, Philadelphia, PA, ²Thomas Jefferson University, Philadelphia,
PA, ³Temple University School Of Medicine, Philadelphia, PA

Purpose

To determine a reliable visualization improvement method based on a T2-weighted gradient echo (GRE) images of pediatric spinal cords, and evaluate the performance of the method(s) in healthy subjects and patients with various severity of spinal cord injury as determined by both diagnostic and clinical examination.

Materials and Methods

A total of 15 subjects (10 healthy and five spinal cord injury patients) were recruited for this study with a mean age of 11.41 years. All patients were assessed clinically using the motor and sensory examinations of the International Standards for Neurological Classification of Spinal Cord Injury (ISNCSCI); severity of injury was determined according to the American Spinal Injury Association Impairment Scale (AIS) (1). The magnetic resonance imaging (MRI) scans were performed using a 3.0T Siemens Verio MR scanner with 4-channel neck matrix and 8-channel spine matrix coils. The axial T2 gradient echo (GRE) scan was prescribed from the sagittal T2-weighted image to cover the entire cervical spinal cord (C1-C7 levels). Following data

acquisition, axial T2-weighted GRE images then were converted to the color images (Fig. 1) by using five different proposed techniques including Hue-Saturation-Value (HSV), Rainbow, Red-Green-Blue (RGB) and two RGB techniques incorporated with different enhancement approaches using image normalization (2) (RGB1) and intensity inhomogeneity correction (3) (RGB2). Performance of these techniques was scored visually by two independent board certified neuroradiologists with a combined experience of 30 years (22 and 8 years) and quantified using signal to noise ratio (SNR) and contrast to noise ratio (CNR).

Results

Visual inspection: The control subjects showed mean \pm standard deviation GRE = 0.78 ± 0.17 , RGB = 0.67 ± 0.17 , RGB1 = 0.86 ± 0.17 , RGB2 = 0.83 ± 0.17 , Rainbow = 0.66 ± 0.16 and HSV = 0.59 ± 0.22 . The subjects with SCI showed reduced values: GRE = 0.67 ± 0.21 , RGB = 0.56 ± 0.19 , RGB1 = 0.73 ± 0.23 , RGB2 = 0.73 ± 0.22 , Rainbow = 0.56 ± 0.18 and HSV = 0.5 ± 0.31 (Figs. 2 and 3). Reliability tests showed moderate to strong agreement between the two examiners. The ICCs and their 95% CIs were GRE [ICC= 0.73, CI (0.69–0.77)], RGB [ICC= 0.83, CI (0.58– 0.65)], RGB1 [ICC= 0.85, CI (0.75–0.83)], RGB2 [ICC= 0.81, CI (0.74– 0.82)], Rainbow [ICC= 0.79, CI (0.58–0.66)] and HSV [ICC= 0.91, CI (0.49–0.6)]. The averaged SNR and CNR values were: GRE [SNR= 76.92 (1:1), CNR= 45.1 (1:1)], RGB [SNR= 130.6 (1.7:1), CNR= 14.76 (0.33:1)], RGB1 [SNR= 50.58 (0.66:1), CNR= 61.35 (1.36:1)], RGB2 [SNR= 110.69 (1.44:1), CNR= 38.27 (0.85:1)], RAINBOW [SNR= 82 (1.07:1), CNR= 4.84 (0.11:1)] and HSV [SNR=97.29 (1.26:1), CNR= 22.51 (0.5:1)]. RGB, RGB2, rainbow and HSV techniques show improvement in the SNR by 70%, 44%, 7% and 26% respectively compared to conventional GRE images and RGB1 shows improvement in CNR by 36%.

Conclusions

It was determined that the color mapping techniques improved image quality for CSF homogeneity, delineation of cord/CSF interface and separation of the GM and WM in the spinal cord and may help in the diagnosis along with the conventional grayscale MRI images.

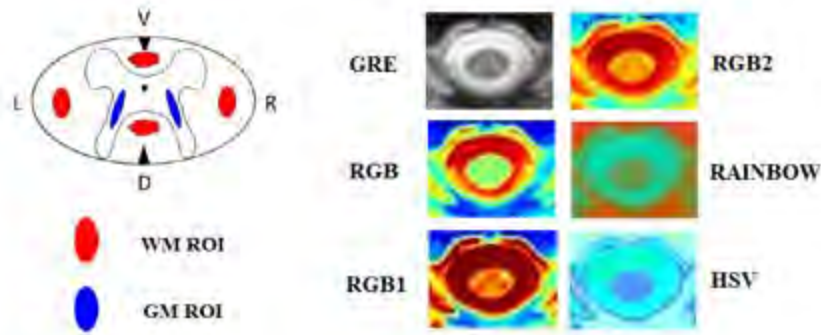


Figure 1. 8 ROIs were drawn to calculate SNR and CNR values. These included 2 ROIs of GM (2 samples in lateral sides), 4 ROIs of WM (frontal, posterior and lateral regions), 1 ROI of the whole cord and 1 ROI of the surrounding region outside the FOV.

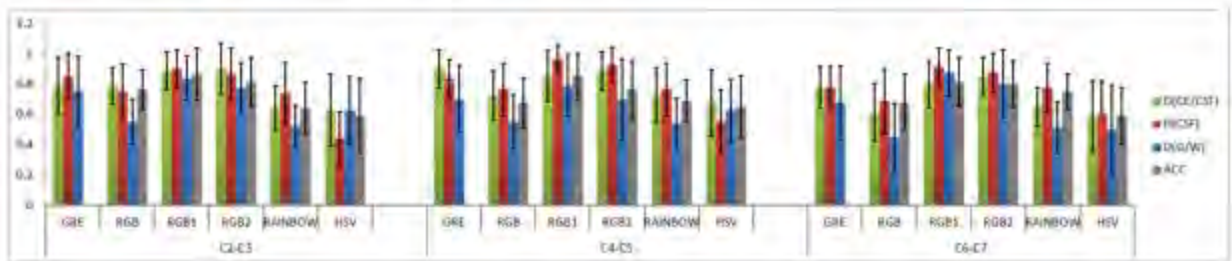


Figure 2. Visualization parameters included accuracy (ACC), differentiating of GM from WM ($D(GM/WM)$), differentiating of cord edge from CSF ($D(CE/CSF)$) and homogeneity of CSF ($H(CSF)$) as a function of cord level (upper (C2-C3), middle (C4-C5) and lower (C6-C7) cervical spinal cord levels) at control subjects.

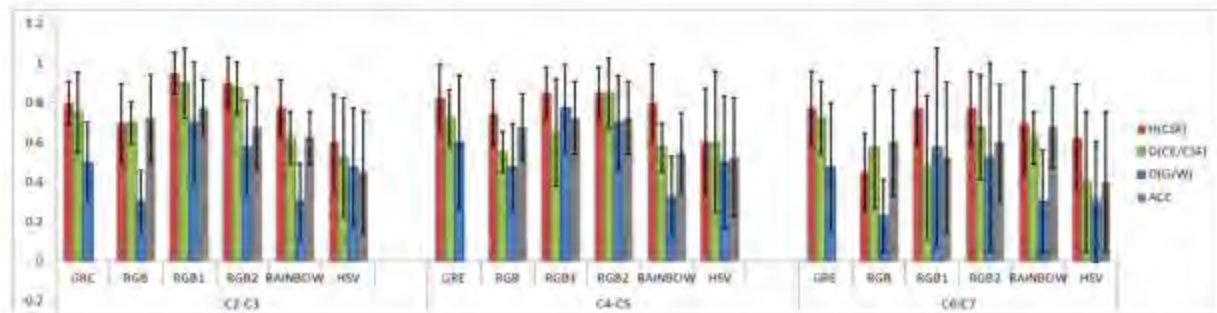


Figure 3. Visualization parameters included ACC, $D(GM/WM)$, $D(CE/CSF)$ and $H(CSF)$ as a function of cord level (upper (C2-C3), middle (C4-C5) and lower (C6-C7) cervical spinal cord levels) at SCI subjects. (Filename: TCT_O-141_color.png)

O-142

4:48PM - 4:51PM

Diffusion Tensor Imaging of the Cervical and Thoracic Spinal Cord in Pediatric Subjects using an Inner FOV 2DRF Pulse Sequence.

S SAKSENA¹, D Middleton², L Krisa¹, P Shah², S Faro³, R Sinko¹, J Gaughan³, J Finsterbusch⁴, M Mulcahey¹, F Mohamed¹

¹Thomas Jefferson University, Philadelphia, PA, ²Temple University, Philadelphia, PA, ³Temple University School of Medicine, Philadelphia, PA, ⁴University Medical Center Hamburg-eppendorf, Hamburg, Hamburg

Purpose

The purpose of this study was to (a) investigate the feasibility of obtaining reliable diffusion tensor imaging (DTI) parameters along the entire cervical and thoracic spinal cord (SC) in typically developing (TD) healthy children and children with spinal cord injury (SCI) using an inner field of view (FOV) sequence, (b) examine the reproducibility of DTI parameters, (c) determine whether microstructural changes quantified by DTI are associated with clinical neurological deficits.

Materials and Methods

Twenty-two TD children (mean age, 11.03 years) without evidence of SC pathology and 15 patients (mean age, 11.42 years) with chronic SCI were recruited. ISNCSCI were used to define the clinical level and severity of injury in SCI patients. Subjects underwent two identical scans (minimum time between scans=2 h) using 3T Verio MR scanner with 4-channel neck matrix and 8-channel spine matrix coils. The protocol consisted of conventional T1- and T2-weighted structural scans and axial DTI scans based on inner FOV sequence described previously (1). Diffusion tensor images were acquired axially using two overlapping slabs, to cover the cervical (C1-upper thoracic region) and thoracic (upper thoracic-L1) SC. The imaging parameters: three averages of 20 diffusion directions, six b0 acquisitions, b=800s/mm², voxel size=0.8x0.8x6mm³, axial slices=40, TR=7900ms, TE=110ms, and acquisition time=8:49min and no gating. Data Analysis: A central mask was applied to the raw DTI images to eliminate the anatomy outside the SC. A mean b0 image was calculated, generated from the coregistration of all 6 b0 acquisitions. After motion correction, the diffusion-weighted images were corrected for motion using a rigid body correction algorithm (2). Tensor estimation was done on a voxel-by-voxel basis using in-house software developed in MATLAB. For robust diffusion tensor estimation, RESTORE technique was used (3). Regions of interest (ROIs) were manually drawn on the whole cord on grayscale FA maps along the cervical and thoracic SC for both scans. Analysis of covariance for repeated measures was performed to compare data from TD and SCI. Test-retest reliability was calculated using the intra-class correlation coefficient (ICC) (4).

Results

The images obtained with inner FOV sequence showed excellent delineation of both cervical and thoracic SC with minimal distortions (Fig. 1). Fractional anisotropy (FA) values were significantly lower while radial diffusivity (RD) was significantly higher

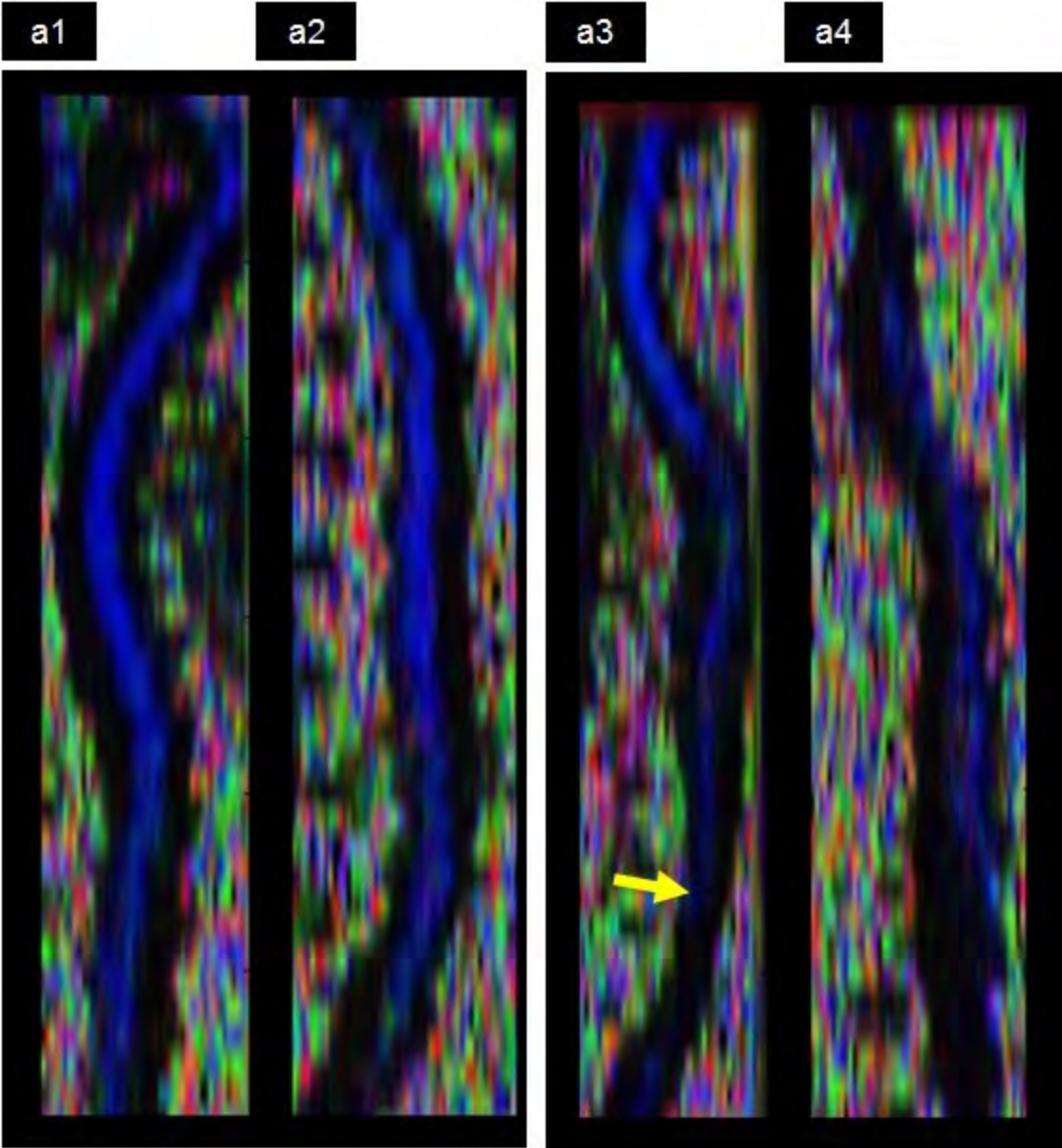
along the SC in patients with SCI compared to TD; however, mean diffusivity (MD) and axial diffusivity (AD) values were not statistically significant (Table 1, Fig. 2). There was a strong reliability for all DTI parameters along the SC in all subjects (ICC: 0.79-0.94). MD, AD and RD showed the greatest number of correlations with ISNCSCI followed by FA indicating that better neurological function is associated with greater unidirectional diffusion.

Conclusions

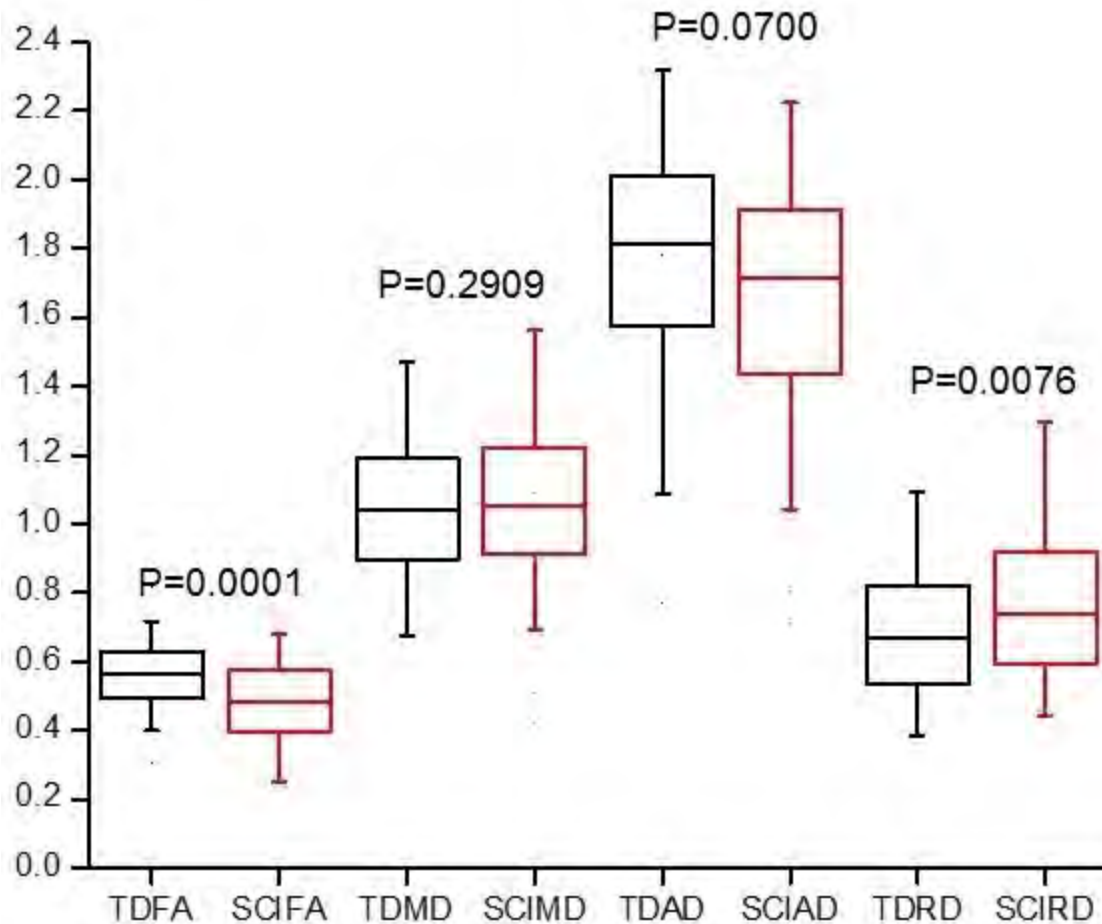
This study demonstrates that DTI has a potential to be used as an imaging biomarker for evaluating the extent of injury, which may be useful to prognosticate as well as monitor patients with SCI.

| | DTI Parameters | | |
|-----|----------------|-----------|-----------|
| | FA | MD | AD |
| TD | 0.56±0.09 | 1.05±0.25 | 1.78±0.38 |
| SCI | 0.47±0.12 | 1.09±0.29 | 1.68±0.37 |

(Filename: TCT_O-142_Table1.jpg)



(Filename: TCT_O-142_Fig1.jpg)



(Filename: TCT_O-142_Fig2.jpg)

O-143

4:51PM - 4:54PM

Reduced FOV Diffusion Tensor MR Imaging and Fiber Tractography of the Pediatric Cervical Spinal Cord

M Alizadeh¹, A Intintolo¹, D Middleton¹, C Conklin², S Faro³, M Mulcahey², F Mohamed²

¹Temple University, Philadelphia, PA, ²Thomas Jefferson University, Philadelphia, PA, ³Temple University School Of Medicine, Philadelphia, PA

Purpose

The purpose of this study was to (a) evaluate the feasibility of generating diffusion tensor tractography (DTT) images of the cervical spinal cord in pediatric, (b) to measure the diffusion tensor imaging (DTI) indices as well as tract specific information using regions of interest (ROIs) generated at every axial slice location along the entire cervical spinal cord based on DTT images, and (c) to investigate if

there are differences in these values between the typically development (TD) subjects and patient group with SCI.

Materials and Methods

Twenty volunteers (mean age of 14.85 years) including 10 healthy subjects who had no evidence of spinal cord injury (SCI) or pathology and 10 subjects with SCI in the cervical area were recruited. The magnetic resonance imaging (MRI) scans were performed using a 3.0T Siemens Verio MR scanner with 4-channel neck matrix and 8-channel spine matrix coils. Diffusion tensor images were acquired axially in the same anatomical location prescribed for the T2-weighted images using a reduced FOV (rFOV) DTI sequence. The DTI parameters used were: number of directions=20, $b=1000\text{s/mm}^2$, voxel size= $1.2 \times 1.2 \times 3.0\text{mm}^3$, matrix size= 36×208 , axial slices=35-45 (depending on the subject's height), TR=6100-8000ms, TE=115ms, number of averages=3 and acquisition time=7min.

Results

The mean fractional anisotropy (FA) values in the controls and patients were 0.6 ± 0.13 and 0.45 ± 0.14 , respectively. Fractional anisotropy values were decreased significantly in the patients with SCI ($p=0.0003$). Apparent diffusion coefficient (ADC) values in the controls and patients were $0.738 \pm 0.181 \times 10^{-3}\text{mm}^2/\text{sec}$ and $0.767 \pm 0.237 \times 10^{-3}\text{mm}^2/\text{sec}$, respectively, however they were not statistically significant. These FA and ADC values in controls and patients with SCI were comparable to what is published in the current literature (1-3). The mean number of fiber tracks in the controls and patients were 1157 ± 156.1 and 750 ± 259.4 , respectively and was significantly decreased in the SCI group ($p=0.00001$). However, the mean length of fiber tracks ($24.30 \pm 15.85\text{mm}$ and $23.06 \pm 15.11\text{mm}$ in the controls and patients, respectively) did not show significant differences. Previous studies on adult subjects demonstrate that FA values of injured cords were much lower than those of uninjured normal cord and ADC values do not differ between abnormal and normal cords in patients and controls (1, 4). However, the mean FA and ADC values of the cervical spinal cord observed in this pediatric study are different from the values quoted in the literature for adult population. The difference in the values may be primarily due to the biologic developments associated with white matter maturation, namely axonal growth and myelination (5). Figures 1 and 2 show tractography images of the entire cervical spinal cord of a normal subject and a patient with SCI, respectively.

Conclusions

These results show that DTI and DTT could be used a surrogate marker for quantification and visualization of the injured spinal cord and has the potential to improve our understanding of damage and recovery in diseases of the spinal cord.

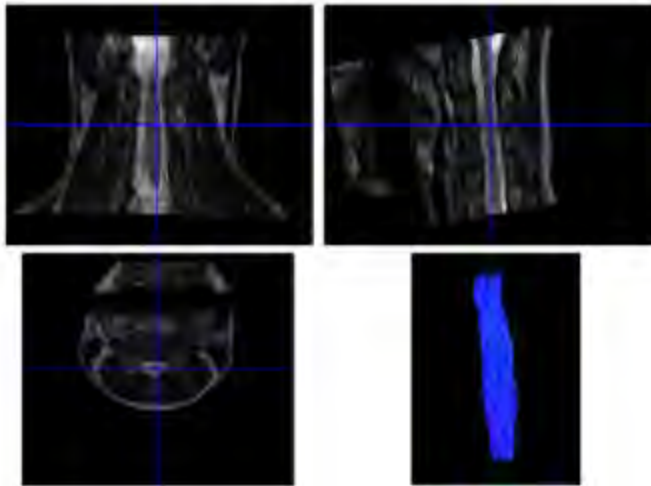


Figure 1. T2- and diffusion tensor tractography of a healthy subject acquired from entire cervical spinal cord. T2 weighted axial (lower left), along with reconstructed coronal (upper left) and sagittal (upper right) views and diffusion tractography of entire cervical spinal cord (lower right).

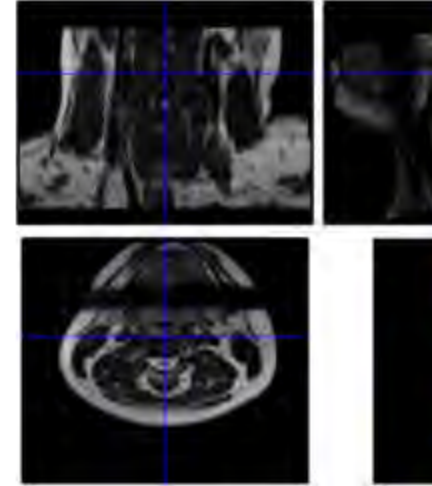


Figure 2. T2- and diffusion tensor tractography from entire cervical spinal cord. T2 weighted with reconstructed coronal (upper left) and sagittal (upper right) views and diffusion tractography of entire cervical spinal cord (lower right). Three dimensional tractography shows the entire cervical spinal cord exactly at the level of the T2 weighted image.

(Filename: TCT_O-143_tract.png)

O-144

4:54PM - 4:57PM

Atrophy and DTI in Pediatric Spinal Cord Injury: Correlation of DTI Metrics to Spinal Cord Cross Sectional Area

D Middleton¹, S Shahrampour¹, S Faro², S SAKSENA³, M Alizadeh¹, C Conklin³, G Nair⁴, W Liu⁵, L Krisa³, M Mulcahey³, F Mohamed³

¹Temple University, Philadelphia, PA, ²Temple University School Of Medicine, Philadelphia, PA, ³Thomas Jefferson University, Philadelphia, PA, ⁴National Institutes of Health, Bethesda, MD, ⁵University of Maryland, College Park, MD

Purpose

The goal of this study was to examine correlations between diffusion tensor imaging (DTI) metrics and spinal cord cross-sectional area (SCCSA) in pediatric subjects with spinal cord injury (SCI).

Materials and Methods

Nine pediatric subjects (mean age 11.8) with chronic SCI were scanned using a 3T Siemens Verio MR scanner. Diffusion tensor imaging data (Fig. 1a) was acquired with an axial inner-FOV sequence(1) with parameters: voxel = 0.8 x 0.8 x 6 mm³, slices = 40, 3 averages, 20 directions, b = 800 s/mm², TE = 110 ms, TR = 7900 ms, TA = 8:49. Data for SCCSA measurement was acquired with a sagittal 3D-TSE T2

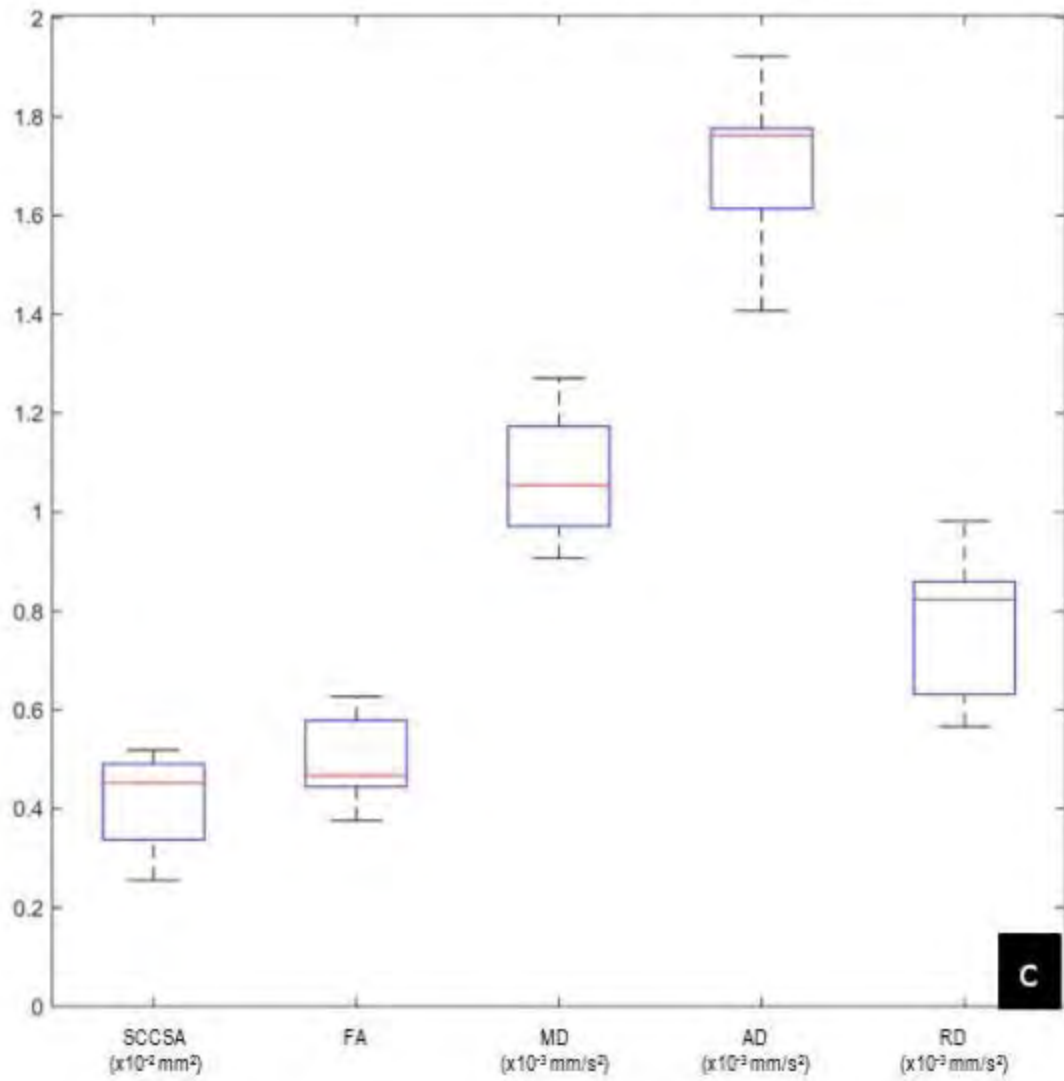
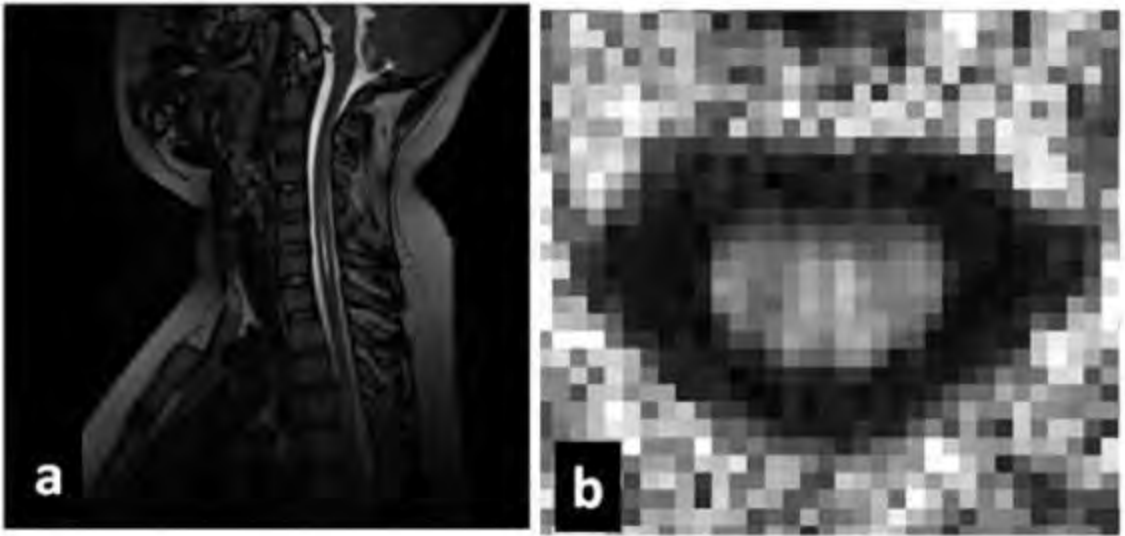
sequence (Figure 1b) with parameters: voxel = 1 x 1 x 1 mm³, TE = 122 ms, TR = 1500 ms, TA = 3:21. Two acquisitions were obtained per subject to provide full cord coverage. Spinal cord cross-sectional area measurement was performed using a newly developed technique where automatic segmentation and cross-section measurement is performed in the axial plane (2). Diffusion tensor images were corrected for motion (3) and tensor estimation was performed. Whole cord regions of interest (ROIs) were drawn on axial slices at each vertebral level.

Results

The DTI parameters and SCCSA were calculated (Fig. 2) and correlations were examined between averaged values for the full cord. A strong and statistically significant correlation was found between FA and SCCSA (Spearman's $r = 0.75$ and $p < 0.02$). Moderate but not significant correlations were found with AD ($r = 0.50$, $p = 0.12$) and RD ($r = -0.58$, $p = 0.07$).

Conclusions

It is possible normal appearing tissue is functionally unaffected, correlation of decreased FA and atrophy suggests that this is not necessarily the case since remaining tissue shows decreased directionality with loss of volume. This suggests that DTI may be a critical compliment to conventional methods when assessing SCI.



(Filename: TCT_O-144_ASNR16.jpg)

O-145

4:57PM - 5:00PM

Accuracy of Neuroimaging to Detect Retinal Pathology in Children Suffering From Accidental and Non-accidental Trauma; Can Ophthalmic Ultrasound Serve as a Screening Tool?

B Riggs¹, C Kraus¹, B Shivakumar², C Trimboli-Heidler³, J Cohen⁴, M Repka⁵, A Tekes⁶

¹Johns Hopkins School of Medicine, Baltimore, MD, ²Johns Hopkins University, Baltimore, MD, ³Children's National Health Systems, Washington, DC, ⁴Children's National Health System, Washington, DC, ⁵Johns Hopkins, Baltimore, MD, ⁶Johns Hopkins Hospital, Baltimore, MD

Purpose

At least one-third of abusive head trauma (AHT) cases are not identified upon initial presentation to the emergency department (ED) (1, 2). Abusive head trauma has a mortality rate of 30%, and 80% of survivors suffer permanent neurological damage (2-4). Retinal manifestations of AHT are identified in 80% of victims by dilated fundus exam (4). We propose that ophthalmic ultrasonography (5) can identify retinal pathology, faster and more accurately than head computed tomography (CT) or head magnetic resonance imaging (MRI) when compared with dilated fundus exam.

Materials and Methods

Retinal pathology was evaluated by dilated fundus exams in all patients. A GE LOGIQ E ® ultrasound machine with a high frequency linear array 10-22 MHz probe was used. No sedation was required. Each globe was evaluated on 37 ophthalmic ultrasounds, 35 head CTs, and 27 head MRIs.

Results

Thirty-seven patients, 27 males and 10 females, 5 days to 5 years of age were enrolled in this IRB approved prospective observational cohort. Abusive head trauma was diagnosed in 27 patients and accidental trauma in 10 patients. According to fundus exams (gold standard), 22 patients had significant bilateral retinal hemorrhages, one had unilateral retinal hemorrhages, and 14 patients had no retinal pathology. Relative to hospital arrival time, ophthalmic ultrasounds were obtained within 3.2 hours (± 2), head CTs within 4 hours (± 4.7), head MRIs within 59 hours (± 77), and dilated fundus exams within 70 hours (± 62). Compared with fundus exam sensitivity and specificity for each modality were as follows (with 95% confidence intervals): head CT sensitivity 23% (CI: 9-43.6) and specificity 100% (CI: 66-100), T2 weighted MRI images sensitivity of 42.9% (CI: 22-67) and specificity of 100% (54-100), susceptibility-weighted imaging (SWI) sensitivity of 62% (CI: 38-82) and specificity

of 66.7% (CI: 22-95.7), ophthalmic ultrasound sensitivity 100% (CI: 88-100) and specificity of 100% (CI: 66-100).

Conclusions

Ophthalmic ultrasound is an accurate, rapid, radiation-free, bedside imaging modality which can be used as a screening tool to identify retinal pathology in children with suspected AHT.

O-146

5:00PM - 5:03PM

Bridging veins rupture correlates with subdural hemorrhages in abusive head trauma: a volumetric SWI study

G Zuccoli¹, M Tamber¹, I Amoddeo¹, A Khan¹, S Bartoletti¹, A Panigrahy¹

¹*Children's Hospital of Pittsburgh of UPMC, Pittsburgh, PA*

Purpose

Bridging vein thrombosis (BVT) is described in abusive head trauma (AHT) in infants. Susceptibility-weighted imaging (SWI) related hypo-intensity and the deformation of the bridging veins resembling a "tadpole" is felt to reflect BVT in the setting of AHT. We aimed to verify whether the tadpole sign truly reflects thrombosis or just traumatic deformation of the bridging veins by using a volumetric SWI approach.

Materials and Methods

Seventeen patients were evaluated retrospectively based on a final multidisciplinary diagnosis of AHT. Images were evaluated by two experienced pediatric neuroradiologists for the presence of the tadpole sign or bridging vein thrombosis on 2-3 mm skip 1 mm SWI axial images. By using the localizer tool (Philips Isite Radiology) we localized the affected bridging veins on coronal volumetric (1 mm skip) SWI images. Contingency table analysis was used to evaluate the strength of association between the presence of BVT on axial versus coronal SWI images.

Results

Among 17 patients that met study criteria, the median age was 8 (IQR 4-13) months, and 53% were male. Eleven out of 17 cases (65%) were identified with possible thrombosis on axial SWI 2mm images [5 = tadpole sign (29%), 6 = thrombosis (35%)]. Among patients showing findings consistent with thrombosed cortical veins on axial imaging, volumetric coronal SWI confirmed the presence of findings consistent with BVT in only four out of 11 patients (36%). The presence of the tadpole sign on axial images did not predict the presence of thrombosed veins on volumetric SWI [OR=0.3 (0.02, 5.01), p=0.538]. Volumetric coronal SWI showed patency of the lumen in 13 out of 17 cases. However, volumetric acquisition disclosed additional irregularities of the bridging veins' walls, a finding that was associated with

the presence of subdural hematoma on MR imaging ($p=0.03$), suggesting traumatic injury.

Conclusions

In our patient population, axial SWI images overestimated findings consistent with thrombosis of the bridging veins as demonstrated by volumetric SWI coronal sequences. Our findings suggest that confounding factors such as volume averaging artifacts may account for previously described findings in the literature, with thrombosis of the bridging veins being confirmed only in a minority of the cases. On the other hand, diffusely irregular contours of the veins observed on volumetric SWI in AHT was a major finding supporting traumatic injury. Further studies using volumetric SWI are warranted to confirm our preliminary findings.

O-147

5:03PM - 5:06PM

Repeated Exposure to Gadolinium-based Contrast Material is Associated with Increased Unenhanced T1 Signal Intensity in the Pediatric Brain.

T Flood¹, N Stence², J Maloney², D Mirsky²

¹University of Colorado Denver - Anschutz Medical Campus, Aurora, CO, ²Children's Hospital Colorado, Aurora, CO

Purpose

Gadolinium-based contrast agents have been shown to deposit in the adult brain and result in increased unenhanced parenchymal signal intensity; however, a rigorous pediatric analysis is lacking (1-5). We conducted a controlled analysis to determine the effect of gadolinium exposure on the pediatric brain.

Materials and Methods

This is a single center retrospective study. Pediatric patients with a history of multiple contrast-enhanced exams (≥ 3) using a linear gadolinium-based contrast agent (gadopentetate dimeglumine) and age-matched contrast-naïve controls were analyzed. Unenhanced axial T1 MR sequence region of interest signal intensity measurements from the globus pallidus (GP), thalamus (TH), dentate nucleus (DN), and pons (PN) were obtained. GP:TH and DN:pons ratios were calculated. Neuroanatomical signal intensity ratios were compared within and between subjects, relative to contrast-naïve patient and control brains, respectively. The relationship between signal intensity and age, gender, and the total number and mean duration between contrast-enhanced exams were investigated. Analysis included Student's T test and Spearman's correlation coefficient.

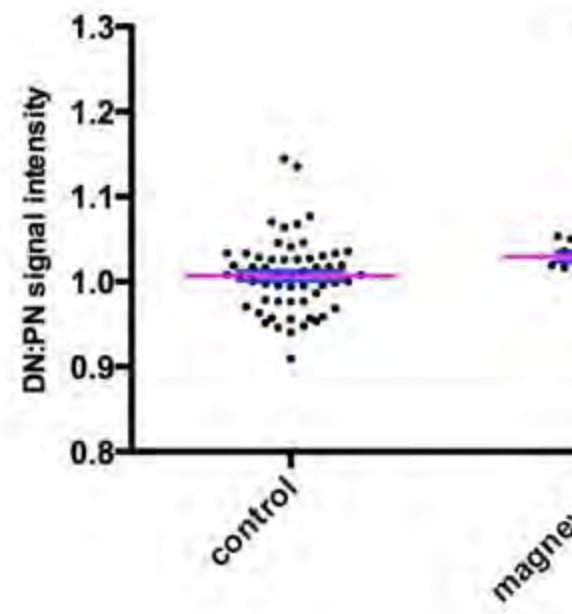
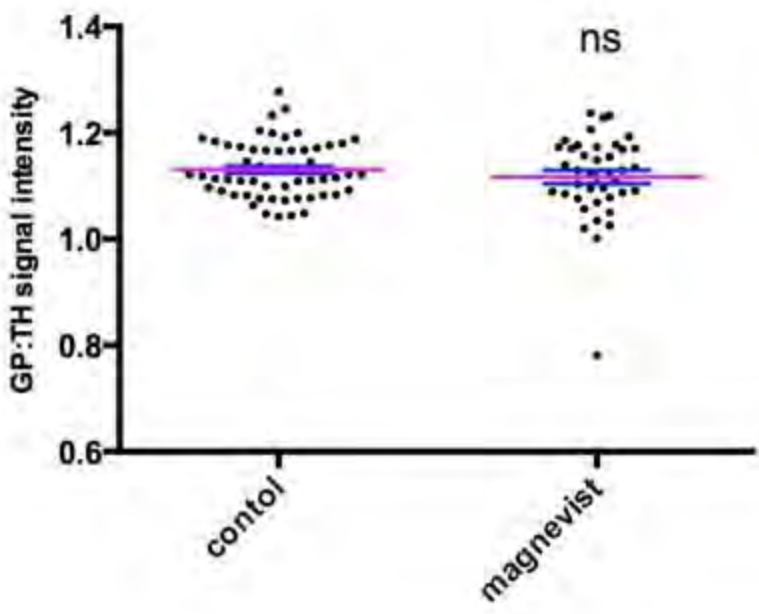
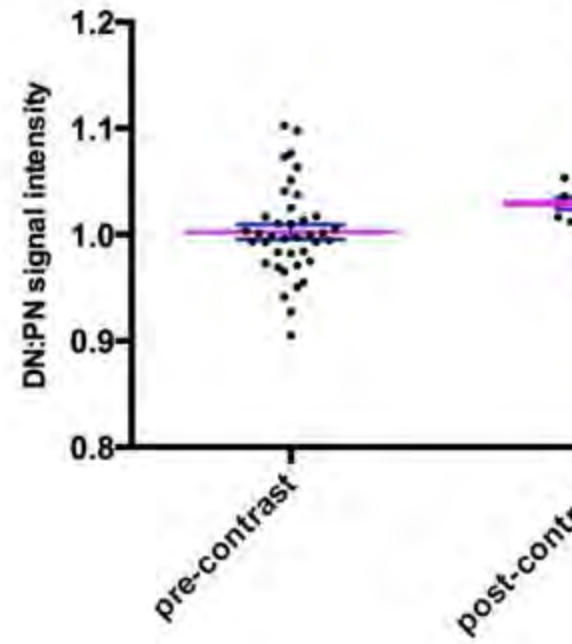
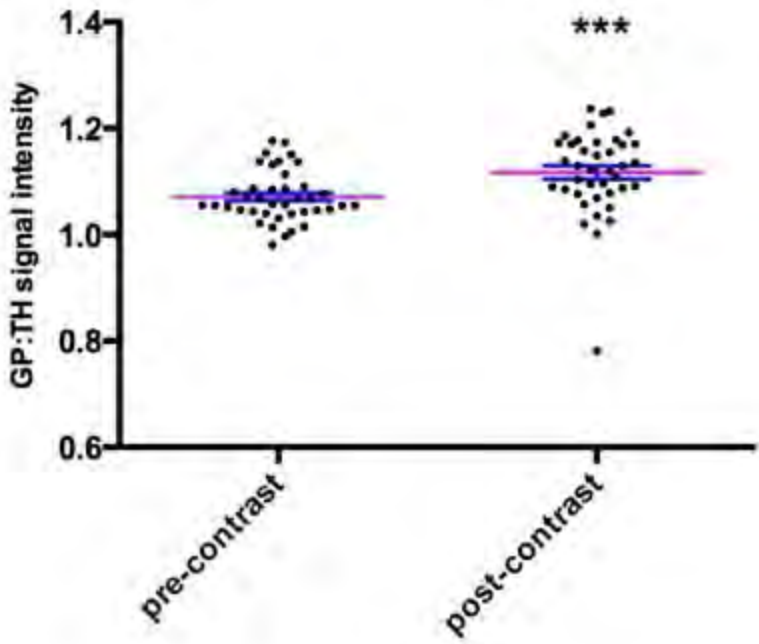
Results

Pediatric patients ($n=40$; age range: 6 months – 18 years) receiving multiple gadolinium-based contrast-enhanced exams (mean: 4.8 exams/patient) demonstrated

increased signal intensity ratios within the GP and DN relative to within subject, contrast-naïve brains ($p < 0.001$ for GP:TH; $p < 0.01$ for DN:PN; Student's T test, paired). Between subject analysis, relative to contrast-naïve age-matched controls, demonstrated an increased signal intensity ratio within the DN ($p < 0.01$) but not within the GP ($p = 0.61$; Student's T test, unpaired). There was no significant relationship between signal intensity and patient age, gender, number of contrast-enhanced exams, or mean duration between contrast-enhanced exams.

Conclusions

Pediatric brain signal intensity increases with exposure to gadolinium-based contrast material. This is the first controlled pediatric study, demonstrating findings consistent with the adult literature (1-5). Additional studies evaluating the clinical significance in this vulnerable population, with a potential lifetime of repeated gadolinium exposure, are needed.



(Filename: TCT_O-147_ASNR_Figure1_07Dec2015.jpg)

O-148

5:06PM - 5:09PM

Intracranial Gadolinium Deposition in the Pediatric Population Following Contrast Enhanced MRI.

R McDonald¹, J McDonald¹, M Jentoft¹, D Murray¹, M Paolini¹, E Williamson¹, D Kallmes¹, L Eckel²

¹Mayo Clinic, Rochester, MN, ²Mayo Clinic, Rochester, Rochester, MN

Purpose

To determine if repeated intravenous exposures to gadolinium-based contrast agents (GBCAs) are associated with deposition of elemental gadolinium in neuronal tissues within the pediatric population.

Materials and Methods

Following antemortem consent and IRB-approval of this single center study, we compared post-mortem neural tissue samples on three pediatric patients who underwent gadolinium-enhanced brain magnetic resonance imaging (MRIs) between 2004-2014 (contrast exposed group) to three pediatric patients who underwent at least one unenhanced brain MRI during their lifetime yet were never exposed to a GBCA (control group). All contrast exposed patients received gadodiamide (Omniscan). Neuronal tissues from the dentate nuclei, pons, globus pallidus, and thalamus of these six deceased pediatric patients were retrieved from our institutional biospecimen archive. Gadolinium tissue concentrations were quantified by inductively coupled mass-spectrometry (ICP-MS) and localized using transmission electron microscopy with energy dispersive x-ray spectroscopy (TEM-EDS). Associations between cumulative gadolinium dose and ICP-MS tissue gadolinium concentrations were assessed by Spearman's rank correlation coefficient (ρ).

Results

All contrast-exposed patients (6-13 years) underwent MRI for evaluation of a primary CNS neoplasm whereas control patients (5-7 years) underwent MRI for non-neoplastic intracranial processes. All contrast-exposed patients had normal renal and hepatobiliary function near the time of gadolinium exposure. Following 4-11 intravenous gadolinium doses, neuronal tissues of the contrast exposed group contained between 0.1-3.0 mg gadolinium/g tissue in a significant dose-dependent trend (dentate nucleus: $\rho = 0.99$, $p < .0001$). Control group patients had undetectable levels of gadolinium in all sampled neuroanatomical locations. Gadolinium deposition in the capillary endothelium and neural interstitium was observed only in the contrast-exposed group using TEM-EDS.

Conclusions

In the pediatric population, intracranial deposition of gadolinium in neural tissues from intravenous administration of GBCAs occurs in a dose-dependent manner in the setting of normal renal and hepatobiliary function and an intact blood-brain barrier.

O-149

5:09PM - 5:12PM

Retention of Linear Gadolinium-based Contrast Agents in the Dentate Nuclei and Globus Pallidus in Pediatric Patients with CNS Neoplasm Who Are Long-term Survivors

V Lau¹, M Atlas², C Filippi³

¹North Shore LIJ, Manhasset, NY, ²Cohen Children's Medical Center, New Hyde Park, NY, ³Hofstra North Shore-LIJ School of Medicine, Manhasset, NY

Purpose

The purpose of this study is to detect increased signal within the dentate nuclei and globus pallidus in long-term surviving pediatric patients with CNS neoplasm as evidence of retention of linear gadolinium-based contrast agents (GBCA).

Materials and Methods

In this retrospective, IRB-approved study, 13 pediatric patients, 5 boys, 8 girls, average age 6.2 years, range 1-11 years at the time of diagnosis, who are all long-term survivors of central nervous system neoplasm. None had neoplasm involving the posterior fossa or deep gray nuclei. All had over six contrast-enhanced brain magnetic resonance (MR) scans (average 15.8 scans, range 6-31 scans), all of which used the identical linear gadolinium-based contrast agent (GBCA). Follow up, on average, was 5.7 years (range 3-9 years). Signal intensity on axial T1-FLAIR images, all performed on the same GE 1.5 MR scanner, were obtained using identical region of interest (ROI) measurements of the dentate nucleus bilaterally and globus pallidus bilaterally; ROIs were obtained of the thalami and pons as reference standards. Regions of interest were placed by a diagnostic radiology resident and a neuroradiology attending with certificate of added qualification. Interobserver and intraobserver reliability for the values obtained for the SI exceeded 0.85 (85%) for the dentate, globus pallidi, pons, and thalami. The signal intensity (SI) ratios of dentate to pons and globus pallidus to thalami were obtained on the first and final exams to assess for changes of T1 shortening (GBCA retention), and independent two-tailed t-tests were used to assess for changes in the ratio and significance was set to $p < .05$.

Results

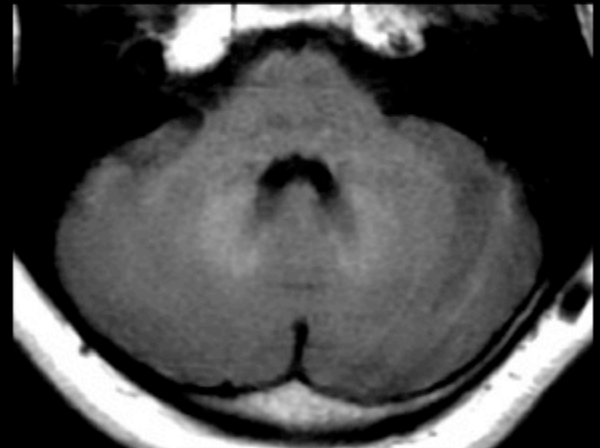
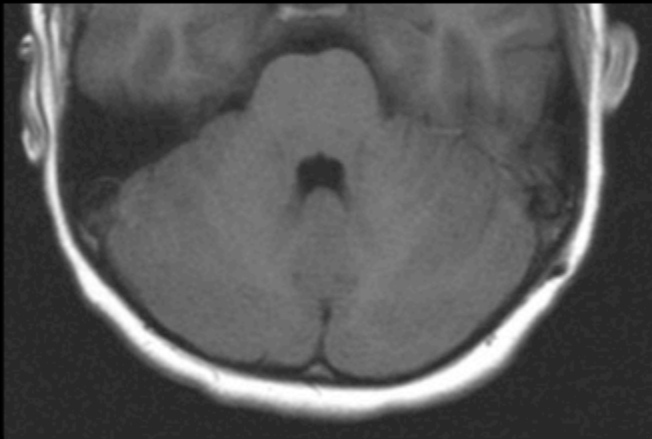
The SI ratio of dentate to pons averaged 1.03 +/- .03 on initial MR exams and 1.12 +/- .05 on the final MR exam. The change in SI ratio of dentate to pons over time was significant ($p < .0002$). The SI ratio of globus pallidus to thalamus averaged 1.02 +/-

.06 on the initial and 1.13 +/- .06 on the final exam. The change in SI ratio of globus pallidus to thalamus over time was significant ($p < .002$). Figure 1 shows an example of increasing SI in the dentate from baseline MR scan in 2003 to MR scan in 2011.

Conclusions

This study shows increased SI in the dentate and globus pallidus from linear GBCA retention in these pediatric patients who are long term cancer survivors. Consideration should be given to the use of macrocyclic GBCAs which is not yet associated with brain retention, and the clinical significance of this observation on brain development remains unknown at this time.

7 year old female patient with increasing T1 retention in the dentate nuclei from 2003 MR scan on the left to MR scan from 2011 on the right (the 19th contrast-enhanced brain MR exam) in this patient with craniopharyngioma



(Filename: TCT_O-149_Slide1.jpg)

O-150

5:12PM - 5:15PM

In pediatric patients, increased T1 signal intensity in the dentate nucleus on unenhanced T1-weighted MR images correlates to number of previous gadolinium contrast administrations

G Bolles¹, B Marebwa¹, A Chatterjee¹, T Brown², D Roberts¹

¹Medical University of South Carolina, Charleston, SC, ²Medical University of South Carolina, Charleston, SC

Purpose

Recently, there have been reports of gadolinium accumulation in the brain of adult patients with normal renal function who have undergone multiple gadolinium contrast administrations. Here we describe a series of pediatric patients who, following multiple contrasted magnetic resonance imaging (MRI) exams, demonstrated progressive hyperintense signal on unenhanced T1-weighted imaging involving the dentate nucleus, a finding which previously has been shown to represent gadolinium deposition in adults.

Materials and Methods

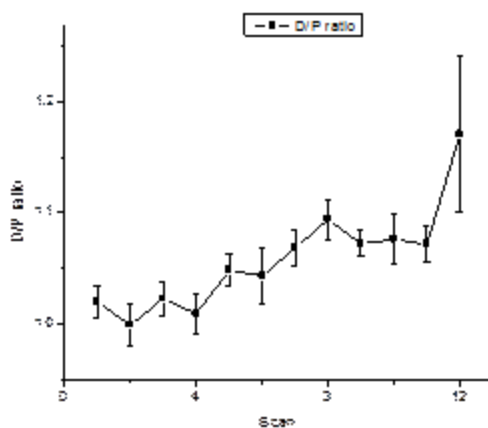
In this retrospective case series at a single large academic institution, we measured signal intensity of the dentate nucleus and pons on unenhanced T1-weighted images in 17 pediatric patients (range 2 months-15 years, median 6 years) who had undergone contrasted MRI exams (on average 9.75 exams, SD 5.23) using a linear contrast agent. Clinical presentations ranged from supratentorial or extra-cranial neoplasms, cerebrospinal fluid (CSF) leaks, vascular malformations and infectious processes, not involving the posterior fossa. None of the 17 patients had renal failure. Eight of the 17 patients received chemotherapy. Eight of the 17 patients had undergone radiation therapy. To avoid subjectivity of region of interest selection, we used an automated software system called "SUIT" to define the dentate nucleus. SUIT is a high-resolution atlas template of the human cerebellum and brainstem based on the SPM-toolbox (<http://www.icn.ucl.ac.uk/motorcontrol/imaging/suit.htm>). We calculated the dentate-to-pons ratio and performed a repeated measures ANOVA to test if the main effect of scan repetition was significant.

Results

The dentate-to-pons ratio showed a significant correlation with the number of previous gadolinium contrast administrations ($p=0.038$) (Fig. 1).

Conclusions

The clinical significance of gadolinium accumulation in the human body is currently unknown but is of concern, particularly in pediatric patients who have a lifetime to manifest any potential adverse consequences. Therefore, research is needed to address the clinical significance, if any, of gadolinium deposition in the developing pediatric brain.



(Filename: TCT_O-150_Picture1.gif)

O-151

5:15PM - 5:18PM

Asymptomatic gadolinium deposition in the dentate and other deep grey nuclei in children and adults: influence of cumulative dose and radiochemotherapy

S Kinner¹, T Schubert¹, S Rebsamen¹, R Bruce¹, S Reeder¹, H Rowley¹

¹University of Wisconsin Madison, Madison, WI

Purpose

T1 hyperintense signal has been noted on magnetic resonance imaging (MRI) in deep gray nuclei after multiple doses of gadolinium-based contrast agents (1-4). The aim of this study was to determine whether T1 shortening also is observed in children, and to analyze the anatomical patterns and clinical profiles seen in affected patients.

Materials and Methods

In this IRB-approved, single-center study, we reviewed all patients with normal renal function who had received at least four gadobenate dimeglumine enhanced MRIs since 08/09. Amongst 326 children, 76 had solely gadobenate (4-20 injections, mean: 8); 16 had brain tumors and radiochemotherapy (RCTX). Amongst 3567 adults, of the top 349 cases with the most injections (n=9-34) analyzed to date, 100 had solely gadobenate (all but four with RCTX). T1 signal change of the dentate between first and last MRI was measured and signal intensity ratios (SIR) for dentate-to-pons (DNP) calculated and correlated in the pediatric group.

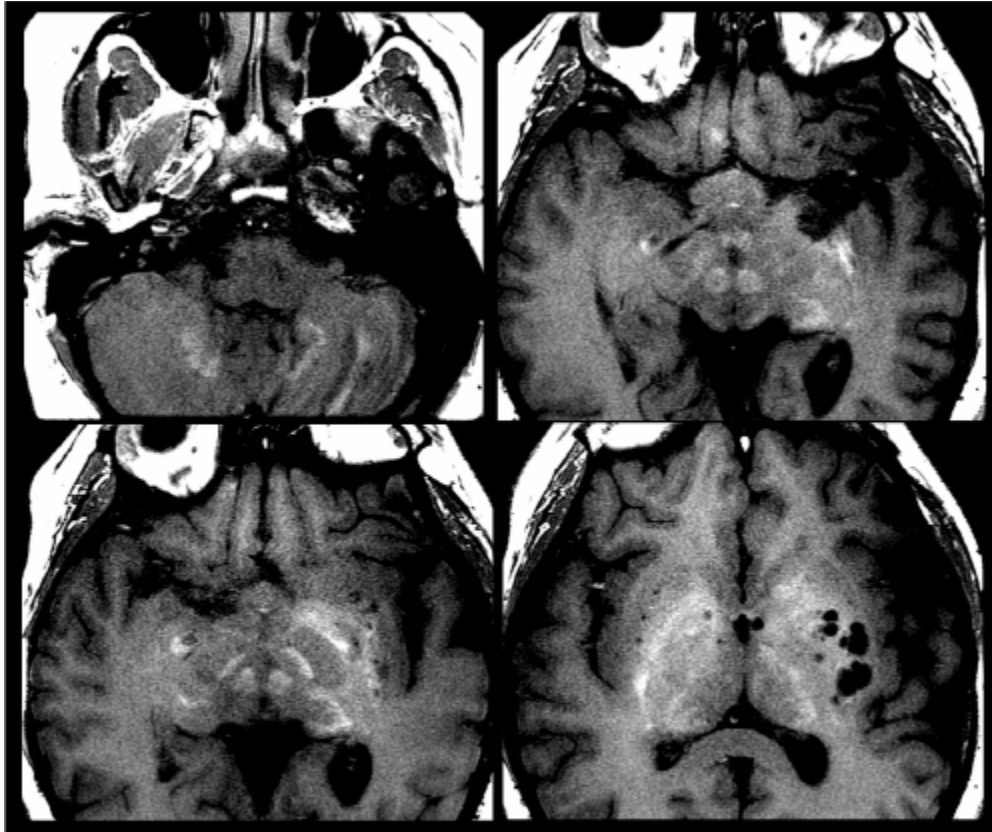
Results

Twelve of 16 pediatric patients with tumors and RCTX had dentate hyperintensities while only 2/60 children without these confounders showed signal increase. Eighty-six of 100 adults with high cumulative exposures showed dentate hyperintensities. A statistically significant increase in SIR change for number of injections ($p < 0.001$) as

well as the amount of gadolinium ($p=0.008$), but not for inter-scan-time interval ($p=0.35$) was noted. There was a significant difference in average change in SIR over time in favor of those with RCTX ($p<0.001$). Hyperintensities in other deep nuclei including the globus pallidus, pulvinar, and red nucleus also were observed (Fig.). Chart review revealed no referable neurological deficits in any subject.

Conclusions

Children and adults show a similar pattern of asymptomatic T1 hyperintensity in the dentate and other deep gray nuclei after multiple injections of gadobenate. The appearance in children may have a later onset, and is accelerated by radiochemotherapy.



Non-contrast T1-weighted images from a 16 year old girl with neurofibromatosis and hypothalamic glioma, treated with RCTX, who received over 22 contrast-enhanced MRIs since age 3. Hyperintense signal changes are seen in the dentate, red nucleus, substantia nigra, globus pallidus, and thalamus.

(Filename: TCT_O-151_ASNRimage.gif)

O-152

5:18PM - 5:21PM

Absence of T1 Hyperintensity in the Dentate or Globus Pallidus in 48 Subjects Receiving 4 or More Doses of Gadobenate Dimeglumine Before Age 3

M DeLano¹, B Betz¹, M Hicks², A Nash¹

¹Michigan State University, Advanced Radiology Services, PC, Spectrum Health System, Grand Rapids, MI, ²Michigan State University College of Human Medicine, Grand Blanc, MI

Purpose

Increased awareness of the potential for gadolinium-based contrast deposition in the brain after repeated exposures prompted a retrospective review of our pediatric brain imaging data. Since 2008 our institution has been using gadobenate dimeglumine for brain magnetic resonance (MR) studies. Since no known harm has been described in patients with contrast-related persistent hyperintensity, we focused on those <3 years of age as they would have the greatest risk of time dependent adverse events. Our aim was to determine if our patients have imaging evidence of persistent gadolinium contrast in brain tissues after four or more exposures to contrast.

Materials and Methods

Forty-eight subjects were identified that had four or more Gd doses (range 4-15 doses) before 3 years of age. Nine of these subjects had 10-15 Gd doses before 3 years of age. Imaging was performed with T1 FLAIR techniques. Occasional conventional spin echo also was provided. Qualitative assessment of the brain by visual inspection and quantitative assessment of selected regions of interest in the dentate nucleus, globus pallidus, thalamus and pons was performed. Total contrast volume administered, renal function, primary diagnosis, and any exposure to radiation therapy was documented.

Results

Patient exposure to gadobenate dimeglumine varied considerably as it is administered by patient weight. No instances of residual T1 hyperintensity were identified in the brain by visual inspection or quantitative interrogation of regions of interest. T1 hyperintensity was not identified in our patient cohort.

Conclusions

Standard MR imaging does not reveal evidence of residual gadolinium-based contrast in the brain of 48 children <3 years of age who have been exposed to 4-15 doses of gadobenate dimeglumine. Additional attention to the influence of the choice of T1 pulse sequence should be given. Background cerebellar and internal capsule white matter hyperintensity may mask the identification of subtle T1 hyperintensity putatively related to contrast administration.

O-153

5:21PM - 5:24PM

Placental vascular pathology correlates with MRI in perinatal ischemic stroke

P Caruso¹, M Naqvi¹, D Roberts¹

¹Massachusetts General Hospital, Boston, MA

Purpose

Perinatal ischemic stroke (PIS) is a leading cause of cerebral palsy (CP). Recent studies of PIS suggest that a definite causative risk factor is established in only 50% of cases. Placental disorders are highly plausible risk factors for PIS. Our study seeks to determine if placental fetal vasculopathy correlates with radiographic and clinical findings in radiologically proven cases of PIS.

Materials and Methods

We searched the MGH pathology database from 1994-2015 for the clinical history of PIS. The obstetrical, neonatal, and pediatric follow-up records were reviewed. The imaging was reviewed by a pediatric neuroradiologist; the imaging findings were grouped into arterial ischemic stroke (AIS), cerebral sinovenous thrombosis, presumed perinatal ischemic stroke, and periventricular venous infarction, in keeping with recent published groupings. In cases of AIS, the arterial vascular territory was recorded. The placental pathology was reviewed by perinatal pathologist: placental pathology was grouped into three categories: fetal vascular malperfusion (FVM), fetal inflammatory pathologies (FIP), and other.

Results

Sixteen cases of radiologically proven PIS with placental pathology were found. The obstetrical, neonatal, and pediatric follow-up data are presented in the attached table. All neonates presented by the third day of life with signs of hypoxia or seizure. All 16 cases fell into the category of AIS. The location of the IPS in all cases was the middle cerebral artery. Twelve of the 16 cases of AIS showed placental fetal vascular pathology. Fetal vascular malperfusion, five cases, FIP, six cases, and other placental pathology, three cases, were found. Placentas classified as FVM trended with earlier clinical presentation of IPS ($p=0.13$).

Conclusions

Of the 16 cases of radiologically proven perinatal AIS, 12 showed evidence of placental fetal vasculopathy. Although not associated with specific outcomes, our study supports a role for placental factors in the pathophysiology of IPS.

O-155

5:27PM - 5:30PM

Texture analysis features reveal selective vulnerability of thalamic nuclei in mice after hypoxic-ischemic injury

M Wagner¹, M Wurnig², A Narayan³, T Huisman⁴, F Northington⁵, A Poretti⁵

¹Johns Hopkins Hospital, Baltimore, MD, ²University Hospital Zurich, Zurich, AK, ³Johns Hopkins Hospital, Baltimore, MD, ⁴Johns Hopkins, Baltimore, MD, ⁵The Johns Hopkins University School of Medicine, Baltimore, MD

Purpose

Neonatal hypoxic-ischemic injury (HII) damages the thalamus, with the ventrolateral nuclei being a selectively vulnerable target. We aimed to identify thalamic nuclei damage in HII mice to assess the role of hypothermic management using texture analysis (TA) features of diffusion tensor imaging (DTI) data.

Materials and Methods

Hypoxic-ischemic injury was induced at postnatal day 10 by a right carotid artery ligation followed by 45 minutes of hypoxia. Mice were randomized to a healthy control group (N=20) and a hypothermia (31°C) (N=32) or normothermia (36°C) (N=25) group following HII. Diffusion tensor imaging data were acquired at postnatal (p) day 11, 18, and 30. Fractional anisotropy (FA) and mean diffusivity (MD) maps were generated. Single slice regions of interest were drawn manually to cover the entire thalamus at its greatest diameter on FA and MD maps. Nineteen TA features were calculated using a MATLAB based semi-automated algorithm.

Results

Quantitative evaluation of TA features of the right thalamus on both FA and MD maps revealed statistically significant results ($p < 0.005$) for 1st, 2nd, and 3rd order texture features comparing p11, p18, and p30 control mice and 1) mice with hypothermia therapy and 2) mice with normothermia therapy. Statistically significant differences were predominant in 3rd order texture features including short and long runs emphasis (SRE/LRE), gray level nonuniformity (GLN), run percentage (RP), and long run high gray level emphasis (LRHGE). Homogeneity (2nd order feature) was significantly different comparing p18 mice with hypothermia and normothermia.

Conclusions

Texture analysis identifies thalamic injury in mice after HII. Our results most likely reflect the selective vulnerability of the ventrolateral nuclei. Immunohistochemistry is needed to confirm these findings and human studies are needed to determine relevance of these findings. In addition, studies correlating TA features with neurodevelopmental outcome of children with HII are needed to assess the potential role of TA measures as outcome biomarker of neonatal HII.

O-156

5:30PM - 5:33PM

Brain Injury Detected with MRI scan in Neonates with Hypoxic-Ischemic Encephalopathy and Seizures

B Kline-Fath¹, P Horn¹, M Schapiro¹

¹*Cincinnati Children's Hospital Medical Center, Cincinnati, OH*

Purpose

Seizures are common in neonates with hypoxic-ischemic encephalopathy (HIE). Our aim was to determine the magnetic resonance (MR) brain imaging findings in neonates with HIE with seizures (HIESz+) compared to those without seizures (HIESz-).

Materials and Methods

EPIC medical record was reviewed for all term (> 36 weeks) neonates with HIE admitted to our institution between 2008 and 2013. Subjects with acceptable MRI scans obtained within 2 weeks of birth were included: 23 HIESz- and 46 HIESz+. Charts were reviewed for demographic, clinical and laboratory variables. Neonates were imaged with conventional T1, proton density, T2-weighted, gradient echo, and diffusion-weighted sequences at 1.5T or 3T. Images were rated using a MRI injury grading score (higher scores more abnormal): brainstem, cerebellar, white matter, cortical, hippocampal, parenchymal hemorrhage, basal ganglia, posterior limb of internal capsule (PLIC), intraventricular hemorrhage, watershed, and ventriculomegaly.

Results

There were no significant group differences (Student's t tests or Fisher's Exact test, where appropriate) in gestational age, birth weight, sex, age at MRI scan, or arterial and cord pH and base excess. HIESz- required more resuscitation at birth ($p=0.0004$), and had lower 5 minute Apgar score ($p=0.0164$) and a greater percentage received therapeutic hypothermia ($p=0.0179$). HIESz+ had significantly more injury within white matter ($p=0.00025$), basal ganglia ($p=0.004$), PLIC ($p=0.0421$), and watershed ($p=0.0091$) when compared to HIESz-. In neonates who received therapeutic hypothermia (19 HIESz- and 24 HIESz+), HIESz+ had an abnormal distribution of ratings compared to HIESz- for white matter ($p=0.004$), basal ganglia ($p=0.0258$), and PLIC ($p=0.0181$), but not watershed ($p=0.1396$).

Conclusions

Despite better Apgar score and less resuscitation, HIESz+ surprisingly had more injury in the white matter, basal ganglia and PLIC than HIESz-. Seizures themselves may cause brain damage. However, it is possible that confounding factors (such as not receiving therapeutic hypothermia) lead both to seizures and brain injury.

HIE MRI Injury grading

- **Brainstem injury**

0 = none
1 = focal
2 = diffuse

- **Cerebellar injury**

0 = none
1 = less than 3 punctate lesions (<2 mm)
2 = more than 3 punctate lesions or confluent large areas

- **White matter injury**

0 = normal
1 = minimal (3 or less wm lesions)
2 = moderate (>3 lesions, bilateral)
3 = severe (multiregional lesions/watershed)

- **Cortical injury**

0 = normal
1 = single focal infarction
2 = abnormal cortex anterior or posterior
3 = abnormal cortex in both anterior and posterior watershed zone
4 = extensive cortical injury

- **Hippocampal injury**

0 = none
1 = unilateral
2 = bilateral

- **Parenchymal hemorrhage – not grade 4**

0 = negative
1 = positive microhemorrhage
2 = positive hemorrhage greater than 2mm

- **Posterior Limb of the internal capsule**

0 = negative/myelination present
1 = impaired myelination
2 = myelination absent with reversed/abnormal signal on T1 or T2

- **Basal Ganglia**

0 = normal
1 = abnormal signal thalamus
2 = abnormal signal in thalamus and lentiform
3 = abnormal signal thalamus, lentiform, per
4 = extensive

- **Intraventricular hemorrhage**

0 = none
1 = grade 1
2 = grade 2
3 = grade 3
4 = grade 4

- **Watershed**

0 = Normal
1 = Single focal infarction
2 = Abnormal signal in anterior or posterior w
matter
3 = Abnormal signal in anterior or posterior w
white matter
4 = Abnormal signal in both anterior and post
5 = More extensive cortical involvement

- **Ventriculomegaly**

0 = normal
1 = mild (10-15mm)
2 = moderate to severe (>15mm)
3 = obstructive hydrocephalus

(Filename: TCT_O-156_HIEMRIInjurygrading.gif)

Monday

4:45PM - 6:15PM

Washington Marriott Wardman Park, Maryland A/B/C

6E - Study Group - Clinical Translation of Functional Diffusion MRI (non-CME)

Monday

4:45PM - 6:21PM

Washington Marriott Wardman Park, Roosevelt 4

6F-PARALLEL PAPER SESSION-Thrombosis, Clot Detection and CNS Hemorrhage

O-157

4:45PM - 4:53PM

Carotid MPRAGE Improves Detection of Simultaneous Bilateral Stroke Sources

M McLaughlin¹, S Kim¹, A DeHavenon¹, G Treiman¹, D Parker¹, S McNally¹

¹University of Utah, Salt Lake City, UT

Purpose

The presence of bilateral acute ischemic stroke often is assumed to be secondary to cardiac emboli, especially in the absence of severe bilateral carotid stenosis or other lumen markers of vulnerable plaque. Carotid intraplaque hemorrhage (IPH) is an essential predictor of ipsilateral ischemic stroke, and is reliably detected by the MPRAGE sequence. The purpose of this study was to determine if carotid MPRAGE detection of IPH was additive to the predictive value of conventional lumen markers in the setting of simultaneous bilateral stroke.

Materials and Methods

In this retrospective cross-sectional study, patients undergoing evaluation for acute stroke were imaged with brain and carotid magnetic resonance imaging (MRI). Acute ischemic stroke was determined using the standard AHA definition of cerebral infarction aided by diffusion-weighted imaging. Patients with noncarotid source strokes (e.g., cardiac sources) and complete or near-complete carotid occlusion were excluded. A total of 425 patients were analyzed. Carotid lumen imaging characteristics were recorded including stenosis, plaque thickness, ulceration, intraluminal thrombus, and IPH. Patient clinical factors including cerebrovascular risk factors and medications also were recorded. Receiver operating characteristic (ROC) curve analysis was performed to determine if information on bilateral carotid IPH increases the predictive value for bilateral carotid stroke sources compared to lumen markers.

Results

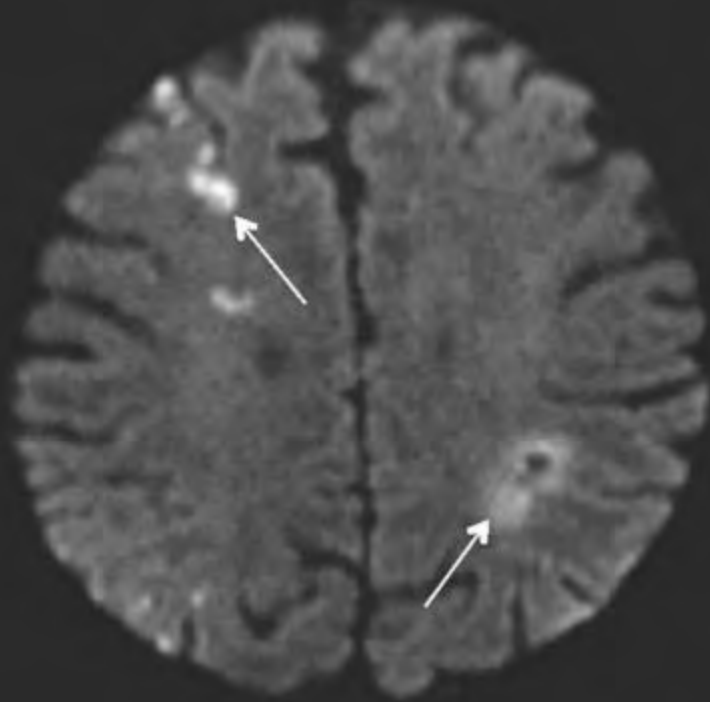
Of the 425 patients imaged, 112 had an acute ischemic stroke, 17 of which were bilateral. Carotid IPH was present in 89/425 of cases, and was bilateral 27.0% of the time (24/89). Bilateral carotid IPH was associated with bilateral stroke (AUC=0.808, 95%CI 0.690-0.925) (Figs. 1A and 1B), and was a better predictor than either bilateral $\geq 70\%$ stenosis (AUC=0.523, $p < 0.001$) or bilateral plaque ulceration (AUC=0.625, $p = 0.011$). In addition, bilateral carotid IPH improved the predictive value of a model including bilateral average stenosis and bilateral ulceration (AUC=0.891 versus 0.800, $p = 0.001$). Receiver operating characteristic results are displayed in Fig. 2, with the

blue curve representing bilateral ulceration combined with average bilateral stenosis and the green curve showing the improved predictive value of including bilateral IPH.

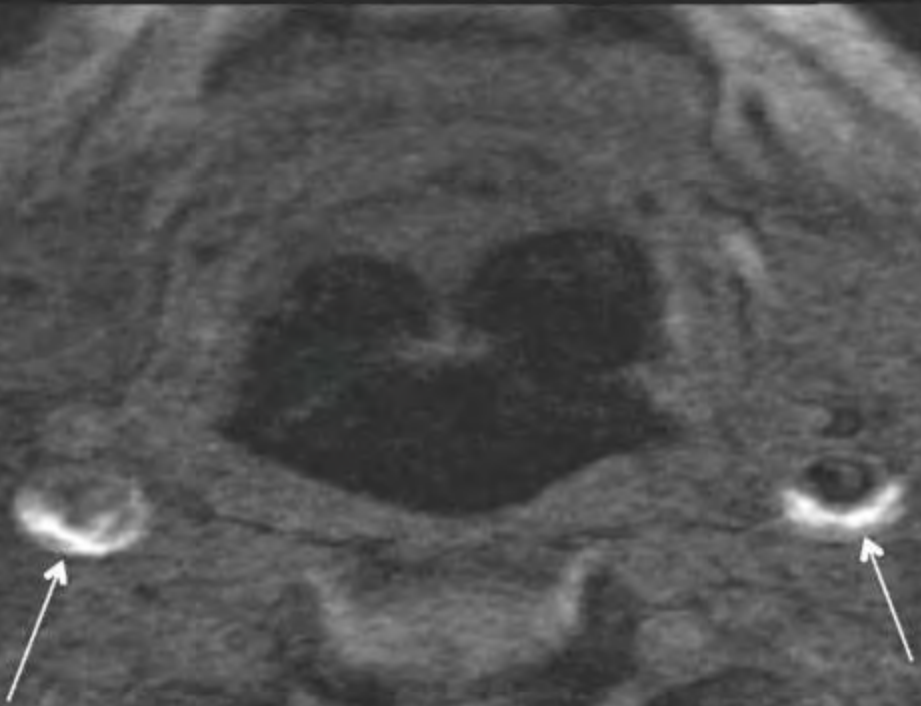
Conclusions

Bilateral carotid IPH is highly associated with simultaneous bilateral stroke, even in the absence of severe bilateral stenosis or ulceration. The carotid MPRAGE sequence provides critical information in determining sources of simultaneous bilateral stroke in patients without cardiac sources.

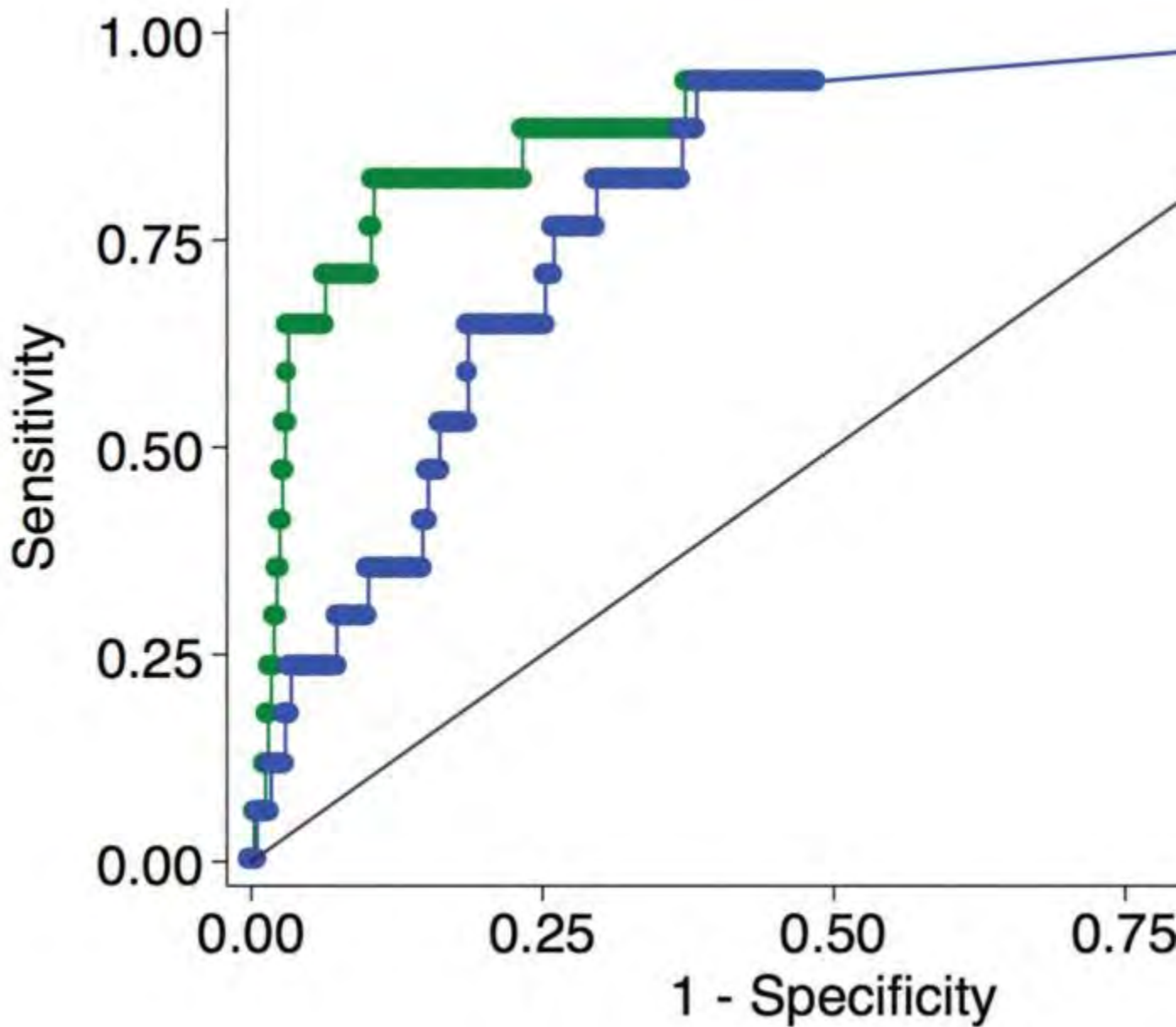
A



B



(Filename: TCT_O-157_Figure1.jpg)



(Filename: TCT_O-157_Figure2.jpg)

O-159

5:01PM - 5:09PM

The susceptible vessel sign (SVS) for detection of arterial occlusive thrombosis on Susceptibility Weighted Images (SWI) in acute stroke patients: correlation with infarct volume.

S Payabvash¹, J Benson², S Taleb¹, B Hoffman³, M Oswood³, A McKinney¹

¹University of Minnesota, Minneapolis, MN, ²University of Minnesota, St. Paul, MN, ³Hennepin County Medical Center, Minneapolis, MN

Purpose

To determine the diagnostic accuracy of susceptible vessel sign (SVS) for detection of arterial occlusive thrombosis on susceptibility-weighted (SWI) sequence in patients presenting with acute ischemic stroke, as well as its correlation with clinical outcome and infarct volume.

Materials and Methods

The medical and imaging records of all patients presenting with acute ischemic stroke to two university affiliated hospitals from 1/2011 to 12/2014 were reviewed. Those patients who underwent an magnetic resonance imaging (MRI) with a SWI acquisition within 24 hours of witnessed symptom onset or last-seen-well were included in this study. Simultaneous MRA (or CTA performed within 3 hours of MRI) was used as the gold standard to determine the presence of intracranial arterial occlusion. Infarct volumes were also measured on diffusion-weighted imaging (DWI).

Results

A total 192 patients with an average age of 63.4 ± 16.5 years were included in this study. The MRI scan was performed within 14 ± 7 hours after symptom onset or last-seen-well. On simultaneous MRA/CTA, 45 (23.4%) patients had arterial occlusion. The SVS was seen on SWI scan of 22 patients – including three false positive subjects without arterial occlusion. The SVS had 42.2% sensitivity, 98.0% specificity, 84.7% negative predictive value, and 86.4% positive predictive value for detection of the arterial occlusion, with an area under the receiver operating characteristics (ROC) curve of 0.701 ($p < 0.001$). The SVS was almost equally sensitive for detection of thrombosis in ICA, MCA, and PCA (Table). Among patients with arterial occlusion, those with SVS had significantly larger infarct volume compared to those without (177.9 ± 169.9 mL versus 86.3 ± 125.6 mL, $p = 0.048$). However, there was no significant difference between patients with SVS versus those without, in terms of the admission and discharge NIHSS scores, as well as for the 3-month modified Rankin score.

Conclusions

The SVS is highly specific (98%), but is only moderately sensitive (42.2%), in the detection of arterial occlusive thrombosis in acute stroke patients. Among stroke patients with arterial occlusion, those with positive SVS have significantly larger infarct volume compared to those without SVS. Hence, SWI is a useful adjunct in the acute stroke MRI evaluation.

| Arterial occlusion | SVS |
|---------------------------|--------------------|
| ICA | 3/5 (60%) |
| MCA | 12/29 (41%) |
| ACA | 0/1 (0%) |
| Basilar artery | 0/1 (0%) |
| PCA | 4/9 (40%) |

Rate of SVS among patients with cerebral arterial occlusion

(Filename: TCT_O-159_ScreenShot2015-12-09at55904PM.png)

O-160

5:09PM - 5:17PM

Imaging-based venous biomarkers in acute stroke patients

J Puig¹, M Hernandez-Perez², G Blasco³, J Daunis-i-Estadella⁴, M Terceño⁵, J Serena⁵, Y Silva⁵, C van Eendenburg⁵, M Wintermark⁶, B Menon⁷, S Pedraza³, J Munuera²

¹Imaging Research Unit, IDI-IDIBGI, Hospital Dr Josep Trueta, Girona, Spain, ²Hospital Universitari Germans Trias i Pujol, Badalona, None, ³Imaging Research Unit, IDI-IDIBGI, Hospital Dr Josep Trueta, Girona, None, ⁴University of Girona, Girona, None, ⁵Hospital Dr Josep Trueta, IDIBGI, Girona, None, ⁶Stanford

University, Stanford, CA, ⁷Calgary Stroke Program, Department of Clinical Neurosciences, Calgary, Alberta

Purpose

Although endovenous thrombolysis is the treatment of choice within 4.5 hours of stroke onset, mechanical thrombectomy also has proven useful recently. The role of the venous system in ischemic stroke is unclear. Imaging-based venous biomarkers would detect alterations in brain perfusion from the dynamic viewpoint or secondary to optimization of oxygen consumption mechanisms (misery perfusion). We aimed (1) to correlate potential imaging-based venous biomarkers, such as hypodense internal cerebral vein ratio (rHdV), between pathological and contralateral, hypointense vein on T2* (HVt), and asymmetrical venous drainage (AVd), with hypoperfusion of the ischemic territory, and (2) to assess possible relationships between imaging-based venous biomarkers and functional outcome.

Materials and Methods

We analyzed two patient groups with anterior ischemic stroke within 12 hours of onset: (1) Patients treated with endovenous thrombolysis [computed tomography (CT) group], who underwent perfusion CT and CT angiography and (2) candidates for mechanical thrombectomy [magnetic resonance imaging (MRI) group], who underwent diffusion-weighted imaging, T2*, susceptibility-weighted imaging, and dynamic magnetic resonance angiography (Olea Sphere V.3.0). We analyzed demographics, stroke etiology, National Institutes of Health Stroke Score (NIHSS), modified Rankin Scale at 3 months, infarct volume, and arterial recanalization (Thrombolysis in Myocardial Infarction criteria).

Results

In the CT group (n=123; 45 women; mean age: 78 years; 54% cardioembolic; baseline NIHSS=18) rHdV correlated negatively with penumbra volume ($r=-0.42$), and $rHdV \geq 0.83$ predicted good functional outcome at 90 days ($p < 0.001$) and arterial recanalization ($p=0.005$). In the MRI group (n=25; 16 women; mean age: 65 years; 41% cardioembolic; baseline NIHSS=17), 96% had HVt, 16% had AVd in deep veins, and 52% had AVd in superficial sinuses; HVt was associated with greater penumbra volume ($p=0.002$).

Conclusions

Imaging-based venous biomarkers are associated with increased hypoperfused tissue volume, worse recanalization rate, and poor functional outcome.

Prediction of recanalization

| Variable | ROC analysis | | | |
|--------------------------------|-----------------------|----------|-------------|-------------|
| | Area under curve (CI) | Cut-off | Sensitivity | Specificity |
| Ratio internal cerebral venous | 0.645 (0.549-0.740) | 0.8392 | 0.667 | 0.56 |
| ASPECTS score at 24 h | 0.645 (0.549-0.741) | 4 | 0.929 | 0.40 |
| Stroke onset to CT | 0.643 (0.547-0.739) | 142.9066 | 0.500 | 0.75 |
| NIHSS at admission | 0.669 (0.575-0.763) | 15 | 0.531 | 0.75 |
| MULTIVARIATE | | | | |
| Stroke onset to CT | | 205 | | |
| ASPECTS score at 24h | 0.711 (0.620-0.802) | 4 | 0.833 | 0.53 |
| NIHSS at admission | | 22 | | |
| Ratio internal cerebral venous | 0.710 (0.619-0.801) | 0.8287 | 0.422 | 0.88 |
| ASPECTS score at 24h | | 4 | | |
| Ratio internal cerebral venous | 0.702 (0.611-0.794) | 1.1259 | 0.714 | 0.64 |

(Filename: TCT_O-160_Figure_Imaging-basedvenousbiomarkersinacutestrokepatients.jpg)

O-161

5:17PM - 5:25PM

Quality of Resident MRI Preliminary Reports following a 6-Minute MRI Stroke Protocol in the setting of hyperacute stroke.

J Becker¹, S Hur¹, W Erly¹, K Nael²

¹University of Arizona, Tucson, AZ, ²Icahn School of Medicine at Mount Sinai, New York, NY

Purpose

To evaluate the quality of resident magnetic resonance imaging (MRI) preliminary reports in patients presenting with hyperacute stroke symptoms. Residents at all levels of training provide a preliminary report for all patients undergoing our 6-minute MRI protocol in the setting of acute stroke. This study has been performed to prove that

these preliminary reports are accurate, not only for assessment of findings related to the acute stroke symptoms, but also for evaluation of other intracranial pathologies. To our knowledge this has not been performed previously.

Materials and Methods

The preliminary reports for 1153 consecutive patients undergoing MRI for symptoms of acute stroke over a 1-year period were evaluated by two attending neuroradiologists. There were no exclusions.

Results

Acute infarcts were present in 215 (19%). Two hundred two of these were correctly identified by our residents (94%), with 13 (6%) overlooked. The resulting resident sensitivity is 94%, with specificity of 99%. This is excellent, and compares very favorably with errors in resident computed tomography (CT) reports in acute stroke and for errors in resident magnetic resonance imaging (MRI) reports of other body parts (2, 3). The overlooked infarcts were most likely to be tiny, single, peripheral cortical infarcts (10/13 cases) or symmetrical hypoxic basal ganglia/ thalamic infarcts without a clear history (3/13 cases). Nine hundred thirty-eight did not have an acute infarct. Nine hundred thirty-one (99.3%) of these were reported correctly. Seven (0.7%) infarcts were overcalled. These were all peripheral cortical or posterior fossa artifacts, mimicking an acute tiny, single embolic type infarct. Evaluation for other nonstroke related pathology resulted in a clinically significant discrepancy rate of 1.8%.

Conclusions

The resident MRI preliminary reports for patients presenting with acute stroke are of excellent quality with a specificity of 99%, and sensitivity of 94%.

O-162

5:25PM - 5:33PM

Role of Prothrombin Complex Concentrate (PCC) in Acute Intracerebral Hemorrhage with Positive CTA Spot Sign: An Institutional Experience at a Regional and State Designated Stroke Center

R REHMANI¹, A Han², J Hassan³, J Farkas⁴

¹NYU LANGONE, NEW YORK, NY, ²AT Still University of Osteopathic Medicine in Arizona, Huntingdon Valley, PA, ³St George's University, Brooklyn, NY, ⁴NYU Langone, Brooklyn, NY

Purpose

Our objective is to identify the effect of prothrombin complex concentrate (PCC) in acute intracranial hemorrhage (ICH) patients by evaluating intracranial hematoma expansion between initial head computed tomography (CT) and follow-up CT at 5-24 hour, in patients with positive CTA spot sign. Computed tomography angiography

spot sign is an independent predictor of hematoma growth (1). Acute ICH regardless of etiology, can present with quick mental status decline and pose as a neurosurgical emergency, requiring urgent surgical intervention, often resulting in irreversible brain damage. Hematoma expansion appears to be a modifiable predictor of clinical outcome and an appropriate target for medical therapy. Clinical trials in the past have shown reduction in hematoma growth with the use of rFVII in ICH patients (2); however without significant improved clinical outcomes, likely due to its thromboembolic effects. Researchers in S. Korea have used positive CTA spot sign as a guide for surgical evacuation of hematomas (3). This trial was shown to lower mortality rates but increased the length of inpatient stay and complications due to it being an invasive procedure (3). Prothrombin complex concentrate is a procoagulant containing factors II, VII, IX, X, Protein C, and Protein S. Advantages of PCC include smaller fluid volumes, rapid reversal of INR <1.5 within 30 minutes of administration and better clinical outcome when compared to rFVII (4). Disadvantages include risk of thromboembolic complications (4). Limited data comparing PCC and FVII suggests better clinical response with PCC regarding bleeding cessation, albeit slower changes in INR, likely due to a greater portion of the clotting cascade (4). We propose that PCC is a promising noninvasive, easily administered quick tool to contain hemorrhage in critical patients with ICH regardless of etiology.

Materials and Methods

We retrospectively reviewed patients with ICH at our NY State designated Stroke Center from November 2013 to September 2015. Out of 85 patients, 23 received PCC, of which eight had positive CTA spot sign (E=8). Out of the remaining 62 patients without PCC, four had a positive spot sign (C=4). ICH volume was measured on the initial head CT and follow-up CT at 5-24 hours using ABC/2 formula, which is an accurate predictor of ICH volume (5). Inclusion criteria were acute ICH (within 24 hours) and positive CTA spot sign (any age, sex, cause or size). Exclusion criteria were negative spot sign, lack of follow up or death or surgical intervention, only infratentorial/intraventricular hemorrhage and use of platelets/FFP. A T test for correlation was performed.

Results

Control group (C) showed increase in mean ICH volume of 46% (SD=37.3%), whereas experimental group (E) showed a decrease of 13% (SD=29.9%), (p value =0.012).

Conclusions

We found a strong statistical correlation favoring our hypothesis. In patients with active ICH denoted by positive CTA spot sign, use of PCC resulted in overall decrease in the mean hematoma size at 24 hours, whereas the control group showed an overall increase. We propose randomized controlled trials to further evaluate the effectiveness and safety of PCC use.

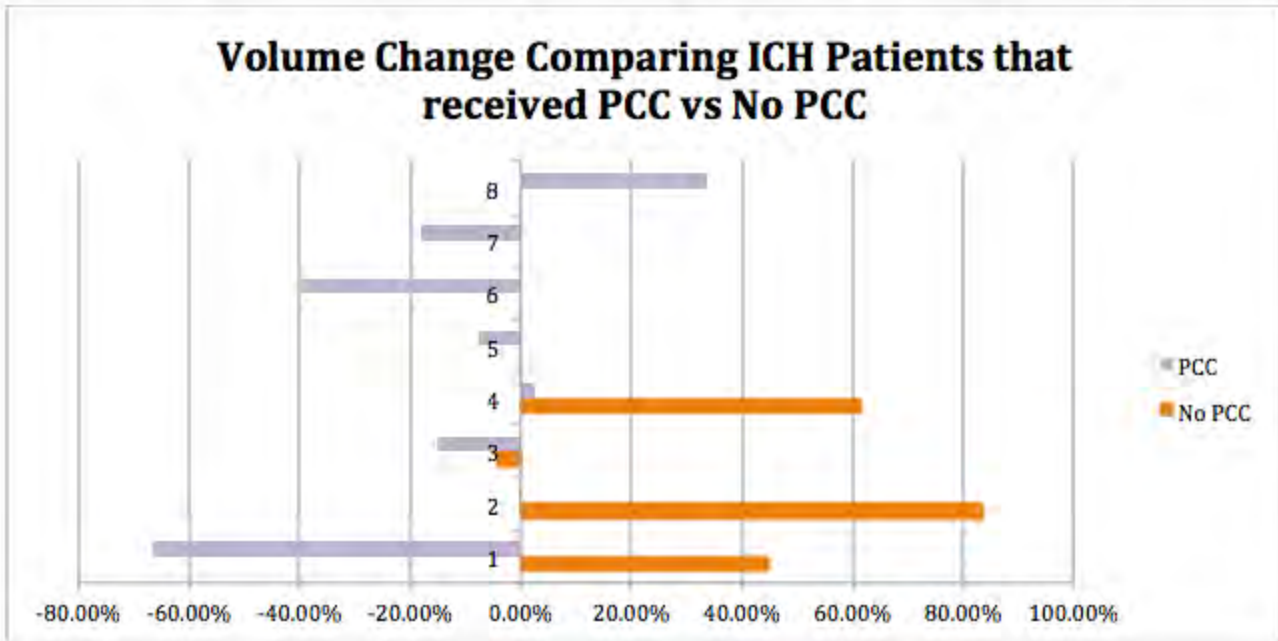
Group Statistics

| | Group | N | Mean | Std. Deviation | Std. Error Mean |
|-------------|-------|---|----------|----------------|-----------------|
| Latest Test | 1.00 | 4 | 46.4696 | 37.29824 | 18.64912 |
| Percentage | 2.00 | 8 | -13.9679 | 29.85605 | 10.55571 |

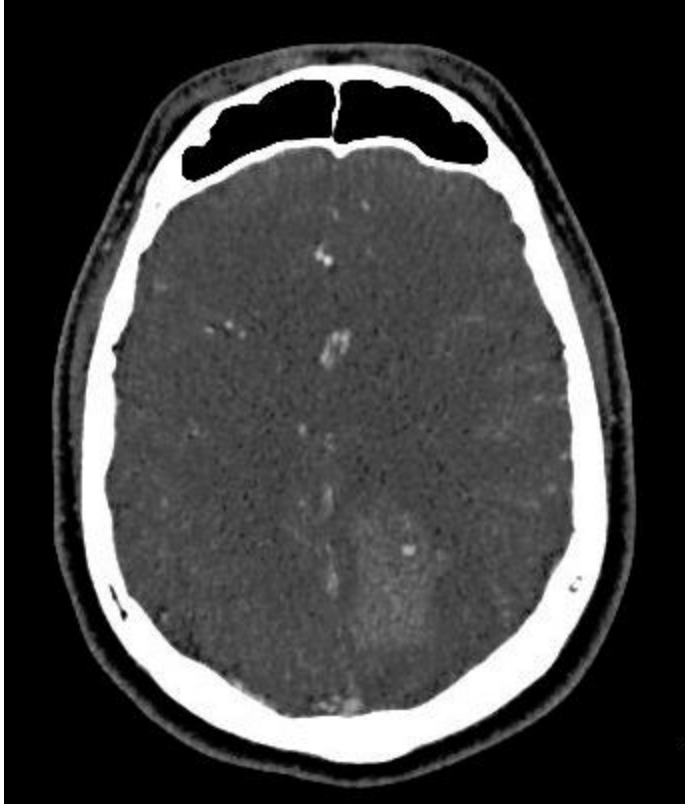
Independent Samples Test

| | | Levene's Test for Equality of Variances | t-test for Equality of Means | | |
|----------|-----------------------------|---|------------------------------|-----------------|-----------------------|
| | | Sig. | Sig. (2-tailed) | Mean Difference | Std. Error Difference |
| Latest | Equal variances assumed | .694 | .012 | 60.43748 | 19.76091 |
| Test Pct | Equal variances not assumed | | .037 | 60.43748 | 21.42925 |

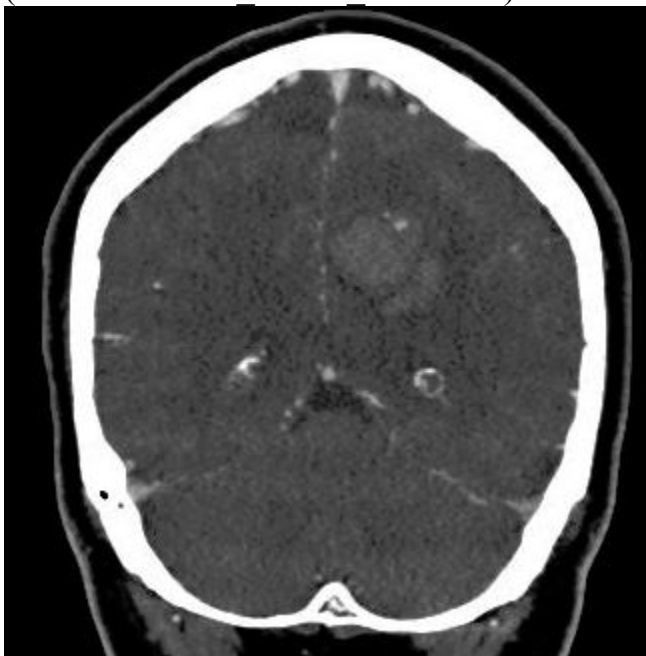
| | Initial Volume on Admission | Initial Standard Deviation (SD) on Admission | 24-Hour Follow Up Volume | 24-Hour Follow Up SD | % Change | % Change SD |
|---------------------|-----------------------------|--|--------------------------|----------------------|----------|-------------|
| Control | 15.8750 | 6.00 | 24 | 11.14 | 46.47% | 37.30 |
| Experimental | 26.48 | 19.69 | 23.76 | 16.47 | -13.97% | 29.86 |



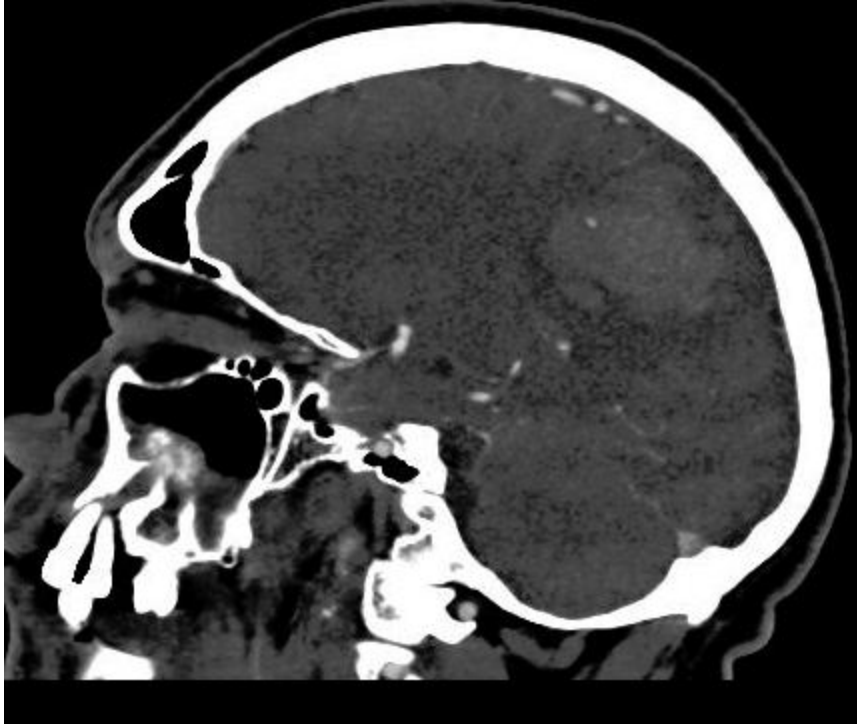
(Filename: TCT_O-162_ASNRImages.jpg)



(Filename: TCT_O-162_star1.JPG)



(Filename: TCT_O-162_Star2.JPG)



(Filename: TCT_O-162_Star3.JPG)

O-163

5:33PM - 5:41PM

Utility of diffusion and perfusion MRI for predicting perihemorrhagic edema growth after intracerebral hemorrhage

J Puig¹, G Blasco², J Daunis-i-Estadella³, G Carbo², V Cuba², M Terceño⁴, Y Silva⁴, C van Eendenburg⁴, J Serena⁴, B Menon⁵, M Wintermark⁶, P Salvador²

¹Imaging Research Unit, IDI-IDIBGI, Hospital Dr Josep Trueta, Girona, Spain, ²Imaging Research Unit, IDI-IDIBGI, Hospital Dr Josep Trueta, Girona, None, ³University of Girona, Girona, None, ⁴Hospital Dr Josep Trueta, IDIBGI, Girona, None, ⁵Calgary Stroke Program, Department of Clinical Neurosciences, Calgary, Alberta, ⁶Stanford University, Stanford, CA

Purpose

Intracerebral hemorrhage (ICH) is a devastating disease. Intracerebral hemorrhage volume is the main predictor of poor outcome, but growing evidence suggests that perihematomal edema (PHE) contributes to secondary brain injury. Methods for predicting PHE growth in clinical scenarios are lacking. We aimed to determine the utility of diffusion (DWI) and perfusion (PWI) magnetic resonance imaging (MRI) indexes for predicting PHE growth in patients with ICH.

Materials and Methods

We prospectively studied 25 patients with spontaneous ICH admitted within 12 hours

of symptom onset. Patients underwent MRI including DWI and PWI sequences on admission and at 72 hours. We measured ICH and PHE volumes on fluid-attenuated inversion recovery images; we used Olea Sphere V.3.0 to determine apparent diffusion coefficient (ADC), cerebral blood volume (CBV), cerebral blood flow (CBF), mean transit time (MTT), and time to peak (TTP). To measure ICH and PHE growth, we calculated the difference between volumes on baseline and 72-hour follow-up studies. We also considered age, sex, blood pressure, National Institutes of Health Stroke Score (NIHSS), and Rankin Scale score.

Results

Perihematomal edema growth correlated with NIHSS at baseline ($r=0.430$; $p=0.036$), PHE-MTT values ($r=0.486$; $p=0.026$), and PHE-ADC values ($r=0.632$; $p=0.001$). We found no significant correlations for ICH growth. Multivariate linear regression identified baseline PHE-ADC as an independent predictor of increased PHE volume at 72 hours ($p=0.024$).

Conclusions

Our preliminary results suggest that DWI can be useful for predicting PHE growth in the first 72 hours and therefore should be evaluated further as a potential imaging biomarker to guide therapeutic strategies in ICH.

O-164

5:41PM - 5:49PM

Predicting Motor Outcome in Acute Intracerebral Hemorrhage

J Puig¹, G Blasco², M Terceño³, J Daunis-i-Estadella⁴, M Hernandez-Perez⁵, V Cuba², G Carbo², J Serena³, C van Eendenburg³, A Alberich-Bayarri⁶, G Schlaug⁷, B Menon⁸, M Wintermark⁹, Y Silva³, P Salvador²

¹Imaging Research Unit, IDI-IDIBGI, Hospital Dr Josep Trueta, Girona, Spain, ²Imaging Research Unit, IDI-IDIBGI, Hospital Dr Josep Trueta, Girona, None, ³Hospital Dr Josep Trueta, IDIBGI, Girona, None, ⁴University of Girona, Girona, None, ⁵Hospital Universitari Germans Trias i Pujol, Badalona, None, ⁶Hospital Universitario y Politecnico La Fe-QUIVIM, Valencia, None, ⁷Beth Israel Deaconess Medical Center, Harvard Medical School, Boston, MA, ⁸Calgary Stroke Program, Department of Clinical Neurosciences, Calgary, Alberta, ⁹Stanford University, Stanford, CA

Purpose

Over half of patients have residual motor deficits 3 months after intracerebral hemorrhage (ICH). Accurate prediction of motor outcome within hours after ICH would enable realistic goal-setting and efficient resource allocation, guide therapeutic management, and help design more efficient rehabilitation programs. Given the lack of studies in the hyperacute phase, we aimed to determine whether combining clinical

scores and diffusion tensor imaging (DTI)-derived measures from the first few hours after symptom onset improves prediction of motor outcome in patients with ICH.

Materials and Methods

We prospectively studied consecutive patients within 12 hours of onset of primary ICH. Patients underwent multimodal magnetic resonance imaging (MRI) including DTI. We assessed ICH and perihematomal edema location and volume, and corticospinal tract (CST) involvement by ICH. We calculated ratios of affected-to-unaffected CST for fractional anisotropy (FA), mean diffusivity, and axial and radial diffusivities (Olea Sphere V.3.0). Paresis was graded by the motor subindex scores of the modified National Institutes of Health Stroke Score (mNIHSS). Motor outcome at 3 months was classified as good (mNIHSS 0-3) or poor (mNIHSS 4-8). Poor functional outcome was defined as modified Rankin Scale >2.

Results

Of 62 consecutive patients, 49 were included in the study (37 men; median age 69.5 years, IQR 59-76). At admission, median NIHSS was 11.5 (QR5-17), and 25 (71.4%) patients had some motor deficit [median mNIHSS 4 (IQR2-7)]. At 3 months, 13 (22.41%) had poor motor outcome. Independent predictors of motor outcome were NIHSS, mNIHSS, rFA of the whole CST, posterior limb of internal capsule (PLIC) involvement by ICH, 72h-NIHSS, and 72h-mNIHSS. The sensitivity, specificity, and positive and negative predictive values for poor motor outcome at 3 months by combined mNIHSS >6 and PLIC-involvement <12h were 84%, 80%, 64%, and 94%, respectively (AUC=0.91, CI=0.82-0.99).

Conclusions

Combined assessment of motor function and PLIC damage during hyperacute ICH may predict functional motor outcome.

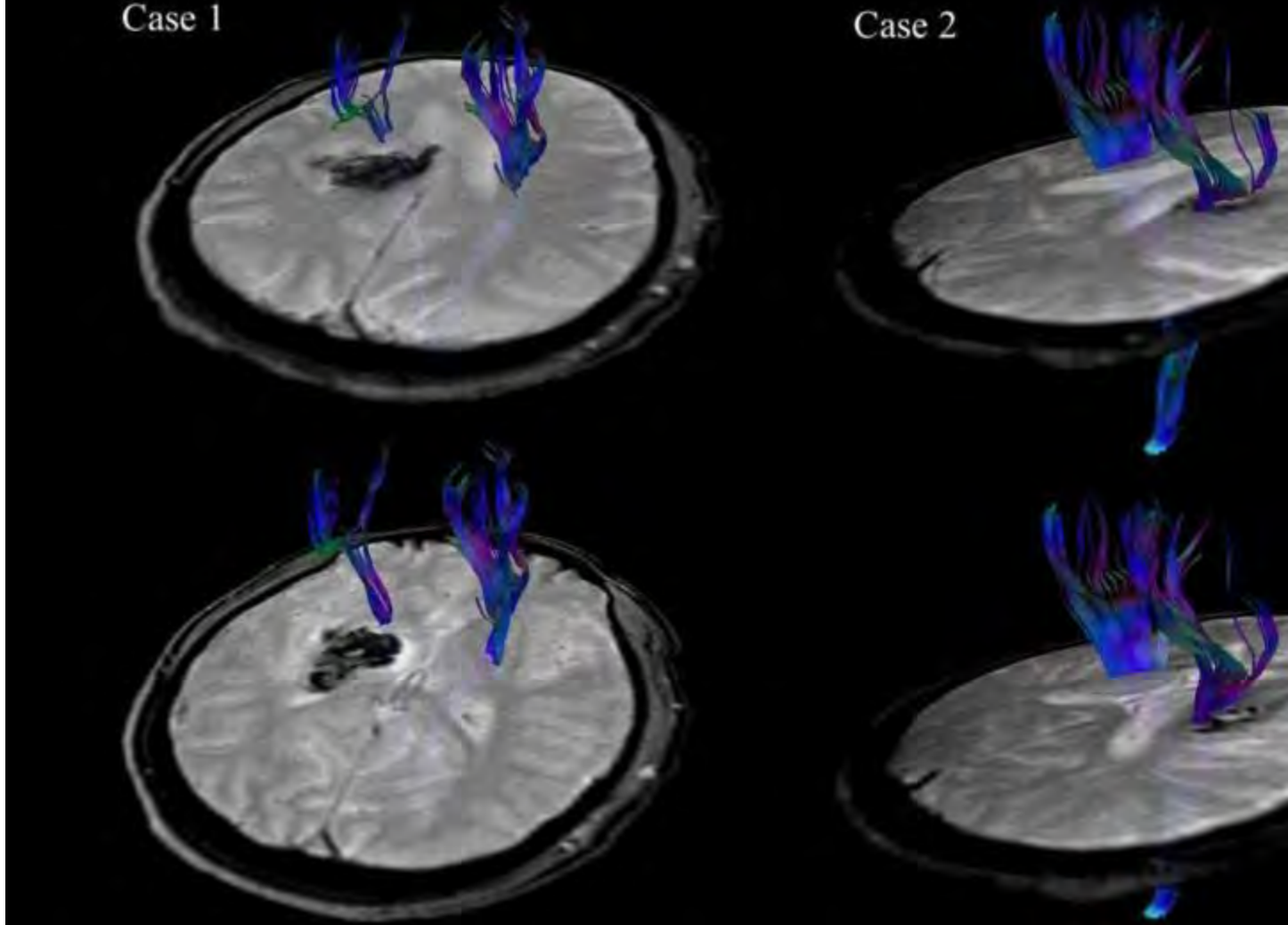
Corticospinal tract diffusion tensor tractography: involvement

Absent

Present

Case 1

Case 2



(Filename: TCT_O-164_Figure_DTIandmotoroutcome.jpg)

O-165

5:49PM - 5:57PM

Diagnostic Value of the MRI in Spontaneous Subarachnoidal Hemorrhage of Unknown Origin

H Schemuth¹, C Deuschl², S Göricke³, C Moenninghoff², A Ringelstein³

¹University Clinic Essen, Essen, Deutschland, ²University Clinic Essen, Essen, Germany, ³Institute of Diagnostic and Interventional Radiology and Neuroradiology, University Hospital Essen, Essen, NRW

Purpose

Spontaneous subarachnoidal hemorrhage (SAH) of unknown origin is reported in up to 27% of all cases in the first digital subtraction angiogram (DSA). The aim of this study was to investigate the value of cerebral and spinal magnetic resonance imaging (MRI).

Materials and Methods

We retrospectively analyzed 122 patients with a SAH of unknown origin in at least one negative DSA who received a cerebral and spinal MRI including a time of flight (TOF) angiography, transversal FLAIR, transversal T2-weighted turbo spin echo, transversal T1-weighted turbo spin echo, and sagittal T2-weighted turbo spin echo of the spine.

Results

In a total of three cases (2.5%) the origin of the DSA-negative SAH could be detected only with the MRI. In these cases the MRI showed two cavernomas and one spontaneous spinal bleeding. The cavernomas caused one perimesencephalic SAH and one nonperimesencephalic SAH, the spinal bleeding was proven by a blood-positive CSF.

Conclusions

Additional cerebral and spinal MRI for patients with a spontaneous SAH can determine the cause of the SAH in 2.5 % of the cases, however in two of three cases we found, the origin of the SAH may need a surgical treatment. The bleeding pattern of the SAH does not help determine whether an additional MRI should be performed. Therefore we think, an additional cerebral and spinal MRI for patients with at least one negative DSA should be performed.

O-166

5:57PM - 6:05PM

Changes in Cerebral Perfusion with Induced Hypertension in Aneurysmal Subarachnoid Hemorrhage

A Murphy¹, L Manoel², R Macdonald³, A Baker², T Marotta², W Montanera¹, R Aviv⁴, A Bharatha¹

¹University of Toronto, Toronto, ON, ²St. Michael's Hospital, Toronto, ON, ³St. Michael's Hospital, Toronto, On, ⁴Sunnybrook Research Institute, Toronto, Ontario

Purpose

Induced hypertension (IH) is a common therapeutic intervention used to treat delayed

cerebral ischemia (DCI) following subarachnoid hemorrhage. The goal of this treatment is to maintain or improve cerebral blood flow (CBF) by increasing cerebral perfusion pressure to the brain. Despite suggestions that IH may result in improved outcomes, recent studies have been equivocal. The potential for induced hypertension to improve outcomes may be dependent on early cerebral perfusion status. The objectives of this investigation are: (1) determine if there are differences in CBF and mean transit time (MTT) at baseline and after induced hypertension; (2) evaluate differences in DCI, infarction and clinical outcome between patients with and without induced hypertension.

Materials and Methods

A retrospective analysis of aneurysmal subarachnoid hemorrhage patients presenting to a single tertiary care center identified 24 patients who had CT perfusion (CTP) imaging performed early (<72 hours after aneurysm rupture) and late (7-10 days after aneurysm rupture). We compared patients who underwent induced hypertension (IH) with those that had no induced hypertension (no-IH). For each group, CBF and MTT were quantified in both the early and late CTP images. Differences in CBF and MTT were quantified between the IH and no-IH group, and between the early and late CTP images in each group. Cerebral infarctions were assessed on magnetic resonance imaging (MRI) or computed imaging (CT) prior to discharge. Clinical DCI was assessed. Clinical outcome was defined as good [modified Rankin score (mRS) ≤ 2] or poor (mRS > 2) at 3 months.

Results

There were 13/24 patients that received norepinephrine (IH group, 54%) and 11/24 patients that did not (no-IH group 46%). Norepinephrine was started in the IH group after the early CTP in all cases (5.2 ± 3.2 days). Early MTT was significantly higher in the IH group (6.8 ± 1.2 sec) compared to the no-IH group (5.7 ± 0.8 sec) ($p = 0.001$), but there was no difference in early CBF between the two groups. In the IH group, CBF significantly increased and MTT significantly decreased after norepinephrine was started. The IH group had a significantly higher incidence of DCI (11/13 versus 0/12; $p < 0.0001$). There was no difference in the incidence of infarction (5/13 versus 2/11) or poor outcome (3/11 versus 6/13) between the IH and no-IH groups respectively ($p > 0.05$).

Conclusions

Aneurysmal SAH patients that received norepinephrine to induce hypertension had higher MTT prior to treatment than patients who were not treated. The use of IH was associated with DCI in most cases. IH improved CT perfusion parameters, but differential clinical outcomes were not demonstrated in this small sample. Early MTT increase may be an indicator of patients that will develop DCI and may benefit from induced hypertensive therapy, but relationship of improvements in cerebral perfusion to clinical outcome remains to be established. Therapies to prevent DCI and improve

clinical outcome may need to be initiated earlier, when cerebral perfusion abnormalities are first identified.

O-167

6:05PM - 6:13PM

Correlation of Histological Evidence of Remote Hemorrhage and Susceptibility-Sensitive MRI for the Assessment of Rupture Risk in Brain AVM

E Meram¹, T Tihan², H Kim², H Su², C Hess²

¹*Koc University School of Medicine, Istanbul, Turkey*, ²*University of California San Francisco, San Francisco, CA*

Purpose

Brain arteriovenous malformations (bAVMs) cause significant morbidity and mortality, especially when associated with acute hemorrhage. Quantifying the risk of rupture is critical for determining the timing and choice of treatment. Hemosiderin, an iron storage product developing after recent or remote hemorrhage, can be recognized readily on histological evaluation and identified on susceptibility-sensitive magnetic resonance imaging (MRI). We previously have demonstrated a strong association between bAVM rupture and silent intralesional microhemorrhage as detected by tissue hemosiderin deposition. The aim of this study was to assess the relationship between susceptibility-sensitive MRI and the histological presence of hemosiderin in surgically resected bAVMs in patients without clinical history of hemorrhage.

Materials and Methods

To detect evidence of prior hemorrhage in patients prior to undergoing surgical bAVM resection, we used susceptibility-weighted angiography (SWA) (GE, Waukesha, WI) with the following parameters: 2.8 mm partition thickness with 0.4 mm x 0.4 mm in-plane resolution, TR/TE=40/25 msec, flip angle 10°, and approximately 4 min. scan time. Resected tissue specimens were analyzed for the presence of hemosiderin and other histological variables postoperatively. Radiological and histological evidence of prior hemorrhage then were correlated with clinical parameters.

Results

Thirty-two subjects with no prior hemorrhage were identified, 29 had both MRI and pathology available for review. Sensitivity and specificity for detecting hemosiderin with SWA were 45% (5/11 patients) and 100% (0/18 patients), respectively. There was significant association between hemosiderin deposition in tissue and MRI detection of susceptibility (Fischer's exact p=0.004).

Conclusions

While the number of subjects in this study was small, these results suggest that SWA has high specificity for the presence of hemosiderin deposition on histological

analysis. The sequence may be useful to identify patients with higher incipient risk of hemorrhage.

O-380

6:13PM - 6:21PM

The effects of glioma in corticospinal tract area on motion function: evaluation with diffusion tensor imaging

B Gao¹

¹*Keck School of Medicine, University of Southern California, Los Angeles, CA*

Purpose

To explore the influence of glioma in the area of corticospinal tract (CST) on muscle strength using quantitative parameters based on diffusion tensor imaging (DTI) and provide a reliable imaging assessment evidence to CST injury as well as motion function.

Materials and Methods

Forty-five patients with postsurgical pathologically confirmed glioma were included in this prospective study. Manual muscle testing (MTT) method was used to measure in all patients. According to Lovett staging classification (Robert Lovett taxonomy), the contralateral knee joint muscle strength were classified. Fractional anisotropy (FA) values and relative FA ($rFA = \text{injured FA} / \text{contralateral FA}$) of injured and contralateral side in posterior limb of internal capsule were measured. The damages from brain tumor close to CSF were divided into three grades (grade 1: displacement, grade 2: displacement and infiltration, grade 3: displacement and disruption). The fiber density index (FD) and relative FDi ($rFDi = \text{injured FDi} / \text{contralateral FDi}$) of injured and contralateral CST were measured. Bilateral CSTs were tracted manually and the values of injured and contralateral CST FA, relative FA (rFA), CST fiber density (FD) and relative FDi (rFDi) were measured. The correlations between muscle strength and damage grade of CST, rFA, injured FDi and relative FDi were calculated using Pearson rank correlation analysis, rFA and rFDi values of different groups were analyzed with one-way ANOVA analysis of variance.

Results

Muscle strength was negatively correlated with injury degree of CST ($r = -0.840$, $P < 0.001$). Muscle strength was positively correlated with rFA, FD and rFA (r values were 0.615, 0.643, 0.567 respectively, $P < 0.001$). Except the differences of rFA between grade 3 and 4 groups muscle strength, of rFDi in grade 2 and 3 groups, grade 4 and 5 groups of muscle strength had no significant difference ($P > 0.05$), the remaining groups all were of significant difference ($P < 0.05$).

Conclusions

Diffusion tensor imaging and tractography based on DTI can accurately reflect

damage degrees of CST and are also helpful in the accurate evaluation of limb dysfunction degrees pre-operatively.

Tuesday

7:30AM - 8:30AM

Washington Marriott Wardman Park, Marriott Ballroom

7A-Tuesday Morning SAM - Spine - Audience Response (AR) Self Assessment Module (SAM)

7A-1

7:30AM - 7:55AM

Unusual Spine Pathology

Torres, C.
The Ottawa Hospital
Ottawa, Ontario

7a-1a

7:55AM - 8:00AM

Questions and Answers

7A-2

8:00AM - 8:25AM

Imaging of Spinal Cord Lesions

Lincoln, C.
Baylor College of Medicine
Houston, TX

7a-2a

8:25AM - 8:30AM

Questions and Answers

Tuesday

8:35AM - 10:00AM

Washington Marriott Wardman Park, Marriott Ballroom

8A-ASPNR Programming: Pediatric Vascular Disease

8A-1

8:35AM - 8:55AM

Congenital Vascular Disorders

Severino, M.

IRCCS Istituto Gianniana Gaslini

Genova

8A-2

8:55AM - 9:15AM

Arteriopathy in Pediatric Stroke

Wintermark, M.

Stanford University

Stanford, CA

8A-3

9:15AM - 9:35AM

Pediatric Stroke: The Neurologist's Perspective

deVeber, G.

Hospital for Sick Children

Toronto, Ontario

8A-4

9:35AM - 9:55AM

Pediatric Venous Disorders

Girard, N.

Hospital Nord

Marseille

Tuesday

8:35AM - 10:00AM

Washington Marriott Wardman Park, Washington 4/5/6

8B-Young Professional Programming: Utilizing Advanced Imaging in Your Practice

8B-1

8:35AM - 9:00AM

Vessel Wall Imaging

Mossa-Basha, M.

University of Washington

Seattle, WA

8B-2

9:00AM - 9:25AM

A Practical Guide to Developing a Clinical fMRI Service

Saindane, A.

Emory University

Atlanta, GA

8B-3

9:25AM - 9:50AM

Interventional Spine Service: Beyond LP's & Myelos

Shah, V.

University of California San Francisco

San Francisco, CA

8B-4

9:50AM - 10:00AM

Discussion

Tuesday

8:35AM - 10:03AM

Washington Marriott Wardman Park, Washington 1/2/3

8C-PARALLEL PAPER SESSION: Multiple Sclerosis / Adult Brain MRI

O-168

8:35AM - 8:43AM

T1 Relaxation Times in Multiple Sclerosis Lesions improve correlation with clinical disability in Multiple Sclerosis patients: A longitudinal survey.

*C Thaler¹, T Faizy¹, J Sedlacik¹, J Stellmann², C Heesen², J Fiehler¹, S Siemonsen¹
¹University Medical Center Hamburg-Eppendorf, Hamburg, Germany, ²University Medical Center Hamburg-Eppendorf, Hamburg, Hamburg*

Purpose

Hyperintense fluid attenuated inversion recovery (FLAIR) lesions (FLAIR-L) in multiple sclerosis (MS) are thought to indicate a wide spectrum of histopathological changes, ranging from edema and mild demyelination to glial scars or liquid necrosis. However, clinical-radiological correlations are still limited. As just recently shown by this research group, assessing MS lesions by its T1 relaxation time (T1-RT) helps to increase correlations with disability. We therefore hypothesized, that longitudinal changes of lesional T1 values are associated with changes in Expanded Disability Status Scale (EDSS) scores.

Materials and Methods

Magnetic resonance imaging (MRI) was performed in 18 MS patients at baseline and after 12 months including 3D-FLAIR, T1-weighted magnetization prepared rapid gradient echo (T1-W MPRAGE) before and after gadolinium injection and double inversion-contrast magnetization-prepared rapid gradient echo (MP2RAGE) sequences. T2 hyperintense lesions were semi-automatically segmented on FLAIR images using an open source lesion segmentation software (LST: Lesion Segmentation Tool). Additionally, T1 hypointense lesions [commonly known as 'black holes' (BH)] were detected by two raters on MPRAGE images. Lesion maps for FLAIR-L and BH were registered to MP2RAGE images at baseline and after 12 months and T1-RT differences (T1-RT-diff) were calculated for all lesion regions of interest (ROIs). Also, changes in clinical status were assessed by using the EDSS at both dates (EDSS-diff).

Results

At baseline and after 12 month, mean T1-RT-diff were obtained for all lesion ROIs patient wise and differences ranged from -132.11 to 87.32 ms (-10.3 to 6.7 %) in FLAIR-L and -280.53 to 65.02 ms (-18.6 to 4.1 %) in BHs. Correlations between T1-RT-diff and EDSS-diff were found significant for values measured in FLAIR-L

(Spearman rank coefficient = 0.62; $p = 0.003$) (Fig. 1) but were not significant for those derived from BHs (Spearman rank coefficient = 0.399; $p = 0.09$)

Conclusions

T1-RT alterations were found in all patients after 12 months compared to baseline. Our findings suggest, that longitudinal changes in T1-RT values seem to be more pronounced within FLAIR lesions and changes for these therefore are associated more closely with longitudinal changes in disability than those changes only detected in black holes. In conclusion, assessing MS lesions by its T1-RT might lead to a better lesion classification and helps to increase clinical-radiological correlations.

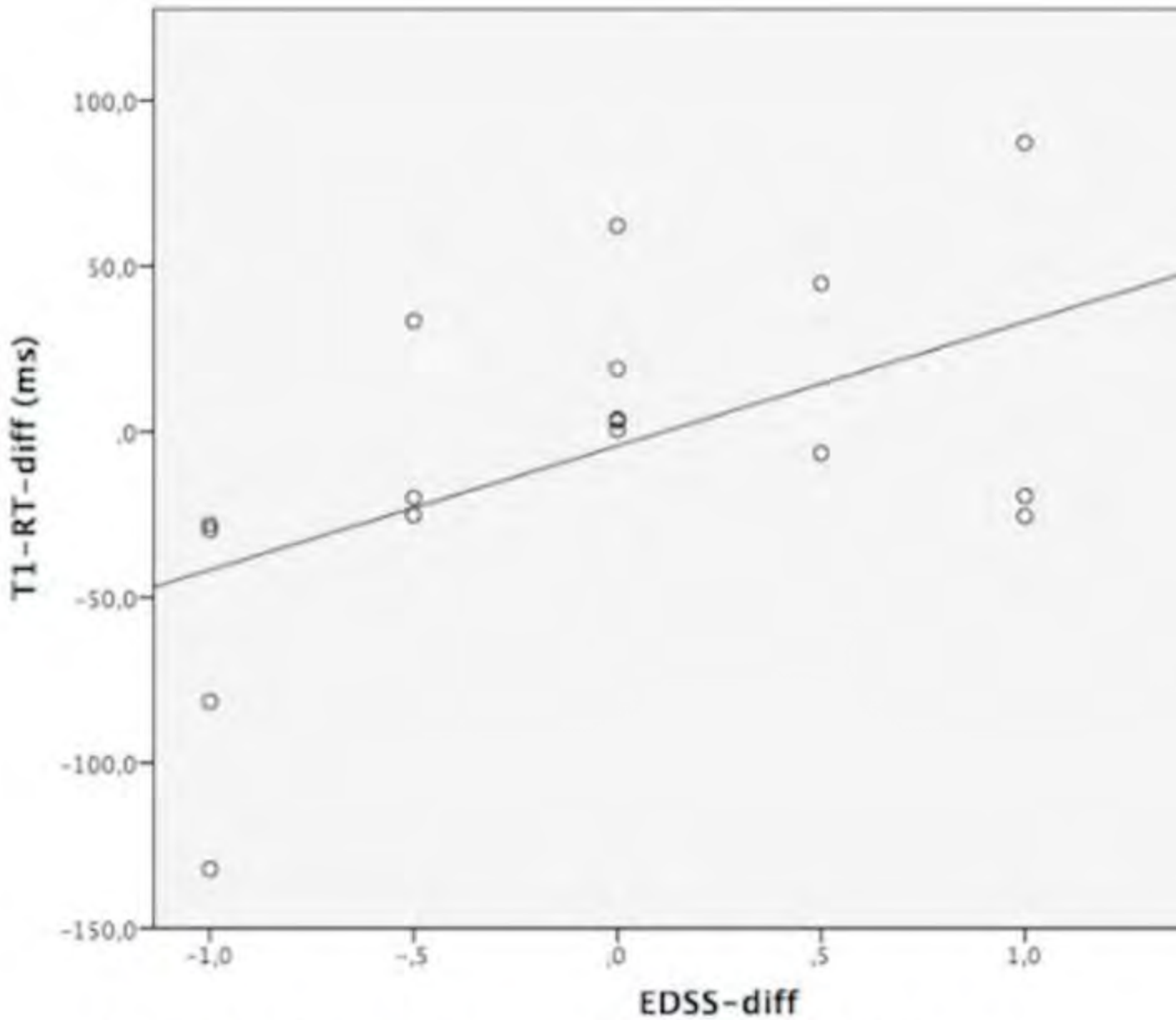


Figure 1: Correlation of T1-RT-diff and EDSS-diff
 T1-RT-diff = T1 relaxation time difference, EDSS-diff = Expanded Status Scale difference

(Filename: TCT_O-168_Figure1.jpg)

O-169

8:43AM - 8:51AM

Reproducibility of Cortical Lesion Detection on Double Inversion Recovery MRI applying the MAGNIMS-Criteria in Multiple Sclerosis Patients Within a 16-Months Period

T Faizy¹, T Ceyrowski¹, C Thaler¹, J Stellmann¹, K Stuermer¹, C Heesen¹, J Sedlacik¹, J Fiehler¹, S Siemonsen¹

¹*University Medical Center Hamburg-Eppendorf, Hamburg, Germany*

Purpose

In patients with multiple sclerosis (MS), double inversion recovery (DIR) magnetic resonance imaging (MRI) can be used to detect and evaluate cortical lesions (CL). Since the identification of cortical lesions in DIR is challenging, consensus recommendations for MS cortical lesion scoring using DIR MRI were established. Nevertheless, longitudinal studies assessing the repeated reproducibility of cortical lesions are rare. We therefore sought to evaluate the reproducibility of intracortical lesions on DIR identified by applying the MAGNIMS criteria longitudinally.

Materials and Methods

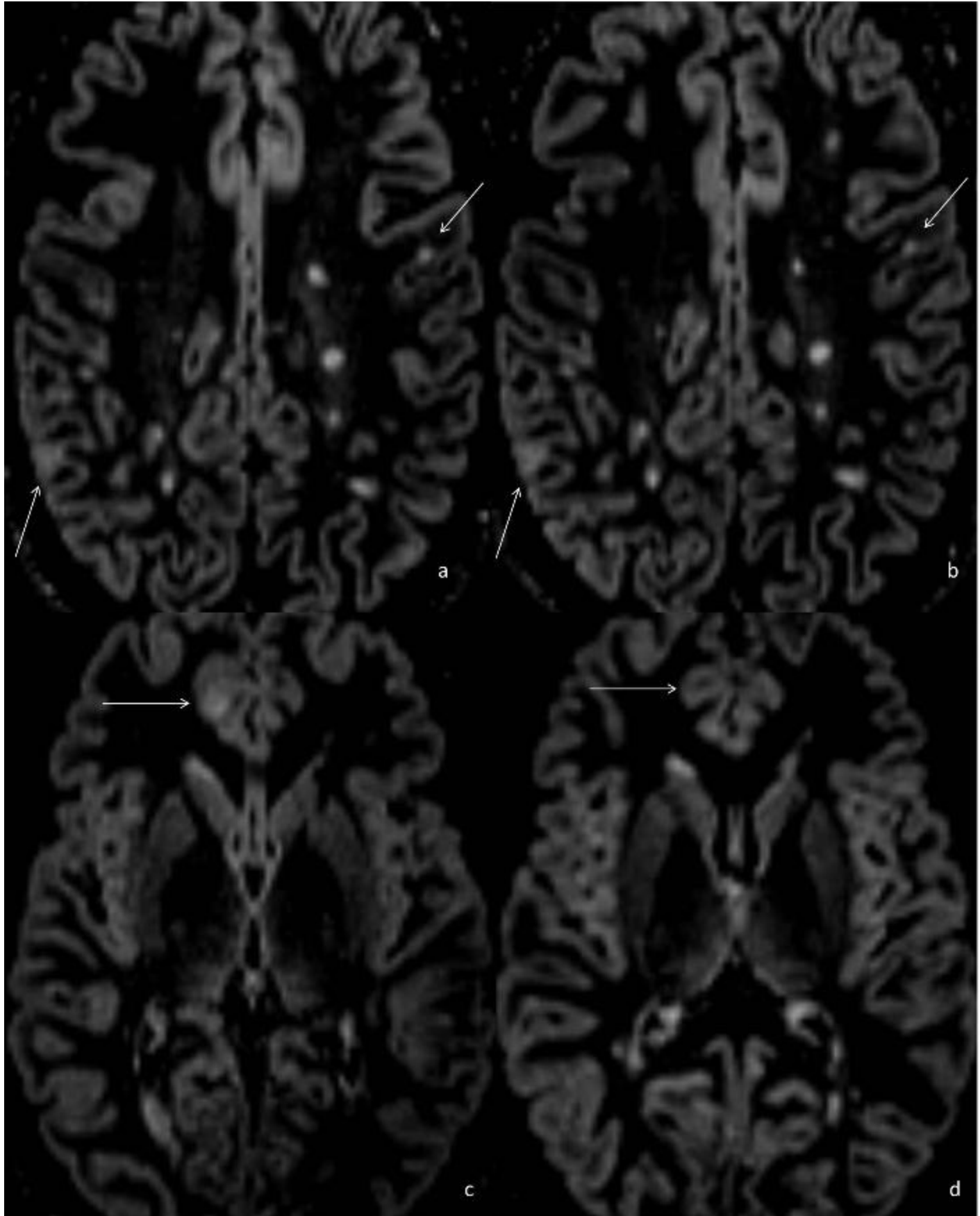
Double inversion recovery images were analyzed for 10 MS patients, all receiving a 3T-MRI (Siemens, Skyra) at 12 time points (TP) within 16 months as part of a phase IIa clinical trial (scans were conducted at months 1-7, 9-12 and 16). Initially, CLs were marked on each scan separately, blinded to previous scans and total lesion numbers were obtained for each scan-timepoint and patient. In a second run, each previously marked lesion on baseline scans was monitored for reproducibility in every follow-up scan and visibility (yes/no) was documented for each time-point. Additionally, the evolution of new lesions during the time-course was noted.

Results

We found a cumulative number of n=80 CLs in 10 MS patients over 12 TPs. Sixty-five percent of CLs were found to be reproducible in all 12 TPs, while 8.75% of CLs were detected in 11 of 12 TPs. 17.5% of CLs were reproducible in less than six TPs. 7.5% (n=6) lesions were found to be newly developed over time and reproduced in at least three of the following TPs. Ninety percent of CLs showed reproducibility in at least two immediately consecutive TPs. 13.75% of CLs that initially were reproducible in at least three consecutive TPs and not reproducible in all following scans were considered as genuine, but during the time course disappearing CLs.

Conclusions

The application of the MAGNIMS criteria for the identification of CLs on DIR led to a high reproducibility of the majority of MS lesions in 12 follow-up scans within 16 months and therefore seems to be a valid system. Lesions that were not reproducible seem to be characterized by lower signal intensity, smaller size or resulted to be artificial.



Ex
ra
se
De
re
le
af
(b)
Im
le
ex
sh
af
(d)

O-170

8:51AM - 8:59AM

T1 dark blood technique increases sensitivity for detection of contrast enhancing lesion in MS

S Siemonsen¹, T Schneider², D Kutzner², J Fiehler³, J Sedlacik²

¹University Medical Center Hamburg-Eppendorf, Hamburg, Germany, ²University Medical Center Hamburg-Eppendorf, Hamburg, Hamburg, ³University Medical Center Hamburg-Eppendorf, Hamburg, AK

Purpose

In multiple sclerosis (MS) the sensitivity for detection of contrast enhancing lesions (CEL) in T1-W scans is essential for diagnostics and therapy decisions. The purpose of our study was to evaluate the sensitivity of T1mprage scans in comparison to T1 dark blood technique (T1-DB) for CEL in MS.

Materials and Methods

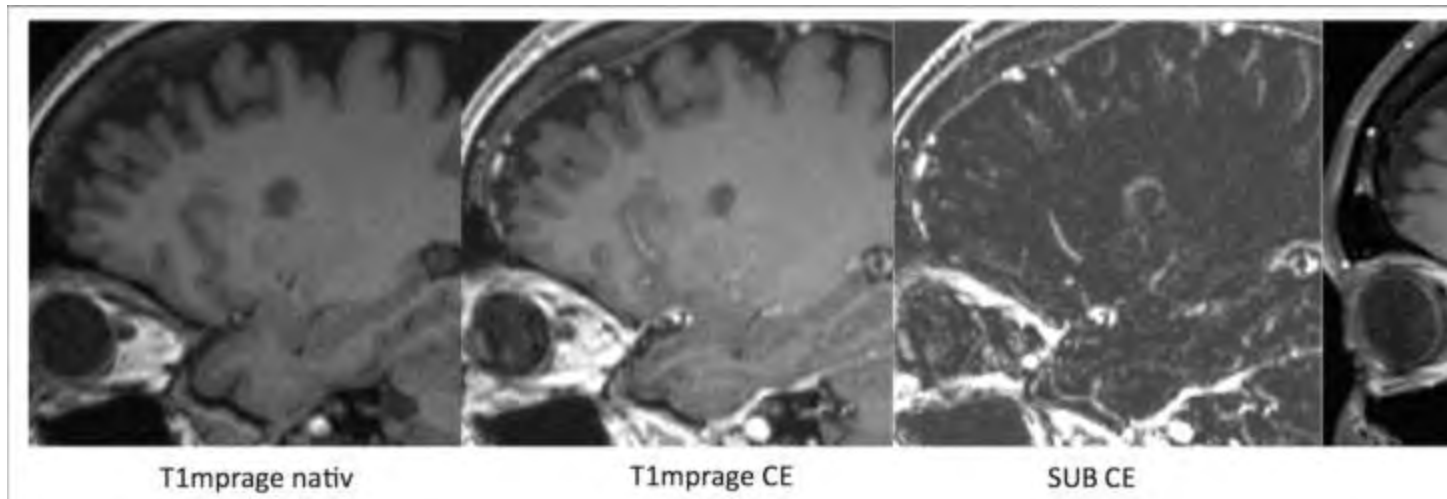
Twenty-one MS patients received 3T MRI with T2-weighted imaging and T1mprage pre (T1nat) and postgadolinium (T1-GD) sequences. After GD application, the T1-DB scan was performed prior to T1-GD. From pre and post T1mprage GD scans, subtraction images (SUB) were calculated. The number of CEL was determined separately on T1-GD and T1-DB by two raters independently. Lesions only detected on T1-DB scans then were verified on SUB images. Only lesions detected by both raters were included in further analysis.

Results

Twenty-three of 21 T1-GD lesions were detected by rater 1/2. In comparison, 8/7 more lesions were detected on T1-DB; all of these lesions could be verified on SUB images. In retrospective evaluation, CEL only detected in T1-DB were lesions that became hypo- or iso-intense on T1-GD in comparison to T1nat. In 13 patients, no CEL was detected in any of the sequences.

Conclusions

The application of T1-DB technique increases the sensitivity for CEL in MS, especially for those lesions that show a subtle increase in intensity after GD application but remain hypo- or iso-intense to surrounding tissue.



(Filename: TCT_O-170_T1DB_MS_Fig1.jpg)

O-171

8:59AM - 9:07AM

Regional quantitative susceptibility mapping of the thalami, not volumes, is associated with clinical disability in multiple sclerosis

J Hu¹, G Chiang¹, Y Wang¹, S Gauthier¹

¹Weill Cornell Medical College, New York, NY

Purpose

Studies using susceptibility-weighted imaging techniques have described increased phase or R2* in the thalamus of multiple sclerosis patients compared to normal controls, suggestive of increased iron. Similarly, thalamic atrophy compared to normal controls has been described as an early event in multiple sclerosis. The purpose of our study was to determine how measures of thalamic iron and volumes relate to clinical disability, measured by the Expanded Disability Status Scale (EDSS), and disease duration.

Materials and Methods

One hundred twelve patients with relapsing-remitting multiple sclerosis underwent 3T magnetic resonance (MR) imaging with a standardized protocol that included quantitative susceptibility mapping (QSM) to assess iron concentration and a 3D T1 SPGR sequence for volumetric analysis. Four regions of interest (ROIs) were delineated manually on the QSM image of the thalamus to encompass the pulvinar nucleus, dorsomedian nucleus (MD), the ventral anterior/lateral nuclei (VAL), and ventral posterior medial/lateral nuclei (VP). Thalamic volumes were obtained using Freesurfer software. Multivariate regression analyses were performed to identify associations between thalamic volumes and QSM of substructures with EDSS and disease duration.

Results

Quantitative susceptibility mapping of the pulvinar was significantly associated with EDSS (coeff=6.5, p=0.01) and disease duration (coeff=-1.4, p=0.03), adjusting for age, gender, use of multiple sclerosis disease-modifying agents, and steroids.

Quantitative susceptibility mapping of the VP also was associated with EDSS (coeff=1.9, p=0.02), whereas QSM of the MD and VAL were associated marginally with EDSS (coeff=3.0, p=0.05; coeff=1.5, p=0.07). There was no significant association between thalamic volumes, adjusted for total intracranial volumes, and EDSS or disease duration. In addition, QSM of thalamic substructures were not associated with thalamic volumes.

Conclusions

Quantitative susceptibility mapping of thalamic substructures may be a better measure of clinical disability in multiple sclerosis patients than thalamic volumes.

O-172

9:07AM - 9:15AM

Comparison of quantitative cerebral blood flow between pseudo-Continuous Arterial Spin Labelling and Bookend perfusion imaging in Relapsing Remitting Multiple Sclerosis

S Hojjat¹, R D'Ortenzio¹, R Vitorino¹, C Cantrell², P O'Connor³, A Feinstein¹, L Lee¹, T Carroll², R Aviv¹

¹Sunnybrook Research Institute, Toronto, Ontario, ²northwestern university, Chicago, IL, ³St. Michael's Hospital, Toronto, Ontario

Purpose

Quantitative cerebral blood flow (CBF) usage as a biomarker for cognitive impairment and disease progression in multiple sclerosis (MS) is potentially a powerful tool for longitudinal patient monitoring. Dynamic susceptibility contrast perfusion with Bookend T1-calibration (Bookend Technique) and pseudo-continuous arterial spin labeling (ASL) recently have been used for CBF quantification in relapsing-remitting MS. The noninvasive nature of pseudo-continuous ASL is potentially advantageous over gadolinium-based techniques in relapsing-remitting MS (RRMS) but correlation between the techniques is not well established.

Materials and Methods

We compared pseudo-continuous ASL CBF to the Bookend technique in a prospective cohort of 19 healthy controls, 19 relapsing-remitting MS subjects without cognitive impairment and 20 relapsing-remitting MS subjects with cognitive impairment on a voxel-wise and Brodmann regional basis. Linear Pearson correlation, SNR and coefficient of variation were tested.

Results

Voxel-wise paired T-tests revealed no significant CBF differences between techniques. Highest Pearson correlations were observed in deep gray matter (GM) structures (average $r = 0.69$ basal ganglia, and $r = 0.63$ thalamus) but remained robust for cortical GM and white matter (WM) (average $r = 0.53$ each). Brodmann regional correlations were significant for all groups. All correlations were maintained in healthy controls and in RRMS disease. Highest SNR was present in Bookend perfusion while the highest coefficient of variation was present in WM.

Conclusions

Agreement between pseudo-continuous ASL and Bookend technique CBF measurements is demonstrated in healthy controls and RRMS patients, supporting the potential use of pseudo-continuous ASL CBF as a potential noninvasive biomarker of RRMS patients.

O-173

9:15AM - 9:23AM

Molecular Imaging Profiling of Treatment Effects in Experimental Multiple Sclerosis Reveals a Novel Mechanism of Action of Interferon-beta

B Pulli¹, R Forghani², G Wojtkiewicz¹, C Wang¹, M Zeller¹, J Chen¹

¹Massachusetts General Hospital and Harvard Medical School, Boston, MA, ²Jewish General Hospital and McGill University, Montreal, Quebec

Purpose

Treatment effects of interferon beta (IFN) and glatiramer acetate (GA), two first-line agents used in multiple sclerosis (MS), are similar as evaluated by conventional magnetic resonance imaging (MRI). Myeloperoxidase (MPO) is a pro-inflammatory and oxidative enzyme secreted by inflammatory myeloid cells. In vivo MPO activity can be noninvasively measured with MPO-Gd, an activatable molecular MR imaging probe sensitive and specific to MPO (1). The purpose of this study was to profile and study the effects of IFN, GA, and ABAH (a preclinical MPO inhibitor) on the innate immune response in vivo using MPO-Gd.

Materials and Methods

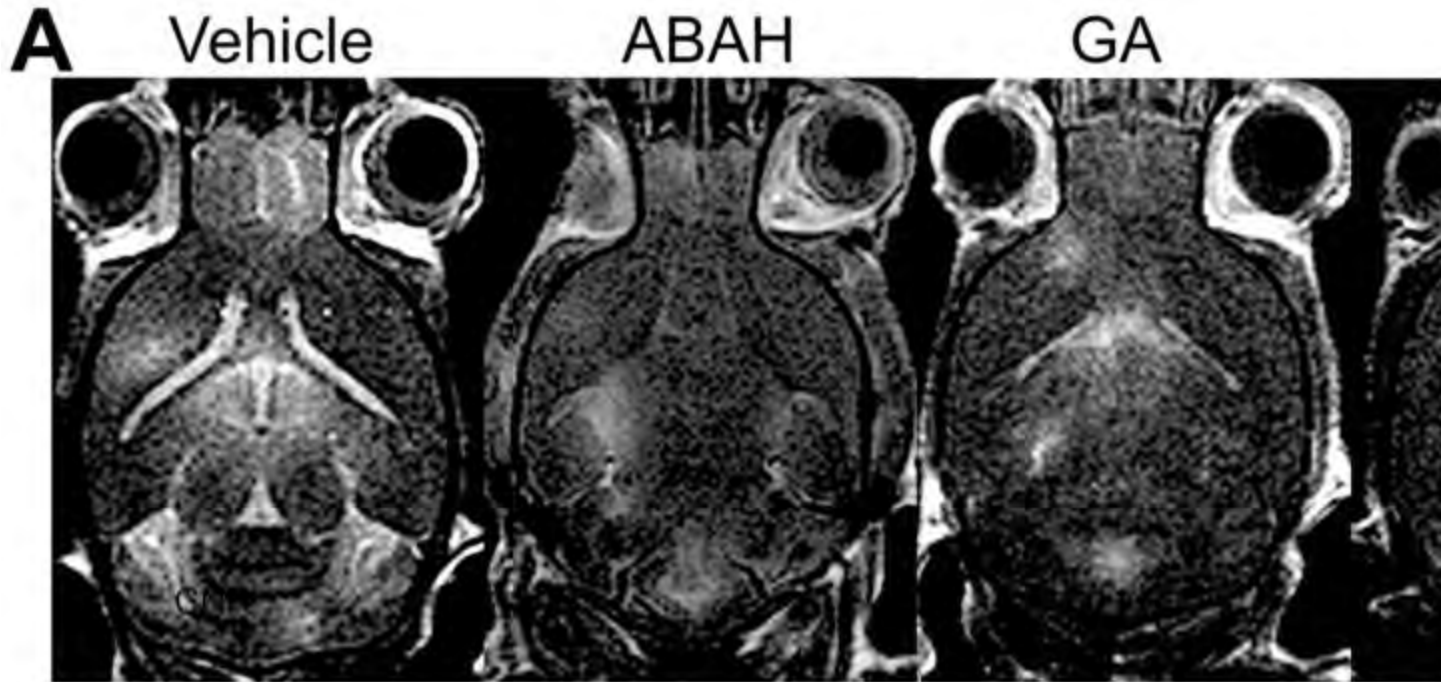
Thirty-five female SJL mice were injected with proteolipid protein to induce experimental autoimmune encephalomyelitis, a mouse model of MS, and treated with IFN (1 $\mu\text{g}/\text{day}$), GA (150 $\mu\text{g}/\text{day}$), MPO inhibitor ABAH (0.8 mg/day), or saline. Mice underwent MRI at 4.7T with MPO-Gd at disease peak (day 12). Lesion volume, number, contrast-to-noise ratio (CNR), and total MPO-Gd enhancement were quantified on delayed images. Mechanistic in vitro experiments and EAE experiments with wildtype and MPO knockout mice were performed.

Results

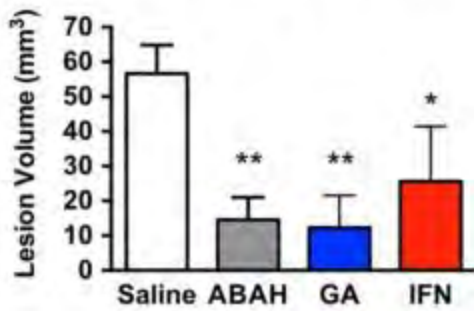
Contrast-to-noise (MPO activity in vivo) was decreased with ABAH and IFN, but not with GA. Lesion volume, lesion number, and total MPO-Gd enhancement (defined as product of CNR and lesion volume) was decreased with all three agents (Fig. A-B). These findings reveal unique imaging signatures for both GA and Ifn- β , where Ifn- β demonstrates an imaging signature similar to the MPO inhibitor ABAH. However, direct enzymatic inhibition was found only with the MPO inhibitor ABAH, but not with IFN or GA. When primary neutrophils were stimulated to secrete MPO, we observed a surprising decrease in MPO activity with IFN, similar to ABAH (C), while GA did not have a similar effect (C). Myeloperoxidase can be inactivated by certain reactive oxygen species. Indeed, when neutrophils were incubated with IFN, we found increased superoxide anion production (as measured by dihydroethidium fluorescence). Conversely, inhibition of superoxide anion production by apocynin (an inhibitor of NADPH oxidase) resulted in the restoration of MPO activity from stimulated neutrophils. Spectrophotometry revealed that IFN-mediated superoxide anion production abolished absorbance of MPO at 430 nm, consistent with irreversible destruction of the iron-containing prosthetic group. On immunohistochemistry, less demyelination was seen in wildtype mice treated with IFN compared to vehicle, similar to vehicle-treated MPO knockout EAE mice (D), suggesting that inactivation of MPO by IFN protects from demyelination.

Conclusions

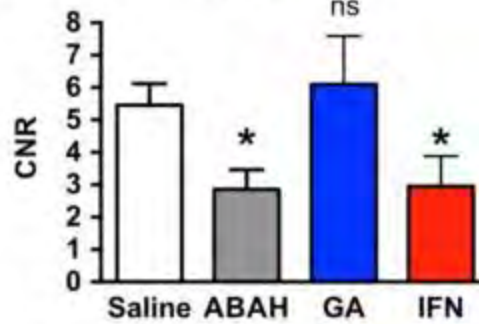
Molecular imaging profiling with MPO-Gd reveals differential treatment effects of the two first-line drugs used in the treatment of MS, and led to the discovery of a novel mechanism of action of IFN: IFN triggers superoxide anion production in myeloid cells to irreversibly inactivate MPO and ameliorate demyelination. In the future, molecular imaging profiling with imaging agents that probe the immune response could open up a new avenue to study the effects of current and future novel therapeutic drugs for MS.



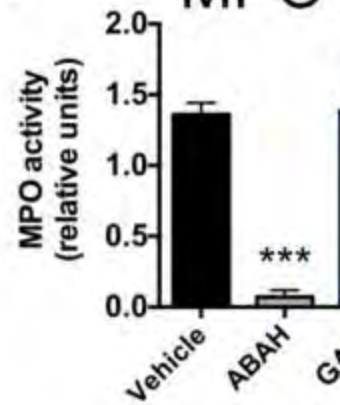
B Lesion volume



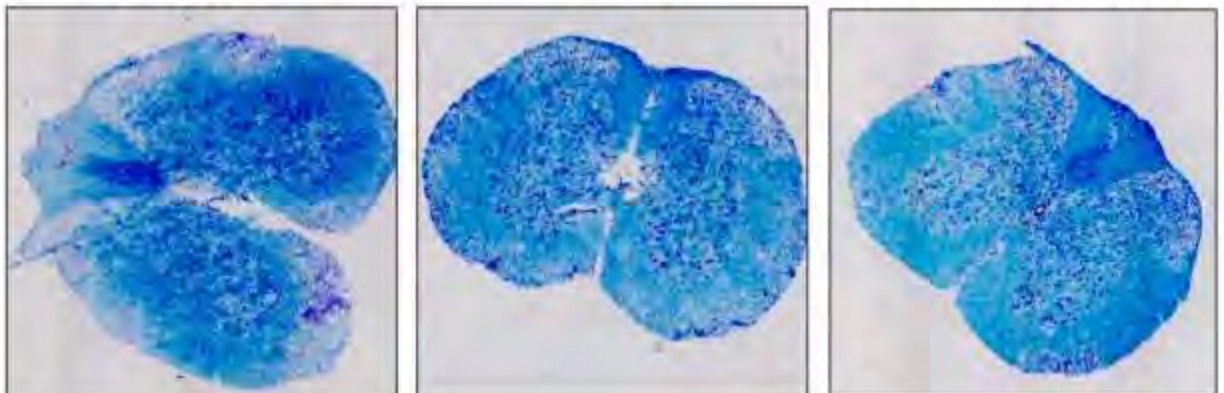
CNR



C MPO



D Vehicle IFN MPO-knockout



Demyelination, grade

(Filename: TCT_O-173_figure.jpg)

O-174

9:23AM - 9:31AM

Sodium MRI in Multiple Sclerosis: A Biomarker for Intracellular Sodium Accumulation in Acute Lesions of the Brain?

A Biller¹, I Pflugmann¹, S Badde², R Diem¹, B Wildemann¹, A Nagel³, J Jutta³, J Kleesiek¹

¹University of Heidelberg, Heidelberg, MA, ²University of New York, New York, NY, ³German Cancer Research Center (DKFZ), Heidelberg, MA

Purpose

Sodium magnetic resonance imaging (MRI) can provide different image contrasts, which reflect the average tissue sodium concentration (average tissue sodium signal; ATS), and sodium ions with short relaxation times thereby achieving a weighting towards the intracellular sodium compartment (intracellular-weighted sodium signal; IWS). Based upon preclinical findings (1, 2) and results of previous sodium MRI studies in MS patients (3, 4) we hypothesize that the IWS signal provides new information to estimate intracellular sodium accumulation, and differs between acute and chronic lesions due to the diverging expression of sodium channels.

Materials and Methods

We enrolled relapsing-remitting MS patients with acute and/or chronic cerebral lesions. Brain sodium MRI data were acquired at 7T providing ATS and IWS signals. Segmentation of MS lesions was performed on clinical routine proton MRI assessed at 3T (Fig. A). Lesion type was defined by the presence or absence of contrast enhancement. Generalized linear mixed models were applied to predict lesion type; thus controlling for varying numbers of lesions among patients. Several factors possibly associated with lesion type like e.g. disease duration were additionally controlled for by including them into the prediction model.

Results

Three hundred two 302 MS brain lesions were detected and analyzed. Thereby, we defined 232 lesion as chronic and 70 as acute. Hierarchical model comparisons revealed that ATS ($\chi^2(1)=27.89$, $p<0.001$) and IWS signal ($\chi^2(1)=5.76$, $p=0.016$) improved lesion type classification. Both sodium MRI signals were elevated significantly in acute compared to chronic lesions (Figs. A and B).

Conclusions

In this study, we are able to demonstrate that sodium MRI reveals new information on MS lesions compatible with the pathogenetic events of MS leading to intracellular sodium accumulation. Sodium MRI information is very specific whereas conventional MRI yields a nonspecific T2 signal of MS lesions and even contrast-enhancement is

considered nonspecific because it is a marker of blood-brain barrier disruption, not inflammation (5). Therefore, sodium MRI could serve as biomarker for diagnostic assessment of MS, and as readout parameter in trials promoting attenuation of chronic inflammation. If confirmed in further studies, sodium MRI could serve as biomarker for diagnostic assessment of MS, and as readout parameter in trials promoting attenuation of chronic inflammation.

Sodium MRI of Cerebral MS Lesions

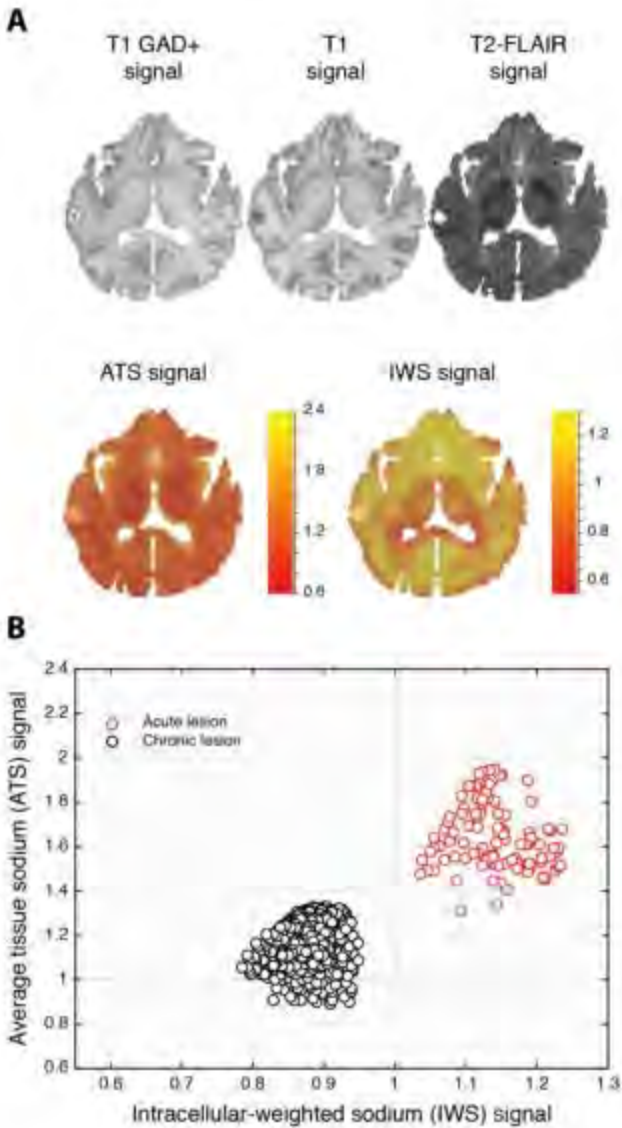


Figure: Axial proton and sodium MR images of an exemplary patient demonstrating an acute right-temporal MS lesion with contrast enhancement and elevated T2-FLAIR, ATS and IWS signals (**A**). Statistical analyzes revealed that both ATS and IWS signals improve prediction of lesion type; both signals were significantly increased in acute compared to chronic brain MS lesions; the scatterplot visualizes these findings (**B**) showing a near perfect discrimination between lesion types which is, of course, not achieved in every case. Sodium MRI information is very specific whereas conventional MRI yields a non-specific T2 signal of MS lesions and even contrast-enhancement is considered non-specific because it is a marker of blood-brain barrier disruption, not inflammation [5]. Therefore, sodium MRI could serve as biomarker for diagnostic assessment of MS, and as readout parameter in trials promoting attenuation of chronic inflammation

(Filename: TCT_O-174_Figure-01.jpg)

O-175

9:31AM - 9:39AM

Imaging CNS inflammation in patients with genetic mutations in the essential immune checkpoint inhibitor, Cytotoxic T-lymphocyte Antigen-4 (CTLA4).

M Schindler¹, G Uzel¹, S Pittaluga¹, D Reich¹, I Cortese¹

¹NIH, Bethesda, MD

Purpose

Genetic mutation in cytotoxic T-lymphocyte antigen-4 (CTLA4), leads to systemic immune dysregulation with autoimmune cytopenia, abnormal lymphoproliferation in lymphoid organs, hypogammaglobulinemia, and infiltrative lymphocytosis in nonlymph organs (gut, lungs, and brain), as recently described (Kuehn et. al., Science 2014). The extent of central nervous system (CNS) involvement and imaging features in this newly described disease are not known.

Materials and Methods

A retrospective review and prospective imaging study of patients with CTLA4 mutations followed at the National Institutes of Health between 2009 and present. Of 30 genetically confirmed CTLA4 patients, 17 had brain magnetic resonance images (MRIs) available for review.

Results

The average age of onset of neurologic signs, symptoms, or imaging findings was 19 years (range 9 to 35 years). Focal inflammatory lesions were present in the supratentorial white matter (11 patients), infratentorial compartment (7), and spinal cord (2), including one longitudinally extensive lesion. Many lesions were large (>64mL) and most enhanced with gadolinium, but many showed little to no distortion of the surrounding tissue. Leptomeningeal enhancement was seen in five patients, including one in whom focal enhancement developed in advance of parenchymal signal change. Lesions responded quickly to steroids with dramatic shrinkage and little residual abnormal signal. Clinically, the most common symptoms were headache (9) and seizure (6). Few patients had focal neurological deficits, and those noted were subtle, in stark contrast to the imaging findings. Limited biopsy samples showed lymphocyte or histiocyte infiltration without overt tissue destruction.

Conclusions

Imaging patients with CTLA4 mutations captures an important feature of neuroinflammation in this disease, i.e., immune-cell infiltration in the relative absence of associated neural-destruction in contradistinction to other CNS inflammatory diseases, like multiple sclerosis. Studying rare genetic syndromes, like CTLA4

haploinsufficiency, therefore may be of value for understanding the pathological basis of MRI signal changes in neuroinflammatory disease.

O-176

9:39AM - 9:47AM

Imaging biomarkers in Neuropsychiatric Lupus- Are they robust enough?

J Chaganti¹, B Brew²

¹St Vincents Hospital, Sydney, NSW, ²ST VINCENT'S HOSPITAL, SYDNEY, NSW

Purpose

Aim: to identify the cytoarchitectural changes in the clinically early neuro psychiatric SLE using multiparametric MRI techniques.

Materials and Methods

We evaluated 21 female patients (20-49 years) with lupus with mild neuro psychiatric symptoms and equal number of normal volunteers to identify and detect early ultrastructural changes in different parts of the brain. All the patients underwent MRS (2DCSI) , ASL (pCASL) and diffusion tensor imaging (DTI) (32 directions) using Philips 3T-Ingenua. Diffusion metrics ADC, FA were measured in in the regions of all the major association fibers as well as commissural fibers (FSL) and cerebral blood flow (CBF) was measured from splenium of corpus callosum, cingulate gyrus, and dorsolateral prefrontal cortex (FSL). Magnetic resonance spectroscopy (MRS) was done using 2D CSI with long TE and the basal ganglia, fronto parietal cortex and centrum semiovale and the peritrigonal white matter were evaluated (LC MODEL). All patients underwent repeat MRI after 1 year. Statistical analysis was done using SPSS version22 using one way ANOVA

Results

The conventional MR images of patients are normal in four patients while the rest demonstrated small bright foci in the central white matter on FLAIR Imaging. Diffusion tensor imaging (DTI)/ASL/MRS measurements: All the patients have demonstrated statistically significant DTI abnormalities and correlated well with MRS. The ASL was equivocal in four patients and demonstrated reduced CBF in five patients and borderline abnormality in 12. Spectroscopy was uniformly abnormal with high Choline to Creatine ratio and mildly reduced NAA to Creatine ratio in nine patients. Correlation: All patients who had abnormal MRS in NAA/CH and NAA/ CR have shown clinical correlation with activity of the disease based on symptoms as well as immune markers. Diffusion tensor imaging metrics were favorably compared with clinical abnormality and mostly associated with reduced FA and increased MD in the superior longitudinal fasciculus (SLF) and splenium of the corpus callosum as well as posterior cingulate. The ASL showed no significant correlation with disease

activity but correlated well with MRS and DTI in those subgroups where there is more reduction in NAA and high mean diffusivity.

Conclusions

The diagnosis of NP-SLE often is clinical and the imaging biomarkers are not well recognized. We have used the three most reproducible imaging modalities to identify the ultrastructural changes and could be used as markers to measure the disease response with the treatment.

O-177

9:47AM - 9:55AM

Diagnostic Value of Apparent Diffusion Coefficient for the Accurate Assessment and Differentiation of Postoperative Intracranial Abscesses

E Lotan¹, S HarNof¹, O Komisar¹, A Fardman¹, C Hoffmann¹

¹*Sheba Medical Center and Tel-Aviv University, Tel-Aviv, Israel*

Purpose

Current radiologic knowledge employs the presence of restricted diffusion as a hallmark of brain abscess in contrast to a cystic tumor. However, it can lead to misdiagnosis in the postoperative setting. The purpose of this study was to compare apparent diffusion coefficient (ADC) values of intracranial abscesses that occurred without ("spontaneously") and after a primary neurosurgical procedure ("postoperatively") and to assess their diagnostic value.

Materials and Methods

This retrospective comparative study was approved by the local institutional review board. The requirement to obtain written informed consent was waived. A total of 73 consecutive patients who underwent a pre-operative magnetic resonance (MR) imaging with diffusion-weighted imaging (DWI) from February 2005 to May 2015 were divided into two cohorts depending on whether the abscess identified after a primary neurosurgical procedure (n=43) or not (n=30). Abscesses were assessed for ADC values by two readers independently. ADC values were described with median and interquartile range (IQR). Chi-square and Mann-Whitney tests were used to compare ADC values between the two cohorts. Correlation between continuous variables was calculated by Spearman's rank correlation coefficient. Chi-squared automatic interaction detection analysis was used to classify the ADC values into categories according to the cohorts.

Results

Apparent diffusion coefficient value of postoperative abscesses [1.34 (1.00-1.62) x10⁻³mm²/s, (median, IQR)] was significantly higher than ADC value of spontaneous abscesses [0.68 (0.58-0.79) x10⁻³mm²/s, P<0.001]. Eighty-three percent (n=24) of abscesses with ADC value <0.79x10⁻³mm²/s were found to be spontaneous, while

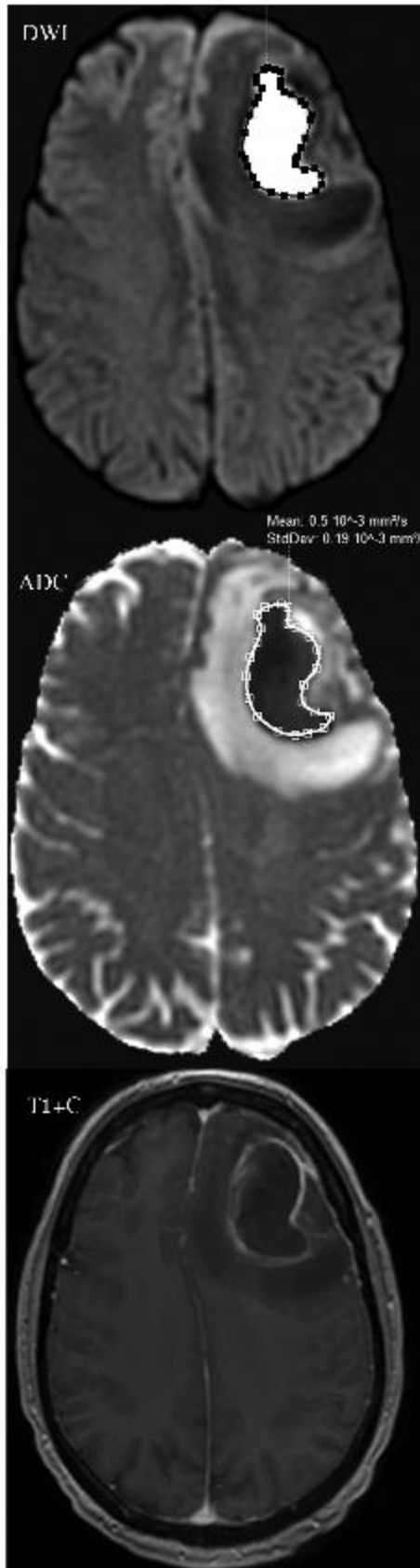
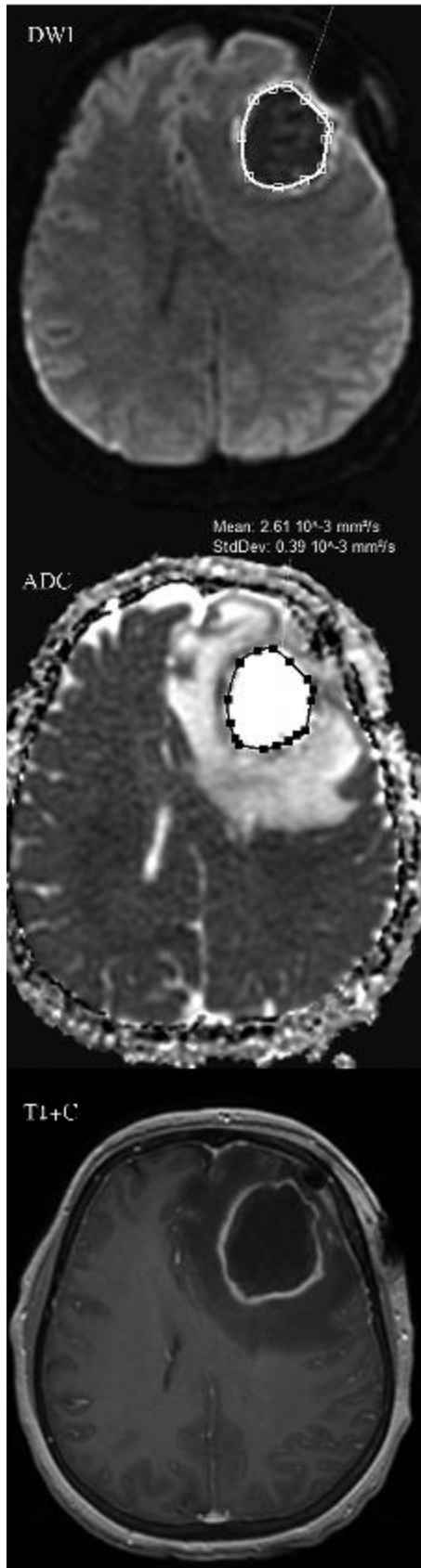
only 27% (n=6) of abscesses with ADC value between 0.79 to 1.33 x10⁻³mm²/s and no abscesses with ADC value above 1.33 x10⁻³mm²/s were spontaneous (P<0.001). There was significant correlation between interval from the initial surgery to re-operation for abscess drainage and the abscess's ADC values (r=-0.352, P=0.026), hence lower ADC values were associated with longer period after the initial surgery.

Conclusions

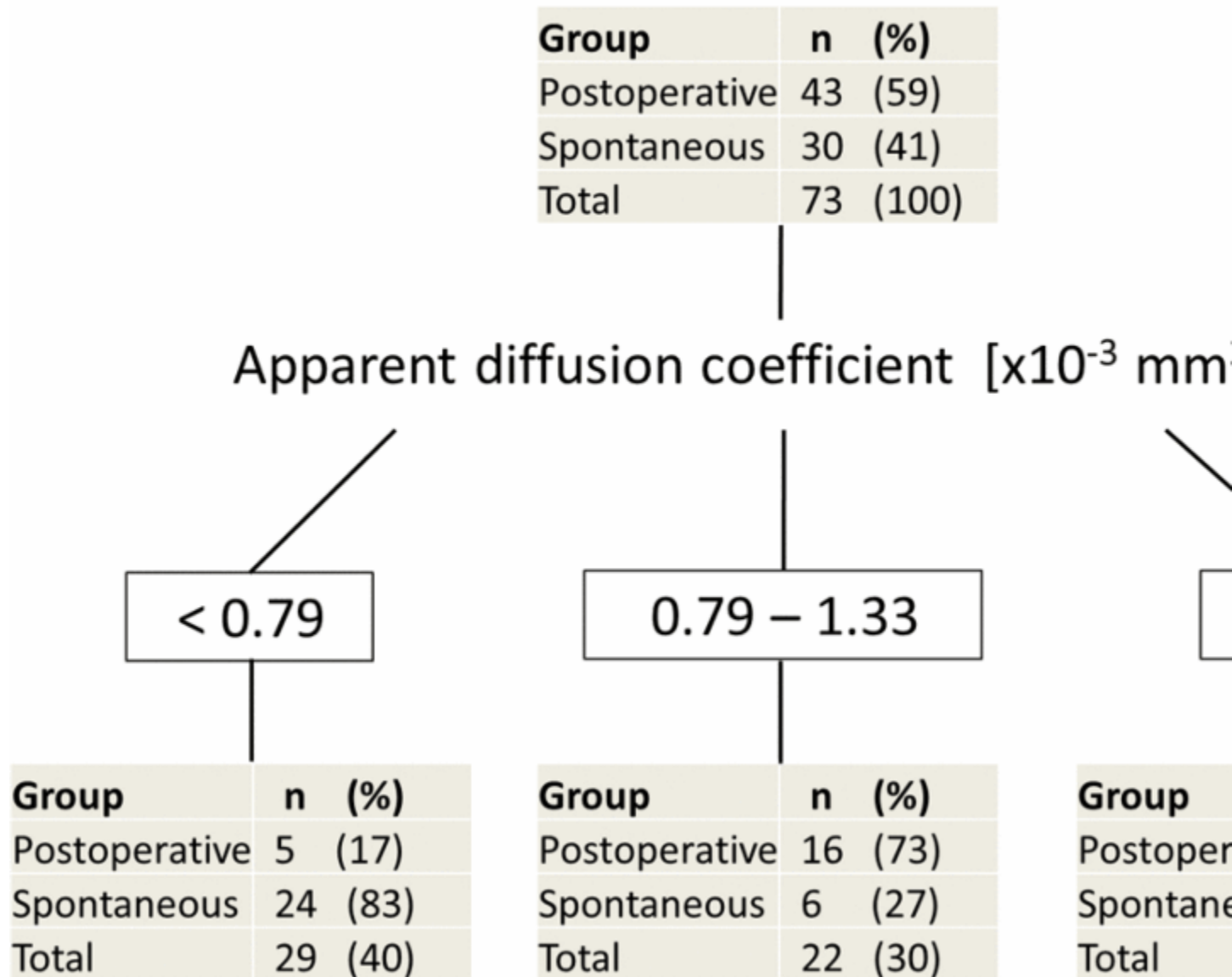
There are significantly higher ADC values of postoperative abscesses compared to spontaneous abscesses. Longer interval from the initial surgery to re-operation for abscess drainage was associated with lower ADC values. Although DWI with an ADC map is an excellent tool for diagnosis spontaneous brain abscesses, it is not sufficient for excluding postoperative intracranial abscess. Clinical suspicion of abscess should not be negated by absence of restricted diffusion in DWI and high ADC value in the ADC map.

Postoperative
Abscess

Spontaneous
Abscess



(Filename: TCT_O-177_Figure-1.jpg)



(Filename: TCT_O-177_Figure2.gif)

O-178

9:55AM - 10:03AM

Imaging of Intracranial Central Nervous Complications after Solid Organ Transplantation

Y Chen¹, M Chan¹, W Kucharczyk²

¹University of Toronto, Toronto, Ontario, ²Toronto General Hospital, Toronto, ON

Purpose

To investigate the imaging spectrum and temporal course of intracranial central nervous system (CNS) complications after solid organ transplantation.

Materials and Methods

Institutional ethics approval was obtained for this retrospective study. The medical records and brain imaging data of 125 consecutive solid organ transplant patients (age 52.6 \pm 13.5 years; 48.4% females) who had positive CT and/or MRI brain findings between January 2010 and November 2015 were reviewed. Central nervous system (CNS) complications were divided into four categories: vascular (including infarct and hemorrhage), toxic/metabolic, infectious/inflammatory and neoplastic. The onset of CNS complications was grouped into four post-transplantation intervals including acute (< 1 month), early subacute (1-3 months), late subacute (3-12 months), and chronic (> 1 year).

Results

Patients with acute intracranial findings on imaging included 50 post-liver (40%), 36 post-lung (28.8%), 16 post-cardiac (12.8%), 19 post-renal (15.2%), and 4 post-multi-organ (3.2%) transplants. Vascular disorders were the most common etiology overall (69, 55.2%), followed by toxic/metabolic (38, 30.4%), infectious/inflammatory (10, 8%), and neoplastic (8, 6.4%) disorders. The average time between acute imaging findings and transplant is 3.2 \pm 6 years, with 55 cases occurring within 1 month (44%), 11 between 1 and 3 months (8.8%), 13 between 3 months and 1 year (10.4%) and 46 more than 1 year (36.8%). In the acute < 1 month group, 54.6% of cases were post-liver and 27.2% post-lung transplants. Vascular disorders were the most common etiology during the acute period (30, 54.6%), followed by metabolic encephalopathy (22, 40%). In the chronic > 1 year group, 34.8% of the cases were post-renal and 26.1% post-lung transplants. Vascular disorder remained the most common etiology (31, 67.4%), followed by neoplastic disorders (6, 13%).

Conclusions

The etiology of CNS complications after solid organ transplant changes depending on the time post-transplant. Vascular and metabolic disorders were the most common in the acute period whereas vascular and neoplastic disorders were the most common in the chronic period.

| Pathology Category | # | Percent | Transplant Type | | | | | |
|-------------------------|------------|-------------|-----------------|-----------|-----------|-----------|-------------|----------|
| | | | Liver | Lung | Heart | Renal | Multi-organ | Other |
| Infarct | 42 | 33.6% | 7 | 19 | 5 | 10 | 1 | 0 |
| Hemorrhage | 27 | 21.6% | 14 | 3 | 8 | 2 | 0 | 0 |
| Toxic/metabolic | 38 | 30.4% | 26 | 8 | 0 | 2 | 2 | 0 |
| Infectious/inflammatory | 10 | 8% | 3 | 4 | 3 | 0 | 0 | 0 |
| Neoplastic | 8 | 6.4% | 0 | 2 | 0 | 5 | 0 | 1 |
| <i>Total</i> | <i>125</i> | <i>100%</i> | <i>50</i> | <i>36</i> | <i>16</i> | <i>19</i> | <i>3</i> | <i>1</i> |

(Filename: TCT_O-178_ASNRabstracttable.PNG)

Tuesday

8:35AM - 10:00AM

Washington Marriott Wardman Park, Roosevelt 1-3

8D-PARALLEL PAPER SESSION: Turbo Talks - Traumatic Brain Injury /

Epilepsy Advances

O-179

8:35AM - 8:38AM

Standard versus Extended CT Protocols in Head Trauma: radiation dose versus workflow considerations from a Level I Trauma Center

M Pinho¹, J Pond¹, B Boren¹

¹University of Texas Southwestern, Dallas, TX

Purpose

Although the standard head computed tomography (CT) covers only the skull base to vertex, our medical center uses a dedicated trauma protocol that extends coverage below the mandible. The rationale is that some patients may eventually need a maxillofacial CT, which can be reconstructed from the original dataset without a second scanning session, facilitating workflow and potentially avoiding duplicated radiation exposure where the brain and face overlap. Additional coverage also enables screening of clinically unsuspected facial lesions. In this study we compare benefits and disadvantages of the two head CT protocols in trauma patients, considering radiation dose and impact to workflow in a level I trauma center.

Materials and Methods

We performed a chart review of 378 consecutive patients that had head CTs performed for trauma, corresponding to a span of 1 month. Maxillofacial CTs for

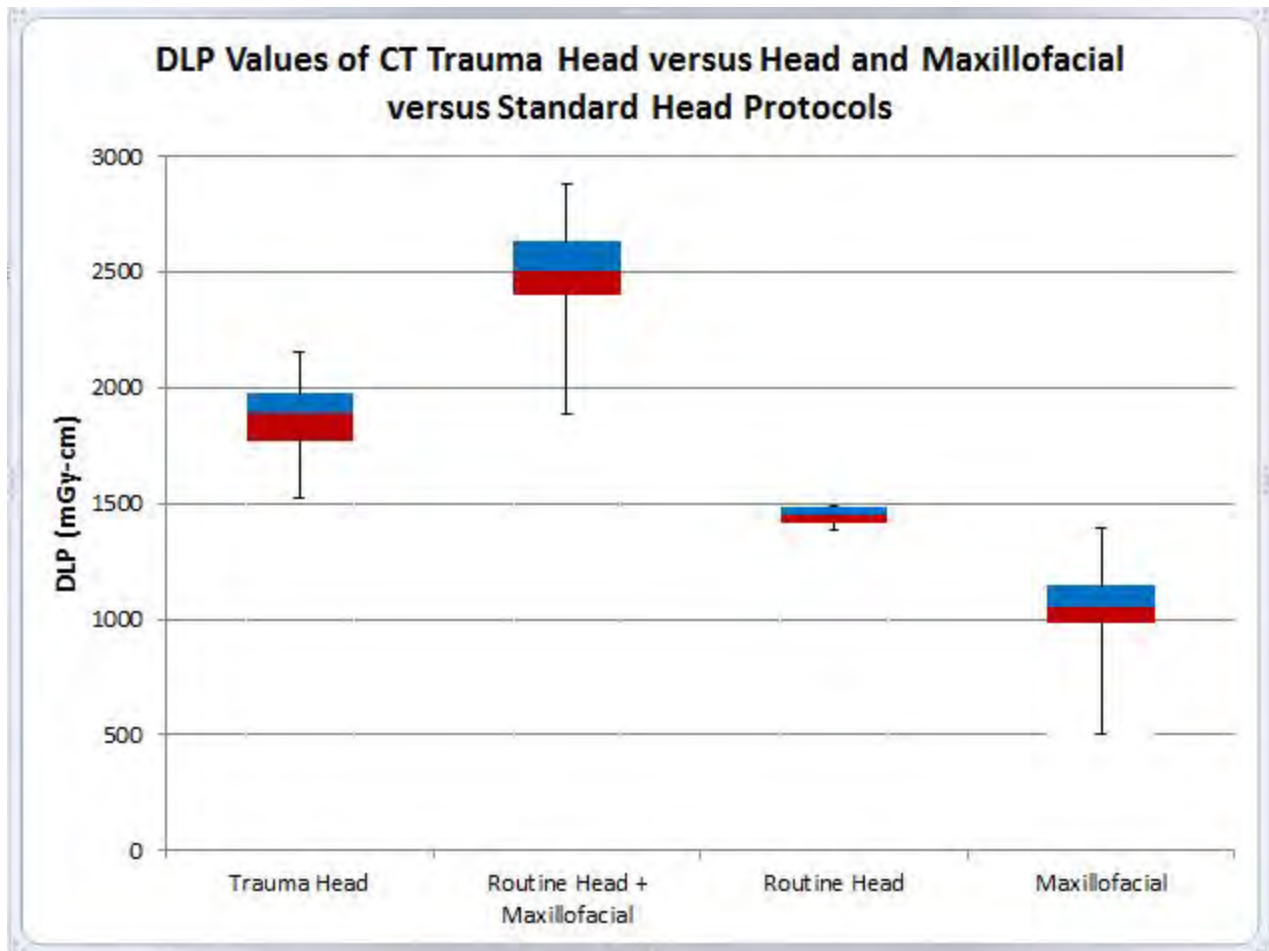
these patients also were computed and we reviewed all clinical and imaging data to determine whether it was reconstructed from the head CT data retrospectively (ordered after the head CT) or at the time of the scan (ordered with the head CT). Head and maxillofacial CT reports were reviewed for traumatic findings. CTDIvol and DLP were recorded for all 378 patients and compared to average radiation doses of a separate sample of 30 consecutive patients who underwent standard head CTs and 60 consecutive patients who underwent maxillofacial CTs.

Results

Of the original 378 patients, 67 (17.7%) also had a dedicated maxillofacial CT. Sixty of these maxillofacial CTs were ordered at the same time as the head CT. Seven CTs were ordered later and reconstructed from the original extended head coverage. All seven patients had evidence of facial trauma on clinical exam and the lack of a prospective maxillofacial CT order was uniformly a clinical oversight. The average radiation dose saved for each of the seven patients was 598 mGycm (24% 4186 mGycm total); however, the mean dose for the extended head protocol is significantly higher compared to the routine protocol ($p < .0001$). The average added dose to the remaining 311 patients (extended head CT protocol without maxillofacial CT) was 427 mGycm each (30% 132,821 mGycm total) resulting in a net added dose of 128,636 mGycm (29%) to the entire group. Eight trauma-related facial findings were detected incidentally in the 311 patients without dedicated maxillofacial imaging due to extending coverage. None of these patients required additional treatment but ophthalmology consultation was requested in two cases.

Conclusions

To our knowledge, the advantages and disadvantages of a "standard" versus "extended" head CT trauma protocol have not been evaluated systematically in the literature. Our results demonstrate that the extended protocol results in a workflow advantage and radiation dose savings for a small fraction of patients (2.2%), but imparts significantly increased (29%) radiation dose on average to the entire group. These results suggest that extended coverage (from vertex to mandible) is justifiable only in patients with prospectively ordered head and maxillofacial studies based on clinical findings.



(Filename: TCT_O-179_Capture.JPG)

O-180

8:38AM - 8:41AM

Longitudinal White Matter Changes Following Traumatic Brain Injury

J Ware¹, J Detre¹, J Kim²

¹University of Pennsylvania, Philadelphia, PA, ²The City College of New York, New York, NY

Purpose

Traumatic brain injury (TBI) is a leading cause of morbidity and disability in the United States, and functional outcomes for patients with TBI remain heterogeneous. Patient stratification based on advanced neuroimaging eventually may lead to more appropriately tailored and/or effective rehabilitation strategies. Diffusion tensor imaging (DTI) in particular has demonstrated the ability to detect white matter changes which occur as a result of shear injury in patients with TBI, though the evolution of DTI changes and their relationship to functional recovery are only

beginning to be characterized. In this study, we investigated longitudinal changes in white matter DTI abnormalities following TBI to determine their relationship to longitudinal changes in disability and brain function.

Materials and Methods

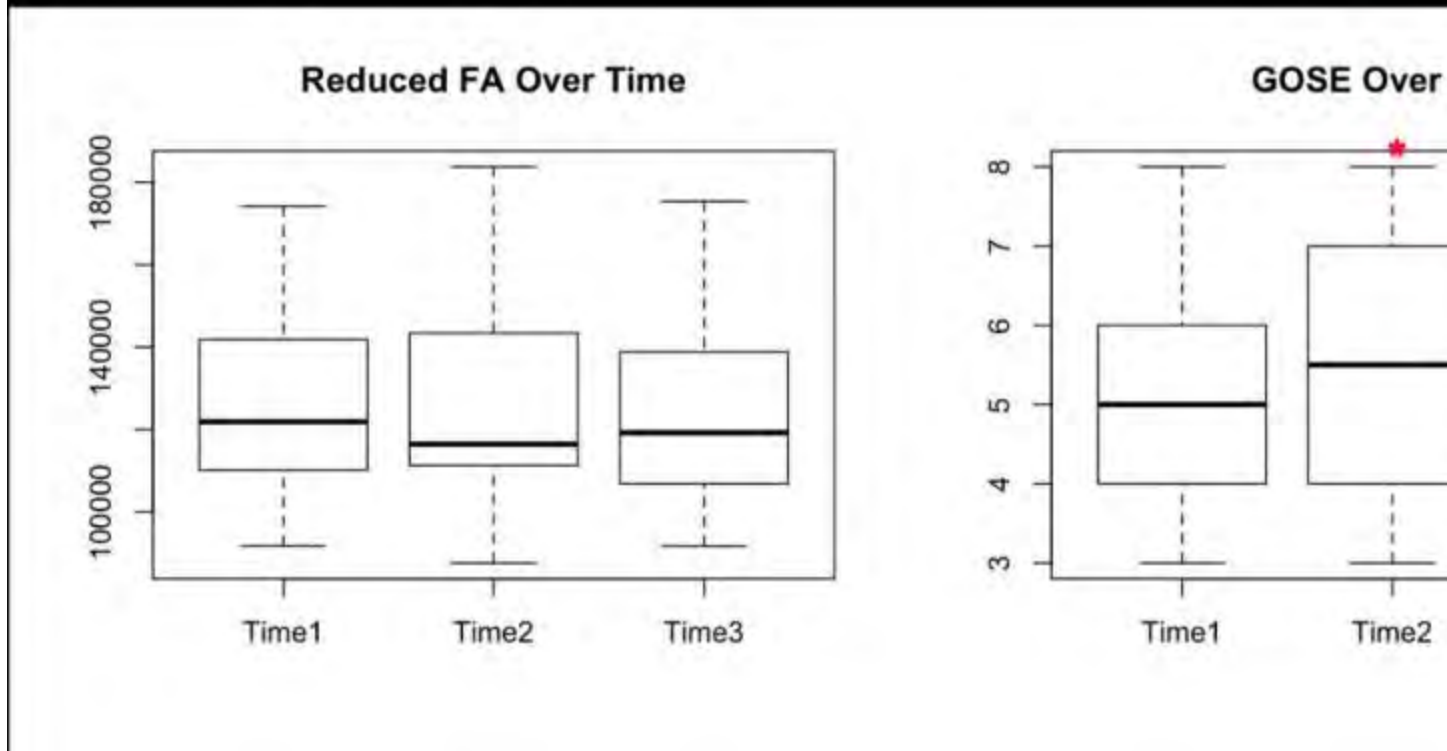
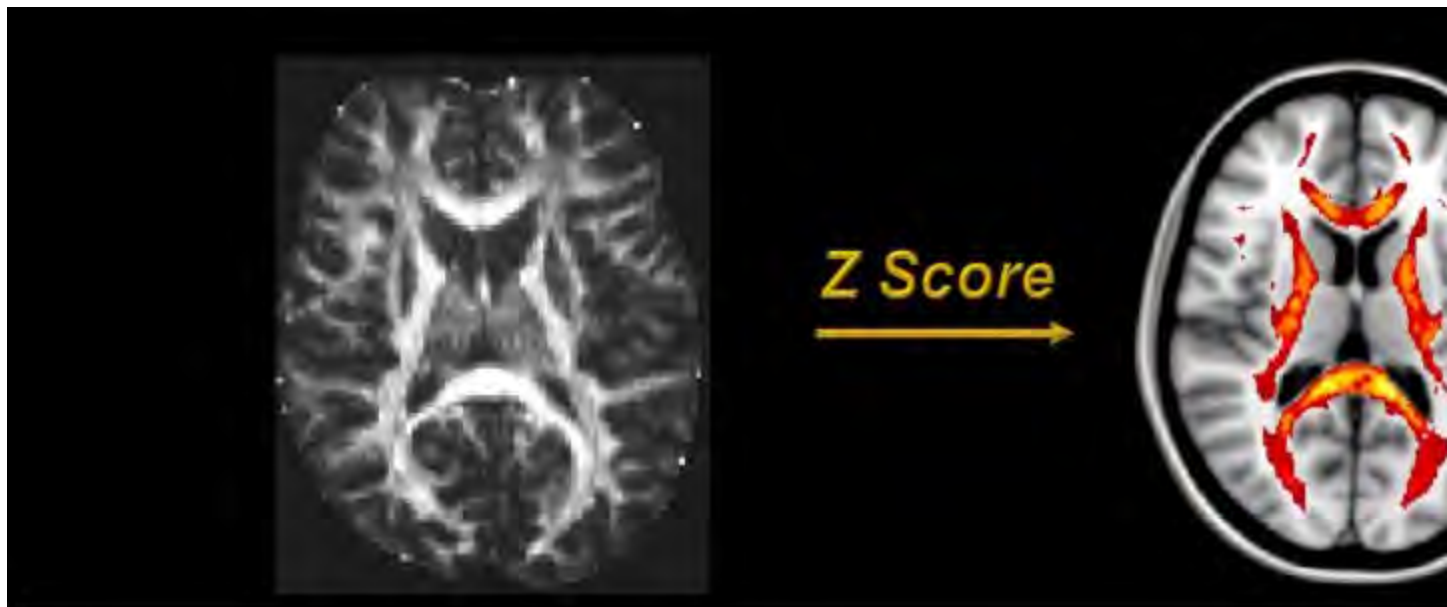
Eighteen adults with at least moderate traumatic brain injury were examined at 3, 6, and 12 months following injury. At each time point, each subject was assessed with DTI as well as the Disability Rating Scale (DRS), Glasgow Outcome Scale-Extended (GOSE), and a test of processing speed (PSI from WAIS-IV). Subject-specific maps of white matter fractional anisotropy (FA) and radial diffusivity (RD) were co-registered and converted to Z-score maps of DTI abnormality based on a control population of 34 normal subjects matched for demographic characteristics, then thresholded to determine regions of abnormally low FA and abnormally high RD. The total number of abnormal voxels derived from each subject's thresholded Z-score map was used to quantify the extent of white matter abnormality for each time point in each subject. Repeated measures analysis of variance and paired t-tests were used to test for significant differences in clinical and imaging measures between time points.

Results

All subjects demonstrated several regions of abnormally reduced FA and abnormally increased RD ($|Z| > 2$, cluster size $p < 0.05$) within otherwise normal-appearing white matter. Over the three time points, there was significant longitudinal improvement in both processing speed ($p = 0.001$) and disability scores ($p = 0.02$). Across all subjects, there was a correspondingly significant increase in the number of abnormal RD voxels ($p = 0.006$) over time, however there was no significant longitudinal change in the number of abnormal FA voxels. The number of abnormal FA and RD voxels at the 3 month time point were predictive of disability score at the 12 month time point ($p < 0.05$).

Conclusions

Despite persistent changes in DTI indices suggesting tract disruption (FA) and progressive dysmyelination (RD) up to 12 months following TBI, there was significant group improvement in function and reduction in disability over time. These findings suggest that functional recovery may depend primarily on compensatory mechanisms rather than normalization of microstructural white matter changes.



(Filename: TCT_O-180_asnr.jpg)

O-181

8:41AM - 8:44AM

Opposing Patterns of Altered Microstructure in Anterior Versus Posterior Cerebral White Matter After Mild Traumatic Brain Injury

E Yuh¹, D McCoy¹, A Ferguson¹, D Ramanan², F Ezekiel¹, M Vassar¹, G Manley¹, P Mukherjee³

¹University of California at San Francisco, San Francisco, CA, ²Ayasdi, Menlo Park, CA, CA, ³San Francisco VA Med Ctr, San Francisco, CA

Purpose

We used topological data analysis (TDA), a powerful technique for querying massive data sets for patterns that may not be apparent using more conventional analysis techniques, to analyze diffusion tensor imaging (DTI) data in the subacute time frame after mild traumatic brain injury (mTBI). We also used region of interest (ROI) methods in conjunction with TDA techniques to assess for tract-specific alterations in DTI parameters after mTBI.

Materials and Methods

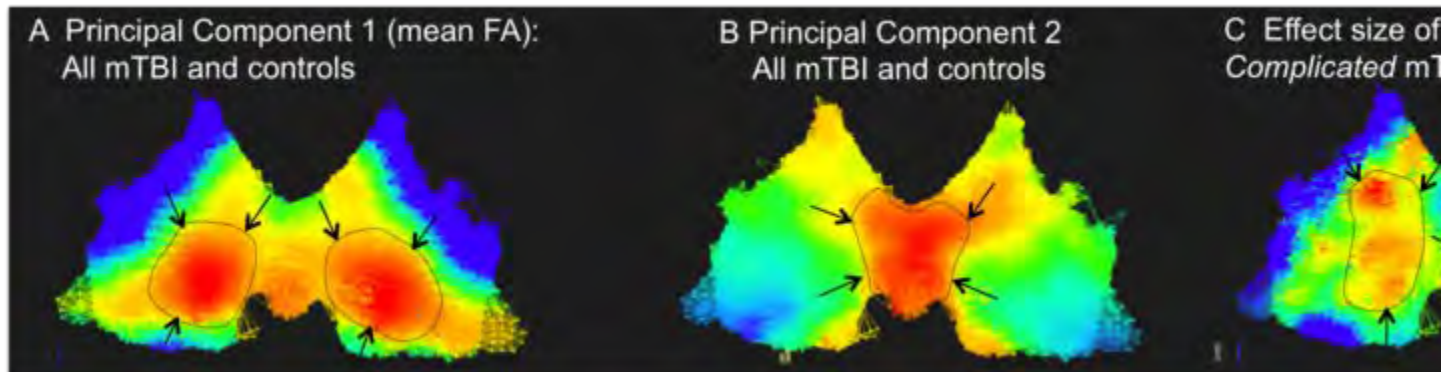
We studied 3T DTI data from 76 adults at 11.2 ± 3.3 days after mTBI. Patients were enrolled at San Francisco General Hospital as part of the Transforming Research and Clinical Knowledge in Traumatic Brain Injury study. Tract-based spatial statistics were used to align each subject's fractional anisotropy (FA) and mean diffusivity (MD) data to a white matter skeleton. We used the TDA software Iris (Ayasdi, Menlo Park, CA) to search for patterns in the DTI data. For the ROI analysis, 45 white-matter-skeleton ROIs were delineated using the JHU ICBM-DTI-81 White Matter Labeled Atlas. For each subject, we calculated global FA and MD based on the entire white matter skeleton, and then normalized FA and MD in each voxel by the subject's global value. For each ROI, we compared the normalized mean FA and MD in that ROI in mTBI versus controls using two-tailed t-tests.

Results

Region of interest analysis: Using normalized FA values, we observed geographic-tract-specific variations in the alterations in DTI parameters. Statistically significant increases in FA in mTBI patients were observed only in anterior tracts (anterior corona radiata, $p=3 \times 10^{-6}$; anterior limb of internal capsule, $p=8 \times 10^{-4}$; superior fronto-occipital fasciculus, $p=0.03$) while significant decreases in FA were observed only in posterior tracts (splenium, $p=7 \times 10^{-8}$; posterior corona radiata, $p=0.03$; posterior limb of internal capsule; $p=0.06$). Topological data analysis: We also used TDA to demonstrate the presence of striking subdivisions within traditional tractography-defined tracts. For example, Figures A and B show the spatial dependence of Principal Components 1 and 2 for FA within the splenium. Regions with highly coherent FA values across all 126 patients and control subjects have similar PC1 and PC2 values, and are manifested as regions of coherent color (encircled regions in Figures A and B). Figure C shows the effect size of alterations in complicated mTBI versus control subjects (red denoting the largest size effects and blue denoting the smallest). Comparison of Figure C to Figures A and B shows that the largest effect sizes in FA differences (red regions in Figure C) are in the same regions with the highest magnitudes of PC1 and PC2 (red regions in Figures A and B).

Conclusions

We demonstrate geographic variations in changes in FA and MD at a subacute timepoint after mTBI. Statistically significant decreases in FA were seen only in anterior tracts, and significant increases only in posterior tracts. We also used TDA to demonstrate the presence of substructures within JHU ROIs; these may be a basis for new ROI schemes that complement traditional tractography-based ROIs for DTI analysis.



(Filename: TCT_O-181_ASNR2016-FigureFinal.png)

O-182

8:44AM - 8:47AM

Blood in the brain: MRI Differentiation of cerebral fat embolism (CFE) from diffuse axonal injury (DAI)

A Rutman¹, E Rapp¹, D Hippe¹, M Mossa-Basha¹

¹University of Washington, Seattle, WA

Purpose

In the setting of high impact trauma with long bone fractures, a diagnostic challenge may arise as the magnetic resonance imaging (MRI) findings of cerebral fat embolism (CFE) can mimic those of diffuse axonal injury (DAI). Our study attempts to differentiate the findings of CFE and DAI using the size, shape, location and number of intracranial lesions with MR imaging.

Materials and Methods

Adult patients with CFE and DAI were selected retrospectively upon review of the radiology database at an adult Level 1 trauma center between 1/1/07 and 7/30/14. Selection criteria of CFE patients were according to Gurd's criteria, with initial GCS of 14-15 and latent decline to <6T, and presence of long bone fractures. Diffuse axonal injury patients had evidence of hemorrhagic lesions on MRI, initial GCS<6T and no long bone fractures to exclude the possibility of concomitant CFE. Two independent, blinded raters evaluated the MRI examinations for number, shape, and

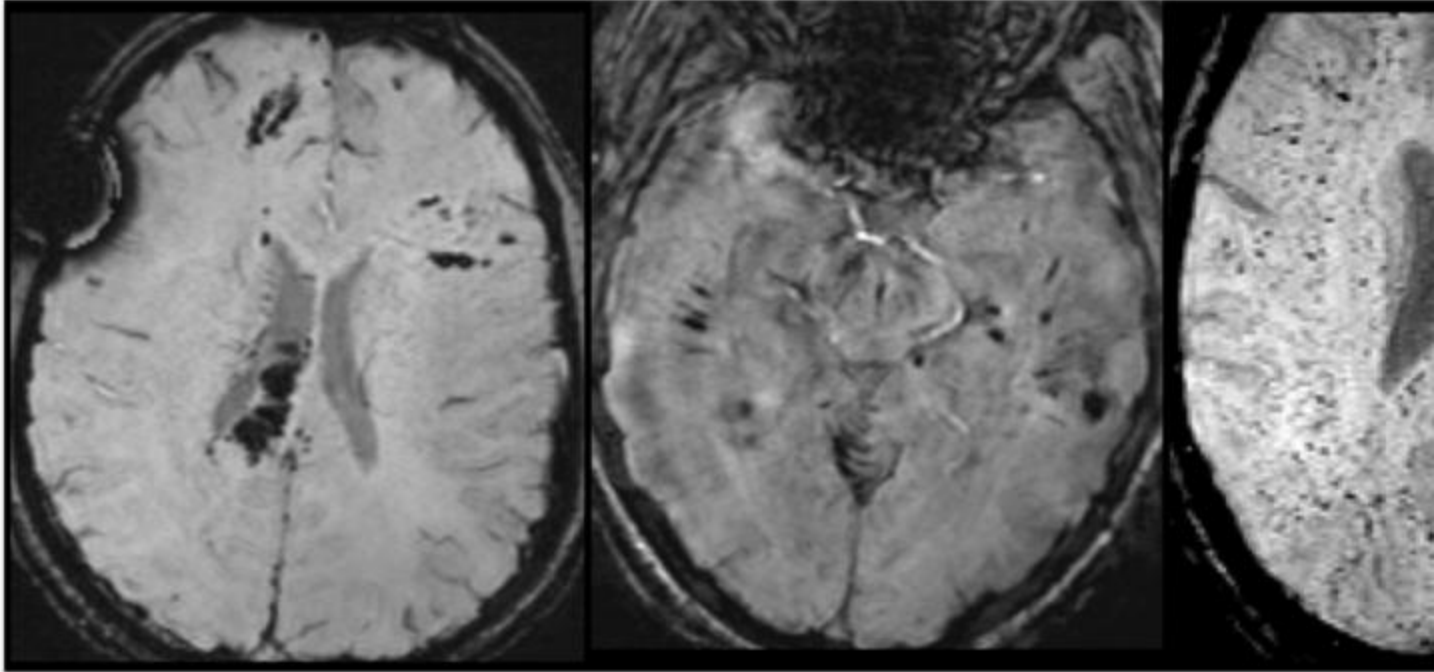
size of hemorrhages on susceptibility-weighted imaging (SWI) and gradient recall echo (GRE) sequences at the following anatomical stations: frontal, parietal, temporal, and occipital white matter, corpus callosum, striatocapsular/insular, thalamus, brainstem, and cerebellum. Hemorrhage shape was round/elliptical or linear and size was characterized as punctate (0-3mm), small (4-10mm), medium (11-20mm), or lobar (>21mm). Statistical analysis was performed with Mann-Whitney test for number of hemorrhages at each station, and Fisher's exact test for hemorrhage shape and size. P-values were adjusted for multiple comparisons across stations to maintain a false discovery rate < 5%.

Results

Seven patients with CFE and 20 with DAI were selected based on inclusion/exclusion criteria. There was overall good interobserver agreement between the two raters, with ICC between 0.66 and 0.88 for number of hemorrhages at the various stations. Of the patients with hemorrhages, cases of CFE had an overall tendency to have more hemorrhages than DAI. Specifically, there were significantly more hemorrhages in the parietal (mean: 120±55 versus 13±11, p=0.005) and occipital lobes (mean: 103±67 versus 3±2, p=0.025), the corpus callosum (mean: 98±46 versus 20±20, p=0.022), and cerebellum (mean: 82±32 versus 12±10, p=0.025). Number of hemorrhages in the frontal and temporal lobes, brainstem, thalamus, and striatocapsular/insular regions, while greater in CFE cases, did not reach statistical significance compared to DAI. Cerebral fat embolism microhemorrhages were typically punctate and round when present, while patients with DAI were significantly more likely to have small or medium-sized hemorrhages (100% versus 0%, p<0.001). Additionally, the presence of linear hemorrhages was significantly more prevalent in DAI (85% versus 0%, p<0.001).

Conclusions

Cerebral fat embolism can be differentiated from DAI with MR imaging. Specifically, CFE patients demonstrate more hemorrhages in parietal and occipital white matter, corpus callosum and cerebellum. Additionally, linear hemorrhages and nonpunctate hemorrhages are both significant indicators of DAI.



Patients with DAI demonstrate small and medium sized hemorrhages (a), as well as linear-shaped hemorrhages (b), while cases of CFE demonstrate numerous round and punctate white matter hemorrhages (c).

(Filename: TCT_O-182_ASNRabstractfig.jpg)

O-183

8:47AM - 8:50AM

Prevalence of Microhemorrhages, White Matter Changes, and Cavum Septum Pellucidum in Fighters: Part of the Professional Fighters Brain Health Study

J Lee¹, S Jones², P Ruggieri³, M Massand¹, M Modic¹, S Banks⁴, C Bernick⁴, J Wu¹

¹Cleveland Clinic, Cleveland, OH, ²Cleveland Clinic, Shaker Heights, OH, ³Cleveland Clinic Foundation, Cleveland, OH, ⁴Cleveland Clinic, Las Vegas, NV

Purpose

Multiple sports such as boxing, mixed martial arts, football, and soccer involve cumulative head trauma over many years, some of whom have developed neurodegenerative disease. Multiple studies have attempted to describe magnetic resonance imaging (MRI) findings associated with repetitive head trauma but these studies usually involve a small number of patients and use advanced imaging techniques such as diffusion tensor imaging (DTI), perfusion, and connectivity. The purpose of this investigation is to study a large number of patients with well defined

multiple mild head trauma and investigate imaging findings seen using conventional MRI techniques.

Materials and Methods

A total of 495 patients who were martial artists, mixed martial artists, or boxers were compared to a cohort of 25 control patients using conventional MR at 3T.

Conventional T1, T2, FLAIR, and susceptibility-weighted imaging (SWI) were obtained and evaluated for microhemorrhages, cavum septum pellucidum (CSP), and white matter changes. All studies were reviewed by four neuroradiologists with an average 20 years of experience and a neuroradiology fellow. All statistics were obtained by SPSS using Fisher exact test and Student's t-test.

Results

The average age of the fighters and controls was 30 and 29, respectively. White matter changes were present in 116 (23%) fighters and five (20%) controls. Cerebral microhemorrhages were present in 34 (6.9%) fighters and 0 controls ($p=0.176$ by Fisher exact test, $p=0.000$ by T-test). Cavum septum pellucidum was present in 95 (19%) fighters and one (4%) control ($P=0.037$). Fighters with microhemorrhages had a higher average of total fights than those without microhemorrhages (79 versus 47, $p=0.029$). Similarly fighters with CSP had a higher average of total fights (80 versus 42, $p=0.000$). Fighters with white matter changes trended toward having a higher average of total fights (60 versus 46, $p=0.098$).

Conclusions

This study presents the largest number of subjects who have been exposed to cumulative head trauma, demonstrating a significantly higher prevalence of microhemorrhages and CSP in fighters than controls. However, a limitation of this study includes selection bias from fighters that volunteered to be imaged. Study of traumatic brain injury is reaching a new pinnacle given the advanced imaging techniques now available and larger databases of patients that are being studied. Given the number of fighters and the increasing popularity of combat sports, conventional MR remains an important tool to continue to monitor and try to prevent sequelae of repetitive head trauma. This study shows that microhemorrhages and CSP are more prevalent with more fights. Whether these MR findings result in future neurodegenerative disease or observable neuropsychiatric adverse outcomes is still up for debate.

O-184

8:50AM - 8:53AM

Splenic Axonal Diffusion in Patients with Mild Traumatic Brain Injury.

G Parikh¹, S Chung¹, E Fieremans², J Smith³, S Flanagan⁴, Y Lui¹

¹NYU Medical Center, New York, NY, ²New York University School of Medicine, New York, NY, ³New York University, New York, NY, ⁴New York University, New York, NY

Purpose

Mild traumatic brain injury (mTBI) is an under-reported public health problem for which there is the need for more informative diagnostic imaging. The corpus callosum is vulnerable to diffuse axonal injury in the setting of shear-strain and tensile forces with the splenium of the corpus callosum frequently being affected because of its close proximity to the falx (1,2). The known microstructural changes in TBI seen in histopathology are not appreciated on conventional imaging; however, diffusion imaging is sensitive to these changes. Many groups have observed alterations with diffusion tensor imaging (DTI), namely in the fractional anisotropy (FA) and mean diffusivity (MD) in the white matter (WM) after injury (3). Recently, diffusion kurtosis imaging (DKI) combined with biophysical modeling allow us to specifically study intra-axonal diffusion (Daxon), a potential marker of axonal injury (4). We also have visually observed a focal, rounded area of relatively high Daxon centered in the splenium of the corpus callosum (sCC) on axial parametric maps, we termed the "splenial dot", in control subjects. We hypothesize here that Daxon may be a more sensitive marker of WM injury than the empiric measure FA. Therefore, we set out to compare mTBI patients with normal controls using both visual inspection and quantitative analysis of FA and Daxon parametric maps in the sCC.

Materials and Methods

Approval for conducting the study was obtained from the institutional review board and informed consent was obtained from all subjects. Eighteen patients (36 ± 11 years; 8 male) with well-characterized, recent (< 2 weeks) mTBI as defined by American College of Rehabilitation Medicine and 16 healthy controls (32 ± 8 years; 9 male) underwent DKI on a 3T MR scanner (Skyra, Siemens). The region of sCC was extracted by using the JHU WM label atlas (5) after nonlinear registration using the FA template and was corrected manually for each subject. Student's t-test was performed. Two observers (one neuroradiology attending with > 10 years of subspecialty experience and one neuroradiology fellow) blinded to the clinical information, also visually reviewed Daxon parametric maps in all subjects and assessed for presence or absence of the splenial dot.

Results

Comparing with controls, patients with TBI showed significantly lower FA (0.54 ± 0.05 versus 0.50 ± 0.05 ; $p = 0.021$) and Daxon (1.18 ± 0.05 versus $1.10 \pm 0.07 \text{ mm}^2/\text{s}$; $p = 0.001$) in the sCC. The splenial dot was observed visually in 50% of the TBI group and in 50% of the healthy control group and is not found to be statistically significant.

Conclusions

Mild traumatic brain injury is associated with lower FA and intra-axonal diffusion in the sCC. Differences in Daxon were greater and more statistically significant than differences in FA between MTBI and controls. Although there is a clear quantitative

difference using group analysis, the change was not easily discerned on visual inspection of parametric maps with regard to individual subjects.

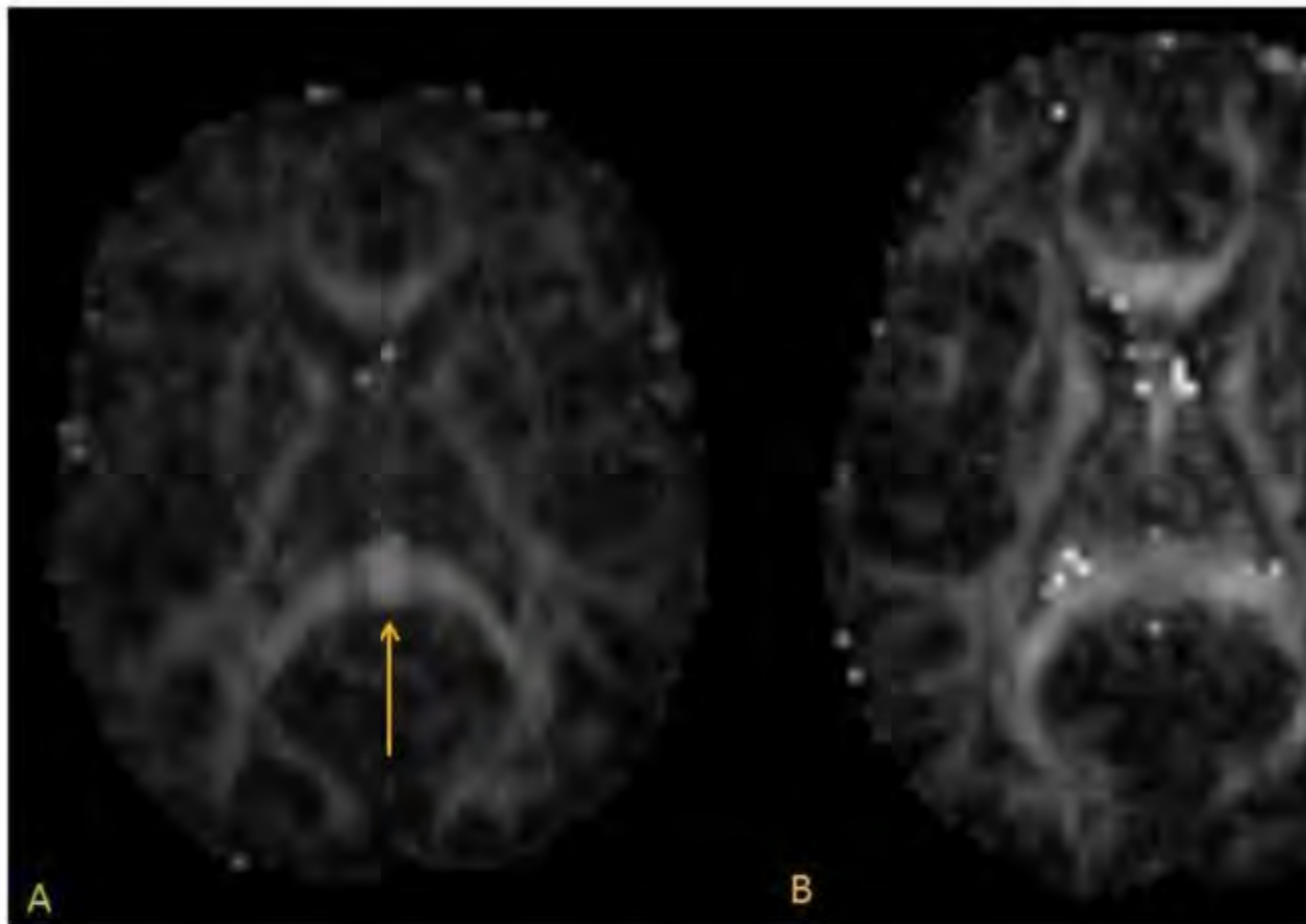


Figure 1: Axial D_{axon} map (A) in a 33-year-old female control shows a focal rounded relative hyperintensity within the splenium of the corpus callosum (arrow). D_{axon} similar level in a 28-year-old male with recent mild traumatic brain injury shows the "splenial dot". Although we found a clear quantitative difference in splenial D_{axon} maps, the splenial dot was not reproducibly discerned on visual inspection using maps.

(Filename: TCT_O-184_Spleniumdotimage_JPEG.jpg)

O-185

8:53AM - 8:56AM

Altered Default Mode Network Connectivity and Task-related Deactivation in Patients with Mild Traumatic Brain Injury

D Chen¹, C Chen¹

¹Taipei Medical University - Shuang Ho Hospital, New Taipei City, Taiwan

Purpose

Mild traumatic brain injury (mTBI) is a substantial public health problem. Difficulty in working memory (WM) and attention frequently is reported in patients with TBI (1). The default mode network (DMN) is active at rest and suppressed during tasks that require attention and decision making. Several functional magnetic resonance imaging (fMRI) studies revealed disruption of resting state DMN connectivity and alterations of brain activation during WM task in mTBI patients, but very few studies addressed on the task-related deactivation in mTBI (2). In this study, we investigated the mTBI effect on the DMN, by means of both resting state functional connectivity and task-related deactivation.

Materials and Methods

This study was approved by the local research ethics committee. Thirty-six patients (male/female: 11/25; age: 33.6 ± 8.6 ; 22-49 years) with mTBI and 24 normal controls (NCs) (male/female: 7/17; age: 34.5 ± 8.9 ; 21-49 years) were recruited. All participants underwent resting state fMRI and task fMRI (1-back verbal working memory task) sequentially in a 3T MRI scanner within 1 month after injury. Resting state DMN connectivity was estimated by a seed-based correlation method (4) with the seed centered at posterior cingulate cortex (PCC) (3). The brain activity (represented by beta values) during the 1-back WM condition was obtained by using the general linear model approach in SPM8. The areas showing negative beta values were considered as deactivation regions. Region of interest (ROI) analysis was carried at the core regions of the DMN, including PCC, inferior parietal lobule (IPL) and medial prefrontal cortex (mPFC). We used one sample t test for the first level group analysis, two sample t test for the second level group comparison and Pearson's correlation coefficient for correlation analysis in the study.

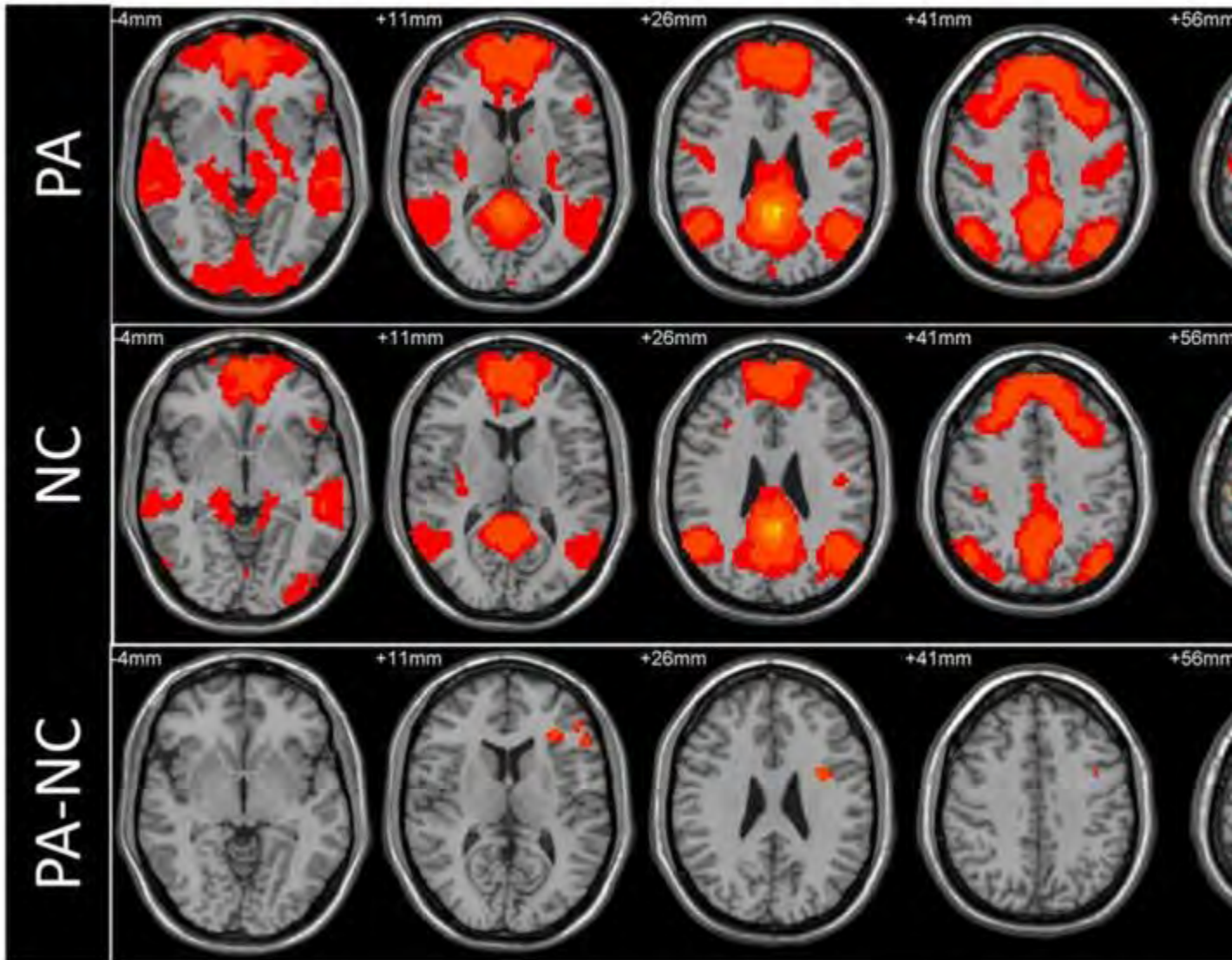
Results

The resting state DMN connectivity in mTBI patients and NCs were presented in Figure 1. Voxel wise group comparison indicates that the patients had increased connectivity to the left inferior frontal gyrus compared to the NCs. However, ROI analysis of the connectivity within the PCC, MPFC and bilateral IPCs revealed no significant group difference between patients and NCs. Figure 2 shows the brains deactivate predominantly in the DMN regions during 1-back WM condition both in the patients and NCs. The patients had more profound deactivation. Region of interest analysis showed that the patients had more deactivation in right IPL ($p = 0.047$) and left IPL ($p = 0.00012$). Correlation analysis revealed significant correlation ($r = -0.638$, $p = 0.00079$) between the mean connectivity and the mean deactivation within the DMN ROIs in healthy controls, while no correlation in the patients ($r = 0.143$, $p = 0.405$) (Fig. 3).

Conclusions

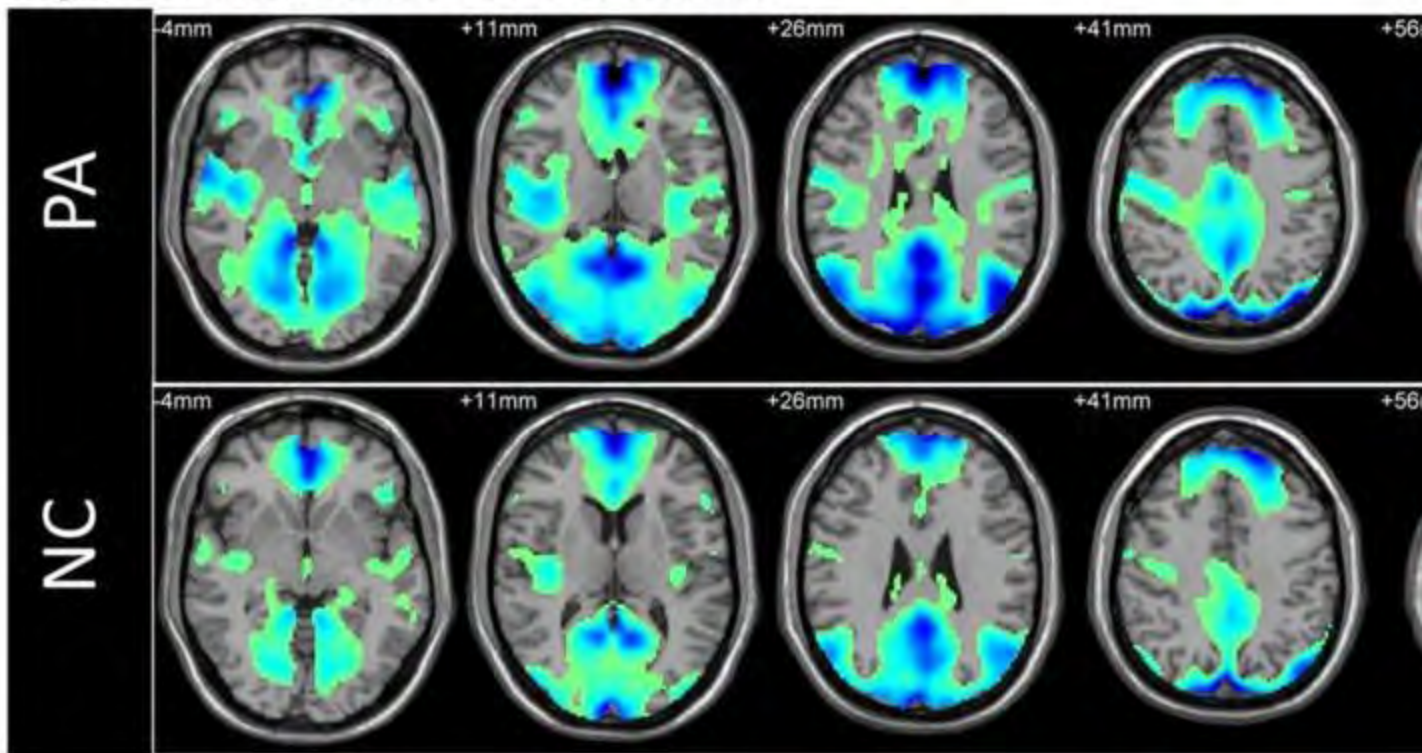
We found alterations in resting state DMN connectivity and task-related deactivation in mTBI patients. Significantly more profound task-related deactivation in the patients may imply more attention needed on performing the WM tasks. Furthermore, significant correlation between resting state connectivity and task-related deactivation of DMN was found in NCs but this rest-task correlation was disrupted in the patients.

Figure 1. Resting-state DMN Connectivity



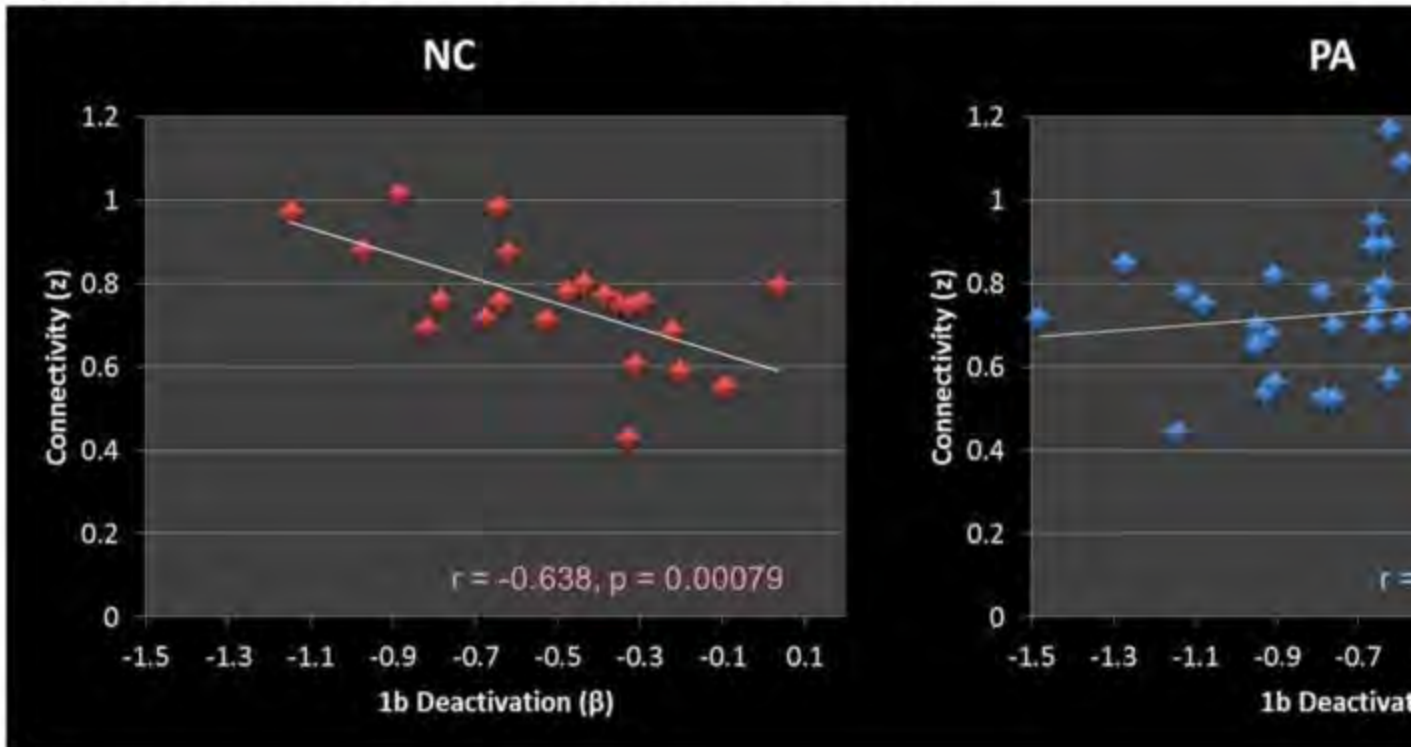
(Filename: TCT_O-185_Figure1.jpg)

Figure 2. Task-related Deactivation.



(Filename: TCT_O-185_Figure2.jpg)

Figure 3. Rest–Task Interaction within DMN.



(Filename: TCT_O-185_Figure3.jpg)

O-186

8:56AM - 8:59AM

Evaluation of Cerebrovascular Injuries in Blunt Trauma Patients at a Level 1 Trauma Center; the Usefulness of CT Screening

M Dahse¹, C Sitton¹, R Patel¹, B Behzad¹

¹The University of Texas Health Science Center at Houston UTHealth, Houston, TX

Purpose

Injury of the cerebrovasculature can occur in blunt trauma patients and can result in devastating consequences. The incidence of injury in blunt trauma patients has been reported to range from 0.9- 2.7% in the literature (1). It has been reported that the risk of stroke from untreated carotid dissections with flow limiting stenosis range from 32-67% and mortality rate from 17-38% (2). Early recognition and early intervention is necessary to avoid neurologic morbidity (3). In order to avoid these devastating outcomes, our institution has instituted an aggressive screening protocol for trauma patients with computed tomography (CT) angiography to evaluate for vascular injury. Our indication for screening is much broader than the traditional Denver criteria (4). The purpose of this study is to evaluate the incidence of cerebrovascular injuries in

blunt trauma patients at a level one trauma center. We also want to investigate the grades of vascular injury to determine if there is a significant difference in the detection rate compared to the reported literature.

Materials and Methods

Utilizing software to search the electronic medical record, we were able to isolate blunt trauma patients who underwent CT of the cervical spine and CT angiography of the head and neck. A total of 446 trauma patients from January 2014 to June 2014 were included in the patient population and a retrospective review of the imaging reports was performed. A database was created to document the findings on cervical spine CT and head and neck CT angiography. Radiology reports utilizing the vascular injury grading scale (5) for each vascular injury were analyzed and the pertinent findings were documented. The location of the vascular injury and any spine fracture or soft tissue injury also was documented. Analysis of the database to determine the incidence of vascular injury and the breakdown of the grades of injury was performed.

Results

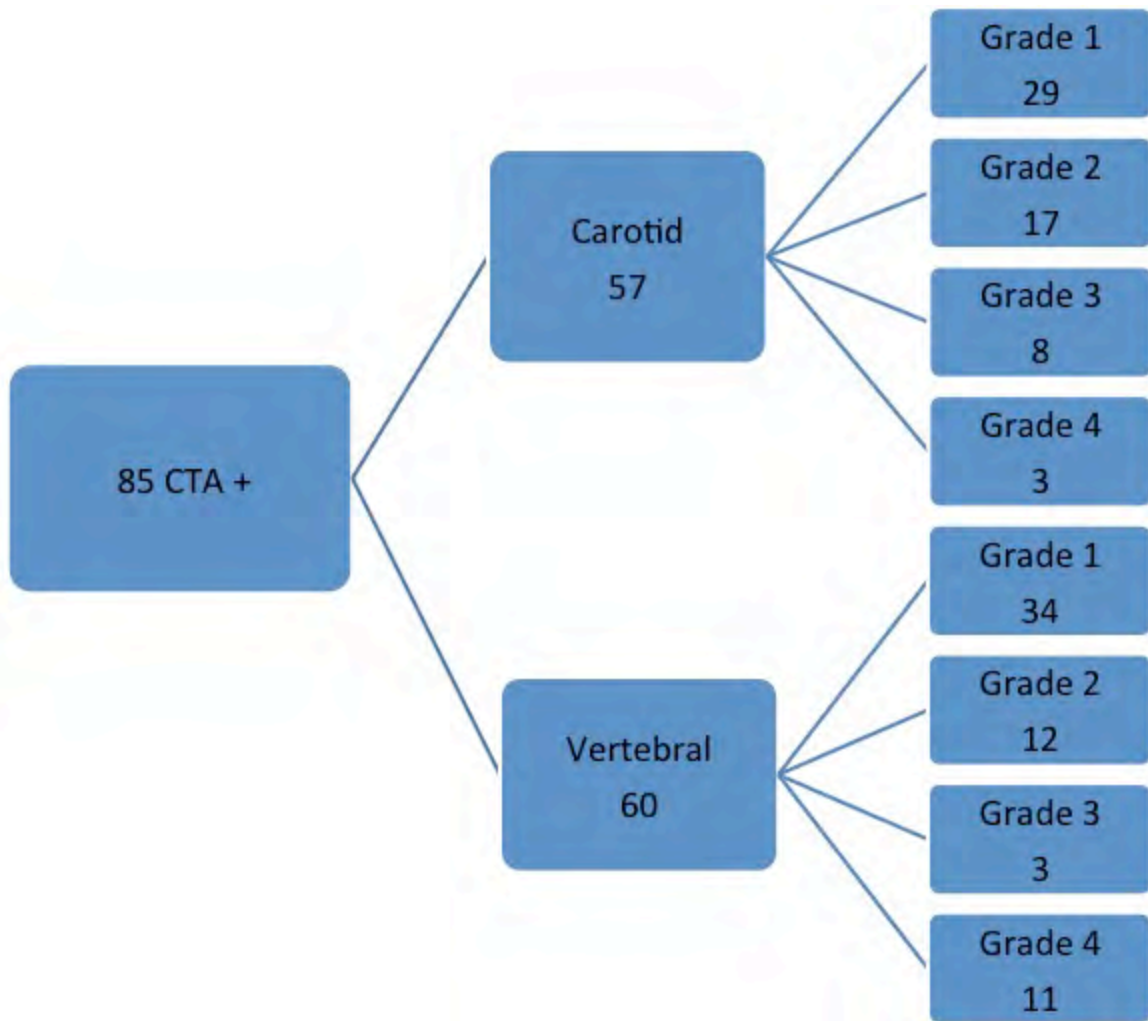
Four hundred forty-six total patients were evaluated and 83 CT angiograms were positive for vascular injury, for a total of 117 injuries. The incidence in our population for a vascular injury was 18.6%. Of the injuries reported, 53.8% were Grade 1, 24.8% were Grade 2, 9.4% were Grade 3, and 11.9% were Grade 4.

Conclusions

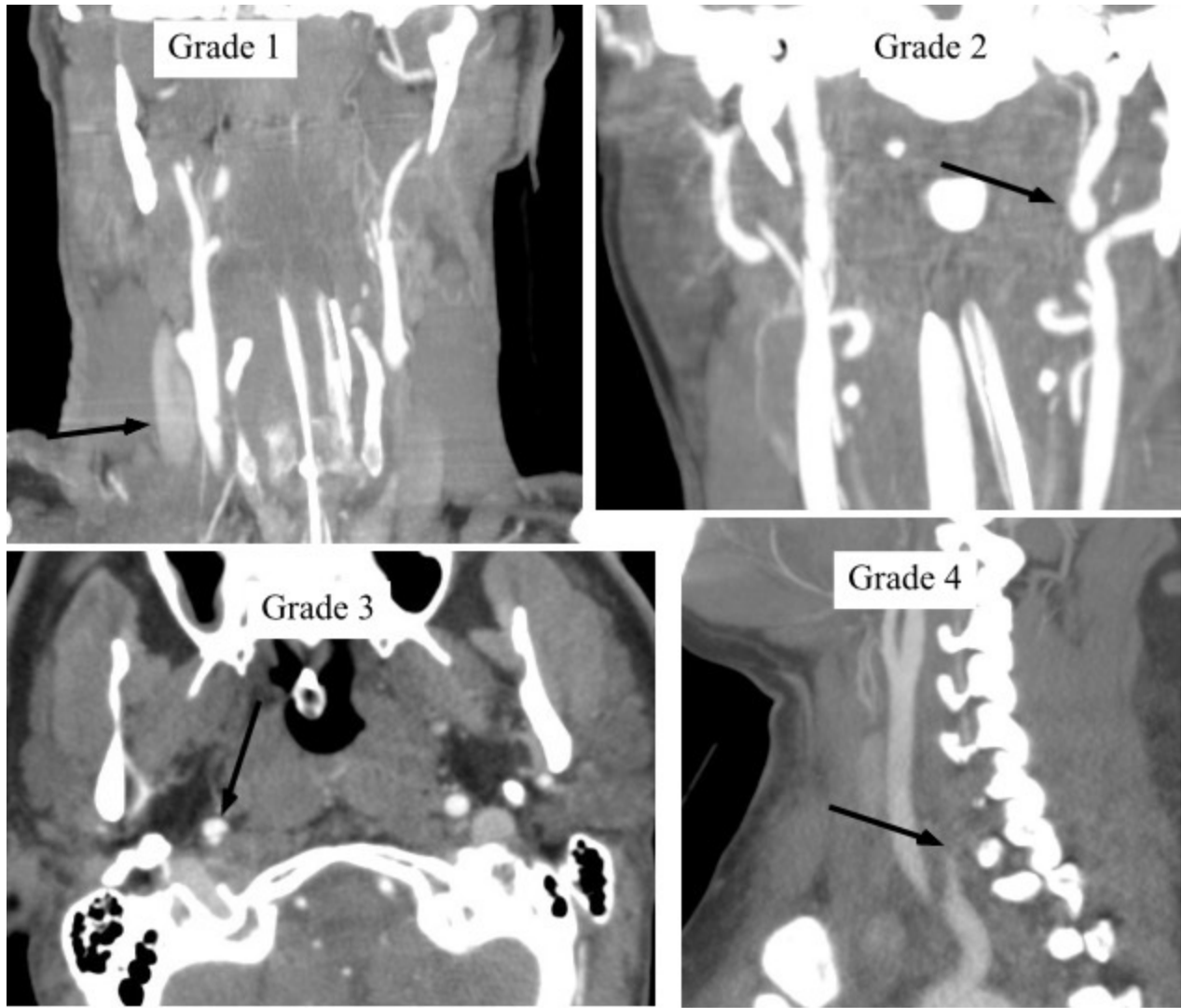
Evaluation of the neck vasculature using CT angiography is extremely important in blunt trauma patients to prevent devastating outcomes of untreated injuries. We found a detection rate for vascular injuries of 18.6%, much higher than previously reported rates of 0.9% to 2.7%. We suspect this increased rate may have been secondary to a high number of grade one injuries, but when grade one injuries were excluded, the rate was still 12.1%. Another explanation for the increased incidence may be a bias toward more severely injured patients at our large level one trauma center with a helicopter ambulance. Further evaluation of the database will be performed for future projects such as evaluation of the progression of injury on subsequent CT angiograms.

| Grade 1 | Grade 2 | Grade 3 | Grade 4 | total | percentage |
|--------------------|-------------------|-------------------|-------------------|--------------------|------------|
| 19 right vertebral | 7 right vertebral | 1 right vertebral | 6 right vertebral | 33 right vertebral | 28.20% |
| 15 left vertebral | 5 left vertebral | 2 left vertebral | 5 left vertebral | 27 left vertebral | 23.10% |
| 13 left carotid | 10 left carotid | 4 left carotid | 3 left carotid | 30 left carotid | 25.60% |
| 16 right carotid | 7 right carotid | 4 right carotid | 0 right carotid | 27 right carotid | 23.10% |
| 63 | 29 | 11 | 14 | 117 | 100% |

(Filename: TCT_O-186_Table1.jpg)



(Filename: TCT_O-186_Graphic1.jpg)



(Filename: TCT_O-186_grading.jpg)

O-187

8:59AM - 9:02AM

Imaging Atlas of Type I and Type II Focal Cortical Dysplasia

E Morimoto¹, H Yokota¹, A Yogi¹, H Ullman¹, Y Hirata¹, I Orosz², M Linetsky¹, B Ellingson³, N Salamon²

¹David Geffen School of Medicine at UCLA, Los Angeles, CA, ²UCLA, Los Angeles, CA, David Geffen School of Medicine at UCLA, Los Angeles, CA, Los Angeles, CA, ³University of California Los Angeles, Los Angeles, CA

Purpose

Focal cortical dysplasia (FCD) is one of the most common causes of intractable epilepsy. Many examples of type I FCD and some of type II FCD are subtle and

difficult to detect with magnetic resonance imaging (MRI). Precise identification of the site of FCD is important in obtaining improved surgical outcomes and seizure freedom. The purpose of this study was to create an atlas of different types of FCD to better understand its topographic distribution and to facilitate more accurate diagnosis.

Materials and Methods

Twenty-six cases of pathologically proven FCD (Type I and Type II) were included. Cases with multilobar FCD were excluded. Regions of interest were generated manually for all 26 cases on T2-weighted images with reference to hypometabolic areas on FDC-PET using Analysis of Functional NeuroImages (AFNI). All regions of interest (ROIs) were spatially normalized and registered to Montreal Neurological Institute (MNI) brain atlas. Existence frequency of FCDs in each lobe was calculated and corrected by the known percentage of the gray matter volume in the lobe relative to that of the whole brain.

Results

The distribution atlas demonstrates that the frontal lobes are the most frequent location of FCD (all types); however existence frequency per volume for FCD type I is highest in the temporal lobes (Fig. 1). In FCD type II, the corrected frequency in temporal lobes (30.5%) was similar to frontal lobes (33.3%) and occipital lobes (23.7%, Fig. 1). Within the temporal lobes, four of the six FCD type I cases and one of the 3 FCD type II cases were in the mesial portions of the temporal lobes (Fig. 2).

Conclusions

Existence frequency per volume for subtle type I FCD is highest in the temporal lobe while Type II FCD is distributed relatively equally. The use of a FCD radiographic atlas may aid in the localization and diagnosis of FCD.

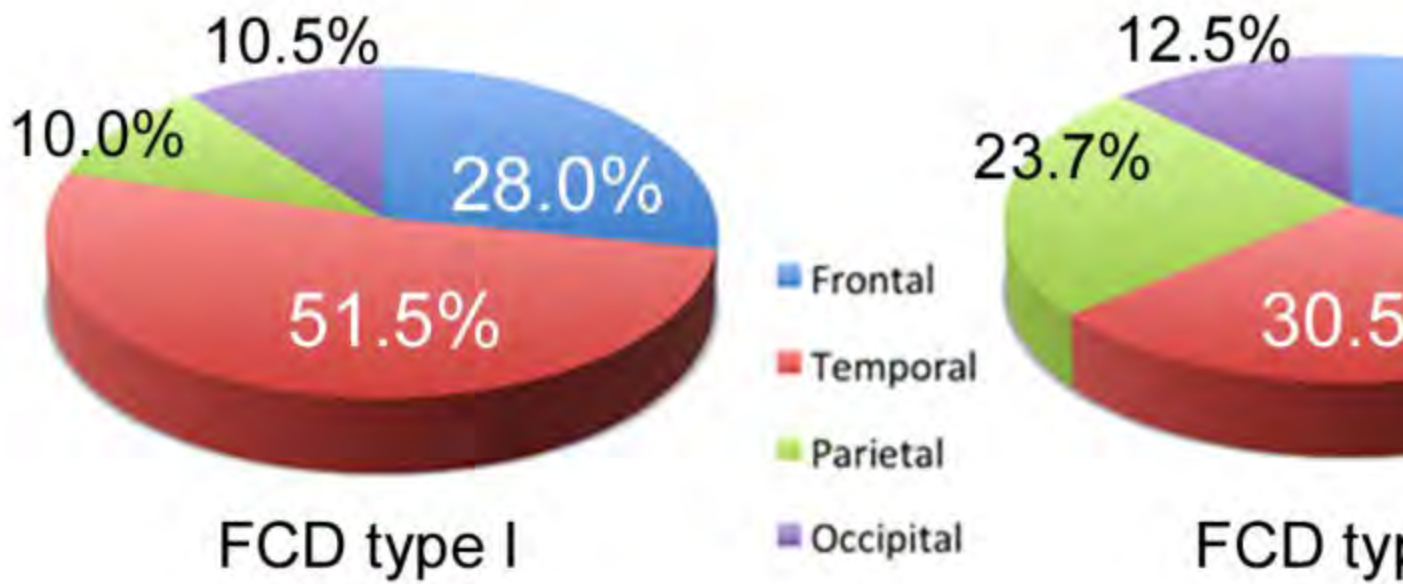


Figure 1. Corrected frequency of FCDs in each lobe

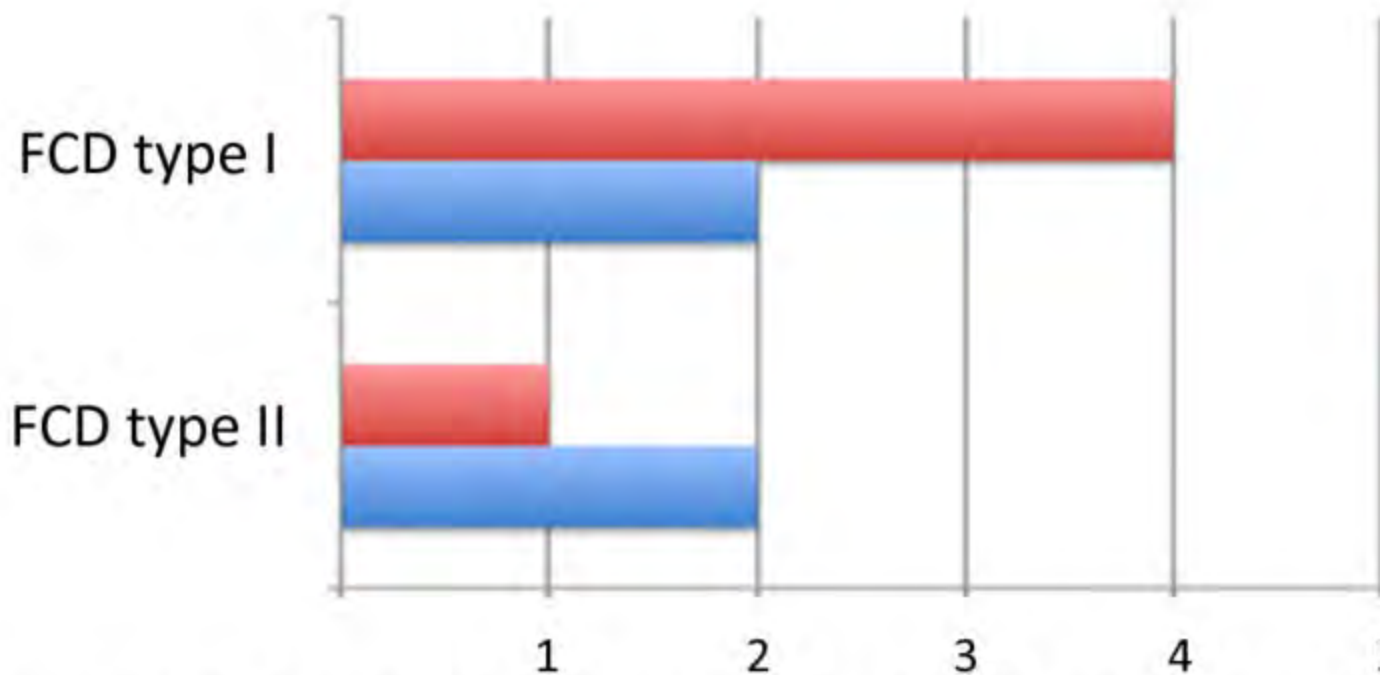


Figure 2. Location difference of FCDs in the temporal lobe

O-188

9:02AM - 9:05AM

Discrepancy between MRI and FDG-PET on focal cortical dysplasia

H Yokota¹, E Morimoto¹, I Orosz², Y Hirata¹, A Yogi¹, H Ullman¹, N Salamon³
¹David Geffen School of Medicine at UCLA, Los Angeles, CA, ²UCLA, Los Angeles, CA, David Geffen School of Medicine at UCLA, Los Angeles, CA, Los Angeles, CA, ³David Geffen School Of Med. at UCLA, Los Angeles, CA

Purpose

Magnetic resonance imaging (MRI) and FDG-PET are essential tools to detect focal cortical dysplasia (FCD). However, discrepancy between MRI and FDG-PET often are observed and confuses diagnosis. We revealed characteristics of the discrepancy by visual assessment.

Materials and Methods

We evaluated pathologically proven 41 type I and type II FCD of 40 patients (2-55 years; mean age, 18.0 years; woman 23, man 17), from the UCLA epilepsy program focal cortical dysplasia cohort between 2004-2014. Focal cortical dysplasia extending multiple lobes were excluded. All patient had nonictal PET scan. Using MRI-PET coregistration, the area of abnormality on MRI and zone of PET hypometabolism were delineated manually. The cases were divided into three groups. Group A: PET hypometabolism is larger than the MRI lesion. Group B: PET hypometabolism zone is same as MRI abnormality. Group C: PET hypometabolism zone is smaller or less evident in the area of MRI abnormality.

Results

Fifteen cases showed larger hypometabolism, 23 cases showed equivalent PET and MRI abnormality and two cases showed no obvious PET hypometabolism. Most of Group A cases was in temporal lobe. Although FCD type I and II were classified significantly as group A and B, respectively ($p=0.04$), FCD type I was major in temporal lobe (12 of 14). All 14 FCDs of temporal lobe were located in anterior part (pole 11, superior temporal gyrus 1, middle temporal gyrus 1, inferior temporal gyrus 1). On temporal lobe, hypometabolic area on PET was extended mainly along medio-basal part, lateral part or both parts (7, 1 or 6, respectively). Some of the frontal lobe FCD shows no obvious hypometabolism.

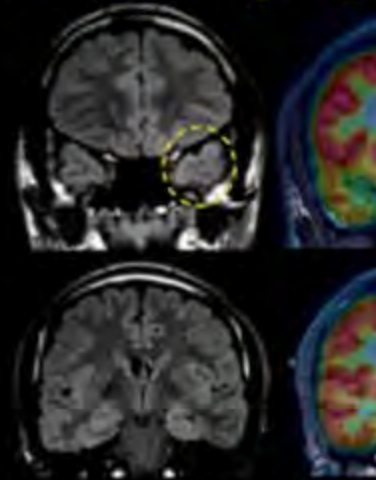
Conclusions

PET hypometabolism is larger than MRI abnormality in temporal lobe. Frontal lobe FCD does not always demonstrate hypometabolism. This may reflect of seizure propagation network. FDG PET will be a helpful modality to identify temporal lobe FCD when the MRI is not obvious.

Summary of location and types of FCD on each group

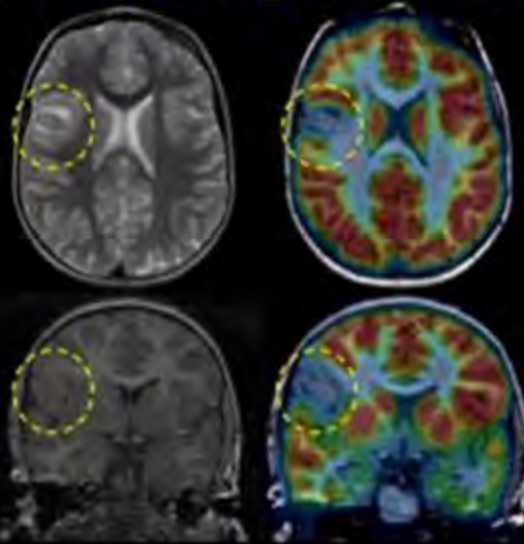
| | Group A | Group B | Group C |
|------------------|---------|---------|---------|
| Frontal | | | |
| FCD I | | 5 | 1 |
| FCD II | | 9 | 1 |
| Temporal | | | |
| FCD I | 12 | 4 | |
| FCD II | 2 | 1 | |
| Parietal | | | |
| FCD I | | 1 | |
| FCD II | 1 | 3 | |
| Occipital | | | |
| FCD I | | 1 | |
| FCD II | | | |

FCD I on the right temporal lobe



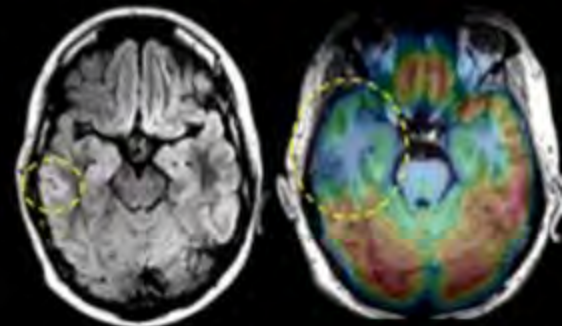
Group A. Hypometabolic area of temporal lobe on PET. Hyperintense area on MRI. Hypometabolic area on PET and hyperintense area on MRI along medio-basal temporal lobe.

FCD IIb on the right frontal lobe



Group B. Hypometabolic area on PET is localized in abnormal area on MRI findings.

FCD IIa on the right frontal lobe



Group A. There is focal cortical thickening on right frontal lobe. Hypometabolic area is localized in abnormal area on MRI findings.

(Filename: TCT_O-188_figures.jpg)

O-189

9:05AM - 9:08AM

Hybrid PET/MR shows reduced CBF and glucose uptake in Subdural Electrode Identified Seizure Foci

X Zong¹, H Shin¹, S Park¹, X Cao², S Todorova¹, V Jewells¹, S Hung³, W Lin¹, D Shen⁴

¹University of North Carolina at Chapel Hill, Chapel Hill, NC, ²Northwestern Polytechnical University, Chapel Hill, NC, ³Taipei Veterans General Hospital, Taipei, Taipei, ⁴UNC School of Medicine, Chapel Hill, NC

Purpose

Recent availability of hybrid positron emission tomography/magnetic resonance (PET/MR) scanners have offered new opportunities to assess structural, functional, and metabolic abnormalities in patients with neurological diseases. To this end, we evaluated how hybrid PET/MR may aid routine clinical workup for identifying epileptic foci by simultaneously assessing MR cerebral blood flow (CBF) and PET glucose metabolism in epilepsy patients. Specifically, we directly evaluated cerebral blood flow (CBF) and glucose uptake in brain regions that were clinically proven epileptic foci using intra-operatively placed subdural electrodes (SDE).

Materials and Methods

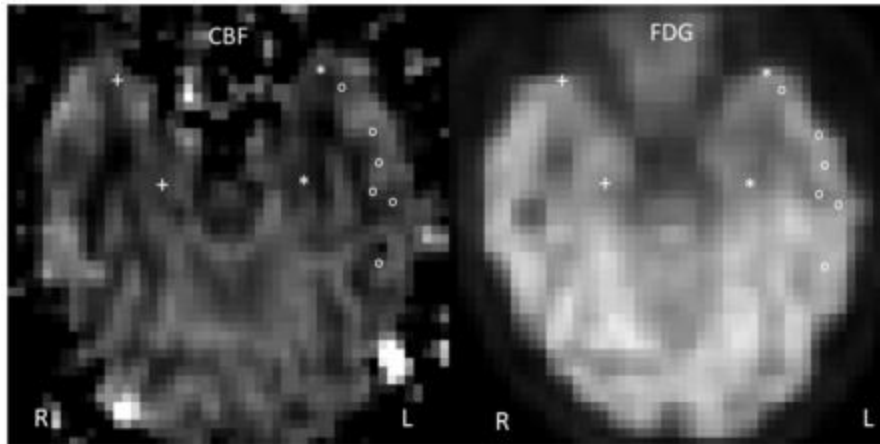
Seven patients underwent pre-operative clinical PET/MRI using the Siemens mMR Biograph. Positron emission tomography images were acquired 30-45 min after intravenous infusion of ~5mCi FDG. Cerebral blood flow images were acquired using a pseudo-continuous arterial spin labelling sequence. After subdural electrode (SDE) placement, CT scans were performed to determine the anatomical locations of the electrodes. The CT images then were registered onto pre-op PET/MR images using a framework developed by our group capable of accurately registering the implanted electrodes onto pre-op PET/MR images. The seizure foci then were determined using the SDE. Regions with reduced FDG uptake were identified on PET images. Cerebral blood flows and body-weight-normalized standardized uptake value (SUVbw) of FDG were calculated in regions of interest (ROIs) (~125 mm³) around the electrodes indicating seizure foci. Cerebral blood flows and SUVbws at the homologous regions in the contralateral hemisphere also were obtained for comparison.

Results

Two patients were excluded due to inconsistent voxel size and failure to obtain consent for data analysis. Representative CBF and FDG-PET maps from a patient with left medial temporal lobe epilepsy are shown. With the exception of one patient, all patients showed decreased CBF and FDG uptake on the lesion foci identified by EEG (see asterisks) when compared to the homologous regions (see '+' signs) in the contralateral hemisphere. In contrast, one patient (RAT0207) who had both temporal and parietal-occipital lobe foci showed increased CBF and glucose uptake. Finally, all patients exhibiting decreased CBF and glucose uptake at the epileptic foci achieved good surgical outcomes (see the Table).

Conclusions

Our results suggest that hybrid PET/MR may provide clinically relevant information on localizing epileptic foci.



| Patient # | SDE lobar seizure foci | PET decrease d uptake | CBF ² (ipsi) | CBF ² (contra) | SU |
|-----------|---|-----------------------|-------------------------|---------------------------|----|
| RAT 0103 | Lateral & Inferior R temporal | R Temporal | 51.5 | 55.4 | |
| LMT 0235 | L medial temporal/Hippocampus | L Temporal | 55.5 | 72.6 | |
| RAT 0207 | inf and Lat R Temporal & R Parietal Occipital | R Temporal | 65.7 | 58.6 | |
| LAT 0213 | L superior temporal gyrus | L Temporal | 55.8 | 70.2 | |
| LMT 0234 | L medial temporal | L temporal | 32.1 | 59.1 | |

¹No surgery because the lesion foci involved language area

(Filename: TCT_O-189_Fig1.jpg)

O-190

9:08AM - 9:11AM

Coupling of FDG uptake and CBF using simultaneous MR-PET measurements in human temporal lobe epilepsy

X Zong¹, H Shin¹, S Park¹, X Cao², S Todorova¹, V Jewells¹, S Hung³, W Lin¹, D Shen⁴

¹University of North Carolina at Chapel Hill, Chapel Hill, NC, ²Northwestern Polytechnical University, Chapel Hill, NC, ³Taipei Veterans General Hospital, Taipei, Taipei, ⁴UNC School of Medicine, Chapel Hill, NC

Purpose

Whether or not there is an uncoupling between cerebral blood flow (CBF) and glucose metabolism (CMRglu) at the epileptic foci remains controversial in the literature (1, 2). One highly plausible explanation for the inconsistent results in the literature may be time-dependent changes of CBF and CMRglu at the epileptic foci since these two measurements typically were acquired at two separate sessions. To this end, simultaneous PET and MR images were acquired using a hybrid PET/MR scanner allowing simultaneous assessments of CBF and glucose metabolism in temporal lobe (TL) epilepsy patients.

Materials and Methods

Ten patients with clinically confirmed unilateral TL epilepsy were included in the study. Interictal FDG-PET and MRI images were acquired on a Siemens mMR Biograph. After intravenous infusion of ~5 mCi of FDG, patients were kept in a quiet room for 30-45 min prior to PET/MR imaging. Cerebral blood flow images were acquired using a pseudo-continuous arterial spin labelling sequence. High resolution T1-weighted images were acquired for segmenting the temporal lobes bilaterally.

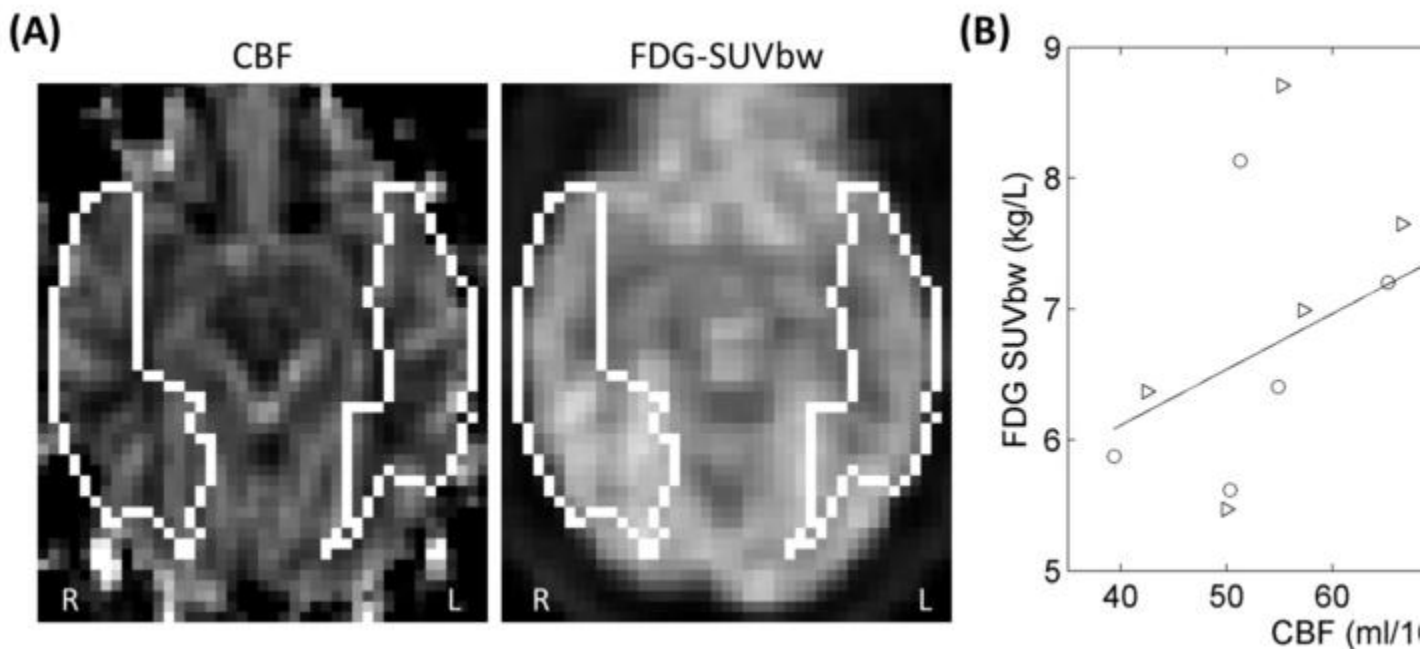
Cerebral blood flow and body-weight-normalized standardized uptake value (SUVbw) of FDG were obtained for the ipsi-lesional and contra-lesional TLs.

Results

Figure (A) shows representative CBF and SUVbw maps overlaid with the TL masks in a left TL epilepsy patient. The left TL shows reduced CBF and SUVbw. The group-averaged CBF and SUVbw both were decreased significantly on the ipsi-lesional TL when compared to the contra-lesional TL ($p = 0.028$ (CBF) and 0.057 (SUVbw); paired t-test). In addition, a strong correlation was observed between the SUVbw and CBF across the patients ($R = 0.53$; $p = 0.016$), as shown in Figure (B). No apparent difference was observed for the CBF versus SUVbw relationship between the ipsi- and contra-lesional hemispheres, suggesting a coupling between CBF and glucose metabolism in both TLs.

Conclusions

Our results demonstrate that although significant CBF and marginally significant SUVbw reductions in the ipsi-lesional TL were observed, the CBF and glucose metabolism remained coupled.



(Filename: TCT_O-190_Fig2.jpg)

O-191

9:11AM - 9:14AM

Amygdala Enlargement in Temporal Lobe Epilepsy

A Capizzano¹, N Mallak¹, P Kirby², M Werz³, T Moritani¹

¹Department of Radiology. University of Iowa Hospitals and Clinics, Iowa City, IA, ²Department of Pathology. University of Iowa Hospitals and Clinics, Iowa City,

Purpose

Amygdala enlargement (AE) on brain magnetic resonance imaging (MRI) ipsilateral to the seizure focus recently has been recognized as a biomarker of a new subtype of mesial temporal lobe epilepsy (mTLE) (1). The purpose of this study is to review clinical, imaging and pathological features in a series of mTLE patients with AE without mesial temporal sclerosis (MTS) and to compare them to a group of mTLE without AE but with pathologically proven MTS.

Materials and Methods

Institutional Review Board approval was obtained for this retrospective study.

Amygdala enlargement patients were selected based on clinical diagnosis of mTLE without MTS and enlarged uncus including the amygdala ipsilateral to the video EEG defined seizure focus. Patients with mass lesions or with MTS were excluded. Eleven patients with AE were entered in the study (4 women, 7 men) with mean age of 35.5 years. An age-matched group of 16 mTLE patients followed up for a minimum of 2 years after anterior temporal lobectomy with pathologically proven MTS without AE with favorable seizure outcome (Engel class I, II or III) was compared to the AE group.

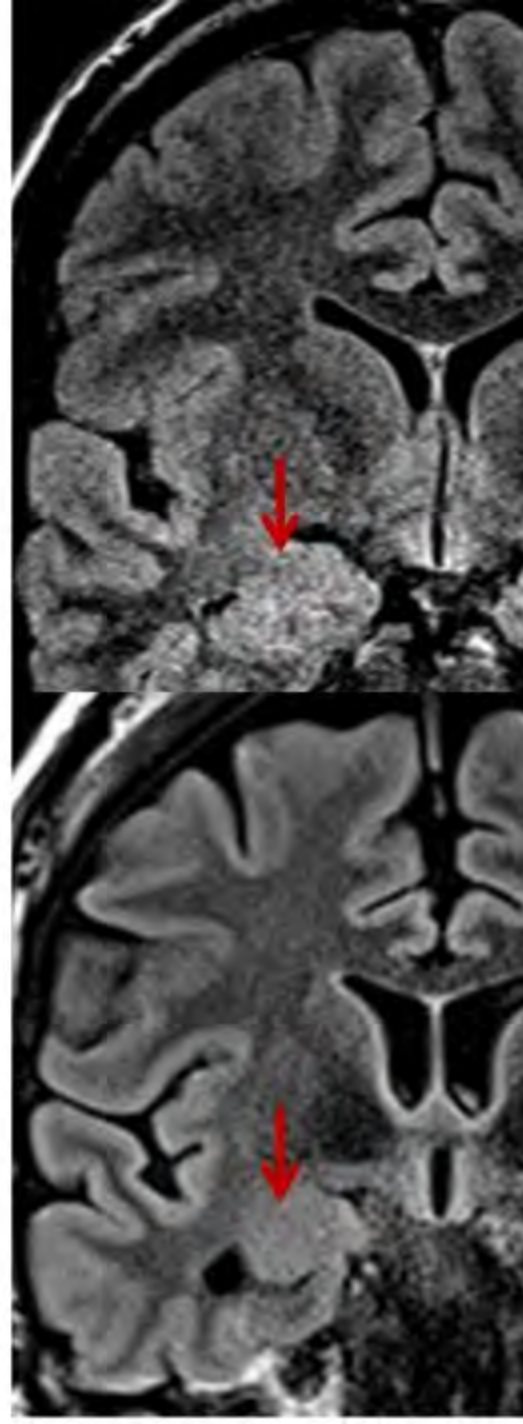
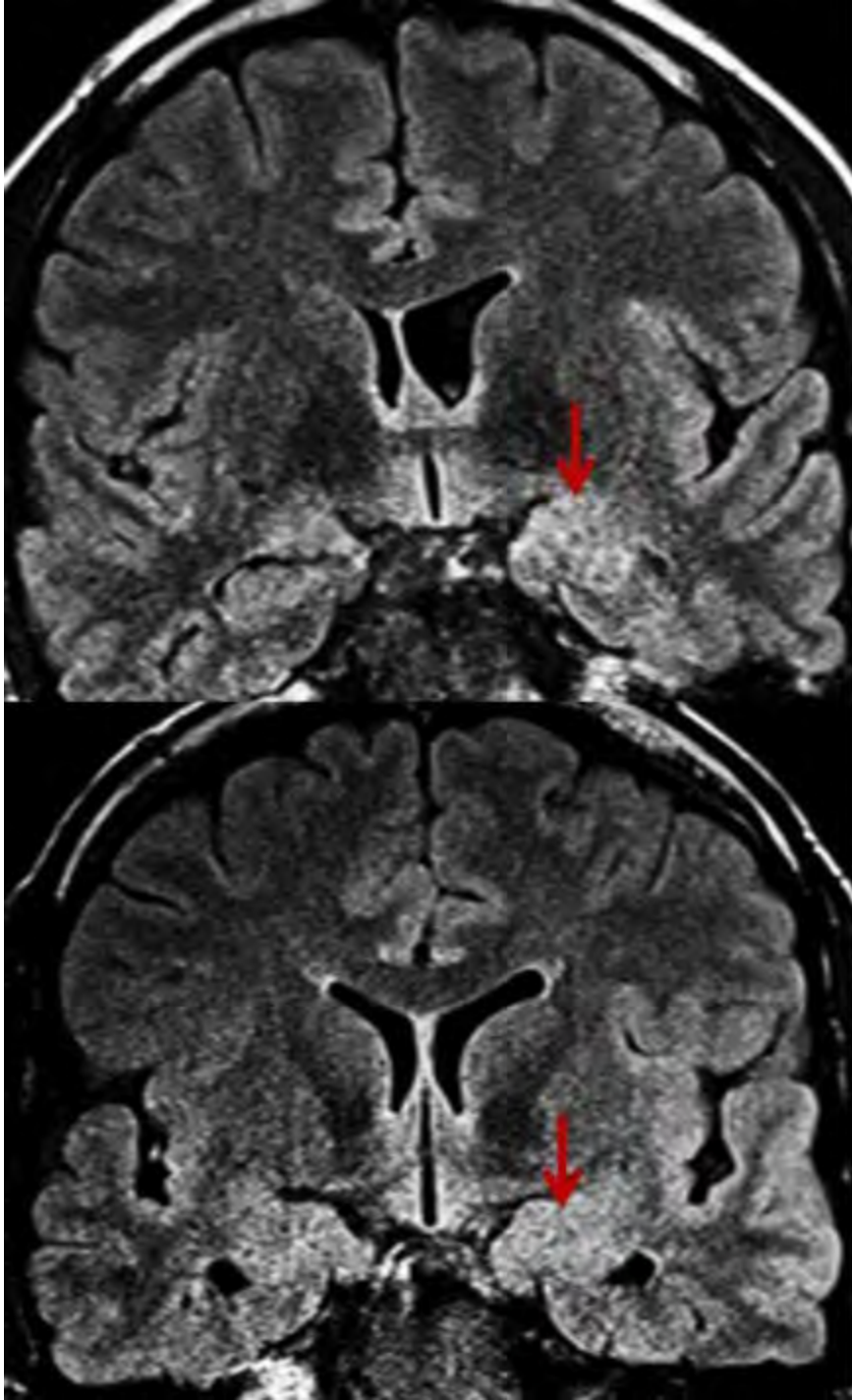
Results

Amygdala enlargement patients were older at seizure onset (27.2 versus 11.3 years, $p < 0.01$) and had less prevalence of childhood febrile seizures ($p < 0.05$) compared to MTS patients. Amygdala enlargement had predominantly complex partial seizures with limbic auras, followed by generalized convulsions. No significant difference in seizure type was noted between groups. Ten AE patients had unilateral AE and one had bilateral AE. For the 10 unilateral AE, ADC of the ipsilateral amygdala was 828.4 mm^2/s versus 803 mm^2/s in the contralateral side ($p < 0.05$). FLAIR signal of the ipsilateral amygdala normalized to the corpus callosum was higher compared to the contralateral one (1.9 versus 1.75, $p < 0.01$). Five AE patients are seizure free on medications, while six had refractory seizures. Four of the latter underwent ipsilateral anterior temporal lobectomy. The figure shows pre-operative coronal FLAIR with arrows pointing to the abnormal side. Pathology disclosed amygdala dysplasia in three and gliosis in one. These 4 AE patients became seizure free with a mean follow up of 21 months.

Conclusions

Amygdala enlargement may represent the only imaging abnormality in a subset of mTLE patients. The most common pathologic underpinning of AE is cortical dysplasia (2). As reported, AE patients have lower prevalence of febrile childhood seizures and later onset of seizures (2). A significant proportion of patients are well controlled on medications and therefore do not become surgical candidates (3, 4). On

imaging, AE has to be distinguished from tumors of the uncus or transient postictal changes. Amygdala enlargement appears as an asymmetric bulging of the uncus imperceptibly merging with the adjacent temporal lobe with homogeneously high FLAIR signal compared to the normal contralateral side. Apparent diffusion coefficient values are slightly higher on the abnormal side suggesting lower cellular density. In conclusion, neuroradiologists should search for features of AE in mTLE patients without MTS, which is particularly important in patients evaluated for surgery for refractory seizures in whom AE can be the only MRI finding.



(Filename: TCT_O-191_Picture2.jpg)

O-192

9:14AM - 9:17AM

Differentiation of Seizure and Other Seizure Mimickers: Clinical Utility of Arterial Spin Labeling Perfusion MRI

R Yoo¹, T Yun¹, C Sohn¹, J Kim¹, S Choi¹, K Kang¹, S Park²
¹Seoul National University Hospital, Seoul, Republic of Korea, ²Seoul National University Boramae Medical Center, Seoul, Republic of Korea

Purpose

Various diseases including acute ischemic stroke may mimic seizure in practice. Our aim was to evaluate the utility of arterial spin labeling perfusion-weighted imaging (ASL-PWI), a noninvasive perfusion imaging technique with no need for contrast administration, in differentiating seizure from other seizure mimickers.

Materials and Methods

One hundred and seventy-one consecutive patients, who underwent MR imaging including diffusion-weighted imaging and ASL-PWI with the suspicion of seizure in the acute setting, were included. Perfusion abnormality was analyzed for: (1) pattern (hypo- or hyperperfusion relative to the gray matter of normal contralateral parenchyma), (2) multifocality (focal, multifocal, or hemispheric), and (3) territory (territorial or non-territorial). Normalized CBF ($nCBF_{lesion} = CBF_{lesion} / CBF_{gray\ matter}$) was calculated. Fisher exact test and unpaired t test were used to compare the perfusion abnormality.

Results

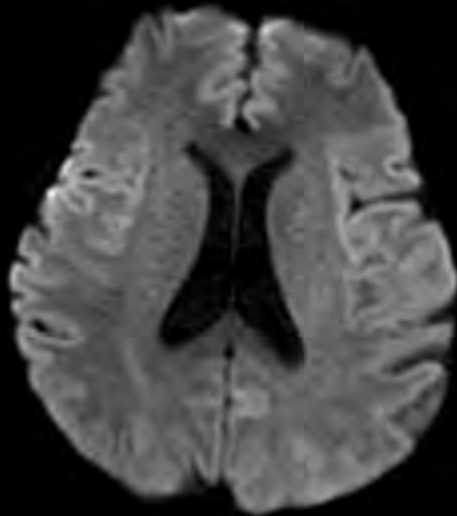
Final diagnoses included seizure (n=133), stroke (n=1), poststroke seizure including stroke onset seizure (n=19), and nonseizure, nonstroke group (n=18).

Hyperperfusion was significantly more common in peri-ictal scans (n=42) than in interictal (n=77) scans (62% versus 26%, respectively; $P < .001$). Incidence of hyperperfusion did not significantly differ between patients who presented with convulsive symptoms and those with nonconvulsive symptoms in both peri-ictal ($P = .501$) and interictal scans ($P = .100$). Hypoperfusion, multifocality, and territorial distribution were significantly more common in stroke onset seizure (n=12) than in seizure ($P < .001$; $P = .024$; $P < .001$). Mean $nCBF_{lesion}$ was significantly higher in seizure than in stroke onset seizure (2.359 ± 0.973 versus 1.318 ± 1.405 , respectively; $P = .006$). In addition, hyperperfusion was significantly more common in seizure than in the nonseizure, nonstroke group (38% versus 0%, respectively; $P < .001$).

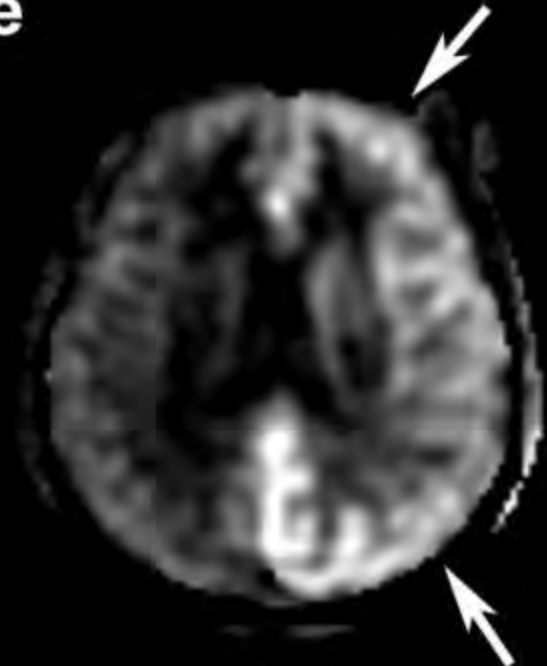
Conclusions

Arterial spin labeling-perfusion-weighted imaging may provide a convenient and noninvasive means of delineating transient perfusion abnormality in seizures and thus assist in discriminating seizures from other seizure mimickers.

Seizure

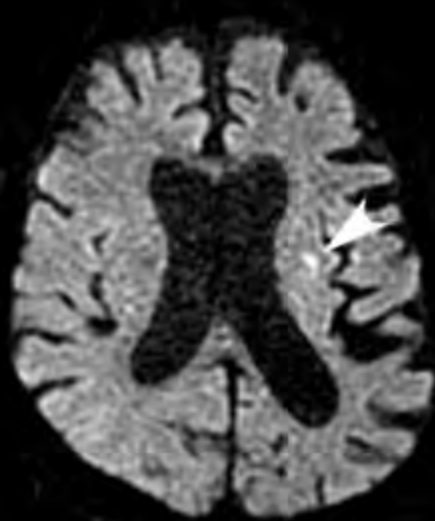


DWI

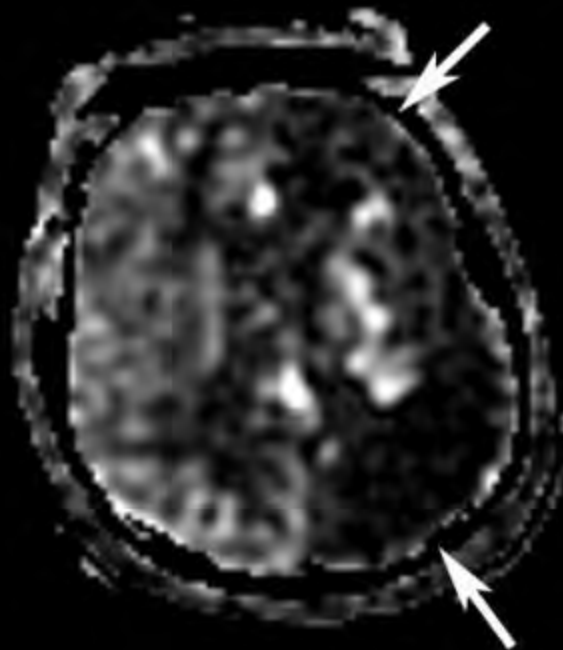


ASL

Stroke onset seizure



DWI



ASL

O-193

9:17AM - 9:20AM

Predicting Laterality of Seizure Onset Zone by Diffusion Tensor Tractography of Intracranial Depth Electrodes in Patients with Temporal Lobe Epilepsy

I Orosz¹, D Woodworth¹, S Weiss², A Yogi³, H Ullman⁴, J Qiao⁵, V Patel¹, I Fried⁶, J Stern², B Ellingson⁷, N Salamon¹

¹Department of Radiological Sciences, Section Neuroradiology, UCLA, Los Angeles, CA, David Geffen School of Medicine at UCLA, Los Angeles, CA, Los Angeles, CA, ²Department of Neurology, UCLA, Los Angeles, CA, David Geffen School of Medicine at UCLA, Los Angeles, CA, Los Angeles, CA, ³Department of Radiological Sciences, Section Neuroradiology, UCLA, Los Angeles, CA, David Geffen School of Medicine at UCLA, Los Angeles, CA, ⁴Department of Radiological Sciences, Section of Neuroradiology, UCLA, Los Angeles, CA, David Geffen School of Medicine at UCLA, Los Angeles, CA, ⁵Department of Radiological Sciences, Section Neuroradiology, UCLA, Los Angeles, CA, David Geffen School of Medicine at UCLA, Los Angeles, CA, Los Angeles, CA, ⁶Department of Neurosurgery, UCLA, Los Angeles, CA, David Geffen School of Medicine at UCLA, Los Angeles, CA, Los Angeles, CA, ⁷Department of Radiological Sciences, UCLA, Los Angeles, CA, David Geffen School of Medicine at UCLA, Los Angeles, CA

Purpose

The success of temporal lobe epilepsy (TLE) surgery relies on accurate lateralization of the seizure onset zone (SOZ). In patients with multiple SOZs, extended electroencephalogram evaluation with intracranial electrodes is needed for further SOZ localization. Previous diffusion tensor imaging (DTI) studies have demonstrated white matter degeneration beyond the presumed epileptogenic zones, which can help to localize the SOZ. The purpose of this study is to determine whether DTI tractography of the intracranial electrodes can complement conventional presurgical evaluations of SOZ localization in TLE. This is the first DTI study performed in conjunction with intracranial electrodes, providing an evaluation of the closest white matter bundles underlying to the epileptogenic zone.

Materials and Methods

Nineteen adult patients (mean age 40.57 years, sd=3.4) with intractable TLE and without hippocampal sclerosis were analyzed retrospectively. All patients underwent stereotactic, MR-guided implantation of four to eight intracranial electrodes in each hemisphere with the majority placed into mesial temporal structures. The SOZ was determined according to the intracranial EEG recording, and patients were divided into unilateral and bilateral TLE subgroups. Tract analysis was performed by

manually drawing seed regions of interest (ROIs) around each intracranial electrode and calculating the mean fractional anisotropy (FA) along the traversing streamlines.

Results

In patients with unilateral TLE (n=10), we demonstrated significantly increased mean FA ($p=0.02$, paired two tailed t-test) in the tracts computed from the intracranial electrodes under the epileptogenic zone compared to the homologues electrodes of the contralateral hemisphere. No significant difference of mean FA was found in the SOZ versus non-SOZ of the contralateral hemisphere in patients with bilateral TLE (n=9).

Conclusions

White matter regions near the SOZ appear to have increased axon directional coherence and density compared with nonepileptogenic regions as evidenced by altered diffusion characteristics. This information pursued by our method may be valuable to localize epileptogenic brain regions in TLE patients.

O-194

9:20AM - 9:23AM

Registering Post-Op CT and Pre-Op MR Images for Accurate Localization of Intraoperative EEG Electrodes

S Park¹, X Cao², S Hung³, X Zong¹, V Jewells¹, W Lin¹, H Shin¹, D Shen¹

¹*University of North Carolina at Chapel Hill, Chapel Hill, NC*, ²*Northwestern Polytechnical University, Shaanxi, China*, ³*Taipei Veterans General Hospital, Taipei, Taipei*

Purpose

Accurate localization of subdural electrodes on multimodality images is necessary for detection of brain subregion connectivity of epilepsy patients to accurately localize seizure onset foci. However, localization is challenging because the brain is significantly displaced due to craniotomy, atmospheric pressure, edema and intracranial hemorrhage. Accordingly, the electrodes shown in post-op computed tomography (CT) images often are localized to incorrect positions with conventional registration methods. To address this problem, we propose a novel two-step registration method.

Materials and Methods

We developed a framework capable of aligning post-op CT images to the pre-op MR images in six epilepsy patients who were imaged using MR pre-operatively and underwent intra-operative placement of electrodes and subsequent CT/MR imaging. The developed framework included several steps. First, post-op CT images were aligned to the pre-op magnetic resonance (MR) images by using a rigid registration method (Flirt registration). Although most structures were aligned correctly, electrodes near the seizure zone could not be registered to the correct positions by

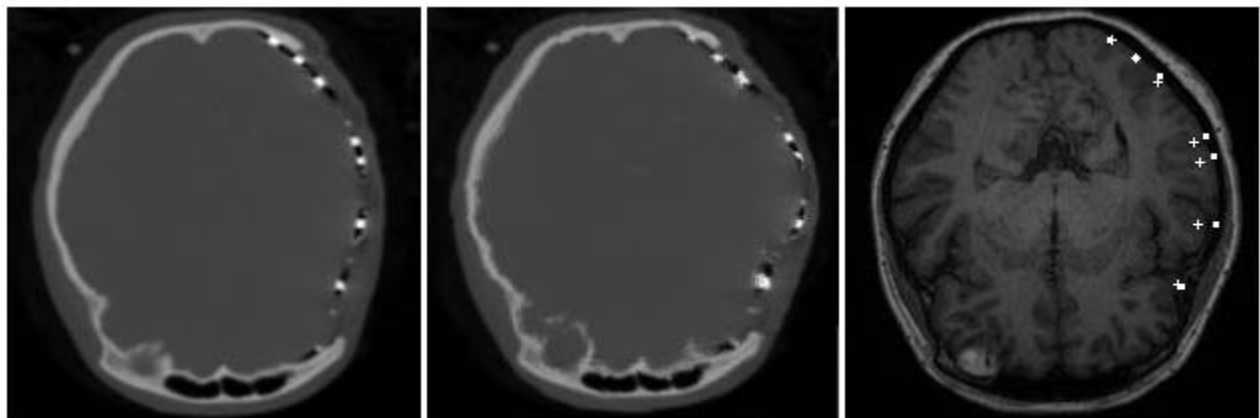
rigid registration due to large local deformations. To mitigate this problem, we performed skull stripping on both the post- and pre-op MR images, and then further aligned them using nonrigid registration (Demon registration) to correct for the registration errors resulted from Flirt. In addition, subdural hematoma regions were removed during the skull stripping, followed by visual inspection and manual editing if needed. Based on the deformation fields, the post-op CT image was aligned to the pre-op MR images allowing extraction of the coordinates of the electrodes to provide a direct link between electrode location and pre-op MR images. Finally, to evaluate accurate localization, we measured the average error distance between the coordinates of electrodes and the closest surface of brain tissue.

Results

The average error distance was obtained as 3.63mm for the Flirt method, while 1.45mm for our method from all six images. The aligned CT images using the Flirt registration and our method are shown in the left and middle of Figure 1, respectively, and the pre-op MR image overlying the electrodes is shown on the right. The crosses and squares indicate the positions of electrodes obtained by the Flirt registration and our method, respectively. It is apparent that our proposed method was much more robust for edema/subdural hematoma compared to the simple rigid registration method.

Conclusions

The newly developed registration method successfully localized the subdural electrodes to the appropriate positions on brain tissue even in very ambiguous regions with edema and subdural hematoma. Continuing refinements focusing on completely automating the procedures are ongoing. This technique can serve as an important basis where all of pre-operative MR results can be combined accurately with information obtained from electrodes.



(Filename: TCT_O-194_abstract_figure_300dpi.jpg)

Tuesday

8:35AM - 10:00AM

Washington Marriott Wardman Park, Maryland A/B/C

8E-Quantitative Imaging
8E-1

8:35AM - 8:52AM

Quantitative Imaging in Context

Herskovits, E.
University Of Maryland
Baltimore, MD

8E-2

8:52AM - 9:09AM

Neuroimaging Analysis

Shen, D.
UNC School of Medicine
Chapel Hill, NC

8E-3

9:09AM - 9:26AM

A Local Level Learning Health System for Head and Neck Radiation Oncology

McNutt, T.
Johns Hopkins University
Columbia, MD

8E-4

9:26AM - 9:43AM

Applications of Imaging Quantification

Bhagavatheeshwaran, G.
NINDS, NIH
Bethesda, MD

8E-5

9:43AM - 10:00AM

Tools For High - Throughput Neuroimage Analysis and Personalized Medicine

Faria, A.
Johns Hopkins University
Baltimore, MD

Tuesday
8:35AM - 10:00AM
Washington Marriott Wardman Park, Roosevelt 4

**8F-Healthcare Policy Programming: Payment Policy Update (2016 - J. Arliss
Pollock Memorial Lecture)**
8F-1

8:35AM - 8:45AM

Presentation of the J. Arliss Pollock Memorial Award

8F-1a

8:45AM - 9:05AM

The Dawn of a New Day: Goodbye SGR, Hello MACRA

Hirsch, J.
Massachusetts General Hospital
Boston, MA

8F-2

9:05AM - 9:30AM

Diving Deep on APMs and Succeeding with MIPS

Nicola, G.
Hackensack Radiology Group
River Edge, NJ

8F-3

9:30AM - 10:00AM

How Imaging 3.0 Fits into New Paradigm for Neuroradiologists

McGinty, G.
Weill Cornell Medicine Radiology
New York, NY

Tuesday
10:30AM - 11:00AM
Washington Marriott Wardman Park, Marriott Ballroom

9-ASNR Annual Business Meeting (Members Only)
Tuesday
11:00AM - 12:00PM
Washington Marriott Wardman Park, Marriott Ballroom

9A-Healthcare Policy Programming: National Initiatives and the Role of the Government ("Public Policy Matters")
9A-1

11:00AM - 11:30AM

Updates from CMS

Goodrich, K.
Centers for Medicare and Medicaid Services
Baltimore, MD

9A-2

11:30AM - 12:00PM

News from the FDA

Krainak, D.
FDA
Silver Springs, MD

Tuesday
1:15PM - 2:45PM
Washington Marriott Wardman Park, Marriott Ballroom

10A-ASHNR Programming: Update on Orbital Imaging Audience Response (AR) Self Assessment Module (SAM)
10A-1

1:15PM - 1:40PM

Visual Loss: Understanding the Patterns

Kennedy, T.
University Of Wisconsin Hospital
Madison, WI

10A-2

1:40PM - 2:05PM

Diplopia: Anatomy and Pathology

Schmalfluss, I.
NF/SG Veterans Administration
Gainesville, FL

10A-3

2:05PM - 2:30PM

Orbital Infections: What You Need to Know

Avey, G.
University of Wisconsin
Madison, WI

10A-4

2:30PM - 2:45PM

Questions & Answers

Tuesday

1:15PM - 2:45PM

Washington Marriott Wardman Park, Washington 4/5/6

10B-ESNR Programming: Cases

10B-1

1:15PM - 2:45PM

Cases

Van Goethem, J. · Thurnher, M. · Kucharczyk, W.
University Hospital Antwerp · Medical University Of Vienna · Toronto General
Hospital
Antwerp · Vienna · Toronto, ON

Tuesday

1:15PM - 2:45PM

Washington Marriott Wardman Park, Washington 1/2/3

10C-Healthcare Policy Programming: Challenges Along the Road from Volume to Value

10C-1

1:15PM - 1:45PM

Management of Incidental Thyroid Nodules: ACR White Paper and Controversies

Hoang, J.
Duke University Medical Center
Durham, NC

10C-2

1:45PM - 2:15PM

A Surgeon's Perspective on Incidental Thyroid Nodules

Sosa, J.
Duke Cancer Institute and Duke Clinical Research Institute
Durham, NC

10C-3

2:15PM - 2:45PM

ACR Perspective on the Shift from Volume to Value

McGinty, G.
Weill Cornell Medicine Radiology
New York, NY

Tuesday

1:15PM - 2:45PM

Washington Marriott Wardman Park, Roosevelt 1-3

10D-PARALLEL PAPER SESSION: Turbo Talks - Degenerative Diseases / Gadolinium Deposition

O-195

1:15PM - 1:18PM

Human lifespan age-related changes of the brain proton density by quantitative MRI

H Kuno¹, O Sakai¹, H Jara¹

¹*Boston Medical Center, Boston University School of Medicine, Boston, MA*

Purpose

Calibrated proton density (PD) measurements using quantitative MRI (qMRI) approximate the mobile water content in the human brain (1). Noninvasive, quantitative PD (qPD) mapping has demonstrated the ability to provide important disease-related parameters associated with focal or global change in tissue water homeostasis (2-4). Prior qPD studies used weighting inversion with cerebrospinal fluid (CSF) calibration have hinted age-related changes over the human lifespan (5). In this work, we use a more accurate qPD technique based on T1 relaxometry.

Materials and Methods

The protocol was approved by the IRB of our institution, and all subjects were consented following NIH HIPAA guidelines. The brain data of 63 healthy subjects (28 males and 35 females; median age, 24.5 years; age range, 0.5 to 87 years) were obtained with the mixed-TSE pulse sequence with a 1.5T MR unit. The whole brain including cerebrospinal fluid (CSF), white (WM), gray matter (GM), and meninges were segmented using a 3-channel dual-clustering algorithm programmed in Mathcad (PTC, Needham, MA). PD histograms of the whole brain were generated and resolved into specific tissues (CSF, GM, and WM) by Gaussian functions.

Results

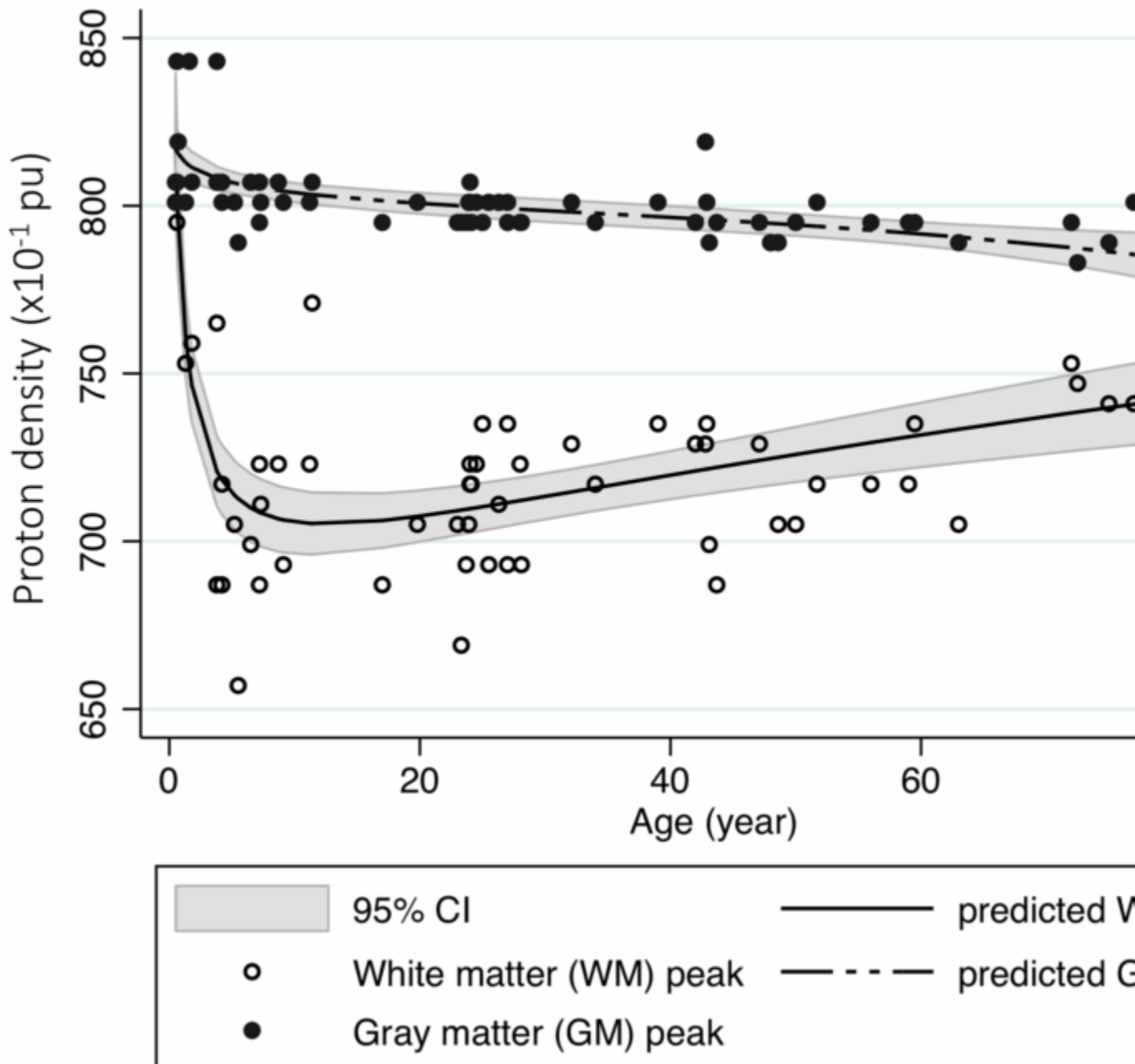
Subjects younger than 2 years of age and older than 78 years of age, had unimodal PD histograms. All other subjects had bimodal histograms with differentiated WM and GM peaks. Peak PD values for GM and WM as a function of age are plotted (Fig.): PD of GM decreased from 0 to 20 years of age and remained approximately stable during adulthood and senescence periods. PD of WM also decreased in the 0-to-20 year range, stabilized during early adulthood, and increased thereafter.

Conclusions

Proton density age-related changes of the normal brain tissues have been studied

throughout life. These results could contribute to establishing a quantitative mapping of water content baseline of the normal brain, covering the full human life span.

Peak values of the PD histograms plotted as a function of age



(Filename: TCT_O-195_Figure_PD_submit.gif)

O-196

Structural Connectivity of Distributed Cortical Association Networks Reflects Cognitive Reserve in Autosomal Dominant Familial Alzheimer's Disease

J Prescott¹, J Petrella¹

¹*Duke University Medical Center, Durham, NC*

Purpose

To assess whether structural connectivity changes in distributed cortical association networks predict cognitive reserve, as determined by estimated years until onset (EYO) of dementia in cognitively normal (pre-symptomatic) autosomal dominant Alzheimer mutation carriers, and to determine whether such changes precede known functional connectivity changes in this population.

Materials and Methods

We studied all cognitively normal subjects enrolled in the Dominantly Inherited Alzheimer's Network (DIAN) who had T1-weighted magnetic resonance imaging (MRI), resting state functional (f)MRI, and diffusion tensor (DT) imaging MRI at baseline. The T1 images were segmented using an empirically derived standard atlas of seven resting-state networks in FreeSurfer. Figure 1 demonstrates a standard parcellation of the human cortex into seven separate distributed cortical association networks based on resting state fMRI from 1000 young healthy subjects; example networks of interest for this study include the ventral attention network (purple), default mode network (red), and frontoparietal control network (orange). Structural connectivity of each of the seven networks was calculated as the weighted global efficiency of structural connections calculated from tractography of DT images; tractography was performed using DSI Studio. The weighted global efficiency is the average inverse shortest path length between any two nodes in the network.

Functional connectivity was calculated as the average timeseries correlation between the nodes of each region in each resting state network. General linear models were created for mutation carriers (M+) and noncarriers (M-), which examined the relationship between cortical functional connectivity and EYO, and white matter structural connectivity and EYO, after covarying for sex, education, cognitive performance (mini mental state examination - MMSE), ApoE4 allele status (positive or negative), and normalized white matter volume. A p-value less than 0.05 was considered significant.

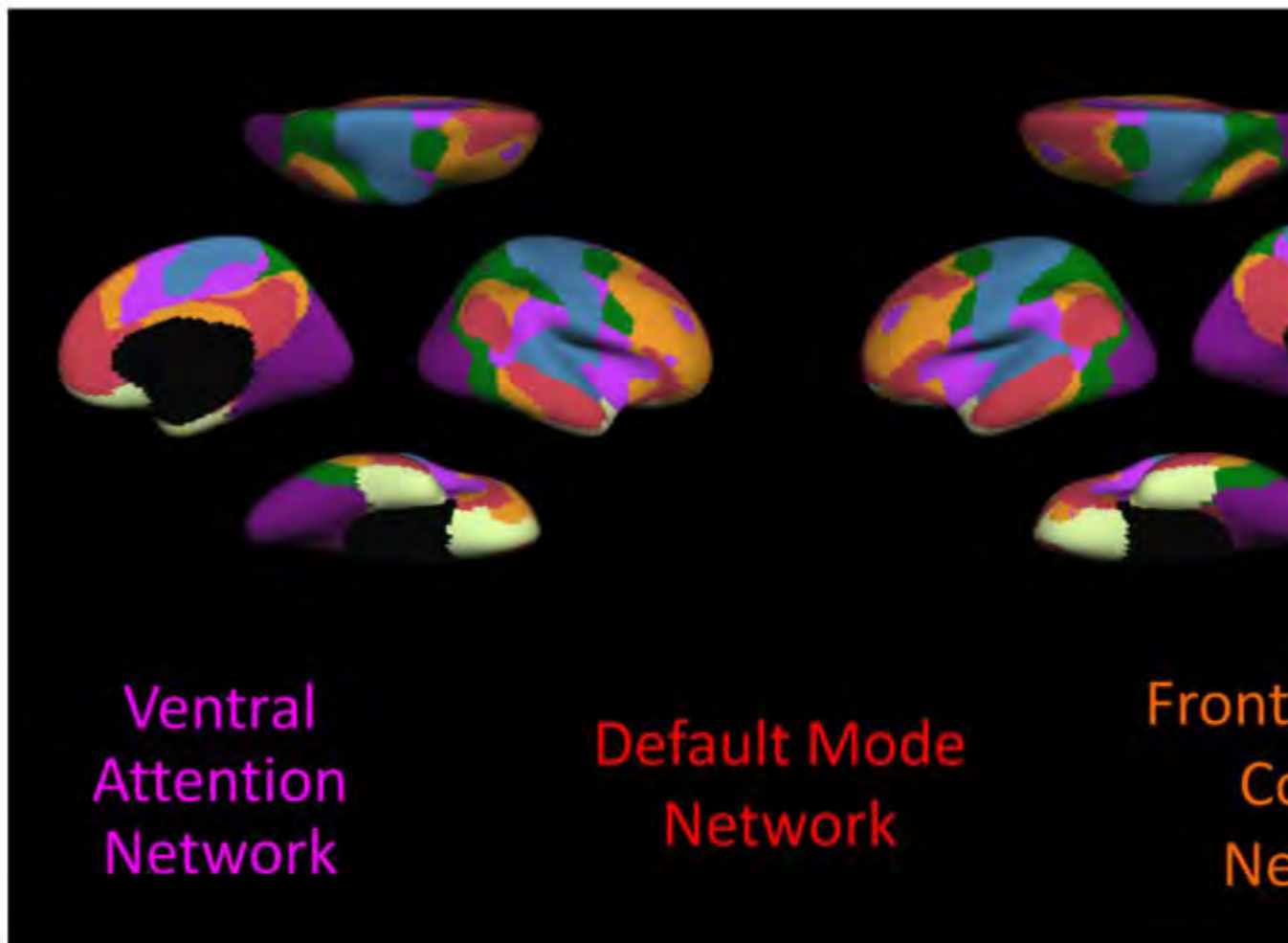
Results

There were 75 subjects analyzed: 37 mutation carriers and 38 controls (no mutation). Among cognitively normal mutation carriers, there was a significant change in white matter structural connectivity versus EYO in the default mode network, ventral attention network, and frontoparietal control network ($p < 0.05$), but not in any other network. There was no significant change in functional connectivity. There was no

significant change in either structural or functional connectivity versus EYO in the controls.

Conclusions

Significant decreases in white matter structural connectivity with decreasing EYO in mutation carriers, but not in controls, in the default mode network, ventral attention network and frontoparietal control network, suggest that the pathologic underpinnings of AD disrupt the cognitive substrate early and progressively in those with an autosomal dominant genetic mutation corresponding to early onset AD.



(Filename: TCT_O-196_Presentation1.png)

O-197

1:21PM - 1:24PM

Personalized genetic prediction of age-associated Alzheimer's disease risk

R Desikan¹, C Fan², W Dillon¹, D Wilson¹, C Hess¹, A Dale²

¹UCSF, San Francisco, CA, ²UCSD, San Diego, CA

Purpose

Identifying individuals at risk for developing Alzheimer disease (AD) is of clinical and societal importance. Genetic risk factors may be useful for predicting the age-specific risk for developing AD.

Materials and Methods

Using genotype data from 11,840 AD patients and 10,931 cognitively normal older individuals from the Alzheimer's Disease Genetics Consortium, we developed a polygenic hazard score (PHS) for predicting age of AD onset. We integrated known AD associated single nucleotide polymorphisms (SNPs) into a Cox proportional hazards model. For each individual, we calculated the AD hazard rate conditioned on the polygenic profile using established population-based incidence proportion and the hazard ratios from our final Cox model.

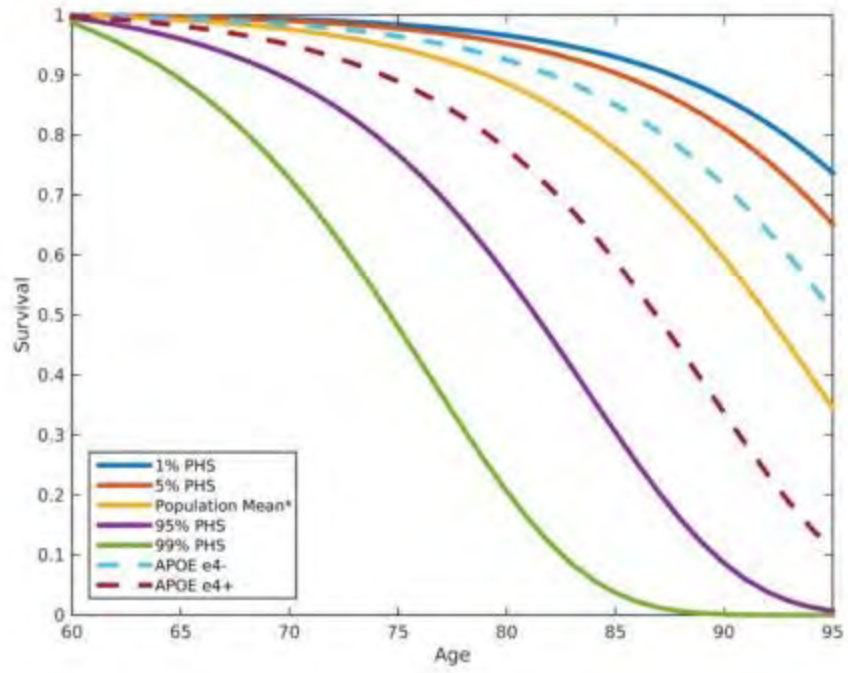
Results

Using age of onset and polygenic profile, we were able to quantify a single individual's risk (hazard) for developing AD. Between 60 and 95 years, increasing PHS strongly predicted decreased median age of AD onset. Accounting for established population incidence, we additionally found that the PHS could inform AD incidence proportion in the US population. The PHS strongly correlated with intracranial neurofibrillary tangles and amyloid plaques, magnetic resonance imaging (MRI) measures of medial temporal lobe volume loss, CSF amyloid- β 1-42 levels and baseline CDR-Sum of Box scores.

Conclusions

We have developed and validated a polygenic hazard score for predicting AD age of onset. Quantification of genetic risk in AD may prove useful for early detection, disease prevention, determining prognosis, and cohort enrichment in clinical trials.

Figure 1



(Filename: TCT_O-197_Figures.jpg)

O-198

1:24PM - 1:27PM

Apolipoprotein E Genotype and Mesial Temporal Atrophy: Two - year Follow-up in Patients with Stable Mild Cognitive Impairment and with Conversion from Mild Cognitive Impairment to Alzheimer's Disease

B Stevens¹, M Spampinato², S Bickley¹

¹Medical University of South Carolina, Charleston, SC, ²Medical University Of South Carolina, Charleston, SC

Purpose

To examine the relationship between Apolipoprotein E (APOE) genotype and mesial temporal atrophy in patients with mild cognitive impairment (MCI) with and without conversion to Alzheimer disease (AD).

Materials and Methods

We evaluated 172 MCI patients with (N = 85, 60 APOE4 - positive) and without (N = 87, 36 APOE4 - positive) AD conversion. Longitudinal magnetic resonance imaging (MRI)-based hippocampal volume (HV) and entorhinal cortex (ERC) thickness measurements were obtained using FreeSurfer V4 software. The Clinical Dementia Rating Sum of Boxes (CDR-SB) score was used for cognitive assessment. APOE genotype was determined from peripheral blood DNA.

Results

We found a significant effect of APOE4 ($F = 5.1$, $p = 0.025$) and clinical course of the disease (stable MCI versus MCI-AD conversion, $F = 18.5$, $p < 0.001$) on longitudinal HV measurements. There was a significant effect of the clinical course ($F = 14.9$, $p < 0.001$), but not of APOE4 ($F = 1.374$, $p = 0.244$), on serial ERC thickness measurements. There were significant differences in cognitive performance measured using CDR-SB scores between patients with and without MCI-AD conversion but not between APOE4 carriers and noncarriers.

Conclusions

The trajectory of HV is influenced by the APOE genotype to a greater extent than the trajectory of ERC thickness in patients with MCI. The effects of APOE4 on structural MRI biomarkers such as HV and ERC thickness should be considered when designing clinical trials that rely on neuroimaging measures of disease progression.

O-199

1:27PM - 1:30PM

Parkinson Disease: Diagnostic Utility of Large-Scale Structural Covariant Networks

W Lin¹, K Chou², P Lee³, H Chen⁴

¹*Kaohsiung Chang Gung Memorial Hospital, Kaohsiung, -- SELECT -- Taiwan,* ²*Institute of Neuroscience, National Yang-Ming University, Taipei, Taiwan,* ³*National Yang-Ming University, Taipei, Taiwan,* ⁴*Kaohsiung Chang Gung Memorial Hospital, Kaohsiung, Taiwan*

Purpose

Disregulation between the striatum and other neo-cortices have been found to be related to clinical impairments associated with Parkinson's disease (PD). By using structural covariance for assessing large-scale structural covariant networks (LSSCN), we had demonstrated that altered striato-cortical networks are an important hallmark in PD. In present study, we used independent component analysis (ICA) to explore the whole brain LSSCN in PD and to examine the usefulness and reproducibility of LSSCN in the diagnosis of PD.

Materials and Methods

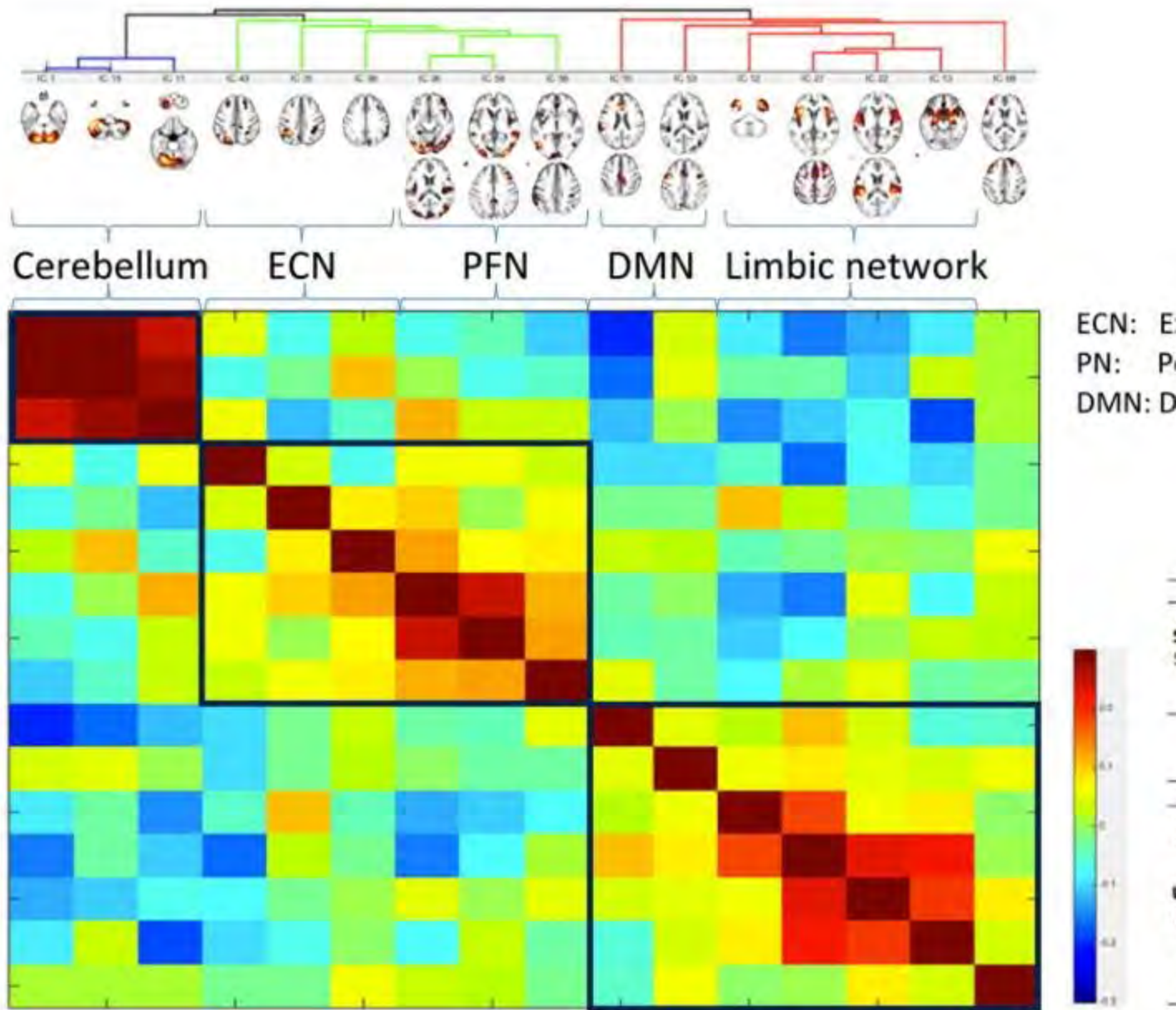
High resolution T1-weighted magnetic resonance imaging was performed in 72 patients with idiopathic PD (mean age, 61.08 years) and 73 healthy subjects (mean age, 58.96 years). The whole brain LSSCNs were extracted using spatial ICA with 70 components. With the forward stepwise feature selection scheme, we identified the set of LSSCNs which provided the most predictive accuracy among 70 components. The leave-one-out cross-validation test, a relatively unbiased estimation, tested the practicability and reproducibility of the PD classifier. Receiver operating characteristic analysis was used to determine the diagnostic performance of the classifier. Pearson correlation analysis was further performed to correlate the outcome measurement of the PD classifier with disease severity.

Results

We found that the LSSCN achieved a well predictive power in the diagnosis of PD (sensitivity 93%; specificity 84%, and accuracy 88%). Further leave-one-out cross-validation tests revealed a high reproducibility of LSSCN in the diagnosis of PD (the mean sensitivity 82%, specificity 77%, and accuracy 79% respectively). Alterations of LSSCN in cerebellar network, executive networks, posterior network, default mode network, and limbic network were associated with higher risk of PD (Fig. 1). Furthermore, outcome measure of this regression model was associated with disease severity.

Conclusions

Consistent with network degeneration hypothesis, brain LSSCN with multiple logistic regression modeling can be a complementary tool in the diagnosis of PD.



(Filename: TCT_O-199_Figure1.jpg)

O-200

1:30PM - 1:33PM

Dentate Nucleus Iron Deposition Is a Potential Biomarker for Tremor-dominant Parkinson's Disease

N He¹, F Yan¹, C Liu²

¹Department of Radiology, Ruijin Hospital, Shanghai Jiao Tong University School of Medicine, Shanghai, shanghai, shanghai, ²Department of Radiology, Duke University Medical Center, Durham, NC 27710, USA, Durham, NC

Purpose

Parkinson disease (PD) is a heterogeneous neurodegenerative disorder with variable clinicopathologic phenotypes and underlying neuropathologic mechanisms. Tremor is the most frequent initial motor symptom of PD and is the most difficult symptom to treat. The dentate nucleus (DN) is a deep iron rich nucleus in the cerebellum and may be involved in PD tremor. In this study, we test the hypothesis that DN iron may be elevated in tremor dominant PD patients using quantitative susceptibility mapping.

Materials and Methods

Forty-three patients with PD [19 tremor dominant (TD)/24 akinetic-rigid dominant (AR)] and 48 healthy gender- and age-matched controls were recruited. Multi-echo gradient echo data were collected for each subject. Similar to our prior study [cite], susceptibility values were obtained using the quantitative susceptibility mapping method [cite]. Bilateral DNs were drawn manually on the susceptibility maps using MRIcro software (www.mricro.com) by two neuroradiologists who were blinded to the diagnosis of each subject. The volume of the DNs was determined by multiplying the sum of voxels within the entire structure by the size of each voxel ($0.86 \times 0.86 \times 1.0 \text{mm}^3$). Inter-group susceptibility and volume differences in bilateral dentate nucleus were investigated and correlations of clinical features with susceptibility also were examined.

Results

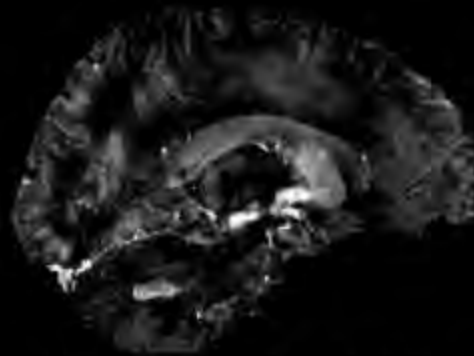
In contrast to the AR group, the TD group was found to have increased susceptibility in the bilateral DN, when compared to healthy controls. In addition, susceptibility was positively correlated with tremor score in TD patients. And other clinical features, such as disease duration, akinetic rigidity score, and Unified Parkinsonian Disease rating scale (UPDRS)-III score were correlated moderately with bilateral DN susceptibility in the TD group. No significant difference in DN volume was found among the PD groups and healthy control group.

Conclusions

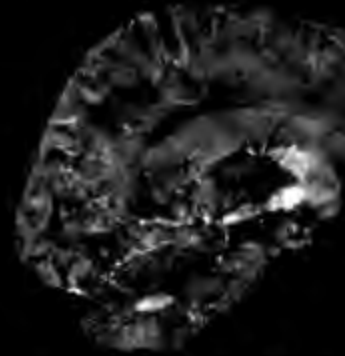
These findings indicate that iron load within DN may make an important contribution to motor phenotypes in PD.



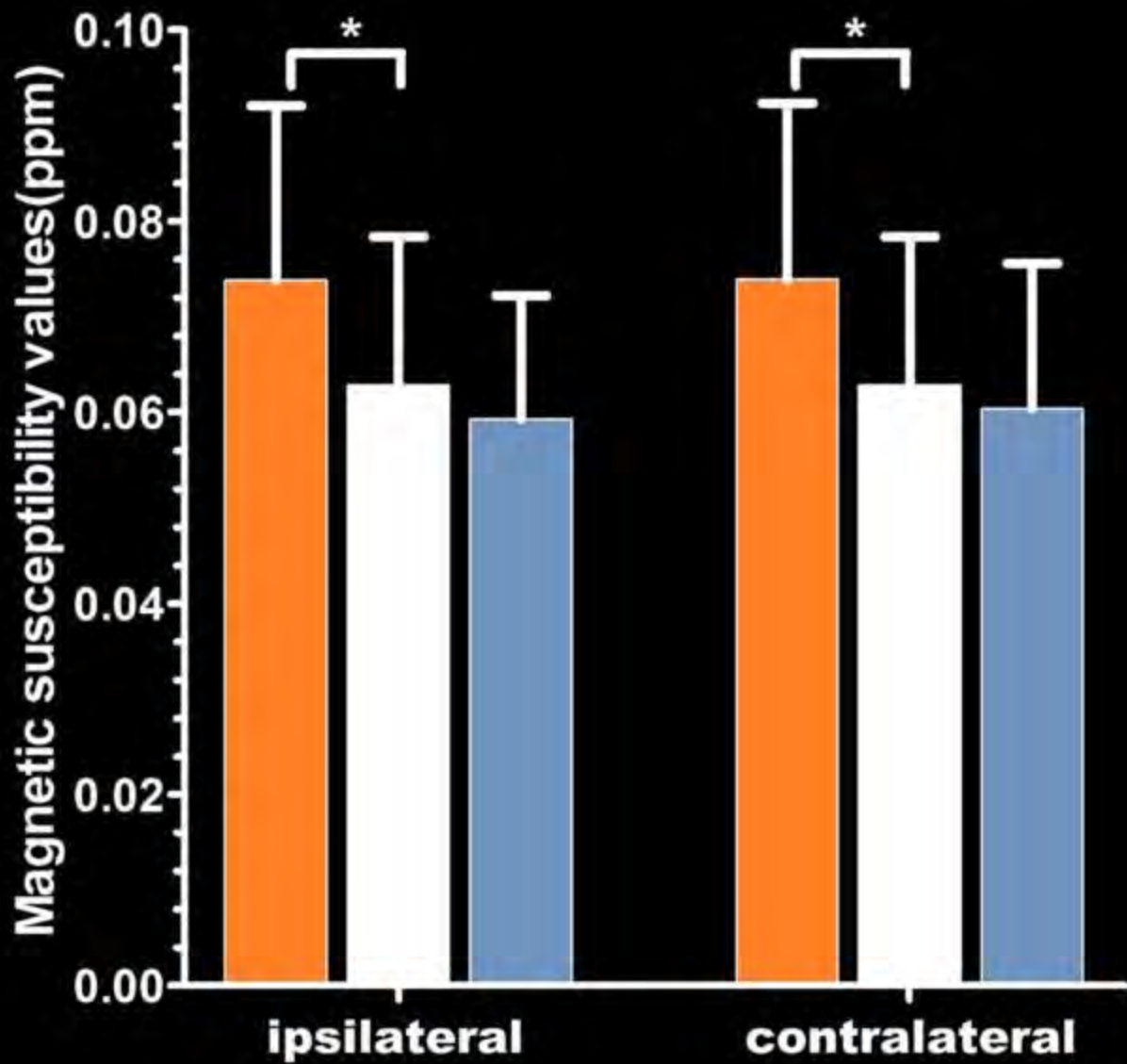
Tremor



Healthy Control



Akinetic-Rigid



(Filename: TCT_O-200_Graphical.jpg)

O-201

1:33PM - 1:36PM

Sex Differences in the Association Between Glycemic Control and Cerebral Blood Flow in African Americans with Type-2 Diabetes: The African-American Diabetes Heart Study MIND

Y Nguyen¹, N Bahrami², J Divers¹, J Xu³, Y Jung¹, B Freedman³, J Maldjian⁴, C Whitlow⁵

¹Wake Forest School of Medicine, Winston-Salem, NC, ²Virginia Tech-Wake Forest University School of Biomedical Engineering & Sciences, Winston Salem, NC, ³Wake Forest School of Medicine, Winston Salem, NC, ⁴University of Texas Southwestern, Dallas, TX, ⁵Wake Forest University School of Medicine, Winston-Salem, NC

Purpose

Growing evidence suggests that women suffer more end-organ complications of type-2 diabetes (T2D) compared to men. Hemoglobin A1C (HA1c) is a biomarker reflecting glycemic control over a 2-3 month period used to gauge the effectiveness of T2D clinical management. This study aimed to characterize the relationship between HA1c and whole brain gray matter (GM) cerebral blood flow (CBF) in the understudied African American population with well controlled T2D. We hypothesized that higher levels of HA1c would be associated with reduced cerebral blood flow (CBF) in GM, and that this relationship would be stronger in women compared to men.

Materials and Methods

African Americans with reasonably well controlled T2D (%HA1c Mean±SD; 8.2±2.1) were recruited as part of an IRB approved NIH funded study. We included 449 participants (268 women and 180 men) in our analysis who had HA1c and measures of CBF using pseudocontinuous arterial spin labeling (PCASL) magnetic resonance imaging (MRI). Magnetic resonance scanning with PCASL was performed with a 3T Siemens Skyra. Regression analysis of the entire cohort (males and females) was conducted to characterize the overall relationship between whole brain GM CBF and HA1c levels (adjusted for age, body mass index, hypertension, education, and diabetes duration), and then repeated separately for males and females.

Results

No statistically significant difference in HA1c was identified between males and females. There was also no statistically significant relationship between HA1c and whole brain GM CBF in the total cohort or among men separately. There was, however, a statistically significant linear relationship between HA1c and whole brain

GM CBF among women, with higher HA1c associated with lower rates of CBF ($p < .0.04$).

Conclusions

HemoglobinA1C is associated with global rates of CBF in African American women, but not men, despite similar between-sex levels of HA1c that were all within the clinically recommended range for management of T2D. One concerning interpretation of these findings is that recommended guidelines for glycemic control based upon HA1c are inadequate for African American women, who may need more aggressive management to avoid brain end-organ complications and cognitive sequelae.

O-202

1:36PM - 1:39PM

Quantitative Gray Matter Calculations in Antiphospholipid Antibody Syndrome: A Novel Tool for Early Detection

s cantrell¹, E Quigley², J Anderson¹

¹University of Utah, Salt Lake City, UT, ²University Of Utah, Salt Lake City, UT

Purpose

We present the spectrum of intracranial findings associated with antiphospholipid antibody syndrome (AAS) with emphasis on early identification of parenchymal volume loss. We propose that quantitative methods may aid in early detection of subtle volume loss in patients with known AAS and may help distinguish volume loss in AAS from other etiologies such as CADASIL, multiple sclerosis and Alzheimer disease.

Materials and Methods

Retrospective review of MR images of patients with AAS presenting to a tertiary academic institution from 2012-2015 was performed. Quantitative gray matter volume calculations were performed using open source toolboxes for MATLAB (SPM 12b, Wellcome Trust). All patients with available MPRAGE images with at least 2x2x2 mm isotropic resolution and history of AAS were included. Gray matter segmentation (SPM12b, normalized to MNI space) was performed and number of gray matter voxels within 116 regions of the AAL brain atlas was compared to an age-matched database.

Results

Sequela of antibody mediated vascular endothelial damage including recurrent thromboses, strokes and advanced microvascular changes related to arteriolosclerosis were identified. Additionally, characteristic biparietal volume loss was observed, helping to differentiate AAS from CADASIL and Alzheimer, both of which characteristically demonstrate early involvement of the temporal lobes. Quantitative gray matter maps were helpful in detecting subtle, disproportionate biparietal volume

loss, which may be difficult to discern on conventional sequences. Given the growing variety of prophylaxis for the CNS manifestations of AAS, including immune modulating drugs and anticoagulants, early detection of CNS manifestations may become increasingly relevant.

Conclusions

Quantitative volumetric analysis may assist in detecting subtle volume loss not readily apparent on conventional sequences. In a patient with suspected AAS, early detection may prove clinically relevant given the opportunity for new therapeutic intervention and prevention of CNS manifestations. Additionally, when confronted with a patient with dementia or thrombotic sequela advanced for age, characteristic biparietal volume loss may prompt testing for antiphospholipid antibody syndrome.

O-203

1:39PM - 1:42PM

Brain Volume and Cell Volume Fraction in Adult Survivors of Pediatric Acute Lymphocytic Leukemia measured by Quantitative ^{23}Na MR Imaging at 9.4 Tesla

N Narayan¹, I Atkinson¹, D Choi¹, M Schmidt¹, K Thulborn¹

¹*University of Illinois at Chicago, Chicago, IL*

Purpose

Long term survivors of pediatric acute lymphocytic leukemia (ALL) have been demonstrated to have a slightly decreased neuropsychological performance compared to age-matched healthy controls but the biological basis of this difference is not known (1). Our hypothesis is that the treatment of ALL with both systemic and intrathecal chemotherapy and sometimes whole brain radiation results in a decrease in brain tissue cell density and brain volume due to tissue cell death although often conventional anatomical MR images are not revealing. We have measured tissue sodium concentration (TSC) and its derived parameter of cell volume fraction (CVF) using quantitative ^{23}Na MR imaging at 9.4T (2) in a group of ALL survivors and age-matched control subjects and correlated tissue loss with TSC and CVF.

Materials and Methods

Adult ALL survivors (N=10, 40% male, age range 19-29 years, age at diagnosis 2-17 years) and age-matched healthy controls (N=8, 50%M, age range 21-30 years) provided signed informed consent in IRB and FDA approved protocols. Magnetic resonance imaging (MRI) was performed on a customized 9.4T magnet equipped with a head gradient set and ^{23}Na volume head coil (2). Quantitative sodium imaging was performed using a ultrashort TE twisted projection imaging (TPI) pulse sequence with both B0 and B1 corrections on each subject and a three compartment sodium calibration phantom (30, 70 110 mM aqueous NaCl) to obtain TSC maps from which

CVF maps were derived. The spatial resolution was nominally 2.5 x 2.5 x 2.5 mm³ with an acquisition time of 10 minutes providing a signal to noise ratio (SNR) of greater than 12. The B0 and B1 mapping each required additional 10 minute acquisitions. The TSC values for the frontal, parietal, temporal and occipital lobes and of the basal ganglia and thalami were measured by customized software and summarized by means and standard deviations (SD). The TSC maps also were used to measure the fraction of cerebrospinal fluid (CSF) space within the calvarium occupied by the cerebral hemispheres. Fractional CSF volumes were compared between ALL survivor and control groups by two-tailed t-test. Linear correlations were performed between regional TSC values and fractional CSF values for both groups.

Results

The fractional CSF volume of the ALL survivor group was statistically larger than the control group ($p < 0.015$) indicating the decreased brain volume of the survivor group. The TSC values for the frontal and parietal lobes and for the basal ganglia and thalami but not of the occipital and temporal lobes showed significant linear correlations with increasing TSC values for the ALL survivor group. In contrast, the normal group showed constant TSC and CVF values across all regions of the brain.

Conclusions

The ALL survivors have smaller brain volumes that show statistically significant trends of increased TSC and decreasing CVF in the frontal lobes, parietal lobes, basal ganglia and thalami compared to age-match normal controls. These results suggest that the disease or its treatment during childhood has a measurable impact on regional brain structure. This trend may relate to age of diagnosis.

O-204

1:42PM - 1:45PM

Practical Low SAR Protocol at 1.5T using Two Magnet Systems for Patients Undergoing Staged DBS Insertion

A Franceschi¹, G Wiggins¹, A Mogilner², T Shepherd¹, S Chung¹, Y Lui¹
¹NYU Medical Center, New York, NY, ²NYU, New York, NY

Purpose

Obtaining high-resolution brain magnetic resonance imaging (MRI) in patients with previously implanted deep brain stimulator (DBS) has been challenging and avoided by many centers due to safety concerns relating to implantable devices. Pre-operative MR sequences routinely used for DBS placement guidance include a high-resolution T1-weighted sequence, used to identify standard anatomical landmarks such as the anterior and posterior commissures, as well as high-resolution T2-weighted MR imaging routinely used to target the subthalamic nucleus (STN), the most common structure targeted in DBS for Parkinson's disease. We present our experience using a

practical clinical MR protocol optimized for both therapeutic image quality in patients with implanted DBS electrodes and lowest possible SAR on two 1.5T magnet systems.

Materials and Methods

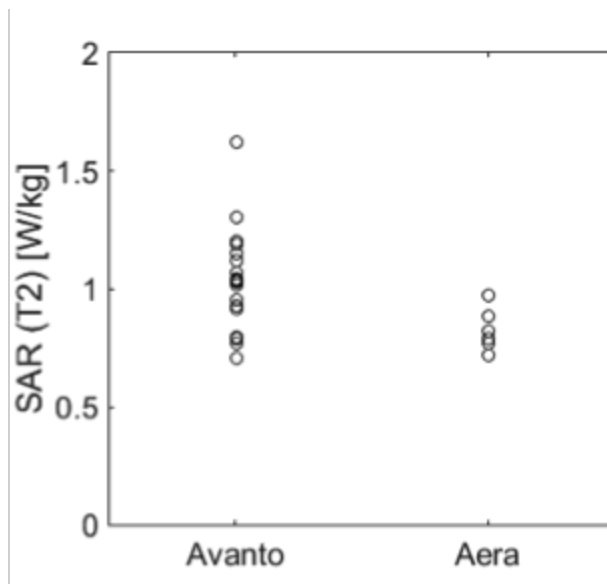
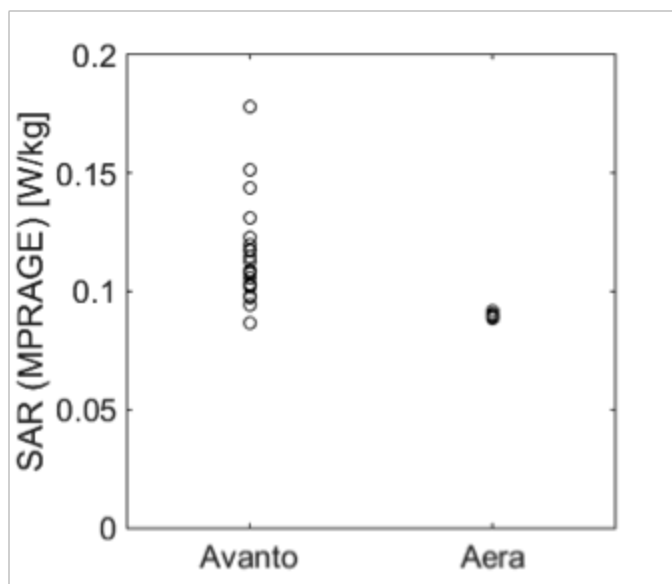
We reviewed MRI studies performed with minimal SAR protocol in patients with DBS in place at our institution between 2/1/2012-8/1/2015. Our initial tests showed that at SAR=0.1W/kg and 0.4W/kg the quality of the study was insufficient for stereotaxis. At SAR of ~0.7W/kg SAR we were able to achieve images adequate for intra-operative stereotaxis and the following protocol was set up: MPRAGE obtained in the axial plane with the following parameters: TR=1870ms, TE=4ms, FA=15, Nav=1, FOV=260x260mm, Matrix size 256x256, slice thickness=1.5mm, 176 slices; T2-weighted sequence obtained in the axial plane with the following parameters: TR=2500ms, TE=80-83ms, FA=150, Nav=4, FOV=260x260mm, Matrix size=256x256, slice thickness=2.5mm). Images were reviewed by a neuromodulation neurosurgeon and a neuroradiologist for adequacy.

Results

Twenty-nine patients (22 Parkinson's disease, six dystonia, one essential tremor) were imaged with at least one neuromodulation implant in situ (Medtronic, Minneapolis, MN). There were 25 subthalamic and four globus pallidus implants. Average imaging time was 6 minutes 17 seconds for MPRAGE and 12 minutes and 16 seconds for T2. Average SAR deposition for MPRAGE was 0.114 ± 0.021 for the Avanto system, 0.090 ± 0.001 for the Aera system and 0.109 ± 0.021 overall. Average SAR deposition for T2 weighted sequence was 1.037 ± 0.214 for the Avanto system, 0.828 ± 0.091 for the Aera system and 0.987 ± 0.210 overall. SAR deposition for both MPRAGE and T2-weighted sequences were significantly lower on the Aera system; $p=0.012$ and $p=0.03$, respectively with lower standard deviation. All pre-operative studies were adequate for guidance of second DBS placement. There were no complications.

Conclusions

Low SAR MRI protocol can be used to obtain high quality and high-resolution preoperative images for DBS surgical guidance safely in patients with a previously implanted electrode. In our multi-year experience with average T2 head SAR of 0.987 (less than a third of usual SAR limit), there were no recorded adverse effects to date. Optimized coil design, such as the incorporation of a multi-element receive array in a geometry that still allows for use of the stereotactic frame, could further improve image quality without increasing SAR.



(Filename: TCT_O-204_ImageforASNR2016.gif)

O-205

1:45PM - 1:48PM

Intracranial Gadolinium Deposition Following Contrast Enhanced MRI in Adult Patients with Normal Brain Pathology.

R McDonald¹, J McDonald¹, M Jentoft¹, D Murray¹, M Paolini¹, L Eckel², E Williamson¹, D Kallmes¹

¹Mayo Clinic, Rochester, MN, ²Mayo Clinic, Rochester, Rochester, MN

Purpose

Recent reports have detected gadolinium deposits in neural tissues of patients with intracranial pathology following intravenous gadolinium-based contrast agent (GBCA) exposure. In the current study, we sought to determine if this deposition might be related to blood-brain barrier integrity by studying adult patients with normal brain pathology.

Materials and Methods

After obtaining antemortem consent and IRB-approval for this single center study, we compared post mortem neuronal tissue samples on five patients who received between four and 16 gadolinium-enhanced abdominal magnetic resonance imaging (MRI) exams between 2005-2014 (contrast exposed group) to 10 gadolinium-naïve patients who underwent at least one MRI exam during their lifetime (control group). All contrast exposed patients received gadodiamide (Omniscan). Neuronal tissues from the dentate nuclei, pons, globus pallidus, and thalamus of these 15 deceased patients were harvested from our institutional biospecimen archive and analyzed by inductively coupled mass-spectrometry (ICP-MS), transmission electron microscopy

with energy dispersive x-ray spectroscopy (TEM-EDS) and light microscopy to quantify, localize, and assess the effects of gadolinium deposition.

Results

Tissues from the four neuroanatomical regions of gadodiamide-exposed patients contained between 0.1-19.4 μg gadolinium/g tissue in a significant dose-dependent relationship (globus pallidus: ρ : 0.90 p = .04). In contradistinction, control group patients had undetectable levels of gadolinium using ICP-MS. All contrast exposed (47-72 years) and control group patients (56-92 years) had normal brain pathology at the time of autopsy. Two of the five contrast exposed patients had borderline renal function (eGFR \sim 30) and hepatobiliary dysfunction at the time of MRI examination(s). Gadolinium deposition in the contrast-exposed group was localized to the capillary endothelium and neuronal interstitium using TEM-EDS.

Conclusions

Gadolinium deposition in neural tissues following GBCA administration occurs in the absence of intracranial pathology that might affect the permeability of the blood-brain barrier. These findings challenge our understanding of the biodistribution of these contrast agents and their safety.

O-206

1:48PM - 1:51PM

Longitudinal Monitoring of Gadolinium Retention in the Dentate Nucleus and Globus Pallidus in Multiple Sclerosis Patients Within a 16-Months Period

S Siemonsen¹, J Stellmann², K Stuermer², C Heesen², J Fiehler³, J Sedlacik²

¹University Medical Center Hamburg-Eppendorf, Hamburg, Germany, ²University Medical Center Hamburg-Eppendorf, Hamburg, Hamburg, ³University Medical Center Hamburg-Eppendorf, Hamburg, AK

Purpose

Recent studies showed an increase in signal intensity (SI) of the dentate nucleus (DN) and globus pallidus (GP) in association with the serial application of gadolinium-based contrast agents (GBCAs). Nevertheless, most of these studies are cross-sectional and data monitoring SI increase longitudinally is rare. The purpose of this analysis was to longitudinally assess the SI increase of the DN and GP on native T1-weighted (T1-W) images in multiple sclerosis (MS) patients and its association with the number of gadolinium administrations for magnetic resonance imaging (MRI).

Materials and Methods

Native T1-W images were analyzed for 16 MS patients, who all received 3T MRI for 12 time points within 16 months as part of a phase II clinical trial (scans were conducted at months 1-7, 9-12 and 16). The average T1-W SI of the DN, the GP and the cerebrospinal fluid (CSF) was obtained, and the DN-CSF and GP-CSF SI-ratio

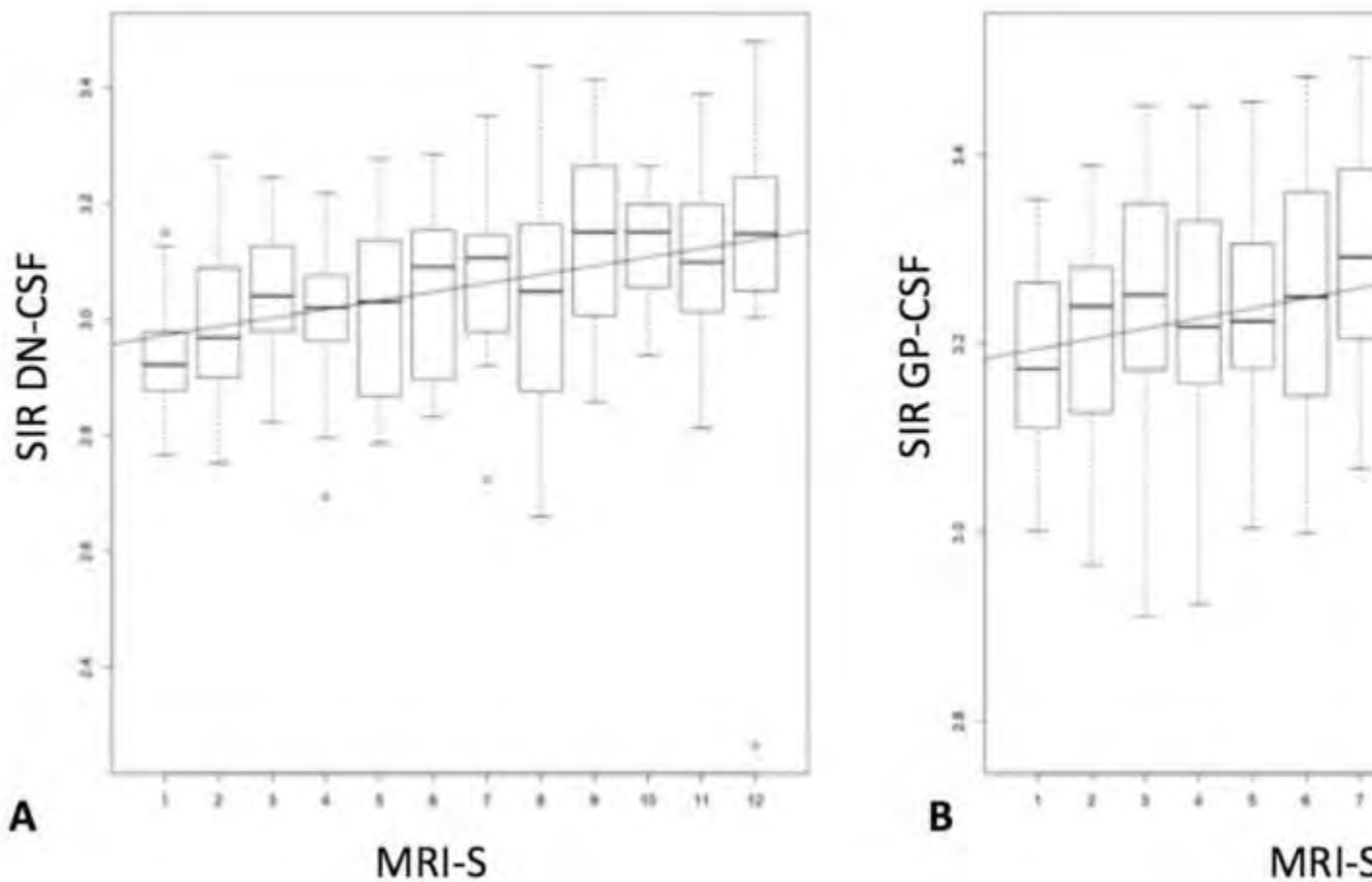
(SIR) was calculated for each scan. Signal intensity ratio was correlated with the number of MR scans and not time, since no GBCA was administered between the scans, even if they were more than 1 month apart. A linear GBCA (gadopetate meglumine; Magnograf) was used.

Results

The SIR for DN-CSF and GP-CSF was significantly increased in comparison to the baseline scan beyond the fifth scanning time point ($p < 0.01$) and showed an overall contiguous increase towards the twelfth scan. The DN-CSF and GP-CSF SIR showed a significant positive correlation with the cumulative number of MR scans (for all $p < 0.01$).

Conclusions

Our data suggest a linear increase of the DN and GP signal intensity on native T1-W scans in MS patients, caused by serial application of a linear GBCA within a relatively short period of time of 16 months. Figure Caption: Boxplots and regression line displaying the longitudinal increase of the SIR of the DN-CSF (A) and GP-CSF (B) for each MRI scan.



(Filename: TCT_O-206_SABA_CE_Figure.jpg)

High T1 Signal Intensity of Brain Parenchyma after Repetitive Gadobenate Dimeglumine Administration: Evaluation of Multiple Sclerosis versus Tumor Patients

S Metting¹, B Bigjahan¹, o boyko², J Acharya¹, M Shiroishi¹, S Cen¹, W Gibbs³, G Ho², L Amezcua¹, M Law¹, A Lerner¹

¹University of Southern California, Keck School of Medicine, Los Angeles, CA, ²University of Southern California, Los Angeles, CA, ³University of Southern California, Keck School of Medicine, Pasadena, CA

Purpose

High T1 signal intensity (SI) in the brain parenchyma has been implicated as an indirect sign of gadolinium (Gd) deposition in patients administered gadolinium-based contrast agents (GBCA) (1). Patients with intracranial neoplasms (IN) and multiple sclerosis (MS) have been studied (1, 2). Recent dynamic contrast enhanced magnetic resonance imaging (DCE MRI) permeability studies revealed increased regional permeability in normal appearing white matter (NAWM) of MS patients suggesting diffuse derangements in blood-brain barrier (BBB) (3, 4). Abnormal permeability in the globus pallidus (GP) and dentate nucleus (DN) is possible, but not yet confirmed. Regions of increased vascular permeability in MS consequently may be more susceptible to Gd deposition than patients with only local BBB derangement. We assessed for increased T1 signal after multiple doses of gadobenate dimeglumine in MS and IN patients, and evaluated for group differences possibly related to BBB derangements.

Materials and Methods

Retrospective analysis of MS and IN patients was performed. Only patients with five consecutive administrations of gadobenate dimeglumine were included. Whole brain radiation was an exclusion criterion and irradiated regions of interest (ROIs) were excluded from measurement. Seventy patients were selected. Regions of interest measured SI on T1-W axial scans immediately prior to consecutive dosing, after five doses, and on the last scan. The ratios obtained were GP:thalamus (TH), DN:pons, white matter (WM):TH, and WM:pons. When possible bilateral measurements were averaged. Linear trajectory slopes of SI ratio were created for change per 10 units GBCA and change per year. The difference in trajectory slopes was compared using the interaction term.

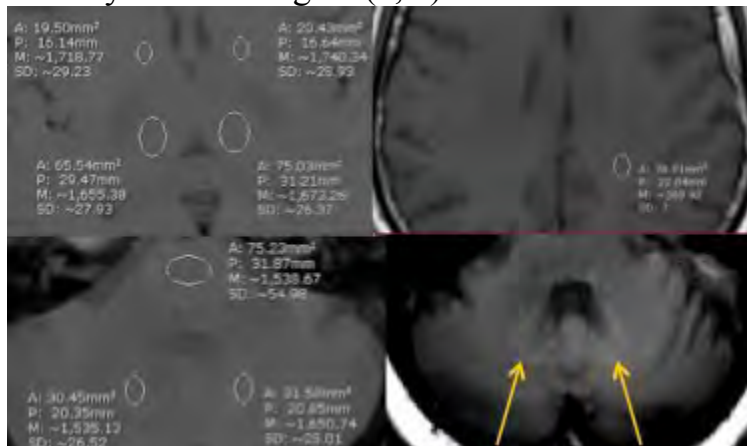
Results

Initial analysis of 16 MS and 15 IN patients revealed a trend for increased DN:pons SI per units of GBCA in the IN group ($p = 0.1$), but not in the MS group. The slope interaction approached significance ($p = 0.1$). The DN:pons SI change per year in the

IN group was significant ($p = 0.03$), but not in the MS group. The slope interaction was significant as well ($p = 0.03$). The slopes for GP:TH in MS and IN were positive, but the trend was weak. The interaction terms were not significant for GP:TH. No significant increase of WM:TH or WM:pons SI was identified for MS and IN patients, and the interaction term was not significant.

Conclusions

Our study shows a significant increase of DN SI in IN patients per year and a strong trend per units GBCA, which was not seen for MS patients. A significant difference between the groups exists counter to our expectations based on recent DCE MRI permeability studies for SI to be greater in MS. Greater frequency of GBCA dosing for IN patients could overwhelm clearance mechanisms such as glymphatics or perhaps chemotherapy plays a role. Additionally, no difference between groups was found in the GP and WM. Given previously analyzed data in MS patients at our institution and by Ramalho et al. demonstrating no signal change related to gadobenate dimeglumine in the GP, and only a trend in the DN 5, this may further evidence suggesting Gd deposition is more a function of neuroanatomical location and stability of the Gd agent (1, 5).



(Filename: TCT_O-207_ASNR2016JPG.jpg)

O-208

1:54PM - 1:57PM

Comparison of Tissue Deposition Rates in Multiple Murine Organs Following Intravenous Administration of Linear vs Macrocyclic Gadolinium Chelates

R McDonald¹, J McDonald¹, D Dai¹, D Schroeder¹, B Cao¹, R Kadirvel¹, L Eckel², D Kallmes¹

¹Mayo Clinic, Rochester, MN, ²Mayo Clinic, Rochester, Rochester, MN

Purpose

Recent studies of gadolinium deposition in neural tissues following intravenous administration of gadolinium-based contrast agents (GBCAs) suggest deposition rates

may vary with chelate stability, yet little data exist using direct methods to quantify tissue deposition (1-3). In the current study, we compared gadolinium tissue deposition in multiple murine organs following injection of more stable macrocyclic chelates [gadobutrol (Gadavist)] to linear chelates [gadobenate dimeglumine (Multihance), gadodiamide (Omniscan)] that have intrinsically lower stability.

Materials and Methods

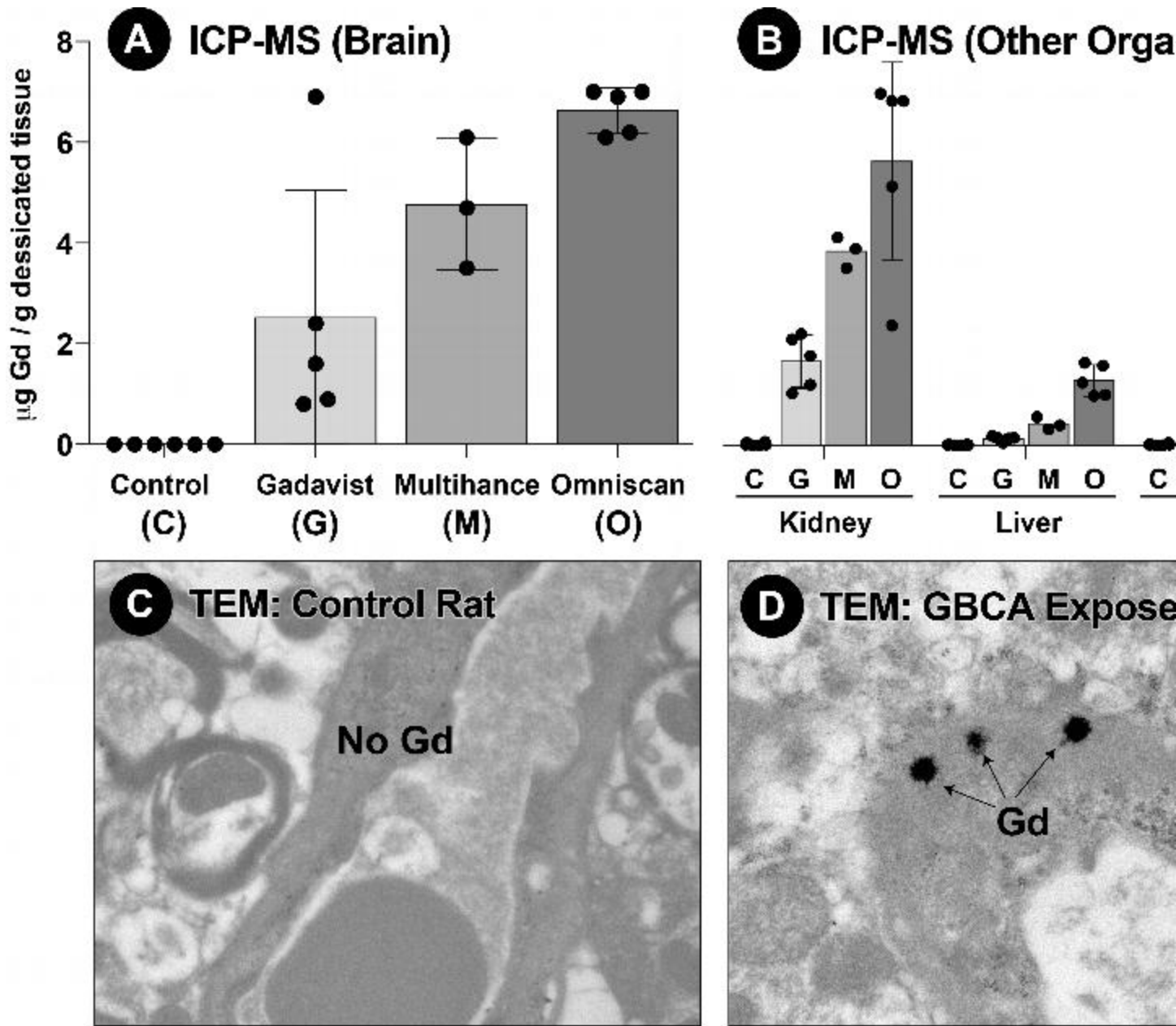
Healthy rats received 20 intravenous injections of 2.5 mmol Gd/kg (gadolinium-exposed group) or saline (control group) over a 26-day period. Unenhanced T1 signal intensities of the dentate nucleus were measured from MR exams performed prior to the initial GBCA injection and 4 days after the final injection. Murine brain, renal, hepatic, and splenic tissues were harvested post mortem 7 days after the final injection and subjected to inductively coupled plasma mass spectrometry (ICP-MS) for elemental gadolinium quantification and transmission electron microscopy (TEM) for characterization of gadolinium deposits (4).

Results

Brain tissue deposition of gadolinium varied with GBCA, with a median concentration of 1.6 ug Gd/g brain tissue (95% CI 0.9-4.7) in Gadavist-injected rats (n=5), 4.7 ug/g (3.5-6.1) in Multihance-injected rats (n=3), and 6.9 ug/g (6.2-7.0) in Omniscan-injected rats (n=5) (Fig. A). Similar relative differences in gadolinium deposition were observed in renal, hepatic, and splenic tissues, albeit at much higher tissue concentrations (Fig. B). No significant tissue deposition was observed in control rats (n=6). Gadolinium deposits were visualized directly in the endothelial capillary walls and neural interstitium in GBCA injected rats, but not in control rats (Figs. C, D).

Conclusions

In this murine model, organ tissue deposition of gadolinium was 2-4 fold higher following administration of the linear agents Omniscan or Multihance compared to the macrocyclic agent Gadavist. These findings suggest organ tissue deposition is reduced but not eliminated by using more stable macrocyclic GBCA chelates in lieu of less stable linear chelates.



(Filename: TCT_O-208_ASNRanimalgadolinium.jpg)

O-209

1:57PM - 2:00PM

Diffusion Tensor Analysis of white matter effects of Gadolinium Deposition

A Paul¹, J Pinto², P Schaefer¹, G Gonzalez¹, O Rapalino³

¹Massachusetts General Hospital, Boston, MA, ²Instituto Estadual do Cerebro, rio de janeiro, Brazil, ³Massachusetts General Hosp., Boston, MA

Purpose

To characterize changes in diffusion tensor analysis (DTI) metrics of anatomically relevant white matter tracts in patients with different levels of gadolinium exposure compared to age-matched controls.

Materials and Methods

Twenty MR datasets obtained from patients without prior gadolinium administration (control group) or after different levels of previous gadolinium administration (<5, 5-10 and > 10 scans) were identified retrospectively and collected for analysis.

Magnetic resonance (MR) studies were obtained using a 1.5T MR scanner (Signa, GE Healthcare, Waukesha, WI) and for different clinical indications. Scans with pathologies potentially affecting the target white matter tracts were excluded from the analysis. T1 signal measurements were obtained from the pons, dentate nuclei, thalami and globi pallidi using uniform regions of interest (ROIs). Diffusion tensor measurements (FA, ADC, longitudinal and radial diffusivity) also were obtained from the central pons, middle cerebellar peduncles, superior cerebellar peduncles, dentate nuclei, cerebellar white matter, red nuclei and ventrolateral thalami using the NordicICE software (NordicNeuroLab, Bergen, Norway) with the same template of ROIs. Measurements and subsequent analysis were blinded to the group assignments. Paired t-test analyses were performed between the gadolinium and control groups.

Results

Relative ratios of T1 signal intensity in the dentate nuclei in relation to the pons were increased significantly in the groups with prior gadolinium administration compared to the control group ($p < 0.05$). There was no significant difference in the relative ratios of T1 signal between the globi pallidi and thalami. There also were no statistically significant differences in the DTI metrics (FA, ADC, radial and longitudinal diffusivity) between the different gadolinium groups and the control group.

Conclusions

Despite the demonstration of increased T1 signal in the dentate nuclei after multiple gadolinium administrations, there were no significant abnormalities in the diffusion parameters of the main white matter tracts connected to these anatomical structures.

O-210

2:00PM - 2:03PM

How are Radiologists Responding to Gadolinium Deposition?

R Fitzgerald¹, V Agarwal², J Hoang³, F Gaillard⁴, A Dixon⁵, E Kanal⁶

¹University of Arkansas for Medical Sciences, Little Rock, AR, ²University of Pittsburgh Medical Center, Pittsburgh, PA, ³Duke University Medical Center, Durham, NC, ⁴The Royal Melbourne Hospital, Parkville, Victoria, ⁵Alfred Hospital, Prahran, Australia, ⁶Univ of Pittsburgh Med Ctr, Pittsburgh, PA

Purpose

Deposition of gadolinium within the brains of patients with normal renal function following the repeated administration of at least some gadolinium-based contrast agents (GBCAs) was reported initially in 2013. Intracranial gadolinium retention/accumulation now is recognized as a dose-dependent consequence of exposure manifested by T1 shortening within several brain regions including the dentate nuclei. The potential clinical implications of gadolinium deposition are not yet understood. The purpose of this study was to determine radiologists' reporting practices in response to these recent findings.

Materials and Methods

We conducted an anonymous online survey of radiologists using <https://www.surveymonkey.com> over 17 days spanning November-December 2015. The questionnaire was distributed by study authors using social media. Questions included basic respondent characteristics such as practice type/location, frequency of detection of gadolinium deposition, and reporting habits.

Results

Our study sample included 94 respondents (50% academic; 27% private practice; 23% hybrid) from 30 different countries (USA 18%). Detection of brain gadolinium deposition was reported by 62% of surveyed radiologists. Most respondents (71%) reported never or rarely (<1/month) detecting dentate T1 shortening as a marker of gadolinium deposition. Among those who reported detecting gadolinium deposition, 58% do not include the finding in the radiology report; only 13% report the finding in the impression of their reports. The most common reason for not reporting gadolinium deposition was the risk of provoking unnecessary patient anxiety (29%). Recent data on gadolinium deposition have led to a reported change in practice in 28% of respondents.

Conclusions

Recognition of and attitudes toward brain gadolinium deposition were inconsistent in this worldwide sample. More than three quarters of radiologists do not routinely report dentate T1 shortening as a marker of gadolinium deposition and only a small minority include this finding in their report impressions. Fear of provoking patient/clinician anxiety and an incomplete understanding of the implications of gadolinium deposition contribute to inconsistencies in reporting.

**Tuesday
1:15PM - 2:51PM**

Washington Marriott Wardman Park, Maryland A/B/C

**10E-PARALLEL PAPER SESSION: Pediatric CNS: Vascular Techniques
O-211**

1:15PM - 1:23PM

Plural-contrast 3D multi-echo GRE for TOF MR angiogram of the Pediatric Brain.

B Lanzman¹, S Holdsworth¹, M Iv¹, K Yeom²

¹Stanford University Medical Center, Stanford, CA, ²Lucile Packard Children's Hospital, Palo Alto, CA

Purpose

T2* imaging often is used for clinical brain magnetic resonance imaging (MRI). 3D multi-echo GRE (ME-GRE) is a type of T2* technique that can generate multiple (or 'plural') tissue contrasts from a single sequence (1-3), including a susceptibility-weighted image (SWI), R2*map, local field map, and quantitative susceptibility map (QSM). Additionally, time-of-flight angiogram (pTOF) can be generated from 3D ME-GRE. We sought to assess clinical performance of pTOF versus conventional TOF-MRA.

Materials and Methods

We retrospectively identified 80 consecutive children (ages 0.01-17 years) presenting for 3T brain magnetic resonance imaging (MRI) who obtained both pTOF and TOF-MRA. 3D ME-GRE used six echoes with a TE ranging from 4.3 ms -37.ms, TR = 40.8 ms (5.44 min). The pTOF images were produced from maximum intensity projection over the first echo. Two neuroradiologists independently and blindly reviewed each image (pTOF and TOF-MRA) and assessed for vascular lesion. Additionally, the readers scored for two categories: lesion conspicuity and diagnostic confidence, using a 5-point Likert scale.

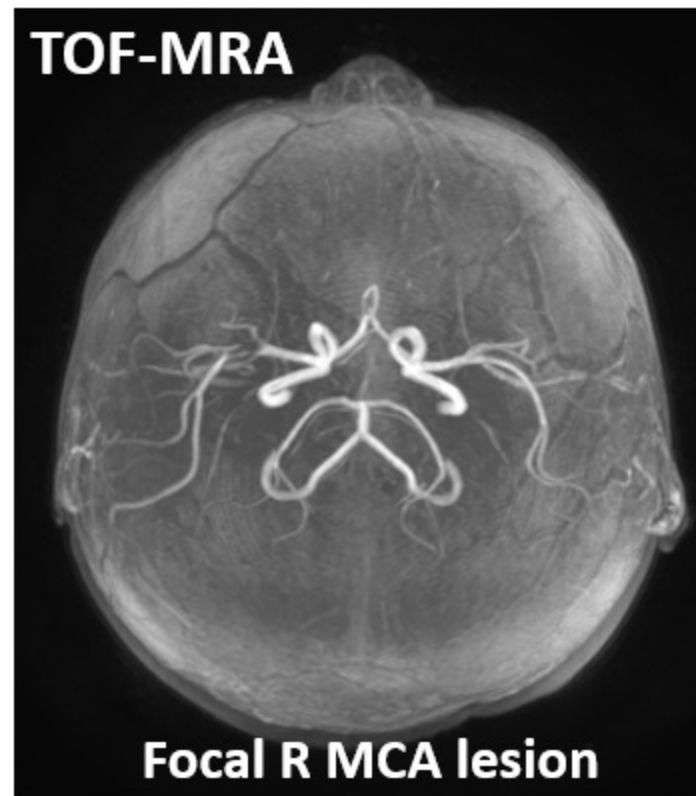
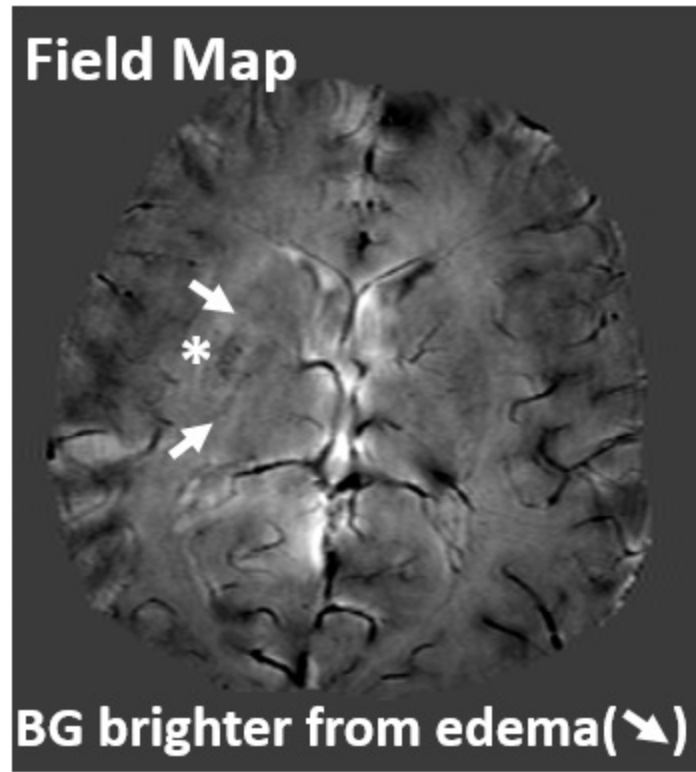
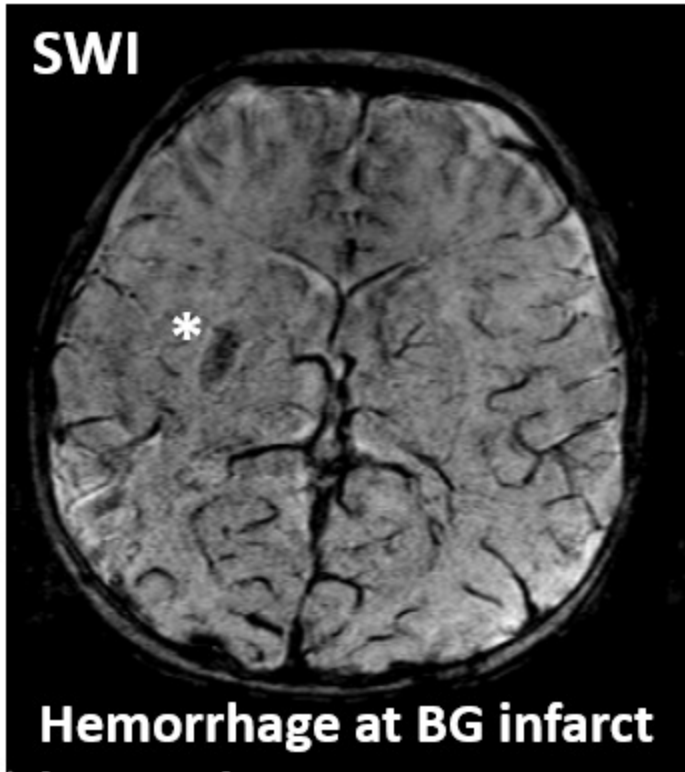
Results

Thirty-two children had vascular pathology (moyamoya disease, vascular dysplasia, AVM, and aneurysm). The readers were in substantial agreement for the specific ratings between the sequences (kappa: lesion conspicuity 0.66; diagnostic confidence 0.71). Sample pTOF and TOF-MRA are shown in Figure 1. For lesion conspicuity, the scores did not differ statistically between pTOF and TOF-MRA. For diagnostic confidence, the readers rated TOF-MRA significantly higher than pTOF. The readers were in perfect agreement (kappa = 0.98) for lesion count. Significantly more lesions were found on pTOF versus TOF-MRA (43% of patients versus 40%, respectively, p = 0.005).

Conclusions

This is the first study to show potential clinical utility of pTOF angiogram generated

from a 3D ME-GRE technique. Our results suggest pTOF may be a suitable alternative MR angiogram method without incurring additional scan time when 3D ME-GRE is performed for clinical T2* imaging.



(Filename: TCT_O-211_Figure1.jpg)

3T MRA Cavernous ICA Segment Anatomy

D Davidson¹, M Whitehead²

¹*George Washington University Hospital, Washington, DC*, ²*Children's National Medical Center, Washington, DC*

Purpose

3T time-of-flight (TOF) magnetic resonance angiography (MRA) is a sensitive technique for detection of normal arterial branch vessels not visible at lower field strengths. It is important that origin of normal cavernous ICA branches not be confused with vasculopathy or aneurysms. The purpose of this study is to evaluate number, size, and course of normal cavernous internal carotid segment branch vessels using 3D TOF MRA at 3T.

Materials and Methods

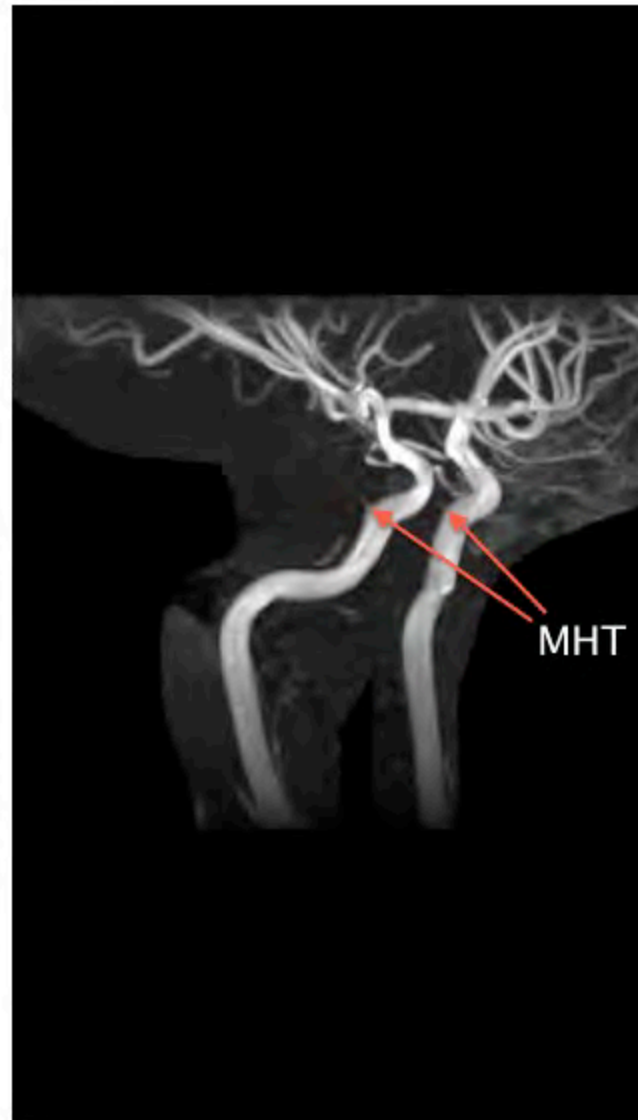
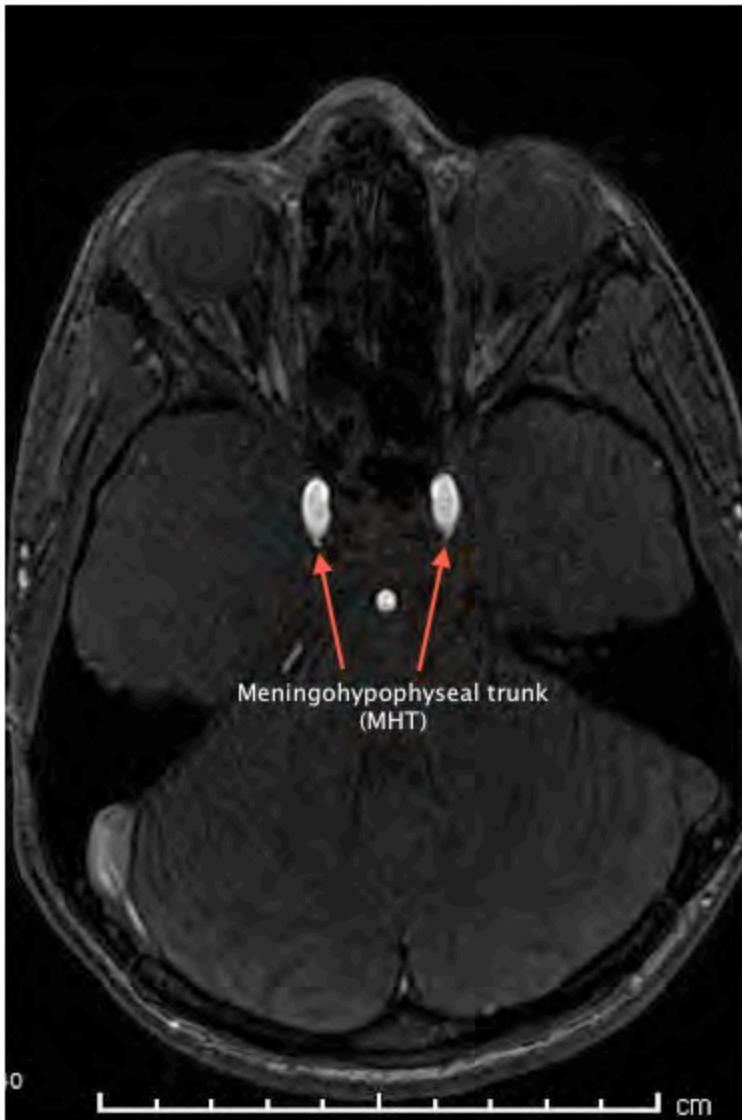
One hundred seventy-five consecutive MRAs from different patients performed over a 2-year period were reviewed. Motion artifact, incomplete coverage, vascular and brain abnormalities were exclusion criteria. Cavernous ICA segments were assessed for the presence of branch vessels. Each ICA was evaluated separately to tabulate unilateral and total ICA vessel scores weighted by conspicuity. Kruskal-Wallis and Student's t-test were performed when appropriate to assess the association between variables; Spearman's rank coefficients were used to evaluate correlations. P values < 0.05 were considered significant.

Results

One hundred six exams met inclusion criteria (60 female, 46 male; mean 9.6 +/- 5.6 years, range 3 days to 20 years). Right and left inferolateral trunk origins were visible in 22% and 26%; right and left meningohypophyseal trunk origins were visible in 63% and 59%. No other cavernous ICA branch vessels were detectable. Age and score were positively correlated (p=0.02). Right- and left-sided scores were not significantly different (p=0.61).

Conclusions

Normal inferolateral and meningohypophyseal arteries commonly are visible on 3D TOF MRA at 3T. It is important that the origin of these vessels not be mistaken for aneurysms.



(Filename: TCT_O-212_MRAcavernousMHT.jpg)

O-213

1:31PM - 1:39PM

Normal Quantitative Luminal Metrics of the Major Intracranial Arteries in Infants, Children, & Young Adults

M Chang¹, L Linscott¹, T Abruzzo¹

¹*Cincinnati Children's Hospital Medical Center, Cincinnati, OH*

Purpose

To establish the normal range of quantitative luminal metrics for the major cerebral

arteries in the pediatric population, across different age groups from infancy to young adulthood.

Materials and Methods

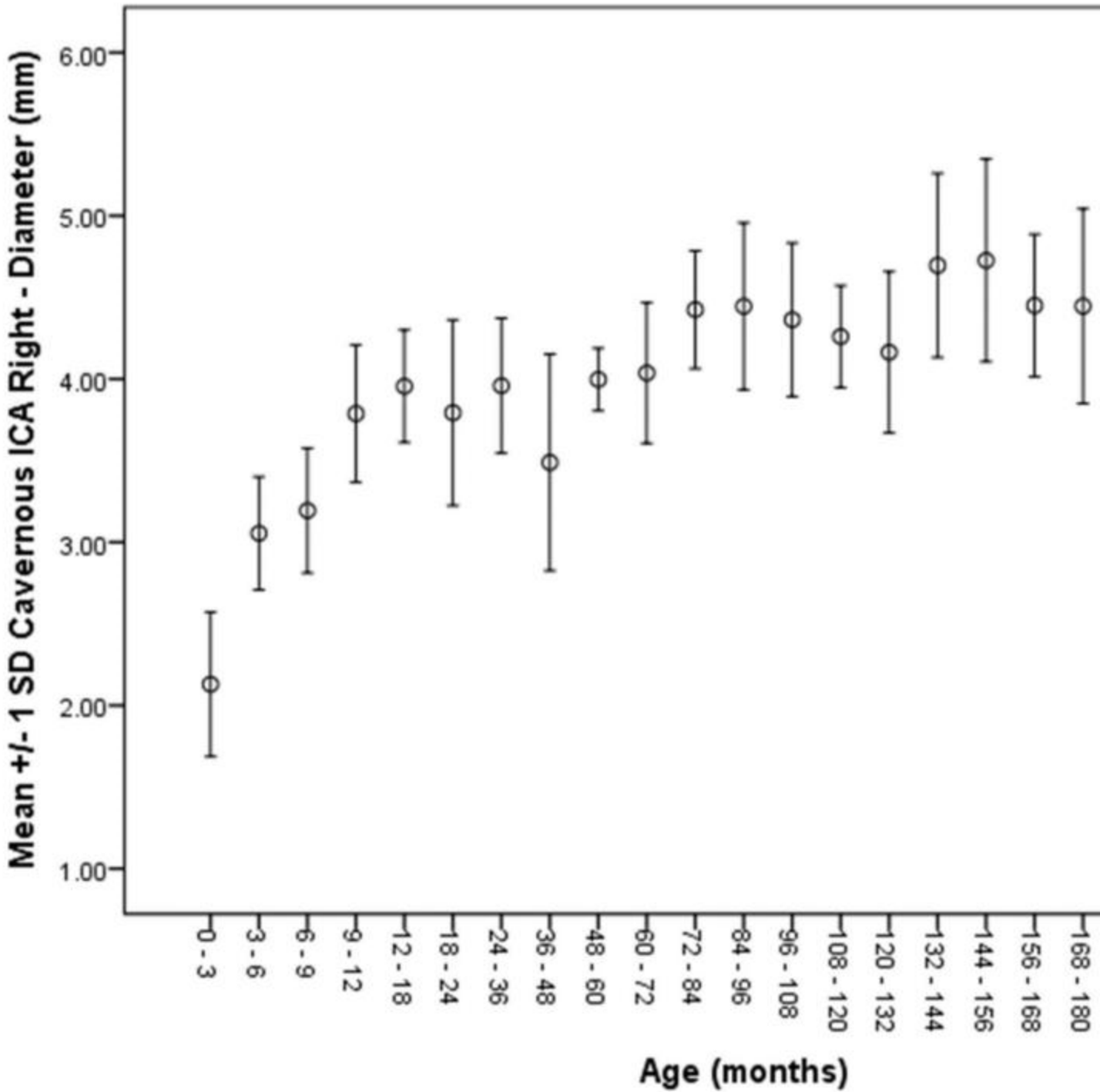
The radiology database of a large tertiary care children's hospital was queried for patients 18 years or younger with normal brain MRI performed for indications of seizure, headache, or hearing loss from January 2010 to May 2015. Axial and coronal T2-weighted fast spin-echo (FSE) images were analyzed to determine the luminal diameter of the major intracranial arteries (cavernous and communicating segments of internal carotid artery (ICA), M1, basilar artery). Measurements were made perpendicular to the long axis of each index vessel. Imaging was performed at 1.5T or 3T magnetic field strength with a slice thickness of 3 mm and 0 mm gap. Cases were classified into 23 age groups ranging from 3 months of life to 18 years. The mean and standard deviation of each metric were calculated for each age group.

Results

Three hundred eighteen patients (147 males, mean age: 99 months) met study criteria. No less than 10 cases were evaluated in each age group. Luminal diameter shows moderate variability (mean variability: 23%; range: 10-42%) in each age group, and demonstrates a marked increase during the first 18 months of life. The growth curve for the cavernous segment of the ICA is provided as an example (Fig.). Luminal diameter shows a small increase between 18 months and 12 years of life, and plateaus thereafter.

Conclusions

Quantitative luminal metrics of the major cerebral arteries, as assessed by magnetic resonance imaging (MRI), demonstrate a relatively predictable growth trajectory in normal children, which closely approximates previously reported head circumference growth reported by the WHO (1). Magnetic resonance imaging criteria for quantitative luminal metrics should be evaluated as a biomarker for pediatric cerebral arteriopathies.



(Filename: TCT_O-213_ASNRgraphcropped.jpg)

O-214

1:39PM - 1:47PM

Improved Visualization of Pediatric Brain Arteriovenous Malformations Using High-Resolution Vascular MRI and Blood Pool Agent (Ferumoxytol)

M Iv¹, O Choudhri², R Dodd³, S Vasanawala¹, M Alley¹, m moseley⁴, S Cheshier⁵, S Holdsworth¹, K Yeom⁵

¹Stanford University Medical Center, Stanford, CA, ²University of California San Francisco, San Francisco, CA, ³Stanford University, Stanford, CA, ⁴stanford, Stanford, CA, ⁵Lucile Packard Children's Hospital, Palo Alto, CA

Purpose

Ferumoxytol, an ultrasmall superparamagnetic iron oxide nanoparticle, has been used widely as a blood pool contrast agent in MR angiography with most applications described in adults outside of the central nervous system (1-4). In this study, we compare ferumoxytol-enhanced high-resolution vascular magnetic resonance imaging (MRI) with time-of-flight (TOF) angiography and the gold standard, digital subtraction angiography (DSA), for the visualization and grading of brain arteriovenous malformations (AVMs) in children.

Materials and Methods

In this IRB-approved retrospective study, we identified 16 children with a diagnosis of brain AVM who had MRI and DSA between April 2014 and June 2015. Magnetic resonance imaging included time-of-flight (TOF) angiography and post-ferumoxytol 3D T1-weighted SPGR sequence using minimum repetition time (TR) and echo time (TE) (Fig. 1). Three experienced raters (two neurointerventionalists and one board-certified diagnostic neuroradiologist) graded AVMs using Spetzler-Martin criteria (5) and assessed for peri-nidal aneurysms on TOF, SPGR, and DSA. Lesion conspicuity (LC), diagnostic confidence (DC), and diagnostic confidence to treat (DCT) were assessed with a 5-point Likert scale. Inter-rater reliability also was calculated.

Results

The distribution and percentages of AVMs assigned each Spetzler-Martin grade were similar between SPGR and DSA in contrast to TOF (Fig. 2). Kappa agreement between readers in assigning grades for DSA, SPGR, and TOF was 0.72, 0.48, and -0.18, respectively. Using a 5-point Likert scale, scores for LC, DC, and DCT based on imaging appearance of AVMs were significantly higher with SPGR (with scores closer to those obtained with DSA) than with TOF across all readers ($p < 0.001$). Amongst all readers, no peri-nidal aneurysms were identified on either SPGR or TOF. However, all readers detected a 4 mm intranidal aneurysm in one subject on DSA.

Conclusions

Ferumoxytol-enhanced high-resolution vascular MRI improves visualization over TOF and yields accurate grading of brain AVMs in children.

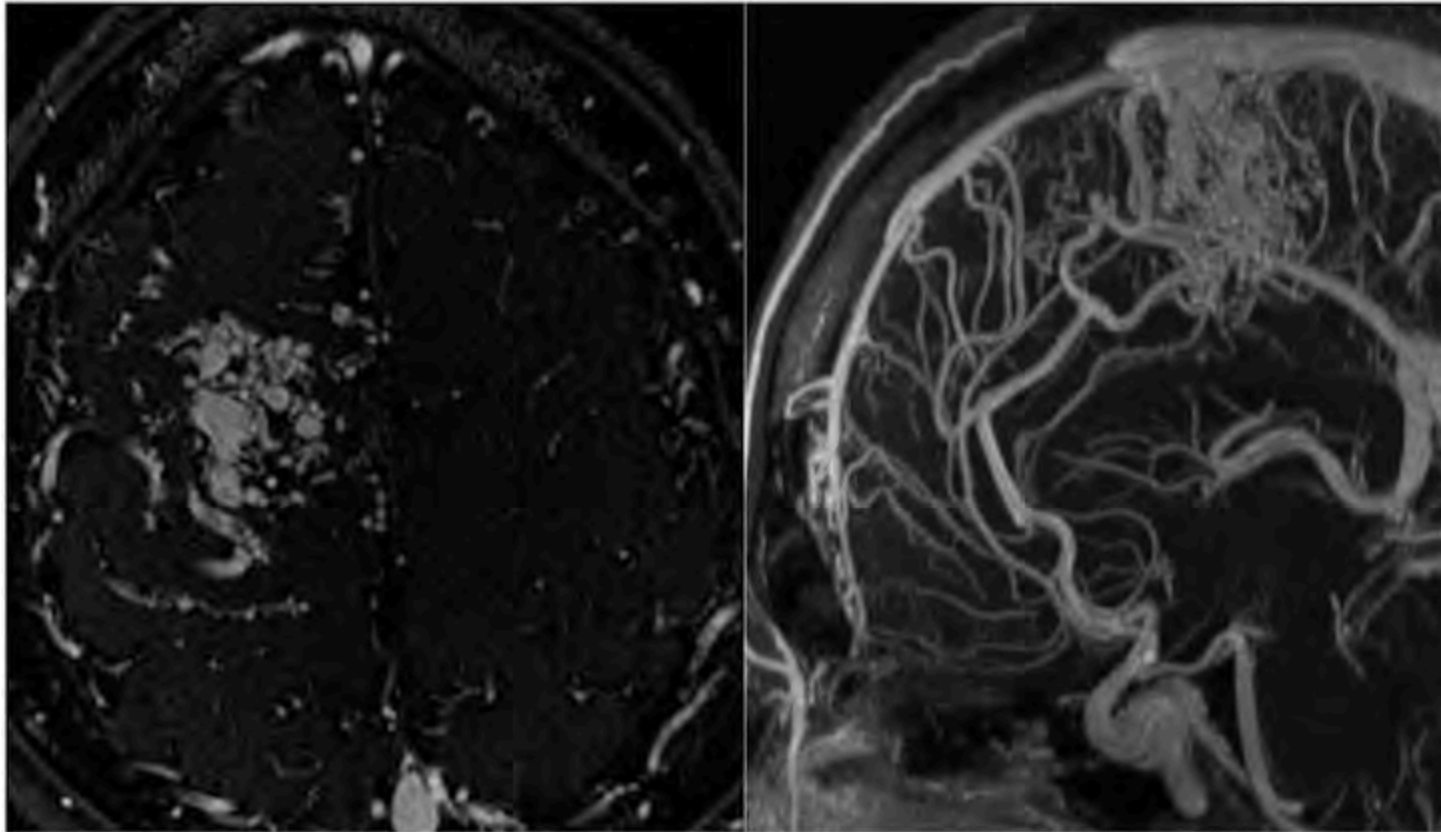


Figure 1

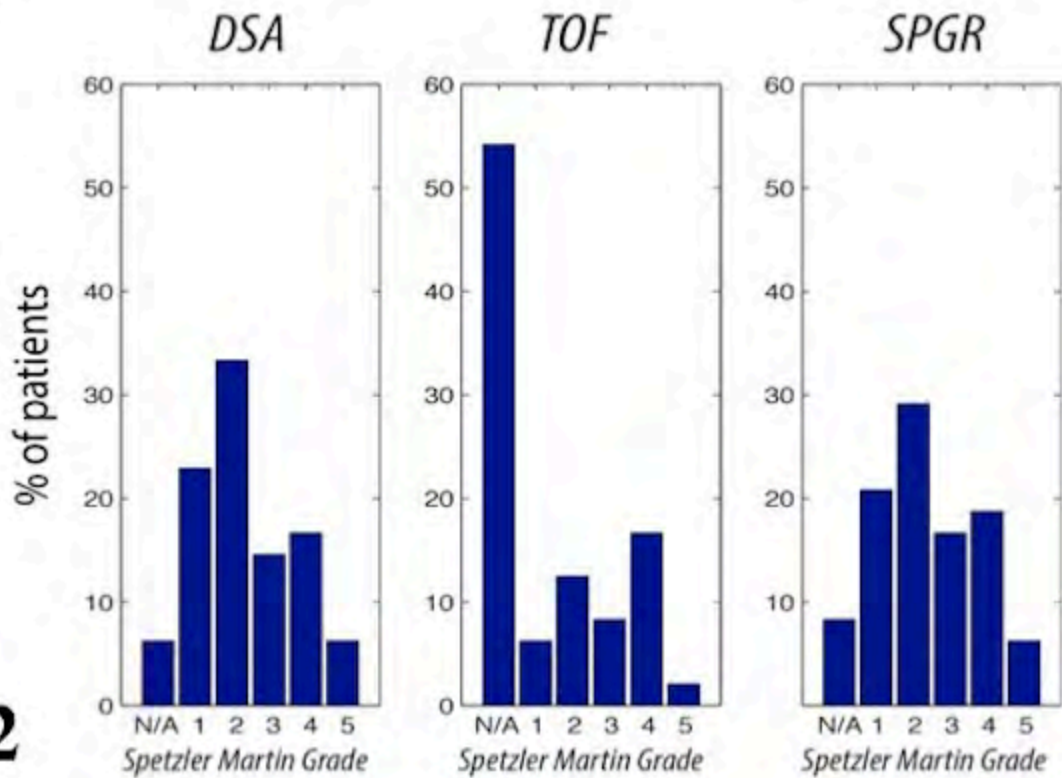


Figure 2

(Filename: TCT_O-214_AVM_graphic_file.jpg)

O-215

1:47PM - 1:55PM

Pediatric Acetazolamide Perfusion Challenge Using Magnetic Resonance Arterial Spin Labeling Perfusion with and without Sedation.

A McAllister¹, J Leach¹, L Linscott¹, M Sjoblom¹, S Vadivelu¹

¹*Cincinnati Children's Hospital Medical Center, Cincinnati, OH*

Purpose

To describe our initial clinical experience with the acetazolamide (ACZ) challenge using arterial spin labeling (ASL) perfusion in pediatric patients to investigate cerebral vascular reserve without and with sedation. Evaluating cerebral vascular reserve is an essential part of the workup for cerebrovascular steno-occlusive disease, particularly in cases of bilateral disease, and potentially direct future revascularization procedures. Acetazolamide challenge is a well known method of determining cerebral vascular reserve in adults typically coupled with nuclear medicine perfusion techniques, computed tomography (CT) perfusion, magnetic resonance imaging (MRI) perfusion, or xenon CT (1). Radiation exposure and time requirements (i.e., most of these methods require the study be performed at two separate times, usually on two separate days) may be considered key impediments in pediatric practice. Limited data are available on the use of ASL perfusion in a quantitative fashion in children (2). Second, there is no data on the effects of sedation on the ACZ challenge, which often is required in pediatric patients.

Materials and Methods

A retrospective review of our clinical experience with ACZ challenge using MRI ASL perfusion performed between 2012 and 2015. Cases performed both with and without sedation were included. Clinically implemented PCASL ASL technique was used, using 1025 ms PLD, and 4mm slice thickness for whole brain coverage. Identical baseline and post ACZ ASL sequences were obtained (20 minutes after 14 mg/mg ACZ infusion). Standardized regions of interest were placed in each hemisphere and changes in cerebral blood flow (CBF) in each region calculated using clinically available software.

Results

A total of 15 MRI ASL ACZ perfusion studies were performed on 10 patients (ages 3-17 years, mean 9 year). Five patients had follow-up examinations. Five examinations were performed under sedation, two with dexmedetomidine and three with propofol. Seven patients had unilateral (4) or bilateral (3) ICA stenocclusive disease. Other indications were: marked arterial tortuosity, large DVA, and prior MCA infarct with residual MCA stenosis. Six subjects were classified as having abnormal responses

(<15% increase in CBF in > one ROI, 2 bilateral), three subjects had normal but asymmetric responses, one had normal symmetric response. Mean CBF increases in ROIs of between 13% and 102% (mean 42%) were noted in hemispheres with normal vascular supply, compared with -11% to 99% (mean 27%) in hemispheres with abnormal vascular supply. Mean CBF increases were similar in patients under sedation (50% in hemispheres with normal vasculature, 26% in hemispheres with abnormal vasculature) as those awake (38% and 24% respectively). Three patients underwent revascularization procedures (2 bilateral) partly on the basis of individual acetazolamide study results.

Conclusions

Acetazolamide challenge using ASL perfusion can be performed successfully in the pediatric population to evaluate cerebral vascular reserve with or without sedation.

O-216

1:55PM - 2:03PM

Assessment of Arterial Spin Labeling (ASL) Sequence in the Pediatric Population Presenting with Hemiplegic Migraines.

M Yasrebi¹, V Kandula², Y Akyol³, N Jambhekar⁴, A Choudhary⁵

¹AI DuPont Hospital for Children/Nemours, Wilmington, DE, ²AI duPont Hospital for Children/Nemours, Wilmington, DE, ³Thomas Jefferson University Hospital, Philadelphia, PA, ⁴New Jersey Medical School, Newark, NJ, ⁵AI duPont Hospital for Children/Nemours, Wilmington, DE

Purpose

Hemiplegic migraine typically is a clinical diagnosis. Arterial spin labeling (ASL) is a magnetic resonance (MR) perfusion imaging sequence which is noninvasive and does not require contrast. The aim of this study is to investigate the efficacy of the ASL sequence in diagnosing hemiplegic migraines in the pediatric population.

Materials and Methods

IRB approval was obtained. From 4/2012 to 5/2015, 23 MRI brain exams (8 Males, 15 Females, Mean age: 13.7 years) with ASL sequences were conducted at AI duPont Hospital for Children in patients presenting with hemiplegic migraines. The ASL sequences were assessed for hyperperfusion, hypoperfusion, versus normal perfusion, particularly focusing on the area of intracranial concern.

Results

On the ASL sequences, 17/23 cases demonstrated hyperperfusion in the area of intracranial concern within 18.6 hours of clinical symptoms (Range: 4 hours-72 hours), 3/23 demonstrated hypoperfusion in the area of intracranial concern within 7 hours of clinical symptoms (Range: 4 hours-11 hours), and 3/23 studies demonstrated no areas of hyper/hypoperfusion in the area of intracranial concern on ASL sequences

within 241 hours of clinical symptoms (Range: 4 hours- 20 days). The remainder of the sequences, including the diffusion-weight imaging (DWI), demonstrated no abnormalities.

Conclusions

Preliminary data suggest that when evaluating ASL sequences in the pediatric population presenting with hemiplegic migraines that the radiologist should search for areas of hypoperfusion in the area of intracranial concern during the acute setting and for areas of hyperperfusion in the area of intracranial concern during the subacute setting. Arterial spin labeling sequences should be considered as a sequence to be used for patients with hemiplegic migraines.

O-437

2:03PM - 2:11PM

Evidence Based Imaging in Pediatrics: the Yield of MR Imaging in Investigating Isolated Pediatric Nystagmus.

V Batmanabane¹, E Heon¹, T Dai¹, P Muthusami¹, A Reginald¹, M Shroff¹

¹*The Hospital for Sick Children, Toronto, Ontario*

Purpose

1. To assess the yield of magnetic resonance imaging (MRI) in isolated pediatric nystagmus. 2. To define a management algorithm to minimize avoidable MRI referrals and to streamline MRI protocols.

Materials and Methods

Chart review of 148 children who underwent neuro MR imaging for isolated nystagmus between January 2008 and September 2014 was conducted. Age at onset of nystagmus, clinical characteristics such as nystagmus direction and symmetry also were noted and compared with the MRI features and visual electrophysiology (VE) results.

Results

Eighty-five boys and 63 girls (average age at MR imaging 4.24 ± 4.19 years) were included. Only 10 (6.75%) children had medically significant intracranial findings on MRI that was responsible for or related to the nystagmus which included optic pathway glioma (2.02%; n=3), and Chiari I malformations associated with end-gaze nystagmus (2.02%; n=3). The time of onset of nystagmus was found to be a weak predictor of abnormal MRI (p=0.07). Seventy patients underwent VE testing but this test could not predict abnormality in MRI (p=0.51).

Conclusions

Less than 7% of children with isolated nystagmus have significant findings on MRI, but neither the clinical characteristics of nystagmus nor the VE results allow prediction of intracranial pathology. We were unable to formulate a management

algorithm for the optimal sequence of investigations (MRI preceding VE or vice versa) but suggest a limited sequence protocol for MRI study of isolated pediatric nystagmus to optimise resource utilization.

Table 1. Abnormal intracranial MR imaging findings of children with isolated nystagmus

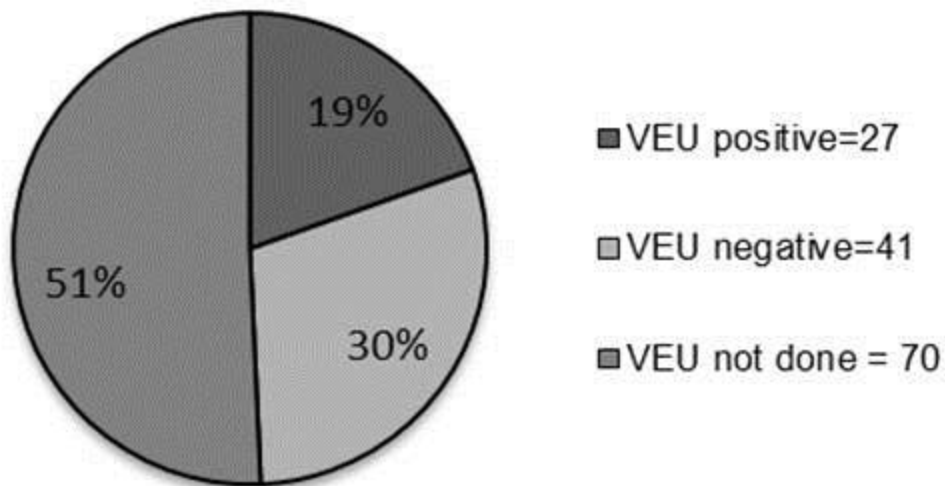
| Abnormal MRI^a | Cases N=10 | Percentage^b (%) (6.75%) |
|---------------------------------|-----------------------|---|
| Astrocytoma | 1 | 0.67% |
| Optic pathway glioma | 2 | 1.35% |
| Chiari I malformation | 3 | 2.02% |
| Optic nerve atrophy | 1 | 0.67% |
| Septo-optic dysplasia | 1 | 0.67% |
| Diffuse hypomyelination | 1 | 0.67% |
| Periventricular leukomalacia | 1 | 0.67% |

a-refers to those with medically significant intracranial findings on MRI that was responsible for or related to the nystagmus.

b-refers to percentage of the total included patients (n=148).

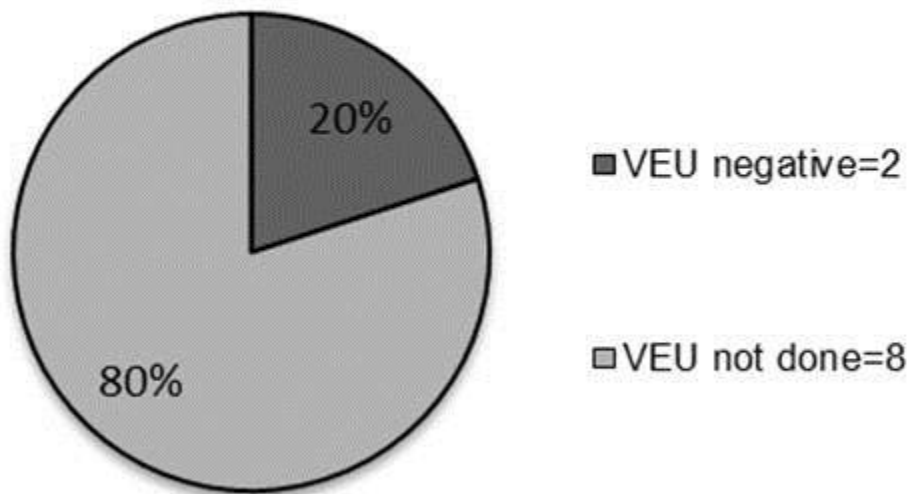
(Filename: TCT_O-437_MRInys.jpg)

Normal MRI^a (n= 138)



(Filename: TCT_O-437_fig1a.JPG)

Abnormal MRI (n=10)



(Filename: TCT_O-437_fig1b.JPG)

O-219

Aberrant Regional Cerebral Cortical Blood Flow Following Preterm Birth

M Bouyssi-Kobar¹, M Brossard-Racine¹, J Murnick¹, C Loucas¹, T Chang¹, C Limperopoulos¹

¹Children's National Health System, Washington, DC

Purpose

The role of altered perfusion on emerging cerebral cortical networks important for socio-cognitive development in very preterm (VPT) infants currently is unknown. The aim of this study was to compare regional cerebral cortical perfusion in VPT infants with/without parenchymal brain injury (BI) at term-equivalent age (TEA)] with healthy full-term (FT) newborns.

Materials and Methods

We prospectively enrolled 155 VPT infants [gestational age (GA) at birth <32 weeks; birthweight <1500 g] and 40 healthy FT controls. We performed unsedated 3T brain magnetic resonance imaging (MRI) studies and acquired a 3mm pseudocontinuous arterial spin labeling sequence. We quantified cerebral blood flow (CBF) using neonatal specific parameters (units=mL/100g/min; software=Functool) and coregistered the anatomical T2-weighted images to the CBF maps (software=IRTK). Regions of interest included right/left: medial/dorsal prefrontal cortex (mPFC, dPFC), anterior/posterior cingulate cortex (ACC, PCC), insular cortex, perirolandic cortex (PRC), posterior parietal cortex (PPC), and hippocampus (Fig. 1). We compared regional relative CBF for each cortical area (regional CBF/global CBF) controlling for GA at MRI.

Results

Fifty-seven VPT infants had parenchymal BI and 58 had a normal MRI [noBI] (Table 1). Global cerebral perfusion was the highest in VPT infants without BI (global CBF=20.7±3.9), followed by VPT infants with BI (global CBF=17.6±3.6); and FT newborns have the lowest global CBF (global CBF=12.9±2.7) (All p<.05). Relative regional cerebral cortical CBF was decreased significantly in the mPFC, ACC, insula, and hippocampus; and significantly increased in the PRC of VPT infants with/without BI compared to FT controls (Fig. 2).

Conclusions

We report for the first time altered regional CBF patterns in VPT infants, in a number of cortical areas that are an integral part of the salience network (ACC; insula) and default-mode network (mPFC; hippocampus) known to mediate socio-cognitive processing. These data suggest early aberrant maturation of the neurocognitive networks involved in higher-order cognitive skills in VPT infants by TEA. These novel findings offer promising avenue towards implementing early imaging biomarkers of impaired cerebral cortical development. The impact of altered cerebral

cortical perfusion on socio-cognitive disturbances in surviving VPT infants currently is under investigation.

Table 1. Clinical characteristics of the cohort.

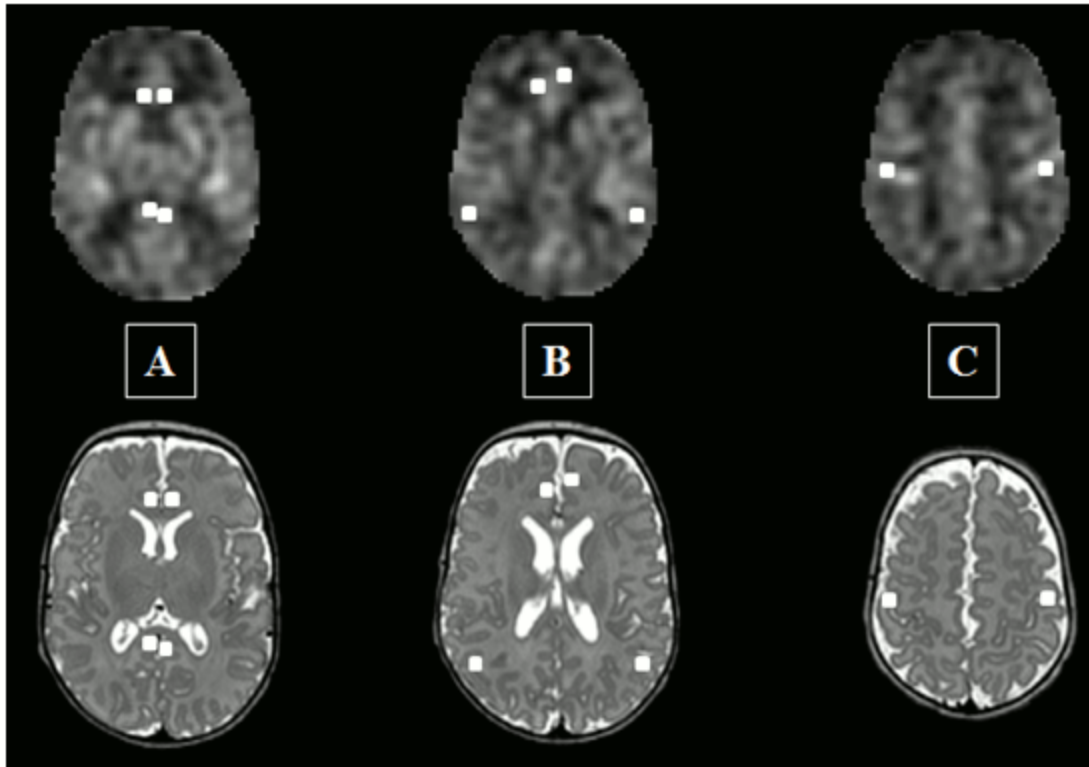
| | VPT-BI N=57 | VPT-noBI N=58 | FT contro N=40 |
|--------------------------------------|------------------------|--------------------------|---------------------------|
| Birth GA (weeks), means±SD | 25.8 ± 2.6 | 27.3 ± 2.5 | 39.5 ± 1.1 |
| Birthweight (grams), means±SD | 823 ± 306 | 902 ± 293 | 3327 ± 390 |
| Vaginal delivery, n (%) | 25 (45%) | 21 (36%) | 30 (75%) |
| Female gender, n (%) | 28 (49%) | 31 (54%) | 21 (52%) |
| Apgar 5 min, median [range] | 7 [1-9] | 8 [8-9] | 9 [8-9] |
| GA at MRI (weeks), means±SD | 40.3 ± 1.5 | 40.3 ± 1.7 | 41.3 ± 1.2 |

^: Between groups: All p-value <.05

#: Between groups: p-value (VPT-noBI vs. FT) <.05 and p-value (VPT-BI vs. FT) <.05

(Filename: TCT_O-219_mbouyssi-kobar_abstract_1527_table1_300dpi.GIF)

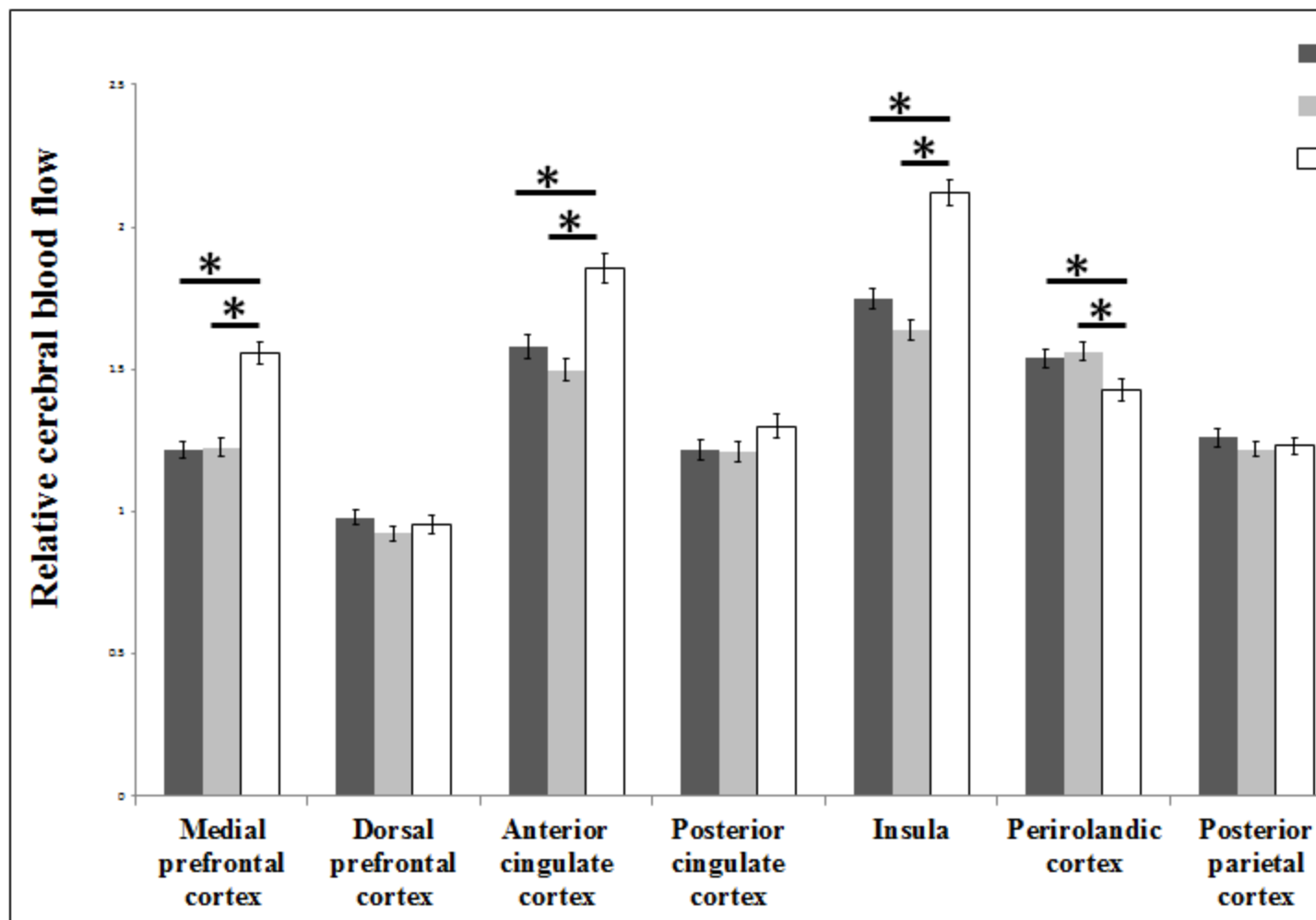
Figure 1. Cerebral cortical regions of interest overlaid on cerebral blood flow map (top row) and aligned anatomical T2-weighted image (bottom row).



A: Anterior and posterior cingulate cortex. B: Medial prefrontal cortex and posterior parietal cortex.
C: Perirolandic cortex.

(Filename: TCT_O-219_mbouyssi-kobar_abstract_1527_figure1_300dpi.GIF)

Figure 2. Regional cerebral cortical perfusion relative to global brain perfusion



(Filename: TCT_O-219_mbouyssi-kobar_abstract_1527_figure2_300dpi.GIF)

O-220

2:27PM - 2:35PM

Impaired Preoperative Brain Metabolism in Newborns with Congenital Heart Disease

M Wien¹, G Vezina¹, J De Asis-Cruz¹, S Bauer¹, D Lanham¹, C Limperopoulos¹
¹Children's National Health System, Washington, DC

Purpose

Neonates with congenital heart disease (CHD) are at increased risk of neurological deficits. Recent studies have demonstrated that CHD neonates have extensive structural and metabolic brain abnormalities that precede surgical correction. The aim of our study was to compare brain metabolic profiles in a cohort of term neonates with

congenital heart disease and healthy controls using quantitative proton magnetic resonance spectroscopy (1H-MRS).

Materials and Methods

We prospectively evaluated a cohort of CHD and healthy control newborns using single voxel 1H-MRS. Patients with suspected CHD were recruited as part of a larger research protocol at the time of prenatal imaging. Those with confirmed fetal CHD (by fetal echocardiogram) were recruited as cases while those with normal fetal echocardiograms were recruited as controls. We performed single voxel MRS using the point resolved spectroscopy (PRESS) technique obtained with a region of interest in the basal ganglia and thalamus. Quantitative analysis of spectroscopy data was processed retrospectively using LCModel. We specifically quantified ratios of metabolites: N-acetylaspartate (NAA), Creatine (Cr), Choline (Cho), [tNAA/tCr, tNAA/tCho, tCr/tCho, and tCho/tCr] as well as the presence of lactate (marker of anaerobic metabolism). Lactate was processed using predetermined criteria for percent certainty. Clinical data were obtained from the electronic medical record and correlation with spectroscopy data were made. ANCOVA analyses were used to evaluate the differences in tNAA/tCho, tNAA/tCr, and tCr/tCho between the two groups relative to gestational age (GA).

Results

We analyzed data from 150 1H-MRS spectra: 73 acquired from neonates diagnosed with CHD (mean GA \pm std: 39.29 \pm 1.32 weeks, range: 36.29-44.71) and 77 obtained from healthy neonates (mean GA \pm std: 41.42 \pm 1.59, range: 36.57-46.43). Of those neonates with CHD, 22/94 (34%) have single ventricle CHD and 59/94 (63%) have cyanotic CHD. Newborns with CHD showed significantly lower tNAA/tCho and tNAA/tCr pre-operatively compared to healthy controls ($p < 0.05$). The ratio of tCr/tCho was not significantly different between the two groups. Lactate was present in 15 neonates, all of which had cyanotic CHD. One third (33%) of neonates with CHD also have structural (intraparenchymal) injury on magnetic resonance imaging (MRI).

Conclusions

Newborns with CHD show decreased concentrations of NAA and increased lactate compared to healthy controls when evaluated with quantitative spectroscopy analysis, suggesting neuronal injury and anaerobic metabolism that precede surgical correction. Aberrant cardiac physiology with hemodynamic impairment likely plays a central role in pre-operative alterations in cerebral metabolism. Our data suggest that quantitative MRS may be useful for studying metabolic profiles in neonates at risk for cerebral hypoxic-ischemic injury prior to cardiac repair.

O-221

2:35PM - 2:43PM

Default Mode Network (DMN) Activation in Children with Sickle Cell Disease (SCD) Using a Word-Stem Paradigm

S Palasis¹, B Sun², C Brown¹, L Hayes², R Jones¹

¹*Children's Healthcare of Atlanta & Emory University School of Medicine, Atlanta, GA*, ²*Children's Healthcare of Atlanta, Atlanta, GA*

Purpose

The purpose of this abstract is to present the findings of our study on default mode network (DMN) activation in children with sickle cell disease (SCD) as compared to normal controls following a word-stem paradigm.

Materials and Methods

The study was performed on a 3T Siemens Trio scanner using the standard head coil. The repetition time was 3 seconds and sufficient slices were acquired to cover the whole brain. This study used a block functional magnetic resonance imaging (fMRI) word-stem paradigm during the activation blocks and a cross-hair during the control blocks. Each block consisted of 10 images (30 seconds) and a total of five control and five activation blocks were acquired for each subject (11 controls, 12 sickle cell patients). There was no significant difference in the ages of the two groups and all the subjects were African-Americans. A T1-weighted anatomical volume was acquired to permit inter-subject registration. The data were processed using FSL 5.06 and contrast masking was used to separate the activation and DMN responses. A spherical region of interest (ROI) was drawn within the area showing statistically significant differences in the DMN deactivation (signal decreases during the activation blocks) between the two groups. This region then was registered to each subject to allow the time course of the signal response to be derived for each subject and hence allow a mean time course to be obtained. The signal from the ROI was fitted to a linear function to estimate the mean signal and this was used to allow an estimation of the percent change in signal.

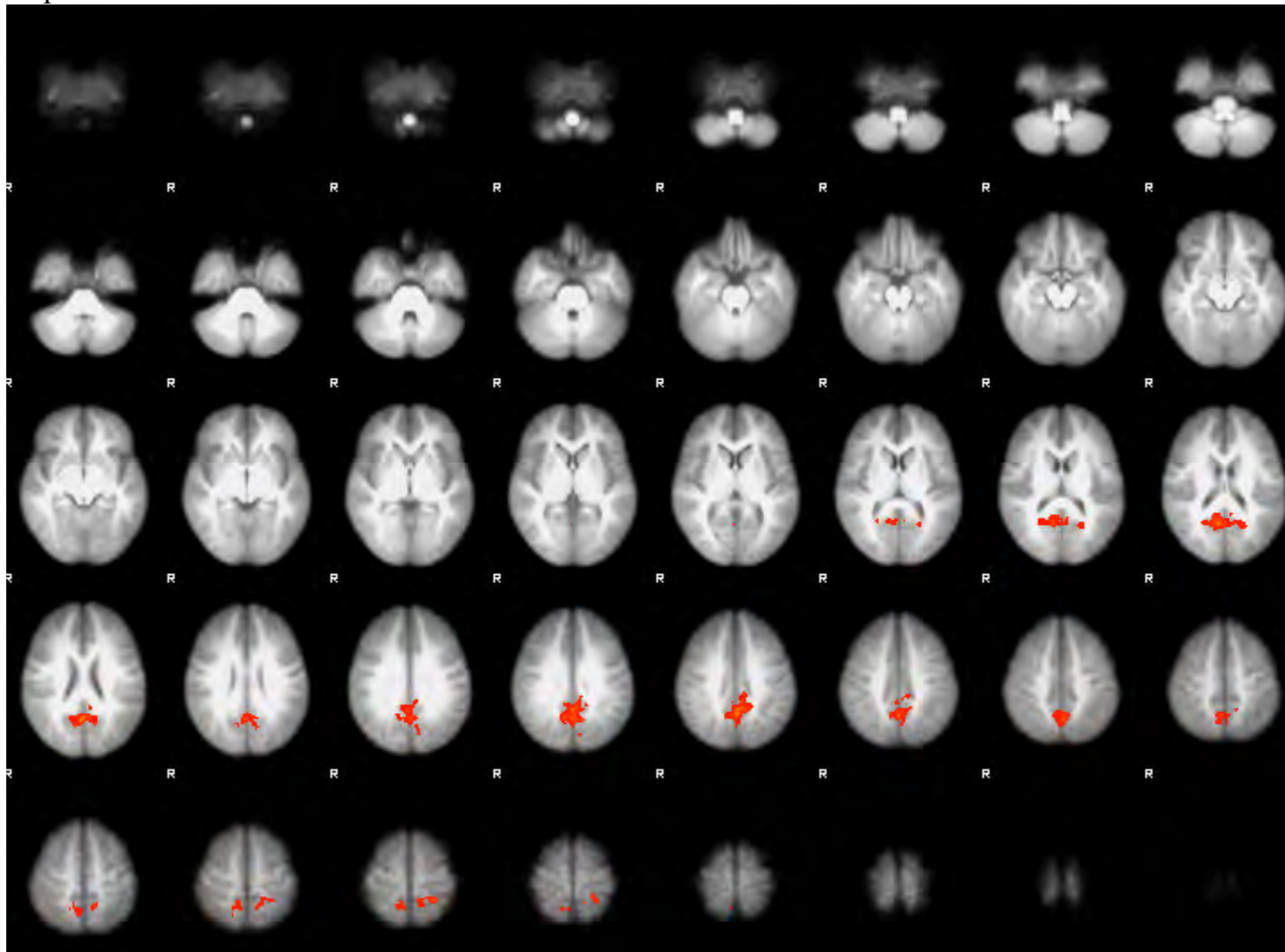
Results

The SCD subjects showed a pattern of less extensive and attenuated activation, however, there was only one small area that was statistically significant between the two groups. For the DMN there was a similar pattern of less extensive and attenuated deactivation, however, there was a prominent area in the precuneus/posterior cingulate gyrus that showed a statistically significant difference between the two groups (Fig. 1). The mean time-course for each of the groups is shown in Figure 2 with the timing of the activation periods shown in orange.

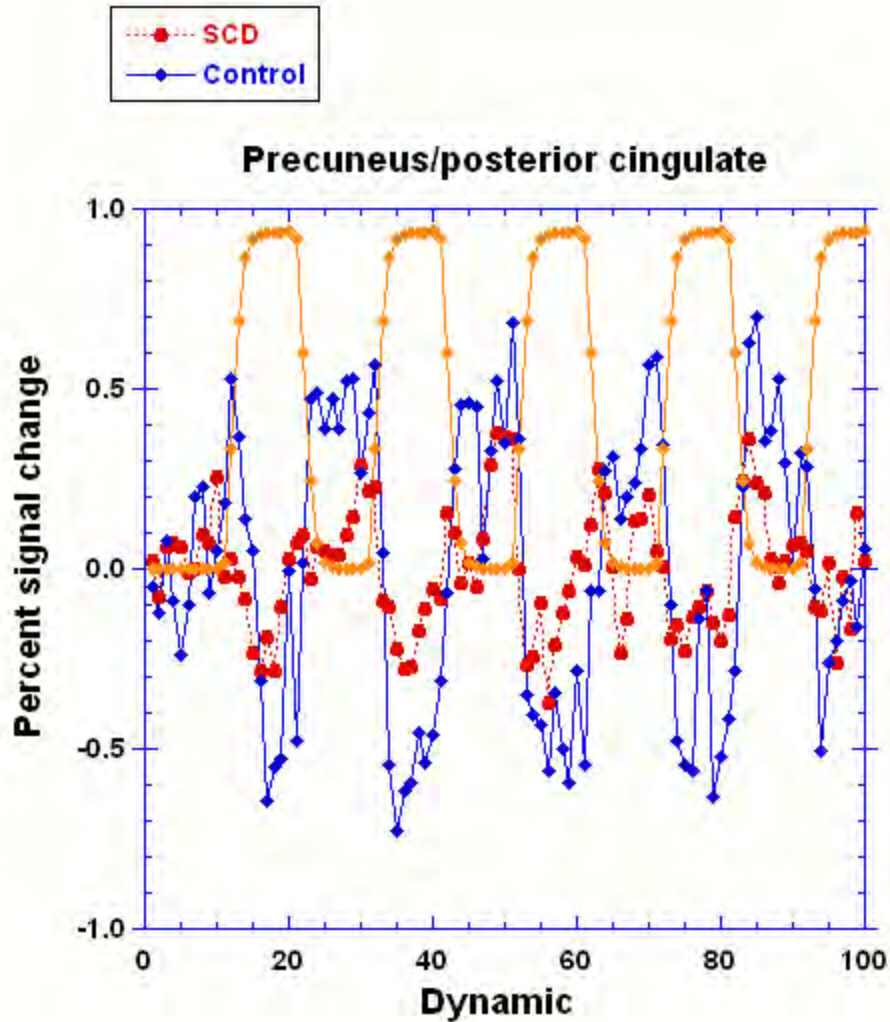
Conclusions

For the control group, compared to the sickle cell subjects, the signal level can be seen to be higher during the rest (cross-hair) periods and with more significant deactivation occurring during the active periods. The DMN deactivation (signal decreases during

the activation blocks) showed a prominent statistically significant area in the precuneus/posterior cingulate in the SCD group as compared to normal controls. We have two hypotheses for the observed difference between the two groups: 1) Differences in the vascular hemodynamics of the two groups, with the higher baseline flow in the SCD group resulting in changes to the hemodynamic response, notably in deoxyhemoglobin levels and/or cerebral blood volume. 2) The precuneus/posterior cingulate have the highest metabolic activity of any area in the brain and it may be that, even with the elevated blood flow levels in SCD patients, the oxygen delivery is insufficient to fully maintain the DMN activity, leading to an attenuated DMN response.



(Filename: TCT_O-221_Figure1.jpg)



(Filename: TCT_O-221_Figure2.JPG)

O-386

2:43PM - 2:51PM

Identification of Novel Gene-Specific Biomaging Markers in Autism Spectrum Disorder

J Gadde¹, J Yu²

¹University of Wisconsin, Madison, WI, ²University of Wisconsin-Madison, Madison, WI

Purpose

To develop novel gene-specific diffusion tensor imaging (DTI) biomarkers in the assessment and characterization of autism spectrum disorder (ASD).

Materials and Methods

Ex vivo imaging methods were used in male rats to examine the structural differences in a *Fmr1* and *Pten* genetic model of ASD (derived from outbred Sprague Dawley rats; $n = 4$) as compared to age-matched male controls (outbred Sprague-Dawley rats; $n = 4$). At PND 45, animals were deeply anesthetized with isoflurane and were transcardially perfused with fresh 4% paraformaldehyde (PFA). Fixed brains were removed and stored in 4% PFA until imaging, whereupon they then were rinsed in 0.9% saline for 48 hours prior to imaging to minimize attenuating effects of fixative on the magnetic resonance imaging (MRI) signal. The brains were placed in a custom-built holder and immersed in Fluorinert (FC-3283, 3M, St. Paul, MN, USA) for image acquisition. For ex vivo diffusion tensor imaging acquisition, brains were simultaneously imaged for ~ 7 h using a 4.7-T Agilent magnetic resonance imaging (MRI) system and 3.5-cm diameter quadrature volume RF coil. A series of multi-slice, diffusion-weighted, spin echo images were acquired with three nonweighted ($b \sim 0$) and 30 diffusion weighted ($b \sim 1200$ s/mm²), using noncolinear weighting directions. Other imaging parameters were TE/TR = 24.17/2000 ms, FOV = 30×30 mm², matrix = 192×192 reconstructed to 256×256 , slice thickness = 0.5 mm, number of slices = 35 and two signal averages. Diffusion tensor imaging maps were created offline using a combination of FSL software and custom MatLab code. Subsequent region of interest (ROI) analysis was performed in the native imaging space. Diffusion tensor imaging values of the corpus callosum (CC) and other principle white matter tracts were performed.

Results

Animals harboring the *Fmr1* and *Pten* deletions demonstrated widespread changes in gray and white matter structure and organization. These include areas of significant change in FA as previously reported in the superior and inferior colliculus, cerebral cortex of the frontal lobe, and in several areas within the deep gray nuclei including the globus pallidus and thalamus. Significant differences between our *Fmr1* and *Pten* genetic models of ASD as compared to wild-type animals also were noted in our region of interest (ROI) analysis including the corpus callosum and several white matter tracts including the medial longitudinal fasciculus, internal capsule, forceps minor, and occipitotemporal tracts.

Conclusions

The etiology of ASD remains elusive. The development of advanced structural and functional MR imaging-based methodologies, including fMRI and DTI, has spurred tremendous interest towards their application in ASD research, especially towards the identification of a neuroimaging biomarker. Our results are the first to demonstrate a truly cogent gene-specific neuroimaging marker in the assessment of ASD on DTI. As further work proceeds with the identification of additional gene-specific DTI neuroimaging markers in other gene-specific knockouts, the collective sum of these

findings will allow for the identification of cogent gene-specific neuroimaging biomarkers, which can contribute to the diagnosis and treatment of ASD.

Tuesday

1:15PM - 2:45PM

Washington Marriott Wardman Park, Roosevelt 4

10F-CSI programming: The Neuroradiology Work Environment

10F1

1:15PM - 1:35PM

Mistakes and How to Avoid Them

Torres, C.
The Ottawa Hospital
Ottawa, Ontario

10F-2

1:35PM - 1:55PM

How to Avoid Interruptions in the Work Place

Yu, J.
University of Wisconsin-Madison
Madison, WI

10F-3

1:55PM - 2:15PM

Structured Reporting

Wiggins, R.
University Of Utah
Salt Lake City, UT

10F-4

2:15PM - 2:35PM

Image Sharing with Patients

Phillips, C.
Weill Med. College Of Cornell/NY Presby'n
New York, NY

10F-5

2:35PM - 2:45PM

Discussion

Tuesday

3:00PM - 4:30PM

Washington Marriott Wardman Park, Marriott Ballroom

**11A-ASFNR Programming: Advanced Neuroimaging Techniques in Brain Tumor:
Current Updates (AR) (SAM)**

11A-1

3:00PM - 3:15PM

Proton MR Spectroscopy

Barker, P.
Johns Hopkins Univ. School Of Medicine
Baltimore, MD

11A-2

3:15PM - 3:35PM

Functional MRI Pre-Treatment Planning for Brain Tumor: Pitfalls and Progress

Welker, K.
Mayo Clinic
Rochester, MN

11A-3

3:35PM - 3:55PM

Perfusion: Treatment Response from Pseudoprogression

Boxerman, J.
Rhode Island Hospital
Providence, RI

11A-4

3:55PM - 4:15PM

Diffusivity and Genomics: Current Thoughts and Metrics

Pope, W.
David Geffen School Of Medicine at UCLA
Los Angeles, CA

11A-5

4:15PM - 4:30PM

Questions and Answers

Tuesday

3:00PM - 4:36PM

Washington Marriott Wardman Park, Washington 4/5/6

**11B-PARALLEL PAPER SESSION-Stroke: Advanced CT and MR Techniques
O-222**

3:00PM - 3:08PM

Combined noncontrast CT (NCCT) ASPECT score and CTA collateral score could predict a small DWI lesion with high specificity.

R Hakimelahi¹, K Buch², T Leslie-Mazwi¹, J Hirsch², G Gonzalez², P Schaefer²
¹Massachusetts general hospital, Boston, MA, ²Massachusetts General Hospital, Boston, MA

Purpose

Small initial diffusion-weighted imaging (DWI) lesion volume is a significant predictor of favorable outcome following intra-arterial (IA) thrombectomy and has been used for patient selection in multiple clinical trials. We sought to investigate if NCCT ASPECT and/or CTA collateral scores could predict a small DWI lesion volume.

Materials and Methods

We identified 135 consecutive patients with initial CTA showing ICA and/or

proximal MCA occlusions who underwent DWI immediately afterward and within 8 hours of stroke symptom onset. Diffusion-weighted imaging lesion volumes were measured and dichotomized to small (≤ 70 ml) and large (> 70 ml). Collateral vessels were categorized into five groups: 0: no collaterals, 1: minimal collaterals, 2: $< 50\%$ of the MCA territory, 3: $> 50\%$, but $< 100\%$ of the MCA territory, 4: = contralateral (CL) MCA vascularity and 5: $> CL$ MCA vascularity. Logistic regression and receiver operating characteristic (ROC) curve analyses were performed to measure predictive value of NCCT ASPECT and CTA collateral scores for a small DWI lesion volume.

Results

Sixty-five of 135 patients were female. Mean (range) were: age 69 (18 - 97) years, NIHSS 17 (8-30), time from stroke onset to MRI 236 (46-480) minutes, DWI volume 53 (0.5 -319) ml, NCCT ASPECT score 8 (1-10) and collateral score 3 (0-5). 97/135 cases had DWI < 70 ml. Age, NIHSS and time to MRI were not significant predictors ($p > 0.05$) of a small DWI volume. Both NCCT ASPECT (OR 2.68, coefficient 0.98, $P < 0.0001$) and collateral scores (OR 2.95, coefficient 1.08, $P < 0.0005$) significantly contribute to prediction of a small DWI lesion. Receiver operating characteristic curve analysis showed AUC of 0.91 (95% CI 0.85 to 0.96). For a specificity $> 80\%$ to predict DWI volume < 70 ccs, different combinations of ASPECT and collateral scores could be used: ASPECT ≥ 7 with collateral score ≥ 3 (specificity 81.6%, sensitivity 79.4%), ASPECT ≥ 8 with collateral score ≥ 2 (specificity 92.1%, sensitivity 75.3%), and ASPECT ≥ 9 with collateral score ≥ 2 (specificity 97.3%, sensitivity 54.6%).

Conclusions

Combined NCCT ASPECT and single phase CTA collateral scores can predict a small DWI lesion volume with high specificity and relatively high sensitivity. This method potentially could be used to help select patients likely to benefit from intra-arterial thrombectomy if MRI is not available.

O-223

3:08PM - 3:16PM

Evaluation of a clinical prototype software for rapid automated display and density measurement of ASPECTS regions on CT images

K Busch¹, L Aulmann¹, P Schramm², A Kemmling²

¹Universitätsklinikum Lübeck, Lübeck, DEUTSCHLAND, ²Universitätsklinikum Lübeck, Lübeck, Germany

Purpose

The Alberta Stroke Program Early CT Score (ASPECTS) is the primary rater-based scoring system for extend of early cerebral infarction. However, interobserver reliability of ASPECTS is limited. We systematically examined a novel imaging

prototype that uses a probabilistic ASPECTS template registered onto individual computed tomography (CT) images to improve rater consistency and provide automated ASPECTS by topographical density measurements.

Materials and Methods

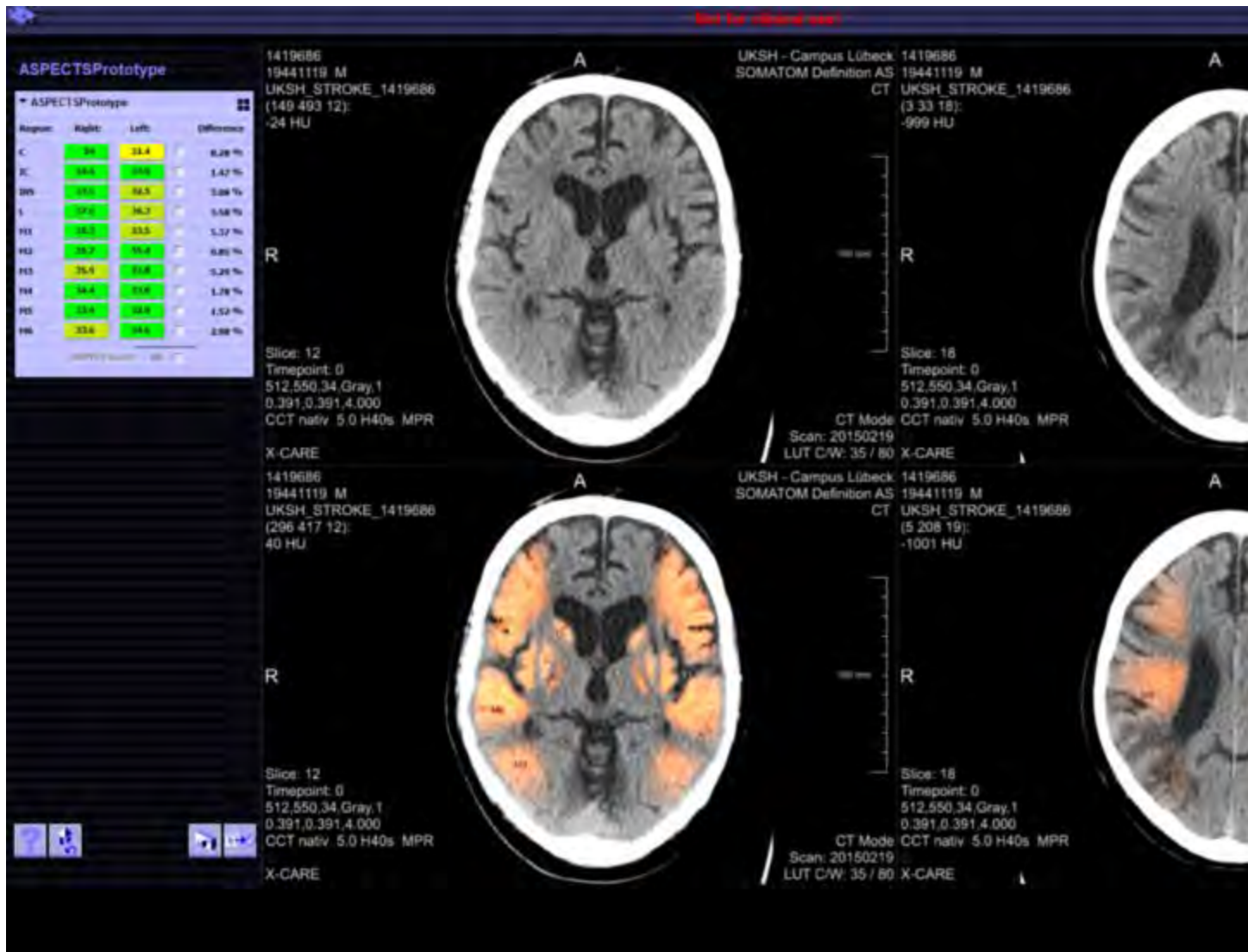
A population based probabilistic ASPECTS atlas was created by manual segmentation of ASPECTS region in 200 cranial CT of healthy subjects followed by affine registration to standard MNI space with nonlinear refinement. The ASPECTS atlas was integrated into a clinical software prototype for automated display and assisted ASPECTS scoring. ASPECTS scoring with and without software-assisted atlas overlay was performed in 99 admission CT images of patients with anterior circulation stroke. Interobserver reliability was evaluated by kappa statistics. Automated ASPECTS scoring was accomplished in every region by logistic regression analysis using atlas-based density measurement and rater-based scores. Performance of Auto-ASPECTS was assessed by area under ROC-curve analysis (AUC).

Results

Interrater reliability of ASPECTS rating was intermediate and improved significantly with display of registered ASPECTS template (kappa 0.72 versus 0.83, respectively), Mean ASPECTS user rating without software assisted atlas overlay was 4.8, with overlay 4.9. Mean Auto-ASPECTS was 5.3 with a root mean squared error of 1.2 from reference score. Discriminative power of Auto-ASPECTS to predict infarct in individual ASPECTS regions was good (ROC AUC range 0.73 to 0.91).

Conclusions

Rapid automated display and overlay of ASPECTS atlas improves interrater reliability of ASPECTS rating in early stroke CT. Automated ASPECTS prediction in CT by atlas based density measurement is reliable. This may help standardize patient stroke triage.



(Filename: TCT_O-223_fig.png)

O-224

3:16PM - 3:24PM

Angiographic Reconstructions From Whole-Brain Perfusion CT for the Detection of Large Vessel Occlusion and Recanalization in Acute Stroke

J Zhang¹

¹Huashan Hospital, Shanghai, -

Purpose

The aim of this study is to assess the value of angiographic thin-slice volume perfusion computed tomography (CT) reconstructions for the detection of intracranial large vessel occlusion and recanalization after receiving intravenous thrombolytic therapy in patients with stroke.

Materials and Methods

Twenty-five patients with acute cerebral infarction treated by recombinant tissue plasminogen activator (rt-PA) were enrolled in this study. They all underwent admission and 24-hour whole-brain perfusion CT. All images were obtained on a 256-slice multidetector CT scanner. Dynamic 3D CT angiographic images (4-dimensional CTA) generated from perfusion source data were obtained in all patients. Images were assessed for the presence of intracranial vessel recanalization. The cerebral hemodynamics changes in distribution of ischemic lesions were analyzed on perfusion parameter maps.

Results

Of 25 patients with an infarct on follow-up imaging, 19 had infarcts in the middle cerebral artery territory, five had infarcts in the posterior cerebral artery territory, and one had an infarct in the internal carotid artery territory. Average image quality scoring of baseline CT angiography (CTA) was the same as one of 24-hours volume perfusion CTA (VPCTA) ($P>0.05$), four cases with middle cerebral artery occlusion and one case with internal carotid artery received partial recanalization on 24-hours VPCTA.

Conclusions

In acute stroke, whole-brain PCT may be an optimal method to evaluate patients for thrombolysis, detect intracranial arterial recanalization of cerebral arteries after receiving intravenous thrombolytic therapy, and have the potential to decrease radiation dose and contrast media by substituting for intracranial CTA in stroke CT.

O-225

3:24PM - 3:32PM

Whole Brain CT Perfusion In Acute Stroke Patients With Mild Neurological Symptoms Identifies Ischemic Events

S Chakraborty¹, R Frank¹, G Stotts²

¹University of Ottawa, The Ottawa Hospital, Ottawa, Ontario, ²The Ottawa Hospital, Ottawa, Ontario

Purpose

More than half of ischemic stroke patients present as minor strokes (NIHSS<6). A lack of thrombolysis guidelines for this population leads to untreated strokes and erroneously treated stroke mimics, producing adverse outcomes. Data suggest that whole brain computed tomography (CT) perfusion (WB-CTP) improves detection of ischemia, offering a potential method of ameliorating diagnostic uncertainty in these patients. HYPOTHESIS: WB-CTP can guide clinical decisions by identifying patients with ischemic episodes that would benefit from thrombolysis or early intervention.

Materials and Methods

This retrospective chart review enrolled 524 consecutive patients receiving WB-CTP with a Toshiba 320 detector scanner, for acute stroke less than 6 hours from onset and NIHSS<6, and who showed no evidence of intracranial hemorrhage. Patients were excluded for nondiagnostic (n=25) or unreported (n=8) scans and nonischemic pathologies (7). For diagnostic accuracy calculations, the reference standard was the final clinical impression suggesting ischemic events during follow up, as only 51% had follow-up imaging. Subgroup analyses were performed in patients receiving follow-up imaging.

Results

A total of 484 patients (age 17-101, 54% men, mean NIHSS 2.48) were included. Follow-up imaging was performed in 249 patients; 148 underwent magnetic resonance imaging (MRI) with diffusion-weighted imaging (DWI). Whole brain CTP is highly specific with a high positive predictive value in all groups and has moderate to high negative predictive value. Positive and negative likelihood ratios were 21.24 and 0.5 in the primary analysis. Diagnostic accuracy of WB-CTP against different reference standards are shown in detail in Table 1.

Conclusions

Positive WB-CTP findings may warrant early intervention, including thrombolysis, while negative findings alone are not a sufficient basis upon which to confidently withhold interventions.

| Reference Standard | Sensitivity (%) | Specificity (%) | PPV (%) | NPV (%) | LR+ | LR- |
|--|-----------------|-----------------|---------|---------|-------|------|
| Clinical Diagnosis: Acute Ischemic Event | 51 | 98 | 98 | 41 | 21.24 | 0.50 |
| F/U Scan | 55 | 91 | 98 | 24 | 6.27 | 0.49 |
| No F/U Scan | 44 | 100 | 100 | 53 | N/A* | 0.56 |
| MRI DWI | 61 | 91 | 89 | 67 | 6.94 | 0.43 |

*no false positives; undefined

(Filename: TCT_O-225_Capture.PNG)

O-226

3:32PM - 3:40PM

CT Perfusion in Acute Lacunar Infarct: Detection Capabilities Based on Infarct Location

J Benson¹, S Payabvash², S Mortazavi², B Hoffman³, M Oswood³, A McKinney²

¹University of Minnesota, St. Paul, MN, ²University of Minnesota, Minneapolis, MN, ³Hennepin County Medical Center, Minneapolis, MN

Purpose

Recently studies indicate that computed tomography (CT) perfusion (CTP) has superior diagnostic value to noncontrast CT/CT angiography (NCCT/CTA) alone in the detection of lacunar infarcts. The purpose of this study was to compare the accuracy of CTP to NCCTA/CTA in lacunar stroke detection based on infarct location.

Materials and Methods

We completed a retrospective review of 1087 CTP examinations performed over a 5.5-year period for patients with acute stroke symptoms, selecting for studies in which patients underwent CTP imaging within 4.5 hours and magnetic resonance imaging (MRI) within 30 days of symptom onset. Selected studies had either 1) lacunar infarct <2 mm on diffusion-weighted imaging (DWI) or 2) no acute infarct on DWI. Patients with co-existing infarcts >2 mm on DWI were excluded. CTP postprocessing was automated by a single delay-corrected algorithm, DC-SVD. Three blinded reviewers were given patients' NIHSS scores and symptoms. Presence or absence of infarct was recorded based on NCCT/CTA, CBF, CBV, MTT, TTP, and DWI.

Results

One hundred fifty-nine patients met inclusion criteria (51.6% male). Lacunar infarcts were present on DWI in 62/159 (39.0%); 97/159 (61.0%) had no infarct on DWI. On CTP, lacunar infarcts appeared as regional perfusion defects larger than the infarcts observed on DWI. Interobserver kappa ranged from 0.35 (CBV) to 0.68 (TTP) for CTP, depending on perfusion parameter; interobserver kappa was 0.85 for DWI. Sensitivity of infarct detection on CTP ranged from 17.7% (CBV) to 35.5% (MTT and TTP); specificity ranged from 97.9% (CBF and MTT) to 99.0% (CBV and TTP). Area under the curve for MTT (0.67) and TTP (0.67) was significantly higher than NCCT/CTA (0.52) ($p < 0.001$ for both). CTP was most sensitive for infarcts within the cortex and/or subcortical white matter (30.0-53.3%), followed by periventricular white matter (14.3-35.7%); infarcts within the thalamus or basal ganglia were not identified correctly in any patients (0/9).

Conclusions

CTP has added value to NCCT/CTA for the detection of acute lacunar infarcts. The sensitivity of CTP is highest within the cortex and/or subcortical white matter; lacunar infarcts in the basal ganglia and thalamus were not detected.

| | TP | TN | FP | FN | Sens. | Spec. | PPV | NPV | Kappa | ROC (95% Confiden |
|----------|----|----|----|----|-------|-------|-------|-------|-------|-------------------|
| NCCT/CTA | 2 | 97 | 0 | 60 | 3.2% | 100% | 100% | 61.8% | 0.13 | 0.516 (0.423-0 |
| CBF | 17 | 95 | 2 | 45 | 27.4% | 97.9% | 89.5% | 67.9% | 0.39 | 0.627 (0.534-0 |
| CBV | 11 | 96 | 1 | 51 | 17.7% | 99.0% | 91.7% | 65.3% | 0.35 | 0.584 (0.490-0 |
| MTT | 22 | 95 | 2 | 40 | 35.5% | 97.9% | 91.7% | 70.4% | 0.59 | 0.667 (0.576-0 |
| TTP | 22 | 96 | 1 | 40 | 35.5% | 99.0% | 95.7% | 70.6% | 0.68 | 0.672 (0.581-0 |

(Filename: TCT_O-226_2015-12-10Image.jpg)

O-227

3:40PM - 3:48PM

High Accuracy of MR T2*W Sequences compared to CTA for Detection of Intracranial Vessel Thrombus in Middle Cerebral Artery Stroke

A Liberato¹, S Shah¹, I Barnaure¹, N Maza¹, G Gonzalez¹, J Romero¹
¹Massachusetts General Hospital, Boston, MA

Purpose

Rapid detection of vessel occlusion is pivotal in the intra-arterial (IA) treatment of patients with acute stroke. Magnetic resonance imaging (MRI) has been demonstrated to detect intravascular thrombus but its diagnostic accuracy compared to computed tomography (CT) angiography (CTA) is not well established. We set out to determine the accuracy of 1.5 T MR T2-W sequences compared to CTA as the reference imaging modality for detection of IA thrombus in patients with acute MCA infarction.

Materials and Methods

Two investigators reviewed DWI and T2-W sequences (GRE/GRE-EPI) for the presence of infarction and susceptibility vessel sign (SVS) (Figure), on consecutive cases with MCA stroke who presented over a period of 20 months. SVS was compared to the corresponding arterial segments on CTA (intracranial internal carotid artery (ICA), M1 and M2 segments of the MCA). Accuracy, sensitivity, specificity, positive and negative predictive values (PPV/NPV) were calculated.

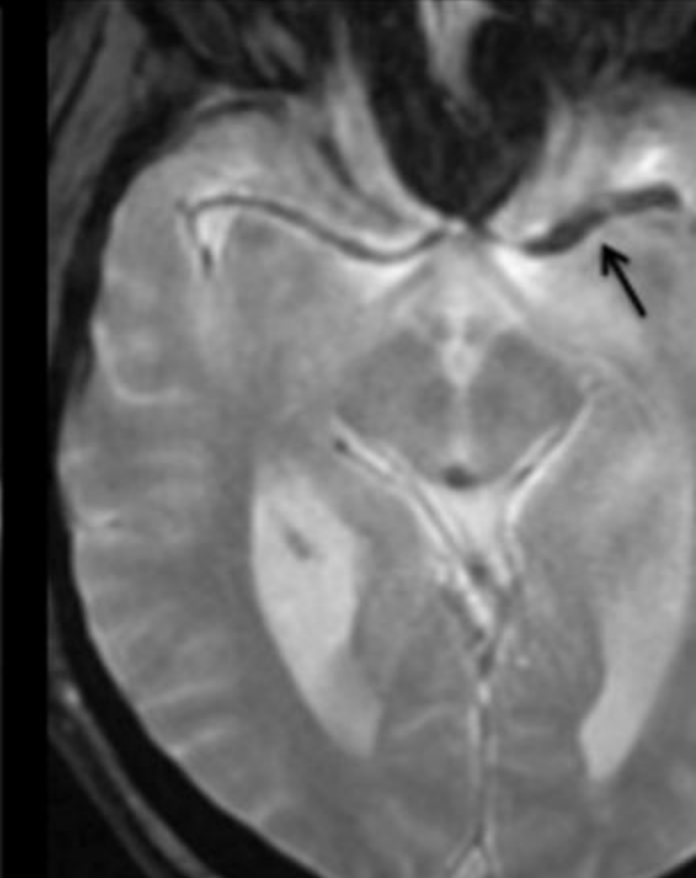
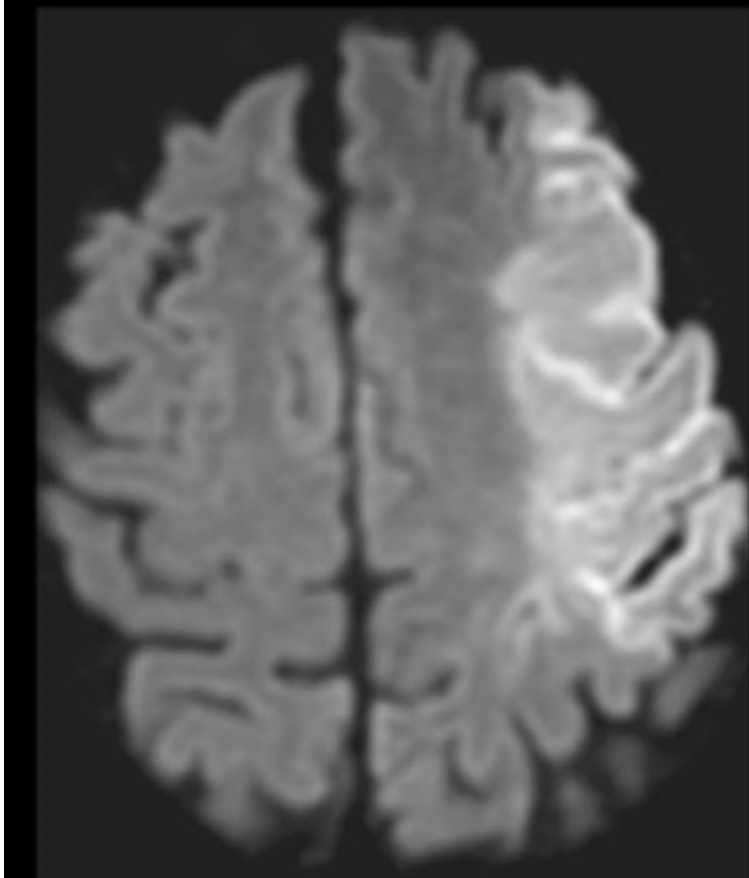
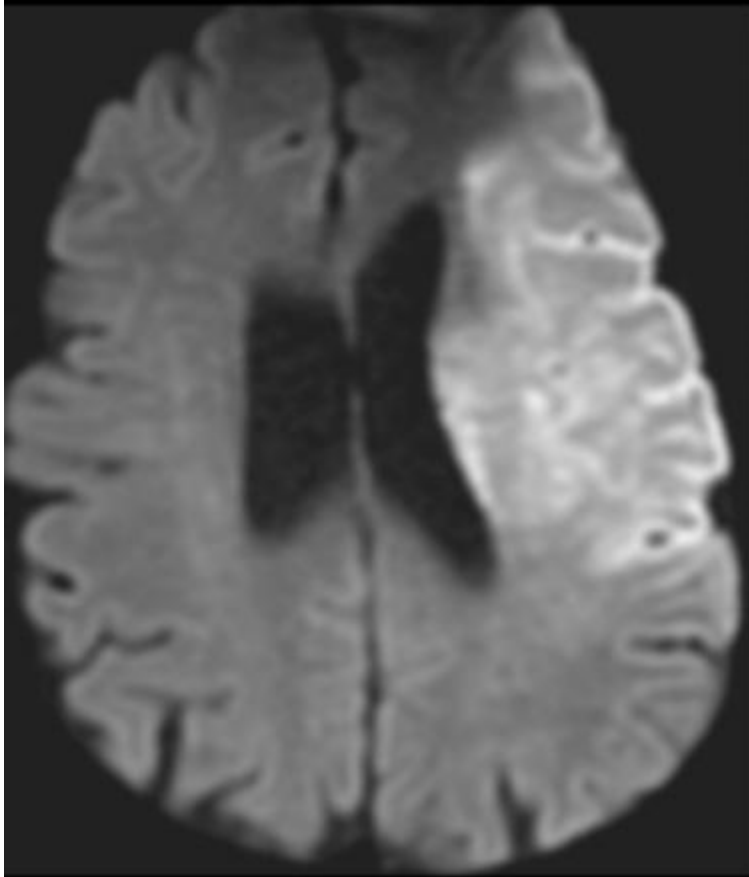
Results

Seventy-one consecutive patients with proven MCA territory stroke were screened. Fifty-one patients who underwent CTA and MRI within 12 hours of clinical symptom onset were included in the study. Forty patients had IA thrombus on CTA and the mean time interval from stroke onset to CTA was 4.2 +/- 2.3 hours (range, 0.4-12 hours). The mean time interval from CTA to MRI was 29.5 +/- 11.1 min. Twenty-six patients showed M1 thrombus on CTA. Of these, 22 patients had corresponding SVS on T2-W sequences and four had no abnormality on MRI. In the remaining 25 patients without M1 thrombus on CTA, no M1-SVS was detected on T2-W sequences. We found an accuracy of 92%, sensitivity of 85%, specificity of 100%,

PPV of 100% and NPV of 86% for M1 occlusion. The interobserver agreement was $k=0.79$.

Conclusions

T2-W sequences demonstrate high accuracy and strong interobserver agreement for detection of thrombus in the M1 segment of the MCA in patients with acute MCA ischemic stroke.



(Filename: TCT_O-227_ASNR1.jpg)

O-228

3:48PM - 3:56PM

Does Cerebrovascular Reserve measured by CT Perfusion using Acetazolamide challenge predict future Stroke/TIA in Cerebro-vascular Steno-occlusive Disease

S Biswas¹, C Denby¹, K Das¹

¹*The Walton Centre, Liverpool, Merseyside*

Purpose

To retrospectively assess whether changes in cerebrovascular reserve (CVR) values following acetazolamide (ACZ) challenged CT perfusion (CTP) in patients with steno-occlusive disease has the ability to predict future cerebrovascular events versus stroke and transient ischemic attack (TIA).

Materials and Methods

Twenty-six patients who underwent CTP with acetazolamide challenge for cerebrovascular steno-occlusive disorders (including moyamoya disease, carotid artery stenosis and occlusion) were studied retrospectively. We gathered together the following diagnostic and clinical information: symptomology, clinical diagnosis, degree of stenosis, number of ACZ procedures, post-ACZ complications, pre- and post-ACZ CBV, CBF and TTP values and CVR percentage change. Information regarding mode of further management (surgical versus conservative) as well as of future cerebrovascular events (stroke or TIA) at 3, 6 or 12+ month intervals was obtained.

Results

On the basis of CBV or CBF values, out of the 26 patients, 19 patients (73%) had normal CVR and seven patients (27%) had decreased CVR. Of the 19 patients with normal reserve, six patients (32% of patients with normal reserve) had a cerebrovascular event (TIA=6, stroke=0). Of the nine patients with decreased reserve one patient had a cerebrovascular event (stroke=1, TIA=0). The association between status of CVR and outcome (TIA/stroke) was not shown to be statistically significant ($p>0.5$). Out of the six patients having a TIA, two of six patients had undergone revascularization. The patient having a documented stroke had not undergone revascularization. Five patients in our study had coronary artery bypass graft surgery and none of them had any cerebrovascular event during our follow up.

Conclusions

No correlation is established between status of CVR and cerebrovascular outcome. Measurement of CVR, independently, is unable to predict the risk of future TIA/stroke. It therefore appears that the outcome is determined by a number of

clinical factors. Decisions regarding management (e.g., surgical versus conservative management) should not be based solely on presence or absence of CVR.

O-229

3:56PM - 4:04PM

Performance of User-independent CT Perfusion Software in Predicting Vasospasm After Aneurysmal Subarachnoid Hemorrhage.

B Knepper¹, S Dehkharghani², R Beck³, B Howard³, A Prater³, J Allen³

¹Emory University Hospital, Atlanta, GA, ²Emory University Hosp, Atlanta, GA, ³Emory University, Atlanta, GA

Purpose

Vasospasm due to aneurysmal subarachnoid hemorrhage (aSAH) is a significant source of morbidity and mortality. Computed tomography (CT) perfusion (CTP) has been advocated as a screening tool for vasospasm, although CTP interpretation requires significant user experience. We examined the power of a custom, user- and vendor-independent perfusion analysis tool configured for prediction of cerebrovascular ischemia to predict significant vasospasm detected on digital subtraction angiography (DSA).

Materials and Methods

Patients with aSAH and CTP performed to assess for vasospasm within 12 hours of DSA were included (n=57). Degree of vasospasm on DSA report was dichotomized: (1) none, minimal, or mild; or (2) moderate or severe. CTP were processed retrospectively using our software. Patients were classified into presence or absence of tissue with Tmax values of > 4s, > 6s, > 8s, and > 10s. Prior studies have proposed Tmax > 4-6s threshold value in the trial setting as a robust predictor of at-risk tissues in the setting of acute ischemia, although this has not been validated in the setting of aSAH. Therefore, a wider range of Tmax values was investigated. Sensitivity, specificity, negative predictive value (NPV), and positive predictive value (PPV) of the presence of ischemic tissue on CTP to predict moderate or severe vasospasm using DSA as the gold standard were calculated.

Results

Forty-one patients (72%) had moderate or severe vasospasm on DSA. Using Tmax > 6s threshold, 34 patients (60%) had ischemic tissue estimated by CTP (mean ischemic volume of 63 cc) and 24 of these patients had moderate or severe vasospasm on DSA with a PPV of 0.71 (true positive mean ischemic volume of 61 cc). However, NPV for Tmax > 6s was only 0.26. Remaining test characteristics and values for other Tmax thresholds tested are shown in Table 1.

Conclusions

Estimation of ischemic tissue using automated CTP analysis software had relatively

good PPV in predicting moderate to severe vasospasm on DSA across Tmax threshold values (0.70-0.76). However, NPV was poor (0.26-0.33).

Table 1. Test characteristics of CTP predicting DSA vasospasm

| | Estimated Value (95% Confidence Interval) | | | |
|------------|---|---------------------|---------------------|---------------------|
| | Sensitivity | Specificity | PPV | NPV |
| Tmax > 4s | 0.85 (0.70-0.94) | 0.19 (0.05-0.46) | 0.73 (0.58-0.84) | 0.33 (0.09-0.69) |
| Tmax > 6s | 0.58 (0.42-0.73) | 0.38 (0.16-0.64) | 0.71 (0.52-0.84) | 0.26 (0.11-0.49) |
| Tmax > 8s | 0.54 (0.38-0.69) | 0.56 (0.31-0.79) | 0.76 (0.56-0.89) | 0.32 (0.17-0.52) |
| Tmax > 10s | 0.39 (0.25-0.55) | 0.56 (0.31-0.79) | 0.70 (0.47-0.86) | 0.26 (0.14-0.45) |

(Filename: TCT_O-229_Table1.jpg)

O-230

4:04PM - 4:12PM

White matter lesion penumbra shows abnormalities on structural and functional MRI in the CARDIA study

I Nasrallah¹, M Hsieh¹, H Battapady¹, G Erus¹, L Launer², D Jacobs³, C Davatzikos¹, R Bryan¹

¹University of Pennsylvania, Philadelphia, PA, ²NIA/NIH, Bethesda, MD, ³University of Minnesota, Minneapolis, MN

Purpose

White matter lesions (WML) are readily visible on structural magnetic resonance imaging (MRI) of the brain and have been linked to future stroke and other neurologic complications. Studies, mainly in the elderly, indicate that WML are associated with broader white matter abnormality. We hypothesized that surrounding 'penumbral' tissue, which is not clearly abnormal by visual inspection, would show abnormalities that are quantifiable by MRI even in young, healthy subjects. We evaluated signal abnormalities in WML penumbra using structural parameters, diffusion tensor imaging, arterial spin label cerebral blood flow (CBF), and blood oxygen level dependent cerebral vascular reactivity (VR).

Materials and Methods

The IRBs of participating institutions approved this study and written informed consent obtained prior to the start of this HIPAA compliant retrospective study of data

acquired prospectively from 8/19/2010 to 8/31/2011. Four hundred sixty-three subjects, mean age 50 years, from the Coronary Artery Risk Development in Young Adults (CARDIA) longitudinal observational cohort study participated. White matter lesions were defined using the established White Matter Lesion Segmentation (WMLS) technique. Voxel-based analysis defined 0-2mm and 2-4 mm penumbral tissue surrounding WML and distant normal appearing white matter (dNAWM), regions shown in color on a FLAIR image in the Figure, top left. Mean signal intensity for FLAIR, T1, fractional anisotropy (FA), mean diffusivity (MD), CBF, and VR were measured. Group comparisons were made using Kruskal-Wallis and pairwise t-tests. Correlations between parameters were calculated using Pearson's R.

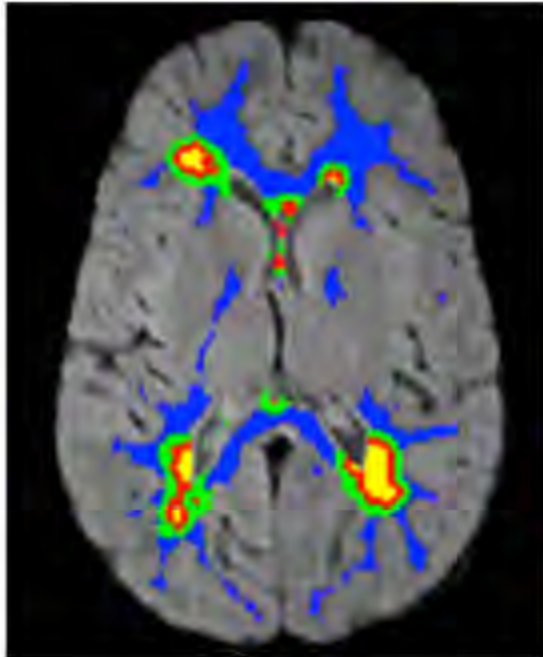
Results

White matter lesions volumes averaged 0.550 ± 0.751 cm³ (range 0-6.79 cm³). Only one subject had no tissue classified as WML while 84% of the sample had greater than 0.1 cm³ defined as WML. Mean signal intensity for FLAIR and MD were increased while T1, FA, and CBF were decreased in WML versus dNAWM.

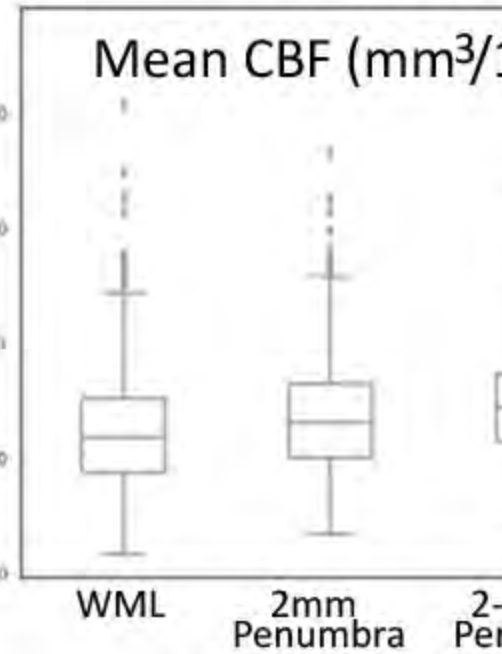
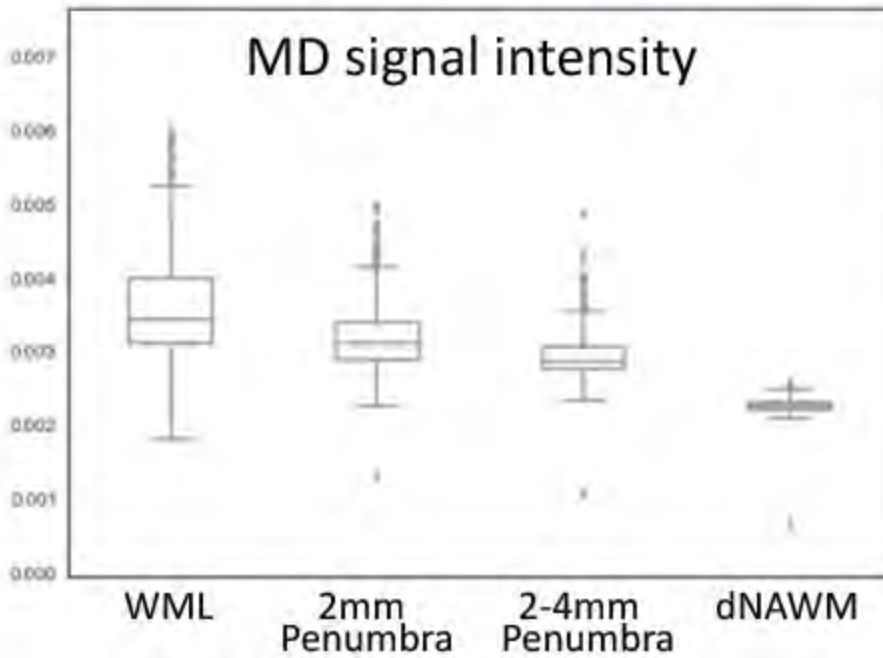
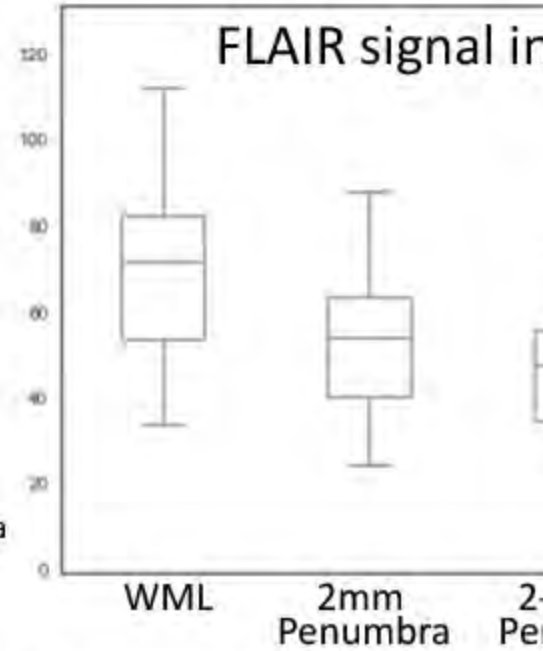
Penumbral tissues show graded intermediate values (corrected $p < 0.001$ for all group and parameter comparisons); the Figure box plots show these significant differences for FLAIR, MD, and CBF. VR showed little activation in lesional and nonlesional white matter. There was no consistent correlation among parameters between the four regions except between MD and FA.

Conclusions

Even in healthy, normotensive subjects with small WML burden, significant abnormalities are detected in MRI structural and functional imaging parameters in penumbral tissue. Findings suggest that white matter injury onset starts by middle age and is more widespread than evident from WML burden visualized on structural imaging. Integrating multiple MRI parameters may provide more detailed delineation of injured white matter compared to traditional approaches.



■ WML
■ 2mm Penumbra
■ 2-4mm Penumbra
■ dNAWM



(Filename: TCT_O-230_Abstract_figure2.jpg)

O-231

4:12PM - 4:20PM

Acquiring and Validating Temporal Information in 4D DSA Reconstructions

J Xu¹, G Shaughnessy¹, J Jiang², S Schafer¹, C Mistretta³, C Strother³

¹University of Wisconsin School of Medicine and Public Health, Madison, WI, ²Michigan Technical University, Houghton, MI, ³University of Wisconsin Madison, Madison, WI

Purpose

Four dimensional DSA generates time-resolved 3D vascular volumes. Blood flow can be quantified if pulsatility in time-attenuation curves is unperturbed by contrast injection parameters. Goals: 1) evaluate a novel quantitative method for detecting time-attenuation curve pulsatility and, 2) evaluate the impact of injection parameters on time-attenuation curves.

Materials and Methods

Forty-seven studies were performed in six canines with carotid artery vein patch aneurysms. Doppler measurements were acquired proximal, and distal to the aneurysms. Injection rate, catheter size, and injector rate-rise were varied. Rotational acquisitions were acquired and reconstructed as 4D volumes. EKG was recorded during the acquisitions. For each 4D reconstruction, time-attenuation curves were analyzed at locations corresponding to the Doppler measurements. The curves were scored qualitatively on pulsatility by two blinded reviewers using a binary scale. A Fourier Transformation was done to determine signal power at each frequency and was compared with EKG and Doppler heart rate measurements. To optimize pulsatility recognition, the peak power and six adjacent points were used to calculate a sideband ratio (SBR). Sideband ratio magnitude was compared to reviewer scores.

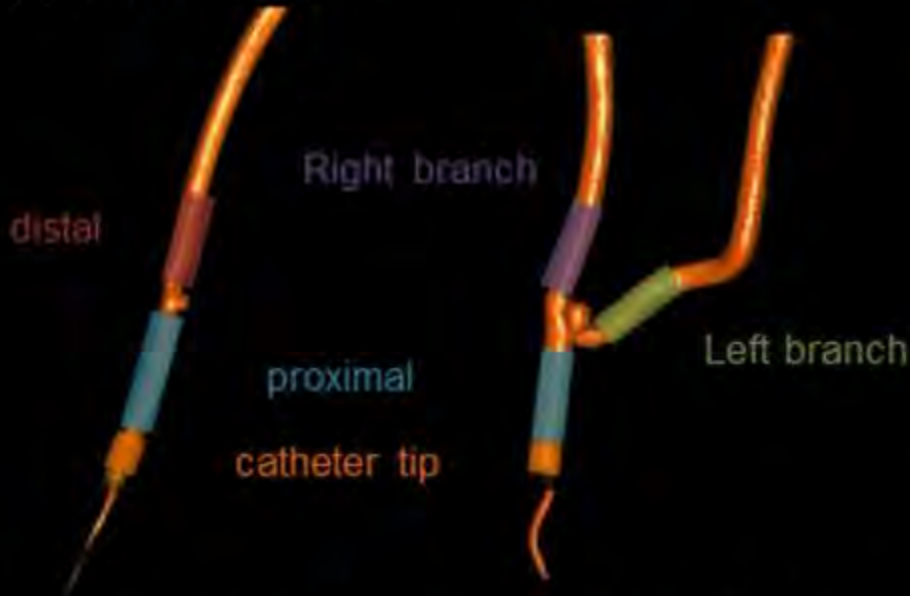
Results

EKG/US and Fourier Transformation calculated heart rates were highly similar (102.3 versus 105.3, $p=0.44$). Sideband ratios between 5-10, and greater than 10 had average reviewer scores of 0.902, and 0.944 respectively. Sideband ratios below five had an average score of 0.567. The nine cases with the highest SBRs and scores were acquired with injection parameters of 2.5-3 ml/s, catheter size of 5-6F, and a rate-rise >0.3 sec.

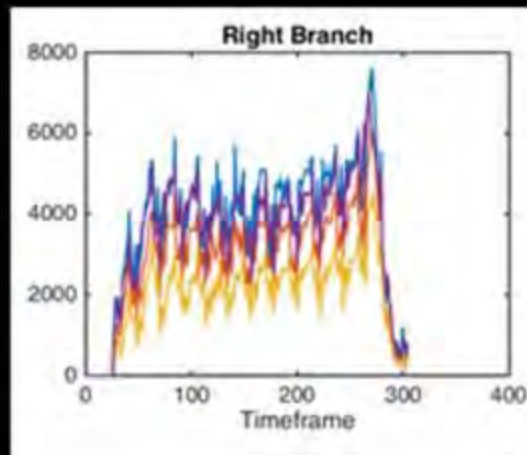
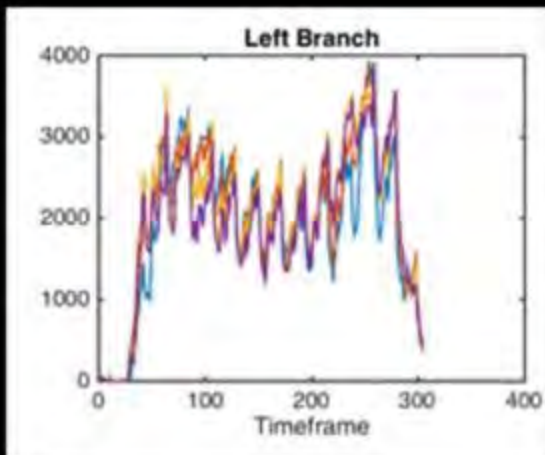
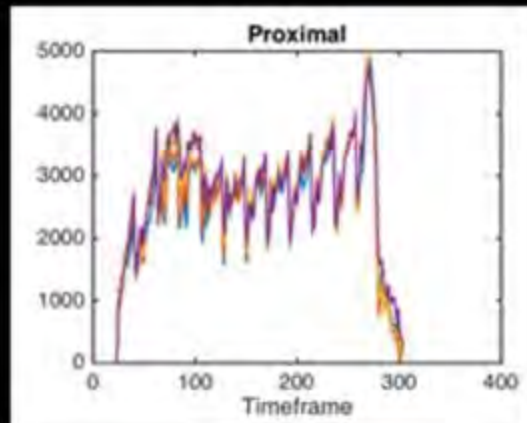
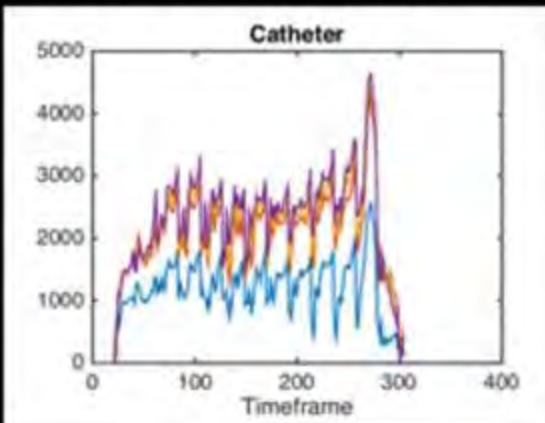
Conclusions

There was excellent concordance between heart rates and Fourier Transformation pulsatility detection. High correlation between reviewers' scores and SBR provides an automatic method to evaluate pulsatility - a $SBR > 5$ indicates an acceptable waveform. Injection rates of 2.5-3 ml/s, 5-6F catheter, and a longer rate-rise provided consistently preserved temporal information.

1. For each 4D reconstruction, time-attenuation curves were analyzed at locations corresponding to the Doppler Measurements.



2. At each location 4 samples were taken for qualitative and quantitative analysis.



(Filename: TCT_O-231_ASNRFigure4.jpg)

O-232

4:20PM - 4:28PM

Improved T1 weighted, black blood, vessel wall imaging using distributed spirals, variable density sampling and constrained reconstruction: Initial clinical experience.

K Johnson¹, L Rivera-Rivera¹, T Kennedy¹, P Turski¹

¹*University of Wisconsin, Madison, WI*

Purpose

Effective black blood imaging is challenging due to complex slow flow resulting in confounding residual intravascular signal. We introduce a variable flip angle, fast spin echo sequence with distributed spiral sampling (1); with the goals of 1) improved suppression of intravascular signal, 2) higher spatial resolution, 3) gating and 4) pure T1 contrast.

Materials and Methods

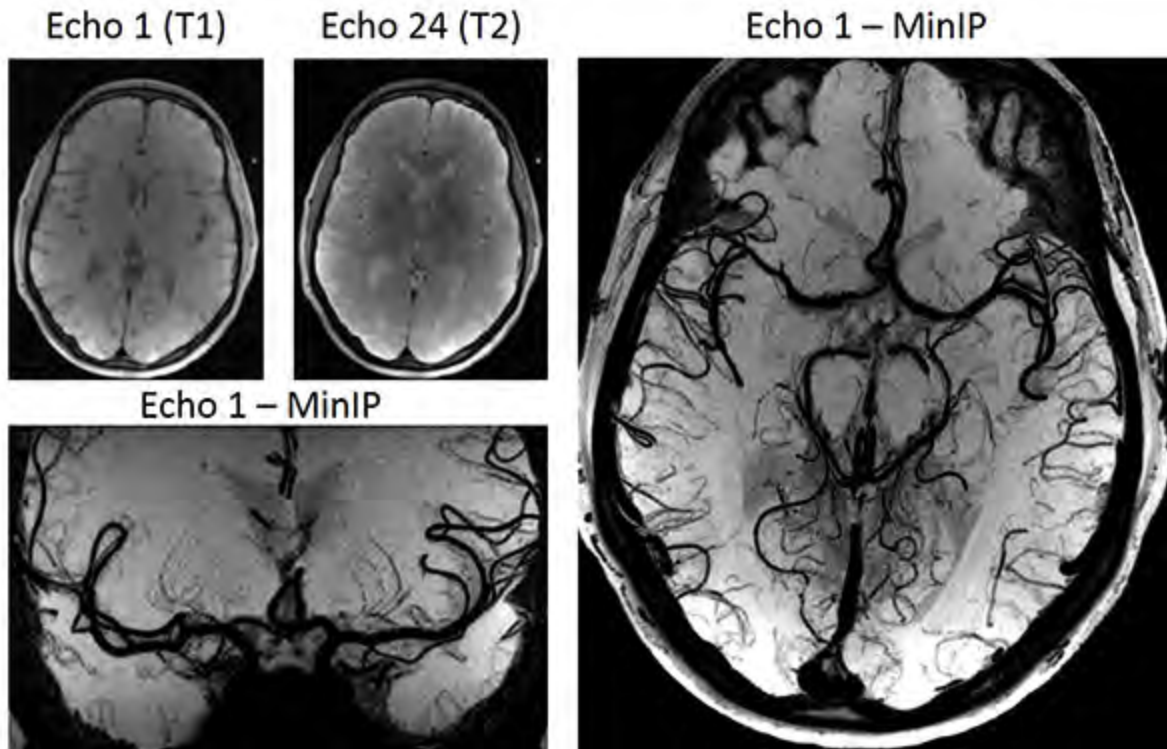
During a variable flip angle fast spin echo readout, samples are collected with spiral arms which are distributed onto kxy with the kz phase encode set continuously in a pseudo-random fashion. These arms are interleaved in a fashion such that flow suppression is 3 dimensional (3D) and T2 decay manifests as a diffuse artifact rather than blurring. Using acceleration in three directions, this artifact can be removed by a constrained reconstruction which learns the echo train signal evolution from the data allowing recovery of images at each echo time (2). Here we present our experience for high resolution intracranial imaging with a practical scan time of ~5 minutes.

Results

In phantom experiments, the spiral image acquisition shows less directional sensitivity and an overall improvement in flow suppression (median black blood suppression of 0.93 for spiral versus 0.69 for Cartesian). The figure shows images of one of the volunteer subjects. The constrained reconstruction, fit to echo train signal evolution, provides image contrast that progresses from T1 dominated (Figure 1, Echo 1) to T2 dominated (Figure, Echo 24). Utilizing the first echo from the reconstruction, high quality T1-weighted black blood images can be generated; later echoes provide T2-weighted images.

Conclusions

We introduce an innovative variable flip angle distributed spiral fast spin echo sequence for black blood vessel wall imaging with increased spatial resolution, suppression of intravascular flow signal, and simultaneous depiction of T1 and T2-weighted contrasts; without the incorporation artifact prone black blood preparation modules.



(Filename: TCT_O-232_Picture1.jpg)

O-232a

4:28PM - 4:36PM

Intracranial Vessel Wall MRI: Recommendations for Clinical Practice

D Mandell¹

¹University of Toronto, Toronto, Ontario

Purpose

-

Materials and Methods

-

Results

-

Conclusions

-

Tuesday

3:00PM - 4:30PM

Washington Marriott Wardman Park, Washington 1/2/3

11C-Incidental Findings

11C-1

3:00PM - 3:20PM

General Overview of Incidental Findings

Poussaint, T.
Boston Children's Hospital
Boston, MA

11C-2

3:20PM - 3:40PM

Incidental Findings in CT Angiography Neck Examinations

Chapman, P.
University of Alabama Birmingham
Birmingham, AL

11C-3

3:40PM - 3:55PM

Incidental Findings in 10,000 Research Volunteer MR Exams

Rowley, P.
University of Wisconsin
Madison, WI

11C-4

3:55PM - 4:20PM

Best Practices: Clinical and Research Incidental Findings

Zaharchuk, G.
Stanford University
Stanford, CA

11C-5

4:20PM - 4:30PM

Questions and Answers

Tuesday

3:00PM - 4:30PM

Washington Marriott Wardman Park, Roosevelt 1-3

11D - PARALLEL PAPER SESSION: Turbo Talks-16 Shades of Grey and White Matter

O-233

3:00PM - 3:03PM

Comparison of 3D FLAIR and 3D T2-w Fast Spin-Echo Sequences for Detection of Infratentorial Multiple Sclerosis Lesions

X Wu¹, S Mansourian¹, V Kalra¹, N Makhani¹, A Malhotra¹

¹*Yale University School of Medicine, New Haven, CT*

Purpose

Infratentorial lesions predict long-term disability prognosis in patients with multiple sclerosis (MS). FLAIR has been considered suboptimal for posterior fossa evaluation and for this reason, imaging protocols include conventional T2-W sequences in addition to FLAIR. We assess the intra- and interobserver agreement for posterior fossa lesion detection among MS patients of 3D FLAIR versus 3D T2-W fast spin echo (FSE) at 3T magnetic resonance imaging (MRI).

Materials and Methods

Fifty patients with clinically definite MS with both 3D FLAIR and 3D T2-W FSE sequences were evaluated retrospectively for number of brainstem and cerebellum lesions, confidence score for each lesion, and overall image sequence quality by two neuroradiologists independently. Statistical analysis was performed to assess for differences between the results of the two sequences. Intra- and interobserver agreements were calculated using the Wilcoxon Signed-Ranked Test and Spearman's Rank Correlation.

Results

Three dimensional FLAIR identified more brainstem and cerebellar lesions compared to 3D T2-W FSE for both readers, however this was only statistically significant for the number of cerebellar lesions ($p = 0.001$) for both readers. The confidence score is statistically significantly higher on FLAIR than on T2 for Reader 1 at brainstem and both readers at cerebellum. There is no significant difference in quality score, except for a higher quality T2 from Reader 2 at brainstem, with detailed confidence and quality scores presented in Table 1. The interobserver agreement has a slightly higher correlation coefficient on T2 (brainstem: 0.83; cerebellum: 0.92) than on FLAIR (brainstem: 0.81; cerebellum: 0.87).

Conclusions

Three dimensional FLAIR identified more infratentorial lesions than 3D T2-W FSE for both brainstem and cerebellum. Conventional T2-W may not need to be performed for MS patients. Additional studies with reference standard lesions would help further investigate the utility of FLAIR compared to T2.

| | Reader 1 | | | Read |
|---|----------|-------|--------------|------|
| | T2 | FLAIR | <i>p</i> | T2 |
| Mean brain stem lesion confidence score | 3.88 | 4.12 | 0.019 | 3.98 |
| Mean brain stem lesion quality score | 4.58 | 4.58 | 1.000 | 4.22 |
| Mean cerebellum lesion confidence score | 3.88 | 4.14 | 0.017 | 3.88 |
| Mean cerebellum lesion quality score | 4.54 | 4.58 | 0.648 | 4.64 |

(Filename: TCT_O-233_MStable.jpg)

O-234

3:03PM - 3:06PM

Absolute quantification of normal appearing and lesional tissue in Relapse Remitting Multiple Sclerosis with and without cognitive impairment

S Hojjat¹, M Kincal¹, R Vitorino¹, C Cantrell², A Feinstein¹, L Zhang¹, L Lee¹, P O'Connor³, T Carroll², R Aviv¹

¹Sunnybrook Research Institute, Toronto, Ontario, ²northwestern university, Chicago, IL, ³St. Michael's Hospital, Toronto, Ontario

Purpose

The role of gray matter in multiple sclerosis (MS) is increasingly evident, however conventional magnetic resonance (MR) images demonstrate limitations in cortical lesion (CL) identification. Perfusion imaging appears sensitive to changes in tissue type and disease severity in MS. We sought to utilize bookend perfusion to quantify parameters in healthy controls (HC), normal appearing and lesional tissue at different relapse remitting MS (RRMS) stages.

Materials and Methods

Thirty-nine RRMS patients and 19 age-matched HC were prospectively recruited. MACFIMS battery was used to assess cognitive performance. Perfusion parameters including cerebral blood flow (CBF) and volume (CBV) and mean transit time (MTT) were compared for HC, normal appearing and lesional tissue for all study groups. Dispersion of perfusion measures for white matter lesion (WML) and CLs was assessed.

Results

Twenty of the 39 RRMS patients were cognitively impaired (RRMS-I). Significant differences were displayed between all RRMS subgroups and HC except for normal appearing gray matter (NAGM) CBV between HC and RRMS-NI and for all normal appearing white matter (NAWM) perfusion parameters between HC and unimpaired RRMS patients (RRMS-NI). White matter lesion but not CL perfusion was significantly reduced in RRMS-I versus RRMS-NI. Perfusion reduction with disease progression was greater in NAGM and NAWM compared to CL and WML. Smaller dispersion was observed for CLs compared to WML for each perfusion parameter.

Conclusions

Quantitative GM and WM analysis demonstrates significant but disproportionate WML, CL, NAWM and NAGM changes present between healthy controls and RRMS patients with and without cognitive impairment necessitating absolute rather than relative lesion perfusion measurement.

O-235

3:06PM - 3:09PM

Can Sequential MR diffusion weighted imaging be used to detect active multiple sclerosis lesions and reduce potential risk of gadolinium deposition in patients with multiple sclerosis ?

W Tian¹, X Liu¹, H Wang²

¹University of Rochester Medical Center, Rochester, NY, ²University of Rochester Medical Center, Rochester, NY

Purpose

Multiple sclerosis (MS) is the most common neurodegenerative disease and one of the leading causes of neurological disability in adults in the United States. Postcontrast T1-weighted imaging (T1WI) is standard imaging protocol for detection of MS activity. However, recent studies suggested that repeated administration of intravenous gadolinium-based contrast agents could induce gadolinium deposition in neuronal tissues in the setting of relatively normal renal function. Therefore, it is important to use noninvasive MR technique to clarify activity status so that to avoid unnecessary injection of MR contrast agents and subsequently reduce potential risk of gadolinium deposition in patients with stable MS lesions. The purpose of our study is to evaluate the screening performance of diffusion imaging to select optimal patients with active MS lesions for further postcontrast T1WI examination.

Materials and Methods

We retrospectively reviewed MR imaging examinations (including postcontrast T1WI and DWI sequence) of 200 MS patients from 2008 to 2014. We only selected the new MS lesions which had prior MR examination(s). The imaging characteristics of these

new MS lesions, including enhancing patterns, and signal intensity changes on diffusion-weighted imaging (DWI) and apparent diffusion coefficient (ADC) were evaluated. Fisher's exact test was performed to determine whether the DWI and ADC abnormalities are associated with enhancement status in these new MS lesions. The sensitivity, specificity, positive predictive value (PPV), and negative predictive value (NPV) were calculated to assess the accuracy of DWI and ADC in predicting MS activity.

Results

Ninety-eight new MS lesion in 45 patients were enrolled in this study, and there were 92 new enhancing lesions and six new nonenhancing lesions. All 98 new lesions presented as hyperintensity on DWI image. Compared to the previous baseline MR examinations, 97 new MS lesions presented as new appearance of hyperintensity on DWI image, and one new MS lesion presented enlarged hyperintensity on DWI image. On ADC maps, 52 enhancing lesions and four nonenhancing lesions showed hyperintensity (54.2% and 4.2%), 35 enhancing lesions and two nonenhancing lesions as isointensity (36.5% and 2%) and five enhancing lesions as hypointensity (5.1%), Figure 1. The hyperintensity on DWI is significantly associated with lesion enhancement ($P < 0.001$). The sensitivity, accuracy and PPV of new and/or enlarged hyperintensity on DWI to predict MS enhancing status were 100%, and 93.9%, 93.9% respectively. The sensitivity and specificity of new and/or enlarged hyperintensity on DWI to predict MS activity status were 100%.

Conclusions

Our preliminary study suggests that lesions with new and/or enlarged hyperintensity on DWI are associated with MS activity, and sequential DWI examination can be used for selecting patients with active MS lesions for further postcontrast T1WI sequences. This may lead to an updated imaging strategy based on appearance of new and/or enlarged hyperintensity on DWI, that could avoid repeated intravenous exposures to the patients with stable MS lesions.

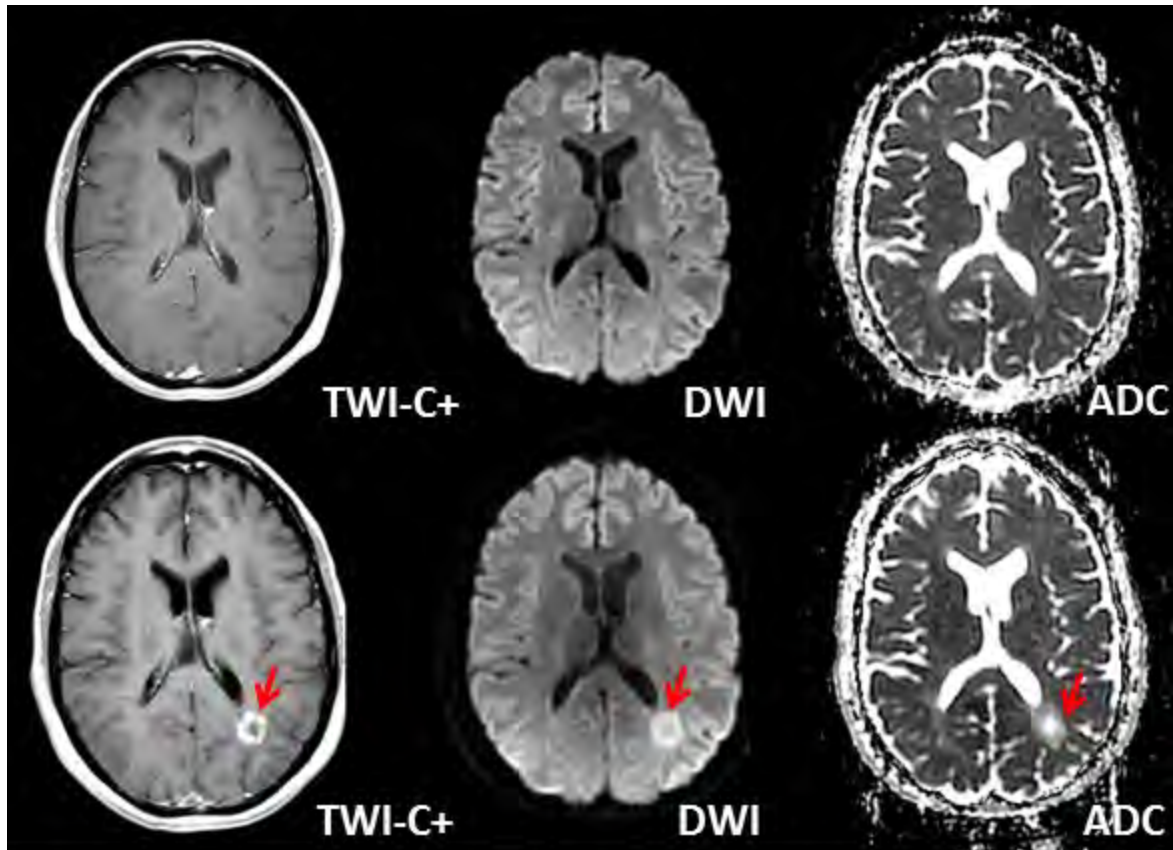


Figure 1: Compared to baseline MR examination (upper row), the new ring-enhancing lesion presented hyperintensity on DWI and ADC images (red arrow)

(Filename: TCT_O-235_Figure1-ASNR2016.jpg)

O-237

3:12PM - 3:15PM

Natalizumab-PML-IRIS: Multiparametric MRI Findings and Time Course

D Titelbaum¹, J Katz², E Lathi², R Dhillon³, E Schwartz¹

¹Shields Health Care, Brockton, MA, ²The Elliot Lewis Center for MS Care, Brighton, MA, ³Sturdy Memorial Hospital, Attleboro, MA

Purpose

During the diagnosis and initial treatment of natalizumab-progressive multifocal leukoencephalopathy (NTZ-PML), imaging leads to difficulty in distinguishing between immune reconstitution inflammatory syndrome (IRIS) and continued PML. We sought to characterize the expected imaging findings and time course of post-treatment IRIS by using multiparametric magnetic resonance imaging (MRI) assessment.

Materials and Methods

Six patients with diagnosed NTZ-PML were followed by MRI, including FLAIR, T1W, diffusion-weighted imaging, gadolinium enhancement, with some patients also undergoing MR spectroscopy (MRS) and diffusion tensor imaging (DTI).

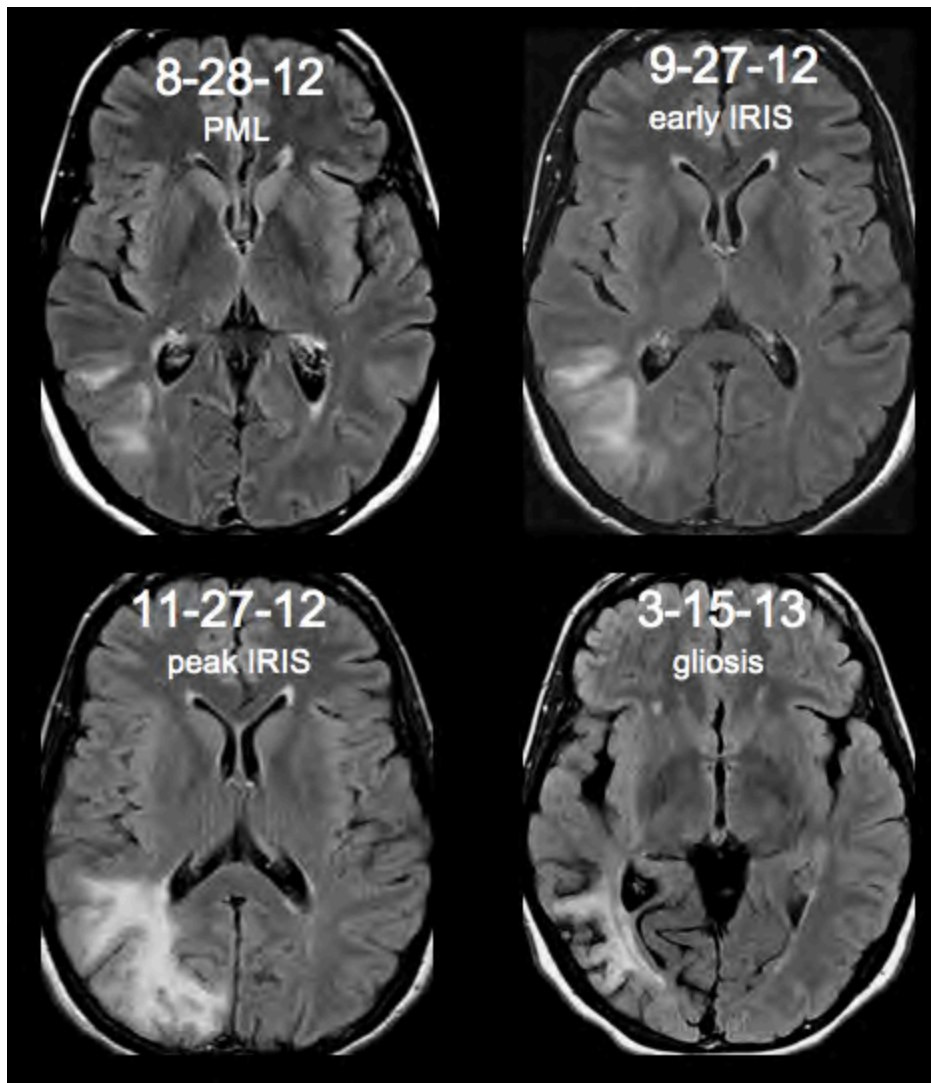
Multiparametric timeline maps were created to identify patterns of changes during early and peak IRIS.

Results

IRIS typically began 3-4 weeks after diagnosis of PML independent of whether patients received plasma exchange, and was accompanied by clinical deterioration that resolved with corticosteroid treatment. Peak IRIS occurred at 7-12 weeks, and resolved to final baseline in 3-6 months (Fig. 1). Early IRIS was seen as worsening FLAIR abnormality in the bed of PML, gadolinium enhancement often involving perivascular space enhancement, and diffusion hyperintensity. Peak IRIS was characterized by maximal FLAIR hyperintensity and gadolinium enhancement, well-demarcated subcortical T1 hypointensity, progression of diffusion hyperintensity from subcortical to deep white matter, decreased fractional anisotropy (FA), and elevated lipid-lactate peak. Cortical laminar necrosis was identified on T1W images shortly after peak IRIS. Resolved IRIS showed contraction of FLAIR abnormality to stable gliotic-appearing residua, resolved enhancement and diffusion abnormality, resolved lipid-lactate, and in some cases improved fractional anisotropy.

Conclusions

Worsening of MR appearance following initial management of PML is an expected manifestation of IRIS, and can be confused with worsening PML. Familiarity with the multiparametric appearance during evolution of PML-IRIS will facilitate accurate diagnosis and management.



(Filename: TCT_O-237_Fig1.jpg)

O-238

3:15PM - 3:18PM

Early MRI Characteristics of Cerebral Lesions in Asymptomatic Boys with X-linked Adrenoleukodystrophy: Focus on the Hot Spots

P Caruso¹, A Liberato¹, R Aziz-Bose¹, A Lauer¹, P Musolino¹, F Eichler¹

¹Massachusetts General Hospital, Boston, MA

Purpose

X-linked adrenoleukodystrophy (ALD) is caused by mutations in the ABCD1 gene leading to accumulation of very long chain fatty acids in plasma and tissues. Its most severe manifestation is childhood cerebral ALD (CCALD), a rapidly progressive form of inflammatory demyelination. Identification of cerebral lesions prior to onset of

symptoms is paramount in selecting patients who will benefit from rescue therapies. We set out to analyze cerebral lesions in a unique cohort of asymptomatic boys with CCALD.

Materials and Methods

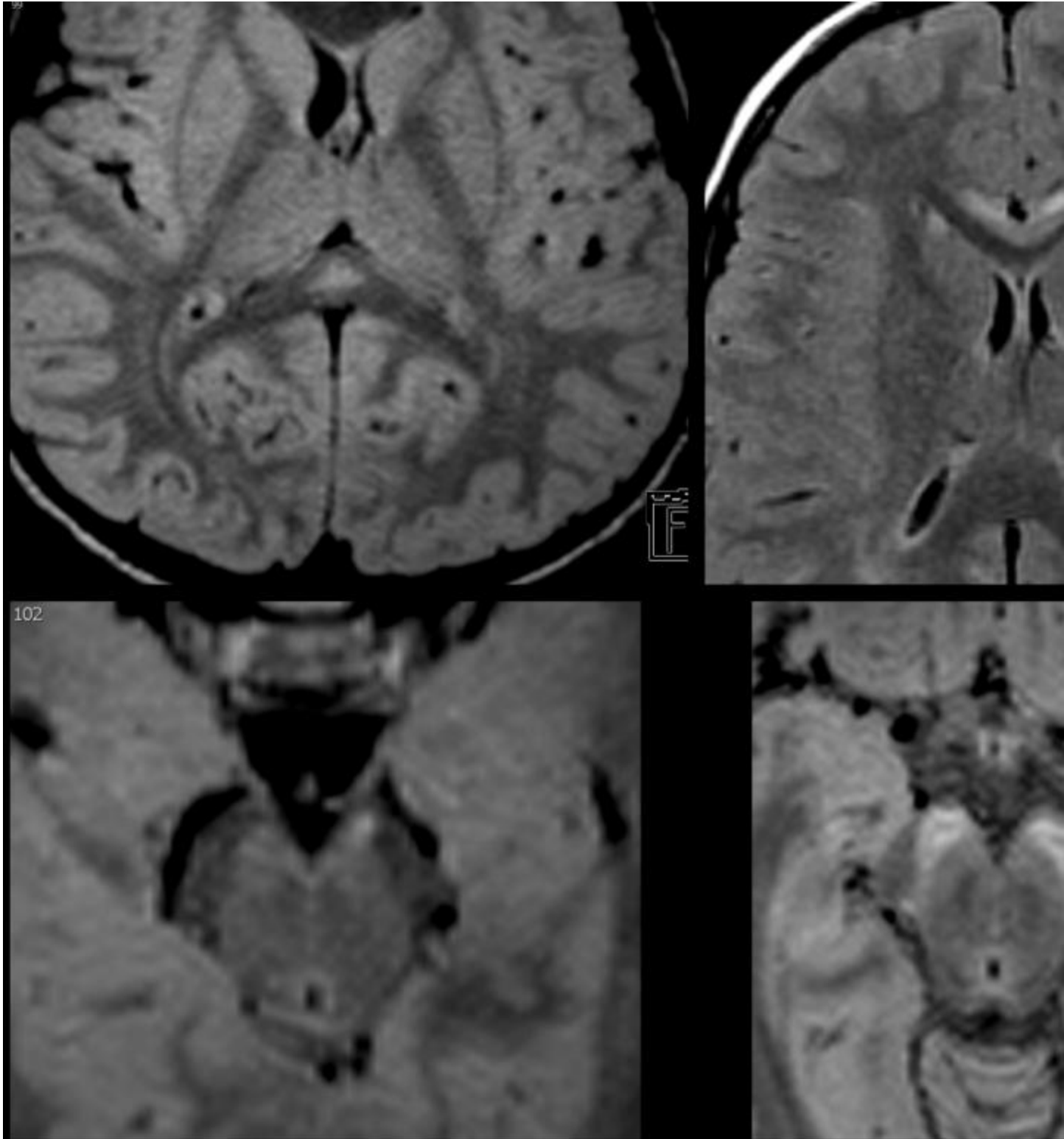
We reviewed 193 brain magnetic resonance images (MRIs) from 44 neurologically asymptomatic (Neurologic Functional Scale=0) boys with biochemical or genetically confirmed ALD followed at Massachusetts General Hospital between 2001 and 2015. Only scans of patients with no history of hematopoietic stem cell transplantation were included. Two neuroradiologists blinded to clinical information recorded the number of patients with lesions, the Loes score¹, the pattern of white matter involvement, and the presence and pattern of enhancement.

Results

Of the 44 boys, 59% (26) showed brain lesions (median age 6.7 years; range 3.6-15.5 years). The median Loes score found was 3.0 points (range 0.5-11). The most frequent lesion pattern was parieto-occipital white matter and splenium of corpus callosum (15) followed by frontal white matter and genu of corpus callosum (5), frontopontine and corticospinal tracts (4), and combined splenium and genu of corpus callosum (2). Among all patients with lesions, 85% (22/26) had contrast enhancement, either at baseline (50%) or on follow-up MRI (50%). Rim, patchy and solid lesion enhancement patterns were seen. Ten patients showed normal baseline MRI and subsequently converted to CCALD (median age 6.4 years).

Conclusions

Magnetic resonance imaging can detect brain lesions and development of disease in the absence of neurological symptoms. As newborn screening is implemented, familiarity with the characteristics of early lesions will help improve disease detection and guide monitoring and treatment in ALD.



(Filename: TCT_O-238_ok.jpg)

O-239

3:18PM - 3:21PM

The Current MRI Scoring System for Cerebral Adrenoleukodystrophy does Not Reliably Reflect Disease Progression in Early Lesions

A Liberato¹, P Caruso¹, A Lauer¹, R Aziz-Bose¹, F Eichler¹, P Musolino¹
¹*Massachusetts General Hospital, Boston, MA*

Purpose

The magnetic resonance imaging (MRI) Loes scale¹ (0-34 points) quantifies the extent of white matter lesions in patients with cerebral adrenoleukodystrophy (ALD). Higher scores represent greater disease burden. It currently is used to assess cerebral ALD severity, progression, and to guide treatment. However, evaluation of disease progression using volumetric measurements of cerebral lesions in asymptomatic patients has not been studied. We set out to evaluate the MRI Loes scale in asymptomatic boys with ALD by comparing the Loes scores to volumetric measurements of cerebral lesions.

Materials and Methods

We reviewed 193 brain MRIs from 44 neurologically asymptomatic (Neurologic Functional Scale=0) boys with biochemical or genetically confirmed ALD followed at Massachusetts General Hospital between 2001 and 2015. Only scans of patients with no history of hematopoietic stem cell transplantation were analyzed. Two neuroradiologists, blinded to clinical information, recorded the Loes scores and lesion volumes for all MRI scans. Lesion progression was defined as Loes score increase of ≥ 1 point and lesion volume increase $\geq 30\%$, in sequential follow-up scans.

Results

Of the 44 boys, 59% (26) showed brain lesions (median age 6.7 years; range 3.6-15.5 years). The median Loes score found was 3.0 points (range 0.5-11). Lesion progression by Loes was present in 48% of patients (12/25) over a follow-up period of 14.2 months (range 0-90.2 months). Twenty patients had sequential MRI scans with unchanged Loes scores during follow-up and 50% displayed lesion volume progression. Of these, the rate of progression was higher among the patients with unchanged Loes score of ≤ 1 (9) compared to the patients with other unchanged Loes scores (1; $p=0.0011$).

Conclusions

Our results showed that cerebral ALD lesions may progress even despite stable Loes scores in follow-up imaging. The current MRI Loes scale for cerebral ALD does not reliably reflect lesion progression in asymptomatic boys with early disease.

O-240

3:21PM - 3:24PM

Volumetric and Diffusion Tensor Imaging Outcomes Associated with Adult Measures of Criminality in a Cohort with Childhood Lead Exposure

K Cecil¹, T Beckwith², J Wright³, K Dietrich³

¹*Cincinnati Children's Hospital Med. Ctr., Cincinnati, OH*, ²*CCHMC, Cincinnati, OH*, ³*University of Cincinnati, Cincinnati, OH*

Purpose

The purpose is to determine if an association exists between measures of adult criminal behavior and neuroanatomical structure in a birth cohort with childhood lead exposure longitudinally followed for nearly 30 years. International epidemiological studies of childhood lead exposure report positive relationships between blood lead concentrations with juvenile delinquency and adult criminality.

Materials and Methods

High-resolution, 3-dimensional, anatomical (volumetric) T1-weighted and 32-direction diffusion tensor imaging (DTI) (spin-echo echo planar imaging, b-value 1000 s/mm²) were acquired with a 3T MR scanner from the adult cohort (N=105, 44 male, mean age at imaging 26.8 +/- 1.1 y). Blood lead levels were measured every 3 months for the first 5 years of life, every 6 months from 5 - 6.5 years of age, at 15 years of age, and at the time of imaging. Criminal arrest records since turning 18 years old were electronically assessed from local, public databases to determine violent arrests and total arrests. Voxel-based morphometry (VBM) utilized Statistical Parametric Mapping (SPM) software. Voxel-based analyses of DTI employed custom software in IDL. Statistical analyses of VBM and DTI outcomes were performed with multiple regression analyses employing a log (x+1) function of total arrest and violent arrests, respectively, as dependent variables, the log of blood lead at 78 months as an independent variable with evaluation of additional confounders such as age at imaging, sex, gestational age, socioeconomic status, full-scale IQ, maternal IQ, and prenatal exposure to cigarettes, alcohol and marijuana considered when constructing the final models.

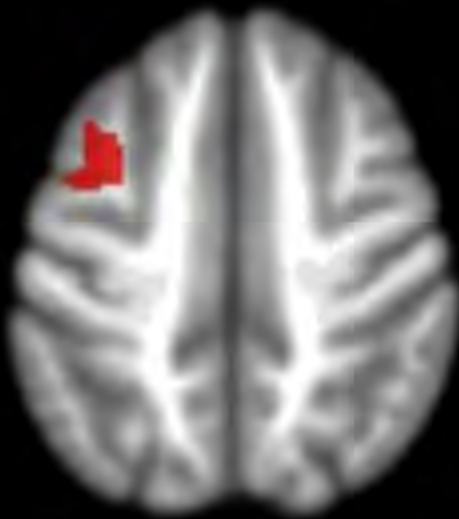
Results

Gray matter loss was observed in the left middle frontal gyrus for all participants in relation to violent arrests, and white matter loss in the left paracentral lobule for males in relation to total arrests. Diffusion tensor imaging data presented patterns of altered myelin structure (such as elevated radial diffusivity) primarily in ascending and descending white matter pathways in relation to total arrests. Similar patterns were observed in relation to total violent arrests with the inclusion of abnormalities in the frontal and temporal lobes. The four-part figure illustrates representative examples of neuroimaging outcomes associated with violent arrests.

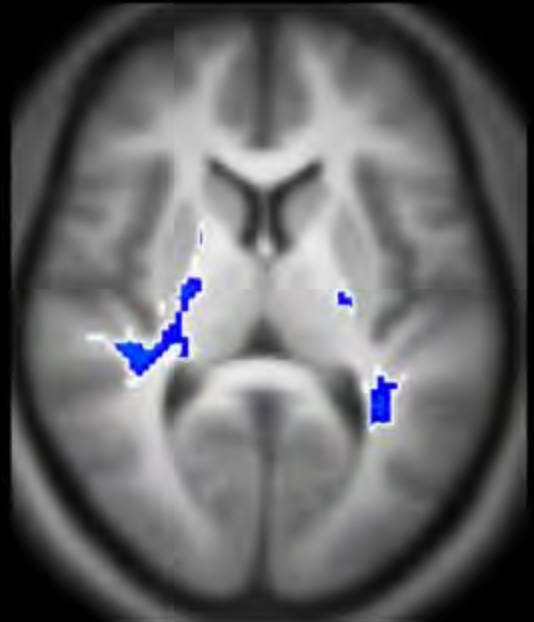
Conclusions

The results of this study suggest that elevated arrest rates associated with childhood lead exposure may be influenced by altered brain structure and organization, especially in white matter.

Voxel Based Morphometry

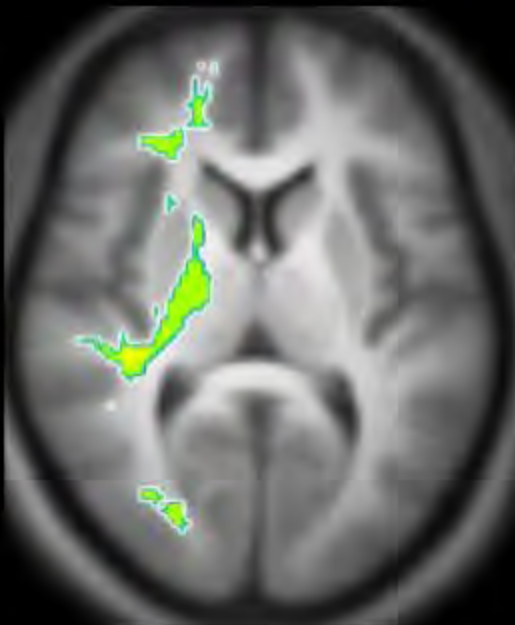


Fractional Anisotropy

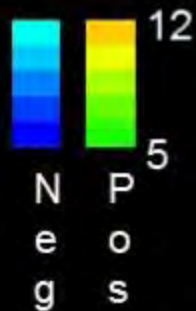
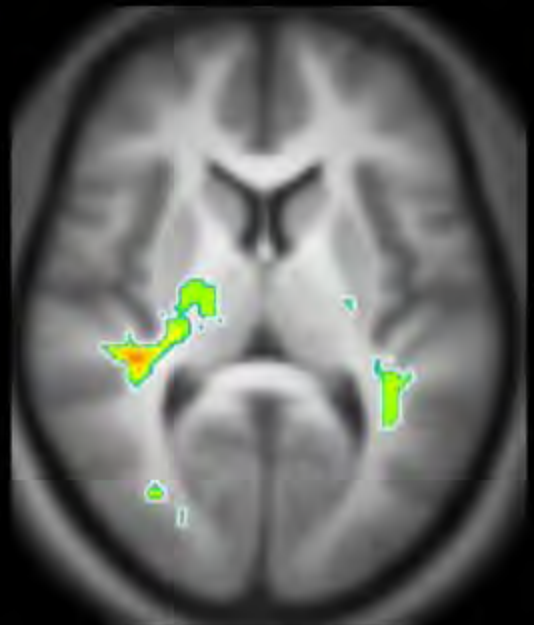


Z
Statistic
For
Diffusion
Tensor
Imaging

Mean Diffusivity



Radial Diffusivity



(Filename: TCT_O-240_BeckwithCecil_Figure.jpg)

O-241

3:24PM - 3:27PM

Determining tumor infiltration in the normal appearing white matter using radiomic characterization.

A Kotrotsou¹, G Thomas², S Abrol¹, P Zinn³, R Colen¹

¹MD Anderson Cancer Center, Houston, TX, ²The University of Texas MD Anderson Cancer Center, PEARLAND, TX, ³Baylor College of Medicine, Houston, TX

Purpose

To determine whether computationally derived MR image-based texture radiomic features can identify infiltrating cancer cells in the peritumoral normal appearing white matter (NAWM). Glioblastoma (GBM) harbors infiltration beyond the region of nonenhancing T2/FLAIR hyperintense component of the tumor (aka NAWM). We hypothesized that texture features obtained from the peritumoral NAWM that contain infiltrating cells, will be different from other white matter regions distant from the tumor.

Materials and Methods

Forty patients with newly diagnosed GBM were identified from The Cancer Genome Atlas (TCGA) database. Presurgical gadolinium-enhanced T1 and FLAIR MR images were obtained from The Cancer Imaging Archive (TCIA). We investigated peritumoral white matter in regions defined by the radiologists as normal nonpathological tissues, but which were adjacent to the tumor boundaries. To assess this texture-captured microinfiltration, we defined one region-of-interest (ROI) adjacent to the tumor beyond the border of edema/invasion, and another on the contralateral hemisphere. All ROIs were carefully selected to include only white matter avoiding signals from adjacent tissues. Prior to feature extraction, an intensity normalization process was carried out to control for scanner/acquisition induced variations. Three hundred second-order textural features (Haralick gray level features) for each ROI along with the corresponding volumes were computed using an in-house software. A support vector machine (SVM) classifier acting on z-score normalized features was used to classify ROIs into peritumoral or contralateral. Performance of the classifier was tested using 80% of the data for training and 20% for testing (100 bootstrap copies).

Results

Overall, we found that SVM-based classification of texture patterns is a promising approach for identifying regions with microinfiltration. The binary SVM classification accuracy, sensitivity, and specificity, assessed by bootstrap analysis, were 84%, 84%, and 85% respectively.

Conclusions

Texture features classified these regions in a distinct class from other white matter regions, thus suggesting that invisible infiltrating cells could be captured by radiomic texture analysis. In the future, correlation with histological image-guided biopsies can be done to further elucidate the pathological infiltrating and genomic characteristics in this region (when obtained in *passé* at the trajectory towards tumor).

O-242

3:27PM - 3:30PM

Altered White Matter Metabolite Concentrations in Diabetic Patients with and without Diabetic Ketoacidosis.

C Fleischer¹, G Umpierrez¹, X Hu¹, S Dehkharghani², J Doan¹, S Moffat³, J Allen¹
¹*Emory University, Atlanta, GA*, ²*Emory University Hosp, Atlanta, GA*, ³*Georgia Institute of Technology, Atlanta, GA*

Purpose

Diabetes is associated with metabolic changes detectable with ¹H-MR spectroscopy (MRS). The impact of hyperglycemic crises on brain metabolites in adults is not known. We compared metabolite concentrations in diabetic patients with and without a history of diabetic ketoacidosis (DKA), the most common hyperglycemic emergency.

Materials and Methods

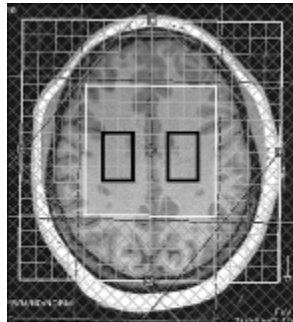
Patients with a history of >3 DKA episodes (n=11) and <72 hours after admission for acute DKA were imaged, along with diabetic controls without DKA history (n=11) and healthy subjects (n=9) on a 3T Siemens Prisma using multivoxel MRS (TR=1700 ms, TE=35 ms, 10 x 10 x 15 mm³ voxel size, 3 averages). A 2 x 3 voxel grid spanning the bilateral centrum semiovale was used to obtain metabolite concentrations (Fig. 1). LC Model (v6.3-1H) was used to estimate absolute metabolite concentrations and concentrations normalized to creatine plus phosphocreatine (/Cr). Values with Cramer-Rao lower bound values >20% were excluded. One-way ANOVA followed by a post-hoc Tukey's test between groups was used to determine significance (p<0.05).

Results

Metabolite concentrations are shown in Table 1. Bilateral myo-inositol (Ins) concentrations were increased significantly in both diabetic controls and DKA subjects versus healthy controls. Significant increases in bilateral Ins/Cr concentrations were detected in diabetic versus healthy controls. Right-sided, normalized N-acetylaspartate (NAA/Cr) concentrations were decreased significantly in DKA subjects versus healthy controls. No significant differences were detected between DKA subjects and diabetic controls.

Conclusions

We detected metabolic changes related to DKA, which may represent a biomarker of neurologic injury. Increased Ins concentrations observed in diabetic controls and DKA subjects may reflect glial cell proliferation or increased size, which may occur during inflammation. This has been described previously in diabetes but not in adult patients with DKA. While alterations in NAA concentrations, a measure of neuronal integrity, have not been reported consistently in diabetes, our findings indicate a measurable decrease in NAA in adult patients with DKA.



| Metabolite | F values | Control (c) vs Diabetic (d) | Control (c) vs DKA (m) |
|--------------|------------------------|-----------------------------|------------------------|
| Right Ins | F[2,30]=8.78 p=.001 | c<d p=.001 | c<m p=.027 |
| Right Ins/Cr | F[2,30]=4.47 p=.021 | c<d p=.016 | ns |
| Right NAA/Cr | F[2,30]=4.03 p=.029 | ns | c>m p=.034 |
| Left Ins | F[2,30]=8.98 p=.001 | c<d p=.001 | c<m p=.037 |
| Left Ins/Cr | F[2,30]=5.80 p=.008 | c<d p=.006 | ns |

Figure 1. Bilateral voxels used in analysis. **Table 1.** Group-wise comparison of absolute and normalized concentrations. (Filename: TCT_O-242_Figure1DKA.jpg)

O-244

3:33PM - 3:36PM

The Widened Sulcus: A New Imaging Sign for Detection of Meningoencephalocele

F Oyedeggi¹, S Hegde¹, B Branstetter¹, J Mettenburg¹, T Rath¹
¹University of Pittsburgh Medical Center, Pittsburgh, PA

Purpose

Acquired meningoencephalocele and persistent cerebrospinal fluid leak (CSF) are potentially life threatening diseases placing patients at risk for intracranial infection and necessitating surgical repair. Identification of meningoencephalocele can be diagnostically difficult due to small size and similar imaging appearance to paranasal sinus and temporal bone inflammatory opacification. Secondary imaging features such as a widened sulcus ("widened sulcus sign"), displaced gyrus ("fallen gyrus sign") and ipsilateral ex-vacuo ventricular dilatation may be useful to confirm the presence of a meningoencephalocele. The purpose of this study was to evaluate the accuracy of the widened sulcus sign, fallen gyrus sign and ipsilateral ventricular dilatation sign in the diagnosis of meningoencephalocele.

Materials and Methods

A retrospective review of magnetic resonance imaging (MRI) and/or computed tomography (CT) scans in patients who were referred for possible

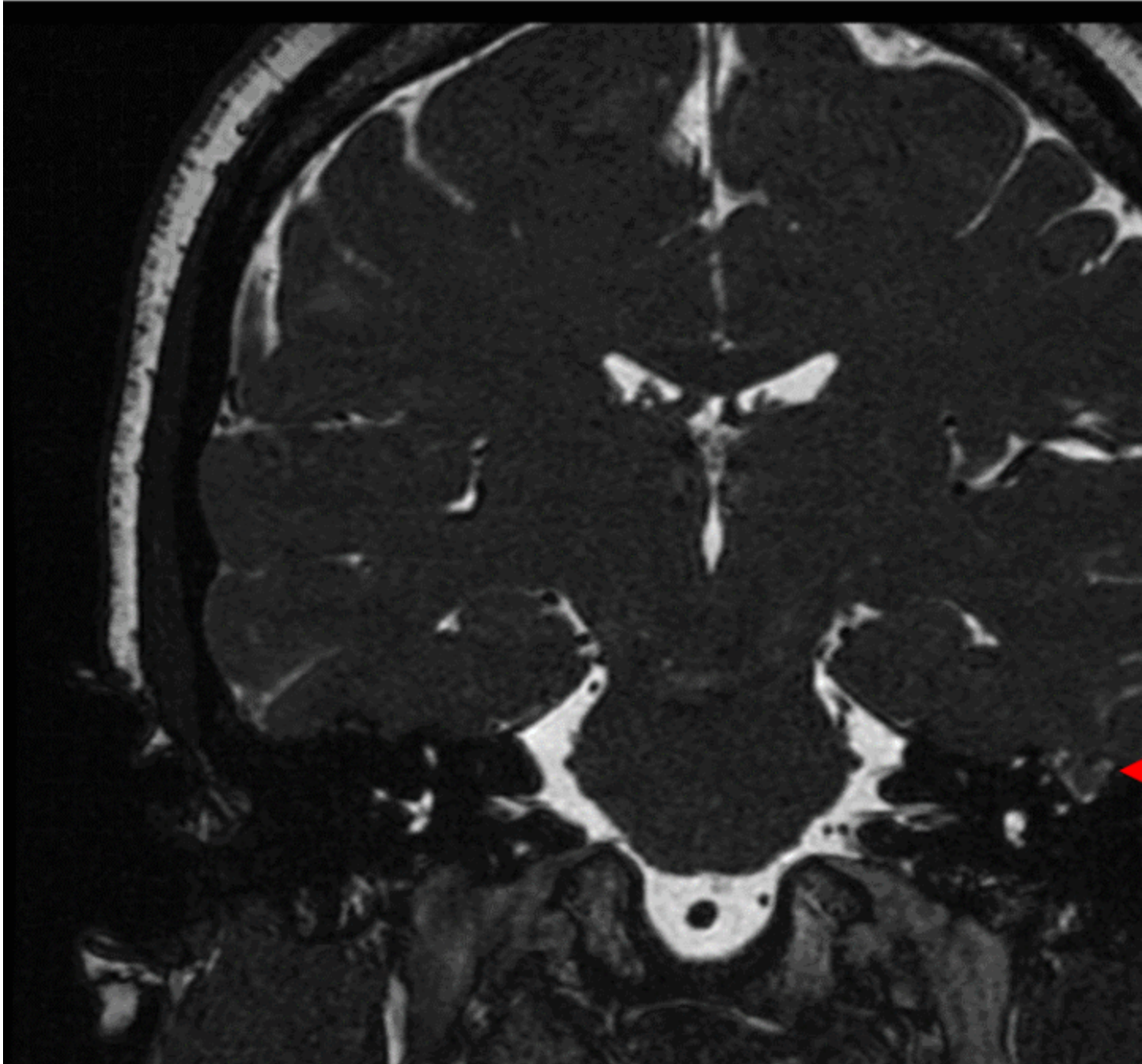
meningoencephalocele or CSF leak was performed. Patients with substantial distortion of the brain from prior surgery or trauma were excluded. Images were analyzed by a single CAQ-certified neuroradiologist for the presence of a widened sulcus sign, a fallen gyrus sign, or ipsilateral ventricular dilatation. The reference standard was surgical repair of a meningoencephalocele or negative endoscopic evaluation with negative beta-2 transferrin assay.

Results

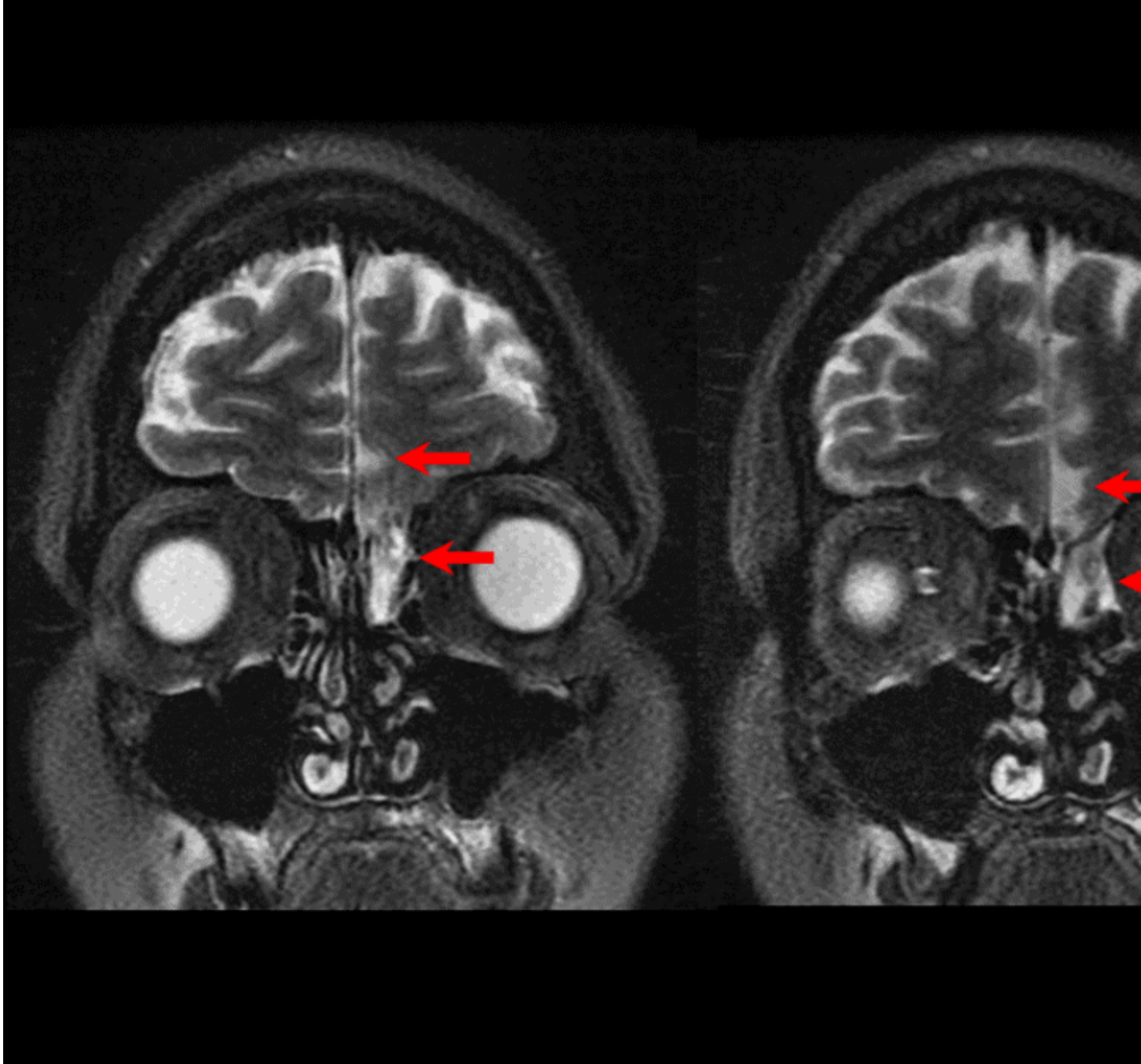
Twenty-eight patients met inclusion criteria. Meningoencephalocele was confirmed surgically in 23 patients. Five patients had no CSF leak or meningoencephalocele following beta-2 transferrin testing and endoscopic evaluation. The sensitivity of the widened sulcus sign, the fallen gyrus sign and the ipsilateral ventricular dilatation sign for meningoencephalocele were 87% (20/23), 45% (10/22) and 27% (6/22), respectively. In patients with a false negative widened sulcus sign (n=3), the fallen gyrus sign and ipsilateral ventricular dilatation sign also were negative. In all five patients without meningoencephalocele, the three signs were all negative (100% specificity).

Conclusions

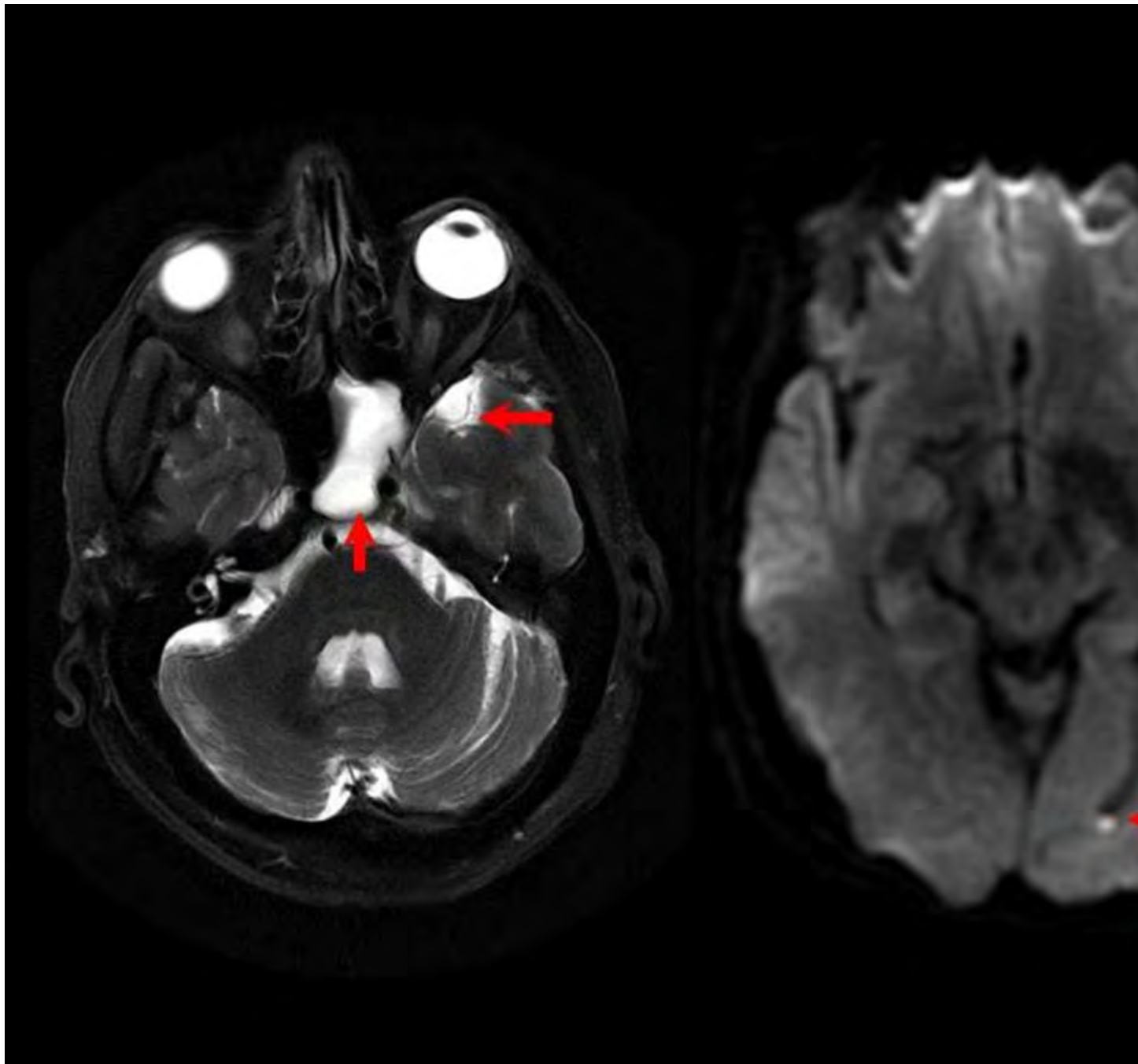
The widened sulcus sign is a highly accurate but previously unreported sign for meningoencephalocele. In patients with paranasal sinus opacification or temporal bone opacification adjacent to the skull base, or clinically suspected CSF leak, the widened sulcus sign should be sought to improve detection of meningoencephalocele.



(Filename: TCT_O-244_encephalocele.gif)



(Filename: TCT_O-244_encephalocele3.gif)



(Filename: TCT_O-244_encephalocelewithmeningitis.jpg)

O-245

3:36PM - 3:39PM

Microstructural changes within the basal ganglia differ between Parkinson disease subtypes

L Nagae¹, J Honce¹, J Tanabe¹, E Shelton¹, S Sillau¹, B Berman¹

¹University of Colorado School of Medicine, Aurora, CO

Purpose

Tremor dominant (TD) and postural instability/gait difficulty (PIGD) subtypes of Parkinson's disease (PD) patients are known to differ in their clinical course, with the PIGD subtype generally having a more severe course and greater association with nonmotor symptoms. Our study aims to investigate differences in microstructural changes in the basal ganglia between TD and PIGD subtypes of PD patients and controls utilizing diffusion tensor imaging (DTI).

Materials and Methods

Twenty-one patients diagnosed with idiopathic PD (12 TD and 9 PIGD) and 20 age-matched healthy controls were evaluated. Diffusion tensor imaging parameters of fractional anisotropy (FA), mean diffusivity (MD), axial diffusivity (AD), and radial diffusivity (RD) were extracted from bilateral caudate, putamen, globus pallidus and substantia nigra with automated regions of interest (ROIs) placement using structural probabilistic atlases (Fig. 1). Fractional anisotropy, MD, AD and RD values were compared across all groups using an analysis of variance (ANOVA) with unequal variance F test followed by pairwise comparisons among the groups using a Tukey-Kramer adjustment for multiple comparisons. A two-sample t-test also was used to compare FA, MD, AD and RD values between PD patients versus controls, and partial Spearman's correlations adjusted for age were used to check for post hoc correlations between FA and MD and clinical measures of disease duration, disease stage, and motor severity.

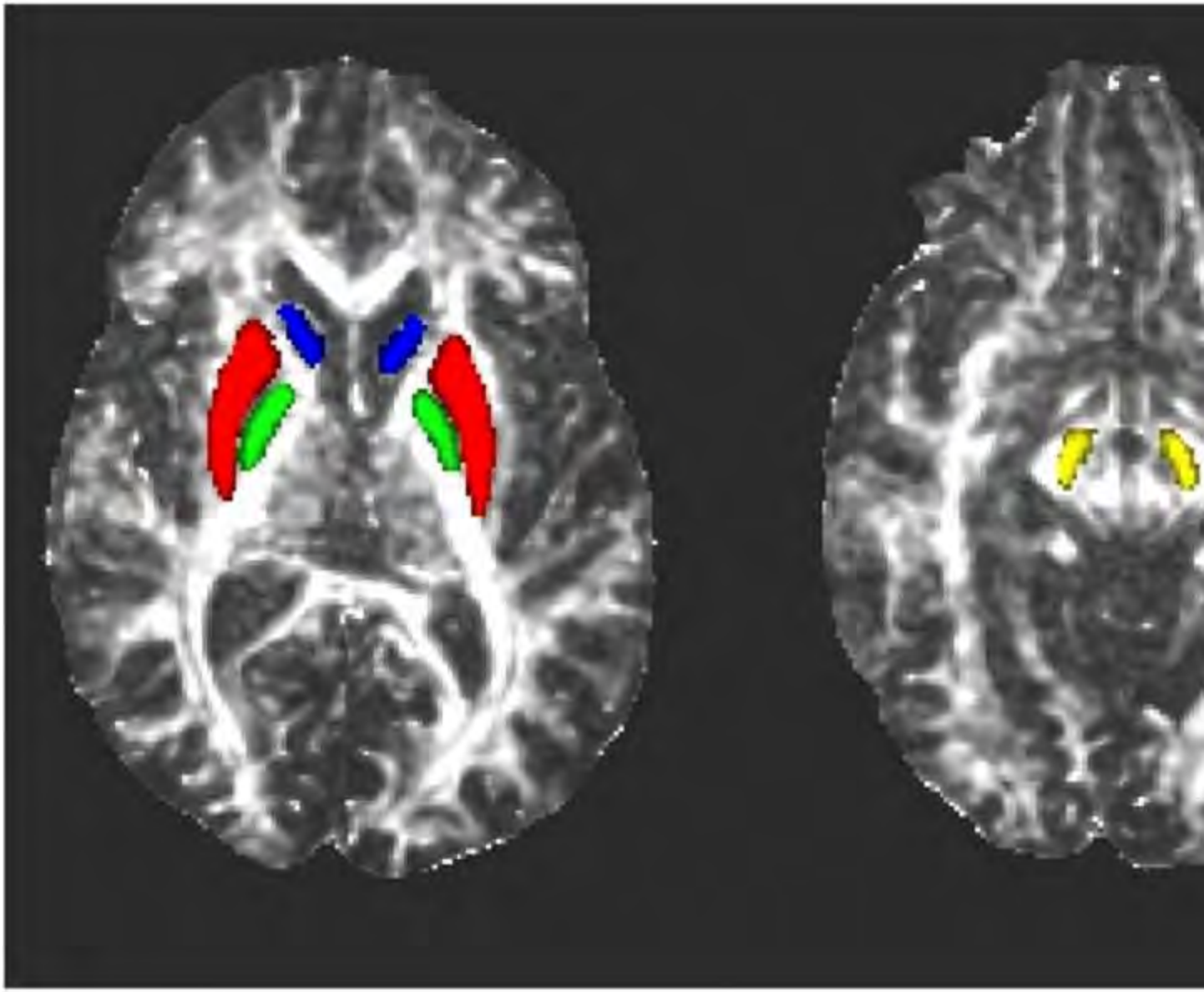
Results

A significant reduction in FA ($p=0.007$) and increases in MD ($p=0.029$) and RD ($p=0.017$) were seen in the left SN when comparing all groups, changes driven by the PIGD subtype. Parkinson's disease and controls differed by reduced FA in the right SN ($p=0.020$); increased MD in the SN (left: $p=0.039$; right: $p=0.020$) and globus pallidus (left: $p=0.020$; right: $p=0.049$); increased RD in the right SN ($p=0.022$) and bilateral globus pallidus (left: $p=0.026$; right: $p=0.049$) (Fig. 2). In the PIGD group, MD in the globus pallidus showed a positive correlation with disease stage (right: $r=0.764$, $p=0.027$) and motor severity (left: $r=0.814$, $p=0.014$).

Conclusions

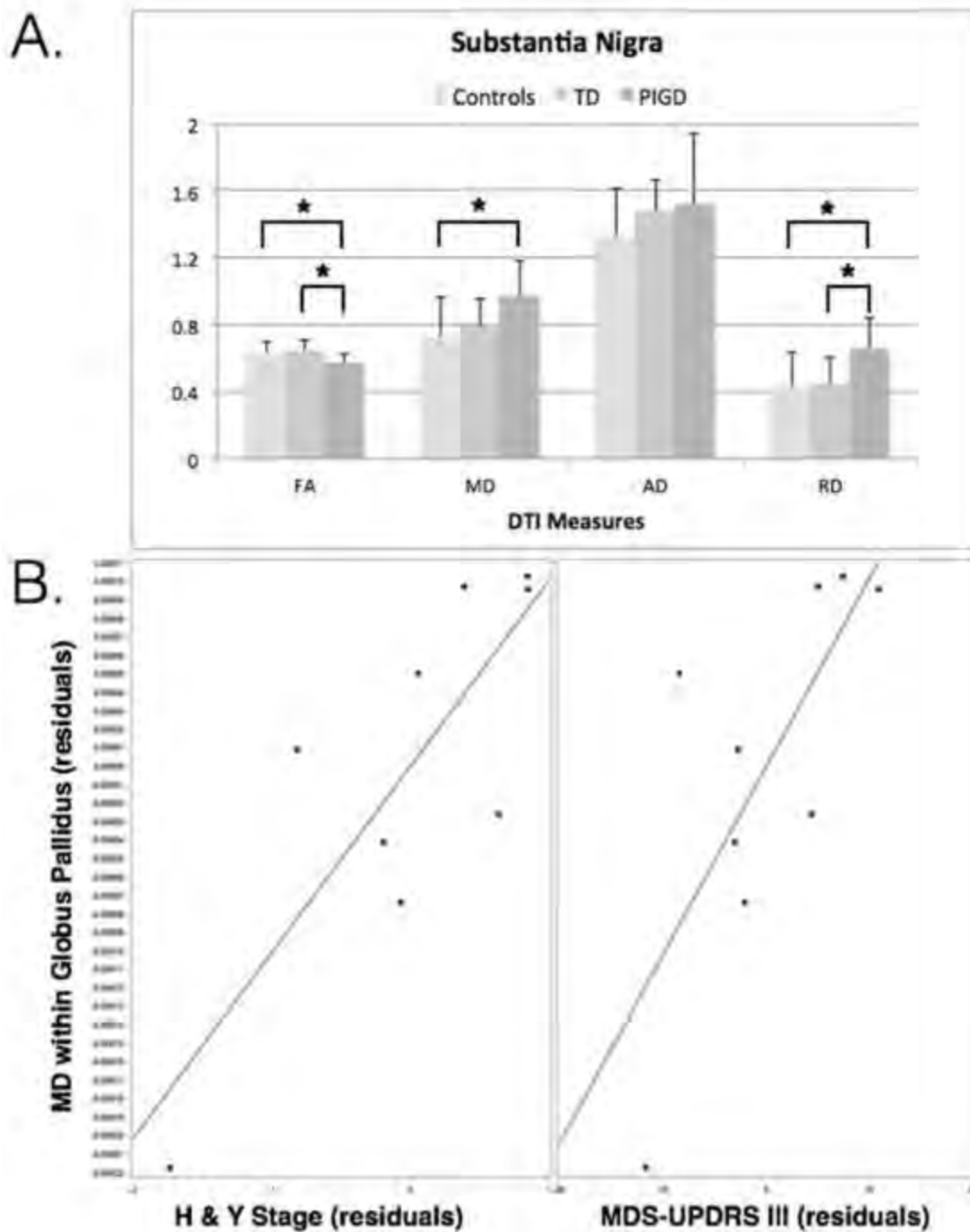
Our results support that DTI can detect microstructural alterations in the SN and globus pallidus of PD patients, and suggest that such changes within the SN may be able to differentiate PIGD and TD motor subtypes. In addition, our findings suggest that diffusivity changes in the globus pallidus are particularly relevant to patients with the PIGD motor subtype and may more accurately reflect motor severity and disease stage than changes affecting the SN.

Figure 1. Representative axial fractional anisotropy (FA) maps from one subject showing the locations of the ROIs after transformation to subject space. Blue – caudate nucleus, putamen, Green – globus pallidus; Yellow – substantia nigra.



(Filename: TCT_O-245_FIG1.jpeg.jpg)

Figure 2. (A.) DTI measures from left substantia nigra across groups showing significant differences ($p < 0.05$, corrected for multiple comparisons using Tukey-Kramer adjustment). **(B.)** Significant partial correlations adjusted for age between mean diffusivity (MD) in the right globus pallidus and H&Y disease stage ($r = 0.764$, $p = 0.027$) and between MD in the left globus pallidus and MDS-UPDRS III scores ($r = 0.814$, $p = 0.014$).



(Filename: TCT_O-245_FIG2_jpeg.jpg)

O-246

3:39PM - 3:42PM

Absence of the "Checkmark" Sign in Patients with Parkinson's Disease.

M Peckham¹, Y Miura¹, M Lee¹, B Bartnik-Olson¹, S Harder¹

¹LLUMC, Loma Linda, CA

Purpose

To determine whether the "checkmark" sign, a mineralized pattern in the region of the dorsolateral substantia nigra, is present or absent in patients with Parkinson's disease (PD). Background: Multiple studies have characterized normal and abnormal midbrain mineralization patterns, specifically in the setting of Parkinson's disease (PD). One pattern seen in normal subjects is a T1 and T2 hyperintense ovoid area within the dorsolateral aspect of the substantia nigra (swallow tail sign). Multiple studies have shown a loss of this hyperintense region in the setting of PD. Another regional pattern, a mineralized "checkmark" extending from the dorsolateral substantia nigra, has never been characterized before in normal or PD subjects (Fig. 1). Because of the checkmark's proximity to the swallow-tail region, we hypothesize that this mineralization pattern will be present in normal subjects and absent in PD.

Materials and Methods

Brain magnetic resonance imagings (MRIs) performed on a 3.0 T magnet of 30 PD and 40 age-matched control subjects were evaluated retrospectively by two investigators. The presence or absence of the checkmark sign, evaluated on SWI, was documented.

Results

A bilateral checkmark sign was significantly associated with disease state [Pearson Chi-square statistic 8.303 (df 1), $p = 0.004$], where the PD group more often had an absence of the checkmark sign bilaterally compared to the control group. When evaluated for laterality, the absence of the checkmark sign was significantly associated with the left side [Pearson Chi-square statistic 9.65 (df 1), $p=0.002$] in the PD group.

Conclusions

We describe a novel mineralization pattern in the midbrain – a "checkmark" extending from the dorsolateral substantia nigra, the same region as the previously described "swallow-tail" sign. This pattern was found to be absent more often in the PD group.

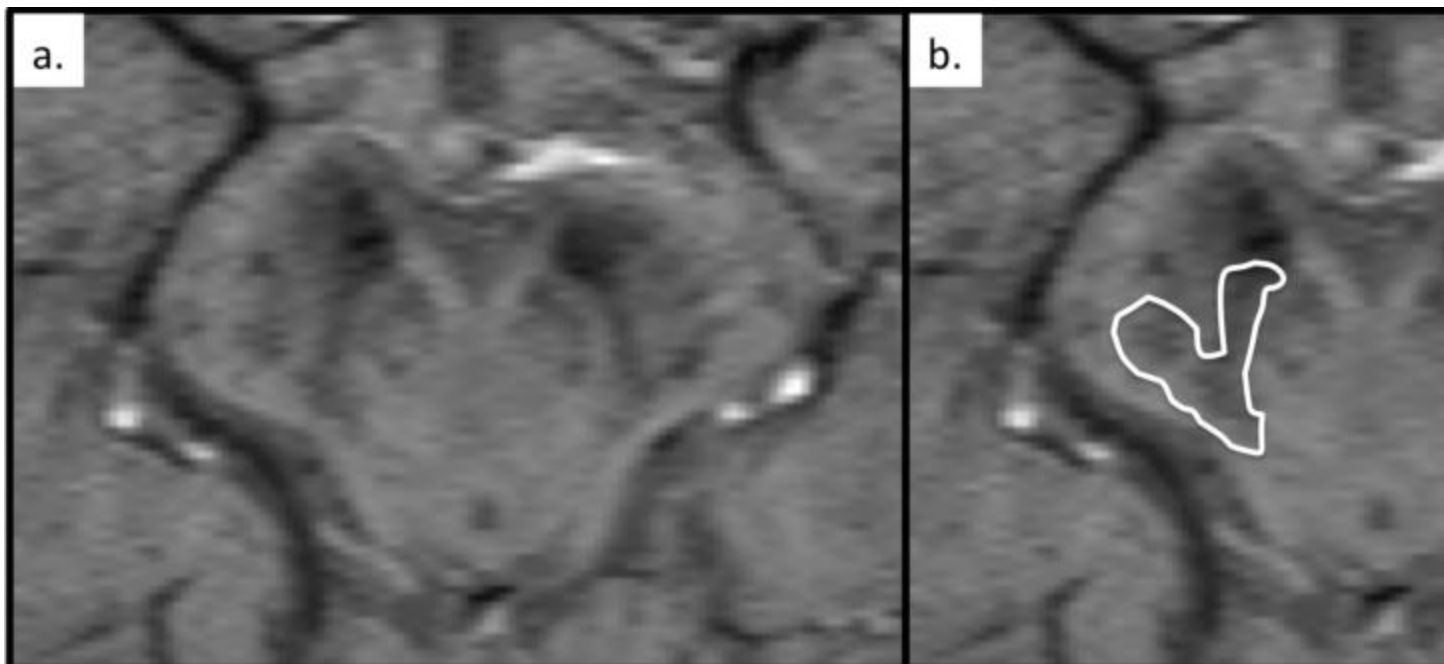


Fig 1. Axial SWI image through the level of the midbrain without (a) and with demonstrating “checkmark” signs bilaterally.

(Filename: TCT_O-246_CheckMarkFinalFig1.jpg)

O-247

3:42PM - 3:45PM

Treatment of Essential Tremors with MRI guided Focused Ultrasound and Post-Procedure Imaging

E Bourekas¹, V Krishna¹, C Fetko¹, D Boulter¹, W Slone¹, A Rezai¹

¹*The Ohio State University, Columbus, Ohio*

Purpose

To describe a new noninvasive magnetic resonance imaging (MRI)-guided technique for the treatment of essential tremors and describe the computed tomography (CT) and MRI findings post-treatment.

Materials and Methods

MRI-guided focused ultrasound (MRgFUS) thalamotomy is an emerging "noninvasive" treatment for essential tremor. The ultrasound energy is delivered across the intact skull, resulting in the thermal lesioning within the target. During the sonication, there is continuous MRI thermal monitoring which guides treatment. Sub-therapeutic sonication allows for clinical testing and precise target identification prior to final therapeutic lesioning. Computed tomography and MRI are obtained

postprocedure for documentation of the lesioning effect and to exclude hemorrhagic complications.

Results

Treatment effects are immediate with the thalamotomy resulting in significant improvement of tremor. CT (Fig. 1) obtained following the procedure demonstrates the left thalamotomy and excludes hemorrhage. Magnetic resonance imaging obtained within 24 hours demonstrates the small thalamotomy with restricted diffusion on diffusion-weighted imaging (Fig. 2), abnormal susceptibility on susceptibility-weighted imaging (Fig. 3) and evidence of edema on FLAIR imaging (Fig. 4) within the thalamus and surrounding the lesion.

Conclusions

Magnetic resonance focused ultrasound allows for the noninvasive treatment of patients with essential tremors with immediate clinical results. The radiologist should be aware of the immediate imaging findings as the technique becomes more available.

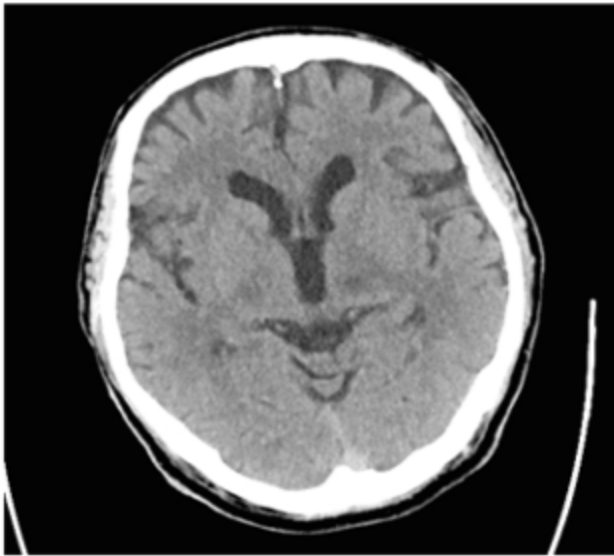


Figure 1

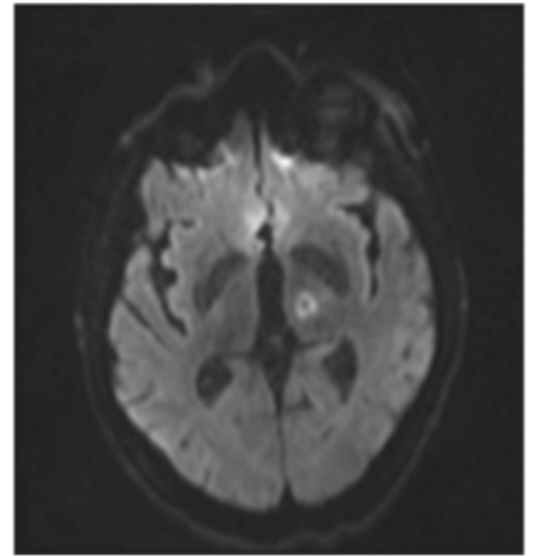


Figure 2

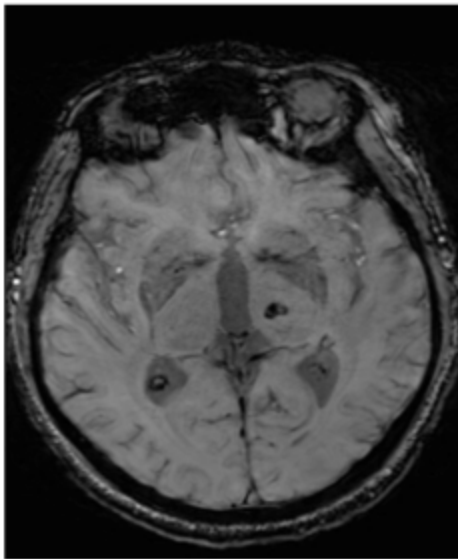


Figure 3

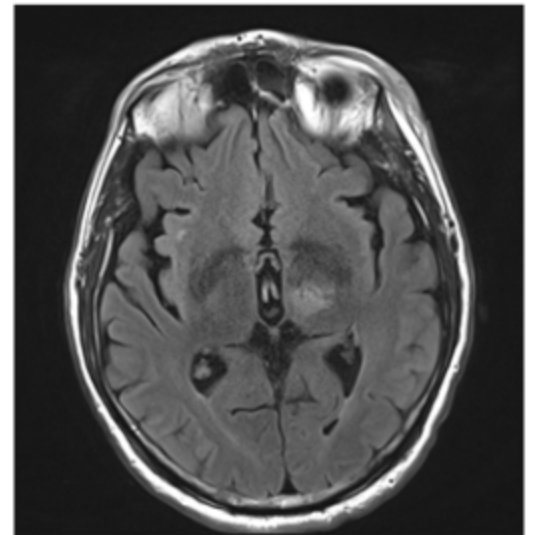


Figure 4

(Filename: TCT_O-247_ASNR2016MRFUSImages.gif)

O-248

3:45PM - 3:48PM

In-vivo T2 Quantification of Brainstem Nuclei in Normal Subjects at 3-T.

M Hoch¹, N Ben-Eliezer¹, S Chung¹, K Chen¹, E Ben-Avi¹, M Bruno², T Shepherd¹
¹NYU Medical Center, New York, NY, ²New York University, New York, NY

Purpose

We have implemented a new clinically feasible and quantitative brainstem magnetic resonance imaging (MRI) protocol that is an improvement over conventional 3T MRI in the direct visualization of brainstem substructures. Using echo modulation curve (EMC) T2 fitting software we sought to generate normal T2 values of brainstem nuclei in living subjects.

Materials and Methods

Six healthy right-handed subjects (Mean age 27.8 years, 2 Male) underwent noncontrast MRI of the head using a 20-channel head and neck coil on a 3T MRI (Skyra, Siemens Healthcare, Erlangen, Germany) using our brainstem protocol (1). For quantitative T2 mapping the multiecho spin echo sequence included 15 echoes at 10 ms intervals (TE = 10-150 ms, TR 5100 ms, Matrix 384 x 234, 2-slice acceleration, 2 mm slice thickness, 2 averages) and required 6 min. T2 and proton density (PD) maps of the brainstem were postprocessed from the multispin echo (MSE) datasets using a recently developed EMC T2 fitting software package, which relies on accurate Bloch simulations to model the exact signal evolution in MSE pulse-sequences by employing the exact radiofrequency pulse shapes and other experimental parameters (2, 3). The software package is custom-written in MATLAB and C++, then executed with MATLAB scripts and a graphical user interface. Manual regions of interest (ROIs) were placed over bilateral brainstem nuclei (Fig. 1) to generate T2 (in ms) and PD values compared within groups.

Results

The quantitative results are summarized in Table 1. Correlation with histology also is provided (4). Values for inferior brainstem nuclei were less reproducible given spin echo blood vessel pulsation artifacts. The lowest T2 value was seen in the red nucleus (RN). The highest PD value was the hypoglossal nucleus (XII). These results need to be validated with a larger group of subjects.

Conclusions

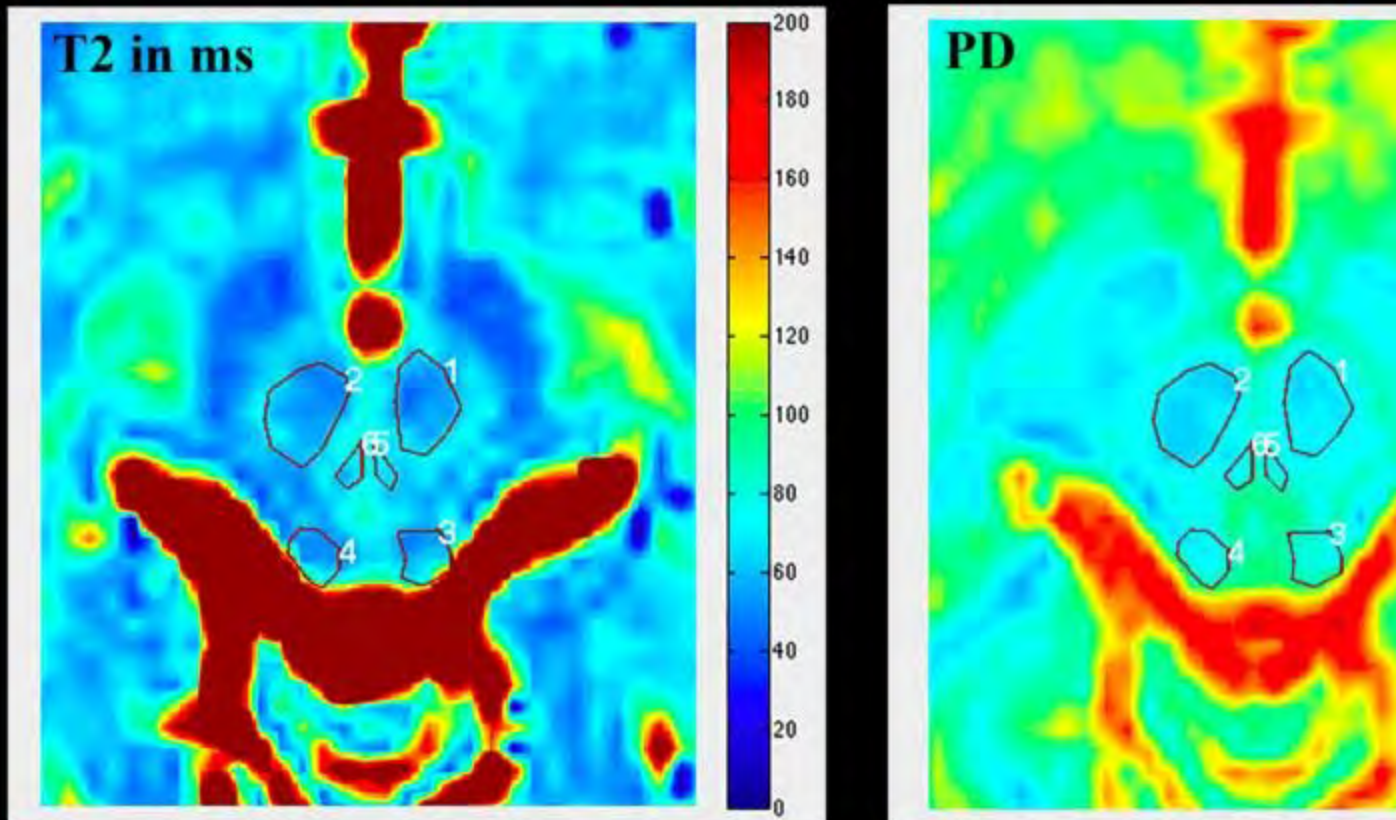
Quantification of directly visualized small brainstem structures was possible at 3T in normal subjects. This method could serve as a future tool for generating potential biomarkers to help diagnose and monitor neurodegenerative disease.

Table 1: EMC T2 and PD values of brainstem nuclei correlated with histology

| Brainstem Nuclei | Avg T2 ms | 95%CI | Avg PD | 95%CI | Dominant Histology |
|---|------------------|--------------|---------------|--------------|---|
| Cuneate Nucleus (CU) | 92.8 | +/-21.5 | 0.43 | +/-0.03 | Pleomorphic cells g |
| DMN Vagus (DMX) | 78.7 | 21.8 | 0.46 | 0.05 | 3 types of medium-s |
| Gracile Nucleus (GR) | 75.2 | 17.9 | 0.48 | 0.04 | Pleomorphic and sca |
| Hypoglossal Nucleus (XII) | 80.2 | 12.6 | 0.49 | 0.04 | Large multipolar mot |
| Inferior Colliculus (IC) | 69.1 | 9.7 | 0.42 | 0.03 | Marked cellularity ar |
| Inferior Olive (IO) | 57.6 | 7.0 | 0.44 | 0.02 | Uniform density, earl |
| Locus Coeruleus (LC) | 86.6 | 8.6 | 0.44 | 0.02 | Dorsal cellularity w/ |
| Medial Vestibular Nucleus (MVN) | 63.9 | 11.6 | 0.48 | 0.05 | Scattered, variable si |
| Mesencephalic Reticular Formation (MRF) | 59.7 | 1.4 | 0.38 | 0.02 | Small cells with glial s |
| Motor Trigeminal Nucleus (MoV) | 69.0 | 7.0 | 0.38 | 0.03 | Large multipolar mot |
| Oculomotor Nucleus (III) | 64.3 | 2.1 | 0.39 | 0.01 | Large multipolar mot |
| Periaqueductal Grey (PAG) | 76.5 | 6.1 | 0.47 | 0.01 | Small cells periphera acellular |
| Red Nucleus (RN) | 55.5 | 2.9 | 0.34 | 0.01 | Medium cells mixed neurons, myelin fiber accumulation |
| Solitary Nucleus (SOL) | 57.0 | 8.1 | 0.44 | 0.02 | Irregularly arranged s |
| Spinal Trigeminal Nucleus (SpV) | 61.4 | 7.3 | 0.42 | 0.03 | Small, closely packed |
| Substantia Nigra (SN) | 56.3 | 5.1 | 0.41 | 0.02 | Large cells w/ abund |
| Superior Colliculus (SC) | 70.5 | 6.7 | 0.41 | 0.01 | 7-layer laminated arr |

(Filename: TCT_O-248_BrainstemTable1.JPG)

Fig 1: EMC T2 & PD maps of rostral midbrain: RN(1,2), SC



(Filename: TCT_O-248_SubmitT2mapMBFLAT.jpg)

Tuesday

3:00PM - 4:30PM

Washington Marriott Wardman Park, Maryland A/B/C

11E-Young Professional Programming: Social Media Programming: Career and Social Media

11E-1

3:00PM - 3:15PM

Becoming a Leader in Private Practice

Barr, R.

Mecklenburg Radiology Associates, P.A.

Charlotte, NC

11E-2

3:15PM - 3:30PM

Becoming a Leader in Academics

Glastonbury, C.
University Of California, San Francisco
San Francisco, CA

11E-3

3:30PM - 3:45PM

WHY all Radiologists Should Use Social Media Professionally

Hoang, J.
Duke University Medical Center
Durham, NC

11E-4

3:45PM - 4:00PM

The Nuts and Bolts of Social Media: AKA How Do I Use This Stuff?

Lall, N.
Cincinnati Children's Hospital Medical Center
Cincinnati, OH

11E-5

4:00PM - 4:30PM

Social Media Super-Users Panel

McGinty, G. · Fitzgerald, R. · Chokshi, F. · Tomblinson, C.
Weill Cornell Medicine Radiology · University of Arkansas for Medical Sciences ·
Emory University School of Medicine · Mayo Clinic
New York, NY · Little Rock, AR · Atlanta, GA · Phoenix, AZ

Tuesday

3:00PM - 4:30PM

Washington Marriott Wardman Park, Roosevelt 4

11F-ASSR Programming: Advanced Interventional Spine Procedures

11F-1

3:00PM - 3:25PM

Regenerative Spine Medicine: A Primer for Neuroradiologists

Johnson, B.
Center for Diagnostic Imaging
Minneapolis, MN

11F-2

3:25PM - 3:40PM

The Future Spine Radiologist: Integrating Imaging and Procedures for Precision Diagnosis and Treatment

Lawler, G.
Neuroimaging and Interventional Spine Services
Danbury, CT

11F-3

3:40PM - 4:00PM

The Spine Clinic: Moving Toward ABR Pain Medicine Certification

Ortiz, A.
Winthrop University Hospital
Mineola, NY

11F-4

4:00PM - 4:20PM

Interventional Pain Management in Failed Back Surgery Syndrome

Georgy, B.
North County Radiology
San Diego, CA

11F-5

4:20PM - 4:30PM

Discussion

Tuesday

4:45PM - 6:15PM

Washington Marriott Wardman Park, Marriott Ballroom

12A-ASPNR Programming: Cased Based Competition (AR)

Tuesday

4:45PM - 6:15PM

Washington Marriott Wardman Park, Washington 4/5/6

12B-Drugs and Bugs: Global Disasters

12B-1

4:45PM - 5:10PM

Outbreak: Illicit Drugs and Infective Bugs

Lim, T.

National Neuroscience Institute

Singapore

12B-2

5:10PM - 5:35PM

Bugs and Drugs: CNS Manifestations Associated with Illicit Drugs and Infections in Brazil

Brandão, L.

Clínica Felipe Mattoso

RIO DE JANEIRO, RJ

12B-3

5:35PM - 6:00PM

Drugs and Bugs: Look What the Boeing Dragged In

Tsiouris, A.

New York-Presbyterian - Weill Cornell Medical Center

New York, NY

12B-4

6:00PM - 6:15PM

Discussion

Tuesday

4:45PM - 6:15PM

Washington Marriott Wardman Park, Washington 1/2/3

12C-Organizational Dynamics

12C-1

4:45PM - 5:20PM

Radiology Group Dynamics-Moving from Dysfunction to Fun Using Leadership and Citizen Training

Lexa, F.

Wharton School, Univ. of Pennsylvania

Philadelphia, PA

12C-2

5:20PM - 5:55PM

There are Many Groups in your Radiology Group: Leading Them to Success

Simon, A.

Seton Hall University

South Orange, NJ

12c-3

5:50PM - 6:15PM

Discussion

Tuesday

4:45PM - 6:15PM

Washington Marriott Wardman Park, Roosevelt 1-3

12D-PARALLEL PAPER SESSION: Turbo Talks: Hot Topics in Neuro

Socioeconomics

O-249

4:45PM - 4:48PM

High Levels of Gadolinium Deposition in the Skin of a Patient with Normal Renal Function

D Roberts¹, K Maravilla², C Welsh¹, S Lindhorst³, W Davis⁴

¹Medical University of South Carolina, Charleston, SC, ²Univ. of Washington, Seattle, WA, ³Medical University of South Carolina, Charleston, SC, ⁴National Institute of Standards and Technology, Charleston, SC

Purpose

Our objective is to raise awareness concerning the potential deposition of high levels of gadolinium in the skin of patients with normal renal function, based on estimated glomerular filtration rate (eGFR) values greater than 59 ml/min/1.73 m², following exposure to large cumulative doses of gadolinium-based contrast agents (GBCAs).

Materials and Methods

Here we present a patient with normal renal function who underwent 61 contrasted brain magnetic resonance imaging (MRI) scans over the course of 11 years. Skin biopsies from the forearm and lower extremity were analyzed with inductively coupled plasma mass spectrometry (ICP-MS), laser ablation ICP-MS (LA-ICP-MS), and hydrophilic interaction liquid chromatography ICP-MS (HILIC-ICP-MS).

Results

Inductively coupled plasma mass spectrometry demonstrated high levels of gadolinium deposition (14.5±0.4 microg/g), similar to previously reported gadolinium levels within the skin of patients with nephrogenic systemic fibrosis. Laser ablation ICP-MS demonstrated deposition of gadolinium within the deep layers of skin. Speciation analysis using HILIC-ICP-MS demonstrated the presence of intact gadolinium-chelate species. Light microscopy demonstrated increased CD34 immunoreactivity in the connective tissue septations of the subcutaneous adipose tissue. The patient had no history of skin disorders, but did have severe joint contractures of unknown etiology.

Conclusions

Our results, in contradiction to published literature, suggest that in patients with normal renal function, exposure to GBCAs in high cumulative doses, can lead to significant gadolinium deposition in the skin. This finding is in line with more recent reports of gadolinium deposition in the brain of patients with normal renal function. Future studies are required to address possible clinical consequences of gadolinium

deposition in the skin, brain and other organs in patients with normal renal function. We recommend, in addition to following FDA and ACR guidelines based on eGFR values, that caution be used when administering large cumulative doses of GBCAs and that total cumulative dose is recorded in the patient's medical record.

O-250

4:48PM - 4:51PM

Prospective Observational Post-marketing Study on the Safety of Gadoterate Meglumine - Final Results in the pediatric cohort of over 1,600 children.

A Gottschalk¹, B Kress¹

¹*Krankenhaus Nordwest, Frankfurt am Main, Germany*

Purpose

To assess the safety profile of gadoterate meglumine (DOTAREM®) in a broad patient population scheduled for contrast-enhanced magnetic resonance imaging (MRI). Secondary objectives were to detect any case of nephrogenic systemic fibrosis (NSF) suspicion and to collect efficacy data (image and diagnosis quality).

Materials and Methods

This global observational study recruited 35,499 patients scheduled for gadoterate meglumine-enhanced MRI. A large pediatric subpopulation of 1,631 patients [53.5% male, mean (\pm SD) age of 10.2 (\pm 4.9) years] from nine countries and including 106 children (6.5%) less than 2 years old was analyzed. Magnetic resonance imaging indications, risk factors and adverse events were recorded. A specific follow up of at least 3 months was planned for detection of any NSF suspicion in patients with moderate to severe renal impairment (3 children among 514 patients). Image quality was analyzed in five classes (very poor, poor, fair, good and very good) and ability to come to diagnosis was assessed.

Results

The main MRI indication for the pediatric population was imaging of the central nervous system (80.4%) followed by musculoskeletal system imaging (11.1%). The most frequent risk factors were nervous system disorders (16.6%), any stage of renal impairment [9.8%; with a mean estimated creatinine clearance or eGFR of 74.1 mL/min (/1.73 m²), (range: 28-89)] and allergies (5.2%). Only one adverse event (mild nonserious vomiting) that was deemed doubtfully related to gadoterate meglumine was described in a 2-year-old child (<0.1%) with brain tumor. No suspicion of NSF was reported. Good to very good image quality was obtained for more than 98% of the pediatric patients and diagnosis could be established for 99.6% of the patients.

Conclusions

The SECURE study confirmed the very good safety profile of gadoterate meglumine

in a large pediatric population as well as its efficacy in terms of image and diagnosis quality in routine practice.

O-251

4:51PM - 4:54PM

Safety of MRI in patients with implantable cardiac electronic devices.

S Mohan¹, J Schmitt¹, H Litt¹, E Motuzko², N Lerner¹, T Brunker¹, S DIXIT¹, L Desiderio¹, L Loevner¹, S Jha¹

¹Perelman School of Medicine of the University of Pennsylvania, Philadelphia, PA, ²Cooper University Hospital, Camden, NJ,

Purpose

A patient with implantable cardiac electronic device (ICED) has a 50-75% lifetime chance of needing an magnetic resonance imaging (MRI) (1, 2). Device-related complications from MRI are speculative. We assess the safety of MRI in patients with ICEDs who needed MRI for clinical management.

Materials and Methods

Between 2008 and 2015, 600 patients with ICED had MRI at 1.5T under an interdisciplinary protocol consisting of pre-approval by an attending radiologist, pre and postprocedure device interrogation and reprogramming, and intraprocedure monitoring. We performed a chart review to search for adverse events within 1 year of MRI. Adverse events were defined as death, arrhythmia requiring urgent treatment during MRI, and permanent device malfunction.

Results

Most patients had MRI of the brain and spine (46%), or heart (44%). There were 32 deaths within 1 year of MRI, all except one was adjudicated as not related to MRI; there was insufficient information concerning one patient to determine cause of death. Two patients with ICDs were removed from the scanner and shocked for symptomatic ventricular tachycardia, one patient developed symptomatic atrial fibrillation during the MRI and was admitted to the hospital. However, in no patient did the ICED malfunction.

Conclusions

With careful patient selection, preparation and monitoring, the adverse event rate related to MRI in patients with implanted devices is very low.

O-252

4:54PM - 4:57PM

RISE (Radiology International Student Education): Creation and Utilization of Virtual Online Classroom for Global Neuroradiology Education

L Busby¹, I Brown¹, G Mwangi², M Rawlings-Fein¹, P Sundaram¹, C Mutch³, W Dillon¹, B Rehani¹

¹UCSF, San Francisco, CA, ²Kenyatta National Hospital, University of Nairobi, Kenya, Nairobi, CA, ³University of California, San Francisco, San Francisco, CA

Purpose

One of the major challenges facing international neuroradiology is a lack of available neuroradiology fellowship training. For example, the entire continent of Africa has no neuroradiology fellowship training available within the region. International travel to complete fellowship training presents financial challenges for trainees and is in practice unsustainable as a routine method of neuroradiology training. We created an innovative solution by designing a virtual classroom, which allows residents from around the world to tune in live during dedicated neuroradiology lectures at UCSF.

Materials and Methods

A virtual classroom was created at UCSF Medical Center to enable international radiology residents to tune in live to a series of dedicated neuroradiology lectures given at UCSF. The pilot project was launched with Kenyatta National Hospital, University of Nairobi, Kenya. Kenyatta National Hospital has 45 radiology residents. Specifically, the live lectures involve two-way audio and video communication with interactive technologic solutions to annotate shared slides. The limitations in internet access, equipment availability, and cross platform technologies were solved with support of local IT staff and the Center of Digital Health and Innovation at UCSF.

Results

The impact of the virtual classroom was studied with close monitoring using pre and postlecture online exams. Advanced result analytics to assess the longitudinal performance of each radiology resident at University of Nairobi is being performed to assess the improvement in knowledge gap in neuroradiology. For asynchronous teaching, the RISE platform provides continuous online access to the recorded lecture database for access across different time zones.

Conclusions

The lack of international subspecialty training in neuroradiology demands innovative solutions to meet the demand for neuroradiology training. Live and interactive online virtual classrooms represent a cost effective and practical method for expanding neuroradiology training to regions with no available fellowship training. In the future, the aim is to expand the RISE curriculum to include other countries around the world for live virtual education in neuroradiology, as well as to develop a defined neuroradiology curriculum.

O-253

4:57PM - 5:00PM

Making Stroke Imaging Better around the World? Global Survey of Radiologists in 20 Countries

I Brown¹, L Busby¹, C Mutch², W Dillon¹, D Cooke¹, B Rehani¹

¹UCSF, San Francisco, CA, ²University of California, San Francisco, San Francisco, CA

Purpose

Stroke poses a major health challenge in today's world. "Time is Brain" in stroke and every minute counts in stroke management. To what extent are we able to provide timely imaging to these patients globally and if not what can be done? Our aim was to survey radiologists across developing countries in Asia, Europe and South America to assess the stroke care and find out what in their opinion are the most effective ways to improvise imaging and management.

Materials and Methods

A standardized questionnaire containing 18 questions was sent to radiologists in 25 developing countries across the world. Radiologists from 20 countries responded (response rate = 80%). These include Kenya, Algeria, Rwanda, Sri Lanka, Malaysia, Costa Rica, Macedonia, Bulgaria, Mexico, China, India, Uruguay, Burma and Venezuela among others.

Results

Survey results indicated that most of the countries (72%), lack access to computed tomography (CT) scanners. Intravenous tissue plasminogen activator (tPA) is the standard of care of ischemic stroke and cannot be given unless hemorrhage is excluded on CT. Also, this only can be administered for a specific time window after symptom onset. To maximize patients who can benefit from thrombolysis, the key is to have a short Emergency Room Door to CT scan time. Unfortunately, Door to CT scanner time is more than 30 minutes in 83% (95% CI being 80.5-85.4%). Moreover, 77% of the countries had shortage of the drug tPA. Overall, radiologists rated their knowledge as "average" in reading stroke imaging and 77% (95% CI being 74.5-79%) believed that further training would be helpful. Minority had access to neurointerventionalist (33%) and Telestroke services (27%). When questioned about the three most powerful ways to improvise stroke imaging in their respective countries, the highest rated choices were: training programs on stroke imaging to improvise knowledge among radiologists, campaigns to increase awareness in the community and improvising access to CT.

Conclusions

This survey helps radiologists around the world communicate the imaging needs in stroke in their respective countries and how they can be met. This can help radiologists who want to reach out in their humanitarian efforts to improve imaging around the world.

O-254

5:00PM - 5:03PM

Centralization Management in Endovascular Treatment of Aneurismal Subarachnoid Hemorrhage The 10 Years Experience of Oversea Transfer in Martinique

M Schertz¹

¹*Pitié Salpetriere, Paris, France*

Purpose

Hospital procedural volume of endovascular therapy is related with outcome in aneurysmal subarachnoid hemorrhage (aSAH). Because of a low volume of patients in Martinique, the further management of SAH consists in transferring overseas by plane patients with aSAH, to a reference center in Paris for endovascular treatment. The aim of this study was to evaluate the cost, the safety and the outcome related to this unique management.

Materials and Methods

We retrospectively identified all patients with aSAH in Martinique from 2004 to 2014. Medical reports were analyzed. Mean cost estimation was done using data from our institution.

Results

In the 10 years study period 120 patients had aHSA in Martinique. Ninety-one of them (76%) were transferred by plane to Paris. Among the transferred patients, 89 had an endovascular treatment of aneurysm (98%) with an average time from diagnostic to treatment of 2 days. Eight transferred patients died within 30 days (Mortality rate = 8.8%). No patients died during the transportation. Total 30 days mortality in Martinique was 25%. Total transportation procedure was estimated at 18.000 euros per transfer.

Conclusions

Long distance plane transfer of aSAH to high volume specialized center is a safe management. This management can be used in isolated areas with low volume of aSAH. It results in a normal regional mortality rate for an acceptable cost.

O-255

5:03PM - 5:06PM

The Use of High-Risk Criteria in Screening Patients for BCVI: A Survey

X Wu¹, V Kalra¹, D Durand¹, R Liu¹, R Bronen¹, K Abbed¹, H Forman¹, A Malhotra¹

¹*Yale University School of Medicine, New Haven, CT*

Purpose

Blunt cerebrovascular injury (BCVI) is uncommon, but delayed detection can have disastrous consequences. Multiple screening criteria are proposed for detection of BCVI, among which Denver criteria is the most commonly used (1). We aim to examine the utilization of screening criteria in the emergency department (ED) of our institution, and assess whether patients with risk factors were imaged.

Materials and Methods

A survey questionnaire was sent out to radiologists in a large, academic institution. Upon the approval of our Institutional Review Board, a search was performed in the database for the use of computed tomography angiography (CTA) and magnetic resonance imaging angiography (MRA) among patients with risk factors. Patients from the last 11 years were included (January 2004 - December 2014).

Results

The survey was sent to a total of 173 radiologists with 41 responses, out of which 35 were complete. Most of the physicians (30 out of 35) surveyed selected CTA as their preferred modality to screen for BCVI whereas the remaining selected MRA. Digital subtraction angiography (DSA) was not preferred by any of the respondents. None of the respondents reported routine use of the screening criteria or Denver Grading scale in their readouts. Only five selected risk factors listed in the Denver criteria correctly. In the institution search, among the 1,069 patients with blunt trauma and risk factors for BCVI, 122 underwent at least one angiographic study, giving a screening rate of 11.4%. There was an increase in the screening rate after February 2010 in all four risk factors, but only statistically significant among patients with foramen transversarium fractures and C1 – C3 fractures.

Conclusions

Both the Denver screening criteria and grading scale of vascular injury have been underutilized in the ED for patients with risk factors. Greater awareness and utilization of imaging potentially can result in decreased incidence of subsequent stroke in patients with blunt injury.

| Fracture Type | Screening Rate Before Feb, 2010 | Screening Rate After Feb, 2010 | <i>p</i> -value |
|------------------------|---------------------------------|--------------------------------|-----------------|
| Skull base | 28.1 | 37.2 | 0.0 |
| Foramen transversarium | 70.8 | 85.3 | 0.0 |
| LeFort | 23.0 | 29.8 | 0.1 |
| C1 – C3 | 27.5 | 36.1 | 0.0 |

(Filename: TCT_O-255_TableforASNR.jpg)

Cost-Effectiveness Analysis of MRI in Cervical Spine Clearance After Blunt Trauma

X Wu¹, V Kalra¹, D Durand¹, R Liu¹, R Bronen¹, K Abbed¹, H Forman¹, A Malhotra¹
¹*Yale University School of Medicine, New Haven, CT*

Purpose

There has been significant controversy on the utility of magnetic resonance imaging (MRI) in cervical spine (CS) clearance after blunt trauma and negative computed tomography (CT) (1-5). This cost-effectiveness analysis aims to assess the utility of MRI by taking many pertinent factors into consideration – including negative predictive value of initial CT, MRI false positive rate, the costs of delayed injury detection.

Materials and Methods

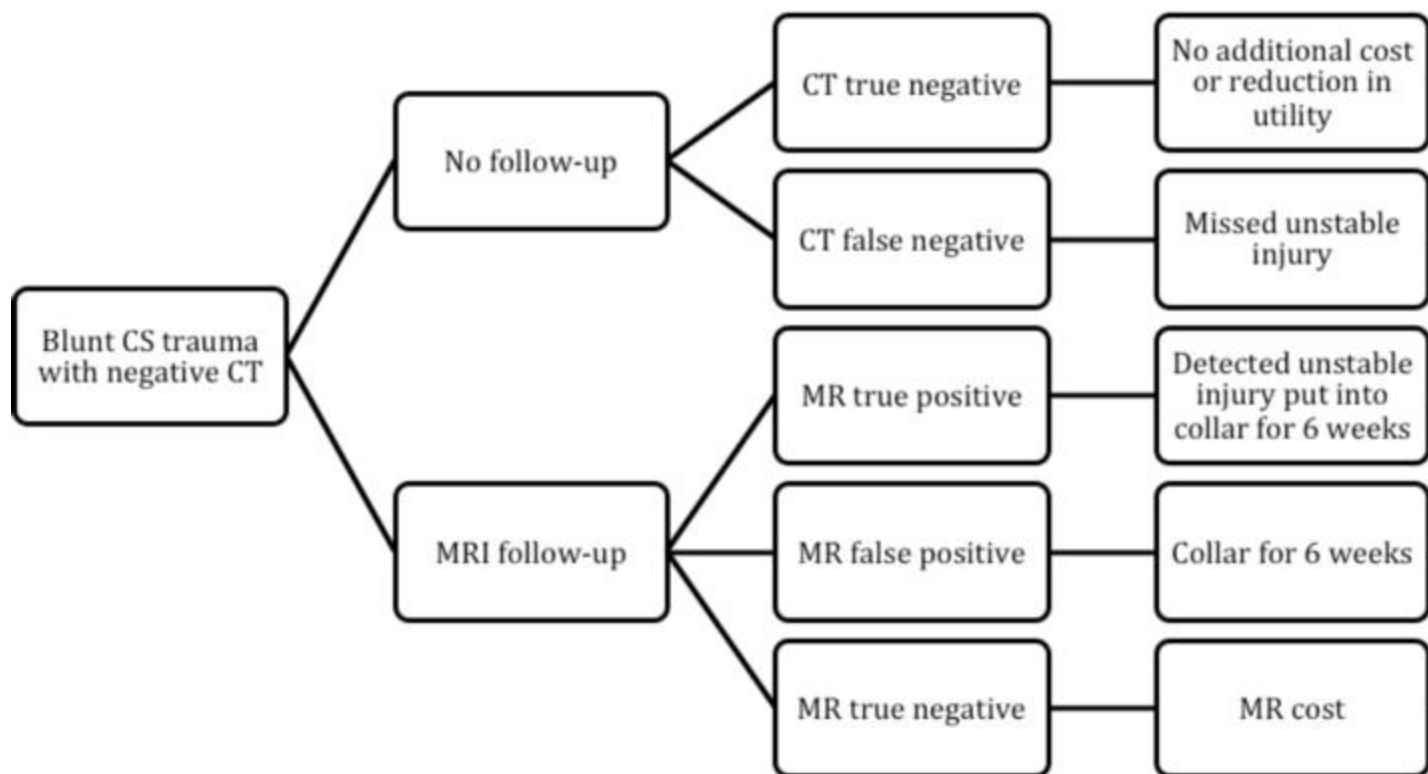
A modeling-based economic decision analysis was performed from a payer's perspective using TreeAge Pro Suite 2014. The two strategies being compared were no follow up after a normal CT, MRI follow up, and Markov model with an annual 3% discount rate was used. Most of the clinical parameters were derived from past literature and a meta-analysis by the authors. Two sets of analyses were carried out using Medicare costs and institutional costs.

Results

Magnetic resonance imaging follow up has an expected cost of \$423 and utility of 18.14 QALY per patient, whereas no follow up has an expected cost of \$1,736 and utility of 18.15 QALY per patient. Magnetic resonance imaging is the more cost-effective strategy, but the difference in effectiveness is minimal. When we assumed the negative predictive value from the pooled meta-analysis average by the inverse of variance, the cost of no follow up drops to \$29.6. In Monte Carlo simulation, no follow up is a better strategy in 40.0% of all iterations. When institutional cost of MRI is used, no follow up is more cost-effective in 99.1%. Sensitivity analyses demonstrate that MRI is the less optimal strategy in most clinical settings and that the percentage of missed ligamentous/soft tissue injury developing into cord injury has the largest impact on the conclusion.

Conclusions

Although MRI has been used as the gold standard to clear CS, its high false positive rate and the rarity of missed injuries on CT render MRI a less cost-effective strategy than no follow up.



(Filename: TCT_O-256_figure1.jpg)

O-257

5:09PM - 5:12PM

Utilization of Inpatient Neuroimaging MRI Studies: Do We Need Guidelines Beyond Existing American College of Radiology (ACR) Appropriateness Criteria?

M Del Guzzo¹, P Mehta¹, S Brown¹, K Mortelet¹, R Rojas¹, R Bhadelia¹

¹Beth Israel Deaconess Medical Center, Boston, MA

Purpose

There is increasing concern about over-utilization of high-cost imaging studies such

as magnetic resonance imaging (MRI) during hospital admissions. Judicious and appropriate use of inpatient MRI services may affect duration of hospital stay and overall healthcare-related costs. Our purpose was to perform a pilot study to assess if existing American College of Radiology (ACR) appropriateness criteria for neuroimaging may be sufficient to identify MRI studies that were performed inappropriately in the inpatient setting.

Materials and Methods

We retrospectively reviewed inpatient MRI scans performed for neurological indications over 1-month period at our tertiary care center. We determined the appropriateness of neuroimaging MRI orders based on the existing ACR appropriateness criteria as well as consensus online medical record review. All inpatient studies were classified as: (1) Appropriate: ACR rating of 4 or more and record review suggesting importance in immediate clinical management. (2) Inappropriate: ACR appropriateness criteria of 4 < and/or a record review suggesting that it could be performed as an outpatient study without altering immediate clinical management. (3) Redundant: If the clinical question had already been answered by another imaging modality.

Results

Of the 293 inpatient MRI studies performed, 235 (80.2%) were considered appropriate, 48 (16.4 %) inappropriate and 10 (3.4 %) redundant. Several additional studies could have been classified as inappropriate provided: (1) there had been a prospective dialogue between the radiologist and referring physician, (2) patient convenience was not accommodated (inpatient MRI to exclude metastasis in the absence of neurologic symptoms), (3) there existed a defined appropriateness criteria for inpatient indications (total spine screening MRI for bacteremia without back pain).

Conclusions

Our results suggest that one out of every five inpatient MRI performed for neuroimaging at our institution was either inappropriate or redundant. Inpatient studies could be further decreased if there were specific criteria for inpatients along with ongoing direct involvement of a radiologist.

O-258

5:12PM - 5:15PM

Prevalence of Repetitive CT and MR Imaging of the Brain at a Tertiary Care Academic Medical Center

D Friedman¹, R Gorniak²

¹*Sidney Kimmel Medical College at Thomas Jefferson University, Philadelphia, PA,* ²*Sidney Kimmel Medical College at Thomas Jefferson University, Philadelphia, PA*

Purpose

Increasing radiation exposure to the population as a result of medical imaging [especially computed tomography (CT)], as well as recently described gadolinium deposition in the brain with repeated use of gadolinium-based contrast agents (as few as four scans), are hot topics in radiology. We assessed the prevalence of repetitive CT and MR imaging of the brain at a tertiary care academic medical center.

Materials and Methods

A radiology database at a tertiary care academic medical center was interrogated for a 45 month period (12/2010 – 9/2014) and then for an additional 12 months through 9/2015 (57 month period). Repetitive imaging was defined as six or more scans for either of these time periods. For CT imaging, the number of patients having 6-10 scans, 11-20 scans, 21-50 scans, and >50 scans was determined for the two time periods; CT/CTA brain performed at the same sitting was counted as one scan. For magnetic resonance imaging (MRI), the number of patients having 6-10 scans, 11-20 scans, and >20 scans was determined for the two time periods; MRI/MRA brain performed at the same sitting was counted as one scan. Scans were performed in emergency department, outpatient office, and/or inpatient settings.

Results

Regarding CT brain imaging, a total of 57,041 patients were scanned during the 45 month time period; 1520 had 6-10 scans; 346 had 11-20 scans; 40 had 21-50 scans; four had greater than 50 scans. A total of 1,910 patients (3.3%) had repetitive CT imaging of the brain during the shorter, 45 month study period. A total of 70,143 patients were scanned during the 57 month time period; 2009 had 6-10 scans; 448 had 11-20 scans; 60 had 21-50 scans; five had greater than 50 scans. A total of 2,522 patients (3.6%) had repetitive CT imaging of the brain during the longer study period; by simply extending the study period by 1 year, an additional 612 patients (+32.0%) were identified. Regarding MR brain imaging, a total of 32,067 patients were scanned during the 45 month time period; 487 had 6-10 scans; 141 had 11-20 scans; four had >20 scans. A total of 632 patients (2.2%) had repetitive MR imaging of the brain during the shorter, 45 month study period. A total of 40,468 patients were scanned during the 57 month time period; 713 had 6-10 scans; 216 had 11-20 scans; 21 had >20 scans. A total of 950 patients (2.3%) had repetitive MR imaging of the brain during the longer study period; by simply extending the study period by 1 year, an additional 318 patients (+50.3%) were identified. An additional 3,568 patients had 3-5 MRI scans during the 57 month time period.

Conclusions

Although repetitive CT and MR imaging of the brain occurred in a small percentage of patients, the absolute number of patients affected was substantial. These data underestimate the prevalence of repetitive imaging, as studies performed at outside facilities in this patient population were not captured; moreover, lengthening the study period by only 1 year captured considerably more patients. Repetitive imaging raises

concerns regarding cumulative radiation dose, accumulation of gadolinium-based contrast agents in the brain, cost effectiveness, and outcomes.

O-259

5:15PM - 5:18PM

Interphysician Variation in the Use and Yield of Non-contrast CT Head Examinations at an Academic Tertiary Emergency Department

Y Chen¹, G Bandiera¹, D Mackinnon¹, D Deva¹, B Gray¹

¹*St. Michael's Hospital, University of Toronto, Toronto, Ontario*

Purpose

The evaluation of variation in test ordering may be a more accurate assessment of quality than solely measuring utilization. We sought to examine the variation in the use and yield of noncontrast computed tomography (CT) head among our institution's Emergency Physicians (EPs).

Materials and Methods

Institutional ethics board approval was obtained. A cross-sectional retrospective study was conducted on 1512 consecutive ED patients who underwent noncontrast CT head examinations. Radiology report data were extracted from our institution's RIS PACS software (Syngo Imaging, Siemens) based on a targeted search of all noncontrast CT head reports from July to December 2013. Utilization rates and positivity rates for full-time individual EPs were calculated and correlated with both years of experience, gender and training certification.

Results

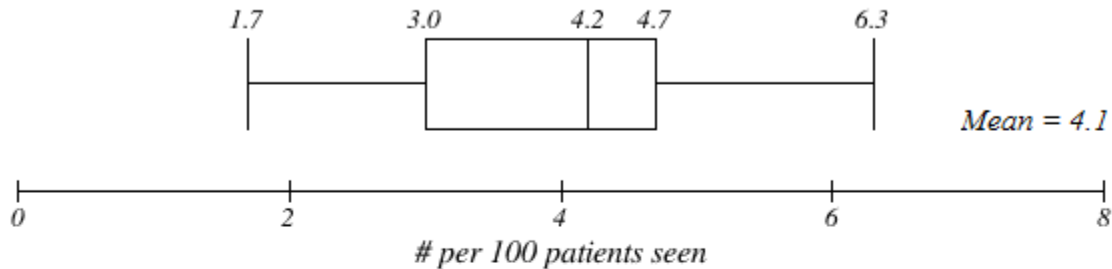
One hundred seventy-four of the 1512 patients (11.5%) evaluated by noncontrast CT head were positive for acute intracranial findings, divided into 43% hemorrhage, 27% infarct, 17% tumor, and 13% other. There was significant variation among full-time EPs in noncontrast CT head use (mean 4.1 +/- 1.3 scans per 100 patients seen, range 1.7 to 6.3 scans) and yield (mean 10.8 +/- 5.6%, range 0 to 22.6%). There was weak correlation between use and yield (Pearson's $r = 0.12$, $p = 0.56$). There was no statistically significant correlation between EP years of experience and use (Pearson's $r = -0.37$; $p = 0.06$), and yield (Pearson's $r = 0.06$; $p = 0.78$). Furthermore, use and yield were not significantly different between male and female EPs ($p = 0.35$ for use, $p = 0.32$ for yield), nor between EPs with emergency medicine certification by the Royal College (FRCPEM) versus by the College of Family Physicians of Canada (CCFP-EM) ($p = 0.27$ for use, $p = 0.09$ for yield).

Conclusions

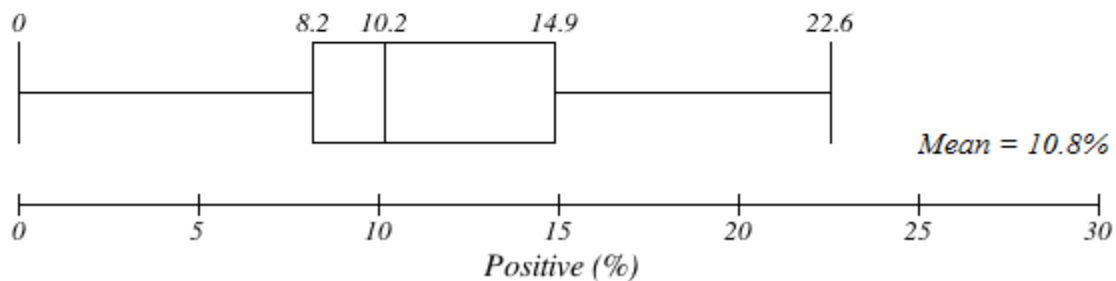
Considerable interphysician variability exists for both use and yield of noncontrast CT head examinations at our institution. Results from our study suggest an opportunity

for a more standardized approach to the use of noncontrast CT head examinations among our EPs.

Non-contrast CT Head Use among Emergency Physicians



Non-contrast CT Head Yield among Emergency Physicians



(Filename: TCT_O-259_FigureVariation.png)

O-260

5:18PM - 5:21PM

Collaboration or Confrontation in a Radiology Utilization Management Program - How Often Do Providers and Radiologists Disagree on the Need for Advanced Imaging Studies?

D Friedman¹, N Smith²

¹Sidney Kimmel Medical College at Thomas Jefferson University, Philadelphia, PA, ²Sidney Kimmel Medical College at Thomas Jefferson University, Philadelphia, PA

Purpose

To determine how often providers and radiologists participating in a collaborative

utilization management (UM) program fail to agree on the need for advanced imaging studies.

Materials and Methods

Using evidence-based guidelines, a UM program (RadConsult) provides peer-to-peer decision support for providers ordering high cost, outpatient imaging studies (CT, MRI, PET, nuclear medicine) on patients enrolled in multiple health plans. After consultation between RBM personnel (tier I, customer service representative; tier II, nurse) and the provider's staff, studies not meeting appropriateness criteria are referred to a radiologist (tier III) for further review. Only a small percentage of cases screened at tiers I/II are referred to tier III. The radiologist can approve the study based upon electronic chart review, or call the provider for more information; determination of appropriateness then is made. If a suitable person cannot take the call, and there is "no callback" in two business days, the study is administratively withdrawn. Studies are not denied. We analyzed the rate of "study approved, but no consensus" after discussion between the provider and radiologist. In this circumstance, although the radiologist felt that the study (1) was not indicated, (2) was not indicated at that time, or (3) should be changed to a different study, the provider still wanted to obtain the study. Aggregated data for all provider specialties enabled comparison to results for each specialty. Approximately 45 radiologists participated in the UM program; 75% were subspecialty trained academic radiologists and 25% were private practice radiologists (some subspecialty trained). Project period was 5 years (7/09-6/14). Studies ordered by cardiologists were excluded, as many were reviewed by cardiologists, not radiologists. We also tracked complaints issued by providers due to interactions involving tiers I, II and III for a 4.5 year period (1/11- 6/15). Complaint data prior to 2011, or for individual tiers, was unavailable.

Results

A total of 168,915 studies ordered by all specialties were reviewed at tier III; 10,068 (6.0%) were approved without consensus. Primary care providers had the highest rates of "no consensus": pediatrics (10.3%); family practice (8.2%); internal medicine (6.6%). Surgical subspecialists had the lowest rates of "no consensus": orthopedic surgery (2.4%); neurosurgery (2.8%); ophthalmology (2.9%); otorhinolaryngology (3.4%); thoracic surgery (3.5%). A total of 6.17 million studies were reviewed in the 4.5 year period; 350 complaints (.006%) were filed by providers during this time.

Conclusions

Peer-to-peer discussion in this UM program achieved consensus in the vast majority of cases; the provider and radiologist "agreed to disagree" regarding the appropriateness of a study in just one of 17 cases. Results were achieved without denials. Despite advice offered by largely subspecialty trained radiologists, disagreements with primary care providers were more frequent than with surgical subspecialists. Rarely, providers filed complaints about interactions with UM personnel.

Neuroradiology Reading Room Interruptions - Workflow Analysis and Optimization

A Schemmel¹, M Lee¹, T Hanley², B Pooler¹, T Kennedy³, A Field⁴, D Wiegmann², J Yu⁵

¹University of Wisconsin Hospital and Clinics, Madison, WI, ²University of Wisconsin Madison, Madison, WI, ³University Of Wisconsin Hospital, Madison, WI, ⁴Univ. Of Wisconsin Hospital, Madison, WI, ⁵University of Wisconsin-Madison, Madison, WI

Purpose

Workplace interruptions and resultant task switching can have deleterious effects on patient safety and quality outcomes (1). By virtue of the varied and complex responsibilities incumbent on radiologists, the radiology workplace is particularly vulnerable to interruptions (2). Anecdotal experiences at our institution suggest that reading room interruptions and ancillary tasks consume a significant portion of the workday in the neuroradiology reading room. The purpose of this study was to: 1) quantify the nature and frequency of the myriad tasks performed in the reading room, 2) dichotomize reading room activities into two distinct workflows: image-interpretive tasks (IIT) and all noninterpretive tasks (NIT), and 3) trial of a new dedicated "Consult Fellow" (CF) to address all reading room NIT.

Materials and Methods

A prospective, randomized, observational investigation of the neuroradiology reading room was performed at our institution. One-on-one observation was performed by two trained observers (AS, TH) over 1 month. Activities were recorded using a time and motion methodology, quantifying the nature and duration of tasks (NIT and IIT) performed by radiologists in the main neuroradiology reading room. As the principal coordinators of reading room workflow, the primary reading room neuroradiology fellow was observed in shifts (8a-12p, 1p-5p), for a total of 48 hr 49 min.

Results

Neuroradiology fellows spent 54% and 46% of their time on IIT and NIT, respectively. There was a mean of 11.2 task switches per hour, with a maximum of 84 task-switching events during a single shift. The median time spent on image interpretation was 3:15 (min:sec) before a task-switching event occurred. Median time spent answering a phone call or responding to a page totaled 0:56, while discrete instances of study protocoling lasted 2:17. In-room consultations, either radiologist-to-radiologist or with referring providers, lasted a median of 1:44. Tasks of the longest duration included staff-out (median 6:07) and out-of-office episodes (median 9:03), which included interventional procedures, direct patient care, and meetings.

Conclusions

Noninterpretive tasks and reading room interruptions place a measurable burden on neuroradiology trainees at our institution consuming up to 46% of their total reading room time. The frequency of these NIT and interruptions, up to 84 in one four-hour span, results in rapid task switching and short duration of time spent per task (e.g., median 3:15 for IIT and 6:07 for trainee staff-out before task-switching event), which may have negative implications for overall reading room efficiency. These data informed the creation of a CF, designed to ameliorate the degree of interruptions trainees experience and to allow for increased time for IIT.

O-262

5:24PM - 5:27PM

Culture Change in Customer Service in an Academic Radiology Department: Paving the Road to Success in a Competitive Outpatient Radiology Market

T Donovan¹, J Bisanti¹, S Williams², J Gross³, M Keiper⁴

¹University of Nebraska Medical Center, Omaha, NE, ²University of Nebraska Medical Center, Omaha, NE, ³University of Nebraska, Omaha, NE, ⁴UNMC, Omaha, NE

Purpose

To evaluate the most effective methods to enact culture change in customer service in an academic radiology department in order to maintain competitive advantage in outpatient radiology services.

Materials and Methods

Multiple programs directed at improving customer service to patients and referring clinicians were implemented over a 2-year period in order to develop and consolidate a uniform culture of dedication to service in an academic radiology department. Radiology exam volumes were followed over that time period to determine if the programs had any effect on overall business development. Programs included scheduled retreats for staff and employees, employee engagement programs, clinical website development, customer survey optimization, and development of radiology blog for staff and employees. Programs were tailored to specific customer service issues identified by optimized electronic patient satisfaction surveys.

Results

Radiology staff and employee retreats introducing a new paradigm of dedication to customer service were scheduled and were possible without disruption to daily workflow. Retreats were successful in establishing a foundation of culture change of service to patients and referring clinicians. The retreats were effectively reinforced with multiple employee engagement programs designed to sustain and consolidate the new culture. These programs included video contests, development of staff and

employee radiology blogs and distribution of radiology news and information on a new radiology clinical website. The new clinical website was successfully developed and introduced as a showcase to the new commitment to customer service. Radiology imaging volumes increased by 14% over the 2-year period in which the culture change was initiated and programs completed. No additional substantive changes in service initiatives, economic variables or market force occurred during that time period to otherwise account for the change in radiology volumes.

Conclusions

Academic radiology practices compete with highly motivated and aggressive outpatient radiology centers in which radiology marketing and promotion is a primary source of radiology business development. By establishing a culture change of complete dedication to customer service and reinforcing these concepts with concrete employee engagement programs and a clinical website, an academic radiology department can remain competitive in outpatient radiology and ultimately realize increased imaging volumes.

O-263

5:27PM - 5:30PM

The Argument for Radiology Business and Marketing Training for Residents in an Academic Radiology Department: Radiology's Future Depends On It

T Donovan¹, S Williams², J Bisanti¹, J Gross³, M Keiper⁴

¹University of Nebraska Medical Center, Omaha, NE, ²University of Nebraska Medical Center, omaha, NE, ³University of Nebraska, Omaha, NE, ⁴UNMC, Omaha, NE

Purpose

To investigate the utility and potential long-term benefits of dedicated radiology marketing and business training in a radiology residency program as an adjuvant to traditional noninterpretive skill development.

Materials and Methods

All residents in an academic radiology residency were exposed to didactic radiology marketing conferences, marketing retreats and direct training through business case scenario exercises over a 1-year period. Residents were taught basic radiology marketing program development, sales techniques and participated in radiology department retreats with radiology staff. Best practices in customer service emphasizing impeccable service to referring clinicians and patients were emphasized as the highest priority in training.

Results

Radiology marketing and sales training was successfully implemented as an adjuvant program to resident noninterpretive skills development. Residents were able to

demonstrate knowledge regarding basic radiology marketing and sales principles as a result of training, applying this knowledge in real life scenario training exercises. The necessity for best practices in customer service to referring clinicians and patients was actively emphasized as was the requirement for impeccable service initiatives for the ultimate success of a radiology practice. Residents were versed in the need for a national consolidated effort in radiology to be best in service and practice as a competitive advantage over other nonradiology-based entities providing imaging services.

Conclusions

Dedicated radiology marketing and sales training provides an effective adjuvant to traditional noninterpretative skills development for radiology residents. Training future radiologists through these programs is essential in ensuring the long term success of radiology practices and the overall health of radiology as a specialty in a competitive imaging market.

Tuesday

4:45PM - 6:15PM

Washington Marriott Wardman Park, Maryland A/B/C

12E - Study Group - Intracranial and Cervical Vessel Wall Imaging (non-CME)

Tuesday

4:45PM - 6:21PM

Washington Marriott Wardman Park, Roosevelt 4

12F-PARALLEL PAPER SESSION: Interventional: Vascular Malformations

O-265

4:45PM - 4:53PM

Sensitivity and Positive Predictive Value of MRI in Hereditary Hemorrhagic Telangiectasia Patients

M Mabray¹, C Glastonbury², M Conrad¹, M Dickey¹, H Kim¹, S Hetts²

¹University of California San Francisco, San Francisco, CA, ²University Of California, San Francisco, San Francisco, CA

Purpose

Hereditary hemorrhagic telangiectasia (HHT) is an autosomal dominant genetic condition characterized by arteriovenous malformations (AVMs) and telangiectasias affecting the skin, mucosa, lungs, liver, and brain. We aim to determine the prevalence of brain AVMs in our HHT cohort and to determine the sensitivity and positive predictive value of MRI as compared to catheter angiography.

Materials and Methods

Retrospective electronic medical record review was performed on our HHT clinic cohort (n=146) to determine if a brain MRI and cerebral angiogram had been performed and to determine the number of AVMs prospectively reported on each imaging study. For patients who had both imaging studies performed, we determined the number of true positives, false negatives, and false positives on a per lesion basis by magnetic resonance imaging (MRI) as compared to cerebral angiography. True negatives were not determined, as patients who had negative MRIs typically did not go to angiography.

Results

One hundred twenty-four of 146 patients (84.9%) underwent brain MRI. Eighty-seven of these MRIs were reported as negative for AVM and 37 MRIs (25.3%) were reported as positive for AVM. Thirty-three patients had both an MRI and an angiogram. There were 33 true positive, 26 false negative, and five false positives on a per lesion basis. Sensitivity of MRI compared to angiography thus was 59.4% (33/59, 95% CI 42.5-68.6%) and positive predictive value was 86.8% (33/38, 95% CI 71.1-95.1%). Overall 27/146 patients (18.5%) had an angiogram-confirmed AVM (60 lesions total). Most of the AVMs were small (<1cm). Eighteen (30%) of these lesions had been treated in 16 patients (8 with gamma knife, 7 with surgery, and 3 with endovascular and surgical treatment). Only one AVM presented with hemorrhage.

Conclusions

Magnetic resonance imaging is only moderately sensitive (~60%) for the identification of AVMs in HHT patients but the positive predictive value is high (~87%). Not all of these generally small lesions go on to treatment (30% in our cohort).

O-266

4:53PM - 5:01PM

Comparison of the Diagnostic Utility of 4D DSA with Conventional 2D and 3D DSA

*C Sandoval-Garcia¹, P Yang², S Till¹, S Schafer³, A Ahmed¹, C Strother¹
¹University of Wisconsin School of Medicine and Public Health, Madison, WI, ²Changhai Hospital, Second Military Medical University, Shanghai, Shanghai, ³Siemens Medical Solutions, USA, IL, USA*

Purpose

Digital subtraction angiography (DSA) evaluations often require multiple 2D DSA acquisitions. These account for the majority of x-ray exposure. Four dimensional DSA provides 3D time resolved vascular volumes viewable at any time of bolus passage at any desired viewing angle. Our purpose was to assess the ability of 4D DSA to

provide diagnostic imaging information equivalent to that of conventional 2D and 3D DSA.

Materials and Methods

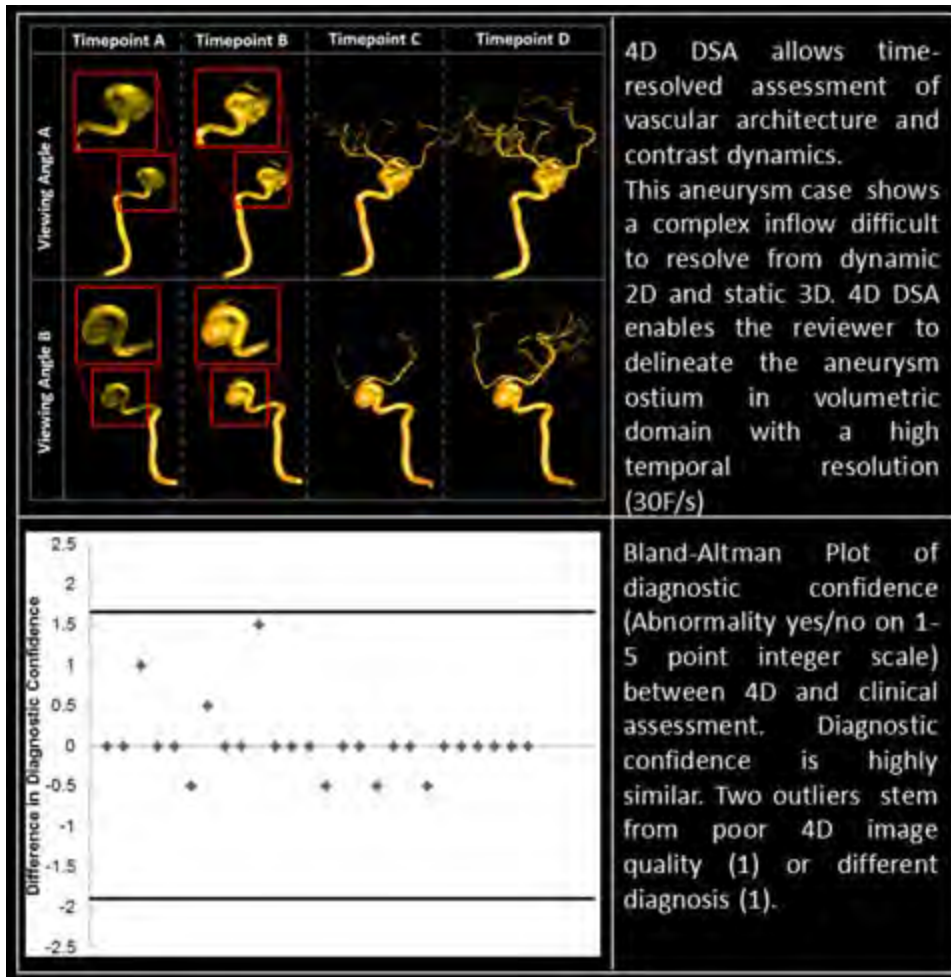
Twenty-six consecutive patients who had one or more 4D DSA as part of their evaluation were selected. There were 10 aneurysm, six avms/avfs, three stenosis and seven normals. The 4D DSAs were reviewed independently by two experienced clinicians. No clinical information was provided. An electronic evaluation form containing essentials e.g., aneurysm measurements, avm angioarchitecture, required in a clinical report was completed for each case. Diagnosis, diagnostic confidence, i.e., abnormality present: definitely not, probably not, unsure, probably yes and definitely yes; and the abnormality characteristics derived from the evaluation forms were compared with the clinical evaluations. The numbers of 2D DSA acquisitions acquired were compiled from PACS.

Results

Paired t-test between the 4D reviewer's scores and between clinical and 4D diagnosis showed no significant difference ($p = 0.82$ and $p = 0.74$ respectively). Agreement between the clinical and 4D diagnosis was found in 24/26 cases. Disagreement was due to poor 4D image quality (1x) and 4D aiding in diagnosing minor occlusive disease (1x). Characteristics, such as aneurysm dimensions, nidus size and stenosis degree were similar to clinical reporting.

Conclusions

In this small study, the information content of the 4D DSAs was, by large, comparable with that of the combined 2D 3D DSA studies. Utilization of 4D-DSA should reduce the requirement for 2D-DSA acquisitions.



(Filename: TCT_O-266_FinalfigureAbstract_Dec16.png)

O-267

5:01PM - 5:09PM

Safety of Conventional Cerebral Angiography in Patients with High-risk for Contrast-induced Nephropathy.

J Kim¹, D Sandhu¹, G Sandhu¹, B Jagadeesan¹, R Tummala¹

¹University of Minnesota, Minneapolis, MN

Purpose

The incidence of contrast-induced acute kidney injury (CI-AKI) is low for general population (~2%). However in patients with high risk factors such as estimated glomerular filtration rate (GFR) < 60 mL/min with diabetes mellitus, this incidence can reach up to 50%. There is paucity of data on patients with high risk features for CI-AKI who underwent conventional cerebral angiography (CCA). We present data on our experience with patients with high risk factors for CI-AKI who underwent CCA at two large tertiary care hospitals.

Materials and Methods

We conducted a retrospective review of clinical and laboratory data on 1913 consecutive CCA procedures performed at our institutions from January 2012 to November 2015.

Results

One hundred sixty-three of 1913 procedures were included in the analysis. All 163 patients had eGFR of < 60. Mean age across the group was 63 years, 68 were male, mean estimated GFR was 45 and 36/163 had eGFR < 30. Visipaque 320 was used in all patients and mean contrast volume injected was 68 cc. Mean 48-72 hours post CCA estimated GFR was 51.6. None of the patients had acute kidney injury (AKI) defined by creatinine increase of 0.5 mg/dL or at least 25% from baseline within 48 to 72 hours post exposure to contrast.

Conclusions

In our experience, CCA is acceptably safe even in patients at high risk for CI-AKI. All our high risk patients received volume expansion (normal saline at 100 cc per hour) prior to and after the procedure for at least 2 hours. Catheters were aspirated after each run to minimize volume of contrast injected. Rotational 3D angiography was avoided whenever possible. Our data suggest that CCA should not be avoided automatically in patients considered high risk for CI-AKI.

O-268

5:09PM - 5:17PM

Outcomes Associated with Treatment of Unruptured Cerebral Arteriovenous Malformations

J Tejada¹, K Riley²

¹Indiana University, Indianapolis, IN, ²Indiana University School of Medicine, Indianapolis, IN

Purpose

In early 2013, patient enrollment in a randomized trial of unruptured brain arteriovenous malformations (ARUBA) was discontinued earlier than planned after an interim analysis revealed statistically significant outcome differences between the treatment groups. At 33 months, it was reported that the incidence of stroke and death was more than three times higher in the intervention group (30.7%) than the nonintervention group (10.1%). In light of the preliminary findings of ARUBA, a retrospective analysis was performed to determine the rates of stroke and death in the population of patients that underwent treatment for unruptured arteriovenous malformations (AVMs) at Indiana University since 2001.

Materials and Methods

A multi-institutional, retrospective search of radiology reports from Indiana

University and its affiliated institutions generated between 2001 and 2015 was performed to identify all patients with arteriovenous malformations. The following data were collected: initial clinical symptoms, presence of hemorrhage at presentation, location, size, drainage pattern (superficial versus deep), treatment (medical management only versus endovascular therapy, surgical excision, radiotherapy, or a combination of these interventions), and subsequent stroke/death. For cases in which these data were not available in the dedicated radiology reports, the corresponding images were assessed directly and the patients' electronic medical records were referenced to collect any excluded information. An analysis was performed to determine the rates of stroke and death in the population of patients that underwent treatment for unruptured arteriovenous malformations.

Results

Four hundred seventy AVMs were identified, 169 (36%) of which were unruptured at diagnosis. Of the unruptured AVMs, 59% presented with headache and 20% presented with seizure. Six percent of AVMs were discovered incidentally and 13% presented with nonspecific symptoms such as altered mental status and dizziness. By the Spetzler-Martin Grading Score, 17% of cases were classified as grade I, 33% grade II, 30% grade III, 16.5% grade IV, and 3.5% grade V. One hundred twenty-nine of the initially untreated AVMs underwent intervention shortly after diagnosis and 40 were treated with conservative medical management alone. Only four of the medically managed AVMs later ruptured. Of the unruptured AVMs that underwent intervention, 14% were embolized, 16% were treated with radiosurgery, and 13% were surgically resected. The remainder were treated with a combination of the above therapies. Following intervention 12.4% experienced subsequent stroke. No deaths were reported.

Conclusions

The results of this study demonstrate a much lower rate of stroke or death following intervention compared to the results of the ARUBA trial (12.4% versus 30.7%). Complication rates for patients treated with intervention in this study (12.4%) were similar to those treated with medical management alone in ARUBA trial (10.1%). These findings suggest that negative patient outcomes following intervention may not be as extreme as suggested in ARUBA.

O-269

5:17PM - 5:25PM

Endovascular Management of Intracranial Arteriovenous Malformations with Various Angioarchitecture Features in the Pediatric Population: Is Spetzler-Martin Grading Predictive?

A Honarmand¹, S Ansari², M Hurley¹, M Potts², B Jahromi², A Shaibani²

¹Northwestern University Feinberg School of Medicine, Chicago, IL, ²Northwestern University, Feinberg School of Medicine, Chicago, IL

Purpose

We performed this study to investigate the potential predictors of long-term outcome in endovascular management of intracranial arteriovenous malformations (AVMs) with/without surgical resection in the pediatric population.

Materials and Methods

Consecutive pediatric patients (<18 years) presenting with intracranial AVMs verified by CT/MR/DSA imaging studies were enrolled in the study. Baseline demographics, presenting symptoms, angioarchitecture characteristics [location, compact/diffuse nidus type, maximum nidus diameter, superficial/deep drainage, associated flow-induced aneurysm and/or venous varix/stenosis/ectasia, number of arterial feeders/draining veins, Spetzler-Martin Grading (SMG) scores, and ruptured/unruptured lesions], treatment strategy (endovascular embolization and/or surgical resection versus conservative management), procedural complication, recurrence, and long-term functional outcome were obtained. Ninety days modified Rankin Scale score of ≤ 2 and achieving developmental milestones were used to determine good functional outcome as appropriate. Independent samples T test, chi square, and logistic regression analyses were performed for statistical analyses.

Results

Fifty-eight cases (m/f: 38/20; mean age [(range) \pm SD: 10.99(0.5-17) \pm 4.09 years] presented with 29 ruptured versus 29 unruptured AVMs. Presenting symptoms included severe headaches (35.8%), occasional mild-moderate headache (22.6%), incidental finding (22.6%), seizure (9.4%), focal neurological deficits (15.1%), and loss of consciousness 20.8%), respectively. Single or multi-session endovascular embolization was performed either alone or prior to surgical resection while three cases were managed conservatively. Procedural complication and lesion recurrence were encountered in 6.9% and 5.2% of cases, respectively. Good functional outcome was achieved in 49 (84%) of cases. Angioarchitecture features of the lesions are presented in the table. No significant association was observed between SMG and final outcome (P=0.80). Regression analysis of clinical presentation, lesion characteristics, and treatment-related variables revealed that rupture and severe onset of headache were independent predictors of poor long-term functional outcome (P=0.006, OR:3.5). Seven out of nine cases with poor clinical outcome presented with ruptured AVMs with unfavorable preprocedural mRS score in eight of them.

Conclusions

In our study, size, eloquent location, and complex angioarchitecture of intracranial AVMs were not predictors of outcome while presentation and ruptured/unruptured status of the lesions were significant predictors of long-term clinical outcome in treatment strategy with endovascular approach.

| | |
|---|---|
| Nidus Type (n, %) | Compact:52 (89.7%) / Diffuse: 6 (10.3 %) |
| Nidus Location (n, %) | Eloquent: 33 (56.9%) / Non-Eloquent: 25 (43.1%) |
| Lesion \geq 3cm (n, %) | 22 (33.9%) |
| Drainage (n, %) | Superficial: 26 (44.9%) / Deep: 15 (25.8%) / Superficial and Deep: 17 (29.3%) |
| Lesions with Multiple Arterial Feeders (n, %) | 43 (74.1%) |
| Lesions with Multiple Draining Veins (n, %) | 27 (46.6%) |
| Intranidal Aneurysm (n, %) | 15 (25.9%) |
| Venous Stenosis (n, %) | 12 (20.7%) |
| Venous Varix (n, %) | 13 (22.4%) |
| Venous Ectasia (n, %) | 20 (34.5%) |

(Filename: TCT_O-269_table.jpg)

O-270

5:25PM - 5:33PM

Headway Duo Microcatheter for Cerebral Arteriovenous Malformation Embolization with n-BCA

J Heit¹, A Faisal¹, N Telischak¹, O Choudhri², H Do¹

¹Stanford University, Stanford, CA, ²University of California San Francisco, San Francisco, CA

Purpose

Cerebral arteriovenous malformations (AVMs) are uncommon vascular lesions, and hemorrhage secondary to AVM rupture results in significant morbidity and mortality. Arteriovenous malformations may be treated by endovascular embolization, and technical advances in microcatheter design are likely to improve the success and safety of endovascular embolization of cerebral AVMs. Here we describe our early experience with the Headway Duo microcatheter for embolization of cerebral AVMs with n-butyl-cyanoacrylate (n-BCA).

Materials and Methods

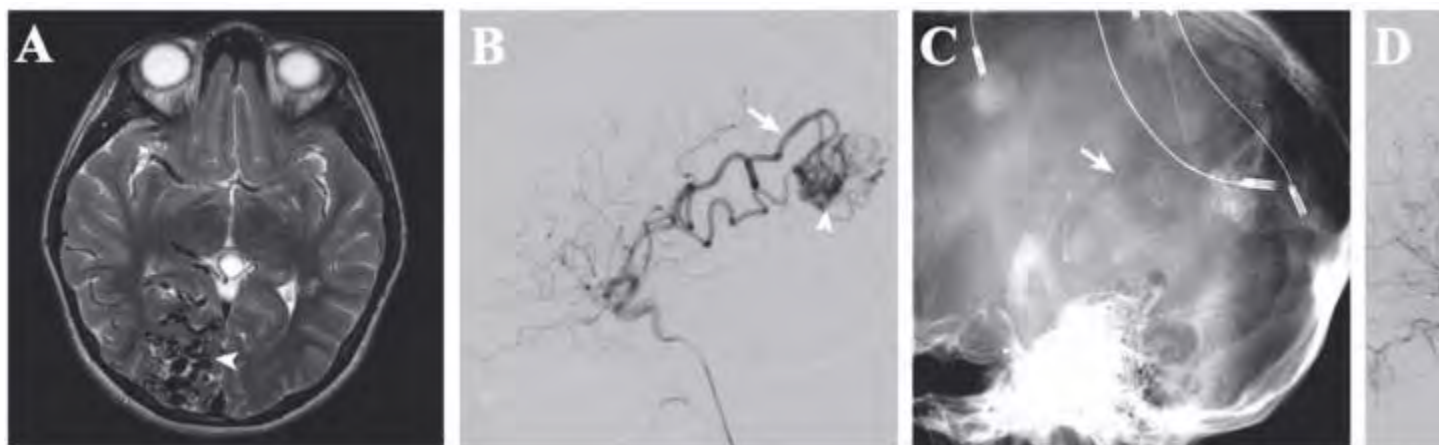
Consecutive patients treated by endovascular embolization of a cerebral AVM with n-BCA delivered intra-arterially through the Headway Duo microcatheter (167 cm length) were identified. Patient demographic information, procedural details, and patient outcome were determined from electronic medical records.

Results

Ten consecutive patients undergoing cerebral AVM embolization using n-BCA injected through the Headway Duo microcatheter were identified. Presenting symptoms included headache, hemorrhage, seizures, and weakness. Spetzler Martin grades ranged from 1 to 5, and AVMs were located in the basal ganglia (2 patients), parietal lobe (4 patients), frontal lobe (1 patient), temporal lobe (1 patient), an entire hemisphere (1 patient) and posterior fossa (1 patient). Fifty arterial pedicles were embolized, and all procedures technically were successful. There was one postprocedural hemorrhage that was well-tolerated by the patient, and no other complications occurred. Additional AVM treatment was performed by surgery and radiation therapy.

Conclusions

The Headway Duo microcatheter is safe and effective for embolization of cerebral AVMs using n-BCA. The trackability and high burst pressure of the Headway Duo make it an important and useful tool for the neurointerventionalist during cerebral AVM embolization.



(Filename: TCT_O-270_Fig1.jpg)

O-271

5:33PM - 5:41PM

CyberKnife Stereotactic Radiosurgery for Brain Arteriovenous Malformations: Single Center Retrospective Review of Safety and Efficacy.

D Eddins¹, E Jacek², S Shah¹, T Sivapatham¹, T Eden¹, D Huisenga¹, G Zoarski¹, S Satti¹

¹*Christiana Care Health System, Newark, DE,* ²*Jefferson University, Philadelphia, PA*

Purpose

Stereotactic radiosurgery is an effective way to eradicate cerebral arteriovenous malformations (AVMs) (1). Previous studies on safety and efficacy have focused on the Gamma Knife Radiosurgery System. This study was performed to determine the safety and efficacy of the CyberKnife Robotic Radiosurgery System in the treatment of cerebral AVMs. The advantage of CyberKnife Robotic Radiosurgery over the Gamma Knife Radiosurgery System is patient comfort as the former does not require use of a metal head frame to be bolted to the patient during treatment; rather the volume targeted is based on bony landmarks.

Materials and Methods

We performed a 7-year retrospective review of imaging studies of all 17 patients who underwent CyberKnife Radiosurgery for the treatment of cerebral AVMs at the Helen F. Graham Cancer Center of the Christiana Care Health System in Delaware between 2008 and 2014. All patients underwent catheter angiography and MRA prior to CyberKnife Radiosurgery. Follow-up imaging included MRA at 1 and 2 years after Cyberknife Radiosurgery. Catheter angiography was performed to confirm eradication of the AVM when MRA demonstrated no residual nidus. Primary endpoints included: 1. Angiographic cure. 2. Complications. 3. Rate of hemorrhage.

Results

Seventeen patients were treated over a 7-year period. Eight patients had prior embolizations, of which one also had a surgical resection, and one had prior radiosurgery. Eight patients (47%) presented to our institution with hemorrhage; nine patients (53%) had unruptured AVMs. Catheter angiography demonstrated high risk features in eight patients (47%): six patients (35.3%) had aneurysms and two (11.8%) had venous stenosis. The average Spetzler-Martin grade was 2.56 (2). Obliteration was confirmed at 1 year in four of 14 (28.6%) treated patients, and in nine of 12 (75%) patients within 2 years. No treated patients suffered a new or recurrent hemorrhage. One patient developed radiation necrosis. Another suffered a stroke, which was considered to be unrelated, more than 2 years after treatment. Three of 17 patients (18%) did not complete/were lost to follow-up imaging protocol and two patients are still within 2 years of treatment.

Conclusions

Our preliminary results suggest CyberKnife Radiosurgery System compares favorably to published Gamma Knife Radiosurgery results in terms of safety and efficacy (1).

O-272

5:41PM - 5:49PM

Head and Neck Endovascular Repair of Vascular Malformations

W Yakes¹

¹*Vascular Malformation Center, Englewood, CO*

Purpose

To determine the efficacy of ethanol embolotherapy of extracranial head and neck vascular malformations of all types, particularly after failure of other endovascular and surgical treatments.

Materials and Methods

One hundred sixty-six patients (64 males, 102 females; mean age: 38 years) presented with extracranial arteriovenous malformations (AVMs) of the head and neck area. Over half of the patients had undergone previous failed therapies. All patients underwent ethanol embolotherapy under general anesthesia. Forty-five patients had AVMs and 121 patients had venous malformations (VM).

Results

Of 45 AVM patients, 36 are cured (mean follow-up 2 ½ years); of 121 venous malformation patients, 65 are at end-therapy (mean follow-up 4 ½ years). The remaining patients are not at end-therapy and are being treated for their residual malformations. In AVM follow up, arteriography is the main imaging modality to determine cure or residual AVM as magnetic resonance (MR) is less sensitive in the evaluation of residual AVM. In VM follow up, MR is the main imaging tool, particularly with T-2 fat suppression and/or STIR imaging. All patients demonstrated improvement post-therapy. Complications were 4.5%, to include bleeding (self-limited), partial 7th nerve palsy (with recovery), skin injury (not requiring skin grafts), infection, and pain.

Conclusions

Ethanol has proven its consistent curative potential at long term follow up for high-flow AVMs and low-flow VM lesions at long term follow up as lesions in the periphery. Complication rates remain low. The procedures are tolerated well by the patients and done on an out-patient basis. Prior surgery and embolization procedures can cause difficulty in lesion access, but does not obviate further ethanol endovascular treatment.

O-273

Mandibular AVM Diagnosis and Curative Endovascular Treatment

W Yakes¹

¹*Vascular Malformation Center, Englewood, CO*

Purpose

To determine optimal management strategies for the treatment of mandibular arteriovenous malformations (AVM).

Materials and Methods

Thirteen patients (10 females, 3 males), age 9 -14 years; mean age 10 years, underwent endovascular therapy to treat their mandibular AVMs. Nine patients had distinct intraosseous AVMs. Three had multiple facial and intramaxillary AVMs requiring treatment. Outside institutions recommended massive hemifacial resections in these patients. Four patients had prior PVA and gel foam embolization, one patient had a lip graft, one had prior mandible surgery, all that had failed.

Results

All thirteen patients have demonstrated MR and angiographic cure of their AVMs. One patient's therapy is not completed and is on-going. The patient's mandibular AVM is cured, a third AVM in this patient in the infratemporal fossa is still undergoing treatment. The follow-up range is 11 months – 41 months, with a mean follow up of 29 months. No complications were noted in treatment of mandibular AVMs. One patient required a minor gingival surgery after treatment of an additional intramaxillary AVM.

Conclusions

Endovascular approaches to manage mandibular AVM can be curative. The intraosseous variety is largely a fistula between artery and vein within the bone. All responded well to endovascular ethanol therapy alone. Surgery was not required in any patient. Surprisingly no complications were encountered in this patient series. Long term cures are noted in this patient series with endovascular approaches alone. No massive surgical resections in any patient, even in patients with multiple AVMs of the soft tissues, mandible and maxilla, was required to effect cure. In patients who suffered hemorrhages from floating teeth, bone formed and stabilized the teeth and no further hemorrhages occurred. Ethanol sclerotherapy proved curative in mandibular intraosseous AVMs in patients who had additional facial soft-tissue AVMs and intramaxillary AVMs that were cured as well at long term follow up.

O-274

Endovascular MR Guided Embolization Using a Magnetically Assisted Remote Controlled (MARC) Catheter System

S Hetts¹, P Lillaney¹, J Yang¹, A Losey¹, D Cooke¹, C Jordan¹, A Martin¹, M Saeed¹, M Wilson¹

¹UCSF, San Francisco, CA

Purpose

The aims of our preclinical study are two-fold while advancing toward the goal of translating the magnetically assisted remote controlled (MARC) catheter system for clinical use. First, our study will assess feasibility for performing a simple endovascular interventional procedure (i.e., renal artery embolization) in vivo using the MARC catheter system under magnetic resonance imaging (MRI) guidance. Second, the same procedure will be performed using x-ray guidance to determine the value added by using MRI guidance, and to pinpoint specific areas where the MARC system can be improved.

Materials and Methods

In concordance with IACUC protocol, in vivo renal artery navigation and embolization was tested in three farm pigs (43±2 kg) under real-time bSSFP imaging at 1.5T. The MARC catheter device was constructed using a 1.2mm diameter intramural copper braided catheter (Penumbra, Inc, Alameda, CA) connected to a laser-lithographed saddle coil (UCSF, San Francisco, CA) at the distal tip. The copper wires were connected to an in-room MRI-compatible cart (UCSF, San Francisco, CA) that allowed the interventionalist to determine the magnitude and polarity of electrical current delivered to create a magnetic moment and deflect the catheter tip in the MR scanner. Contralateral kidneys were embolized similarly under x-ray guidance using standard clinical catheters and guidewires. Changes in renal artery flow and perfusion were assessed pre- and postembolization (for both x-ray-guided and MR-guided procedures) using velocity-encoded MR imaging and perfusion scans of the renal parenchyma. Catheter navigation times, renal parenchymal perfusion, and renal artery flow rates were determined for MR-guided and x-ray-guided embolization procedures and presented as means ± standard deviations in our small pilot study.

Results

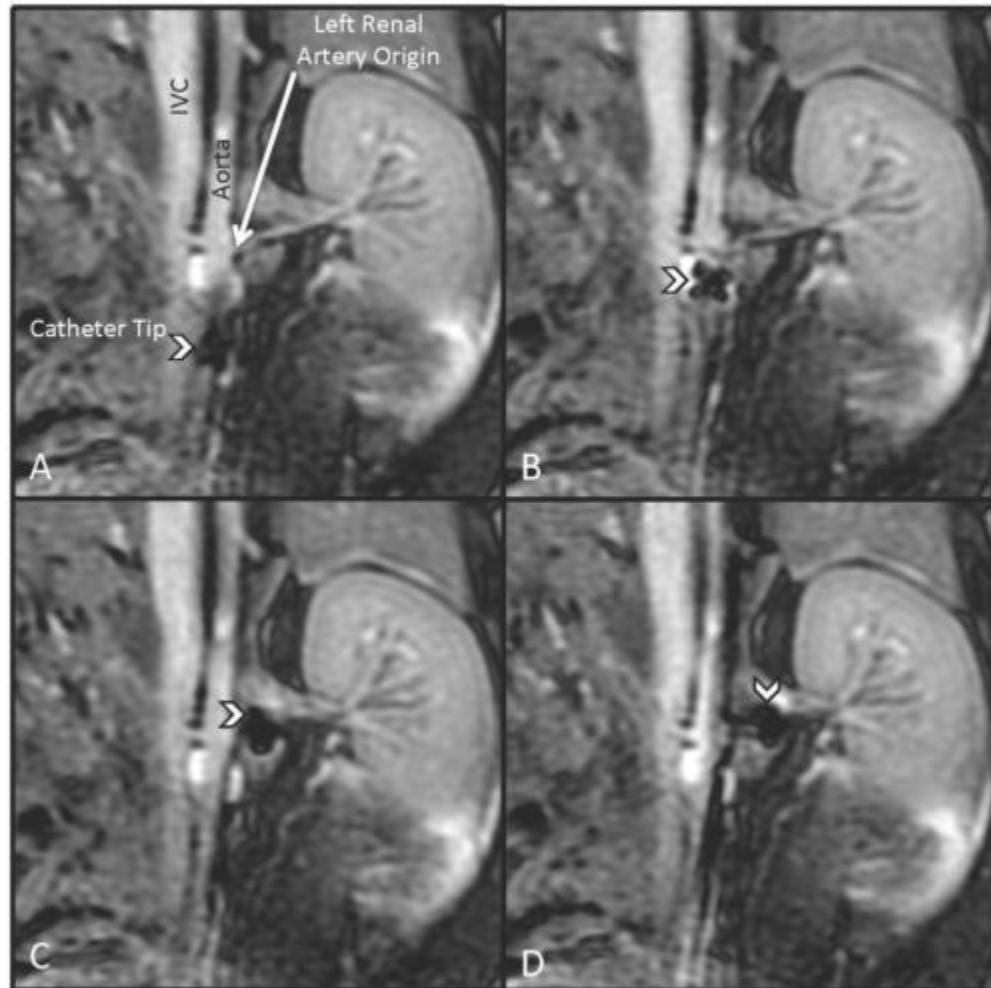
The catheter tip position was visible under MRI guidance. In addition, in vivo injections of microspheres were successful in all six swine kidneys and demonstrated under either x-ray or MRI. Under MR, overall mean catheterization time was 93±56 seconds, change in perfusion rates was 4.9±0.8 A.U./sec, and change in renal flow rate was 2.1±0.2 ml/min/g. X-ray- and MR-guided embolization produced comparable results.

Conclusions

Using a MARC catheter for renal artery catheterization and embolization under real-time MRI in vivo is feasible; it provides a novel opportunity to perform endovascular procedures in interventional MRI environment. Future versions of this technology will

be directed at embolization of tumors in the head and neck as well as endovascular stroke treatment with real-time diffusion-weighted imaging feedback.

Navigation



(Filename: TCT_O-274_MARCRenalNavigation.jpg)

O-275

6:05PM - 6:13PM

Stentrod: minimally invasive endovascular stent-electrode array for high-fidelity, chronic recordings of cortical neural activity

T Oxley¹, N Opie², S John², G Rind², S Ronayne², J Judy³, T Wheeler², A Dornom², T Lovell², C Steward⁴, D Garrett², B Moffat², E Lui⁴, B Campbell⁴, N Yassi⁴, P Mitchell⁴, D Grayden², C May⁵, T O'Brien²

¹University of Melbourne, Melbourne, ²University of Melbourne, Melbourne, AK, ³University of Florida, 1, FL, ⁴Royal Melbourne Hospital, Melbourne, AK, ⁵Florey Institute of Neuroscience and Mental Health, Melbourne, AK

Purpose

High-fidelity intracranial electrode arrays for recording and stimulating brain activity have facilitated major advances in the treatment of neurological conditions over the past decade. Traditional arrays require direct implantation into the brain via open craniotomy, which can lead to inflammatory tissue responses; thus, there is a need to develop minimally invasive approaches that avoid brain trauma. Here, we demonstrate the feasibility of chronically recording brain activity from within a cerebral vein using a passive stent-electrode recording array (stentrode). We were particularly interested in the feasibility of targeting superficial cortical motor areas that may prove useful in brain-machine interface systems.

Materials and Methods

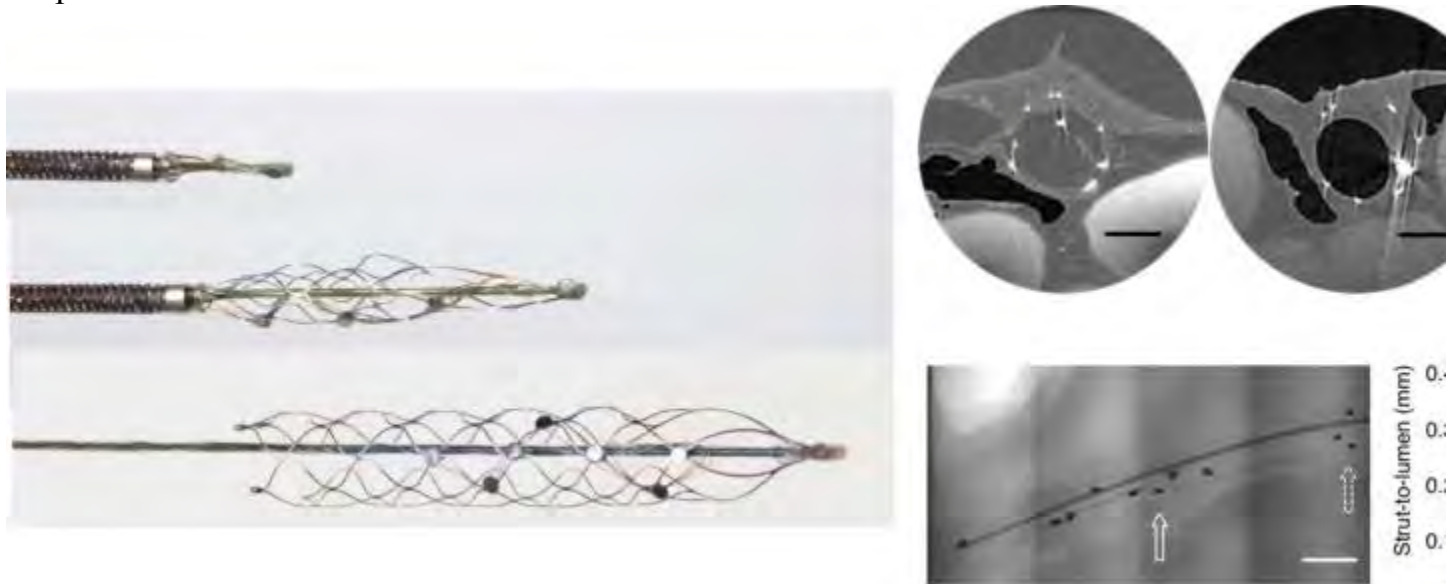
We fabricated stentrododes on intracranial stent technology currently in clinical use. Self-expanding stents (Solitaires) were used as scaffolds for the attachment of 750 μm diameter, laser-cut platinum disk electrodes. We used an angiography-based co-axial catheter technique to deliver a 4F catheter to the 2 mm diameter target vessel in a sheep cerebral angiography model. The process of incorporation of the stentrode into the vessel wall was investigated with synchrotron imaging and impedance spectroscopy. Brain signals recorded from the stentrode were analyzed as functions of both time since implantation and electrode location, and were validated against commercially available surface electrocorticography arrays by assessing somatosensory evoked potentials, theta burst suppression ratios, and maximal bandwidth.

Results

We achieved implantation of the stentrode into a superficial cortical vein overlying the motor cortex via catheter angiography and demonstrated neural recordings in freely moving sheep for up to 190 days. Vessel-wall incorporation of the stentrode into the sheep superior sagittal sinus occurred as early as 6 days. A spatial resolution of at least 2.4 mm (electrode spacing) was achievable with neural recordings from within the blood vessel wall. The maximal bandwidth of the stentrode was 189 Hz. Our findings demonstrate that the performance of the stentrode, measured by spectral content and bandwidth, was similar to an epidural array and marginally inferior to a subdural array. Venous internal lumen patency was maintained for the duration of implantation.

Conclusions

We report the first intracranial stentrode array, deployed via minimally invasive catheter angiography within a cerebral vein to achieve chronic recordings in freely moving sheep for up to 190 days. Early incorporation of the stentrode into the vessel wall was associated with an improvement in recording sensitivity. The recording performance was comparable to epidural electroencephalography. An endovascular neural interface offers a method for safe, reliable and chronic neural recordings. We envisage that future applications of endovascular arrays may include motor cortex sensors in brain-machine interfaces, seizure prediction in epilepsy, and endovascular deep brain stimulation.



(Filename: TCT_O-275_abstractimage.jpg)

Wednesday

7:30AM - 8:30AM

Washington Marriott Wardman Park, Marriott Ballroom

13A-Wednesday Morning SAM - Pediatrics - Audience Response (AR) Self Assessment Module (SAM)

13A-1

7:30AM - 7:55AM

Pediatric Brain Cases

Poussaint, T.
Boston Children's Hospital
Boston, MA

13A-2

7:55AM - 8:00AM

Questions and Answers

13A-3

8:00AM - 8:25AM

Going With the Flow: Pediatric Vascular Disease

Mirsky, D.
Children's Hospital Colorado
Aurora, CO

13A-4

8:25AM - 8:30AM

Questions and Answers

Wednesday

8:30AM - 9:00AM

Washington Marriott Wardman Park, Marriott Ballroom

14-General Session: Future of Neuroimaging / Neuroscience Research

14-1

8:30AM - 9:00AM

NIH and the Future of Neuroimaging for Neuroscience Research

Koroshetz, W.
NIH/NINDS
Bethesda, MD

Wednesday

8:35AM - 10:03AM

Washington Marriott Wardman Park, Roosevelt 4

14F-PARALLEL PAPER SESSION: Venous Disease and CSF Dynamics

O-288

8:35AM - 8:43AM

Imaging Findings in Pediatric Intracranial Hypertension

M Salmela¹, S Khanipour Roshan¹, A McKinney¹, D Nascene¹

¹*University of Minnesota, Minneapolis, MN*

Purpose

To evaluate the imaging findings in pediatric intracranial hypertension.

Materials and Methods

A retrospective search of the electronic medical record was performed to identify pediatric patients who were suspected of having intracranial hypertension and had undergone brain imaging. Clinical features evaluated were height, weight, BMI, presenting symptoms, opening cerebrospinal fluid (CSF) pressure, and presence of papilledema. Imaging features evaluated were the presence and location of cerebral venous stenosis, optic nerve sheath dilation, optic nerve tortuosity, posterior globe flattening, optic disk cupping, slit ventricles, partially empty sella, venous distension sign, and Chiari 1 malformation.

Results

Eighteen patients were identified (aged 1-17.8 years, mean age: 10.4 years; 9 male, 9 female). Presenting symptoms included headache (n=12, 67%), visual symptoms (n=10, 56%), and vomiting (n=2, 11%). Sixty-seven percent (n=12) of patients had elevated CSF pressure > 20cm H₂O; 28% (n=5) were obese; and 83% (n=15) had papilledema. Eighty-three percent (n=15) had cerebral venous stenosis. Locations of cerebral venous stenosis included the transverse-sigmoid sinus junction (n=13), sigmoid sinus (n=3), transverse sinus (n=2), distal straight sinus (n=1), superior sagittal sinus just above the torcula (n=1), and high internal jugular vein (n=1). Two of three patients who did not have venous stenosis had clinical features with known association with intracranial hypertension including renal failure and reduction in steroid dosing. Other imaging findings included optic nerve sheath dilation (n=15, 83%), posterior globe flattening (12, 67%), venous distension sign (n=8, 44%), tortuous optic nerves (n=7, 39%), Chiari 1 malformation (n=4, 22%), partially empty sella (n=3, 17%), optic disk cupping (n=1, 6%), and slit ventricles (n=0, 0%).

Conclusions

The most common imaging findings in pediatric intracranial hypertension found were cerebral venous sinus stenosis, optic nerve sheath dilation, and posterior globe

flattening, all occurring in at least half of cases. If present, the cerebral venous stenosis usually was located at the transverse-sigmoid sinus junction. Partially empty sella and optic disk cupping were rare, and slit ventricles were not seen.

O-289

8:43AM - 8:51AM

Prevalence and Clinical Significance of Unilateral Absent Flow in a Transverse Dural Sinus (TDS) on MR Venography

J Kim¹, R Rojas², Y Chang³, R Bhadelia⁴

¹*Beth Israel Deaconess Medical Center, Brighton, MA*, ²*Beth Israel Deaconess Medical Center, Boston, MA*, ³*Beth Israel Deaconess Medical Center, Newton, MA*, ⁴*Beth Israel Deaconess Medical Center, Boston, MA*

Purpose

Unilateral absence of flow signal in a transverse dural sinus (TDS) frequently is observed on MR venography (MRV) but its exact prevalence and clinical significance is not known. Our purpose was to determine: (1) prevalence of unilateral absence of TDS flow signal on MRV, (2) its clinical significance by assessing thrombosis on contrast-enhanced magnetic resonance imaging (MRI)/CTV, and (3) if asymmetry in TDS size explains the phenomenon of absent flow on MRV.

Materials and Methods

Patients who had both MRV (2D time-of-flight and/or 3D phase-contrast) and gadolinium-enhanced 3D-MPRAGE images or computed tomography (CT) venography between January 2014 and October 2015 were included. All the images were reviewed to determine (1) the number of patients with complete absence of flow in a TDS (Figure 1 a-b), (2) presence of thrombosis on MRI/CTV, and (3) asymmetry between the lateral most portion of the transverse sinuses as measured on postcontrast images (Figure 1c). T-test was used to determine the differences in size of TDS between those with and without absent flow on MRV.

Results

Of the 123 patients, 25 (20.3%) had absence of flow in one TDS on MRV. The absent TDS flow was seen on the left in 15 and on the right in 10 patients. Comparison with postcontrast images (116 MPRAGE; 7 CTV) showed only 5/25 (20%) of patients with unilateral absence of TDS flow had signs of thrombosis on postcontrast images. Patients with absent TDS flow had significant asymmetry of size compared to those without ($P<0.001$).

Conclusions

Unilateral absence of TDS flow is common on MRV examinations, and is a false positive finding in 80% of the patients. Size asymmetry appears to contribute to the phenomenon of absent unilateral TDS flow.

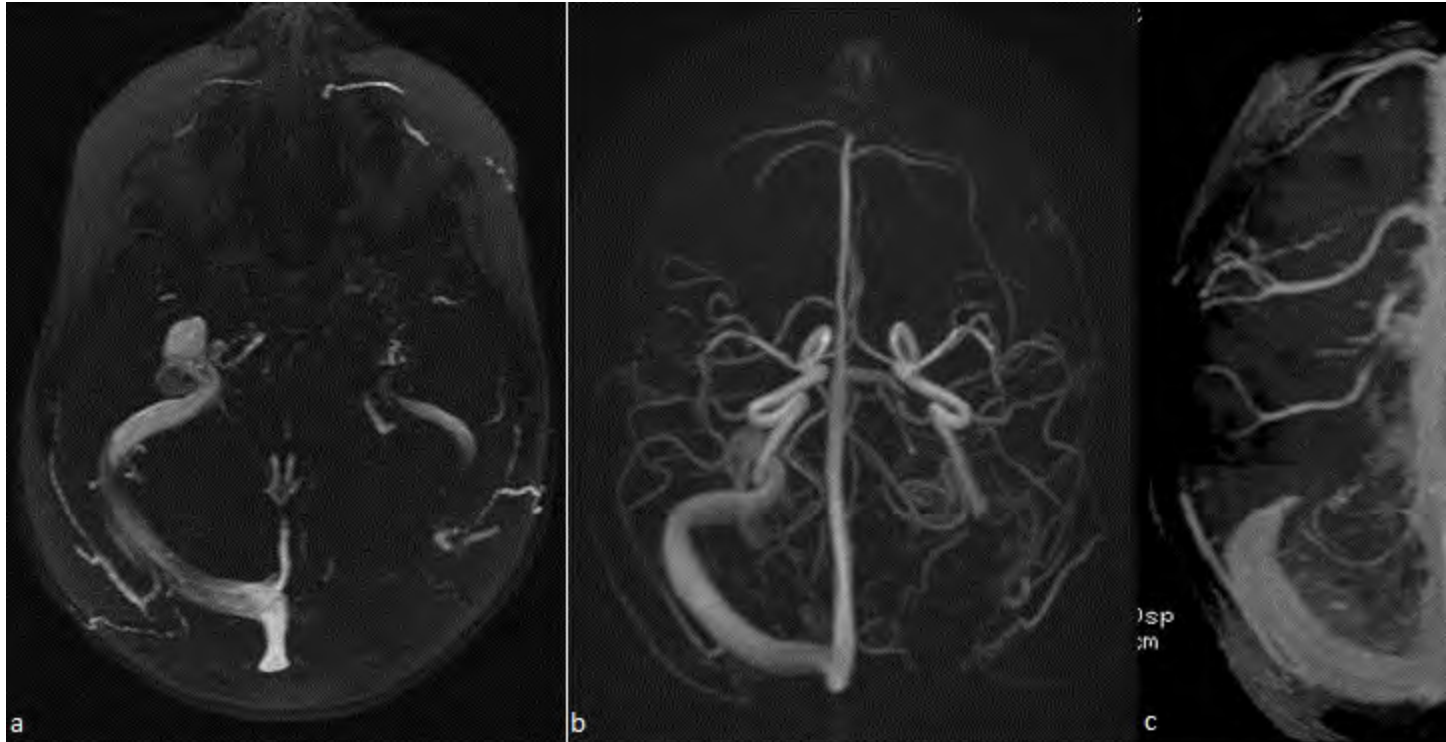


Fig 1) 2D-TOF (a) and 3D-PC (b) demonstrate loss of signal of the left transverse venous sinus while gadolinium (c) demonstrates patency.

(Filename: TCT_O-289_MRVFigure.jpg)

O-290

8:51AM - 8:59AM

Cross-Sectional Measurement of Intracranial Dural Venous Sinuses Towards a Better Diagnosis of Obstruction

I Shelef¹, S Lublinsky², A Friedman³, R Anconina¹, D Zur⁴, A Kesler⁴, I Shelef¹
¹Soroka University Medical Center, Beer-Sheva, n/a, ²Ben Gurion University, Beer Sheva, Israel, ³Ben-Gurion University, Beer-Sheva, n/a, ⁴Tel Aviv Sourasky Medical Center, Tel Aviv, n/a

Purpose

Accurate and precise technique that allows quantitative characterization of differences in the intracranial venous system is a critical diagnostic tool for evaluation of occlusion degree. The purpose of this study was to develop and test a novel quantitative diagnostic technique allowing characterization of dural sinuses anatomy in idiopathic intracranial hypertension (IIH) patients.

Materials and Methods

An automated and validated algorithm to quantify vessels cross-sectional changes was applied (1). The method consists of several steps, which include an automatic vessel

extraction and segmentation from the normalized to standard space brain volume of interest, volumetric skeletonization of the vessel object, numerical definition of cross-sectional planes at each skeleton point, and rendering of vessel cross-sectional circumference based on specially developed clustering technique (Fig. 1). Four large sinuses were tested (right and left transverse sinuses, superior sagittal sinus, and straight sinus). The cross-sectional area and shape measurements were evaluated in three control subjects and four IHH patients [before and after lumbar puncture (LP) treatment with the specific intention of removing 30-40 ml of CSF] (Fig. 2). Three dimensional affine registration based on finite difference optimization was applied to match and align the 4-sinuses skeletons. To this end one control skeleton was chosen as a reference. Iterative closest point matching (2) was applied to register the rest of the skeletons with the reference one. The before and after LP and healthy control matching cross-sectional data were plotted along the length of the sinuses according to its position starting from confluence point. The comparison of the cross-sectional area was performed with a T test. p-value less than .05 was considered significant.

Results

In agreement with previous studies (3-4), it demonstrated an increase in venous diameter after LP due to normalization of intracranial hypertension. All four investigated principal cranial blood sinuses had significant cross-sectional area increase after LP ($p \leq .05$) (Table 1). There was no significant difference between after LP and control in cross-sectional area data.

Conclusions

The presented technique allows quantitative characterization of differences in the intracranial venous system and evaluation of occlusion degree based on the pathology and normal data comparison. Implementation of this technique in neuroimaging could help better characterize differences in the intracranial venous system and aid differentiating pathology and normal.

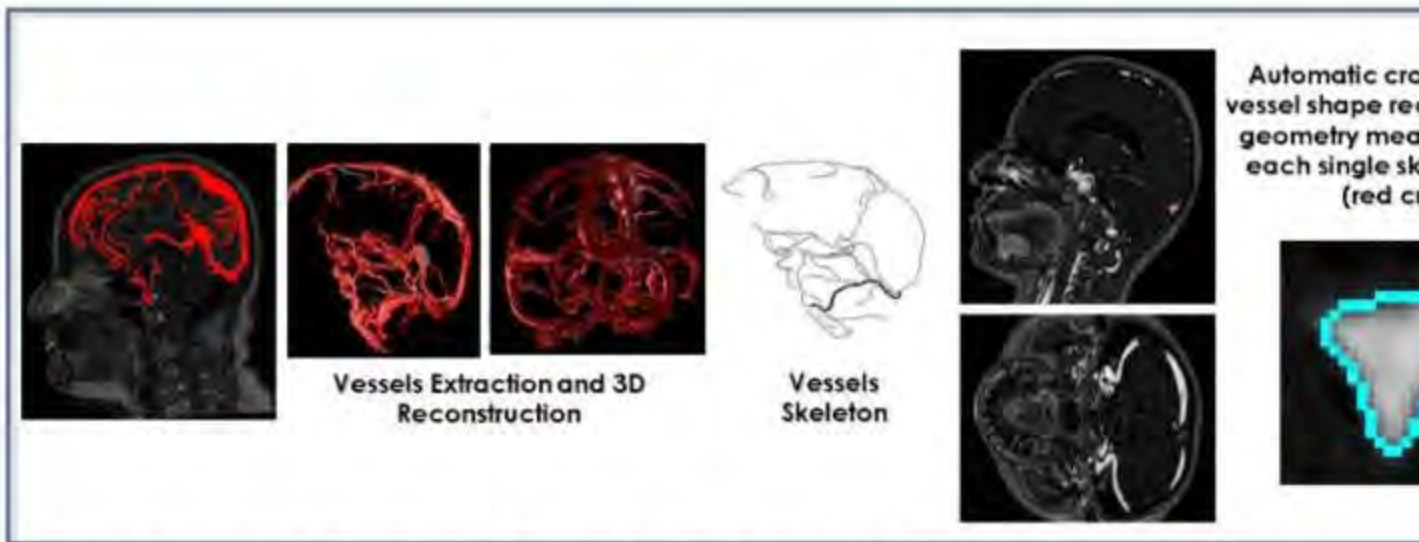


Figure 1. Automated Method for Cross Sectional Analysis of Sinuses in the Brain.

| Sinus | Cross-Sectional Area (mm ²) | | | | | |
|-------------------|---|----------|----------|---------|---------|---------|
| | Before LP | | After LP | | Control | |
| Right transverse | 40 ± 21 [†] | (4-76) | 52 ± 22 | (6-79) | 58 ± 13 | (34-93) |
| Left transverse | 45 ± 20 [†] | (7.5-78) | 52 ± 23 | (8-78) | 54 ± 12 | (36-99) |
| Superior sagittal | 52 ± 21 [†] | (17-88) | 54 ± 21 | (17-88) | 56 ± 17 | (29-91) |
| Straight | 23 ± 13 [†] | (2-45) | 30 ± 16 | (4-48) | 31 ± 12 | (20-57) |

Table 1. Cross-Sectional Area Measurements in Principal Cerebral Sinuses
Data reported as mean ± SD (range, minimum-maximum)

[†]Significant difference ($p \leq .05$) between measurements before and LP.



Figure 2. Changes in cross-sectional area measurements in principal cerebral sinuses before (red) and after (cyan) LP.

(Filename: TCT_O-290_Images.jpg)

O-291

8:59AM - 9:07AM

Transverse Sinus Effacement is the most sensitive MR sign of Pseudotumor Cerebri

P Morris¹, D Black¹

¹Mayo Clinic, Rochester, MN

Purpose

Various magnetic resonance (MR) imaging findings of pseudotumor cerebri have been described, including optic nerve sheath redundancy, optic nerve tortuosity, optic nerve head flattening, empty sella, etc. each with variable sensitivity. We hypothesized that neuroradiologic interpretation of pseudotumor is restricted by the limitations of these signs and that our awareness of this disease entity can be improved by focusing on the stenoses of the transverse sinuses found in this condition.

Materials and Methods

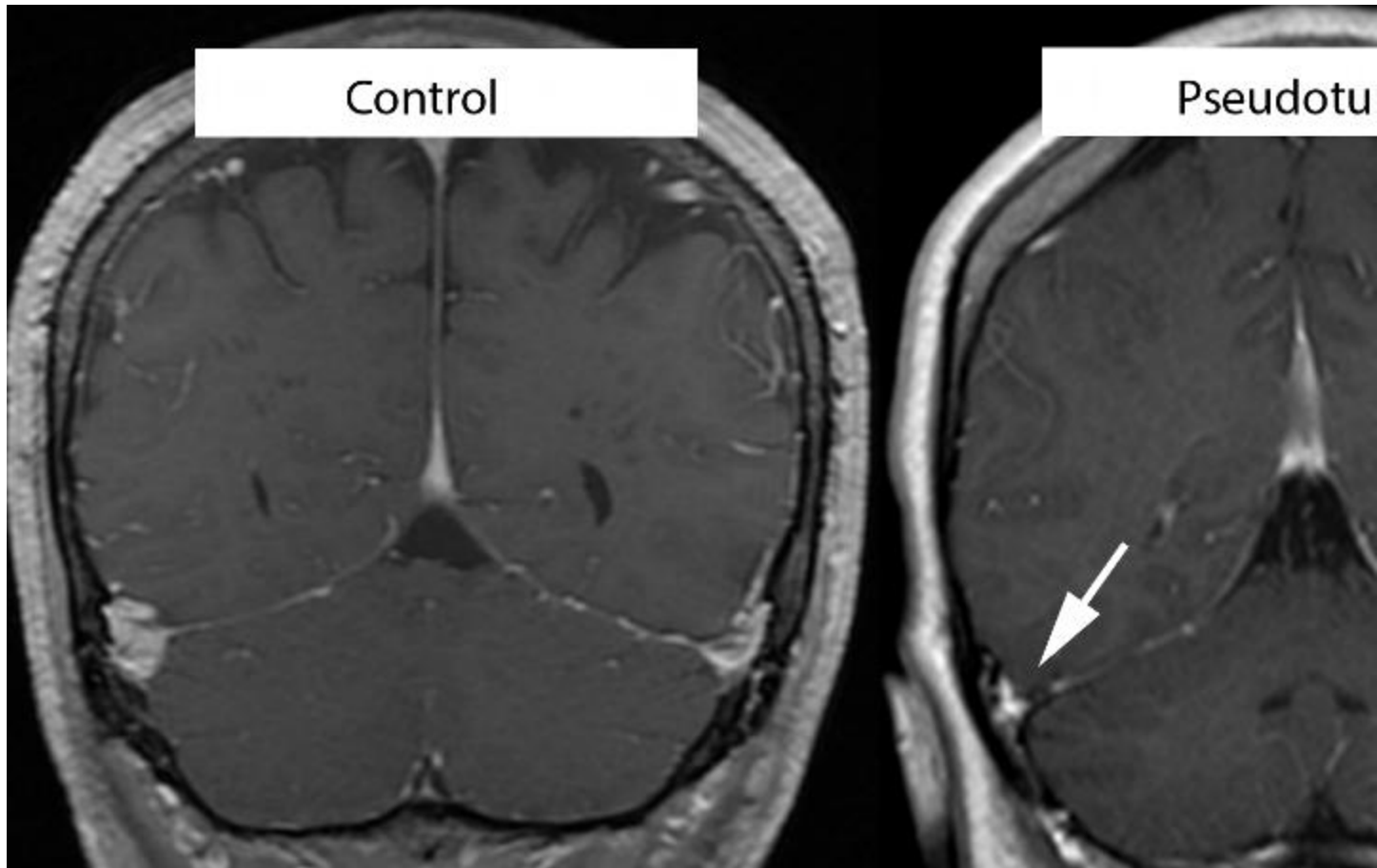
Medical records and imaging of 65 patients with the diagnosis of pseudotumor cerebri according to the Modified Dandy Criteria were reviewed with IRB approval. Parameters including BMI, CSF opening pressure, and fundoscopic findings were gathered. Magnetic resonance imaging and MRV images were reviewed for established signs of elevated ICP. Gadolinium-bolused MRV images were evaluated for TS stenosis using a 4 point categorical scale in 25% increments distally and proximally, and also using a calipers-tool for millimeter measurements in two planes. Coronal postgadolinium images were evaluated on a categorical scale for presence or absence of (1) bilateral TS stenosis/effacement, and (2) prolapse/herniation of temporo-occipital tissue into the expected location of the TS.

Results

Bilateral distal > 50% stenosis of the transverse sinuses, using the proximal sinus as a reference, was the most consistent and sensitive indicator of pseudotumor cerebri ($p < .0001$ Wilcoxon Signed Rank matched-pairs). Bilateral TS stenosis was present in 86% of patients on MRV and in 84% of patients on coronal T1 post-gadolinium images (Fig. 1). This surpassed the sensitivity of other signs such as empty sella 54%, optic nerve sheath dilatation 65%, DWI spot sign at the optic nerve head 10%, flattening of the optic nerve head 34%. Retrospectively, in 33% of patients MRV interpretation on at least one occasion during the period of review ignored the findings of TS stenosis, and in the absence of other signs of PC, therefore did not draw attention to the diagnosis.

Conclusions

In this series, transverse sinus stenosis was the most reliable MR finding in patients with pseudotumor cerebri. Sinus stenosis can be discerned with similar sensitivity on both the gadolinium-bolused MRV sequence and the postgadolinium coronal T1 sequence. Therefore, detection of TS stenosis on MR imaging need not depend on having access to an MRV sequence. Other established MR signs of pseudotumor are less sensitive, and their absence appears to contribute to a significant rate of radiologist oversight of this condition in this series. An awareness of the sensitivity of coronal T1 imaging to TS stenosis and of the lower sensitivity of previously established MR signs of pseudotumor cerebri will enhance the neuroradiologist's interpretation of this diagnosis.



(Filename: TCT_O-291_Figure1.jpg)

O-292

9:07AM - 9:15AM

Transverse Sinus Cross Sectional Areas in Pseudotumor Cerebri: A potential Venturi Phenomenon argues for the validity of Stent Treatment

P Morris¹, D Black¹, J Port¹, N Campeau¹, H Cloft¹, G Lanzino¹, A Alexander¹
¹Mayo Clinic, Rochester, MN

Purpose

Transverse sinus (TS) narrowing is observed in over 80% of patients with pseudotumor cerebri (PC) (1), previously reported in broad increments of percentage narrowing compared with the more proximal sinus. We hypothesized that direct measurement of the cross-sectional area (CSA) of the transverse sinuses in multiple locations and comparison with a control population of non-PC patients would give more precise evaluation of the degree and hemodynamic conditions of the stenoses seen in this disease state, with implications for the treatment options available.

Materials and Methods

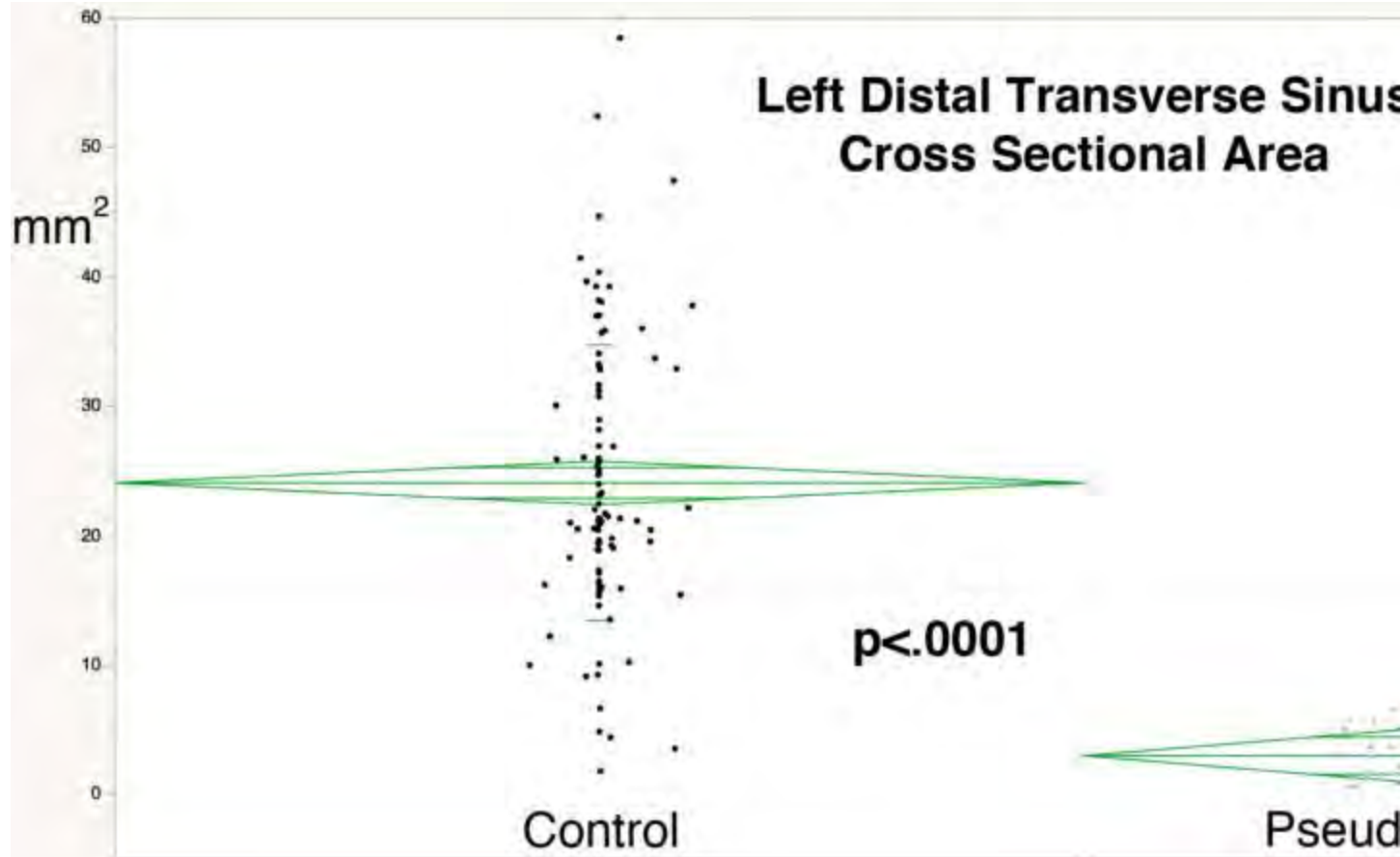
Magnetic resonance imaging (MRI)/MRV examinations from 65 PC patients were reviewed with IRB approval and compared with those of 97 non-PC control patients. The caliber of the distal stenotic segment of the TS was compared with that of the more proximal segments using, firstly, a 4-point nominal scale indicating 25% degrees of incremental stenosis, previously described (1). Secondly, orthogonal direct measurements of the TS were obtained from the MRV raw data, using a calipers tool, and the CSA of the TS was calculated as the area of a triangle, height x ½ width. Intrasubject and between-group comparisons were made using parametric ANOVA and pairwise nonparametric statistics.

Results

Transverse sinuses of PC patients were narrowed significantly distally compared with controls using the nominal scale ($p < 0.005$) and using the calculated CSA ($p < 0.0001$). Both scales yielded results in broad agreement, although CSA estimates were more statistically significant. The left transverse sinus distally measured 2.9 mm² (SD 2.09) compared with 24.03mm² (SD 10.6) in controls (Fig. 1), while the right distal TS measured 4.2mm² (SD 4.18) compared with 29.89mm² (SD 11.3) in controls. The stenotic effect also was evident to a lesser degree in the proximal right TS; PC proximal TS mean CSA 28.5mm², SD 14.6mm², Control 37.4mm² SD 15.9mm² ($p < 0.004$). The left side proximally did not demonstrate a significant difference: TS left proximal mean CSA PC 23.6mm² vs control 24.7mm² ($p = 0.81$). Transverse sinuses measurements were not significantly influenced by age or gender ($p = 0.04$).

Conclusions

Transverse sinuses narrowing in PC patients is more severe than can be reflected in a 4-point categoric scoring system. The severe, focal nature of TS stenosis in PC patients presumably begins as a compressive phenomenon, secondary to elevated intracranial pressure. However, the stenotic conditions conform to that of a Venturi tube whereby the drop in pressure at the level of the stenosis becomes an aggravating factor, further exacerbating the collapse of the dural sinus wall. Therefore, for as long as ICP surpasses the intraluminal pressure of the distal transverse sinus, the sinus will remain collapsed. We suggest that the Venturi phenomenon may be a significant factor in perpetuating this "strange attractor" or "entrapment" condition, arguing that the most effective therapeutic method to reverse this state might be, therefore, an intravascular stent.



(Filename: TCT_O-292_Fig1Abst3.jpg)

O-293

9:15AM - 9:23AM

Sagging of the Tentorium in Pseudotumor Cerebri, a correlate of Transverse Sinus Collapse

P Morris¹, D Black¹, J Port¹, N Campeau¹
¹Mayo Clinic, Rochester, MN

Purpose

Effacement or stenosis of the transverse sinuses is seen in >84% of patients with pseudotumor cerebri (PC). We conjectured that such an effect could not take place unless there was a downward shift of the tentorium cerebelli bringing about this change in the configuration of the venous sinuses. Because the apex of the tentorial incisura is fixed medially at the point of attachment of the falx cerebri and laterally at the margins of the transverse sinuses, we hypothesized that a downward vector of

force on the tentorium would be detectable as a downward "sling" or "hammock" curvature of the tentorium on its midpoint in pseudotumor patients.

Materials and Methods

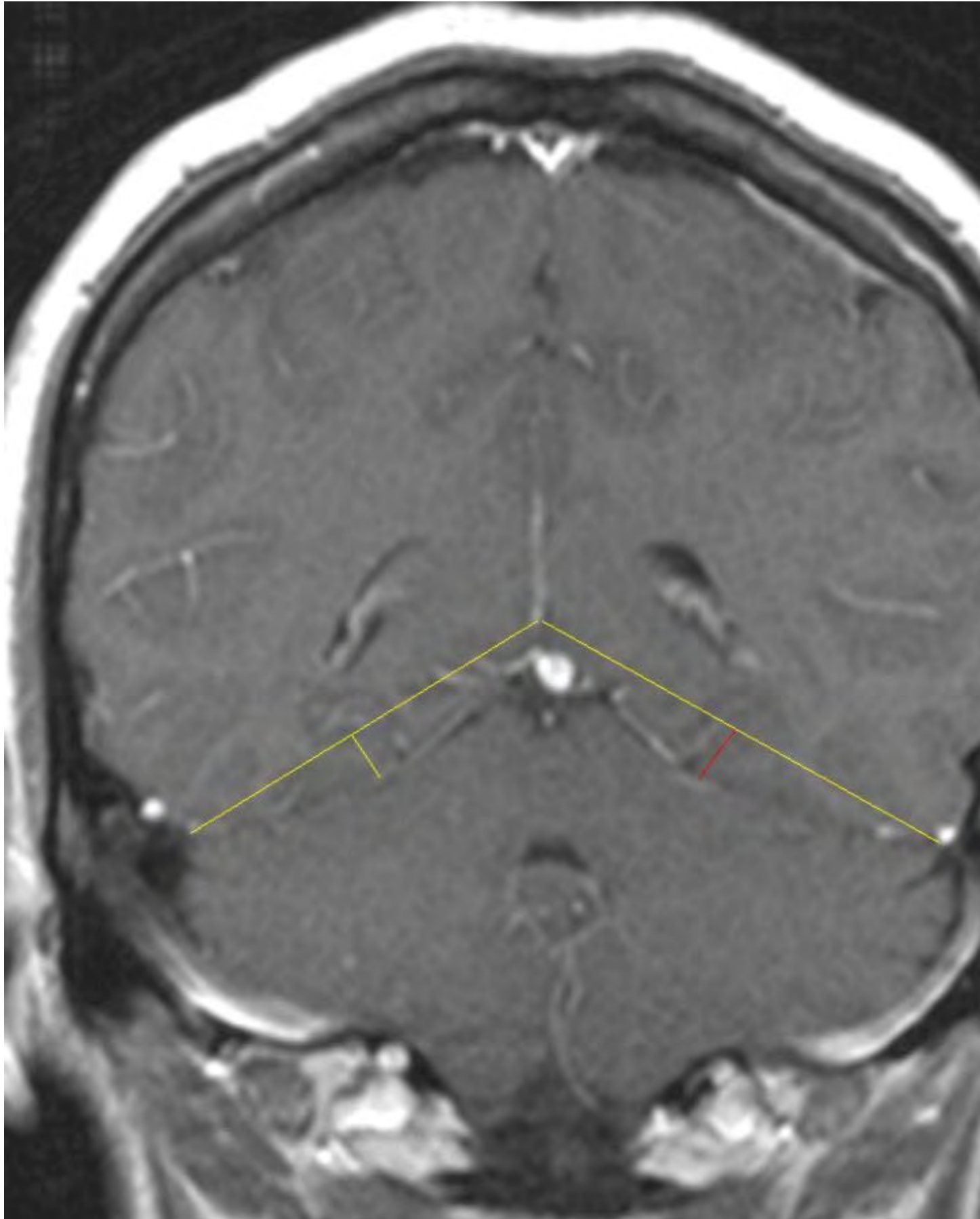
Coronal T1-weighted postgadolinium magnetic resonance (MR) images were analyzed with IRB approval in 50 patients with pseudotumor cerebri and compared with 40 control subjects. An arc of curvature was defined between the points of attachment of the tentorium at the apex of the incisura and laterally at the insertion into the transverse sinus. The perpendicular height of the arc was measured at the point of maximal curvature (Fig. 1), using which the radius of curvature and area of the segment defined by the chord and curvature of the tentorium were calculated.

Results

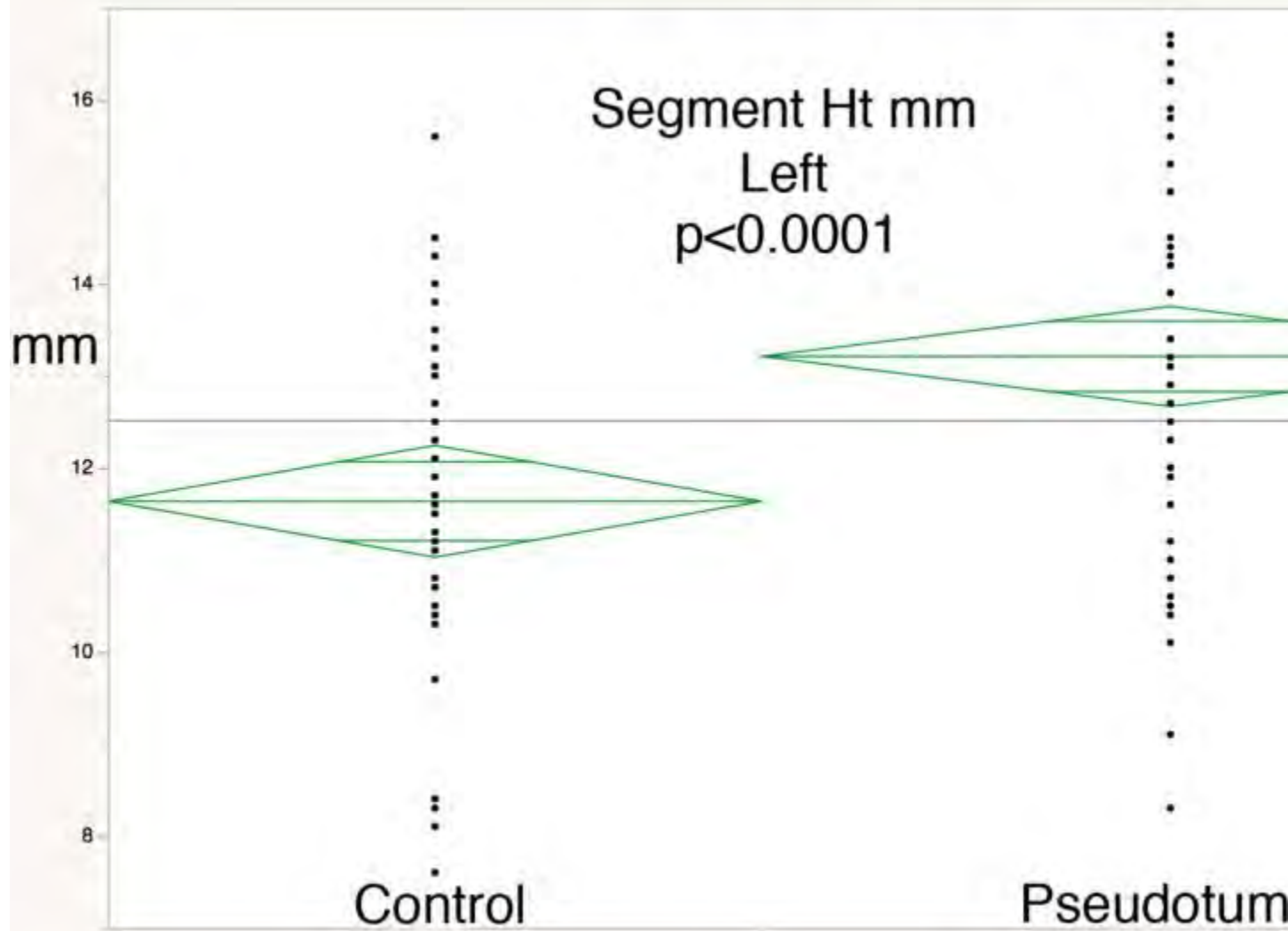
Pseudotumor patients showed a significantly higher height of the arc and area of the defined segment than did the control group. The mean height of the arc in the pseudotumor group was 13.5mm (S.D. 1.8) on the right side, 13.2 mm (S.D. 2.06) on the left, compared with controls 11.93 mm (S.D. 2.04) and 11.6 mm (S.D. 1.76) respectively, $p = .0001$ (Fig. 2). The pseudotumor group showed a mean area of the segment on the right side of 629.72 mm² (S.D.106.21) and on the left side 615.98mm² (S.D. 119.78) compared with controls; Right 527.14 mm² (S.D.106.2) and Left 512.78 mm² (S.D. 101.70), $p < .0001$ (Fig. 3). The calculated radii of curvature on either side showed no significant difference between the two groups.

Conclusions

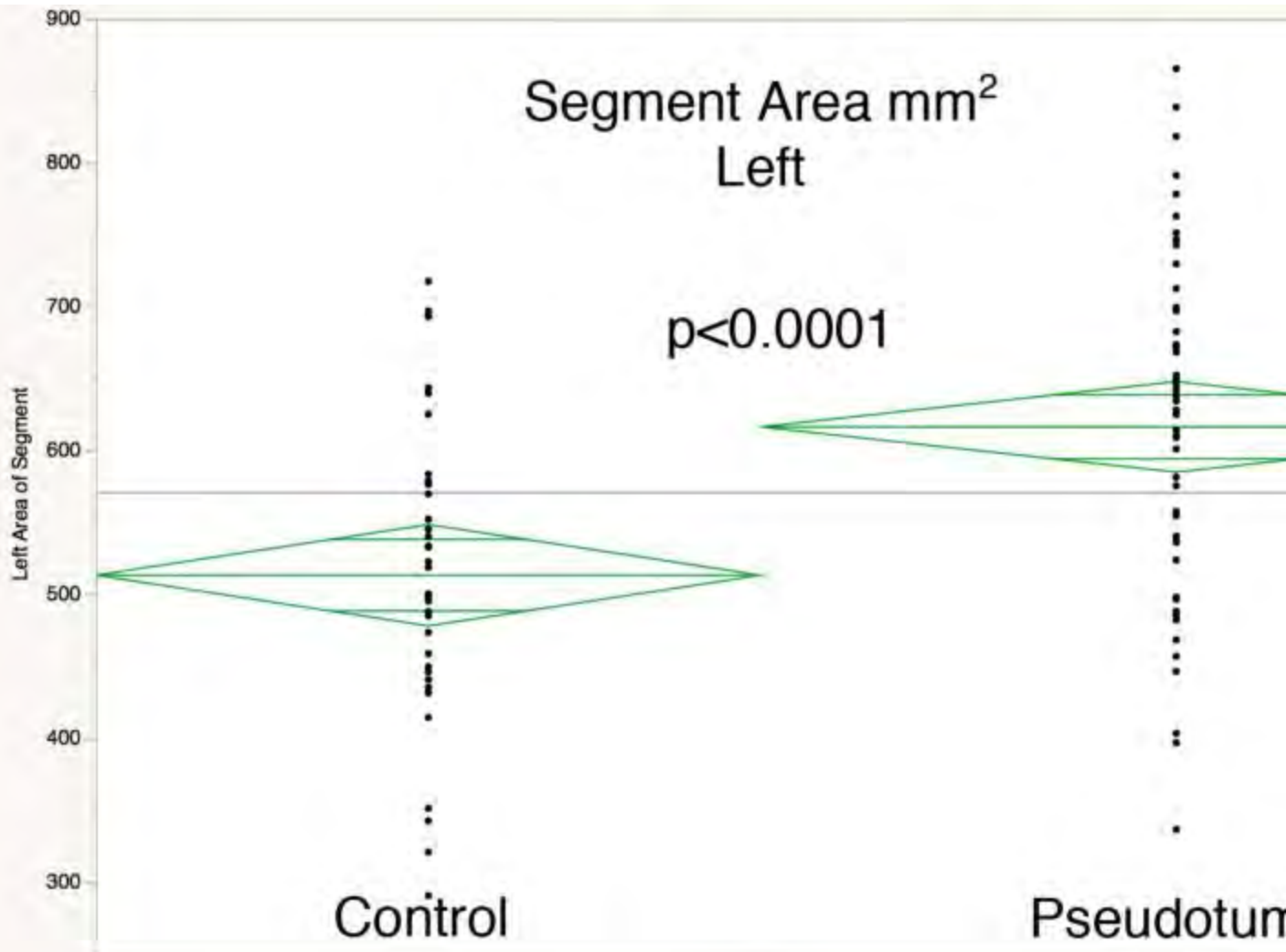
Our results support the hypothesis that an alteration in the configuration of the tentorium cerebelli is present in patients with pseudotumor cerebri, likely occurring in conjunction with changes in the configuration of the transverse sinuses. The tentorium appears to demonstrate a greater degree of downward bowing in pseudotumor, compared with control subjects. This would suggest that the primary genesis of the pressure effects in pseudotumor cerebri is supratentorial/hemispheric, acting from above-down. The narrowing of the transverse sinuses seen in this condition may, therefore, result from a downward translation of the tentorium, rather than being due simply to a diffuse elevation of ICP compressing the transverse sinuses nondirectionally.



(Filename: TCT_O-293_A3Figure1.jpg)



(Filename: TCT_O-293_A3Figure2.jpg)



(Filename: TCT_O-293_A3Figure3.jpg)

O-295

9:31AM - 9:39AM

Pericatheter VP shunt catheter fluid collections in adults. Infection, shunt malfunction or worse? Correlation of CT/MR findings with Indium-111 Disodium Pentetate (In-111 DTPA) scan.

S Hegde¹, H Kale², A Muthukrishnan³, V Agarwal³

¹University of Pittsburgh, Pittsburgh, PA, ²University of Pittsburgh Medical center, Pittsburgh, PA, ³University of Pittsburgh Medical Center, Pittsburgh, PA

Purpose

Chronic fluid collections with edema along ventriculo-peritoneal (VP) shunt catheter

tracts in adults are rare (1, 2) and are seen more frequently in children (3, 4, 5). The cause of these collections frequently is unclear and represents a diagnostic dilemma. In search of the radiology literature, there are no previous studies correlating these findings on CT/MRI with nuclear medicine scans. We hypothesize that when seen in adults, these CT/MR findings represent VP shunt catheter failure.

Materials and Methods

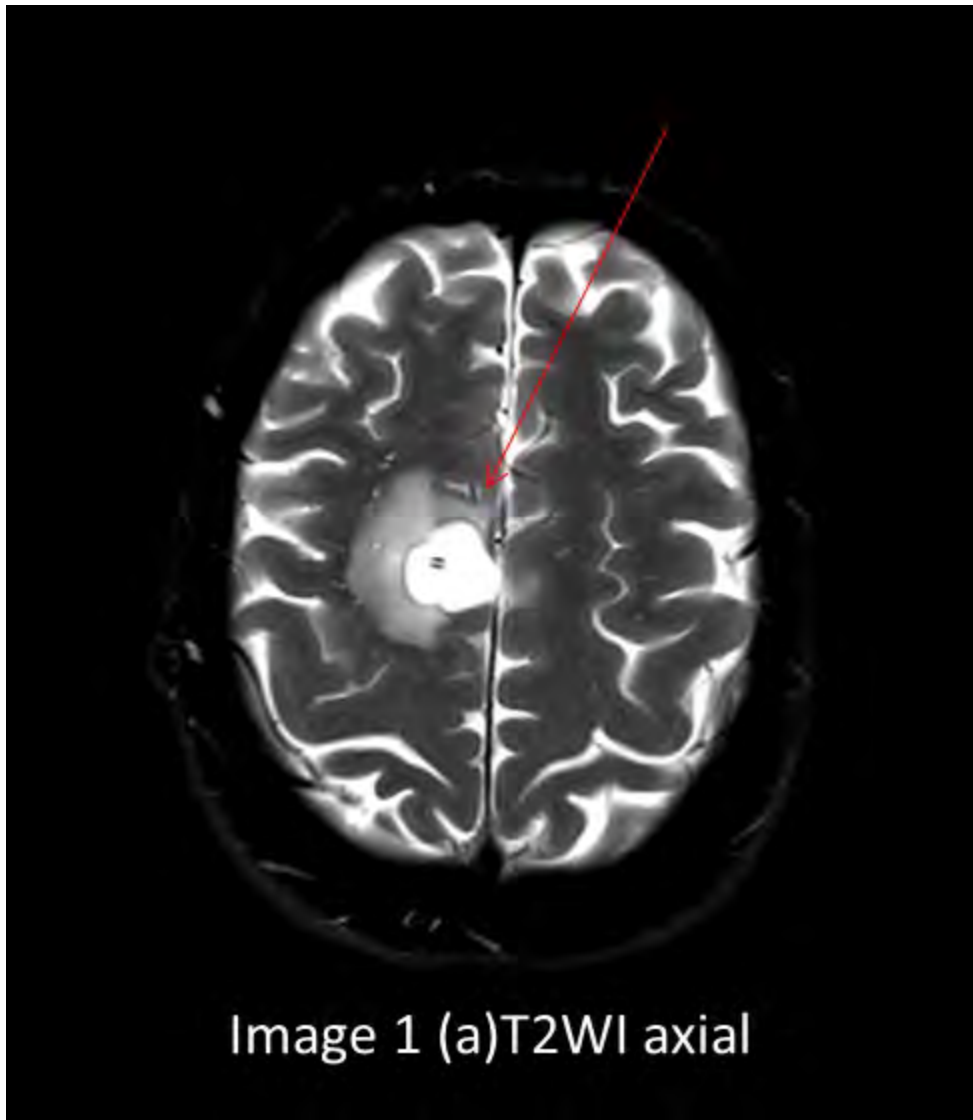
We retrospectively evaluated computed tomography (CT)/magnetic resonance (MR) and Indium-111 Disodium Pentetate (In-111 DTPA) scan findings in six patients with peri-VP shunt catheter collections who presented at our institution. Patients who had recently placed catheters and pericatheter hemorrhage were excluded. All patients selected had prior (immediate postoperative or remote) CT/MRI scans which did not reveal any collection.

Results

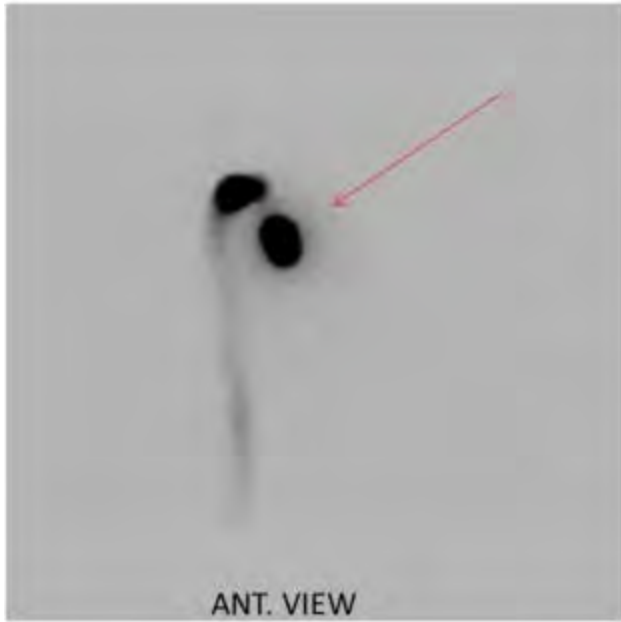
In the series of cases presented here, a majority of patients demonstrated absence of radiotracer reflux into the ventricles on the In-111 DTPA scan. Also, there was focal accumulation of radiotracer corresponding to the loculated fluid collection on correlation with head CT or MRI images. In some, there was good passage of the radiotracer through the distal portions of the tubing which should not be mistaken for a well-functioning shunt system, especially in the absence of ventricular reflux and presence of an intracranial loculated collection of radiotracer activity. We believe this rare finding of pericatheter collection may represent complete or early partial obstruction of the catheter which will ultimately result in shunt failure.

Conclusions

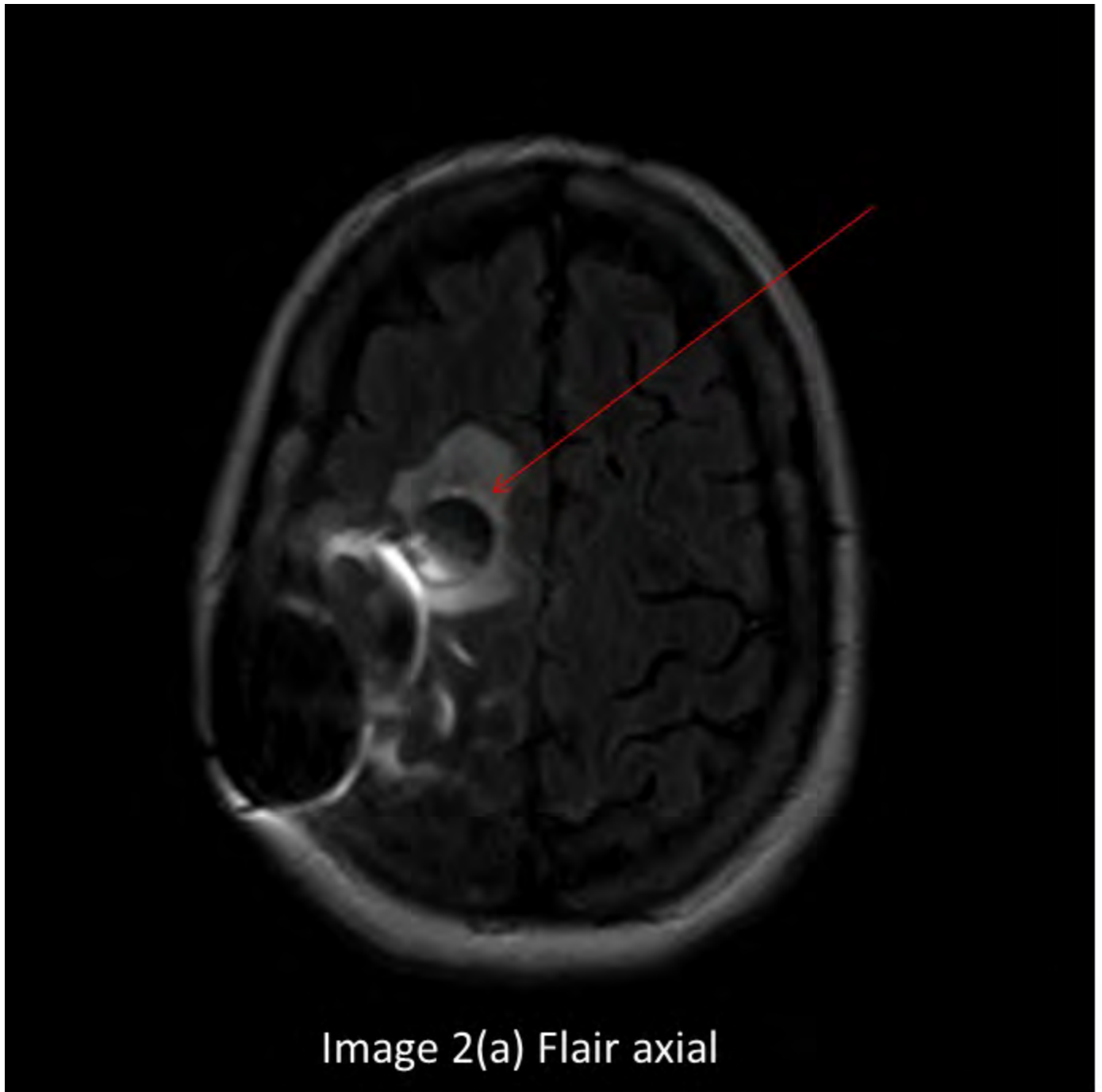
Collections around VP shunt catheters in adults are rare. All of the cases evaluated by us demonstrate that findings on CT/MR represent a malfunction of the VP shunt catheter. A combined interpretation of the findings of nuclear medicine scans and CT/MRI may be useful in differentiation of this rare but important complication of VP shunt catheter placement in adults in order to prevent incorrect diagnosis of abscess or tumor and eliminate the need for unnecessary biopsy.



(Filename: TCT_O-295_Image1aT2WI.jpg)



(Filename: TCT_O-295_Image1bAnteriorView.jpg)



(Filename: TCT_O-295_Image2aFLAIRaxial.jpg)



Image 2(b) Anterior view

(Filename: TCT_O-295_Image2bAnteriorView.jpg)

O-297

9:47AM - 9:55AM

Hyperdense Paraspinal Vein Sign: A Marker of CSF-Venous Fistula in Spontaneous Intracranial Hypotension

P Kranz¹, T Amrhein¹, L Gray¹

¹Duke University Medical Center, Durham, NC

Purpose

Cerebrospinal fluid (CSF)-venous fistula is a cause of spontaneous intracranial hypotension (SIH) that may occur in the absence of myelographic evidence of CSF leak, but has only been reported previously in one small case series of three patients. Identification of these lesions can be challenging, but is important for treatment. The purpose of this report is to describe three additional cases of CSF-venous fistula and to report on a novel imaging sign that may aid in its detection and localization.

Materials and Methods

We retrospectively reviewed cases of patients with SIH treated at our institution in order to identify cases caused by or associated with surgically confirmed CSF-venous fistulae. Pre-operative imaging was reviewed to determine the appearance of these lesions on conventional or digital subtraction myelography and CT myelography (CTM). The presence of abnormal paraspinal blood vessels on CTM was assessed. Attenuation values from regions-of-interest drawn over the paraspinal vessels on pre-myelographic CT and post-myelographic CT were compared. Image postprocessing using automated attenuation-thresholded color overlays was performed on CTM images.

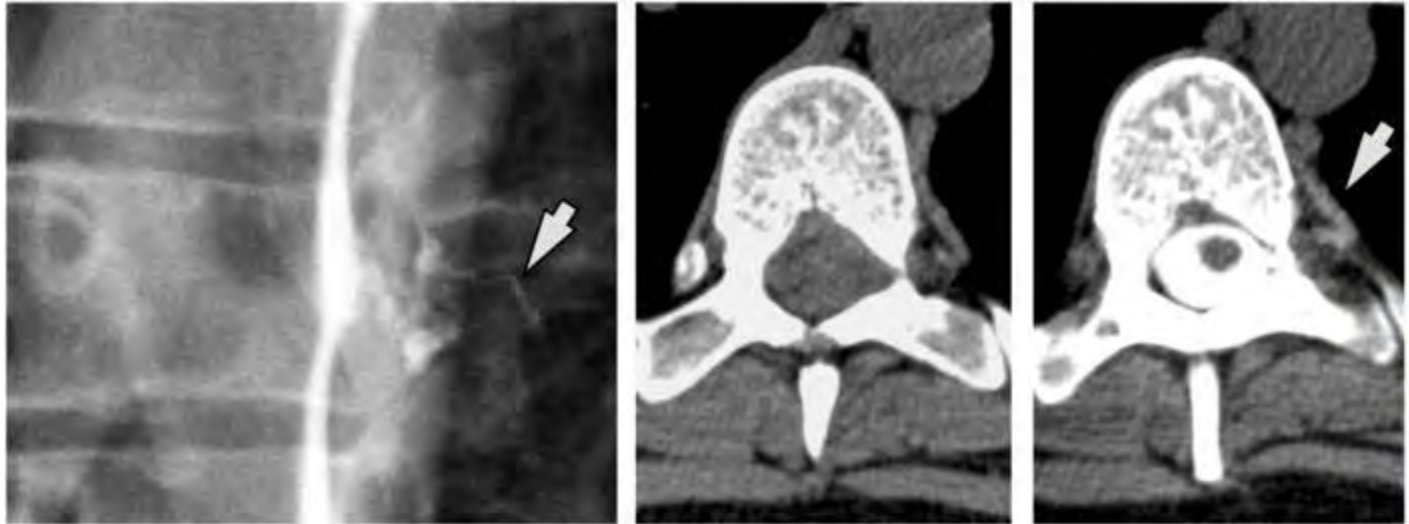
Results

Three cases of CSF-venous fistulae were identified. Myelography with or without digital subtraction was performed in two cases, demonstrating the location of the fistula; the third case was confirmed intra-operatively based on suspicion from the pre-operative CTM. A hyperdense paraspinal vein was observed in all cases ipsilateral to and at the same level of the fistula. The average density of the vessel measured 27.5 ± 6.4 HU on pre-myelographic CT, and 105.7 ± 23.0 HU on postmyelographic CT. Postprocessing with attenuation-thresholded color overlays increased conspicuity of the hyperdense vessel in all three cases. In all three cases, targeted epidural patching failed, necessitating surgical ligation of the fistula. All patients had resolution of symptoms of SIH following surgery.

Conclusions

Cerebrospinal fluid-venous fistulae are a newly recognized cause of SIH that can occur without myelographic evidence of CSF leak. The presence of a hyperdense paraspinal vein on CTM can help identify these lesions, and recognition may be facilitated with image postprocessing using attenuation-thresholded color overlays. Identification of this sign on CTM is important in that it may help guide subsequent

confirmatory imaging tests, and based on our preliminary experience, suggests the need for surgical intervention rather than epidural patching.



(Filename: TCT_O-297_AbstractfigureKranz.jpg)

O-298

9:55AM - 10:03AM

Unsupervised Characterization of Adult Hydrocephalus using CSF Flow and Volumetrics

J Shin¹, G Pagé², A Moghekar¹, O Balédent³, A Blitz¹

¹*Johns Hopkins Medical Institutions, Baltimore, MD*, ²*Centre Hospitalier Universitaire d'Amiens, Salouël, Salouël*, ³*Université de Picardie Jules Verne, Amiens, Amiens*

Purpose

Adult hydrocephalus (AH, including idiopathic normal pressure hydrocephalus and other etiologies) is a curable cause of dementia. Adult hydrocephalus is defined phenotypically by abnormal building up of cerebrospinal fluid (CSF) in the ventricular system, thus indeed represents a heterogeneous group of diseases with diverse etiology, manifestation, prognosis and response to treatments. Systematic categorization and characterization of AH have not been achieved yet, due to a limited number of subjects and difficulty in the volumetric and hydraulic quantification of CSF in the ventricular system. Here, we analyze a large number of subjects using unbiased mathematical approaches to classifying and characterizing AH.

Materials and Methods

We used an unsupervised cluster-based approach to integrating the 70 parameters from the volumetric analysis and the 14 parameters from the aqueductal flow analysis from 495 subjects (mean age: 58.7 years) with varying degree of ventricular enlargement. Volumetric analysis of the ventricles and brain parenchyma was

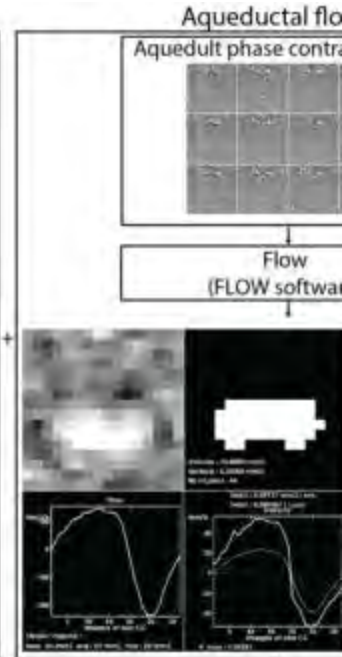
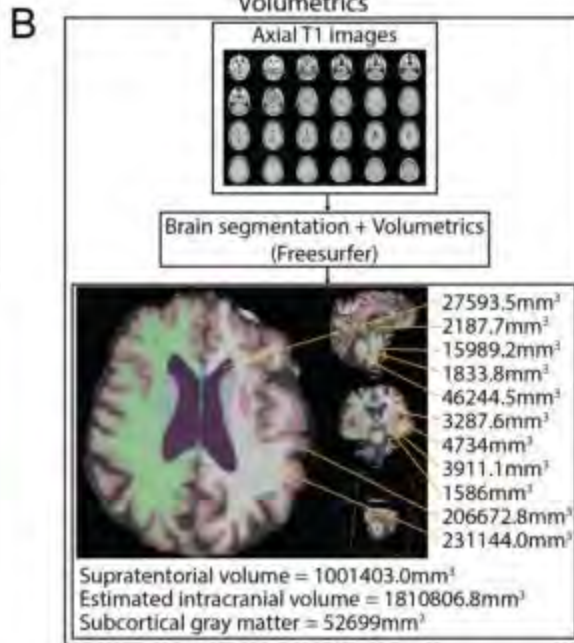
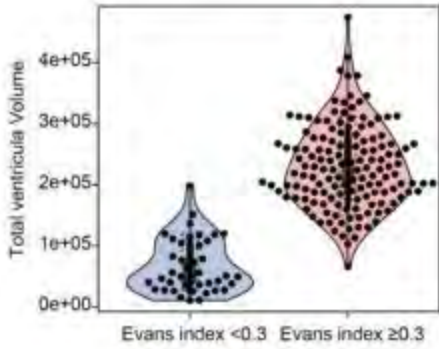
performed using Freesurfer software package. Dedicated CSF flow postprocessing software (Bio Flow Image, CHU Amiens) was used to quantify CSF flow through the cerebral aqueduct including stroke volume and maximal velocity. Subjects were classified based on unsupervised clustering and compared with clinical data including gait abnormality measured by Tinetti and TUG (Timed Up and Go) scores, urinary symptoms, and MMSE (Mini-Mental State Examination) scores. The resulting parameters were merged to determine correlations between over 100 parameters from the volumes of different brain segments, aqueductal flow characteristics and clinical data.

Results

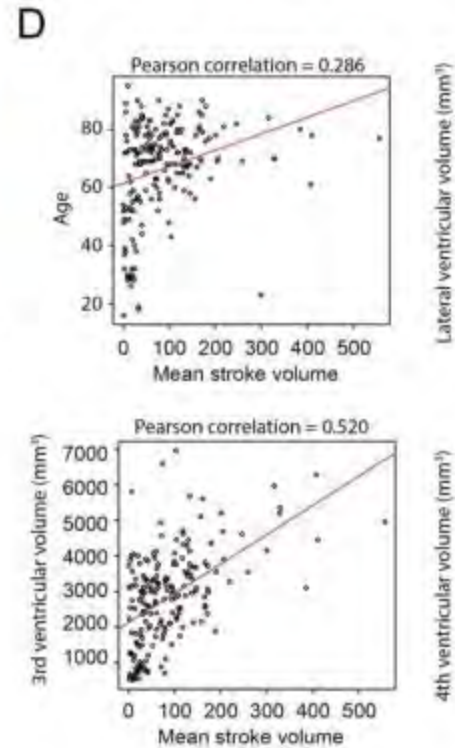
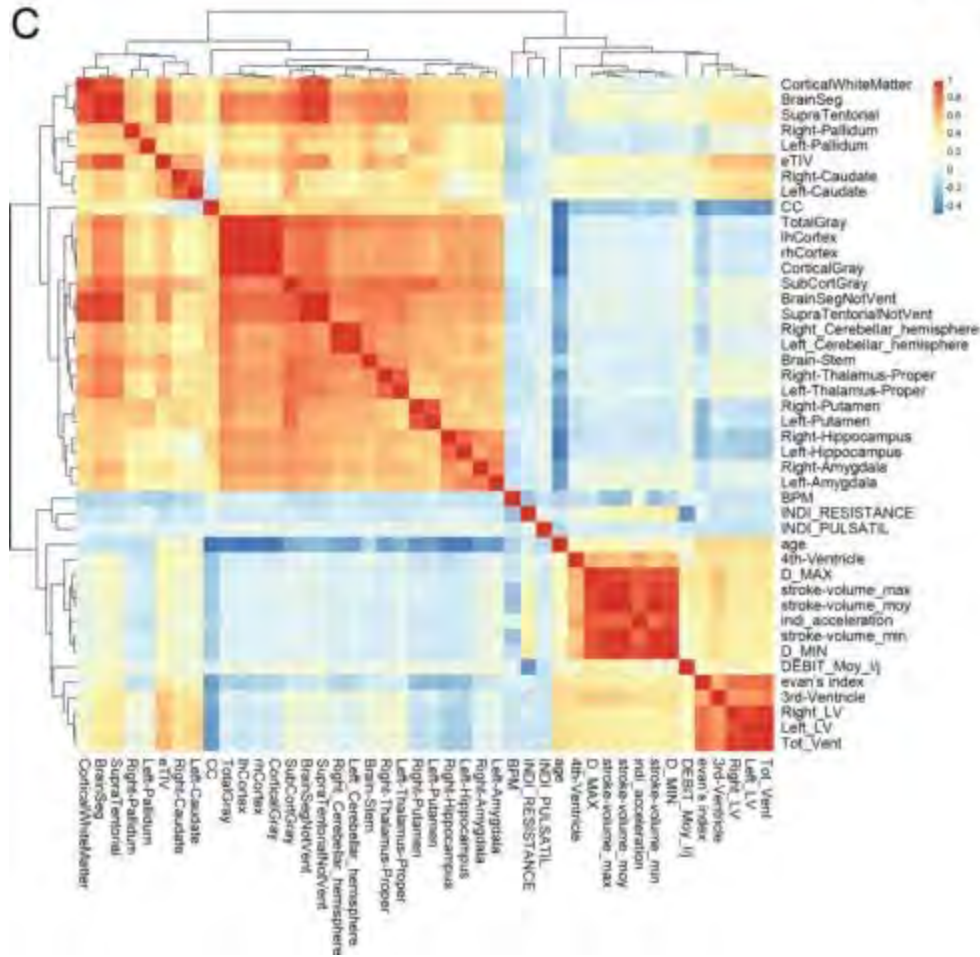
1. Evan's ratio is a poor predictor for the extent of ventricular volume enlargement. 2. Unsupervised clustering of volumetric data provided consistent results to a clinical magnetic resonance imaging (MRI) classification scheme. 3. Cross correlation tables are presented from the results of volumetric analysis and phase contrast imaging and reveal clusters of associated variables (e.g., there is a high correlation between the volume of 4th ventricle and the maximal flow rate through cerebral aqueduct).

Conclusions

Our study used an unbiased mathematical approach to define relationships between data derived from two MRI methods, phase-contrast CSF flow imaging and volumetrics. These relationships provide important insights of various forms of adult hydrocephalus and require further study.



Symptoms and outcomes of shunting



(Filename: TCT_O-298_asnr.jpg)

Wednesday

9:00AM - 10:00AM

Washington Marriott Wardman Park, Marriott Ballroom

14A-Mini Stroke - Acute Triage

14A-1

9:00AM - 9:30AM

A New Standard for Acute Stroke Therapy

Albers, G.
Stanford University
Palo Alto, CA

14A-2

9:30AM - 10:00AM

Stroke Triage: Patient Selection Beyond the 6 hour Window

Chaudry, M.
Medical University of South Carolina
Charleston, SC

Wednesday

9:00AM - 10:00AM

Washington Marriott Wardman Park, Washington 4/5/6

14B-MR Safety-Updates in 2016

14B-1

9:00AM - 9:15AM

Update on Retained GBCA

McDonald, R.
Mayo Clinic
Rochester, MN

14B-2

9:15AM - 9:30AM

Anthropogenic GBCA and Status of GBCA Expose

Kanal, E.
Univ of Pittsburgh Med Ctr
Pittsburgh, PA

14B-3

9:30AM - 9:45AM

The American Board of MR Safety Standardization

Kanal, E.
Univ of Pittsburgh Med Ctr
Pittsburgh, PA

14B-4

9:45AM - 10:00AM

Questions/Answers and Audience Feedback

Wednesday

9:00AM - 10:00AM

Washington Marriott Wardman Park, Washington 1/2/3

14C-Dementia

14C-1

9:00AM - 9:30AM

Molecular and Functional Imaging Techniques in Preclinical Alzheimer's Disease: Implications for Prevention Trials

Sperling, R.
Brigham and Women's Hospital and Massachusetts General Hospital
Boston, MA

14C-2

9:30AM - 10:00AM

Title: Brain Aging and Biomarkers of Alzheimers Disease

Jack, C.
Mayo Clinic
Rochester, MN

Wednesday

9:00AM - 10:00AM

Washington Marriott Wardman Park, Roosevelt 1-3

**14D-PARALLEL PAPER SESSION: Turbo Talks - Brain Physiology in Practice
O-276**

9:00AM - 9:03AM

**Establishing a New Susceptibility-Age Baseline to Assess Iron Content in Basal
Ganglia and Midbrain Nuclei of Healthy Adults**

K Ghassaban¹, M Liu¹, C Habib¹, E Haacke¹

¹*Wayne State University, Detroit, MI*

Purpose

Non-heme brain iron content generally increases in normal aging (1) and is more pronounced in neurodegenerative diseases. Due to its paramagnetic properties, non-heme iron can be detected by magnetic susceptibility mapping. In this study, we present a new approach aimed to establish a baseline of magnetic susceptibility change as function of age in subcortical gray matter structures.

Materials and Methods

Seven basal ganglia and midbrain nuclei, including the caudate nucleus, globus pallidus, putamen, thalamus, pulvinar thalamus, substantia nigra, and red nucleus have been assessed in 175 healthy subjects (89 males/86 females, age range 20-69) using magnetic resonance imaging (MRI). Multislice regions of interest have been manually traced (Fig. 1) on quantitative susceptibility maps (QSM) (2), reconstructed by SPIN software (Detroit, MI). Mean susceptibility in each structure was evaluated as a function of age, also known as global analysis. The upper bound of 95% prediction interval in global analysis then was used to determine age-related thresholds defining high iron content region (RII); for each structure, any pixel value higher than the specified threshold was considered as RII. Susceptibility-age correlation also was analyzed in RII region for each structure (known as regional analysis).

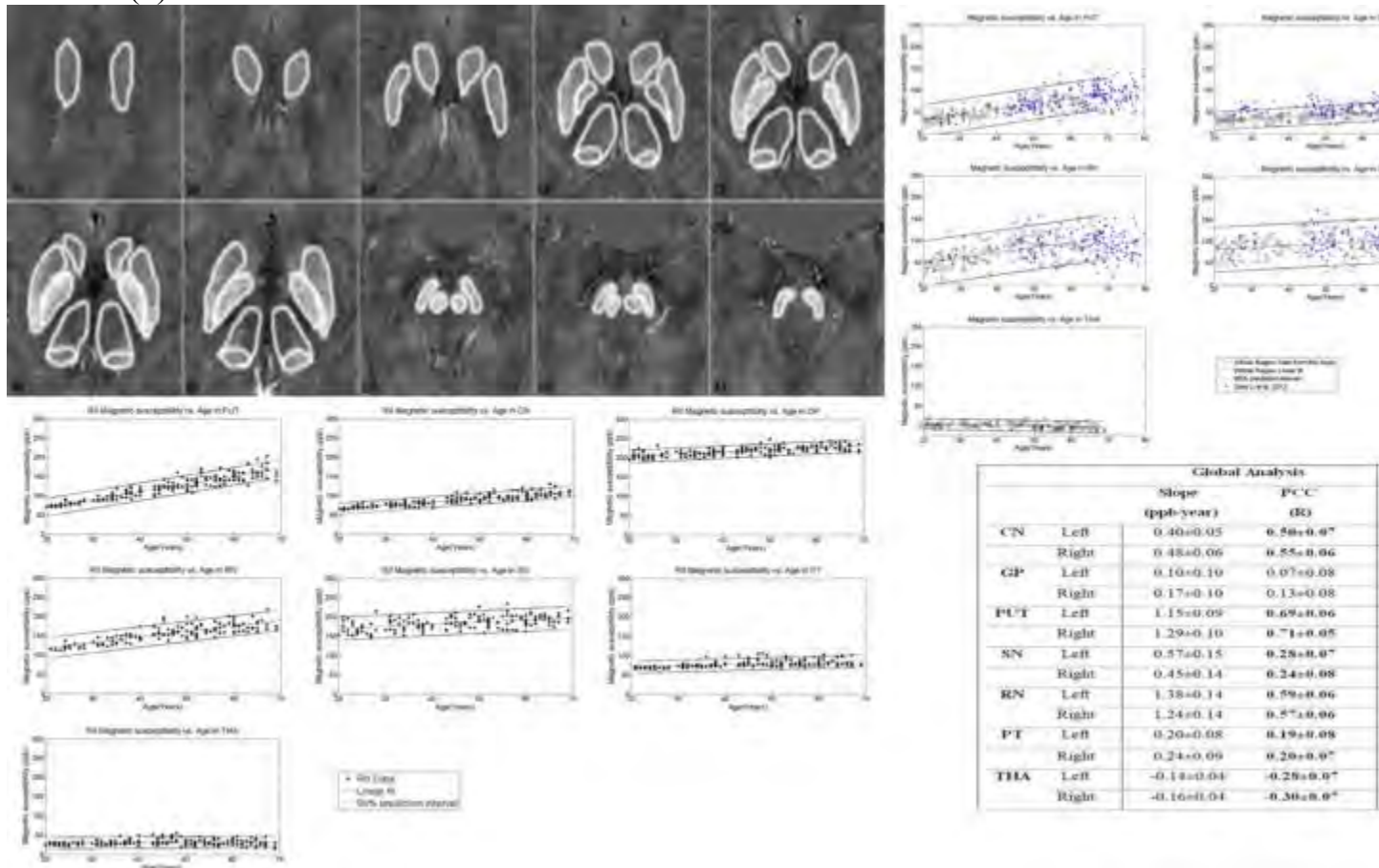
Results

The global analysis showed linear increasing trend in mean susceptibility as a function of age in most of the structures, which is in agreement with the current literature (3) (Fig. 2. Right hemispheres). Linear ascending susceptibility-age correlations also were

seen in regional analysis, even in globus pallidus whose iron content is believed to have no relationship with age (Fig. 3. Right hemispheres). However, these linear trends in RII appeared to be much tighter (higher PCC value) with slopes almost double those in global analysis (Table 1).

Conclusions

Regional analysis has been shown to provide a much more sensitive baseline which can be used to assess abnormal high levels of iron content in neurodegenerative diseases (4).



(Filename: TCT_O-276_Fig1_ROIs_Fig2_Global_Fig3_Regional_Fig4_LinearReg.jpg)

O-277

9:03AM - 9:06AM

Sub-mSv Cerebral CT Perfusion Imaging using Prior Image Constrained Compressed Sensing: A Prospective Comparison of Image Quality at Reduced Dose versus Standard Dose Imaging

K Li¹, P Yang², M Cathey¹, J Tang³, H Rowley⁴, P Turski⁵, V Prabhakaran¹, C Strother⁶, G Chen¹

¹University of Wisconsin-Madison, Madison, WI, ²Changhai Hospital, Second Military Medical University, Shanghai, Shanghai, ³GE Healthcare, Waukesha, WI, ⁴Univ. Of Wisconsin, Madison, WI, ⁵Univeristy of Wisconsin, Madison, WI, ⁶University of Wisconsin Madison, Madison, WI

Purpose

A prospective clinical study was conducted to assess whether cerebral CT perfusion (CTP) imaging can be achieved at sub-millisievert (mSv) radiation dose level by using the prior image constrained compressed sensing (PICSS) reconstruction algorithm.

Materials and Methods

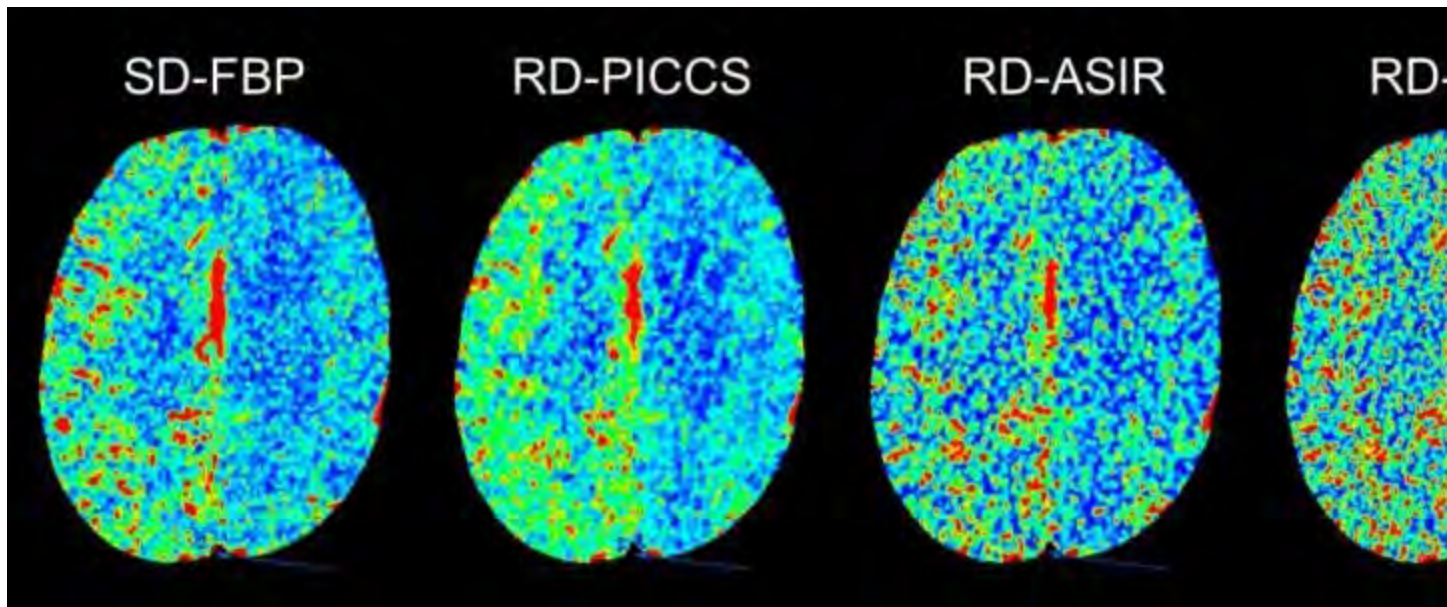
Following standard dose (SD) CTP acquisition, 31 patients (median age, 62 years; 15 M/16 F; median BMI, 27) underwent an additional reduced dose (RD) CTP acquisition at 20% of standard dose level. Three algorithms (PICCS, ASIR, and FBP) were used to reconstruct the CTP source images of the RD series. SD-FBP served as the reference standard. Two clinical observers scored CTP maps using a five-point qualitative scoring system (1: nondiagnostic; 5: excellent), and quantitative noise measurements were performed. Statistical analyses were performed to infer conclusions from qualitative and quantitative assessments.

Results

The CTDIvol and effective dose for the RD series was 44.5 mGy and 0.75 mSv respectively, compared with 222.6 mGy and 3.74 mSv respectively for the SD series. The average image quality scores of the RD-PICCS series were 3.8±0.7 for CBF, 3.5±0.9 for CBV, 3.9±0.9 for MTT. In comparison, subjective image quality scores of SD-FBP were 3.5±0.8 for CBF, 3.5±0.9 for CBV, 3.3±0.8 for MTT. The average noise of RD-PICCS (CBF, 5.8±1.9 mL/100 g/min; CBV, 0.74±0.26 mL/100 g; MTT, 5.5±1.2 s) were lower than those of SD-FBP (CBF, 8.1±2.5 mL/100 g/min; CBV, 0.86±0.28 mL/100 g; MTT, 6.4±1.2 s) with statistical significance ($p < 0.001$). Both subjective scores and objective noise of RD-ASIR and RD-FBP were significantly inferior to those of SD-FBP ($p < 0.001$).

Conclusions

Prior imaging constrained compressed sensing enables sub-mSv cerebral CT perfusion imaging without compromising diagnostic image quality.



(Filename: TCT_O-277_figure.jpg)

O-278

9:06AM - 9:09AM

A Dedicated Cone-Beam CT System for Detection of Acute Intracranial Hemorrhage at the Point of Care

H Dang¹, J Xu¹, A Sisniega¹, W Zbijewski¹, J Stayman¹, X Wang², D Foos², N Aygun¹, V Koliatsos¹, J Siewerdsen¹

¹Johns Hopkins University, Baltimore, MD, ²Carestream Health, Rochester, NY

Purpose

Prompt detection of acute intracranial hemorrhage (ICH) offers potential benefit to diagnosis and management of neuropathology, including traumatic brain injury (TBI) and stroke. Noncontrast-enhanced multidetector CT reliably detects acute ICH but requires patient transport to a radiology suite, increasing time and risk of adverse events. This work reports development of a dedicated cone-beam CT (CBCT) system offering a level of image quality sufficient for detection of ICH in a mobile form consistent with point-of-care application in, for example, the neuro intensive care unit (ICU).

Materials and Methods

The system was designed according to task-based image quality models for optimal performance in ICH detection at 10-25 mGy dose. Image artifacts are diminished using software corrections of x-ray scatter (via GPU-accelerated Monte Carlo scatter simulation), beam hardening, veiling glare, and detector lag. Furthermore, an iterative model-based reconstruction (MBR) method was developed to improve image quality

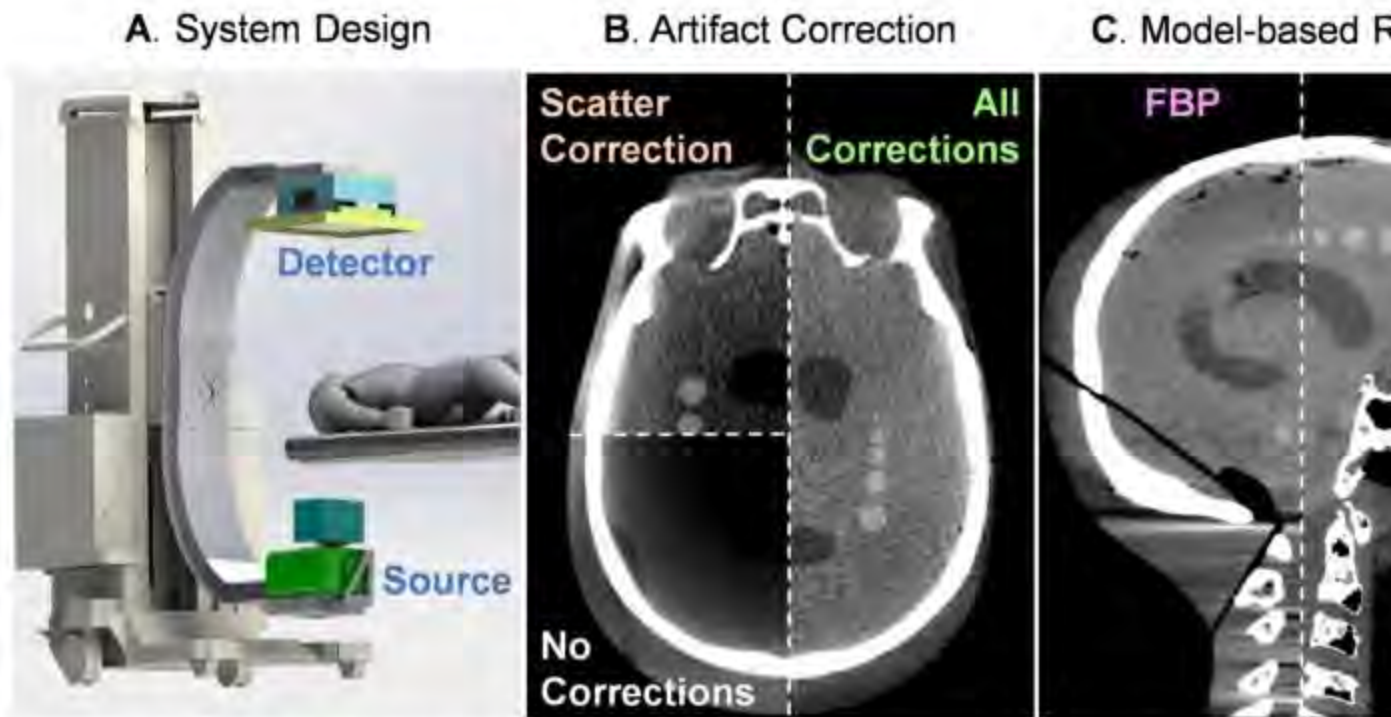
at reduced dose. Performance was evaluated in CBCT phantom and cadaver studies simulating ICH (50 HU contrast, 1.5-12 mm diameter).

Results

The system design guided development of a prototype with system configuration including a rotating anode x-ray source with 15 kW power and 0.6 focal spot size and 43 cm × 43 cm flat-panel detector at source-detector distance of 1000 mm and magnification 1.8. Cupping artifacts were strongly reduced by scatter correction, and blooming and streak artifacts were mitigated by beam-hardening, glare, and lag corrections. The resulting images demonstrated major reduction in artifacts that conventionally plague CBCT, yielding uniformity ~10 HU across the image, including regions adjacent to the cranium, where artifacts can impede detection of epidural hemorrhage. Studies with simulated ICH indicated reliable detection of fresh blood lesions as small as 3 mm diameter using the artifact correction framework combined with MBR algorithm. Cone-beam artifacts also were strongly reduced in MBR images, particularly about the skull base and cervical vertebrae.

Conclusions

A dedicated CBCT system has been designed and a clinical prototype suitable for clinical studies has been realized. Initial studies indicate image quality characteristics beyond conventional limitations of CBCT and are consistent with reliable detection of millimeter-scale acute ICH. These findings support and motivate investigation of feasibility and performance in point of care applications for imaging TBI and stroke, with clinical studies in the neuro ICU now underway.



(A) CAD rendering of the dedicated CBCT scanner prototype, which was designed using task-based image quality models for optimal performance in ICH detection. (B) Simulated ICH demonstrate strong reduction of cupping artifacts by scatter correction, mitigation of blooming and streak artifacts by beam-hardening, glare, and lag correction. (C) Model-based reconstruction (MBR) substantially reduced noise while preserving spatial resolution and strongly reduced cone-beam artifacts, compared to filtered back projection (FBP). The results indicated reliable detection of fresh blood lesions as small as 2 mm using the proposed CBCT imaging technique. These findings support and motivate the feasibility and performance in point of care applications for imaging TBI and are currently being tested in clinical studies in the neuro ICU underway.

(Filename: TCT_O-278_HeadScanner2_crop.JPG)

O-279

9:09AM - 9:12AM

Displacement Encoding with Stimulated Echoes (DENSE) MRI for Noninvasive Assessment of Intracranial Pressure Status

A Saindane¹, J Holbrook¹, D Qiu¹, J Oshinski¹, B Bruce¹, V Biousse¹, N Newman¹, T Lancaster², B Dale³, X Zhong⁴

¹Emory University, Atlanta, GA, ²Emory University School of Medicine, Atlanta, GA, ³MR R&D Collaborations, Siemens Healthcare, Morrisville, NC, ⁴MR R&D Collaborations, Siemens Healthcare, Atlanta, GA

Purpose

Intracranial pressure (ICP) is estimated invasively using lumbar puncture (LP) with cerebrospinal fluid (CSF) opening pressure (OP) measurement. Displacement encoding with stimulated echoes (DENSE) is a magnetic resonance imaging (MRI) technique sensitive to brain motion as low as 0.01 mm. This study utilized DENSE to measure brain displacements in patients with high OP before LP (Pre-LP), after a reduced closing pressure (CP) following LP and CSF removal (Post-LP), and in healthy controls.

Materials and Methods

Seven patients with suspected elevated ICP and nine healthy controls were included in this IRB-approved study. Patients and controls underwent 3T MRI (Tim Trio, Siemens, Erlangen, Germany) in the supine position with peripheral pulse unit gated segmented EPI cine DENSE sequence through the mid-sagittal brain with the following image parameters: displacement encoding frequency $k_e=1.5$ cycle/mm, through-plane dephasing frequency $k_d=0.08$ cycle/mm, TE=8.9-10.4 ms, TR=55-59 ms, EPI factor=8, segments=16, pixel size= 1.2×1.2 mm², slice thickness=7 mm, averages=4, frames=13-16. Motion was measured in the foot-to-head and anterior-to-posterior directions in separate acquisition and combined in postprocessing to create a displacement magnitude. . Patients with suspected elevated ICP underwent standardized protocol of DENSE, LP with OP (within 30 minutes of DENSE), post-CSF removal CP measurement, then repeat DENSE (within 30 minutes of CP). Phase-reconstructed images were processed offline and regions of interest were placed in various brain structures. Patient data were analyzed first with an analysis of covariance (ANCOVA) to determine any effects of brain regions and pressure. To determine treatment effects, control and patient data collectively underwent analysis of variance (ANOVA) to determine the main effects of clinical status and brain regions, where clinical status was pre-LP, post-LP, or control status.

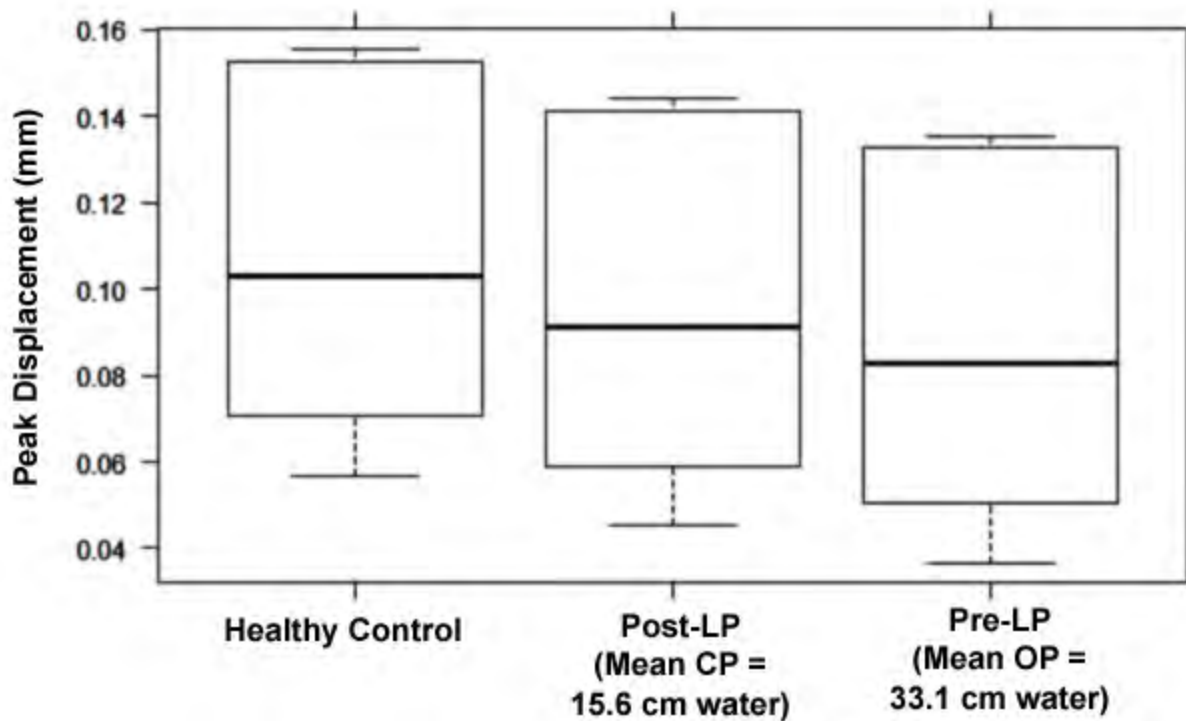
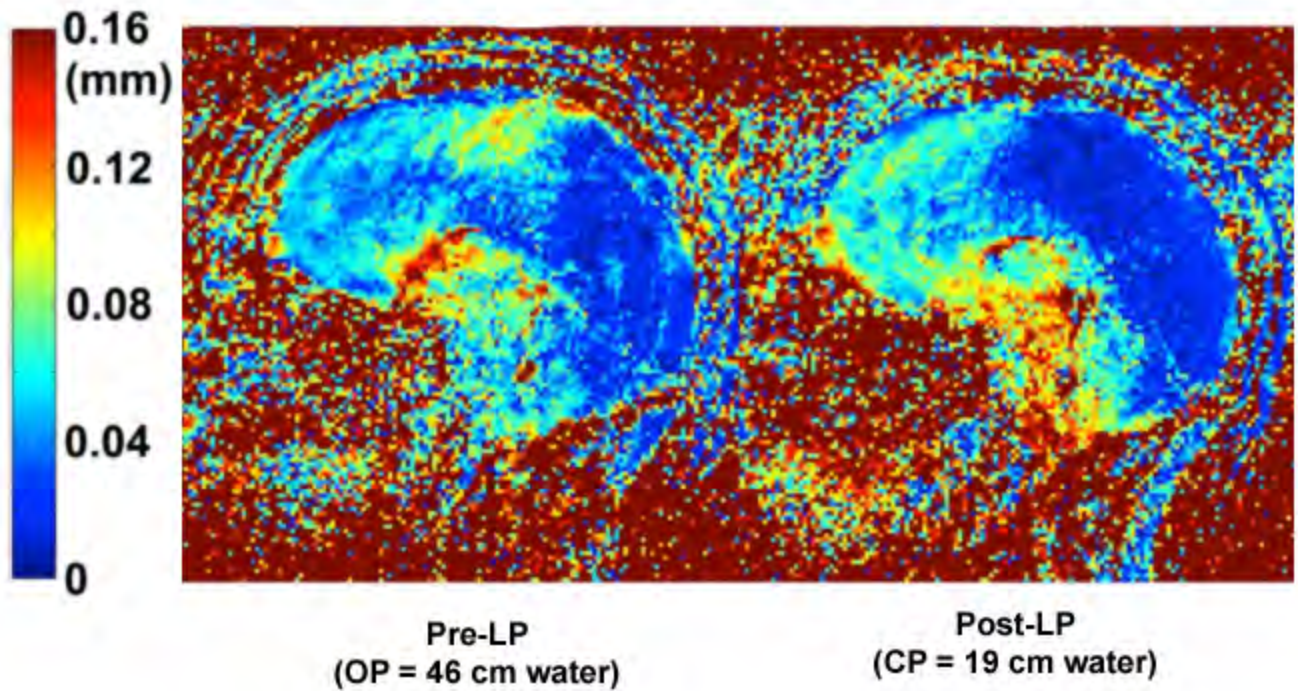
Results

All seven patients with suspected elevated ICP had elevated OP (mean 33.1 cm water) that was decreased by removal of cerebrospinal fluid (CSF) to mean CP of 15.6 cm water. Patients and controls demonstrated no intracranial abnormalities on MRI. For brain displacement in patients, measured pressure had a marginally significant ($p=0.0141$) effect with every unit decrease in pressure leading to 2.22×10^{-4} mm increase in brain displacement. For collective control and patient data, clinical status ($p=0.0021$) had significant effects on brain displacement; controls had significantly larger peak displacements than the Pre-LP group. Post-LP patients had intermediate displacements not significantly different from either control or Pre-LP groups. Please

refer to the figure for representative change in brain displacement from reduction of pressure in a patient, and for effects of clinical status on brain displacement.

Conclusions

This study establishes a relationship between peak brain displacement from DENSE MRI and measured pressure obtained contemporaneously by LP, providing a potential method for noninvasively assessing ICP status.



(Filename: TCT_O-279_Figure.jpg)

O-280

9:12AM - 9:15AM

Towards quantification of hemodynamic parameters in saline perfusion MRI

a mian¹, C Farris¹, O Sakai², H Jara¹

¹*Boston University/Boston Medical Center, Boston, MA*, ²*Boston Medical Center, Boston University School of Medicine, Boston, MA*

Purpose

Gadolinium-based contrast agents can have risks including nephrogenic systemic fibrosis, allergic reactions and limitation of use during pregnancy. Recent literature also has suggested gadolinium deposition in neural tissue in patients with normal renal function. Normal saline (NS) is a nontoxic sodium chloride water solution that can significantly alter the MR relaxation properties of blood by hemodilution. Saline perfusion magnetic resonance imaging (MRI) is novel approach to perfusion MRI which is much safer than currently used contrast agents. The purpose of this study is to develop tools for hemodynamic quantification parameters.

Materials and Methods

This HIPAA compliant prospective study was approved by the IRB of our hospital. Magnetic resonance imaging was performed at 1.5T (Achieva, Philips Healthcare): head array and body coil for RX/TX. Ten patients were scanned with a dynamic inversion recovery turbo spin echo sequence. The IR-TSE pulse sequence was run during and after the NS injection for up to 5min: 100cc of NS were power injected via antecubital veins at 3-4cc/s. Images were processed with Mathcad (2001i, PTC, Needham, MA) algorithms to map maximum enhancement (maxENH), area under the curve (AUC), time-to-peak (TTP), and mean-transit-time (MTT). We further refined the software to generate quantitative maps proportional to cerebral blood volume (CBV), cerebral blood flow (CBF) and MTT.

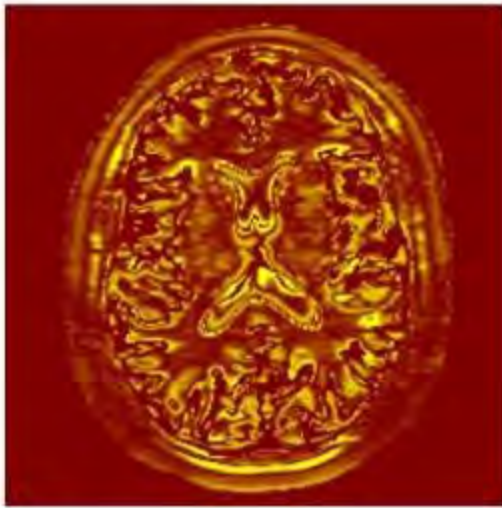
Results

Normal saline injection-related enhancement effects were observed in all patients, particularly in highly vascular intra and extracranial tissues. Maps of CBV, CBF and MTT are shown in Figure 1 demonstrating different MR perfusion parameters for brain. All recruited patients completed the NS injection plus the dynamic-IR-MRI scan without any adverse effects, or expressing discomfort.

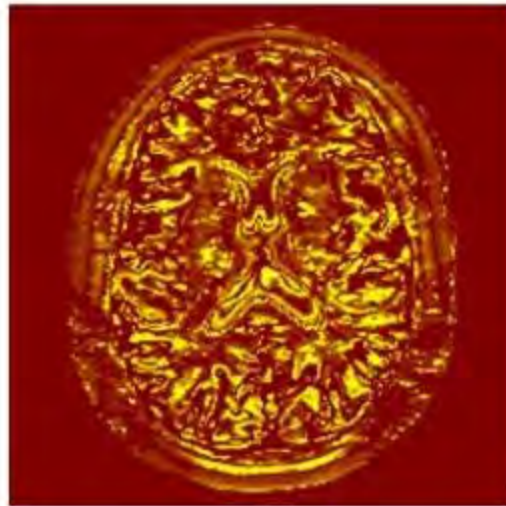
Conclusions

Preliminary maps of CBV and CBF have been generated using NS as an intravascular contrast agent. This work would have implications for validating saline as a perfusion contrast agent in the brain.

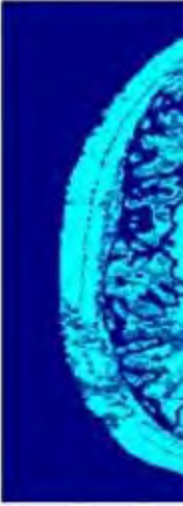
Figure 1.



rCBV



rCBF



$$rCBF = \frac{rCBV}{MTT}$$

(Filename: TCT_O-280_Fig1asnr.jpg)

O-281

9:15AM - 9:18AM

Diffusion Corrected Aneurysm Wall Permeability Correlates with Rupture Risk

C Cantrell¹, P Vakil², S Ansari³, T Carroll¹

¹northwestern university, Chicago, IL, ²University of Illinois Chicago, Chicago, IL, ³Northwestern, Chicago, IL

Purpose

Intracranial aneurysms (IA) affect 2-6% of the population (1). Rupture carries a mortality rate of 50% and devastates the lives of many otherwise healthy people. Unruptured IAs often are discovered incidentally and given the inherent risks

associated with surgical clipping or coiling, treatment remains controversial. The purpose of this study was to quantify IA wall permeability (k_{trans} , v_L) using a diffusion corrected Tofts' model (2). While previous work has shown k_{trans} to be associated with wall thinning and IA rupture risk, as defined by various anatomical, imaging and clinical risk factors, it employed a Tofts' based permeability model (3). For aneurysmal modelling, a diffusion model (4) more accurately represents physiology and provides better resolution of wall thickness and bleb formation zones.

Materials and Methods

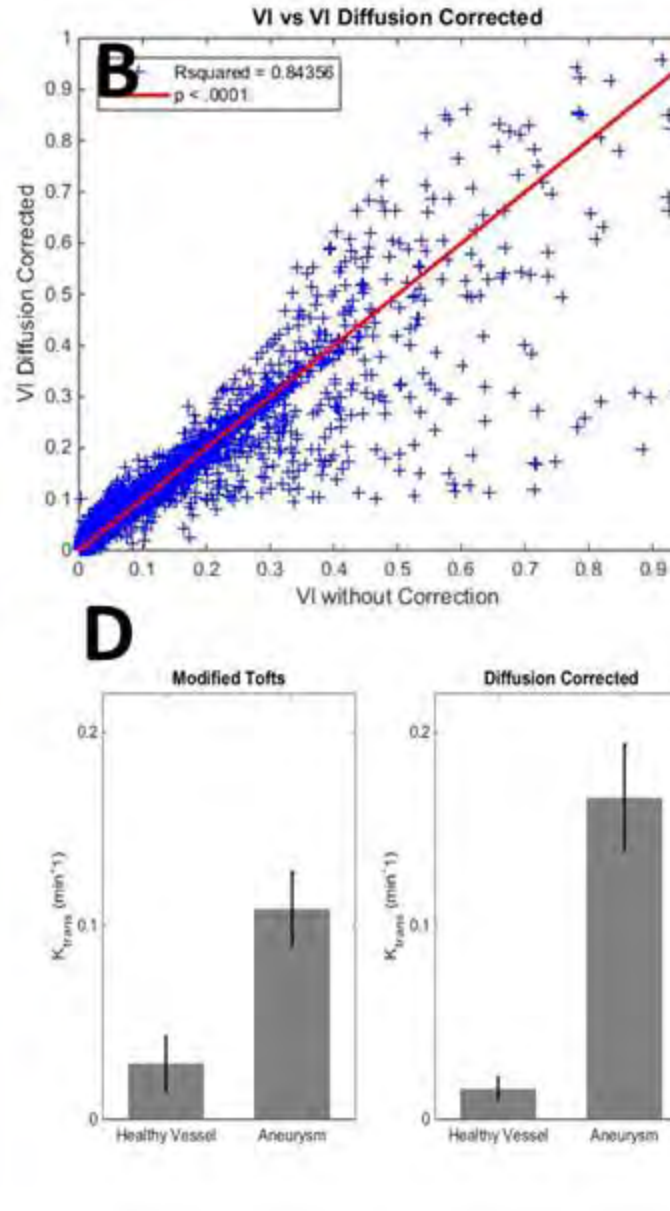
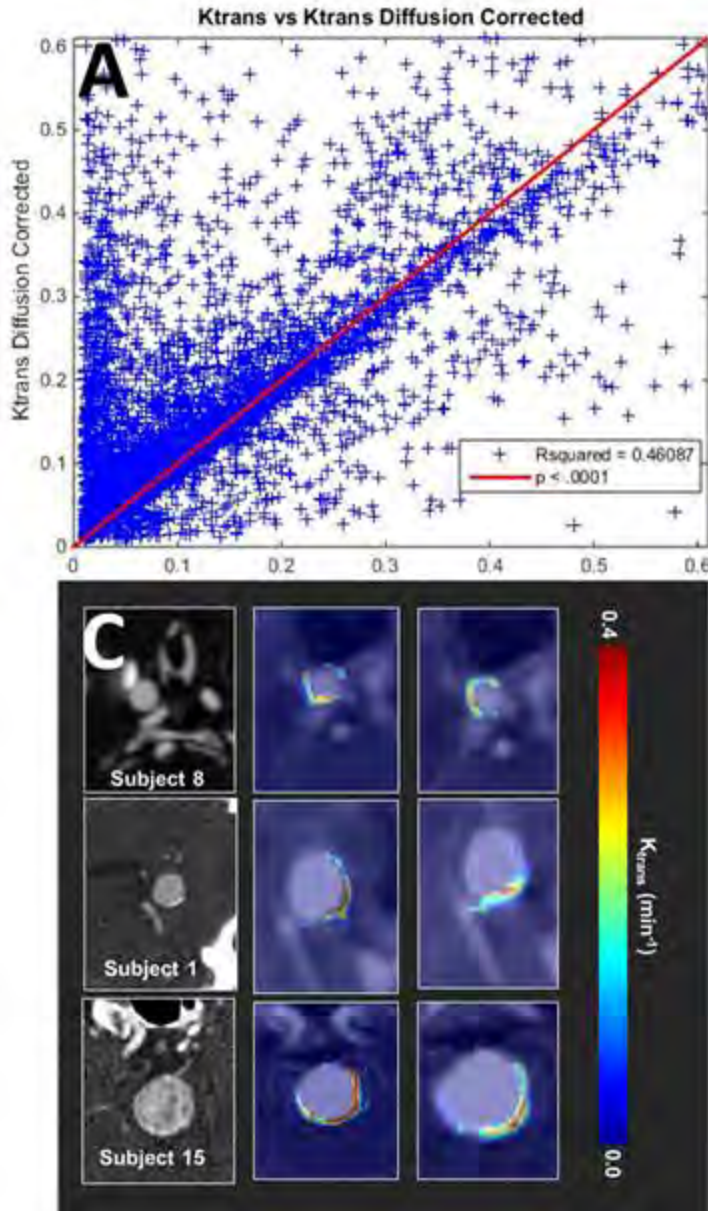
We employ a finite element model (FEM), to quantify leakage and compare to more traditional Tofts modeling. The FEM model improves on the Tofts model by allowing contrast to flow from regions of high concentration towards low concentrations. k_{trans} and v_L were evaluated as markers of rupture risk by comparing against established clinical (symptomatic lesions) and anatomical (size, location, morphology, multiplicity) risk metrics and evaluated against values obtained through the Tofts' Model. One patient opted out of surgical intervention and was imaged 18 months after initial evaluation. Twenty-seven symptomatic, unruptured IAs in 23 patients (M/F, 10/13, = 60.7 ± 12.3) were imaged with dynamic contrast-enhanced magnetic resonance imaging (DCE-MRI), and wall permeability parameters (k_{trans} , v_L) were calculated in regions adjacent to the aneurysm wall. k_{trans} and v_L were calculated using both a Tofts' permeability model as described in (2) and a finite-element diffusion model. Correlation and mean values were compared to test the hypothesis that FEM analysis corrects for parenchymal diffusion of the contrast agent.

Results

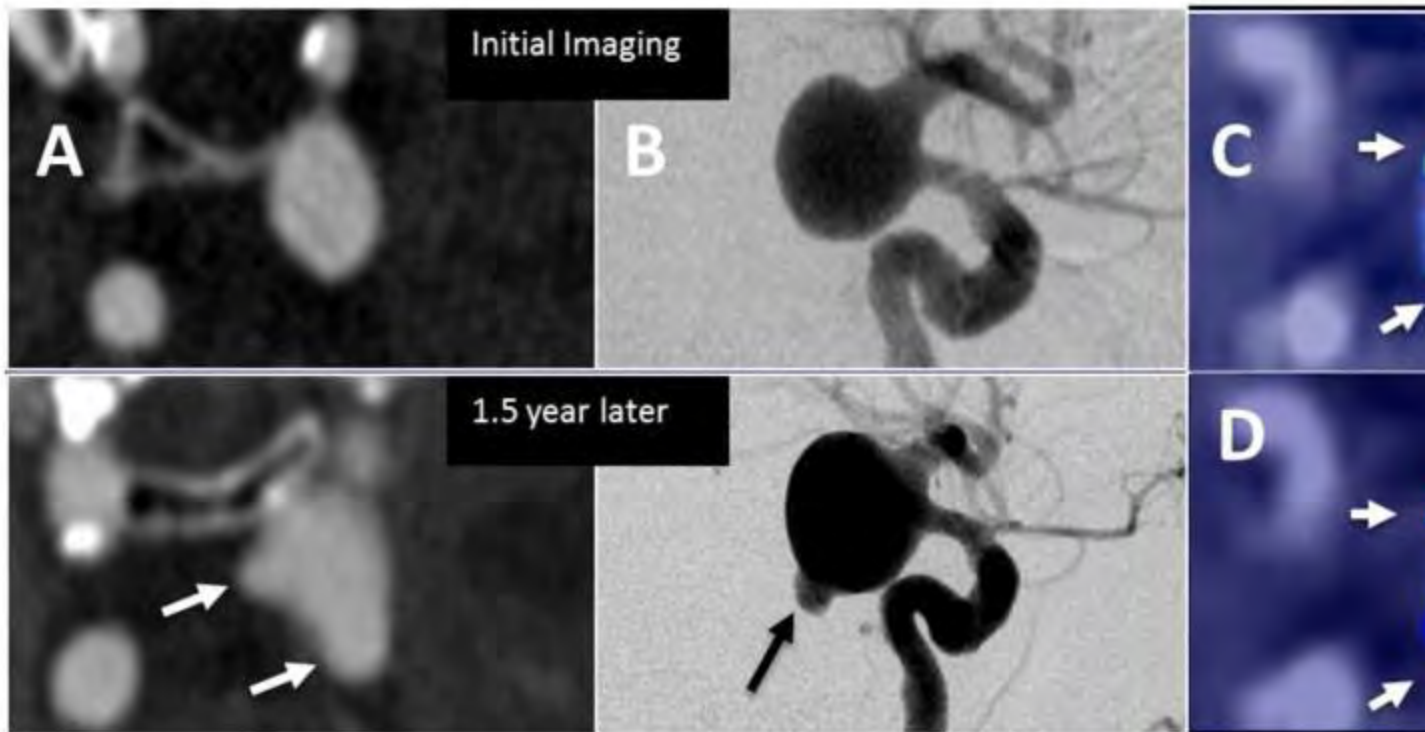
All IAs had a pronounced increase in wall permeability compared to the paired healthy MCA ($p < 0.001$). Regression analysis demonstrated a significant trend toward increased k_{trans} with increasing aneurysm size ($p < 0.05$). Diffusion corrected k_{trans} and v_L values correlate strongly with the Tofts' Model ($p < .001$) (Fig. 1a-b). Diffusion corrected values showed greater permeability distinction between aneurysm wall and healthy vessel ($p < .001$) (Fig. 1d).

Conclusions

We found contrast agent permeability across the aneurysm wall correlated significantly with both aneurysm size as well as size-independent anatomical risk factors. Moreover, we note the diffusion correction shows greater distinction between permeable regions (i.e., leaky aneurysmal wall) and healthy tissue which can be seen in Figure (1d). Additionally we see, in Figure (1a-c), distinct regions of faster leakage even within a single aneurysm. Intuitively this makes sense, as we know physiologically aneurysms can be nonuniform. Figure 2 shows a 61-year-old male who decided to forgo surgical intervention. For this anecdotal case, both methods provided similar results that lined up exceptionally well with future bleb formation.



(Filename: TCT_O-281_Diffusion1.jpg)



(Filename: TCT_O-281_Diffusion2.jpg)

O-282

9:18AM - 9:21AM

Relationship of Brain Temperature and Cerebrovascular Reserve in Patients with Chronic Steno-Occlusive Disease

S Dehkharghani¹, C Fleischer², D Qiu², S Park³, J Wu², F Nahab²

¹Emory University Hosp, Atlanta, GA, ²Emory University, Atlanta, GA, ³Georgia Institute of Technology, Atlanta, GA

Purpose

To demonstrate the utility of magnetic resonance imaging (MRI) and noninvasive brain thermometry in patients with chronic steno-occlusive disease to characterize the relationship between brain temperature and cerebrovascular reserve (CVR).

Materials and Methods

Six patients underwent a two-day MRI scan protocol on a Siemens Magnetom Trio 3.0 T clinical scanner with acetazolamide (ACZ) challenge (1 g slow IV infusion over 3-5 minutes). Arterial spin labeling (ASL) and blood oxygen level-dependent imaging (BOLD) scans were acquired pre- and post-ACZ as previously reported (1). MR spectroscopic imaging-based thermometry scans were acquired with the semiLASER sequence (2) (TR=1700; TE=35 ms; averages=3; 10x10x15 mm³ voxels; 8x8 voxel region of interest) and processed using LCMoel (3) and custom software written in

Matlab (Mathworks). Voxel-wise relationships between CVR calculated from ASL and BOLD scans and temperature difference (post-ACZ – pre-ACZ, ΔT) were determined with least squares regression analysis.

Results

A representative ΔT map is shown in Figure 1. Significant global voxel-wise correlations were observed between ΔT and ASL CVR ($r = 0.30$, $p < .001$). Significant correlations were observed between ΔT and ASL CVR ($r = 0.39$, $p < .001$) and BOLD CVR ($r = 0.39$, $p < .001$) for ipsilateral voxels and between ΔT and ASL CVR ($r = 0.38$, $p < .001$) and BOLD CVR ($r = 0.21$, $p = .03$) for contralateral voxels. Interestingly, the ipsilateral relationship between ΔT and ASL CVR was quadratic while the contralateral relationship for the same parameters was linear suggesting disparate mechanisms relating perfusion and temperature in normal versus impaired tissues.

Conclusions

We report the first use of MRI and brain thermometry to correlate CVR with a dynamic temperature response. These findings suggest that brain temperature is a potential biomarker in patients with chronic steno-occlusive disease and compel further studies exploring the intersection of blood flow, cerebral metabolism, and brain temperature.

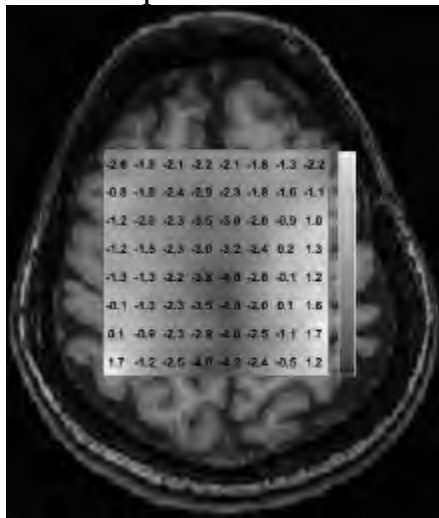


Figure 1. Representative brain ΔT map. Color bar ranges from -5 to 2 °C. Image is displayed in the radiological convention.

(Filename: TCT_O-282_Fig1_withcaption_300ppi.jpg)

O-283

9:21AM - 9:24AM

3D Printing of Diffusion Tensor Tractography: Brave New World of Educational and Surgical Models.

E Quigley¹, R Lobo¹, J Cramer¹, t hutchins², U Rassner¹, L Shah³

¹University of Utah, Salt Lake City, UT, ²University of Utah, Salt lake city, UT, ³University Of Utah, Salt Lake City, UT

Purpose

To demonstrate the utility, feasibility, and application of 3D printing techniques to diffusion tensor imaging (DTI) derived tractography data.

Materials and Methods

Using open source and commercially available software packages (Trackvis, Massachusetts General Hospital, Boston, Mimics 3-Matics, Materialise, Plymouth MI), multidirectional DTI data sets are converted to tractography splines. Subsequently, these spline coordinates were converted to representative 3D volumetric models. These 3D models then are used to create physical models of the white matter tracts. These can be printed in a variety of materials and colors with various transparency of superficial and deep brain anatomy. Selected normal anatomy, anatomical variant, pathologic cases, and high resolution tractography libraries were utilized.

Results

3D models of DTI tractography data can be generated to create useful teaching models. These can add to the demonstration of normal anatomy, anatomical variants such as callosal agenesis, pathologic states such as corticospinal tract displacement by tumor, and models for demonstrating brain connectivity. These can be employed for resident and fellow education, consultant use, patient education, and surgical planning.

Conclusions

Conventionally, diffusion tensor imaging data has been used to extract mathematical splines to represent white matter pathways. We demonstrate that these diffusion tensor representations can be converted to 3D printable models. These models can be used to demonstrate normal anatomy, show white matter variation in anatomical variants, portray displacement or disruption of white matter pathways in pathological states, and generate tangible teaching models. These models provide a novel modality for trainee, consultant, patient education and surgical planning.

O-284

9:24AM - 9:27AM

Opening the Blood-Brain Barrier via Transcranial Sonication Using a Clinical Body MR-guided Focused Ultrasound System

R Airan¹, N Ellens¹, A Partanen², K Farahani³

¹Johns Hopkins Medical Institutions, Baltimore, MD, ²Johns Hopkins Medical Institutions, Philips Healthcare, Baltimore, MD, ³Johns Hopkins Medical Institutions, NCI/NIH, Baltimore, MD

Purpose

Blood-brain barrier (BBB) opening via magnetic resonance (MR)-guided focused ultrasound (MRgFUS) has gained recent attention for its promise to enable therapeutic agent delivery to the brain for devastating diseases such as gliomas and Alzheimer disease (1). A tacit assumption is that for all intracranial focused ultrasound applications, a 'neuro' focused ultrasound transducer is necessary. However, for practical reasons, an institution may only have access to a 'body' system designed for abdominal, pelvic, and extremity applications. We sought to build on our prior simulations (2) and use a clinically relevant model to experimentally demonstrate that a body MRgFUS system may be used for transcranial low power/duty cycle applications, like BBB opening.

Materials and Methods

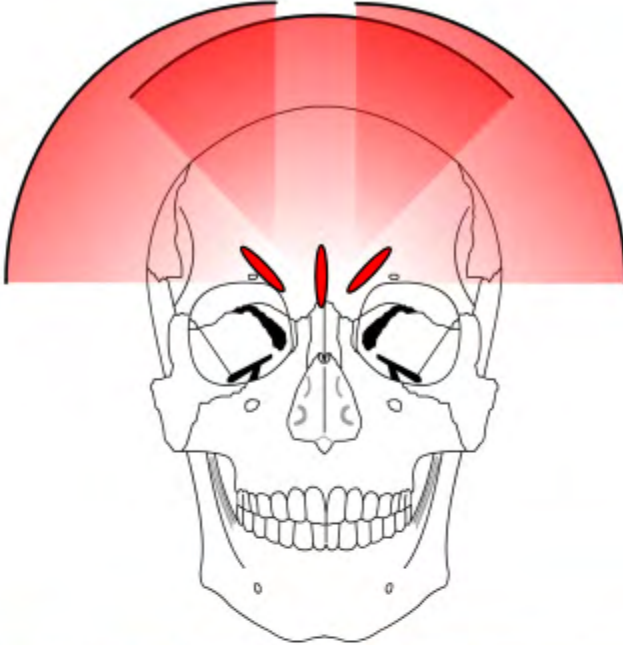
A degassed dorsal human cranium was mounted in degassed water over a clinical body MRgFUS transducer (256 elements, operated at 1 MHz; Sonalleve V2, Philips Healthcare, Vantaa, Finland). A lipstick hydrophone (Onda Corp., Sunnyvale, CA) mounted to a 3D moveable stage made measurements both in free water and transcranially in three orientations at 3-4 depths each; Figure top left and right. 40-cycle sonications at 1 MHz were applied at acoustic powers of 5-20 W in free water, and 20-500 W transcranial. The 3D full-width at half-maximum (FWHM) and the peak negative pressure were measured. The hydrophone was replaced with a living rat (n=3) with dorsal scalp depilated, positioned supine, and under isoflurane anesthesia; Figure bottom left. After planning T2-W MRI (Philips Achieva 3T), microbubbles (0.02 mL/kg, Definity, Lantheus Medical, N. Billerica, MA) were injected via a 24g tail-vein catheter. Simultaneously, 10 ms ultrasound pulses were applied at 1 Hz pulse repetition frequency for 120 s. The acoustic power was chosen to generate an estimated in situ pressure of 0.44-0.60 MPa, based on the prior hydrophone results. Contrast (0.2 mL/kg; Magnevist, Bayer, Pittsburgh, PA) then was injected and T1-W MRI was performed. Animals then were sacrificed and their scalps were examined for signs of external damage.

Results

The ultrasound pressure attenuation ranged -5.8-9.3 dB. The axial FWHM ranged 1.83-3.79 mm. Maximal attenuation occurred with a dorsal midline approach as the beam passed through sutures. Angled, parietal approaches demonstrated less attenuation for most targets. Generally, the insertion loss decreased as the focus was moved away from the skull surface. Postcontrast T1-W MRI indicated successful BBB opening; Figure bottom right. The region of BBB opening did not appear to be shifted from the desired target. For higher estimated in situ pressures (>0.55 MPa), the disruption region was larger and less uniform; left of Figure bottom right. Even without refocusing, the targeting precision appeared adequate. There was no physical or imaging evidence of damage to suggest supra-therapeutic or off-target sonication.

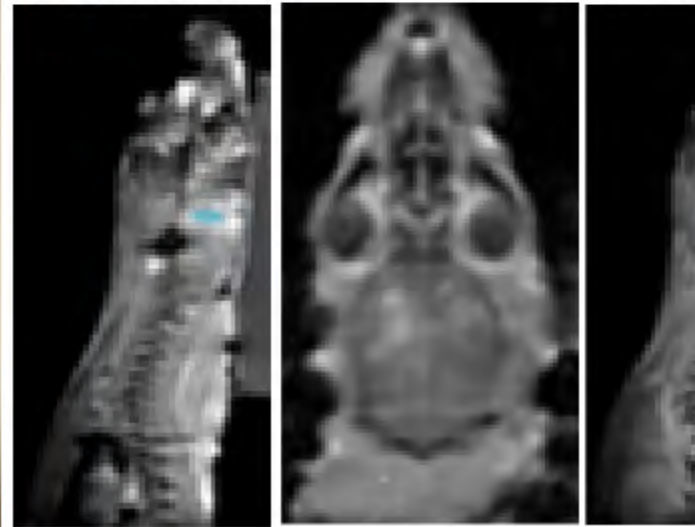
Conclusions

Transcranial, low power/duty cycle MRgFUS applications, such as BBB opening and neuromodulation, can be accomplished with a clinical body MRgFUS system, in agreement with our prior simulation results (2).



0.58 MPa

0.44



Blue oval outlines the desired

(Filename: TCT_O-284_Airan_tcBBB_ASNR2016.jpg)

O-285

9:27AM - 9:30AM

Targeted Release of Anesthetic Agents with Focused Ultrasound

R Airan¹, R Meyer¹, N Ellens¹, K Farahani², J Green¹

¹*Johns Hopkins Medical Institutions, Baltimore, MD*, ²*Johns Hopkins Medical Institutions, NCI/NIH, Baltimore, MD*

Purpose

Pre-operative localization of functional brain regions would ideally involve safe and reversible application of a neuromodulatory agent to a spatially compact brain target that is defined by image guidance. We believe that we can accomplish this with a nanoparticle system that allows release of a drug cargo upon application of focused ultrasound (FUS). This technology would capitalize on the recent successes of magnetic resonance (MR)-guided FUS (MRgFUS), which has received much recent attention for its successful use in clinical deep-brain target ablation for essential tremor (1) and more recently for a clinical blood-brain barrier opening (2). As a first implementation, we have made such a nanoparticle system that allows focused ultrasound mediated targeted release of the small molecule anesthetic agent propofol.

Materials and Methods

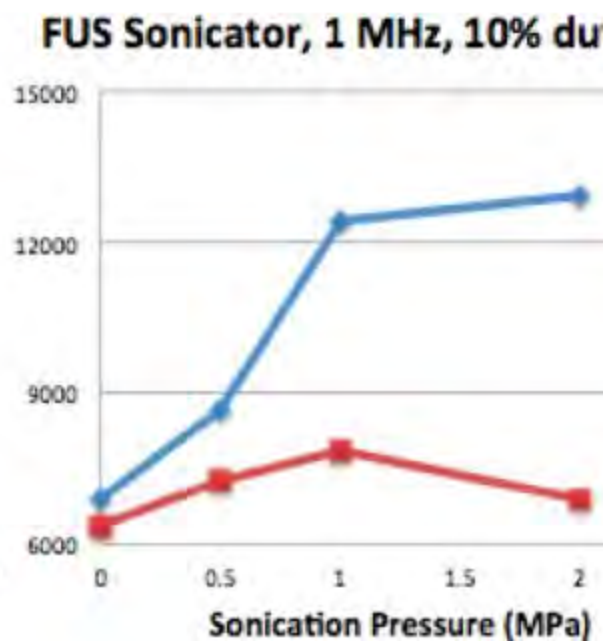
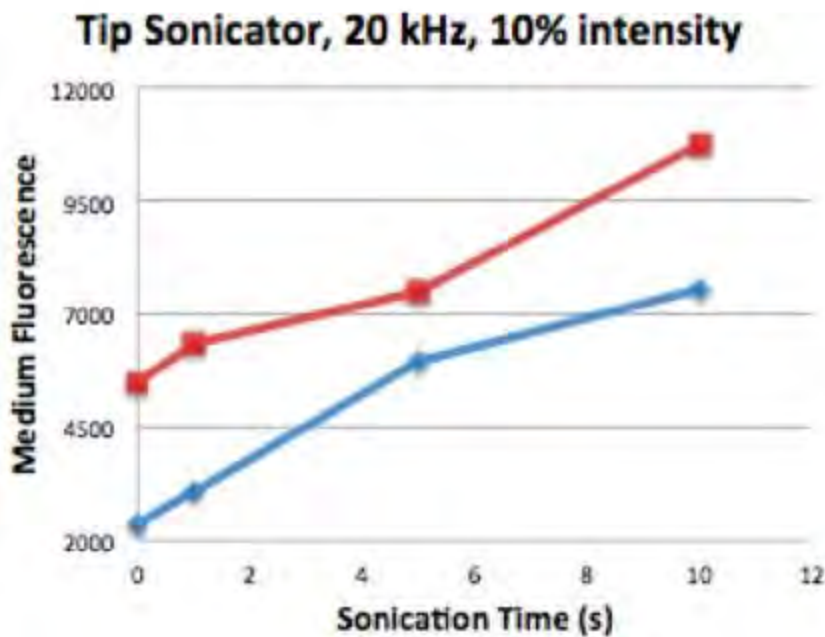
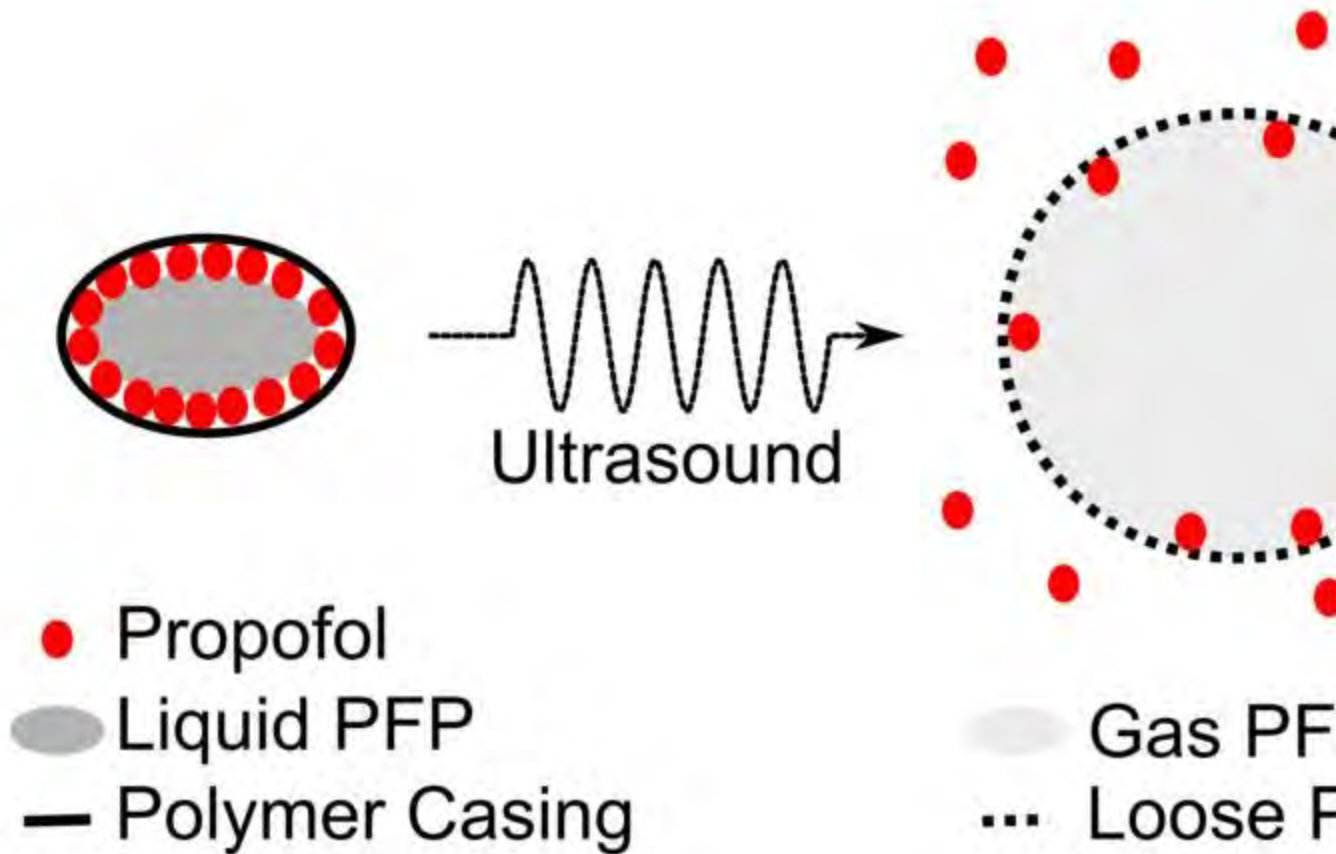
We modified prior described protocols for perfluorocarbon nanoemulsion preparations (3). Micelles of polymer (50 mg; PEGylated poly-caprolactone, PEG-PCL, or PEGylated poly-L-lactide, PEG-PLLA) and propofol (5 mg) were made by dissolving each into 1 mL of anhydrous tetrahydrofuran (THF), then mixing in 1 mL of PBS, and then vacuum evaporation of the THF. Micelles then were diluted 1:5 and perfluoropentane (PFP) was added to a net 1:4 polymer:PFP ratio. The mixture then was placed into a cup sonicator and sonicated at 60% amplitude until the PFP was visibly emulsified, up to 60 sec. The resultant mixture then was washed twice in hexane to remove free propofol. Resultant particle size was assessed. To test particle release capability, the particles were sonicated using a tip sonicator (20 kHz) continuously for 0, 1, 5, or 10 sec; or, using a focused ultrasound transducer (1 MHz) using 10 ms pulses every 1 sec for up to 2 min and nominal in situ pressures of 0, 0.5, 1, or 2 MPa. Released propofol was extracted with hexane and quantified using UV fluorescence at 280 ex/310 em.

Results

Particle diameter was 300-400 nm. Upon sonication particles are expected to undergo a phase transition, which increases their diameter 5-6x thereby inducing drug release (3) (Figure, top). This yields a maximal particle diameter after release of 2.4 μm , suggesting the particles are safe for intravascular applications, with no significant risk of embolization. Sonication at both 20 kHz and 1 MHz was sufficient to induce release of free propofol, with a dose response found with either total sonication time or sonication pressure (Figure, bottom). PCL-based particles had more robust and reliable release than PLLA-based particles.

Conclusions

We have developed a nanoparticle drug delivery system that permits release of drug upon application of focused ultrasound in a sonication dose dependent manner. The individual components of the particles are each FDA-approved for clinical use. When combined with existent clinical MR-guided focused ultrasound systems, this technology may enable image-guided, targeted, safe, and focal delivery of anesthetics to the brain, potentially enabling noninvasive focal neuromodulation of an awake patient. We currently are evaluating the in vivo potential of this technology.



(Filename: TCT_O-285_Airan_Propofol_ASNR2016.jpg)

O-286

9:30AM - 9:33AM

Visualization of CSF Dynamics using 4D time Spatial Spin Labeling Magnetic Resonance Imaging

S Yamada¹, M Yui², S Shimizu³, N Sakashita², T Yamamoto⁴, T Suzuki³

¹*Toshiba Rinkan Hospital, Sagamihara, Tokyo*, ²*Toshiba Medical Systems Corp., Otawara, Tochigi*, ³*Toshiba Medical Systems Corp., Chuo-Ku, Tokyo*, ⁴*Toshiba Medical Systems Corp., Minatoku, Tokyo*

Purpose

Cerebrospinal fluid (CSF) dynamics was investigated with time-spatial labeling inversion pulse (Time-SLIP) magnetic resonance imaging (MRI). This technique allows CSF itself to serve as an endogenous tracer using special RF pulses. In other words, Time-SLIP allows us to perform a tracer study without introducing an external tracer. This technique enables CSF dynamics to be depicted with time resolutions that no other technique can provide. Cerebrospinal fluid dynamics as observed by Time-SLIP have been found to significantly differ from CSF physiology established by prior research and published textbooks. To date, however, Time-SLIP was limited to 2D cine imaging and 3D static imaging. Here, we present the latest findings using 4D (3D imaging with time axis) Time-SLIP.

Materials and Methods

A series of 3D volumes with incremental inversion recovery times was obtained by 3T MR scanner using Time-SLIP sequence with respiratory-gated segmented gradient echo sequence. The scanning conditions were FOV = 25 x 25 cm, acquisition matrix = 192 x 192, slice thickness = 2mm, TR/TE = 4.8/1.5, FA = 3, initial inversion time (TI) = 138ms, TI step = 230ms.

Results

Cerebrospinal fluid dynamics was observed using 4D Time-SLIP MRI. There was active CSF exchange between the lateral ventricle and third ventricle through the foramen Monro. Large CSF displacement was observed at prepontine cistern. Cerebrospinal fluid displacement was observed predominantly in spinal subarachnoid CSF when subject was in the supine position. These CSF displacements were associated with respiration. Cerebrospinal fluid displaced cranio-caudally during expiration and caudo-cranially during inspiration in the entire CSF space in the central nervous system.

Conclusions

Visualization of 4D CSF dynamics was achieved with 4D time-SLIP sequence.

O-287

Smartphone controlled, angle-adjusted external ventricular drainage insertion

F Burn¹, C Eisenring¹, M Baumann¹, J Beck¹, A Raabe¹, M Oertel¹

¹*Department of Neurosurgery, University Hospital of Berne, Berne, Switzerland*

Purpose

Twenty to 40% of external ventricular drainages (EVD) are reported as suboptimally placed on imaging controls. Therefore, the authors evaluated the feasibility and accuracy of smartphone-guided angle-adjusted EVD implantation in both a human artificial cranium and a cadaveric head.

Materials and Methods

A trajectory was drawn from Kocher's point to the center of the ipsilateral ventricular frontal horn according to the horizontal and vertical diameter. Intracranial length and angle of the trajectory towards the midline were measured. A commercially available protractor app of a sterile packed smartphone to adjust the insertion angle was implemented. In total, 20 EVD were inserted, eight of 20 into a human artificial cranium and 12/20 into a cadaver head. Additionally, consecutive CT imaging datasets of 23 patients before EVD insertion were analyzed to determine relevance and influence of ventricle width on application and accuracy of the method.

Results

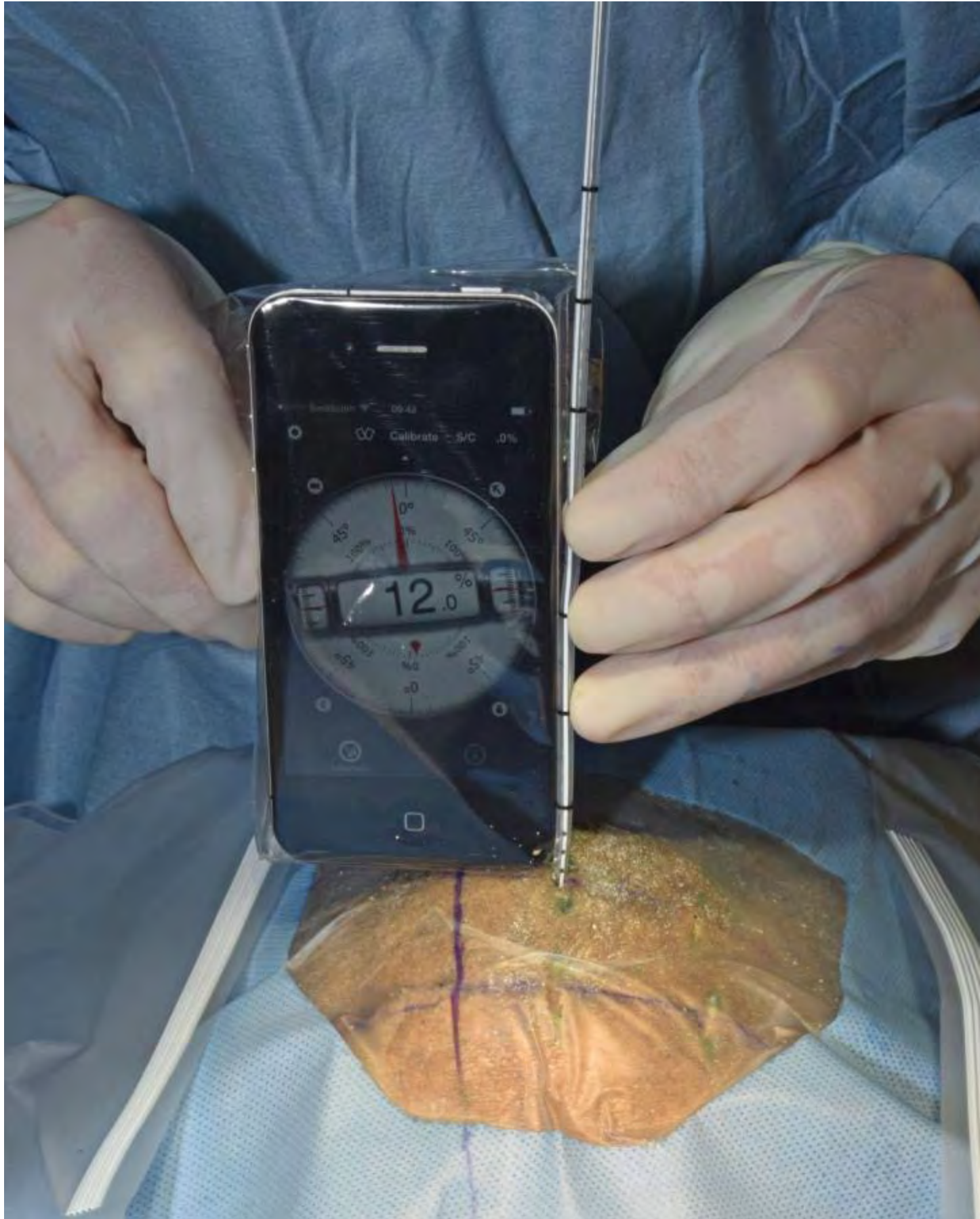
Twenty of 20 EVD were inserted successfully within the ipsilateral ventricle by first attempt. The mean deviation of the intended trajectory was 2.76° with a standard deviation (SD) of 1.98. We measured a tip deviation from the ventricular center of 0.4 cm (SD 0.26) and a maximal deviation of 0.86 cm. 20/23 ipsilateral ventricles analyzed on CT images had a diameter above 0.86 cm. The average duration of measurement of implantation angles and intracranial EVD lengths was 3 min, and of sterile packing, smartphone calibration and angle-adjusted EVD insertion 4 min, respectively.

Conclusions

Results of the current ex vivo study show that smartphone-guided EVD placement is feasible with high accuracy. An ipsilateral ventricular frontal horn diameter above 0.86 cm allowed more optimal EVD insertion. Whether this innovative, easily applicable and broadly available method will be in vivo implementable in clinical routine remains to be investigated.



(Filename: TCT_O-287_graphic1.JPG)



(Filename: TCT_O-287_DSC_0990.jpg)

Wednesday

9:00AM - 10:00AM

Washington Marriott Wardman Park, Maryland A/B/C

14E-Subspecialty & Regional Society Papers, Dyke Award, Foundation of the ASNR Papers

14E-1

9:00AM - 9:10AM

Awards Announcements

14E-2

9:10AM - 9:18AM

A Method to Quantify Injury to White-Matter Pathways Using Diffusion MRI - Norma E. Leeds Award (ENRS)

Ahmadi, E.

Massachusetts General Hospital

Boston, MA

14E-3

9:18AM - 9:26AM

Automated Adaptive Multiplane-Multiangle Oblique (AAMO) Rendering Volumetric Spine CT

Titelbaum, N.

Icahn School of Medicine at Mount Sinai

NEW YORK, NY

14E-4

9:26AM - 9:34AM

CSF Venous Fistula and Renal Contrast in SIH Patients Without CSF Leak at CT Myelography - Louis A. Gilula, MD Mentor Award (ASSR)

Clark, M.
Mayo Clinic
Rochester, MN

14E-5

9:34AM - 9:42AM

Altered Excitation-Inhibition in Knee Osteoarthritis - Gabriel H. Wilson Award (WNRS)

Foerster, B.
Ann Arbor VA Health System
Ann Arbor, MI

14E-6

9:42AM - 9:50AM

Tales From the Crypt: When Vertebral Augmentation Goes Very Wrong - Southeastern Neuroradiology Society (SENRS) Award

Jensen, M.
University of Virginia Health Systems
Afton, VA

14E-7

9:50AM - 9:58AM

Structural Connectivity of Distributed Cortical Association Networks Reflects Cognitive Reserve in Autosomal Dominant Familial Alzheimer's Disease - 2016 Cornelius G. Dyke Award

Prescott, J.
Duke University Hospital
Durham, NC

Wednesday

10:30AM - 12:00PM

Washington Marriott Wardman Park, Marriott Ballroom

15A-SNIS Programming: Point-Counterpoint: Drip-and-Ship vs. Mothership - The NeuroInterventionalist's Role in Large Vessel Occlusion Therapy (AR) (SAM)

15A-1

10:30AM - 10:45AM

Large Vessel Occusion (LVO) Therapy: What is the Current Evidence

Jayaraman, M.
Rhode Island Hospital
Providence, RI

15A-2

10:45AM - 11:00AM

Point: Drip-and-Ship for Acute Ischemic Stroke: What is the Evidence?

Hussein, M.
Cleveland Clinic
Cleveland, OH

15A-3

11:00AM - 11:15AM

Counterpoint: Mothership for Acute Ischemic Stroke: What is the Evidence?

Baxter, B.
Tennessee Interventional Associates
Chattanooga, TN

15A-4

11:15AM - 11:30AM

Speaker Rebuttals

15A-5

11:30AM - 11:45AM

Does the Mobile Stroke Unit (MSU) Change the Rules? Incorporating MSU in Stroke Therapy

Rasmussen, P.
Cleveland Clinic
Cleveland, OH

15A-6

11:45AM - 12:00PM

Questions and Answers

Wednesday

10:30AM - 12:00PM

Washington Marriott Wardman Park, Washington 4/5/6

**15B-WHO's Next and What's New? The 2016 World Health Organization Update
on Brain Tumors: What Neuroradiologists Need to Know**

15B-1

10:30AM - 11:15AM

Updates on Brain Tumors

Osborn, A.
University of Utah
Salt Lake City, UT

15B-2

11:15AM - 12:00PM

What is Next in Pathology

Kleinschmidt-DeMasters, B.
University of Colorado School of Medicine
Aurora, CO

Wednesday

10:30AM - 12:00PM

Washington Marriott Wardman Park, Washington 1/2/3

15C-ASFNR Programming: Resting State Connectivity: Ready for Primetime?

15C-1

10:30AM - 10:50AM

Resting State Connectivity in Language Function

Stufflebeam, S.
Massachusetts General Hospital
Boston, MA

15C-2

10:50AM - 11:10AM

What We Know About Resting State Connectivity in Children

Fulbright, R.
Yale University Medical Center
New Haven, CT

15C-3

11:10AM - 11:30AM

-Resting Connectivity and the Connectome

Shimony, J.
Washington University School of Medicine
Saint Louis, MO

15C-4

11:30AM - 11:50AM

Resting State Connectivity in Neurodegenerative Disease: Biomarker Potential

Sair, H.
Johns Hopkins Medicine
Baltimore, MD

15C-5

11:50AM - 12:00PM

Discussion

Wednesday

10:30AM - 12:00PM

Washington Marriott Wardman Park, Roosevelt 1-3

15D-PARALLEL PAPER SESSION-Turbo Talks - Pediatric CNS: Fetal Imaging / Sickle Cell Disease

O-299

10:30AM - 10:33AM

Functional Brain Connectivity is Altered in Fetuses with Congenital Heart Disease

J De Asis-Cruz¹, A Yarish¹, M Donofrio¹, G Vezina¹, A Du Plessis¹, C Limperopoulos¹

¹*Children's National Health System, Washington, DC*

Purpose

Infants with complex congenital heart disease (CHD) are at elevated risk for neurodevelopmental disabilities. Identifying early deviations from normal brain development and function thus is critical to ensure proper surveillance and timely intervention. Using resting-state functional connectivity magnetic resonance imaging (rs-fcMRI), our objective was to determine whether differences in brain function between CHD and healthy fetuses are detectable in utero. We hypothesized that these differences would manifest in brain regions that are components of complex resting state networks (RSNs).

Materials and Methods

We used noninvasive rs-fcMRI to assess in utero brain function in 52 fetuses [26 diagnosed with CHD (mean±std: 33.34±3.42; 11 single ventricle, 15 two ventricle) and 26 gestational age-matched controls (32.77±3.58)] with no structural brain anomalies. Blood oxygen level dependent (BOLD) signals measured from 90 cortical/sub-cortical regions of interest (45 ROIs per hemisphere) were measured and Fisher z' transformed temporal correlations between regions were computed and compared between cohorts.

Results

We found robust between-hemisphere functional connectivity (t-test, $p < 0.05$) for the majority of ROIs in the CHD (33 out of 45 ROIs) and healthy fetal brain (32/45 ROIs). In both groups, the most highly correlated regions included medially located ROIs: superior frontal gyrus, anterior to mid cingulate regions, medial orbitofrontal

regions, among others. The strength of connectivity between corresponding bilateral structures did not significantly differ between groups, however, inter-regional connectivity was decreased in some association and paralimbic areas of the CHD brain. Specifically, connectivity between the middle orbitofrontal cortex-supplementary motor area, medial orbitofrontal cortex-rectus gyrus, supramarginal gyrus (SMG)-angular gyrus (ANG), SMG-paracentral lobule was decreased in CHD compared to control fetuses (t-test, $p < 0.05$).

Conclusions

We report for the first time that functional connectivity between corresponding bilateral brain regions is intact in CHD fetuses, but connectivity in some association and paralimbic brain regions is decreased compared to controls. Further studies are needed to elucidate how early functional alterations in association regions involved in multimodal integration (i.e., SMG and AG) impact neurodevelopment in CHD.

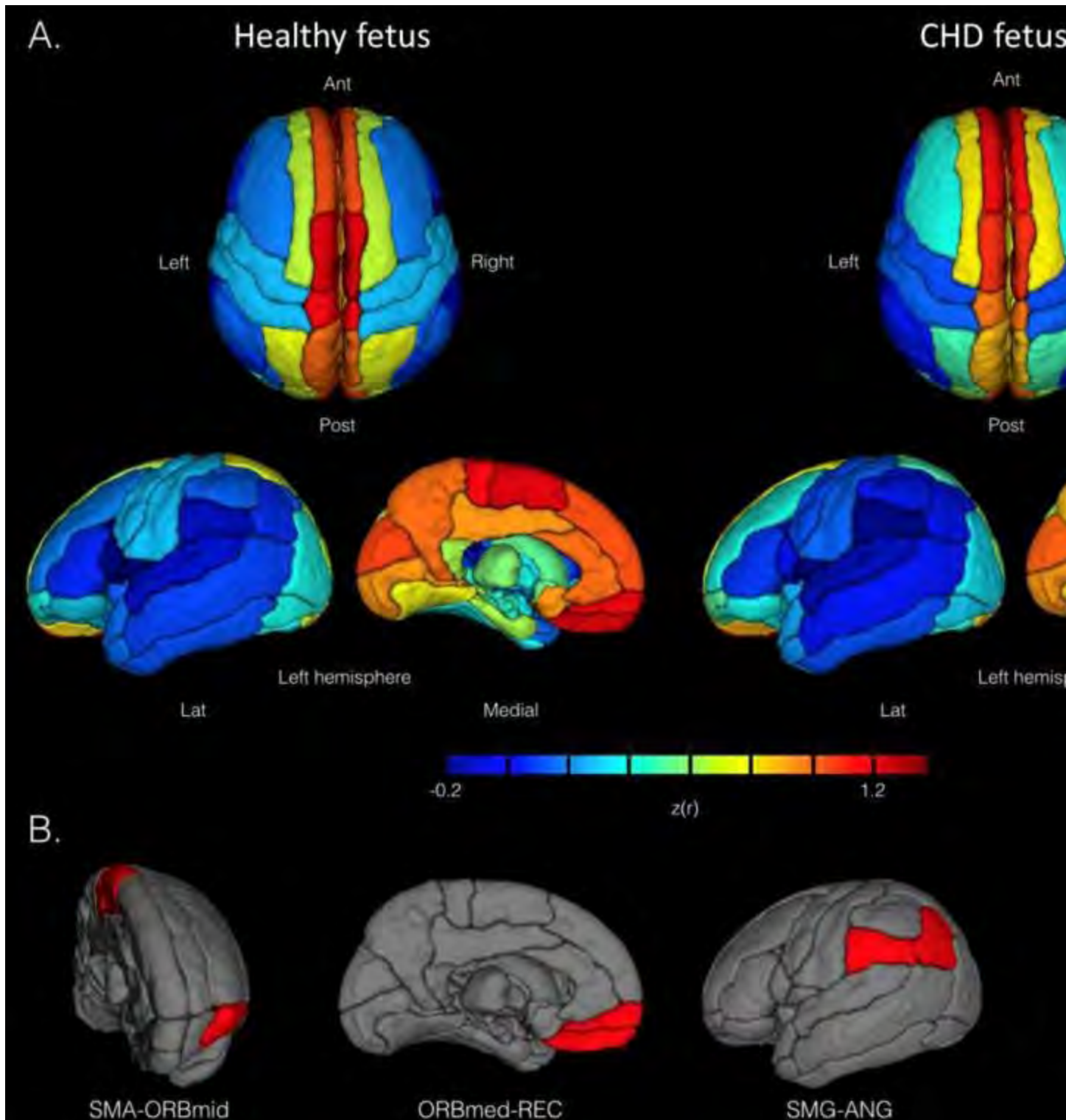


Figure 1. Superior, lateral and medial views of the brain (A) show strength of connectivity ($z(r)$) corresponding bilateral regions in healthy and CHD fetuses. Connectivity pattern is highly similar. Medial areas are more strongly connected (red) than lateral regions (blue). (B) shows areas which were decreased in the CHD cohort: supplementary motor area (SMA)-orbitofrontal cortex, middle (ORBmid)-orbital cortex, medial (ORBmed)-rectus gyrus (REC), supramarginal gyrus (SMG)-angular gyrus (ANG), posterior cingulate cortex (PCL). Brain parcellation and abbreviations are from Shi et al (2011).

(Filename: TCT_O-299_ASNRFigure.jpg)

O-301

10:36AM - 10:39AM

Validation of In Utero Tractography with Histology-based Structure Tensor Analysis in the Human Fetal Brain

C Mitter¹, A Jakab¹, P Brugger¹, G Ricken¹, G Gruber¹, D Bettelheim¹, A Scharrer¹, D Prayer¹, G Kasprian¹

¹*Medical University of Vienna, Vienna, Austria*

Purpose

Diffusion tensor imaging (DTI) offers the unique ability to visualize the developing white matter neuroanatomy of the human fetal brain in vivo and in utero. However, in order to establish in utero DTI as a clinical imaging tool, an anatomical validation of macroscopic imaging results with microscopic histology data in identical subjects is needed. The aim of this study was to validate normal as well as abnormal in utero tractography results of commissural and internal capsule fibers in human fetal brains using postmortem histological structure tensor (ST) analysis (Budde et al. 2012).

Materials and Methods

We included histopathological specimens of two structurally unremarkable and four abnormal fetal brains, for which in utero DTI [1.5T magnetic resonance imaging (MRI)], 16 directions, reconstructed voxel size 0.94mmx0.94mmx3mm, b-values of 0 and 700sec/mm²) had been performed within a 2 week timespan prior to fetal demise. The internal capsule, the corpus callosum, as well as the Probst bundles in three subjects with agenesis of the corpus callosum were defined anatomically using a multiple region of interest (ROI) approach and visualized using a FACT algorithm (Philips Extended MR WorkSpace 2.6.3.3). For histological validation of in utero tractography results, whole hemisphere tissue sections of the same subjects were stained with antibody against neural cell adhesion molecule (NCAM) to identify axonal tracts and digitized using a high resolution scanner. Structure tensor analysis (using OrientationJ for ImageJ) was performed on the digitized histological sections to directly visualize fiber orientation and anisotropy on a microscopic scale. To overcome limitations in correlating in utero tractography to postmortem histology data, an approach to perform deterministic tractography in histological sections was implemented.

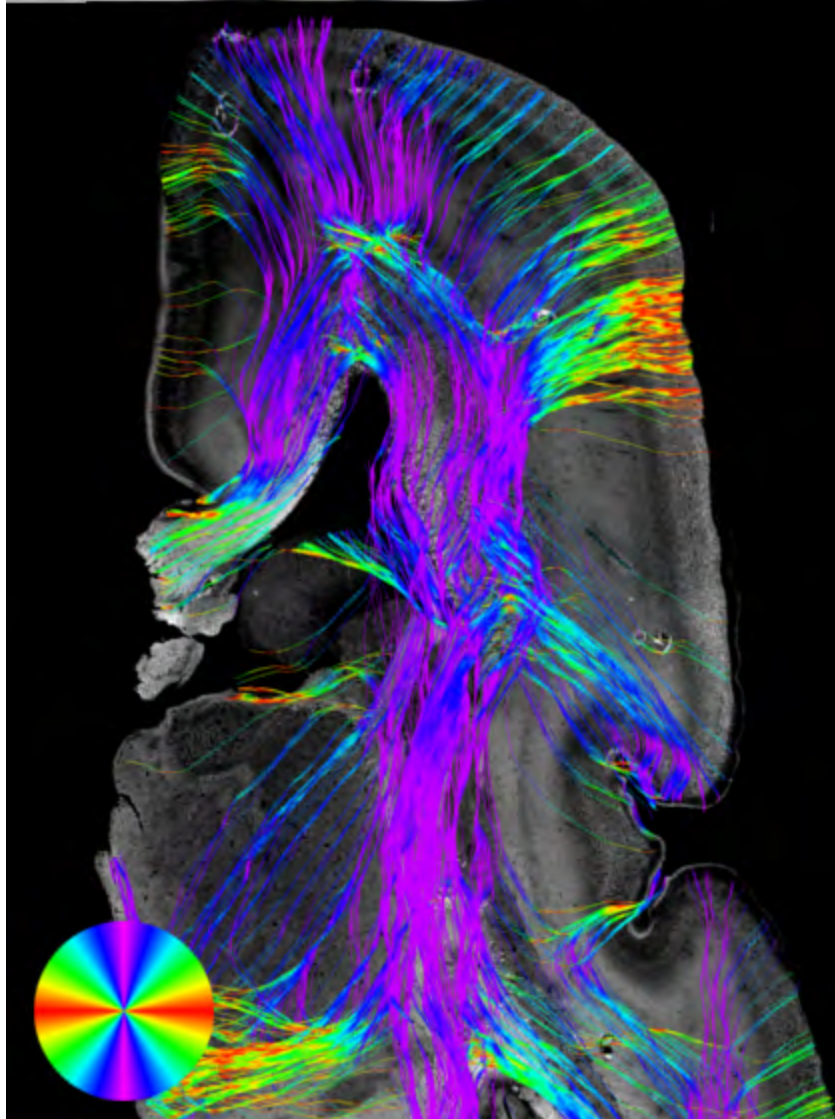
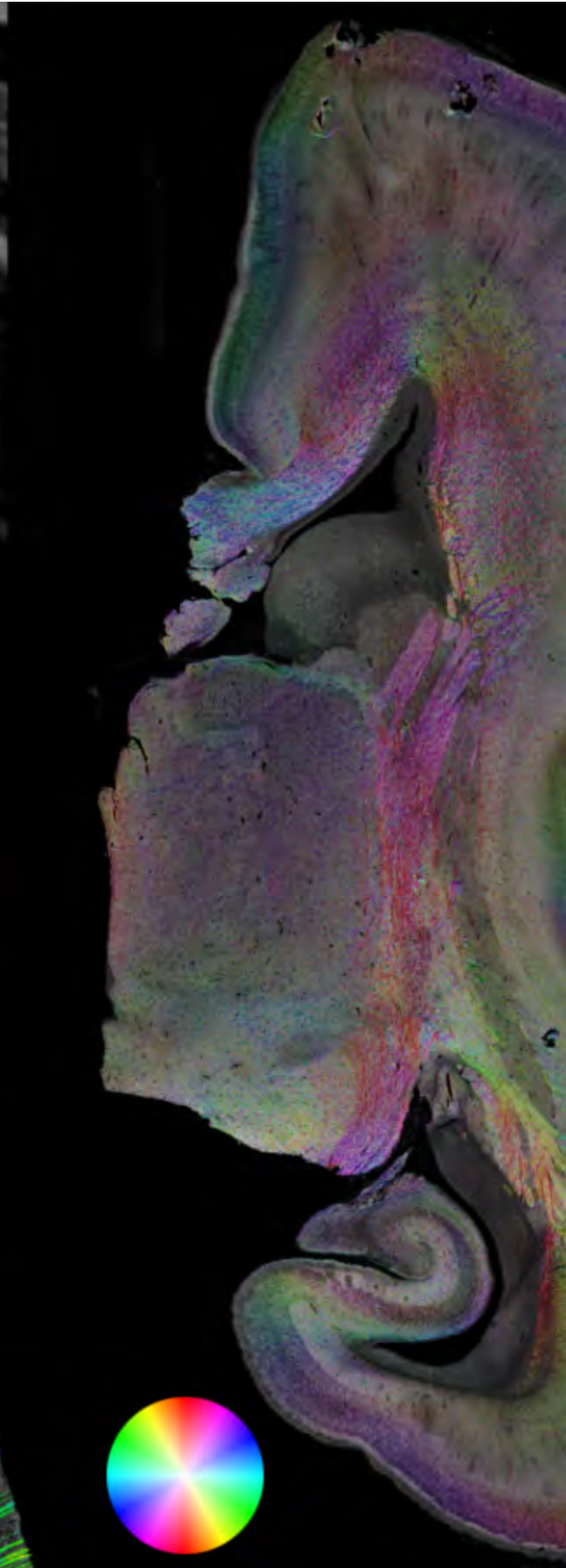
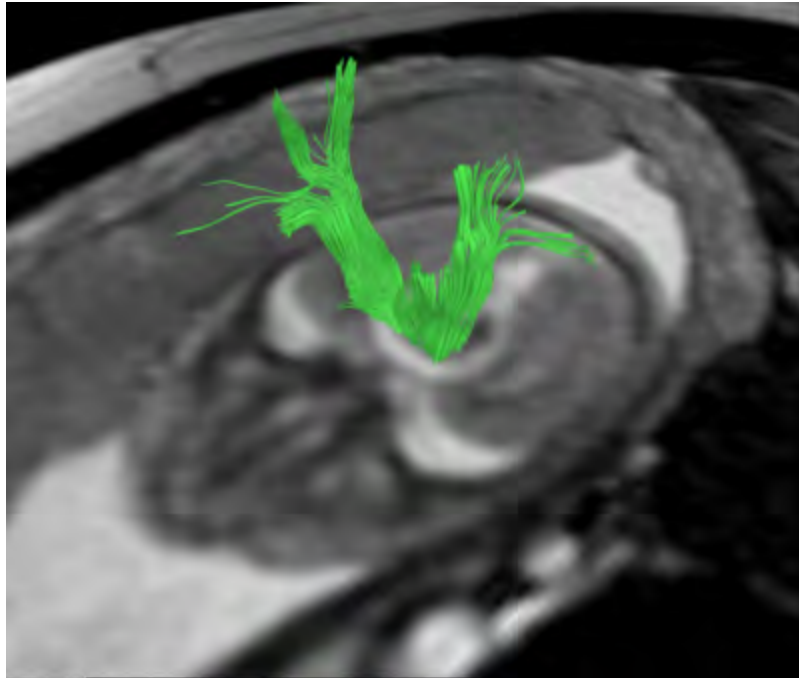
Results

Histological ST analysis and histology-based tractography of fetal brain sections enabled the direct assessment of the anisotropic organization and main fiber orientation of the transient layers of the fetal telencephalic wall. Structure tensor analysis successfully validated abnormal in utero tractography findings of

commissural fibers in subjects with agenesis of the corpus callosum, and revealed additional information about the internal fiber architecture of Probst bundles. The potential for cross-validation of abnormal in utero tractography results of the internal capsule was demonstrated in two subjects with malformations of internal capsule fibers. Potential limitations of DTI-based in utero tractography could be demonstrated in several brain regions.

Conclusions

Histology-based tractography of commissural and internal capsule fibers in NCAM-stained human fetal brain sections corresponds remarkably well to many of the results of in utero tractography. Combining the three-dimensional nature of DTI-based in utero tractography with the microscopic resolution provided by histological ST analysis ultimately may facilitate a more complete morphologic characterization of axon guidance disorders and other malformations of white matter fiber tracts at prenatal stages of human brain development.



(Filename: TCT_O-301_ASNR2016.jpg)

O-302

10:39AM - 10:42AM

Neuronal Injury and Impaired Metabolism in Fetuses with Congenital Heart Disease

E Mahdi¹, G Vezina¹, J De Asis-Cruz¹, M Donofrio¹, D Lanham¹, S Bauer¹, A Du Plessis¹, C Limperopoulos¹

¹*Children's National Health System, Washington, DC*

Purpose

Neurodevelopmental dysfunction is common in infants with congenital heart disease (CHD). There is growing evidence that impaired brain development and metabolism has its origins in the fetal period. However, the exact mechanism of abnormal prenatal brain development is unclear. The aim of this study was to delineate fetal metabolic biomarkers associated with CHD using proton magnetic resonance spectroscopy (1H-MRS).

Materials and Methods

We prospectively studied a large cohort of pregnant women with healthy and CHD fetuses between 17-39 weeks gestational age (GA) using single voxel 1H MRS. The resultant MR spectra were preprocessed retrospectively and quantified using LC Model. Ratios of the main metabolites: N-acetyl aspartate -NAA; Choline-Cho; Creatine-Cr [tNAA/tCho, tNAA/tCr, and tCr/tCho] and presence of lactate (anaerobic marker) were quantified. The correlation strength between GA and metabolites ratios was measured using Fisher z' transformed Pearson Coefficients. ANCOVA analyses were performed to determine differences in the slope of the fitted regression line for each metabolite/group.

Results

We acquired 302 1H-MRS spectra: 82 CHD fetal spectra (mean GA 31.9 +/-4.25 weeks) and 220 healthy controls (mean GA 31.4 +/-5.25 weeks). Among CHD fetuses, 64% had cyanotic CHD and 41% had single-ventricle (1v) physiology. In healthy fetuses, ratios of all measured metabolites increased with advancing GA (p<0.001). In CHD fetuses, tNAA/tCho and tCr/tCho also correlated with increasing GA (p <0.001); however, tNAA/tCr did not. The relationship between tNAA/tCho and tNAA/tCr, and advancing GA was significantly lower in CHD compared to healthy fetuses (p<0.001, for each). There was no difference between the two groups for tCr/tCho. Lactate was detected in 38% of CHD fetuses (39% had 1V, and 57% were cyanotic). The prevalence of minor structural brain injury on fetal MRI was 21% in CHD fetuses, and included prominent subarachnoid spaces and mild ventriculomegaly/asymmetry.

Conclusions

We report a high prevalence of cerebral lactate and decreased NAA concentrations in fetuses diagnosed with CHD suggesting anaerobic metabolism and neuronal injury. These data suggest that metabolic alterations in CHD fetuses may be an important early biomarker for subsequent brain injury in this high-risk population.

O-303

10:42AM - 10:45AM

Robust gestational age prediction framework for cerebral cortical development in healthy and high-risk fetuses

S Dahdouh¹, G Vezina¹, C Limperopoulos¹

¹*Children's National Health System, Washington, DC*

Purpose

Accurate gestational age (GA) prediction is critical for determining normal and aberrant fetal brain development during pregnancy. Our objective was to examine the accuracy of a novel machine learning framework for automatically predicting GA using fetal cortical indices.

Materials and Methods

Using a cerebral cortical framework (1), fetal cortical surfaces from congenital heart disease (CHD) and control fetuses were parceled into 12 regions per hemisphere. A novel local signature composed of a mean: local gyrification index, cortical depth and cortical thickness per region was defined. The sum of these local signatures comprises a global brain signature. The brain signatures then were 'learned' using Regression Forests, a machine learning approach that maps a complex input space (set of multi-dimensional signatures) to a continuous output (e.g., age) based on a training dataset (Fig. 1). First healthy fetuses GA were predicted. Then, fetal CHD cortices were 'learned' and a prediction was carried out. Finally, CHD type (i.e., cyanotic versus acyanotic; 1- versus 2-ventricle CHD) was compared and a final GA prediction was performed.

Results

A total of 119 fetal brains: 61 CHD/58 controls (mean GA: 29.9±3.1 versus 31.0±3.5 weeks, respectively) were studied. GA prediction for healthy fetuses had a mean accuracy of <5 days, with a variability of 0.5 weeks, for an overall accuracy of 8 days. For CHD fetuses, the mean GA accuracy was 7 days, with a variability of 0.8 weeks, with a global accuracy of <13 days. Stratification of the CHD fetuses (1- versus 2v/cyanotic versus acyanotic) does not change the global prediction accuracy.

Conclusions

We present for the first time a novel, fully automated GA prediction framework in healthy and high-risk fetuses. Our data suggest a highly accurate GA prediction,

particularly for healthy fetuses. The wider GA global accuracy in CHD fetuses likely reflects greater variability in cortical development. Future work will extend this framework for diagnostic prediction and quantifying local cerebral cortical delays.

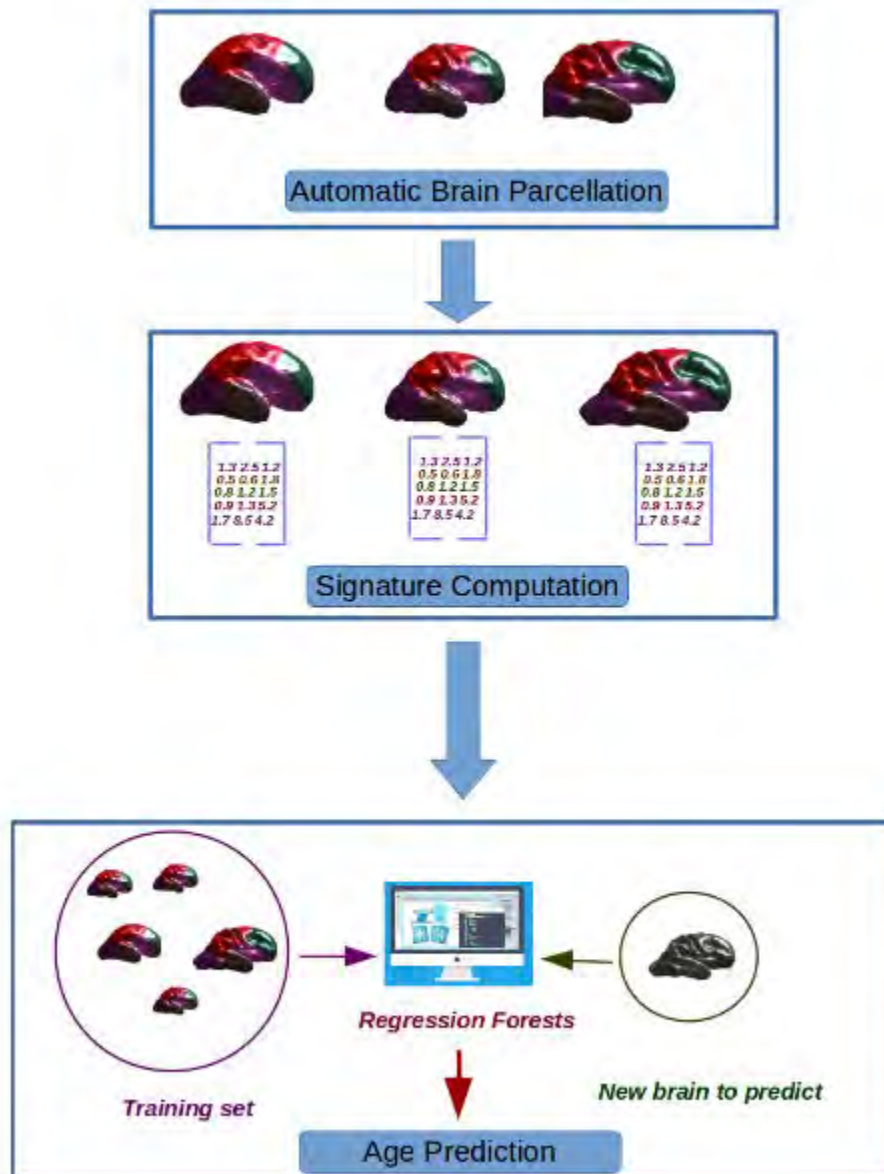


Figure 1: Age prediction framework based on local cortical signatures

(Filename: TCT_O-303_figure1_2.png)

O-304

10:45AM - 10:48AM

Normal Developmental Globe Morphology on Fetal MR

M Whitehead¹, G Vezina¹

¹Children's National Medical Center, Washington, DC

Purpose

Age-dependent structural changes occur in the globes over the course of gestation. In the second and early 3rd trimester, the posterolateral globe margins bulge outward, and the eyes are conical in the sagittal plane. Later, the globes are ellipsoid. The purpose of this study is to establish normal developmental fetal globe morphology.

Materials and Methods

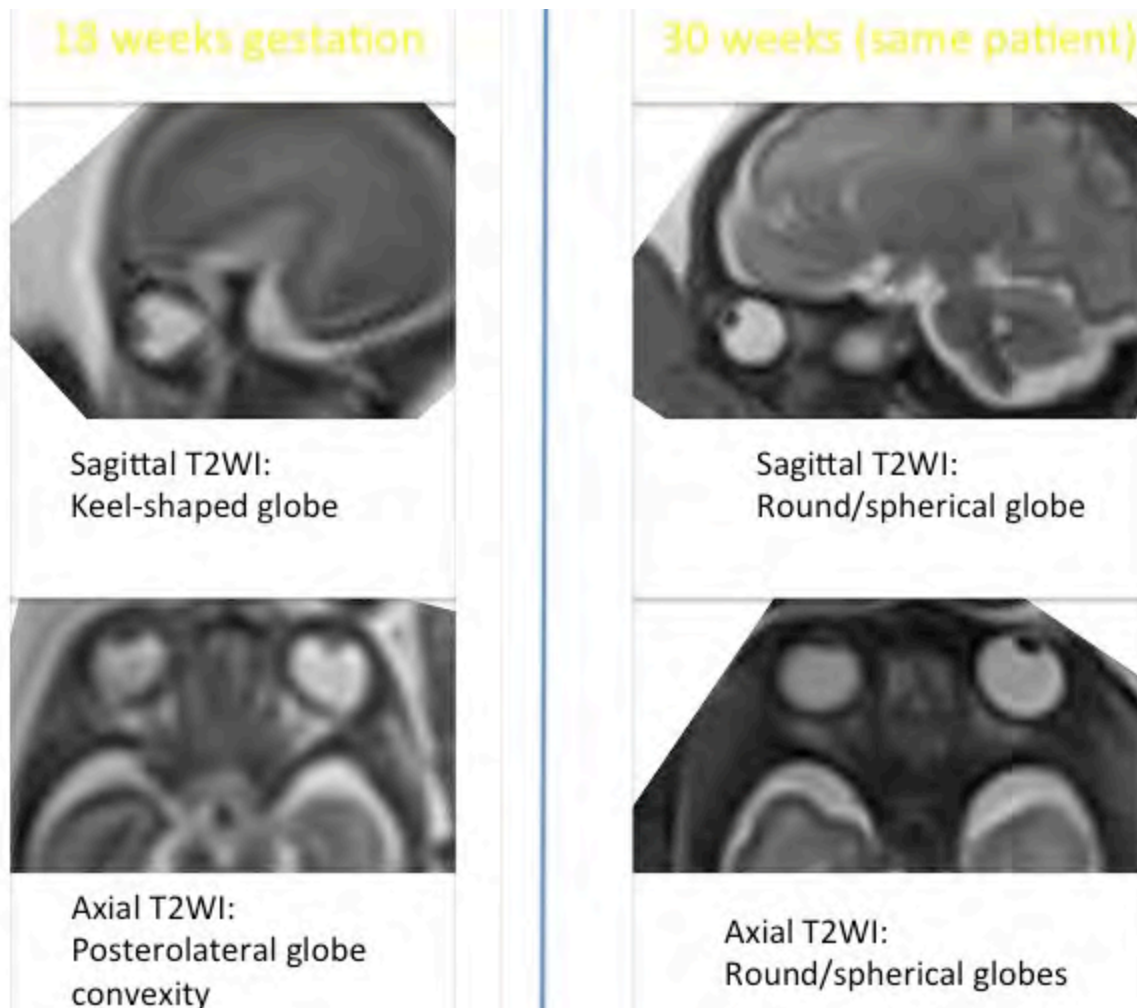
The fetal magnetic resonance (MR) database at an academic children's hospital was queried for all brain MRIs performed over 8 years. Motion artifact, brain/craniofacial/globe malformations, and chromosomal defects were exclusion criteria. Two board certified neuroradiologists evaluated examinations in consensus. Logistic regression and Spearman's rank coefficients were used to evaluate correlations among variables.

Results

Twelve hundred forty-three exams from 1177 patients were identified. Six hundred eighty-two exams met inclusion criteria (17-39 weeks). Nonelliptical globes with posterolateral protrusions were universal up to 22 weeks. Thereafter, globes gradually assumed an elliptical shape, present in nearly all patients over 29 weeks. The hyaloid vasculature was visible in most patients up to 19 weeks, and occasionally up to 24 weeks. Subsequently, the hyaloid vasculature was no longer detectable. Receiver operating characteristic (ROC) analysis showed that age was highly predictive of globe shape (AUC=0.99) and visibility of fetal vasculature (AUC=0.94). There was a weak negative association between hyaloid visibility and elliptical globe shape (Spearman's rank coefficient= -0.36).

Conclusions

Physiologic nonspherical globe shapes are normal up to 29 weeks gestation, and should not be misinterpreted as pathologic. Thereafter, globes are generally elliptical. The timing of this process coincides with the resolution of the primary vitreous, and may be related.



(Filename: TCT_O-304_Fig.jpg)

O-305

10:48AM - 10:51AM

Spectrum of Systemic Disorders in Fetuses with Orbital Lesions and their Associations with Cerebral Anomalies.

A Maddocks¹, A Pollock², B Coleman¹, T Feygin¹

¹Children's Hospital of Philadelphia, Philadelphia, PA, ²Children's Hospital of Philadelphia, Philadelphia, PA

Purpose

Fetal orbital anomalies may be associated with an underlying systemic disorder. The purposes of this study include: 1. Description of fetal imaging appearance of orbital anomalies. 2. Assessment of congenital disorders associated with orbital anomalies, with focus on a spectrum of cerebral pathology in each disorder.

Materials and Methods

With IRB approval, retrospective selection of fetal orbital anomalies was performed using keywords "microphthalmia", "coloboma", "cataract", "fetal". Cases were selected from fetal ultrasound and fetal magnetic resonance (MR) imaging performed at our institution from 2008-2015 for assessment of suspected fetal anomalies on obstetric ultrasound. Available imaging in the selected cases was reviewed independently by three neuroradiologists, and one senior sonographer.

Results

Evaluation of MRI/US examinations and patient's charts revealed 11 patients with confirmed vitreous coloboma; 36 patients with microphthalmia and three patients with cataracts. Orbital lesions were diagnosed during work up of suspected fetal central nervous system anomalies. The gestational age at the time of imaging was between 16-36 weeks. The lesions were diagnosed on obstetric ultrasound and fetal MRI. All colobomas and microphthalmia were seen equally on fetal MRI and ultrasound. Cataracts were detected on ultrasound only. No single case of isolated coloboma nor cataract was evident in our study, although four cases of seemingly isolated microphthalmia were revealed. Cases with detected coloboma were associated with a variety of underlying syndromes, including three cases of PHACES, two cases of CHARGE, two cases of Walker-Warburg, two cases of Aicardi, one case of Wolf-Hirschhorn syndromes and one case of unclassified multiple congenital anomalies. Two cases with detected cataract were associated with Walker-Warburg syndrome and one case was associated with CHARGE syndrome. Thirty-two cases with detected microphthalmia were associated with multiple underlying syndromes, most often with unclassified multiple congenital anomalies and trisomy 13. The spectrum of cerebral anomalies in cases with orbital lesions extensively varied and among others included abnormal corpus callosum, holoprosencephaly and migrational cortical anomalies.

Conclusions

Detection of fetal orbital lesions should prompt a diligent search for associated birth defects arising at the same time or sharing the same progenitor cell. Fetal orbital anomalies may be helpful as a discriminator in order to narrow a long list of underlying systemic disorders. Precise assessment of associated cerebral anomalies is very important for decision making and future planning.

O-306

10:51AM - 10:54AM

Hypogenesis of the Corpus Callosum: Brain Findings in Fetal MR Imaging

J Alves¹, X Mu², A Barkovich³, D Xu², A Foster-Barber², O Glenn²

¹*Centro Hospitalar do Porto, Porto, Portugal*, ²*Univ. California San Francisco, San Francisco, CA*, ³*UCSF Benioff Children's Hospital, San Francisco, CA*

Purpose

Agenesis of the corpus callosum is one of the most frequently diagnosed brain malformations prenatally, but most studies focus on complete absence rather than hypogenesis. The aim of this study was to characterize brain MR findings in fetuses with hypogenesis of the corpus callosum (HCC), pointing out similarities and differences to fetuses with complete agenesis, and to assess the impact of fetal MR information on diagnosis and postnatal outcome of the children.

Materials and Methods

Out of 44 fetuses with potential HCC, brain magnetic resonance (MR) findings were reviewed retrospectively in those without bilateral severe ventriculomegaly and whose callosal length was below normal reference values.

Results

Twenty-one fetuses with HCC were included in this study, with a median gestational age of 23 weeks, 14 weeks at the time of fetal MRI. Prenatal ultrasound suspected a callosal abnormality in 48% of cases. On fetal MR, HCC was associated with other brain abnormalities in 81% of fetuses, including mild ventriculomegaly (n=9), interhemispheric lesions (n=9), sulcation delay (n=9), abnormal sulcal morphology (n=8), infratentorial anomalies (n=7), periventricular heterotopia (n=5) and thalamic fusion (n=1). Extracranial abnormalities were detected in seven fetuses. Out of six children with postnatal follow-up, three had good neurodevelopmental outcome and three poor outcome. None of the three children with a good outcome had abnormal sulcal morphology.

Conclusions

Fetal MR was a valuable tool in the diagnosis of unsuspected cases of HCC and showed that associated brain abnormalities are common and phenotypically heterogeneous. Although sulcation delay was present in a moderate proportion of cases, it was less frequent than what has been reported in complete agenesis, supporting the hypothesis that it may be secondary to abnormal commissuration and not an independent brain malformation. Information provided by fetal MR helps to clarify its etiology in some individual cases and constitutes an invaluable tool in assessing neurodevelopmental prognosis and parental counseling.

O-307

10:54AM - 10:57AM

Neuroimaging findings in Chiari II malformation on fetal and postnatal MRI

U Nagaraj¹, K Bierbrauer¹, J Peiro¹, B Kline-Fath¹

¹*Cincinnati Children's Hospital Medical Center, Cincinnati, OH*

Purpose

To examine neuroimaging findings in fetuses with open spinal dysraphisms and compare with postnatal imaging features.

Materials and Methods

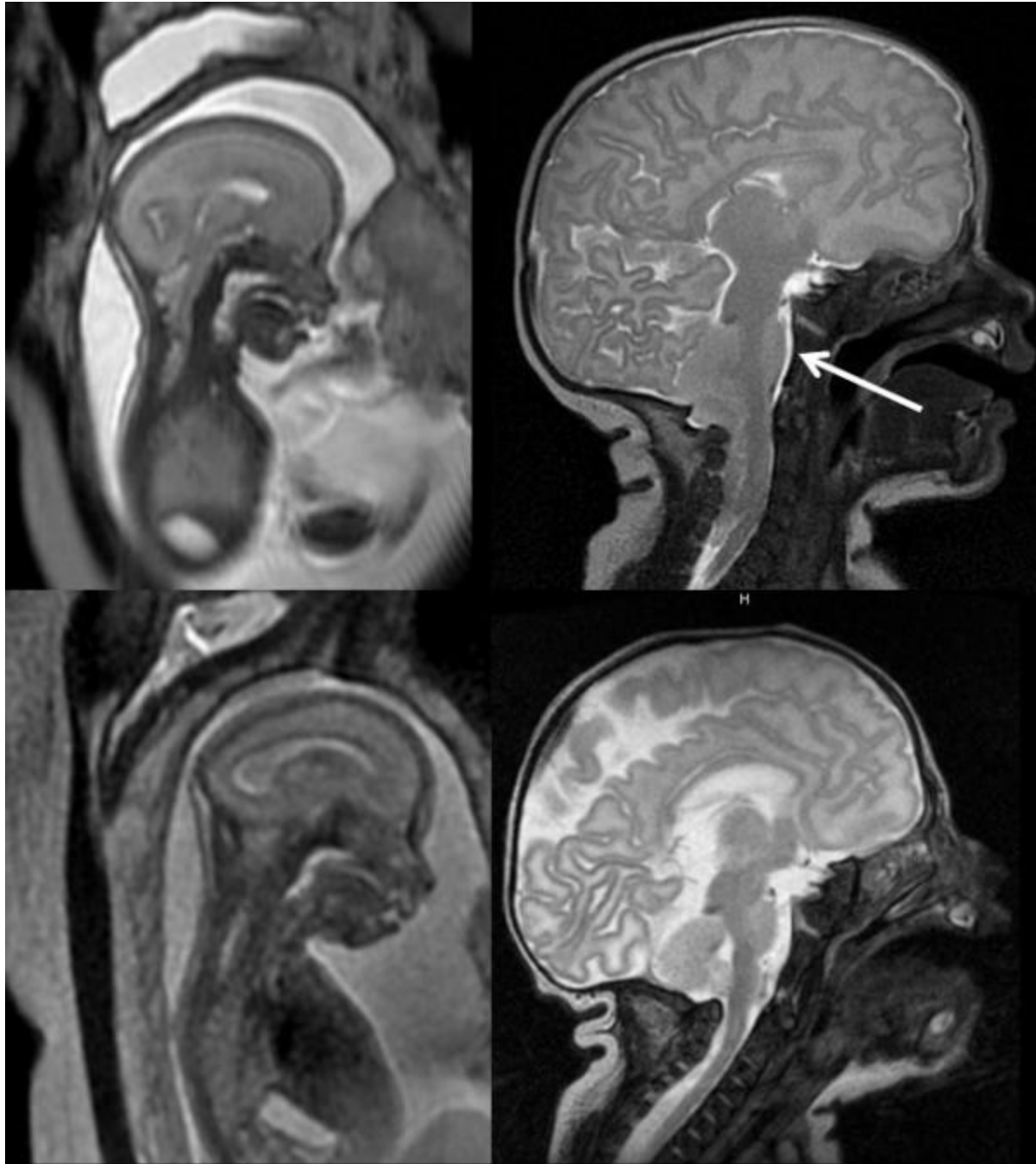
A single center HIPPA compliant and institutional review board approved retrospective analysis was performed of magnetic resonance imagings (MRIs) of fetuses with open spinal dysraphism from 1/2004 through 7/2015 with available postnatal imaging. Images were reviewed by two board certified fellowship-trained pediatric neuroradiologists. Corresponding obstetrical ultrasound and clinical/operative reports were reviewed.

Results

One hundred eight fetal MRIs of open spinal dysraphisms with available postnatal neuroimaging and clinical/neurosurgical follow up were included. Average gestational age at fetal MRI was 23.9 ± 3.7 weeks. Cerebellar ectopia was seen in 90.7% (98/108) of fetuses, 86.7% (85/98) severe (grade 3) and 13.3% (13/98) moderate (grade 2). 90.7% (98/108) of fetuses had effacement of the pre-pontine cistern. In utero repair was performed in 30.6% (33/108) of fetuses, 81.8% (27/33) with severe Chiari II malformation. 97.2% (105/108) had postnatal brain MRI within the first year of life at average age of 26.2 ± 57.9 days. 14.8% (16/108) of patients had postnatal effacement of the prepontine cistern. Of 10 fetuses without cerebellar ectopia, 20% (2/10) developed ectopia postnatal ($p=0.08$). Of nonprenatal repaired severe cases 58.6% (34/58) were stable, 37.9% (22/58) had improved Chiari II, and 3.4% (2/58) had resolved cerebellar tonsillar ectopia postnatal. In fetuses with severe Chiari II that underwent in utero repair 74.1% (20/27) had no cerebellar ectopia, 11.1% (3/27) had improved Chiari II, and 11.1% (3/27) had no improvement by postnatal imaging.

Conclusions

In fetuses with open spinal dysraphism and severe Chiari II malformation that do not undergo prenatal repair, majority (58.6%) have no change in the severity of Chiari grade, however the majority (82.8%, 48/58) have improved mass effect on the brainstem postnatal. In fetuses that had in utero repair majority (74.1%, 20/27) had no postnatal imaging findings of cerebellar ectopia.



Chiari II malformation
 postnatal MRI
 repair:
 Fetal MRI (10 weeks gestation)
 severe Chiari II
 Postnatal MRI
 age (upper cervical)
 severe Chiari II
 now with posterior
 cistern (arrow)

Chiari II malformation
 prenatal MRI
 repair:
 Fetal MRI (10 weeks gestation)
 severe Chiari II
 Postnatal MRI
 age (lower cervical)
 marked improvement
 cerebellar enlargement

(Filename: TCT_O-307_ASNRPre-PostFigure.jpg)

O-308

10:57AM - 11:00AM

Fetal MRI Assessment in Rhombencephalosynapsis

J Alves¹, A Barkovich², X Mu³, D Xu³, A Foster-Barber³, O Glenn³

¹Centro Hospitalar do Porto, Porto, Portugal, ²UCSF Benioff Children's Hospital, San Francisco, CA, ³University Of California, San Francisco, San Francisco, CA

Purpose

Rhombencephalosynapsis (RS) is a likely underestimated brain malformation and its pathogenetic mechanisms remain largely unknown. We describe prenatal brain magnetic resonance imaging (MRI) findings in a large cohort of fetuses with RS, showing how this imaging technique can improve our understanding of this pathology.

Materials and Methods

Review of prenatal MR features in an institutional cohort of 16 fetuses with prenatally diagnosed RS.

Results

The prevalence of fetal RS in our institution was 1.2%. Nine fetuses had complete RS and seven had partial RS. The cerebellum was small in 81% and the pons anteroposterior diameter was reduced in 69%. The most common supratentorial associated findings were ventriculomegaly (n=14), absence of septal leaflets (n=13) and partial or complete agenesis of the corpus callosum (n=8). Abnormalities outside the brain were found in half of our fetuses, including two cases of lumbar myelomeningoceles and one with cervical meningocele, all without cerebellar or brainstem herniation through the foramen magnum.

Conclusions

Rhombencephalosynapsis is more common than originally considered and likely an underdiagnosed entity, in part due to the fact that a vermian remnant is found in a substantial number of cases. Fetal MR accurately characterizes cerebellar abnormal morphology and associated brain findings. Our results show that RS is frequently part of a more extensive malformation complex that includes neural tube defects, mesencephalon- and diencephalosynapsis and holoprosencephaly and that these entities likely share some common biological mechanisms, involving midline dorsoventral patterning defects.

O-309

11:00AM - 11:03AM

Placental Structural Evolution in Healthy and Congenital Heart Disease Fetuses using MRI

S Yewale¹, S Dahdouh², J De Asis-Cruz³, D Bulas¹, S Bauer³, D Lanham³, C Limperopoulos³

¹Children's National Medical Center, Washington DC, DC, ²Children's National Medical Center, Washington, DC, ³Children's National Health System, Washington, DC

Purpose

Placental insufficiency remains a common cause of perinatal mortality and neurodevelopmental morbidity. In utero congenital heart disease (CHD) may result in alterations in oxygen delivery and blood flow in the fetal and placental circulation. The extent to which placental structure is altered in CHD fetuses is unknown. We sought to characterize global and regional placental structural evolution in healthy and CHD fetuses using volumetric and texture-based magnetic resonance imaging (MRI) analyses.

Materials and Methods

We prospectively studied singleton pregnancies with healthy and CHD fetuses who underwent fetal MRI between 18- 40 weeks gestational age (GA). Manual segmentation of maternal and fetal compartments was carried out. We measured: (1) total, maternal and fetal placental volumes, (2) normalized entropy (nentrop), a descriptor of textural randomness, and (3) normalized variance (nvar), a measure of textural variability. An ANCOVA analysis was performed to study the evolution of all descriptors with regard to GA and condition. Partial correlation analysis between nvar, nentrop and volume also was performed.

Results

Placenta data from 200 fetal MRI scans, 84 CHD (mean GA \pm sd: 30.83 \pm 4.89 weeks) and 116 healthy controls (30.99 \pm 4.89 weeks) were analyzed. Placental volume, nentrop and nvar for total, maternal and fetal compartments increased linearly with advancing GA for control and CHD fetuses ($p < 0.01$). Maternal placental volume was significantly lower in CHD fetuses compared to controls ($p = 0.001$) throughout gestation. The difference in slopes between CHD and control fetuses was significant for nvar in the fetal compartment only ($p = 0.03$). Normalized entropy correlated with placental volumes ($p = 0.0014$) in healthy fetuses, while both nentrop ($p = 0.0020$) and nvar correlated with CHD placental volume ($p = 0.04$).

Conclusions

We report for the first time that global and regional maternal/fetal placental growth and textural variability increase with advancing GA in healthy and CHD fetuses. We demonstrate that regional maternal placental volumes are reduced significantly in CHD fetuses. The lack of correlation between placental volume and nvar in healthy fetuses likely reflects an evolving placental textural pattern evident with increasing GA, that is nonevident in CHD placenta. The functional significance of these intriguing preliminary placental findings in CHD fetuses awaits further study.

O-310

11:03AM - 11:06AM

MRI texture analysis in sickle cell disease

P Croal¹, P Kosinski², M Shroff¹, A Kassner¹

¹The Hospital for Sick Children, Toronto, Ontario, ²The University of Toronto, Toronto, Ontario

Purpose

Up to 40% of children with sickle cell disease (SCD) are afflicted with silent cerebral infarcts (SCI) (1), associated with cognitive decline (2, 3) and increased stroke-risk (4); however the pathophysiology remains poorly understood. Here, we propose the application of texture analysis (TA) in children with SCD with and without SCI, to assess whether SCI are associated with widespread white matter (WM) changes. We focus on the watershed areas due to increased risk of ischemic damage in SCD, with the internal watershed damage thought to arise from chronic hemodynamic compromise, and external watershed damage from acute microembolic events (5).

Materials and Methods

Data were acquired on a 3T magnetic resonance imaging (MRI) system as part of a larger study and retrospectively analyzed. T1-weighted (TR/TE=2300/2.96ms, resolution=1×1×1mm and T2-weighted (TR/TE=2500/13ms, resolution=3.4×3.4×4.5mm) were acquired and reviewed by an experienced neuroradiologist (MS). Data from 14 patients were analyzed; seven subjects with SCI (14.4±2 years) and seven subjects without (14.5±3 years). Gray-level co-occurrence matrix (GLCM) based TA was applied to T1-weighted data in four slices (Fig. 1). Features were compared between SCI and non-SCI patients using a Student's t-test (corrected for multiple comparisons).

Results

For the internal watershed area, significant differences were observed in 10/11 features ($p < 0.05$) across all pixel distances. There were no significant group differences in texture features for the external watershed area.

Conclusions

Results suggest that microscopic structural changes in normal appearing WM occur in addition to focal damage, although not yet visible on structural scans. Differences were observed in internal but not external watershed areas, supporting the notion that SCI in children with SCD are associated with chronic hemodynamic compromise rather than acute microembolic events. Texture analysis is a cost-effective image processing method which may provide additional insight into low-grade WM damage in SCD. By better understanding how damage is associated with SCI, it may become possible to predict SCI occurrence and better target therapeutic intervention.

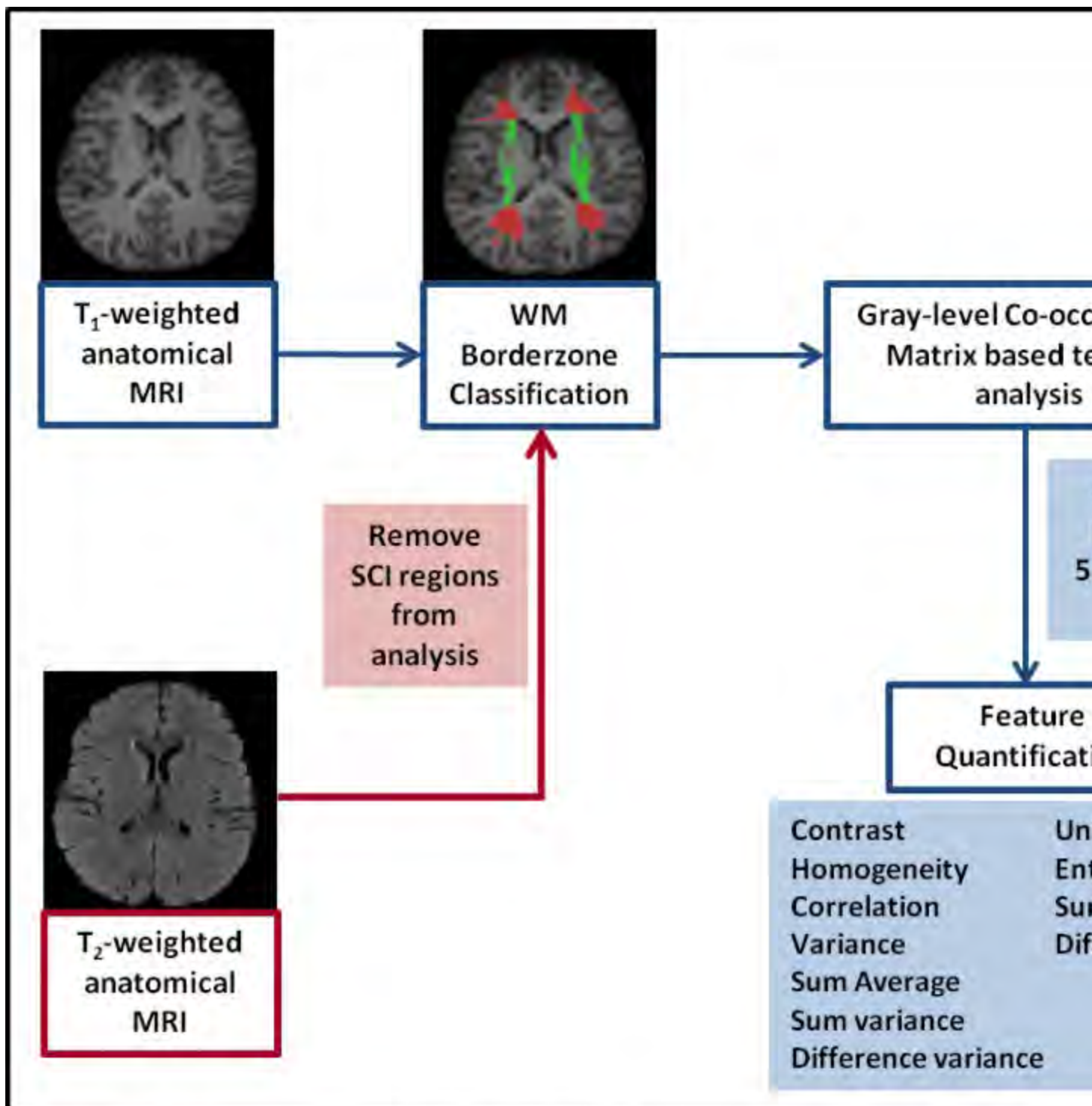


Figure 1: Texture analysis pipeline. External and internal borderzone regions of interest were identified on T₁-weighted anatomical images, and gray-level co-occurrence matrix (GLCM) texture analysis applied. If silent cerebral infarctions were identified on T₂-weighted anatomicals, these voxels were excluded from analysis.

(Filename: TCT_O-310_TA_ASNR.png)

O-311

11:06AM - 11:09AM

Altered Temporal Dynamics in BOLD Measurements of Vascular Reserve in Children with Sickle Cell Disease

J Leung¹, J Duffin², A Kassner¹

¹*The Hospital for Sick Children, Toronto, Ontario*, ²*University of Toronto, Toronto, Ontario*

Purpose

Cerebrovascular reactivity (CVR) is a measure of the change in cerebral blood flow (CBF) in response to a vasoactive stimulus, such as carbon dioxide (CO₂). However, the response of cerebral blood vessels is limited by both a temporal lag and a period of transient increase (1, 2) (Fig. 1). Recently, a method that accounts for such delays into CVR analysis was introduced, known as transfer function analysis (TFA), which uses frequency analysis instead of a direct temporal correlation (2). In this study, we compared TFA to standard temporal correlation for BOLD-CVR calculation in children with sickle cell disease (SCD) as they have known cerebrovascular impairment (3). We hypothesize that the maps computed with TFA will exhibit higher CVR than with standard correlation, and this improvement will be more pronounced in SCD compared to healthy controls.

Materials and Methods

Data from 62 children with SCD (age 10 to 18 years) and 35 age matched healthy controls were analyzed for this study. Subjects were scanned on a 3T clinical magnetic resonance imaging (MRI) (MAGNETOM Tim Trio, Siemens Healthcare, Erlangen Germany) with a 32-channel head coil. BOLD data were acquired using a gradient-echo EPI (TR/TE=2000/30ms, FOV=220mm, matrix=64×64, slices=25, slice=4.5mm, time=8min) in synchrony with a CO₂ stimulus. The gas stimulus cycled between 60 seconds of normocapnia (CO₂=40mmHg, O₂=100mmHg) and 45 seconds of hypercapnia (CO₂=45mmHg, O₂=100mmHg). In addition, a high resolution anatomical scan was acquired. BOLD images were corrected for motion using FSL and the CO₂ waveforms were temporally aligned to the BOLD data. Using the TFA tool, voxel-wise Gain and Phase maps were generated. Standard CVR maps computed from temporal correlation also were calculated. The anatomical images were segmented into gray and white matter regions using FSL. CVR, Gain, and Phase maps for each subject were co-registered to anatomical space and averaged across gray and white matter regions. Group differences were determined with a Student's t-test. A linear regression analysis was performed between CVR and Gain and we tested for

significant differences between slopes in the patient data versus control data (4). A p-value <0.05 was considered statistically significant.

Results

Representative slices from CVR, Gain, and Phase maps for a SCD patient are provided in Figure 2. We see that CVR maps underestimate the CBF response compared to the Gain maps, especially in the white matter where the Phase maps indicate a delayed response. Group averages comparing CVR and Gain exhibit the same pattern in both groups, as shown in Table 1. Figure 3 plots CVR versus Gain for patients and controls, showing that the slope for patients is significantly higher in both grey and white matter with $p<0.01$ in both cases.

Conclusions

Using TFA, a more robust measure of CVR can be obtained as it is less sensitive to small variations in BOLD response time. We found that the difference between CVR and Gain is more prominent in children with SCD compared to healthy controls, suggesting that the disease may be affecting the response time of the cerebral vasculature.

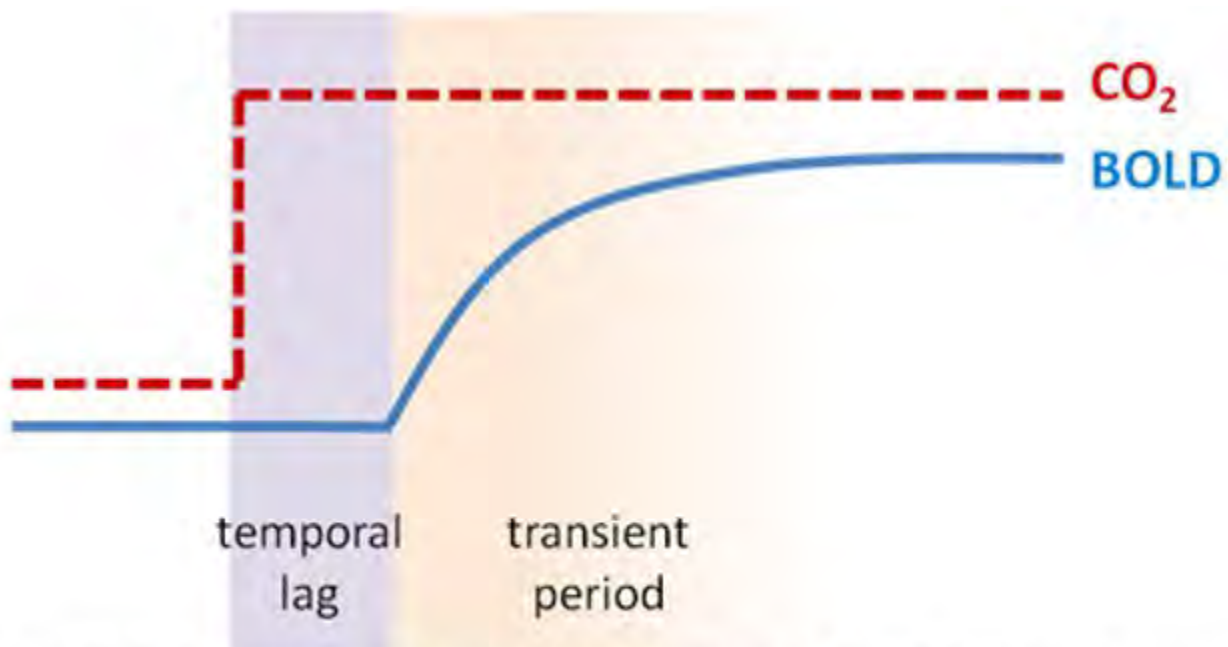


Figure 1. Diagram illustrating the sources of BOLD temporal delay in response to a step increase in CO₂.

(Filename: TCT_O-311_TFA_Figure1.jpg)

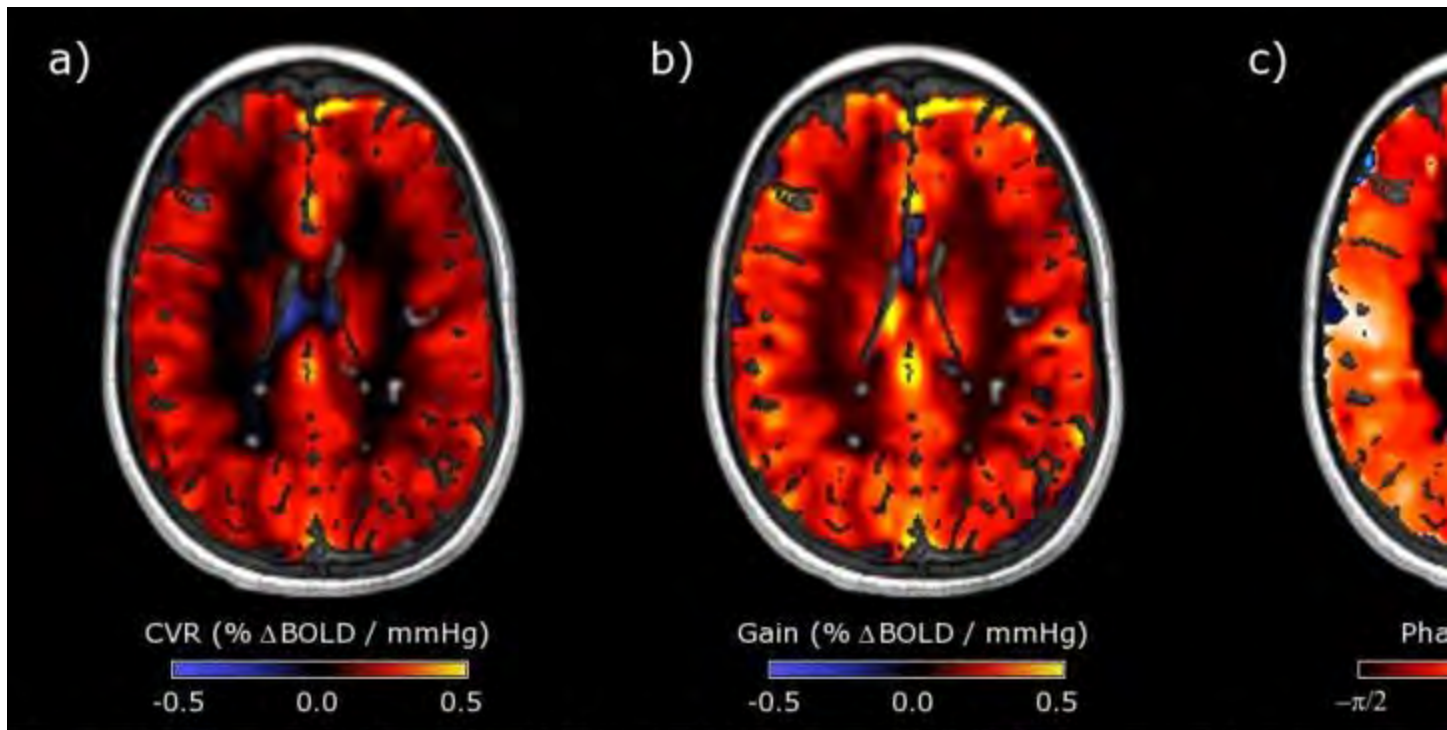


Figure 2. Example slice of a (a) CVR, (b) Gain, and (c) Phase map of a representative subject. (Filename: TCT_O-311_TFA_Figure2.jpg)

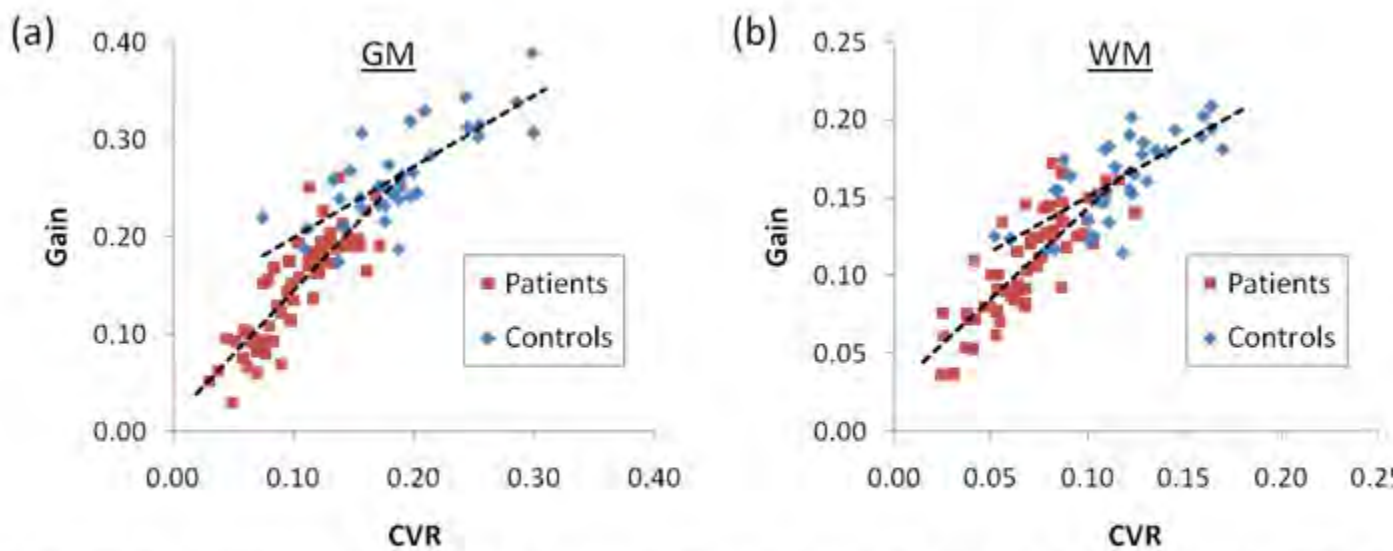


Figure 3. Mean CVR plotted against mean Gain in the (a) grey matter and (b) white matter. Trend lines have been added in black to show differences in slope between the patient and control groups.

(Filename: TCT_O-311_TFA_Figure3.jpg)

| | SCD Patients | | | Healthy Controls | | |
|----|---------------|---------------|--------------------------|------------------|---------------|--------------------------|
| | CVR | Gain | p-value | CVR | Gain | p-value |
| GM | 0.134 ± 0.058 | 0.191 ± 0.076 | 2.13 × 10 ⁻⁷ | 0.187 ± 0.052 | 0.262 ± 0.049 | 2.78 × 10 ⁻⁷ |
| WM | 0.086 ± 0.034 | 0.127 ± 0.041 | 1.13 × 10 ⁻¹¹ | 0.116 ± 0.029 | 0.162 ± 0.028 | 2.39 × 10 ⁻¹¹ |

Table 1. Regional group mean ± standard deviation for CVR and Gain.

(Filename: TCT_O-311_TFA_Table1.jpg)

O-312

11:09AM - 11:12AM

Physiological Fluctuations in the White Matter of Children with Sickle Cell Disease

J Leung¹, B MacIntosh², Z Shirzadi³, A Kassner¹

¹The Hospital for Sick Children, Toronto, Ontario, ²Sunnybrook Health Sciences Centre, Toronto, Ontario, ³The University of Toronto, Toronto, Ontario

Purpose

Sickle cell disease (SCD) is a genetic hemoglobinopathy affecting oxygen transport throughout the body due to the transformation of red blood cells into a rigid sickled shape. This leads to a cascade of physiological changes, including vascular impairment in the brain. Cerebrovascular dysfunction in SCD may be further exacerbated by arterial stiffness, which is a potential biomarker for cardiovascular mortality (1). One of the potential consequences associated with poor arterial compliance is increased intracranial pulsatility. Stiff arterial walls are unable to act as an elastic buffer to convert arterial pulsatile flow into steady peripheral flow (2). This effect has been observed in studies on small vessel disease and adult dementia, and has been termed physiological fluctuation in the white matter (PFwm), and can serve as a proxy of cerebrovascular dysfunction (3). Using resting state blood-oxygen level dependent (BOLD) magnetic resonance imaging (MRI) the fluctuations can be detected as temporal variations in the white matter (WM) signal, as defined by the equation in Figure 1. In the present study, we acquired PFwm data in children with SCD, and compared them to healthy controls. We hypothesize that SCD patients will exhibit greater WM fluctuations reflecting their underlying pathophysiology.

Materials and Methods

Nine pediatric patients with SCD (5 male, 4 female, age 10-17 years) and six age-matched healthy controls were imaged on a clinical 3T MRI scanner (MAGNETOM Tim Trio; Siemens Medical Solutions, Germany) using a 32-channel head coil. Baseline fluctuation data were acquired using a BOLD sequence (TR/TE =

2000/40ms, FOV = 220mm, matrix size = 64×64, slices = 25, slice thickness = 4.5mm, volumes = at least 120). In addition, a T1-weighted image (MPRAGE, voxel = 1 mm isotropic) was acquired for anatomical information. A WM mask was generated by segmenting the T1-weighted data and coregistered into the BOLD space using AFNI. The BOLD data were corrected for motion (MCFLIRT, FSL) and the temporal mean and variance across the time-series in each voxel was computed. Next, we calculated the spatial average of the variance and mean within the regions defined by the WM mask. Thermal noise variance was calculated from a region drawn outside of the brain. Differences in PFwm between groups were calculated using Student's t-test, with significance defined as $p < 0.05$.

Results

Figure 2 shows representative PFwm maps superimposed onto anatomical slices comparing a SCD and healthy subject. The mean PFwm was significantly higher in children with SCD (0.182 ± 0.096) compared to the control group (0.085 ± 0.019), with $p = 0.016$. A plot comparing the two groups is provided in Figure 3.

Conclusions

The increased WM pulsatility in SCD patients supports a possible link between PFwm and cerebrovascular dysfunction. This increase may be driven by the combination of anemia-induced vasodilation and reduced nitric oxide bioavailability (4), each contributing to arterial stiffening. Our results show that PFwm has the potential to be a clinically relevant tool in the assessment of SCD and other cerebrovascular diseases.

$$PF_{wm}^2 = \frac{\sigma_{wm}^2 - \sigma_{thermal}^2}{\mu_{wm}^2}$$

Figure 1. Equation for Physiological Fluctuation, where σ^2 is the temporal variance and μ is the temporal mean.

(Filename: TCT_O-312_PFwm_Figure1.jpg)

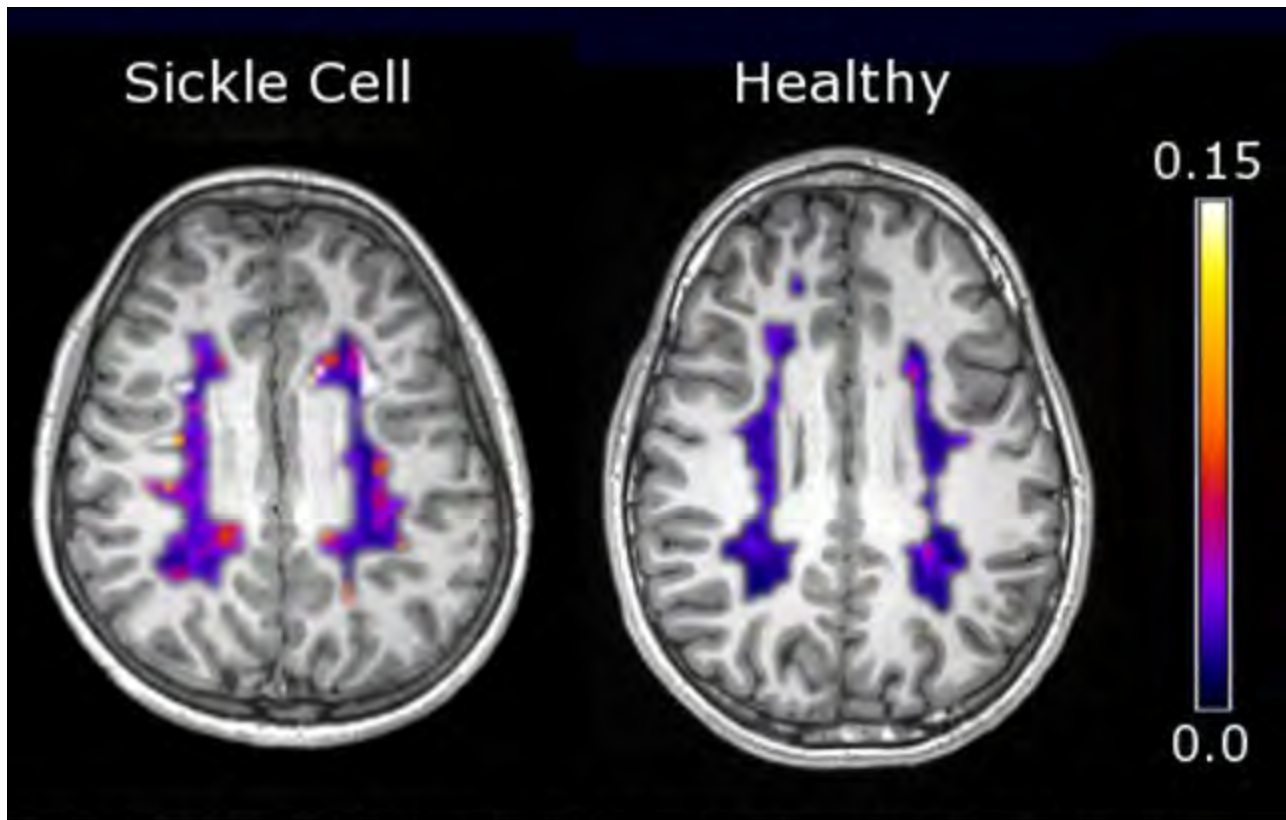


Figure 2. Representative PFwm maps in a sickle cell and healthy subject.

(Filename: TCT_O-312_PFwm_Figure2.jpg)

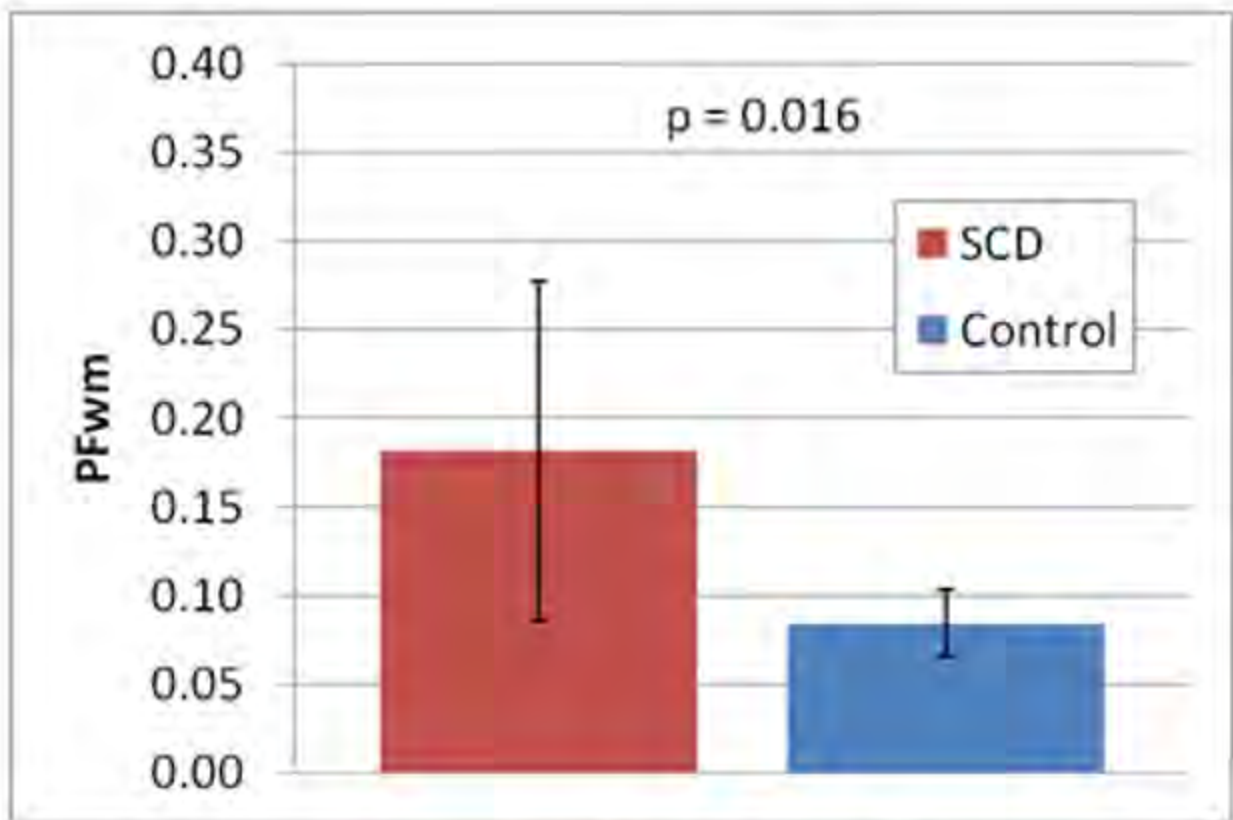


Figure 3. Group mean and standard deviation of PFwm in sickle cell patients and healthy controls.

(Filename: TCT_O-312_PFwm_Figure3.jpg)

O-313

11:12AM - 11:15AM

Quantification of Global Phase-based Venous Oxygenation in Children with Sickle Cell Disease

P Croal¹, M Serafin², J Leung¹, A Kassner¹

¹The Hospital for Sick Children, Toronto, Ontario, ²The University of Toronto, Toronto, Ontario

Purpose

Venous oxygen saturation (Y_v) enables quantification of oxygen extraction fraction (OEF) and cerebral metabolic rate of oxygen (CMRO₂). In this study we compare two approaches for global quantification of Y_v based on clinically available magnetic resonance imaging (MRI) sequences. Firstly, the infinite cylinder (IC) method (1), the most commonly used MR-susceptometry technique and secondly, the forward field (FF) method (2), a recent modification of the IC method which accounts for specific

vessel geometry of each subject. We implement these methods in children with sickle cell disease (SCD), in whom oxygen dynamics are likely to be disrupted, due to high risk of overt ischemic stroke in children.

Materials and Methods

Eleven SCD patients (8M/3F, 13.5 ± 3 years) and eight healthy controls (4M/4F, 13.8 ± 3 years) were imaged on a 3T MRI system. Magnitude and phase data were acquired using an SWI sequence (TR/TE=28/20 ms, FA=15°, $0.8 \times 0.7 \times 1.2$ mm³, 5 minute). Regions of interest (ROIs) were drawn on the magnitude image; (i) within and (ii) around the superior sagittal sinus (SSS), and applied to the filtered phase image to calculate the phase difference (Fig. 1). For both methods, Y_v was quantified from phase difference according to Equation 1, assuming a susceptibility difference between tissue and deoxyhemoglobin of $\Delta X_{do} = 0.27$ ppm (cgs) and a gyromagnetic ratio $\gamma = 2.675 \times 10$ for 3T. Hematocrit (Hct) was assumed to be 0.41 for healthy males, 0.39 for healthy females, and obtained via a blood sample for patients. The IC method was applied in five slices in which the SSS was most parallel to the main magnetic field (B_0), such that $A \approx 1/3$, where A is a geometric scaling factor accounting for shape. For the FF method, $\Delta\phi$ was calculated in slices where the SSS was clearly visible, and a forward field calculation (3) applied to estimate field perturbation within the SSS, from which A was calculated, accounting for SSS geometry.

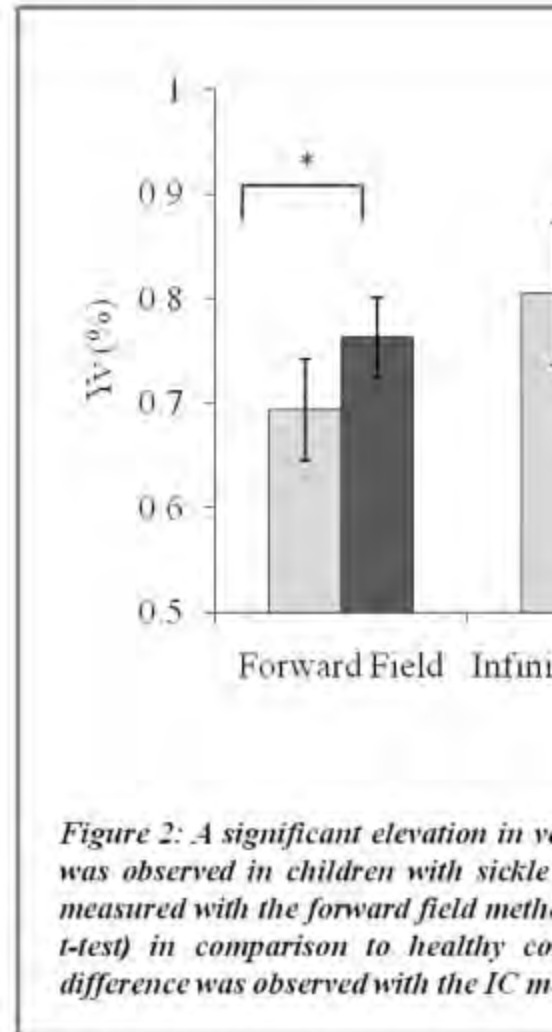
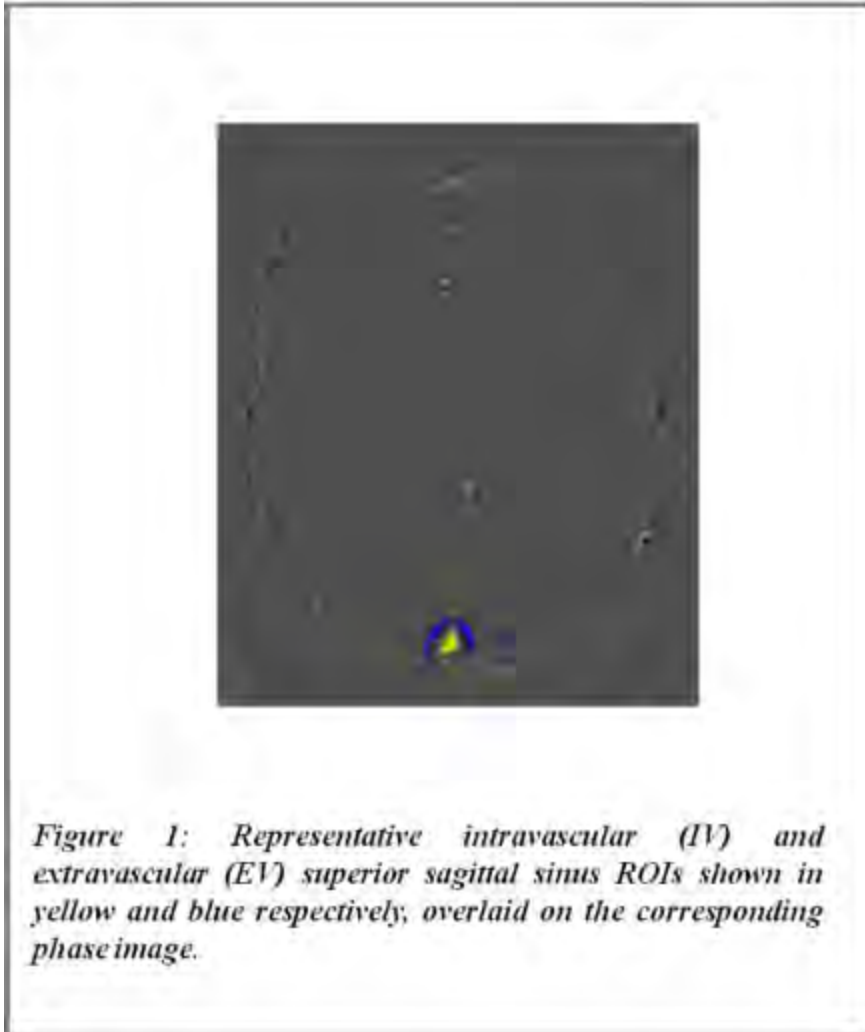
Results

Figure 2 shows a significant elevation in Y_v in SCD patients in comparison to healthy controls, as quantified with the FF method. The IC method showed a trend for increased Y_v in SCD patients in comparison to controls. For both groups, Y_v was significantly higher when quantified with the IC method in comparison to the FF method.

Conclusions

Here we observed elevated Y_v in children with SCD in comparison to controls, demonstrating both the first implementation of the FF method in a clinical population. This was significant only for the FF method, suggesting that by capturing individual variations in venous shape, sensitivity to pathophysiological changes in Y_v is increased. The FF method therefore may be preferable to the IC method in clinical populations.

$$Y_v = 1 - \frac{\Delta\phi_{IV}}{\Lambda \cdot \gamma \cdot TE \cdot B_0 \cdot Hct \cdot \Delta\chi_{do}}$$



(Filename: TCT_O-313_Yv_ASNR.png)

O-314

11:15AM - 11:18AM

Improvement of Neurocognitive Function, BOLD fMRI Activation and Transcranial Doppler Velocities in Pediatric Sickle Cell Anemia Patients Treated with Hydroxyurea

K Helton¹, A Jones¹, P Zou¹, J Hankins¹, J Schreiber¹, R Ogg¹
¹St. Jude Children's Research Hospital, Memphis, TN

Purpose

Sickle cell anemia (SCA) is a hereditary hemoglobinopathy, associated with cerebral vaso-occlusive disease, elevated transcranial doppler (TCD) velocities, silent infarctions, and stroke. Even with normal appearing brains by magnetic resonance imaging (MRI) declining neurocognitive function is well described in school aged children with SCA. We previously have shown that Intelligence Quotient (IQ) was associated with the blood oxygenation level-dependent (BOLD) MRI response to visual contrast stimulus (VCS) in children with SCA. This study utilizes BOLD functional magnetic resonance imaging (fMRI) and TCD velocities to compare hydroxyurea-treated and untreated groups of children with SCA to evaluate the effect of therapy on brain function.

Materials and Methods

After informed consent, untreated pediatric SCA patients without clinical history of stroke were enrolled in an Institutional Review Board approved prospective neuroimaging study. Patients underwent laboratory, BOLD functional MRI with VCS, TCD velocities and neuropsychological testing at baseline and after 12 ± 3 months. Patients were divided into two groups based on treatment status: hydroxyurea (HU) treated ($n=15$, mean age 12.7 ± 3.4 years) and untreated ($n=9$, mean age 11.4 ± 2.9 years).

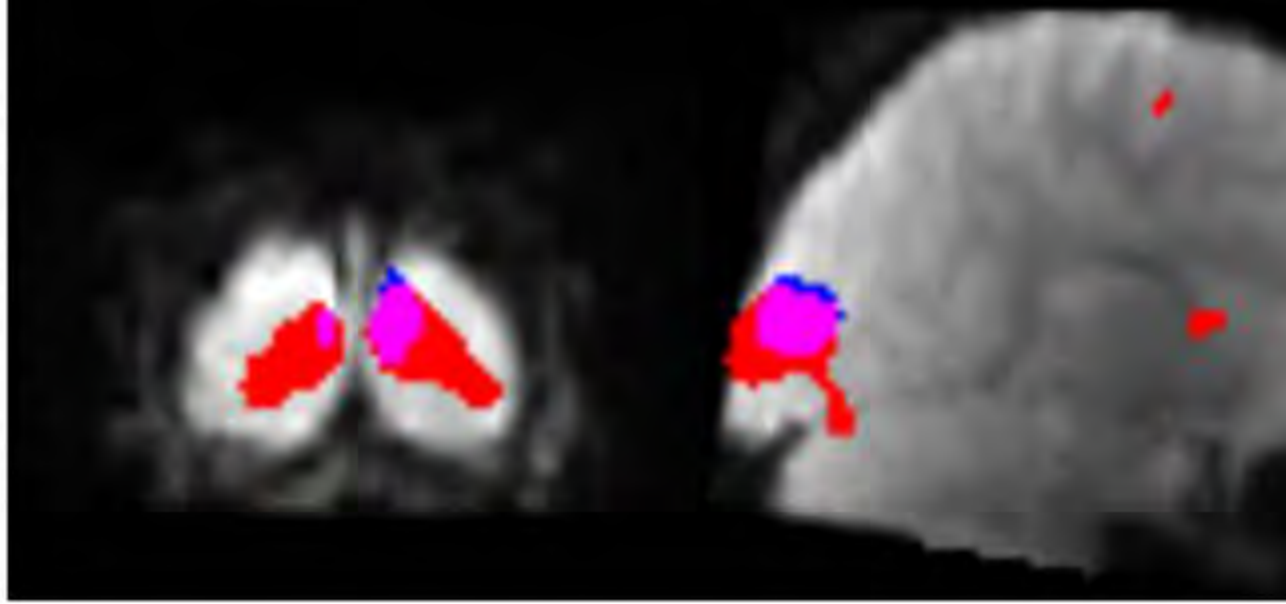
Results

All measures improved in the treated group: [increased BOLD response to VCS ($p=0.032$), decreased middle cerebral artery (MCA) TCD velocities ($p=0.005$), increased IQ score ($p=0.018$)] compared with baseline examinations. All measures systematically declined in the untreated group [decreased BOLD response ($p=0.352$), increased MCA TCD velocities ($p=0.191$), decreased IQ score ($p=0.130$)] compared with baseline examinations, but the differences were not significant.

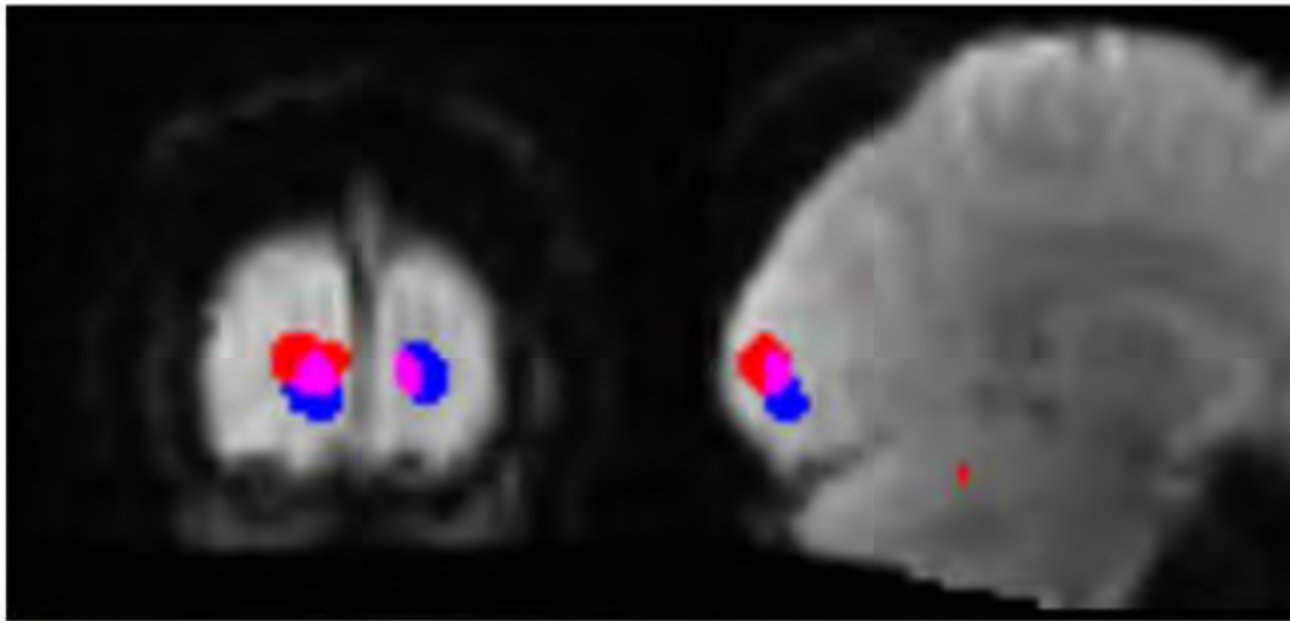
Conclusions

One year of hydroxyurea therapy leads to measureable improvement of global IQ in previously untreated children with SCA. Corresponding improvement in MCA velocities and visual cortex BOLD response suggest that improved brain function after hydroxyurea therapy is mediated in part by normalization of neural-hemodynamic coupling. Hydroxyurea therapy may not only prevent decline, but actually improve neurocognitive function in patients with SCA.

HU treated



untreated



■ BASELINE ■ +1 YEAR ■ OV

$T > 4.6$, $p < 0.05$ (Family-Wise Error Cor

(Filename: TCT_O-314_HeltonASNR2016_v2.jpg)

Wednesday

10:30AM - 12:00PM

Washington Marriott Wardman Park, Maryland A/B/C

15E-CSF Programming: Normal Pressure Hydrocephalus (NPH) and Chiari I

15E-1

10:30AM - 10:55AM

Diagnosis and Management of Chiari

Rekate, H.
The Chiari Institute
Great Neck, NY

15E-2

10:55AM - 11:20AM

Computational Flow Dynamics of Chiari

Haughton, V.
University of Wisconsin School of Medicine and Public Health
Oconomowoc, WI

15E-3

11:20AM - 11:45AM

PC-MRI in Evaluation of NPH

Bradley, W.
USD Medical Center
San Diego, CA

15E-4

11:45AM - 12:00PM

Discussion

Wednesday

10:30AM - 12:06PM

Washington Marriott Wardman Park, Roosevelt 4

15F-PARALLEL PAPER SESSION: Informatics: Analysis Tools and Optimized Workflow

O-315

10:30AM - 10:38AM

Development and Optimization of a Bayesian Expert System for Diagnosis Support in Neuroradiology

E Botzolakis¹, S Mohan¹, I Nasrallah², H Kundel¹, E Herskovits³, R Bryan¹
¹*University of Pennsylvania, Philadelphia, PA*, ²*HUP, Philadelphia, PA*, ³*University Of Maryland, Baltimore, MD*

Purpose

Applications capable of providing diagnosis support in neuroradiology currently are limited. We therefore aimed to develop a novel diagnosis support system which takes as input key features (KFs) extracted from brain magnetic resonance images (MRIs) and outputs a rank-ordered differential diagnosis (DDx) using a Bayesian network. We hypothesized that a Bayesian expert system could distinguish a nearly comprehensive list of adult neuroradiology diseases with better performance than a radiology resident.

Materials and Methods

A naïve Bayesian network (BN) was developed based on expert beliefs, which incorporated 123 diseases (including normal) and 13 KFs (brain MRI signal and spatial characteristics, and patient age). To evaluate network performance, 450 brain MRIs were selected randomly from our imaging archives (77 diseases represented thus far), with ground truth (GT) determined after review of clinical, radiologic, and pathologic records. Six readers (2 neuroradiology attendings, 2 neuroradiology fellows, and 2 radiology residents) reviewed each case, extracted KFs, and provided a "top 3" DDx for each case. Reader-extracted KFs were entered into the BN, which also generated a DDx for each case. We compared reader and BN DDx to GT using receiver operating curve (ROC) analysis. Partial area under the curve (pAUC) from 0 to 0.15 was calculated based on reader and BN ability to identify GT among their top 3 DDx. To improve network performance, reader-extracted KFs were used to "train" the expert BN using established machine learning algorithms, resulting in a hybrid data-driven network composed partly of probabilities calculated from observed KFs, and partly from expert beliefs for disease entities where data were sparse.

Results

Performance of the readers improved with higher levels of training (attendings,

fellows, and residents had overall accuracy rates of 54%, 45%, and 32% and pAUCs of 0.06, 0.04, and 0.02, respectively). Performance of the preliminary expert BN also was dependent on training level of radiologist extracting the KFs, but with decreased performance at all levels compared to the radiologists themselves (overall accuracy rates of 32%, 26%, and 23% and pAUCs of 0.02, 0.01, and 0.01 for attending-, fellow-, and resident-extracted KFs, respectively). Performance of the hybrid BN improved compared to the expert BN (overall accuracy rates of 48%, 40%, and 32% and pAUCs of 0.03, 0.02, and 0.01 for attending-, fellow-, and resident-extracted KFs, respectively).

Conclusions

Bayesian networks represent a promising approach to neuroradiology diagnosis support. Using a combination of expert beliefs and reader-extracted KFs from brain MRIs, we demonstrated that a hybrid BN can achieve diagnostic performance as good as a radiology resident regardless of KF source, and similar to neuroradiology fellows with attending-level KF extraction. With further optimization, we anticipate BNs can achieve even higher levels of diagnostic performance.

O-316

10:38AM - 10:46AM

Validation of an Expert-Based Bayesian Network for Discriminating Diseases Affecting the Basal Ganglia and Thalamus

E Botzolakis¹, I Nasrallah², H Kundel¹, E Herskovits³, R Bryan¹, S Mohan¹
¹University of Pennsylvania, Philadelphia, PA, ²HUP, Philadelphia, PA, ³University Of Maryland, Baltimore, MD

Purpose

Diseases affecting the basal ganglia and thalamus are challenging to diagnose on imaging, requiring consideration of multiple imaging features and often complex clinical history. Several studies have demonstrated the potential utility of Bayesian networks (BNs) for assisting imaging interpretation, reflecting their ability to integrate large amounts of probabilistic information for the purposes of generating a differential diagnosis. We aimed to develop an expert-based BN capable of discriminating diseases affecting the basal ganglia and thalamus, with the potential of eventually providing neuroradiology diagnosis support.

Materials and Methods

Using commercially available software (Netica, Norsys Software, Vancouver, Canada), a naïve BN was generated consisting of a parent "disease" node connected to multiple daughter "key feature" (KF) nodes. The disease node contained a broadly inclusive list of 52 diseases affecting the basal ganglia and thalamus in adults. A total of 26 KF nodes included magnetic resonance imaging (MRI) signal and spatial

characteristics, plus patient age and symptom acuity. Conditional probabilities, defined as KF probability given a particular disease, were generated from a combination of expert opinion and literature review. Bayesian network performance was evaluated using 120 clinically proven cases randomly selected from the imaging archives of our tertiary care university hospital, including 30 normals. A neuroradiology attending and fellow extracted KFs from these cases and entered them into the BN. By comparing the BN differential diagnosis to ground truth (GT) for each case, a confusion matrix was generated and used to evaluate BN performance.

Results

Of the 52 diseases represented in the BN, 34 were included within the set of test cases, with the number of cases per disease ranging from 1 to 4. When the highest probability diagnosis for each case was compared to GT, the expert-based BN demonstrated overall accuracy of 0.73, with sensitivity and specificity of 0.65 and 0.97, respectively. However, when the BN "top 3" differential diagnosis for each case was compared to GT (i.e., when the BN was given three chances to make the correct diagnosis), sensitivity increased to 0.85, with specificity unchanged. Based on sensitivity analysis, the five most discriminating KFs were (in decreasing order of entropy reduction): acuity of clinical presentation, mass effect, FLAIR signal, diffusion signal, and T1 signal.

Conclusions

An expert-based BN was developed with high discriminatory capacity for diseases affecting the basal ganglia and thalamus using reader-extracted KFs. With further parameter and structural optimization, we anticipate this BN eventually could be used for real-time neuroradiology diagnosis support.

O-318

10:54AM - 11:02AM

Natural Language Processing to Identify Type 1 Modic Endplate Changes in Older Adults

H Huhdanpaa¹, K Tan¹, S Rundell¹, P Suri², F Chokshi³, B Comstock¹, P Heagerty¹, K James¹, A Avins⁴, S Nedeljkovic⁵, D Nerenz⁶, J Jarvik⁷

¹University of Washington, Seattle, WA, ²VA Puget Sound Health Care System, Seattle, WA, ³Emory University School of Medicine, Atlanta, GA, ⁴Kaiser Permanente, Northern California - Division of Research, Oakland, CA, ⁵Brigham and Women's Hospital, Boston, MA, ⁶Henry Ford Health System, Detroit, MI, ⁷Univ of Washington, Seattle, WA

Purpose

Natural language processing (NLP) has the potential to extract meaningful data from free-text such as radiology reports. One use would be to identify potential subjects for

clinical trials. Recent work from Albert et al (1), implicate Propionibacterium as an infectious agent possibly associated with Type 1 Modic endplate changes. Their single center randomized trail indicated that some patients might benefit from antibiotic therapy. Our goal was to determine the validity and predictive value of an NLP algorithm to identify patients with Type 1 Modic endplate changes.

Materials and Methods

We annotated 154 randomly selected lumbar spine MR reports from a prospectively assembled cohort of older adults with back pain (2). Two annotators identified all reports that contained Type 1 Modic endplate change, and a senior neuroradiologist adjudicated discrepancies to create the reference standard. We then applied a rule-based NLP algorithm using Regular Expression, a string matching algorithm easily implemented in Python (Table 1). We calculated sensitivity, specificity, positive and negative predictive values (PPV and NPV).

Results

The prevalence of Type 1 Modic endplate changes was 6%. The sensitivity and negative predictive value of rule-based NLP were perfect, although the positive predictive value was only 67%. Most of the false positives were due to fracture-associated edema.

Conclusions

Rule-based NLP is a feasible approach for identifying patients with Type 1 Modic endplate change if the emphasis is on case finding and there is low concern regarding false-positives. If the research question requires better PPV, then consider other approaches, such as machine-learning NLP. We also plan to report how this approach performs in a larger cohort with greater age diversity, the Lumbar Imaging with Reporting of Epidemiology (LIRE) study.

Table 1: Details of Regular Expression Rule-based NLP

Synonyms:
 Endplate edema
 Endplate Modic change
 Modic type (1/I/one)
 Type 1 endplate/Modic change
 Modic type 1 degenerative endplate change
 Type 1 Modic degenerative endplate change
 Bone marrow edema
 (High/increased) signal
 High STIR signal
 Endplate changes are again seen
 Reactive marrow edema

Rules:
 Look ahead and behind in the same sentence that these words aren't there:
 Fracture
 Fat

Negations:
 Pre: No, negative, without, rule out, no existing, unremarkable, none, no evidence, no significant
 Post: not seen, not identified, cannot be excluded

Table 2: Comparison of NLP with Reference Standard Annotation for Type 1 Modic Change

| Rule-based NLP | Reference Standard Annotation | | | Total |
|----------------|-------------------------------|------------|--|------------|
| | Present | Absent | | |
| Present | 10 | 5 | | 15 |
| Absent | 0 | 139 | | 139 |
| Total | 10 | 144 | | 154 |

| Prevalence | Sensitivity | Specificity | PPV | NPV | Fscore |
|------------|-------------|-------------|------|------|--------|
| 0.06 | 1.00 | 0.97 | 0.67 | 1.00 | 0.80 |

(Filename: TCT_O-318_Tables.JPG)

O-319

11:02AM - 11:10AM

Computer Aided Reporting of Accurate Spine Level and Laterality According to Standardized Nomenclature: “Smart Annotation” in the Value-Based Imaging Era.

M Morris¹, B Saboury¹, J Hostetter¹, S Boateng¹, R Whiting², S Rothenberg¹, R Tu³, E Siegel¹

¹University of Maryland Medical Center, Baltimore, MD, ²George Washington University, Washington, DC, ³George Washington University Hospital, Washington, DC

Purpose

Spine laterality and disk level mistakes are critical reporting errors with potential major consequences affecting patients safety. In computed tomography (CT) or

magnetic resonance imaging (MRI) studies of the spine laterality and disk level of an abnormality guide the procedural approach and therefore accurate reporting is essential (1, 2). It was evaluated whether computer-aided reporting through the use of "smart annotations" and natural language generation (NLG) could provide accurate and reproducible structured reports for spinal disease according to the new Combined Task Force (CTF) standardized nomenclature.

Materials and Methods

Standardized annotation tracking with annotation image markup (AIM) can provide a method for computational processing of radiologist annotations as common data elements (CDEs) (3). A nearest neighbor mathematical algorithm is utilized in order to define the laterality and disk level based on annotation of the vertebral bodies. These CDEs then are formatted as xml and populated into a web-based graphical user interface to assign standard descriptors. The radiologist reviews the web form and adds additional observations. When the form is submitted, a structured report is generated according to the updated standardized CTF spine nomenclature.

Results

Computer-aided reporting of spinal disease allows for reliable structured reporting of the laterality and level of spine pathology, which is critical. A simple to use web interface was created and allowed for structured reporting using the standardized CTF nomenclature for spine disease through natural language generation.

Conclusions

This smart annotation tool for spine imaging can be used to extract essential report elements in real time during radiologist interaction with spine CT and MRI in a reliable and convenient way. Standardized reporting is essential to communicate consistent findings, to reduce misinterpretation of the intent of the radiologist, to reduce errors in medical settlements/judgements, and disability payments.

O-320

11:10AM - 11:18AM

Interrogating Log File Data to Understand the Effect of Imaged Body Region on the Occurrence of Repeated and Terminated Sequences.

J Andre¹, T Amthor², C Hall³, W Cohen¹, N Beauchamp¹

¹University of Washington, Seattle, WA, ²Philips Research Europe, Hamburg, Germany, ³Philips Healthcare, Bothell, WA

Purpose

Modality log files, like a "black box" used in modern aircraft, track metrics of magnetic resonance (MR) scanner efficiency including repeated sequences and patient table motion. We sought to document the effect of scanned body region on the

probability of sequence repetition and termination as a function of time during the examination.

Materials and Methods

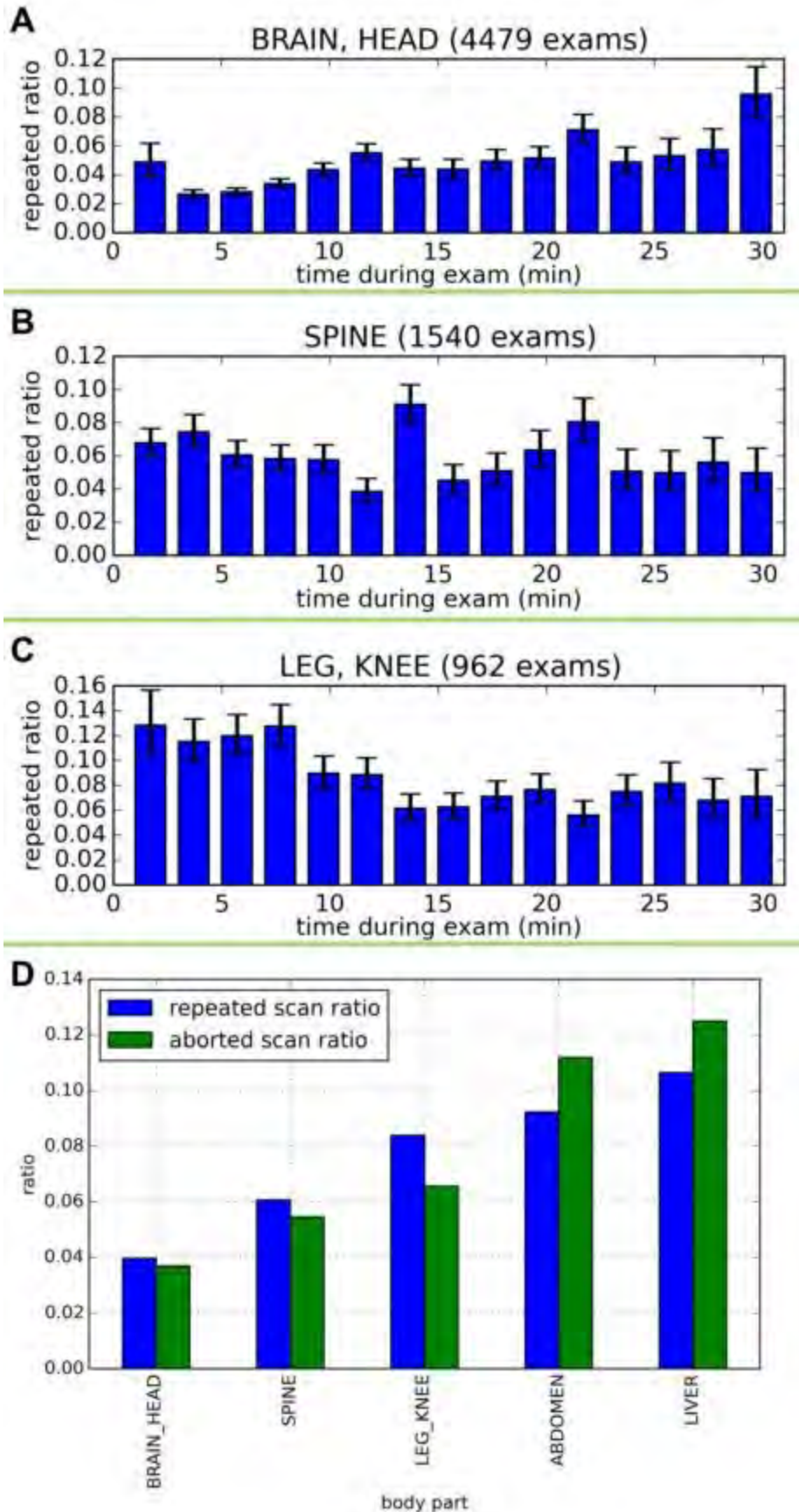
We retrospectively interrogated the log files of two identical 3T MR systems (Ingenia, Philips Healthcare, Best, The Netherlands) over a 2-year period (06/29/2013 – 09/10/2015). Log file data were evaluated and analyzed using in-house Python scripts. Statistical analysis was performed using a Wilson score to determine 95% confidence intervals for all probabilities.

Results

There were 4479 head and/or brain, 1540 spine, 438 abdomen, 1656 liver, and 962 leg/knee examinations evaluated. Log file-based probabilities are depicted as a function of the time the patient spends inside the magnet bore in Figure 1A-C, where the bars indicate the probability of a sequence begun within the respective time interval to be repeated. For head and/or brain exams, there is a higher repetition probability at the beginning of the exam, a clear minimum near 2.5-10 minutes, followed by a general trend of rising scan repetition probability as the scan approaches 30 minutes. However, this trend is not followed for spine and leg/knee exams suggesting that the shape of the motion curve varies based on scanned anatomical region, and may be potentially influenced by sequence-specific sensitivity to motion (secondary to the employed readout method), as well as patient position within the bore of the magnet (feet-first positioning routinely used for abdomen, liver and leg exams, and head-first positioning used for brain, head and spine exams). Figure 1D depicts the cumulative ratio of repeated and aborted sequences relative to scanned anatomical region (where "scan" = sequence).

Conclusions

The use of log files can detect patterns of scanner and exam performance, that may vary based on anatomical region scanned, and may be useful in identifying pitfalls to diagnostic imaging in a clinical environment.



(Filename: TCT_O-320_plots_BRAIN_HEAD_LEGV2.jpg)

O-321

11:18AM - 11:26AM

Radiological Assessment of Patient Motion Correlated with the Incidence of Repeat Sequences Documented by Log Files.

J Andre¹, T Amthor², C Hall³, W Cohen¹, N Beauchamp¹

¹*University of Washington, Seattle, WA*, ²*Philips Research Europe, Hamburg, WA*, ³*Philips Healthcare, Bothell, WA*

Purpose

Modality log files, like a "black box" used in modern aircraft, track metrics of MR scanner efficiency including repeated sequences and patient table motion. We sought to compare the radiological assessment of motion with the incidence of repeated sequences documented by scanner log files.

Materials and Methods

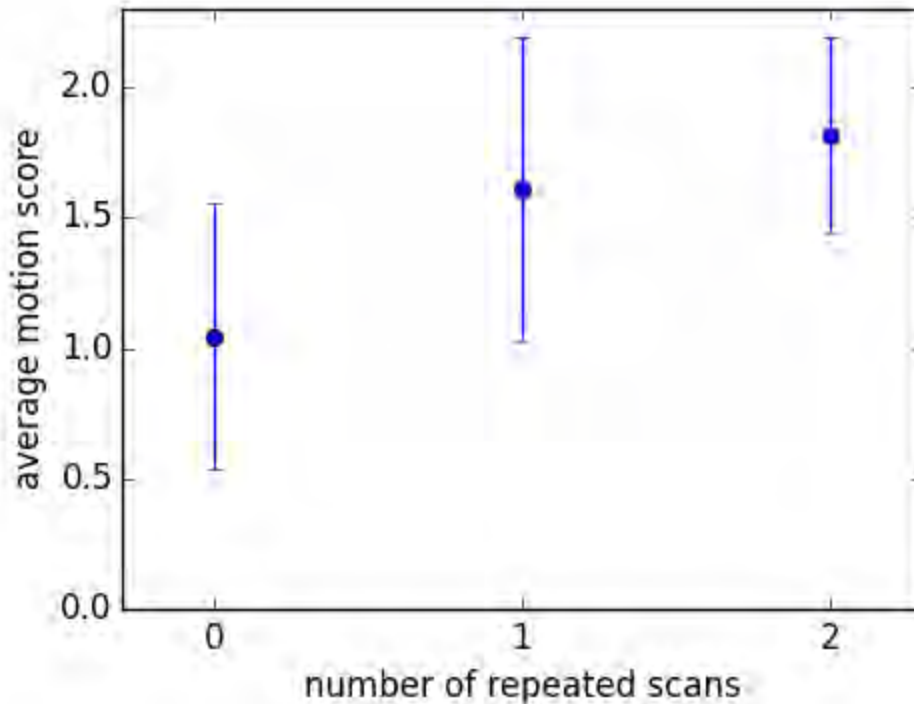
One neuroradiologist, blinded to all patient history and log file data, retrospectively evaluated one full calendar month (August 2014) of sequentially obtained clinical MR exams of the head and/or brain for the presence of motion artifacts using a previously defined clinical grading scale (1). All exams were acquired on one of two identical 3T MR systems (Ingenia, Philips Healthcare, Best, The Netherlands). Log file data from these exams were analyzed using in-house Python scripts. Statistical calculations included a Wilson score to determine 95% confidence intervals for the score ratios, and Welch's t-test to exclude the hypothesis of equal means.

Results

Two hundred fourteen examinations of the head and/or brain, comprising 1600 sequences, were evaluated. Radiological motion assessment scores (0, none – 4, severe), evaluated as a function of time within the magnet bore, varied over the course of the exam generating the following trend: initially higher motion score near the beginning of the exam, a minimum at 5 to 10 minutes, and a steady rise in subsequent motion scores. Figure 1 depicts the average motion score per brain and head exams (cumulative scores divided by the number of sequences), relative to the log file documented incidence of repeated sequences within an examination. The hypothesis of equal means was rejected for the samples with 0 and 1 ($p=0.0009$), and 0 and 2 ($p=0.022$) repetitions, respectively, but not for samples with 1 and 2 repetitions ($p=0.26$). The number of exams with 0, 1, and 2 repetitions were 186, 18, and 4, respectively.

Conclusions

Log file data may help predict patterns of scanner and exam performance in a clinical environment, particularly with respect to patient motion.



(Filename: TCT_O-321_Fig_5_nrepeats_vs_motion_score.png)

O-322

11:26AM - 11:34AM

Accessible and Cost-effective 3D Printing in Neuroimaging.

A Krishnamoorthy¹, T Burtonwood²

¹Swedish Covenant Hospital, Chicago, IL, ²School of the Art Institute of Chicago, Chicago, IL

Purpose

The excitement surrounding open source three-dimensional (3D) printing is based primarily on how accessible desktop 3D printers have become in the past few years. Despite this trend, anatomical 3D printing in radiology for the most part remains a high cost endeavour which limits its accessibility. We present results from a 3D printing service started at a radiology practice that utilizes relatively low cost, widely available 3D printing equipment.

Materials and Methods

Anatomical data from computed tomography (CT) and magnetic resonance images (MRIs) of the brain, spine, and head and neck were translated into segmented anatomical models using Slicer (slicer.org). These models subsequently were processed for 3D printing utilizing a free open source software tool chain including

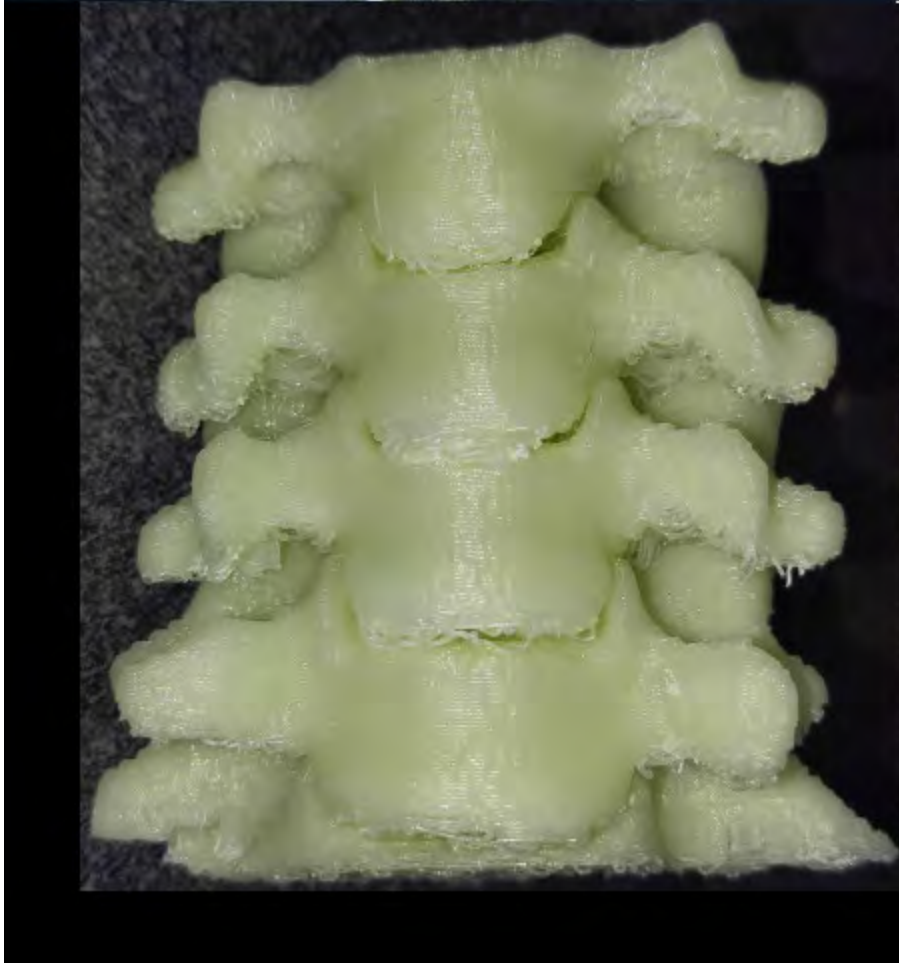
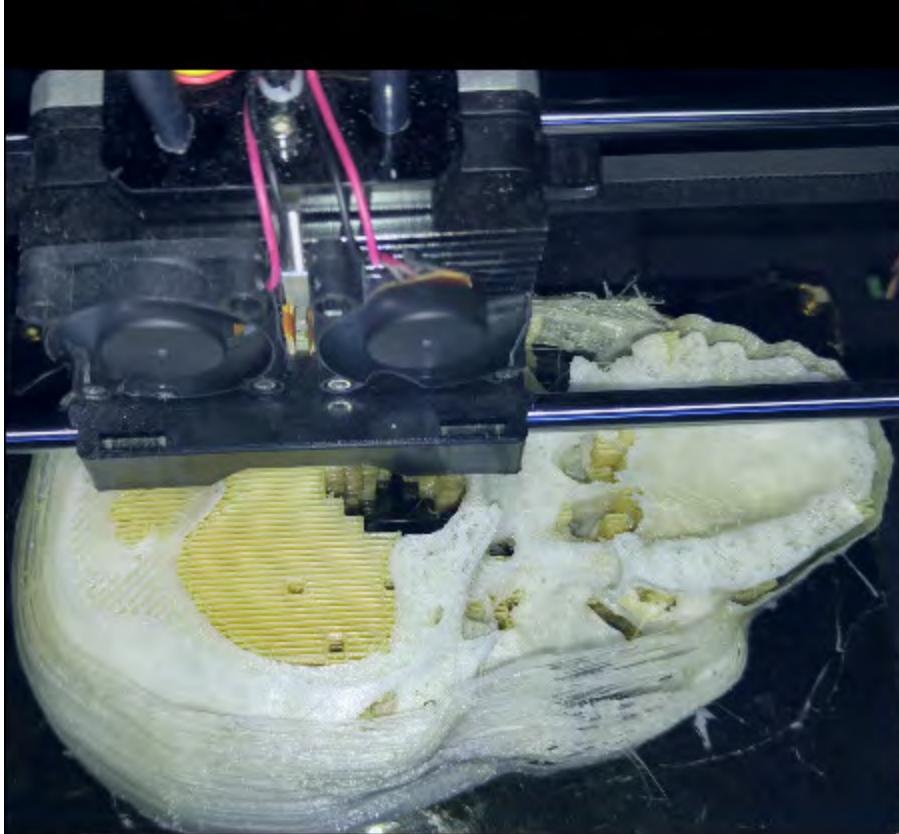
MeshLab (meshlab.sourceforge.net), ReplicatorG (replicat.org), Slic3r (slic3r.org) and GPX (github.com/whpthomas/GPX). The 3D printer employed was a Flash Forge Creator Pro (flashforge-usa.com) which can print with two materials simultaneously, produce structures with resolution of up to 0.1 mm, and has a build area suited for most head/neck and spine models. The plastic filament material used for model fabrication was polylactic acid (PLA) with polyvinyl alcohol (PVA) used occasionally for support material.

Results

So far, 17 anatomical 3D models of the head, neck and spine have been printed from CT and MR data since the acquisition of the equipment 7 months previously with increasing interest among our clinical colleagues. These life size, physical anatomical models have served as an adjunct to currently available computer graphic 3D renderings of anatomical data and were utilized primarily to assist with surgical planning and communicating planned procedures with the patient.

Conclusions

The popularity of 3D printing in large part is due to its accessibility and affordability, and we demonstrate how this model of open source 3D printing can be applied to medical imaging and specifically in a neuroimaging practice.



(Filename: TCT_O-322_3DprintAKTB_abstract2413.jpg)

O-323

11:34AM - 11:42AM

Demystifying the Course of the Facial Nerve Utilizing 3D Printing

D Davidson¹, M Bansal¹, A Choudhri², M Taheri³, R Javan¹

¹*George Washington University Hospital, Washington, DC*, ²*University of Tennessee Health Center, Memphis, TN*, ³*George Washington University, Washington, DC, DC*

Purpose

The goal of this exhibit is to demonstrate the methodology of designing a highly detailed custom educational physical 3D model depicting the complex three-dimensional course of the facial nerve. This is achieved by utilizing 3D printing from high-resolution computed tomography (CT) images combined with custom graphic design.

Materials and Methods

Images from a normal high-resolution CT of the temporal bone was used to three-dimensionally reconstruct the bony anatomy using Materialise Mimics 17.0, after manually perfecting the segmentation of bony anatomy on each thin slice of the scan. This 3D model was imported in Autodesk 3D Studio Max 2013 and split with a curved plane (craniocaudal) along the course of the facial nerve from its cisternal portion extending to the stylomastoid foramen. The parotid gland and retromandibular vein were added as landmarks for the extracranial portion of the course. The facial nerve itself also is graphically designed to fit the anatomical facial canal. The intracanalicular portion is designed to demonstrate the cross-sectional appearance relative to the Vestibulocochlear nerve branches. Subsequently 3D printing was performed through commercially available services utilizing rapid prototyping technology on polyamide material with minimum detail of 0.3 mm. Magnets also were embedded in the model for assembly. An additional small dual-material model was created with bone tissue represented as transparent material and the facial nerve as opaque color material.

Results

An enlarged detailed multipart physical model of the temporal bone was created with intricate detail for the specific use of teaching the complex course of the facial nerve.

Conclusions

Highly customized physical models easily can be developed for very specific teaching purposes. This exhibit is to demonstrate an example of such 3D printed models for a concept that is commonly difficult to grasp and visualize by radiology trainees, i.e., the three-dimensionally complex course of the facial nerve. This technique can be applied to numerous other areas of the head and neck, such as the pterygopalatine

fossa and the cavernous sinus, to simplify understanding complex anatomy with specifically tailored physical models. Knowing the exact course also helps the interpretation of pathologic conditions, such as trauma to the temporal bone or abnormal enhancement of the facial nerve when interpreting MRIs in the setting of peri-neural spread of tumor, clinical concern for Bell's palsy or presence of a nerve sheath tumor.

O-324

11:42AM - 11:50AM

Efficacy of Double-Blinded Peer Review in Neuroradiology

E O'Connor¹, M Cousar¹, J Lentini², M Castillo³, K Halm⁴, T Zeffiro⁵

¹Lewis Katz School of Medicine at Temple University, Philadelphia, PA, ²Temple University Hospital, Philadelphia, PA, ³Univ. Of North Carolina School Of Medicine, Chapel Hill, NC, ⁴American Journal of Neuroradiology, Oak Brook, IL, ⁵Temple University, Philadelphia, PA

Purpose

The American Journal of Neuroradiology (AJNR) uses double-blinded peer review to minimize potential reviewer bias concerning content, quality and recommendations. However, in a relatively small medical subspecialty such as neuroradiology, there are potential reasons why this process may be limited by reviewers' prior knowledge of the authors' work or ongoing studies at associated institutions. We sought to investigate the efficacy of blinding reviewers in AJNR and to determine the impact that unblinding may have on outcome of submitted manuscripts.

Materials and Methods

For manuscripts submitted to AJNR, from January through June 2015, AJNR reviewers completed a brief anonymous questionnaire after their blinded reviews. Questions assessed whether reviewers were familiar with the research prior to their reviews and their knowledge of the authors or institutions from which the work originated (Appendix A).

Results

Response rate for a total of 1,079 questionnaires offered to reviewers was 98.8%. 12.7% of reviewers knew or suspected that they knew the manuscript's author(s) and 15.1% knew or suspected that they knew the institution(s) from which the work originated. Reviewers who made guesses, correctly identified the author(s) of the submitted manuscripts in 90.3% of cases and correctly stated the institution(s) in 86.8% of cases. Unblinding resulted from self-citation in 34.1% of occurrences for both authorship and institutions. The rate of acceptance when reviewers knew or suspected they knew the author(s) was 57/137 (41.6%) and the rate of acceptance when reviewers did not identify the authors was 262/929 (28.2%). A binomial test

comparing proportions showed that familiarity with authors was associated with greater acceptance for manuscripts ($p < .0019$). Familiarity with institution also was associated with greater acceptance ($p < .046$).

Conclusions

The process of double-blinded peer review utilized by AJNR is largely effective in minimizing reviewer bias. Unblinding of authors is associated with a higher rate of manuscript acceptance.

Appendix A

AJNR Reviewer Questionnaire

| |
|---|
| 1. Can you identify principal author/s of manuscript reviewed? (A) I know I could (B) I suspect I could (C) I do not think I could |
| 2. Can you identify the institution/s from which the reviewed work originates? (A) I know I could (B) I suspect I could (C) I do not think I could |
| 3. Can you identify either the author/s or institution/s? (A) I know I could (B) I suspect I could (C) I do not think I could |
| 4. If you answered (A) or (B) for the above question, please enter the suspected author, institution or both. |
| 5. Were you familiar with the research finding before review? (A) Yes (B) No (C) Not sure |

(Filename: TCT_O-324_QuestionnaireTable.jpg)

O-325

11:50AM - 11:58AM

Comparison of Citation Frequency and Almetric Score in Articles Published by the American Journal of Neuroradiology

H Kelly¹, A Choudhri², J Ross³

¹Massachusetts General Hospital, Boston, MA, ²University of Tennessee Health Center, Memphis, TN, ³Mayo Clinic, Phoenix, AZ

Purpose

Our purpose was to evaluate the top articles from AJNR in altmetric score (a measure of online and social media mentions of an article) and citation frequency and to determine the characteristics of each of these groups of articles.

Materials and Methods

A SCOPUS search was used to identify the top 50 articles with the highest number of citations published in AJNR between January 2012 and December 2015. An Altmetric Explorer search was performed to identify the 50 AJNR articles with the highest altmetric scores. These groups were cross-referenced to identify any articles that appeared in both categories. Characteristics including citation data, altmetric score, topic and article type were compared.

Results

Only one article appeared in both the top 50 most cited and top 50 highest altmetric score groups. The most frequently cited articles averaged 10.8 citations/year compared to 3.1 citations/year for the articles with the highest altmetric scores ($p < 0.00001$). The average altmetric score in the top 50 articles was 41.9 compared to 0.8 for the 50 most frequently cited articles ($p < 0.03$). There was no correlation between the altmetric score and the rate of citations per year in either the top altmetric score group or the most frequently cited group ($R = 0.08$ and 0.16 respectively).

Conclusions

The most frequently cited articles published in AJNR are not the most likely to be mentioned online. There is no significant correlation between citation frequency and altmetric score, suggesting that online and social media mentions do not influence citation patterns and vice versa. These metrics may be independent measures of impact for neuroradiology articles.

O-326

11:58AM - 12:06PM

It's about time: A Time-Activity Study in Neuroradiology

A Al Yassin¹, M Salehi Sadaghiani², S Mohan², E Botzolakis², R Bryan², I Nasrallah²
¹New York Institute of Technology, Glen Cove, NY, ²University of Pennsylvania, Philadelphia, PA

Purpose

Although efficiency is critical to modern radiology practice, the specific distribution of activities performed by neuroradiologists at the workstation remains poorly understood. Indeed, knowledge of the timing and steps leading to final report

generation is essential for workflow optimization and departmental staffing decisions. We measured the time spent on each step from study opening to report signing to identify potential targets for optimization. Furthermore, we evaluated how these patterns differed between attendings and trainees.

Materials and Methods

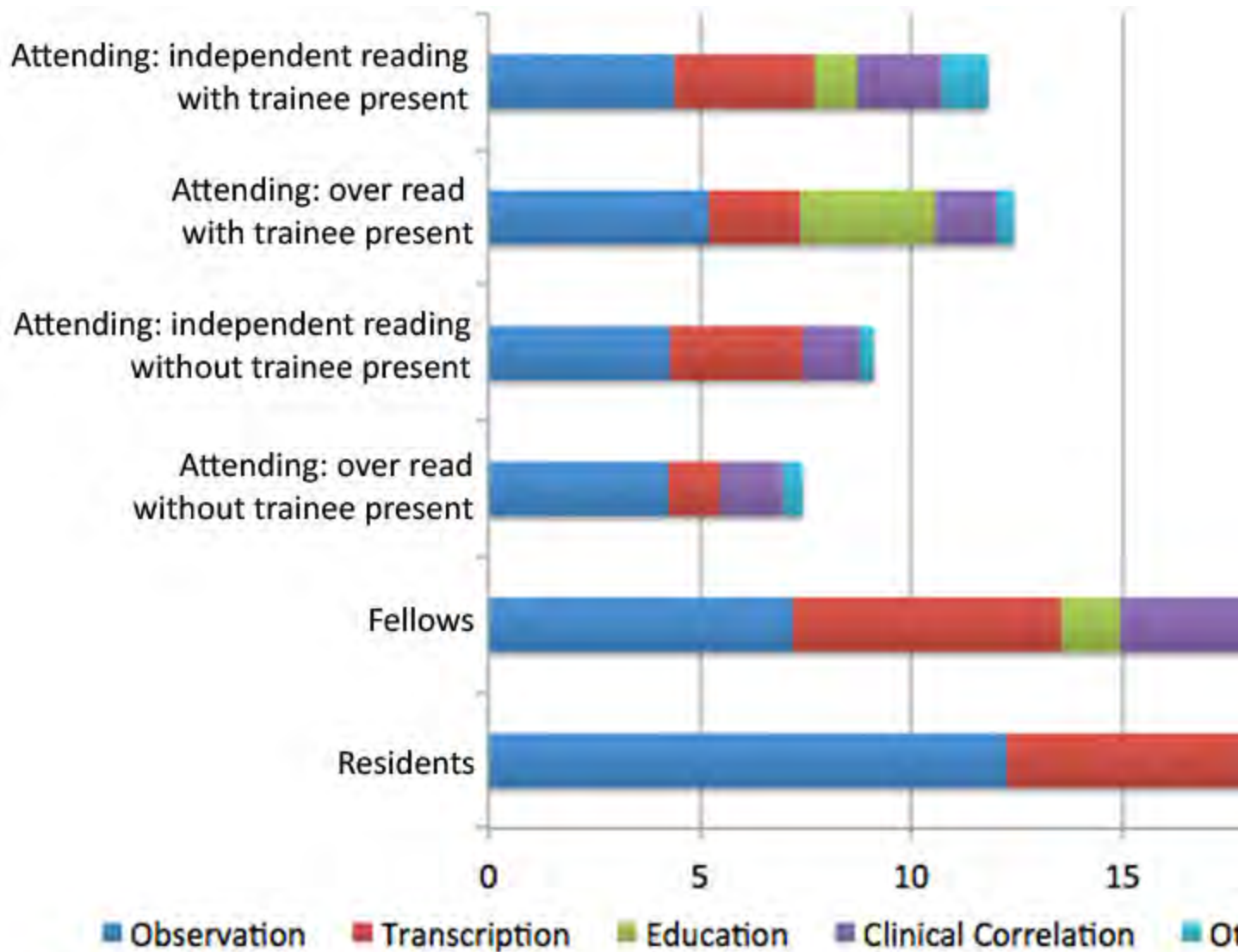
In this prospective observational study, radiologists were timed while interpreting 201 brain magnetic resonance images (MRIs) in a tertiary care academic practice over 5 weeks. We measured the total duration from study opening to report signing and time spent on five distinct activities during this period: image review, report transcription, obtaining correlative clinical data, trainee education, and other. Attendings, fellows and residents reading studies independently and attendings over-reading trainee-previewed studies were observed. ANOVA and t-tests were performed for statistical analysis.

Results

Attendings, fellows, and residents respectively spent a total of 13 +/- 8, 20 +/- 9 and 23 +/- 6 minutes (mean +/- standard deviation) when independently generating a brain MRI report. Mean duration was significantly different between attendings and fellows ($p=0.0002$) or residents ($p=0.003$) but not between fellows and residents. Although slightly less, mean duration for attendings reading independently was not significantly different from attendings over-reading trainees, with offsetting time spent on transcription/obtaining clinical data versus trainee education between the two settings. Attendings spent the same time on image viewing (mean 4.4 min) with or without trainees. Mean attending transcription time was shortest when over-reading trainees (about 1.2 min, with or without trainees present at the time of the attending read) and longest when reading independently (3.3 min), showing benefit of having a draft report. Fellows and residents had longer mean times for image viewing (7.2 min and 12.3 min, respectively) and transcription (about 7 min). Measurements of reading times showed high agreement between different observers.

Conclusions

Neuroradiologist time/activity distribution for brain MRI studies was measured, establishing a benchmark for future efforts to improve efficiency and decrease reporting times, specifically showing precedent for decreasing attending transcription time with the availability of a draft report. Furthermore, we show differences in total duration of report generation by level of training due to longer observation, transcription, and clinical correlation reporting times in trainees compared to attendings.



* p < 0.01 versus Attending: independent reading with trainee present, all others not significant

(Filename: TCT_O-326_Abstractfigure_1.jpg)

Wednesday

1:15PM - 2:45PM

Washington Marriott Wardman Park, Marriott Ballroom

16A-SNIS Programming: Trauma and the NeuroInterventionalist: The Management of the Endovascular Emergency

16A-1

1:15PM - 1:35PM

Diagnostic Neuroradiology in the Setting of Trauma of the Head and Neck: Spotting the Problem

Sunshine, J.
Univ. Hospitals Of Cleveland, Case Western Reserve Univ.
Cleveland, OH

16A-2

1:35PM - 1:55PM

Management of Traumatic Dissections of the Great Vessels of the Neck: Current Level of Evidence

Ansari, S.
Northwestern University, Feinberg School of Medicine
Chicago, IL

16A-3

1:55PM - 2:15PM

Acute Management of the Traumatic CCF

Armonda, R.
MedStar Health
Washington, DC

16A-4

2:15PM - 2:35PM

Acute Endovascular Management of Trauma of the Face and Neck

Gandhi, C.
Rutgers New Jersey Medical School
Newark, NJ

16A-5

2:35PM - 2:45PM

Panel Discussion

Wednesday

1:15PM - 2:45PM

Washington Marriott Wardman Park, Washington 4/5/6

16B-TBI - Advanced

16B-1

1:15PM - 2:45PM

Advanced Biomarkers of Traumatic Brain Injury for Precision Medicine

Mukherjee, P.

San Francisco VA Med Ctr

San Francisco, CA

16B-2

1:15PM - 2:45PM

Brain Imaging and Subconcussive Impacts in Sports-related mild TBI

Maldjian, J.

University of Texas Southwestern

Dallas, TX

16B-3

1:15PM - 2:45PM

Radiology Findings in Military TBI Using Advanced MR Imaging

Riedy, G.

The National Intrepid Center of Excellence

Arlington, VA

Wednesday

1:15PM - 2:45PM

Washington Marriott Wardman Park, Washington 1/2/3

**16C-ASFNR Programming: Cutting Edge Functional Imaging in
Neurodegenerative Disorders: New Concepts**

16C-1

1:15PM - 1:35PM

**Advanced Translational Approach to Functional Connectivity MRI in
Neurodegenerative Disorders**

Anderson, J.
University of Utah
Salt Lake City, UT

16C-2

1:35PM - 1:55PM

Functional MR in Alzheimers Disease

Petrella, J.
Duke University Medical Center
Durham, NC

16C-3

1:55PM - 2:15PM

Models of Graph Spread Can Predict the Spatio-Temporal Distribution of Neurodegenerative Disorders

Raj, A.
Weill Cornell Medical College, Cornell University
New York, NY

16C-4

2:15PM - 2:35PM

Metabolic Connectivity Pathways in Neurodegenerative Disease

Eidelberg, D.
The Feinstein Institute for Medical Research
Manhasset, NY

16C-5

2:35PM - 2:45PM

Discussion

Wednesday

1:15PM - 2:45PM

Washington Marriott Wardman Park, Roosevelt 1-3

16D-PARALLEL PAPER SESSION: Turbo Talks - Spine Innovations

O-327

1:15PM - 1:18PM

Novel Interventional Neuroradiology Techniques for the Treatment of Spinal CSF Leak as a Cause of Spontaneous Intracranial Hypotension

J Masur¹, J Stephen², B Pukenas³, P Marcotte², J Schuster², E Zager², L Bagley¹
¹*Pennsylvania Hospital, Philadelphia, PA*, ²*Hospital of the University of Pennsylvania, Philadelphia, PA*, ³*Hospital Of the Univ. Of Pennsylvania, Philadelphia, PA*

Purpose

Spontaneous intracranial hypotension (SIH) secondary to spinal cerebrospinal fluid (CSF) leaks causes significant neurological morbidity. While nontargeted lumbar epidural blood patch (EBP) can be an effective treatment for many, precise diagnostic localization of the CSF leak site and targeted treatment often is required in patients that fail EBP. The purpose of this study is to describe novel interventional neuroradiology techniques in the treatment of challenging spinal CSF leak cases, including working closely with neurosurgery to achieve cure through the least invasive approach. Specifically, we describe the use of pre-operative and intra-operative CT myelography to localize the leak and also targeted ventral epidural blood patch for ventrally located leaks.

Materials and Methods

Herein, we report a case series of eight patients undergoing diagnosis and subsequent treatment of spontaneous intracranial hypotension (SIH) secondary to spinal CSF leak. Each patient's clinical course through diagnosis and various treatment modalities is reported, as is the outcome for each patient. The novel techniques of ventral epidural blood patch (VEBP) and intra-operative CT myelography also are presented.

Results

We identified eight patients (mean age 37 years) diagnosed with spontaneous intracranial hypotension secondary to spinal CSF leak with diagnostic imaging. Localization of the leak site in our series was cervical in one case, thoracic in seven, with multiple sites in three. Utilizing a multidisciplinary approach to treatment, five cases underwent autologous blood patch, including two ventral epidural blood patches. During VEPB, iodinated contrast material was added to the autologous blood to delineate the extent of the autologous blood patch postinjection. Three of five

patients undergoing blood patch had resolution of symptoms not requiring further interventions. Three patients underwent neurosurgical intervention from a posterior approach. Intra-operative myelography was performed in two of these three cases. Reasons for patients undergoing surgical treatment included post-traumatic etiology of leak or failure of conservative management. Seven of eight patients reported a good outcome (resolution or significant improvement of symptoms) at a mean follow up of 8 months. Complications of treatment included development of hydrocephalus requiring shunting in one patient and possible concomitant skull base CSF leak in another patient.

Conclusions

In addition to the critical diagnostic role of identifying and localizing a spinal CSF leak, the neuroradiologist has an integral role in the treatment of spinal CSF leaks, as many patients may be treated successfully in the Interventional Suite alone. Our series demonstrates that VEBP appears to be an effective intervention for ventrally located leaks which are challenging to reach through open neurosurgical approaches. Also, intra-operative CT myelogram may be invaluable in cases requiring open neurosurgical leak repair. While SIH remains a diagnostic and therapeutic challenge, our series illustrates novel interventional neuroradiology techniques to supplement a multidisciplinary approach.

Figures:

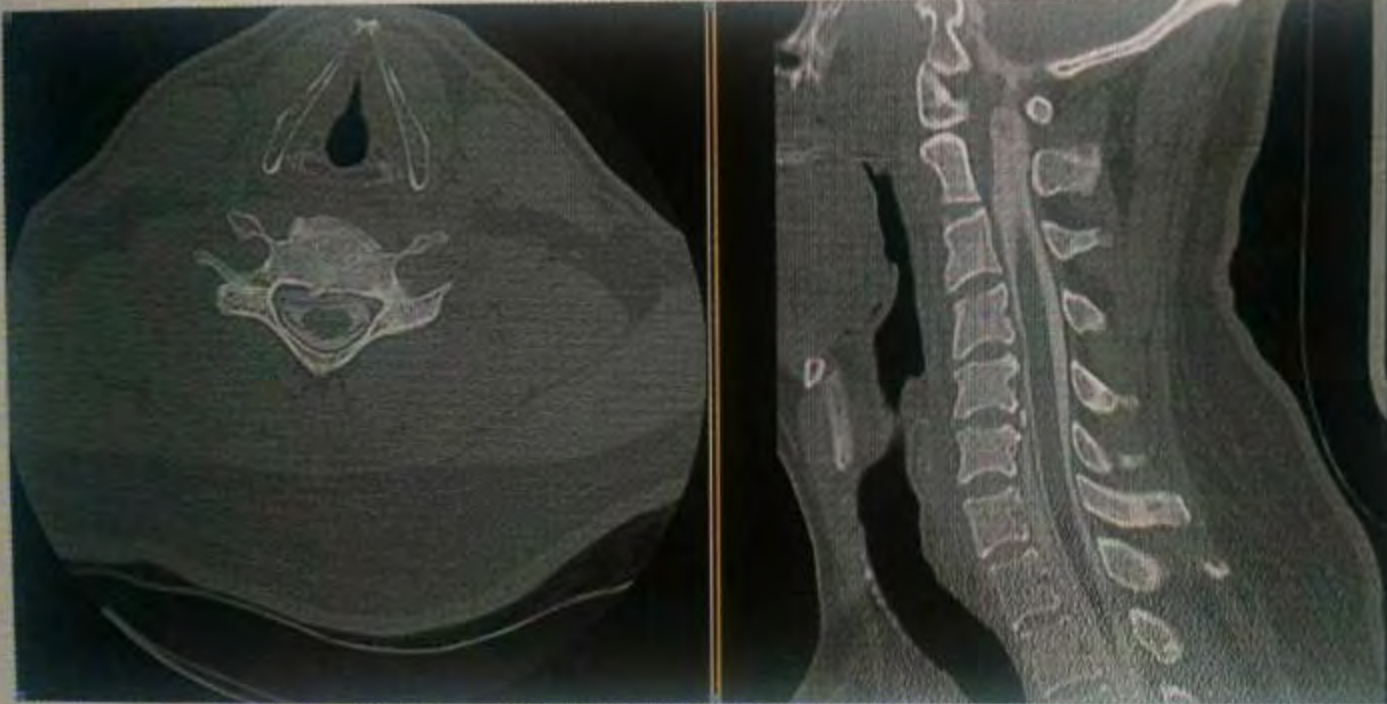


Figure 1. CT myelogram demonstrating a calcified disk/osteophyte complex at C5-6 ventral to the dural sac, consistent with a dural tear/CSF leak at C5-6.

(Filename: TCT_O-327_Image1.jpg)

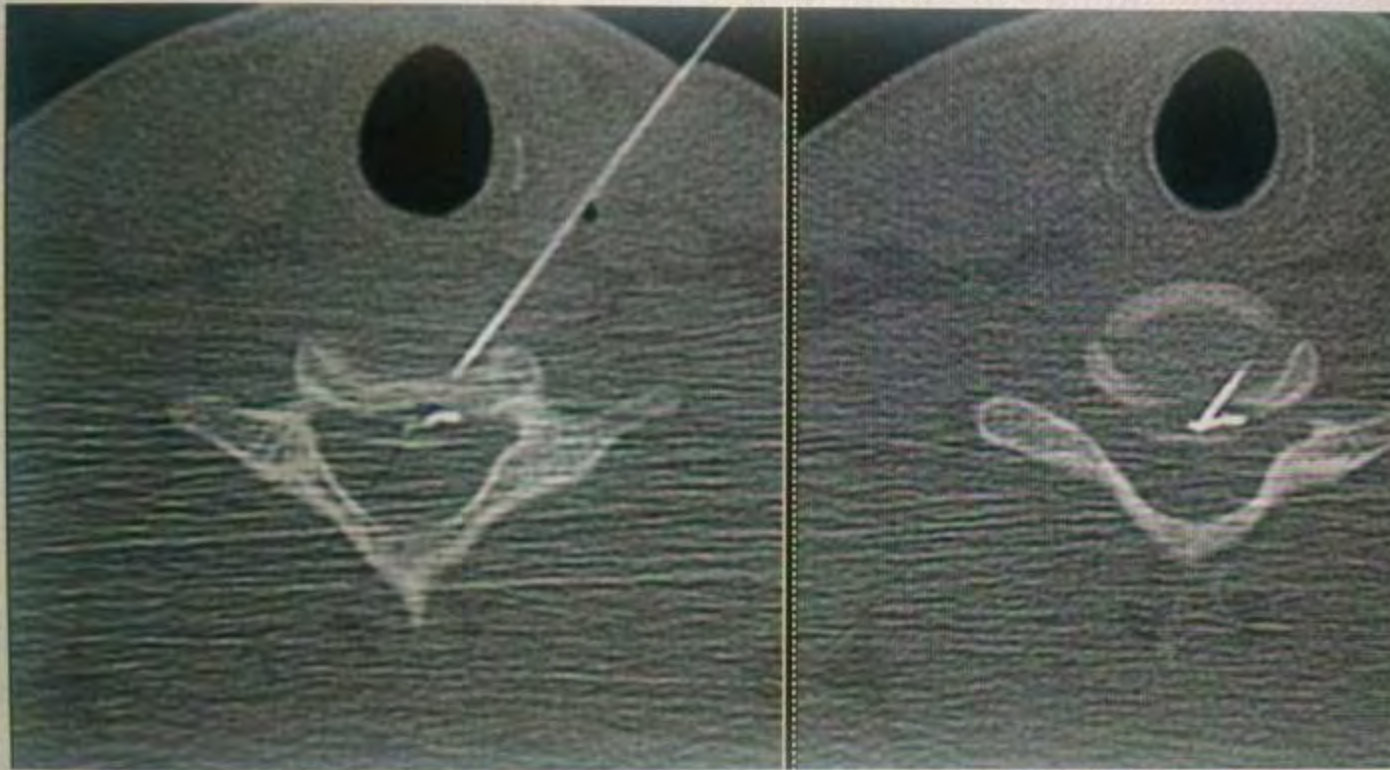


Figure 2. Contiguous axial CT images during injection of contrast confirming epidural needle tip, within the ventral fluid collection.

(Filename: TCT_O-327_Image2.jpg)

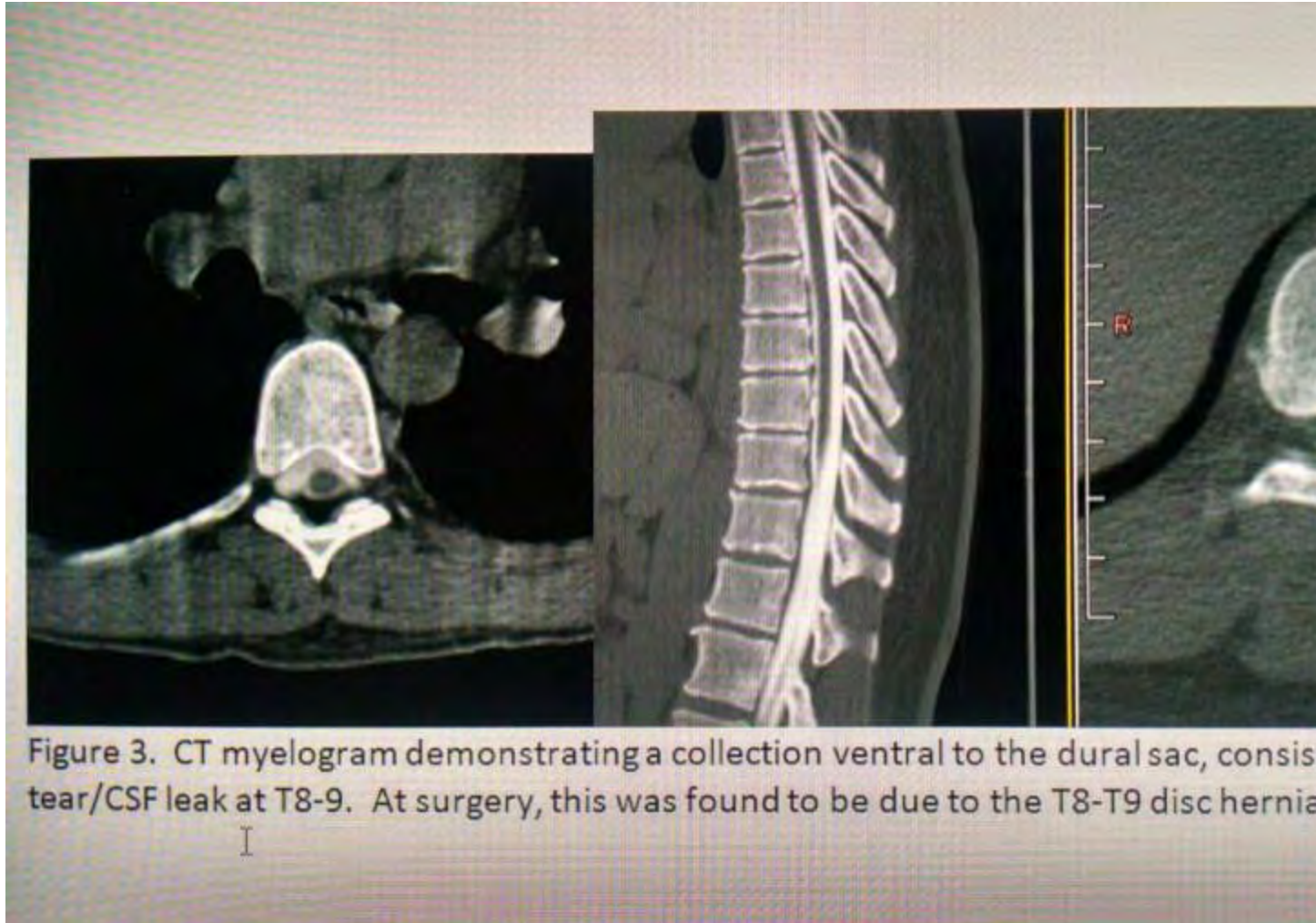


Figure 3. CT myelogram demonstrating a collection ventral to the dural sac, consisting of contrast material, consistent with a dural tear/CSF leak at T8-9. At surgery, this was found to be due to the T8-T9 disc herniation.

(Filename: TCT_O-327_Image31.jpg)

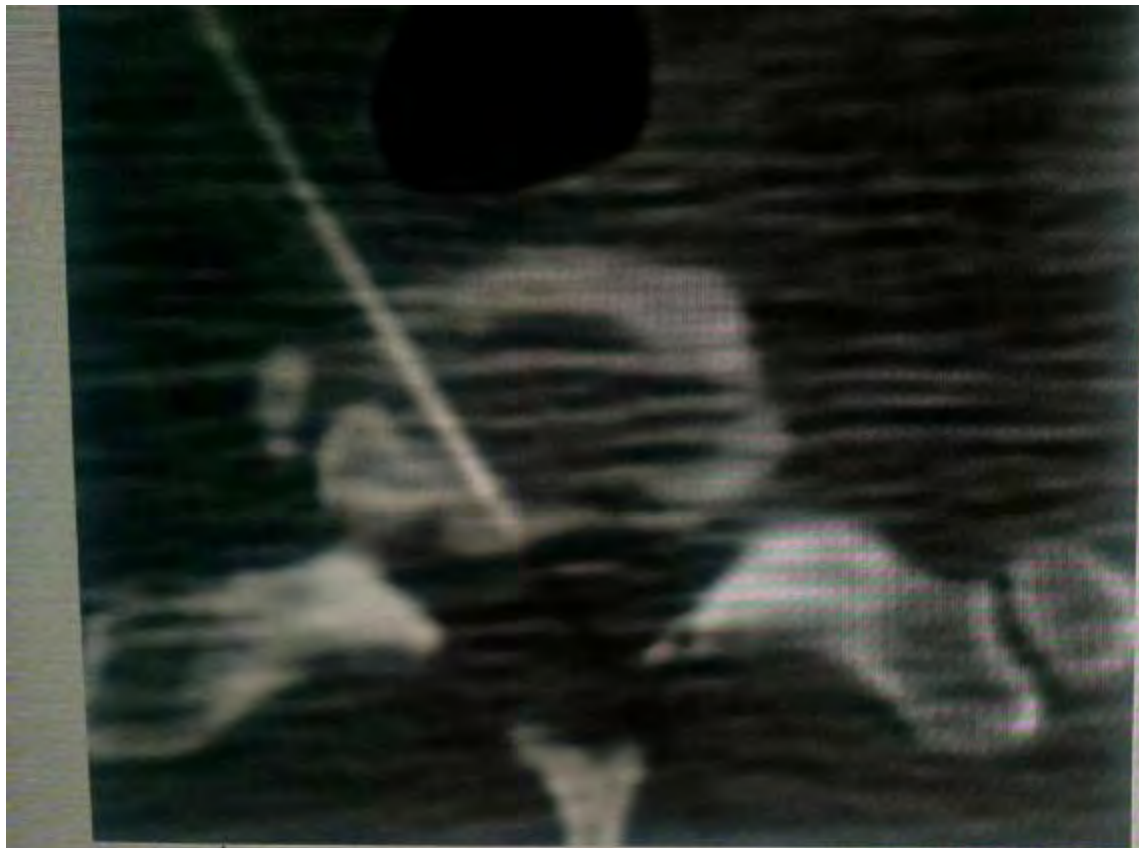


Figure 4. CT images during injection of contrast confirming epidural location of the the ventral fluid collection.

(Filename: TCT_O-327_Image4.jpg)

O-328

1:18PM - 1:21PM

Evaluation of the Intraforaminal Location of Prominent Anterior Radiculomedullary Arteries Using Flat Panel Catheter Angiotomography.

L Gregg¹, P Gailloud¹, D Sorte²

¹Johns Hopkins University School of Medicine, Baltimore, MD, ²University of New Mexico, Albuquerque, NM

Purpose

Flat-panel catheter angiotomography (FPCA) acquired during the selective injection of intersegmental arteries (ISA) has enabled multiplanar visualization of anterior spinal artery (ASA) contributors within the neural foramen. Unwarranted injection and/or injury of ASA contributors during transforaminal epidural steroid injections (TFESI), can result in spinal cord damage (1). Prior evaluations of the intraforaminal

location of these arteries have been limited to either the anteroposterior view (2) or to examination of cadaveric material (3, 4). The purpose of this study was to document the in vivo intraforaminal location of prominent thoracolumbar anterior radiculomedullary arteries using FPCA acquisitions.

Materials and Methods

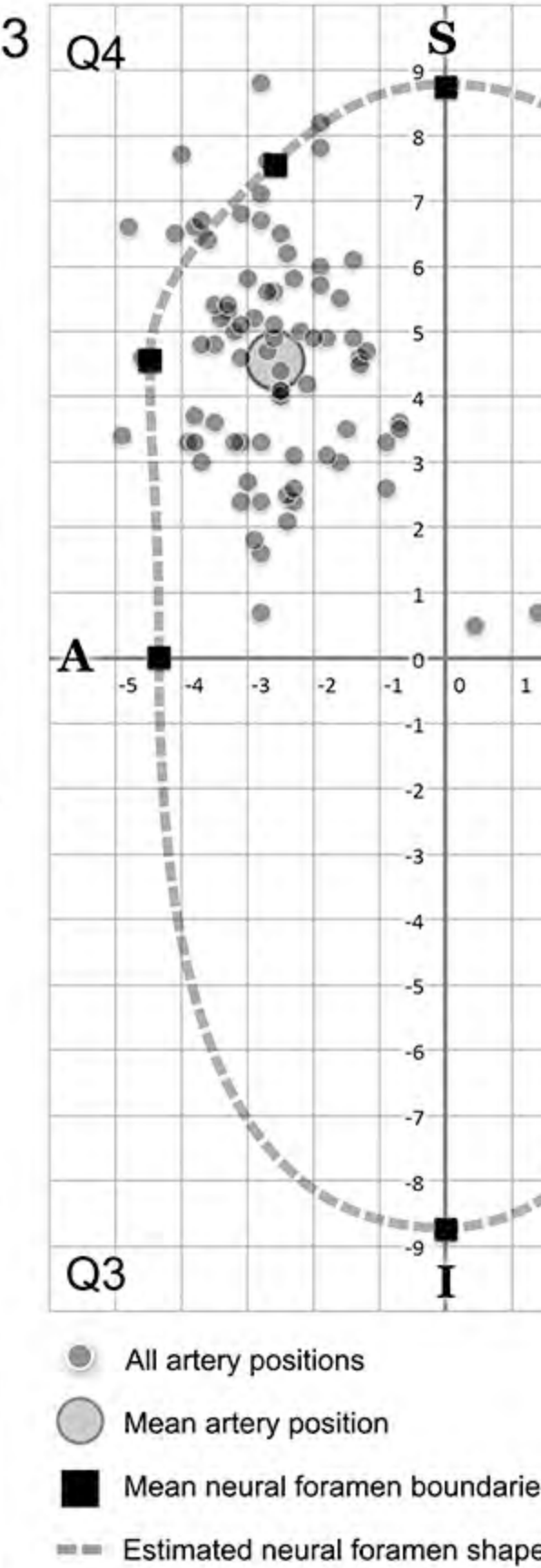
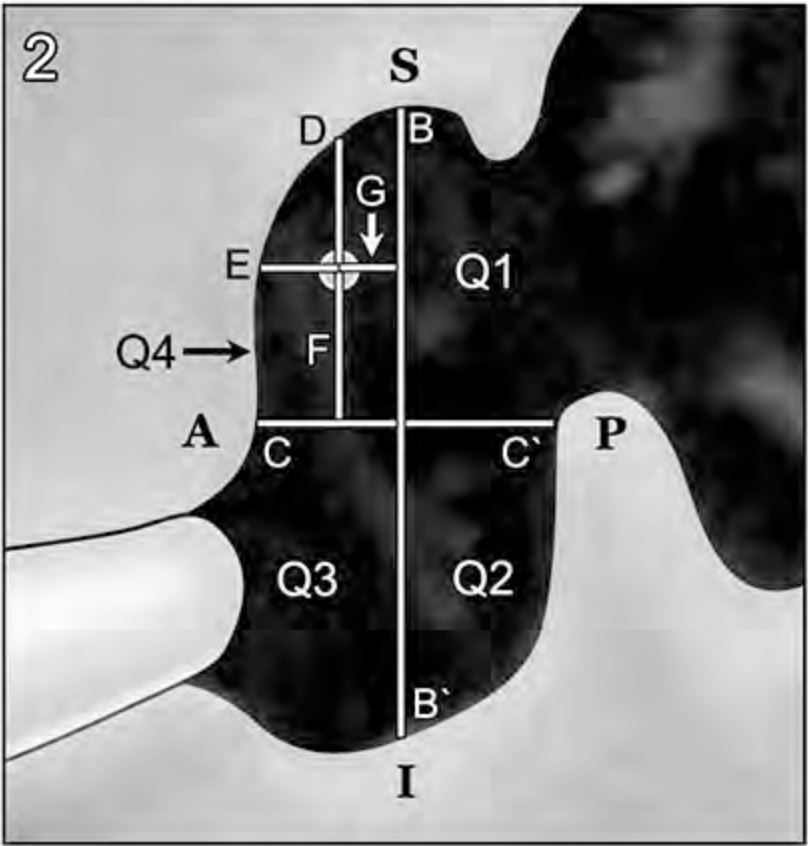
Ninety-four FPCA acquisitions obtained during the selective injection of ISAs providing an anterior radiculomedullary artery were reviewed. Measurements were obtained in a sagittal view (Figs. 1 and 2) and converted into a scatter plot visualization (Fig. 3). Patients' age, gender, site of injection, and level of injection were recorded.

Results

The intraforaminal location of the ASA contributors could be ascertained in 78 of the 94 FPCA acquisitions (33 women and 45 men, with ages ranging between 22 and 82). Fifty-three (68%) acquisitions were on the left and 25 (32%) on the right, at vertebral levels extending from T2 to L3. The anterior radiculomedullary arteries were found in the anterosuperior quadrant of the neural foramen in 76 (97%) cases (Fig. 3, Q4) and in the posterosuperior quadrant in two (3%) cases (Fig. 3, Q1). No contributors were located in the inferior quadrants. No differences in location were observed with age, gender, site of injection, or vertebral level.

Conclusions

Anterior radiculomedullary arteries were found in the superior half of the neural foramen (100%), particularly in its anterosuperior quadrant (97%). Avoiding needle placement in these areas can reduce the likelihood of injury to the spinal arterial system during TFESI. Figure 1. FPCA, left L1 ISA injection, sagittal reconstruction, documenting the location of an anterior radiculomedullary artery within the neural foramen (white arrow). Figure 2. Illustration of measurements and quadrants corresponding to Figure 1. The neural foramen height (B to B') was defined as the long axis from the posterior edge of the vertebral pedicle to the superior edge of the pedicle below. The neural foramen was divided into quadrants (Q1-4) by measuring the width (C to C') at the midpoint of the height. ASA contributor location was evaluated by measuring the distance from the center of the artery to the superior (D) and anterior (E) wall of the neural foramen and the vertical (F) and horizontal (G) distance to the quadrant divisions. A = anterior, P = posterior, S = superior, I = inferior. Figure 3. Scatter plot of measurements in millimeters. Zero values for the x and y-axis represent the approximate center of the neural foramina (n = 78).



(Filename: TCT_O-328_figures1-gregg.jpg)

O-329

1:21PM - 1:24PM

C1-2 Puncture: Prevalence of High-Risk Vascular Variants

W Gibbs¹, A Rajamohan¹, M Law¹

¹*University of Southern California, Keck School of Medicine, Los Angeles, CA*

Purpose

Lateral C1-2 puncture for collection of cerebrospinal fluid or injection of myelographic contrast or chemotherapy is perceived to be more dangerous and difficult to perform than lumbar puncture. Computed tomography (CT) guidance diminishes the risk of cord puncture, but injury to an anomalous origin or low-lying loop of the posterior inferior cerebellar artery (PICA) or a variant vertebral artery course overlying the posterior third of the spinal canal remains a concern. The purpose of this study was to investigate the prevalence of these variants on CT angiography in order to assess the risk of vascular injury in lateral C1-2 puncture.

Materials and Methods

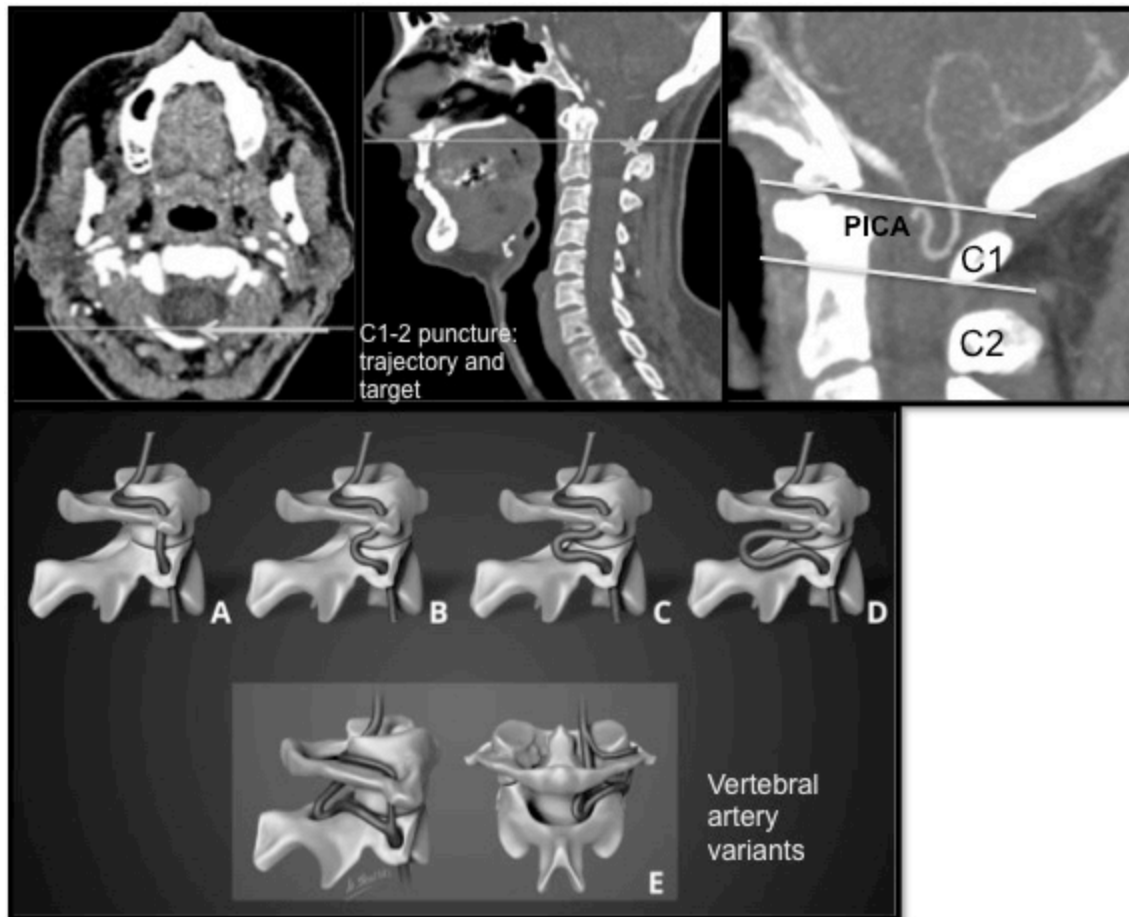
Three hundred ten consecutive CT angiography studies were evaluated. Characteristics that would contraindicate C1-2 puncture (elevated intracranial pressure, Chiari malformation, craniocervical mass or stenosis) prompted exclusion. In each subject the inferior extent of the PICAs (or AICA-PICA loop) and the PICA origins were characterized as intracranial, below the foramen magnum but above the inferior margin of C1, or below C1. The location of the vertebral artery at the C1-2 level was characterized as anterior to the canal, overlying the anterior 2/3 of the canal, or overlying the posterior 1/3 of the canal.

Results

Three hundred three patients met criteria. In eight patients (2.6%) a PICA originated below the foramen magnum but above C1. No patients had a PICA origin at or below C1. In 34 patients, 38 PICAs (11.2%) extended below the foramen magnum but remained above the inferior C1 margin. The PICA did not extend below C1 in any patient. No patients had vertebral arteries overlying the posterior third of the canal at the C1-2 level.

Conclusions

The most feared complication of C1-2 puncture is injury to the PICA or vertebral artery. In this study no variants were found that would put these patients at risk of vascular injury in a properly performed lateral C1-2 puncture.



(Filename: TCT_O-329_2016ASNRC1-2.jpg)

O-330

1:24PM - 1:27PM

Percutaneous CT Guided Laminotomy and Fenestration for Treatment of Symptomatic Lumbar Synovial Cysts.

A Bress¹, B Pukenas²

¹University of Pennsylvania, Philadelphia, PA, ²Hospital Of the Univ. Of Pennsylvania, Philadelphia, PA

Purpose

To report on the effectiveness and need for subsequent surgery on in patients treated with a novel technique – computed tomography (CT)-guided percutaneous laminotomy and synovial cyst fenestration.

Materials and Methods

This retrospective study was conducted on patients from December 2011 to November 2015. Electronic medical record and PACS were reviewed. Patient demographics, symptoms, location, short-term results (within 1 week of treatment),

long-term results (up to 2 years), and surgical treatment were recorded. All patients had monitored anesthesia and procedures were performed utilizing CT fluoroscopy. Direct injection of 1-3 cc of diluted Iovue M200 contrast was injected into the facet joint in order to visualize cyst. Then a manual (Bonopty) or mechanical (On-Control) bone drill was used to create a laminotomy in order to directly fenestrate the cyst. Next, the cyst was ruptured by injecting contrast until seen in the epidural space. Then 1-2 ml of 1% lidocaine and 2 ml dexamethasone (10mg/cc) was injected.

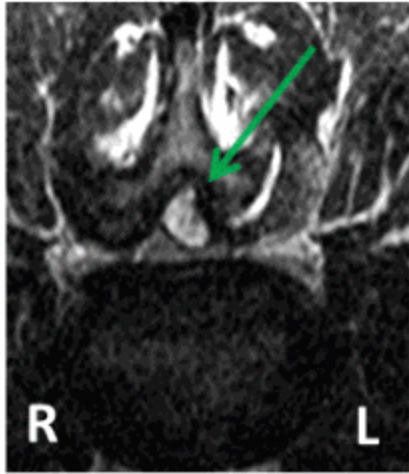
Results

A total of 38 patients were included in our study. Immediate follow up was not documented in four patients and five patients had no documented long-term follow up. All cysts were fenestrated successfully and there were no complications from the procedure. Ages ranged from 42-82 years old with mean of 63.4 and median of 64. There were 19 males and 19 females. The levels treated were L3-4 (7 patients), L4-5 (28 patients), and L5-S1 (three patients). Immediately postprocedure 29/38 (76.3%) significantly improved. A total of 14/38 (36.8%) patients had some or complete recurrence of symptoms. Surgery was performed in 9/38 (23.7%) patients. There were four patients who had a repeat procedure and only one of them eventually went to surgery while the other three improved.

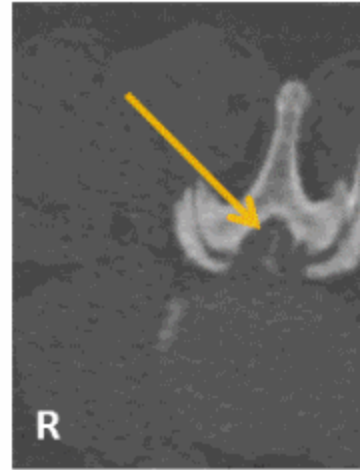
Conclusions

Percutaneous CT guided laminotomy and synovial cyst fenestration is a minimally invasive, safe, and effective treatment that eliminated the need for surgery in 76% of our patients.

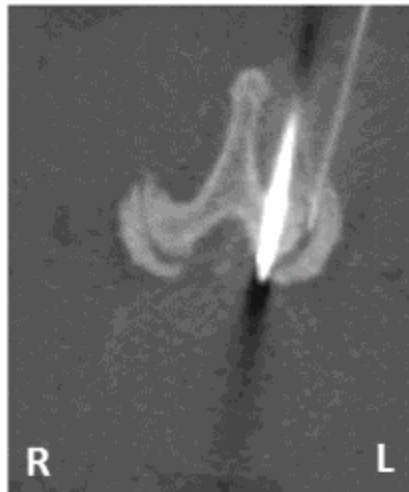
Left L3-4 Synovial Cyst Fenestration



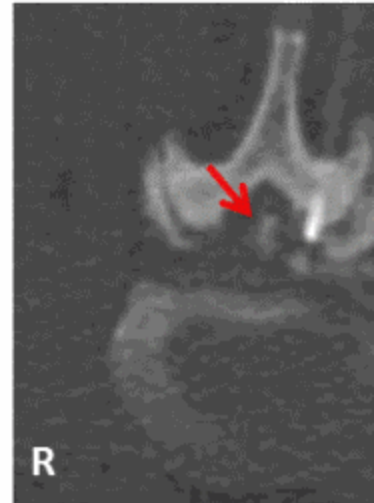
Pre-treatment axial T2 MRI



22g Spinal Needle with injection outlining the cyst



11g On-Control Laminotomy Needle into the cyst



Post injection through Laminotomy Needle flows along left nerve root and dural fenestration.

(Filename: TCT_O-330_Fenestration_Images.gif)

O-331

1:27PM - 1:30PM

Cervical Percutaneous Vertebroplasty: 13 years' Experience in a Single Center

F Clarençon¹, E Cormier¹, R Fahed¹, L Mollet-Benhamou¹, V Degos¹, J Chiras¹
¹Pitié-Salpêtrière Hospital, Paris, France

Purpose

To present our experience in cervical percutaneous vertebroplasty (cPVP).

Materials and Methods

From January 2001 to October 2014, 141 cPVP procedures (170 vertebrae) were performed in 134 consecutive patients (91 females, 43 males; mean age = 56 years). Among the treated lesions, 76.1% were bone metastases (mostly from breast cancer), 9% were related to a hemopathy and 14.9% were nonmalignant lesions (hemangiomas, aneurysmal bone cyst, ...). Procedure-related complications (minor and major) were recorded systematically. Effectiveness in terms of analgesia was evaluated using a semi-quantitative grading scale at 1-month follow up.

Results

One fatal complication was reported due to cement migration in the vertebrobasilar system. Three cervical hematomas were recorded, one having required a prolonged oral intubation. One case of vertebral artery spasm was observed, without any clinical consequence. At 1 month, pain reduction was observed in more than 80% of the cases.

Conclusions

Cervical percutaneous vertebroplasty is a safe technique with an acceptable major complication rate. Its effectiveness in terms of analgesia is good at midterm follow up.

O-332

1:30PM - 1:33PM

Effect of Systemic Therapies on Outcomes Following Vertebroplasty Among Patients with Multiple Myeloma

J McDonald¹, R McDonald¹, D Kallmes¹, V Lehman¹, F Diehn¹, J Wald¹, K Thielen¹, P Luetmer¹

¹Mayo Clinic, Rochester, MN

Purpose

Published clinical evidence in support of vertebral augmentation of pathologic fractures in the myeloma population remains limited. With this study we seek to better define the effectiveness of vertebroplasty for myeloma associated fractures and determine if outcomes and complications are dependent upon procedure timing relative to initiation of systemic therapy.

Materials and Methods

In this single center retrospective study, we retrieved demographic and clinical data on 172 multiple myeloma patients treated with vertebroplasty since October 2000. Laboratory and medication data were retrieved to determine the extent of myeloma and presence of systemic therapy at the time of vertebroplasty. Quantitative outcome data including the Roland Morris Disability Questionnaire (RDQ) and numerical

rating scale (NRS) for pain and qualitative outcome data (self-reported pain, mobility, narcotic use) were collected pre-operatively, immediately postoperatively and at 1 week, 1 month, 6 months, and 1 year following treatment. Peri- and postoperative complications also were collected.

Results

Significant improvements in all outcome measures were observed postoperatively and throughout the duration of follow up. Significant median improvements in RDQ (0-23), and analogue pain scale (0-10) rest and activity of 15, two, and six points respectively ($p < .0001$) persisted at 1 year without significant change from immediate postoperative scores ($p > .36$). Patients on systemic therapy for myeloma at time of procedure were more likely to achieve responded status when compared to patients not on systemic therapy, with no difference in complication rates between groups.

Conclusions

Vertebroplasty is an effective therapy for myeloma patients with symptomatic compression fractures. Favorable outcomes more likely are to be achieved when spinal augmentation is performed after systemic therapy is initiated. Complication rates are not affected by timing of systemic therapy.

O-333

1:33PM - 1:36PM

Vertebral Augmentation for Myeloma-Related Spinal Fractures: A 2002-2012 Population-Based SEER-Medicare Study

F Chokshi¹, D Howard², R Duszak¹, J Jarvik³

¹Emory University School of Medicine, Atlanta, GA, ²Emory Rollins School of Public Health, Atlanta, GA, ³Univ of Washington School of Medicine, Seattle, WA

Purpose

To evaluate trends in the use of vertebral augmentation (VA) among Medicare beneficiaries with myeloma-related spinal fractures.

Materials and Methods

Using the SEER-Medicare database [Medicare claims linked with Surveillance, Epidemiology and End Results (SEER) tumor registry records] (1), we identified myeloma patients age 65 and older who had a pathological fracture between 2002 and 2012. From claims, we identified those undergoing VA. We used logistic regression to estimate the impact of patient age, gender, race, education and poverty level (both by ZIP code), comorbidity count, and year of fracture on the receipt of VA.

Results

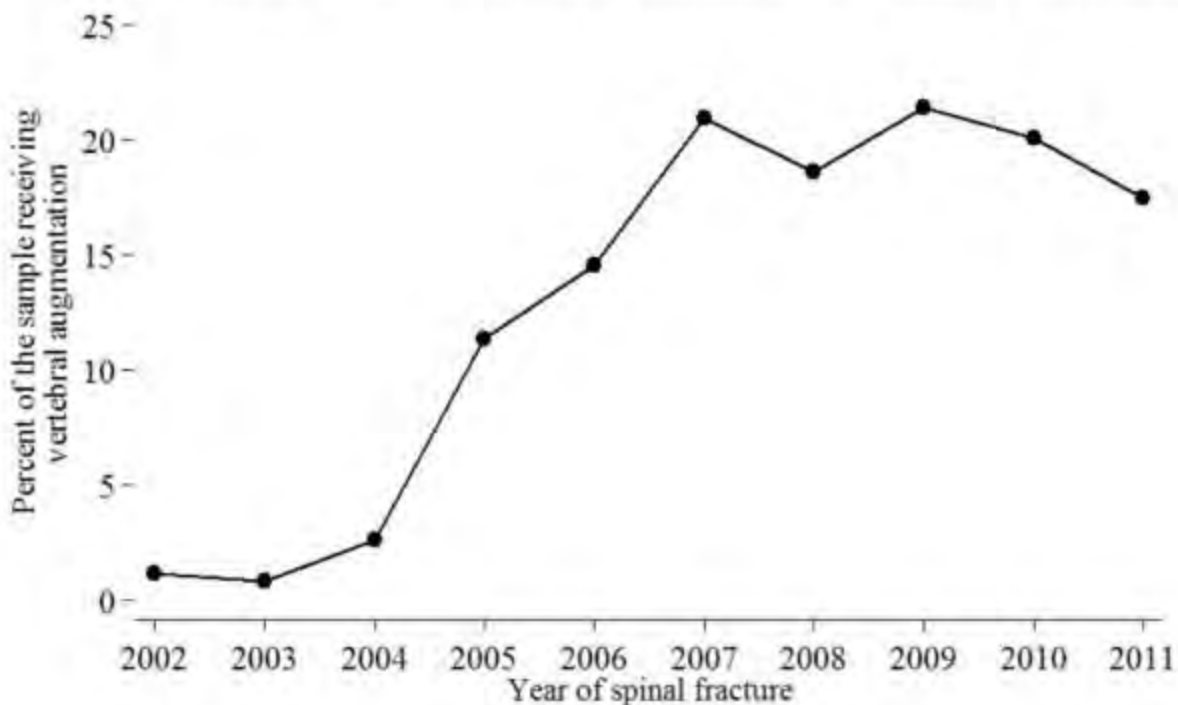
Of 25,516 myeloma patients, 4,725 had pathological spinal fractures; of these, 653 (13.8%) underwent VA. Similar to studies of osteoporotic fractures (2, 3), procedure volume increased from 2002-2007 and plateaued in 2008-2011. Patients who had a

spinal fracture before a myeloma diagnosis (959; 20.3%) were more likely to undergo VA than patients who had a spinal fracture after their myeloma diagnosis (3,766; 79.7%). Use of VA was 7.6 percentage points lower among black patients ($p < 0.0001$), but other socioeconomic variables had little or no effect on the receipt of VA. Patients with less comorbidity were more likely to undergo VA ($p = 0.003$).

Conclusions

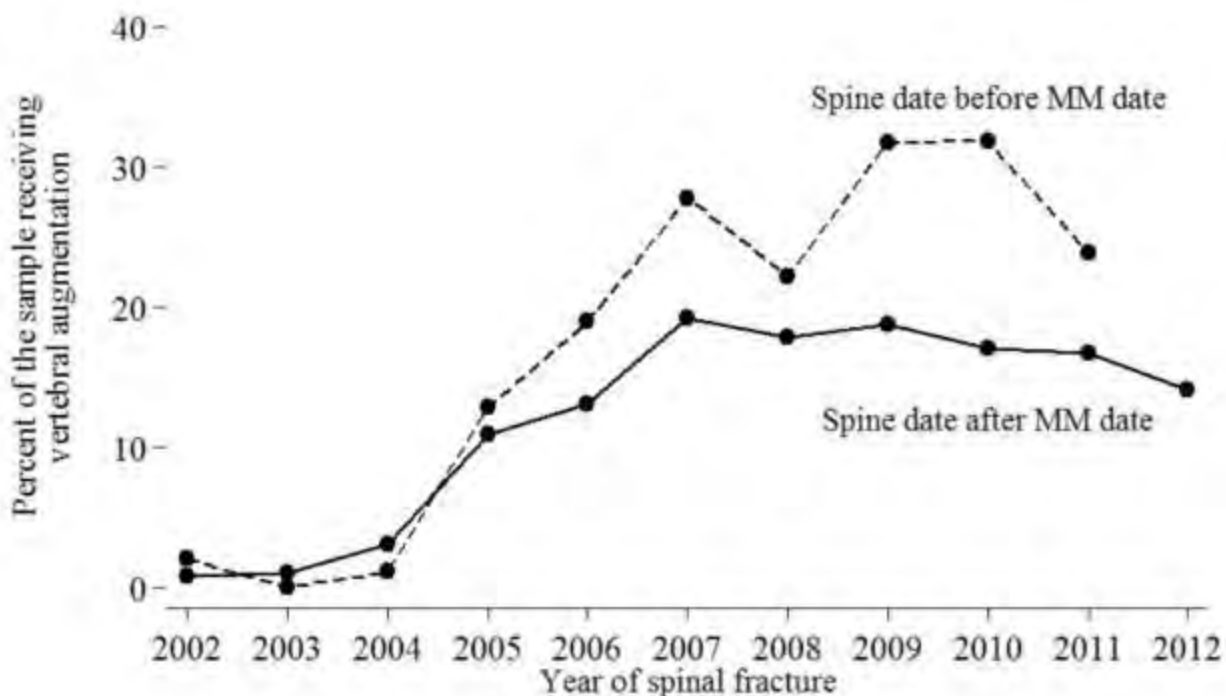
1. National trends in VA in myeloma patients follow trends in its use in patients with osteoporotic fractures. Practitioners may be applying results of two RCTs focused on osteoporotic fractures (2, 3) to patients with myeloma.
2. Patients experiencing a fracture before an established myeloma diagnosis may be being treated as those having osteoporotic fractures.
3. Black patients may have less access to vertebral augmentation compared to Caucasians.
4. Interventionalists and surgeons may be selecting healthier patients for performing vertebral augmentation.

Figure 1: Trends in Use of Vertebral Augmentation in Myeloma Spinal Fractures



SOURCE: Authors' analysis of SEER-Medicare.

Figure 2: Subgroup Trends in the Use of Vertebral Augmentation in Myeloma Spinal Fractures



SOURCE: Authors' analysis of SEER-Medicare.

O-334

1:36PM - 1:39PM

Detection of Stellate Ganglion and Thoracic Sympathetic Chain Ganglia on Noncontrast CISS MRI

A Chaudhry¹, A Kamali², A Blitz³

¹*Johns Hopkins Medicine, Elkridge, MD*, ²*Johns Hopkins University Hospital, Baltimore, MD*, ³*Johns Hopkins, Baltimore, MD*

Purpose

Three-dimensional constructive interference in steady state (3D-CISS) refocused-gradient-echo magnetic resonance imaging (MRI) sequence is a high spatial resolution imaging technique. The technique generates images using ratio of T2 relaxation time: T1 relaxation time, generating what appears to be heavily T2-weighted images (3). Currently, this technique is being used widely to evaluate small intracranial structures most notably the cranial nerves and spinal nerve roots. In our experience, we found that 3D-CISS provided comprehensive in vivo evaluation of the sympathetic chain ganglion. In this retrospective study, we aim to evaluate the normal anatomy of the stellate ganglion as well as thoracic sympathetic chain ganglia and assess the detectability of each of the thoracic sympathetic chain ganglion (SCG) on precontrast CISS images.

Materials and Methods

In this IRB-approved HIPPA compliant study, 300 normal thoracic sympathetic chain ganglion were evaluated in 25 patients. The detectability of the sympathetic chain ganglion was evaluated using precontrast-enhanced 3D-CISS MR imaging.

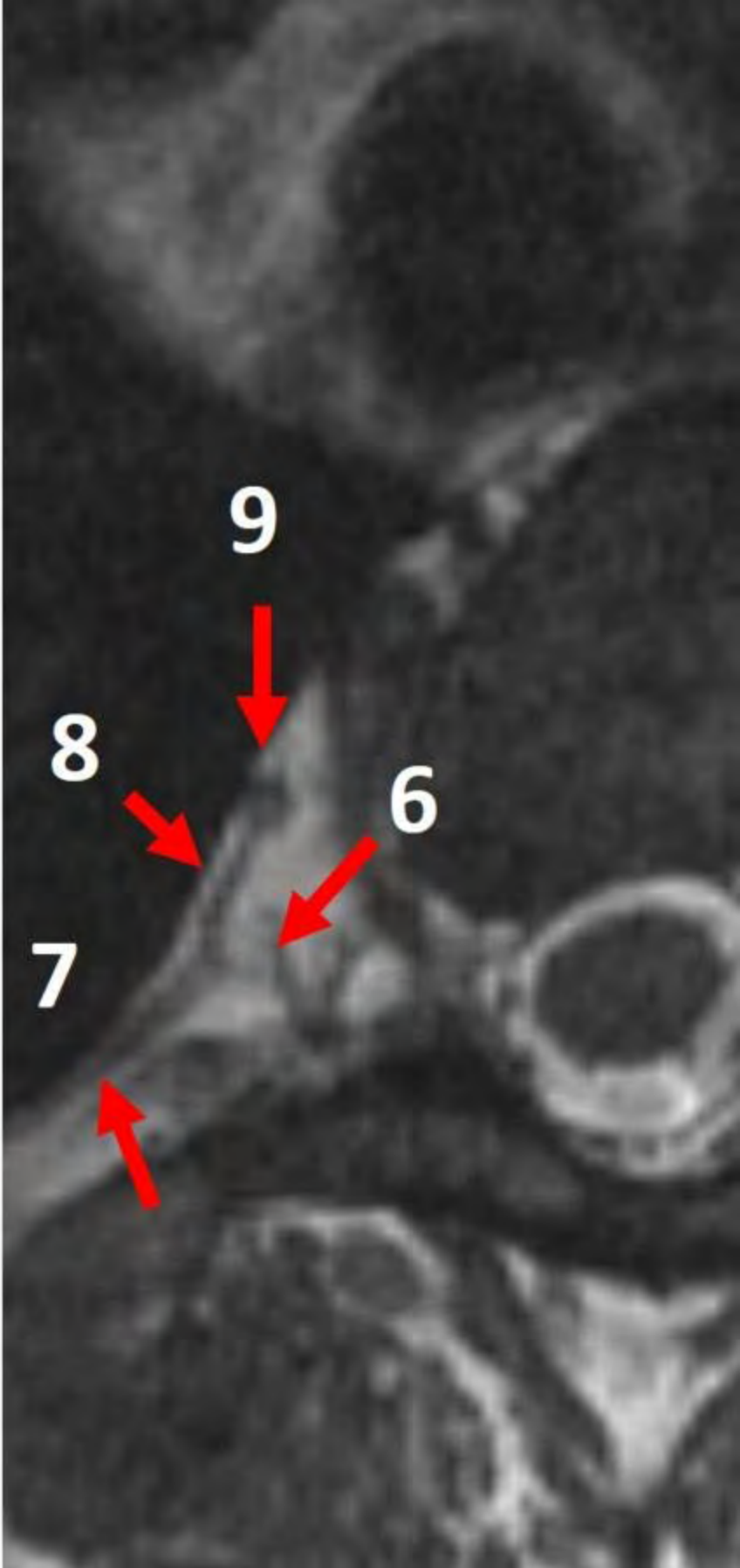
Confirmation of stellate and SCG was made ensuring connection of the ganglia with spinal nerves and interconnection within the SCG chain. Measures of central tendency were performed as well as t-test were performed for statistical analysis. Additionally, kappa test was performed to evaluate for inter-rater reliability.

Results

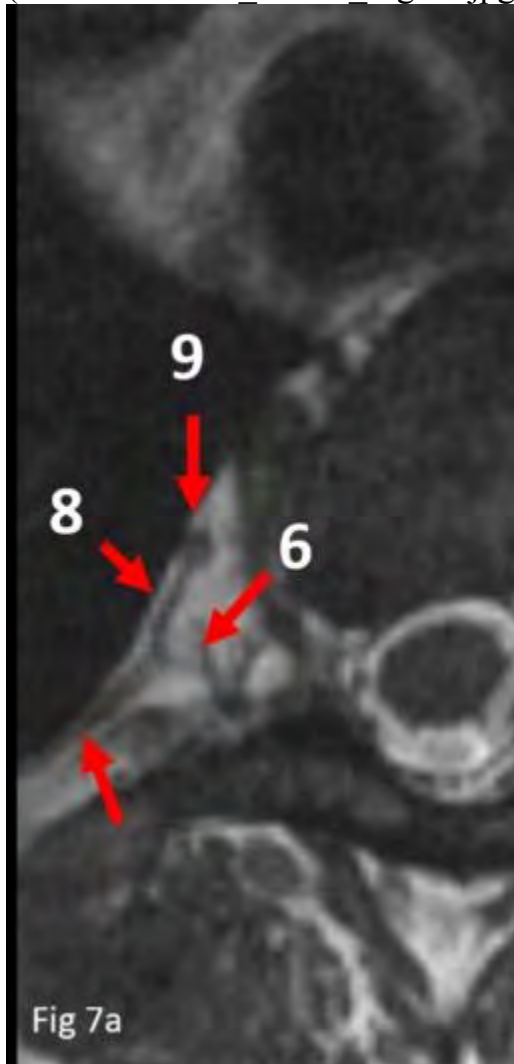
In our cohort of 13 males and 12 females (mean age 45 years), stellate ganglion and thoracic chain ganglia were identified successfully in all patients except at T10-T11 and T11-T12 level. Precontrast CISS demonstrated stellate ganglia to be isointense relative to gray matter noted in the spinal cord. Stellate ganglion was found inferomedial to the subclavian artery inferior to the transverse process of C7 in all patients. Thoracic SCG were identified ventral to the costovertebral junction. There is strong interobserver agreement with Kappa-value > 0.80. Mean size of stellate ganglia was 35.75 mm² while thoracic SCG ranged from 6.5 mm² to 17.4 mm².

Conclusions

Thoracic sympathetic chain ganglia can be seen readily and well characterized on precontrast 3D-CISS MRI. This technique can aid in initial evaluation of potential stellate and/or SCG pathology as well allow for post-treatment follow up.



(Filename: TCT_O-334_Figure.jpg)



(Filename: TCT_O-334_figure1.jpg)

O-335

1:39PM - 1:42PM

A comparison of contrast-enhanced portal venous phase CT vs MRI in the assessment of lumbar spinal canal stenosis

R Kavanagh¹, A Carroll¹, R Killeen¹, E Heffernan¹
¹*St. Vincent's University Hospital, Dublin 4, Ireland*

Purpose

Magnetic resonance imaging (MRI) is the gold standard imaging modality for lumbar spinal canal assessment. However, in certain patients, MRI is contraindicated and an alternative imaging modality is required. The usual next option for assessment is formal or computed tomography (CT) myelography, which have been shown to be

highly sensitive and specific for the diagnosis of lumbar spinal stenosis (1); however, myelography requires a lumbar puncture and injection of contrast into the subarachnoid space and reported complications from this procedure, although uncommon, include headache, infection, bleeding, adverse contrast reaction and seizures (2). We postulate that with the high spatial and contrast resolution of modern CT scanners, IV contrast-enhanced CT alone may be useful in the assessment of lumbar spinal stenosis and the aim of this study was to assess if portal venous phase CT is accurate in assessing the lumbar spinal canal as compared to MRI as the gold standard.

Materials and Methods

Sample size calculation gave a result of $n=202$ for the detection of a 10% difference in the measurements with 90% power at a significance level of 0.05. A total of 202 lumbar spinal levels were assessed in 60 consecutive patients who underwent contrast-enhanced portal venous phase CT scanning and MRI of the lumbar spine within 28 days of each other. The mean time between scans was 6.6 days. The cross-sectional area of the thecal sac was measured on equivalent slices at the level of the intervertebral disks on the axial/oblique axial images from the CT and T2-weighted MRI sequence and the results were compared. Student's t-test was used to assess difference of means, correlation coefficient was calculated and the Bland-Altman method was used to assess the agreement between the two modalities (3).

Results

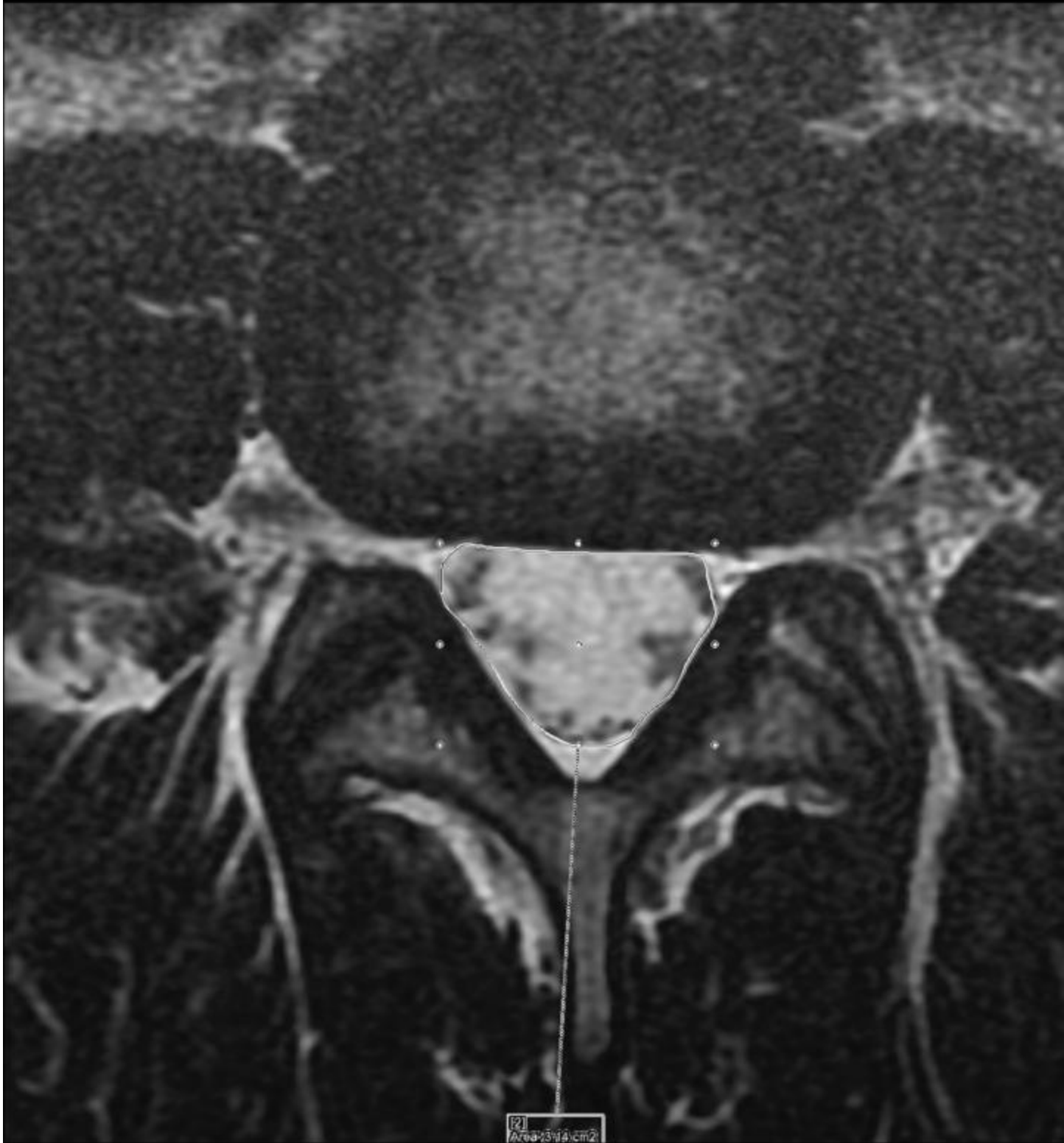
The mean thecal sac area on MRI was found to be 1.77cm^2 and on CT was found to be 1.79cm^2 , with $p=0.30$ indicating no significant difference between these measurements. A scatter plot demonstrates good correlation between the measurements with a correlation coefficient of 0.94. Bland-Altman plot also demonstrates good agreement between the measurements with 95% of the CT measurements lying within $\pm 0.4\text{cm}^2$ of the MRI measurements. Previous research has defined lumbar spinal canal stenosis as a thecal sac area $<1\text{cm}^2$ (4); using this figure our results show contrast-enhanced portal venous phase CT has a sensitivity of 75% and specificity of 99% in the diagnosis of lumbar spinal stenosis with a positive predictive value of 94% and negative predictive value of 97%.

Conclusions

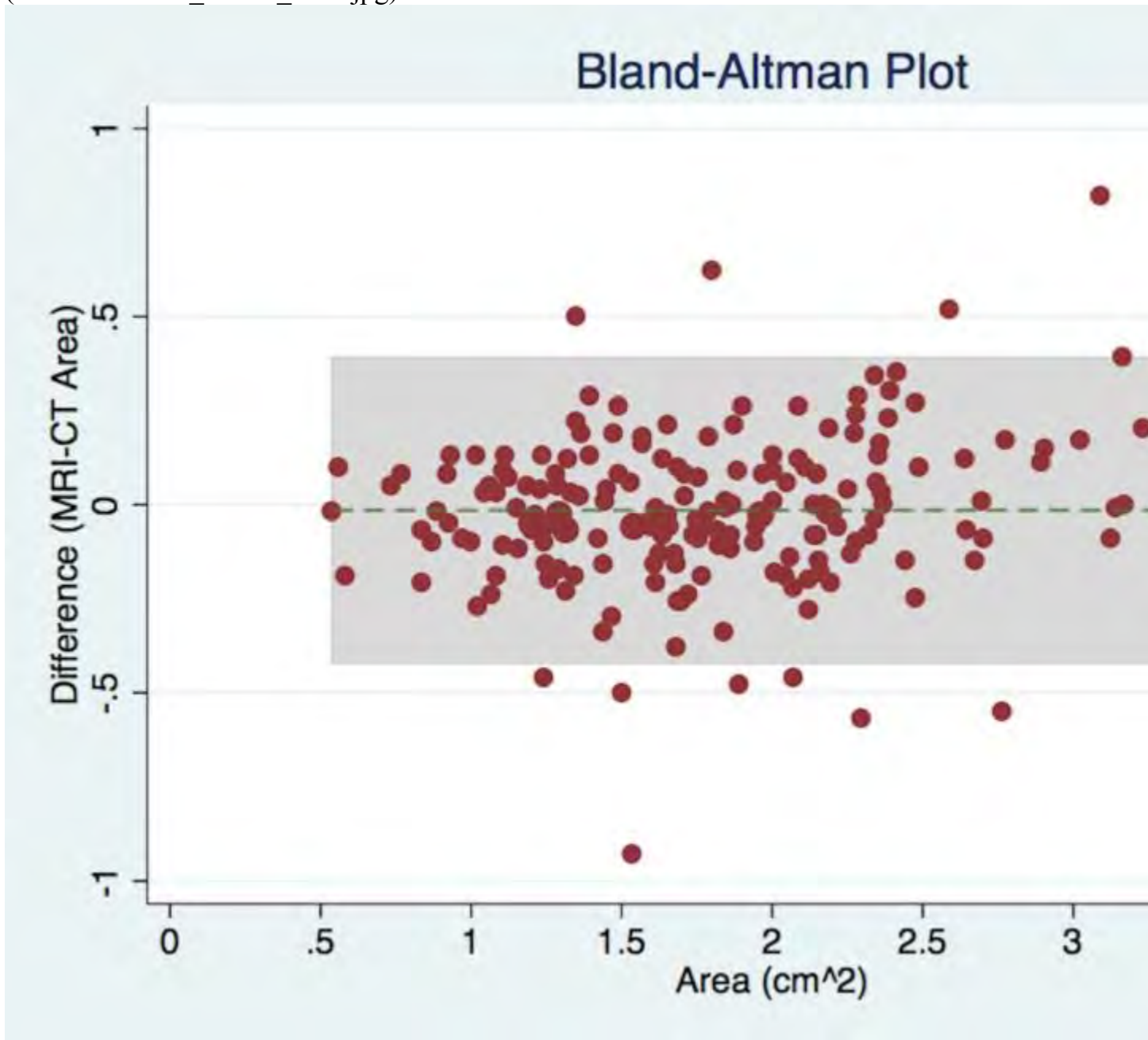
Contrast-enhanced portal venous phase CT is a reliable modality in the assessment of lumbar spinal canal stenosis.



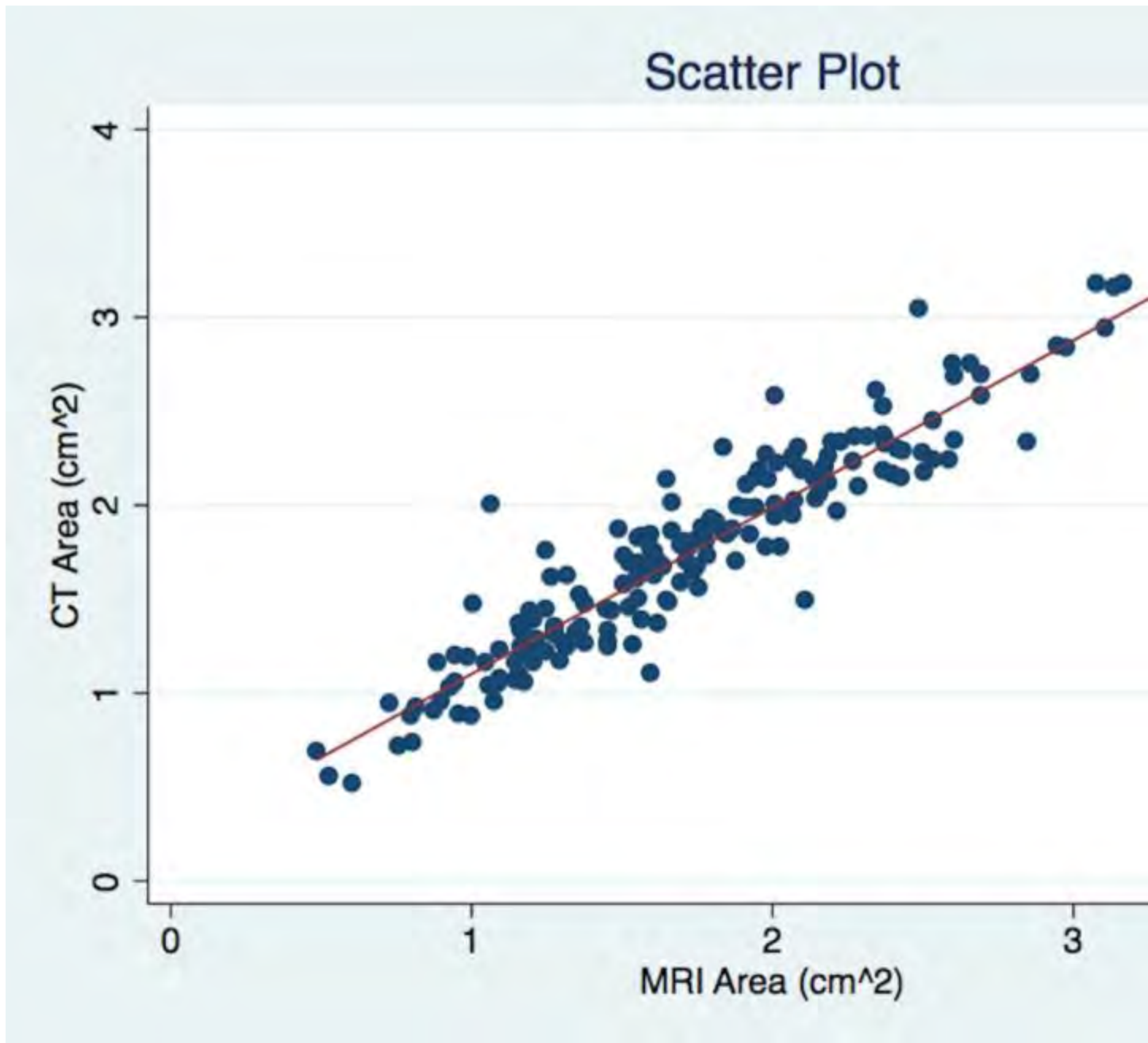
(Filename: TCT_O-335_CT.jpg)



(Filename: TCT_O-335_MRI.jpg)



(Filename: TCT_O-335_Bland-AltmanPlot.jpg)



(Filename: TCT_O-335_ScatterPlot.jpg)

O-336

1:42PM - 1:45PM

Cranio-Spinal CSF Redistribution Following Lumbar Puncture in Patients with Idiopathic Intracranial Hypertension

N Alperin¹, A Bagci¹, B Lam¹, S Lee¹

¹University of Miami, Miami, FL

Purpose

The physiologic effect of lumbar puncture (LP) in idiopathic intracranial hypertension (IIH) has not been studied adequately and automated quantitation of cerebrospinal fluid (CSF) volumes in the entire cranio-spinal system by magnetic resonance imaging (MRI) is lacking. We characterized the physiologic effect of LP by determining the change of cranio-spinal CSF distribution before and after LP. To achieve this aim, we developed a new automated method for delineating spinal CSF spaces.

Materials and Methods

The study subjects consists of eight young overweight women with newly diagnosed untreated IIH (Age 29 ± 5.9 years, BMI 34 ± 6.7). Research cranio-spinal MRIs were performed immediately before and immediately after the diagnostic LP to establish IIH (opening pressure 33 ± 9.1 cm water). Magnetic resonance imaging included T1W MPRAGE and T2W SPACE sequences of the brain and two separate T2W SPACE sequences covering the upper and lower portions of the spinal canal. Ventricular and cranial CSF volumes were quantified using FreeSurfer and SPM software packages, respectively. The segmentation of the spinal CSF spaces was achieved using an iterative approach to overcome the effect of potential image nonuniformity associated with imaging of a large field of view. The automated segmentation approach made use of a 2D-matched filter to detect the size and position of the cord and an active contour algorithm. Cranio-spinal CSF volumes prior and following LP were compared to the amount of CSF withdrawn.

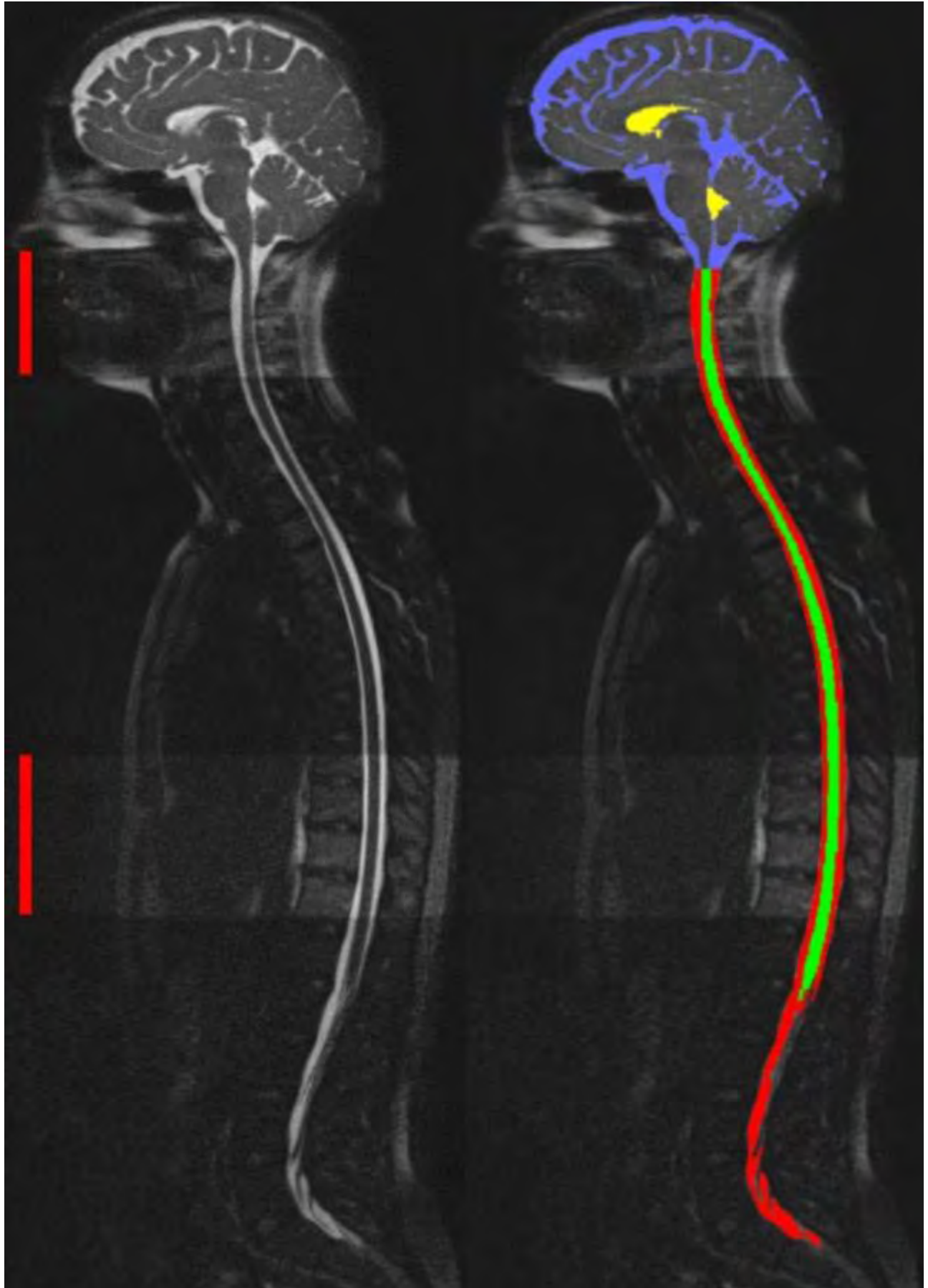
Results

The enclosed Figure is an example of the merged MRI image of the entire CNS CSF with the superimposed segmented cranial and spinal CSF spaces. The reduction of the CSF volume following CSF withdrawal by LP was predominantly from the spinal canal and was localized near the region of the LP. Cranial CSF volume was nearly unchanged. Spinal CSF and cord volumetric automated measurements were highly reproducible with mean variability of less than 1%, $-0.7 \pm 1.4\%$, $-0.7 \pm 1.0\%$, respectively. The pre-to-post CSF withdrawal differences in the cranio-spinal CSF volumes were consistently smaller and strongly correlated with the CSF amounts removed ($R=0.86, p=0.006$). The smaller measured pre-to-post LP CSF differences compared to the CSF amount withdrawn can be accounted for by assuming a net CSF formation of 0.41 ± 0.18 ml/min.

Conclusions

An automated method for delineation of the spinal CSF spaces has been developed and applied to study the effect of lumbar CSF withdrawal on the cranio-spinal CSF redistribution in IIH. The study reveals that the drop in the opening pressure following CSF withdrawal is primarily related to an increase in the spinal canal compliance caused by reduction in spinal CSF volume localized to the lumbar region. The study demonstrates the central role of the spinal compartment in ICP regulation and the

automated method developed will permit future longitudinal studies to assess cranio-spinal CSF volumetry to further elucidate the pathophysiology of IIH and other CSF-related diseases.



(Filename: TCT_O-336_whole_spine_csf.jpg)

O-337

1:45PM - 1:48PM

Influence of Normative Data on Diffusion Tensor Imaging Metric Comparisons in Cervical Spondylotic Myelopathy

K Wang¹, O Idowu², I Izbudak²

¹*Johns Hopkins School of Medicine, Baltimore, MD*, ²*Johns Hopkins University, Baltimore, MD*

Purpose

The use of diffusion tensor imaging (DTI) in evaluating cervical spondylotic myelopathy (CSM) is limited by the lack of standardized methods for data acquisition and postprocessing analysis. For example, when comparing DTI metrics of patients with CSM to those of controls, studies differ in the vertebral segments chosen for designated control groups. For instance, disk levels utilized as control groups have included C2-C3, C2-C5, C5-C6, and C4-C7 in healthy volunteers, and nonstenotic levels (e.g., C2-C3) in CSM patients. It is uncertain to what extent such variation affects interpretation of DTI metrics. In this study, we aim to use receiver operating characteristic (ROC) curves to characterize the influence of the intervertebral disk levels chosen as controls on DTI metrics' ability to discriminate between patients with CSM and controls.

Materials and Methods

Magnetic resonance (MR) imaging of the cervical spinal cord was performed in eight CSM patients and in five healthy volunteers on a 3T MR scanner. For each patient, fractional anisotropy (FA) and mean diffusivity (MD) were measured at the level of maximal stenosis and regions of interests (ROIs) were placed to approximate the lateral white matter, posterior white matter, and anterior gray matter. Fractional anisotropy and MD also were measured in larger ROIs that provided near-entire interrogation of the sagittal cord and hemi-axial cord. For each control, similar ROIs were placed at intervertebral disk levels as utilized in prior studies (ex. C2-C3, C2-C5, C2-C6). Receiver operating characteristics analysis was used to assess the discriminatory ability of FA and MD when utilizing different disk levels as control groups. Differences in areas under the curve across the controls groups were considered statistically significant if $p < 0.05$.

Results

The highest area under the curve (AUC) in MD was 0.80 when analyzing the hemi-axial cord region and utilizing level C4-C7 in healthy volunteers as a control. There were statistically significant differences in the area under the curve when analyzing the MD measure in the hemi-axial cord across the control groups with varying chosen

intervertebral disk segments ($p=0.040$). No significant differences in AUC among the control groups were noted for MD or FA when analyzing other regions of the spinal cord, including posterior white matter, lateral white matter, and anterior gray matter.

Conclusions

There may be significant differences in discriminatory power depending on which region of interest of the cord is analyzed. Consistent with a prior study (1), highest AUCs were demonstrated with MD, suggesting diagnostic utility of MD may be superior to that of FA. There also may be significant differences in discriminatory power depending on the intervertebral segments chosen as controls, as suggested by the significant differences in AUC when analyzing the MD measure in the hemi-axial cord across the different control groups. Being mindful of the influence of using differing disk levels in designating controls groups, which have been highly variably in prior studies, may allow for more accurate interpretation DTI data in the evaluation of CSM.

O-338

1:48PM - 1:51PM

Better Look Twice: Incidental Findings in the Extra-Spinal Soft Tissues on Outpatient Thoracic Spine MRI

S Sogge¹, K Diehl¹, T Ouyang¹, C Jamis-Dow¹, D Nguyen¹

¹*Penn State Hershey Medical Center, Hershey, PA*

Purpose

An incidental finding is defined as an asymptomatic lesion found on an imaging exam performed for an unrelated reason. These findings are occasionally more clinically significant than the original reason for the examination. The purpose of this research was to examine the prevalence of both clinically and nonclinically relevant extra-spinal incidental findings in patients that undergo magnetic resonance imaging (MRI) of the thoracic spine and evaluate the rate of undetected findings in radiology reports.

Materials and Methods

The study was approved by our Institutional Review Board and was HIPAA compliant. Our PACS (GE Centricity Radiology Information System) was searched for thoracic spine MRI exams without contrast performed between July 1 2012 and June 30 2013. Only adult patients between the ages of 18 and 99 years of age were included. Patients with known malignancy were excluded to avoid over detection of extra-spinal malignancy. Three board certified radiologists reviewed 187 MRIs. Extra-spinal abnormalities were classified according to a modified CT colonography Reporting and Data System (C-RADS). Incidental findings were categorized using C-RADS criteria reported elsewhere: E0 - exam compromised by artifact, examination severely limited. E1 - Normal exam or anatomical variant. E2 – clinically unimportant

finding without work up indicated. E3 – likely unimportant finding that is incompletely characterized. E4 – potentially important finding, communicate to referring physician as per local practice guidelines.

Results

Overall, 48.6% (91 of 187) of patients had ESFs. There were a total of 139 incidental ESFs, with some patients having more than one ESF. Among studies with more than one ESF, the findings may fit into more than one C-RADS category. 50.2% (94 of 187 scans) had no discernible extra-spinal findings (E1). Two patients with incidental normal variants also were classified into the E1 category. These were retro-aortic left renal vein and aberrant right subclavian artery. Of the 48.6% of patients with ESFs, 11.7% had clinically significant abnormalities, a large portion (75%) of which was not reported originally. Figure A: Heavily weighted T2 myelogram sequence showing sample E3 findings including large bilateral glenohumeral joint effusions (white arrows) along with large hiatal hernia (open white arrow). Also seen are renal (white arrowhead) and hepatic simple cysts (red arrow) which are E2 findings. Figure B: Left paraspinal mass, a sample E4 finding.

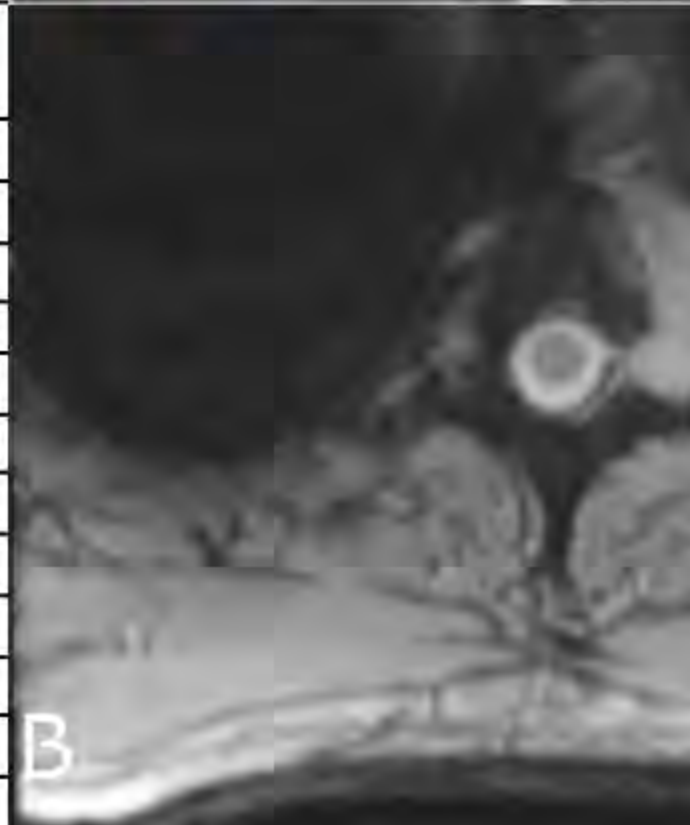
Conclusions

Incidental extra-spinal findings are common on thoracic MRI and can be overlooked easily. Our findings are similar to studies in the lumbar spine including a high nondetection rate of potentially clinically significant incidental findings. A mental checklist or structured reporting system may help to identify more of these findings. Consensus for further recommendation and work up of the potentially significant incidental findings are not available universally, but communication with the referring services and a multidisciplinary approach could improve patient care by aiding early diagnosis.

| Type of E3 finding | Number |
|---|--------|
| Sub-centimeter thyroid nodules | 3 |
| Complicated liver cyst | 5 |
| Simple pleural effusion | 8 |
| Complicated renal cyst with well-defined borders and no solid component | 5 |
| Dilated bile ducts | 3 |
| Splenomegaly | 2 |
| Renal atrophy | 1 |
| Dilated esophagus | 2 |
| Hiatal hernia | 5 |
| Para-costal cystic lesion | 1 |
| Patchy airspace disease | 3 |
| Enlarged central pulmonary arteries | 1 |
| Mediastinal cyst | 1 |
| Ectatic (but non-aneurysmal) thoracic aorta | 1 |
| Prominent bowel loop | 1 |
| Para-spinal muscle atrophy | 1 |
| Shoulder/bursal effusion | 10 |



| Type of E4 finding | Number |
|-----------------------------|--------|
| Adrenal nodule > 1 cm | 5 |
| Thyroid nodule > 1 cm | 5 |
| Chest wall mass (NSCLC) | 1 |
| Lung nodule > 5 mm | 7 |
| Mediastinal lymphadenopathy | 2 |
| Loculated pleural effusion | 1 |



(Filename: TCT_O-338_ASNRtspinesubmissionwithnumbers1.jpg)

O-339

1:51PM - 1:54PM

The Clivoaxial Angle Measured on High-Resolution T2-Weighted MR Images in Normal Adult Volunteers with both Flexion and Extension

E Munoz¹, F Berkowitz², A Sayah³

¹Georgetown, Washington, DC, ²Georgetown University Hospital, Washington, DC, ³Medstar Georgetown University Hospital, Washington, DC

Purpose

The clivo-axial angle currently is used by spine surgeons to predict potential benefit of occipitocervical fusion, and need for surgical correction of clivo-axial deformities. Normal clivo-axial angles range from 150 degrees to 180 degrees in a neutral position. Recent literature demonstrates that the clivo-axial angle is affected by patient positioning at time of imaging. The purpose of this study is to determine a range of normal values for the clivo-axial angle using high-resolution magnetic resonance (MR) imaging of healthy adults during neck flexion and extension.

Materials and Methods

High-resolution T2-weighted MR images of the cervical spine in 10 adult volunteers were reviewed. Inclusion criteria included ages 18 and older. Exclusion criteria included a history of cervical spine injury, prior cervical spine surgery, neck pain, and degenerative spondylosis. The clivo-axial angle was measured as the angle subtended by a line drawn along the dorsal surface of the clivus and a second line drawn along the dorsal surface of the odontoid process. The clivo-axial angle was measured on midline sagittal images in the following neck positions: supine extension, supine flexion, prone extension, and prone flexion.

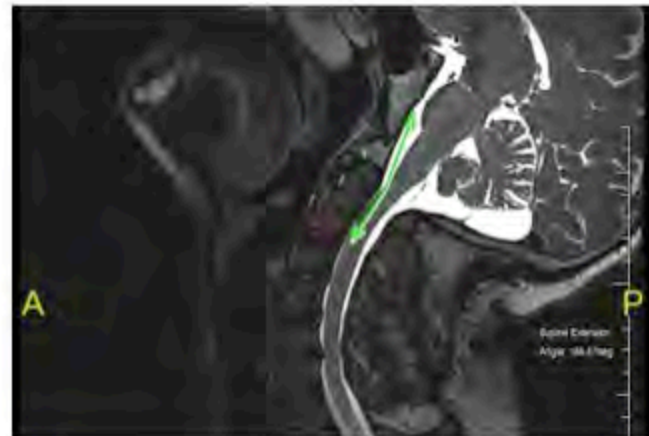
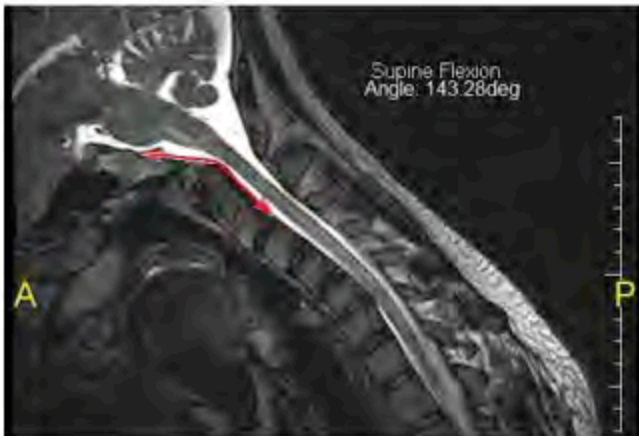
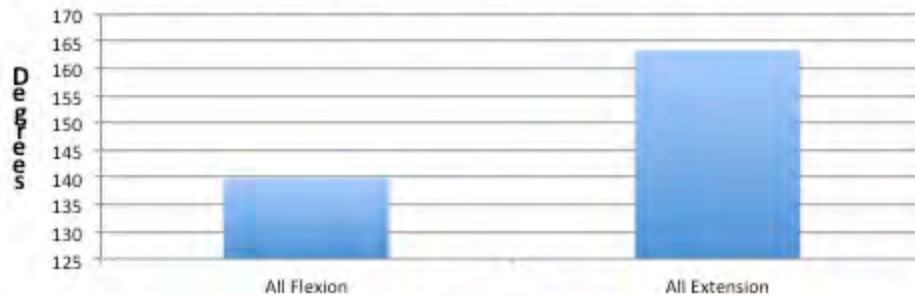
Results

The mean clivo-axial angle (in degrees) was as follows: 160.0 for supine extension, 140.0 for supine flexion, 166.8 for prone extension, 139.6 for prone flexion, 139.8 for all flexion, and 163.4 for all extension. The minimum clivo-axial angle recorded was 124.0 (n=40). The maximum clivo-axial angle recorded was 178.6 (n=40).

Conclusions

Anthropometric data of normal adult volunteers reveal a clivo-axial angle range from 124.0 to 178.6 degrees, with angles less in neck flexion than in extension, irrespective of spine or prone positioning. These values likely will be helpful for the surgeon deciding on potential occipitocervical fusions, and may be applicable to general brain MR and CT imaging.

Mean Clivoaxial Angles Measured on High-Resolution T2-Weighted MR Images in Normal Adult Volunteers with both Flexion and Extension



(Filename: TCT_O-339_Slide2.jpg)

O-340

1:54PM - 1:57PM

Diffusion Tensor Microscopy of Human Intervertebral Disc-interrogation of mechanics and structure relationships in complete human discs

R Alkalay¹, D Hackney²

¹Beth Israel Deaconess medical Center, Boston, MA, ²Beth Israel Deaconess Medical Center, Boston, MA

Purpose

This study investigated the association between structural parameters computed from diffusion tensor magnetic resonance (MR) images (DTI) of intact human discs and the

viscoelastic response of the disks to a loading condition simulating standing (700N) posture.

Materials and Methods

Six lumbar L2-L3 disks from human donors age 49-70 years were imaged (9.4T BioSpec 4.7T, Bruker BioSpin Inc., MA) using 72mm coil (Bruker BioSpin) with the disk's transverse (TR) and caudal-cranial (C-C) axes aligned with the imager Z, X-Y axes. 3D spin-echo echo-planar (SE-EPI) diffusion tensor image data were acquired using 30 noncollinear directions with 2 averaged b0 images, b value: 670 s/mm², (TE/TR: 29/700) ms, NEX = 2, FOV: (56 x 50 x 16) mm, matrix: (500 x 500 x 16), reconstructed resolution: (500 x 500 x 1000) μ m. The disk was segmented (3Dslicer 4.1, www.slicer.org) and tensor data computed from the diffusion-weighted images. Diffusion tensor imaging parameters computed were mean diffusivity (MD), eigenvalues, ($\lambda_1, \lambda_2, \lambda_3$), axial ($\lambda_l = \lambda_1$) and radial diffusivity ($\lambda_t = (\lambda_2 + \lambda_3)/2$), fractional anisotropy (FA) and anisotropy projected with respect to the axial (RIAMax-E(Z)) and radial (RIAMax-E (X)) component of λ_1 . General linear models (JMP 8.0, SAS, NC) tested for association of MR parameters with degenerative grade.

Results

The disk's instantaneous (E1) and long term (E2) stiffness were positively associated with the following annular parameters, magnitude of radial (E: p<0.01, E2: p<0.001), λ_l (E: p<0.001, E2: p<0.001) λ_t (E: p<0.01, E2: p<0.01), RIAMax-E(Z) (E: p<0.05, E2: p<0.01), RIAMax-E (X) (E: p<0.001, E2: p<0.0001) diffusivity and TR (E: p<0.01, E2: p<0.001). The viscous damping (η_1) was positively associated with the magnitude of radial diffusivity (p<0.01) and RIAMax-E (X) (p<0.01) and negatively associated with magnitude of radial (p<0.05) diffusivity.

Conclusions

Magnetic resonance DTI parameters can predict disk mechanical performance. This information should functional derangements the spine due to degenerative disk disease and may assist in analyzing back pain and the expected natural history of this disease.

O-341

1:57PM - 2:00PM

Can STIR “Claw Sign” Differentiate Infectious and Degenerative Intervertebral Disc Space Disease?

S Shrot¹, A Sayah², F Berkowitz³

¹Medstar Georgetown University Hospital, Washington, DC, DC, ²Medstar Georgetown University Hospital, Washington, DC, ³Georgetown University Hospital, Washington, DC

Purpose

Recently, the diffusion-weighted "claw sign" was proposed to discriminate between infection and degenerative changes involving the intervertebral space. Our hypothesis was that the "claw sign" was caused by Modic I changes at the interface between normal marrow and Modic III changes. If this is the case, then the "claw sign" also should be visible on STIR images. Our purpose was to test if the STIR "claw sign" can be used to differentiate between infection and degenerative disease in cases where imaging is suspicious for diskitis.

Materials and Methods

Seventy-two consecutive patients with imaging features of suspicious or probable diskitis (T2 hyperintense signal within the intervertebral disk) and available clinical follow up were reviewed blindly for appearance of vertebra marrow edema "claw sign" on sagittal STIR images. A STIR "claw sign" was defined as well marginated, linear, area of hyperintensity situated within the vertebral bodies with an interface of hypointense marrow signal adjacent to the suspicious intervertebral space (Figure: Cervical spine CT (Right) and MRI (Left) showing C6-C7 Modic III changes with STIR "claw sign"). When available, concurrent CT studies were evaluated for Modic III changes. Clinical follow up including blood culture and bone biopsies were used as the standard of reference.

Results

Of our cohort, 47 patients had clinical diagnosis of infectious diskitis. STIR "claw sign" appeared in 11 patients, four with clinical diagnosis of diskitis and seven of noninfectious degenerative endplate changes. Sensitivity and specificity of STIR "claw sign" for diagnosis of noninfectious endplate changes were 63.6% and 70.5%, respectively. The negative predictive value was 91.5%. Eight out of 11 patients with STIR "claw sign" had concurrent CT study demonstrating sclerotic endplates changes.

Conclusions

The STIR "claw sign" is not sufficiently reliable to exclude infection. It often represents Modic I changes (edema) adjacent to Modic III changes (sclerosis). Infection also can cause endplate sclerosis with adjacent edema resulting in the "claw sign".



(Filename: TCT_O-341_Image.jpg)

O-342

2:00PM - 2:03PM

Cervical MRI vs. CT Myelography: Is That the Anterior Median Fissure or the Central Canal?

v perez¹, E Peak¹, L Wang², T Tomsick¹

¹University of Cincinnati, Cincinnati, OH, ²University of Cincinnati Medical Center, Cincinnati, OH

Purpose

Hyperintense foci (HIF) and the anterior median fissure (AMF) on axial T2 cervical MR images have been shown to be associated with identification of a T2 hyperintense line simulating a channel on T2 sagittal images. We hypothesize that the HIF may represent the central canal of the spinal cord, or the base of the AMF in some instances. Our aim is to compare the ability of computed tomography myelography (CTM) versus magnetic resonance imaging (MRI) to identify HIF and AMF, and aid

in distinguishing not only the central canal versus AMF, but also sagittal lines as a manifestation of the central canal versus an AMF channel.

Materials and Methods

Cervical MRI and CTM from 34 consecutive patients who underwent both studies from 2012-15 were reviewed retrospectively. The images for each study (3mm T2 fast-spin-echo axial and sagittal MR, 2.5 mm soft-tissue algorithm axial CTM with 3 mm sagittal reconstruction) were reviewed initially separately by a neuroradiologist and a neuroradiology fellow, and then were reviewed jointly and adjudicated for the presence or absence of HIF, AMF, and sagittal lines on MRI and CTM.

Results

Magnetic resonance identified more HIF than AMF/pt. (191 versus 103, ratio 1.85), with sagittal lines in 19/34 (55.9%) patients (Table 1). Lines were associated with HIF and AMF (7.6 versus 3.5 patients, respectively), and none were identified in their absence. Computed tomography myelography demonstrated far fewer total HIF than AMF (16 HIF versus 123 AMF, ratio 0.13), with two short sagittal lines. Fifty of 103 (48.5%) MR AMF demonstrated concordant demonstration of CT AMF at the same patient level. Twenty-eight of 191 (14.7%) MR HIF were associated with CTM AMF at the same level. Of 16 CTM HIF, 15 were continuous with the base of the AMF; only one was an isolated focus unassociated with AMF. Six of 15 were associated with MR AMF as well, and 10 with MR HIF.

Conclusions

Concordant demonstration of MR and CTM AMF was common, confirming reliability in identification of AMF. Magnetic resonance HIF were identified in the absence of identified MR AMF, yet associated with CTM AMF at the same level. The presence of CT AMF associated with MR HIF without MR AMF suggests some AMF may be present in conjunction with MR HIF, but not resolved on MR imaging. Hyperintense foci were uncommonly identified on CTM, and almost exclusively as a continuation of an AMF. These observations are evidence that some MR HIF and MR sagittal lines may represent the base of a CTM-demonstrated AMF, and not the central canal of the spinal cord. While not conclusive, data supports previous observations that MR HIF and AMF may represent portions of the same structure, the AMF, which may appear as a sagittal line or channel in some instances. It is further hypothesized that this sagittal channel may more rarely be wider, and mimic hydromyelia.

| Table 1 | CT AMF (n=122) | CT HIF (n=16) |
|-----------------|----------------|---------------|
| MR AMF (n=103) | 50 | 67 |
| MR HIF (n= 191) | 28 | 10 |

(Filename: TCT_O-342_PerezTable.jpg)

Wednesday

1:15PM - 2:45PM

Washington Marriott Wardman Park, Maryland A/B/C

16E-SILAN Programming: Cerebral Venous System: Update in Diagnostic and Novel Treatments

16E-1

1:15PM - 1:20PM

Introduction: What is SILAN?

Diaz, O.
The Methodist Hospital
Bellaire, TX

16E-2

1:20PM - 1:40PM

Diagnosis of Venous Infarct: Where Do We Stand?

Gonzalez, R.
Massachusetts General Hospital
Boston, MA

16E-3

1:40PM - 2:00PM

Venous Sinus Stenting for Endovascular Treatment of Idiopathic Intracranial Hypertension

Tejada, J.
Indiana University
Indianapolis, IN

16E-4

2:00PM - 2:20PM

Endovascular Treatment of Venous Lesions of the Head and Neck

Berenstein, A.
Mount Sinai Hospital
New York, NY

16E-5

2:20PM - 2:40PM

Current State of Endovascular Treatment of Acute Dural Venous Sinus Thrombosis

Delgado, J.
Consulting Radiologists, Ltd
Minneapolis, MN

Wednesday

1:15PM - 2:45PM

Washington Marriott Wardman Park, Roosevelt 4

16F-PARALLEL PAPER SESSION: Pediatric Brain Tumors: Pre- and Post-Treatment

O-343

1:15PM - 1:23PM

Assessment of Brain Tumors in Pediatric Patients with Amide Proton Transfer MRI: Preliminary Experience

J Curran¹, A Pokorney¹, J Chia², H Hu¹, J Miller¹, J Keupp³
¹Phoenix Children's Hospital, Phoenix, AZ, ²Philips Healthcare, Cleveland, OH, ³Philips Research Laboratories, Hamburg, Germany

Purpose

The purpose of this study is to evaluate the feasibility and clinical utility of a nongadolinium contrast amide proton transfer (APT) magnetic resonance imaging

(MRI) technique in assessing pediatric brain tumors. Amide proton transfer MRI is particularly sensitive to amide proton groups, which are prevalent in gadolinium contrast positive brain tumors (1-4).

Materials and Methods

This pilot APT study was approved by our institutional review board and conducted on two 3T Philips Ingenia MRI platforms with dual channel RF transmission and 32 channel head coils. To date, we have successfully acquired APT MRI data in 15 pediatric patients and our study is ongoing. In the following presentation, we will particularly focus on four pediatric case examples with positive findings of brain tumors. The patients underwent both APT MRI and standard brain MRI examinations with gadolinium (Dotarem, Guerbet) contrast agent. The first patient was a 9-month-old male with a large lobulated right cerebellar hemisphere and vermian mass. The second patient was a 11-year-old male with two intra-axial masses of metastatic Ewing's sarcoma, one in the right temporal lobe, the other in the right parietal lobe. The third patient was a 4-year-old male with a large solid and cystic mass centered in the hypothalamus, and findings are consistent with a craniopharyngioma. The fourth patient was a 11-year-old male with a malignant neoplasm of the right parietal lobe. Two pediatric neuroradiologists assessed the diagnostic utility of the APT data by comparing it to conventional T1, T2, and postgadolinium images. Regions of interest (ROIs) analysis was performed on the APT-weighted images to quantify the asymmetric magnetization transfer ratio (MTR_{asym}), a recently reported potential biomarker of tumor activity and underlying tissue protein content. Regions of interest were drawn in tumor and adjacent healthy brain tissue for comparison. The APT technique was based on a 3D turbo-spin-echo pulse sequence. The protocol consisted of 9-12 slices of 4.4mm thickness, with a 180-220 mm field-of-view, an in-plane voxel size of 1.8mm, and an approximate TE/TR of 6.2ms/5s. APT scan time was between 4-5 min.

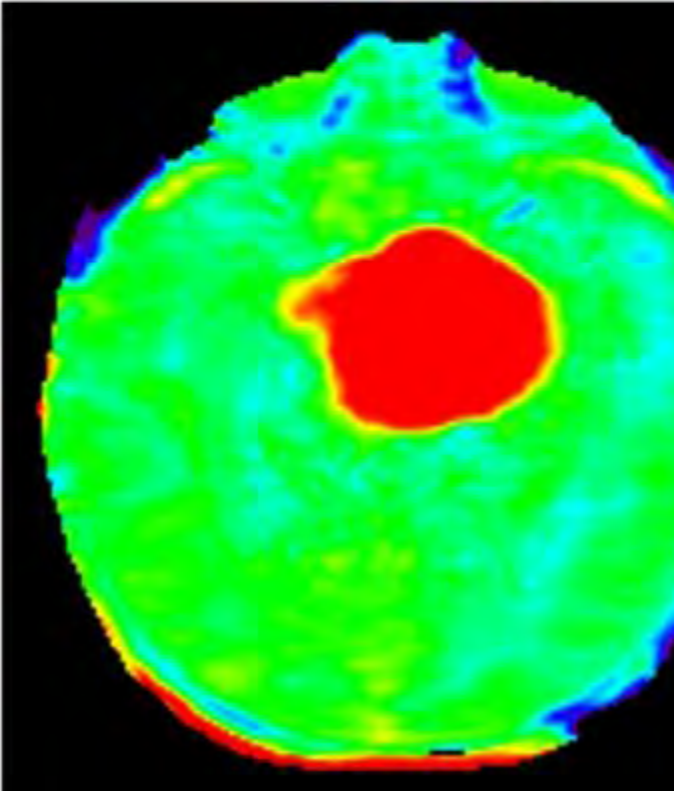
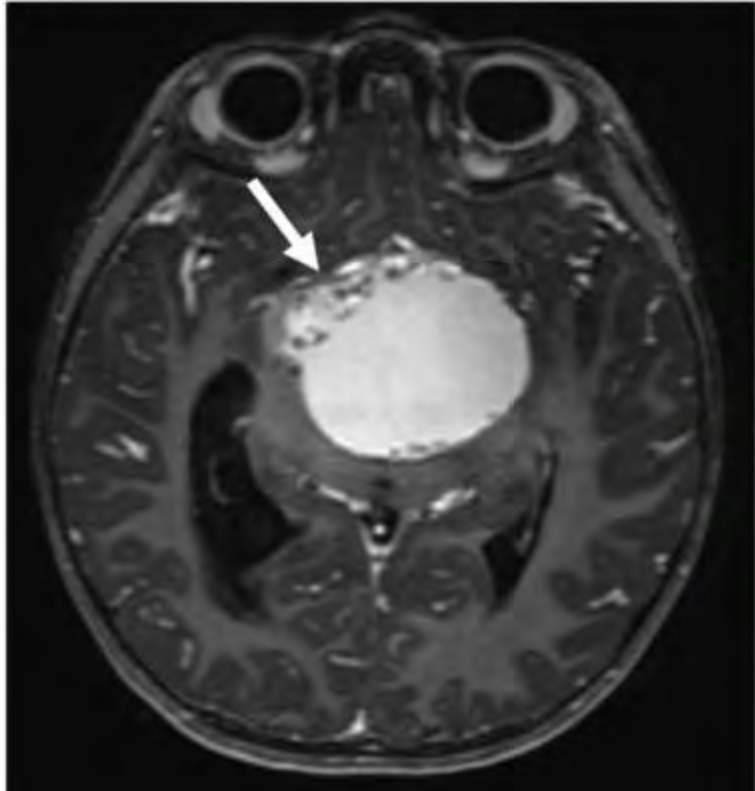
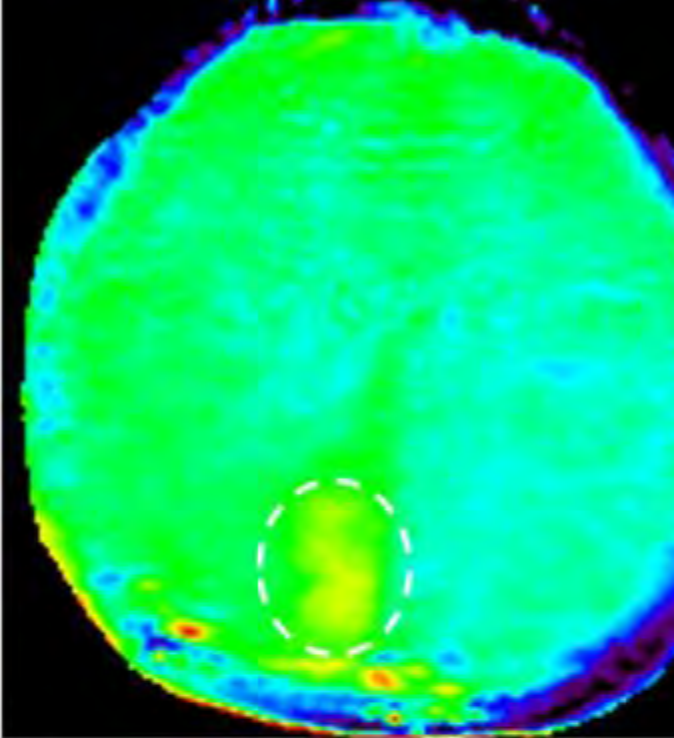
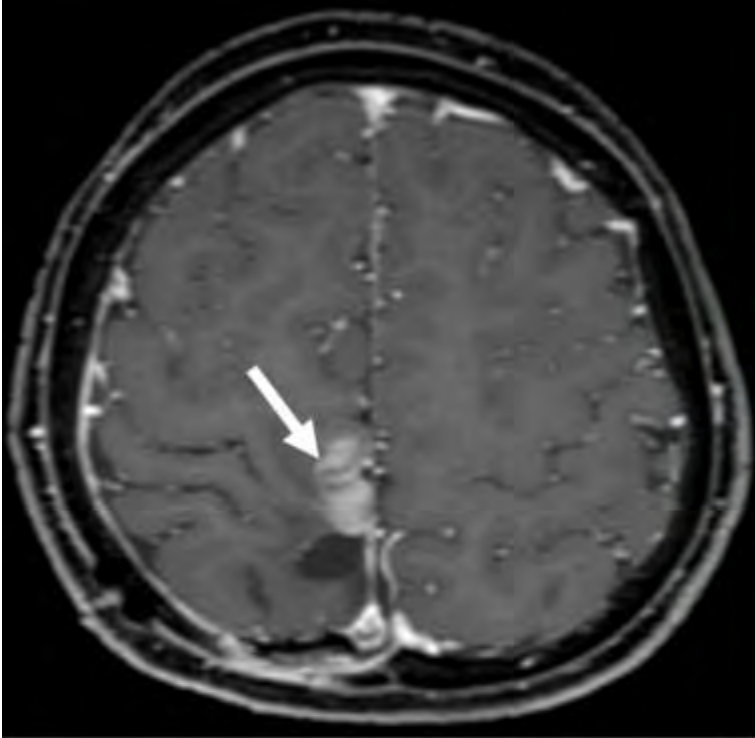
Results

The figure illustrates data from patients #3 (top) and #4 (bottom). Amide proton transfer color maps of the tumor are shown for one slice, although the data acquisition was 3D. The color bar is a scale of the MTR_{asym} metric. Postgadolinium images illustrate tumor enhancement (arrows) in each case. Note the evident signal contrast in the tumor APT signal versus background normal appearing gray and white matter in patient #4. The signal contrast is subtle but still visible in patient #3 (dashed oval). Amide proton transfer tumor signal measures in the 4-6% range, whereas healthy gray matter signal measures in the 1-2% range and healthy white matter shows minimal signal.

Conclusions

Our preliminary experience with nongadolinium contrast APT MRI in pediatric patients suggest promising clinical feasibility of the technique in the assessment of

contrast-enhancing brain tumors. Amide proton transfer may eventually supplement or potentially supplant traditional gadolinium-based imaging for brain tumor imaging.



(Filename: TCT_O-343_Figure1.jpg)

O-344

1:23PM - 1:31PM

MRI Evaluation of Non-Necrotic T2 Hyperintense Foci in Pediatric Diffuse Intrinsic Pontine Glioma

Z Patay¹, O Clerk-Lamallice¹, Y Li¹, A Edwards¹, J Glass¹, W Reddick¹

¹*St. Jude Children's Research Hospital, Memphis, TN*

Purpose

The conventional magnetic resonance imaging (MRI) appearance of diffuse intrinsic pontine glioma (DIPG) suggests intralesional histopathological heterogeneity. Previous publications have described and elucidated the putative nature and significance of various distinct lesion components, including T2-hypointense foci and "occult" enhancement. In this paper, we report the prevalence, conventional MRI semiology, and advanced MRI features of non-necrotic T2-hyperintense foci within DIPG.

Materials and Methods

Twenty-one patients with DIPG were included in this study (F:M=12:9; mean age, 7.77 years; age range, 2.08-17 years). All MRI studies were performed at 3T by using routine conventional and advanced MRI (DSC-perfusion, DCE, and DTI) sequences. Perfusion (CBV), vascular permeability (ve, Ktrans) and diffusion (ADC) metrics were calculated and used to characterize non-necrotic T2-hyperintense foci in comparison with other lesion components, namely necrotic T2 hyperintense foci, T2-hypointense foci, peritumoral edema, and normal brainstem (from a cohort of patients without posterior fossa pathology). Statistical analysis was performed by using Kruskal Wallis testing and pairwise comparisons.

Results

Sixteen non-necrotic T2-hyperintense foci were found in 12 tumors. In non-necrotic T2-hyperintense foci, apparent diffusion coefficient (ADC) values were significantly higher than those in either T2-hypointense foci ($p<0.002$) or normal parenchyma ($p<0.0001$), and relative CBV values were significantly lower than those in either T2-hypointense ($p<0.001$) or necrotic T2-hyperintense ($p<0.006$) foci. Ktrans in T2HrF was lower than that in T2-hypointense ($p<0.0006$) or necrotic T2-hyperintense ($p<0.0348$) foci.

Conclusions

Non-necrotic T2 hyperintense foci are common, distinct lesion components within DIPG. Surrogate advanced MRI biomarkers indicate that those are characterized by relatively low cellularity yet somewhat increased vascular permeability, the latter suggesting an early stage of angiogenesis with leaky vessels. We speculate that these foci may correspond to poorly understood biological events in tumor evolution,

possibly representing clones of transforming cell populations evolving towards foci of anaplasia.

| | ADC ($\times 10^{-3} \text{ mm}^2/\text{s}$) (Mean \pm SD) | relCBV (Mean \pm SD) | K^{trans} (min^{-1}) (Mean \pm SD) |
|---|--|---------------------------|--|
| <i>Normal brainstem (n=17)</i> | 0.75 \pm 0.04 | 1.36 \pm 0.21 | NA |
| <i>Peritumoral edema (n=22)</i> | 1.42 \pm 0.27 | 1.04 \pm 0.31 | 0.0028 \pm 0.0020 |
| <i>Non-necrotic T2^{HrF} (n=16)</i> | 1.48 \pm 0.41 | 1.38 \pm 0.68 | 0.0034 \pm 0.0025 |
| <i>T2_{HoF} (n=13)</i> | 0.82 \pm 0.16 | 3.82 \pm 1.32 | 0.0112 \pm 0.0071 |
| <i>Necrotic T2^{HrF} (n=9)</i> | 1.47 \pm 0.23 | 3.61 \pm 1.63 | 0.0108 \pm 0.0072 |

(Filename: TCT_O-344_Table.jpg)

O-345

1:31PM - 1:39PM

Embryonal tumor with multilayered rosettes: Correlation between Radiographic, Clinical, Histopathologic, and Molecular Findings.

J Pavaine¹, P Sin-Chan², A Huang², S Laughlin¹

¹Department of Diagnostic Imaging, The Hospital for Sick Children, Toronto, Ontario, ²Division of Hematology-Oncology, Arthur and Sonia Labatt Brain Tumor Research Centre, Toronto, Ontario

Purpose

Some of the known rare pediatric high grade embryonal tumors including embryonal tumor with abundant neuropil and true rosettes (ETANTR), ependymoblastoma (EPB), medulloepithelioma (MEPL) and central nervous system primitive neuroectodermal tumor (CNS-PNETs) with variable differentiation have been shown to have common molecular features including amplification of 19q13.42 and LIN28A immunopositivity and a single diagnostic category of embryonal tumor with multilayered rosettes (ETMR) for these has been suggested (1, 2). We reviewed the imaging features of these rare tumors to see if they also were similar and to assess if these were distinct from other more common malignant pediatric brain tumors.

Materials and Methods

Eighteen cases of the rare, highly aggressive embryonal CNS neoplasms were histopathologically diagnosed as ETANTR, ependymoblastoma, medulloepithelioma and CNS-PNETs with variable differentiation at the Hospital for Sick Children in Toronto, Canada from 1981 to 2015. For 14 of these cases, a molecular diagnosis of

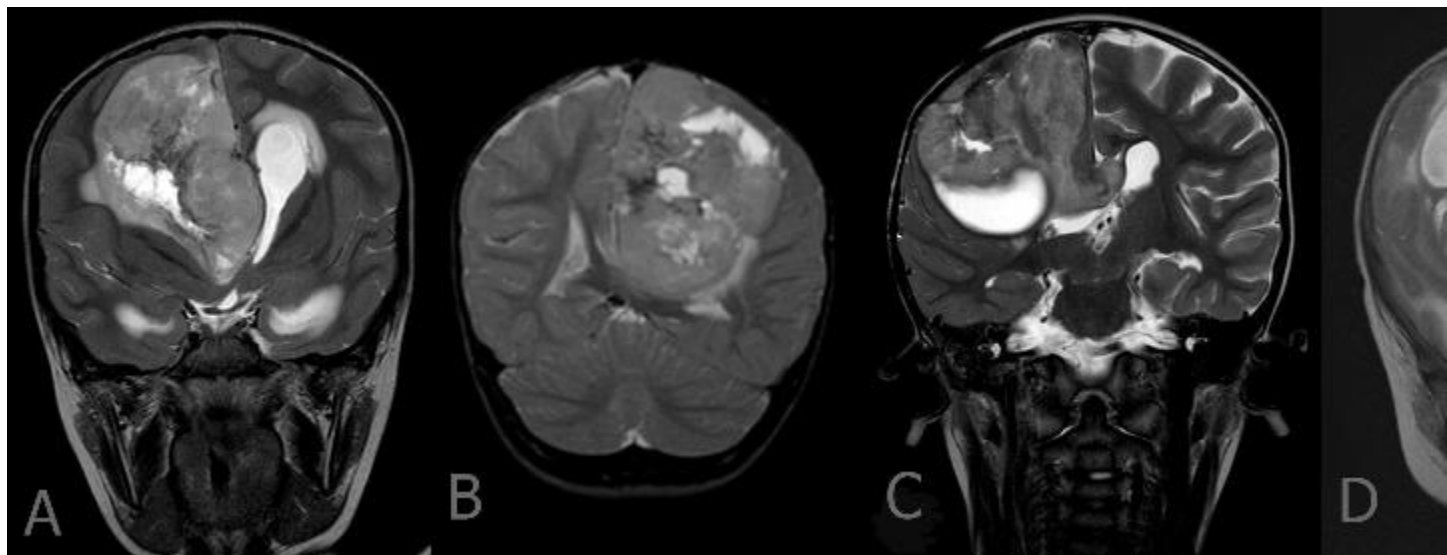
ETMR was available based on gene expression profiling, copy number analysis, C19MC FISH, and/or LIN28 expression. Magnetic resonance (MR) and computed tomography (CT) imaging features were assessed for each of these tumors and separately for supratentorial and infratentorial tumors in correlation with clinical, histopathological and molecular findings.

Results

The tumors occurred in children younger than 4 years of age with an almost 2:1 female predominance and were more frequently supratentorial than infratentorial. Common MR imaging features for ETMR supratentorial tumors included large size at presentation, features of hypercellularity, heterogeneity with solid and cystic components including predominantly low T1 and isointense or slightly hyperintense T2 signal relative to cortex for the solid components and intratumoral areas of cystic/necrotic change and a patchy pattern of enhancement. Most did not demonstrate frank tumor vascularity but often an encased enhancing vessel coursing through the solid component of the tumor was seen (Fig. 1). Figure 1. MR imaging of the supratentorial ETMR histological subtypes. Coronal T2-weighted images for ETANTR (A), EPB (B), recurrent PNET (C), MEPL (D).

Conclusions

Our study found similar imaging features and overlap between the rare pediatric high grade embryonal tumors including ETANTR, EPB, MEPL and CNS-PNETs with variable differentiation at the time of presentation and when these recurred and is supportive of the previously suggested single ETMR entity based on unifying molecular features.



(Filename: TCT_O-345_E712A577A2F43BA45CC7778773FFDC7552635C06230F0EC73Cpimgpsh_fullsize_distr.jpg)

O-346

Radiographic Response of Tectal Gliomas Following Proton Radiotherapy

P Caruso¹, J Ryan Alkasab², A Baer¹, B Buchbinder¹, Y Torunn¹, S Rincon¹

¹*Massachusetts General Hospital, Boston, MA*, ²*University of Massachusetts Medical School, Worcester, MA*

Purpose

Proton radiotherapy is an effective modality for the treatment of brainstem tumors and in pediatric neurooncology offers the advantage of high conformal control that limits radiation dose to the developing brain. While the imaging findings in tumors treated with proton radiotherapy have been described, distinguishing between radiographic response and tumor progression in the early post-treatment period remains an important but challenging task: many tumors including tectal gliomas may respond to proton radiotherapy initially by increasing in size, and this may be misinterpreted as tumor progression. The purpose of our study is to assess the quantitative response of tectal gliomas by performing serial magnetic resonance imaging (MRI) measurements of tumor volume over time in order to identify a predictable trend in tumor response to proton radiotherapy.

Materials and Methods

Following IRB approval, a retrospective search of clinical and imaging databases was performed for patients with tectal gliomas. Patients ages 0 through 25 years with tectal gliomas who underwent proton beam radiotherapy were included. Patients with tumors previously treated with radiotherapy or surgical resection were excluded. Cubic volume measurements were obtained from FLAIR MRI scans at all available timepoints.

Results

Five subjects met inclusion criteria with median age 14.4 years (average, 16.2 years; range, 12.6-20.8 years). Median imaging follow-up was 2.6 years (average, 3.0 years; range, 1.4-5.4 years) with a median of eight post-treatment timepoints (average, 7.6; range, 4-10). Each of the five tumors followed a pattern of post-radiotherapy enlargement followed by reduction in size. The peak tumor volume occurred at a median of 7.0 months (average, 6.3 months; range, 3.6-8.3 months) from initiation of radiotherapy (Figure 1).

Conclusions

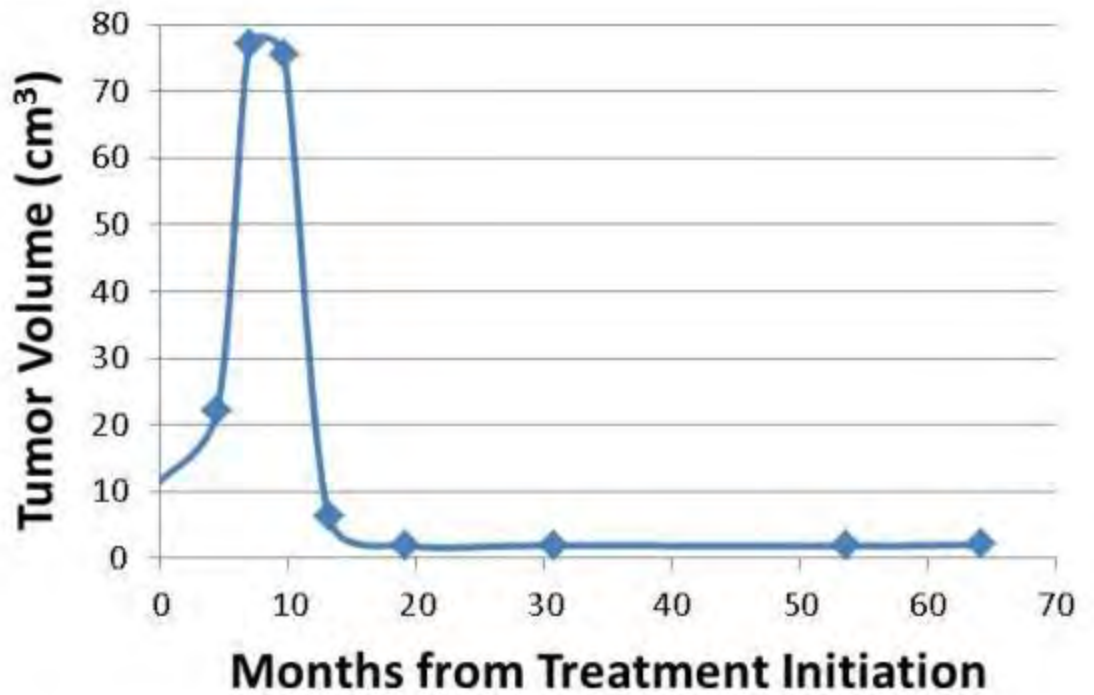
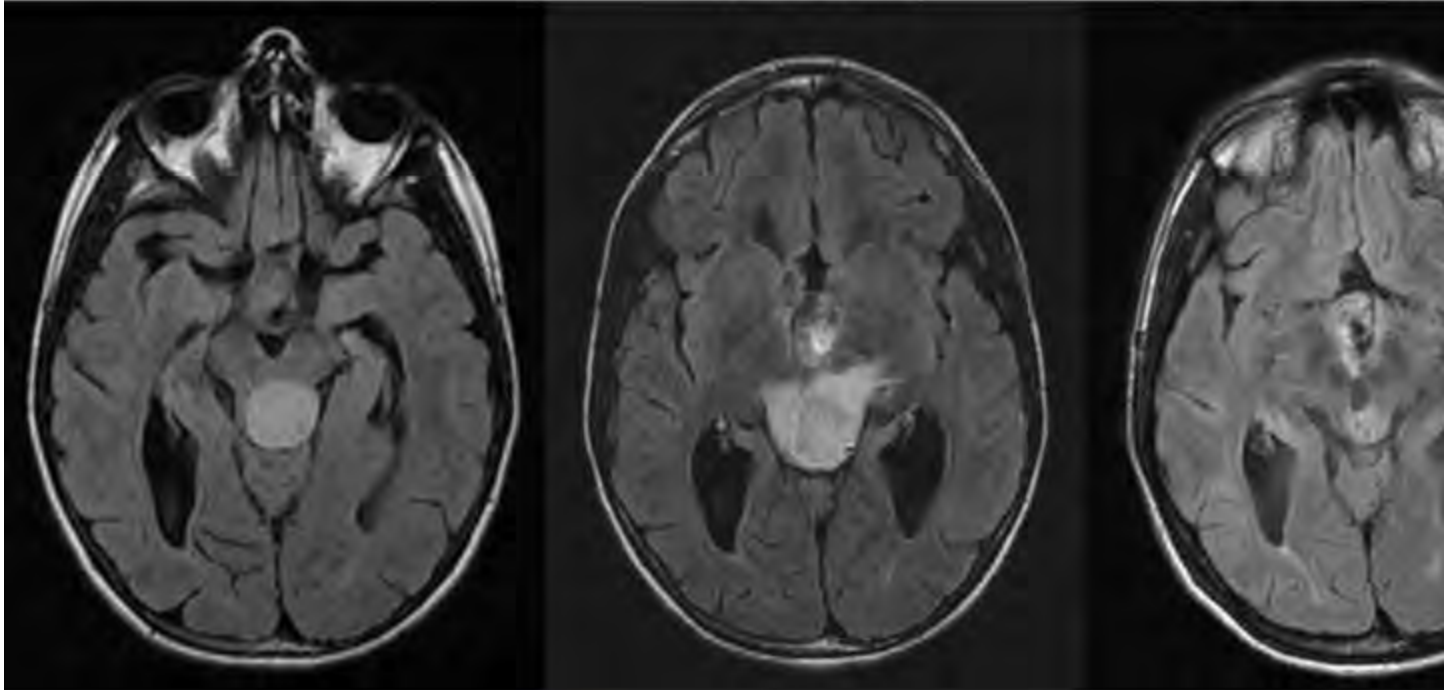
Following proton radiotherapy, tectal gliomas demonstrate a predictable trend of enlargement and subsequent reduction in tumor size. This trend may be helpful in distinguishing between expected radiographic response and tumor progression in tectal gliomas.

Subject 1

Pretreatment

Peak volume
(7.0 months)

Final volume
(65.1 months)



O-347

1:47PM - 1:55PM

Imaging characteristics of pediatric diffuse midline gliomas based on the presence of a poor prognostic marker histone H3 K27M mutation

M Aboian¹, D Solomon¹, E Felton¹, S Mueller¹, S Cha¹

¹*University of California San Francisco, San Francisco, CA*

Purpose

The molecular basis underlying pediatric gliomas is distinct from adult gliomas. One unique molecular alteration that has been identified in pediatric gliomas is K27M missense mutation in histone H3 variants and presence of this mutation correlates with poor prognosis. The forthcoming 2016 WHO Classification will include "diffuse midline gliomas with histone H3 K27M mutation" as a new diagnostic entity. We identify imaging characteristics of diffuse midline gliomas in pediatric patients based on the presence or absence of histone H3 K27M mutation.

Materials and Methods

We identified 31 pediatric patients (<18 years old) with diffuse gliomas with available magnetic resonance imaging (MRI). Histopathologic subtypes included diffuse astrocytoma, anaplastic astrocytoma, and glioblastoma. We evaluated the imaging patterns of these diffuse gliomas based on their location, enhancement pattern, and necrosis.

Results

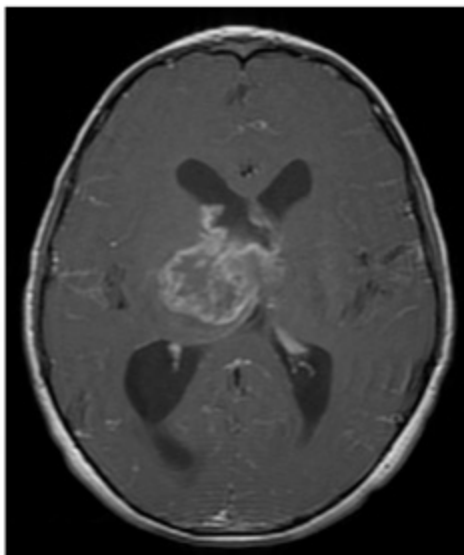
In these 31 patients, tumors were supratentorial in origin in 42% of cases, infratentorial in 52%, and cervical spine in 6%. Seventy percent of the tumors were midline (thalamus, pons, or spinal cord) with 90% of these harboring K27M mutation. All of the tumors arising supratentorially in the cerebral hemispheres had wild type histone H3 and were associated with a high amount of necrosis ($p < 0.003$). Both of the two cervical spine tumors were K27M positive and demonstrated distal subependymal metastases within the lateral ventricles on follow-up imaging at 5-13 months. When comparing histone H3 mutant to wild type diffuse gliomas, there was no statistically significant correlation between enhancement or border characteristics, infiltrative appearance, presence of edema, or ADC value.

Conclusions

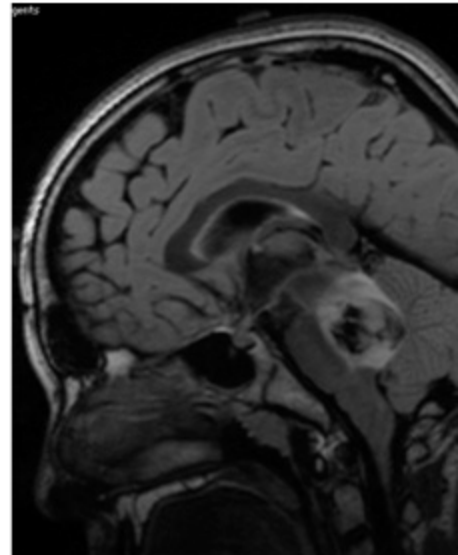
The majority of diffuse midline gliomas originating in the thalamus, pons, or spinal cord were found to harbor histone H3 K27M mutation and showed a propensity for distal metastatic spread, particularly for those arising in the cervical cord. In contrast, diffuse gliomas arising in the cerebral hemispheres were uniformly negative for K27M mutation and were more likely to demonstrate necrosis.

**Histone H3
K27M**

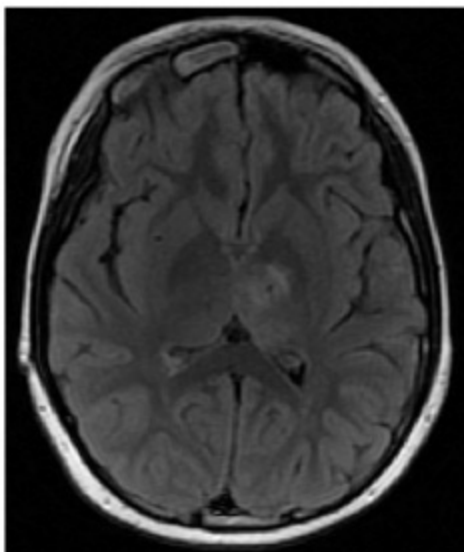
**Thalamus
72%**



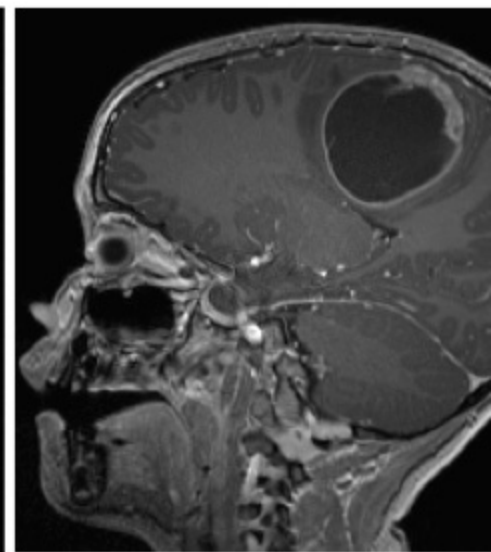
**Pons
100%**



**Thalamus
28%**



**Peripheral
100%**



**Histone H3
WT**

(Filename: TCT_O-347_12102015Ed.jpg)

O-348

1:55PM - 2:03PM

Use of ADC Histogram Metrics in Characterization and Survival Prediction in Pediatric Brain Tumors: A Report from the Pediatric Brain Tumor Consortium

S Vajapeyam¹, D Brown¹, K Ricci², M Kocak³, A Onar⁴, M Fouladi⁵, T Poussaint¹
¹*Boston Children's Hospital, Boston, MA*, ²*Massachusetts General Hospital, Boston, MA*, ³*University of Tennessee Health Science Center, Memphis, TN*, ⁴*St. Jude Children's Research Hospital, Memphis, TN*, ⁵*Cincinnati Children's Hospital, Cincinnati, OH*

Purpose

To characterize pediatric brain tumors based on apparent diffusion coefficient (ADC) histogram metrics, and explore correlations of these metrics with survival for various tumor types.

Materials and Methods

A framework for quantitative ADC histogram analysis was developed using a retrospective review of 121 patients in five newly diagnosed brainstem glioma (BSG) treatment protocols (1). The methodology was applied to a cohort of 14 patients in a non-NF1 optic pathway/low-grade glioma (LGG) protocol to test feasibility in a different tumor type. Postcontrast T1 images and ADC maps were registered to the corresponding FLAIR images using a mutual information algorithm in FSL2. Three dimensional regions of interest (ROIs) comprising FLAIR and enhancement tumor volumes were generated automatically using a thresholding feature available in Fiji3. Quantitative histogram analysis of the FLAIR and enhancing tumor volumes also was done using Fiji, using a uniform bin width and uniform range of ADC values chosen to limit the ADC values to solid tumor. For each histogram, the following metrics were assessed for FLAIR and enhancement volumes: number of peaks, mean ADC, standard deviation (SD), mode, median ADC, skewness and kurtosis. For bimodal distributions, metrics for each peak were assessed separately.

Results

In our previous work, ADC histogram metrics in the BSG cohort demonstrated significant correlations with survival, with lower mean, mode and median baseline ADC, higher skewness, and presence of enhancement associated with shorter survival (1). The same histogram technique was translated easily to a small LGG cohort, proving the versatility of the technique and ease of use for other pediatric brain tumor types. The LGG cohort typically showed baseline high ADC mean values.

Conclusions

Apparent diffusion coefficient histogram metrics in pediatric brain tumors provide a 3D analysis of tumor volume diffusion characterization, which recently has been applied in children with diffuse intrinsic brainstem glioma (1). This technique can be used in other brain tumor types and future work will evaluate associations with treatment and survival.

O-349

Utility of Post-contrast FLAIR Imaging in Pediatric Brain Tumors: Initial Experience

G Zuccoli¹, M Tamber¹, M Utz², F Kamal¹, G Mason¹, I Pollack¹, A Panigrahy¹

¹Children's Hospital of Pittsburgh of UPMC, Pittsburgh, PA, ²University of Pittsburgh Medical Center, Pittsburgh, PA

Purpose

Spoiled gradient echo contrast-enhanced T1-weighted imaging (T1-WI) is used routinely for initial evaluation and re-evaluation of pediatric brain tumors.

Postcontrast volumetric fluid attenuated inversion recovery (FLAIR) has emerged as a useful sequence in evaluating both morphology of the primary lesion and the presence of intracranial metastases. On postcontrast FLAIR images, edema and nonenhancing parenchymal tumor appear hyperintense. Since FLAIR imaging nulls the signal of cerebrospinal fluid (CSF) in the subarachnoid spaces, we believe that postcontrast FLAIR also has utility in the evaluation of leptomeningeal dissemination of tumor. Our study compares the performance of postcontrast volumetric FLAIR imaging compared to T1-WI in depicting the local extent and leptomeningeal seeding of primary brain tumors.

Materials and Methods

IRB approval was obtained. A retrospective review of the radiology database was performed for patients with a history of a primary brain tumor. Patients were included if they had a study which had both postcontrast SPGR and postcontrast volumetric FLAIR sequence. A total of 46 patients were included. The age, sex, and diagnosis were collected from the electronic medical record. Two reviewers reviewed each study, a pediatric neuroradiologist with 15 years of experience, and a neuroradiology fellow. Each reviewer recorded the number of lesions observed on precontrast axial 2D FLAIR, postcontrast SPGR, and postcontrast volumetric FLAIR. Thirty lesions was used as a maximum cutoff, beyond which they were considered too many to individually count. The Wilcoxon signed rank-test was used to compare the number of lesions visualized on postcontrast SPGR and postcontrast volumetric FLAIR. Each reviewer also decided whether postcontrast FLAIR depicted better extent of parenchymal tumor into the extra-axial spaces.

Results

A total of 46 studies were reviewed. Ten studies (19.6%) had lesions which were seen on postcontrast FLAIR but not on SPGR. The median number of lesions was 3.5 on postcontrast FLAIR (IQR 1.75-16.5) and one on SPGR (IQR 0.75-5.5), which was a statistically significant difference ($p=0.011$). Two studies demonstrated lesions on postcontrast FLAIR and no lesions on SPGR (ependymoma and low grade glioma). Two studies had lesions that were better seen on SPGR (germinoma and glioblastoma).

multiforme). A full assessment of the inter-rater reliability of the quantification of additional lesions on postcontrast FLAIR is in progress.

Conclusions

In conclusion, our preliminary results show that postcontrast FLAIR may represent an additional tool in depicting new lesions in intracranial metastases or tumor recurrence in children affected by primary brain tumors. Our results suggest that postcontrast FLAIR can have a significant clinical impact by discovering lesions not identifiable on standard volumetric postcontrast imaging.

O-350

2:11PM - 2:19PM

Intracranial Inflammatory Germinoma: A Pathologic and Imaging Pitfall

R Lobo¹, G Hedlund², C Palmer¹, A Osborn¹

¹University of Utah, Salt Lake City, UT, ²Primary Children's Hospital, Intermountain Healthcare, Salt Lake City, UT

Purpose

Inflammatory changes associated with extra central nervous system (CNS) germinomas are well recognized. That intracranial germinomas can be associated with granulomatous inflammation is less well recognized with only a few scattered case reports in the literature. In this paper we identify and characterize the imaging and pathologic spectrum of intracranial germinoma-associated inflammatory changes.

Materials and Methods

An IRB-approved query of our imaging databases for "germinoma" and MR brain yielded 28 pathologically-proven cases. Demographic, clinical and laboratory data were documented and imaging findings (tumor location, size, signal intensity, enhancement, and presence/extent of T2/FLAIR hyperintensity outside the enhancing neoplasm's margin) were tabulated. Surgical pathology including the presence of associated inflammatory and/or granulomatous change was recorded.

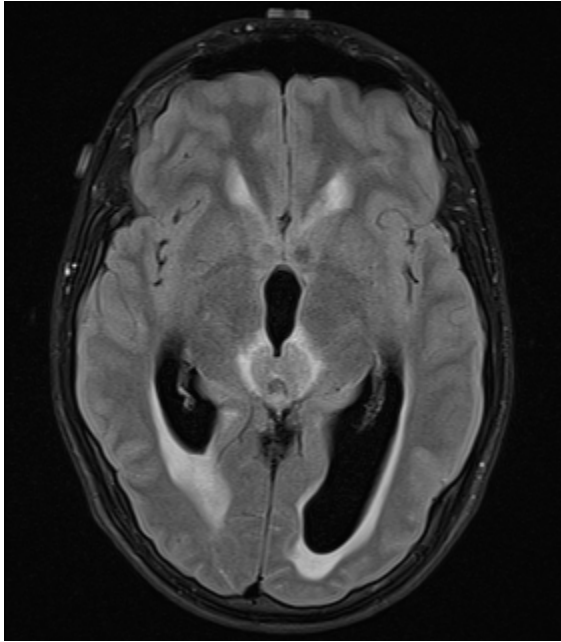
Results

Fourteen tumors were located in the pineal gland, 11 in the pituitary/infundibulum/hypothalamus, and three in the basal ganglia/thalami. Seven cases had multiple sites of involvement. Twelve of 14 pineal lesions (86%) exhibited T2/FLAIR hyperintensity that extended beyond the enhancing tumor margin, most commonly into the thalami (83%), tectum (75%), midbrain (42%) and pons (25%). Extratumoral extent varied from minimal (2mm) to striking (7 mm). Histopathology in six cases specifically referenced inflammatory changes infiltrating along the tumor including lymphocytes, lymphoplasmacytic cells, or nests of inflammatory cells that in some cases almost completely obscured the neoplasm. Initial biopsy in three cases disclosed only granulomatous change/inflammatory cells "without evidence of

tumor." Repeat biopsies were all positive for germinoma. All cases were treated with steroids, chemotherapy and/or radiation with subsequent imaging showing retracting tumoral enhancement together with complete resolution of the pre-operative T2/FLAIR abnormalities in the adjacent parenchyma.

Conclusions

Inflammatory reaction commonly is associated with intracranial germinoma and is seen as confluent T2/FLAIR hyperintensity extending beyond the enhancing tumor into the adjacent parenchyma. Initial biopsy in inflammatory germinoma may be negative, showing only inflammatory cells. Repeat biopsy should be performed as robust lymphoplasmacytic infiltrates may obscure neoplastic cells.



(Filename: TCT_O-350_1075648392.jpg)

O-351

2:19PM - 2:27PM

Radiation Induced Cerebral Microbleeds in Pediatric Patients with Brain Tumors Treated with Proton Radiotherapy

L Grignon¹, S Kralik¹, W Finke¹, C Ho¹
¹Indiana University, Indianapolis, IN

Purpose

Cerebral microbleeds have been demonstrated to occur following conventional (photon) radiation therapy for brain tumors in both pediatric and adult patients with an incidence ranging from 3.4-50%. In pediatric patients, proton radiotherapy has a theoretical advantage compared to conventional radiotherapy of reduced radiation dose to normal brain parenchyma. The goal of this study was to determine the

incidence, time to development, and imaging characteristics of radiation therapy-induced cerebral microbleeds in pediatric patients with brain tumors treated with proton radiotherapy.

Materials and Methods

Following institutional review board approval, a retrospective review of clinical and radiologic data was performed on 16 consecutive pediatric patients with primary brain tumors who had undergone cranial proton beam radiotherapy from January 2010 to October 2012, and had clinical and MR imaging follow up performed at our institution with susceptibility-weighted imaging (SWI) sequences. Radiation therapy-induced cerebral microbleeds were defined as focal areas of susceptibility artifact in the brain parenchyma which did not correspond to normal vessels, were not present on initial presentation imaging, and which did not correspond to hemorrhage within residual tumor or at the resection site. A review of clinical data and the SWI sequence was performed to determine the incidence of microbleeds, number of microbleeds per patient, new or progressive enlargement of microbleeds, time from radiation therapy to development of microbleeds, and imaging follow-up duration.

Results

The median patient age at time of brain tumor diagnosis was 6 years (range 1.5 -18 years). All of the patients underwent MR imaging prior to radiation therapy and none of them were found to have microbleeds prior to treatment. A total of 14/16 (87.5%) of patients developed microbleeds with median time to development of 2.6 years (range 0.75-4.1 years). All of these patients demonstrated multiple microbleeds rather than a single lesion. The largest cerebral microbleed was 1.1 cm with a median size of 0.65 cm (range 0.1-1.1 cm). A total of 2/16 (12.5%) patients did not develop cerebral microbleeds following radiation therapy with median follow-up duration of 3.5 years (range 3-3.9 years).

Conclusions

The majority of pediatric patients with primary brain tumors treated with proton radiotherapy develop multiple cerebral microbleeds. The incidence of radiation therapy-induced microbleeds in pediatric patients treated with proton therapy radiation may be greater than patients treated with conventional radiation therapy.

O-352

2:27PM - 2:35PM

Clinical Validation of Synthetic Brain MRI in Children

H West¹, J Leach², B Jones², S Serai², M Care², R Radhakrishnan³, E Alvarado³, A Merrow²

¹CCHMC, Cincinnati, OH, ²Cincinnati Children's Hospital Medical Center, Cincinnati, OH, ³Cincinnati Children's Hospital, Cincinnati, OH

Purpose

To determine the diagnostic accuracy of synthetic magnetic resonance (MR) sequences generated using postacquisition processing of a single sequence that measures inherent R1, R2 and PD tissue properties [multi-dynamic and multi-echo sequence (Qmap)] compared with conventionally acquired sequences as part of a routine clinical pediatric brain MR exam (1).

Materials and Methods

Thirty-two patients (mean age 10.4 years) underwent routine clinical brain MRI with both conventional and synthetic sequences (22 abnormal). Exams were performed at 3T(18) and 1.5T(13) (GE Healthcare, Waukesha, WI). Synthetic axial T1, T2 and T2 FLAIR or PD sequences were made to match the comparable clinical sequences in each case (1). Two exams (conventional and synthetic) for each patient were de-identified. Four blinded reviewers each reviewed eight patients and were asked to generate clinical reports on each exam at two different times with different sequence origin (synthetic or conventional) separated by a mean of 33d. Exams were rated for overall and specific finding agreement (synthetic/conventional and compared to gold standard consensus review by two senior reviewers with knowledge of clinical report), quality and diagnostic confidence.

Results

Overall agreement between conventional and synthetic exams was 97%. Agreement with consensus readings was 84% (conventional) and 81% (synthetic), $p=0.61$. There were no significant differences in sensitivity, specificity or accuracy for specific imaging findings involving the ventricles, cerebrospinal fluid (CSF), brain parenchyma, or vasculature between synthetic or conventional exams ($p>0.05$).

Although there were some subtle differences between exams, no significant difference in exam quality or diagnostic confidence (sufficient or better for diagnosis) or significant difference in noise/artifacts (that would compromise diagnosis) was noted comparing studies with synthetic or conventional sequences ($p<0.0001$).

Conclusions

Diagnostic accuracy and quality (sufficient for diagnosis) of synthetically generated T1, T2, T2 FLAIR and PD sequences is comparable to conventionally acquired sequences as part of a standard pediatric brain exam. Further confirmation in a larger study is warranted.

O-353

2:35PM - 2:43PM

Real-time Rigid Body Registration of Ventricle Check MRI Using Commercial Thin-Client Software: A Feasibility Study.

E Yang¹, J Vaughn¹, P Hill¹, J Schulte¹, P Ketwaroo¹, J Frost¹, G Colleran¹, T Meehan², C Stamoulis¹, S Prabhu¹

¹*Boston Children's Hospital, Boston, MA*, ²*Massachusetts General Hospital, Boston, MA*

Purpose

Detection of longitudinal change is a fundamental task performed by all neuroradiologists. However, day to day differences in proscribed imaging planes can frustrate accurate comparison of features (e.g., ventricle size or lesion load). These day to day variations can be corrected using image registration software though such software has received limited clinical use to date. We investigated the feasibility of using real time rigid body image registration on a thin client module attached to our PACS system. This real time registration was studied using ventricle check magnetic resonance images (MRIs) and analysis of speed, confidence, and accuracy of interpretation by seven trainee radiologists.

Materials and Methods

Thirty ventricle check MRIs (HASTE or T2-weighted with extended echo train length) from 24 individuals were compared to other ventricle check MRIs or T2-weighted series from diagnostic brain MRIs at a different point in time. After manual and software-assisted review by two attending pediatric radiologists with a total of 12 years experience, consensus for changes in the ventricle system was determined (timepoint A, timepoint B, or unchanged). After removing subjects who were presented more than twice and choosing a range of comparison difficulty (6 "easy", 5 "medium", and 17 "hard"), a total of 28 image pairs from 22 subjects remained (mean age 8.2 years) with a mean comparison interval of 116 days. Seven trainee radiologists (5 fellows, 2 residents) compared the images from the two time points in randomized order, indicating larger time point (or neither) and confidence in rating (1="completely uncertain" to 5="certain"). A subset of five "hard" cases were separately timed. Subsequently, the same exercise was performed using the Synapse 3D "Fusion" module opened from the Synapse PACS.

Results

Using PACS only, the concordance of the seven trainee radiologists was in the range 71.4%-89.3% (median = 82.1%, (25th, 75th) quartiles = (73.2%, 82.1%)) whereas with image registration assisted review, it was in the range 82.1%-89.3% (median =85.7%, (25th, 75th) quartiles = (82.1%, 88.4%)). The median time of interpretation for the five timed cases was 122 seconds by eye [(25th, 75th quartiles) = (83.8, 179.3)] seconds and 97 seconds with software assistance [(25th, 75th) quartiles = (82.0, 119.5)] seconds. Despite trends favorable for the utility of the coregistration-assisted image review, there was no statistically significant advantages in speed of interpretation or accuracy. For interpretative confidence, statistically significant increases in confidence were demonstrated for four of seven subjects only.

Conclusions

Although diagnostic superiority cannot be asserted based on the available data, this

study indicates the feasibility of performing real time image registration in a clinical environment. Caveats of this work include potential for geometric distortion between scans and obscuration of parenchymal features due to use of nonisotropic data sets.

Wednesday

3:00PM - 4:30PM

Washington Marriott Wardman Park, Marriott Ballroom

17A-SNIS Programming; New Devices in NeuroInterventional Space

17A-1

3:00PM - 3:20PM

The FDA and the NeuroInterventional Space: Helping to Define New Horizons

Jensen, M.

University of Virginia Health Systems

Afton, VA

17A-2

3:20PM - 3:40PM

Quality and Training in the World of New Devices: Who is Responsible?

Prestigiacomo, C.

Neurological Institute Of New Jersey

Newark, NJ

17A-3

3:40PM - 4:00PM

New Devices for Hemorrhagic Stroke (Aneurysm and AVM): A Synopsis

Turk, A.

Med. Univ. of So. Carolina

Charleston, SC

17A-4

4:00PM - 4:20PM

New Devices for Ischemic Stroke: A Synopsis

Rai, A.
West Virginia University
Morgantown, WV

17A-5

4:20PM - 4:30PM

Panel Discussion

Wednesday

3:00PM - 4:30PM

Washington Marriott Wardman Park, Washington 4/5/6

17B-ASSR Programming: Advanced Imaging of the Spine (AR) (SAM)

17B-1

3:00PM - 3:20PM

MR Neurography: Plexus and Peripheral Neurography

Carrino, J.
Hospital for Special Surgery
New York, NY

17B-2

3:20PM - 3:40PM

Optimized Imaging of the Instrumented Spine

Tanenbaum, L.
RadNet, Inc.
Baltimore, MD

17B-3

3:40PM - 4:00PM

Spinal Cord Imaging: Advanced Techniques

Law, M.
Keck Medical Center of USC
Los Angeles, CA

17B-4

4:00PM - 4:20PM

Spinal 4D MRA

Chokshi, F.
Emory University School of Medicine
Atlanta, GA

17B-5

4:20PM - 4:30PM

Questions and Answers

Wednesday

3:00PM - 4:30PM

Washington Marriott Wardman Park, Washington 1/2/3

17C-PET-MR

17C-1

3:00PM - 3:25PM

Introduction to PET/MRI Neuroimagers

Zaharchuk, G.
Stanford University
Stanford, CA

17C-2

3:25PM - 3:50PM

PET/MRI of Dementia

Nasrallah, I.
HUP
Philadelphia, PA

17C-3

3:50PM - 4:15PM

Multimodality Imaging of Epilepsy: Role of PET/MRI

Stufflebeam, S.
Massachusetts General Hospital
Boston, MA

17C-4

4:15PM - 4:30PM

Panel Discussion

Wednesday

3:00PM - 4:30PM

Washington Marriott Wardman Park, Roosevelt 1-3

17D-PARALLEL PAPER SESSION-Turbo Talks-Acute Stroke: Imaging and Intervention

O-354

3:00PM - 3:03PM

Differences in neuroimaging utilization in acute stroke: A population based study

A Vagal¹, P Sanelli², H Sucharew³, K Alwell⁴, J Khoury⁴, P Khatri⁵, M Flaherty⁴, B Kissella⁴, O Adeoye⁴, F De Los Rios La Rosa⁴, S Martini⁴, J Mackey⁴, D Kleindorfer⁴
¹Univ. Hosp./Univ. Cincinnati College Of Medicine, Cincinnati, OH, ²North Shore - LIJ Health System, Manhasset, NY, ³Cincinnati Childrens Hospital Medical Center, Cincinnati, OH, ⁴University of Cincinnati, Cincinnati, OH, ⁵University Of Cincinnati Medical Center, Cincinnati, OH

Purpose

Rates of diagnostic work up in stroke have increased over time. However, less is known about differences in utilization of neuroimaging for stroke from a population perspective. Our primary objective was to assess whether race-, sex- and age-related differences exist in neuroimaging utilization in a population-based study.

Materials and Methods

Stroke (ischemic and hemorrhagic) and transient ischemic attack (TIA) patients were identified in a metropolitan population of 1.3 million served by 15 different inpatient hospitals in the Greater Cincinnati area in calendar years of 2005 and 2010. Patient charts and imaging records were abstracted by research nurses and reviewed by study physicians. The proportion of imaging use within 2 days of stroke/TIA onset or hospital admission date including noncontrast head CT (NCCT), magnetic resonance imaging (MRI) head, computed tomography (CT) angiogram (CTA), (MR) angiogram (MRA), digital subtraction angiogram (DSA) and carotid ultrasound was computed. Multivariable logistic regression was used to examine the odds of advanced imaging utilization (CTA/MRI/MRA) adjusting for insurance, baseline NIHSS, ED presentation and hospital type (academic versus community).

Results

In 2005, there were 3471 stroke/TIA events with imaging data available in 3226 patients and, in 2010, there were 3431 stroke/TIA events with imaging data in 3213 patients. A higher proportion of males received MRI (55% versus 51%) and MRA (36% versus 31%) as compared to females in both 2005 and 2010 with no gender differences in utilization of NCCT, CTA, DSA or carotid ultrasound. A higher proportion of blacks received NCCT (96% versus 92%), MRI (59% versus 51%), MRA (42% versus 41%) as compared to whites ($P < 0.01$) with no racial difference in CTA and DSA. All imaging utilization except NCCT and carotid ultrasound was higher in younger (< 55 years) as compared to older patients (> 55 years) ($P < 0.01$). Multivariable regression demonstrated that the odds of receiving NCCT did not differ significantly by age, sex, and race. Adjusting for covariates, younger age (< 55) was associated with higher odds of additional advanced imaging (CTA/MRI/MRA) compared to older age (> 55) patients, and white race was associated with lower odds of additional advanced imaging compared to black race patients. (Table).

Conclusions

In a large population-based study, age, racial and gender related differences exist in the utilization of neuroimaging for patients with acute stroke. The differences may be partly driven by age, with younger patients getting more extensive work ups. However, further understanding of the contributors can provide an important basis for newer lines of inquiry into environmental, socioeconomic and access to health care issues.

| | OR (95% CI) | P-value |
|------------------------------------|-------------------|---------|
| Age | | |
| <55 years | 1.90 (1.63, 2.22) | <0.01 |
| Sex | | |
| Female | 0.95 (0.85, 1.06) | 0.32 |
| Race | | |
| Whites | 0.79 (0.67, 0.93) | <0.01 |
| Percentage below poverty | | |
| ≥20% | 0.85 (0.69, 1.03) | 0.10 |
| Academic | 1.43 (1.20, 1.71) | <0.01 |
| ED event | 1.95 (1.65, 2.29) | <0.01 |
| Insurance | 0.91 (0.70, 1.18) | 0.47 |
| Baseline NIHSS | 0.93 (0.92, 0.94) | <0.01 |
| Event type (TIA reference) | | |
| ICH/SAH | 1.22 (0.99, 1.50) | 0.07 |
| Infarct | 2.51 (2.19, 2.88) | <0.01 |
| Seen by stroke team or neurologist | 2.33 (2.07, 2.63) | <0.01 |
| Study year | | |
| 2010 | 1.66 (1.48, 1.85) | <0.01 |

(Filename: TCT_O-354_Table_ASNRabstract.jpg)

O-355

3:03PM - 3:06PM

ESCAPE to reality: Post-trial outcomes in an ESCAPE centre

A Nixon¹, M Jamison², I Rennie¹, P Flynn¹, A Hunter¹, P Burns¹

¹Royal Victoria Hospital, Belfast, AK, ²Royal Victoria Hospital, Belfast, AK

Purpose

The Royal Victoria Hospital, Belfast provides the regional neuroendovascular service for Northern Ireland and was an enrolling center for the ESCAPE endovascular stroke trial. Our endovascular service for acute ischemic stroke continues to be time limited. The purpose of this study was to assess outcomes for patients presenting with acute stroke following discontinuation of trial enrollment at our center.

Materials and Methods

We collected data on all patients presenting with acute stroke between Nov 1st 2014 and Oct 31st 2015 who received endovascular treatment or received IV thrombolysis (IV-tPA) alone. ESCAPE eligibility of each patient was assessed. Presenting and discharge National Institute for Health Stroke Scale (NIHSS) score was recorded. The primary outcome was modified Rankin Score (mRS) at 3 months. Favorable mRS was defined as a score of ≤ 2 at 3 months.

Results

One hundred thirty-two presented with acute stroke symptoms during the time period. Seventy-three of 132 (55.3%) patients were treated with IV-tPA only. Of these 73 patients, 45 (61.6%) had identified thrombotic occlusion [via CT angiography or hyperdense vessel on unenhanced computed tomography (CT)]. Fifty-nine of 132 (44.4%) patients received endovascular treatment. Forty-six of 59 (78.0%) patients treated with endovascular treatment were considered ESCAPE eligible and 17/73 (22.3%) patients treated with IV-tPA were considered ESCAPE eligible. Of the patients considered ESCAPE eligible, 27/46 (58.7%) patients had mRS ≤ 2 at 3 months following endovascular treatment. Four of 17 (23.5%) patients considered ESCAPE eligible had mRS ≤ 2 at 3 months following IV-tPA treatment only, of which six died (35.3%). Thirteen of 59 (22.0%) patients who had endovascular treatment were considered ESCAPE ineligible (basilar occlusion, n=6; M2 occlusion, n= 6, M1 occlusion with ASPECTS < 6 n=1). Of these patients, 6/13 (46.2%) patients had mRS ≤ 2 at 3 months. Fifty-six ESCAPE ineligible patients were treated with IV-tPA only, of which 27 (48.2%) had identifiable thrombotic occlusion. Eleven of 27 (40.7%) patients with identifiable thrombotic occlusion had mRS ≤ 2 at 3 months. Twenty-three of 29 (79.3%) of ESCAPE ineligible patients without definite thrombotic occlusion had mRS ≤ 2 at 3 months.

Conclusions

ESCAPE eligible patients in our center had a favorable outcome rate comparable to the published trial data. ESCAPE ineligible patients tended to do slightly less well, but still much better than the favorable outcome rates achieved with IV-tPA alone. There is potentially a wide discordance between the threshold for futility and trial eligibility criteria when considering endovascular treatment for acute ischemic stroke.

O-357

Establishing the first Mobile Stroke Unit in Argentina.

C Bleise¹, J CHUDYK², J Cirio², J Chudyk³, R Ceratto¹, P Lylyk⁴

¹*Instituto Médico ENERI - Clínica Sagrada Familia, Buenos Aires, CABA*, ²*Instituto Médico ENERI - Clínica Sagrada Familia, BUENOS AIRES, Buenos Aires*, ³*Instituto Médico ENERI - Clínica Sagrada Familia, Buenos Aires, Buenos Aires*, ⁴*Clinica ENERI, Buenos Aires, Buenos Aires*

Purpose

We present the first mobile stroke unit (MSU) in Argentina. New units and trials have been developed in the last 10 years starting with the German concept. We develop this unit as an emergency support for pre hospital stroke management of our institution with a competitive medical and paramedic staff.

Materials and Methods

The MSU is equipped with a mobile CT scanner, a telemedicine program (was develop as a stroke telemedicine/teleneurology software) and point of care laboratory. Since March 2015 to July 2015, 10 patients were evaluated with a primary diagnosis of acute ischemic stroke (AIS). Only three patients were diagnosed with a stroke. One patient was treated with iv-tPA, other with iv-tPA plus mechanical thrombectomy (bridging technique), and the last one only with mechanical thrombectomy.

Results

The use of the MSU resulted in faster times to evaluation and treatment, compared to traditional models. Telemedicine and point of care laboratory were the key points for the diagnosis and treatment. All the treatment options were analyzed directly with the hospital neurologist via telemedicine, allowing us to minimize the treatment times.

Conclusions

The first MSU in Argentina has been introduced in Buenos Aires, after about one year of preparation. Major obstacles to establish the MSU were obtaining funding, licensure, documenting radiation safety protocols, and establishing a locally tailored communication with the emergency system. Preliminary data during a run-in phase indicate no complications. Further studies are in progress to determine the time savings, clinical outcomes, telemedicine reliability, and cost effectiveness of the MSU strategy.



(Filename: TCT_O-357_msuasnr.jpg)

O-358

3:12PM - 3:15PM

Stent Retriever Based Endovascular Reperfusion Therapy in Octogenarians

J Gomori¹, J Cohen², R Leker²

¹Hadassah Hebrew University Medical Center, Jerusalem, Israel, ²Hadassah Hebrew University Medical Center, Jerusalem, NA

Purpose

Endovascular reperfusion therapy (ERT) may be beneficial in a subset of patients with large hemispheric stroke. Previous studies concluded that favorable outcomes are far less frequent in older patients but have not explored outcomes in the era of newer generation stent retrievers.

Materials and Methods

Consecutive patients with large hemispheric stroke treated with stent retriever-based ERT (SERT) were included. We compared neurological and functional outcomes between patients younger and older than 80 years.

Results

We included 16 patients older than 80 years (22.5%, mean age 84.1±4.4 years, 56% females) and compared them to 55 patients that were younger than 80 years (77.5%, mean age 63.1±12.5 years, 51% females). Cerebrovascular risk factor profile, admission NIH stroke scale scores, stroke etiology and procedure-related variables including excellent target vessel recanalization (thrombolysis in cerebral infarction score 2b-3) did not differ between the groups. Favorable outcome at 90 days (modified Rankin Score ≤2) was more common in younger patients (77% versus 23%; p=0.031). In contrast mortality rates were higher in octogenarians (40% versus 7%; p=0.01). Logistic regression analysis adjusting for neurological severity and collateral state identified age over 80 years (OR 0.15 95% CI 0.03-0.75; p=0.02) and

reperfusion state (OR 7.4 95% CI 1.1-49.9; p=0.04) as significant modifiers of favorable outcome. Similarly, age over 80 years was identified as a positive predictor of mortality (OR 8.1 95% CI 1.8-36.7; p=0.007).

Conclusions

Very old patients have higher chances of mortality and a lower probability of achieving functional independence even after SERT. Nevertheless, because some elderly patients do achieve favorable outcomes the cost-effectiveness of SERT in this population needs to be studied further.

O-359

3:15PM - 3:18PM

Acute Ischemic Infarct Topology: Correlation with Lesion Volume and Severity of Clinical Symptoms

S Payabvash¹, J Benson², S Taleb¹, A McKinney¹

¹University of Minnesota, Minneapolis, MN, ²University of Minnesota, St. Paul, MN

Purpose

To determine the correlation between acute ischemic infarct location and lesion volume and severity of stroke symptoms at presentation.

Materials and Methods

Patients with acute ischemic stroke who underwent magnetic resonance imaging (MRI) within 24 hours of symptom onset or last-seen-well between 1/2011 and 12/2014 in two university-affiliated hospitals were included in this study. The infarct lesions were segmented on admission diffusion-weighted imaging (DWI) scans and were coregistered on standardized MNI-152 brain map. The clinical severity was determined by the admission National Institute of Health Stroke Scale (NIHSS) score. The Voxel-based Lesion Symptom Mapping (VLSM) analysis was used to determine the correlation between the infarct location with lesion volume, admission NIHSS, and the NIHSS/volume ratio.

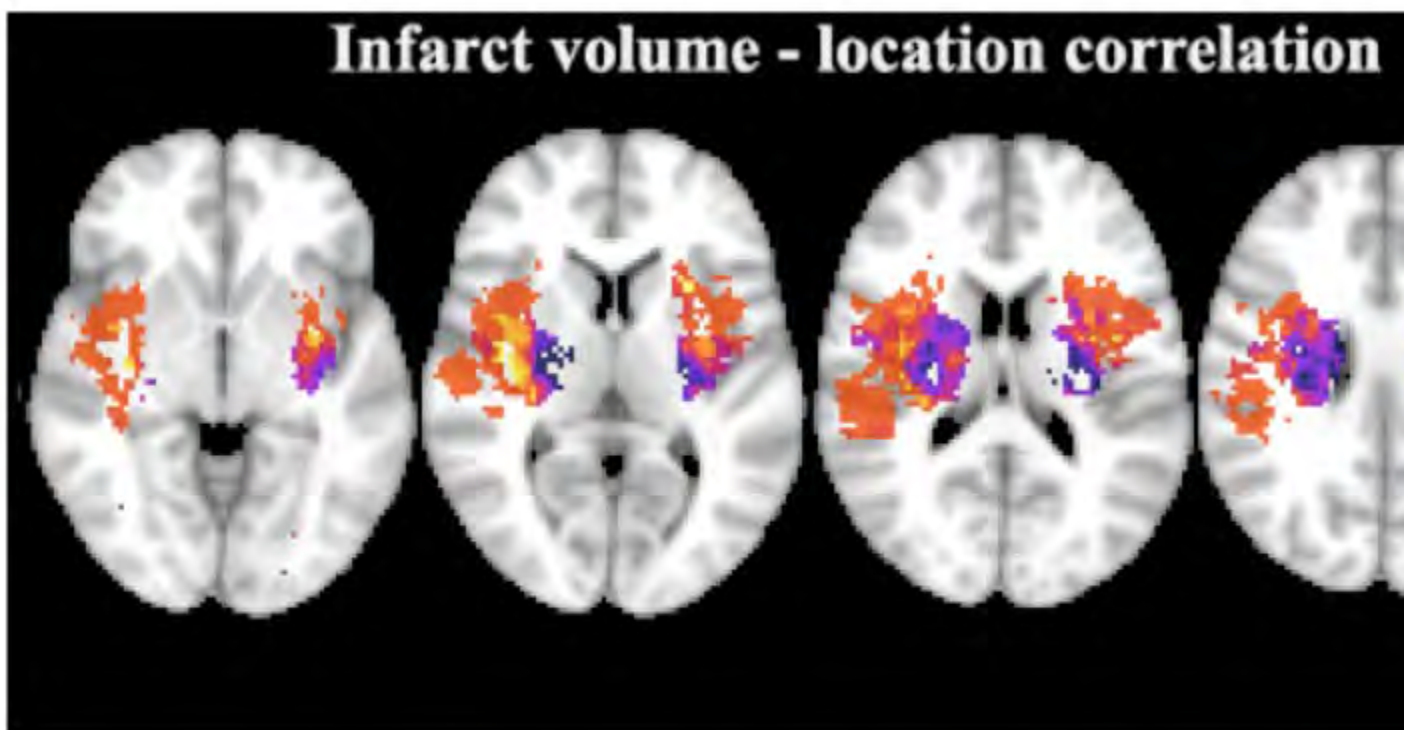
Results

A total of 238 patients were included. On voxel-based analysis, ischemic infarct in bilateral striatocapsular nuclei, insular ribbons, central corona radiata and the right precentral gyrus was associated with larger infarct volume, and higher admission NIHSS. The average volume of ischemic infarcts involving aforementioned regions (76.7 ± 125.6 mL) was higher than infarcts sparing these regions (16.4 ± 24.0 mL, $p < 0.001$). However, infarction of brainstem (i.e., midbrain, pons, and medulla) and/or thalami was associated with higher NIHSS/volume ratio. While the average volume of ischemic infarcts involving the brain stem/thalami (21.5 ± 35.1 mL) was less than infarcts sparing these regions (43.6 ± 92.1 mL, $p = 0.010$); patients with

brainstem/thalami infarction had higher admission NIHSS (median: 6, interquartile: 3 – 11) compared to the rest of patients (median: 4, interquartile: 2 – 7, $p=0.006$).

Conclusions

Ischemic infarcts with larger volume and worse clinical presentation tend to involve the insular ribbon, lentiform nuclei, and central corona radiata. On the other hand, ischemic infarcts of brain stem and thalami are associated with worse clinical presentation despite a small volume. These findings can explain recent reports underscoring the role of insular ribbon infarction as a biomarker for stroke prognostication. These regional findings potentially can be integrated to develop a hazard atlas of the brain for prediction of acute ischemic stroke clinical outcome and treatment triage.



Voxel-based lesion symptom mapping (VLSM) analysis of infarct volume range shows Z scores resulting from Brunner–Munzel testing (threshold higher scores (yellow) indicating areas associated with larger infarct volume).

(Filename: TCT_O-359_ScreenShot2015-12-09at62553PM.png)

O-360

3:18PM - 3:21PM

Slice Accelerated Isotropic Diffusion Imaging (SAIDWI) of the brain in acute ischemic stroke.

J Becker¹, J Probst¹, K Johnson², K Nael³

¹University of Arizona, Tucson, AZ, ²Siemens Medical Solutions USA, Inc, Malvern, PA, ³Icahn School of Medicine at Mount Sinai, New York, NY

Purpose

To evaluate the utility of slice accelerated isotropic diffusion imaging of the brain (SAIDWI) in acute stroke compared with conventional diffusion weighted imaging (DWI).

Materials and Methods

Two hundred fifty consecutive patients presenting with acute symptoms of acute stroke underwent both conventional diffusion imaging and slice accelerated isotropic DWI (SAIDWI) at 3T (Skyra; Siemens Medical Systems, Erlangen, Germany) using a 20 Channel head and neck receive only coil. SAIDWI images were obtained by using a slice accelerated spin-echo single-shot echo-planar (EPI) sequence and a monopolar diffusion gradient scheme for reduced echo time. Multiple slices were acquired simultaneously with a blipped CAIPIRINHA technique with individual slices reconstructed using a Slice GRAPPA reconstruction method. Imaging parameters were as follows: TR/TE of 4400/75 ms, FOV of 27x27 cm, an acquisition matrix of 124 x 124, and section thickness of 2.2 mm with an intersection gap of 0 mm. Voxel Size 2.2 x 2.2 x 2.2 interpolated to 1.1 x 1.1 x 2.2. Seventy four axial slices were obtain using an iPat factor 3 in-plane, and a slice acceleration factor of 2, Diffusion-weighted MR images were acquired with diffusion-weighted factor of 0 and 950 s/mm². Axial, sagittal and coronal DWI and ADC maps were generated. Scanning time was 2:34 minutes.

Results

SAIDWI demonstrated superior signal to noise ratios for acutely restricted lesions compared with conventional DWI, demonstrating significantly more DWI positive lesions than conventional DWI. This allowed for the diagnosis of acute stroke rather than TIA in four cases. SAIDWI also enabled confident diagnosis of small peripheral infratentorial and cortical infarcts that had been mistaken for artifacts on conventional DWI.

Conclusions

SAIDWI is superior to conventional DWI in evaluation of acute ischemic infarcts in patients presenting with acute stroke.

O-361

3:21PM - 3:24PM

TraveStroke (Therapeutic recanalization after vascular events in acute Stroke) Prototype— a clinical software prototype to predict voxelwise time-dependent infarct probability in an acute stroke setting

L Aulmann¹, M Heinrich², F Flottmann³, P Schramm⁴, A Kemmling⁴

¹Universitätsklinikum Lübeck, Lübeck, DEUTSCHLAND, ²Universität zu Lübeck, Lübeck, DEUTSCHLAND, ³Universitätsklinikum Hamburg-Eppendorf, Hamburg, HH, ⁴Universitätsklinikum Lübeck, Lübeck, Germany

Purpose

TraveStroke is a novel imaging prototype aiming to support physicians in acute stroke settings. A patient's individual infarct probability map, considering stroke severity, patient's characteristics, radiological images and time between onset and endovascular treatment is calculated. Results can be displayed as a probability map or a visualization of infarct core and penumbra with changing expected time of recanalization. This visualization shows the predicted patient's individual benefit of endovascular treatment. We evaluated the prototype to test the reliability of the probability maps and the clinical feasibility.

Materials and Methods

The software prototype calculates voxelwise infarct probability from CT perfusion parameter maps using a multivariate logistic regression model published by Kemmling et.al. (1). The algorithm integrates further information with effect on infarct probability (e.g., tissue specific susceptibility to ischemia) into perfusion space. Global variables including age and gender are read automatically out of the imaging dicom-header. The clinical user enters NIHSS-Score (National Institutes of Health Stroke Scale), time of stroke onset and approximated time of recanalization. Patient specific infarct probability maps then are calculated and displayed as infarct core and tissue at risk with changing expected time of recanalization. The prototype was tested in 36 patients with proximal occlusion in anterior circulation. For each patient, the final lesion was segmented manually in a follow-up CT and registered onto the initial CT. Predicted infarct probability maps were binarized by stepwise increasing thresholds and compared to the final lesion by ROC curve analysis. Area under the ROC curve (AUC) was used to test the discriminative power of calculated infarct probability maps to predict infarct lesions.

Results

Automated calculation of the CT perfusion parameter maps (5mm slice thickness) and registration was reliable (88 sec). Treatment time dependent infarct probability maps predicted binary infarct lesions reliably with a ROC-AUC of 0.79 at an optimal probability cut-off of 10% with sensitivity of 71.5% and specificity of 74.2%.

Conclusions

The TraveStroke software prototype rapidly calculates and displays infarct probability maps from CT perfusion imaging that depict infarct core and tissue at risk as a function time to recanalization. The evaluated clinical software prototype may help

physicians in acute stroke triage to estimate individual treatment benefit especially in patient's with prolonged treatment intervals.

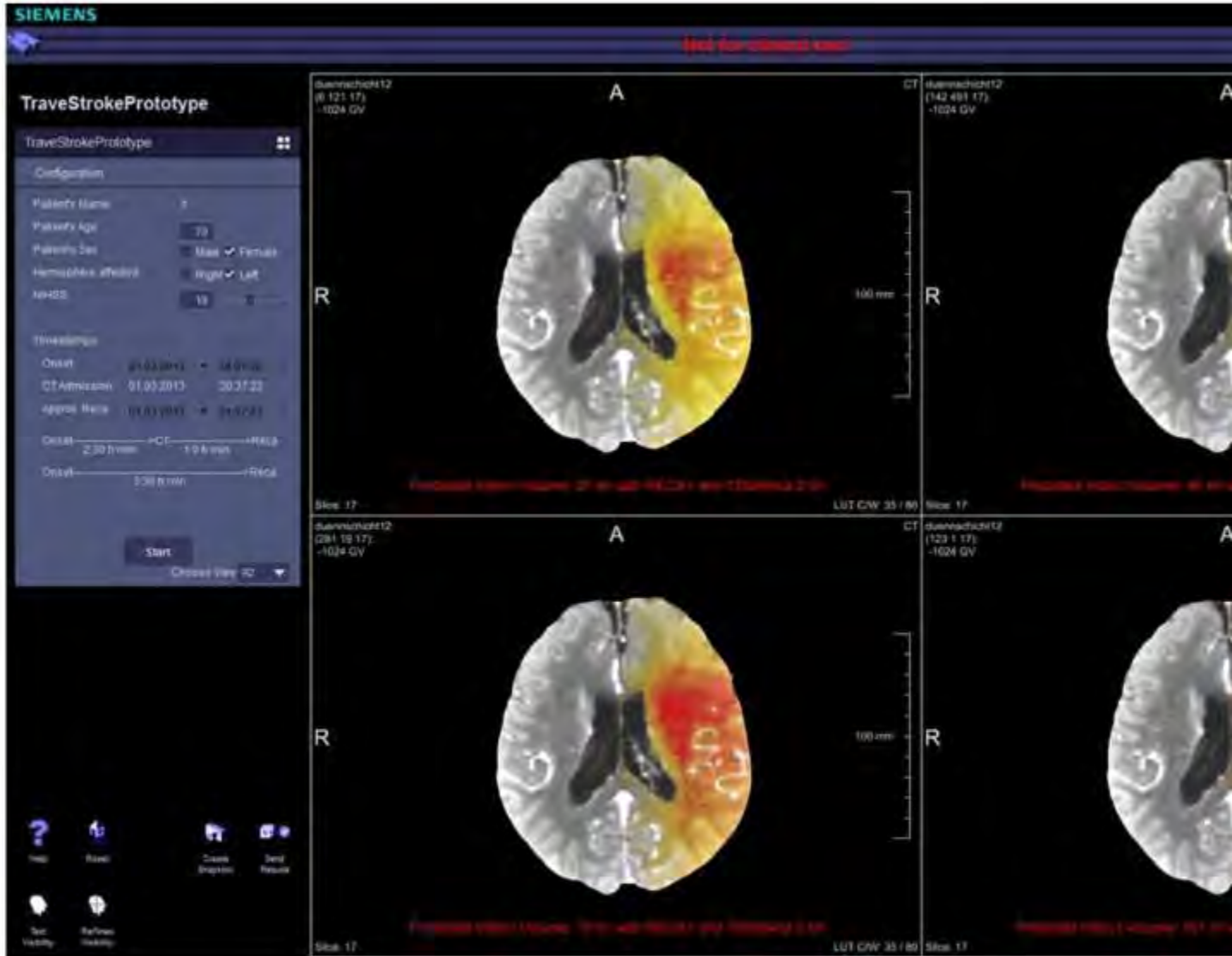


Figure 1: Time-dependent infarct prediction of a patient with acute middle cerebral artery occlusion, NIHSS of 18 and onset 2.5 hours ago. The different pictures show the infarct outcome after successful recanalization (TICI 2b-3) with different time intervals between onset and recanalization (top left: 2.5h, top right: 3.5h, bottom left: 5.5h, bottom right: 7.5h).

(Filename: TCT_O-361_fig1.jpg)

O-362

3:24PM - 3:27PM

Quantitative T1 Rho MR imaging of Acute Ischemic Infarct

D Chow¹, J Soun², C Esenwa², J Grinband³, C Filippi⁴

¹University of California, San Francisco, San Francisco, CA, ²Columbia University Medical Center, New York, NY, ³Columbia University, New York, NY, ⁴North Shore University Hospital, New York, NY

Purpose

Establishing a timeline of acute infarct is prone to uncertainty but remains important in selecting time-sensitive treatments. In an acute stroke animal model, T1 Rho increased linearly in the first 6 hours after middle cerebral artery occlusion, making it possible to objectively date stroke onset. In this feasibility study, we show that a rapid, noncontrast T1 Rho MR sequence during acute stroke can be obtained, and T1 rho values in infarct core and surrounding brain tissue can be quantified in humans.

Materials and Methods

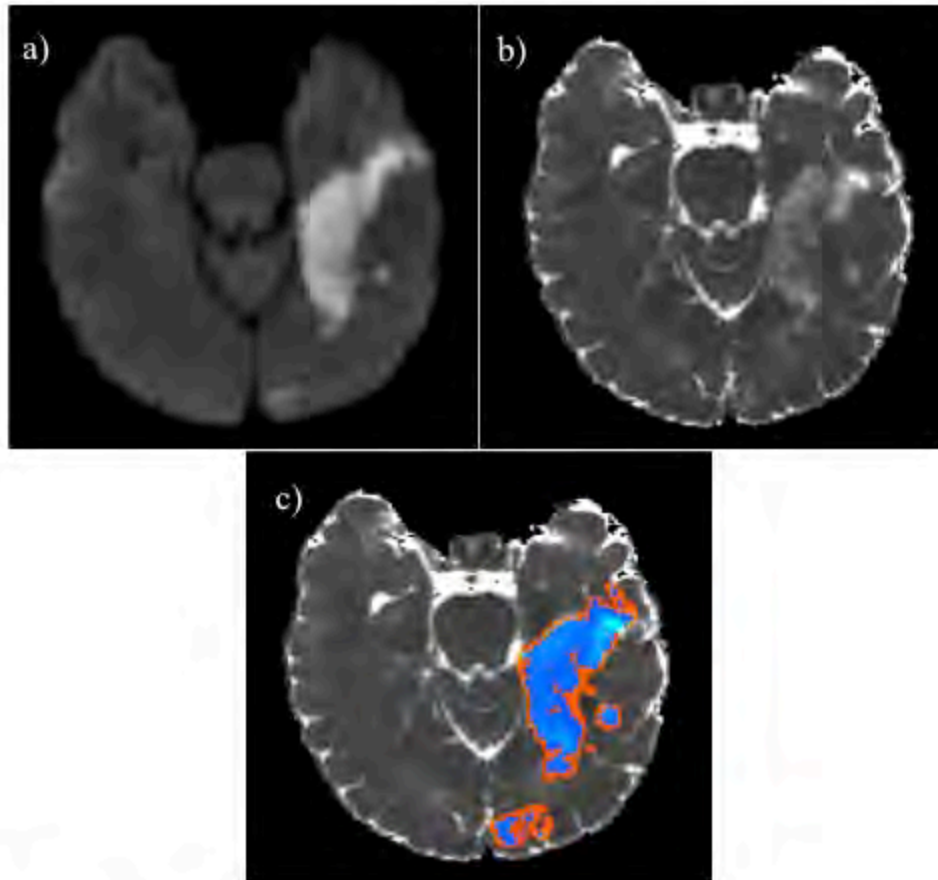
This prospective IRB-approved study included seven acute stroke patients scanned at 3T. Standard diffusion-weighted imaging (DWI) was obtained. T1 Rho MR used a whole-brain 3D technique with spin lock times (TSL) of 1, 10, 30, 50 and 70 ms at spin lock frequency of 300 Hz (acquisition time ~ 7 minutes). Postprocessing used FSL and Matlab. Each spin lock time was registered linearly to the first time point (TSL = 1 ms), and mono-exponential decay was applied to the 5 TSLs to generate a T1 Rho map. Regions of interest were drawn around the infarct on DWI and coregistered to T1 Rho images. Peri-infarct ROIs also were created on T1 Rho images using a mask dilation method. Contralateral normal brain parenchyma served as within subject controls. Mean T1 Rho were quantified and compared using a Student's t-test.

Results

Mean T1 Rho within the infarct ROI were significantly higher compared to contralateral normal brain ROI ($p < 0.005$, 111.16 ± 13.4 and 94.13 ± 14.8 ms, respectively). Mean T1 Rho within the peri-infarct ROI were higher compared to the corresponding contralateral region but not significant ($p < 0.08$, 105.89 ± 16.36 and 94.65 ± 22.06 ms, respectively).

Conclusions

T1 Rho is feasible and can both detect and quantify acute ischemic stroke in humans. A trend of abnormal peri-infarct T1 Rho signal suggests that T1 Rho may be able to assess penumbra. Longitudinal measurements to document how T1 Rho changes with infarct progression are needed.



Acute infarct on a) DWI and b) T1 Rho. ROIs of infarct (blue) and peri-infarct (orange) are shown in c).

(Filename: TCT_O-362_Slide1.jpg)

O-364

3:30PM - 3:33PM

Natural fate of ischemic penumbra is less time dependent and more a measure of collateral flow

A Vagal¹, R Aviv², H Sucharew³, M Reddy⁴, H Hua⁵, P Michel⁶, T Jovin⁷, M Wintermark⁸, P Khatri⁹

¹Univ. Hosp./Univ. Cincinnati College Of Medicine, Cincinnati, OH, ²Sunnybrook Research Institute, Toronto, Ontario, ³Cincinnati Childrens Hospital Medical Center, Cincinnati, OH, ⁴University Of Cincinnati Medical Center, Cincinnati, OH, ⁵University of Virginia, Charlottesville, VA, ⁶University of Lausanne, Lausanne, AL, ⁷University of Pittsburgh, Pittsburgh, PA, ⁸Stanford University, Stanford, CA, ⁹University Of Cincinnati Medical Center, Cincinnati, OH

Purpose

Perfusion and collateral imaging is being used increasingly in the evaluation of acute ischemic stroke with ischemic penumbra as a potential therapeutic target, particularly in later time windows. However, the natural history of the fate of penumbra without reperfusion treatment is understudied. We sought to determine how time from stroke onset to imaging and collaterals affect penumbral salvage in untreated stroke patients.

Materials and Methods

We analyzed all untreated acute stroke patients (without IV tPA or endovascular treatment) who received baseline CT angiogram (CTA) and CT perfusion (CTP) within 24 hours and follow-up CTA or MR angiogram within 24-48 hours utilizing a large, prospectively collected, multicenter acute stroke registry. Baseline CTA was reviewed for arterial occlusion and collateral status, and follow-up CTA/MRA was reviewed to determine recanalization status. Baseline CTP was assessed for ischemic core (rCBF<30%) and penumbra volume (Tmax >6). Final infarct volume (FIV) was measured on follow-up computed tomography (CT) and magnetic resonance imaging (MRI). Penumbra salvage was defined as Penumbra-FIV and penumbral fraction was defined as Penumbra / Penumbra + Ischemic core volume. Associations were assessed between penumbral salvage and time from onset to imaging and collaterals.

Results

Among 110 untreated ischemic stroke subjects, 16 had nondiagnostic perfusion studies. Among 94 remaining subjects, mean age was 65 years, median NIHSS was 13, and median (range) time from stroke onset to baseline imaging was 2.9 (0.4-23) hours. The median (range) of ischemic core volume was 31 (0.4-172), penumbra 42 (0.4-412) FIV 9.8 (0-253) cc. There was no significant correlation between salvaged penumbra and time ($r=0.06$; $p=0.56$). There was a trend towards a positive correlation between penumbral fraction and time ($r=0.20$; $p=0.05$) without statistical significance. Better collaterals were associated with larger salvaged penumbra ($r=0.32$, $p<0.01$).

We further analyzed the data by stratifying according to recanalization status. There was no evidence of an association between spontaneous recanalization and collateral score (median: 1 versus 2, p -value = 0.54), baseline ASPECTS (median: 14 versus 13, p -value = 0.57), penumbral salvage (median: 0 versus 0, p -value=0.35) or penumbral fraction (median: 0.54 versus 0.54, p -value = 0.85).

Conclusions

In this multicenter cohort of untreated acute stroke patients, we found no evidence of time dependence of the natural tissue fate of penumbra, but rather an association with collateral flow. Larger studies are warranted to understand natural history of penumbra that can inform future trials and could have treatment implications particularly in delayed or unknown onset time.

O-365

MR Perfusion to Determine the Status of Collaterals in Patients with Acute Ischemic Stroke: Look Beyond Perfusion Time-maps

K Nael¹, J Knitter¹, A Doshi¹, J Mocco¹, R Deleacy¹, J Bederson¹, T Naidich¹

¹*Icahn School of Medicine at Mount Sinai, New York, NY*

Purpose

Collateral flow is an independent predictor of reperfusion, infarct size, and clinical outcome in patients with acute ischemic stroke (AIS). Magnetic resonance perfusion time-maps show delayed perfusion but are unable to differentiate antegrade from collateral flow if used alone. In this study, using a multiparametric approach, we aimed to identify a perfusion biomarker that can represent the extent of collaterals in comparison to angiographic findings.

Materials and Methods

Acute ischemic stroke patients with anterior circulation proximal occlusion who had baseline MR perfusion and cerebral angiography were evaluated. MR perfusion data were processed using Bayesian method to generate arterial tissue delay (ATD) maps at thresholds of 2, 6 seconds. The volume of delayed perfusion (Vol-ATD2sec), critical hypoperfusion (Vol-ATD6sec), and hypoperfusion (Vol-ATD 2sec-6sec) in addition to corresponding values of rCBV and rCBF were calculated using volume-of-interest (VOI) analysis. Collateral status was dichotomized to poor (TICI 1-2a) or good collaterals (TICI 2b, 3), using baseline cerebral angiography. The association of perfusion biomarkers was assessed with the status of collaterals using repeated measure of analyses. Receiver operating characteristic (ROC) analysis was performed to determine the optimal parameters and threshold for predicting the status of collaterals.

Results

In 37 patients included, 20 (54%) had good collaterals (TICI \geq 2b) using cerebral angiography. After controlling for age, baseline NIHSS and infarct volume, multivariate logistic regression analysis identified rCBV (p=0.001) and hypoperfused volume (Vol-ATD 2sec-6sec) (p=0.01), but not rCBF (p=0.08), Vol-ATD 2sec (p=0.3) or Vol-ATD 6sec (p=0.07), as independent predictors of good collaterals. For rCBV, ROC analysis showed the greatest AUC (0.89) at the threshold > 2.1 with sensitivity/specificity of 85%/90%. For Vol-ATD 2sec-6sec, ROC analysis showed the greatest AUC (0.78) at a threshold > 51 ml with sensitivity/specificity of 70%/82%. Hypoperfused tissue volume (Vol-ATD 2sec-6sec) multiplied by its rCBV, termed hypoperfused tissue collateral index, remained an independent predictor of good collaterals, with improved diagnostic accuracy over each measure alone (AUC: 0.96 at a threshold > 90, sensitivity/specificity of 91%/100%).

Conclusions

Multiparametric MR perfusion can be used to assess the status of collaterals in patients with AIS. Hypoperfused tissue collateral index defined as hypoperfused volume (Vol-ATD 2sec-6sec) x rCBV is a new perfusion index with diagnostic accuracy of 96% compared to angiographic findings to predict status of collaterals.

O-366

3:36PM - 3:39PM

Recanalization and Outcome Comparisons in Acute Ischemic Stroke Patients Treated with Mechanical Thrombectomy Selected by CT/MR Perfusion Imaging Versus CT Angiography

A Honarmand¹, A Shaibani², M Hurley², M Potts², B Jahromi², S Ansari²

¹*Northwestern University Feinberg School of Medicine, Chicago, IL*, ²*Northwestern University, Feinberg School of Medicine, Chicago, IL*

Purpose

Several randomized controlled trials, have demonstrated improved percentages of independent clinical outcomes with computed tomography (CT)/magnetic resonance (MR) perfusion selection in acute ischemic stroke (AIS), albeit with more stringent patient exclusion. Conversely, preprocedure CT angiography (CTA) is gaining increasing credence among neurointerventionalists for documenting emergent large vessel occlusion and as a surrogate for tissue selection via collateral imaging. In this study, we compared the level and times to recanalization as well as clinical outcomes in patients selected for endovascular thrombectomy based on their perfusion versus single phase CTA imaging selection.

Materials and Methods

We performed a prospective IRB approved multicenter study of consecutive AIS patients presenting <6 hours from symptom onset that underwent mechanical thrombectomy. Patients were selected after CTA/MRA confirmed ICA/MCA M1-M2 occlusion and either CTP/MRP (favorable mismatch ratio/core infarct volumes) or CT/CTA (ASPECTS > 6 and pial collaterals > 2/3 MCA) imaging selection. Patient demographics, baseline NIHSS score, THRIVE score, symptom onset to groin puncture times, and the type of thrombectomy devices utilized for recanalization were studied. Modified Rankin Scale score of 0-2 at 90 days defined good functional outcome. Recanalization was delineated by the neurointerventionalist at the end of the thrombectomy according to modified TICI classification. Ordinal recanalization scores of 0, 1, 2, 3, and 4 were assigned to TICI classification of 0, 1, 2a, 2b, and 3, respectively for further evaluation of recanalization/reperfusion level. TICI scores of 2b and 3 defined successful recanalization. Chi-square, student t test, Mann-Whitney U, and Kruskal-Wallis tests were utilized for statistical analysis as appropriate.

Results

Seventy patients (37 F/33 M, mean age±SD of 64.43±15.08 years) were recruited into the study. Based on preprocedure imaging, consecutive patients were selected for endovascular thrombectomy either by CTA (n=35) or perfusion studies (n=35). Both groups were comparable in terms of demographics, NIHSS score, THRIVE score, and thrombectomy devices utilized for recanalization. Symptom onset to groin puncture time was significantly lower in the CTA group (mean= 138.50 min in CTA VS. 224.25 min in perfusion groups, P=0.012). Recanalization scores were not significantly associated with the type of thrombectomy devices (P=0.782). Although recanalization scores were significantly higher in patients selected by CTA compared with perfusion imaging (P=0.020), successful recanalization (TICI 2b/3) was not significantly different (P=0.155). There was a nonstatistically significant trend for good functional outcome in CTA group (P=0.07). Good functional outcome was associated significantly with successful recanalization (P<0.005).

Conclusions

Mechanical thrombectomy patients selected by CTA or perfusion imaging demonstrated no difference in successful recanalization rate, but higher level of recanalization/reperfusion and a trend of improved outcomes with CTA selection that may be attributed to improved treatment times.

O-367

3:39PM - 3:42PM

Clinical Utility of Arterial Spin Labeling Perfusion Images in the Emergency Department for the Work-up of Stroke-Like Symptoms

K Buch¹, W Copen², O Wu¹, G Gonzalez¹, P Schaefer¹

¹Massachusetts General Hospital, Boston, MA, ²massachusetts general hospital, Boston, MA

Purpose

Discrimination between acute stroke and stroke-like conditions can be a diagnostic dilemma. While diffusion-weighted imaging (DWI) is highly sensitive and specific for diagnosing acute stroke, arterial spin labeling (ASL) imaging may improve the differentiation of stroke from stroke mimics and may improve risk stratification.

Materials and Methods

Arterial spin labeling and DWI images from 282 consecutive magnetic resonance imaging (MRI) examinations performed in the emergency department were reviewed. Diffusion-weighted images were evaluated for presence of restricted diffusion, and lesion volumes were calculated. FLAIR and GRE sequences were evaluated for additional abnormalities. Arterial spin labeling-derived cerebral blood flow (CBF) maps were evaluated for decreased, normal or increased CBF, and volumes of lesions

with decreased CBF were calculated. NIHSS, length of hospital stay, and incidence of future neurologic events were extracted from medical records. Correlations between abnormalities on ASL and NIHSS and clinical outcomes were evaluated using a two-tailed T-test.

Results

Of 282 MRI exams reviewed, 95 patients had a final diagnosis of acute infarction, 20 of seizures, and 167 of transient neurologic symptoms. Eighty-two patients had an ASL abnormality and 200 had no ASL abnormality. Arterial spin labeling showed elevated CBF in 29 patients, and decreased CBF in 53 patients. Of the 29 patients with elevated CBF, 26 had reperfusion hyperemia in the setting of infarction, and none of these infarcts grew substantially on follow-up imaging. Three had normal DWI with hyperemia due to seizures. Forty-seven of 53 patients with low CBF had acute infarction with a diffusion abnormality. Ten of 47 had a CBF/DWI mismatch (ratio of > 1.8 CBF/DWI). In follow-up imaging, those with a mismatch demonstrated significantly larger lesion growth ($P < 0.05$) compared to those without a mismatch. Six of 53 had low ASL without a diffusion abnormality. Two of six developed a DWI abnormality on follow-up. The negative predictive value (NPV) of the ASL in predicting a neurologic event requiring hospital admission was 93.5%. The NPV of ASL related to an abnormality detected on other MRI sequences was 91.3%. Statistically significant differences were seen in the NIHSS (median 6.0 versus 1.0, $P < 0.0001$), length of hospital stay (mean 5.7 versus 1.0 days, $P < 0.0001$), and incidence of a future neurologic event (71% versus 6.0%, $P = 0.003$) in patients with versus without an ASL abnormality.

Conclusions

Arterial spin labeling is highly useful in the evaluation of patients with stroke-like symptoms in the emergency setting. Patients with acute neurologic deficits and normal ASL are unlikely to require hospital admission, to have abnormalities identified on other MRI sequences, to have major neurologic deficits, to require a lengthy hospital stay or to have future neurologic deficits. Arterial spin labeling may demonstrate low CBF in patients with normal DWI, thereby confirming that a lesion is due to ischemia and not a stroke mimic. Patients with an CBF/DWI mismatch have significantly more infarct growth, compared to those without a mismatch.

O-368

3:42PM - 3:45PM

Noninvasive assessment of quantitative oxygen extraction fraction in ischemic stroke by MRI susceptibility: a pilot study

A Fan¹, A Khalil², J Fiebach², A Villringer³, G Zaharchuk¹, K Villringer², C Gauthier⁴

¹Stanford University, Stanford, CA, ²Charité Universitätsmedizin Berlin, Berlin, N/A, ³Max Planck Institute for Human Cognitive and Brain Sciences, Leipzig, N/A, ⁴Concordia University, Montreal, Quebec

Purpose

The ability to noninvasively quantify oxygen extraction fraction (OEF) would provide meaningful metabolic data to inform diagnosis and selection of therapy for patients with stroke (1). However, this measurement is technically challenging and no standard method currently exists to image OEF by magnetic resonance imaging (MRI). This study tests a new MRI approach, quantitative susceptibility mapping (QSM) (2, 3), to measure absolute OEF (%) along cerebral veins in patients with ischemic stroke at baseline and follow up.

Materials and Methods

Five patients (ages 60-86 years) were scanned on average 18.2 hours after stroke onset at 3T. Patients were admitted with median NIHSS score of 8 and discharged with median score of 4. Flow-compensated gradient echo phase images were acquired for OEF assessment: TR/TE = 20/12ms; 0.63x0.63x0.8mm³; bandwidth = 220Hz/pixel; 2x GRAPPA acceleration; scantime ~5 min. Each patient received a follow-up QSM scan on average 3.8 days after the first scan; two of five patients received thrombolysis between the two scans. Bolus-tracking perfusion and T1-weighted scans also were collected after gadolinium injection to look at mean transit time (MTT) and vascular anatomy, respectively. For preprocessing, background fields were first removed from the phase images with a spherical harmonic approach. Quantitative susceptibility maps then were reconstructed through a dipole inversion of the phase map with an L1-norm smoothness prior (4). On these maps, susceptibility values in veins (χ_{vein}) are sensitive to oxygenation levels due to the presence of paramagnetic deoxyhemoglobin molecules in venous blood. We identified two of three cortical veins near the infarct and three veins in the contralateral hemisphere for OEF assessment. We quantified $\text{OEF} = 1 - (\chi_{\text{vein}} - \chi_{\text{water}}) / (\Delta\chi_{\text{do}} \times \text{Hct})$ where χ_{vein} was estimated from the 10% brightest voxels in the vessel, $\Delta\chi_{\text{do}} = 0.27\text{ppm}$, and χ_{water} was estimated from cerebrospinal fluid (CSF).

Results

Bright signals on QSM maps corresponded to venous structures seen on gradient echo magnitude and postcontrast T1 scans (Fig. 1). Patients with larger areas of MTT delay (Case 1) tended to have higher OEF in areas of stroke relative to the normal hemisphere; patients with smaller areas of MTT delay tended to have more similar OEF between affected and unaffected areas (Case 2). In all patients, the OEF ratio between the symptomatic and contralateral hemispheres was ≥ 1 (Table 1). In two patients, this OEF ratio normalized between the baseline and follow-up scans, while in all other patients this OEF ratio remained stable between the two time points.

Conclusions

Quantitative OEF assessment by susceptibility mapping in veins is feasible for stroke patients and is consistent with previous qualitative vessel assessment in patients (5). Ongoing work focuses on the relationship between longitudinal OEF changes and clinical and imaging metrics, to better characterize tissue metabolism at various stages of stroke progression.

Figure 1: Quantitative susceptibility MRI for oxygenation



Case 1: 86 yr patient,

Mean transit time (day 1)

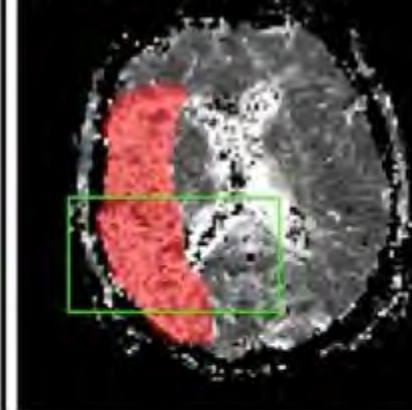
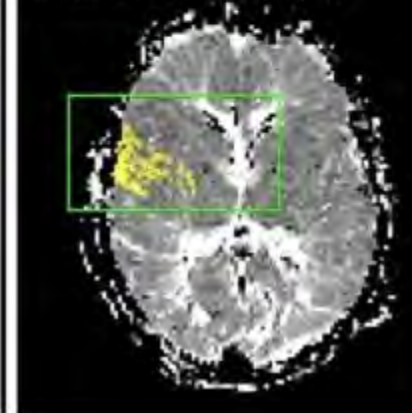


Table 1: Oxygen extraction fraction (OEF) from area of stroke and contralateral hemisphere

| Patient | Baseline | | | Follow-up | | |
|---------|--------------|--------------|-----------|--------------|--------------|-----------|
| | OEF (stroke) | OEF (normal) | OEF ratio | OEF (stroke) | OEF (normal) | OEF ratio |
| 1 | 35.5 | 27.3 | 1.3 | 31.8 | 26.5 | 1.1 |
| 2 | 33.0 | 33.5 | 1.0 | 25.6 | 25.8 | 1.0 |
| 3 | 27.4 | 20.6 | 1.4 | 23.0 | 22.6 | 1.0 |
| 4 | 29.7 | 22.2 | 1.4 | 31.6 | 24.1 | 1.3 |
| 5 | 22.6 | 21.1 | 1.1 | 24.7 | 23.1 | 1.1 |

Case 2: 60 yr patient,

Mean transit time (day 1)



(Filename: TCT_O-368_ASNR_Figure_total.jpg)

O-369

3:45PM - 3:48PM

Extent of Insular Infarct on CT as a Prognostic Indicator of Intraarterial Treatment for Acute MCA Occlusion

J Gadde¹, A Iaia², C Flores², R Hu³, M Lev³, S Kamalian³

¹University of Wisconsin, Madison, WI, ²Christiana Care Health System, Newark, DE, ³Massachusetts General Hospital, Boston, MA

Purpose

The purpose of this study was to determine whether the extent of insular infarct on admission computed tomography (CT) in patients with acute MCA occlusion can predict clinical outcome after intra-arterial treatment.

Materials and Methods

A retrospective review was performed of patients treated for acute MCA infarct as a Stroke Code or Stroke Alert at our institution. Inclusion criteria included patients who received intra-arterial treatment (IAT), documented NIHSS at presentation and discharge and mRS at discharge and 90 days. Two independent CAQ certified neuroradiologists categorized the degree of insular infarction on noncontrast CT exam as <25%, 25-50%, or >50% involvement. A consensus reading was reached between the two reviewers. A TICI score of 2b or 3 was used as the definition of recanalization.

Results

Twenty-eight patients met the inclusion criteria. Patients with insular infarct of <50% had significant clinical improvement after recanalization ($p=0.005$), and those with insular infarct >50% did not have significant improvement ($p=0.87$). However, multivariate analysis demonstrated no significant interaction of insular infarct and recanalization on overall patient outcome.

Conclusions

In this cohort of IAT patients with acute MCA occlusion, the greatest clinical benefit of IAT was seen in the subgroup of patients with "small" insular infarcts on admission CT. We currently are investigating whether the extent of insular infarct on CT is an independent outcome marker compared to admission ASPECTS, and/or whether the difference in predictive value between CT-insula score and diffusion-weighted imaging (DWI)-insula score can be attributed to the different time sensitivities of these modalities.

Wednesday

3:00PM - 4:30PM

Washington Marriott Wardman Park, Maryland A/B/C

17E-PARALLEL PAPER SESSION: Brain Tumors: Diffusion and Perfusion

Techniques

O-370

3:00PM - 3:08PM

A MULTI CENTRIC 3T MR ASSESSMENT OF T2 PERFUSION AND T1 PERMEABILITY IN BRAIN GLIOMAS (MAPPING STUDY): comparison of diagnostic accuracy in preoperative grading.

n anzalone¹, a castellano², g conte¹, v cuccarini³, a bizzi³, a costa⁴, m grimaldi⁵, g grillea⁶, p vitali⁷, m cadioli², m caulo⁸

¹sraffaele hospital, milan, Italy, ²s raffaele hospital, milan, Italy, ³istituto neurologico besta, milan, Italy, ⁴ospedale policlinico, milan, Italy, ⁵istituto clinico humanitas, rozzano milano, Italy, ⁶neuromed, isernia, Italy, ⁷istituto neurologico mondino, pavia, Italy, ⁸itab, chieti, Italy

Purpose

Dynamic contrast-enhanced (DCE) magnetic resonance imaging (MRI) recently has demonstrated to have similar accuracy to dynamic susceptibility contrast (DSC) MRI in glioma grading, but still lacks standardization for MRI data acquisition and analysis. This prospective study aims to verify the diagnostic accuracy of both DCE and DSC techniques for glioma grading applying a definite protocol for data acquisition and processing in a multicentric setting.

Materials and Methods

This prospective study included 92 patients with newly diagnosed gliomas; pre-operative MR studies were performed on 3T magnets in seven centers. Histologic diagnosis was obtained for all the patients through a biopsy or surgery procedure (26 WHO II and 66 III/IV WHO). The acquisition protocol included two injections of 5 ml of gadobutrol one for DCE and one for DSC MR imaging in the same setting. Perfusion data were analyzed with NordicIce (NordicNeuroLab, Bergen, Norway). Parametric maps of Ktrans, Vp, Ve and area under concentration curve (AUC) were obtained from DCE data sets; parametric map of relative CBV (rCBV) from DSC data sets. For each parameter the maximal abnormality through hotspots-based method was evaluated. Diagnostic accuracy was assessed using receiver operating characteristic (ROC) analysis.

Results

In differentiating low- from high-grade astrocytomas, the accuracy of Vp, Ktrans, Ve, AUC and rCBV (area under the curve = 0.88, 0.90, 0.90, 0.91, 0.90 respectively) resulted to be very similar. Cutoff values of Vp, Ktrans, Ve, AUC and rCBV (1.73%, 0.025 min⁻¹, 1.75%, 0.049, 3.67 ml/100g respectively) showed a sensitivity and specificity of 83%, 81% for Vp, 83%, 88% for Ktrans, 88%, 85% for Ve, 86%, 85% for AUC and 85%, 88% for rCBV.

Conclusions

A definite DCE and DSC protocol is feasible for multicentric studies with different MR equipments and central analysis. The results confirmed the high diagnostic accuracy of DCE and DSC for glioma grading.

O-371

3:08PM - 3:16PM

Correlation between Histopathology Defined Percentage Tumor Recurrence, Dynamic Contrast Enhanced (DCE), and Dynamic Susceptibility Contrast (DSC) Perfusion Parameters in Treated High Grade Gliomas.

N Zakhari¹, T Nguyen², A Boivin³, G Jansen⁴, J Woulfe², G Cron², R Thornhill²
¹The Ottawa Hospital, Ottawa, Ontario, ²The Ottawa Hospital University of Ottawa, Ottawa, Ontario, ³University of Ottawa, Ottawa, Ontario, ⁴The Ottawa Hospital University of Ottawa, Ottawa, Ontario

Purpose

New enhancing lesions after surgery and chemoradiation for high grade glioma commonly contain variable proportions of tumor recurrence (TR), tissue necrosis and treatment-related changes. Our purpose is to determine whether magnetic resonance (MR) perfusion parameters correlate with the percentage of TR in these lesions.

Materials and Methods

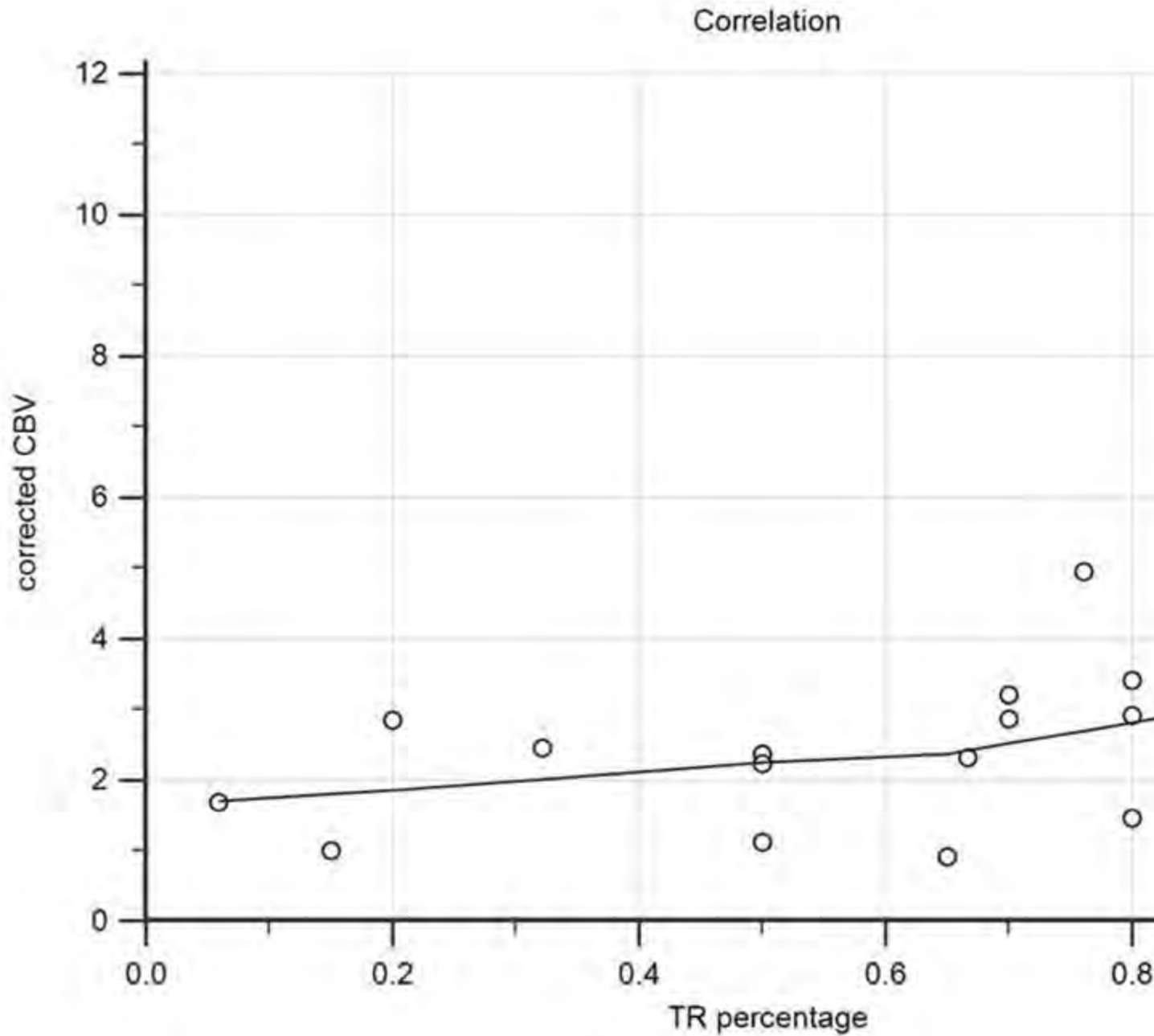
Patients with treated high grade gliomas who developed a newly enhancing lesion on follow-up MRI and who underwent re-resection were enrolled prospectively. Each patient underwent dynamic contrast-enhanced (DCE) and dynamic susceptibility contrast (DSC) perfusion MR. Histogram and hot spot analysis were performed for each parametric map (Ktrans, AUC, Vp, uncorrected cerebral blood volume (CBV) and leakage corrected CBV. Tumor recurrence percentage was defined histopathologically. The lesions were categorized into predominant TR (=tumor>50%), predominant treatment related changes (T=<20%) and mixed lesions (20 %< T=<50%). Spearman's rho correlation coefficient was used to express the correlation between TR percentage and perfusion parameters. Differences between the groups were assessed via Kruskal-Wallis and Mann-Whitney U tests.

Results

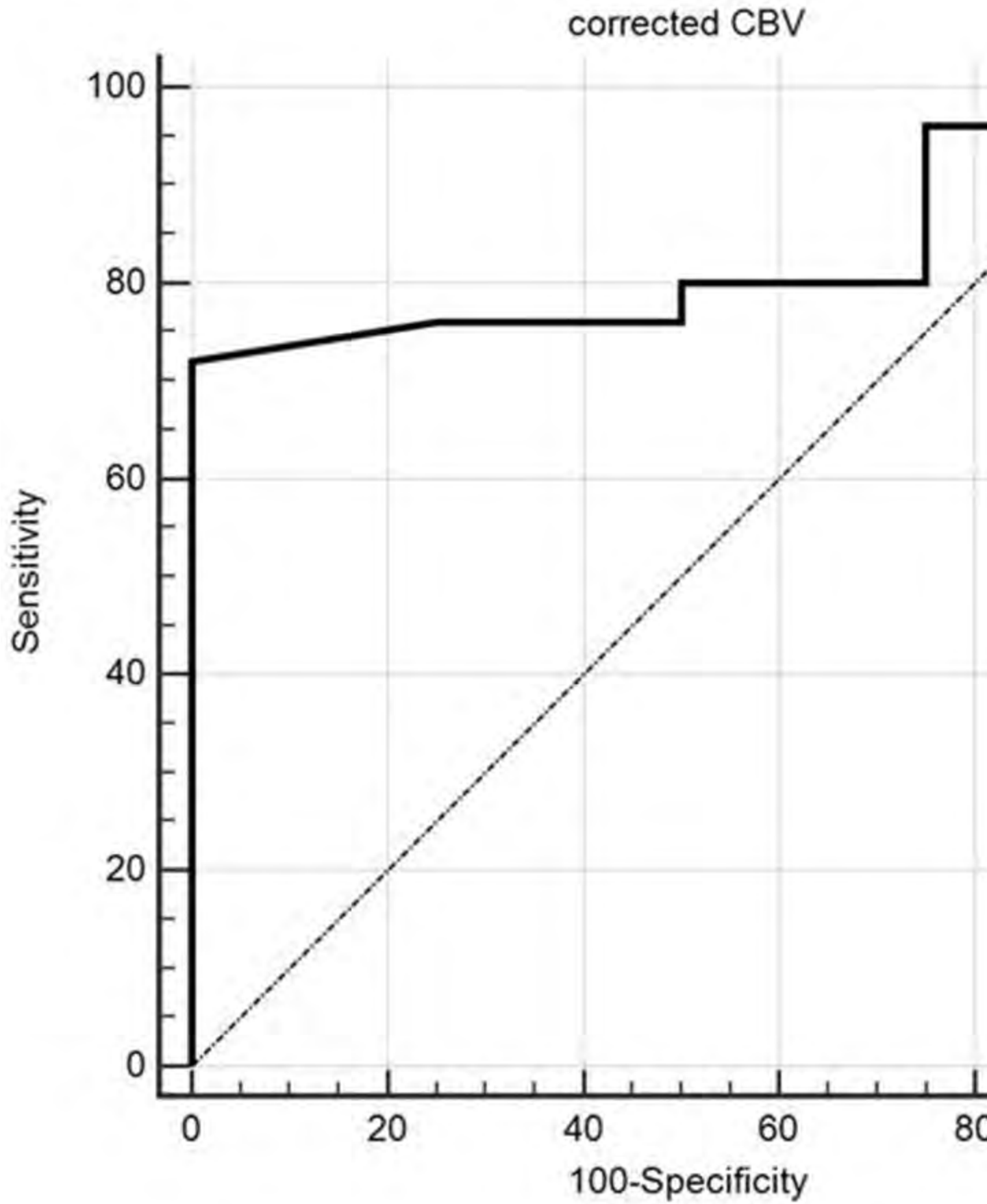
There were 25 predominant tumors, three predominant treatment-related lesions and four mixed lesions. Moderate correlation with TR percentage was seen only with corrected CBV values on hot spot analysis ($r = 0.53$, 95% CI 0.23 to 0.74, $p = 0.002$) (Fig. 1) and noncorrected CBV peak height position on histogram analysis ($r = 0.41$, 95% CI 0.07 to 0.66, $p = 0.022$). Statistically significant difference was seen only for hot spot corrected CBV between the three groups ($p = 0.048$), mainly between the mixed and predominant tumor groups (median (IQR) 2.31 (1.69 - 2.42) versus 3.23 (2.44 - 4.31); $p = 0.046$) (Figs. 2 and 3). Other parameters showed no statistically significant difference between the groups and weaker or no statistically significant correlation with TR proportion.

Conclusions

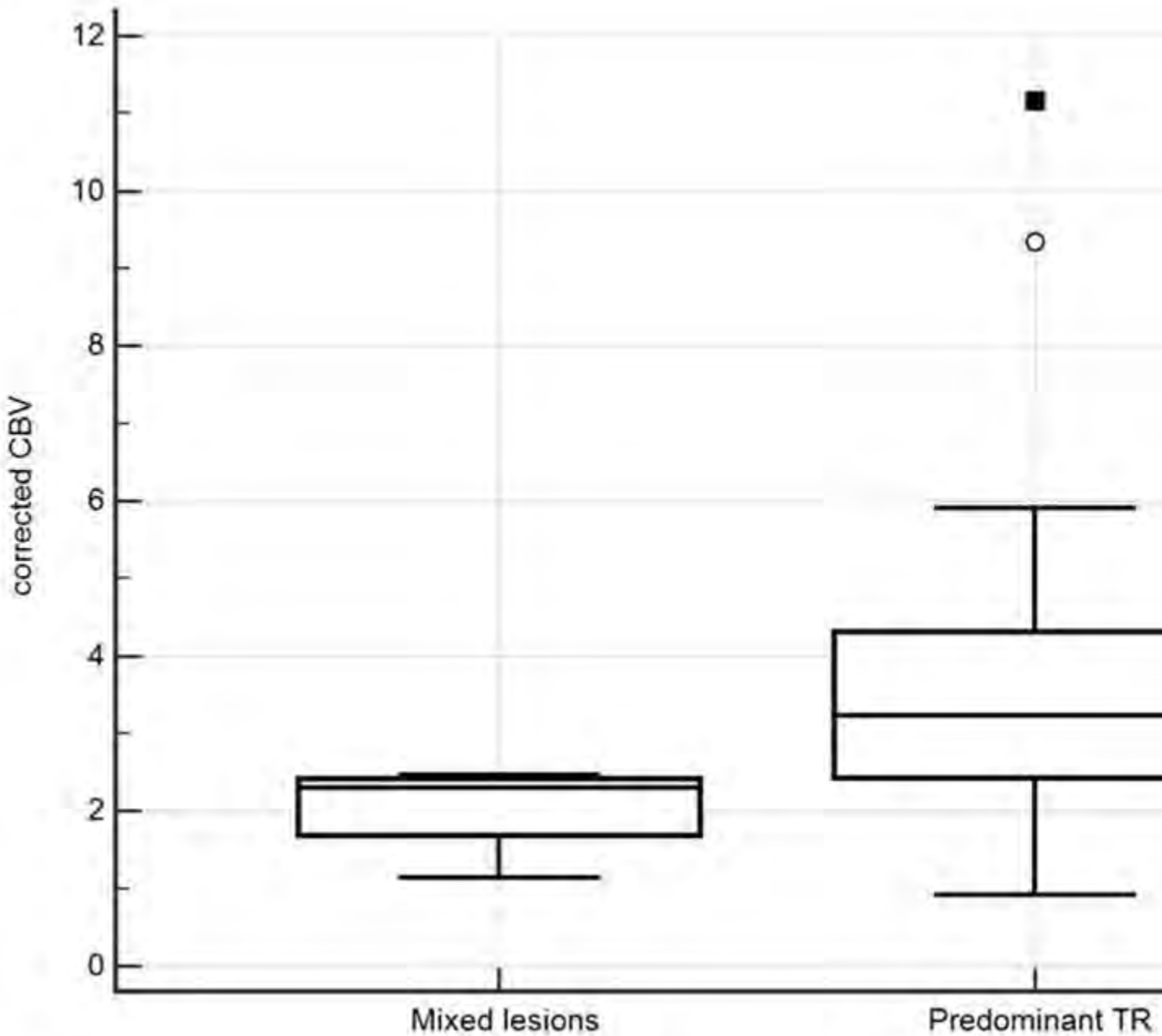
Leakage-corrected CBV might be useful in predicting the TR proportion and to differentiate between the different causes of abnormal enhancing lesions in post-treatment high grade gliomas.



(Filename: TCT_O-371_Fig1ScatterdiagramshowsmoderatecorrelationbetweentheTRpercentageandthecorrectedCBVvaluesonhotspotanalysisr0534p00016.jpg)



(Filename: TCT_O-371_Fig2ROCcurveofcorrectedCBVbetweenmixedlesionsandTRAreaunderthecurve0815p00002.jpg)



(Filename: TCT_O-371_Fig3DatacomparisongraphofdifferencebetweencorrectedCBVvaluesbetweenmixed lesionsandTRmedianIQR2305016850-24200versus3230024350-43075p00.jpg)

O-372

3:16PM - 3:24PM

Prognostic Utility of Diffusion Tensor Imaging and Dynamic Susceptibility Contrast MR Perfusion in Patients with Brain Metastases

Y Chen¹, S Wang¹, S Chawla¹, L Loevner¹, M Alonso-Basanta¹, H Poptani², S Mohan¹

¹*Perelman School of Medicine at the University of Pennsylvania, Philadelphia, PA*, ²*University of Liverpool, Liverpool, United Kingdom*

Purpose

Graded prognostic assessment [GPA (1)] and recursive partitioning analysis [RPA (2)] generally are used clinically for prognosis in patients with brain metastases. A recent study reported borderline significant survival differences ($p \approx 0.04-0.05$) in patients grouped by mean diffusivity (MD) (3). Besides MD, diffusion tensor imaging (DTI) (measure of anisotropy) and dynamic susceptibility contrast (DSC) MR perfusion (measure of vascularity) are biomarkers of tumor micro-environment that may be more biologically relevant. This study evaluated the prognostic potential of DTI, along with cerebral blood volume (CBV), which has not been reported previously in brain metastases.

Materials and Methods

Magnetic resonance imaging (MRI) from 101 patients (49 M:52 F, age 59 ± 12 years) diagnosed with brain metastases in 2006–2013 were analyzed retrospectively. Primary tumor was lung ($n=56$), breast ($n=15$), and other ($n=30$). All patients had brain MRI with DTI and DSC prior to any treatment for brain metastases. Six patients were excluded from DSC analysis due to susceptibility artifacts. Clinical data included tumor type, Karnofsky Performance Scale (KPS), GPA, RPA, and length of survival after initial diagnosis of brain metastasis. Diffusion tensor imaging metrics and CBV (based on DSC) were quantified from enhancing areas of dominant metastasis segmented semi-automatically (4). Diffusion tensor imaging metrics included MDmin (average of lowest 10% of segmented voxels), as well as fractional anisotropy (FA) and linear (CL)/planar (CP)/spherical (CS) anisotropy coefficients [average of lowest 25% (Q25) and average of highest 25% (Q75) of segmented voxels, to account for tumor heterogeneity]. Relative CBVmax (rCBVmax) was average of highest 10% of segmented voxels normalized to contralateral white matter. For each metric, patients were placed into two groups [based on literature (3) for MDmin and preliminary results for other metrics]: 1) MDmin – above and below median MDmin; 2) FA/CL/CP/CS – above and below first quartile of respective metric; 3) rCBVmax – above and below third quartile of rCBVmax. Kaplan-Meier analysis was used to detect significant group differences in survival ($p < 0.05$).

Results

Median KPS score was 80 and median survival was 301 days. Survival differences by GPA class ($p < 0.001$) and RPA class ($p < 0.001$) were significant, indicating a valid

cohort. Survival by tumor type (lung/breast/other) was not significantly different ($p=0.23$). Significant group differences in survival were seen with MDmin ($p=0.013$), FA Q25 ($p=0.009$), CL Q25 ($p=0.049$), and CP Q25 ($p=0.009$) (Figure). However, CS did not predict survival. In addition, no significant group difference in survival was observed with rCBVmax (Figure).

Conclusions

This study suggests that brain metastases with lower FA/CL/CP (lower anisotropy suggesting disorganized tumor micro-environment) have a more favorable prognosis. In contrast to primary brain tumors, rCBVmax did not predict survival in brain metastases. These findings need to be validated in a multi-institutional setting to evaluate prognostic utility of DTI in this patient population.

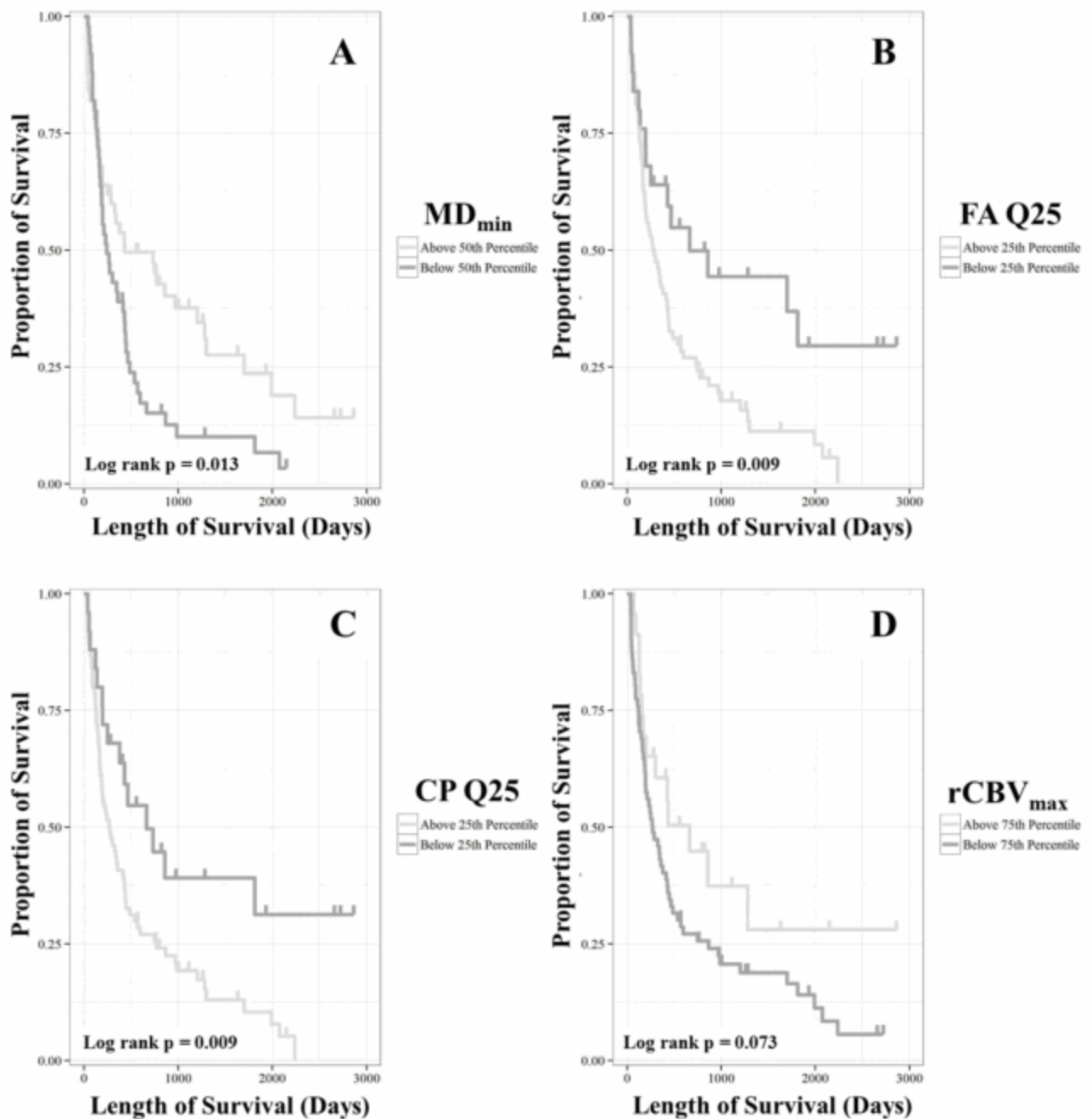


Figure. Kaplan-Meier survival analysis shows significant group differences in survival with MD_{min} (A), FA Q25 (B), and CP Q25 (C) (similar result with CL Q25, not shown). In contrast, no significant group difference in survival was seen with rCBV_{max} (D). For each metric, patients were placed into two groups as defined in the Materials and Methods section.

(Filename: TCT_O-372_ASNR2016BrainMetsDTIFigureBW.gif)

O-373

3:24PM - 3:32PM

Perfusion Weighted Imaging in the Study of Brain Gliomas: Reproducibility and Comparison of Data Obtained by Using Two Different Software Platforms

g conte¹, a castellano², A Iadanza³, M Cadioli³, N Anzalone³, A Falini³

¹*San Raffaele Hospital, Milan, Italy*, ²*s raffaele hospital, milan, CA*, ³*San Raffaele Hospital, Milan, CA*

Purpose

The aim of this study was to evaluate the effect of using different softwares on reproducibility of perfusion parameters in a group of gliomas. We evaluated intra- and interobserver reproducibility (intrasoftware reproducibility) and intersoftware reproducibility.

Materials and Methods

We retrospectively evaluated dynamic contrast-enhanced magnetic resonance imaging (MRI) (DCE) and dynamic susceptibility contrast MRI (DSC) data sets of 20 patients with gliomas (8 WHO II, 4 WHO III and 8 WHO IV) using a 3.0T magnet. Perfusion data were postprocessed with two software: NordicIce (NordicNeuroLab, Bergen, Norway) and Olea Sphere (Olea Sphere, Olea Medical Solutions, La Ciotat, France); in Olea Sphere both automatic and manual detection of vascular input function (VIF) was used. Parametric maps of K_{trans} and V_p were obtained from DCE data sets; parametric map of cerebral blood volume (CBV) from DSC data sets. For each parameter we evaluated the maximal abnormality through hotspots method. All patients were analyzed by two independent observers blinded to the histological grade using both softwares. Each observer repeated the analysis after 1 month to evaluate intra-observer reproducibility. Additionally, in each patient we compared DCE and DSC parameters obtained selecting the same regions of interest (ROIs) with the two softwares. To assess reproducibility of data we used intraclass correlation coefficient (ICC) and Bland-Altman analysis.

Results

Intraclass correlation coefficient for intra- and interobserver reproducibility was higher than 0.8 in almost all cases for each parameter and each software suggesting almost perfect agreement. Intraclass correlation coefficient for intersoftware reproducibility ranged from 0.3 to 0.6 suggesting poor to moderate agreement; we obtained similar results selecting same ROIs with the two softwares.

Conclusions

Our results show that each software guarantees almost perfect intra- and interobserver reproducibility. Best reproducibility is obtained when automatic detecting of VIF is

selected in Olea Sphere. The finding of low intersoftware reproducibility suggests that caution should be taken when comparing results obtained with different softwares.

O-374

3:32PM - 3:40PM

Arterial Spin Labeling Perfusion in Differentiation of Primary and Secondary Glioblastomas

A Tonoyan¹, T Ovcharenko², L Shishkina¹, I Pronin³

¹*Burdenko Neurosurgery Institute, Moscow, Russian Federation*, ²*Pirogov Russian National Research Medical University, Moscow, Russian Federation*, ³*Burdenko Neurosurgery Institute, Moscow, Russian Federation*

Purpose

Glioblastoma (GBM) is the most frequent malignant primary brain tumor in adults. Glioblastomas are subdivided into two groups based on their origin and genetic alterations: primary and secondary GBMs (1, 2). It is believed that secondary GBMs have better prognosis than primary. Due to the fact that vascularization increases with higher glioma malignancy grade (3), we were interested whether primary and secondary GBMs exhibit different tumor tissue perfusion values. Therefore, our purpose was to investigate with the use of arterial spin labeling (ASL) if there is a correlation between tumor blood flow (TBF), clinical data, and origin of GBMs.

Materials and Methods

We studied 37 patients with histologically proved GBM: 14 primary and 23 secondary GBMs. Then these patients were reformed into two groups based on the duration of symptoms: 24 patients had a clinical history less than 3 months, 13 – more than 3 months. Absolute and normalized (to contralateral normal white matter) maximum (aTBFmax, nTBFmax) and mean (aTBFmean, nTBFmean) values of tumor blood flow were measured for each patient in the contrast-enhanced tumor areas. All of these parameters were compared in the groups of patients using the Mann-Whitney test.

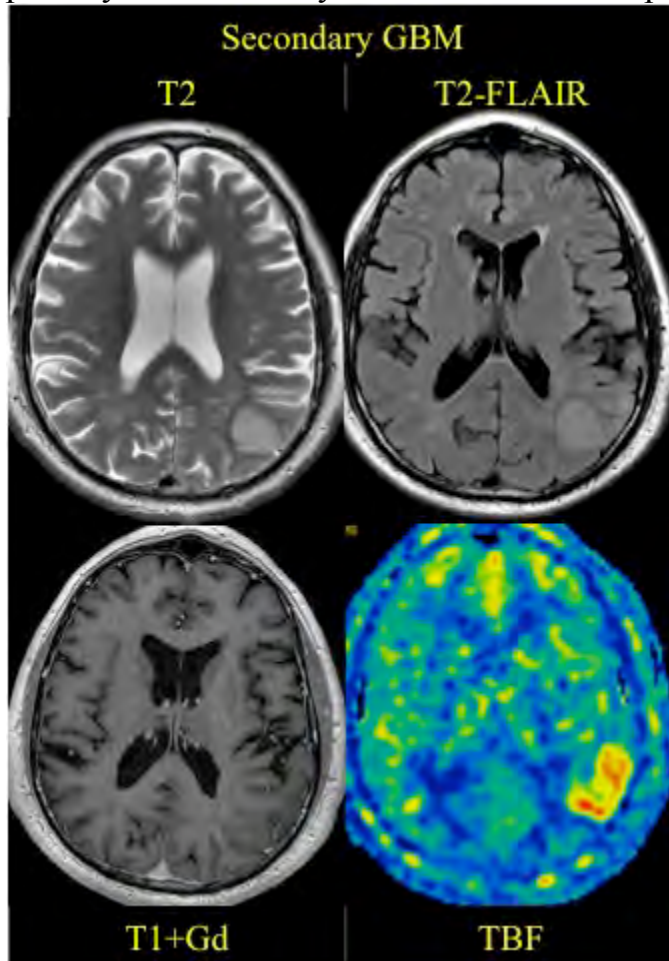
Results

The values of aTBFmax, aTBFmean, nTBFmax, nTBFmean tend to be higher in primary GBMs (169 ± 72 ml/100g/min, 115,1 ± 36,5 ml/100g/min, 11,1 ± 6,6 ml/100g/min, 7,3 ± 3,6 ml/100g/min respectively) compared to secondary GBMs (152,2 ± 65,4 ml/100g/min, 103,9 ± 48,8 ml/100g/min, 8,4 ± 4,5 ml/100g/min, 5,6 ± 3,1 ml/100g/min respectively), but without any statistic significance (p>0,05). The values of aTBFmax, aTBFmean, nTBFmax, nTBFmean were higher in GBMs with clinical history less than 3 months (153,5 ± 55,2 ml/100g/min, 109,1 ± 34,2 ml/100g/min, 9,1 ± 5 ml/100g/min, 6,4 ± 3,1 ml/100g/min respectively) compared to GBMs with clinical history more than 3 months (147 ± 64,5 ml/100g/min, 98,1 ± 55,2

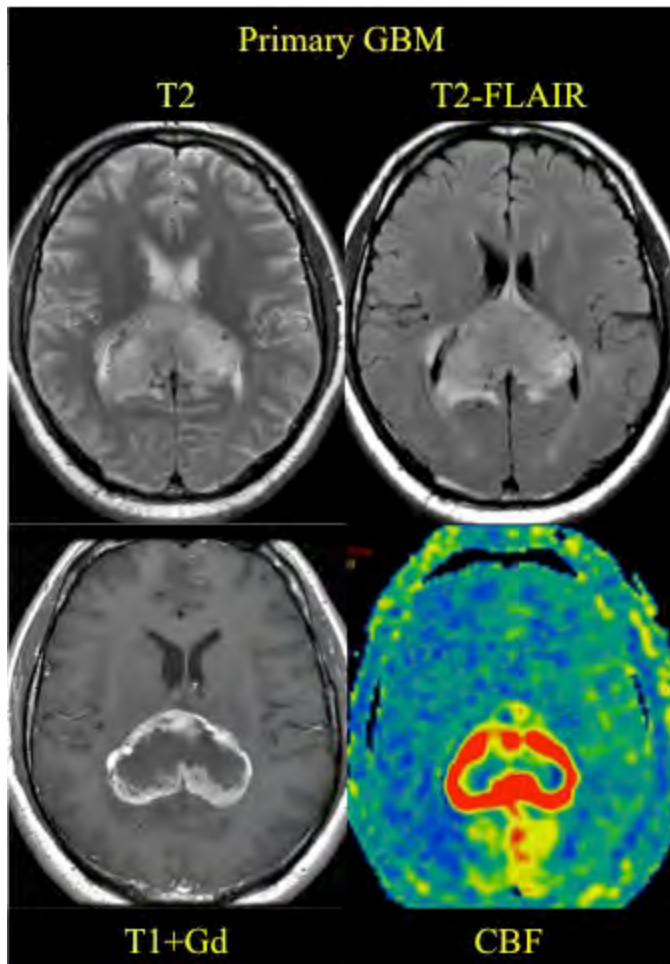
ml/100g/min, $8,9 \pm 4,8$ ml/100g/min, $5,8 \pm 3,5$ ml/100g/min respectively), but also without any statistic significance ($p > 0,05$).

Conclusions

It is well known that tumor vascularization and blood flow values significantly increase with higher glioma malignancy grade. In spite of that fact tumor blood flow values obtained by ASL cannot be used as reliable criteria for differentiation of primary and secondary GBMs and do not depend on aggressiveness of GBMs.



(Filename: TCT_O-374_SecondaryGBM_1.jpg)



(Filename: TCT_O-374_PrimaryGBM_1.jpg)

O-375

3:40PM - 3:48PM

A study of high signal intensity on using ASL outside the contrast-enhanced area in brain tumors using a DSC perfusion technique.

T Abe¹, H Kabasawa², T Matsuda², M Harada³

¹Tokushima University Graduate School, Institute of Biomedical Sciences, Tokushima, Tokushima, ²GE Healthcare Japan, Hino, Tokyo, ³Tokushima University Graduate School, Tokushima, Tokushima

Purpose

We previously reported the finding of high signal intensity on an arterial spin labelled (ASL) image, outside a contrast-enhanced (CE) area [ASL-dominant (ASL-d), Figure 1, arrow] in an intra-axial brain tumor, which suggested glioma and lymphoma, but not metastasis (T Abe, et al. Magn Reson Med Sci. 2015. doi:10.2463/mrms.2014-

0083). In this study, we investigated the changes in perfusion parameters observed in dynamic susceptibility contrast (DSC) magnetic resonance (MR) imaging.

Materials and Methods

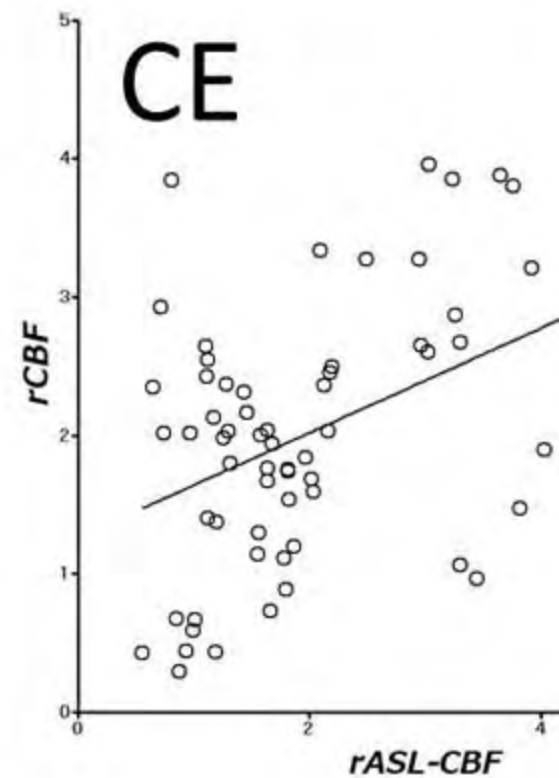
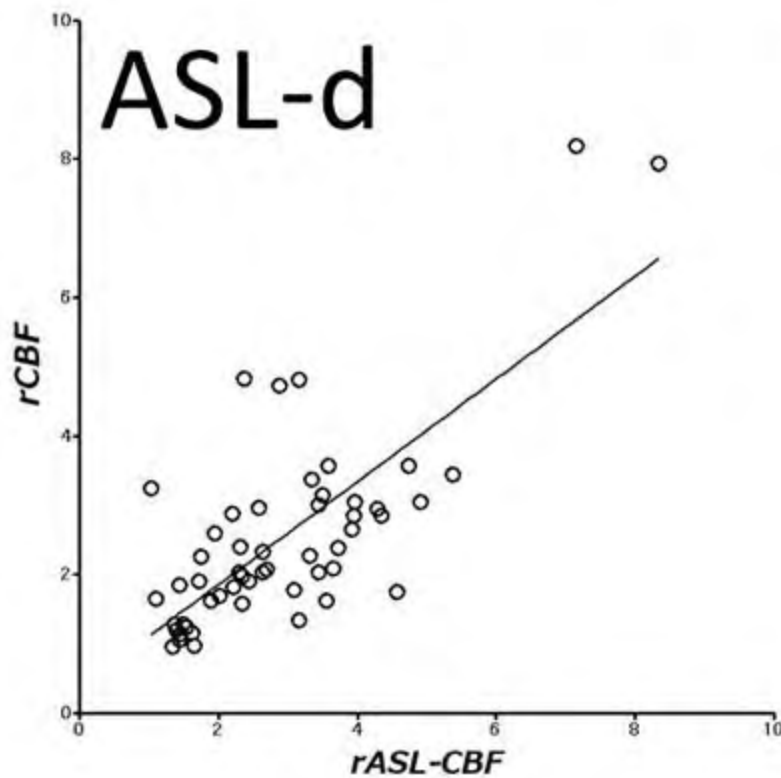
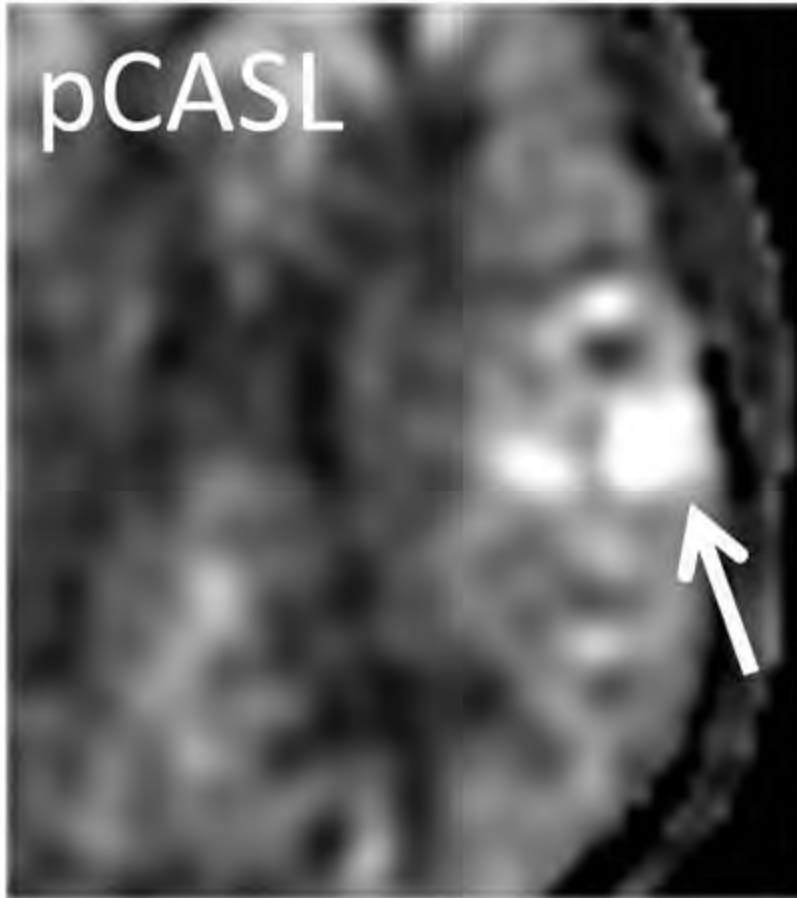
We examined images from 13 consecutive patients with malignant glioma who underwent ASL, DSC, and CE-MR imaging using a 3T MR scanner. CBV, CBF, MTT, and Tmax from DSC data and CBF from ASL data (ASL-CBF) were obtained. Using relative CBV (rCBV), each parameter was normalized using brain parenchyma that appeared unaffected. A maximum of eight round-shaped regions of interest (ROIs), each with an area of 60 mm², were selected on the ASL-d and CE images of each tumor. We investigated the correlation between the perfusion parameters in ASL-d and CE areas. In addition, the differences in each perfusion parameter between the ASL-d and CE-d areas were assessed using the Mann–Whitney U test, with a p-value < 0.05 required to achieve significance.

Results

The rASL-CBF on ASL-d area correlated with rCBV, rCBF, and rMTT (R = 0.67, 0.64, and 0.29 respectively). However, rASL-CBF correlated with rCBF, and rTmax on CE area (R = 0.41, -0.46, respectively). Difference: rASL-CBF was significantly higher on the ASL-d area compared with the CE-d area, whereas rCBF did not show a significant difference. The parameters, rCBV, rMTT, and rTmax were significantly lower on the ASL-d area. The value of rMTT and rTmax on ASL-d area was 1.04 and 1.01, respectively, which is almost the same as the normal appearing brain parenchyma.

Conclusions

The ASL-d area showed different perfusion characteristics compared with the CE area, and some perfusion parameters were almost the same as the normal appearing brain parenchyma. This indicates that the vessels on the ASL-d area have relatively natural features, probably resulting in these impressive imaging findings.



(Filename: TCT_O-375_DSC_ASNR2016_figure_300by300_3inches.jpg)

O-376

3:48PM - 3:56PM

A study of high signal intensity on using ASL outside the contrast-enhanced area in brain tumors using a DCE permeability imaging.

T Abe¹, T Matsuda², H Kabasawa², M Harada³

¹*Tokushima University Graduate School, Institute of Biomedical Sciences, Tokushima, Tokushima,* ²*GE Healthcare Japan, Hino, Tokyo,* ³*Tokushima University Graduate School, Tokushima, Tokushima*

Purpose

We previously reported that presence of high signal intensity outside the contrast-enhanced (CE) area on arterial spin labeling (ASL) images of intra-axial brain tumor indicated glioma and lymphoma, and not metastasis (T Abe, et al. Magn Reson Med Sci. 2015. doi:10.2463/mrms.2014-0083). Here, we used dynamic contrast-enhanced (DCE) magnetic resonance imaging (MRI) to investigate characteristics of vessels in areas showing ASL hyperintensity in regions outside the CE area (ASL-d areas).

Materials and Methods

We examined images from 16 patients with malignant glioma who underwent ASL, DCE, and CE-MR imaging on a 3T MR scanner. We acquired parameters for permeability (Ktrans), extravascular extracellular volume (Ve), and fractional plasma volume (fPV) from DCE data, and CBF from ASL data (ASL-CBF). A circular region of interest (ROI) of 60 mm² was set on each tumor. Up to eight ROIs were set in the ASL-d and CE areas for each tumor. Regions of interest also were set on brain parenchyma of normal appearance. We performed correlations between parameters and tested for significance using the Mann-Whitney U test at P < 0.05.

Results

Arterial spin labeling CBF from ASL-d areas correlated with fPV (R = 0.41) but not with any other parameters. Arterial spin labeling CBF from the CE area did not correlate with any parameters. Arterial spin labeling CBF, Ktrans, Ve, and fPV from ASL-d and CE areas were significantly higher than those from normal brain parenchyma, and Ktrans and Ve from CE areas were significantly higher than those from ASL-d areas. Arterial spin labeling CBF and Ve from CE areas indicated a nonsignificant trend towards higher values than in ASL-d areas.

Conclusions

Within ASL-d areas, fPV was significantly higher than in normal appearing brain parenchyma, although not significantly different from CE areas. Ktrans and Ve were higher than in normal appearing brain parenchyma, but significantly lower than that

from CE areas. This suggested that the ASL-d finding resulted from an enlarged vascular bed that was otherwise relatively normal in structure.

O-377

3:56PM - 4:04PM

Additive value of Arterial Spin-Labeling (ASL) to Diagnose Residual or Recurrent Meningioma

K Kikuchi¹, A Hiwatashi¹, O Togao¹, K Yamashita², R Kamei¹, H Honda¹

¹*Kyushu University, Fukuoka, Fukuoka*, ²*Kyushu University, Fukuoka, Japan*

Purpose

Arterial spin-labeling (ASL) imaging is useful to evaluate tumor blood flow. Arterial spin labeling could be useful in the detection of hyper vascular tumor. The purpose of this study was to evaluate the additive value of ASL on conventional postcontrast T1-weighted images (CE-T1-WI) to diagnose residual or recurrent meningiomas.

Materials and Methods

This retrospective study included 25 patients with residual or recurrent meningioma (20 females and 5 males; age range 32-85 year, median 65 years) and 25 sex- and age-matched controls without intracranial masses. Arterial spin labeling was obtained using pseudo-continuous method with labeling time of 1650 ms and post labeling delay of 2000 ms. Other imaging parameters were as follows: TR/TE = 4200/8.6 ms, EPI factor = 35, FOV = 240 x 240 mm², matrix = 64 x 64, slice thickness = 6 mm, slices = 20, total scan time = 4 m 40 s. Seven independent observers (four radiology residents and three neuroradiologists) took part in two reading sessions. In the first session, the observers read only conventional CE-T1-WI. In the second session, they read simultaneously ASL along with CE-T1-WI. We evaluated sensitivity and diagnostic performance for detecting residual or recurrent meningiomas. Diagnostic performance was assessed with figure-of-merit (FOM) calculated by jackknife free-response receiver-operating characteristic (ROC). Statistical analysis was performed by paired t-test. A p value < 0.05 was considered significant.

Results

Using only CE-T1-WI, the sensitivity and FOM for the residents, neuroradiologists and all readers were 69.0/97.7/81.3% and 0.80/0.95/0.86, respectively. Using CE-T1-WI with ASL, the sensitivity and FOM for the residents, neuroradiologists and all readers were 79.3/100/88.2% and 0.88/0.99/0.93, respectively. All but neuroradiologists showed statistically significant improvement when adding ASL to diagnose (p < 0.01).

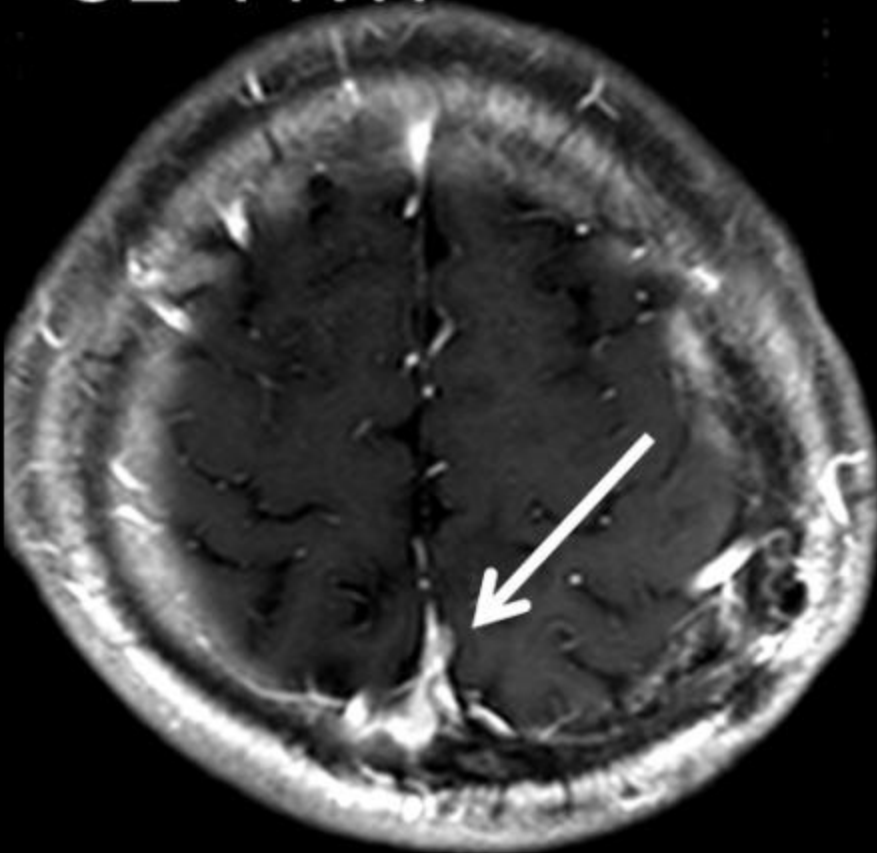
Conclusions

It is beneficial to add ASL to diagnose residual or recurrent meningiomas on postcontrast T1-WI.

40M atypical meningioma

CE-T1WI

ASL



(Filename: TCT_O-377_20151208_ori01_mg_fig.jpg)

O-378

4:04PM - 4:12PM

**Anaplastic Astrocytoma versus Glioblastoma Histological Grading with MRI
DSC Perfusion Technique: Cerebral Blood Volume versus Cerebral Blood Flow
Utilizing Standard, Time Insensitive and Bayesian Deconvolution Methods**

I Littig¹, G Fatterpekar², A Francheschi³, A Davis⁴

¹New York University, New York, NY, ²NYU School of Medicine, New York, NY, ³NYU, New York, NY, ⁴NYU Langone Medical Center, New York, NY

Purpose

Tumor cerebral blood volume and blood flow has been shown to broadly differentiate low-grade from high-grade gliomas (1, 2). However, there is sparse literature on utilization of magnetic resonance imaging (MRI) perfusion techniques to distinguish grade III anaplastic astrocytomas from grade IV glioblastoma (3). This might be related to MRI perfusion techniques utilizing simplistic area under the curve algorithms and single arterial input function limiting detailed analysis. Time insensitive and Bayesian models and multiple arterial input function measurements have been shown to improve accuracy (4, 5). We revisited the investigation using these models to determine which method and perfusion index might best differentiate grade III from IV glioma.

Materials and Methods

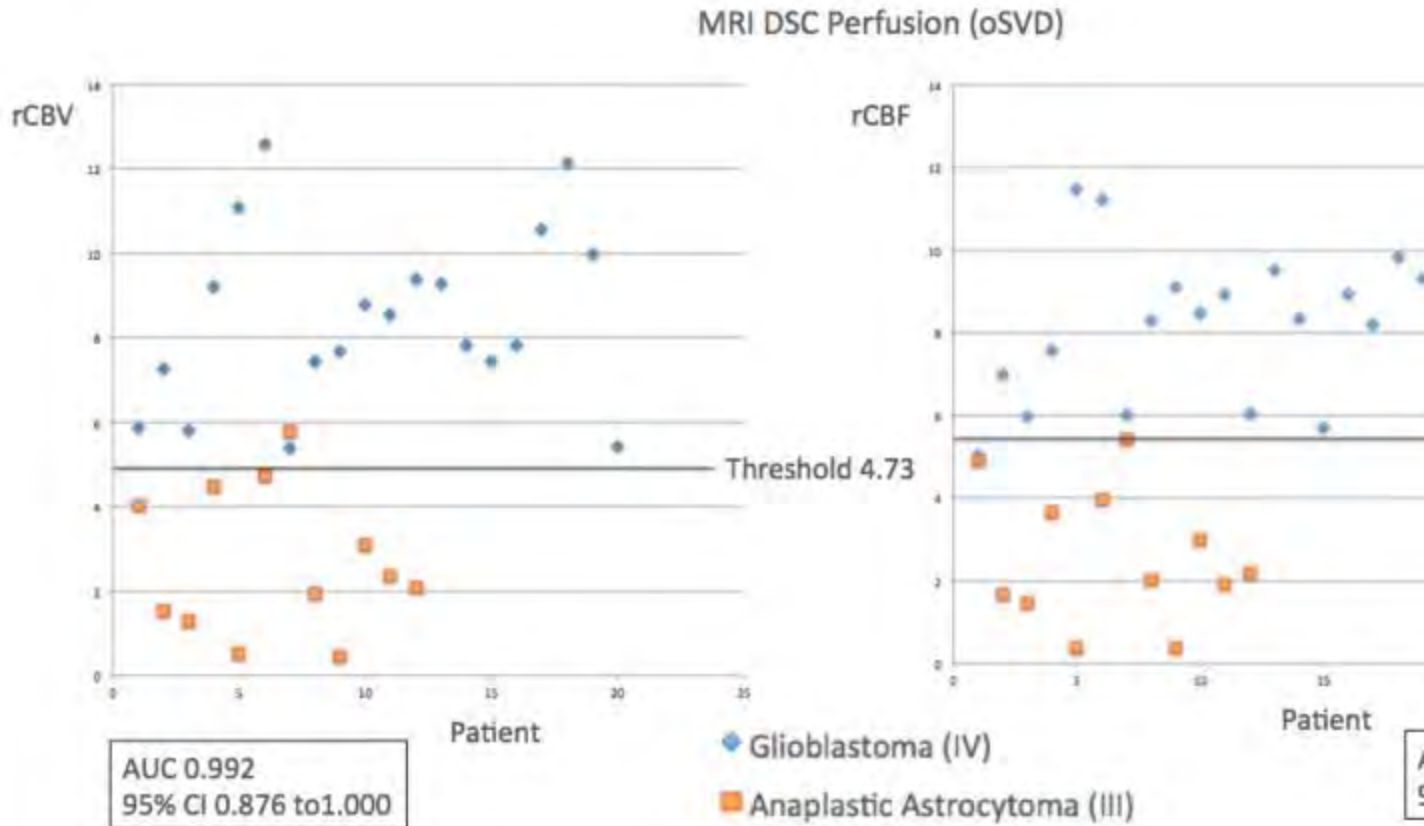
A HIPAA compliant IRB approved prospective study was performed. Surgical pathology and radiology reports were reviewed to identify 20 GB and 12 AA patients with MR dynamic susceptibility contrast (DSC) perfusion performed prior to surgical or medical treatment. Studies marred by artifact or significant co-synchronous pathology were eliminated. Perfusion analysis with standard (sSVD), time insensitive (oSVD), and Bayesian algorithms were performed. Four standardized intra-tumoral regions with greatest values were averaged. Statistical analysis using receiver operating characteristic (ROC) analysis was performed.

Results

Receiver operating characteristic analysis demonstrates that both rCBV and rCBF differentiate AA from GB (AUC 0.892 to 0.992). Varying algorithms conferred no difference within rCBV analysis although oSVD was the most superior rCBF analysis. Utilizing a 4.73 rCBV and a 5.42 rCBF threshold provides a 91.7% and 100% sensitivity and 100% and 95% specificity respectively of differentiating AA from GB.

Conclusions

Our study demonstrates that both rCBV and rCBF can be utilized to clearly differentiate anaplastic astrocytoma from glioblastoma utilizing MR DSC technique.



(Filename: TCT_O-378_finalgraph.jpg)

O-379

4:12PM - 4:20PM

Progressive bevacizumab induced diffusion-restricted lesions indicate coagulative necrosis surrounded by non-enhancing tumor and are associated with decreased survival in recurrent glioblastoma patients

P LaViolette¹, H Nguyen¹, S Hurrell¹, J Connelly¹, E Cochran¹, S Rand¹

¹Medical College of Wisconsin, Milwaukee, WI

Purpose

The current standard of care for recurrent glioblastoma (GBM) patients is treatment with bevacizumab. In a subset of patients diffusion-restricted lesions have been seen on apparent diffusion coefficient (ADC) maps. The presence of these lesions has been associated with both increased and decreased overall survival (OS) in discrepant studies. This study investigates these lesions at autopsy to determine the underlying histology and their impact on OS.

Materials and Methods

Seven patients with recurrent GBM and progressive diffusion-restricted lesions were recruited for brain donation. To reduce tissue distortion during fixation and to align

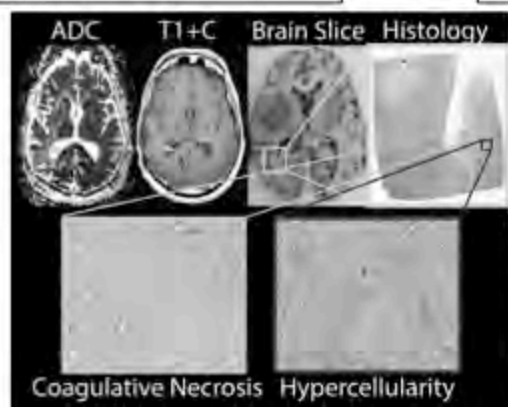
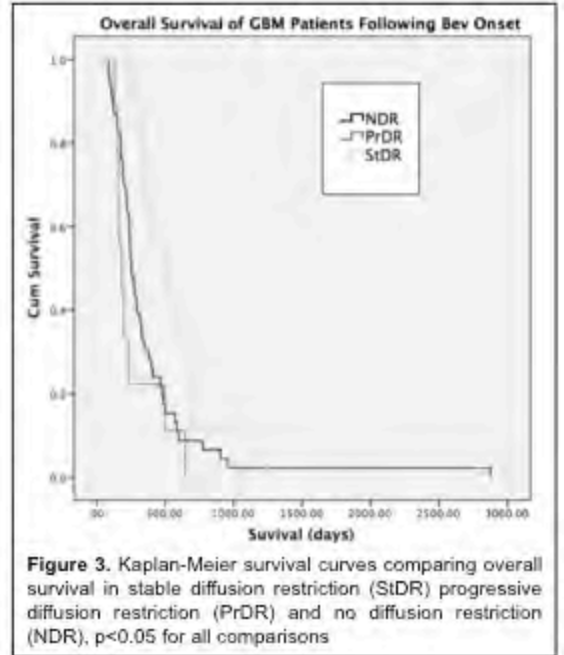
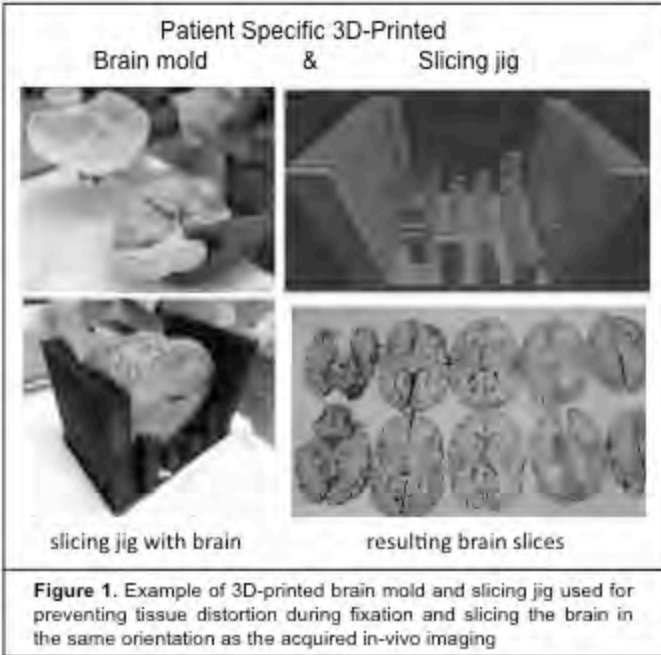
brain slices with pre-mortem imaging, patient-specific 3D-printed molds and slicing jigs were created (Fig. 1). Tissue specimens were taken from regions identified radiographically as diffusion-restricted, H&E stained, digitized, and pathologically interpreted (Fig. 2). A second dataset from a retrospective patient population of 64 GBM bevacizumab cases was analyzed to assess the effect of diffusion restriction on OS. Patients were separated into three groups: no diffusion restriction (NDR), progressive diffusion restriction (PrDR), and stable diffusion restriction (StDR). A Kaplan-Meier analysis was performed.

Results

Six of the seven patients had progressive DRN at time of death while the seventh patient had recurrent tumor elsewhere. These lesions were comprised of coagulative necrosis surrounded by nonenhancing hypercellular tumor. Fig. 3 shows the survival curves comparing NDR, PrDR, and StDR, where StDR patients had significantly greater OS and PrDR had significantly lower OS than NDR patients (both $p < 0.05$).

Conclusions

We found diffusion-restricted lesions were coagulative necrosis. Importantly, PrDR further indicated that the necrotic region was surrounded by viable nonenhancing tumor. StDR was associated with greater OS while PrDR indicated decreased OS compared to NDR patients. Our autopsy results double the number of diffusion-restricted necrosis cases reported in current literature, but further research is needed to establish the biological basis for bevacizumab causing DRN.



(Filename: TCT_O-379_Slide1.jpg)

O-455

4:20PM - 4:28PM

Pretreatment Diagnosis of Suprasellar Papillary Craniopharyngioma and Germ Cell Tumors of Adult Patients

H Lee¹, F Chang¹, W Guo¹

¹Taipei Veterans General Hospital & National Yang Ming University, Taipei, Taiwan

Purpose

Suprasellar papillary craniopharyngiomas and germ cell tumors in adults share some clinical and imaging similarities but have different therapeutic strategies and outcomes. This study aimed to evaluate the pretreatment diagnosis of these two tumors to improve the therapeutic outcome.

Materials and Methods

We retrospectively enrolled 18 adults with papillary craniopharyngiomas and 17 with germ cell tumors. The magnetic resonance imaging (MRI) findings were evaluated, including signal change and anatomical extension. The medical records were reviewed to collect clinical findings, management, and outcomes.

Results

The clinical findings of papillary craniopharyngiomas versus germ cell tumors were as follows: age: 46 +/- 13.9 years versus 23 +/- 7.1 years ($P < .0001$); diabetes insipidus: 2/18 (11%) versus 11/17 (65%) ($P < .001$); recurrence 13/16 (81%) versus 4/17 (24%) ($P = .0031$). The MR imaging findings of papillary craniopharyngiomas versus germ cell tumors were as follows: pituitary stalk thickening: 1.6 +/- 0.4 mm versus 5.4 +/- 4.2 mm ($P < .0001$); vertical infundibular extension: 1/18 (6%) versus 16/17 (94%) ($P < .0001$); sagittal spheric shape: 17/18 (94%) versus 1/17 (6%) ($P < .0001$); diffusion restriction: 1/17 (6%) versus 8/12 (67%) ($P = .0009$).

Conclusions

Younger age, diabetes insipidus, MR imaging characteristics of restricted diffusion, and vertical infundibular extension favor the diagnosis of germ cell tumors. Spheric shape without infundibular infiltration provides clues to papillary craniopharyngiomas, which originate from the pars tuberalis and are located outside the third ventricle. We suggest that suprasellar germ cell tumor is possibly an intraventricular lesion. Appropriate treatment planning can be initiated according to the diagnosis and anatomical location.

Location:

https://ww4.aievolution.com/asn1601/files/content/abstracts/abs_2156/2016asnr2.

Wednesday

3:00PM - 4:30PM

Washington Marriott Wardman Park, Roosevelt 4

**17F-PARALLEL PAPER SESSION: Pediatrics: Epilepsy, Autism, & Development
O-381**

3:00PM - 3:08PM

Is heterogeneity of cortical tubers useful for predicting the epileptogenicity in tuberous sclerosis complex (TSC) patients?: The preliminary results.

A Yogi¹, Y Hirata¹, P Pan¹, H Ullman¹, E Morimoto¹, H Yokota¹, I Orosz¹, M Linetsky¹, G Mathern², N Salamon¹

¹*Department of Radiology, David Geffen School of Medicine at UCLA, Los Angeles, CA,* ²*Department of Neurosurgery, David Geffen School of Medicine at UCLA, Los Angeles, CA*

Purpose

It is challenging to identify the epileptogenic tubers in tuberous sclerosis complex (TSC) patients presurgically. This study aims to test whether the heterogeneous magnetic resonance (MR) feature of tubers can help predicting epileptogenic tubers.

Materials and Methods

Twenty-two consecutive patients with intractable epilepsy who underwent presurgical MRI including diffusion tensor imaging (DTI) between 2004 and 2013 were selected retrospectively from UCLA TSC cohort. Epileptogenic tubers were defined by presurgical work up with FDG-PET/MRI fusion, magnetoencephalography, intra-operative electrocorticography, and postoperative seizure outcome. A total of 33 epileptogenic tubers were selected as well as 92 nonepileptogenic tubers. Minimum, maximum, mean, median, and standard deviation (SD) of apparent diffusion coefficient (ADC) values in each tuber were measured. We categorized the tubers' spatial heterogeneity according to the classification shown in Table 1 and Fig.1. We used the Mann-Whitney U test to compare all quantitative variables between epileptogenic and nonepileptogenic groups and performed Pearson's correlation test to examine the correlation between SD and other parameters. Subsequently, we used analysis of variance (ANOVA) with the Kruskal-Wallis test to evaluate differences in frequency of epileptogenic tubers among the classes. We also used receiver operating characteristic (ROC) analysis for standard deviation (SD) of ADC and the classes of tubers, and the area under the curve (AUC) values were calculated.

Results

Maximum, minimum, and SD of ADC showed significant difference ($p < 0.01$, $p = 0.03$, and $p < 0.001$, respectively). Standard deviation of ADC positively correlated with maximum ADC of tuber ($r^2=0.86$, $p<0.001$). Sixty-one, 29, 10, six, and 19 tubers were classified from classes one to five, respectively (Fig. 2). ANOVA demonstrated that the frequency of epileptogenic tubers was significantly different among each class ($p<0.01$). The AUC value of SD of ADC and five scales were 0.67 and 0.77, respectively.

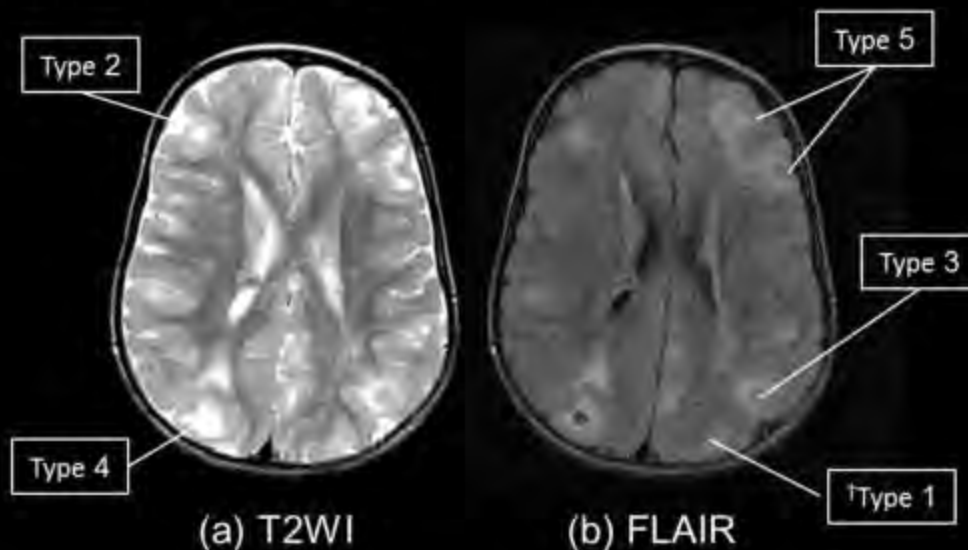
Conclusions

Assessments of tubers' heterogeneity, especially spatial heterogeneity, may help to identify epileptogenic tubers in presurgical patients with TSC.

Table. 1 Five categories for spatial heterogeneity of tubers

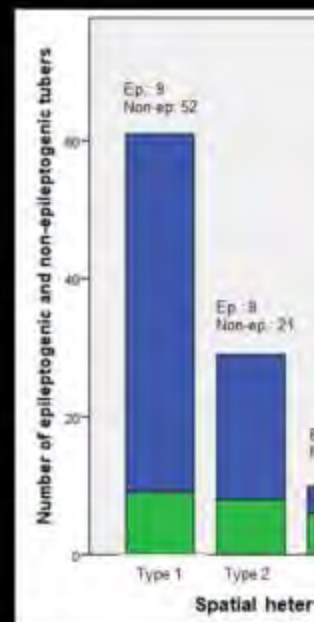
| Categories | Imaging characteristics |
|------------|--|
| Type 1 | Mildly hyperintense on T2WI and FLAIR and isointense on T1WI |
| Type 2 | Homogenous hyperintense on T2WI and FLAIR and hypointense on T1WI |
| Type 3 | Heterogeneous hyperintense on T2WI and FLAIR and hypointense on T1WI |
| Type 4 | Hyperintense on T2WI and hyperintense with a internal hypointense area degeneration on FLAIR |
| Type 5 | Hyperintense on T2WI and hyperintense with multiple internal hypointense cystic degenerations on FLAIR |

Fig. 1 An example of tuber's spatial heterogeneity



† The tuber in left parietal lobe was isointense on T1WI (not shown) so that it was categorized as type 1.

Fig. 2 The results of spatial heterogeneity analysis



(Filename: TCT_O-381_tableandfigures_v6.jpg)

O-382

3:08PM - 3:16PM

Predicting the epileptogenic tubers in tuberous sclerosis complex (TSC) patient using machine learning.

A Yogi¹, H Ullman¹, Y Hirata², E Morimoto¹, H Yokota¹, I Orosz¹, M Linetsky¹, B Ellingson¹, N Salamon¹

¹*Department of Radiology, David Geffen School of Medicine at UCLA, Los Angeles, CA*, ²*David Geffen School of Medicine at UCLA, Los Angeles, CA*

Purpose

It is challenging to identify the epileptogenic tubers presurgically in patients with tuberous sclerosis complex (TSC). This study aims to predict epileptogenic tubers by applying a machine learning method to diffusion tensor imaging (DTI) parameters and positron emission tomography (PET) with 2-deoxy-2-[fluorine-18]fluoro- D-glucose integrated (FDG PET) uptake.

Materials and Methods

Between March 2007 and January 2014, 33 patients with 605 tubers received MRI examinations including DTI. Of these, 14 patients with 300 tubers who underwent FDG-PET imaging were selected retrospectively from the TSC cohort. Epileptogenic tubers were defined by presurgical work up, including FDG-PET/MRI fusion, magnetoencephalography, intra-operative electrocorticography, and postoperative seizure outcome (Table). Two observers manually generated regions of interest (ROIs) of all of the tubers in consensus, and ROIs were inflated by 4mm to generate the ROI of tuber plus perituberal tissue (ROI tuber+perituber). Minimum, maximum, mean, and median values of all DTI parameters and the FDG uptake values in all ROIs were compared between epileptogenic and non-epileptogenic groups. Logistic regression models were built from the DTI and FDG-PET data. Class weights were adjusted to obtain different degrees of sensitivity and specificity. The models were evaluated by a leave-one-out cross-validation procedure, and the performance of the different modalities was compared using receiver operating characteristics (ROC) analysis.

Results

Maximum ADC, RD, and AD, mean ADC, and minimum FA showed significant differences between the epileptogenic and nonepileptogenic groups ($p < 0.001$, 0.01, 0.05, and 0.05, respectively). None of FDG measurements showed significant difference. Receiver operating characteristic curves for predicting epileptogenic tubers are shown in figures. Receiver operating characteristic curves of both machine learning models of FDG-PET and DTI were improved compared to those of

maximum ADC or minimum FDG uptake. AUC values in both models of DTI and FDG-PET were 0.65 and 0.74.

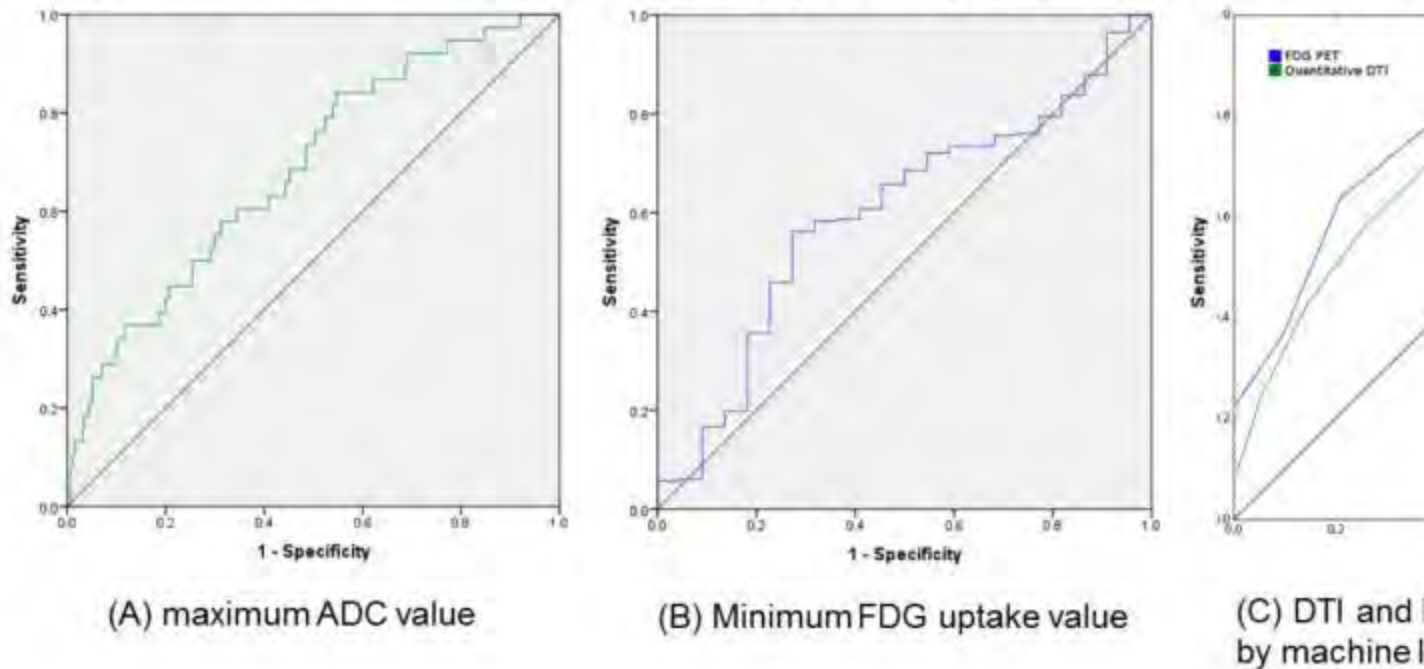
Conclusions

Machine learning method, where multiple measurements could be added for the comparison, may help predicting epileptogenic tubers more effectively.

Table. The number of epileptogenic and non-epileptogenic

| | No. of patients | No. of epileptogenic tubers | No. of epilept tubers |
|-----------------------|-----------------|-----------------------------|-----------------------|
| Patients with DTI | 33 | 38 | |
| Patients with FDG-PET | 14 | 22 | |

Figures. ROC curves predicting the epileptogenic tubers



(Filename: TCT_O-382_tableandfigures.jpg)

O-383

3:16PM - 3:24PM

Brain Network Architecture Predicts Global Intelligence in Pediatric Patients with Localization-related Epilepsy

Z Chu¹, W Zhang¹, F Golriz¹, M Paldino¹
¹*Texas Children's Hospital, Houston, TX*

Purpose

The biologic basis for intelligence rests to a significant degree on the capacity for efficient integration of information across the cerebral network. As a result of advances in computational neuroscience and magnetic resonance imaging (MRI), network architecture of the brain now is accessible to systematic study. The clinical value of such techniques has yet to be realized, however, in large part because the physiologic meaning of network metrics has not been established in the setting of cerebral pathology. Normal rewiring of the cerebral network during development as well as the known impact of anesthesia on the MR measurement of brain networks further complicate the situation in children. We therefore sought to measure: 1. the relationship between network architecture and intelligence in the pediatric, epileptic brain; 2. the impact of anesthesia during MRI on this relationship.

Materials and Methods

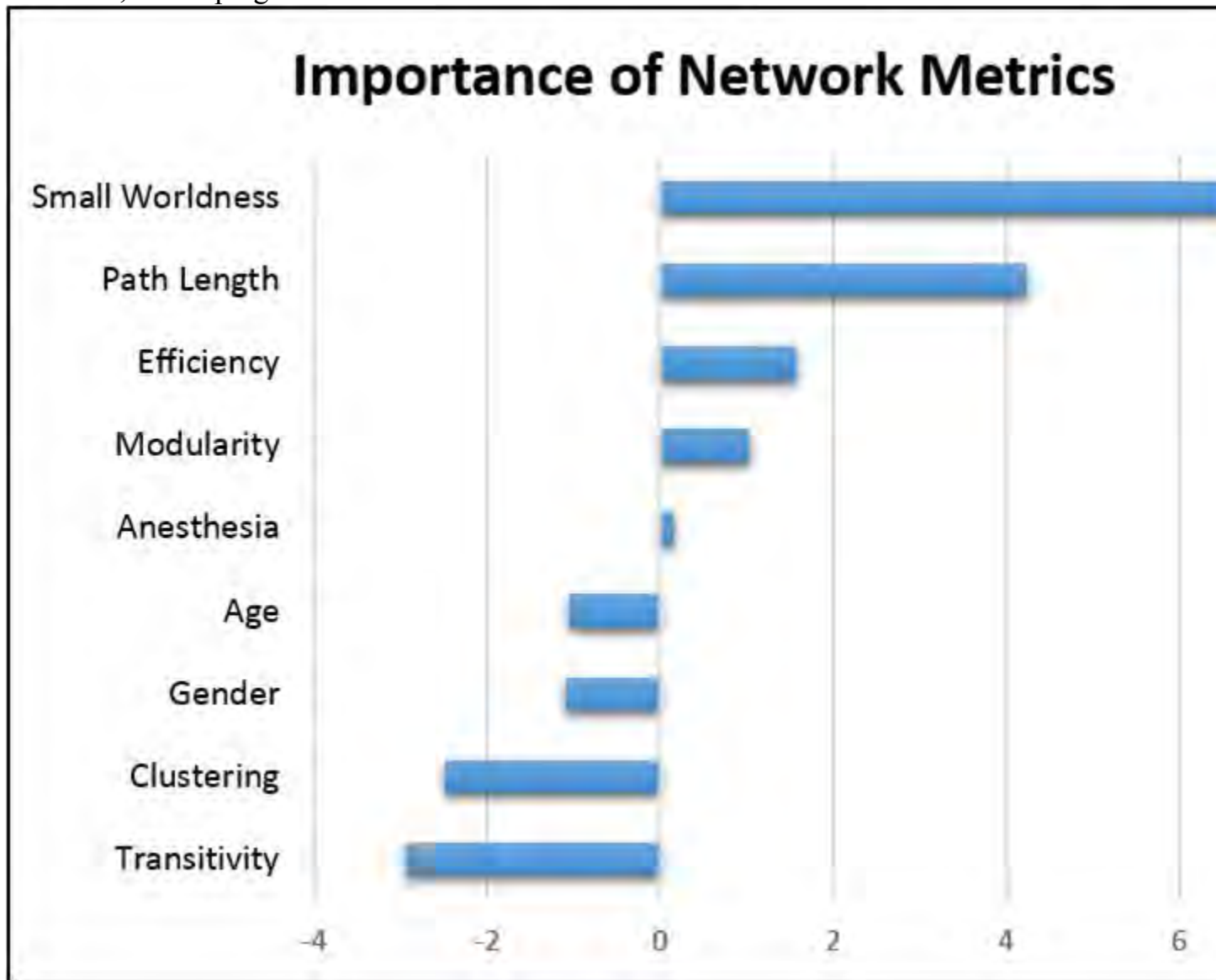
This cross-sectional study was IRB approved. Patients were identified retrospectively with the following inclusion criteria: 1. A diagnosis of localization related epilepsy; 2. MRI of the brain acquired at 3T, including a resting state functional MRI sequence; 3. Global IQ measured (according to an age-appropriate version of the Wechsler Intelligence Test) by a pediatric neuropsychologist. Patients with prior brain surgery were excluded. Resting-state time series were co-registered to a T1-weighted image, corrected for motion, and high-pass filtered (0.01 Hz). Network nodes then were defined based on subdivision of the brain into 800 gray matter volumes of interest. Voxel-wise blood oxygen level dependent (BOLD)-signal time series were averaged over each node. The strength of an edge (connection) between two nodes was defined as the absolute value of the correlation between their BOLD time series. For each weighted, undirected connection matrix, the following network properties were calculated using matlab scripts provided in The Brain Connectivity Toolbox (<http://www.brain-connectivity-toolbox.net>): clustering coefficient, transitivity, modularity, path length, small worldness, and global efficiency. A machine learning algorithm was used to: 1. measure the independent contribution of each metric to IQ after adjusting for the contribution of all other metrics; 2. model the impact of anesthesia on this contribution.

Results

Twenty-eight patients met criteria (age: 7-18 years). Path length and small worldness independently predicted global intelligence after accounting for all other variables (Fig. 1). Direct and inverse relationships were observed to IQ for small worldness ($p=0.008$) and path length ($p=0.004$) respectively. Administration of anesthesia did not impact the metrics contributing intelligence.

Conclusions

We report two main findings in this cohort of pediatric epilepsy patients: 1. Two metrics of network integration strongly contributed to full scale IQ; 2. These relationships to intelligence were robust to anesthesia. These findings support the physiologic relevance of imaging-based metrics of network architecture in the abnormal, developing brain.



(Filename: TCT_O-383_ASNR1.jpg)

Whole-Brain MEG-Recorded Delta Activity Decreases During Normal Pediatric Brain Maturation

E Libove¹, E Davenport¹, M Espeland¹, J Urban¹, J Stitzel¹, J Maldjian², C Whitlow¹
¹Wake Forest University School of Medicine, Winston-Salem, NC, ²University of Texas Southwestern, Dallas, TX

Purpose

Delta waves are low frequency (0-4 Hz) signals produced by brain that traditionally have been detected via electroencephalography (EEG), and are emerging as an important biomarker of brain injury and disease. The purpose of this investigation was to characterize whole brain delta wave activity using magnetoencephalography (MEG) in healthy pediatric subjects, thus providing normal baseline data for comparison.

Materials and Methods

Ninety-eight healthy male subjects (ages 9 to 18 years) were recruited as part of a larger study investigating brain structure/function in youth and high school football players. Eight minutes of eyes open continuous resting-state MEG data were acquired using a 275 channel radial gradiometer whole-head CTF Omega 2005 (VSM MedTech Ltd., Coquitlam, Canada) at a sampling rate of 600 Hz and acquisition bandwidth of 0.25–150 Hz. Magnetic resonance imaging (MRI) data were acquired for each subject immediately after MEG on a 3T Siemens Skyra scanner. Whole brain mean delta wave power was computed from band-limited source space projections using a scalar beamformer. Structural T1 images were segmented into gray matter (GM), white matter (WM) and cerebrospinal fluid (CSF), normalized to Montreal Neurologic Imaging space, and processed to generate volumetric tissue maps using SPM8 in the VBM8 toolbox for evaluating normal developmental changes in GM volume.

Results

Regression analysis revealed a significant inverse linear relationship between age and delta wave activity ($p < 0.0001$, $R^2 = 0.189$). Age-related decreases in delta wave activity correlated with normal developmental decreases in whole brain GM volume ($p < .0001$, $R^2 = 0.199$).

Conclusions

We demonstrate that MEG-recorded delta wave activity decreases with increasing age in healthy pediatric subjects, and is associated with developmental associated decreases in GM volume, which extends previous studies reporting similar findings using EEG. It is possible that normal developmental changes in delta wave activity

may reflect synaptic pruning and could be useful as a biomarker for mTBI, as well as other neurological diseases that are otherwise occult to conventional neuroimaging.

O-385

3:32PM - 3:40PM

Construction of a 3D Printed MEG Phantom for Validation of MEG Source Localization

E Davenport¹, P Brown¹, L East¹, J Urban¹, B Wagner², M Espeland¹, R Moran³, P Santago⁴, C Whitlow¹, J Stitzel¹, J Maldjian⁵

¹Wake Forest University School of Medicine, Winston-Salem, NC, ²University of Texas Southwestern, 5323 Harry Hines Blvd. , TX, ³Virginia Polytechnic & State University, Roanoke , VA, ⁴Wake Forest University, Winston-Salem, NC, ⁵University of Texas Southwestern, Dallas, TX

Purpose

The purpose of this study is to design an anatomically accurate magnetoencephalography (MEG) compatible phantom that will allow for validation testing of inversion source localization methods across a range of source locations.

Materials and Methods

From an ongoing study of youth football, a normal subject's MEG and magnetic resonance imaging (MRI) scans were chosen as models for the MEG phantom. The MRI was segmented using SPM8. The Slicer 3D software was used to clean and smooth the cortical surface mask. The 3D reconstruction was imported into Geomagic Studio (v14.1.0 Geomagic, Research Triangle Park, NC), and a hollow mold-like model of the brain surface was created. Supports, spouts to fill the brain with gelatin, and a mechanism to connect the two halves were designed in Solidworks.

Physiologically relevant dipoles holders were placed at anatomically predetermined locations (e.g., amygdala, default mode nodes) based on literature values and MNI coordinates. The final 3D model was printed using PolyJet by Stratasys Direct Manufacturing (Valencia, CA). Dipoles were constructed from semi-rigid coaxial cable (8216 Coax- RG-174/U Type, Belden) in accordance with Leahy et al. (2) The halves were joined and the model then was filled with a saline-gelatin mixture. The mixture was prepared with 0.75mg/ml concentration saline solution and gelatin at 0.6% by weight to provide a conductivity matching that of gray matter.³⁷ A computed tomography (CT) was acquired of the phantom for localization of the physical dipoles. Specific currents at prespecified dipole locations were constructed using MATLAB and the Simulink toolbox with a frequency ranging from 1-50Hz and amplitude range of +/-5µA in order to mimic true neuronal signals. Continuous MEG signals, sampled at a rate of 600 Hz, were recorded using a 275 channel radial gradiometer whole-head CTF Omega 2005.

Results

The phantom was successfully constructed. The CT measured dipole locations served as ground truth for testing inversion techniques. The error between the intended and the ground truth dipole location was an average of 8.2mm with a standard deviation of 1.6mm. Currents were generated and measured by the MEG on the same scale of human neuronal signals; several issues related to electrical noise and digital-to-analog converter (DAC) performance were identified.

Conclusions

This study demonstrates the construction and use of one of the most geometrically advanced and anatomically accurate MEG phantoms to date. Source localization errors were on the order of 1 cm. Improvements in DAC performance and electrical noise are expected to further refine source localization.



(Filename: TCT_O-385_marvin.jpg)

O-387

3:48PM - 3:56PM

Hemispheric Asymmetry of White Matter Microstructure and Language Ability in Autism

M Hwang¹, L Blaskey¹, J Owen², T Roberts¹, J Berman¹

¹Children's Hospital of Philadelphia, Philadelphia, PA, ²UCSF, San Francisco, CA

Purpose

The hemispheric specialization of language and leftward lateralization of the superior longitudinal fasciculus (SLF) volume is a well known finding in normally developing children. In autism spectrum disorder (ASD), language circuits develop abnormally and some research indicate that structural and functional asymmetry is absent or even reversed (1). It is largely unknown how abnormal patterns of lateralization impact language ability and if compensatory mechanisms exist. This study investigates the relationship between SLF microstructural asymmetry of diffusion MR metrics and language ability in ASD.

Materials and Methods

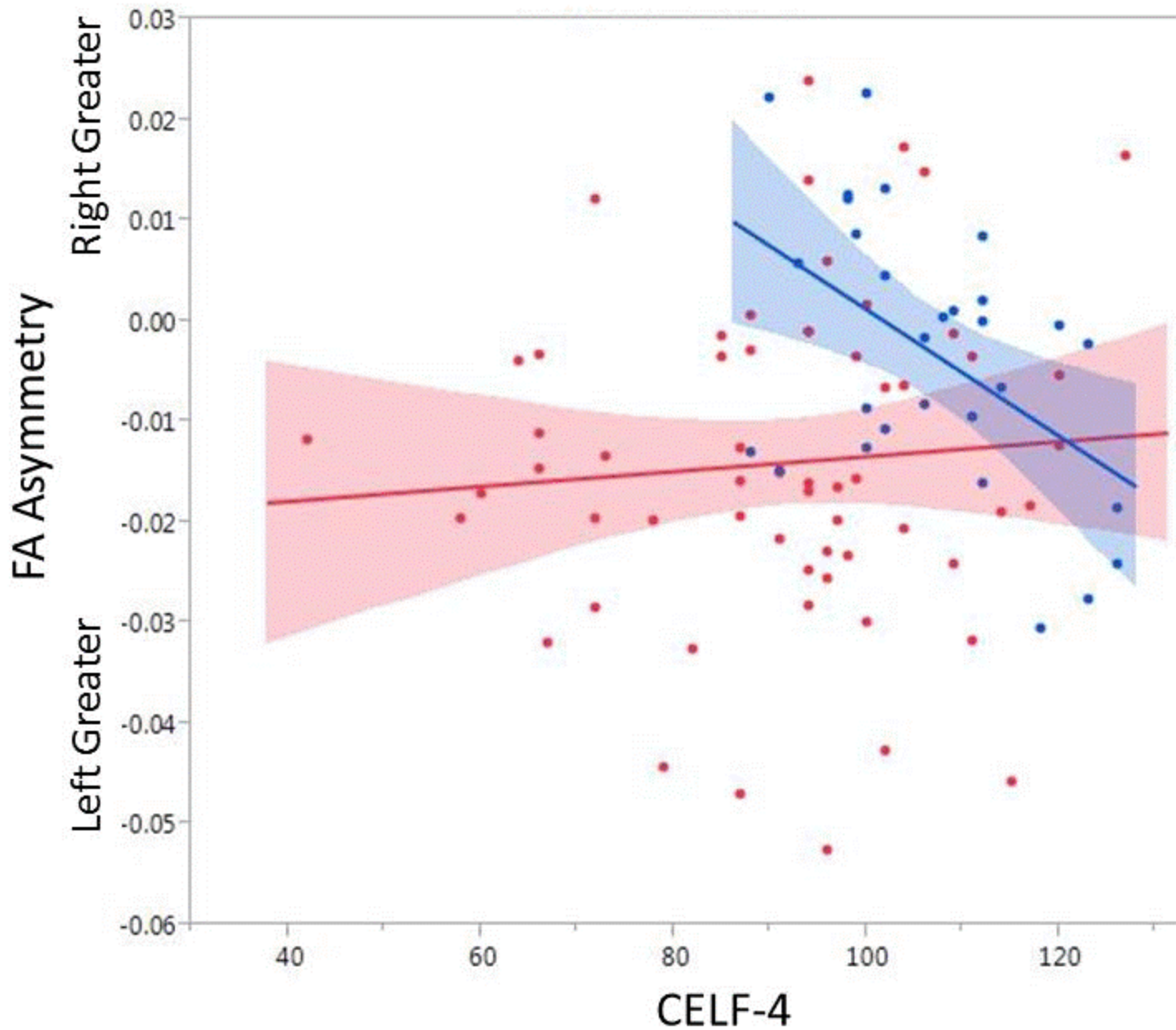
The study included 30 controls (mean age 10.6 ± 2.5 years) and 61 age-matched children with ASD [prior diagnosis made by expert clinician, confirmed by Autism Diagnostic Observation Schedule, 2nd Edition (ADOS-2) and parent report measures] (mean age 10.5 ± 2.5 years). Diffusion tensor imaging (DTI) was acquired at 3T (Siemens Verio) with 2mm isotropic resolution, $b=1000s/mm^2$, and 30 diffusion directions. Atlas-based SLF regions of interest (ROIs) were placed on each subject's TBSS generated skeleton of diffusion maps (2). Asymmetry of fractional anisotropy (FA), mean diffusivity (MD), and radial diffusivity (RD) were calculated. The association of microstructural asymmetry with language ability, as measured on the Clinical Evaluation of Language Fundamentals (CELF-4), was examined.

Results

Degree of leftward lateralization of FA and rightward lateralization of RD were predictive of language ability (CELF-4) in controls ($p < 0.05$, each) (Fig.). In ASD, the correlation slope between DTI metrics (FA and RD) and CELF-4 was significantly different than in controls ($p < 0.05$ each). In ASD, there was a trend of positive correlation between rightward FA and CELF-4 and negative correlation between leftward RD and CELF-4, indicating a possible reversal of the modulating effect of SLF microstructure on language ability.

Conclusions

The abnormal and possibly reversed relationship between SLF asymmetry and language function in ASD suggests a compensatory role of the right SLF in language function. This altered structure-behavior relationship in ASD may underlie the heterogeneity of language ability in ASD.



(Filename: TCT_O-387_FinalFigure.gif)

O-388

3:56PM - 4:04PM

In Vivo Assessment of Phase One Pharmacological Intervention Using GABA Spectroscopy in Awake Children with Single Gene (NF1) Autism.

S Stivaros¹, M Tziraki², S Garg², H Haroon², A Kapasi², S Williams², J Green³

¹Royal Manchester Children's Hospital, Manchester, Lancs, ²University of Manchester, Manchester, Lancs, ³University of Manchester, Manchester, Lancs

Purpose

Neurochemical dysregulation is thought to have potential as a basis to model developmental abnormalities in autism. The most common noninvasive technique used to acquire measures of neurochemistry in vivo is proton magnetic resonance spectroscopy (1HMRS). Simvastatin is an HMG-CoA reductase inhibitor. There is extensive clinical experience of its use in young children with disorders such as familial hypercholesterolemia and Smith Lemli Opitz syndrome. Our aim was the in vivo 1HMRS quantitation of GABA using a preparation and scanning protocol which allowed us to acquire a range of neurochemistry measures in nonsedated children with neurofibromatosis type 1 (NF1) single gene model autism who were undergoing a phase 1 trial of Simvastatin intervention.

Materials and Methods

The children with single gene (NF1) autism were acclimatized to awake MRI scanning using a social story and 2 weeks of exposure to mp3 recordings of specific MRI scan sequence noises at specified time points during the day when both awake and during sleep preparation. Scanning was performed at time zero, then again following 12 weeks treatment of placebo or Simvastatin. We measured the concentration of GABA and other neuro-metabolites in the left frontal white matter and deep gray nuclei. We applied a single-voxel MEGA-PRESS sequence, TR/TE 2000/68 ms, FA 90°, NSA 4, phase cycles 4, samples 1024, spectral BW 2000 Hz, VOI size 30×30×30 mm³, dynamics 44, dynamics interval 8 s, BASING pulse MEGA basic, pulse duration 15 ms, water freq 4.68 ppm, pulse 1 freq 1.9 ppm, pulse 2 freq 7.6 ppm, pulse FA 180°, water suppression by excitation. Nonwater suppressed spectra also were acquired in both locations for quantification purposes. Datasets were analyzed using the jMRUI v.5 software; AMARES, was utilized to calculate metabolite concentration with tissue percentages extracted from a participant's T1 image for partial volume correction.

Results

In total 32 children presented for imaging, 24 males. The mean age was 7.9 years (range 4.6-10.4 years). Time zero scans were obtained successfully in the deep gray nuclei in 24 and in the frontal white matter in 27. Following drug/placebo treatment successful scanning was performed in 21 children in the deep gray nuclei and 19 in the frontal white matter. Comparison of the GABA values at time zero and at week 12 demonstrated no significant difference in GABA measurements in the frontal white matter ($p=0.19$) or deep gray nuclei ($p=0.66$).

Conclusions

We have demonstrated that in this age group, made more challenging by the diagnosis of autism, careful patient preparation can result in successful quantitative GABA

assessment. The results of our GABA imaging demonstrate stability over time validating its use in the assessment of the Ras-Raf-MEK-ERK pathway in this age group during this phase one phamaco-intervention study. We also present the changes seen in the neurochemistry of these children following simvastatin intervention.

O-389

4:04PM - 4:12PM

Negative Brain Connectivity: A General Maladaptive Trait and Imaging Biomarker For Neurodevelopmental Disorders

A Mallik¹, L Shah², J Anderson¹

¹University of Utah, Salt Lake City, UT, ²University Of Utah, Salt Lake City, UT

Purpose

Abnormal brain functional connectivity MRI (fc-MRI) findings now have been demonstrated in numerous neurodevelopmental and neuropsychiatric disorders. For example, evidence for an abnormal ratio of excitation and inhibition in autism is thought to contribute to brain hyperconnectivity (Supekar et al. 2013). Studies that span different neurodevelopmental disorders have been proposed as a mechanism to study brain phenotypes that may be shared across disorders (Research Domain Criteria, Cuthbert 2015).

Materials and Methods

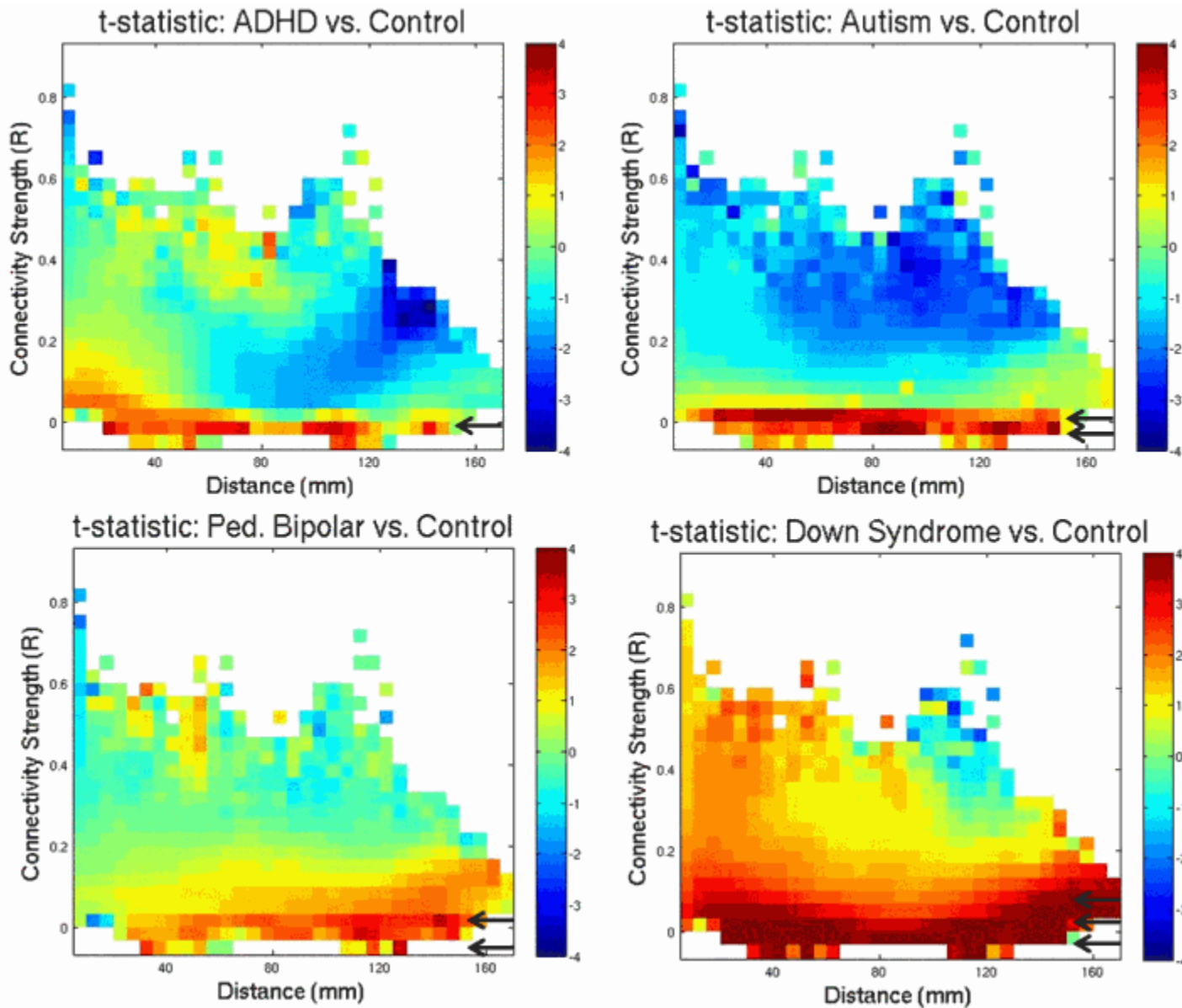
We examined connectome wide fc-MRI relative to age-matched controls for autism (autism=447, control=517, ABIDE), ADHD (n=248; 476, ADHD-200), Down syndrome (n=21,16, University of Utah), pediatric bipolar disorder (n=32,48, University of Utah) and adult schizophrenia (n=60, 68, COBRE). Functional connectivity MRI correlations were organized by distance between 7266 regions of interest (ROIs) and by calculated strength of those connections in 476 typically developing (TD) young adults (Human Connectome Project, HCP). We calculated a negative connectivity score (NCS) consisting of the average correlation for all "connections" for which the Human Connectome Project sample averaged functional connectivity less than zero.

Results

All pediatric neurodevelopmental and neuropsychiatric disorder patient groups demonstrated increased correlation in typically negative connections relative to age-matched controls ($p < 0.05$), while adult schizophrenia did not. These findings suggest a common shared pathophysiology of increased connectivity in negative connections across these neurodevelopmental disorders, as can be seen with decreased inhibition. In TD young adults, increased connectivity among negative functional connections was correlated with impaired performance on behavioral metrics involving executive function and attention ($q < 0.05$, FDR).

Conclusions

The NCS may be a useful diagnostic imaging biomarker or prognostic metric for the evaluation of patients for neurodevelopmental disorders. Findings in TD young adults suggest a novel diagnostic or prognostic tool for patients with suspected mood disorders.



(Filename: TCT_O-389_mallik_anderson_ASNR_figure_4.gif)

O-390

4:12PM - 4:20PM

Childhood Cerebral Adrenoleukodystrophy: MR Perfusion Measurements and their Use in Predicting Clinical Outcome after Hematopoietic Stem Cell Transplantation

J Benson¹, M Salmela², D Nascene², J Eisengart², D Loes³, L Zhang⁴, A McKinney²
¹University of Minnesota, St. Paul, MN, ²University of Minnesota, Minneapolis, MN, ³Suburban Radiologic Consultants, Ltd., Burnsville, MN, ⁴Clinical and Translational Science Institute, University of Minnesota, Minneapolis, MN

Purpose

To prospectively measure magnetic resonance perfusion (MRP) parameters in patients with cerebral adrenoleukodystrophy (cALD) pre and posthematopoietic stem cell transplantation (HSCT), and to correlate those measurements with the clinical outcome.

Materials and Methods

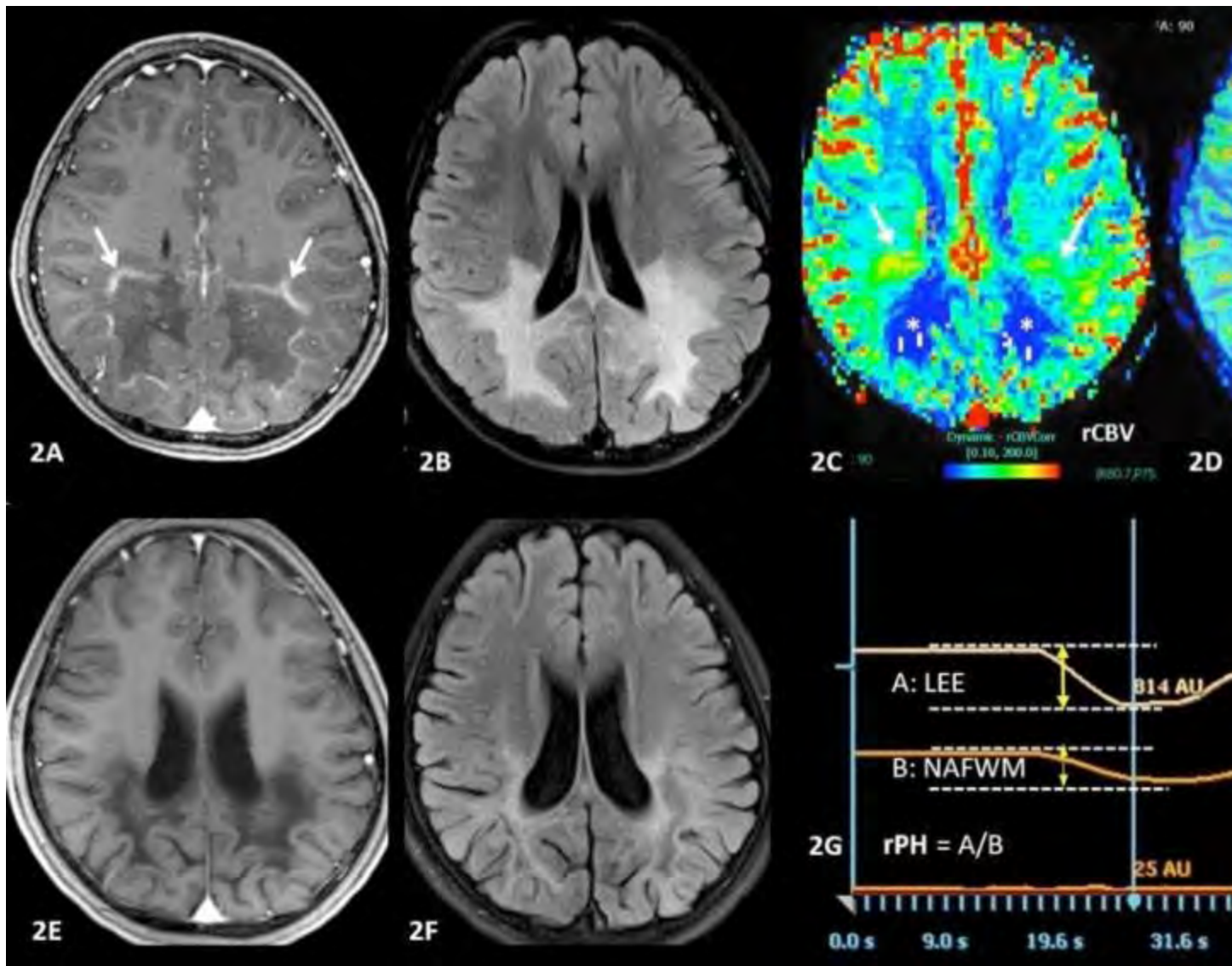
Ten cALD patients prospectively underwent DSC-MRP at <45 days pre-, 30-60 days post-, and 1 year post-HSCT. Magnetic resonance perfusion measurements in the 10 cALD patients and eight controls were obtained from the parietooccipital WM (POWM), callosal splenium (SCC), leading edge of enhancement (LEE), and normal-appearing frontal white matter (NAFWM). Magnetic resonance severity (Loes) scores, neurologic function scores (NFS), and neurocognitive scores also were obtained. Magnetic resonance perfusion values were analyzed in the cALD patients at each time point, and compared to controls. Correlations were calculated between the pre-HSCT MRP values and 1-year clinical scores, with p-value adjustment for multiple comparisons.

Results

Pre-HSCT (baseline) in cALD patients, both rCBV and rCBF within the SCC and POWM significantly differed from controls ($p=0.005-0.031$), and remained so at 1 year post-HSCT ($p=0.003-0.005$). Meanwhile, no MRP parameter within the LEE differed significantly from controls ($p=0.074-0.999$), nor significantly changed by 1 year post-HSCT ($p=0.142-0.887$). The baseline Loes scores correlated with the 1 year NFS ($r=0.813$, $p<0.0001$), while SCC rCBV significantly correlated with the 1 year NFS and neurocognitive scores ($r=-0.730-0.815$, $p=0.007-0.038$).

Conclusions

Leading edge of enhancement MRP measurements likely remain normal post-HSCT in cALD, which suggests local disease stabilization. Meanwhile, the POWM and SCC rCBV and rCBF values worsen, suggesting irreversible injury. This study found that certain baseline (pre-HSCT) MRP values may predict the eventual outcome following HSCT.



(Filename: TCT_O-390_201512-1Image1abstract.jpg)

O-391

4:20PM - 4:28PM

Inherited Disorders of Sulfite Metabolism: evolution of brain MRI findings

P Caruso¹, P Musolino¹, R Aziz-Bose¹, D Loes², F Eichler¹

¹Massachusetts General Hospital, Boston, MA, ²Suburban Radiologic Consultants, Ltd., Burnsville, MN

Purpose

Isolated sulfite oxidase deficiency (ISOD) and molybdenum cofactor deficiency (MOCD) are genetic disorders that lead to rapid neurodegeneration due to

intracellular accumulation of sulfites. While both gray and white matter are known to be affected, the timing and extent of injury remains poorly understood.

Materials and Methods

Twenty patients with proven biochemical and/or genetic defects for ISOD or MOCD were screened. Of the cohort, 18 patients (3 with ISOD and 15 with MOCD) with magnetic resonance imaging (MRI) were included in the study. All MR images were reviewed by two experienced neuroradiologists and two neurologists for the location and timing of gray and white matter injury, cavitations, atrophy, and malformations.

Results

Forty-three brain magnetic resonance scans in the 18 patients were reviewed. Fifteen patients presented in the first year of life (classic infantile form) and three patients presented between 12 months and adulthood (late onset type). Of the classic infantile patients, MRI showed diffuse multilobar white matter lesions in all patients, white matter cavitation in 6/15 (40%), and an abnormally long posterior fossa in 14/15 (93%). Subsequent imaging showed cavitation in 13/15 (86%) patients. Cavitations developed within an average of 35 days (range 15-96 days). Among the late-onset group, only one patient had a deep gray matter cavitation; one patient had a completely normal MRI; and the posterior fossa was normal in all three patients.

Conclusions

Brain MR abnormalities in ISOD and MOCD exhibit two patterns: the classic pattern where onset occurs in the infantile period and progresses over weeks to month to diffuse panlobar white matter cavitation, and the other, a late onset pattern, associated with a more mild course. Interventions before or during the acute phase may impact the onset and severity of the disease.

Wednesday

4:45PM - 6:15PM

Washington Marriott Wardman Park, Marriott Ballroom

18A-One Stop Shop Symposium

18A

4:45PM - 4:50PM

Introduction

18A-1

4:50PM - 5:10PM

Technology Enabling Multimodality Imaging in the Angiography Suite

Chen, G.
University of Wisconsin-Madison
Madison, WI

18A-2

5:10PM - 5:30PM

**Rationale and Feasibility of Multimodality Imaging in the Angiography Suite.
How This Adds Value**

Dörfler, A.
University of Erlangen
Erlangen

18A-3

5:30PM - 5:50PM

The Erlangen Experience with Multimodality Imaging in the Angiography

Struffert, T.
University of Erlangen-Nuremberg
Erlangen

18A-4

5:50PM - 6:10PM

Capabilities of Multi-Modality Imaging Using Cone-beam CT

Aagaard-Kienitz, B.
University of Wisconsin Hospital and Clinics
Madison, WI

18A-5

6:10PM - 6:15PM

Wrap-up

Wednesday

4:45PM - 6:15PM

Washington Marriott Wardman Park, Washington 4/5/6

18B-CSI Programming: 3D Print

18B-1

4:45PM - 5:15PM

**Incorporation of 3D Printing into a Quaternary Referral Center: Emphasis on
Craniofacial**

Morris, J.

Mayo Clinic

Rochester, MN

18B-2

5:15PM - 5:45PM

3D Printing for Pediatric Neurosurgical Surgical Simulation

Prabhu, S.

Boston Children's Hospital

Boston, MA

18B-3

5:45PM - 6:15PM

**Using 3D Printing in the Creation of Plastic Surgery Guides and Maxillofacial
Prosthetic Molds**

Liacouris, P.

Walter Reed National Military Medical Center

Bethesda, MD

Wednesday

4:45PM - 6:15PM

Washington Marriott Wardman Park, Washington 1/2/3

18C-ASNR/SNMMRI Joint Session: Integrated Molecular Imaging

18C-1

4:45PM - 5:15PM

Imaging Biomarkers for AD - PET and MRI

Johnson, S.
University of Wisconsin Madison
Madison, WI

18C-2

5:15PM - 5:45PM

Amyloid PET and IDEAS Study

Nasrallah, I.
HUP
Philadelphia, PA

18C-3

5:45PM - 6:15PM

Clinical Dopamine Imaging in Movement Disorders

Seibyl, J.
Yale University
New Haven, CT

Wednesday

4:45PM - 6:15PM

Washington Marriott Wardman Park, Roosevelt 1-3

18D-PARALLEL PAPER SESSION: Turbo Talks - Head and Neck: All Neck

Extravaganza

O-392

4:45PM - 4:48PM

Comparison of Dual-Energy CT (DECT) Iodine Overlay, Virtual keV Monochromatic Series, and Single-Energy CT in the Visualization of Head and Neck Cancer.

M Kraft¹, A Srinivasan¹, M Ibrahim¹, M Spector¹

¹*University of Michigan, Ann Arbor, MI*

Purpose

To compare lesion margin, enhancement, conspicuity, and staging amongst dual-

energy computed tomography (DECT) derived iodine overlay maps, virtual keV monochromatic series, and single-energy CT (SECT) in squamous cell carcinomas of the head and neck (HNSCC).

Materials and Methods

This retrospective study included 33 patients with histopathologically proven HNSCC who underwent DECT scanning from 2008-2015. Dual-energy CT scans were processed to create three monochromatic series (40, 45, and 50 keV) and iodine overlay series. Two blinded board-certified neuroradiologists compared these images against a control series of either SECT images (if performed within 1 month) or 70 keV DECT derived monochromatic series. The images were randomized and evaluated ordinarily (1-poor, 2-adequate, and 3-excellent visualization) for lesion margin, enhancement, and overall conspicuity. Additionally, each cancer was staged, and an image preference was chosen. Results were compared using a Wilcoxon signed-rank test.

Results

The 45 and 50 keV images were significantly better (p-values 0.003 to <0.001) than the controls in determining lesion enhancement, margins, and overall conspicuity for both readers. The iodine overlay was not significantly better than the controls in nearly all assessments, and one reader found the conspicuity worse. The monochromatic series performed better in tumor staging for reader 1, while having the same accuracy as SECT for reader 2. Both readers most preferred the 50 keV monochromatic series, with the 45 and 40 keV images as the second and third most preferred image series, respectively. No reader preferred the iodine overlay images.

Conclusions

The improved lesion margin, enhancement, and conspicuity in HNSCC on the 40, 45, and 50 keV monochromatic series can be crucial for a comprehensive evaluation of lesion extent and accurate staging. The 50 keV series was the most preferred series, suggesting this may have the best balance of image noise and enhancement of the lesion.

O-393

4:48PM - 4:51PM

Image quality and radiation dose of third generation dual-energy CT of the head and neck compared with a standard acquisition.

S Suntharalingam¹, E Stenzel², A Wetter², N Guberina², A Ringelstein³, M Forsting², K Nassenstein²

¹University Hospital Essen, Essen, Germany, ²University Hospital Essen, Essen, NRW, ³Institute of Diagnostic and Interventional Radiology and Neuroradiology, University Hospital Essen, Essen, NRW

Purpose

To evaluate the radiation dose and image quality performance of head and neck imaging between a third-generation dual-energy CT (DECT) and a standard acquisition (SECT).

Materials and Methods

For the baseline exam 30 cancer patients underwent SECT with automated tube current modulation and automated tube voltage selection. The follow-up CT was performed on DECT (80 and Sn150 kVp). Radiation doses and attenuation measurements of the internal jugular vein, submandibular gland and sternomastoid and tongue muscles were compared. Objective image noise was compared at five anatomical levels. Image quality also was visually evaluated by two radiologists.

Results

CTDI_{vol} was 54 % lower with DE than with SECT (4.2 versus 9.2 mGy; $p = 0.002$). Median objective noise was lower in DECT at all anatomical levels (nasopharynx: 4.3 versus 6.2 HU; $p = 0.02$ - floor of mouth: 3.2 versus 4.5 HU; $p = 0.02$ - arytenoids: 3.5 versus 4.9 HU; $p = 0.08$ - lower thyroid: 4.7 versus 30.2 HU; $p = 0.03$ - arch of aorta: 6.6 versus 27.1 HU; $p = 0.002$). No different attenuation measurements were observed between DECT and SECT in submandibular gland (106.1 versus 119.6 HU; $p = 0.85$), in sternomastoid (65.8 versus 70.0 HU; $p = 0.38$) and tongue muscles (77.5 versus 76.4 HU; $p = 0.42$). Only signal intensity in internal jugular vein was lower in DECT (196.4 versus 263.2 HU; $p = 0.002$). Visual image quality showed no significant differences between both examinations.

Conclusions

Head and neck imaging with third-generation DECT can reduce radiation dose significantly, while maintaining excellent image quality.

O-394

4:51PM - 4:54PM

Quantitative Assessment of Variation in CT Scanning Parameters on Texture Features: Pilot Study Using a Non-Anatomic Phantom

K Buch¹, B Li², M Qureshi², S Anderson², O Sakai²

¹*Boston Medical Center/Massachusetts General Hospital, Boston, MA*, ²*Boston Medical Center, Boston University School of Medicine, Boston, MA*

Purpose

Texture analysis is becoming increasingly used in the field of radiology given that it is a quantitative, noninvasive, postprocessing, multimodality technique. The objective of this study is to evaluate how changes in computed tomography (CT) scanning parameters results in variations in texture features.

Materials and Methods

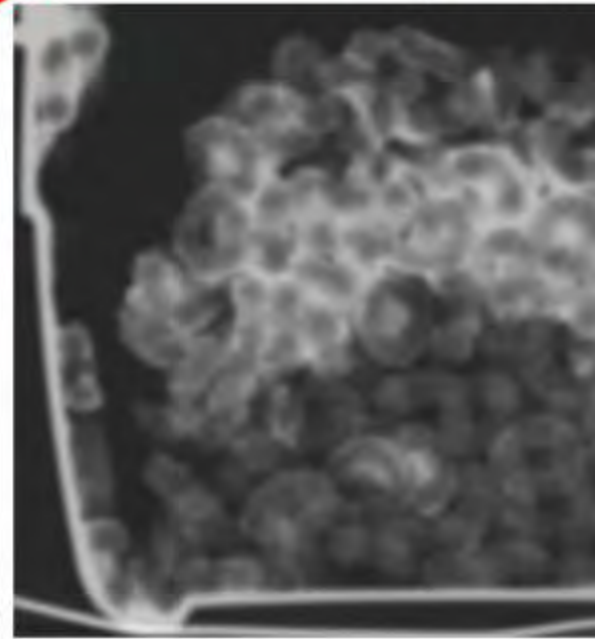
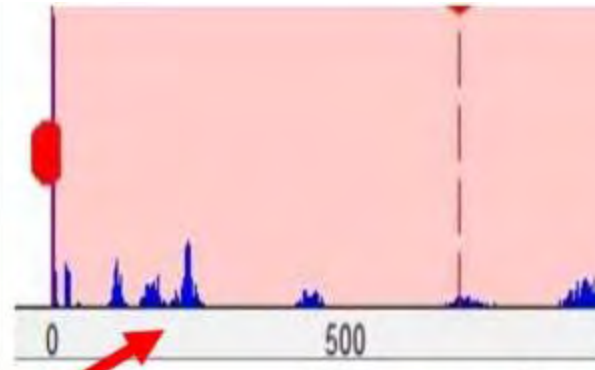
Serial CT scans were performed on two cylindrical acrylic phantoms containing a randomized mixture of air, fat, and solid cereal rings of varying size using both 64-multidetector row CT and 16-multidetector row CT scanners. Computed tomography scan parameters including the mA, kVp, slice thickness, helical pitch, ASIR setting, and acquisition mode were varied. A total of 42 texture features were extracted from each scan using an in-house developed Matlab program including histogram, gray level co-occurrence matrix (GLCM), gray level run-length (GLRL) and Law's features. A two-tailed t-test was performed to evaluate for differences in texture features.

Results

Statistically significant differences were seen in the histogram features with variations in phantom size, acquisition mode, and number of detectors ($P < 0.0001$ - $P = 0.044$). Gray level co-occurrence matrix features of entropy, correlation, and energy demonstrated significant differences with variations in slice thickness, kVp, pitch and phantom size ($P < 0.001$). Gray level run-length features significantly varied with differences in the acquisition mode (axial versus helical scanning), and slice thickness. The Law's features demonstrated statistically significant differences for all tested variations in CT scanning parameters. Changing mA had no significant effect on the texture parameters.

Conclusions

Subtle changes in image texture become significantly different based on changes in basic CT scanning parameters. While these changes may not affect image interpretation with the human eye, quantitative assessments such as texture analysis are impacted significantly by alterations in these parameters. Therefore, during the noninvasive quantitative assessment of pathology on CT, standardized CT scanning parameters are of paramount importance.



(Filename: TCT_O-394_CTphantomtexturepic.jpg)

Variations in Texture Features Based on Variations in CT Slice Thickness

| | 0.625 (N=7) | | 1.25 (N=7) | | 2.5 (N=7) | | 5 (N=7) | |
|------------------------|-------------|----------|------------|----------|-----------|----------|----------|----------|
| | Mean | SD | Mean | SD | Mean | SD | Mean | SD |
| Histogram | | | | | | | | |
| Mean | 226.18 | 3.86 | 224.19 | 5.05 | 220.76 | 15.07 | 222.81 | 17.4 |
| Median | 236.29 | 2.43 | 235.86 | 2.97 | 228.43 | 9.32 | 218.14 | 11.1 |
| STD | 193.20 | 5.60 | 189.53 | 11.45 | 164.39 | 25.18 | 147.36 | 28.1 |
| Range | 81.05 | 0.77 | 74.91 | 2.16 | 60.35 | 2.48 | 46.79 | 2.8 |
| Geometric mean | 171.93 | 4.28 | 174.93 | 5.68 | 182.13 | 14.29 | 197.38 | 15.1 |
| Harmonic mean | 90.46 | 4.23 | 99.54 | 5.01 | 116.02 | 8.96 | 141.97 | 7.8 |
| 2 nd STD | 27.81 | 0.26 | 25.68 | 0.75 | 20.67 | 0.85 | 15.99 | 0.9 |
| STD5 | 45.27 | 0.42 | 41.87 | 1.17 | 33.68 | 1.32 | 25.95 | 1.5 |
| STD9 | 74.10 | 0.72 | 68.96 | 1.63 | 55.88 | 1.95 | 42.96 | 2.5 |
| 4 th moment | 6.79E+09 | 7.49E+08 | 6.73E+09 | 1.67E+09 | 4.37E+09 | 2.37E+09 | 3.07E+09 | 1.84E+09 |
| IQR | 225.86 | 9.30 | 220.14 | 12.82 | 180.14 | 10.51 | 144.71 | 13.1 |
| Entropy | 7.07 | 0.02 | 7.02 | 0.03 | 7.01 | 0.09 | 7.00 | 0.3 |
| Test | 0.38 | 0.29 | 0.44 | 0.31 | 0.57 | 0.39 | 0.52 | 0.3 |
| GLCM | | | | | | | | |
| Entropy | 1.21 | 0.02 | 1.08 | 0.06 | 1.13 | 0.06 | 1.20 | 0.3 |
| Contrast | 4.61 | 0.16 | 4.07 | 0.10 | 2.99 | 0.17 | 2.23 | 0.2 |
| Correlation | 0.97 | 0.001 | 0.97 | 0.002 | 0.98 | 0.004 | 0.98 | 0.0 |
| Energy | 0.02 | 0.001 | 0.02 | 0.002 | 0.02 | 0.001 | 0.02 | 0.0 |
| Homogeneity | 0.59 | 0.002 | 0.61 | 0.01 | 0.64 | 0.01 | 0.68 | 0.0 |
| GLRL | | | | | | | | |
| SRE | 0.09 | 0.003 | 0.09 | 0.01 | 0.08 | 0.004 | 0.07 | 0.0 |
| LRE | 0.10 | 0.003 | 0.09 | 0.01 | 0.08 | 0.004 | 0.07 | 0.0 |
| GLN | 0.09 | 0.003 | 0.09 | 0.005 | 0.08 | 0.003 | 0.06 | 0.0 |
| RLN | 0.10 | 0.003 | 0.09 | 0.01 | 0.08 | 0.004 | 0.07 | 0.0 |
| RP | 92.17 | 2.58 | 89.16 | 3.79 | 84.19 | 9.66 | 84.18 | 12.1 |
| LGRE | 89.55 | 2.44 | 86.81 | 3.46 | 81.80 | 9.23 | 81.69 | 11.1 |
| HGRE | 91.91 | 2.51 | 89.73 | 3.68 | 85.78 | 9.50 | 85.38 | 11.1 |
| SRLGE | 90.50 | 2.71 | 87.76 | 3.65 | 82.33 | 9.71 | 82.02 | 11.1 |
| SRHGE | 3.47E+04 | 2.24E+03 | 3.18E+04 | 1.28E+03 | 2.23E+04 | 1.32E+03 | 1.53E+04 | 2.36E+03 |
| LRLGE | 4.84E+04 | 2.47E+03 | 4.46E+04 | 2.25E+03 | 3.40E+04 | 2.35E+03 | 2.57E+04 | 3.88E+03 |
| LRHGE | 3.46E+04 | 1.71E+03 | 3.14E+04 | 1.50E+03 | 2.17E+04 | 1.60E+03 | 1.48E+04 | 2.19E+03 |

(Filename: TCT_O-394_CTTexturetable.jpg)

O-395

4:54PM - 4:57PM

CT texture analysis potentially predicts local failure in head and neck squamous cell carcinoma treated with chemoradiotherapy

H Kuno¹, B Li¹, M Qureshi¹, M Chapman¹, V Andreu¹, M Truong¹, O Sakai¹

¹Boston Medical Center, Boston University School of Medicine, Boston, MA

Purpose

Human papillomavirus (HPV) positive head and neck squamous cell carcinomas (HNSCC) are known to have a good response to chemoradiotherapy (1-3), yet treatment failure has been reported (4). The purpose of this study is to assess various texture features of a primary lesion from pretreatment computed tomography (CT) to predict potential local failure in HNSCC patients treated with chemoradiotherapy.

Materials and Methods

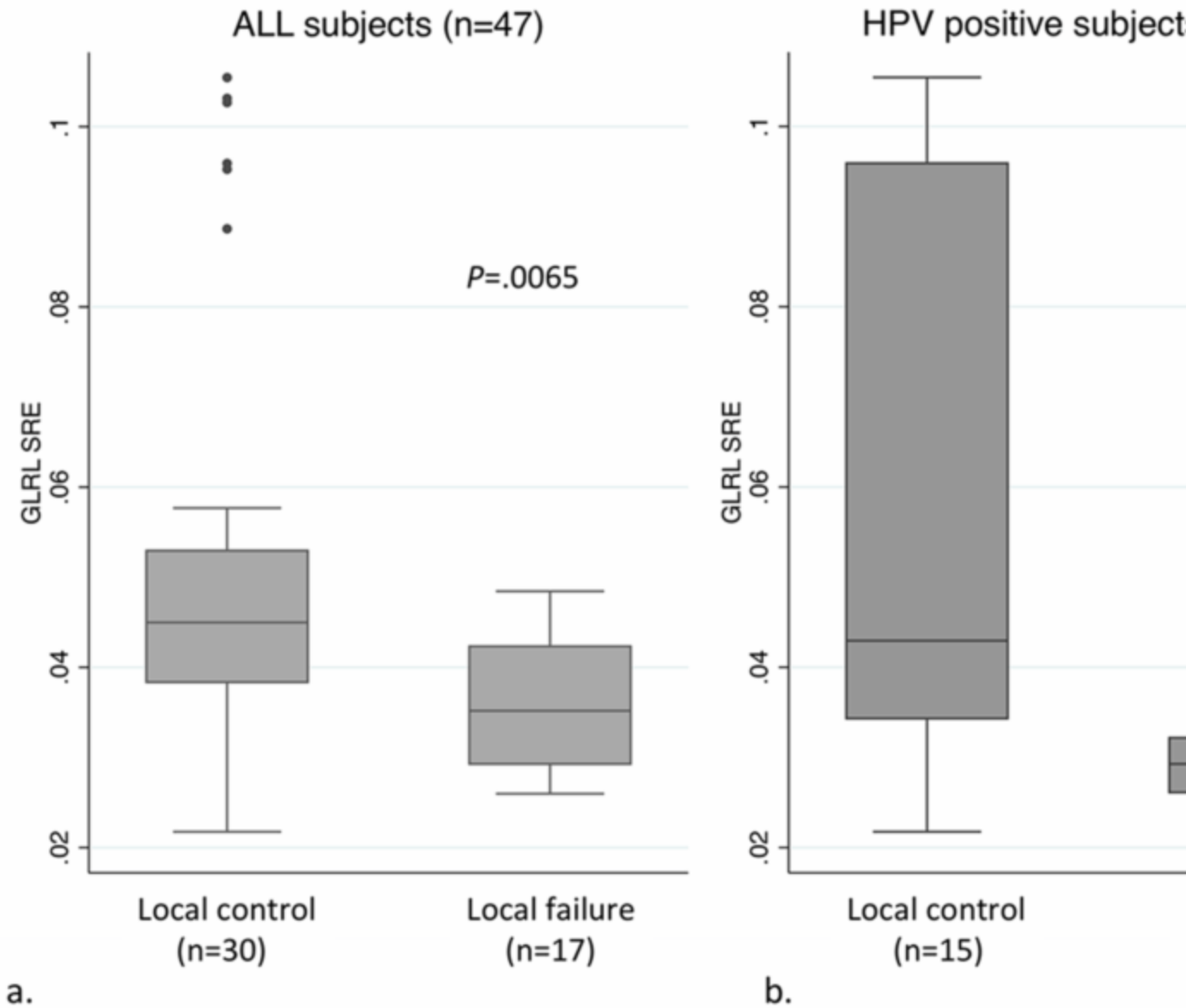
Forty-seven patients (40 men, 7 women; 31–80 years; median age, 57 years) diagnosed with primary HNSCC (25 oropharynx, 7 hypopharynx, 13 larynx and 2 oral cavity, including 20 HPV-positive and 19 HPV-negative) who underwent contrast-enhanced CT for staging between March 2008 and March 2014 followed by chemoradiotherapy were reviewed retrospectively. Segmentations of the primary lesion were performed manually, and an in-house developed MATLAB-based texture analysis program extracted 42 texture features from each segmented volume (5). Mann-Whitney U test was used to compare locally controlled patients with patients who developed local failure. A P value of less than 0.05 was considered statistically significant.

Results

Seventeen patients developed local failure (follow-up periods; 2 to 23 months), and the remaining 30 showed local control (12 to 76 months). There were eight gray-level run-length (GLRL) features that demonstrated significant difference ($P < 0.007$; Fig. a) between these two groups. Among 20 HPV positive patients, five patients (4 oropharynx and 1 larynx) developed local failure, and seven GLRL features were significantly different such as long run emphasis ($P = .016$; Fig. b) and short run emphasis ($P = .026$) features.

Conclusions

The results suggest that the GLRL matrix features from CT texture analysis may serve as a potential indicator of local failure in HNSCC treated with chemoradiotherapy or radiotherapy regardless of HPV status. Additional studies are needed to investigate the clinical significance of these findings with larger sample size.



Box plots of GLRL SRE between local control and local failure. Note: GLRL, gray-level run-length; SRE, short-range entropy.

(Filename: TCT_O-395_ASNR_Figure1.gif)

O-396

4:57PM - 5:00PM

Using texture analysis to differentiate between nasopharyngeal carcinoma and age-matched normal adenoid controls

A Tsai¹, K Buch², A Fujita³, B Li⁴, M Qureshi⁴, M Truong⁴, O Sakai⁴

¹*Boston Medical Center/Boston University Medical Center, Boston, MA,* ²*Massachusetts General Hospital, Boston, MA,* ³*Jichi Medical University School of Medicine, Shimotsuke, Japan,* ⁴*Boston Medical Center, Boston University School of Medicine, Boston, MA*

Purpose

Early nasopharyngeal carcinoma (NPC) may have subtle imaging findings on contrast-enhanced computed tomography (CECT), making it difficult to differentiate from normal adenoid tissue. Texture analysis has been employed increasingly as a postprocessing image analysis tool, which extracts quantitative texture features from an image to evaluate subtle pathologic changes not easily perceived by the human eye. The purpose of this study was to investigate the use of texture analysis applied to CECT to aid in the differentiation of NPC from normal adenoid tissue.

Materials and Methods

Following IRB approval, 13 patients with NPC and 13 age-matched normal adenoid controls, who underwent CECT between 2010-2014 were included in this study. The adenoid tissue of NPC and control patients was contoured manually, segmented, and imported to an in-house developed texture analysis program, which extracted 42 texture features from each segmented volume. These texture features included spatially independent features (histogram features) as well as spatially dependent features (gray-level co-occurrence matrix (GLCM) and gray-level run length (GLRL) features). Statistically significant differences in the texture features between NPC and controls were evaluated using a two-tailed t-test.

Results

Statistically significant differences ($p < 0.05$) between NPC and controls were seen in all but two of the 42 extracted texture features. In particular, all of the spatially dependent texture features demonstrated statistically significant differences between the NPC and control groups. Only histogram features median ($p = 0.52$) and test ($p = 0.71$) did not demonstrate statistically significant differences.

Conclusions

Significant differences were seen in spatially dependent texture features suggestive of a specific tissue architecture seen in NPC that is not present in normal adenoid tissue. Texture analysis may therefore aid in differentiating early NPC from normal adenoid tissue.

| Statistically significant differences in texture features between NPC and adenoid controls | | | |
|--|------------------------|---------|---------|
| Texture feature | | p-value | q-value |
| histogram | mean | <0.0001 | 0.0002 |
| | median | 0.5233 | 0.5361 |
| | std | <0.0001 | 0.0002 |
| | entropy | <0.0001 | 0.0002 |
| | 2dstd | <0.0001 | 0.0002 |
| | range | <0.0001 | 0.0002 |
| | std9 | <0.0001 | 0.0002 |
| | geo mean | <0.0001 | 0.0002 |
| | harmonic mean | <0.0001 | 0.0002 |
| | iqr | 0.0011 | 0.0015 |
| | 4 th moment | 0.0006 | 0.001 |
| | test | 0.7092 | 0.7092 |
| | MGR | <0.0001 | 0.0002 |
| | VGR | <0.0001 | 0.0002 |
| | skewness | <0.0001 | 0.0002 |
| kurtosis | <0.0001 | 0.0002 | |
| GLCM | entropy | <0.0001 | 0.0002 |
| | contrast | <0.0001 | 0.0002 |
| | correlation | <0.0001 | 0.0002 |
| | energy | <0.0001 | 0.0002 |
| | homogeneity | <0.0001 | 0.0002 |
| GLRL | SRE | <0.0001 | 0.0002 |
| | LRE | 0.002 | 0.0024 |
| | GLN | 0.0028 | 0.0033 |
| | RLN | <0.0001 | 0.0002 |
| | RP | 0.011 | 0.0122 |
| | LGRE | 0.0054 | 0.0061 |
| | HGRE | 0.0113 | 0.0122 |
| | SRLGE | 0.0155 | 0.0163 |
| | SRHGE | <0.0001 | 0.0002 |
| | LRLGE | <0.0001 | 0.0002 |
| | LRHGE | <0.0001 | 0.0002 |
| Laws | L1 | 0.0002 | 0.0004 |
| | L2 | 0.0013 | 0.0017 |
| | L3 | 0.0009 | 0.0013 |
| | L4 | 0.0008 | 0.0012 |
| | L5 | 0.0008 | 0.0012 |
| | L6 | 0.0017 | 0.0022 |
| | L7 | 0.0009 | 0.0013 |
| | L8 | 0.0020 | 0.0024 |
| | L9 | 0.0006 | 0.0010 |

(Filename: TCT_O-396_pandqvaluetable.jpg)

O-397

5:00PM - 5:03PM

Texture analysis of CT in the larynx between normal subjects and patients with localized amyloidosis

T Kakigi¹, K Hassan², M Qureshi², M Chapman², B Li², J Berk², O Sakai²

¹*Boston Medical Center, Boston University/Kyoto University Graduate School, Boston, MA*, ²*Boston Medical Center, Boston University School of Medicine, Boston, MA*

Purpose

Calcification often is seen in lesions of head and neck amyloidosis, however detection of noncalcified amyloid lesions is difficult on computed tomography (CT) as noncalcified lesions demonstrate similar density to normal tissue. The purpose of this study was to evaluate the difference between noncalcified amyloid lesions and normal tissues in the larynx using texture analysis of CT.

Materials and Methods

This study was IRB-approved and HIPAA-compliant with a waiver of the need for informed consent. Fourteen patients with biopsy-proven AL amyloidosis (5 males and 9 females; mean age 57.2 years, ranged from 35 to 72 years) and 14 control subjects without amyloidosis (4 males and 10 females; mean age 51.4 years, ranged from 24 to 81 years) who underwent noncontrast neck CT were included in the study. The glottis on nonenhanced CT was evaluated using texture analysis. Differences in 42 texture parameters were examined in these groups using Student's t-test and a false discovery rate (FDR) correction.

Results

Thirty-one parameters (excluding standard deviation, entropy, harmonic mean and test of the histogram feature, gray-level co-occurrence matrix (GLCM) entropy, short-run emphasis (SRE), long-run emphasis (LRE), gray-level nonuniformity (GLN), run-length nonuniformity (RLN), high gray-level-run emphasis (HGRE), and short-run low gray-level emphasis (SRLGE) of the gray-level run length (GLRL) texture feature, (harmonic mean and test) demonstrated statistically significant differences between the groups ($P < .05$). After using FDR correction, 30 parameters (excluding fourth moment of the histogram feature) showed significant differences ($Q < .05$).

Conclusions

Amyloidosis of the head and neck may be the first clinical sign of systemic disease. We need to diagnose head and neck amyloidosis in the early period before it develops systemic manifestations. Texture analysis of CT imaging is a noninvasive procedure

that has the potential to differentiate noncalcified amyloid lesions from normal tissue in the larynx.

O-398

5:03PM - 5:06PM

Preoperative 18F-FDG-PET/CT versus contrast-enhanced CT to identify regional metastasis among patients with head and neck squamous cell carcinoma

J Cho¹, T Ow², A Lee², N Schlecht¹, R Smith², B Schiff², A Tassler², J Lin¹, R Moadel², J Bello², K Shifteh²

¹Albert Einstein College of Medicine, Bronx, NY, ²Montefiore Medical Center, Bronx, NY

Purpose

For head and neck squamous cell carcinoma (HNSCC), metastasis to the cervical lymph nodes portends a worse prognosis (1). Imaging is used to help identify suspicious lymph nodes pre-operatively. The primary aim of this study is to compare the accuracy of positron emission tomography (PET)/computed tomography (CT) to contrast-enhanced CT (CECT) in the detection of cervical lymph node metastasis when compared to histopathology as the gold standard.

Materials and Methods

Of 214 patients who received neck dissection for primary staging and treatment of newly diagnosed HNSCC from 1999 to 2014, 73 patients had reviewable pre-operative PET/CT and CECT studies within 6 months prior to surgery. All PET/CT and CECT studies were reviewed independently by board-certified specialists, blinded to pathology reports and cancer stage. A lymph node satisfying any one the following criteria: (1) necrosis, (2) extra-capsular extension (ECE), (3) round or irregular shape with enhancement and >0.5cm, (4) round or irregular in shape without enhancement and >1.0cm, (5) oval shape with enhancement and >1.0cm, (6) oval shape without enhancement and >1.5cm, or (7) grouping of three or more suspicious lymph nodes, was determined positive on CECT (2, 3). Any lymph node with abnormally increased focal tracer uptake was determined positive on PET/CT (4). The neck level or neck side was designated positive if at least one lymph node was suspected within the defined borders (5). Concordance between radiology and histopathology was measured both by neck level and by neck side. The sensitivity, specificity, overall accuracy, positive predictive value (PPV), and negative predictive value (NPV) were calculated for each modality and compared using a two-sample proportion with significance set to a p-value of 0.05 or less.

Results

Eighty-three of 579 (14%) neck levels and 53 of 116 (46%) neck sides were positive for metastasis on histopathology (Table 1). By neck level, PET/CT was significantly

less specific than CECT (85 versus 90%, $p=0.007$). On analysis by neck side, PET/CT was significantly more sensitive (87 versus 66%, $p=0.022$), while CECT showed higher specificity (79 versus 51%, $p=0.001$). A significant difference was not found between the modalities in overall accuracy by neck side ($p=0.39$). However, CECT tended to have higher overall accuracy, an association that did not quite reach significance by neck level (86 versus 82%, $p=0.056$). Twenty-seven of 73 (37%) patients ultimately were staged N0 by histopathology. In the N0 cohort, nodal involvement was detected falsely by PET/CT in 17 of 27 patients (63%) and falsely detected by CECT in eight of 27 patients (30%).

Conclusions

Our data suggest that PET/CT is more sensitive than CECT to rule out cancer involvement of a given neck side prior to surgery. However, CECT appears to be more specific overall, with fewer false positive results. Although CECT showed higher overall accuracy, the trend did not reach statistical significance. One must consider these distinct but perhaps complementary attributes when using results of these modalities for clinical decision making.

Table 1. Relationship between FDG-PET/CT and CECT results with neck histopathology correlates

| Imaging Modality | TP (n) | FP (n) | FN (n) | TN (n) | Sensitivity (%) | Specificity (%) | Accuracy (%) |
|-----------------------------|--------|--------|--------|--------|-----------------|-----------------|--------------|
| Neck Level (n = 579) | | | | | | | |
| PET/CT | 53 | 77 | 30 | 419 | 64 (53, 74) | 85 (81, 88) | 82 (78, 85) |
| CECT | 49 | 48 | 34 | 448 | 59 (48, 70) | 90 (87, 93) | 86 (83, 89) |
| p value | | | | | 0.632 | 0.007 | 0.056 |
| Neck Side (n = 116) | | | | | | | |
| PET/CT | 46 | 31 | 7 | 32 | 87 (74, 94) | 51 (38, 63) | 67 (58, 76) |
| CECT | 35 | 13 | 18 | 50 | 66 (52, 78) | 79 (67, 88) | 73 (64, 81) |
| p value | | | | | 0.022 | 0.001 | 0.389 |

PPV: Positive Predictive Value, NPV: Negative Predictive Value.

(Filename: TCT_O-398_ASNRTable.jpg)

O-399

5:06PM - 5:09PM

PET/CT in patients treated for advanced head and neck cancer: what do you say when the tumor improved, but didn't completely resolve?

P Wangaryattawanich¹, T Rath¹, B Branstetter¹

¹University of Pittsburgh Medical Center, Pittsburgh, PA

Purpose

Positron emission tomography (PET)/computed tomography (CT) performed for surveillance of head and neck cancer has demonstrated a wide range of false positive and false negative rates, depending on imaging and interpretation protocols. One

potential area of confusion is in patients who present with bulky disease that is treated with chemoradiation, and has dramatic improvement in tumor size without complete resolution. The purpose of this study was to evaluate the accuracy of initial post-treatment PET/CTs in patients with advanced head and neck squamous cell carcinoma (HNSCC), when the examination demonstrates marked improvement but not complete resolution of tumor mass or fluorodeoxy glucose (FDG) avidity.

Materials and Methods

We performed a retrospective chart review to identify patients with HNSCC who initially presented with bulky tumor and were treated with chemoradiation. We selected patients whose first post-treatment PET/CT was interpreted as showing marked improvement in tumor size and FDG avidity, but with residual tumor mass or faint residual FDG avidity. Seventy-nine such patients were identified. These patients were followed clinically and radiographically for 2 years after to determine recurrence rates. Treatment failure was confirmed by histopathology or unequivocal disease progression on subsequent imaging or clinical evaluation.

Results

Seven of the 79 patients (9%) experienced locoregional treatment failure within 2 years after definitive treatment, yielding a negative predictive value of 91.1%.

Conclusions

In patients with advanced HNSCC treated with chemoradiation, a first post-treatment PET/CT showing dramatic improvement in tumor volume has a high negative predictive value, even when there is a residual tumor mass. The negative predictive value of these PET/CTs is high at 91%, similar to literature values for initial complete response post-treatment PET/CTs.

O-400

5:09PM - 5:12PM

Should we evolve from whole body 18F-FDG-PET-CT protocol to more disease tailored HN -PET -CT in the management of head and neck cancers?

p gopalan¹

¹*Leeds and Bradford Teaching Hospitals, Wakefield, United Kingdom*

Purpose

18F-FDG positron emission tomography (PET) computed tomography (CT) plays a significant role in the management of head and neck (H&N) malignancies. The main indications of PET-CT in H&N cancers are: For unknown primary, pretreatment staging, and following tumor recurrence/relapse. Whole body PET CT protocol is used unanimously for all purposes. The study looked at significant findings above and below diaphragm in view of changing to more disease tailored PET CT protocols, as

there has been recent suggestions that half- body (above diaphragm) PET CT may be sufficient for the management of head and neck cancer patients.

Materials and Methods

Sixty-six consecutive patients suspected of having head and neck malignancy (48 men, 18 women; age range, 22–94 years) that underwent standard whole-body PET/CT in 1-year period (2014-2015) were selected retrospectively. Patients who were referred for identifying unknown primary lesions in the setting of nodal enlargement were (n=29) and who had known primaries were (n=37). The patients referred for staging of known malignancies (n=13) and for detecting recurrence of treated malignancies (n=32), which included both known and unknown primaries. Of the known 37 proven malignancies: 23 patients had oropharyngeal cancer, four had nasopharyngeal cancers, two had oral cavity tumors, two had hypo pharyngeal cancers, and three had laryngeal cancers. Of the 29 unknown primaries, five were probable nasopharyngeal, 14 oropharyngeal, two were lymphomas, one metastatic adenocarcinoma and in six no primaries were identifiable.

Results

Results demonstrated 10.6% significant findings above diaphragm, which predominantly included lung nodules (n=18) the remainder were: Mediastinal nodes, activity in thyroid, esophagus, lung, bone and vocal cords. Significant activity was found only in three cases below diaphragm, which includes nodal disease in lymphoma and metastatic adenocarcinoma and a patient with known renal cancer. The rest were benign adrenal uptake, suspected liver, bone and splenic flexure activity, which were not of any pathological significance on subsequent investigations. Other causes of benign activity below diaphragm includes colonic and marrow activity.

Conclusions

This study cohort did not demonstrate significant findings below diaphragm pertaining to squamous cell carcinoma of head and neck. Considering the proven disease pattern spread of HNSCC and nasopharyngeal cancers, worth switching to more disease tailored PET CT protocols. Propositions: Index scans for staging all head and neck cancers should continue to be whole body PET to identify distant metastasis and concurrent primaries. Follow-up scans for HNSCC can be switched to half body (above diaphragm) particularly if they were low-grade tumor and in the lower spectrum of TNM staging. This is more so in the management of SCC compared to nasopharyngeal cancer. If there is specific question of nodal recurrence then dedicated HN PET CT should be considered rather than using whole body PET CT. Switching the follow-up scans from whole body PET CT to dedicated HN PET CT may improve sensitivity in picking up nodal recurrence.

O-401

5:12PM - 5:15PM

Recurrence Rates Among Category 2 “Questionable Recurrence” Lesions Using NI-RADS Head and Neck Squamous Cell Carcinoma Surveillance Imaging Template: Initial Experience.

G Nayak¹, D Krieger², A Corey³, K Baugnon¹, P Hudgins¹, J Beitler⁴, A Aiken⁵
¹Emory University, Atlanta, GA, ²Emory University School of Medicine, Atlanta, GA, ³Emory, Fayetteville, GA, ⁴Winship Cancer Institute of Emory University, Atlanta, GA, ⁵Emory University Hospital, Atlanta, GA

Purpose

To determine the incidence of local and regional recurrence among lesions scored as "Questionable recurrence," or category 2, using the previously described NI-RADS scoring system in post-treatment contrast-enhanced computed tomography (CECT) surveillance of squamous cell carcinoma (SCC) of the head and neck (HN).

Materials and Methods

This study was classified as a quality improvement project by the IRB. A multidisciplinary team at our institution developed NI-RADS, a standardized template for reporting results on surveillance CECT of the neck in patients previously treated for HN cancer (1). This includes a numerical assessment of suspicion for recurrence, rated 1 through 4, linked to specific management recommendations, both for the primary site and for cervical lymph nodes. Category 2, our "questionable recurrence" category is reserved for ill-defined, non-discrete abnormalities, and if performed with PET, have only intermediate or low fluorodeoxyglucose (FDG) uptake. Category 2 recommendations include direct visualization for mucosal lesions (category 2a), short interval follow up with PET/CECT or CECT for deeper primary site abnormalities (2b if < 1cm, or 2c if > 1cm), or biopsy if a target is identified and is clinically indicated. An EMR database search yielded 500 consecutive cases using the NI-RADS template. Cases without a numerical score or with non-SCC primary tumors, new primary tumors, and primary SCC outside of the HN and skin were excluded. A total of 403 cases were included. The EMR was reviewed to determine the subsequent management, pathology results and outcome of clinical and radiologic follow up.

Results

The incidence of a Category 2 score was 13.6% (55/ 403 cases) with a total of 62 targets identified, 41 at the primary site and 21 in the neck. Eleven of 62 (17.7%) Category 2 targets underwent biopsy and/or surgery following the index study, 9/11 for lesions at the primary site and 2/11 for neck disease. Two of 11 (18.2%) biopsies, both at the primary site were positive for recurrence, and nine were negative. An additional seven Category 2 lesions demonstrated progression during follow up. Therefore, 9/62 (14.5%) target lesions (5 primary and 4 nodal) demonstrated pathology proven recurrence or clear imaging/clinical recurrence during follow up (average follow-up time: 9 months).

Conclusions

13.6% scans (55/403) were scored as Category 2 with a total of 62 lesions. The overall rate of recurrence for targets categorized as "questionable recurrence" was 14.5% (9/62). The relatively low positivity rate reflects that the Category 2 lesions represent an intermediate risk group. This also reinforces that ill-defined abnormalities without significant FDG uptake are often non-neoplastic treatment-related changes and short interval follow up is often the best course of action, with biopsy indicated only in the minority. Knowledge of recurrence rates in this group will be helpful to counsel patients and to further refine surveillance and management recommendations.

O-402

5:15PM - 5:18PM

Recurrence Rates in Category 3 “Highly Suspicious” Lesions Using the NI-RADS Head and Neck Squamous Cell Carcinoma Surveillance Imaging Template: Initial Experience

D Krieger¹, P Hudgins², G Nayak², K Baugnon², A Corey³, J Beitler⁴, A Aiken⁵
¹Emory University School of Medicine, Atlanta, GA, ²Emory University, Atlanta, GA, ³Emory, Fayetteville, GA, ⁴Winship Cancer Institute of Emory University, Atlanta, GA, ⁵Emory University Hospital, Atlanta, GA

Purpose

To determine the incidence of local and regional recurrence among lesions scored "High Suspicion" or Category 3 using the previously published NI-RADS scoring system in post-treatment contrast-enhanced computed tomography (CECT) surveillance of squamous cell carcinoma (SCC) of the head and neck (HN).

Materials and Methods

A multidisciplinary team at our institution developed NI-RADS, a standardized template for reporting results on surveillance neck CECT in patients previously treated for HN cancer (1). This process includes a discrete numerical assessment of suspicion for recurrence, rated into four main categories, linked to specific management recommendations, both for the primary site and for cervical lymph nodes. Category 3 "highly suspicious" lesions are defined as new or enlarging, discrete abnormalities (with significant FDG uptake if performed with PET/CT) with biopsy recommended if clinically indicated. This study was classified as a quality improvement project by the IRB. An EMR database search yielded 500 consecutive cases using the NI-RADS template. Cases without a numerical score or with non-SCC primary tumors, new primary tumors, as well as primary SCC outside of the HN and skin were excluded, leaving 403 evaluable studies. The EMR was reviewed to

determine the subsequent management, pathology results and outcome of clinical and radiologic follow up.

Results

The incidence of a Category 3 score was 7.2% (29/403 cases), with a total of 33 Category 3 targets identified (4 patients received 3's for both primary and nodes), 22 at the primary site and 11 in the neck. Twenty-one of 33 (63.6%) Category 3 targets had pathologic investigation by subsequent biopsy and/or salvage surgery (13/33 primary site, 8/33 nodal). The pathologically confirmed true positive rate was 47.6% (10/21), 30.8% (4/13) at the primary site and 75.0% (6/8) at nodal sites. The remaining 12/33 targets did not have pathological confirmation; eight because it would not affect management, three because no correlate could be found when biopsy was attempted, and one without explanation. Seven of 12 (58.3%) had clinical or radiological evidence for recurrence (6 primary site lesions and 1 nodal site), defined as progression at the target site on subsequent imaging or clinically obvious tumor. Overall, the positive predictive value of recurrence (pathologic or clinical/radiologic) among Category 3 lesions was 17/33 (51.5%): 10/22 (45.5%) at the primary and 7/11 (63.6%) nodal sites.

Conclusions

7.2% (29/403) scans were scored with Category 3 lesions, with a total of 33 lesions, 17 of which had definitive or clinical evidence of recurrence. The low rate of biopsy recommendation and relatively high yield was considered a favorable initial benchmark for the performance of NI-RADS in this clinical setting. The higher PPV for neck nodes (63.6%) compared with primary site (45.5%) is expected, given the complex appearance of post-treatment changes and mucositis at the primary site. Knowledge of recurrence rates in this subcategory will be helpful to counsel patients and to further refine surveillance and management recommendations.

O-403

5:18PM - 5:21PM

Testing Susceptibility Weighted Imaging and Double Inversion Recovery Sequences in the Evaluation of Oropharyngeal Squamous Cell Carcinoma

A Richardson¹, M Bashir², N Dunlap¹, R Rebecca¹, R Bert¹

¹University of Louisville, Louisville, KY, ²University of Wisconsin, Madison, WI

Purpose

Staging and treatment strategies for oropharyngeal squamous cell carcinoma (OPSCCa) depend upon radiologic guidance with significant implications for patient morbidity and mortality. Hypoxia and tumor microstructure may be important predictors of treatment failure in OPSCCa by identifying resistance to radiation and chemotherapy. Susceptibility-weighted imaging (SWI) is a magnetic resonance

imaging (MRI) technique utilizing tissue magnetic susceptibility differences that can demonstrate deoxyhemoglobin in tissues. Double inversion recovery (DIR) is a MRI sequence which employs two inversion pulses to suppress signal from two different tissue types, possibly better delineating tumor boundaries. We hypothesized that such features of SWI and DIR may be of clinical utility in the staging of OPSCCa, adding prognostic value and guiding therapy. We have begun testing of SWI and DIR in patients with OPSCCa.

Materials and Methods

After obtaining IRB approval, six patients with P16+, HPV+ OPSCCa were enrolled and imaged (3T MAGNETOM Skyra) before and 2 weeks following initial chemoradiation treatment. Isotropic 3D SWI imaging parameters: voxel size=1.5mm, TR=27ms, TE=20ms, NSA=1, bandwidth=120, FA=15, PE steps=222. 3D DIR imaging parameters: slice thickness=1.4mm, TR=5000ms, TE=202ms, TIa=2200ms, TIb=300, NSA 2, Echotrain=193, bandwidth=870Hz, FA=120, PE steps=213. Susceptibility-weighted imaging and DIR images were compared to conventional structural images (T1 conventional spin echo pre and postcontrast fat-sat and DWI). Contrast/noise ratios were calculated for mean regions of interest (ROIs) from tumor and control tissues using OSIRIX software.

Results

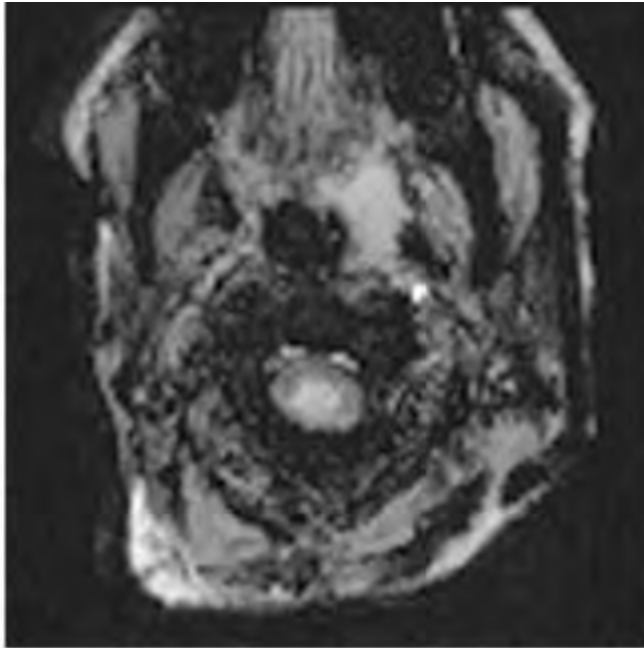
Six OPSCCa patients successfully underwent pre/post-treatment SWI and DIR imaging. Only one patient did not undergo pretreatment postcontrast FST1 imaging (patient 5). Representative pre/post-treatment DIR and SWI images are shown below, demonstrating the often drastic and rapid diminution in tonsillar and nodal tumor burden as early as 2 weeks post-treatment. Contrast to noise ratios (CNRs) are shown in the table below with corresponding delta values reflecting patients with both interval increased and decreased CNRs. The wide variability in these values potentially may be prognostically relevant, however additional follow up is necessary.

Conclusions

Susceptibility-weighted imaging and DIR MRI are potentially useful tools in the staging and therapeutic decision-making of OPSCCa if proven directly relevant to chemotherapeutic/radiation treatment resistance. Our initial optimization of these sequences in a small population of OPSCCa patients supports their clinical feasibility/utility, and further research is planned into their prognostic value.

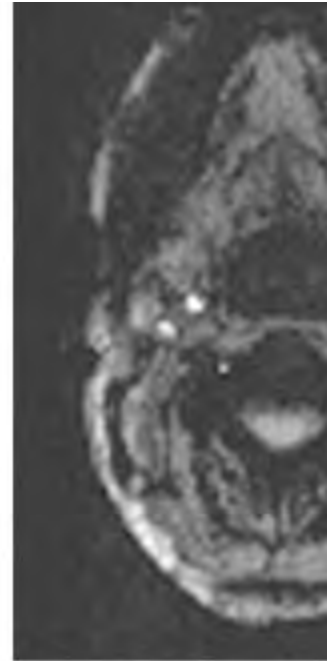
| | Pre-Rx SWI | Post-Rx SWI | Δ | Pre-Rx T1FS w/ | Post-Rx T1FS w/ | Δ | Pre-Rx DIR |
|-----------|---------------|----------------|-------------|-------------------|--------------------|--------------|---------------|
| Patient 1 | 2.7 | 6.5 | 3.8 | 57.7 | 98.3 | 40.6 | 70.5 |
| Patient 2 | 3.9 | 1.8 | -2.1 | 19.2 | 20.4 | 1.2 | 40.8 |
| Patient 3 | 5.4 | 0.5 | -4.9 | 35 | 20.6 | -14.4 | 41.4 |
| Patient 4 | 1.2 | 1.5 | 0.3 | 22.1 | 28.3 | 6.2 | 76.1 |
| Patient 5 | 0.7 | 4.3 | 3.6 | | 26.1 | | 34.9 |
| Patient 6 | 5.6 | 6.9 | 1.3 | 81.2 | 57.1 | -24.1 | 64.9 |

(Filename: TCT_O-403_table.jpg)

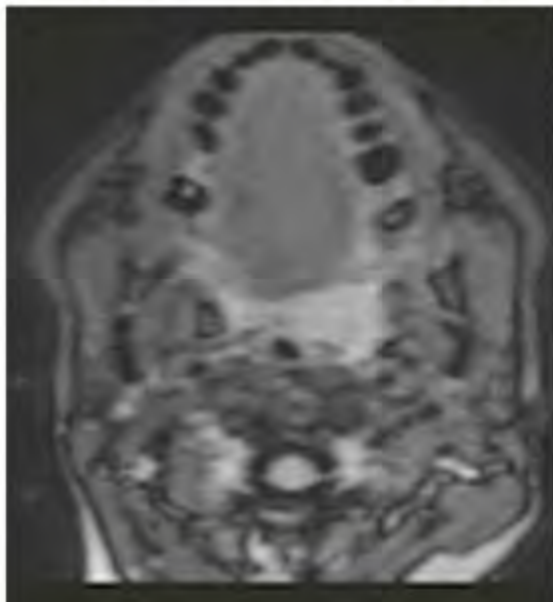


Pre-Treatment

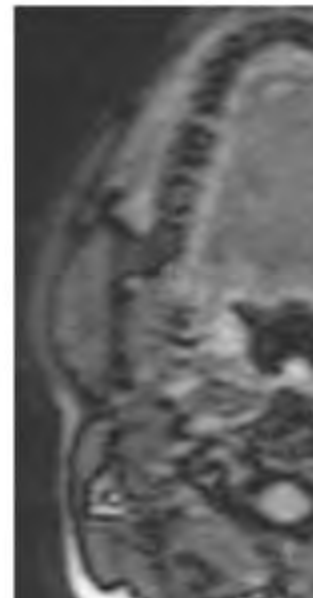
SWI



Post-Tre



DIR



(Filename: TCT_O-403_AbstractGraphic.jpg)

O-404

5:21PM - 5:24PM

Determination of Oropharyngeal Wall Thickness: Implications for Transoral Laser Microsurgery

C Tomblinson¹, G Fletcher¹, A Patel¹, J Hoxworth¹

¹Mayo Clinic, Phoenix, AZ

Purpose

While conventional oropharyngeal cancer resection employs wide local margins, the margins in transoral laser microsurgery with margin mapping are limited by the thickness of the oropharyngeal wall, which has not been well defined. Oropharyngeal wall thickness was measured on magnetic resonance imaging (MRI) to determine the extent of variability in the general population and whether it changes as a function of age and gender.

Materials and Methods

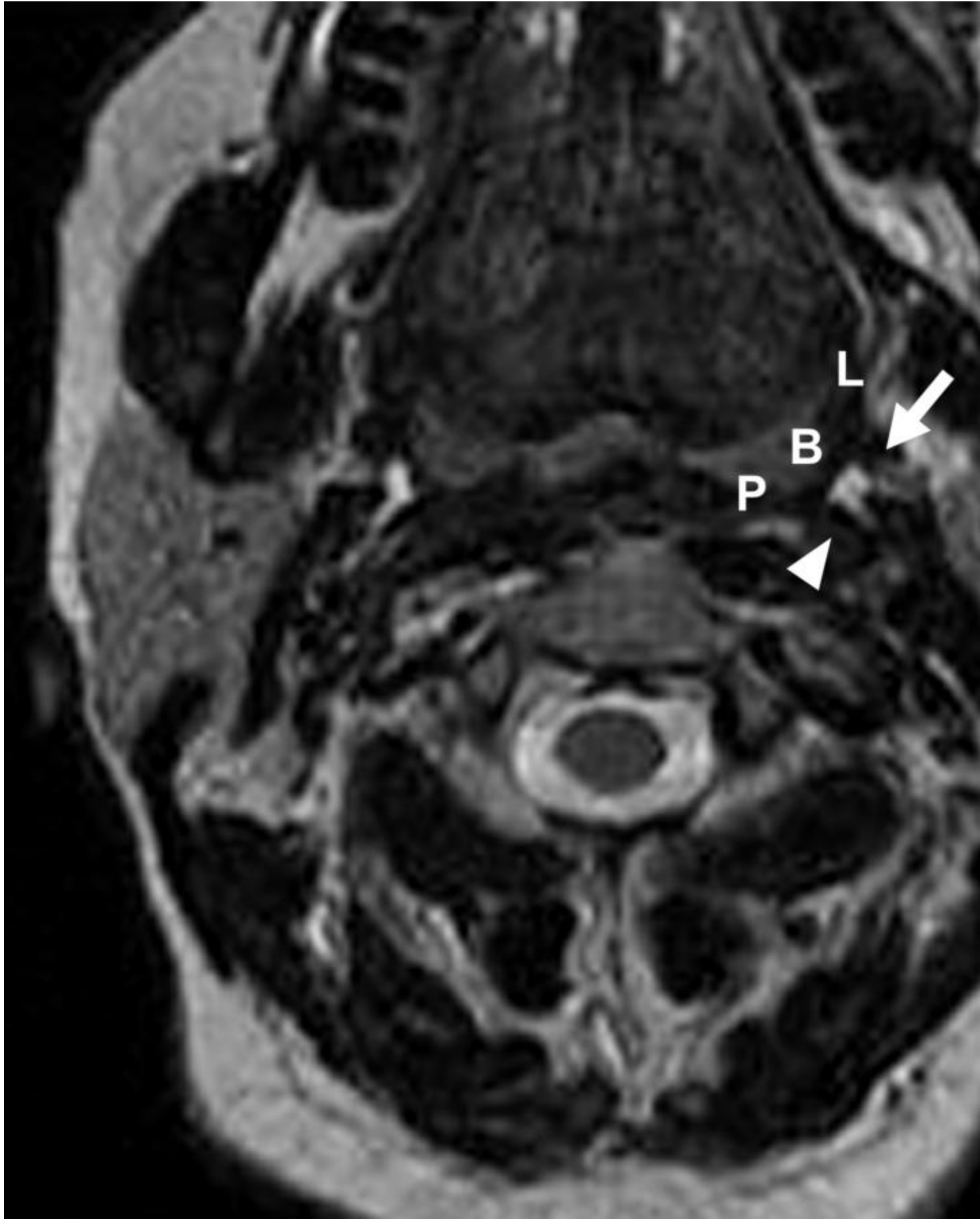
This retrospective study was approved by the institutional review board, and the need for informed consent was waived. The radiology database was queried to identify consecutive neck MRIs which were stratified by decade and gender to ensure equal sampling (10 patients per decade per gender were enrolled between 20 and 80 years; i.e., 240 sides). Patients with a history of head and neck surgery, irradiation, malignancy, and neurologic disorders were excluded. Oropharyngeal wall thickness was measured on axial T2-weighted fast spin echo sequences (3 mm slice thickness) posterior (P), between (B), and lateral (L) to the styloglossus (arrow) and stylopharyngeus (arrowhead) muscles. Statistical analysis was performed to assess for potential correlation between oropharyngeal wall thickness, age and/or gender.

Results

The oropharyngeal constrictor measured (mean \pm standard deviation) 3.7 ± 0.9 mm (P), 1.9 ± 0.6 mm (B), and 5.1 ± 2.0 mm (L). The distance between the styloglossus and stylopharyngeus muscles at the point of insertion into the constrictor was 5.5 ± 1.5 mm. Multivariate regression suggests that P may decrease slightly with age and the distance between the styloglossus and stylopharyngeus muscles increases with age ($p < 0.01$). The remaining constrictor measurements did not vary with age, and no significant gender effects were identified.

Conclusions

Oropharyngeal wall thickness is relatively constant in healthy subjects except that the distance between the styloglossus and stylopharyngeus muscles increases with age and posterior wall thickness slightly decreases with age. These results suggest that the classically taught 5 mm negative margin thought necessary for oropharyngeal cancer resection may not be routinely obtainable with transoral laser microsurgery because the constrictor thickness frequently measures less than 5 mm.



(Filename: TCT_O-404_FigureforAbstract.jpg)

O-405

5:24PM - 5:27PM

Correlation of neck CT finding of piriform sinus morphologic abnormality with Otolaryngology direct visualization: How specific are we?

K Hassan¹, M Chapman², B Setty¹, O Sakai¹

¹*Boston Medical Center, Boston University School of Medicine, Boston, MA,* ²*Boston University Medical Center, Boston, MA*

Purpose

Hypopharyngeal squamous cell carcinomas (SCCa) account for 5% of head and neck malignancies (1), with 70% of cases involving the piriform sinus (2). Cancers here are clinically "silent," with small or early stage tumors producing no or mild clinical symptoms (3). Tumors often are large at diagnosis, reflecting the significant morbidity and mortality associated with these cancers (4-5). Partial or completely effaced piriform sinuses are often found during computed tomography (CT) evaluations of the neck. Radiologists often recommend direct inspection to avoid missing treatable cancer. The purpose of this study is to evaluate piriform sinus abnormalities on CT, and to correlate with findings seen on direct inspection.

Materials and Methods

We retrospectively reviewed our patient database to identify patients with documented piriform sinus abnormalities on CT examinations including the neck [CT neck, cervical spine, and neck positron emission tomography (PET)/CT] from January 2009 through December 2010, utilizing "piriform" and "pyriform" as a keyword search. Imaging studies and medical records were reviewed.

Results

9,175 CT examinations were performed during that time. Two hundred eleven patients (2.3%) demonstrated abnormal piriform sinus morphology (60% male (n=127), 40% female (n=84); 58% smokers (n=116) and 56% with history of alcohol use (n=110)). Ninety-nine (47%) underwent visualization with fiberoptic examination or rigid laryngoscopy. Fifty-seven percent (n=120) of abnormalities were left-sided, 25% (n=53) were right-sided, and 10% (n=38) were bilateral. Thirty-five (17%) patients with visualization demonstrated hypopharyngeal or laryngeal abnormality, with four (2%) patients diagnosed with biopsy proven malignancy, all of which were SCCa. Additional features on neck CT scans analyzed included lymphadenopathy and hypermetabolism on neck PET/CT scans. Seventy-six (36%) patients demonstrated cervical lymphadenopathy and 12 (14%) of those who underwent neck PET/CT scans demonstrated hypermetabolism in the piriform sinuses.

Conclusions

Morphologic abnormalities of the piriform sinuses commonly are found on CT. Direct inspection of the abnormalities may find a small number of early treatable cancers.

O-406

5:27PM - 5:30PM

Accuracy of Preoperative CT in Detecting Pathologic Nodal Extracapsular Spread in Oropharyngeal Squamous Cell Carcinoma.

J Telleria¹, P Hudgins¹, K Magliocca¹, M Patel¹, J Beitler¹, J Arora¹, A Aiken¹

¹Emory University, Atlanta, GA

Purpose

Nodal extracapsular spread (ECS) carries a higher risk for locoregional recurrence and distant metastases in head and neck squamous cell carcinoma (SCC), although the significance of ECS in HPV P16+ tumors is debated (1-2). Recent management trends for oropharyngeal (OP) SCC rely on pretreatment radiographic ECS (rECS) evaluation where imaging specificity is critical. Imaging in predominantly non-HPV SCC has demonstrated sensitivities of 63%-81% and specificities of 60%-91% (3-4). A recent study examining HPV P16+ (predominantly OP) SCC reported sensitivities of 47-55% and specificities of 70-85%, but did not subdivide pathologic ECS (pECS) into microscopic (<1mm) and macroscopic (>1mm) ECS (5). Our purpose was to determine if imaging accuracy is improved using macroscopic ECS as the pathologic gold standard. We also assessed the predictive value of individual nodal imaging features for macroscopic pECS.

Materials and Methods

This retrospective study included 24 consecutive patients who underwent primary TORS and neck dissection for OP SCC. Two CAQ-certified neuroradiologists independently reviewed pre-operative contrast-enhanced CT (CECT) images to evaluate the largest suspicious lymph node. For each case, the radiologist recorded lymph node size and features: matted appearance, lobular contours, perinodal stranding (subtle versus gross), necrosis (small versus >75% or "cystic"), invasion of adjacent structures, and overall impression of rECS. Radiographic results were correlated with pathology.

Results

Radiographic ECS was reported in 13/24 and 12/24 patients by radiologist 1 and radiologist 2, respectively. Pathologic examination revealed that 8/24 (33%) had pECS, with five having macroscopic ECS. Imaging sensitivity for all pECS was 100% for both readers. Specificity for all pECS was 69% and 75% for radiologist 1 and 2, respectively, but decreased to 58% and 63%, respectively, for macroscopic ECS. Interobserver agreement was high for all ECS, lobular contours, all stranding, and all

necrosis. Interobserver agreement was poor when stranding was subdivided into subtle or gross. On logistic regression analysis, size [OR 45.8, p=.003, 95% CI ([2.1, 999])] and lobular contours [OR 25.2, p=.003 CI (3.9-999)] demonstrated a positive correlation with macroscopic ECS. All stranding (C-index 0.79) and all necrosis (C-index 0.76) also demonstrated positive correlation with macroscopic ECS, however, were not statistically significant. Subtle stranding was not a predictor of macroscopic ECS.

Conclusions

This study found a much higher sensitivity (100%) of imaging for detecting pECS in OP SCC than previously reported, but with low specificity, especially for macroscopic ECS (58%-63%). Therefore, when applying criteria used for ECS in non-HPV SCC, the false positive rate is unacceptably high to base treatment decisions. We hypothesize that using subtle stranding as a criterion for macroscopic rECS in HPV P16+ nodal disease may result in false positives due to the inflammatory reaction present on pathologic examination which may mimic ECS radiographically. Size and lobular contours best predicted macroscopic ECS.

O-407

5:30PM - 5:33PM

Choi Criteria as a measure of treatment efficacy in patients with metastatic head and neck squamous cell cancer patients treated with axitinib

E Dickerson¹, P Swiecicki¹, E Bellile¹, F Worden¹, A Srinivasan¹

¹*University of Michigan, Ann Arbor, MI*

Purpose

Axitinib is a small-molecule inhibitor of VEGFR and EGFR which has been evaluated for treatment of metastatic head and neck squamous-cell carcinoma (mHNSCC). The most frequently used tool for assessing response to chemotherapy, response evaluation criteria in solid tumors (RECIST), evaluates tumors by size. However, size alone may not reflect underlying intermediate tumor changes such as tumor necrosis. An alternate means of evaluation, the Choi Criteria, assesses factors including attenuation and size on CT. This was a retrospective, exploratory study assessing the utility Choi Criteria in assessing the response of HNSCC to axitinib.

Materials and Methods

This study examined radiologic and clinical data from a phase II clinical trial of axitinib for the treatment of unresectable recurrent or metastatic HNSCC. Forty-two patients initially were recruited to this trial of which 30 had imaging which could be assessed for disease response and 29 had computed tomography (CT) imaging of neck, chest, and/or abdominal metastasis for which Choi Criteria could be applied in a

retrospective, exploratory analysis. Outcomes were evaluated by Kaplan-Meier survival-analysis.

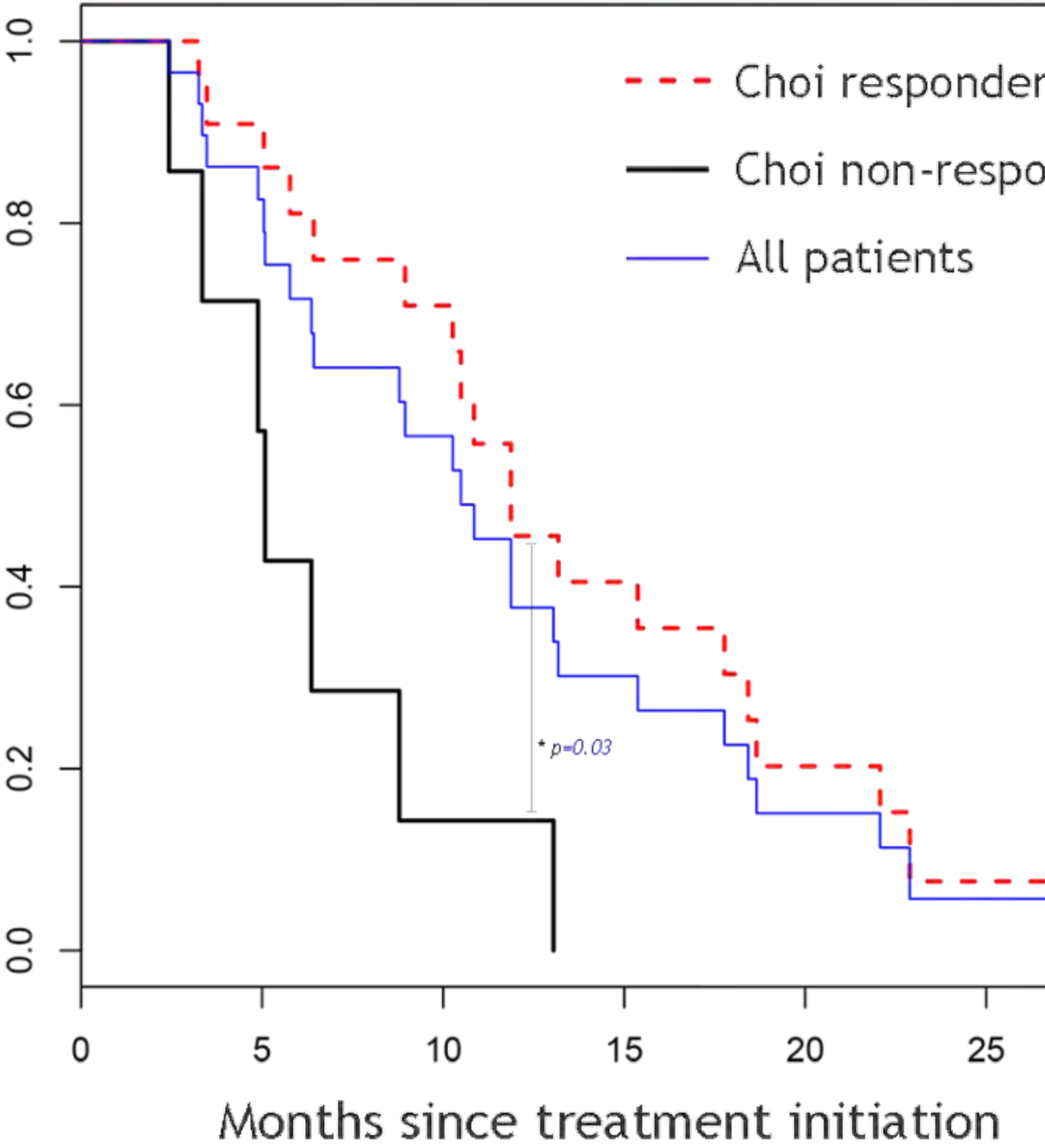
Results

By RECIST, 2/29 (6.9%) patients demonstrated partial response (PR) at any point and the disease control rate (CR, PR or stable disease) was 23/30 (76.7%). Applying Choi Criteria, 19/29 (65.5%) patients demonstrated PR at any point with a disease control rate of 21/29 (72.4%). No patients had complete response to therapy. Exploratory estimate of survival demonstrated a statistically significant difference between Choi responders versus nonresponders (63% versus 20% respectively, $p=0.03$). Common reasons for patients leaving the trial included disease progression (31/42; 73.8%), unacceptable toxicity (6/42; 14.3%), or noncompliance (2/42; 4.8%).

Conclusions

This analysis suggests that the Choi Criteria are useful in evaluating response to axitinib therapy in patients with mHNSCC. They merit consideration as a means of evaluating response to therapy in future prospective clinical trials.

Comparing overall survival among Choi cri responders and non-responders



(Filename: TCT_O-407_Choi_Survival_Plot_1_w_p_value.png)

Wednesday

4:45PM - 6:15PM

Washington Marriott Wardman Park, Maryland A/B/C

18E - Excerpta - II

E-20

4:50PM - 4:55PM

Increased Conspicuity of a Skull Base Meningioma Using ASL vs. DSC Perfusion

A Sung¹, R Lee², N Farid³

¹UC San Diego, San Diego, CA, ²UCSD/VA Medical Center, San Diego, CA, ³University of California, San Diego, San Diego, CA

Purpose

To demonstrate the advantages of arterial spin labeling (ASL) in imaging a skull base meningioma.

Materials and Methods

59 year-old female with right skull base meningioma status-post subtotal resection and fractionated radiation treatment presents for routine follow-up MRI.

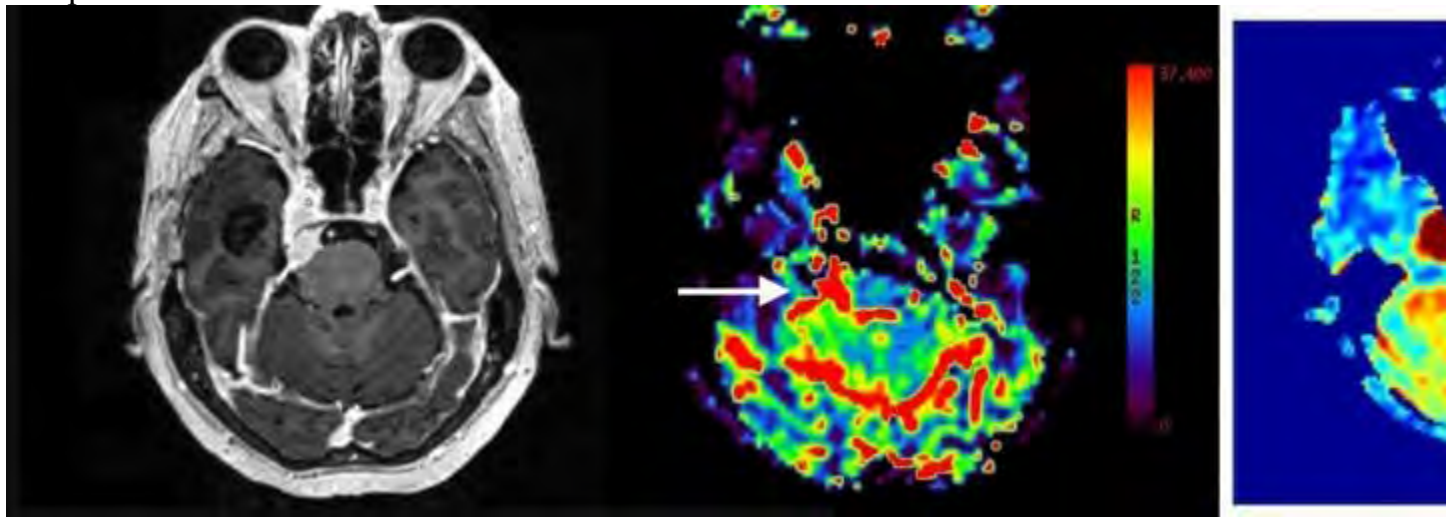
Results

Axial T1 contrast enhanced image shows an enhancing right skull base mass involving the right cavernous sinus, Meckel's cave, and pre-pontine cistern, consistent with residual meningioma. Dynamic susceptibility contrast (DSC)-derived cerebral blood flow (CBF) map shows high cerebral blood flow within the right skull base meningioma. (ASL)-derived CBF map also demonstrates high cerebral blood flow within the right skull base meningioma, with much greater conspicuity compared to the DSC-derived CBF image.

Conclusions

Perfusion imaging at the skull base is particularly challenging with traditional MR perfusion techniques, such as dynamic susceptibility contrast (DSC), due to the high susceptibility artifacts that are produced with echo planar imaging (EPI). ASL perfusion imaging is an emerging technology that is becoming popular in the clinical setting. With recent advances in ASL technology, we are now able to perform whole brain 3D volumes using fast spin echo sequences, which are advantageous in imaging areas of high susceptibility, such as the skull base. Recently, ASL has been shown to be useful in distinguishing between meningiomas and schwannomas at the skull base. We present this case as a direct comparison between DSC and ASL perfusion in imaging a skull-base meningioma. The increased conspicuity on ASL stems from the

use of fast spin echo (FSE) imaging, which produces less susceptibility artifact compared to EPI.



(Filename: TCT_E-20_linearcombined.jpg)

E-21

4:55PM - 5:00PM

Tracheal Chondrosarcoma, Imaging and Clinical Features of a Rare Entity

M Neimark¹, A Spiro², J Bello², K Shifteh²

¹Montefiore Medical Center/Albert Einstein College of Medicine, Bronx, NY, ²Montefiore Medical Center, Bronx, NY

Purpose

To describe a case and to review the clinical and imaging findings of tracheal chondrosarcoma.

Materials and Methods

76 year old man with chronic tobacco use presented to the ED with 1 month history of worsening shortness of breath. On exam, there was a mobile nontender mass above the right clavicle. Tracheostomy was performed due to severe narrowing of the trachea seen on imaging. Sample biopsy was taken and sent to pathology which resulted in low grade chondrosarcoma. Patient returned to the operating room one week later for tracheal resection, hemithyroidectomy, and tracheal anastomosis.

Results

CT demonstrates a 4.9 cm hypodense, partially calcified mass, with invasion of and extension into the posterior trachea, severely narrowing it at the level of the thoracic inlet. The lesion appears to arise from the right thyroid lobe. There is no evidence of metastatic disease including lymphadenopathy, bone lesions, or lung nodules.

Conclusions

Tracheal chondrosarcoma is a rare entity with, including this case, 23 reported cases.

9 cases, including the last six consecutive cases, involved the upper 1/3 of the trachea. The tumor arises from the cartilaginous rings of the trachea. Differential entities include local extension from thyroid, esophageal, and lung masses, and primary squamous cell carcinoma or adenoid cystic carcinoma of the trachea. Tracheal chondrosarcoma occurs overwhelmingly in male patients (95%), and tends to occur in older patients, with mean age 64. Two cases were associated with Maffucci syndrome, and one case was associated with remote radioiodine therapy for papillary thyroid carcinoma. CT usually describes a polypoid mass extending into the tracheal lumen, often significantly narrowing it. Calcification was present in 75% of cases, distinguishing it from most primary tumors of the trachea including squamous cell carcinoma and adenoid cystic carcinoma.



(Filename: TCT_E-21_TrachealChondrosarcoma300DPI.jpg)

E-22

5:00PM - 5:05PM

Myxofibrosarcoma of the Retropharyngeal Space

B Goldner¹, B Hamilton²

¹Oregon Health & Sciences University, Portland, OR, ²Oregon Health and Sciences University, Portland, OR

Purpose

We present a rare case of a primary myxofibrosarcoma of the retropharyngeal space (RPS) and discuss the anatomical and diagnostic considerations.

Materials and Methods

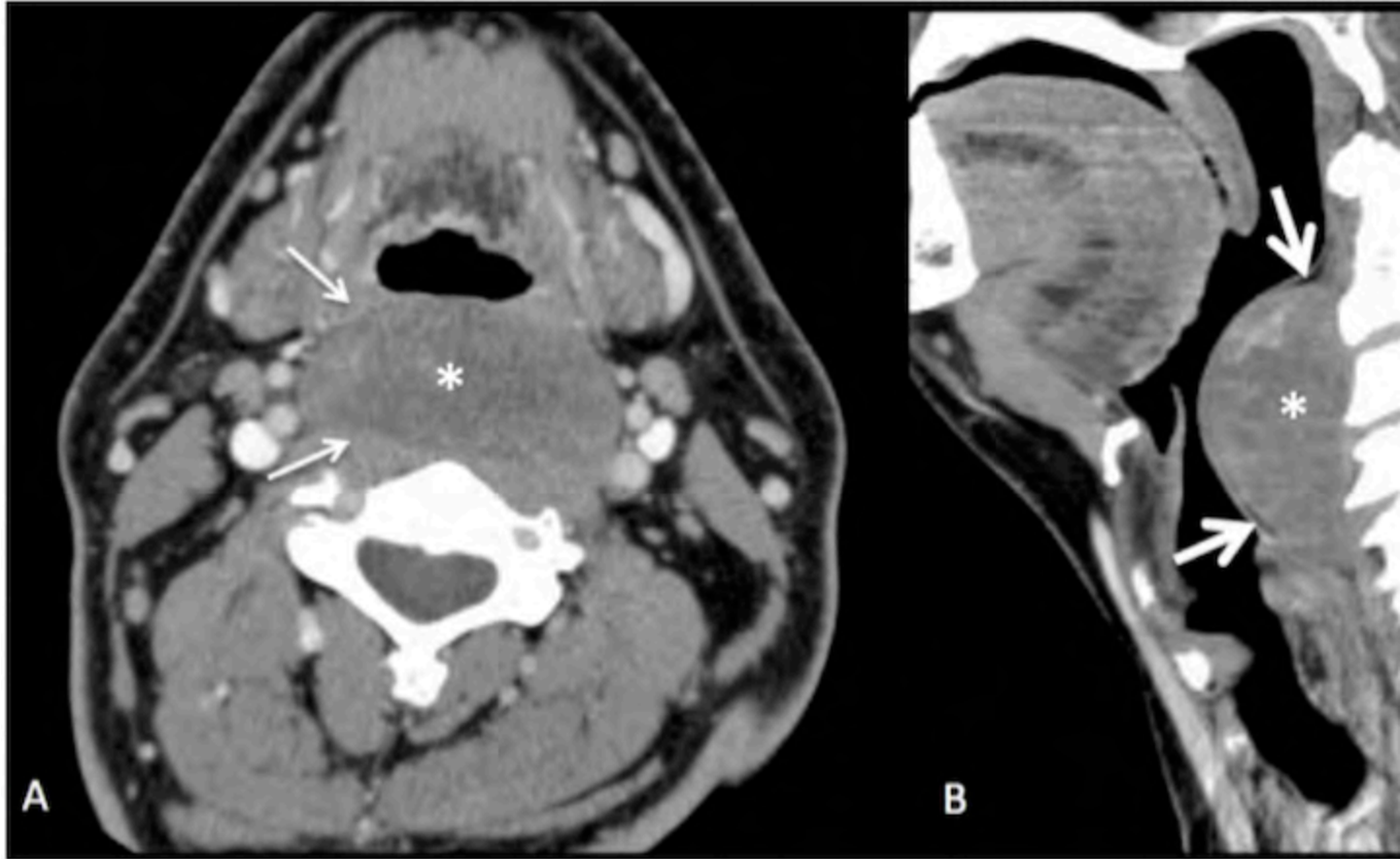
A 55 year old man presented with dysphagia.

Results

Modified barium swallow showed anterior displacement of the hypopharynx and cervical esophagus. Axial (Figure 1A) and sagittal MPR (Fig. 1B) enhanced neck CT demonstrated a 6 cm rounded midline RPS mass. The presence of a thin fat plane along the superior and inferior border of the mass (thick arrows, Fig. 1), along with the lower density (asterisk, Fig. 1) compared to prevertebral muscles and pharynx (thin arrows, Fig. 1) localized this mass to the RPS. Preoperative F-18 FDG PET showed minimal radiotracer uptake. Biopsy and subsequent excision revealed high-grade myxofibrosarcoma.

Conclusions

The usual contents of the RPS include fat and lymph nodes and therefore there is a very limited differential for RPS pathology. The key to diagnosis is recognizing that a lesion is within the RPS. This case demonstrates classic localizing imaging findings of a RPS lesion including preservation of fat planes, midline location within the neck and different enhancement from the pharynx and pre-vertebral muscles. The primary consideration RPS lesions include fluid, lymphoid tissue, and less commonly sarcomas. A solid RPS mass that is morphologically dissimilar to lymphoid tissue is virtually pathognomonic of a sarcoma.



(Filename: TCT_E-22_myxofibrosarcoma.jpg)

E-23

5:05PM - 5:10PM

Importance of MR imaging for guiding management in traumatic abducens nerve palsy: A case report.

P SHAH¹, A Langguth², A Karagianis³

¹Northwestern University Feinberg School of Medicine, CHICAGO, IL, ²Northwestern University, Chicago, IL, ³Northwestern University, Feinberg School of Medicine, Chicago, IL

Purpose

1. Describe imaging findings in abducens nerve avulsion with emphasis on CISS and SPACE/CUBE/VISTA MRI sequences. 2. Review the causes of traumatic abducens nerve palsy. 3. Understand the importance of early and accurate MRI diagnosis in guiding surgical management.

Materials and Methods

84 year-old female presented with diplopia after sustaining a fall and hitting the left side of her head without loss of consciousness. CT brain and face obtained at the time

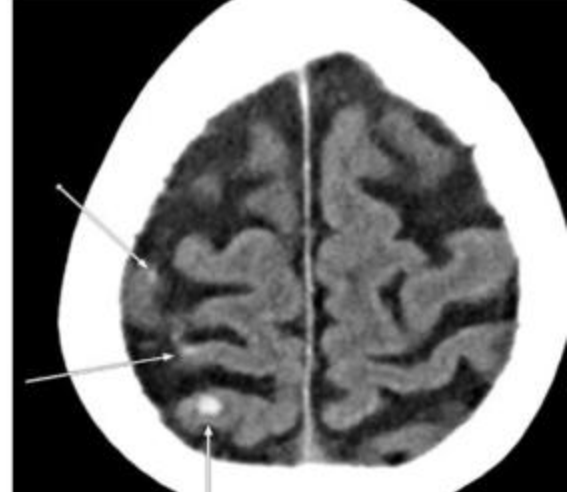
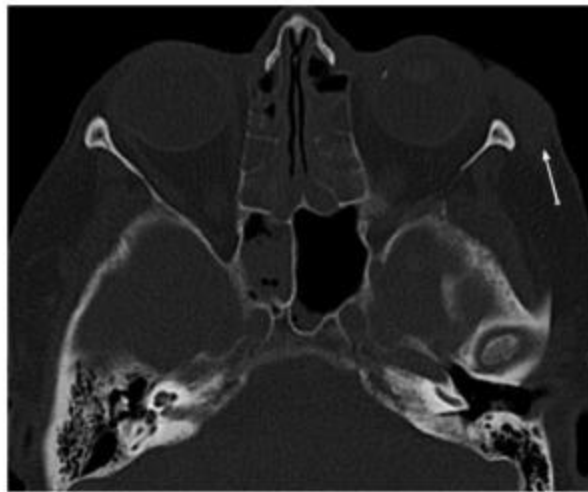
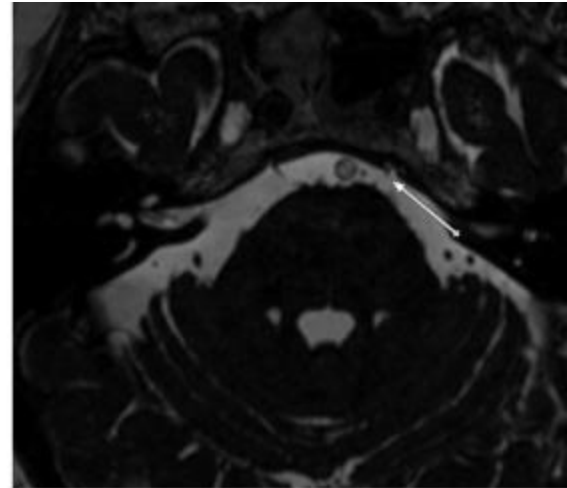
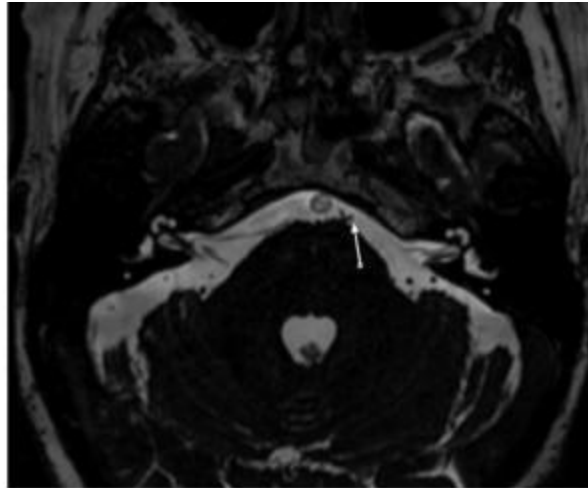
of fall showed scattered subarachnoid hemorrhage and left periorbital and premaxillary soft tissue swelling without skull base or facial fracture. Upon examination, the patient was normal except for a profound (-4) abduction deficit in the left eye. A subsequent MRI orbit demonstrated a left abducens nerve avulsion. Given the imaging findings, return of patient's left lateral rectus muscle function was deemed unlikely. Thus, a decision was made to proceed with a split tendon vertical rectus transposition surgery.

Results

1. CT brain and face showed small parenchymal contusion and scattered subarachnoid hemorrhage in the right parietal lobe without acute fractures. 2. MRI brain showed a left abducens nerve avulsion. The proximal cisternal segment arising from the pons and the distal cisternal segment entering Dorello canal were present with absent intervening segment.

Conclusions

A traumatic abducens palsy may be the result of abducens nerve avulsion. It may also occur in the setting of skull base fracture, prepontine hemorrhage, increased intracranial pressure and brain herniation, among other causes. In majority of the cases, abducens nerve palsy may be initially treated conservatively, as most cases improve partially or completely within 6 months. Surgery is usually delayed if there is no improvement after 6 months. With a complete abducens nerve avulsion, return of lateral rectus muscle function is highly unlikely, and an accurate imaging diagnosis of this entity enables early surgical management, as in our case.



(Filename: TCT_E-23_imagesforcasereportabducensnervepalsy.jpg)

E-24

5:10PM - 5:15PM

MR Findings in Wyburn-Mason Syndrome, a Rare Syndrome of Multiple Vascular Malformations of the orbit, brain and face.

M Gule-Monroe¹, N Chasen¹, L Ginsberg²

¹M.D. Anderson Cancer Center, Houston, TX, ²MD Anderson Cancer Center, Houston, TX

Purpose

Describe the MR imaging findings in a patient with Wyburn-Mason Syndrome (WMS), a rare phacomatosis characterized by unilateral retinal, cerebral vascular malformations and vascular skin lesions.

Materials and Methods

A 19 year old male initially came to medical attention at the age of 3 when he

presented with proptosis of the left eye. On ophthalmologic exam he was found to have a large vascular lesion with dilated loops of vessels in the medial conjunctiva with tortuous retinal vessels. MR imaging of the brain and face demonstrated the presence of left orbital, left frontal scalp and intracerebral vascular malformations consistent with WMS. Three years after the initial presentation, at the age 6, the patient developed intracerebral hemorrhage. Since that time, the patient has experienced continued slow increase in left eye proptosis. Visual function has remained stable and thus, further surgical management of the orbital vascular malformation is being deferred.

Results

MR imaging of the face and orbits demonstrates a large, enhancing retrobulbar mass with hemorrhage and fluid-fluid levels, consistent with a vascular malformation. In the left frontal scalp a serpiginous T2 hyperintense, enhancing facial vascular malformation is identified. MRI brain and MRA brain demonstrates a vascular malformation in the left vermis with arterialized venous drainage. Diffuse vascular congestion of the left occipital and temporal lobes with corresponding cerebral volume loss is also seen. Several cavernous malformations, most prominently within the pons, left temporal and occipital lobes are identified.

Conclusions

WMS is a rare, sporadic neurocutaneous disorder characterized by unilateral vascular abnormalities of the orbit, typically the retina, facial soft tissues and brain. Clinically the patients present with sequela related to compression or rupture of intracerebral vascular malformations or ocular symptoms. Imaging with angiography is the gold standard for diagnosis with MR and CT, playing an important adjunct role, particularly with respect to anatomic characterization and imaging of complications.

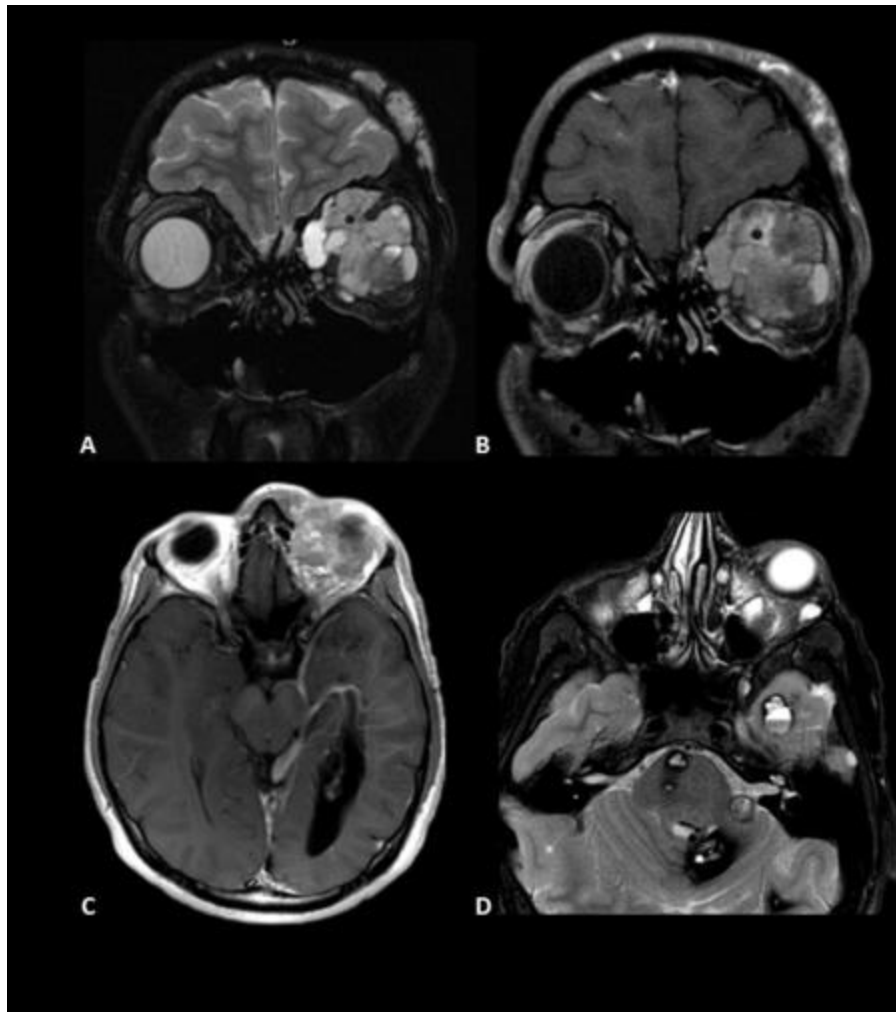


Image A and B: Fat saturated coronal T2 (A) and coronal T1 post contrast (B) images through the brain demonstrate lobulated T2 hyperintense, enhancing venous malformation remodeling the left orbit. Intralesional T1 and T2 hypointensities reflect a phlebolith. T2 hyperintense enhancing left frontal scalp is consistent with a scalp venous malformation .

Image C: Fat saturated axial T1 post contrast image through the brain shows fluid- fluid levels of the vasculature in the left orbit. Dilated, arterialized veins anterior to the tentorium with diffuse venous congestion anterior to the tentorium in the left hemisphere are demonstrated.

Image D: Axial T2 image through the brain illustrates multiple cavernous malformations in the posterior frontal and temporal lobes.

(Filename: TCT_E-24_FiguresWMSjpgcorrected.jpg)

E-25

5:15PM - 5:20PM

Schwannoma of the Oral Tongue

C Davidson¹, J Kim¹

¹*University of Kentucky, Lexington, KY*

Purpose

To present a case of an oral tongue schwannoma. Given that oral tongue lesions are uncommon in the pediatric patient, differential considerations for this case will be reviewed.

Materials and Methods

A 17-year-old male presented with a history of a tongue mass which was discovered incidentally when it was seen by someone else. He described occasional dysphagia to solids, otherwise he was asymptomatic. Physical exam by revealed a 2-3 cm

nontender, soft mass in the musculature of the left lateral oral tongue, and was thought clinically to be a minor salivary gland inclusion cyst. MRI of the face was obtained for further characterization. Submucosal excision was performed due to the potential of the lesion to affect speech and swallowing. Pathology revealed a schwannoma with classic Antoni A and B fibers.

Results

MRI of the face without and with contrast revealed a 2.6 cm well-circumscribed, homogeneously enhancing mass within the dorsum of the oral tongue. The mass demonstrated mild prolongation on T2-weighted images relative to the oral tongue, with prolongation on precontrast T1-weighted images.

Conclusions

Oral tongue schwannomas are relatively rarely reported and examples of imaging of these lesions in case reports are even less common. Oral cavity schwannomas represent as little as 1% of schwannomas of the head and neck, although the tongue is the most common site for schwannomas in the oral cavity. Most lesions are seen in patients between the ages of 10-40 years old. This example followed typical imaging characteristics of a schwannoma, although other differential considerations for a pediatric patient included rhabdomyoma, vascular lesion, granular cell myoblastoma, sarcoma, or minor salivary gland tumor. Even though lesions on imaging have a nonspecific appearance, imaging still has a role in diagnosis and treatment planning. Additionally, familiarity with differential considerations of pediatric oral tongue lesions, which in daily practice are uncommon, may facilitate care.



(Filename: TCT_E-25_schwannomaT2.jpg)

E-26

5:20PM - 5:25PM

A Neonatal Maxillary Mass: Characterization with Time Resolved MRA

J Coburn¹, G Avey²

¹University of Wisconsin Hospitals and Clinics, Madison, WI, ²University of Wisconsin, Madison, WI

Purpose

To explore the differential diagnosis of congenital maxillary masses, and demonstrate the utility of time-resolved MR angiography for lesion characterization and surgical planning.

Materials and Methods

A 13 day old female born via spontaneous vaginal delivery presented for evaluation a left maxillary mass and associated weight loss. The mass was present at birth. The mass interfered with feedings, resulting in weight loss. At the time of presentation the patient was at the 5th percentile for weight and 95th percentile for height. Physical examination revealed a 2 cm left maxillary alveolar mass covered with normal appearing, but thinned mucosa. The anterior face of the mass was soft & boggy on palpation. Laboratory evaluation was significant for thrombocytopenia. Urine catecholamine levels were normal. A clinical differential diagnosis of melanotic neuroectodermal tumor of infancy, congenital hemangioma, rhabdomyosarcoma, and congenital epulis was entertained.

Results

Figure 1: Maxillofacial CT without contrast demonstrates a solitary expansile mass involving the left maxillary alveolus, measuring 1.7 x 2.6 x 2.2 cm in size (A-P, transverse, cranio-caudad). There is a permeative appearance of the maxillary alveolus, with no evidence of overlying periosteal reaction. Figures 2 and 3: MRI of the mass with and without contrast demonstrates no change in the size of the mass over the intervening two weeks. The mass is T2 hyperintense, isointense to muscle on T1, and has homogenous contrast enhancement. There is no associated diffusion restriction. Figure 4: Time-resolved MR angiography demonstrates a very vascular mass, with rapid progressive enhancement of the mass. Homogenous enhancement is achieved approximately 20 seconds after contrast administration. Time-resolved MR angiography confirms hypertrophy of the internal maxillary artery, as well as demonstrating that the dominant arterial supply to the mass arises from the greater palatine artery, with a lesser contribution from the posterior superior alveolar artery.

Conclusions

We present the case of a 13 day old female infant who presented with concern for an enlarging left maxillary mass, which on imaging evaluation was noted to be highly vascular. Time-resolved MR imaging delineated that the mass was fed primarily by an enlarged left greater palatine artery. A combined procedure with plastic surgery and otolaryngology was performed with ligation of the greater palatine artery and open

biopsy of the mass. Pathology results were consistent with a congenital hemangioma (rapidly involuting versus non-involuting). The safety of the procedure and care of the patient were greatly enhanced by recognizing the vascular nature of the lesion and precisely identifying the source of the arterial supply prior to surgical biopsy. Time-resolved imaging can greatly assist in the diagnosis and identification of the arterial supply of congenital vascular anomalies, thereby enhancing safe and successful management of these lesions.



(Filename: TCT_E-26_ASNR2016images.jpg)

E-27

5:25PM - 5:30PM

MR Imaging of an Acute Contrast Reaction with Oropharyngeal Angioedema

R McDonald¹, C Rydberg¹

¹Mayo Clinic, Rochester, MN

Purpose

Allergic reactions to gadolinium based contrast agents (GBCAs) are observed at a frequency of 0.7% to 0.004% with severe anaphylactoid reactions occurring in 0.01% to 0.001% of cases (1). Radiologists must be able to identify and treat these reactions emergently, particularly those reactions associated with respiratory and/or circulatory system compromise. Imaging correlates to these reactions are rarely observed and reported. We present MR imaging of oropharyngeal angioedema during an acute contrast reaction.

Materials and Methods

A 46 year old female developed diffuse hives, facial erythema, throat pain, hoarseness, and difficulty swallowing within minutes of intravenous administration of

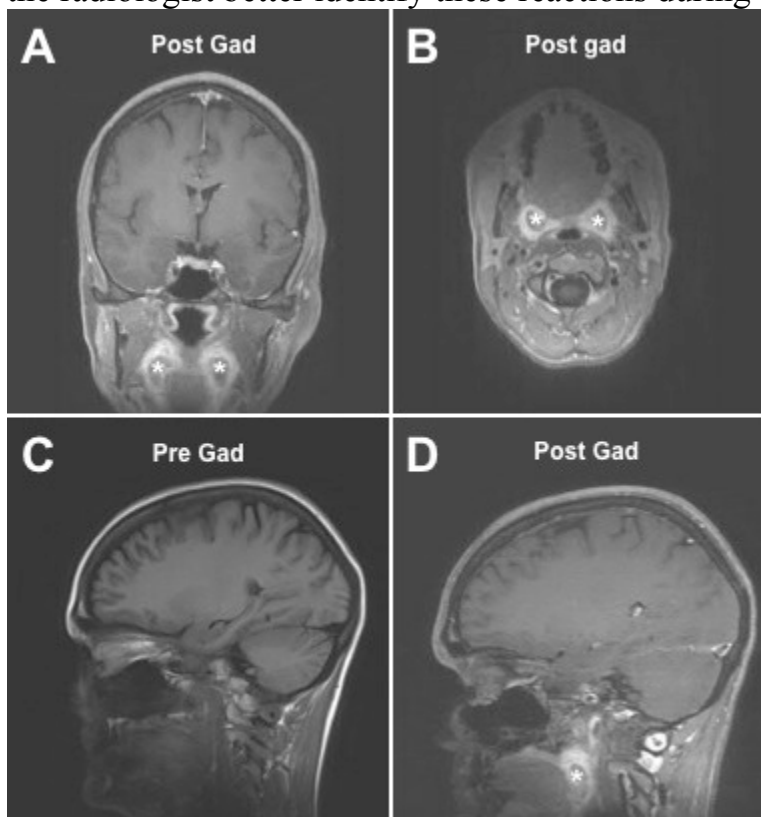
0.1 mmol/kg gadobutrol (Gadavist) for a contrast enhanced MRI of the brain. She did not report symptoms until the exam was completed. Supportive measures were initiated and included oxygen administration via facial mask, intravenous administration of 1L of 0.9 normal saline, 50 mg of IV diphenhydramine, and 40 mg of IV methylprednisolone. Despite some degree of patient distress, vital signs remained stable and there was no evidence of respiratory or cardiovascular compromise. These symptoms gradually resolved over the next hour while under close observation.

Results

Post-contrast T1 images of the MRI demonstrate bilateral edema and prominent mucosal enhancement of Waldeyer's ring predominantly affecting the palatine tonsils bilaterally (Fig A & B). These findings developed after contrast administration, as evidenced by the evolution of findings on the pre and post-contrast images (Fig C & D).

Conclusions

We present an unusual case of an acute allergic reaction to GBCA administration manifesting as oropharyngeal angioedema without associated airway compromise that developed and was observable on MR imaging. These findings illustrate the diverse manifestations of allergic contrast reactions after GBCA administration and may help the radiologist better identify these reactions during the MRI exam.



(Filename: TCT_E-27_ASNRFig1.jpg)

Multiple Myeloma Involving the Thyroid Cartilage: Case Report.

A Mamere¹, L Feltrin¹, R Fava¹

¹*Barretos Cancer Hospital, Barretos, SP*

Purpose

To report a rare pathology-proven case and to show the imaging findings of diffuse involvement of the thyroid cartilage in a patient with multiple myeloma.

Materials and Methods

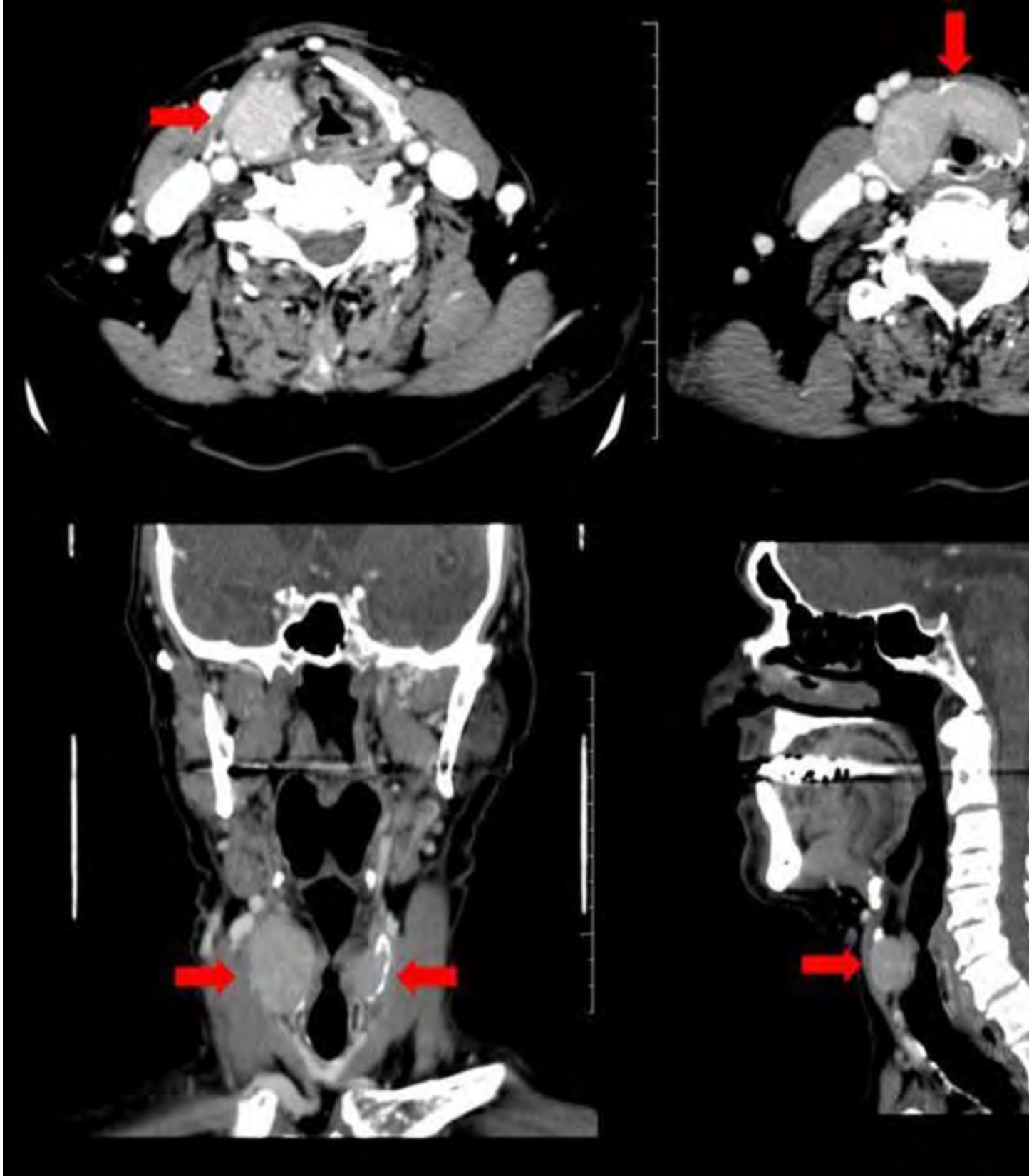
A 75-year-old man with a background of IgA-kappa type multiple myeloma presented with increasing hoarseness 1 year after diagnosis. A mass in the region of the thyroid cartilage was observed on the computed tomography (CT) examination. Percutaneous imaging-guided core-biopsy was performed and the pathological findings were consistent with diffuse plasma cell infiltration.

Results

CT examination of the neck showed homogeneously enhancing solid mass diffusely involving the thyroid cartilage. Slight narrowing of the laryngeal airway was also noted.

Conclusions

Extrasosseous myeloma refers to a rare manifestation of multiple myeloma where there is plasma cell proliferation outside the skeletal system and it can potentially affect any organ system. Lymph node is the most common extrasosseous site of involvement. The presence of extrasosseous myeloma generally implies a poorer prognosis. Involvement of the thyroid cartilage by multiple myeloma is even rarer. In our literature review, we have found only fifteen cases previously reported. Differential diagnosis includes other laryngeal malignancies, chondroma and low-grade chondrosarcoma. These chondroid tumors typically demonstrate chondroid calcifications which are not present in plasma cell tumors. The most likely mechanism suggested for cartilaginous involvement in cases of multiple myeloma seems to be that of osseous metaplasia of the cartilage with subsequent myelomatous involvement of this extraskelatal marrow. Despite its extreme rarity, thyroid cartilage plasma cell infiltration should be included in the differential diagnosis in patients with multiple myeloma presenting with cervical mass and/or hoarseness and it may be the first manifestation of the disease.



(Filename: TCT_E-28_MM.jpg)

Dentures Mimicking Traumatic Pharyngeal Blood on a Cervical Spine CT.

I Ikuta¹, J Ewell¹, F Yang¹

¹*Norwalk Hospital, Norwalk, CT*

Purpose

While the appearance of oral dentures have been described on CT, the appearance of ectopic denture prosthetics can be difficult to identify and may mimic the appearance of blood. We provide an example to demonstrate dentures in the setting of trauma as an imaging pitfall, and review the imaging characteristics of dentures.

Materials and Methods

A 43-year-old man presented to the Emergency Department with massive facial lacerations and head trauma, status post assault. A CT of the cervical spine was ordered to evaluate the extent of trauma. The radiology resident was present at the CT scanner when the patient arrived, and upon direct visual inspection noticed a large volume of blood covering the patient's head. The patient was unconscious upon arrival and intubated, and was therefore unable to provide any additional history.

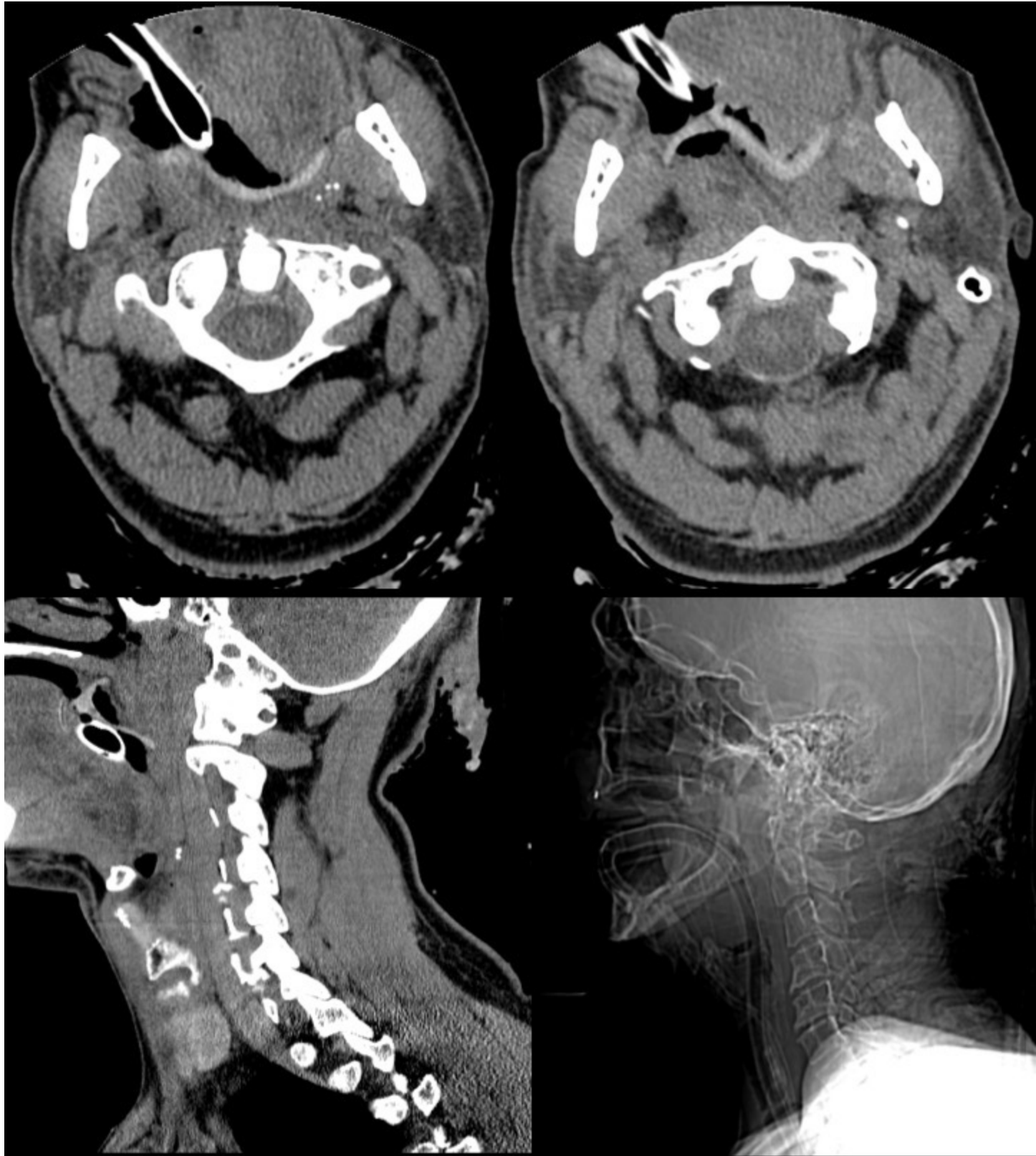
Results

The CT of the cervical spine soft tissue windows demonstrated high-attenuation material initially appearing to layer within the dependent portion of the posterior oropharynx (top left image). Given the clinical history, the high attenuation material was believed to represent hemorrhage, which seemed to be a reasonable consideration in the setting of facial and oral trauma with copious hemorrhage. Upon further evaluation, portions of the high-attenuation material demonstrated an S-shaped morphology with some portions in an anti-dependent location, not the expected appearance for hemorrhage (top right image). On examination of the sagittal multiplanar reformatted images, the posterior cephalad end of the high-attenuation structure demonstrated a hooked appearance, which would also be atypical for a hemorrhagic collection (bottom left image). Review of the lateral localizer image demonstrated that the patient was edentulous, which raised the possibility of denture prosthetics (bottom right image). The high-attenuation material is also not readily visible on the lateral localizer image.

Conclusions

Dentures have an attenuation which may mimic blood, and in the setting of trauma it presents a potential imaging pitfall. Careful evaluation of the gastrointestinal tract (including the posterior oropharynx) and airways (trachea and bronchi) may reveal a high-attenuation material concerning for hemorrhage; however, when a morphology is not characteristic of blood, ectopic location of dentures in an edentulous patient may

be suspected and direct visualization recommended. The radiolucent polymer of dentures may not be readily appreciated on x-ray and CT localizer images, and note of an edentulous or partially edentulous patient may be one of the few clues to help avoid this imaging pitfall.



(Filename: TCT_E-29_Dentures_AbstractImage_ASNR2016_cropped.jpg)

Supraglottic Laryngeal Paraganglioma

Y Sun¹, S Bobra¹, H Mehta¹, M Tenner¹, B Rigney¹, A Arneja¹

¹Westchester Medical Center, Valhalla, NY

Purpose

Paragangliomas are highly vascular, slow growing and often benign tumors that arise from neural crest cell derivatives with a low malignant transformation potential.

Together with tumors of epithelial origin, they comprise the majority of laryngeal neuroendocrine neoplasms. Laryngeal paraganglioma is exceedingly rare and it is the only laryngeal neuroendocrine tumor that has a female predilection with a reported female-to-male incidence ratio of 3:1 (1). We present a novel case of a 63 year-old female with supraglottic laryngeal paraganglioma.

Materials and Methods

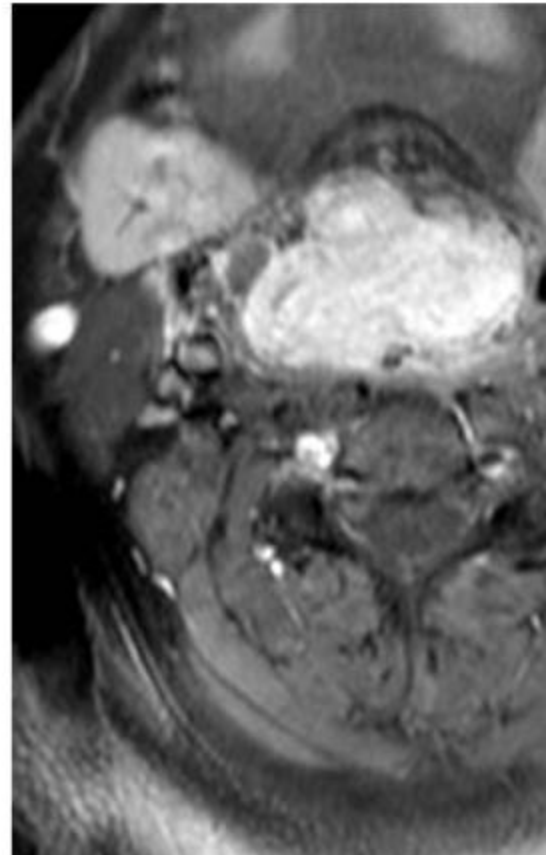
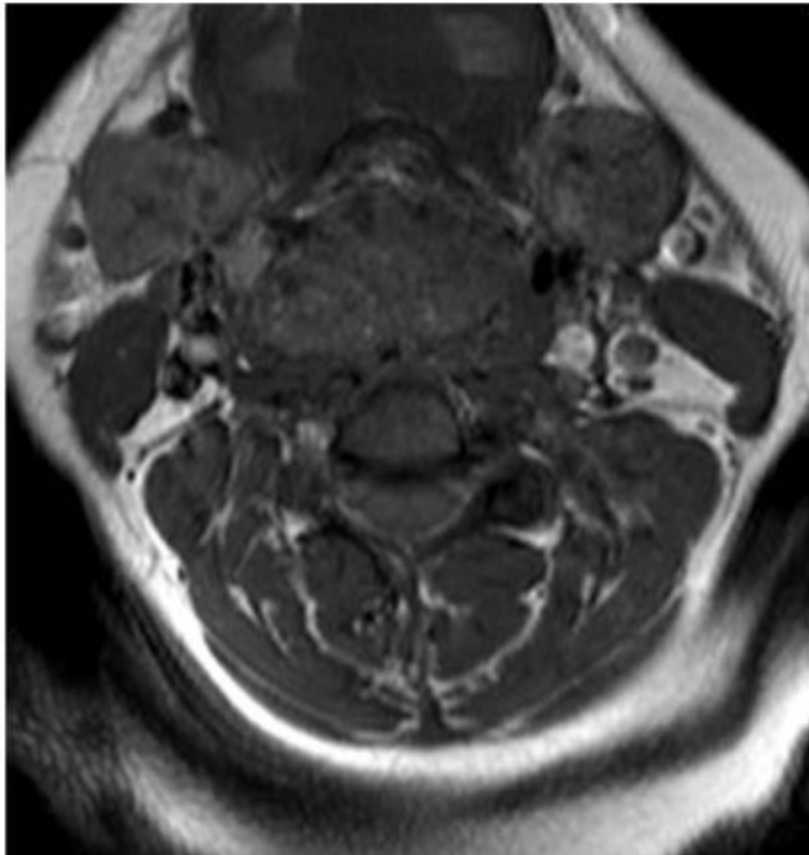
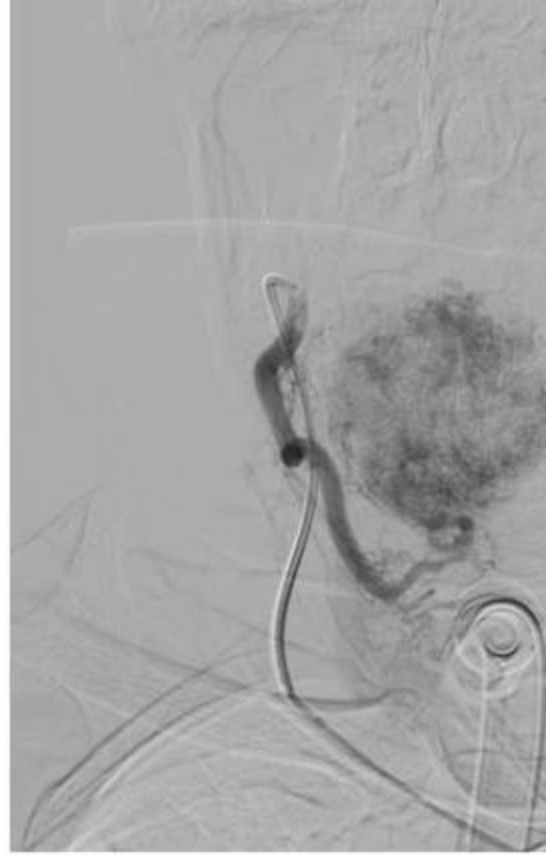
A 63-year-old female presented with a large anterior neck mass and long standing history of progressive dysphonia. Patient underwent a tracheostomy for airway protection and subsequently underwent transpharyngeal/translaryngeal excision of the tumor. Pathology revealed paraganglioma.

Results

CT of the neck demonstrates a large avidly enhancing mass lesion in the supraglottic larynx that measures approximately 4.5cm CC x 4.4cm TV x 2.8cm AP. There is severe effacement of the aerodigestive tract. MRI demonstrates prominent vascular flow voids along the periphery of the avidly enhancing mass. Selective right external carotid artery catheter angiogram shows a large tumor blush in the anterior midline of the neck with arterial supply mainly from the right superior and inferior thyroid arteries. A second tumor blush is noted near the left vertebral artery origin with arterial supply from branches of the left thyro-cervical trunk.

Conclusions

Laryngeal paragangliomas are rare with roughly 80% supraglottic and 20% infraglottic in location. Less than 10% of the paragangliomas are extra-adrenal in location and less than 1% localize to the head and neck region (2). CT and MRI are essential for characterization. T1-weighted image may show a "salt and pepper" appearance; representing blood products from internal hemorrhage and flow voids secondary to increased vascularity. Preoperative angiography and possible embolization are important imaging/management considerations. Surgical excision is the treatment of choice (3).



(Filename: TCT_E-30_Paraganglioma.jpg)

E-31

5:45PM - 5:50PM

Dual Energy CT Cisternography in the Evaluation of CSF Leaks: A Novel Approach

A Alfieri¹, D Boulter², W Slone², X Nguyen³, B Gans², M Luttrull¹, E Bourekas⁴, E Miller⁵, L Prevedello³

¹The Ohio State University Wexner Medical, Columbus, OH, ²The Ohio State University Wexner Medical, Columbus, OH, ³Ohio State Wexner Medical Center, Columbus, OH, ⁴The Ohio State University, Columbus, OH, ⁵Ohio State University, Columbus, OH

Purpose

Cerebrospinal fluid (CSF) leaks pose a serious threat to patients as they represent an unchecked communication between the subarachnoid space and the external environment. Potential complications include meningitis, stroke, stupor, and death. Accurate localization of leakage site is essential for treatment planning. We describe the novel utilization of dual energy CT technology in cisternography for the evaluation of CSF leaks.

Materials and Methods

A 66 year old female presented with tinnitus and positional right nasal drainage while recumbent for the past several months. The patient denied any associated symptoms. She had a history of right CSF otorrhea status post surgical repair via craniotomy with dural patching in the 1980s and reported no similar complaints during the interim. A brain MRI performed at an outside institution suggested the possibility of a CSF leak and recommended cisternography for further evaluation.

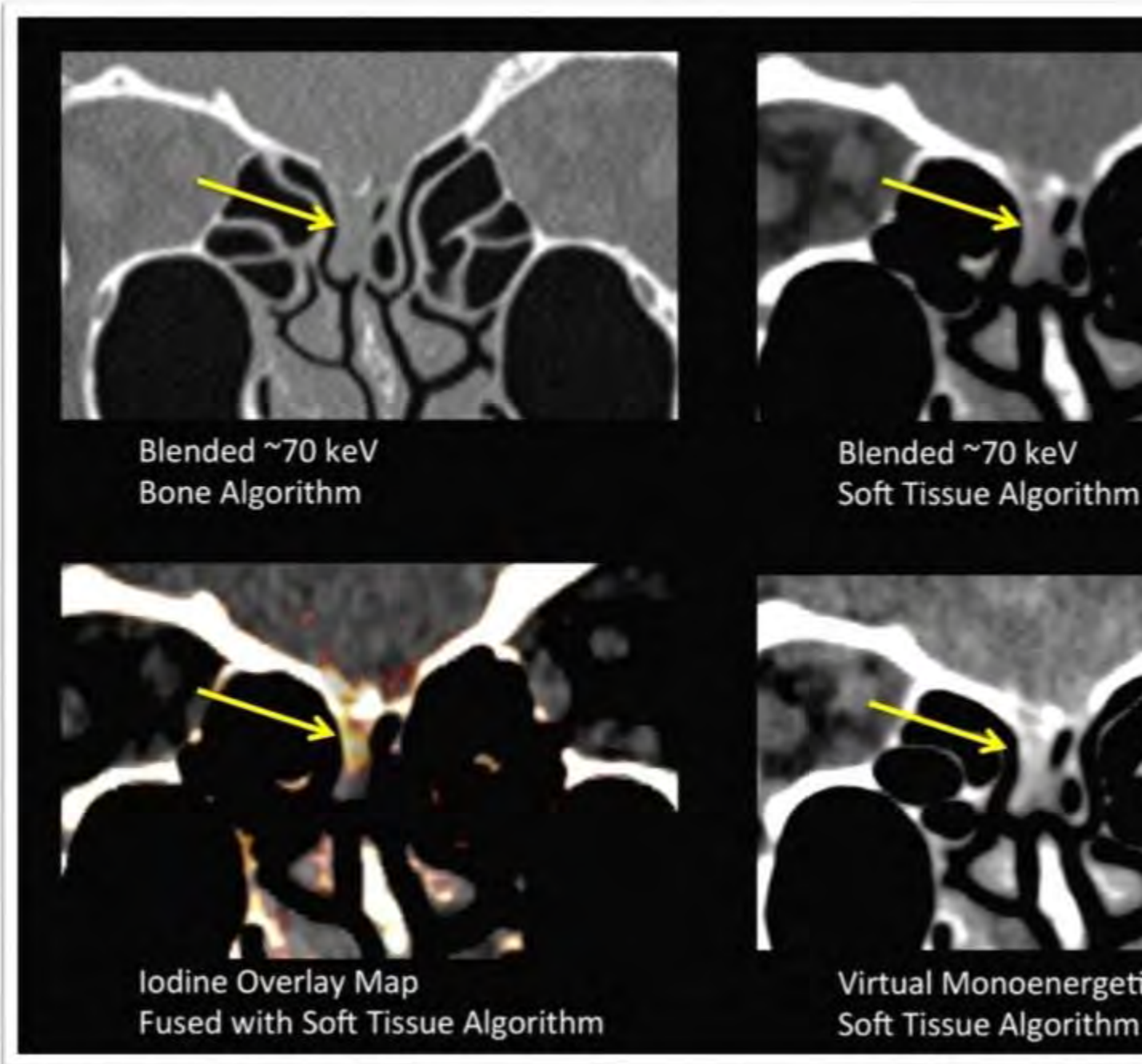
Results

Following intrathecal injection of iodinated contrast, high-resolution dual energy CT of the skull base revealed contrast filling the extra-axial CSF spaces. Focal fluid opacification of the right olfactory recess was noted on standard linearly blended images (60% of 80 kVp tube, 40% of 140 kVp tube with tin filter). Noise-optimized monoenergetic reconstructions at 40 keV markedly increased the attenuation and conspicuity of fluid in the right olfactory recess, confirming iodinated contrast leakage. Iodine overlay map fused on anatomic images further increased conspicuity of contrast leakage. Dual energy reconstructions simplified separation of contrast leakage from adjacent structures and allowed for clear visualization of a direct pathway of CSF communication.

Conclusions

CSF leaks have important clinical complications, and accurate diagnosis of leak

presence and location are critical to surgical planning. While conventional CT cisternography allows for accurate identification of CSF leakage in many cases, the addition of dual energy CT may significantly improve visualization of leakage without considerably altering radiation exposure.



(Filename: TCT_E-31_DualEnergyCTCisternogramImages.jpg)

E-32

5:50PM - 5:55PM

Rare case of bilateral hypoglossal nerve enhancement in Guillain Barre syndrome

M Ma¹, S Lin¹, R Pandit¹

¹*Santa Clara Valley Medical Center, San Jose, CA*

Purpose

Guillain-Barre syndrome (GBS) is an acute autoimmune post infectious or inflammatory demyelination of peripheral nerves. Cranial nerve involvement of GBS is most commonly seen in the facial nerves, followed by bulbar and trigeminal nerves (1,2). Review of literature shows that involvement of the hypoglossal nerve is rare in GBS clinically (3), with only 1 previously reported case with imaging abnormalities (4). We present an unusual case of GBS variant with extensive bilateral cranial nerve enhancement, including that of CN XII.

Materials and Methods

42 yo previously healthy female was admitted with 1 week of bilateral ascending numbness, parasthesia, and pain in her extremities. This was accompanied by dysphagia, dysarthria, blurred vision, and progressive ascending weakness. She underwent 2 courses of IVIG and recovered some motor function. However, 3 weeks following initial presentation, she developed new left facial weakness, right facial parasthesia, and increased difficulty speaking. On exam, she had dysarthria, left upper and lower facial droop, right V1-V3 decreased facial sensation, gaze evoked nystagmus with lateral gaze bilaterally, and mild sensory ataxia. Tongue protrusion was midline. She had diffuse muscle weakness and decreased sensation, greater in the lower extremities, and she was areflexic throughout. CSF studies showed albuminocytologic dissociation, and microbiology studies were unremarkable. AntiGq1b serology was negative (5). EMG showed axonal loss in the lower greater than upper extremities and prolonged latency, consistent with GBS.

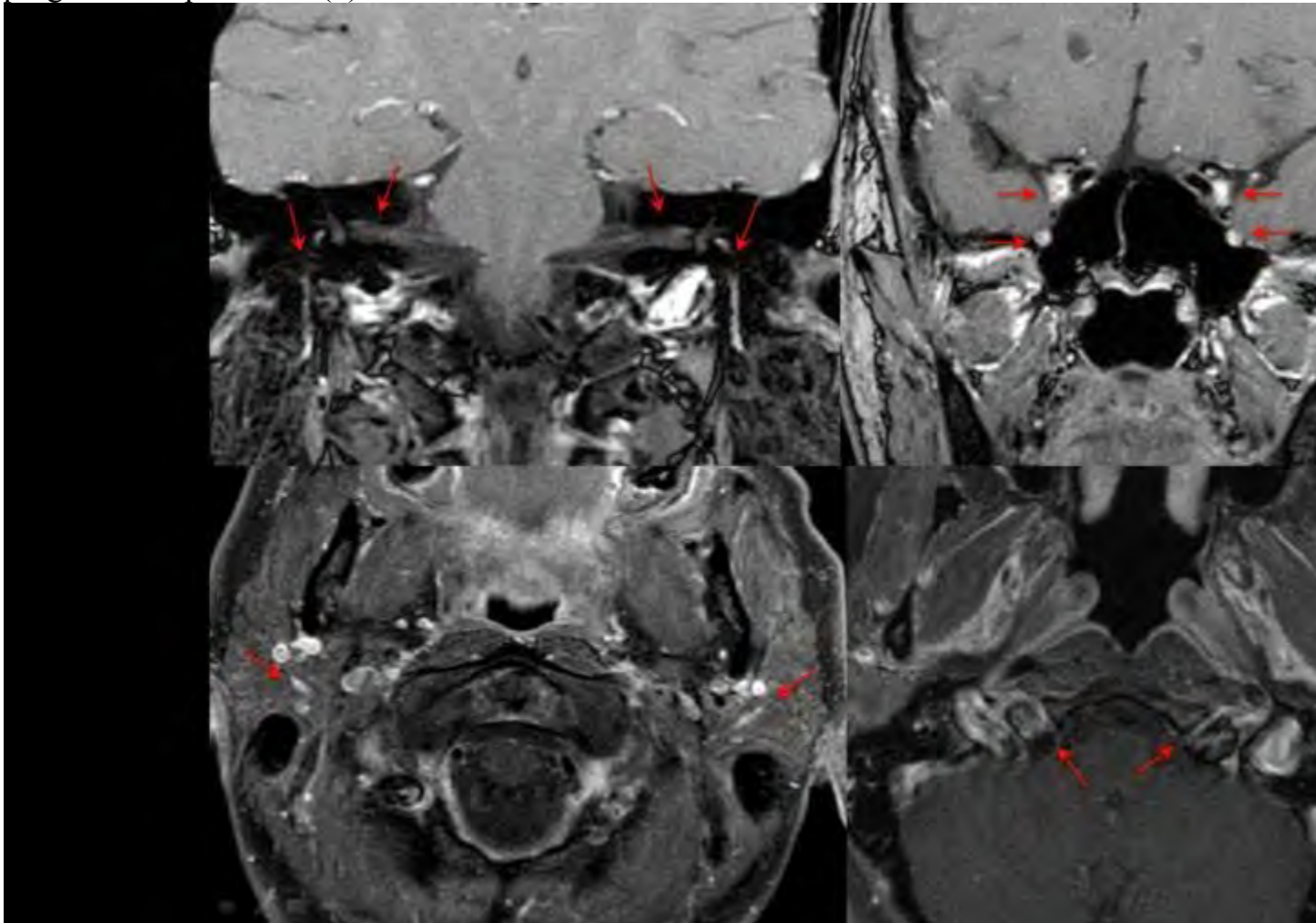
Results

T1 post contrast fat saturated images show extensive long segment enhancement of CN VII from the intracannalicular through parotid portions bilaterally. In addition, the patient has enhancement of bilateral CN V from the cavernous segment to its divisions in foramen rotundum and the vidian canal, of bilateral CN IX-X complex at the jugular foramen, and of bilateral CN XII as they traverse the hypoglossal canal. No intraparenchymal lesions are identified. Spinal imaging was not performed.

Conclusions

This patient is best described as a case of GBS variant, given her presentation of delayed onset of multiple cranial neuropathies. Although cranial nerve involvement is a well described manifestation of GBS, our case is unique in that bilateral CNXII involvement has only rarely been observed. Understanding the spectrum of disease

presentation is valuable in evaluating acute inflammatory neuropathies and may have prognostic implications (1).



(Filename: TCT_E-32_ASNRimage.jpg)

E-33

5:55PM - 6:00PM

Masticator Space Parasitosis: Rare Presentation for a Common Infection

M Ramírez-Guzmán¹, L Garcia-Posada², E Sarda-Inman², R Valenzuela³, G Godoy-Brewer¹, D Ruiz⁴, R Riascos⁵

¹The University of Texas Health Science Center at Houston, Houston, TX, ²Diagnostico Especializado por Imagen, Zapopan, Jalisco, ³The University of Texas, Houston, TX, ⁴The University of Texas Health Science Center at Houston UTHSC, Houston, TX, ⁵UTHSC-Houston, Houston, TX

Purpose

- Presenting a rare case of a middle age female, who demonstrated inflammation of

the left cheek. The ultrasound (US) and magnetic resonance (MR) images demonstrated a cystic lesion in the left masseter muscle compatible with cysticercosis.

- To contribute with our imaging findings to consider cysticercosis in masseter muscle in future cases as a differential diagnosis of cyst mass.

Materials and Methods

Female patient in her mid-thirties. No medical background, who assists claiming volume increase on the lower left face region since three months ago, during the physical exam, a volume increase on the left parotid region was evidenced, firm, nodular, no adhesion to deep planes, painful when touched. An echographic and MR study was requested under the suspicion of a parotid tumor. After imaging studies cysticercosis diagnosis was made. The patient was treated with Albendazole 50mg/Kg day per 14 days, showing clinical improvement within the following days. The control US and MR studies showed no cyst mass.

Results

Gray scale and color Doppler US shows a cyst lesion on the left masseter muscle with heterogenic appearance irregular edges, echogenic center, and peripheral vascularization. MR demonstrated in T1, T2 with fat suppression, FIESTA, and T2 with heavy contrast where a well-defined round lesion was shown localized on the left masseter muscle, hypointense behavior on T1 hyperintense on T2 and a nodular image with less intensity to the periphery, compatible with the scolex.

Conclusions

Cysticercosis is one of the most common parasitic infections worldwide. A rare case of an isolated cysticercosis lesion in the left masticator space was presented, diagnosed by US and MR imaging, where cysticercosis characteristics are shown, such as the scolex. A clinical improvement was shown after the treatment with oral Albendazole, and Praziquantel might be used as well, with the disappearance of the edema and symptoms. It is important to be familiar with the uncommon manifestations of the infection and consider this entity as a part of the differential diagnosis when we see cystic intramuscular lesions.

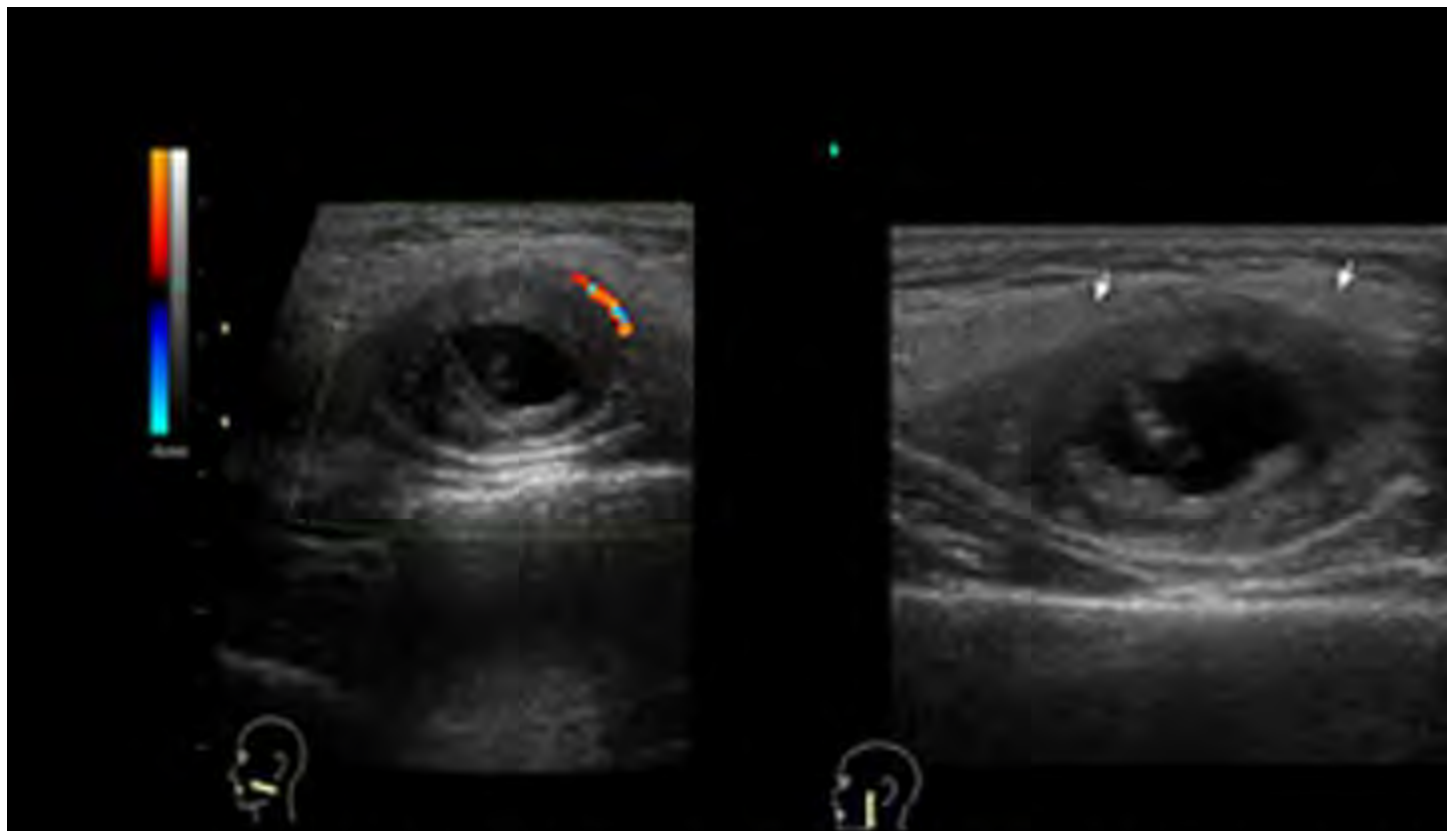


Figure 1 Gray scale (A) and doppler (B) ultrasound Where an heterogeneous intramuscular lesion is observed presenting cystic areas and solid material to the periphery, showing an echogenic area in its interior

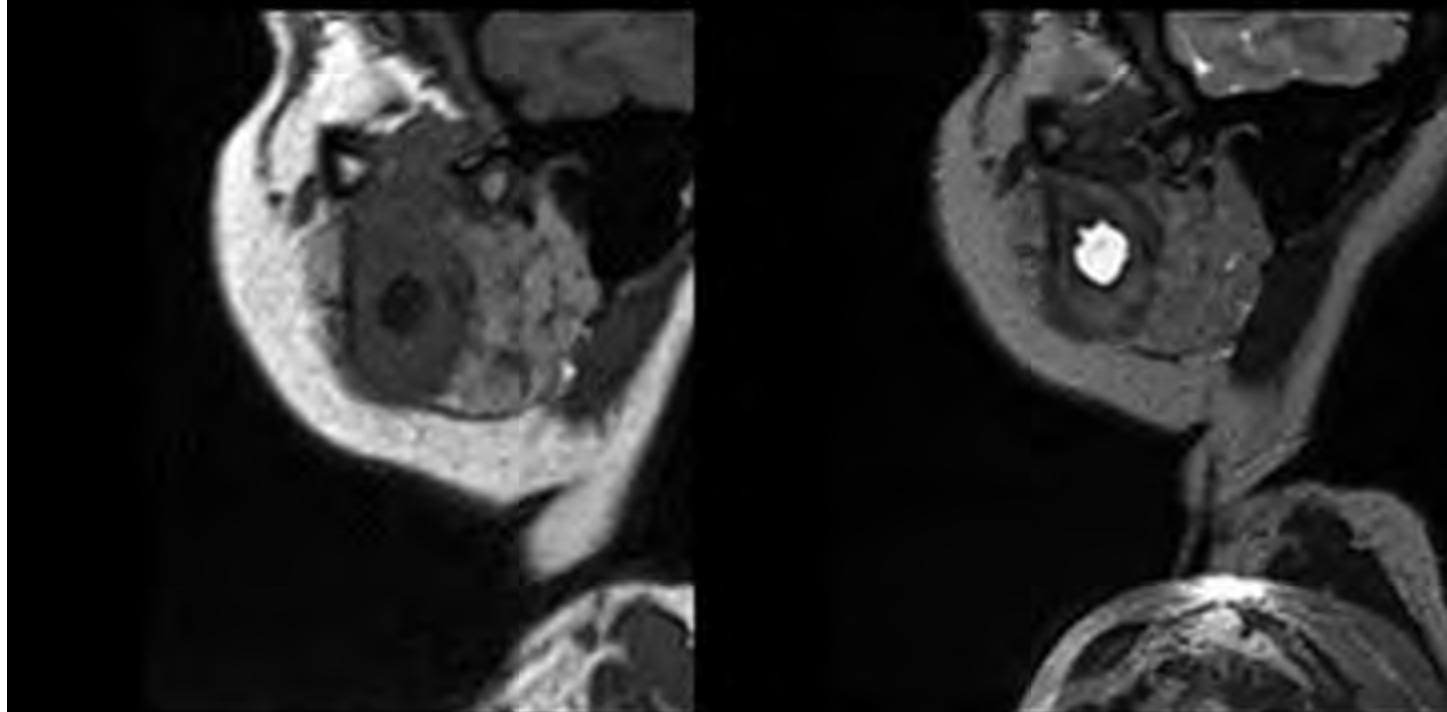


Figure 2 Sagittal images on MR potentiated on T1 (A) and T2 with fat suppression (B) where a cystic lesion can be observed on the left masseter muscle, well defined, no perilesional edema.

(Filename: TCT_E-33_MasseterCisticercosis.jpg)

E-34

6:00PM - 6:05PM

Unique Arterial Cause of Fallopian Canal Enlargement in a Patient with PHACES

J Lam¹, M Cunnane², D Zimmerman³

¹Hartford Hospital, Middletown, CT, ²Massachusetts Eye and Ear Infirmary, Boston, MA, ³Hartford Hospital, Hartford, CT

Purpose

We describe a PHACES patient showing a vascular phenomena with respect to the left tympanic facial nerve canal from the sequelae of a developmentally hypoplastic left internal carotid artery (ICA).

Materials and Methods

A 9 years old female with PHACES syndrome was presented for further evaluation of an extensive vascular facial birthmark and possible segmental hemangioma. Her initial study revealed a hypoplastic left ICA. Progressive narrowing of the left supraclinoid ICA with incidental dilation of the right internal auditory canal (IAC) was noted on subsequent imaging. Thus, a dedicated computed tomography scan (CT) of the temporal bone was ordered to better delineate the structures of the posterior fossa.

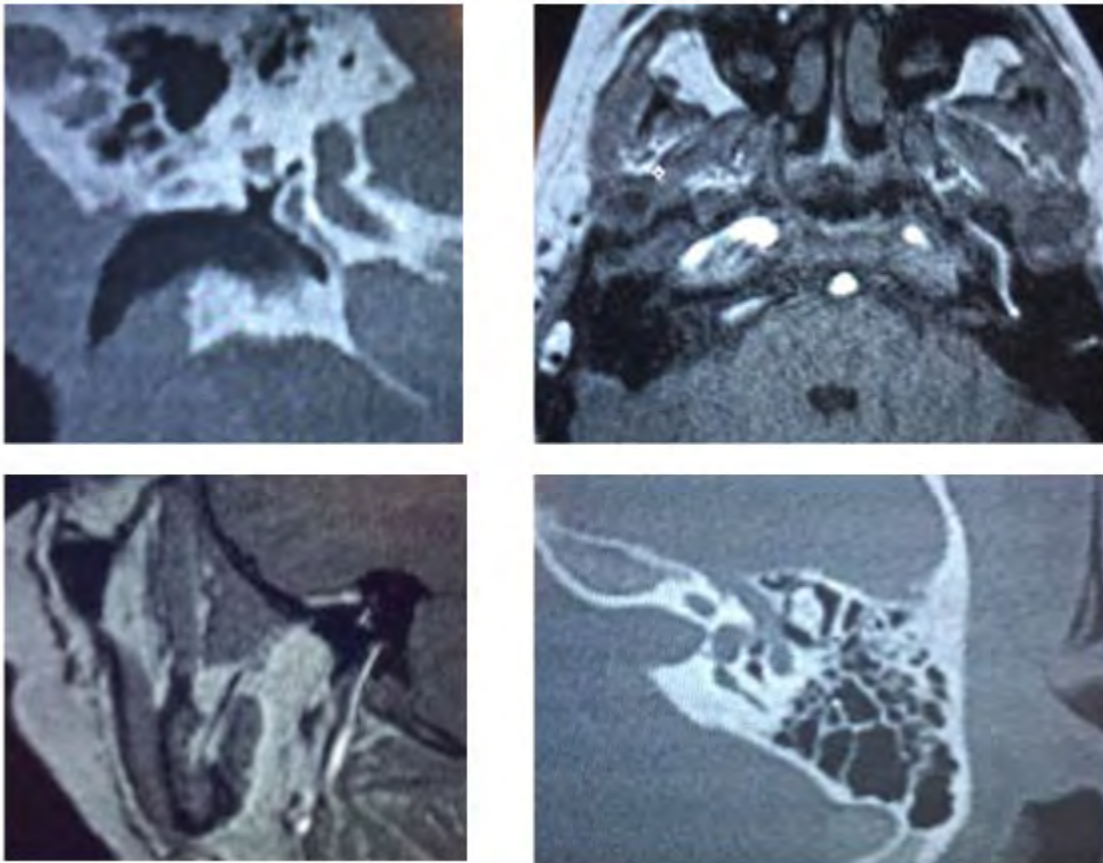
Results

The tympanic segment of the left facial nerve (FN) canal is abnormally enlarged (Top right image). An aberrant vascular channel is seen communicating with it at the level of the oval window niche, descending into the skull base, medial to the mastoid segment of the FN canal (Bottom right image: the stylomastoid artery comes off from the posterior auricular artery). Reviewing prior magnetic resonance (MR) angiography with the CT, a prominent vascular structure communicates between the anterior portion of the tympanic facial canal near the geniculate ganglion (Top left image). This vessel represents a prominent superficial petrosal (SP) artery. MR time of flight reveals an anastomosis between the SP branch of the middle meningeal artery (MMA) and enlarged stylomastoid artery within the tympanic segment of the fallopian canal. Incidentally, the patient also has a persistent stapedial artery, a known vascular phenomenon in patients with PHACES syndrome (Bottom left image).

Conclusions

Intracranial vascular anomalies have been observed in conjunction with PHACES syndrome in many instances.¹ The petrosal artery (PA) is commonly the first branch off the MMA after it exits the FS.²⁻⁵ It travels with the greater superficial petrosal nerve (GSPN) through the GSPN hiatus. The superior tympanic artery, the second

branch off the MMA, can sometimes joins with the PA or continues into the facial canal with the lesser petrosal nerve.²⁻⁴ The stylomastoid artery from the posterior auricular artery goes through the stylomastoid foramen to supply the mastoid segment and later joins the PA in the tympanic segment of the FN.^{3,4} Consequently, because the left ICA of this patient is developmentally hypoplastic, this anastomosis between the SP artery and the SM artery persisted, resulting an enlarged left tympanic segment FN canal. The findings of all three occurrences are extremely rare, but explainable due to the known abnormal vasculature that can occur in patients with PHACES syndrome.



(Filename: TCT_E-34_PHACES.jpg)

E-35

6:05PM - 6:10PM

Don't Pop This Pimple: Facial Varix, a Rare Entity

P Shah¹, J Huang¹, V Yedavalli²

¹Advocate Illinois Masonic Medical Center, Chicago, IL, ²Illinois Masonic Medical Center/ University of Chicago, Chicago, IL

Purpose

Varices of the facial vein are extremely rare, with only a handful of cases being reported in the literature. We present a case of symptomatic varix of the facial and angular vein with suspected arteriovenous fistula.

Materials and Methods

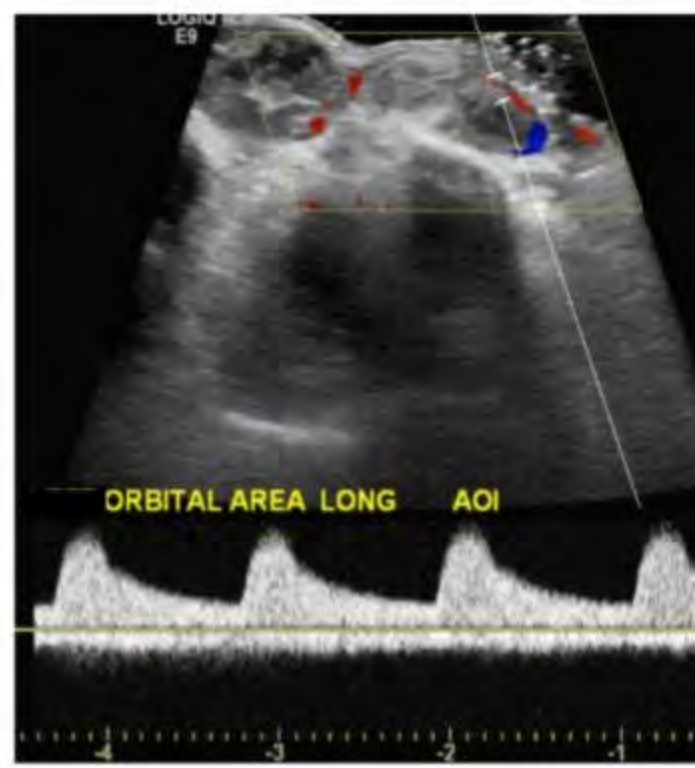
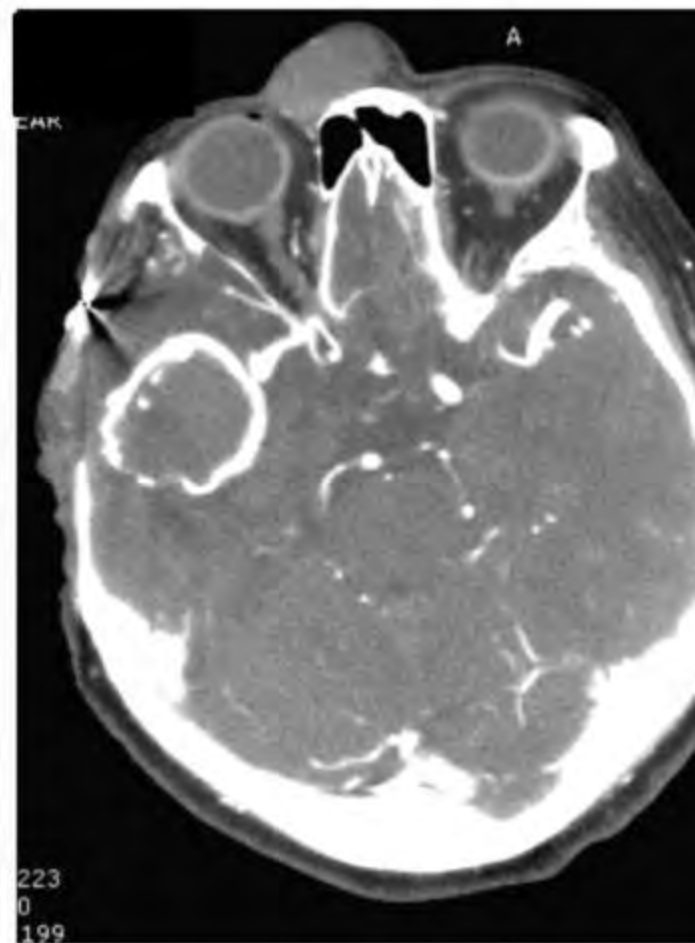
A 69 year old female with history of a thrombosed giant right middle cranial fossa aneurysm status post right craniectomy and right external carotid artery to right middle cerebral artery bypass presented with two weeks of progressive pain, swelling and ecchymosis in the right periorbital region. She reported no history of trauma, malignancy, or infection. Due to history of prior aneurysm and patient's presentation, underlying vascular etiology was suspected and computed tomography angiography (CTA) of the head and neck was performed.

Results

CTA revealed a large tubular soft tissue structure in the region of swelling in the right periorbital region with contrast in its inferior aspect that communicates with the right external jugular vein, thus representing a partially thrombosed facial varix. Doppler ultrasound was performed to further characterize flow dynamics. This revealed mixed arterial and venous Doppler waveforms, raising suspicion for underlying arteriovenous malformation. The patient was then discharged with close follow up for future conventional cerebral angiography and possible endovascular intervention.

Conclusions

Facial varices are rare causes of facial swelling and are typically thrombosed upon diagnosis. Typically overlooked, vascular etiologies should also be considered in addition to infectious and inflammatory causes of focal facial swelling.



(Filename: TCT_E-35_varix.jpg)

E-36

6:10PM - 6:15PM

Spontaneous Regression of a Large High-Flow Intracranial Dural Arteriovenous Fistula

A Yen¹, S Hetts¹

¹*University of California, San Francisco, San Francisco, CA*

Purpose

Intracranial dural arteriovenous fistulas (DAVFs) are rare vascular malformations that connect meningeal arteries to dural venous sinuses or cortical veins. Few DAVFs have been reported to resolve spontaneously since the phenomenon was first described in 1976. The mechanism for spontaneous closure is unknown, although some possibilities have been proposed. Here we describe a case of spontaneous resolution of a large DAVF in a patient with a hypercoagulable state.

Materials and Methods

A 47-year-old female with a history of rheumatoid arthritis was seen at an outside institution and found to have a large transverse sinus DAVF with high-flow fast arteriovenous shunting. One year prior to discovery of the DAVF, she underwent work-up at an outside institution for a seven-year history of daily occipital headaches and was found on MRI to have left-sided transverse and sigmoid sinus thromboses. She was clinically deemed to have a hypercoagulable state and was prescribed warfarin at the time. After continued headaches and the development of low-pitched ringing in her ears, a catheter angiogram showed a large transverse sinus DAVF, supplied by the left occipital artery and the left middle meningeal artery and drained by the right-sided transverse sinus, sigmoid sinus, and internal jugular vein. She was referred to our institution for embolization of her DAVF. Although the patient was prescribed a low molecular weight heparin injection bridge between her usual warfarin and the time of angiography at our institution, that prescription was not filled. Thus, the patient's warfarin was stopped four days prior to her procedure with no anticoagulant bridging. Her prior diagnostic angiogram and her angiogram performed at our institution were separated by 8 months. Although her initial angiogram clearly showed a large DAVF, the second diagnostic angiogram demonstrated that her DAVF had spontaneously resolved. As a result, no embolization was performed. No treatment was given thereafter. The patient was recently contacted for follow-up but did not respond.

Results

Image 1 (DSA, 2012) - Left external carotid artery lateral angiogram demonstrates a high flow DAVF shunting to the sigmoid sinus with antegrade drainage to the internal

jugular vein. Image 2 (DSA, 2012) - Right occipital artery anteroposterior angiogram demonstrates supply to the contralateral left transverse sigmoid sinus junction DAVF. Image 3 (DSA, 2013) - Left external carotid angiogram demonstrates spontaneous resolution of the DAVF. Image 4 (DSA, 2013) - Right occipital artery anteroposterior angiogram demonstrates no residual supply to previously seen left transverse sigmoid sinus junction DAVF.

Conclusions

In this report, we described a case of a very large DAVF that spontaneously resolved. Despite our institution's extensive familiarity with DAVFs, this is the largest that we have seen to resolve on its own. Although the exact mechanism of why this occurred is unknown, it is likely related to the patient's underlying hypercoagulable state and the high-flow nature of the DAVF.

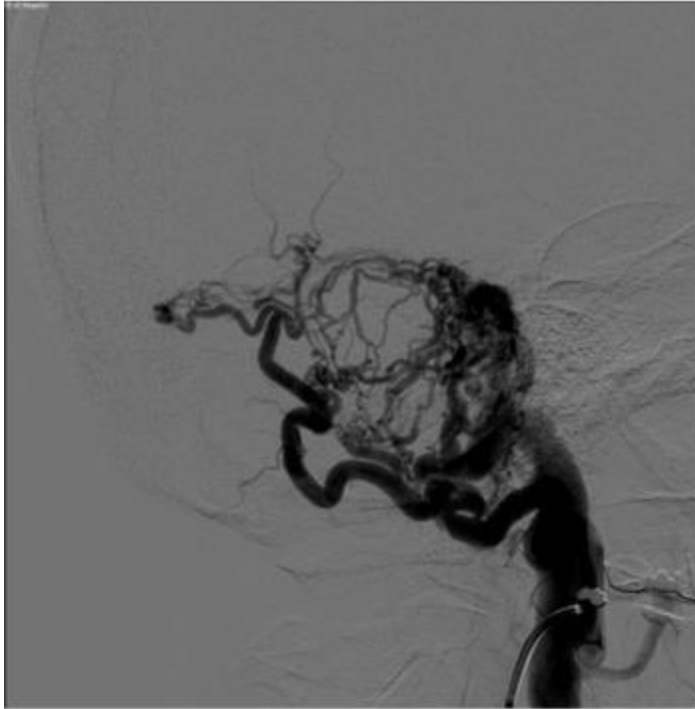


Image 1 – DSA, 2012

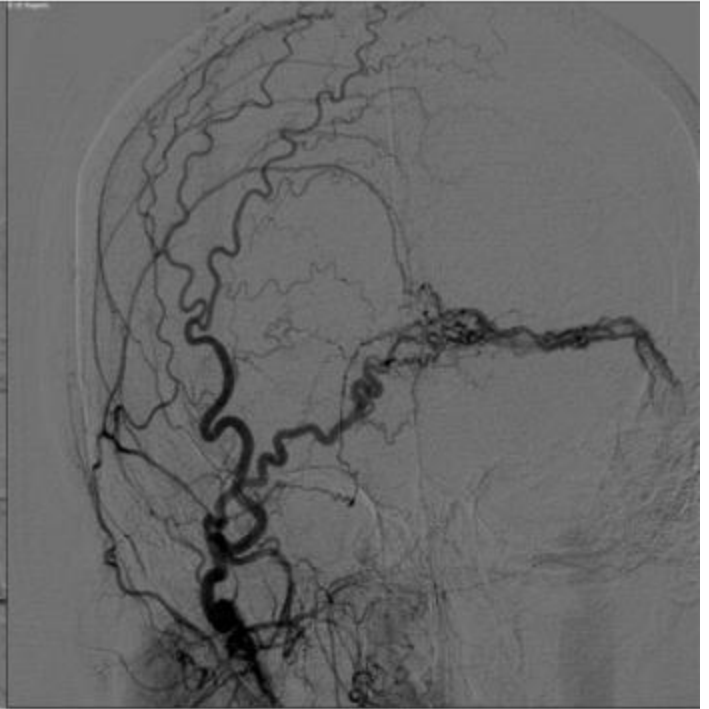


Image 2 – DSA, 2012

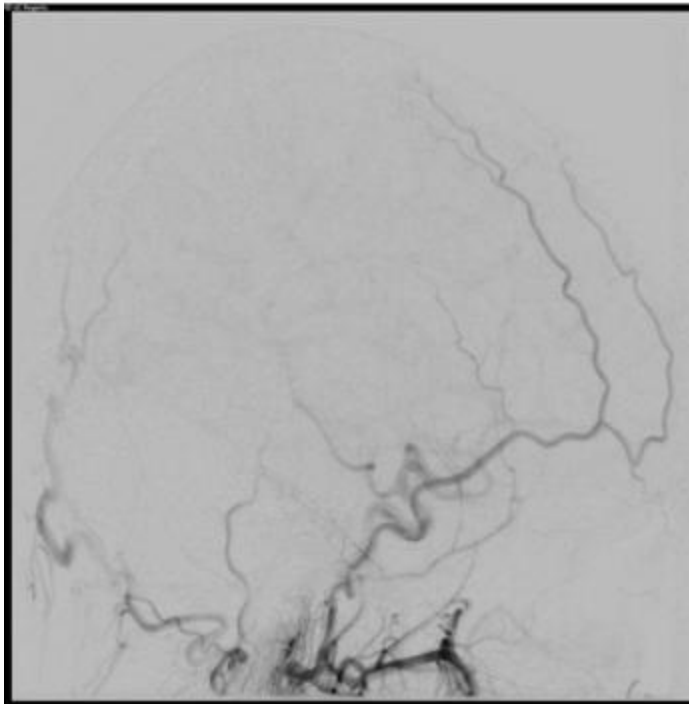


Image 3 – DSA, 2013

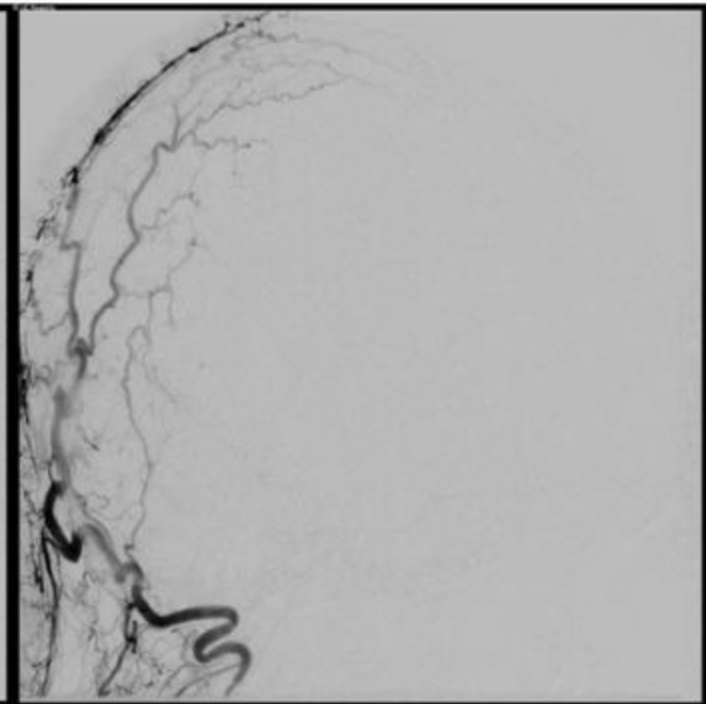


Image 4 – DSA, 2013

(Filename: TCT_E-36_ASNR20164images.JPG)

Wednesday

4:45PM - 6:15PM

Washington Marriott Wardman Park, Roosevelt 4

18F-Study Group - Imaging Genomics (non-CME)

Thursday

7:30AM - 8:30AM

Washington Marriott Wardman Park, Marriott Ballroom

**19A-Thursday Morning SAM - Head and Neck Audience Response (AR) Self
Assessment Module (SAM)**

19A-1

7:30AM - 7:55AM

Salivary Glands

Eliahou, R.

Hadassah Medical Center

Reut

19A-1a

7:55AM - 8:00AM

Questions and Answers

19A-2

8:00AM - 8:25AM

Deep Spaces of the Neck

Hagiwara, M.

NYU Langone Medical Center

New York, NY

19a-2a

8:25AM - 8:30AM

Questions and Answers

Thursday

8:35AM - 10:00AM

Washington Marriott Wardman Park, Marriott Ballroom

20A-SNIS Programming: Difficult Dilemmas: Safe Solutions for Challenging Situations in the Cavernous Sinus

20A-1

8:35AM - 9:00AM

Cavernous Sinus Anatomy and Its Endovascular Implications

Prestigiacomo, C.
Neurological Institute Of New Jersey
Newark, NJ

20A-2

9:00AM - 9:20AM

Intra-arterial Approaches to Cavernous Sinus Lesions: Is the "Direct" Route Always the Best?

Amans, M.
UCSF
San Francisco, CA

20A-3

9:20AM - 9:40AM

Transvenous Approaches to Lesions of the Cavernous Sinus: The "Indirect Solution to a Complex Problem

Amuluru, K.
Rutgers New Jersey Medical School
Newark, NJ

20A-4

9:40AM - 10:00AM

Deconstruction Methods and Alternatives to the Treatment of Vascular Lesions of the Cavernous Sinus

Hui, F.
Johns Hopkins University
Baltimore, MD

Thursday

8:35AM - 10:00AM

Washington Marriott Wardman Park, Washington 4/5/6

20B-Advanced Neuroimaging and Bioinformatics in Neuropsychiatric Disease

20B-1

8:35AM - 8:50AM

Substance Use Disorder and Neuroimaging

Tanabe, J.
University of Colorado School of Medicine
Aurora, CO

20B-2

8:50AM - 9:05AM

MS Spectroscopy in Neuropsychiatric Disorders

Port, J.
Mayo Clinic
Rochester, MN

20B-3

9:05AM - 9:20AM

Imaging Genetics of 22q11 Deletion Syndrome

Schmitt, J.
University of Pennsylvania
Philadelphia, PA

20B-4

9:20AM - 9:35AM

Systems Neuroscience, Neuroimaging and Neuropsychiatric Disease

Yu, J.

University of Wisconsin-Madison
Madison, WI

20B-5

9:35AM - 9:50AM

Overview of Functional Neuroimaging in Neuropsychiatric Disease

Sugrue, L.

UCSF
San Francisco, CA

20B-6

9:50AM - 10:00AM

Discussion

Thursday

8:35AM - 10:03AM

Washington Marriott Wardman Park, Washington 1/2/3

20C-PARALLEL PAPER SESSION: Head and Neck: Parathyroid, Thyroid, and Salivary

O-408

8:35AM - 8:43AM

Diagnostic Accuracy of Parathyroid Imaging: Comparing 4D-CT, Ultrasonography, MIBI and 4D-CT/MIBI Fusion.

B Tantiwongkosi¹, V Nguyen¹, F Yu¹, U Salman¹, H White¹, W Altmeyer², A Singh³, F Miller¹, C Hands¹, O Boyce¹, A Santillan-Gomez¹

¹University of Texas Health Science Center at San Antonio, San Antonio, TX, ²UTHSCSA, San Antonio, TX, ³UT Health Science Center San Antonio, San Antonio, TX

Purpose

The purpose of this study is to assess the diagnostic accuracy of four dimensional computed tomography (4D-CT) for localizing pathologically proven hyperfunctioning parathyroid glands, as compare to ultrasound (US), MIBI and 4D-CT/MIBI fusion.

Materials and Methods

Retrospective review of 4D-CT, US, MIBI and fusion parathyroid imaging at a tertiary referral center between 2011 and 2015 is performed with radiological, surgical and pathological correlation. Inclusion criteria are availability of intra-operative report, pathology and performance of pre-operative imaging. Histology, surgical findings, reduction of intra-operative parathyroid hormone levels are used as gold standards. Accuracy of 4D-CT is determined by including laterality and quadrant of the pathologically proved lesions as compare to US, MIBI and fusion study.

Results

Sixty-eight patients with hyperparathyroidism have 82 glands removed and proven to have parathyroid adenomas or hyperplasia. Sixty-eight, 38, 32 and 24 patients have 4D-CT, US, MIBI, and 4D-CT/MIBI fusion respectively. The accuracy of 4D-CT, US, MIBI and 4D-CT/MIBI fusion are 79%, 64%, 76% and 83% in quadrant localization and 89%, 65%, 78% and 93% in lateralization respectively. When utilizing combination of imaging modalities, the accuracy increases up to 91% and 92% in quadrant localization and lateralization accordingly.

Conclusions

Four dimensional CT is a novel robust method in localization of hyperfunctioning parathyroid glands with high accuracy as compared to conventional imaging.

O-409

8:43AM - 8:51AM

Confidence Grading System for Parathyroid 4D-CT: How Well Does Radiologist Confidence Predict Surgical Findings?

S Kuzminski¹, M Bahl¹, A Sepahdari², J Sosa¹, J Hoang¹

¹Duke University Medical Center, Durham, NC, ²UCLA, Santa Monica, CA

Purpose

Several studies have shown four-dimensional (4D) parathyroid computed tomography (CT) to have superior sensitivity to ultrasound and scintigraphy. Another advantage of 4D-CT is the ability to provide a confidence score based on a combination of imaging findings. The Duke 4D-CT grading system was developed to standardize reporting.

The purpose of this study was to evaluate the performance of this grading system in predicting intra-operative parathyroid lesion location.

Materials and Methods

We retrospectively reviewed 174 consecutive pre-operative 4D-CT scans from UCLA and Duke University in patients with primary hyperparathyroidism who on final surgical pathology were demonstrated to have parathyroid adenomas or hyperplasia. Lesions were categorized according to the Duke 4D-CT grading system based on three enhancement patterns (Types A-C) and three secondary findings (polar vessel, size ≥ 1 cm, cystic change) (Bahl, Sepahdari, Sosa, & Hoang, 2015). "Consistent with" was defined as Type A or B enhancement with at least one secondary finding. "Suspicious" was Type A or B enhancement without a secondary finding or Type C enhancement with at least one secondary finding. "Possible" was Type C enhancement without a secondary finding. We calculated and compared the sensitivity, prevalence, and positive predictive values (PPV) for each confidence grading system category.

Results

One hundred seventy-four patients had 229 parathyroid lesions. All lesions could be categorized by the grading system (Table 1). "Consistent with" was the most common classification, with a prevalence of 39%, sensitivity of 97%, a positive predictive value (PPV) of 97%. "Suspicious" represented 36% of lesions and had a sensitivity of 88% and PPV of 91%. Finally, "possible" represented 25% of lesions and had the lowest sensitivity of 68% and a PPV of 81%.

Conclusions

The Duke 4D-CT grading system performs as intended in reporting parathyroid lesions on 4D-CT. The system is reliable in helping the surgeon decide if further imaging is required and if surgery can be performed using a minimally invasive or focused technique.

Table 1. Enhancement patterns and secondary signs of parathyroid adenomas and hyperplasia on 4DCT.

| | Parathyroid Lesions (Prevalence) | False Positive | Positive Predictive Value |
|---|----------------------------------|----------------|---------------------------|
| Total number of lesions | 229 | 23 | 89% |
| Single | 154 (67%) | 18 | 88% |
| Multiglandular | 75 (33%) | 5 | 91% |
| Enhancement Pattern * | | | |
| Type A – higher attenuation than thyroid on arterial phase with decreasing attenuation on delayed phase | 37 (16%) | 1 | 97% |
| Type B – same attenuation as thyroid on arterial phase but lower in attenuation than thyroid on delayed phase | 79 (34%) | 4 | 95% |
| Type C – similar in attenuation to thyroid on both contrast phases | 113 (49%) | 18 | 81% |
| Secondary findings | | | |
| Size ≥ 1 cm | 116 (51%) | 10 | 91% |
| Cystic component | 37 (16%) | 3 | 93% |
| Polar vessel | 71(31%) | 10 | 86% |
| Grading Scale | | | |
| Consistent with – Type A/B enhancement and 1 or more secondary findings | 90 (39%) | 3 | 97% |
| Suspicious – Type A/B enhancement without secondary findings or Type C enhancement with ≥ 1 secondary findings | 82 (36%) | 10 | 91% |
| Possible – Type C enhancement without secondary findings | 57 (25%) | 10 | 81% |

* All enhancement patterns required the adenoma to be lower in attenuation than the thyroid gland on the noncontrast phase.

(Filename: TCT_O-409_ParathyroidTable.JPG)

O-410

8:51AM - 8:59AM

4D MRI for Preoperative Localization of Parathyroid Adenomas: 2 Year Experience

K Nael¹, S Hur², J Becker², P Pawha¹, P Som¹

¹Icahn School of Medicine at Mount Sinai, New York, NY, ²University of Arizona, Tucson, AZ

Purpose

Recently dynamic magnetic resonance imaging (MRI) has been used for identification and characterization of parathyroid adenomas (PTA) with success (1). The purpose of

this study was to assess the diagnostic performance of 4D MRI for pre-operative localization of patients with PTA in comparison to surgical pathology.

Materials and Methods

From Sep 2013 to Sep 2015, patients with the diagnosis of primary hyperparathyroidism who had surgery and pre-operative MRI were reviewed. Magnetic resonance imaging was performed with inclusion of a high spatial (1.3 x 1.3 x 2 mm) and high temporal resolution (5.5 sec) dynamic contrast-enhanced acquisition. Images were reviewed by a CAQ-certified neuroradiologist who was blinded to the results of surgical pathology. A lesion was identified as PTA if it was in the expected location of parathyroid tissue (orthotopic or ectopic), was T2 hyperintense and demonstrated early arterial enhancement. The location (left or right, superior or inferior gland) as well as the number of PTAs was recorded. If more than one candidate was identified on initial analysis, the reader was instructed to use dynamic information (rapid arterial enhancement, rapid wash-in and washout) to confirm suspicion of a PTA versus other structures such as lymph node. Diagnostic accuracy of 4D MRI was measured against surgical pathology for both side and quadrant location.

Results

A total of 75 patients were reviewed. Thirteen patients were excluded (nondiagnostic dynamic MRI, n=4, unavailable surgical pathology n=5, parathyroidomatosis in re-operative patients, n=4). Among 62 included patients, no lesions were found in three patients (5%) at surgery. A total of 74 PTAs were identified in 59 patients including five patients with multiglandular disease. Among 74 PTAs identified, 66 lesions were correctly localized by 4D MRI (89%). Four dimensional MRI correctly identified unilateral versus bilateral disease in 53/59 (91%) patients. The overall sensitivity was 94% for single gland disease versus 69% for multiglandular disease. For 11 lesions, a second potential candidate was considered initially (based on conventional imaging), that was differentiated correctly and identified as cervical lymph node using dynamic information including rapid washin and washout.

Conclusions

Four dimensional dynamic MRI can be used for pre-operative localization of PTAs with diagnostic accuracies rivaling those with 4D CT. If its potential is realized, 4D MRI can be used as an alternative diagnostic modality in pre-operative parathyroid imaging.

O-411

8:59AM - 9:07AM

Survey of Radiologists on Parathyroid 4D-CT: Variability in Practice Patterns and Protocol

K Williams¹, J Hoang¹, F Gaillard², J Sosa¹, A Dixon³

¹Duke University Medical Center, Durham, NC, ²The Royal Melbourne Hospital, Parkville, Victoria, ³Alfred Hospital, Prahran, Australia

Purpose

Several studies show parathyroid four-dimensional CT (4D-CT) to be more sensitive than scintigraphy and ultrasound for pre-operative localization of parathyroid adenomas, but based on the literature, there is high variability in the imaging protocols and role of 4D-CT in pre-operative planning worldwide. The aim of this study was to describe the current practice role and trends in utilization of 4D-CT.

Materials and Methods

A survey was designed to query radiologists about their different institutional practices with regard to 4D-CT in the pre-operative evaluation of hyperparathyroidism. The survey was distributed by Radiopaedia.org, ASHNR and ASNR in January 2015. The survey questions sought to understand four main categories of practice: primary role of 4D-CT at the institution, details about 4D-CT protocol, volume and trends in utilization, and shared reporting practices among radiologists.

Results

Three hundred sixty radiologists responded. Two hundred of 360 (55.3%) stated that 4D-CT was used in their practices. Nineteen (9.5%) reported that 4D-CT plays a primary role in parathyroid imaging, 155 (77.5%) reported that 4D-CT plays a secondary role, and 26 (13%) reported that it is performed routinely with ultrasound and scintigraphy. A three-phase protocol was most common (50.5%), but imaging also was performed with 4 and 2 phases. In the majority of practices (148/200, 74%), <5 4D-CT studies were performed each month. Overall, 143/200 (71.5%) practices have performed the exam for ≤ 3 years, and 4D-CT volume was perceived to be increasing over time according to 91/200 (45.5%) respondents. Ninety of 200 (45%) radiologists indicated that only one or two radiologists in their practices reported 4D-CT. A first line role for 4D-CT in the evaluation of hyperparathyroidism was more likely if the study had been performed for >3 years and with increasing and larger 4D-CT practice volumes.

Conclusions

More than half of radiologists who responded to the survey perform 4D-CT, and nearly half report increasing utilization of 4D-CT in pre-operative evaluation of hyperparathyroidism. The 3-phase protocol is used most commonly in practice. The majority of radiologists reported that 4D-CT still plays a secondary role.

O-412

9:07AM - 9:15AM

Dynamic 4D CT Imaging of Larynx in Vocal Cord Palsy: Initial Experience using 320 slice MDCT

S Bhuta¹, G Kwan², C Hsu²

¹*Gold Coast University Hospital, Gold Coast, Australia,* ²*Gold Coast University Hospital, Southport, N/A*

Purpose

To describe the utility noninvasive technique of dynamic 4D CT imaging of the larynx in assessment of vocal cord palsy.

Materials and Methods

Dynamic imaging of the larynx was performed with 320 slice mean diffusivity (MD)CT (Toshiba Aquilion One, Japan). Laryngeal imaging was performed in 15 patients with detector ray to scan of 8 cm and 10 cm Z-axis volume to minimize the radiation dose. Acquisition was at 0.5mm and reconstructed at 1 mm slice thickness interval with 350 ms gantry rotation speed. Gantry angulation was used to reduce artifact from mandible FOV from hyoid to upper trachea – 1st or 2nd tracheal ring (Fig.1). Intravenous (IV) contrast was not administered. Patients were rehearsed in a breathing protocol. Multiple phases are acquired as Quiet Breathing, EEE Phonation and Sniff Test. Imaging technique was compared with endoscopy findings.

Results

Vocal cord palsy was well detected on 4D CT. Volume and surface rendering technique was used. Virtual endoscopy also was performed. Widening of the laryngeal ventricle, medial deviation and thickening of the aryepiglottic fold and dilatation of the piriform sinus was observed consistently in all patients. Dynamic assessment using breathing techniques showed the expansion of the pyriform sinus with no change in respiratory phase, similarly alerted cord mobility was visualized directly on cine loop images.

Conclusions

Dynamic vocal cord assessment is innovative and quick and noninvasive imaging test. No IV contrast is required and radiation dose is minimal. Imaging findings are comparable to direct visualization of the larynx. Study can be repeated to assess improvement after voice training and or after surgery.



(Filename: TCT_O-412_Picture1.jpg)

O-413

9:15AM - 9:23AM

Increasing Incidence of Thyroid Cancer: Impact of Neck Imaging Utilization

G Ma¹, M Makary¹, G Abdalhalim¹, S Erdal², L Prevedello¹, T Shujaat¹, X Nguyen¹

¹Ohio State University Wexner Medical Center, Columbus, OH, ²Ohio State University College of Medicine, Columbus, OH

Purpose

Thyroid cancer incidence has nearly tripled in recent decades, with varying magnitude of increase across different demographic groups. Increased detection of asymptomatic thyroid cancers likely contributes to this trend, but few studies directly assess the impact of imaging utilization on rising thyroid cancer incidence. This study quantifies neck CT imaging utilization rates and their relationship with thyroid cancer incidence as a function of age, sex, and race.

Materials and Methods

Medical records of over one million patients receiving care from 2004 to 2011 at our institution were analyzed retrospectively to quantify neck CT utilization, defined as the proportion of patients having at least one neck CT or CTA study. The United States National Cancer Institute's Surveillance, Epidemiology and End Results database was used to compute thyroid cancer incidences from 2004 to 2011 and to calculate fold-change of thyroid incidence over the past 30 years. Both patient populations were partitioned into demographic subgroups of varying age, sex, and race.

Results

Of the three demographic variables, age demonstrated the greatest variability in thyroid cancer incidence and neck imaging utilization, both of which peaked in the 65-74 age group (Fig. 1a). When stratifying by age, neck CT utilization correlated very strongly with national thyroid cancer incidence ($R = 0.97$) and with 30-year fold change in thyroid cancer incidence ($R = 0.87$). Across all demographic subgroups, there was moderate correlation between neck imaging utilization and 30-year fold change in thyroid cancer incidence ($R = 0.46$), greater for whites ($R = 0.63$) and blacks ($R = 0.53$) than other races ($R = 0.07$) (Fig. 1b).

Conclusions

Differences in neck CT utilization account for a large portion of the variation in thyroid cancer incidence among demographic subgroups. The data support a role of increased imaging detection in the observed rise in thyroid cancer incidence.

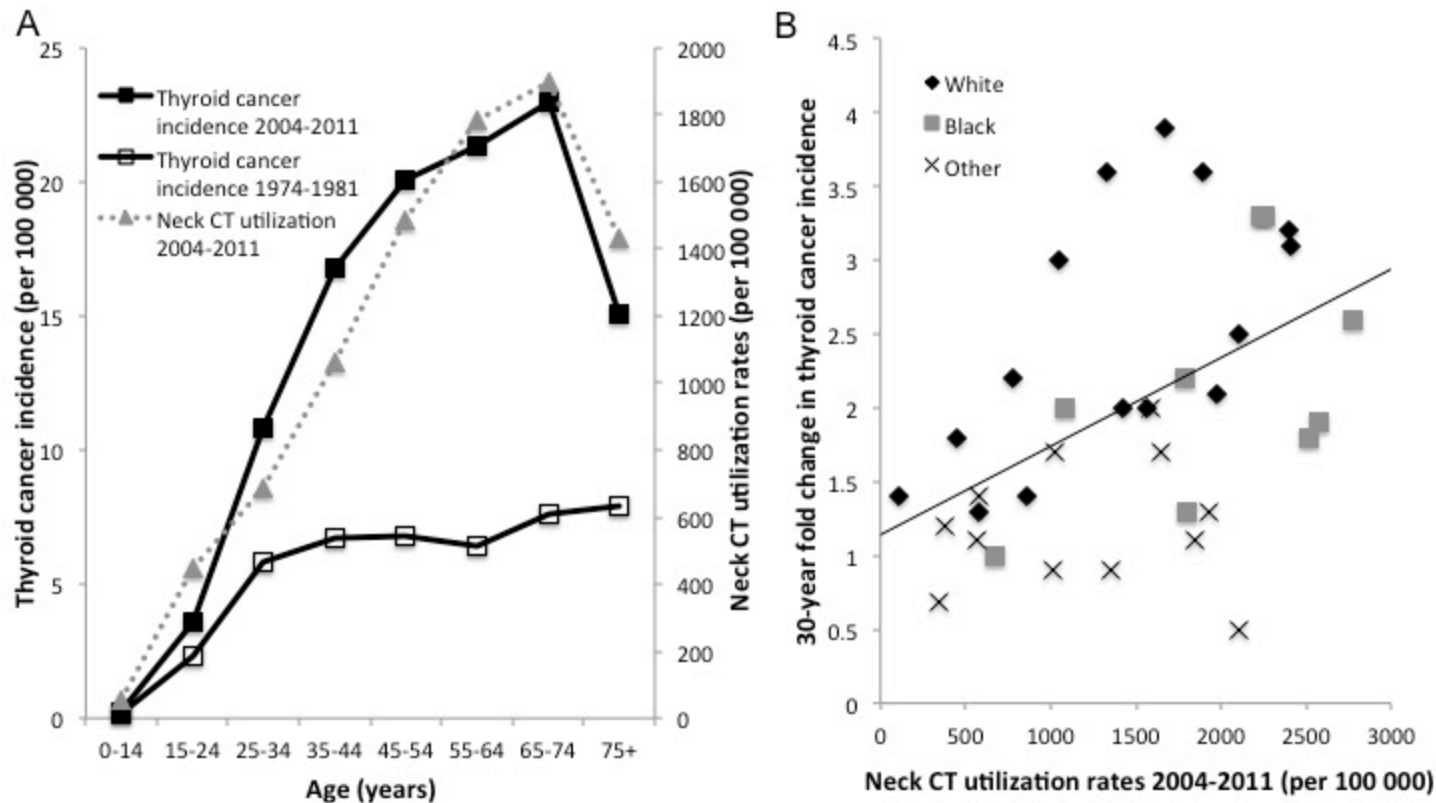


Figure 1. (A) Thyroid cancer incidence and neck CT utilization as a function of age. (B) Scatterplot of 30-year fold change in thyroid cancer incidence versus neck CT utilization rates among demographic subgroups.

(Filename: TCT_O-413_Figure1-Dec8.jpg)

O-414

9:23AM - 9:31AM

Imaging of Anaplastic Thyroid Cancer

S Ahmed¹, M Ghazarian², T Vu¹, J Debnam¹, N Chasen³

¹UT MD Anderson Cancer Center, Houston, TX, ²UT Houston Medical School at Houston, Houston, TX, ³M.D. Anderson Cancer Center, Houston, TX

Purpose

While anaplastic thyroid cancer (ATC) accounts for less than 3% of thyroid cancer cases, there is rapid progression of tumor with significantly higher mortality when comparing to differentiated thyroid cancer which comprises 85-90% of thyroid cancer cases and typically has an indolent course. The aim of this study is to describe the imaging characteristics on contrast-enhanced computed tomography (HRCT) of the neck, in patients with biopsy proven anaplastic thyroid cancer.

Materials and Methods

Hospital database was queried for diagnosis of ATC between 6/2004 and 7/2015. Those patients with pretherapy CT imaging were included. HRCT images were reviewed by CAQ'd neuroradiologists specializing in head and neck imaging. The primary tumor was evaluated for 1) extent of involvement, 2) size, 3) margins, 4) extra-thyroidal extension, 5) morphology, 6) calcifications, 7) esophageal invasion, 8) tracheal invasion, 9) laryngeal invasion, 10) carotid encasement, 11) internal jugular vein (IJV) encasement/invasion, and 12) intrathoracic extension. The presence of central, lateral, and lateral retropharyngeal lymphadenopathy (LAD) was documented. Lateral compartment LAD was assessed for calcification, necrosis, and cystic change.

Results

Query yielded 205 cases of ATC. Fifty-eight of 205 patients had pretherapy CT imaging, and three patients were excluded for poor image quality. Male=28/55, Female=27/55. Age range: 21 to 82 years (Mean=64 years, Median=65 years). Extent of involvement: one lobe=12/55 (22%), one lobe plus isthmus=13/55 (24%), both lobes=30/55 (54%). Size: Mean=5.1 x 4.5 cm, Median=4.9 x 4.1 cm (AP x Transverse). Tumor margins: Ill-defined=45/55 (82%), well-defined=10/55 (18%). Extra-thyroidal extension=50/55 (91%). Morphology: Solid=10/55 (18%), cystic=0/55 (0%), mixed solid and necrotic=45/55 (82%). Calcification: present=34/55 (62%). Of the 34 tumors with calcification, coarse calcifications =19/34, punctate/stippled=19/34, eggshell=5/34. Intrathoracic extension=23/55 (42%), esophageal invasion=34/55 (62%), tracheal invasion=31/55 (56%), laryngeal invasion=16/55 (29%). Carotid artery encasement=22/55 (40%), IJV involvement=23/55 (42%). Central LAD=30/55 (55%), Lateral LAD=4/55 (62%). Lateral retropharyngeal LAD=7/55 (13%). Lateral compartment LAD: necrosis=21/34 (61%), calcification=0/34 (0%) had calcification, cystic=3/34 (8%).

Conclusions

Anaplastic thyroid cancer typically presents in an older patient as a large (≥ 5 cm) solid mass with necrosis involving more than one lobe of the thyroid, and with extracapsular extension. The esophagus and trachea are involved more commonly than the larynx, and there is propensity for vascular encasement/invasion. Majority of the cases will have cervical lymphadenopathy, often with necrosis. It is important for the radiologist to be aware of the above imaging characteristics, and suggest a specific diagnosis of ATC when these features are present in a patient with a thyroid mass, to ensure accurate diagnosis and prevent delays in therapy.

O-415

9:31AM - 9:39AM

Practice Variations in Salivary Gland Imaging and Utility of Virtual Unenhanced Dual-Energy CT Images for the Detection of Major Salivary Gland Stones

R Forghani¹, B Beland², A Srinivasan³, M Levental²

¹*Jewish General Hospital & McGill University, Montreal, H3T 1E2*, ²*Jewish General Hospital & McGill University, Montreal, Quebec*, ³*University of Michigan, Ann Arbor, MI*

Purpose

There can be significant variation in the imaging approach for the evaluation of sialolithiasis. In this study, we performed a survey in order to evaluate the variations in contemporary practice for salivary imaging and evaluated the accuracy of dual energy CT (DECT) virtual unenhanced images (VUE) derived from a contrast-enhanced acquisition for detection of salivary stones.

Materials and Methods

IRB approval was obtained for this study. To evaluate practice variations, a 4-question survey was distributed to the membership of the American Society of Neuroradiology. A search of the CT scan database and reports then was performed at our institution in order to identify scans that were performed using the salivary gland protocol, including both an unenhanced (UE) and a contrast-enhanced (CE) acquisition, with the CE phase performed in DECT mode. Cases positive for at least one major salivary gland stone then were identified and matched with an equal number of cases without any stones, as negative controls. Virtual unenhanced images then were created from the 65s CE acquisition. The UE, VUE, and CE series then were mixed using a randomizer and displayed individually in random order. A head and neck radiologist evaluated each series for the number and minimum size of the stones detected. The number of stones on the UE study was considered as the gold standard. Sensitivity, specificity, positive predictive value (PPV), and negative predictive value (NPV) were calculated for detection of stones on VUE, using the true UE series as gold standard reference.

Results

Among the 280 respondents to the survey, 53.4% indicated using a different imaging protocol for referrals requested to rule out salivary stones compared to those for work up of gland swelling or mass, whereas 46.6% used the same protocol. For the work up of sialolithiasis, 92.9% use CT as first line imaging modality, 4.6% use ultrasound, and the rest other techniques. The most common CT protocols used were an UE CT followed by a single phase CE acquisition (35.3%), an UE CT only (28.1%), or a CE acquisition only (28.1%). For the evaluation of stones, 26 patients having a total of 52 obstructive or nonobstructive major salivary gland calcifications were identified, matched with another 26 patients without any salivary stones. On a per patient basis, the VUE images had 100% sensitivity and specificity. On an individual calcification basis, the VUE had a sensitivity of 96%, specificity of 96%, PPV of 98%, and NPV of 93%. The false negative cases corresponded to clinically insignificant, nonobstructive

parenchymal calcifications in the parotid glands. Stones not seen on the VUE images measured 2 mm or less although in many cases stones as small as 1 mm were visible on VUE images.

Conclusions

There is significant practice variation in the imaging approach and CT protocols used for the evaluation of sialolithiasis. An approach using a single CE dual energy CT acquisition with reconstruction of VUE images may represent an attractive alternative and enable the elimination of the true UE phase and associated radiation exposure.

O-416

9:39AM - 9:47AM

Instantaneous Responses of Parotid Glands to Gustatory Stimulation Evaluated by High Temporal Resolution Echo-planar Diffusion-weighted Imaging

C Juan¹, T Chiu², Y Liu³, H Chang⁴, K Hsu⁵

¹National Defense Medical Center and Tri-Service General Hospital, Taipei, Taiwan, ²Taipei Medical University, Taipei, nil, ³Feng Chia University, Taichung, nil, ⁴The University of Hong Kong, Hong Kong, nil, ⁵National Defense Medical Center, Taipei, nil

Purpose

To evaluate instantaneous responses of parotid glands to gustatory stimulation using echo-planar diffusion-weighted imaging (DWI).

Materials and Methods

This prospective study was approved by a local institutional review board. Written informed consent was obtained from 21 enrolled healthy volunteers [14 men and 7 women; age of 45.2 ± 12.9 years (mean \pm standard deviation)]. All participants underwent 1.5T fat-saturated echo-planar DWI with a temporal resolution of 4 seconds per scan. Imaging quality on T2WI ($b = 0$ s/mm²) and DWI ($b = 200$ s/mm²) was qualitatively assessed. Signal intensity of T2WI, DWI and apparent diffusion coefficient (ADC) of parotid glands was analyzed quantitatively. One way ANOVA with post-hoc group comparisons with Bonferroni correction were used for statistical analysis. $P < 0.05$ was considered statistically significant.

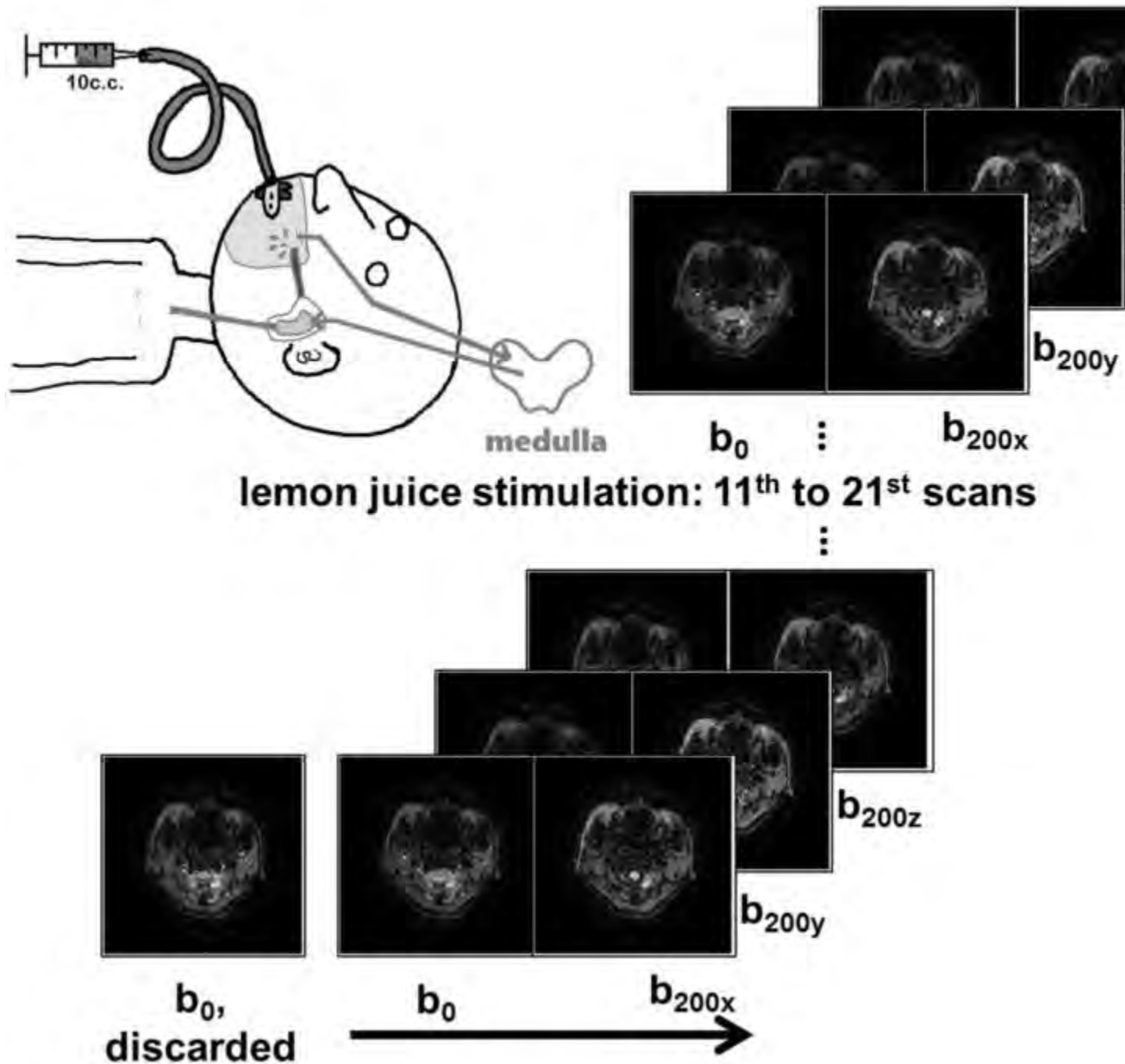
Results

Substantial to almost perfect interobserver agreement was achieved ($\kappa \geq 0.656$) in qualitative analysis. Free from perceptible magnetic susceptibility artifact at the baseline and at the end of scans on all images, parotid glands were partially involved by artifact on DWI during swallowing in three volunteers. Reduced signal intensity of parotid glands on T2WI and DWI and increased ADC occurred immediately after oral administration of lemon juice. Maximal signal change of ADC ($24.8 \pm 10.8\%$) was significantly higher than that of T2WI ($-10.1 \pm 5.2\%$; $P < 0.001$). Recovery ratio of

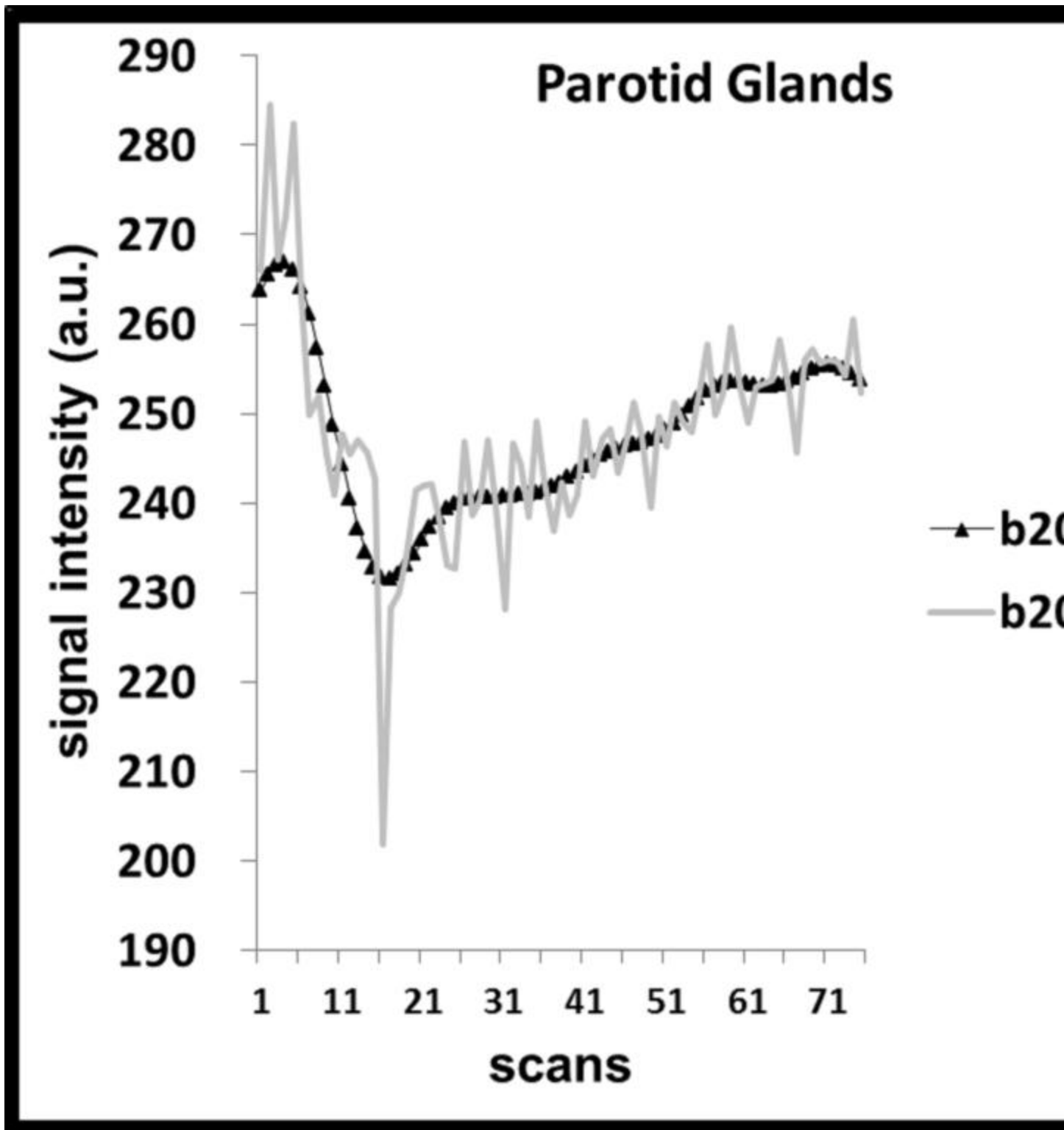
ADC ($100.71\% \pm 42.34\%$) also was significantly higher than that of T2WI ($22.36\% \pm 15.54\%$; $P < 0.001$).

Conclusions

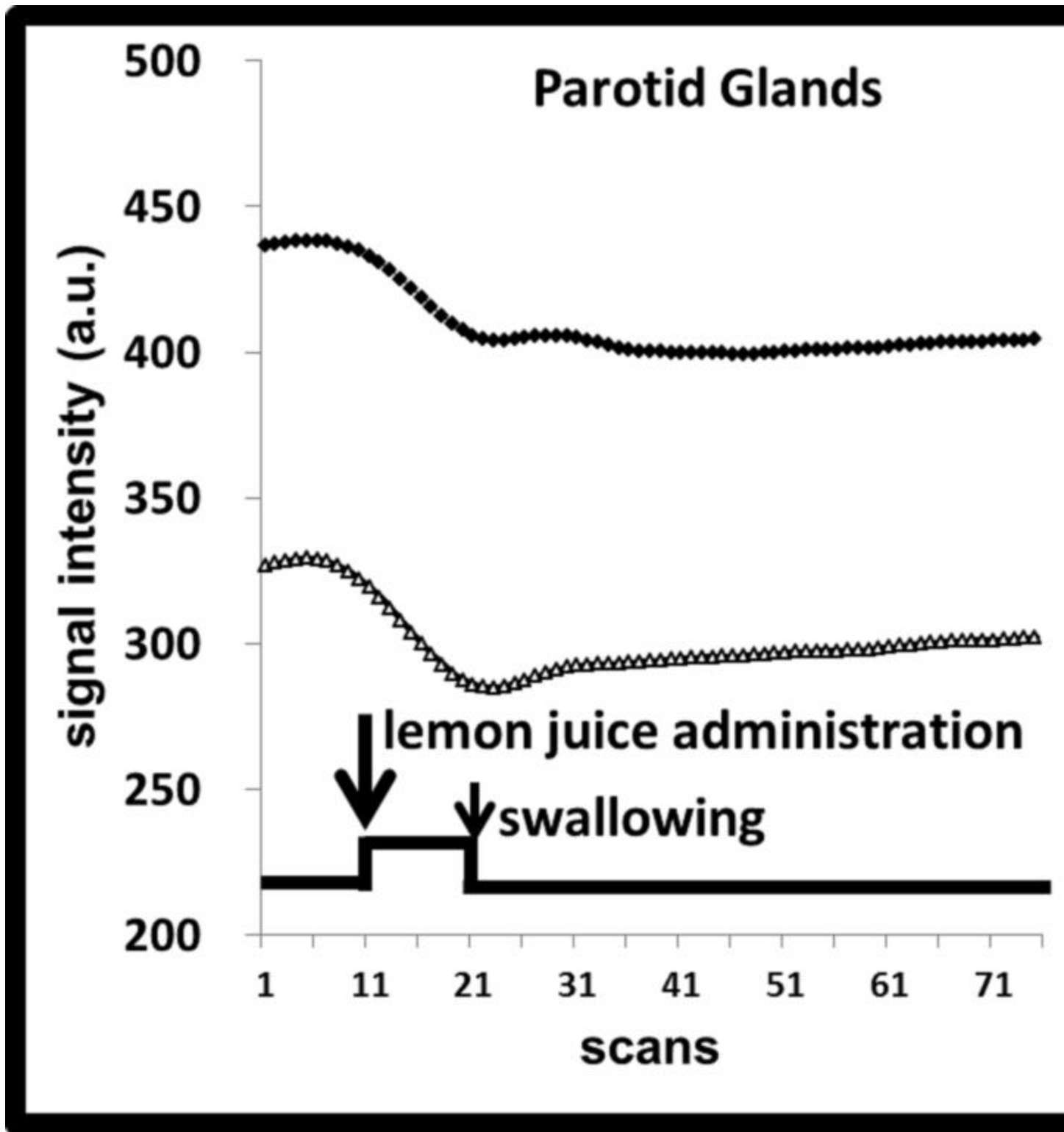
Echo-planar DWI allows evaluation of instantaneous responses of parotid glands to gustatory stimulation at a high temporal resolution of 4 seconds per scan.



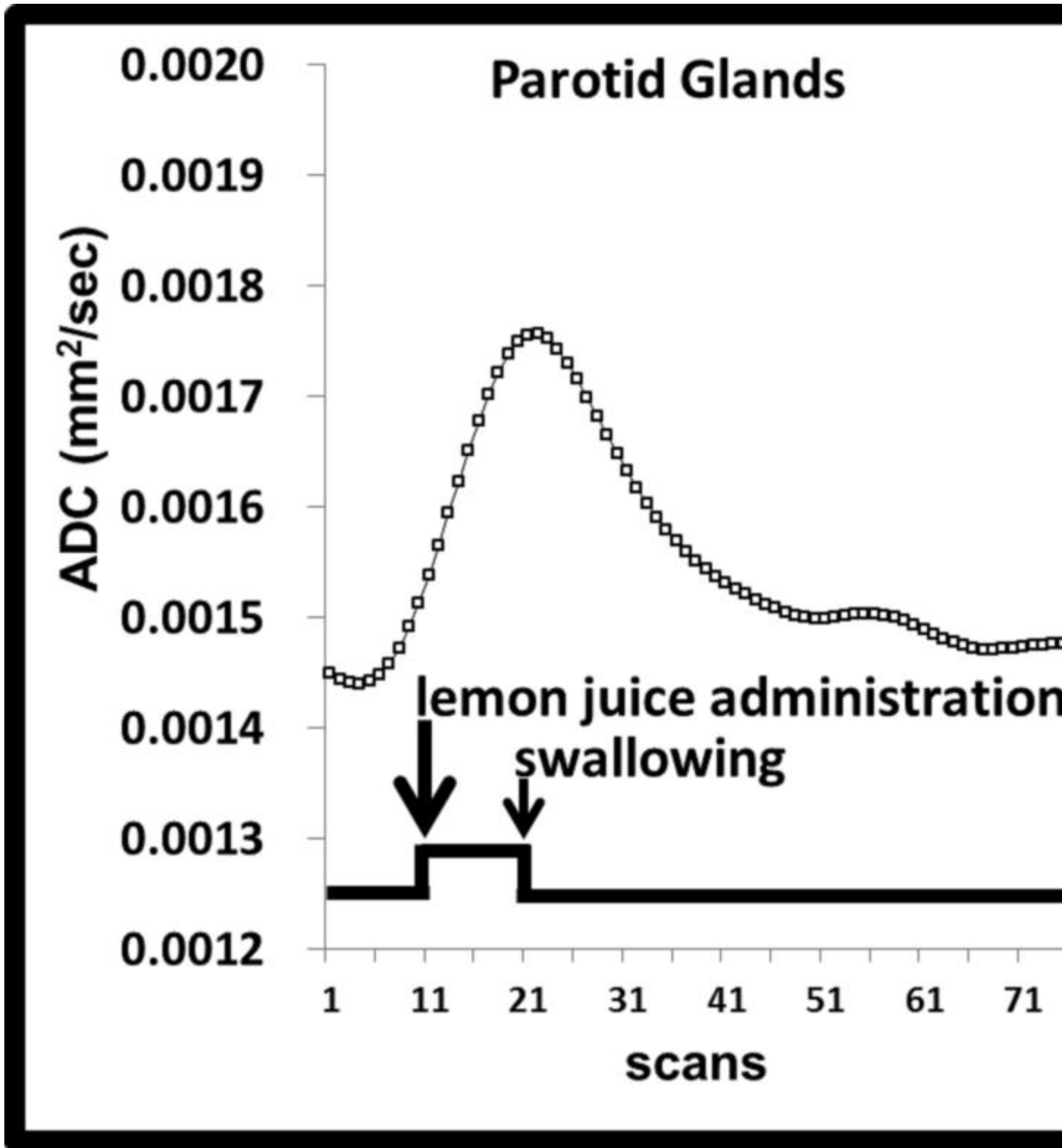
(Filename: TCT_O-416_Fig1.jpg)



(Filename: TCT_O-416_Fig2.jpg)



(Filename: TCT_O-416_Fig3.jpg)



(Filename: TCT_O-416_Fig4.jpg)

O-417

9:47AM - 9:55AM

CT and MRI Characteristics of Benign versus Malignant Palpable Parotid Masses

M Bashir¹, C Britt², G Hartig², L Gentry², T Kennedy³

¹*University of Wisconsin, Madison, WI*, ²*University of Wisconsin Hospitals, Madison, WI*, ³*University Of Wisconsin Hospital, Madison, WI*

Purpose

Parotid gland masses account for 70-85% of all salivary gland tumors, and have a rate of malignancy approaching 15-25%. The palpable, asymptomatic parotid mass presents a common problem for the clinician regarding need for resection. Currently, there is no treatment algorithm for managing palpable, asymptomatic parotid masses, particularly when surgery is wished to be avoided. We examined palpable, asymptomatic parotid masses in order to identify high-risk features within a larger available patient population that may aid in guiding appropriate management for these lesions.

Materials and Methods

This IRB-approved retrospective study evaluated computed tomography (CT) and magnetic resonance (MR) imaging (132 and 27 masses, respectively) of randomized patients between 2007 and 2013 with palpable, asymptomatic parotid gland masses who underwent surgery. Two interpreting radiologists were blinded to the pathology results. The evaluated CT imaging characteristics of the parotid masses included contrast-enhancement, size, location within the gland, density, margins, and calcifications. The evaluated MR imaging characteristics included contrast-enhancement, size, location, T1 and T2 signal intensity. Diffusion characteristics and FDG imaging were included where available. Data analysis was performed using Fisher exact test with the Monte Carlo correction to determine whether or not there is a difference between the benign and malignant groups, as well as to determine if very hyperintense T2 signal (similar to that of cerebrospinal fluid) can help in identification of pleomorphic adenomas versus all other parotid gland masses in this study.

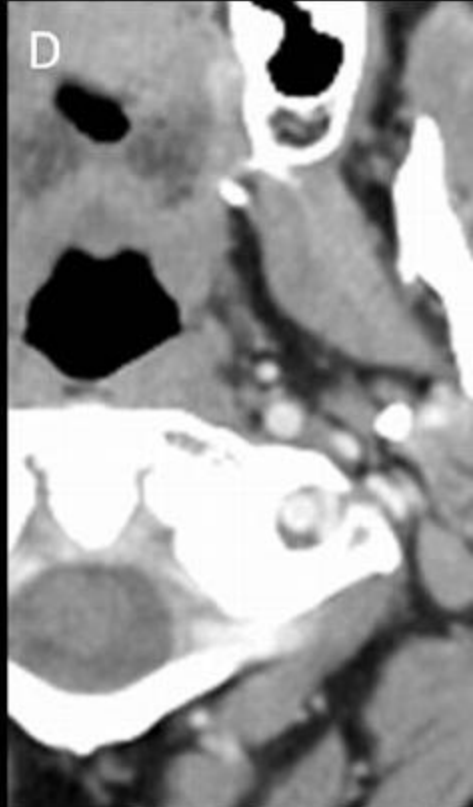
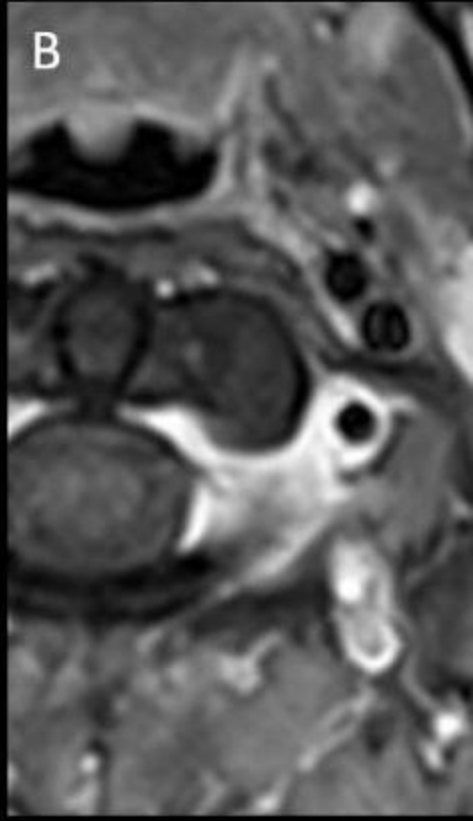
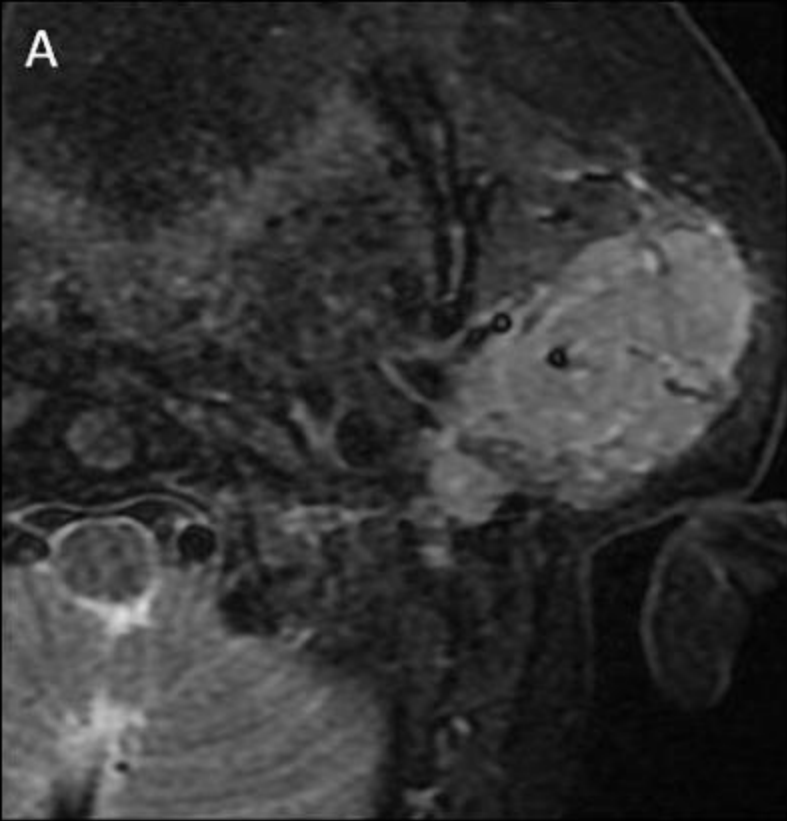
Results

Of the different CT and MRI characteristics evaluated, the presence of irregular margins on both CT and MRI proved to be statistically significant in distinguishing malignant from benign pathology ($p=0.04$, $p=0.04$). Pathology for the malignant lesions included acinic cell carcinoma, carcinoma ex pleomorphic adenoma, and lymphoma, among others. The majority of benign masses were pleomorphic adenomas and Warthin tumors. In addition, T2 signal was significantly different for pleomorphic adenomas ($p=0.01$) compared to other lesions; very hyperintense T2 signal was seen only in pleomorphic adenomas. The degree of enhancement, size, location, or individual MR signal characteristics were not independently useful in distinguishing benign from malignant pathology. Image 1: A) Axial STIR MR image

demonstrates a STIR hypointense left parotid mass with irregular margins. Lymphoma. B) Axial T1 postcontrast fat-saturated image demonstrates a heterogeneously enhancing mass with irregular margins in the left parotid gland. Carcinoma ex pleomorphic adenoma. C) Axial contrast-enhanced CT image demonstrates an enhancing mass with irregular margins in the left parotid gland. Squamous cell carcinoma. D) Axial contrast-enhanced CT image demonstrates an enhancing mass with irregular margins in the left parotid gland. Carcinoma ex pleomorphic adenoma.

Conclusions

The presence of irregular margins on CT and MRI can help distinguish high risk palpable, asymptomatic parotid masses.



(Filename: TCT_O-417_parotidmasses.jpg)

O-418

9:55AM - 10:03AM

Neck Adipose Tissue and Airway Volume: an Imaging Approach to the Obesity Epidemic

S Tal¹, H Maresky¹

¹*Assaf Harofeh Medical Center, Zrifin, HaMerkaz (Central)*

Purpose

Background: Neck adiposity tissue volume (NATV) accumulation, is an indicator for metabolic syndrome and cardiovascular disease (CVD). Neck circumference is a poor measure of NATV, and a quantifier for this entity has not yet been established. Aim: To evaluate volumetric quantification by multidetector computed tomography (MDCT) as a reproducible anthropometric tool to measure NATV and airway volume (AWV), and to correlate these measurements with several comorbidities and overall mortality.

Materials and Methods

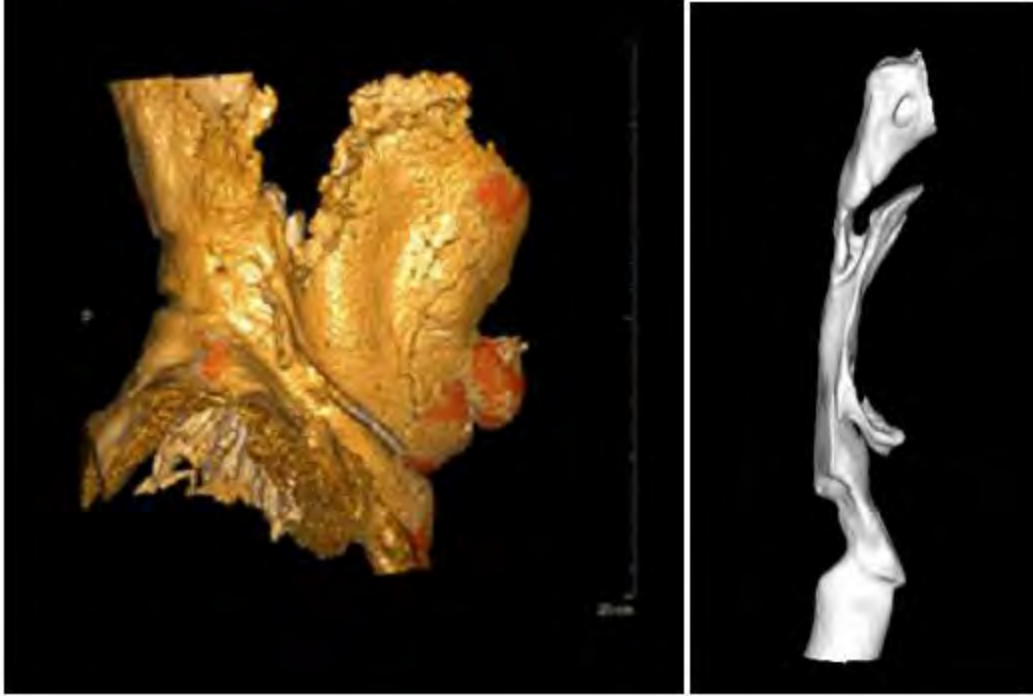
We retrospectively and volumetrically analyzed the neck fat and airways of all patients who underwent head and neck CT in our hospital within 1 year (2013). Included scans were all noncontrast CT (NCCT) and all CT angiography (CTA). Postprocessing 3-dimensional (3D) tissue reconstruction was performed on all patients' neck scans, and their cervical adipose tissue (CAT) and airway volumes (AV) were quantified volumetrically. Neck circumference was traced semi-automatically and expressed as cross-sectional area (mm²). Information on BMI, hypertension, and smoking was obtained, sleep apnea "STOPBANG" questionnaires were gathered.

Results

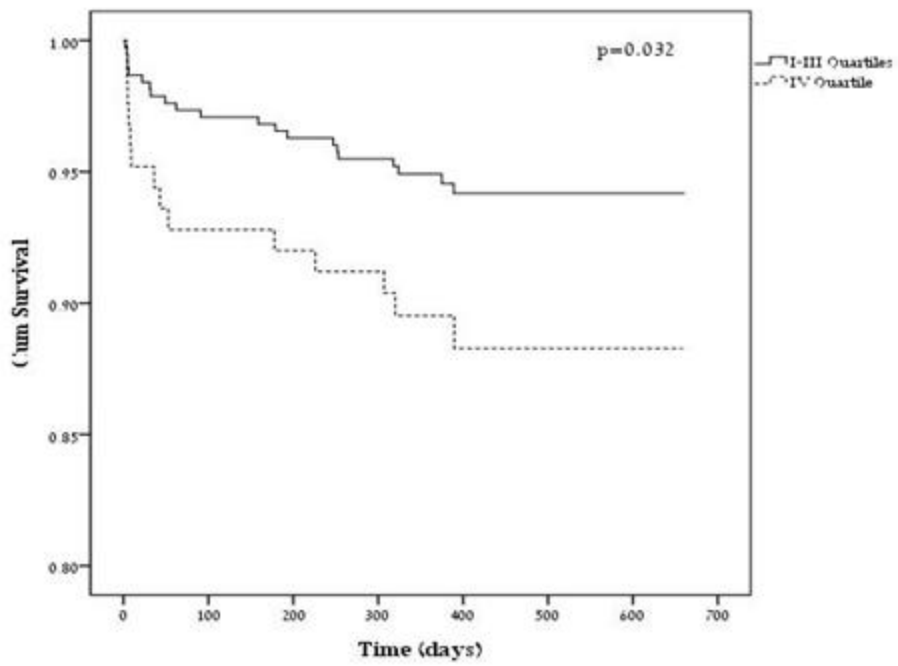
A total of 431 necks were analyzed, corresponding to the completed questionnaires, including 72 NCCT and 359 CTA. Subjects were grouped into three categories based upon STOPBANG score (0-2, 3-4, 5-8), with 135 considered "low risk" (43 NCCT, 92 CTA), 165 "intermediate risk" (18 CT, 147 CTA), and 131 "high risk" (11 CT, 120 CTA) for sleep apnea. Low risk STOPBANG subjects were at a median age of 49 years, with 9,928 mm³ NCSA, mean CAT:AV ratio of 21.3. Intermediate risk patients had a median age of 64 years, 14,388 mm³ NCSA, mean CAT:AV ratio of 32. High risk patients were at a mean age of 64 years, 16,147 mm³ NCSA, mean CAT:AV of 33.5. Mean CAT:AV by scan type, NCCT and CTA were 21.2 and 39.4, respectively (p<0.001). Patients were followed for 670 days, and the top quartile of all CAT:AV patients displayed a significant propensity for overall mortality (7.5%, p=0.032).

Conclusions

Patients with high CAT:AV ratios showed a higher likelihood to suffer from sleep apnea, display stroke-like symptoms on presentation, and a higher predilection for mortality. Further research is warranted to fully understand the anatomical relationship between cervical adiposity and airway volumes, specific comorbidities, and overall mortality. Volumetric quantification of NATV and AWV is a reproducible and prognostic anthropometric tool; future research may further advance our understanding of this phenomenon.



(Filename: TCT_O-418_3dreconstructioncervicaladiposityairway.JPG)



(Filename: TCT_O-418_mortalitycurve.JPG)

Thursday

8:35AM - 10:00AM

Washington Marriott Wardman Park, Roosevelt 1-3

20D-PARALLEL PAPER SESSION: Turbo Talks - Neurovascular Imaging

Advances

O-419

8:35AM - 8:38AM

Extracranial Carotid Artery Imaging and Intervention: Current trends in the U.S. Medicare Population from 2001-2013.

M Cox¹, D Levin¹, L Bagley², R Hurst³, L Parker¹, V Rao¹

¹Thomas Jefferson University, Philadelphia, PA, ²Pennsylvania Hospital, Philadelphia, PA, ³University of Pennsylvania, Philadelphia, PA

Purpose

The purpose of our study was to evaluate recent trends in extracranial carotid artery imaging and intervention from 2006 to 2013 in the Medicare fee-for-service population.

Materials and Methods

Data from the national Medicare part B Physician/Supplier Procedure Summary Master files were used for this study. The Medicare part B files represent the largest database of its kind on Medicare patients, and covers patients enrolled in traditional fee-for-service Medicare (37.3 million patients in 2013). Volume of CEA, CAS, and carotid ultrasound were studied by physician specialty from 2001-2013.

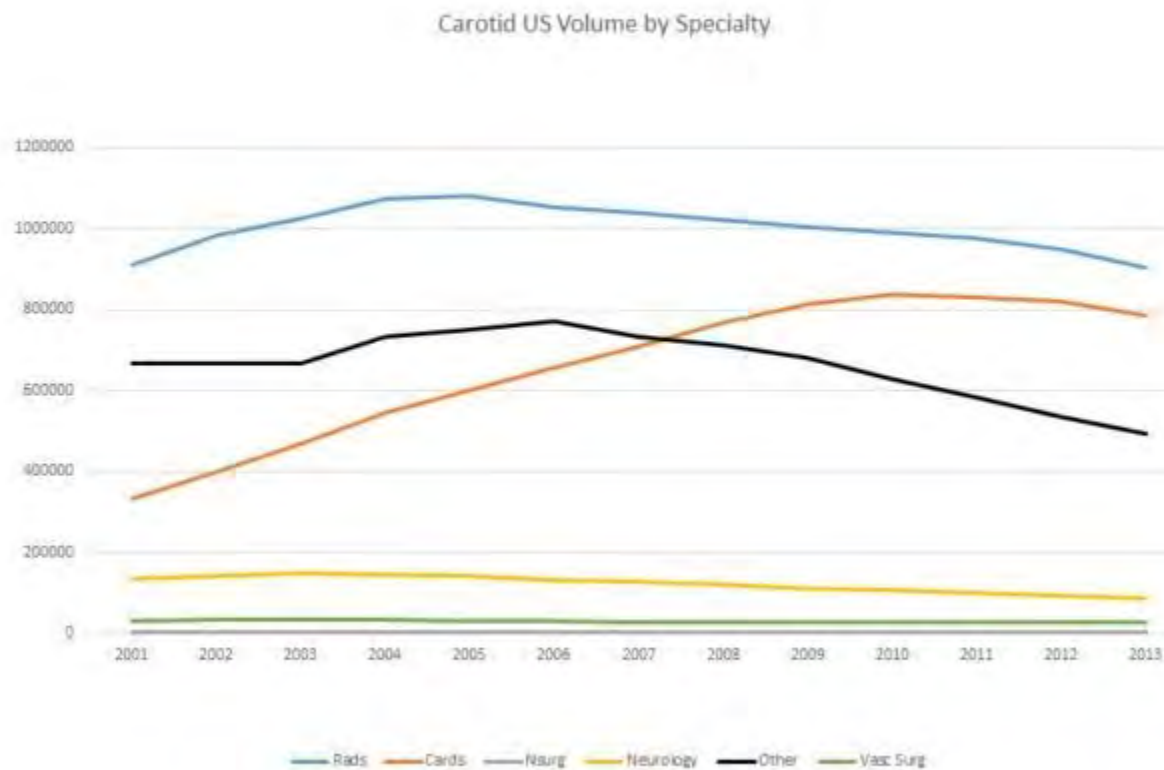
Results

Carotid ultrasound volumes increased from 2,293,866 in 2001 to 2,680,479 (17% increase) in 2013. Radiologists performed the largest number of carotid ultrasound studies, performing 903,688 or 34% in 2013. Cardiologists were the second largest group, performing 785,187 studies or 29% in 2013. Carotid endarterectomy volumes also are increasing: the total volume of carotid endarterectomy was 353,041 in 2001, rising to 445,221 in 2013 (an increase of 26%). Vascular surgeons perform most CEAs in the United States Medicare population, performing 408,173 surgeries in 2013 or 92%. The percentage of carotid endarterectomies performed by vascular surgeons also is increasing: vascular surgeons performed 73% of all carotid endarterectomy surgeries in 2001, increasing to 92% in 2013. Carotid artery stenting also is showing a trend towards an increase in the volume of procedures, with most CAS performed by cardiologists as shown in a recent publication (1).

Conclusions

The volume of extracranial carotid imaging and intervention is increasing.

Radiologists perform the majority of carotid ultrasound (34%), with cardiologists a close second (29%). Carotid endarterectomy appears to be the preferred method of revascularization in the U.S. Medicare population, and vascular surgeons performed 92% of these procedures in 2013.



(Filename: TCT_O-419_CUSvolume.jpg)

O-420

8:38AM - 8:41AM

CT- Angiography Evaluation of Acute Ischemic Stroke- Study From a Tertiary Care Hospital of North India

g_rastogi¹, S GROVER¹

¹*VARDHMAN MAHAVIR MEDICAL COLLEGE, SAFDARJUNG HOSPITAL, DELHI, INDIA*

Purpose

(1) To assess intracranial arterial circulation in acute ischemic stroke patients by computed tomography angiography (CTA). (2) To evaluate the impact of CTA diagnosis on management decisions.

Materials and Methods

Thirty consecutive patients clinically presenting with acute stroke and diagnosed as ischemic stroke on non-contrast CT (NCCT) within 6 hours of onset of symptoms were included in the study. Computed tomography angiography was performed in all patients immediately. Computed tomography angiography was analyzed for territorial distribution, plaques and arterial lumen stenosis. Patients were directed for emergency thrombolysis, carotid endarterectomy, carotid artery stenting and medical management as per CTA findings. Post-treatment 1-year clinical follow up was obtained.

Results

Young strokes were seen in 13% patients who were less than 40 years old with significant male predilection ($p=0.02$). Fifty-eight percent of patients were hypertensive with deranged lipid profile in 26% and diabetes in 12%. Atherosclerotic plaque was the most common etiology with 65% in extracranial segment of internal carotid artery (ICA) and both intracranial and extracranial segments of ICA in 42% patients. Seventy percent of patients were directed for emergency thrombolysis, out of which 46% had successful treatment with excellent clinical recovery. Seventy-five percent of patients had severe stenosis, among them 60% underwent carotid endarterectomy and carotid artery stenting. On one-year clinical follow up only 20% had recurrent attack. One patient with suspected tubercular vasculitis was treated with anti-tubercular therapy and had uneventful post-treatment for 1 year. Remaining were advised conservative medical management.

Conclusions

Computed tomography angiography provides rapid, noninvasive, life saving, comprehensive evaluation in acute stroke and contributes in definitive treatment planning. It reduces morbidity significantly and therefore can be recommended in the standard investigative protocol of this neurological catastrophe even in a developing country like India.

O-421

8:41AM - 8:44AM

International, Multicenter Phase 3 Blinded Study (GEMSAV) of the Structural Visualization, Diagnostic Efficacy and Safety of Gadobutrol (Gadavist) Enhanced MRA of the Supra-aortic Vessels compared to Time-of-Flight MRA using CTA as the standard of reference

E Melhem¹, D Haverstock², C Di Casoli², J Agris³

¹*Diagnostic Radiology and Nuclear Medicine, Baltimore, MD*, ²*Global Clinical Statistics, Bayer, Whippany, NJ*, ³*Bayer, Whippany, NJ*

Purpose

The purpose of the study was to compare the performance of a contrast-enhanced magnetic resonance angiography (CE-MRA) with gadobutrol, a high relaxivity, macrocyclic agent, to 2D time-of-flight (ToF) MRA using computed tomography angiography (CTA) as the standard of reference. Some key primary objectives were to evaluate the superiority for structural delineation and noninferiority for diagnosis of clinically significant vascular disease (50-99% stenosis).

Materials and Methods

Four hundred eighty-seven patients (mean age 68 years, 65% male) suspected of stroke or other supra-aortic disease underwent MRA with gadobutrol at a dose of 0.1 mmol/kg and ToF as well as CTA. The evaluations were based on central blinded read (BR) by three radiologists and investigator reads of the 21 supra-aortic vessel segments including the carotid and vertebral arteries. Exact vessel/stenosis measurements were performed.

Results

Gadobutrol-enhanced MRA demonstrated statistically significant improvement in visualization of vascular segments when compared to ToF 95.0% versus 72.7% ($P < 0.0001$). In the BR, noninferiority for sensitivity was shown for gadobutrol MRA (CE-MRA) compared to ToF MRA (60.1% versus 54.4%) as well as superiority for specificity (96.1% versus 87.3%). The sensitivity improved by 5.7% with CE-MRA and the specificity improved significantly by 8.8%. The corresponding values for the site evaluation were 60.9% sensitivity for CE-MRA and 39.1% for ToF MRA, demonstrating superiority, and 98.1% specificity for CE-MRA versus 89.0% ToF MRA. The gadobutrol MRA vessel measurements were more precise than those in the ToF MRA (0.01mm gadobutrol versus 0.29mm ToF for error in stenosis measurements) shown in Fig 1. Relatively fewer vertebral stenoses were present, but sensitivity was similar to that of the larger carotid arteries. In addition, diagnostic confidence increased and fewer additional imaging studies were recommended with gadobutrol-enhanced MRA.

Conclusions

Gadobutro-enhanced MRA was superior to 2D ToF MRA for delineation of the vascular segments as well as exclusion of disease. Furthermore it showed high accuracy with minimal error in the vascular measurements (Fig. 1). Gadobutrol-enhanced MRA of the supra-aortic vessels has superior visualization, more accurate measurements and is a valuable alternative to CTA without any ionizing.

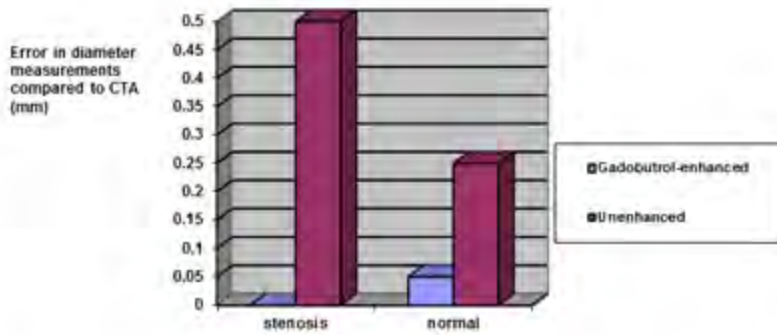


Figure 1: Difference in GEMSAV mean vessel diameter between CTA and (gadobutrol-enhanced or unenhanced) MRA

(Filename: TCT_O-421_ISMRM2016GRAMSFigure1.jpg)

O-422

8:44AM - 8:47AM

Exploring Other Vascular Dimensions: Comparison of 3-dimensional vs. 2-dimensional Vessel Wall Imaging Techniques for the Evaluation of Large Artery Vasculopathies

M Mossa-Basha¹, M Alexander², J Maki³, W Cohen¹, D Hippe¹, H Huhdanpaa¹, C Yuan¹, T Saam⁴

¹University of Washington, Seattle, WA, ²University of California San Francisco, San Francisco, CA, ³university of Washington, Seattle, WA, ⁴Ludwig-Maximilians-Universität München, Munich, Munich

Purpose

Takayasu and giant cell arteritis are chronic, inflammatory large artery vasculopathies (LAV), that necessitate early diagnosis as prompt initiation of treatment can prevent or delay the onset disease-related morbidities including blindness, limb ischemia, and hemorrhage secondary to chronic vessel stenosis, occlusion, aneurysm formation, and the harmful side-effects of overtreatment in later stage disease. Unfortunately, early detection is difficult due to the vague nonspecific clinical presentation and lack of early luminal imaging findings. There has been a recent focus on MR vessel wall imaging techniques (VWI) to establish vessel wall involvement by the presence or absence of enhancement indicative of active inflammation (1-5). This study performs a quantitative and qualitative comparison between a modified 3D T1 VISTA with EKG gating and breathing navigation and 2D T1 double inversion recovery (DIR) black blood imaging of the upper thoracic aorta and cervical arteries to determine the differential quality of each technique in patients referred for suspicion of LAV.

Materials and Methods

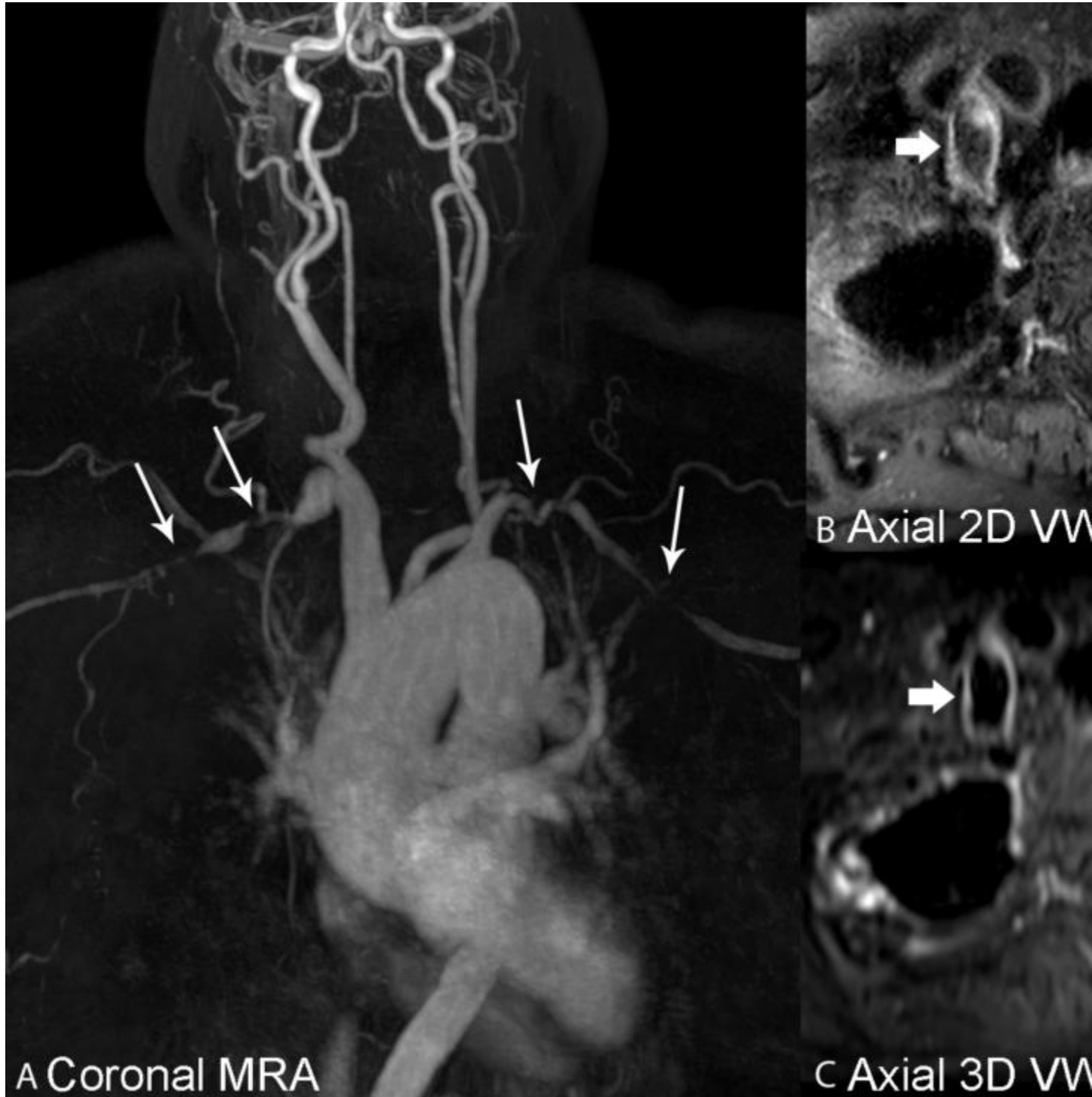
Patients referred for potential LAV who received both modified 3D T1 VISTA with EKG gating and breathing navigation and 2D VWI MRI w/wo contrast were included. Two dimensional and 3D sequences were performed in random order after contrast. Blinded independent review was performed by two radiologists. Blood signal suppression, image quality and diagnostic confidence each were rated using a four-point scale. The ratings from each radiologist were averaged for the data analysis. A separate rater evaluated vessel wall and soft tissue signal to noise ratio (SNR) and contrast to noise (CNR) for cervical and aorta images for both techniques. Two-tailed paired t-tests were performed to compare differences between 2D and 3D techniques.

Results

Eight patients were included. Cervical arteries were imaged in all patients while the superior thoracic aorta was imaged in six of eight. Two dimensional VWI demonstrated significantly increased SNR and CNR of the vessel wall (.031 and .026) for images of the cervical arteries. Three dimensional images had better soft tissue SNR (p=.005) for the thoracic aorta. Blood suppression, overall image quality and diagnostic confidence ratings of the cervical images were significantly higher for the 3D versus 2D images. For the aorta, blood suppression and image quality ratings were significantly higher for the 3D versus 2D images, with a trend towards higher diagnostic confidence (p=0.054). Three dimensional provided increased coverage relative to 2D imaging. Three dimensional VWI scan time was shorter compared to 2D VWI.

Conclusions

Three dimensional VWI for evaluation of LAV should be a clinical consideration based on radiologist-perceived advantages and improved coverage in a shorter scan time.



(Filename: TCT_O-422_Figure1copy.jpg)

Non-Contrast, Inflow Enhanced Inversion Recovery with 3D Fast Spin Echo (IFIR-FSE) with Fast Image Acquisition using Compressed Sensing (CS) technique has potential to be a Viable Alternative to Contrast-Enhanced MRA (CE-MRA) for the evaluation of neck vasculature.

S Lee¹, M Qandeel¹, C Yang¹, S Ali¹, K Jahangir¹
¹University of Chicago Medical Center, Chicago, IL

Purpose

To evaluate the image quality of the neck vasculature with inflow-enhanced inversion recovery with 3D fast spin echo (IFIR-FSE) with compressed sensing (CS) technique, a noncontrast magnetic resonance angiography (MRA) technique.

Materials and Methods

This study was approved by institutional IRB. Six patients who consented to participate were included. Contrast-enhanced MRA (CE-MRA) and IFIR-FSE 3D MRA with combinations of two set of inversion recovery time and three sets of compressed sensing (CS) were obtained on a 1.5T scanner (Optima MR450w, GE) [A (TI=1600, CS=1.0), B (TI=1600, CS=1.5), C (TI=1600, CS=2.0), D (TI=2000, CS=1.0), E (TI=2000, CS=1.5), and F (TI=2000, CS=2.0)]. Three board-certified neuroradiologists blindly reviewed the anonymized image sets using a third party viewer (Visage7®, Visage Imaging, CA, USA). Arterial segments for the semiquantitative image quality assessment included: aortic arch, brachiocephalic trunk, left subclavian artery and bilateral CCAs, ICAs and ECAs. The scoring scale used for image quality assessment was: 4 (excellent; sharply defined arterial borders, diagnostic), 3 (good; minor inhomogeneities not influencing vessel delineation, diagnostic), 2 (fair; ill-defined vessel borders with suboptimal quality, nondiagnostic) and 1 (poor; barely visible lumen, nondiagnostic). For quantitative image analysis, the contrast to noise ratio (CNR) was measured between the right CCA and adjacent soft tissue using $[(SI_v - SI_0)/SD_0]$ formula.

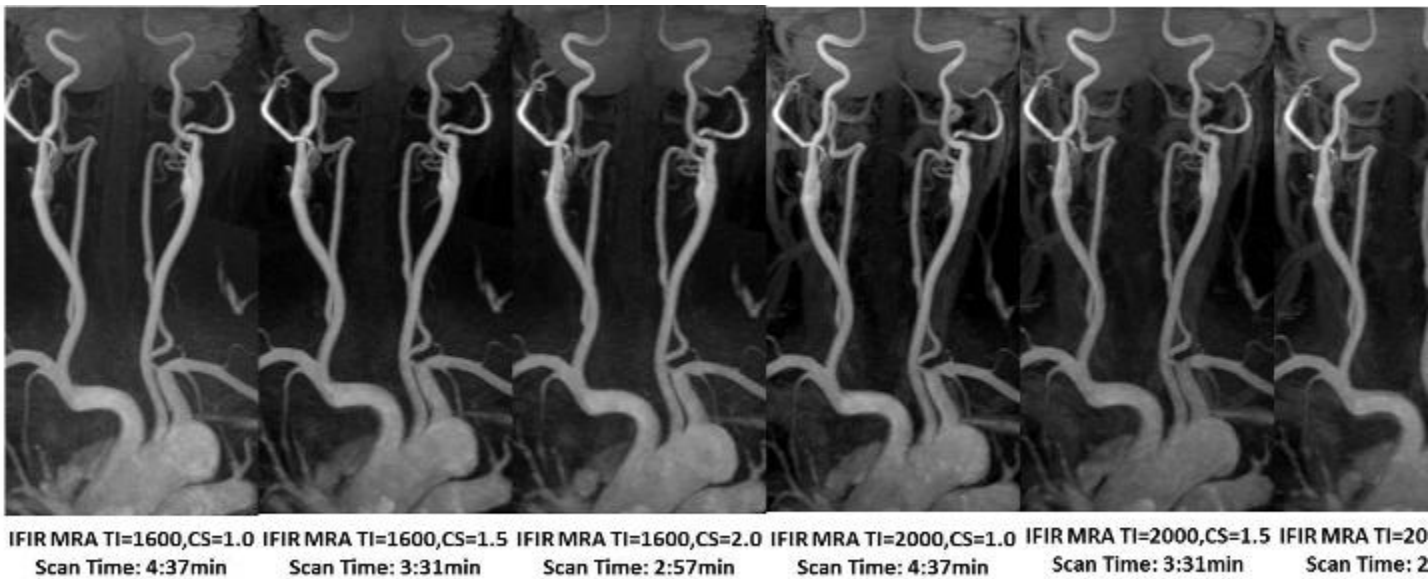
Results

A total of 37 MRA image sets in six patients were obtained. All IFIR-CS MRA image sets and CE-MRAs received a diagnostic quality score (3 or higher). Mean cumulative score for 10 vascular segments and mean scan times of A-F image sets were: A=3.86 (4:37min), B=3.86 (3:31min), C=3.82 (2:57min), D=3.83 (4:37min), E=3.84 (3:31min), F=3.85 (2:57min) and CE-MRA=3.78 (1:03min). All IFIR-FSE MRAs did not show a statistically significant difference in CNR compared to CE-MRA except image set F which showed better CNR than CE-MRA.

Conclusions

Noncontrast-enhanced neck MRA using IFIR-FSE with CS technique demonstrates

high quality images comparable to CE-MRA in reasonably short acquisition time. Considering the benefits of avoiding gadolinium, this technique has potential to be a viable alternative to CE-MRA for the evaluation of neck vasculature.



(Filename: TCT_O-423_figure1.jpg)

O-424

8:50AM - 8:53AM

Reducing Radiation Exposure and Optimizing Cervicocerebral CT Angiographic Quality in Acute Stroke Patients

J Jordan¹, Y Jordan², K Ragland³, J McPherson⁴

¹Providence Little Company of Mary Medical Center, Torrance, CA, ²Washington University St. Louis School of Medicine, St. Louis, MO, ³Long Beach Memorial Medical Center, Long Beach, CA, ⁴Providence Little Company of Mary Medical Center, Marina Del Rey, CA

Purpose

To assess the radiation dose exposure using various computed tomography angiography (CTA) protocols for brain and neck imaging in the diagnosis of acute stroke; and to assess the image quality and optimize protocols by reducing the radiation dose, while maintaining diagnostic efficacy.

Materials and Methods

Computed tomography angiography was performed of the brain and/or cervical carotid arteries as part of an institutional acute stroke management protocol. Seventy-two patients were evaluated and separated into four groups based on variations in tube voltage. KVPs of 135, 120, 100, and 80, (groups 1-4 respectively) were utilized while holding MAS constant. Image quality was assessed quantitatively and qualitatively.

Regions of interest (ROIs) were used to determine maximal vascular enhancement across groups, and calculate signal to noise (SNR) and contrast to noise (CNR) ratios. Effective radiation doses also were calculated for each study. The image quality was also graded qualitatively on a 5 point scale (1=non-diagnostic, 5= excellent diagnostic quality) by two experienced readers. Statistical analysis of the results was performed using analysis of variance (ANOVA) and nonparametric inferential methods. Interobserver agreement also was tested applying Cohen's kappa statistical measures.

Results

Compared with group 1(140 kvp), the effective dose was 4.3 times higher than group 4 (80 kvp). The effective dose of group 1 was also 1.4 and 2.2 times higher than group 2 (120 kvp), and group 3 (100 kvp) respectively. Visual image scoring showed excellent concordance between readers ($k= 0.89$, SE .04, $p< .001$), with good to excellent diagnostic quality consistently demonstrated for groups 1-3, and fair to poor quality consistently shown for group 4. Mean signal to noise and contrast to noise ratios were lowest for group 4 versus group 1, but comparable between groups 1, 2, and 3, despite incremental increases in noise for the lower kvp groups ($p<.0001$).

Conclusions

Substantial reductions in patient radiation exposure for cervicocerebral CTA can be achieved by reducing tube voltage to as low as 100 kvp, without compromising image quality. At 100 kvp, a 55% reduction of radiation dose was calculated versus 27% for the 120 kvp group, but as both protocols demonstrated good to excellent image quality, the 100 kvp protocol was deemed superior because of the greater radiation exposure reductions achieved.

O-425

8:53AM - 8:56AM

Radiation Dose Reduction in 4-dimensional Intracranial CT angiography by Individualized Estimation of Cerebral Circulation Time

M Radon¹, A Chandran¹, M Bhojak¹, K Das¹

¹*The Walton Centre, Liverpool, United Kingdom*

Purpose

Four-dimensional computed tomography angiography (4D-CTA) provides a noninvasive technique for dynamic assessment of the intracranial vessels. Its use has been limited by a high radiation dose. Prior descriptions of the technique use a fixed exposure time protocol of up to 22 seconds. This study examines the potential for dose reduction by individualizing exposure time to patient physiology with the use of recently described time-enhancement curve techniques for CT angiography and venography.

Materials and Methods

Four dimensional CTA examinations performed at our institution were retrospectively reviewed. Two imaging techniques were compared. Method 1 determined start of exposure from peak arterial enhancement and exposure duration was based on radiologist discretion. Method 2 used dual arterial and venous time-enhancement curves from which exposure start time and duration were measured. Data were reconstructed at 500 ms intervals for both methods with method 1 using 750 ms temporal resolution, and method 2 1000 ms with reduced tube current.

Results

One hundred fifty-two examinations were completed using method 1, and 55 with method 2. Method 2 acquired fewer total volumes (method 1: 31, method 2: 19; $p < 0.05$) representing a reduction in exposure time of 39%, fewer precontrast arrival frames (6 versus 1; $p < 0.05$), fewer postvenous phase frames (2 versus 0 ; $p < 0.05$) but had reduced peak venous enhancement (370 versus 324 HU; $p = 0.019$). Subjective quality score was not different between groups 4.7 versus 4.8 ($p = 0.29$). Studies with inadequate temporal coverage were 11 (7.2%) in method 1 versus 2 (3.8%) in method 2. Positive finding rate was not different between studies 36.2% versus 36.5% ($p = 0.63$). Mean dose-length product was 2993 mGy.cm in method 1 and 1508 mGy.cm in method 2.

Conclusions

Exposure time in 4D-CTA can be reduced by use of a dual arterial-venous time-enhancement curve method to match exposure to patient physiology without degrading study adequacy. Subjective study quality was not reduced by the use of the lower temporal resolution technique, suggesting that a higher temporal resolution may not be justifiable against radiation dose.

O-426

8:56AM - 8:59AM

Usefulness of carotid wall imaging for early detection of carotid plaque and intraplaque hemorrhage as a screening tool for outpatients

H KWAK¹, S Jeon², G Chung³

¹Chonbuk National University Medical School and Hospital, Jeonju-si, Korea, Republic of, ²Wonkwang University School of Medicine & Hospital, Iksan, AZ, ³Chonbuk National University Medical School and Hospital, Jeonju-si, Korea

Purpose

To assess the usefulness of carotid magnetization-prepared rapid acquisition with gradient-echo (MPRAGE) added to routine contrast-enhanced carotid magnetic resonance angiography (CE-MRA) as a screening tool for early outpatient detection of carotid plaque and intraplaque hemorrhage (IPH).

Materials and Methods

From November 2012 to November 2014, we recruited 1737 outpatients evaluated with carotid MPRAGE and CE-MRA for detection of carotid plaque and IPH. A carotid plaque was defined as wall thickness greater than 2 mm in at least two consecutive slices of the carotid artery on MPRAGE imaging. Intraplaque hemorrhage was defined as carotid plaques with high signal intensity on MPRAGE more than 200% that of the adjacent wall. The location of IPH within the carotid artery was divided into three areas: common carotid artery (CCA), carotid bifurcation, and internal carotid artery (ICA).

Results

Among the studied population, 291 carotid plaques of 226 subjects (1.3%) were detected on MPRAGE imaging. Of these patients, 146 carotid plaques (50.2%) of 118 subjects (52.2%) demonstrated MR-positive IPH. Among the carotid plaques, 101 (34.1%) had normal angiographic findings on CE-MRA. In 43 of the carotid plaques, IPH was detected in subjects with normal angiographic findings on CE-MRA. Among subjects with IPH in the CCA, 29 (90.6%) had normal angiographic findings on CE-MRA. Normal angiographic findings on CE-MRA were significantly more common in subjects with CCA IPH than in patients with ICA IPH.

Conclusions

Carotid MPRAGE imaging is a useful screening tool for the early detection of carotid plaque and IPH.

O-427

8:59AM - 9:02AM

Vulnerable Carotid Plaque Imaging and Histopathology Without a Dedicated MRI Receiver Coil

N Berkovitz¹, L Fitzpatrick², N Majeed¹, M dos Santos³, R Glikstein¹, S Chakraborty¹, J Venoit¹, G Stotts¹, A Berthiaume¹, R Chatelain¹

¹The Ottawa Hospital, Ottawa, Ontario, ²The University of Ottawa, Ottawa, Ontario, ³The Ottawa Hospital, Ottawa, Ontario

Purpose

Stroke is associated with vulnerable carotid artery plaques showing specific histopathologic characteristics, namely a lipid-rich necrotic core, intraplaque hemorrhage, and thin fibrous cap. While ultrasound (US) and computed tomography (CT) can accurately identify carotid plaques and determine the extent of stenosis, magnetic resonance imaging (MRI) can further delineate plaque vulnerability. We examined the imaging and histopathology for three patients with symptomatic carotid plaques to determine whether these vulnerable features can be detected on MRI without a dedicated receiver coil.

Materials and Methods

Three patients presenting with symptomatic carotid artery plaques with 50-70% stenosis on US underwent CT angiography and MRI, followed by carotid endarterectomy and en-bloc excision of the plaque. A dedicated MRI receiver coil was not used.

Results

All three patients were found to have vulnerable carotid plaque features on histopathologic examination. Computed tomography and ultrasound were used to localize the plaques and assess the degree of stenosis. Vulnerable plaque characteristics were easily identifiable on MRI without a dedicated receiver coil in all three cases. The pre and postcontrast T1W sequences were most useful for identifying the lipid-rich necrotic core and thin fibrous cap, respectively. Plaque ulceration was best appreciated on CE-MRA. Direct comparison of TOF and CE-MRA allowed for distinction of hemorrhage from gadolinium. Overall, the 3T images had superior spatial and contrast resolution compared to the 1.5T images for all sequences.

Conclusions

While US and CT can identify carotid artery plaques, MRI allows for further characterization of vulnerable plaques in moderately stenotic vessels without the use of a dedicated receiver coil. Magnetic resonance imaging has great potential to be used for noninvasive risk stratification given its widespread availability, especially in resources limited centers. Future studies on plaque vulnerability and risk stratification should consider MRI for routine clinical use.

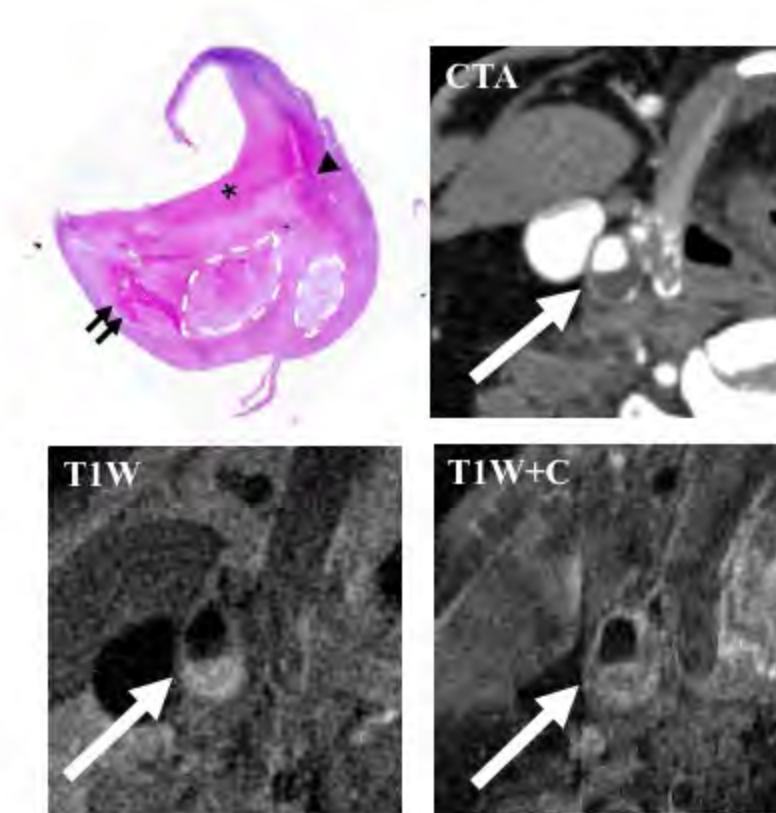


Figure 1: Histopathology of a large plaque in the right common carotid artery (*arrows*) with corresponding CTA and pre- and post-contrast T1W images. Vulnerable carotid plaque features on histopathology include a lipid-rich necrotic core (*dotted lines*), calcification (*arrowhead*), thin fibrous cap (*asterisk*) and small area of intraplaque hemorrhage (*double arrows*). The lipid-rich necrotic core and thin fibrous cap can also be identified on the pre- and post-contrast T1W images.

(Filename: TCT_O-427_ASNRfigure.jpg)

O-429

9:05AM - 9:08AM

Doppler Parameters to Distinguish High Velocity Carotid Near Occlusion from Conventional Stenosis.

S Khangure¹, R Aviv², A Fox³, C Grönlund⁴, A Sjöberg⁴, P Wester⁴, E Johansson⁴
¹University of Toronto, Toronto, Ontario, ²Sunnybrook and Women's College HSC, Toronto, ON, ³Sunnybrook Health Sciences Centre, Toronto, ON, ⁴Umeå University, Umea, Umea

Purpose

Carotid near occlusion is full (Fig. A) or partial (Figs. B-D) collapse of the internal carotid artery (ICA) lumen distal to a tight stenosis. Near occlusions are known from prior study to vary from severe stenoses in criteria for stroke-prevention treatment. Although a tight carotid stenosis with very low or unmeasurable flow velocity is

specific for near-occlusion, the majority of near-occlusions have high peak systolic flow velocities (PSV), mimicking conventional 50-99% carotid stenosis. We aimed to explore if Doppler parameters other than PSV can be used to distinguish near-occlusion and conventional stenoses.

Materials and Methods

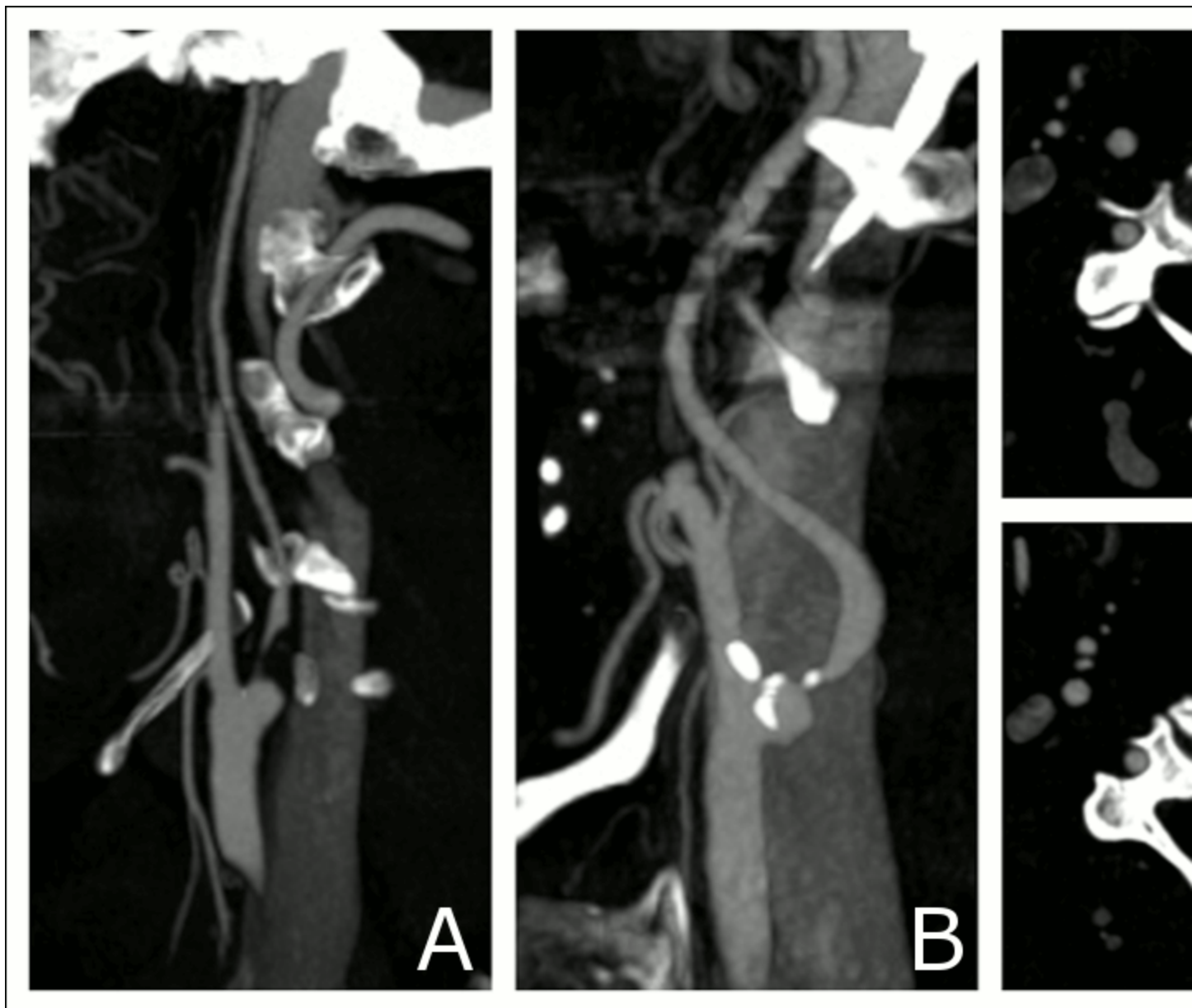
Dual-site retrospective study. Patients were included (n=84) if they had near occlusion or conventional 50-99% stenosis, a carotid Doppler and carotid CT angiogram performed within 30 days of each other, and a PSV of > 150 cm/second in the stenosis. Computed tomography angiograms were reviewed by two blinded expert readers. Velocity measurements in the ICA stenosis and mid common carotid artery (CCA) were recorded. Mean velocity, pulsatility index and ratios were calculated, giving 12 Doppler parameters for analysis.

Results

Of the 84 patients, 49 had conventional stenosis and 35 had near-occlusion on CT angiography. Of the 12 Doppler parameters, nine significantly differed between the near-occlusion and conventional stenosis groups. No single parameter had a high sensitivity and specificity for diagnosing near-occlusion. Several combinations of variables increased sensitivity and specificity. The best combination was pulsatility index of the ICA stenosis (>1.7) and end-diastolic velocity (EDV) ratio (EDV stenosis/EDV CCA) (>7.1) as it could distinguish near-occlusion from conventional stenosis with a sensitivity of 94% and a specificity of 58%.

Conclusions

Near-occlusion may be distinguished from conventional stenosis using Doppler parameters other than PSV. This can improve management decisions for overlooked cases. Optimal parameter combination and threshold values need to be validated before clinical use.



(Filename: TCT_O-429_nearocclusion.gif)

O-430

9:08AM - 9:11AM

Carotid Artery Web and Ischemic Stroke: A Case-Control Study

D Mandell¹, J Coutinho², S Derkatch¹, A Potvin¹, L Casaubon¹, F Silver¹

¹University Health Network, Toronto, Toronto, Ontario, ²Academic Medical Center, University of Amsterdam, Amsterdam, The Netherlands

Purpose

A carotid artery web is a thin shelf of fibrous tissue that extends from the wall of the

carotid artery into the lumen. The lesion is likely developmental in origin. It has been hypothesized that blood stasis along the downstream surface of a web may lead to thrombus formation and thromboembolic stroke (1). However, evidence of an association between carotid web and ischemic stroke has been only anecdotal. We conducted a case-control study to determine whether carotid artery web is a risk factor for ischemic stroke.

Materials and Methods

Patients with ischemic stroke of undetermined etiology (TOAST definition) (2), in a unilateral internal carotid artery territory, were identified from a prospective registry of stroke patients admitted between January 2012 and March 2015. Control subjects were identified from a prospective registry of patients admitted with a brain arteriovenous malformation, cerebral aneurysm, or primary intracerebral hemorrhage during the same time period. Additional inclusion criteria were age under 60 years, and computed tomography (CT) angiography of the neck during admission. A neuroradiologist diagnosed carotid webs according to published criteria (1). We tested for differences in age and sex between groups using a Student's t-test and chi-square test, respectively. We report the strength of association between carotid artery web and ischemic stroke as an odds ratio with 95% confidence interval (CI). We used logistic regression to adjust for age and sex, and also report the adjusted odds ratio.

Results

Sixty-two patients with cryptogenic ischemic stroke and 219 control subjects were included. Control subject diagnoses were aneurysm (n=160), arteriovenous malformation (n=38), or primary hemorrhage (n=21). Patients with stroke were older (mean age 49 versus 45 years; p=0.004) and had a lower proportion of women (34% versus 60%; p<0.001) than controls. A carotid web was present in 8.1% (5/62) of cases compared with 0.9% (2/219) of controls (unadjusted OR = 9.5, 95% CI = 1.8 to 50.3). After adjusting for age and sex, the association remained statistically significant (adjusted OR = 13.7, 95% CI = 2.4 to 78.6). In all five cases with a carotid web, there was a web located in the artery supplying the territory of the stroke. Three patients also had a contralateral web. NIH Stroke Scale scores ranged from two (minor stroke) to 21 (severe stroke).

Conclusions

There is an association between carotid artery web and ischemic stroke in patients who lack an alternative cause of stroke. Carotid web is likely an under-appreciated risk factor for stroke.

O-431

9:11AM - 9:14AM

Silent Brain Infarction in Patients with Asymptomatic Carotid Artery Atherosclerotic Disease

H Baradaran¹, G Gialdini², G Askin², H Kamel¹, A Gupta¹

¹New York-Presbyterian Hosp/Weill Cornell Med Ctr, New York, NY, ²Weill Cornell Medical College, New York, NY

Purpose

Silent brain infarctions (SBIs), strokes in completely asymptomatic patients, confer a two-fold increased risk of incident stroke; however, their relationship with carotid atherosclerosis remains unclear. We tested the hypothesis that unilateral extracranial internal carotid artery (ICA) stenosis results in a greater prevalence of SBI in the cerebral hemisphere ipsilateral to ICA disease compared to the unaffected, contralateral side.

Materials and Methods

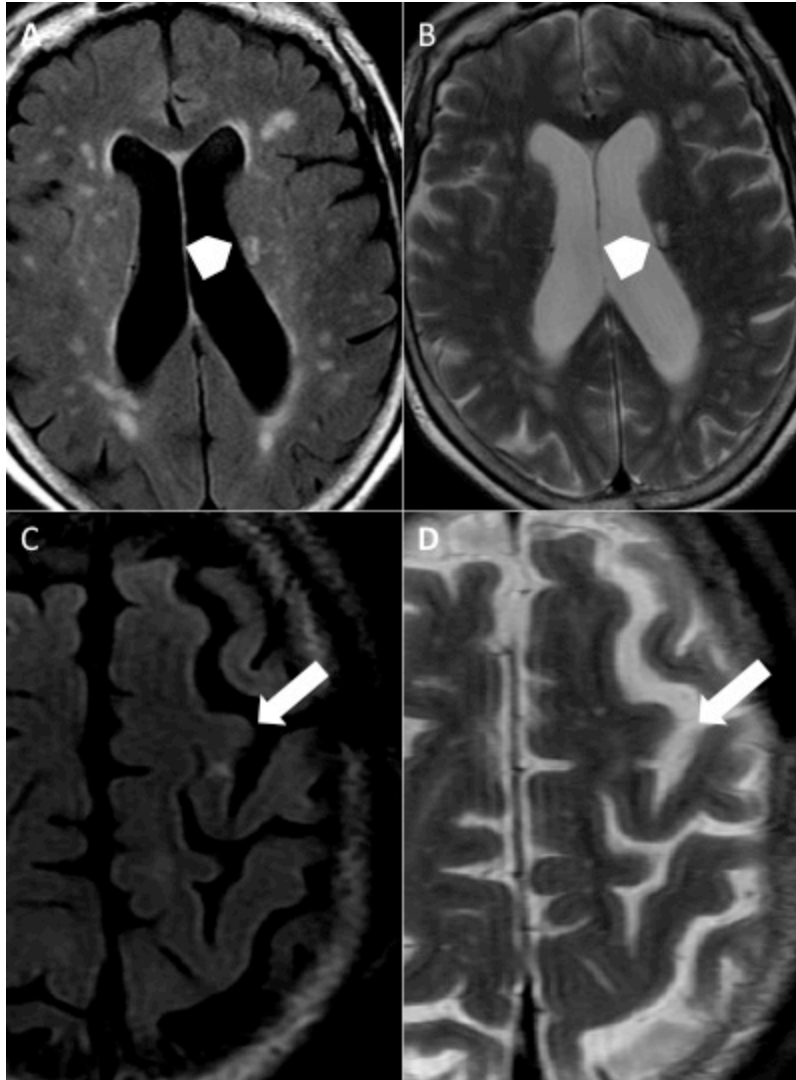
We identified patients with unilateral extracranial ICA stenosis $\geq 50\%$ on CT or MR angiography by NASCET criteria by screening studies from January 2008 through December 2014. We included patients who were asymptomatic without a prior history of stroke or transient ischemic attack and with a recent brain magnetic resonance imaging (MRI). While blinded to the results of angiographic imaging, we evaluated for presence of anterior circulation SBIs both ipsilateral and contralateral to the index diseased carotid artery. Silent brain infarction was defined as either a cavitory lacunar infarction in the white or deep gray matter (Fig. 1, A&B) or cortical infarction defined by T2 hyperintense signal in the cortical gray matter (Fig. 1, C&D). The Wilcoxon signed rank sum test was used to compare SBI downstream from ICA disease versus the unaffected side. Cohen's Kappa was used to assess inter-rater reliability of SBI assessment.

Results

Among the 104 asymptomatic patients with unilateral ICA disease causing luminal stenosis of $\geq 50\%$, we found a higher prevalence of SBIs ipsilateral to ICA disease (33%) compared to the contralateral side (20.8%)($p=0.0067$). There was no significant difference in the prevalence of the lacunar subtype of SBI (including both white and deep gray matter lacunar infarctions) between hemispheres ($p=0.109$), but there were significantly higher prevalence of cortical SBIs occurring downstream from ICA disease ($p=0.0045$). High inter-rater reliability was observed ($\kappa=0.818$).

Conclusions

Asymptomatic patients with ICA disease demonstrate higher prevalence of SBI downstream from their site of ICA atherosclerotic disease compared to the contralateral side, but only of the cortical and not lacunar SBI subtype. Our findings suggest that silent artery-to-artery embolism is responsible for a significant burden of silent brain infarctions in asymptomatic carotid disease. Further studies are warranted to determine whether these patients should be treated more aggressively with stroke prevention measures, including potential consideration of surgical revascularization procedures.



(Filename: TCT_O-431_ASNRabstractSBIfigure.jpg)

O-432

9:14AM - 9:17AM

Hemodynamic Changes Before and After Stenting Evaluated with Quantitative Digital Subtraction Angiography in Patients with Carotid Stenosis

M TENG¹, Y Kao², C Lin³

¹Cheng Hsin General Hospital, Taipei, Taiwan, ²National Yang Ming University, Taipei, Taiwan, ³Taipei Veterans General Hospital, Taipei, Taiwan

Purpose

The absolute and relative time to peak (TTP) were used in evaluation of hemodynamic changes in digital subtraction angiograms for patients with arterial

stenosis receiving stenting treatments. We studied more hemodynamic parameters for clinical application.

Materials and Methods

Digital subtraction angiograms of 35 patients with carotid stenosis receiving stenting treatments were analyzed retrospectively. Nine regions of interest (ROIs) were placed on the arterial and venous vessels on the PA and lateral views. Hemodynamic parameters including TTP, bolus arrival time (BAT), full width half maximum (FWHM), wash in (WI) slope, wash out (WO) slope, maximum enhancement (ME), and area under curve (AUC) were measured from the time-concentration curves of these ROIs. The dependent t-test for paired samples was applied to the parameters before and after the stenting treatment.

Results

We found that the stenting procedure significantly reduced TTP, BAT, FWHM, WO at all arterial ROIs and at some arterial ROIs for AUC. In addition to all arterial ROIs, BAT also showed significant difference in the venous ROIs including PV and SSS. The ME and WI did not show significant changes after the stenting treatment. The carotid stenosis caused in longer transit time not only at the segment containing the stenosis, but also in the distal intracranial segments.

Conclusions

In addition to TTP and rTTP, we found more hemodynamic parameters could be used for evaluation of the integrity of cerebral blood flow at arterial and venous vessels. Bolus arrival time has the potential to be used in future study of brain circulation at arterial and venous sites especially when TTP could not be measured because of incomplete time-concentration curve.

O-433

9:17AM - 9:20AM

ASL derived CBF Changes Post Carotid Intervention Predicts Post-Operative Cognitive Impairment

S Soman¹, W Dai², E Hitchner³, W Duan², P Massaband⁴, D Alsop¹, A Rosen⁵, W Zhou⁶

¹Harvard Medical School, BIDMC, Boston, MA, ²State University of New York at Binghamton, Binghamton, NY, ³Stanford University, Palo Alto Veterans Affairs Hospital, Palo Alto, CA, ⁴Stanford, Veterans Affairs Palo Alto Healthcare System, Palo Alto, CA, ⁵Stanford University, Veterans Affairs Palo Alto Health Care System, Palo Alto, CA, ⁶Stanford, Veterans Affairs Palo Alto Health Care System, Palo Alto, CA

Purpose

Carotid stenosis significantly increases the risk for stroke. Carotid revascularization

surgeries have been shown to reduce this risk, but also can be associated with cognitive impairment that is not clearly linked to cardiovascular risk factors or peri-operative complications (1-4). We performed baseline, 24 hours and 6 month postsurgery arterial spin labeling (ASL) brain cerebral blood flow (CBF) imaging, with baseline and 1 month postop neuropsychological testing to evaluate if CBF change patterns can predict cognitive impairment postsurgery.

Materials and Methods

Patient enrollment: Under institutional guidelines, 55 male veterans scheduled to undergo carotid intervention for a single carotid vessel (CAS or CEA) were enrolled. Seven of these subjects were re-enrolled in the study when undergoing surgery on the contralateral carotid vessel, for a total of 62 subjects. **Imaging:** Patients were imaged as part of a clinical acquisition using the product GE 3D PC-ASL imaging sequence (PLD=2.5 ms, 6-8 arms, 4-5mm slice thickness, 3-4 NEX) using a 3T MRI (Discovery MR 750 Software Rev. 23, GE Medical Systems, Milwaukee, WI, USA). Imaging was performed within a month prior to surgery (PRE), within 24 hours after surgery (POST), and again 6 months after surgery (6MO). **Neuropsychological**

Testing: All subjects underwent cognitive testing prior to and 1 month after surgery that included the Rey Auditory Verbal Learning Test (RAVLT), which is a measure of episodic memory recall for verbal information that tests encoding, consolidating, storing and retrieval of verbal information. **Image Analysis:** Cerebral blood flow maps were generated from product ASL images. Cerebral blood flow maps then were normalized using the method outlined by Dai et al (5). All images were flipped so the side of surgery was on the left, and then an 8 mm smoothing kernel was applied. Next GLMs were computed using SPM 8.

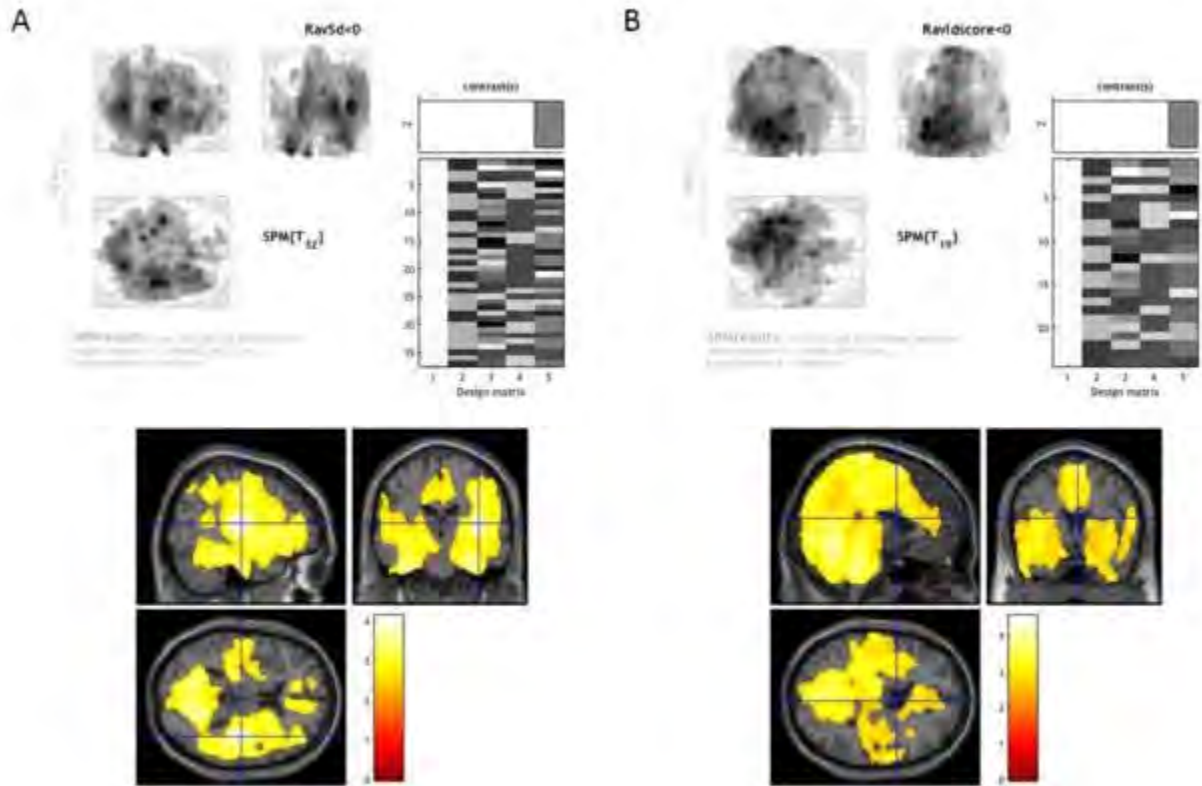
Results

PRE to POST: The cerebral hemisphere ipsilateral to the side of vessel repair experiences significant increased CBF, but less than the opposite hemisphere ($p=0.001$). CEA subjects also demonstrated significantly increased CBF on the hemisphere of vessel surgery compared to CAS ($p=0.05$) on PRE versus POST imaging. Lower increases in CBF from PRE to POST also were associated with greater decline at 1 month of RAVLT short delay. Lower increases from PRE to POST in CBF demonstrated a trend for decline at 1 month on RAVLT sum of trials ($p=0.093$). **POST to 6MO:** There was a significant decrease in CBF ($p=0.05$). **PRE to 6MO:** There was no significant difference in CBF ($p=0.05$). Demonstrating greater CBF increase from PRE to 6MO was associated with greater decline at 1 month on the RAVLT long delay ($p=0.05$). Additionally, greater increase in CBF from PRE to 6MO were associated with cognitive decline on the RAVLT long delay at 1 month ($p=0.05$).

Conclusions

Our finding that subjects with greater increase in CBF from baseline to 6 months after surgery is associated with greater decline on the 1 month RAVLT long delay exam

portion suggests that patients who do not normalize CBF back to presurgical levels may have impaired dynamic cerebral autoregulation.



ASL ce
(CBF) i
analys
A) lowe
from ba
after su
decline
and me
the RAV
portion
B) grea
from ba
after su
with gre
month
exam p

(Filename: TCT_O-433_Figure1.jpg)

O-434

9:20AM - 9:23AM

Correlation of Vitamin D levels with Quantitative Analysis of Carotid Intraplaque Hemorrhage and Local Vitamin D Receptor Expression

B Aldred¹, T Burton², M McLaughlin¹, S Kim¹, D Miller³, A De Havenon², D Parker¹, G Treiman¹, S McNally¹

¹University of Utah, Salt Lake City, UT, ²Univerity of Utah, Salt Lake City, UT, ³University of Utah, Intermountain Healthcare, Murray, UT

Purpose

Patients with carotid intraplaque hemorrhage (IPH) have a high stroke risk despite standard medical therapy. There is a critical need to identify new treatments in this

high-risk population. Vitamin D is an endogenous inhibitor of the angiotensin system, a known stimulator of IPH in animal models. Recently we found that low vitamin D was associated with carotid IPH. The purpose of this study was to build on initial results by evaluating the relationship between vitamin D level and carotid IPH volume quantitatively measured on MRI, and carotid IPH area calculated on histology and VDR receptor expression levels.

Materials and Methods

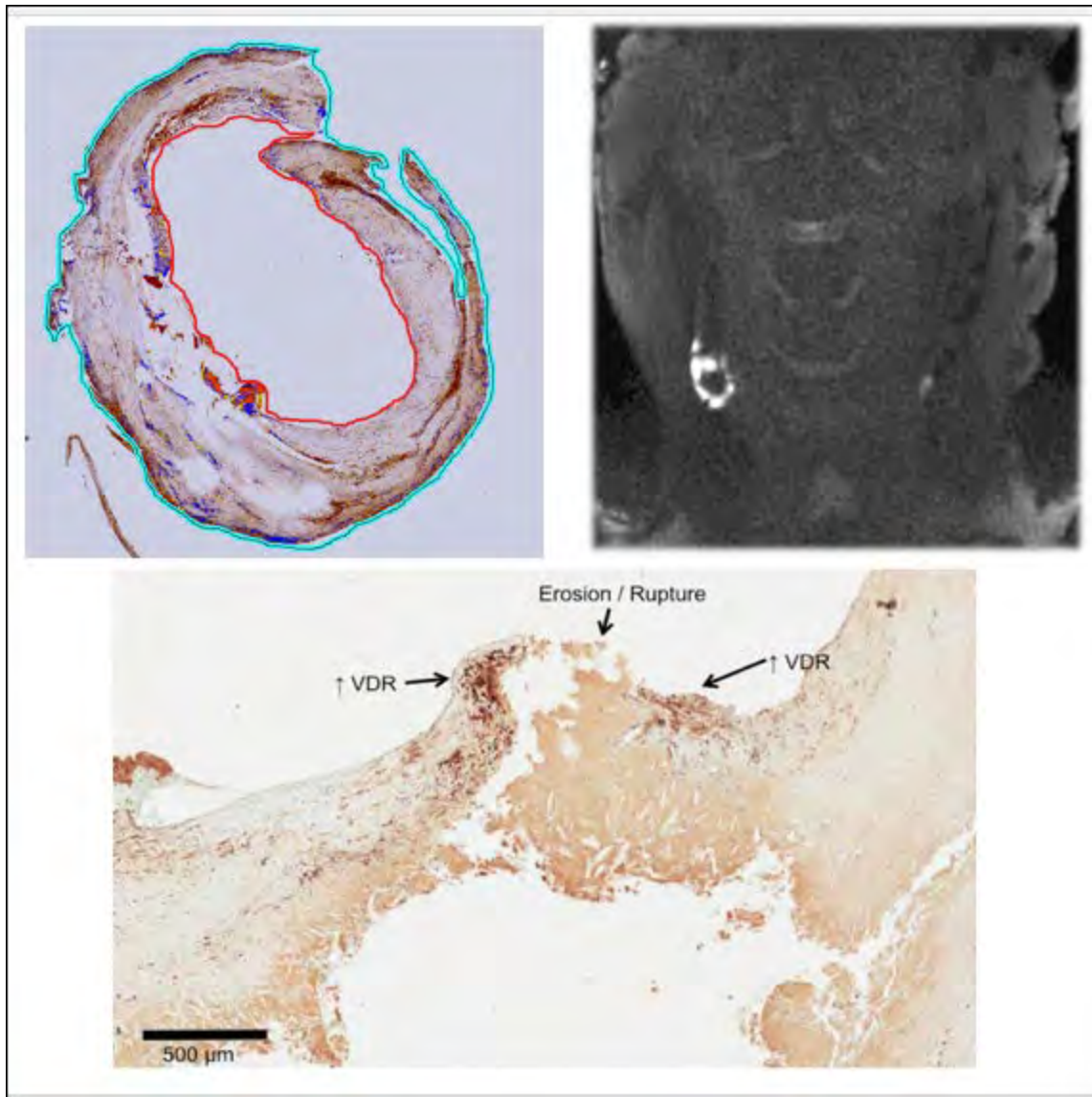
In this IRB-approved prospective cross-sectional study, 65 patients, with carotid disease were recruited for carotid MRI and vitamin D analysis. Intraplaque hemorrhage volume was determined quantitatively using a volumetric MPRAGE sequence. In addition, 35 underwent carotid endarterectomy and carotid IPH area was determined on histology and VDR counts were determined with quantitative immunohistochemistry. Linear regression was used to determine the association of vitamin D levels with carotid IPH volume, IPH area and VDR counts. To account for up to two carotid arteries per patient, we analyzed the in vivo MRI data using a multivariable GEE Poisson regression model. To account for multiple histologic sections per plaque, we used a repeated measures analysis accounting for data grouped within patients.

Results

Low vitamin D (<30ng/mL) was correlated significantly with MPRAGE-detected IPH volume ($r=0.26$, $p=0.003$) after adjusting for maximum plaque thickness. Low vitamin D also correlated with IPH area on histology ($r=0.22$, $p=0.03$) when adjusting for total plaque area. VDR expression was dependent on vitamin D level (normal versus low, $r=0.34$, $p<0.001$) when adjusting for plaque area. Representative images demonstrated VDR expression in areas of carotid plaque vulnerability.

Conclusions

Vitamin D levels are highly correlated with MRI-detected IPH, histology-detected IPH, and total VDR receptor counts. Notably, VDR is highly expressed in areas of vulnerable carotid plaque. Low vitamin D may be a contributing factor to vulnerable carotid plaque, and given local VDR expression, this may represent a potential prevention measure or treatment target against carotid IPH.



(Filename: TCT_O-434_Graphics.jpg)

Thursday

8:35AM - 10:03AM

Washington Marriott Wardman Park, Roosevelt 4

**20F-PARALLEL PAPER SESSION: Pediatrics: Brain Imaging Advances
O-435**

8:35AM - 8:43AM

LAMA1 mutation analysis in cerebellar dysplasia with cysts

A Poretti¹, A Micalizzi², M Romani², E Valente², E Boltshauser³

¹The Johns Hopkins University School of Medicine, Baltimore, MD, ²CSS-Mendel Institute, IRCCS Casa Sollievo della Sofferenza, Rome, MD, ³University Children's Hospital, Zurich, MD

Purpose

Cerebellar dysplasia with cysts and abnormal shape of the fourth ventricle, in the absence of significant supratentorial anomalies and of muscular involvement, defines recessively inherited Poretti-Boltshauser syndrome (PBS, OMIM 615960). Clinical features are also homogeneous and comprise nonprogressive cerebellar ataxia, intellectual disability of variable degree and language impairment, ocular motor apraxia and frequent occurrence of myopia or retinopathy. Recently, loss-of-function mutations in the LAMA1 gene were identified in six probands with PBS. We aimed to report the detailed clinical, neuroimaging and genetic characterization of 17 children with PBS from 14 unrelated families.

Materials and Methods

Information about neurological and cognitive functions were collected from review of the clinical history and follow-up examinations. All magnetic resonance imaging (MRI) studies were evaluated retrospectively for cerebellar structural abnormalities. LAMA1 sequencing analysis was performed in all children.

Results

At the last follow up at the mean age of 7.2 years (range 1.5 to 14.0 years), all children older than two years (n=16) had cerebellar ataxia. All patients but one (94%) had mild or moderate intellectual disability. Eye involvement was present in nine patients (53%), including myopia in eight (47%) and retinal dystrophy in four (24%). Cerebellar dysplasia with cortical-subcortical cysts were present in all children. Hypoplasia of the cerebellar vermis was found in 10 patients (59%). The fourth ventricle was enlarged in 14 children (82%) and elongated in 13 (77%). Biallelic LAMA1 mutations were identified in all families. Sixteen different mutations were identified, which were all novel. In particular, the frameshift mutation p.R979Gfs*4 recurred in six unrelated families on a shared haplotype, suggesting a founder effect.

Conclusions

There is a strong correlation between the clinical and neuroimaging phenotype of PBS and LAMA1 mutations. Brain MRI clearly points to the correct diagnosis of PBS by showing the peculiar association of cerebellar dysplasia, cerebellar cysts and abnormally shaped/sized fourth ventricle.

O-436

8:43AM - 8:51AM

White and gray matter abnormalities in children with LAMA2-related muscular dystrophy: more than meets the eye.

A Meoded¹, J Dastgir², A Vanderver³, A Poretti⁴, C Bonnemann²

¹National Institute of Neurological Disorders and Stroke/NIH, Baltimore, MD, ²National Institute of Neurological Disorders and Stroke/NIH, Bethesda, MD, ³Children's Research Institute, Children's National Health System, Washington, DC, DC, ⁴The Johns Hopkins University School of Medicine, Baltimore, MD

Purpose

LAMA2-related congenital muscular dystrophy (LAMA2-CMD) is caused by partial or complete laminin $\alpha 2$ deficiency. The affected children present with generalized hypotonia, muscle weakness and atrophy, and contractures. Qualitative evaluation of conventional magnetic resonance imaging (MRI) sequences typically show extensive, confluent, and nonprogressive white matter changes sparing the corpus callosum, internal capsule, brainstem, and cerebellum. To date no quantitative evaluation of white and gray matter structures has been reported in children with LAMA2-CMD. In this study, we assessed microstructural and volumetric changes of gray and white matter structures in children with LAMA2-CMD compared to age- and gender-matched controls.

Materials and Methods

We performed tract-based spatial statistics (TBSS) of fractional anisotropy (FA) and mean (MD), axial (AD), and radial diffusivity (RD) maps and voxel-based morphometry (VBM) of 3D-T1WI in children with genetically confirmed LAMA2-CMD and age-matched controls.

Results

Fifteen patients (median age 9.8 years) and 15 age- and gender-matched controls (median age 9.7 years) were included in this study. Tract-based spatial statistics revealed reduced FA and increased MD, AD, and RD in major supratentorial white matter tracts in patients compared to controls. In addition, FA and AD were reduced in cerebellar white matter tracts. Voxel-based morphometry showed reduced volume of cerebellum, basal ganglia, temporal operculum, and cingulate cortex in patients compared to controls.

Conclusions

Quantitative analysis of diffusion tensor imaging (DTI) data confirms extensive supratentorial white matter abnormalities in children with LAMA2-CMD. Changes in DTI metrics within the supratentorial white matter suggest demyelination as the underlying pathomechanism. Quantitative DTI analysis revealed changes of e.g. the cerebellar white matter that remained undetected by qualitative evaluation of conventional MRI sequences. Changes in DTI metrics suggest axonal degeneration as the underlying pathomechanism for cerebellar white matter abnormalities. In addition, VBM showed changes in volume of gray matter structures that may be caused by neuronal loss secondary to white matter disease.

O-438

8:59AM - 9:07AM

Interhypothalamic Adhesions: No Longer Just a Pediatric Finding

A Harrell¹, D Nascene¹

¹*University of Minnesota, Minneapolis, MN*

Purpose

Interhypothalamic adhesions are a recently described anatomical finding in which a connection of tissue can be visualized in the third ventricle connecting the hypothalami. Previous studies have suggested an association of these adhesions with midline abnormalities in pediatric patients. This study aimed to analyze interhypothalamic adhesions in a broader population to further understand its significance.

Materials and Methods

Retrospective review of 779 patients who underwent MRI for evaluation of hearing loss from 2008 to 2014 was performed. The patient ages ranged from 7 months to 95 years old. The presence of interhypothalamic adhesions was characterized, and clinical data were recorded.

Results

Interhypothalamic adhesions were identified in 41 out of 779 patients. The incidence in this patient population is higher than those previously estimated in the pediatric population. Furthermore, the presence of interhypothalamic adhesions could not be correlated with any disease state. This study did reveal three patients with more than one interhypothalamic adhesion.

Conclusions

There does not appear to be an association between interhypothalamic adhesions and midline abnormalities in a broader patient population. Interhypothalamic adhesions may represent an asymptomatic anatomical variant. The presence of interhypothalamic adhesions may be more common than previously estimated, approximately 5%. While certain variants of this anatomical anomaly appear to be more common, the significance of the type, size, and associated disease states remains unknown.



(Filename: TCT_O-438_abstractpicture.gif)

O-439

9:07AM - 9:15AM

Malformations of Cortical Development in HHT

G Palagallo¹, S McWilliams¹, A White², M Goyal¹

¹*Mallinckrodt Institute of Radiology, Washington University School of Medicine, Saint Louis, MO*, ²*Washington University School of Medicine, Saint Louis, MO*

Purpose

Since 2007, we routinely include a high resolution MPRAGE sequence on brain magnetic resonance images (MRIs) to evaluate children with hereditary hemorrhagic telangiectasia (HHT). The purpose of this study was to determine the incidence of malformations of cortical development (MCD) in children with HHT.

Materials and Methods

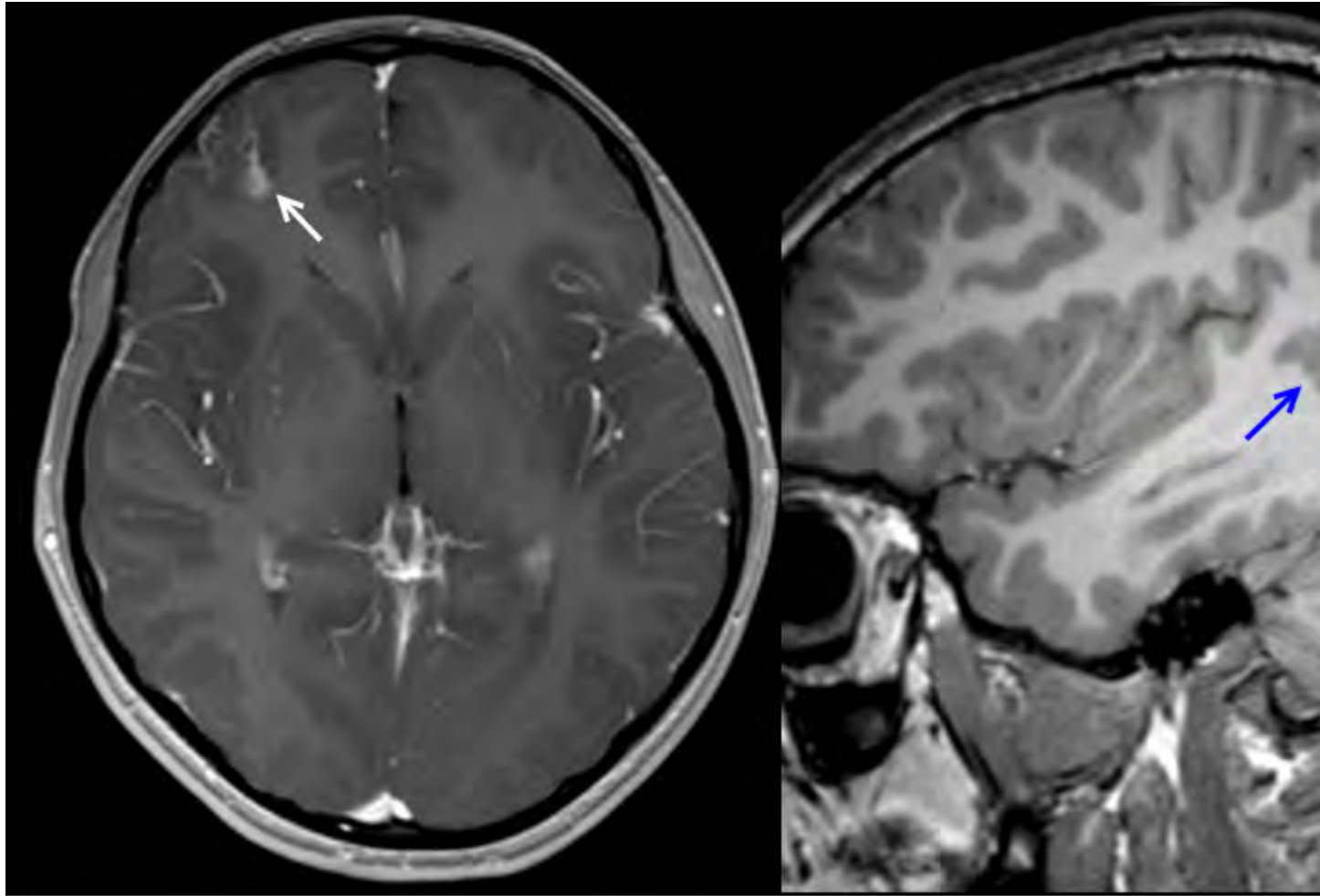
We identified 116 pediatric patients--being evaluated in the HHT Clinic at St. Louis Children's Hospital--who underwent a brain MRI that included at least one high resolution 3D sequence. Of the 116, 72 had definite HHT according to Curacao criteria. Each MRI was evaluated specifically for the presence or absence of MCD by a neuroradiology fellow. Positive cases then were confirmed by a board-certified neuroradiology attending.

Results

Fourteen of 116 (12.1%) patients were found to have MCD. Of the 14 positive cases, 13 had definite HHT by Curacao criteria, and one had possible HHT. There were 12 cases of polymicrogyria and two cases of bifrontal periventricular nodular heterotopia. Polymicrogyria was seen unilaterally in a perisylvian and parietotemporal distribution in 10 cases, and unilaterally in the frontal lobe in two cases. One case lined a large porencephalic cyst and another was adjacent to a previously resected arteriovenous malformation. Additionally, one patient had epilepsy.

Conclusions

When evaluated by a high resolution brain MRI sequence, children with HHT are found to have a high prevalence of MCD, most frequently polymicrogyria.



A

B

FIG 1. Polymicrogyria and an AVM seen simultaneously in an 11-year-old child with HHT. T1-post contrast axial image demonstrates a tangle of small vessels (*white arrow*) feeding a focus of ill-defined enhancement in the right frontal lobe (A). Coronal MPRAGE image demonstrates focally thickened and excessively convoluted cortex (*blue arrow*) in the right frontal lobe (B).

(Filename: TCT_O-439_AbstractFigureGJP.jpg)

O-440

9:15AM - 9:23AM

Predicting Motor Outcome after Hemispherotomy using Pre-surgical FDG PET

H Ullman¹, I Orosz², M Linetsky¹, G Mathern¹, N Salamon³

¹David Geffen School of Medicine at UCLA, Los Angeles, CA, ²UCLA, Los Angeles, CA, ³David Geffen School of Medicine at UCLA, Los Angeles, CA

Purpose

Hemispherotomy can be considered in patients with refractory seizures and multiple

onset zones. While the procedure is effective in controlling seizures, cognitive and motor deficits often are pronounced. In this study we aimed to predict the degree of motor deficit after hemispherotomy based on pre-operative FDG PET. A higher degree of hypometabolism was thought to be a positive predictor of outcome.

Materials and Methods

Materials: Nineteen patients went through FDG PET as part of their presurgical evaluation at UCLA medical center. The patients had refractory epilepsy on the basis of hemimegalencephaly, Rasmussen's encephalitis or perinatal infarction. Clinical motor outcome was graded as relative to presurgical functioning on a scale from -2 to +2 where negative values indicated worsening functioning and positive values indicated an increase in function. Motor function was divided into general motor function, upper limb function and gait function. **Methods:** A hemispheric ratio was calculated by dividing the FDG uptake in the affected hemisphere with the healthy hemisphere. This ratio represented the degree of hypometabolism in the affected hemisphere and thus the degree of hemisphere malfunction. The ratio subsequently was correlated with postsurgical motor outcome.

Results

The ratio of FDG PET hypometabolism correlated inversely with general motor outcome ($\rho=-0.67$, $p=0.001$) and gait ($\rho=-0.53$, $p=0.018$) but not with hand function ($\rho=-0.37$, $p=0.11$).

Conclusions

The degree of hypometabolism in the affected hemisphere is a strong predictor of motor outcome. A pattern with marked hypometabolism indicates tissue dysfunction prior to resection and predicts absence of new motor deficits. FDG PET is a good tool for predicting new motor deficits after hemispherotomy.

O-441

9:23AM - 9:31AM

Morphometric Measurements of the Thalamus in the Pediatric Population

R Hourani¹, R Tutunji¹, L Nasr¹, M El Homs¹, M Hourani¹

¹*American University of Beirut Medical Center, Beirut, Beirut*

Purpose

Observations of thalamic atrophy in children are done subjectively. No normative measures exist for aiding objective diagnosis formation. We aimed to determine normative 2D measurements of the thalamus in the developing brain, and create a general guide for radiologists to use for objective assessments.

Materials and Methods

Magnetic resonance images (MRIs) of 200 patients scanned at the American University of Beirut Medical Center between 2008 and July 2015 were collected

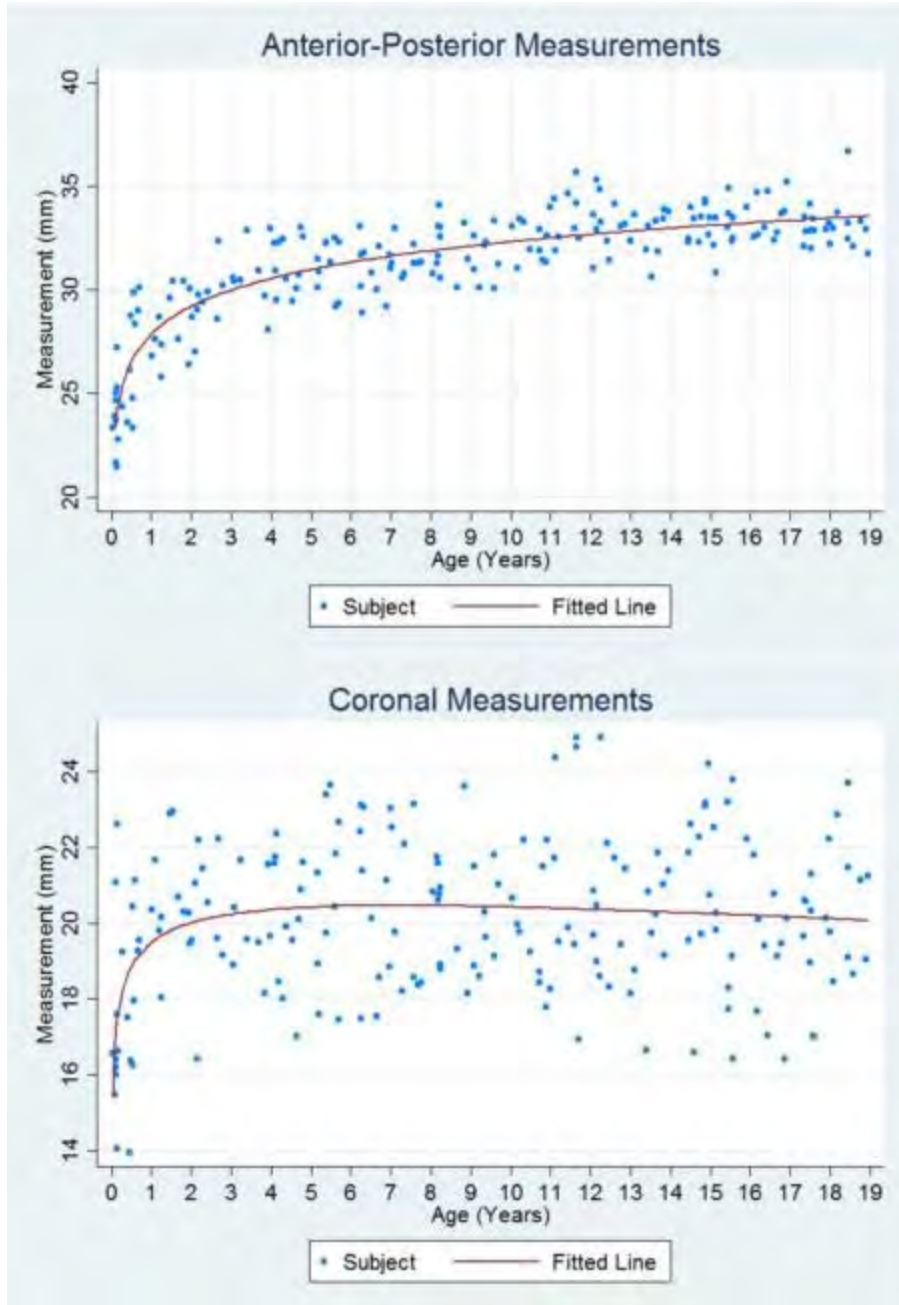
retrospectively for examination. Measurements were taken on the axial and coronal slices showing the thalamus for each participant. Participants were selected based on normal brain MRIs. Exclusion criteria included: i) presence of a brain tumor, ii) history of repeated seizures and epilepsy, iii) Lesions around and in the thalamus and gray matter, iv) periventricular lesions, v) brain infarcts or hemorrhage. Participants who met the criteria had their images uploaded to a database where the measurements were later taken. The diameter of the thalamus was measured in the anterior-posterior, transverse, and craniocaudal dimensions. We expected the measurements to increase until the age of 12, where by measurements would reach those similar to those of adults.

Results

There was a significant increase in the size of the thalamus on the anterior-posterior diameter from 23.91 mm to a plateau of ± 33 mm by the age of 11. Transverse diameters increase from 14.04mm to plateau in the 21mm range by the age of 13. Coronal diameters increase in the first year of life and remain stable in the 20 mm range with no obvious increasing patterns. There was a significant between-group difference as seen by an ANOVA conducted for all measurements ($P < 0.01$).

Conclusions

The thalamus increases in size in its transverse and anterior-posterior diameters in the developing brain. No such pattern was discernible in the coronal measurements. Our measurements can be used while diagnosing to identify whether pediatric patients of different ages have normally sized thalami, and also gives us a glimpse as to how the brain develops in children.



(Filename: TCT_O-441_Figure_2.jpg)

O-442

9:31AM - 9:39AM

Effect of Venous Oxygenation on Cerebral Venous Susceptibility Imaging in Pediatric Patients

C Toensing¹, P Kim¹, P Eaton¹, J Jacobson¹

¹Loma Linda University Medical Center, Loma Linda, CA

Purpose

General anesthesia and conscious sedation have increasing utilization for the acquisition of diagnostic imaging, particularly for pediatric patients. This project was undertaken as an initial effort to understand the effect that these methods of image acquisition have on the images themselves, specifically on cerebral venous systems as quantified by susceptibility-weighted imaging (SWI).

Materials and Methods

All pediatric brain magnetic resonance imagings (MRIs) from June 2013 to May 2014 were queried. Those that were interpreted as "Normal MR findings of the brain," or a variation thereof, were included. Exclusion criteria include history of cardiac, central nervous system and pulmonary disease. Categories included: no sedation (NS), conscious sedation (CS), and general anesthesia (GA). Anesthesia, laboratory and nursing data were acquired. Susceptibility-weighted imaging maps were created with SPIN software (MR Institute, Detroit). Quantitative susceptibility measurements (QSM) of the deep and superficial cerebral venous structures were obtained by placing a region of interest (ROI) along the long axis of the veins and recording the highest value in parts per billion (ppb). Deep venous structures included the bilateral internal cerebral veins (ICV) and the straight sinus (SS); superficial venous structures included the most prominent vein in the bilateral MCA territories (MCA). Standard data analysis was performed, including independent-samples Kruskal-Wallis tests.

Results

Ninety-seven patients were enrolled in our study. The mean age of the CS and GA groups were lower than that of the NS group (GA 4.9 years \pm 3.9, CS 12.2 years \pm 3.4, NS 5 years \pm 4.4). Average venous oxygenation levels also were significantly higher for the GA group than the sedation or NS groups (GA 85%, CS 24%, NS 21%). Quantitative susceptibility measurements were statistically significantly lower for general anesthesia as compared to the no sedation group in all venous territories ($p < 0.000$). Quantitative susceptibility measurements also were statistically significantly lower for GA compared to CS in the right ICV, left ICV and right MCA ($p < 0.000$, $p < 0.000$, $p = 0.076$, respectively), though were not statistically significant in the SS and left MCA. Quantitative susceptibility measurements were statistically significantly lower for CS compared to NS in the straight sinus, right MCA, left MCA and the left ICV, though were not significant in the right ICV ($p = 0.006$, $p = 0.005$, $p = 0.005$, $p = 0.04$, $p = 0.1$, respectively).

Conclusions

Higher venous oxygenation levels had statistically significant effects on the QSM of cerebral venous systems in pediatric patients, primarily when general anesthesia was utilized. This suggests that altered venous oxygenation has an effect on the images themselves. The extent of this effect, and whether or not there are qualitative differences in the images acquired, warrants further study.

Susceptibility-weighted Imaging as a Non-contrast Technique in the Diagnosis of Developmental Venous Anomalies in Children

R Goel¹, A Young², A Poretti³, T Huisman⁴, T Bosemani³

¹Johns Hopkins Hospital, Baltimore, MD, ²John Hopkins School of Medicine, Baltimore, MD, ³The Johns Hopkins University School of Medicine, Baltimore, MD, ⁴Johns Hopkins, Baltimore, MD

Purpose

Developmental venous anomalies (DVAs) are the most common type of cerebral vascular malformation. Gadolinium-enhanced T1-weighted magnetic resonance imaging (MRI) is the gold standard for diagnosis. Gadolinium deposition in the brain (particularly in the dentate nuclei) regardless of renal or hepatobiliary dysfunction has been shown. Susceptibility-weighted imaging (SWI) detects paramagnetic deoxyhemoglobin as hypointense signal within low flow venous vasculature without the need of gadolinium injection. We evaluated the sensitivity of SWI in the diagnosis of DVAs and their complications in children.

Materials and Methods

Inclusion criteria for this study were 1) the diagnosis of DVA based on gadolinium-enhanced T1-weighted MRI and 2) availability of SWI data and T2-weighted magnetic resonance imaging (MRI) (for comparison). T1 postcontrast imaging was used as the reference standard for the diagnosis of DVA. Susceptibility-weighted imaging and T2-weighted MRI were evaluated individually for the diagnosis of DVA. In addition, SWI and T1 postcontrast imaging were evaluated individually for DVA location, morphology, drainage pattern, presence of cavernoma, and associated hemorrhage by an experienced pediatric neuroradiologist.

Results

Fifty-seven children with DVAs (mean age 11.2 years; range 0-18 years) were included in this study. Fifty-one DVAs were classic and six were solitary. Susceptibility-weighted imaging identified 42/57 DVAs with a sensitivity of 73.68%. Five of 15 cases not visible on SWI were related to hyperoxygenation of the patient. T2-weighted MRI could identify 15 DVAs with a sensitivity of only 26.3%. Susceptibility-weighted imaging detected 100 % (12/12) of the cavernomas whereas T1 postcontrast revealed only 50% (6/12). Hemorrhage was noted in 4/57 patients, visible on both SWI and T1 postcontrast.

Conclusions

Susceptibility-weighted imaging identifies DVAs with moderate sensitivity. In addition, it is superior to T1 postcontrast imaging in detecting occult cavernomas.

Susceptibility-weighted imaging may be a valuable pulse sequence that obviates the need for gadolinium.

O-444

9:47AM - 9:55AM

The Evolution of Pituitary Cysts (PC) in Children With Growth Hormone Deficiency (GHD) and Idiopathic Short Stature (ISS)

R Noto¹, N Swiecka¹, A Parlapalli¹, M Tenner¹

¹New York Medical College, Valhalla, NY

Purpose

In this study, we analyzed the change of cyst volume (CV) in short children treated with growth hormone.

Materials and Methods

Materials: Magnetic resonance imaging (MRI) with postgadolinium contrast.

Methods: Brain MRIs with special attention to the pituitary gland of 642 growth hormone deficient and idiopathic short stature patients were reviewed for the presence of pituitary cysts (PC). Seventy-two patients were found to have a pituitary cyst, of these, 24 underwent multiple MRI studies for analysis. Presence of PC, CV, pituitary volume (PV), and the percentage of the pituitary gland occupied by cyst (POGO) were measured and calculated. Large cysts (LPC) were considered to be when more than 15% of the PV was occupied by cyst. All patients were treated with growth hormone during the observation period.

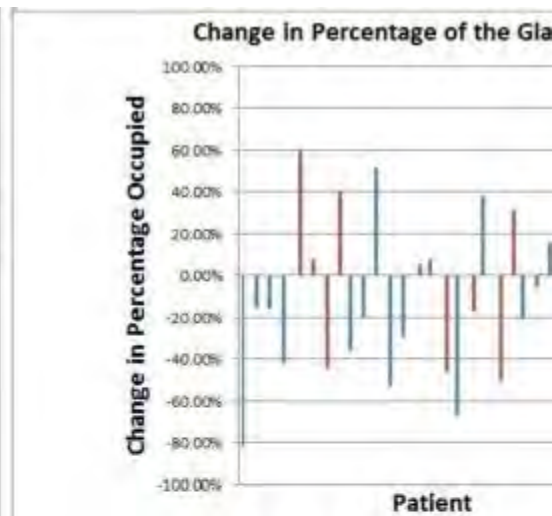
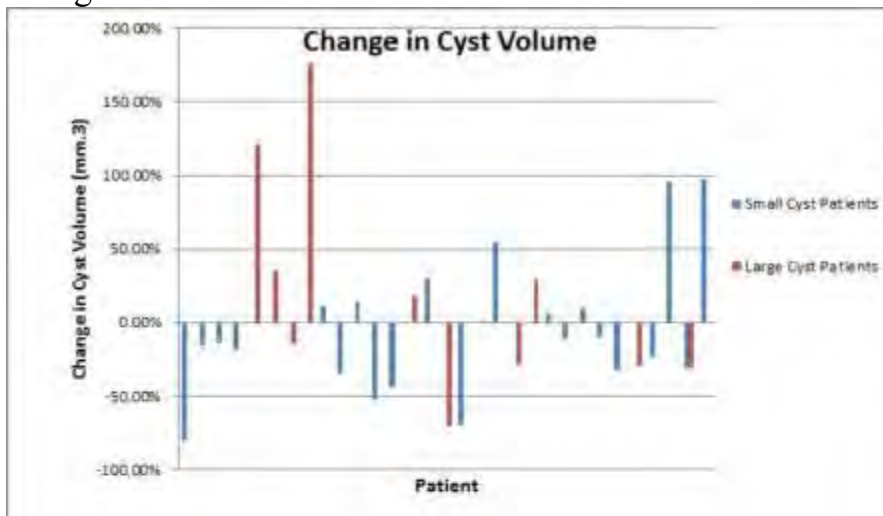
Results

From initial MRI studies of the 24 patients, 14 (58%) patients demonstrated a small cyst (SPC) and 10 (42%) demonstrated a LPC. Analysis from the first to second MRI demonstrate the following: the mean, median, and range change in CV for all patients were 2.07 cu.mm.±18.4, -7.53%, and CV varied from -84.70% to +680.0%. The mean, median, and range change in POGO by the cyst for all of the patients were -5.27 cu.mm.±14.85%, -2.37%, and POGO varied from -60.41% to +7.02%. The mean, median, and range change in CV for patients with a SPC were 90.11% ± 137.97, 21.02%, and CV for SPC varied from -77.48% to +439.6%. The mean, median, and range change in POGO by the cyst for patients with SPC was 0.26% ± 4.81, 0.24%, and POGO varied between -7.4% to +7.02%. The mean and median change in CV for patients with a LPC was +41.82 ± 259.55% and -49.94% respectively, with a CV range of -92.1% to +680%. The mean, median, and range change in POGO by the cyst for patients with a LPC was -20.12 ± 16.28% -13.7% respectively, and POGO varied from -60.01% to -7.0%. The total mean between follow-up dates was 2.96 ± 2.24 years. For patients with two sequential MRIs, analysis of change in POGO in time demonstrated that one of the patients with SPCs

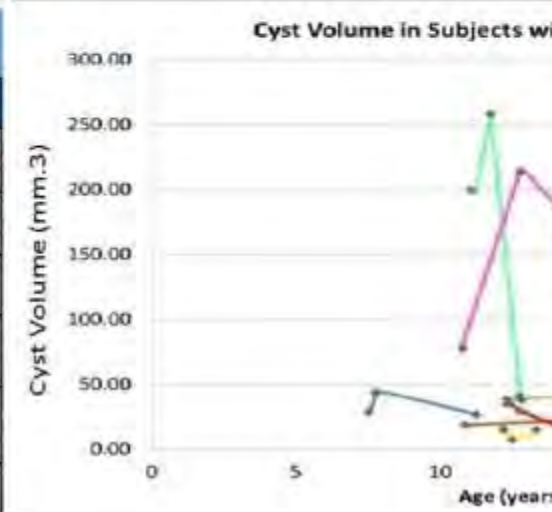
developed into LPCs and six patients with LPCs diminished in size into SPCs. Of the 72 patients, nine had three sequential MRIs. Five of these patients had a SPC, while four had a LPC. None of the patients with a SPC developed into a LPC. The percentage change in CV from the first to second MRI in patients with a LPC was between -20.5% to +40.3%. From the second to third MRI, the range was -34.7% to +77.9%. When comparing groups, the growth hormone deficient patients versus idiopathic short stature (ISS) patients in the male versus females subjects showed significant differences in POGO (Table 1).

Conclusions

Patients with a SPC over short periods of time will unlikely develop into a LPC. However, patients with a LPC can show major changes and should be tracked for CV change in time.



| Table1 : Difference in Data Between Groups | | | | |
|--|---------------------------|-----------------|------------------|----------|
| Patient Groups | Variable | Mean | Median | p-value |
| Male Vs Female | Cyst volume % change | 65.34 vs 27.87 | 14.75 vs. 20.86 | 0.245999 |
| Small Vs Large | Cyst volume % change | 64.25 vs. 33.05 | 21.02 vs. -47.49 | 0.295755 |
| GHD Vs ISS | Cyst volume % change | 1.55 vs. 106.37 | -28.9 vs. 4.04 | 0.018739 |
| Small Vs Large | Change in cyst % of gland | -5.49 vs. -5.05 | -3.26 vs. -1.48 | 0.456975 |
| Male Vs Female | Change in cyst % of gland | 0.26 vs. -20.12 | 0.24 vs. -13.7 | 0.001111 |
| GHD Vs ISS | Change in cyst % of gland | -6.82 vs -3.73 | -3.76 vs. -0.22 | 0.385081 |



(Filename: TCT_O-444_cyst_research_graph_final.jpg)

O-445

9:55AM - 10:03AM

Atypical Diffusion Restriction Patterns in Pediatric Cerebral Malaria

T LoStracco¹, G Birbeck², S Kampondeni³, K Seydel⁴, T Taylor⁴, M Tivarus⁵, M Potchen⁵

¹*University of Rochester, Rochester, NY, USA*, ²*Univeristy of Rochester, Rochester, NY*, ³*Malawi MRI Center, Blantyre, NY*, ⁴*Michigan State University - College of Osteopathic Medicine, East Lansing, MI*, ⁵*University of Rochester, Rochester, NY*

Purpose

Six hundred thousand children per year are diagnosed with pediatric cerebral malaria (CM). Despite a case fatality rate of 15 to 25%, only recently has massively increased brain volume, detected using magnetic resonance imaging (MRI) technology, been identified as a strong predictor of mortality in children with CM (1). One third of CM survivors experience neurologic sequelae (2). Serial MR imaging may offer insights into the evolution of the disease and mechanisms of brain injury that might aid in the identification of potential interventions.

Materials and Methods

Children admitted to the Blantyre Malaria Project with retinopathy-confirmed CM underwent brain MRIs on admission and then daily until death or recovery using a 0.35T GE Signa Ovation MRI. Follow-up studies were obtained at 1 month or later. NeuroInterp (3) was used by interpreting radiologists to systematically capture radiographic data. Diffusion-weighted imaging (DWI) abnormalities on serial imaging are described.

Results

One hundred eighty-two consecutive consented pediatric patients with CM between 2009 and 2014 were imaged. Acute DWI abnormalities were seen in 39/182 (21%). Among these, 31/39 (79%) had diffuse white matter involvement; 14 (36%) showed changes in the corpus callosum; 16 (41%) in the basal ganglia, four (10%) in cortical areas including one (3%) in the hippocampus. Of those with DWI abnormalities on admission, 28/39 had follow-up MRI at least 5 days after their acute presentation. Two paradoxical findings were evident: total resolution of admission restricted diffusion without associated residual structural abnormalities [13/28 (46%) with 11/13 (85%) involving the white matter], while four children had prolonged restricted diffusion persisting greater than 14 days.

Conclusions

Magnetic resonance imaging findings in pediatric CM demonstrated unusual patterns including transient restricted diffusion localized to the white matter without residual structural abnormalities. This phenomenon is consistent with transient sequestration of parasitized red cells in the cerebral microvasculature. Conversely, restricted diffusion that persists after recovery from coma was seen, similar to findings following anti-angiogenic drug therapy, and may indicate prolonged endothelial injury.

Thursday

10:30AM - 12:00PM

Washington Marriott Wardman Park, Marriott Ballroom

21A-ASSR Programming: Oncologic Spine Imaging and Interventional Procedures

21A-1

10:30AM - 10:50AM

Oncology: The New Frontier for the Spinal / Pain Interventionalist

Wong, W.

UCSD

San Diego, CA

21A-2

10:50AM - 11:10AM

MR Perfusion of Spinal Metastatic Disease: Implications for Treatment and Response to Therapy

Karimi, S.

Memorial Sloan-Kettering Cancer Center

New York, NY

21A-3

11:10AM - 11:30AM

Tumor Ablation and Vertebral Augmentation for Spinal Metastatic Disease

Jennings, J.

Washington University

St. Louis, MO

21A-4

11:30AM - 11:50AM

Endovascular Treatment of Spinal Metastatic Lesions

Do, H.

Stanford University

Stanford, CA

21A-5

11:50AM - 12:00PM

Discussion

Thursday

10:30AM - 12:00PM

Washington Marriott Wardman Park, Washington 4/5/6

**21B-CSF Programming: Normal Pressure Hydrocephalus (NPH) and Pseudotumor
21B-1**

10:30AM - 10:55AM

Physiology and Imaging of CSF Flow

Blitz, A.
Johns Hopkins Hospital
Baltimore, MD

21B-2

10:55AM - 11:20AM

TimSLIP in Evaluation of NPH

Law, M.
Keck Medical Center of USC
Los Angeles, CA

21B-3

11:20AM - 11:45AM

Idiopathic Intracranial Hypertension

Dillon, W.
UCSF
San Francisco, CA

21B-4

11:45AM - 12:00PM

Discussion

Thursday

10:30AM - 12:00PM

Washington Marriott Wardman Park, Washington 1/2/3

**21C-PARALLEL PAPER SESSION: Head & Neck: The Orbital Neighborhood
O-446**

10:30AM - 10:38AM

**Orbital Masses: The Usefulness of Diffusion-Weighted Imaging in Lesion
Categorization**

A Youssef¹, M Abdel Aziz¹, M Homos², I Hamed¹

¹National Cancer Institute, Cairo University, Cairo, Cairo, ²Cairo University, Cairo, Cairo

Purpose

Orbital masses represent a spectrum of benign and malignant lesions in adults and children that can be challenging to diagnose and treat. Imaging plays an important role in diagnosis, due to a potentially limited clinical examination and risks associated with biopsy. Magnetic resonance imaging (MRI) is a powerful tool for imaging the globe, due to the excellent tissue contrast it provides. Yet conventional MRI has a limitation in discriminating the benign from malignant lesions. Diffusion-weighted imaging (DWI) is noninvasive rapid technique uses the water diffusion produce contrast among different kinds of tissues. Our propose was to assess the role of DWI and calculated apparent diffusion coefficient (ADC) values in characterization of the orbital masses regarding benignity or malignancy.

Materials and Methods

Fifty-one patients with recently diagnosed orbital masses and who underwent pre-operative conventional MRI and DWI were included in this study. The orbit was divided into six compartments: the eye globe, retro-ocular fat, optic nerve, lacrimal system, bony boundaries and extra-ocular muscles. The average ADC obtained from each tumor was compared with the histo-pathological diagnosis determined from subsequent surgical sample.

Results

Twenty female and thirty-one male patients with orbital masses were included in this study. Their ages ranged from 1 month to 65 years. The globe is the seat of more than one fifth of these lesions (21.6%) followed by optic nerve (17.6%). Thirty (58.8%) of cases was diagnosed as having malignant masses and 21 (41.2%) of cases have benign lesions. The mean ADC value of the malignant orbital tumors ($0.82 \pm 0.69 \times 10^3$ mm²/s) was significantly ($P = 0.001$) lower than that of the benign orbital lesions ($1.48 \pm 0.55 \times 10^3$ mm²/s). Receiver operating characteristic (ROC) analysis showed a sensitivity of 83.33 % 90.5% and a specificity of 83.3% when using an optimal cut off ADC value of 0.89×10^3 mm²/s for differentiating malignant from benign lesions.

Conclusions

Apparent diffusion coefficient values provide an accurate, sensitive, fast, and noninvasive means of characterization of pediatric orbital tumors. A prior tumor characterization is useful in timing and treatment planning for orbital tumors.

O-447

10:38AM - 10:46AM

Using DWI Thermometry to Measure Globe Temperature Differences: Retrospective Case-Control Study of Orbital Cellulitis

J Derakhshan¹, L Loevner², F Wehrli¹

¹University of Pennsylvania, Philadelphia, PA, ²University of Pennsylvania, Philadelphia, PA

Purpose

Diffusion-weighted imaging (DWI)-based thermometry is a new technique (1), which uses the diffusion coefficient in regions of nonrestricted diffusion to measure temperature (2). Prior studies are limited to studying the "core brain temperature" in the lateral ventricles (3, 4) and the technique has not been studied in the orbit. The purpose was to assess the ability to perform DWI thermometry in the orbits using existing DWI data by measuring globe temperature in patients with and without orbital cellulitis.

Materials and Methods

A retrospective case-control study was performed at our institution from all studies in our database. The database (Montage Healthcare Solutions v2.0) was mined for all magnetic resonance imaging (MRI) studies with orbital cellulitis. Inclusion criteria included a diagnosis of pre or postseptal orbital cellulitis by MRI as well as having both DWI and apparent diffusion coefficient (ADC) maps. Exclusion criteria were bilateral disease, prior surgery, trauma, radiation, stroke, seizure, severe artifacts on DWI and aspherical globe. A circular region of interest (ROI) was drawn in the center

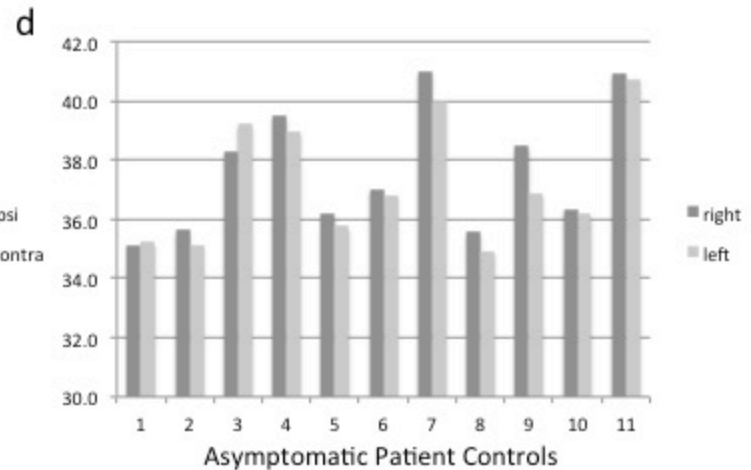
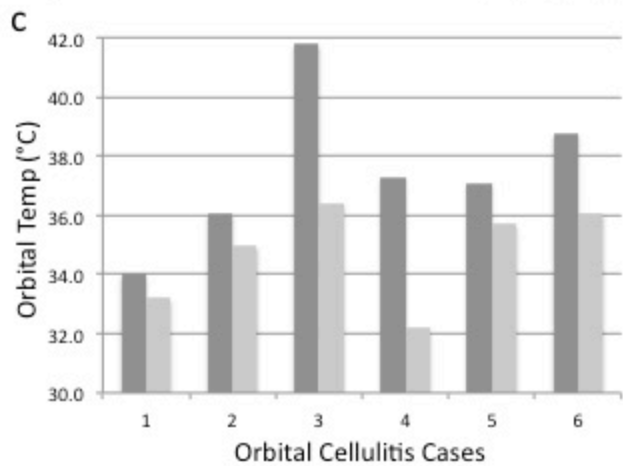
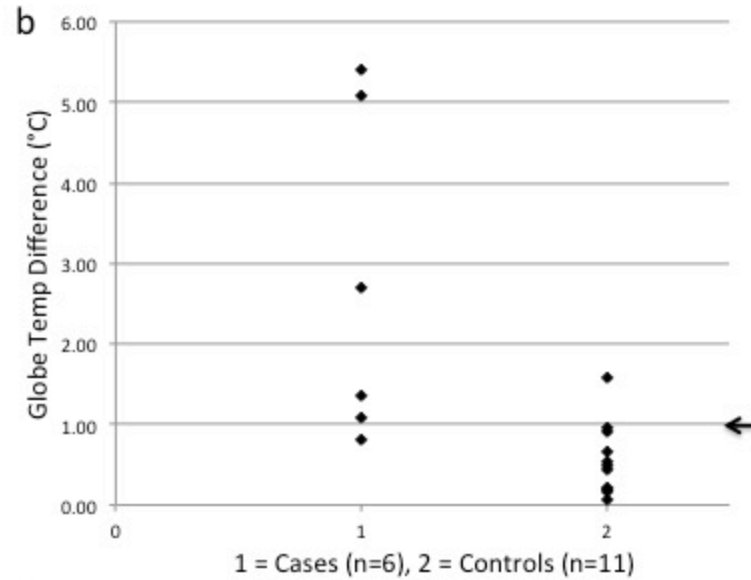
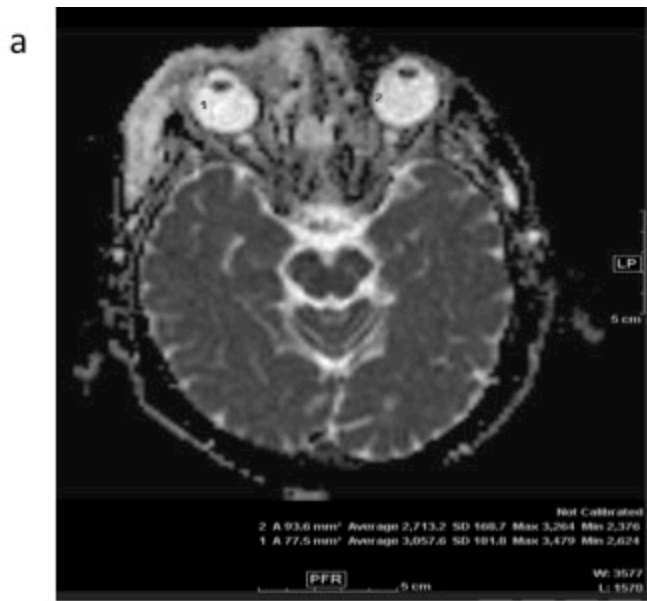
of the orbit at the level of the optic nerve insertion and the mean ADC value was recorded, taking care to avoid clear artifacts on the corresponding DWI images. The ADC was converted to temperature using equation 2 in Ota et al (5). Twice the number of cases of age-matched controls were identified with a "normal brain MRI", excluding patients with sinus disease. Paired t-tests were performed in Matlab to assess globe temperature differences in both the cases and controls. Nonpaired t-test was used to assess the difference in globe temperatures between the cases and controls.

Results

A sample ADC map obtained in one of the cases is provided in Fig. 1a showing the circular ROIs superimposed. Fig. 1b provides the globe temperature differences for all cases (n=6) and controls (n=11). Globe temperatures are provided for all cases (Fig 1c) and controls (Fig 1d). The mean globe temperature in the ipsilateral eye of the cases was $37.5 \pm 2.6^{\circ}\text{C}$. The mean globe temperature in the contralateral globe was $34.8 \pm 1.7^{\circ}\text{C}$. The globe temperature was increased in the ipsilateral eye in all cases with a mean difference of $2.7 \pm 2.1^{\circ}\text{C}$, which was highly significant ($p=0.003$, paired one-sided t-test). In the controls, the mean globe temperature in the warmer eye was $37.7 \pm 2.2^{\circ}\text{C}$ while in the cooler eye was $37.2 \pm 2.0^{\circ}\text{C}$. The mean difference in globe temperature was $0.6 \pm 0.5^{\circ}\text{C}$, which was significant ($p=0.02$). The mean difference in globe temperature between the cases and controls was highly statistically significant ($p=0.003$). Using a globe temperature difference threshold of 1°C (arrow), there was 83% sensitivity and 91% specificity for the diagnosis of orbital cellulitis.

Conclusions

Diffusion-weighted imaging thermometry can be used to measure differences in globe temperature in patients with and without orbital cellulitis revealing significant differences. Diffusion-weighted imaging thermometry has high sensitivity and specificity for the diagnosis. Future studies are warranted to study other infectious, inflammatory and vascular pathologies using DWI thermometry in the globe.



(Filename: TCT_O-447_Slide1.jpg)

O-448

10:46AM - 10:54AM

Infra-orbital nerve involvement on MRI in European patients with IgG4-related ophthalmic disease.

A Lecler¹

¹Fondation Rothschild, Paris, France

Purpose

To measure the frequency of infra-orbital nerve involvement (IONE) on magnetic resonance imaging (MRI) in European patients suffering from IgG4-related orbital disease (IgG4-ROD), as compared to patients suffering from non-IgG4 orbital inflammation (non-IgG4-OI).

Materials and Methods

Between January 2006 and April 2015, 132 patients consulted and/or were admitted for nonlymphoma, nonthyroid-related orbital inflammation in our tertiary center. Among these patients, 38 had both pretherapeutic orbital MRI and histopathological IgG4 immunostaining. We conducted a systematic retrospective of their medical charts and MRI images. Fifteen patients were classified as cases of IgG4-ROD and 23 patients were classified as cases of non-IgG4-OI. Two readers performed blinded analysis of MRI images. The main criterion for this study was infra-orbital nerve enlargement (IONE), defined as a diameter of the infra-orbital nerve superior to the diameter of the optic nerve in coronal section. Prevalence of IONE was compared between IgG4-ROD patients and non-IgG4-OI patients.

Results

Infra-orbital nerve involvement was present in 53% (8/15) of IgG4-ROD cases whereas it was never (0/23) present in cases of non-IgG4-OI ($p < 0.0001$). Infra-orbital nerve involvement was present only in cases where on MRI, inflammation of the inferior quadrant was present and in direct contact with the infra-orbital nerve canal.

Conclusions

In European patients suffering from orbital inflammation, presence of IONE on MRI is a specific sign of IgG4-related etiology. Recognition of this pattern may facilitate definite diagnosis for clinicians and allow adequate management and appropriate care.

O-449

10:54AM - 11:02AM

Correlation of Quantitative Measurements of Intraorbital Optic Nerve and Clinical Features in Thyroid Eye Disease Patients Using Diffusion Tensor MRI

H Seo¹, H Lee², Y Lee², s suh³

¹Korea University Ansan Hospital, Ansan-si, Korea, Republic of, ²Korea University Ansan Hospital, Ansan-si, Gyunggi-do, ³Korea univeristy Guro Hospital, seoul, Korea, Republic of

Purpose

To compare the quantitative measurements of intra-orbital optic nerve in thyroid eye disease (TED) patients and age-sex matched control using diffusion tensor magnetic resonance imaging (DTI MRI) and analyze the correlation between DTI parameters and clinical features in TED patients.

Materials and Methods

Twenty TED patients (M:F=8:12, mean age=44.3±9.3 years) and age- and sex-matched 20 controls (M:F=7:11, mean age=44.2±10.5 years) were included. Diffusion tensor MRI and thyroid function test including thyroid-stimulating immunoglobulins were performed. Visual field analysis was conducted with and mean deviation (MD)

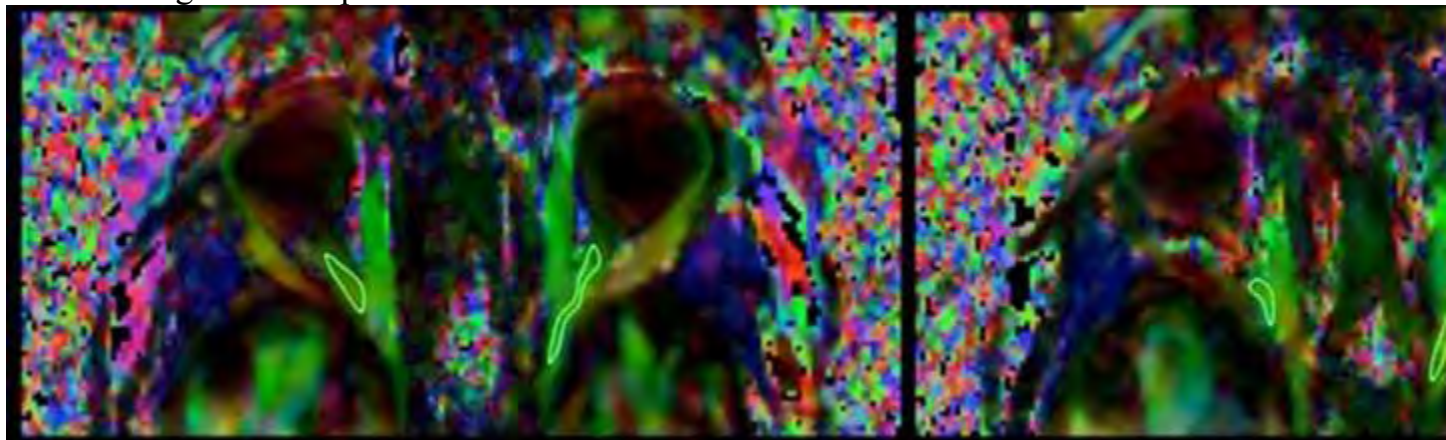
was measured. Fractional anisotropy (FA), apparent diffusion coefficient (ADC), axial diffusivity (Ax), and radial diffusivity (Rad) values were obtained at the intraorbital optic nerves in diffusion tensor MRIs and compared between two groups (Fig.1). The correlation between these DTI values and clinical features of TED (lower eyelid retraction, lagophthalmos, exophthalmos, and extraocular movement limitation), MD in the visual field analysis, clinical activity score (CAS), and modified NOSPECS score, and medial rectus muscle diameter measured on CT scans were assessed.

Results

Diffusion tensor imaging analysis showed that the average FA was larger in patients with TED than in controls (0.5486 ± 0.0779 and $0.4968 \pm 0.0505 \times 10^{-2}/\text{mm}^2/\text{s}$) and the difference was statistically significant ($p < 0.000$) (Table 1). On the contrary, the average ADC was smaller in patients with TED than in controls (0.1166 ± 0.0232 and $0.1312 \pm 0.0162 \times 10^{-2}/\text{mm}^2/\text{s}$, $p = 0.001$) (Table 1). There was a significant correlation between FA and CAS ($r = 0.353$, $p = 0.030$). Modified NOSPECS score showed significant negative correlation with ADC ($r = -0.408$, $p = 0.011$) and positive correlation with FA ($r = 0.419$, $p = 0.009$) (Table 2). The diameter of the medial rectus muscle showed significant negative correlation with ADC and RD ($r = -0.406$, $p = 0.011$ and $r = -0.332$, $p = 0.042$ each) and positive correlation with FA ($r = 0.458$, $p = 0.048$). Thyroid eye disease patients were subdivided with and without enlarged medial rectus muscle and the comparison of DTI parameters between these groups showed that ADC and RD was statistically larger in medial rectus muscle enlarged group.

Conclusions

Changes of DTI parameters reflected the axonal degeneration and ischemic changes of the intra-orbital optic nerve in patient with TED although there was no evident DON. Disease activity and severity with enlarged medial rectus muscle may have a role in changes of DTI parameters.



(Filename: TCT_O-449_Figure1.jpg)

Table 1 | Comparison of DTI parameters between control and TED patients

| DTI parameters | TED | Control |
|----------------|-----------------|-----------------|
| ADC | 0.1166 ± 0.0232 | 0.1312 ± 0.0162 |
| FA | 0.5486 ± 0.0779 | 0.4968 ± 0.0505 |
| Ax | 0.1984 ± 0.0184 | 0.2086 ± 0.0191 |
| Rad | 0.0793 ± 0.0186 | 0.0925 ± 0.0161 |

↵

by paired t-test

* p-value < 0.05

(Filename: TCT_O-449_Table1.jpg)

Table 2| Correlation of DTI parameters and clinical characteristics

| | ADC | | FA |
|------------------------|---------|--------|---------|
| | P-value | r | P-value |
| Exophthalmometry | 0.475 | 0.119 | 0.130 |
| CAS score | 0.728 | -0.058 | 0.030* |
| Modified NOSPECS score | 0.011* | -0.408 | 0.009* |
| MD | 0.492 | -0.115 | 0.119 |

by paired t-test

* p-value < 0.05

(Filename: TCT_O-449_Table2.jpg)

O-450

11:02AM - 11:10AM

Normal Optic Pathway Value Ranges for Routine Pediatric MRI

T Bartsikhovsky¹, I Bekerman², S Tal², A Ben Ely², H Maresky³, S Nagieva²

¹Assaf Harofeh Medical Center, Ramat Gan, Israel, ²Assaf Harofeh Medical Center, Tzrifin, Tzrifin, ³Assaf Harofeh Medical Center, Zrifin, HaMerkaz (Central)

Purpose

To establish objective age-related normal diameter values of the optic pathway in the pediatric population using magnetic resonance imaging (MRI).

Materials and Methods

We retrospectively reviewed all brain MR studies performed from January to June 2015 of pediatric patients referred for reasons unrelated to orbital pathology and were interpreted as normal. The examinations were performed on a 1.5T or 3T Siemens MR system using routine imaging protocols. Orbital optic nerves (OON), prechiasmatic optic nerves (PON) and optic tracts (OT) were measured on T2 axial sequences. Measurements of OON were performed 10 mm posterior to optic disk, without including the optic nerve sheath. PON were measured 5 mm posterior to optic canal. Measurements of each OT were performed at the level of the anterior border of the cerebral peduncle. The optic chiasm (OC) was measured on T2 coronal fat saturated sequences on a slice where its maximal width was identified. All measurements were performed manually. The final study population included 137 studies (72 male, 65 female, average age = 7.7 years). Patients were stratified into five age groups: (I) 0-1.5 years, (II) 1.5-3 years, (III) 3-6 years, (IV) 6–12 years, (V) 12-18 years.

Results

The observed value range of OON mean diameter was 2.7 mm (IQR = 2.4-2.9), PON was 3.2 mm (IQR = 3.05-3.5), OT 2.6 mm (IQR = 2-2.9). A strong positive correlation was established between age and mean diameter of OON ($r=0.73$, $p<0.001$), PON ($r=0.59$, $p<0.001$), OT ($r=0.72$, $p<0.001$), OC weight ($r=0.55$, $p<0.001$). A significant difference in mean OON diameters was found between age groups I-II ($d=0.3$, $p=0.01$), II-III ($d=0.5$, $p<0.001$), III-IV ($d=0.5$, $p<0.001$) followed by a plateau between IV-V ($d=0.10$, $p=0.19$). Orbital optic nerves/optic tracts ratio maintained a steady mean value 1 (IQR =0.93-1.1) regardless of age ($p=0.7$).

Conclusions

Size of optic pathways was found to increase as a function of age, with consistent correlation between nerve and tract for all ages.

O-451

11:10AM - 11:18AM

Prognostic CT Finding for Diplopia after Surgical Repair of Pure Orbital Blowout Fracture

H Jung¹, J Byun², G Park³

¹*Samsung medical center, Sungkyunkwan University School of Medicine, Seoul, Korea, Republic of,* ²*Kangnam St. Mary's Hospital, The Catholic University of Korea, Seoul, Korea, Republic of,* ³*Samsung Medical Center, Sungkyunkwan University School of Medicine, Seoul, Korea, Republic of*

Purpose

To evaluate the prognostic computed tomography (CT) finding for diplopia after surgical repair of pure blowout fracture.

Materials and Methods

We retrospectively reviewed CT images of 181 patients with pure orbital blowout fracture who had at least 6 months postoperative follow up. We evaluated the following factors: (1) site of fracture (orbital floor, medial wall of the orbit, or both), (2) fracture type, (3) fracture size, (4) volume of herniated orbital soft tissue, (5) (volume of herniated orbital soft tissue / fracture size) ratio (6) presence of extraocular muscle (EOM) thickening, (7) EOM swelling ratio, (8) presence of displacement of EOM, (9) presence of deformity of EOM, (10) presence of tenting of EOM, and (11) number of points of contact between EOM and bony edge. The association between diplopia at 6 months after surgical repair and various risk factors was analyzed using logistic regression models in univariable- and multivariable analysis.

Results

Deformity and tenting of EOM, large volume and (volume of herniated orbital soft tissue/fracture size) ratio were found to be statistically significant risk factors for diplopia at 6 months after repair (all $P < 0.05$). Among them, patients who showed tenting or deformity of EOM on CT images had a 5.22 or 10.85 times greater probability of new or residual diplopia after surgery, respectively ($P < 0.001$ and $P = 0.026$; 95% confidence interval of odds ratio, 2.071–13.174 and 1.323–88.915, respectively).

Conclusions

Prognosis of patients was approximately predicted through the evaluation of CT findings. Patients who have deformity or tenting of EOM, or high (volume of herniated orbital soft tissue/fracture size) ratio on CT scan are more likely to have postoperative diplopia.

O-452

11:18AM - 11:26AM

Usefulness of Color Doppler Flow Imaging in the Management of Lacrimal Gland Lesions.

A Lecler¹

¹*Fondation Rothschild, Paris, France*

Purpose

To assess the role of color Doppler flow imaging (CDFI) in the diagnosis and management of lacrimal fossa lesions.

Materials and Methods

Institutional ethical committee approval was obtained. Fifty-one patients with 62

lacrima fossa lesions were retrospectively included between 2003 and 2015. All patients underwent CDFI, with a qualitative and quantitative analysis of the vascularization. All patients had lacrima gland surgery. Definitive diagnosis was based on pathological examination.

Results

The study included 47 nonepithelial lesions (NEL) and 15 epithelial lesions (EL), with 24 (39%) malignant lesions and 38 (61%) benign lesions. Nonepithelial lesions were significantly more likely to present with septa ($p < 0.001$), hypoechogenicity ($p < 0.001$), high vascular intensity ($p < 0.001$), specific vascularization pattern ($p < 0.05$) and a low resistance index (RI) ($p < 0.0001$). Epithelial lesions were significantly more likely to present with the presence of cysts ($p < 0.001$), and a higher RI. Receiver operating characteristic curves (ROC) identified a RI value of 0.72 as the best cut-off to differentiate NEL from EL, with a sensitivity and specificity of 100%.

Conclusions

Color Doppler flow imaging is a simple, valuable and reliable tool in the differential diagnosis of lacrima fossa lesions. Resistance index measurement enables perfect segregation of epithelial and nonepithelial lesions, thus providing crucial data for surgical management.

O-453

11:26AM - 11:34AM

Effects of MR Imaging Technique on “Classic” MRI Findings of Venous Malformations

M Alexander¹, N Hughes¹, D Cooke¹, C Hess¹, I Frieden¹, A Phelps¹, C Dowd², R Darflinger¹, F Settecase¹, A Nicholson¹

¹UCSF, San Francisco, CA, ²Univ. Of California San Francisco, San Francisco, CA

Purpose

Magnetic resonance imaging (MRI) is the best imaging modality for characterization of venous malformations (VMs). Classically, phleboliths suggest a VM, while the fluid-fluid levels (FFLs) suggest a lymphatic malformation (LM) is more likely than a VM. Magnetic resonance technology has advanced considerably since the first description of these key findings. This study seeks to re-examine these traits to see if rates of trait detection have changed as technology and techniques have evolved.

Materials and Methods

A prospectively maintained database from the multidisciplinary birthmarks and vascular anomalies clinic at a major academic medical center was queried. Patients with final diagnosis of VM-based on clinical, radiologic, and vascular anomalies group consensus, who had reviewable contrast-enhanced MRIs were identified. From this group, patient with the oldest and newest MR studies were chosen to identify

equal numbers of patients from the temporal extremes. Imaging was reviewed to assess for presence of FFLs, phleboliths, and presence of enhancement. Enhancement was quantified by measuring signal in the same location of the lesion on both pre and postcontrast sequences, tabulating three enhancement values for each lesion. Such comparison was made with the same MR sequences performed before and after contrast administration. The most avidly enhancing segment of the lesion was targeted for measurement of signal. Percent enhancement was calculated by the formula (postcontrast signal – precontrast signal)/precontrast signal. Time elapsed between contrast injection and image acquisition was noted. Chi-square analysis was performed to compare rates of visualization of FFL, phleboliths, and enhancement between the cohorts. Independent sample t-test was performed to compare percent enhancement between the cohorts. Pearson's coefficient was performed to evaluate the correlation between percent enhancement, time to contrast, and date of imaging.

Results

Forty patients were identified for analysis. Twenty studies were performed between 1995 and 2006; 20 studies were performed between 2011 and 2012. The new imaging cohort had higher rates of FFL visualization (55% versus 5%, $p=0.001$). Phlebolith visualization occurred at similar rates between groups (55% versus 50%, $p=0.50$). Higher average percent enhancement was seen on the older cohort (245% versus 59%, $p<0.001$). Correlation was found between time to imaging following contrast and degree of enhancement ($r=0.60$, $p<0.001$). Inverse correlation was found between scan date and time to contrast ($r=-0.50$, $p=0.001$) and scan date and degree of enhancement ($r=-0.364$, $p=0.021$).

Conclusions

With advanced MR technology, fluid filled levels can be seen more commonly with VMs than classically reported. Fluid filled levels should not be considered exclusionary for diagnosis of VMs. Visualization of phleboliths maintains specificity for VMs using contemporary techniques. Timing following contrast administration should be maximized to increase degree of enhancement to confirm the diagnosis of VMs. Further analysis is needed given limitations in this retrospective study, including heterogeneous protocols, and differences in gadolinium chelates.

Patient Lesion Characteristics

| | Old MRI (n=20) | New MRI (n=20) | All Patients (n=40) | p-value |
|--------------------|-------------------|-------------------|------------------------|---------|
| Male | 7 | 11 | 18 | 0.214 |
| Mean Age (Years) | 21.4 | 10.0 | 15.7 | 0.006 |
| Pediatric | 10 | 16 | 26 | 0.049 |
| Max Dimension (cm) | 10.5 | 16.0 | 13.2 | 0.082 |
| FFL | 1 (5%) | 11 (55%) | 12 (30%) | 0.001 |
| Enhancement | 20 (100%) | 20 (100%) | 40 (100%) | - |
| Mean % Enhancement | 245% | 59% | 152% | <0.001 |
| Phleboliths | 10 (50%) | 11 (55%) | 21 (46.7%) | 0.500 |

(Filename: TCT_O-453_AbstractTable.jpg)

O-454

11:34AM - 11:42AM

Gadolinium Enhanced Constructive Interference in Steady State (CISS) Imaging: Depiction of Oculomotor Nerve and Its Distinction from Adjacent Skull Base Masses.

M Adin¹, A Blitz², N Aygun³

¹Silvan state hospital, Turkey, diyarbakir, Turkey, ²Johns Hopkins Hospital, Baltimore, MD, ³Johns Hopkins University, Baltimore, MD

Purpose

To demonstrate whether contrast-enhanced CISS imaging adds value to postcontrast T1-weighted imaging in distinction of oculomotor nerve from adjacent skull base tumors.

Materials and Methods

We retrospectively reviewed medical records of 324 (168 Female, 156 Male) consecutive patients who were referred to our institution between February 2010 and July 2013 for various skull base tumors (pathologies are listed in the table) for a dedicated high-resolution skull base imaging including submillimetric precontrast and postcontrast T1-weighted (VIBE) and heavily T2-weighted (CISS) sequences. Eighty-one cases met the criteria for inclusion to this study. Radiological

interpretations were done independently by two radiologists (NA with 15 years of post-training experience and MEA sixth year in radiology training) who were blinded to clinical information. Visibility of CN III and distinction from space occupying lesions were assessed on postcontrast series of both high-resolution T1 weighted VIBE images, and CISS images using a 4-tiered visual scoring system (0= invisible CN III or indistinguishable from mass, 1= poor visualization, 2= good visualization, 3= excellent visualization). The relationship between the lesion and CN III was investigated on five segments (cisternal, dural cave, interdural, foraminal and extraforaminal) of the CN III separately.

Results

Our study showed a statistically significant difference between contrast-enhanced T1-weighted VIBE and CISS techniques in favor of postcontrast CISS images. A chi square test showed a statistically significant difference between overall score distributions in two methods (p value < 0.0001). Statistical analyses of each segment were performed using Kolmogorov-Smirnov Two-Sample Test and Kuiper Test for variable rating classified by variable methods, which again demonstrated the superiority of postcontrast CISS images over postcontrast VIBE images for each segment (p value < 0.0001). Contrast material administration significantly increased the visibility of the oculomotor nerve and also improved separation of the oculomotor nerve from skull base tumors.

Conclusions

Postcontrast CISS images significantly improve radiologist's ability to identify the oculomotor nerve and to differentiate the oculomotor nerve from the adjacent tumors.

| pathological diagnosis | n |
|---------------------------------------|-----------|
| pituitary adenoma | 14 |
| meningioma | 10 |
| esthesioneuroblastoma | 8 |
| schwannoma | 8 |
| sarcoma | 7 |
| infectious process/nonneoplastic mass | 7 |
| carcinoma | 6 |
| chordoma | 5 |
| germ cell tumors | 4 |
| nasopharyngeal angiofibroma | 2 |
| other rare neoplasms | 10 |
| total number of cases | 81 |

(Filename: TCT_O-454_Table.jpg)

O-456

11:50AM - 11:58AM

Significance of Severity of Vascular Compression and Vessel Type with Symptoms in Patients with Trigeminal Neuralgia.

J Job¹, M Hughes¹, S Fakhran², L Alhilali³, B Branstetter¹, R Sekula¹

¹University of Pittsburgh Medical Center, Pittsburgh, PA, ²Banner Health and Hospital System, Phoenix, AZ, ³Barrow Neurological Institute, Phoenix, AZ

Purpose

Trigeminal neuralgia is a debilitating disease most commonly caused by vascular compression of the 5th cranial nerve. Asymptomatic vascular compression is known to be common with rates reported between 10-71% (Maarbjerg et al., 2014). However, with improved MR imaging techniques the severity of vascular compression can now be graded. For example, deformity of the nerve by the offending vessel is detectable with thin section SSFP imaging. The purpose of this study is to determine whether the rates of vascular compression, arterial compression, and nerve deformity were higher

in symptomatic trigeminal nerves when compared to asymptomatic nerves in patients with trigeminal neuralgia.

Materials and Methods

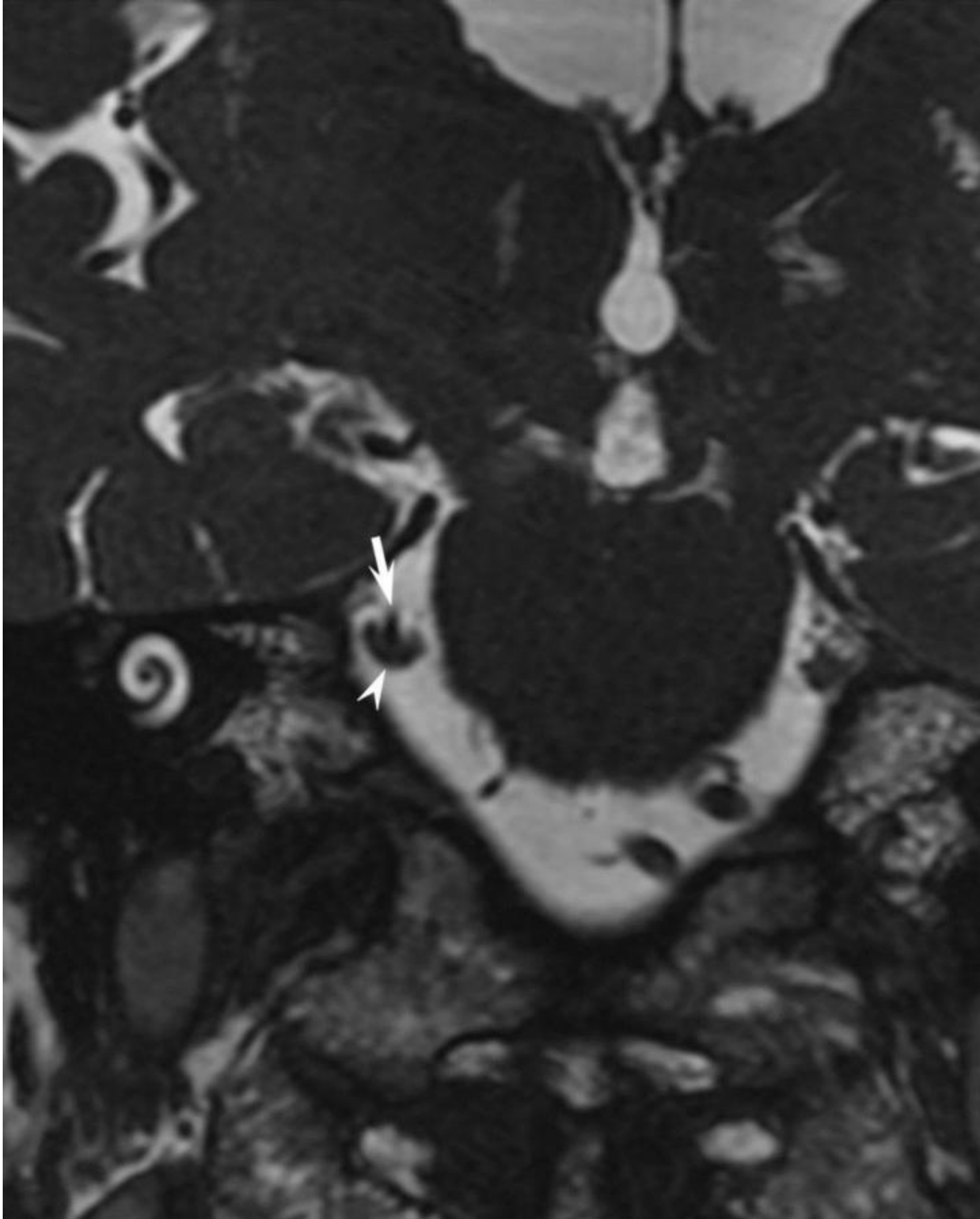
The study includes 104 patients with a history of unilateral trigeminal neuralgia. Patients underwent a dedicated 3T magnetic resonance imaging (MRI) using cranial neuralgia protocol MRI with three-plane thin section steady state free precession imaging. All films were evaluated retrospectively by one of two CAQ-certified neuroradiologists blinded to the laterality of symptoms. The presence of any vessel compressing the trigeminal nerve and whether the culprit vessel was an artery or vein then was recorded. The degree of vascular compression was categorized as contact or deformity. Vascular contact is defined as vessel abutment without mass effect on the trigeminal nerve. Vascular deformity is defined as abutment and associated concave contour deformity of the trigeminal nerve (see Fig. 1). Categorical variables are presented with frequency distributions and the Chi square test was used to assess associations with laterality of symptoms.

Results

Out of a total of 104 symptomatic patients, 94% (98/104) had vascular compression on the symptomatic side. Vascular deformity was present in 61% (60/98) and 39% (38/98) had vascular contact. On the asymptomatic side, vascular compression was less common 64% (66/104). Vascular deformity was seen in only 14% (9/66) and vascular contact in 86% (57/66) on the asymptomatic side. Of the patients who had vascular compression on the symptomatic side, the culprit vessel was an artery in 78% (76/98), a vein in 13% (13/98), and both an artery and vein in 9% (9/98). Of the patients who had vascular compression on the asymptomatic side, the culprit vessel was an artery in 59% (39/66), a vein in 39% (26/66), and both an artery and vein in 2% (1/66). In summary vascular compression, an arterial culprit vessel, and deformity was present more frequently on the symptomatic side. Deformity is uncommon on the asymptomatic side. Chi square tests of association revealed statistically significant rates of association between the symptomatic side and the presence of any vascular compression, an arterial culprit vessel, and deformity of the nerve ($p < 0.05$).

Conclusions

Vascular compression, compression by an artery, and nerve deformity are more commonly seen on the symptomatic side in patients with trigeminal neuralgia. Further studies to correlate the utility of imaging findings such as vascular deformity with surgical outcomes are necessary to best select patients for surgery.



(Filename: TCT_O-456_Figure11.jpg)

Thursday

10:30AM - 12:00PM

Washington Marriott Wardman Park, Roosevelt 1-3

21D-PARALLEL PAPER SESSION: Turbo Talks - Intracranial Vascular Procedures

O-457

10:30AM - 10:33AM

The Effect of General Anesthesia on Pressure Gradients in Transverse Sinus Stenosis: Initial Observations

F Hui¹, M Luciano², S John³, A Blitz⁴

¹*Johns Hopkins University, Baltimore, MD*, ²*Johns Hopkins, Baltimore, MD*, ³*Cleveland Clinic, Cleveland, OH*, ⁴*Johns Hopkins Hospital, Baltimore, MD*

Purpose

The use of transverse sinus stenting in the setting of idiopathic intracranial hypertension has gained increasing acceptance as a management modality in medically refractory patients. Diagnostic manometry prior to stent placement often is used to ascertain whether or not a physiologically significant gradient is present, though operators may differ in their minimum threshold. Given that most intracranial stenting procedures are performed under general anesthesia, differences in the intracranial environment may affect gradients, and thus therapeutic decisions and diagnostic conclusions.

Materials and Methods

Prospectively collected data on patients undergoing diagnostic manometry and stent placement under anesthesia was reviewed for patients that received manometry both before and after anesthesia, and before stent placement were reviewed. There were five patients identified that had appropriate data. Demographics, management, outcome metrics and procedural records were assessed. The change in venous pressures and gradients were recorded before anesthesia, after anesthesia and after stent placement.

Results

Initial pressure gradient across the stenosis was 32 mmHg. After anesthesia, there was reduction in measured gradient across the stenosis in all patients 5/5 (100%), with a mean reduction of 16.4 mmHg ranging from 1 mmHg to 28 mmHg. There was also a reduction of Torcular pressure of 12 mmHg ranging from 0 – 28 mm Hg. The IJ measurement of pressure was increased by 2.4 mmHg postanesthesia. In one case (1), there was apparent resolution of both the gradient (to 5 mmHg) as well as near

resolution of the stenosis. In a second case (3), the intervention was initially performed under local sedation and the stenosis was severe enough such that the stenosis could not be crossed with the stent or intermediate catheter. After anesthesia was induced, the minimum luminal diameter increased from 2 to 4 mm. There was reduction of angiographically measured degree of stenosis in two of five of the patients (40%). In contrast, after stent placement, the pressure gradient across the prior stenosis was 2.4 mmHg, reduced from an initial mean of 32 mmHg. The mean IJ pressure was 18.4 mmHg after anesthesia, up from 11.6 mmHg.

Conclusions

In this limited sample, there was a clear effect of measured torcular pressures in the sample set in which the pressure gradient across the stenosis decreased by a mean value of 12 mmHg after anesthesia, and, in two cases, evidence of reduced degree of stenosis. Use of manometry to determine eligibility for transverse sinus stenting should account for the effect of anesthesia. Furthermore, poststent manometry should be interpreted in light of these findings, as elimination of gradient may in part reflect an anesthetic effect rather than merely stent efficacy.

O-458

10:33AM - 10:36AM

The Clot Thickens: A Large Single Center's Experience with Dural Venous Sinus Thrombosis

W Reyenga¹, E Nyberg¹

¹*University of Colorado, Aurora, CO*

Purpose

Dural venous sinus thrombosis (DVST) is an uncommon condition which can result in venous infarct with or without intracranial hemorrhage and carries the possibility of permanent neurological deficit. The mainstay of treatment is systemic anticoagulation with heparin or low molecular weight heparin, but data regarding interventional therapy with intrasinus thrombolysis or thrombectomy is limited to a few case reports and case series suggesting an increased incidence of hemorrhagic complications. The purpose of this study was to analyze a larger series of consecutively treated patients than is available in previously published series and to analyze any differences in outcomes between patients receiving anticoagulation alone versus those also receiving endovascular therapy.

Materials and Methods

Institutional Review Board approval was obtained for this retrospective study. The electronic medical record was queried based on ICD-9 code for patients treated for DVST at our institution from 2009 to 2015. For each patient, we recorded the clinical presentation, treatment, and clinical course. Follow-up clinical and imaging reports

were reviewed to assess for new hemorrhage or infarct after the initiation of therapy. We compared outcomes of patients receiving and not receiving interventional therapy at discharge and at 90 days after discharge. Statistical significance was assessed using the chi-squared test and unpaired t-test.

Results

Sixty-eight patients were treated for DVST from 2009 to 2015. Thirty-five (51%) of these developed infarct with or without hemorrhage. Thirty-seven (54%) patients were treated with systemic anticoagulation alone. Twenty-nine patients (43%) were treated with endovascular thrombolysis using tissue plasminogen activator (tPA), and 22 of those patients (32%) also were treated with mechanical thrombectomy. Two patients underwent endovascular therapy without tPA administration or thrombectomy, one having a stent placed, and one treated with balloon angioplasty, and were excluded from the outcome comparison. New intracranial hemorrhage or infarct after initiation of therapy was seen in nine (31%) of the patients who underwent endovascular therapy and none of the patients receiving systemic anticoagulation alone ($p < 0.001$). The mean modified Rankin Scale (mRS) at discharge was 1.62 for the endovascular group compared to 1 for the anticoagulation group ($p = 0.0802$), and the mean mRS at follow up was 0.87 for the endovascular group versus 0.84 for the anticoagulation group ($p = 0.901$). Similarly, there was no statistically significant difference between the two groups in the percentage of patients with mRS of 2 or less at discharge and at follow up.

Conclusions

Endovascular treatment of DVST was associated with a higher incidence of new, postprocedural intracranial hemorrhage or infarct compared to patients treated with anticoagulation alone. Possible explanations for this finding, including differences in preprocedural clot burden and clinical status between the treatment groups, will be explored in the discussion. Despite this, both groups had statistically similar good outcomes.

O-459

10:36AM - 10:39AM

ARTS (Aspiration-Retriever Technique for Stroke)

F Massari¹, N Henninger¹, J Lozano¹, A Kuhn¹, M Gounis¹, A Wakhloo¹, A Puri¹
¹*University of Massachusetts, Worcester, MA*

Purpose

New generation of highly navigable large-bore aspiration catheters and retriever devices for intracranial mechanical thrombectomy has markedly improved recanalization rates, time and clinical outcomes. We report a collected clinical data utilizing a new technique based on combined large lumen aspiration catheter and

partially resheathed stent retriever (ARTS: Aspiration Catheter and Stent Retrievers Technique for Stroke). This technique is applied, especially in presence of bulky/rubbery emboli, when resistance is felt while retracting the stent retriever; at that point the entire assembly is locked and removed in-toto under continuous aspiration with additional flow arrest.

Materials and Methods

A retrospective data analysis was performed to identify patients with large cerebral artery acute ischemic stroke treated with ARTS. The study was conducted between August 2013 and February 2015 at a single high volume stroke center. Procedural and clinical data were captured for analysis.

Results

Forty-two patients (median age 66 years) met inclusion criteria for this study. The ARTS was successful in achieving Thrombolysis in Cerebral Infarction (TICI) $\geq 2b$ revascularization in 97.6% of cases (TICI 2b = 18 patients, TICI 3 = 23 patients). Patients median NIHSS score at admission was 18 (6–40). Three-month follow-up mRS value of 0–2 was achieved in 65.7% of the successfully treated patients (average 2.4). Two patients (4.8%) developed symptomatic intraparenchymal hemorrhages. Six procedure unrelated deaths were observed.

Conclusions

We found that ARTS is a fast, safe and effective method for endovascular recanalization of large vessel occlusions presenting within the context of AIS.

O-460

10:39AM - 10:42AM

Single Center Experience with the Trevo XP 6x25 mm. as a Primary Device in Acute Ischemic Stroke Patients with Large Vessel Occlusion.

J Blasco Andaluz¹, L San Roman², N Macias², F Zarco³, O Chirife⁴, L Saenz², S Amaro², X Urrea², L Llull², J Macho²

¹Hospital Clinic of Barcelona, BARCELONA, -- SELECT --, ²Hospital Clinic of Barcelona, Barcelona, Barcelona, ³Hospital Clinic of Barcelona, Barcelona, barcelona, ⁴hospital Clinic of Barcelona, Barcelona, Barcelona

Purpose

To report our early experience with the Trevo XP 6x25 mm. as a primary device in patients with acute ischemic stroke (AIS) and large vessel occlusion at a single comprehensive stroke center.

Materials and Methods

We retrospectively analyzed the safety and efficacy of the Trevo XP 6x25 mm in 45 consecutive patients with proximal vessel occlusions treated between April and November 2015.

Results

Since April 2015 until November 2015, 45 consecutive AIS patients with proximal vessel occlusions were treated with the Trevo XP 6x25 mm. as the primary device. Mean age was 68 years, mean NIHSS at baseline was 17, mean symptom onset to puncture was 225 min. Occlusion site was as follows: 20% terminal internal carotid artery, 53% M1, 7% M2, 11% basilar artery, and 9% tandem lesion with M1 occlusion. Median overall procedure time was 44 minutes with a median number of passes of two needed to achieve good revascularization rate (TICI 2b-3). Good revascularization rate was obtained in 86% of the patients, achieving this reperfusion in just one to two passes in 68% of the patients. In two patients a different stent retriever device was used, not achieving TICI 3-2b in any of them. Vasospasm was not infrequently detected but with no clinical consequences. In one case rupture of the device at the level of the stent retriever-guidewire connection precluded retrieval of the device . Clinical outcome at 90 days was available in 22 patients at submission of this abstract, and was 45.4 % mRs 0-2.

Conclusions

Our initial data suggest that the use of Trevo XP 6x25 in LVO AIS patients is safe and feasible, achieving high revascularization rates with very few number of passes. These results should be confirmed in larger series in order to determine the primary target of this 6 mm device.

O-461

10:42AM - 10:45AM

With MR Selection, Improved Outcomes after Successful Thrombectomy Beyond 6 Hours in Anterior Circulation Large Vessel Occlusion Stroke

B Cristiano¹, M Pond¹, U Oyoyo², S Basu¹, J Jacobson¹

¹Loma Linda University Hospital, Loma Linda, CA, ²Loma Linda University, Loma Linda, CA

Purpose

The benefit of thrombectomy among patients with anterior circulation large vessel occlusion (ACLVO) stroke is unclear beyond 6 hours (1-5). Here we sought to ascertain whether or not successful thrombectomy performed greater than 6 hours after stroke onset is beneficial compared with no intervention.

Materials and Methods

A cohort of 30 patients undergoing thrombectomy after magnetic resonance (MR) selection for ACLVO stroke from 11/1/2012 until 5/15/2015 was studied retrospectively. Patients were selected for thrombectomy based on diffusion-restricted core volume $\leq (100 - \text{patient's age})$ mL. Patients who presented beyond 6 hours from symptom onset who achieved TICI \geq 2B recanalization (n=21) were compared against

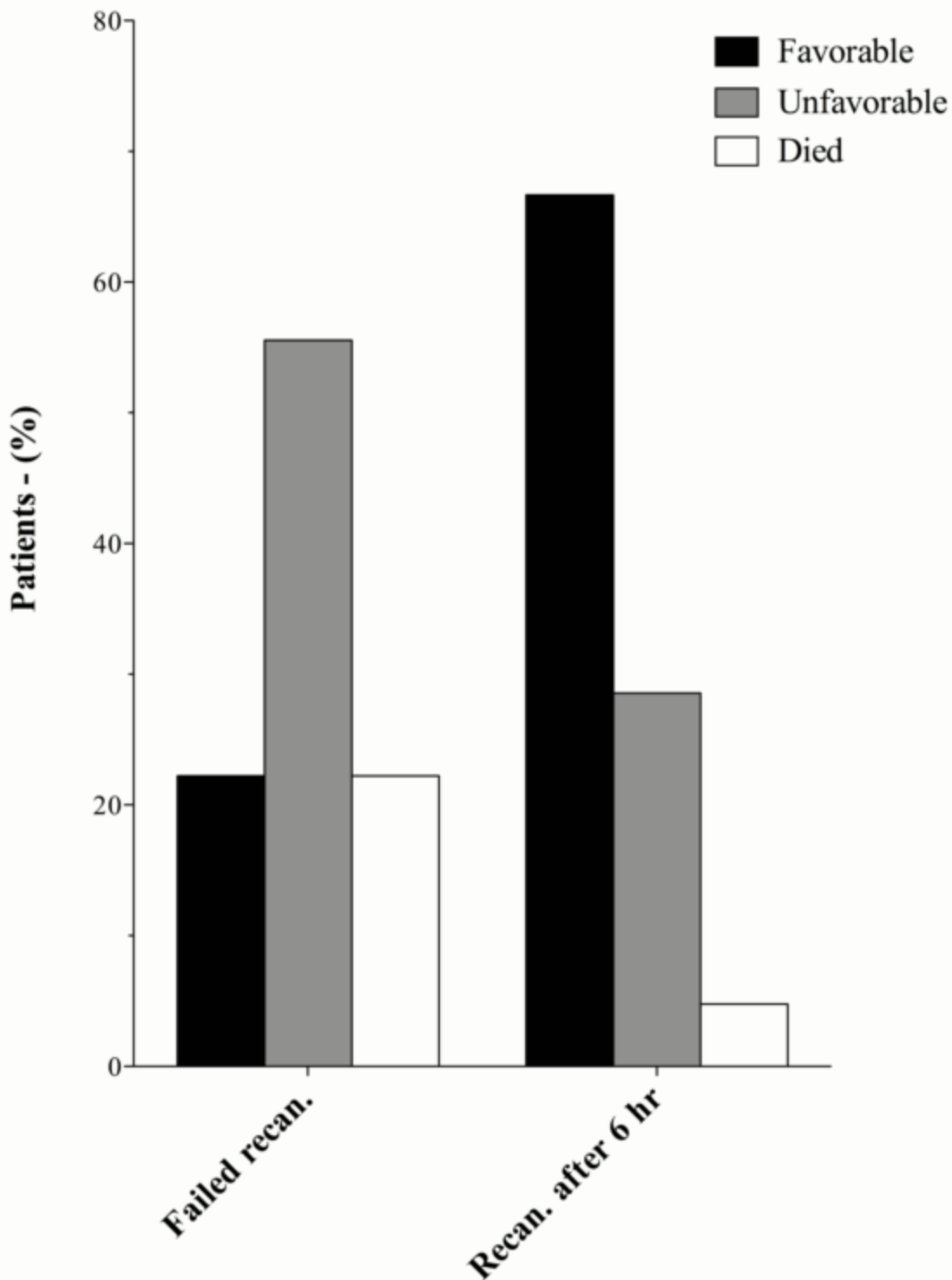
patients with failed thrombectomy at any time (n=9), with final infarct volume the primary outcome.

Results

Baseline characteristics were similar (failed versus late thrombectomy), including admission NIHSS (IQR 11 – 19 versus 11 – 18). The median symptom onset to access time for the late thrombectomy group was 10.6 hours (IQR 7.8 – 14.4). Patients with successful late thrombectomy had significantly smaller median final infarct volume [20 mL versus 53 mL, estimated difference -34 mL (95CI: -211 – +1), $p = 0.045$], median infarct growth [+4 mL versus +43 mL, estimated difference -32 (95CI: -192 – +1), $p = 0.036$], and were more likely to have a favorable outcome defined as discharge home or to rehab [14/21, 66.7%, versus 2/9, 22.2%, odds ratio 7.14 (95% CI: 1.26 – 34.5), $p = 0.046$].

Conclusions

Successful thrombectomy performed beyond 6 hours of ACLVO stroke onset with MR selection is likely beneficial compared with no intervention.



Outcomes with successful late MR-selected thrombectomy in ACLVO stroke. Patients with successful late thrombectomy had increased favorable outcomes (67% vs. 22%), decreased unfavorable outcomes (29% vs. 56%) and death (5% vs. 22%) compared with failed thrombectomy.

(Filename: TCT_O-461_Figure.gif)

O-462

10:45AM - 10:48AM

The Categories of Hyperperfusion Syndrome after Carotid Stenting

H Lee¹, F Chang¹, W Guo¹

¹*Taipei Veterans General Hospital & National Yang Ming University, Taipei, Taiwan*

Purpose

Hyperperfusion syndrome (HPS) occurred only in 0-3% of the patients after carotid endarterectomy or carotid artery stenting (CAS). Impaired autoregulation of intracranial arteries may account for its mechanism. The imaging abnormalities range from slight brain edema to intracranial hemorrhage. Typical clinical presentation includes the triad of headache, seizure and focal neurological deficit. However, atypical symptoms with behavior or emotional change, such as agitation and hypertalkativity, have never been reported. We retrospectively evaluated the cases of symptomatic HPS in our institute and proposed a new category system for the outcomes.

Materials and Methods

Between the years 2000 to 2015, 980 cases of CAS were done in our institute. Of them, 28 patients (2.55%, 25 males and 3 females) after CAS with abnormal symptoms and/ or imaging findings of HPS were included. Three categories of symptomatic HPS were classified according to the imaging findings: type I "Hemorrhagic" HPS with intraparenchymal, subarachnoid, or subdural hemorrhages; type IIa "Severe, nonhemorrhagic" HPS with focal brain edema; type IIb "Slight, nonhemorrhagic" HPS with no abnormal findings on plain CT or MR including T2 FLAIR and diffusion-weighted images. Clinical symptoms, neurological deficits, outcomes and imaging studies before, during and after procedure were reviewed for comparison.

Results

The clinical symptoms of the 11 patients of type I, eight patients of type IIa and nine patients of type IIb HPS were: consciousness disturbance [n= 3 (27%), 2 (25%), 0 (0%)], headache [n= 2 (18%), 2 (25%), 2 (22%)], muscle weakness [n= 2 (18%), 1 (13%), 2 (22%)], convulsion [n= 1 (9%), 3 (38%), 0 (0%)], quadriplegia or hemiplegia [n= 1 (9%), 2 (25%), 1 (11%)], dizziness [n= 2 (18%), 0 (0%), 2 (22%)], agitation [n= 0 (0%), 2 (25%), 5 (56%)], and hypertalkativity [n= 0 (0%), 0 (0%), 1 (11%)]. In 30 days after CAS, 3 (27%) patients of type I HPS had morbidity or mortality. One (9%) patient of type I HPS and 2 (25%) patients of type IIa HPS had dysarthria or hemiplegia. None (0%) of type IIb HPS had related neurological deficits.

Conclusions

We provide a new category system to describe the varied scope of HPS of CAS. The

patients of type IIb "Slight, nonhemorrhagic" HPS can present with emotional or behavior change which was under-recognized before. Early diagnosis and aggressive management with strict blood pressure control can prevent the slight HPS progress to the advanced categories.

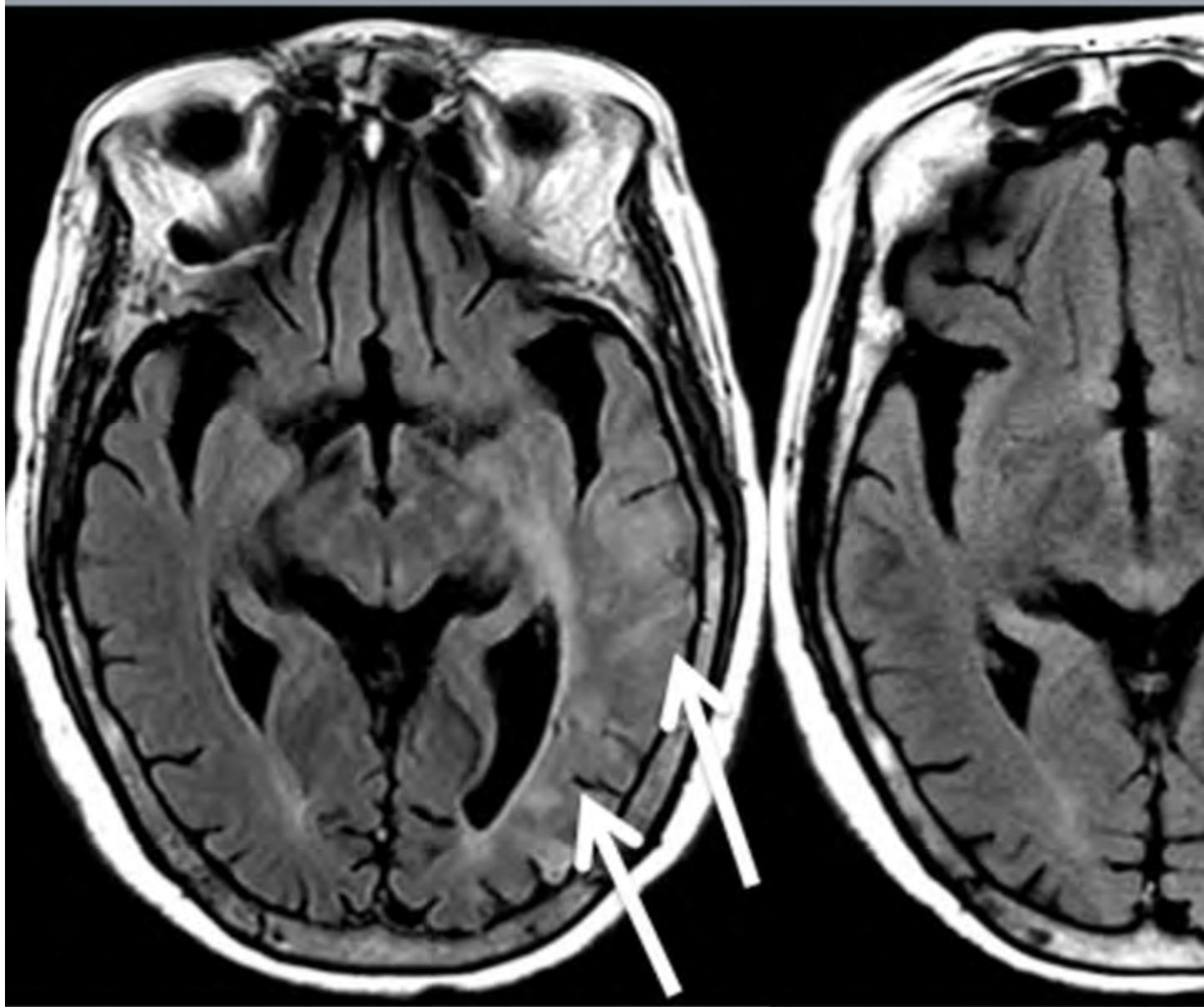


Fig. A 79-year-old woman presented with sudden onset of dysarthria, headache and seizure one week after left carotid stenting. MR T2 FLAIR shows edematous change at left parieto-temporal region (right, arrows) and resolved one week later (left).

(Filename: TCT_O-462_HPS2.png)

O-464

10:51AM - 10:54AM

Pial Artery Supply as a Treatment Risk for Intracranial Dural Arteriovenous Fistulas

S Hetts¹, A Yen², D Cooke³, M Amans³, P Jolivalt², F Settecase³, M Alexander³, R Darflinger³, C Dowd⁴, R Higashida³, H Kim³, V Halbach³

¹University Of California, San Francisco, San Francisco, CA, ²University of California, San Francisco, San Francisco, CA, ³UCSF, San Francisco, CA, ⁴Univ. Of California San Francisco, San Francisco, CA

Purpose

Intracranial dural arteriovenous fistulas (DAVFs) are rare vascular malformations that connect meningeal arteries to dural venous sinuses or cortical veins, accounting for 10-15% of all intracranial arteriovenous lesions. Although DAVFs are supplied by dural branches of the internal carotid, external carotid, and vertebral arteries, they also can be fed by pial arteries that also supply the brain. We sought to determine the frequency of neurological deficits following treatment of intracranial dural fistulas with and without a component of pial supply.

Materials and Methods

A retrospective review of 123 patients who underwent embolization for intracranial DAVFs at our hospital from 2008 to 2015 was conducted. Clinical information was derived from electronic medical records and radiologic imaging data. Patients were examined for postembolization neurological deficits, and those patients with deficits were evaluated for evidence of infarction and for clinical improvement. Data were analyzed using multivariate logistic regression.

Results

Of the 123 treated patients, 30 patients (24.4%) had DAVFs that were supplied by pial arteries and 93 patients (76.4%) had DAVFs supplied by nonpial vessels. Of the 30 patients with pial artery supply, four (13.3%) had post-treatment neurological deficits, compared to two patients (2.2%) out of the 93 patients without pial artery supply. Imaging demonstrated three patients with pial artery supply (10%) had foci of cerebral ischemia, compared to only one patient without pial artery supply (1.1%).

Conclusions

Patients with DAVFs supplied by pial arteries were more likely to experience post-treatment neurological deficits including strokes than patients with no pial artery supply.

O-465

High-Resolution Vessel Wall MRI in the Evaluation of Ruptured Cranial Dural Arteriovenous Fistulas: Preliminary Experience

C Matouk¹, B Cord¹, J Yeung¹

¹*Yale University School of Medicine, New Haven, CT*

Purpose

High-resolution vessel wall magnetic resonance imaging (VW-MRI) is increasingly being used to characterize intracranial vascular disease. Recent studies have begun to explore its utility in the evaluation of ruptured intracranial aneurysms (1-3). For example, we previously demonstrated that VW-MRI could identify the site-of-rupture in patients with SAH and multiple, intracranial aneurysms (1). We hypothesized that VW-MRI also may be useful in the evaluation of a more complex, angioarchitectural vascular malformation; namely, ruptured cranial dural arteriovenous fistulas (dAVFs). Herein, we report for the first time VW-MRI in patients with ruptured cranial DAVFs.

Materials and Methods

A retrospective review was performed of cranial DAVFs treated by a single practitioner (CCM) between December 2011 and December 2015. Patients were included if they underwent VW-MRI in addition to conventional sequences (CT, CTA, MRI, MRA, and catheter angiography) prior to definitive treatment. Vessel wall MRI was performed on a Verio 3.0T scanner with a 32-channel head coil (Siemens Healthcare). The T1-weighted black blood vessel wall sequence (TSE acquisition with FOV=16x16cm acquired matrix=512x512; slice thickness=2mm; total slab thickness=4-6cm; repetition time/echo time 590/10ms) was performed before and after the administration of gadolinium (with constant scan parameters). Each vessel wall sequence was performed in the axial and coronal planes.

Results

Of six patients treated with ruptured cranial dAVFs, three patients underwent VW-MRI in addition to conventional imaging prior to definitive treatment. Case #1. This 39-year-old man presented with spontaneous, focal SAH adjacent to the medulla secondary to a ruptured cranial dAVF of the left hypoglossal canal (Borden Type III). Conventional sequences demonstrated a venous varix at the epicenter of the focal SAH. Vessel wall MRI demonstrated thick enhancement of the wall of the ruptured venous varix. Case #2. This 87-year-old woman presented with spontaneous fourth ventricular hemorrhage secondary to a ruptured posterior fossa dAVF (Borden Type III). Conventional sequences demonstrated a bi-lobed venous varix at the floor of the fourth ventricle. Vessel wall MRI demonstrated thick enhancement of the wall of the anterior lobe projecting into the fourth ventricular clot, but not the posteriorly-directed lobe pointing away from the clot. Case #3. This 54-year-old man presented in extremis with a spontaneous, acute subdural hematoma requiring emergent evacuation

and decompressive craniectomy. Conventional sequences demonstrated a cranial dAVF related to an occluded R transverse sinus (Borden Type III). The presumptive site-of-rupture was a venous varix subjacent to the evacuated subdural hematoma and contiguous with a small intraparenchymal hemorrhage. Vessel wall MRI demonstrated thick enhancement of the wall of the ruptured venous varix and contiguity with the parenchymal clot.

Conclusions

The site-of-rupture in cranial dAVFs demonstrates thick vessel wall enhancement and contiguity with the hemorrhage on high-resolution VW-MRI. These data may be useful in clinical decision-making.

O-466

10:57AM - 11:00AM

Anterior Ethmoidal Dural Arterio-Venous Fistulas (dAVF): Endovascular Treatment Through the Ophthalmic Artery

C Perazzini¹, E Pomero², A Malakhia², A Biondi²

¹*Besançon University Hospital, Besançon, France*, ²*Besançon University Hospital, Besançon, France*

Purpose

Anterior ethmoidal dural arteriovenous fistulas (dAVF) are rare intracranial lesions fed by ethmoidal branches arising from the ophthalmic arteries. The venous drainage is through cortical veins most often draining into the superior sagittal sinus or through the deep leptomeningeal venous system draining into the basilar vein. Dilated venous pouches often are observed. These lesions are associated with a high risk of intracranial hemorrhage (ranged from 62% to 91% of cases). The endovascular treatment of the anterior ethmoidal dAVFs is feasible, however the approach through the ophthalmic arteries (OAs) remains a delicate procedure because of the risk of ischemic complications leading to retinal damage. We report our experience in the treatment of these lesions.

Materials and Methods

Retrospective evaluation was carried out on five patients (3 women and 2 men, mean age 67.6 years) with an anterior ethmoidal dAVF. Two patients (cases 1 and 5) presented with an intracranial hemorrhage, one patient (case 4) with papilledema due to increased intracranial pressure and in two patients (cases 2 and 3) the dAVF was diagnosed incidentally on a MR study performed because of endocarditis in one case and vertigo in the other one. The two patients in whom the dAVF was revealed by intracranial hemorrhage underwent transarterial embolization through the right ophthalmic artery; the patient presenting with vertigo underwent transarterial embolization through both ophthalmic arteries. The 80-year-old patient (case 4)

affected by papilledema refused consent to treatment and the patient (case 2) with endocarditis died because of cardiac failure before any treatment. In case 1, transarterial embolization was performed using glue (Glubran), in case 3 using Onyx (right ophthalmic artery) and Glubran (left ophthalmic artery) and in case 5 using only Onyx. In all cases, transarterial administration of nimodipine (50% diluted in normal saline) including selective infusion in the ophthalmic artery was performed during the endovascular procedure in order to prevent vasospasm of the ophthalmic artery (leading to temporary hypoperfusion of the central retinal artery and subsequent retinal ischemia) due to the maneuvers of microcatheter removal.

Results

After endovascular treatment, complete occlusion of the anterior ethmoidal dAVF was obtained in all cases. No technical or clinical complications (especially regarding a visual deficit) occurred. The angiographic follow-up at 1 year confirmed the persistent occlusion of the lesion. Treated patients were asymptomatic at follow up.

Conclusions

The endovascular treatment of the anterior ethmoidal dAVFs using a transarterial approach through the ophthalmic artery allows the occlusion of these lesions at high risk of neurological complications. The risk of an ischemic damage of the retina due to a vasospasm or an occlusion of the ophthalmic artery due to embolic material reflux must be considered. The precise retinal tolerance time to acute ischemia is still undefined (<4 hours). The selective periprocedural administration of nimodipine is crucial to avoid vasospasm.

O-467

11:00AM - 11:03AM

Imaging Characteristics after Intra-arterial Cytoreductive Chemotherapy for Lacrimal Adenoid Cystic Carcinoma

S Williams¹, B Snelling¹, S Sur¹, N Nagornaya²

¹University of Miami, Miami, FL, ²University of Miami/Jackson Memorial Hospital, Miami, FL

Purpose

Primary lacrimal adenoid cystic carcinoma is a rare, aggressive malignant epithelial cancer. It is a difficult lesion to treat due to its proclivity for perineural spread with intracranial extension, soft tissue and bone infiltration, as well as hematogenous and lymphatic invasion. Despite maximal surgical and medical therapy, recurrence rates of 55-88% within 5 years of diagnosis have been reported. For these reasons, a multimodality treatment approach is required. In our institution neoadjuvant intra-arterial chemotherapy (IAC) usually is performed prior to surgical management to enhance local disease control. Transient post-treatment changes on follow-up imaging

can be extensive and confused for tumor spread. To our knowledge, this is the first evaluation of post-treatment imaging findings after IAC for this disease.

Materials and Methods

Retrospective chart review of all patients receiving intra-arterial chemotherapy for lacrimal adenoid cystic carcinoma. Imaging obtained at the time of diagnosis and pre- and post -IAC were reviewed. Imaging features evaluated include tumor size, perineural spread, and changes in the adjacent bone and soft tissue. Timing of imaging in relation to therapy, vessel catheterized during IAC, number of IAC treatments, chemotherapy agent and dosage utilized, as well as possible concurrent chemoradiation at the time of imaging was evaluated.

Results

Fifteen patients received IAC for lacrimal adenoid cystic carcinoma at a single institution from 2010-2015. Thirteen patients received MR and or CT imaging of the orbits before and after IAC.

Conclusions

Imaging evaluation of adenoid cystic carcinoma plays a critical role in management given the aggressive nature of the disease. Extensive edema and enhancement can be seen on the treated side, especially of the infratemporal fossa, several weeks after IAC that improves on subsequent imaging. Awareness of these findings is important for the neuroradiologist to help differentiate post-treatment changes from disease progression.

O-468

11:03AM - 11:06AM

Eye lens doses imparted during interventional and non-interventional neuroimaging techniques

N Guberina¹, C Mönninghoff², A Ringelstein²

¹*Institute of Diagnostic and Interventional Radiology and Neuroradiology, Essen, NRW,* ²*Institute of Diagnostic and Interventional Radiology and Neuroradiology, University Hospital Essen, Essen, NRW*

Purpose

To assess and compare eye lens doses imparted during interventional and noninterventional imaging techniques for the examination of intracranial vessels.

Materials and Methods

We performed a phantom study on an anthropomorphic phantom (ATOM dosimetry phantom 702-D; CIRS, Norfolk, Virginia, USA) and measured eye lens doses with TLD-s Type 100 (LiF:Mg,Ti) during interventional (3D rotational angiography, 2 plane DSA a/p and lateral projections) and noninterventional neuroimaging techniques [CT-angiography (CTA) with and without lens protectors, with and

without prior assessment of unenhanced cranial CT-protocols (nCT)]. Eye lens doses were calculated following recommendations of the ICRP 103.

Results

In the noninterventional setting following absorbed eye lens doses are measured: (I) CTA 3.9 mGy; (II) CTA with lens-protector 2.3mGy; (III) CTA in combination with prior nCT 31.9mGy; (IV) CTA with +nCT (nCT including head tilt) 16.1mGy; (V) CTA with nCT with lens-protector 23mGy. Eye lens doses for the interventional setting were distributed as follows: (VI) 3D rotational angiography 1mGy (VII) 2 plane DSA p/a+lat.4.5mGy (VIII) 3D rotational angiography and 2 plane DSA 5.5mGy.

Conclusions

Eye lens doses are lower during 3D rotational angiography compared to 2 plane DSA. Gantry angulation in the noninterventional setting and 3D rotational angiography bear considerable capacity for eye dose savings.

O-469

11:06AM - 11:09AM

Estimation of radiation exposure of children undergoing superselective intra-arterial melphalan therapy for retinoblastoma treatment

N Guberina¹, S Göricke², C Mönninghoff², S Sirin², S Suntharalingam³, A Ringelstein²

¹*Institute of Diagnostic and Interventional Radiology and Neuroradiology, Essen, GA,* ²*Institute of Diagnostic and Interventional Radiology and Neuroradiology, University Hospital Essen, Essen, NRW,* ³*University Hospital Essen, Essen, Germany*

Purpose

The purpose of this study was to examine the radiation exposure of children undergoing melphalan therapy for retinoblastoma treatment in the neurointerventional setting.

Materials and Methods

In a retrospective study design the radiation exposure of children undergoing superselective intra-arterial melphalan therapy for retinoblastoma treatment was examined. All neurointerventional procedures were performed on the flat panel angiography system Allura Xper (Philips, Eindhoven, The Netherlands) at University Hospital Essen. Altogether 63 neurointerventional procedures could be included in the time period from 04/2011 till 08/2015. We differentiated patients according to the following variables: age group (infant 1-12 months, child 13-36 months), indication (bulbus preserving first line therapy or in relapse), used microcatheter-system and number of individual melphalan therapies. Fluoroscopy time and dose area product

(DAP) were assessed with dose monitoring software Radimetrics Enterprise platform (BayerHealthcare, Leverkusen, Germany).

Results

In detail, the following data were acquired: (I) fluoroscopy time 16.7min. (II) DAP 9.3 Gy cm^2 . (III) effective dose 1.1mSv. (IV) average number of individual melphalan therapies 1.5 and (V) successful neurointerventional procedure in 49/63 cases.

Reasons for a not carried out melphalan therapy were an unsuccessful microcatheterization and meningeal anastomoses.

Conclusions

This is the first data acquisition of radiation exposure during superselective intra-arterial melphalan therapy of a pediatric cohort at the German Retinoblastoma Referral Centre. The assessment of radiation exposure in a larger population and comparison to international standards are the next necessary step for the determination of diagnostic reference levels.

O-470

11:09AM - 11:12AM

A Novel System Using Multiple Radiophotoluminescence Glass Dosimeters For Radiation Measurements During Diagnostic Cerebral Angiography And Therapeutic Neurointerventional Procedures

K Futatsuya¹, S Kakeda², T Moritake², L Sun², J Moriya², S Ide², N Ohnari², K Fujimoto², E Futagami², J Yamamoto², S Nishizawa², Y Korogi²

¹University of Occupational and Environmental Health, School of Medicine, Kitakyushu, Japan, ²University of Occupational and Environmental Health, School of Medicine, Kitakyushu, Fukuoka

Purpose

There has been a growing concern regarding the detrimental effects of radiation to the patients during neurointerventional procedures. Furthermore, according to the 2011 ICRP statement, the threshold of the crystalline lens dose decreased from 5 to 0.5 Gy. Recently, we developed the direct measurement system (RADIREC) for calculating entrance skin dose (ESD) using multiple radiophotoluminescence glass dosimeters (RPLGDs) set on the surface of the patient's head and neck (Fig.1). The aim of this study was to evaluate the actual radiation exposure of the crystalline lens, the maximum ESD, and distribution of the ESDs during diagnostic cerebral angiography and therapeutic neuro-interventional procedures.

Materials and Methods

By using RPLGDs set, crystalline lens doses, the maximum ESD, and distributions of ESDs were evaluated prospectively in 28 consecutive adult patients (35 sessions

consisting of 22 diagnostic procedures and 13 therapeutic procedures). The crystalline lens doses and the maximum ESD were compared with the dose-area product (DAP).

Results

The mean maximum ESD was 440.2 ± 293.1 mGy (range; 67-1464). The mean doses of the crystalline lens were 48.6 ± 35.7 (1-128) mGy on the right side and 18.3 ± 10.6 (1-46) mGy on the left side; in all patients, the right side dose was higher than the left side dose. For the dose distribution, 24 procedures (22 patients) (68.6%) showed the maximum ESD in the right occipital regions. Although the maximum ESD showed significant positive correlations with the DAP ($r = 0.67$, $p < 0.01$), there were no correlations between the crystalline lens dose and the DAP ($r = 0.04$, $p = 0.82$).

Conclusions

RADIREC is an epoch-making system which can evaluate radiation exposure of the crystalline lens and the distribution of ESD precisely. In contrast, the DAP seems not useful to predict radiation exposure of the crystalline lens.



(Filename: TCT_O-470_ASNR2016abstractimage.jpg)

O-471

11:12AM - 11:15AM

Significant Dose Reduction During Neurointerventional CT Cases Using Table Side Parameter Controls

A Bress¹, S Metzler¹, C Plastaras¹, B Pukenas²

¹University of Pennsylvania, Philadelphia, PA, ²Hospital Of the Univ. Of Pennsylvania, Philadelphia, PA

Purpose

The purpose of this abstract is to show how computed tomography (CT)-guided neurointerventional procedures can be performed safely and effectively utilizing low dose radiation with and without a preplan CT scan. Altering a few basic radiation parameters with the side table control panel has shown marked reduction in dose length product (DLP) when comparing with the previous institutional CT scanner. In our experience, many CT-guided neuro-interventional procedures can be performed with only a scout image and low-dose CT-fluoroscopy when prior imaging is available. Our aim is to demonstrate how relatively simple alterations in the CT scanner parameters can be used in order to significantly decrease radiation exposure to the patient, operator, and staff during the majority of CT-guided procedures. Throughout our presentation we will show how we apply these techniques in several cases depicting how simple and effective these radiation sparing techniques are for guiding the needle(s) to the desired target.

Materials and Methods

A total of 141 patients undergoing CT neuro-interventional procedures were included in this retrospective data analysis study from July 1, 2014 to June 30, 2014. The patients underwent various CT-guided neuro-interventional procedures including spinal biopsy, aspiration, cyst fenestration, vertebral augmentation, epidural injection, epidural blood patch, nerve block and cyst fenestration. The dose-length products (DLP) were obtained from the postprocedural dose report which routinely are uploaded to our institutional PACS system. Only one patient did not have a dose report uploaded to PACS. The patients then were separated into three groups: AS+N (SENSATION 64 slice, Siemens, replaced in January 2015), AS+Y (SOMATOM Definition AS+ 128 slice, Siemens) with pre-plan CT, and AS+Y without preplan CT. Then, the mean DLP and diagnostic sampling rate was compared between the groups.

Results

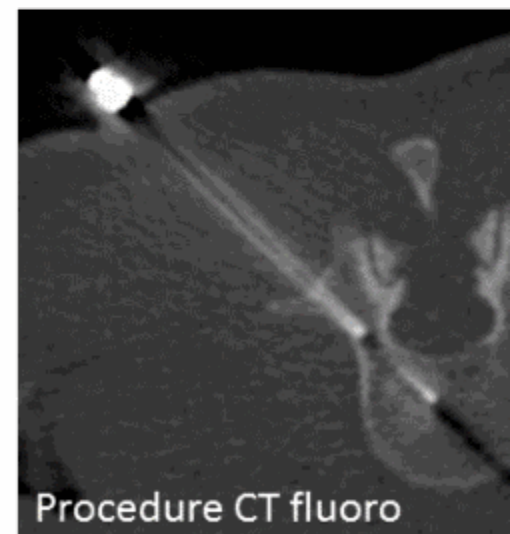
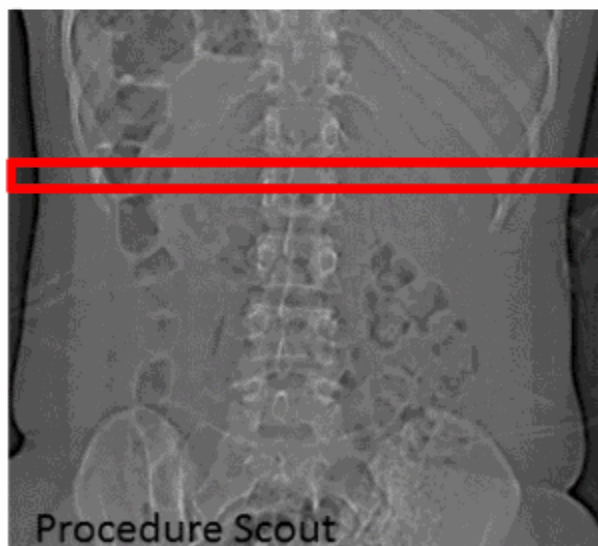
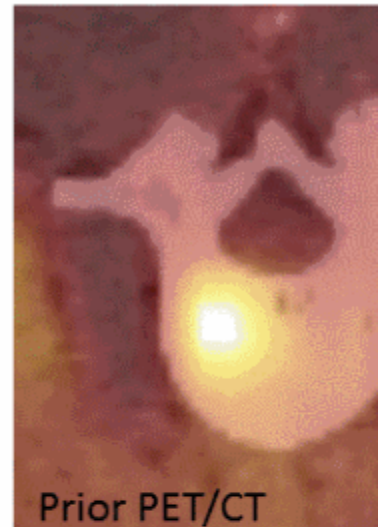
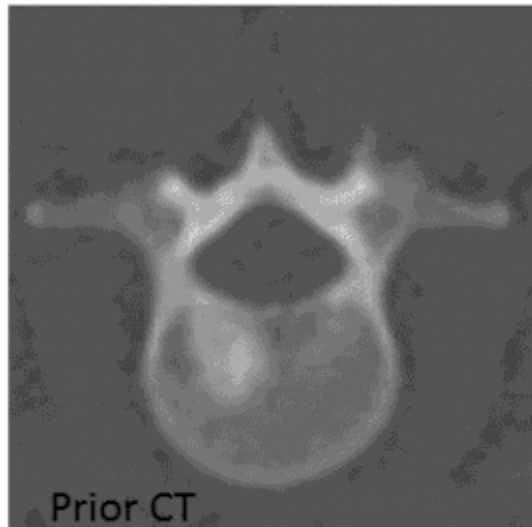
Groups were divided as follows: 54 patients in the AS+N group, 51 in the AS+Y pre-plan CT group, and 35 in the AS+Y no pre-plan CT group. The mean DLP (\pm SD) for the AS+N was 815.84 \pm 246.53, the AS+Y pre-plan CT 233.00 \pm 220.78, and the AS+Y no preplan CT 27.64 \pm 33.75. Diagnostic biopsy sampling rates were 43/47 (91.5%), 37/39 (94.9%), and 28/30 (93.3%), respectively.

Conclusions

Many CT-guided neuro-interventional procedures can be performed using only a scout image for planning purposes, augmenting the mAs and kV for CT fluoroscopy, and reviewing prior imaging. A preplanning CT prior to performing a CT-guided procedure is necessary only for complex cases particularly when the known targeted region cannot be identified confidently using prior imaging and the scout image. Our biopsy yields are consistently over 90% regardless of the chosen technique. Utilizing these relatively simple measures can provide significant radiation dose reduction to

everyone involved as well as adhere to ALARA (As Low As Reasonably Achievable) and Image Gently guidelines.

L2 Vertebral Body Lesion Biopsy



Dx: Metastatic carcinoma – mucoepidermoid
DLP = 28 mGy*cm, KV – 120, mAs - 8

(Filename: TCT_O-471_Images.gif)

Thursday

10:30AM - 12:00PM

Washington Marriott Wardman Park, Roosevelt 4

21F - Excerpta - III

Hemorrhagic Wernicke's Encephalopathy

H Oligane¹, F Oyedeji², J Mettenburg³, M Hughes¹

¹University of Pittsburgh Medical Center, Pittsburgh, PA, ²University of Pittsburgh Medical Center, Murrysville, PA, ³UPMC, Pittsburgh, PA

Purpose

Wernicke's encephalopathy is a serious neurologic disorder characterized by vitamin B1 deficiency. Recognizing typical and atypical imaging characteristics is imperative because of the potential reversibility of this condition. Petechial micro-hemorrhage is a common pathologic finding on autopsy in patients with Wernicke's encephalopathy (1). However, intracranial hemorrhage identified by imaging is very rare and has only been described in non-radiologic literature in a handful of case reports (2, 3).

Materials and Methods

The patient is a 48 year old male who was found unresponsive in his home. Per his family he had a three week history of dizziness, hypersomnia, excessive vomiting, severe anorexia, and progressive mental deterioration. He had a past medical history of coronary artery disease, obesity, myocardial infarction, and diabetes mellitus type II, but there was no history of alcohol abuse or illicit drug use. CSF samples were negative. Initially an MRI was performed at an outside institution and interpreted as bilateral thalamic infarctions and intraventricular hemorrhage. The patient was transferred to our institution. The studies were re-interpreted as an unusual case of Wernicke's encephalopathy complicated by intraventricular hemorrhage. There was no arterial or venous thrombosis on vascular imaging. The patient's vitamin B1 level was found to be critically low. With parenteral thiamine supplementation, the patient's altered mental status gradually improved and he was eventually discharged home.

Results

CT of the Head: Acute intraventricular hemorrhage within the third ventricle and bilateral occipital horns (Figure 1 & 3). Noncontrast MRI of the brain: Symmetric abnormal T2 FLAIR signal within the bilateral thalami (Figure 2), mammillary bodies (Figure 3), and periaqueductal region (Figure 4). No abnormal restricted diffusion was present (not shown).

Conclusions

Intracranial hemorrhage is an atypical imaging characteristic of Wernicke's encephalopathy, which is a potentially treatable life threatening condition.

Radiologists must be aware of both the typical and atypical imaging characteristics of this disorder, as early identification and initiation of treatment can prevent devastating consequences.

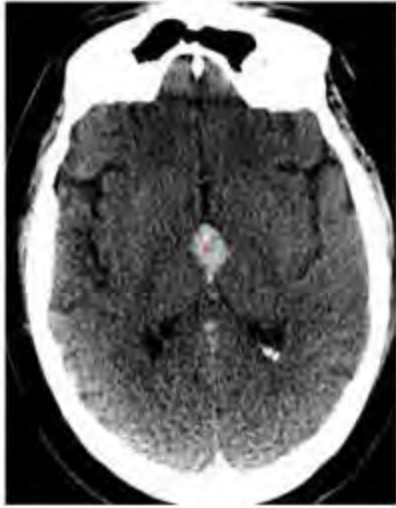


Figure 1

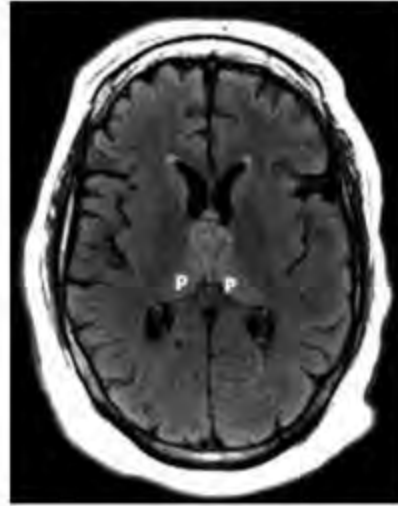


Figure 2

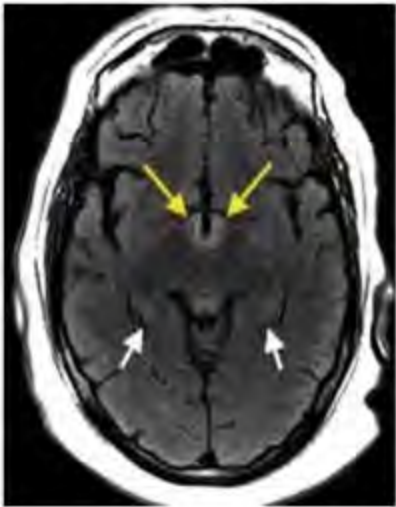


Figure 3

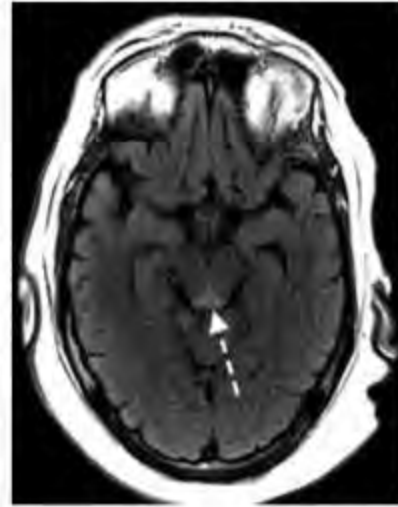


Figure 4

(Filename: TCT_E-37_imagefile.jpg)

E-38

10:35AM - 10:40AM

MRI Findings in Thallium Toxicity

D Johnson¹, P Morris¹

¹*Mayo Clinic, Rochester, MN*

Purpose

Thallium salts are extremely toxic to animals, and were formerly widely used as rodent poison. Because thallium salts are colorless, odorless, and tasteless, human deaths from thallium poisoning, both accidental and purposeful, have been reported. This has fortunately become quite rare, as thallium use is now closely restricted in many countries. Central nervous system manifestations of thallium toxicity include delirium, visual disturbance, seizure, and often coma leading to death in severe cases. Alopecia is a characteristic sign of thallium toxicity, but it often does not occur until other symptoms are well established. Because the vast majority of cases of thallium toxicity occurred prior to the advent of CT or MRI, little is known about the neuroradiological manifestations of this condition.

Materials and Methods

A young adult presented with two weeks of progressive paresthesia, diplopia, and abdominal pain. During the evaluation of these symptoms, the patient experienced a rapid neurological decline, becoming lethargic, non-ambulatory, and non-communicative over several days. Extensive evaluation was nondiagnostic until the patient began to develop alopecia, at which time blood and urine thallium levels were found to be extremely elevated.

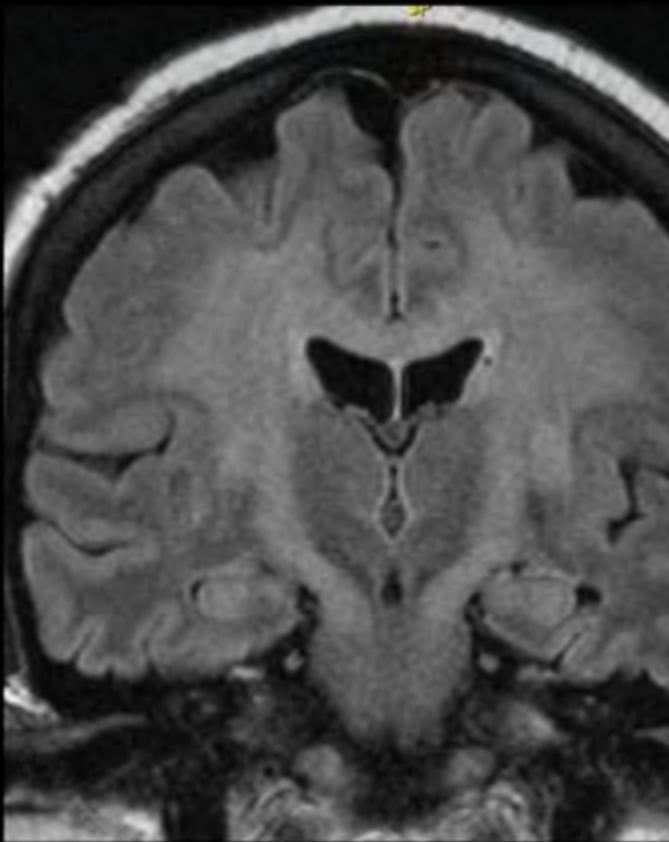
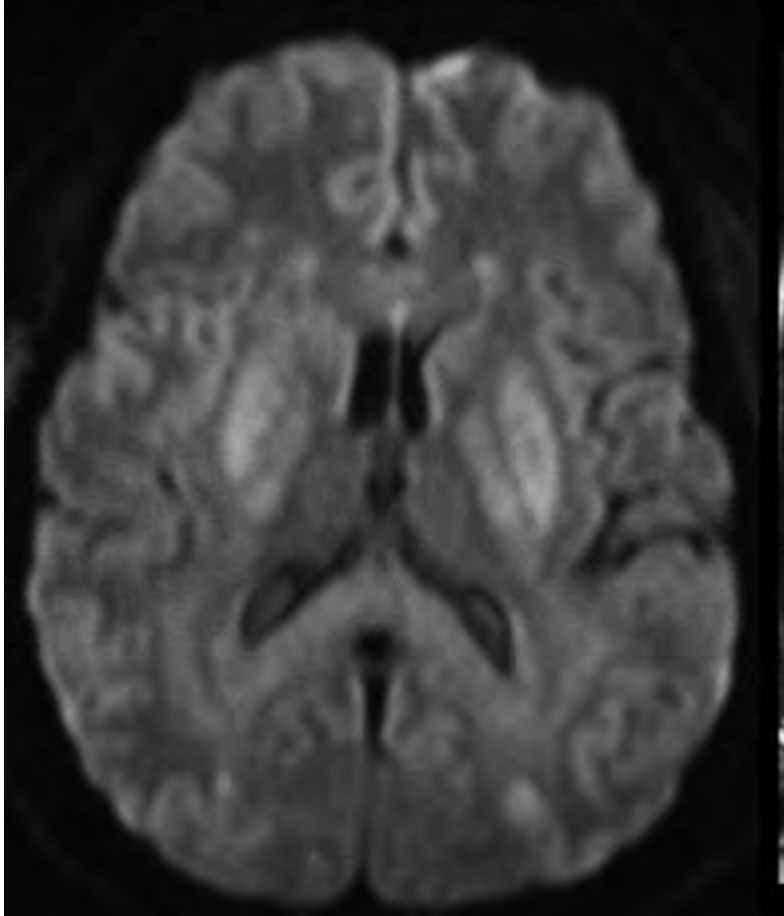
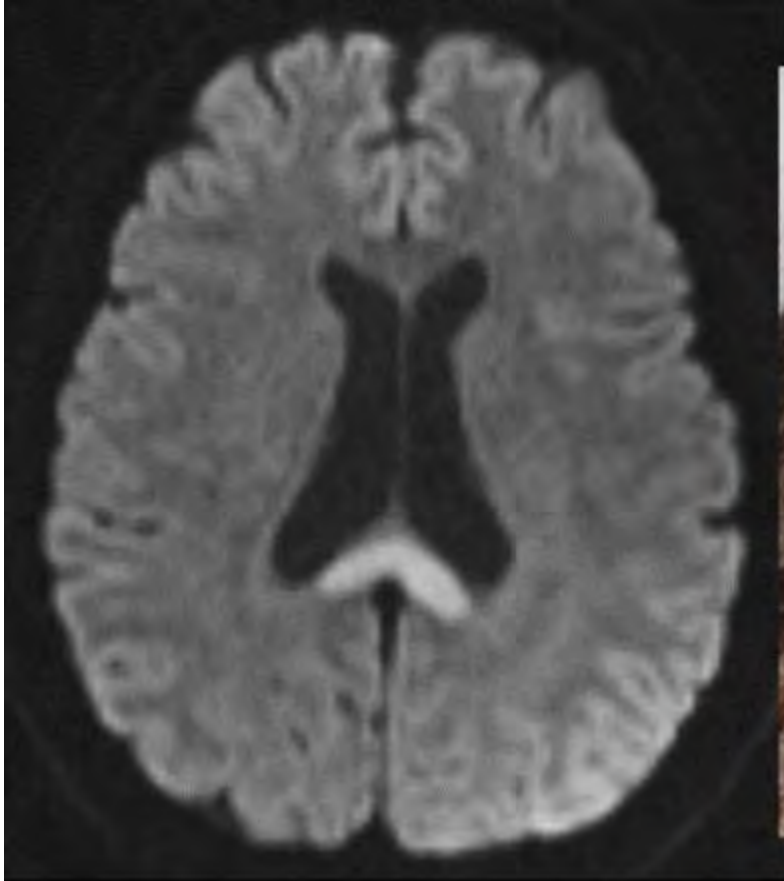
Results

An MRI at the onset of neurological symptoms was unremarkable. A repeat study two weeks later demonstrated new restricted diffusion in the splenium of the corpus callosum (upper left) and the right cingulate gyrus as well as new patchy enhancement in the white matter of the bilateral frontal lobes with corresponding increased FDG uptake on PET. Soon after this, the patient began to develop alopecia (upper right). By one week later the restricted diffusion had progressed to include the deep grey nuclei and multiple regions of cortex (lower left). FLAIR hyperintensity was seen throughout the periventricular white matter, with extension into the brainstem (lower right).

Conclusions

Thallium toxicity is an uncommon cause of rapid neurological decline. Treatment with hemodialysis and oral Prussian blue can limit the severity of disease, though delays in diagnosis may allow irreversible damage to occur prior to the initiation of

these measures. Awareness of the neuroradiological manifestations of this condition may allow earlier diagnosis and appropriate therapy.



(Filename: TCT_E-38_NewFig1.JPG)

E-39

10:40AM - 10:45AM

A Case of Phosphomannomutase 2 deficiency (CDG-Ia): Neurologic and Ophthalmologic Findings

J Guerin¹, M Ho², A Parvinian²

¹Mayo Clinic, Rochester MN, Rochester, MN, ²Mayo Clinic, Rochester, MN

Purpose

To demonstrate a case of phosphomannomutase 2 deficiency (CDG-Ia) with several classic neurologic and ophthalmologic imaging features.

Materials and Methods

Phosphomannomutase 2 deficiency (CDG-Ia), caused by mutation in the gene encoding PMM2, is the most common congenital disorder of glycosylation (CDG). The clinical spectrum is highly variable with more severe forms seen in infancy and more mild phenotypes in those that survive to adolescence and adulthood. The more classic neurologic form with cerebellar dysfunction related to cerebellar hypoplasia/atrophy is nearly always observed in older patients. Other common findings include hypotonia, ataxia, seizures and developmental delay as well as retinitis pigmentosa and nystagmus. We feature a 25 year-old man with the first diagnosed case of this disorder at Mayo, initially discovered in 1993 at the age of three when he presented global developmental delay, ataxia and partial seizures. As an adult, he continues to have drug-resistant epilepsy, chronic global static encephalopathy, myoclonus and movement disorder, demyelinating peripheral neuropathy and progressive retinitis pigmentosa. Patient underwent initial brain MRI in 2014 for his epilepsy. Notable imaging features include severe cerebellar and midbrain atrophy, idiopathic intracranial hypertension, hypomyelination, retinitis pigmentosa and bilateral staphylomas. On MR spectroscopy there is also a characteristic myoinositol peak and decreased NAA related to neuronal loss and gliosis.

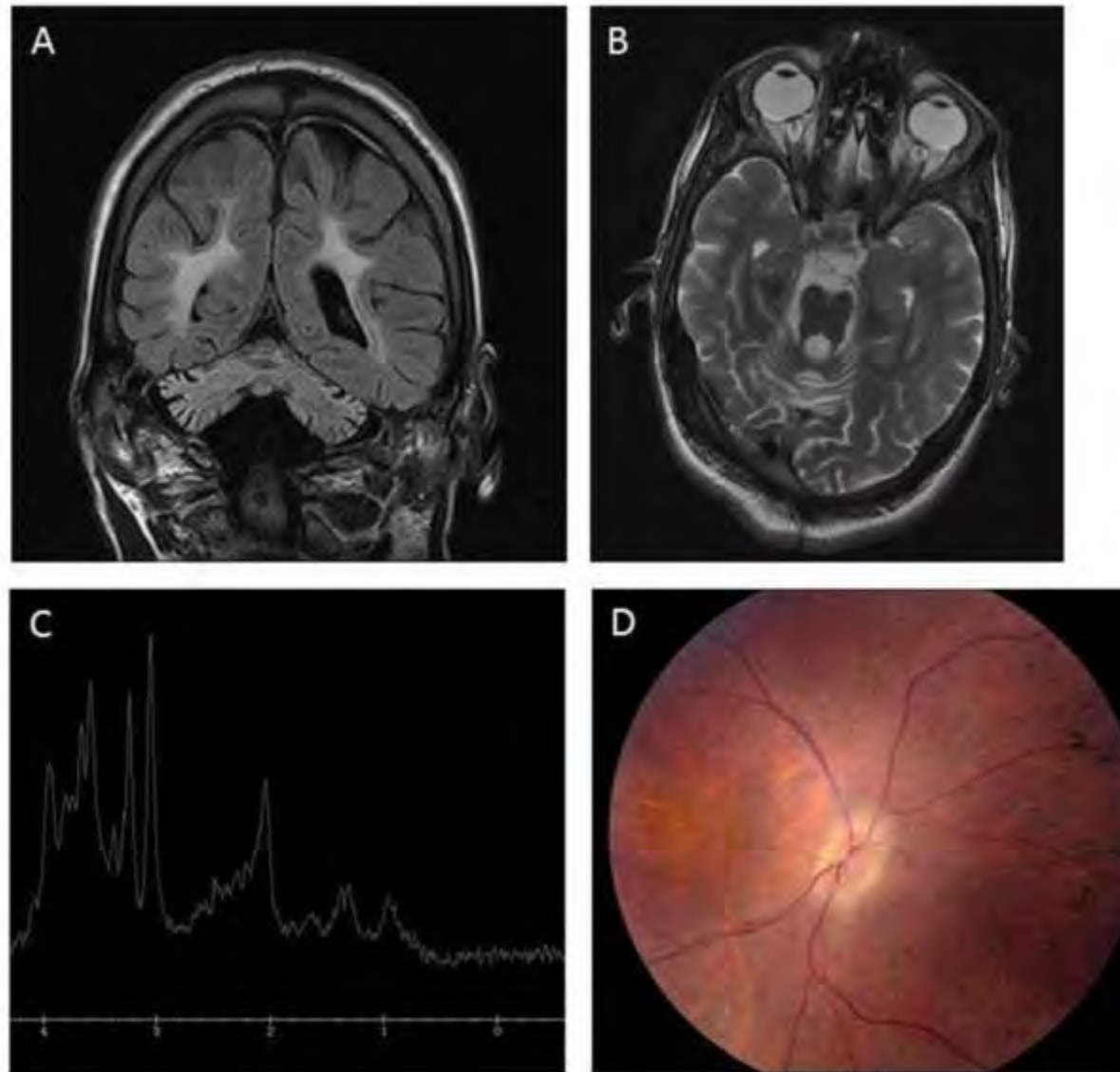
Results

Selected collage of images. A: Coronal T2 FLAIR demonstrates severe cerebellar and more mild cerebral volume loss with increased T2 FLAIR signal and relative decreased white matter. B: Axial T2 sequence shows posterior scleral flattening as can be seen with idiopathic intracranial hypertension. Subtle outpouching of the posterolateral globes, off center from the optic disks, compatible with staphylomas. Severe midbrain atrophy. C: MR spectroscopy from a cerebellar voxel shows elevated myoinositol peak and decreased NAA peak related to neuronal gliosis. D: Fundoscopic

photograph demonstrates a pale optic disk, scattered retinal pigment deposits and thinned blood vessels; these findings are seen with retinitis pigmentosa.

Conclusions

Case report of a 25 year-old man with phosphomannomutase 2 deficiency (CDG-Ia), the most common congenital disorder of glycosylation, with characteristic neurologic and ophthalmologic MRI, MR spectroscopy and fundoscopic findings.



(Filename: TCT_E-39_Images1.jpg)

E-40

Woodhouse Sakati Syndrome

E Lindgren¹, V Lehman¹

¹*Mayo Clinic, Rochester, MN*

Purpose

Demonstration of Woodhouse Sakati Syndrome (WSS) with MRI findings in an adult female. Woodhouse Sakati is an uncommon inherited condition which results in extrapyramidal symptoms, alopecia, mild deafness, intellectual disabilities and hypogonadism.

Materials and Methods

We submit a case of a 38 year-old female from the Middle East who had a normal birth and development, but at the age of 13, started developing muscle weakness with dystonia. She subsequently experienced a progressive decline in health: she never developed any secondary sexual characteristics, nor reached menarche. Later, she experienced difficulty opening her mouth, markedly impaired verbal communication, and developed alopecia and hearing impairment. Family history revealed 4 of her 7 siblings, male and female, had similar symptoms. All children were the product of a consanguineous marriage (first cousins). MRI findings are detailed below. The genetic test for Woodhouse-Sakati syndrome was positive (DCAF17 mutation).

Results

MRI demonstrated innumerable areas of T2 hyperintensity within the subcortical and deep white matter of both cerebral hemispheres; this had progressed since an MRI 8 years prior. There was marked low susceptibility signal within both globi pallidi and the pars reticulata of both substantia nigra, which was compatible with brain iron accumulation.

Conclusions

Previously reported MRI findings have ranged from normal to patchy and confluent periventricular white matter abnormalities and centrum semiovale signal intensities on T2 images suggesting iron accumulation to pituitary abnormalities. To our knowledge, none has shown findings consistent with iron accumulation on susceptibility weighted images (SWI). Moreover, reportedly normal cases previously did not include SWI. Radiologists should consider the use of SWI when WSS is suspected as imaging findings can help prompt genetic testing in the appropriate clinical scenario.

E-41

A Case of Adult-Onset Adrenoleukodystrophy

F Baffour¹, C Carr¹, L Eckel¹

¹Mayo Clinic, Rochester, Rochester, MN

Purpose

To review the MRI imaging findings in Adult-Onset Adrenal Leukodystrophy.

Materials and Methods

34 year old Caucasian male with traumatic brain injury and quadriplegia after a motor vehicular accident at the age of 33. He presented to the emergency department with tachypnea, hypoxia and fevers and was transferred to the intensive care unit where he was intubated due to hypoxic respiratory failure. A brain MRI was obtained due to acute worsening of his mental status with findings supporting a diagnosis of adult onset adrenoleukodystrophy. He failed to wean from mechanical ventilation and comfort care measures were initiated after 9 days on admission. The patient passed away 4 days later. The medical history is pertinent for chemically diagnosed adrenoleukodystrophy at age 11 with symptoms of adrenal insufficiency. He had no neurological symptoms and several brain MRIs were negative. The patient's younger brother was diagnosed with adrenoleukodystrophy at age 9, and has since passed away (age 11).

Results

MRI of the brain demonstrates extensive T2 hyperintensity with some areas demonstrating profound enhancement throughout the cerebral white matter symmetrically, involving the periventricular white matter, internal capsules, corpus callosum, and cortical spinal tracts with extension into the brainstem. No mass effect is demonstrated.

Conclusions

Adult cerebral adrenoleukodystrophy is a relatively rare presentation and compromises between 2% and 5% of all patients with adrenoleukodystrophy. More commonly adults with this disorder present with adrenal myeloneuropathy, characterized by progressive paraparesis, sphincter dysfunction, and adrenal insufficiency. There are reports of head trauma initiating rapidly progressive adult-onset cerebral adrenal leukodystrophy in some patients. Unfortunately there is no treatment for this disorder once the cerebral degeneration has begun. The key imaging features include abnormal white matter signal intensity, primarily within the centrum ovale, pyramidal tracts in the brainstem and internal capsule. No postgadolinium enhancement is seen due to the intact blood-brain barrier.

E-42

10:55AM - 11:00AM

Venous signal on cervical TOF MRA due to “venous subclavian steal

B Winegar¹, E Quigley², U Rassner¹

¹University of Utah, Salt Lake City, UT, ²University Of Utah, Salt Lake City, UT

Purpose

Review causes of high venous signal on TOF MRA with a case of "venous subclavian steal" as an example

Materials and Methods

89 year old female presented to the Emergency department with right sided vision loss. A stroke workup was performed including MRI of the brain and MRA of head and neck. Ultimately the case of vision loss was found to be total retinal detachment

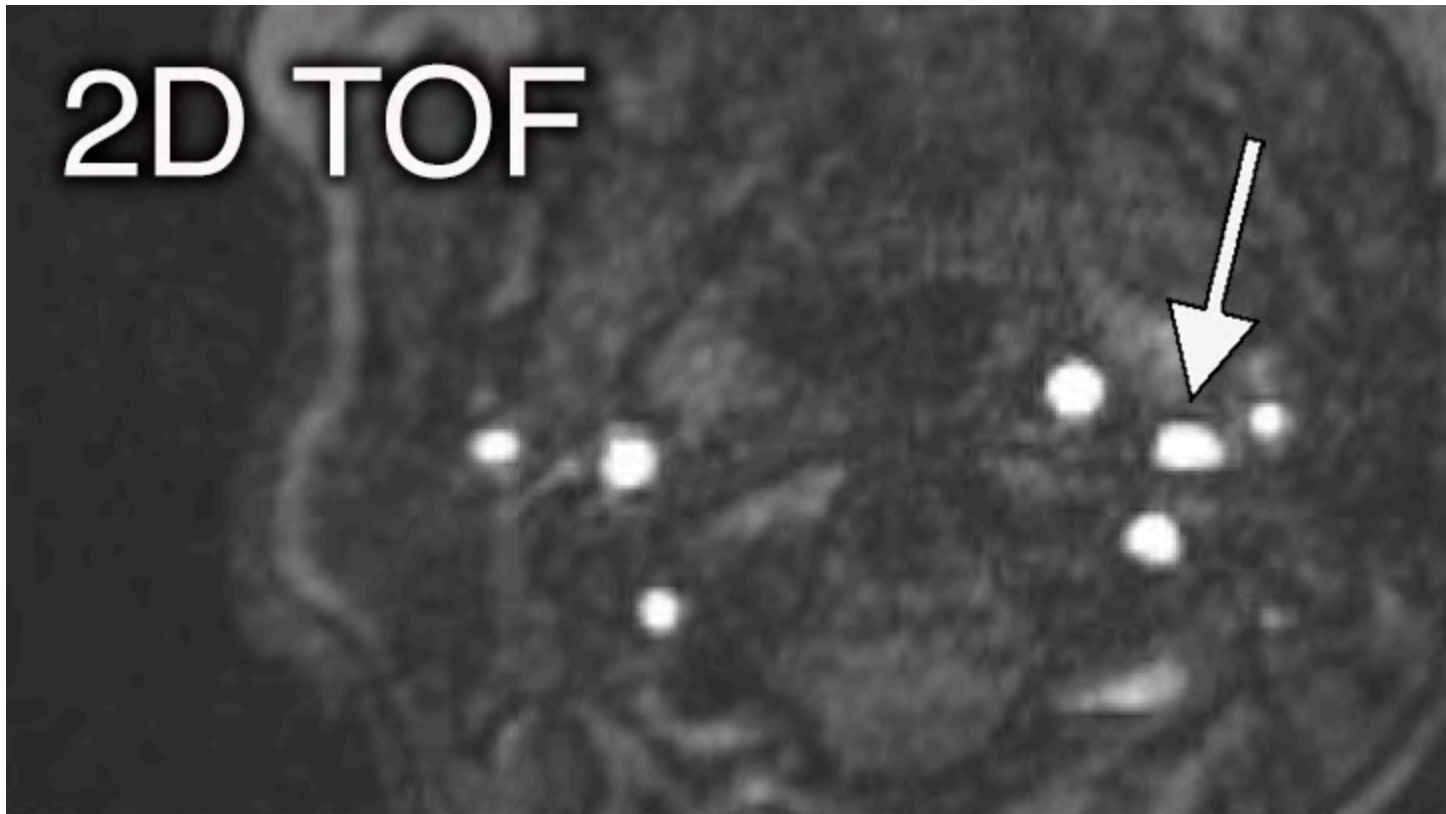
Results

Brain MRI showed senescent changes without signs of ischemic stroke. MRA showed no flow limiting stenosis. Axial 2D time of flight (TOF) of the neck and 3D TOF of the brain showed flow related enhancement in the left transverse and sigmoid sinus as well as in the left jugular vein. Brain MRI showed senescent changes without signs of ischemic stroke. MRA showed no flow limiting stenosis. Axial 2D time of flight (TOF) of the neck and 3D TOF of the brain showed flow related enhancement in the left transverse and sigmoid sinus as well as in the left jugular vein. Venous signal on TOF MRA can be seen with arteriovenous shunting lesions (e.g. AV fistulas), thrombus with T1 shortening, or following the administration of gadolinium contrast agents. Flow reversal, in which venous blood signal is not suppressed by the saturation band cranial to the image slice, is an additional source of increased venous signal. Venous phase post contrast MRA images showed occlusion of the left brachiocephalic vein resulting in reversed flow in the left internal jugular vein.

Conclusions

While venous signal on TOF MRA is commonly seen with AV fistulas or T1 bright thrombus, reversed flow has to be considered. Understanding the physics behind TOF MRA can be important in correct interpretation of venous signal on TOF MRA. This case had reversal of flow in the internal jugular vein due to occlusion of the left brachiocephalic vein, leading to a flow phenomenon akin to arterial steal.

2D TOF



Post gad MRA



(Filename: TCT_E-42_Abstract1.jpg)

E-43

11:00AM - 11:05AM

Progressive Multifocal Leukoencephalopathy Mimicking Gliomatosis Cerebri on MR Spectroscopy and Perfusion.

M Sondag¹, C Kim¹, S Futterer¹, B Liu¹

¹*Northwestern University Feinberg School of Medicine, Chicago, IL*

Purpose

To present a case of progressive multifocal leukoencephalopathy (PML) with MR spectroscopy (MRS) and perfusion (MRP) imaging mimicking neoplasm, specifically gliomatosis cerebri.

Materials and Methods

47-year-old-man with two months of progressive vision loss and cognitive difficulties. Physical exam revealed absence of light perception, left hemineglect and prosopagnosia. Notable lab values include HIV antibody positivity, HIV viral load 190,000 (normal <20), and absolute CD3/CD4 count 37 (normal >340). MR imaging was performed demonstrating findings mimicking gliomatosis cerebri. Subsequent brain biopsy yielded pathology consistent with PML.

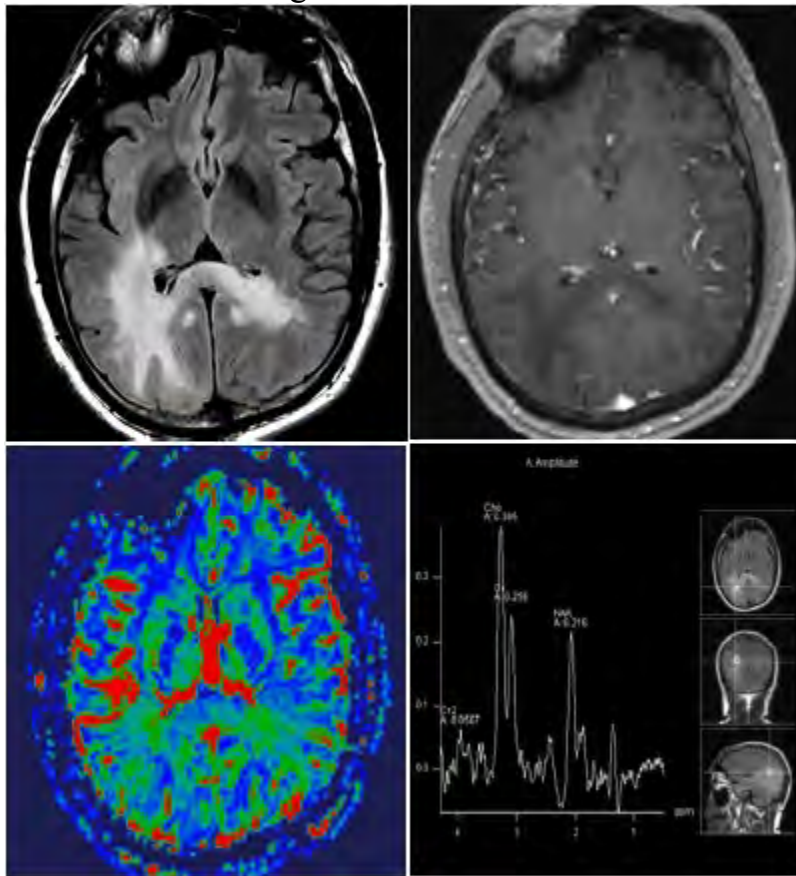
Results

MRI: Nonenhancing confluent FLAIR hyperintensity centered in the right temporal white matter and extending across the splenium of the corpus callosum to involve the left cerebral white matter. PERFUSION: Elevated relative cerebral blood volume (rCBV) ratio approximating 2.5 in regions of bilateral parietooccipital FLAIR hyperintensity. SPECTROSCOPY: Elevated Cho/NAA ratio approximating 1.8 in regions of right parietooccipital FLAIR hyperintensity.

Conclusions

Advanced imaging modalities such as MRS and MRP may assist in differentiating neoplasms from non-neoplastic brain lesions. We present a case of PML mimicking gliomatosis cerebri with false-positive findings on MRS and MRP. Prior studies investigating MRP have demonstrated specificity and positive predictive values (PPV) ranging from 0.58-0.92 and 0.87-0.93, respectively, to diagnose neoplasm using an elevated rCBV threshold of 1.5-1.75 (1,2). Combined MRP and MRS criteria have yielded specificity and PPV as high as 0.92 and 0.93, respectively, for neoplasm using thresholds of rCBV 1.5 and Cho/NAA 1.64 (1). A variety of non-neoplastic lesions may demonstrate increased Cho/NAA (3,4), however PML is not a well-known false-positive entity. This case reviews the variable MRS findings (5) and MRP findings in PML. Discriminating between PML and gliomatosis is important for diagnosis, treatment guidance, and in some cases, prevention of brain biopsy. Recognizing that

PML may show false-positive MRS and MRP findings resembling neoplasm is essential for radiologists.



(Filename: TCT_E-43_Perrypicture2.jpg)

E-44

11:05AM - 11:10AM

Pure Alexia and Palinopsia From Glioblastoma Involving Left Inferior Occipital Gyrus Evaluated with fMRI and DTI Tractography

S Fung¹

¹Houston Methodist Hospital, Houston, TX

Purpose

Lesions involving visual word form area (VWFA) and inferior longitudinal fasciculus (ILF) can cause pure alexia. Palinopsia is a visual disturbance typically caused by occipitoparietotemporal cortical lesions involving the postgeniculate visual pathway. An unusual case of glioblastoma presenting as pure alexia and palinopsia is described, evaluated with language fMRI and DTI tractography.

Materials and Methods

A 67-year-old woman developed acute onset of difficulty recognizing whole words,

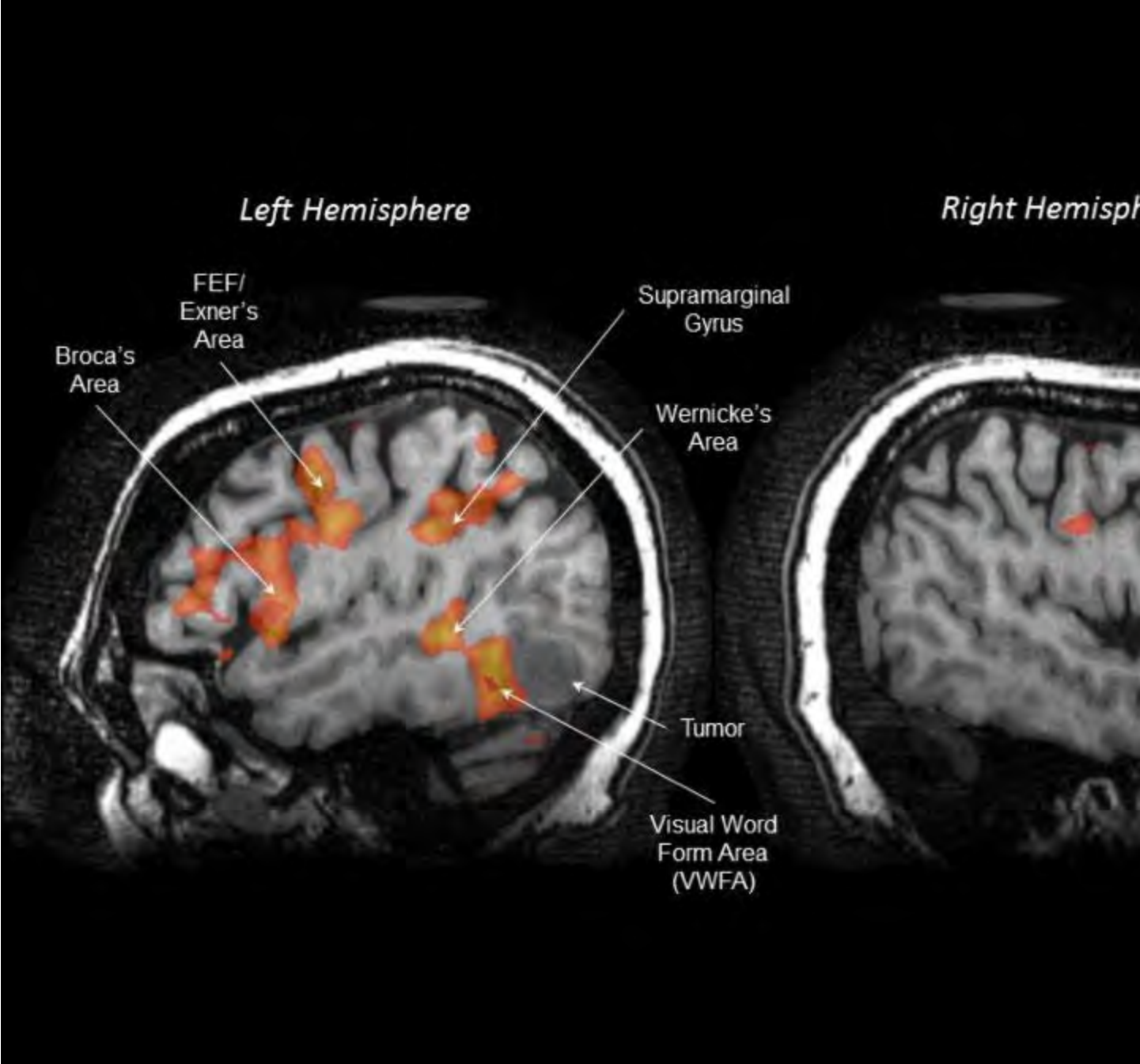
which she described as strings of scrambled characters, although she maintained the ability to spell and write and eventually learned to recognize words using letter-by-letter reading, symptoms consistent with pure alexia. She also complained of seeing persistent afterimages of objects lasting several seconds in her visual field after looking away, symptoms consistent with palinopsia.

Results

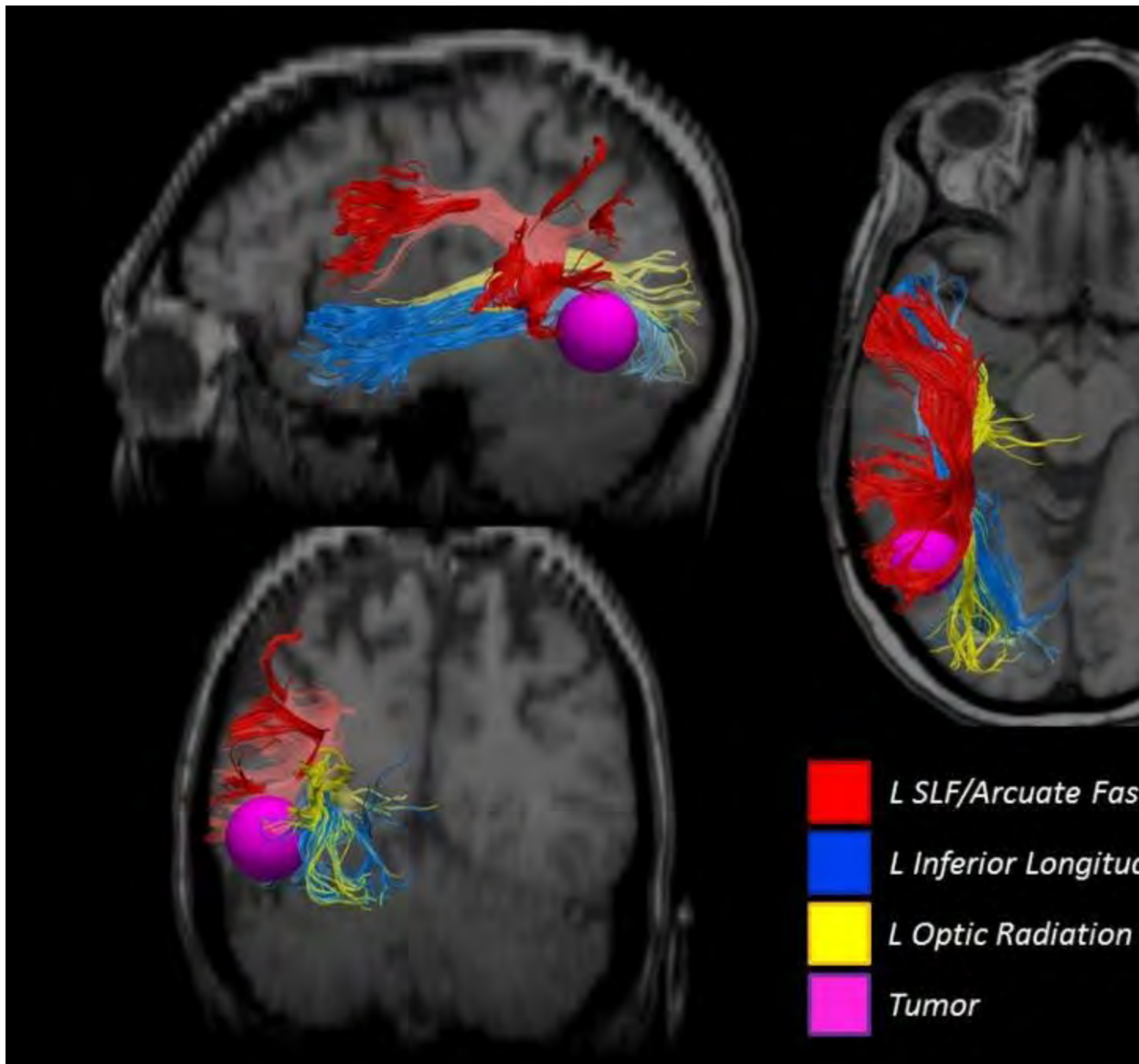
MRI showed 1.9 cm minimally-enhancing nodular mass involving and mildly expanding the cortex and subcortical white matter in the left inferior occipital gyrus. fMRI evaluating language was performed using silent word generation and reading comprehension tasks, which were visually presented as block design consisting of 17 periods of 30 s each with 9 control and 8 active conditions arranged in alternating sequence. Functional activation was relatively consistent across both runs of word creation and reading comprehension tasks. Left-lateralized frontal, temporal, and parietal language activation supported left hemispheric language dominance. Activation corresponding to VWFA was centered in the left fusiform gyrus/inferior occipital gyrus along the anterior margin of the tumor. DTI with 25 diffusion gradient directions was obtained using spin-echo EPI with b-value 1000 s/mm². DTI tractography was then performed using second-order Runge-Kutta propagation algorithm, 35° angle threshold. The vertical segment of the left arcuate fasciculus was just anterior to the margin of the mass. The left ILF and left optic radiation traversed in close proximity to the medial margin of the mass.

Conclusions

VWFA generally localizes to the region of fusiform gyrus and lateral occipitotemporal sulcus, typically in the dominant hemisphere for language involved in identifying words and letters from lower-level shapes. ILF courses along the lateral aspect of the inferior and posterior cornua of the lateral ventricle connecting occipital and temporal lobes and is part of the ventral visual association pathway crucial for object identification. In the dominant hemisphere, ILF is thought to carry afferent and efferent fibers to the VWFA. Lesions involving the VWFA and ILF can cause pure alexia, also known as alexia without agraphia. Patients have difficulty reading but can spell and write, although some can recognize words using letter-by-letter reading. Palinopsia is a visual disturbance with persistent or recurrent images after the stimulus is removed. Lesions are typically in the non-dominant occipitoparietotemporal region involving the postgeniculate visual pathway, although lesions can involve the dominant hemisphere, as in this case.



(Filename: TCT_E-44_FungetalASNR2016AbstractFig1.jpg)



(Filename: TCT_E-44_FungetalASNR2016AbstractFig2.jpg)

E-45

11:10AM - 11:15AM

Toxic Meningoencephalopathy after Intrathecal Gadolinium Administration

J Chetta¹, s Kumar², P Diaz-Marchan¹

¹Baylor College of Medicine, Houston, TX, ²BCM, Houston, TX

Purpose

Intrathecal gadolinium is safe and useful in clinical imaging when administered in low doses. Only three case reports exist citing neurotoxicity when intrathecal gadolinium is used in high doses. We report a rare case of toxic meningoencephalopathy following a MR myelogram.

Materials and Methods

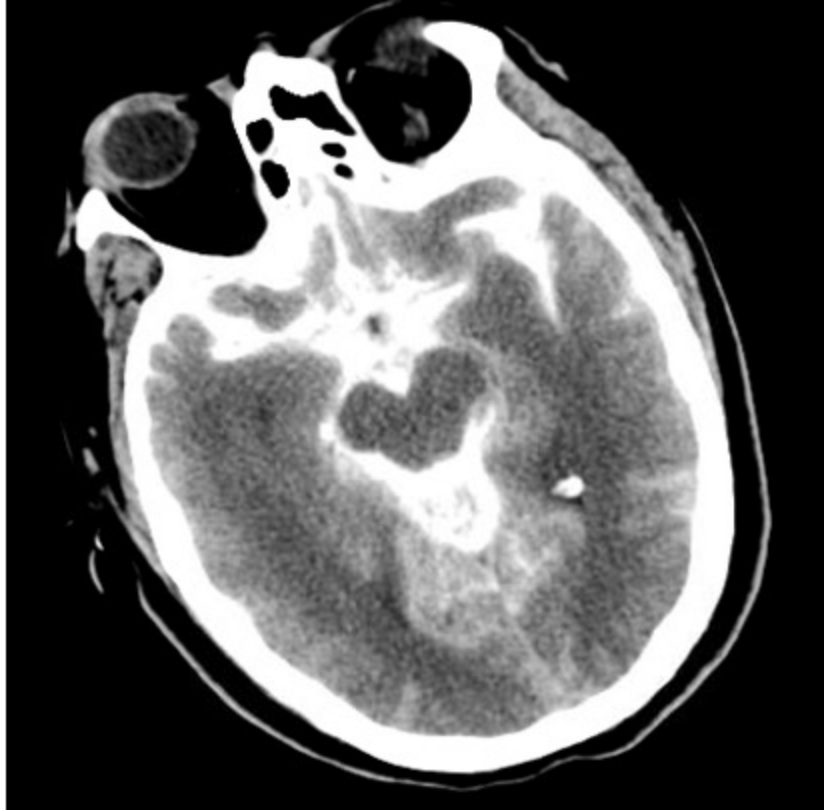
A 64-year-old male presented to our emergency department (ED) with altered mental status following an MR myelogram. He had a history of spinal surgeries and post-surgical seroma which required routine imaging. Ten hours prior to arrival the patient underwent intrathecal administration of gadolinium at an outside facility for a MR myelogram. He was in his usual state of health. After the intervention, the patient reported progressively worsening headache, malaise, and exhibited neurologic decline. Upon entry to our ED, he was febrile and tachycardic. He exhibited somnolence, global aphasia, nuchal rigidity, and dense quadriplegia. Cell counts and blood chemistries were unremarkable. Blood cultures were negative. A head CT was performed. Cerebrospinal fluid (CSF) analysis showed a mild lymphocytic pleiocytosis. CSF cultures were negative although the lumbar puncture was performed after antibiotics were given. The patient returned to his baseline over 24-48 hours and discharged within the week.

Results

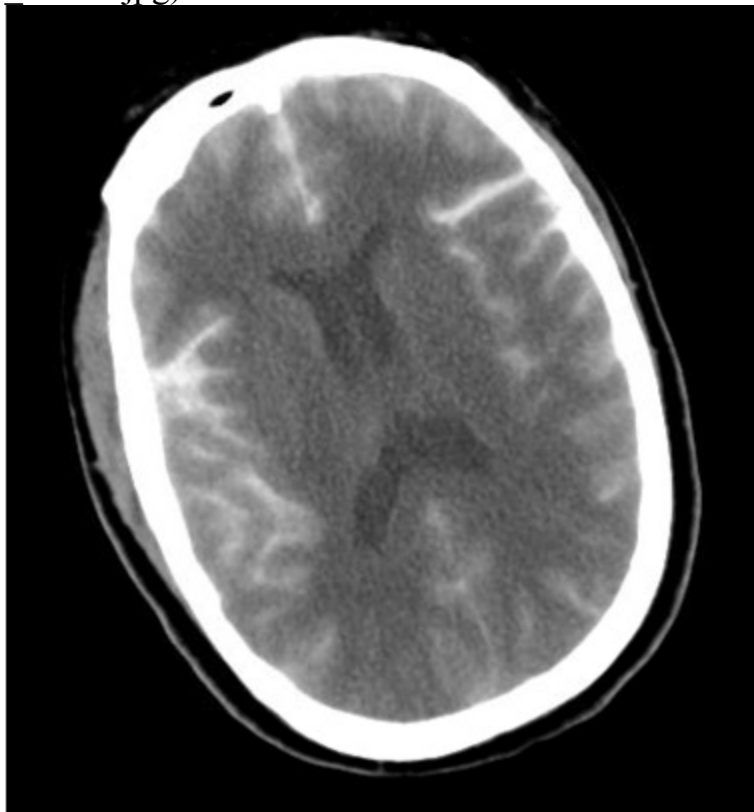
A head CT performed on admission showed diffuse opacification of the subarachnoid spaces and cisterns. A head CT performed 12 hours later showed new complete effacement of the cerebral cortical sulci and basal cisterns, consistent with diffuse cerebral edema. A brain MRI performed on hospital day four showed no abnormalities.

Conclusions

Intrathecal gadolinium is a safe and useful tool for diagnostic imaging purposes. The patient presented to the ED following intrathecal contrast administration. The differential diagnosis included infectious or chemical meningitis however his rapid recovery is inconsistent with an infectious meningoencephalitis. Toxic meningoencephalopathy is a rare complication of intrathecal gadolinium administration.



(Filename: TCT_E-45_Slide2.jpg)



(Filename: TCT_E-45_Slide1.jpg)



(Filename: TCT_E-45_Slide55.jpg)

E-46

11:15AM - 11:20AM

Foreign Body Reaction to Bovine Pericardial Duraplasty

D Goold¹, M Lester¹, T Hijaz², C Therasse¹

¹Northwestern University, Chicago, IL, ²Feinberg School Of Med., Northwestern Univ., Chicago, IL

Purpose

We describe the imaging findings and clinical characteristics of an intracranial foreign body reaction resulting from the use of bovine pericardial duraplasty material in a patient who underwent surgery for meningioma recurrence.

Materials and Methods

We present a case of a 56-year-old woman with imaging findings suggestive of recurrence of a left frontal meningioma leading to repeat surgical resection. During the surgery, a portion of the native dura mater was resected, and the resulting defect was closed at the end of the surgery using bovine pericardial duraplasty material. Delayed post-operative follow-up imaging revealed extensive left frontal lobe edema, an increase in the size of an epidural fluid collection, and local abnormal meningeal enhancement. Given the absence of clinical signs of infection, the patient was treated

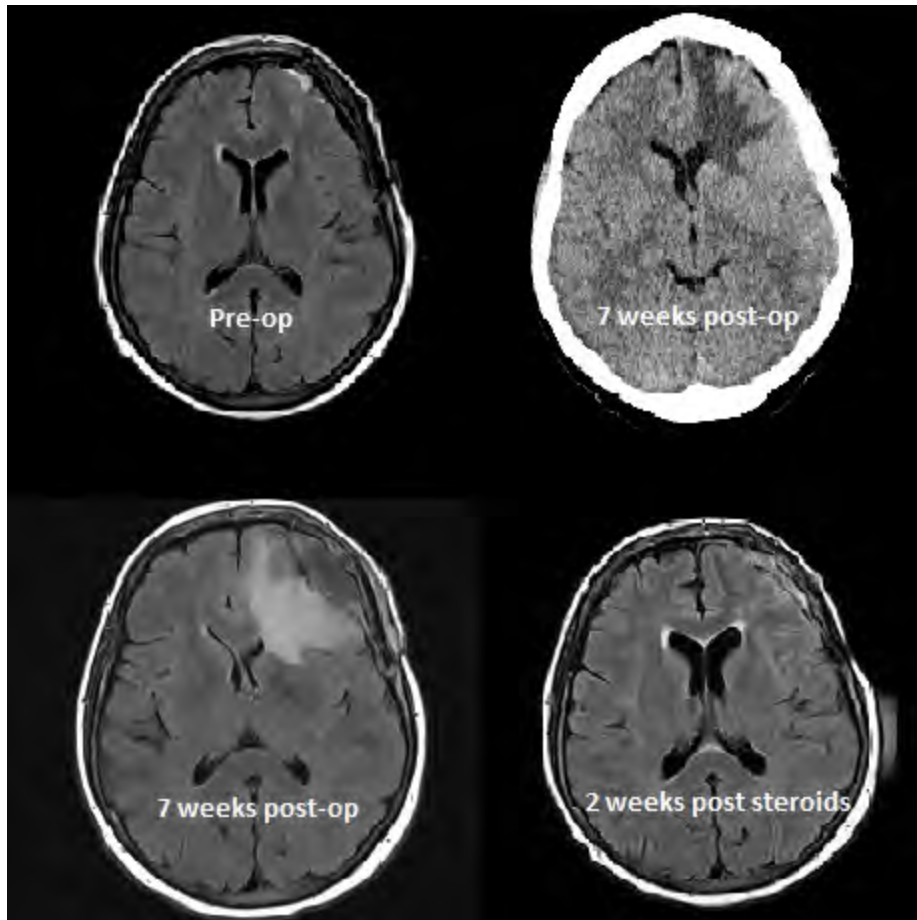
solely with a course of oral steroids. After treatment, there was significant improvement in the imaging appearance compatible with a foreign body inflammatory reaction to the dural graft material.

Results

Noncontrast head CT (7 weeks after surgery): When compared to immediate postoperative imaging, there was an increase in size of an epidural fluid collection beneath the craniotomy and development of new extensive vasogenic edema in the left frontal lobe. Contrast-enhanced brain MRI (7 weeks after surgery): MR imaging confirmed the increase in size of the aforementioned epidural fluid collection and also demonstrated new restricted diffusion within it. Also noted was new hyperintense T2/FLAIR signal in the left frontal lobe and accompanying new abnormal overlying pachymeningeal and leptomeningeal enhancement. Contrast-enhanced brain MRI (9 weeks after surgery and following oral steroid therapy): Compared to the MRI from 2 weeks prior, there was a decrease in size of the epidural fluid collection beneath the craniotomy. Furthermore, hyperintense T2/FLAIR signal in the underlying brain and local abnormal pachymeningeal/leptomeningeal enhancement also substantially decreased.

Conclusions

Extensive efforts have been made to find a graft material to optimize outcomes in patients requiring a duraplasty. Initial efforts began with rubber and gold foil, and later autologous, heterologous, and synthetic graft materials were employed. Bovine pericardium has generally been considered nonreactive in its use as a cardiac graft and has led to its emergence as a dural graft material. Bovine pericardium has been shown to be a suitable option with favorable outcomes and good surgical ease of use, generally lacking the local tissue effects seen with older graft materials. Nevertheless, rare associated foreign body reactions have been reported in the neurosurgical literature. Our case is unique in that it documents the clinical and imaging findings seen in both the development of such a foreign body inflammatory reaction and their improvement following oral steroid therapy alone.



(Filename: TCT_E-46_FBRXN.jpg)

E-47

11:20AM - 11:25AM

Amnesia, seizures, and the limbic system - anti-LGI1 Limbic Encephalitis: An evolving clinical syndrome.

N Cross¹, G Aguirre¹, E Botzolakis¹, J Stein¹, S Mohan¹

¹*University of Pennsylvania, Philadelphia, PA*

Purpose

Anti-LGI1 (Anti-leucine-rich glioma inactivated-1) limbic encephalitis is an uncommon clinical disorder often characterized by memory loss, seizures, and confusion. Whether of primary autoimmune, or more rarely paraneoplastic cause, early diagnosis allows prompt initiation of immune modulatory therapy and a search for possible underlying malignancy.

Materials and Methods

A 61 year old gentleman presented after an evening of more than a dozen episodes of lightheadedness during which he uttered inappropriate, bizarre comments. Each

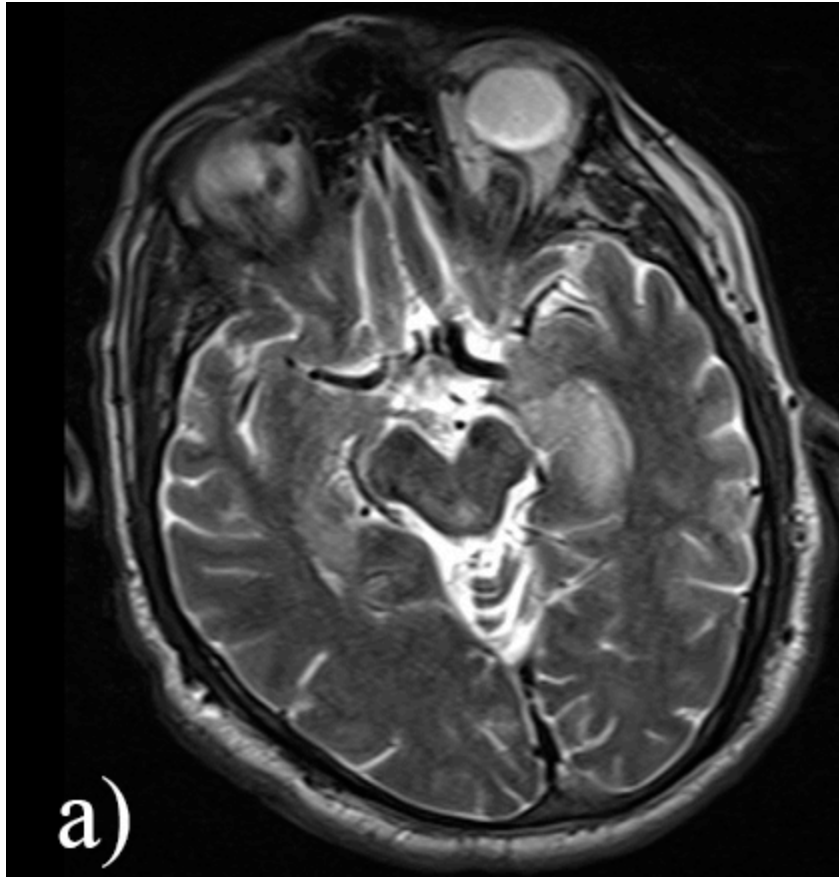
episode resolved quickly and was followed by a short 30-60 second period of confusion. There was no associated headache, weakness, loss of consciousness, diplopia, or shaking. The episodes continued, approximately hourly and were accompanied by body chills, feeling cold, whole body numbness and tingling, and progressive anterograde amnesia. For short periods, all of the patient's hairs would become erect during "chills" which were unrelated to room temperature. The combination of clinical symptoms including amnesia, pilomotor seizures, and imaging findings was considered diagnostic for limbic encephalitis and confirmatory labs were obtained including positive results for anti-LGI1 (Anti-leucine-rich glioma inactivated-1). Whole body imaging was negative for malignancy. Inpatient IVIG and steroid treatment, followed by rituximab, has resulted in gradual improvement in memory and function.

Results

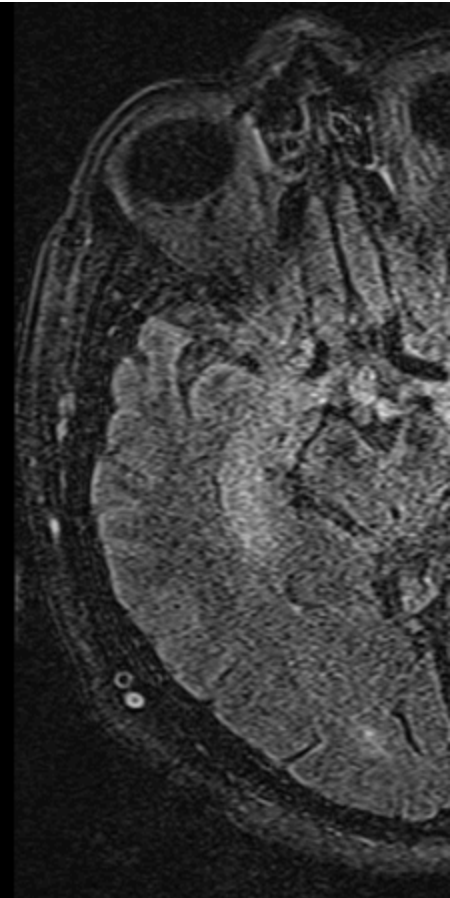
MRI of the brain demonstrated mildly expansile and slightly asymmetric T2/FLAIR hyperintensity throughout the bilateral hippocampi and mesial temporal structures. There was no definite enhancement visualized, and mild diffusion restriction was present in the mesial left temporal lobe. The remainder of the brain and cerebellum was unremarkable.

Conclusions

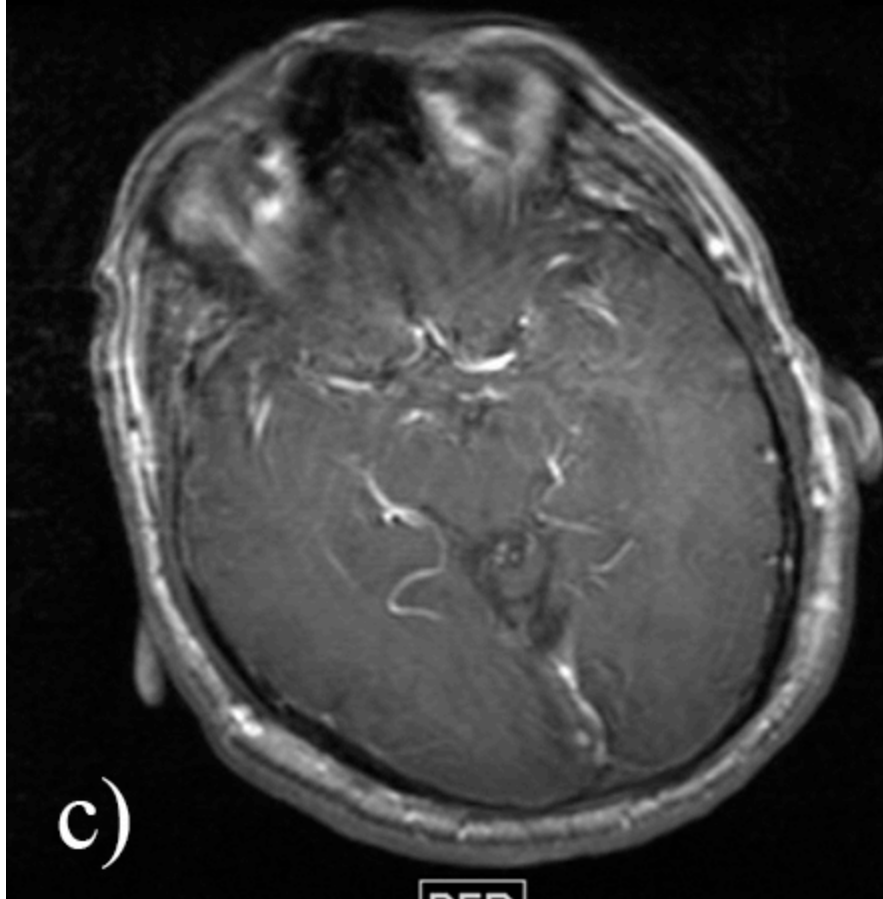
Bilateral mesial temporal signal abnormality with the appropriate clinical presentation including anterograde or retrograde amnesia, and possible seizures should suggest limbic encephalitis. Many of these cases are autoimmune, previously attributed to antibodies to voltage gated potassium channels; the true antibody target is LGI1. The paraneoplastic subset of limbic encephalitis is important because this diagnosis can prompt the search for an otherwise occult malignancy.



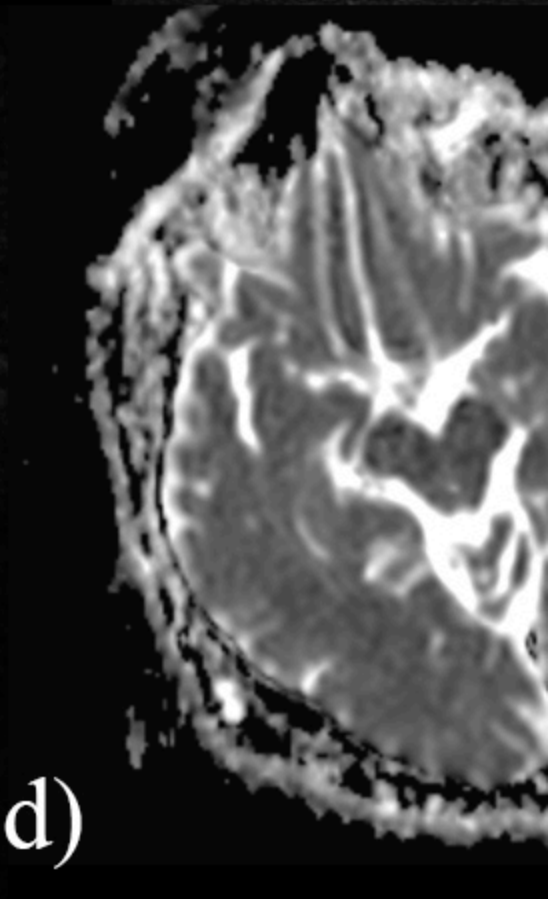
a)



b)



c)



d)

(Filename: TCT_E-47_limbicencephalitisimagefigure1.jpg)

E-48

11:25AM - 11:30AM

CNS Graft Versus Host Disease: Clinical and Radiologic Considerations in Diagnosis and Treatment

S Montoya¹, J Brucker², A Hussain³, M Khadir¹

¹University of Rochester Medical Center, Rochester, NY, ²University of Rochester, Rochester, NY, ³University of Rochester Medical Center, Rochester, NY

Purpose

We present an interesting neuroradiologic case to help illustrate the imaging findings of CNS graft versus host disease (GVHD), as correlated to features of its pathophysiologic and clinical progression, and presented in contrast to other leukoencephalopathies that are commonly encountered in this patient population.

Materials and Methods

The patient is a 30-year-old female who presented with night sweats and increasing fatigue in January 2013. At the time of presentation, the white cell count was markedly elevated at 203.4 with a correspondingly low hemoglobin of 7.5. A bone marrow biopsy was performed and confirmed the diagnosis of acute myelomonocytic leukemia. Subsequently, the patient underwent leukapheresis and induction chemotherapy, followed by multiple cycles of high dose cytarabine. A follow-up bone marrow biopsy performed in February 2014 revealed minimal residual disease. The patient continued treatment with a peripheral blood stem cell transplant and total body irradiation. In June 2015, the patient was re-admitted with mild encephalopathy, associated with focal neurologic findings of left homonymous hemianopia, left sided sensory deficit, and left pronator drift. An EEG was consistent with seizure activity and CSF analysis was negative for malignancy. However, an MRI demonstrated high T2 FLAIR-weighted signal involving the white matter lateral to the right caudate head, along the external capsule. Serial follow-up MRI examinations continued to show significant progression of T2 FLAIR signal abnormalities throughout the majority of the deep cerebral white matter and central brainstem, as well as the deep gray nuclei, despite plateaued Tacrolimus levels and initiation of steroid therapy. A brain biopsy was performed at the end of October, which revealed inflammation, but no evidence of malignancy or demyelination. Currently, the leading differential is CNS graft versus host disease.

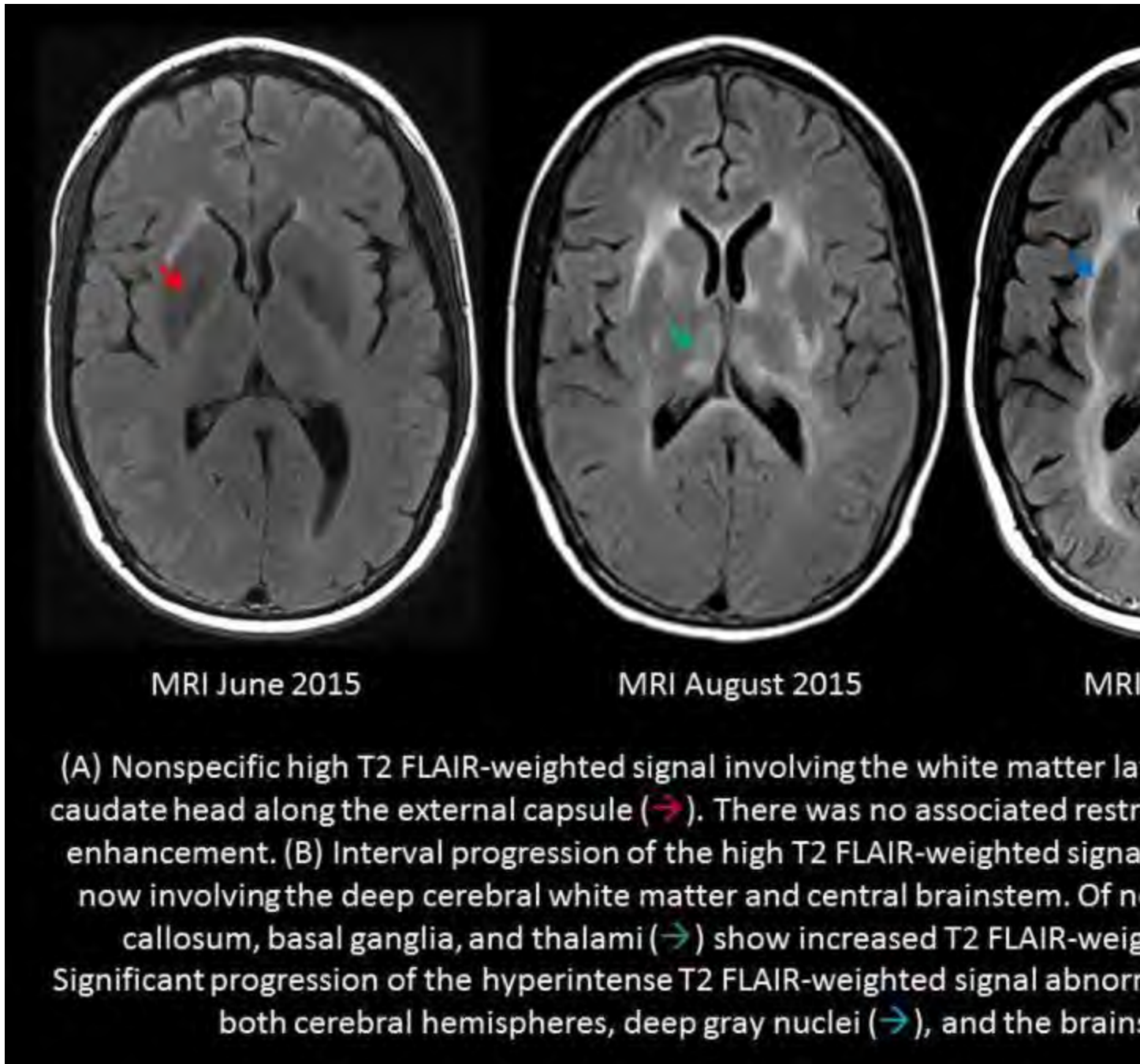
Results

MRI Brain, June 2015: (A) Nonspecific high T2 FLAIR-weighted signal involving the white matter lateral to the right caudate head along the external capsule. There was no associated restricted diffusion or enhancement. MRI Brain, August 2015: Interval

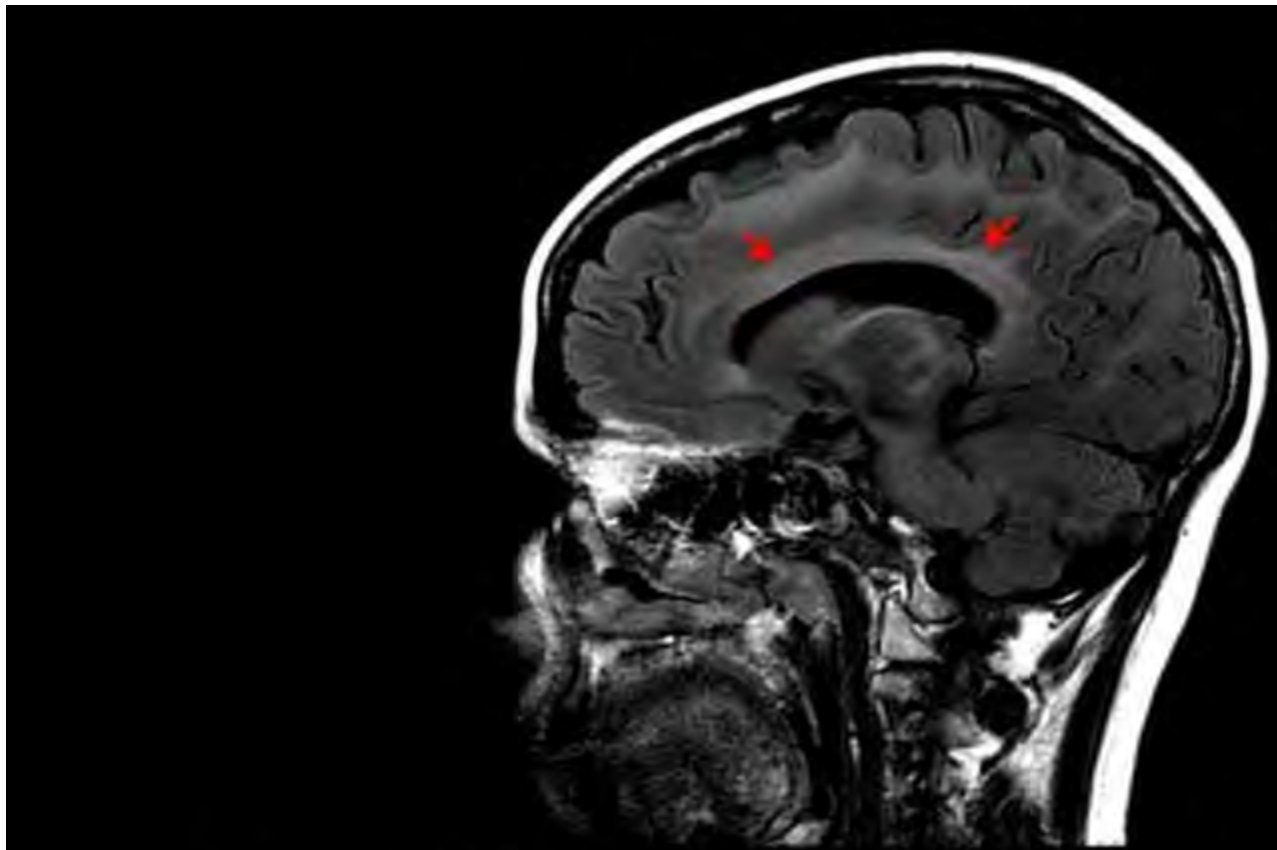
progression of the high T2 FLAIR-weighted signal abnormalities, now involving the deep cerebral white matter and central brainstem. Of note, the corpus callosum, basal ganglia, and thalami show increased T2 FLAIR-weighted signal. MRI Brain, October 2015: Significant progression of the hyperintense T2 FLAIR-weighted signal abnormalities both cerebral hemispheres, deep gray nuclei, and the brainstem.

Conclusions

CNS graft versus host disease is a challenging clinical and radiologic diagnosis that can mimic many other white matter processes in the oncologic patient population. Accurate and timely diagnosis has significant effect on management and clinical outcomes. We review the pertinent features of CNS GVHD to help facilitate recognition of this important clinical entity.



(Filename: TCT_E-48_Slide1.JPG)



Hyperintense T2 FLAIR-weighted signal involving the corpus call

(Filename: TCT_E-48_Slide2.JPG)

E-49

11:30AM - 11:35AM

Post-Radiosurgery Cyst Formation in Brain, a Rare and Delayed Complication

G Parikh¹, M Hoch², D Kondziolka³, R Jain⁴

¹New York University, Secaucus, NJ, ²NYU Medical Center, New York, NY, ³NYU Medical Center, New York, NY, ⁴NYU School of Medicine, New York, NY

Purpose

Post-radiosurgery cyst formation is a rare and delayed complication. This case report displays two patients with cyst formation status post radiosurgery following arteriovenous malformation (AVM) treatment (which has been previously described) as well as a patient following atypical meningioma treatment (which has not been previously described in the literature).

Materials and Methods

Patient A is a 26 year old female status post LINAC radiosurgery (standard dose is of approximately 16Gy) of left parietal AVM in 2008. In 2015, approximately 6.5 years following radiosurgery, patient developed worsening seizures with negative cerebral angiogram with MR revealing cystic findings in radiosurgery bed. Patient B is 72 year old female status post gamma knife radiosurgery (standard dose is of approximately 16 Gy) of right parietal anaplastic meningioma in 2002. In 2015, approximately 8 years following radiosurgery, patient had follow-up MR revealed findings in radiosurgery bed.

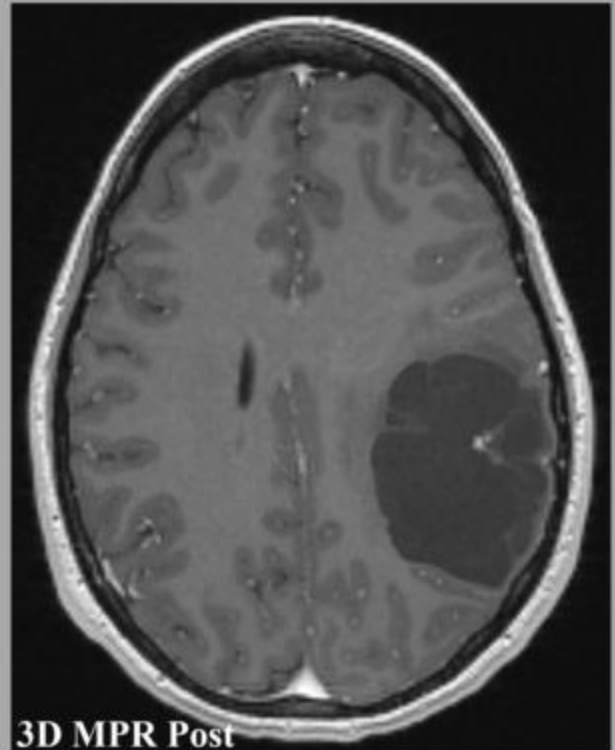
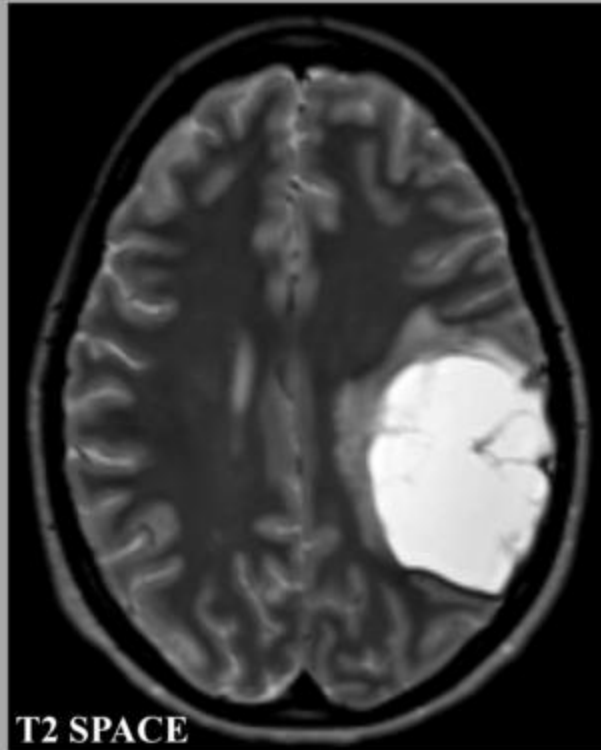
Results

Patient A: There is 3.6 cm well defined lesion within the left parietal radiosurgical bed causing mass effect with surrounding edema. It is hyperintense on T2, and hypointense T1 without enhancement compatible with a multiloculated cyst. There is a thin peripheral rim of enhancement within the radiosurgical cavity. There is a punctate focus of enhancement along the superior margin of the cavity compatible with gliosis. Due to worsening seizures, this cystic lesion was drained and with tissue sampling revealing a cyst. Patient B: There is a 3.0 well-defined lesion within the right parietal surgical bed causing mass effect with surrounding edema. It is hyperintense on T2, and hypointense T1 without enhancement compatible with a multiloculated cyst. There are stable peripheral and nodular areas of enhancement surrounding the cavity compatible with gliosis.

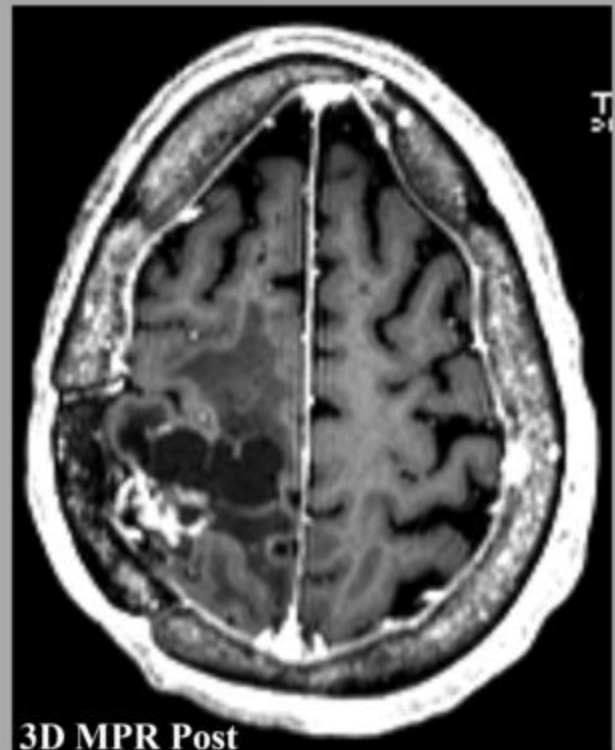
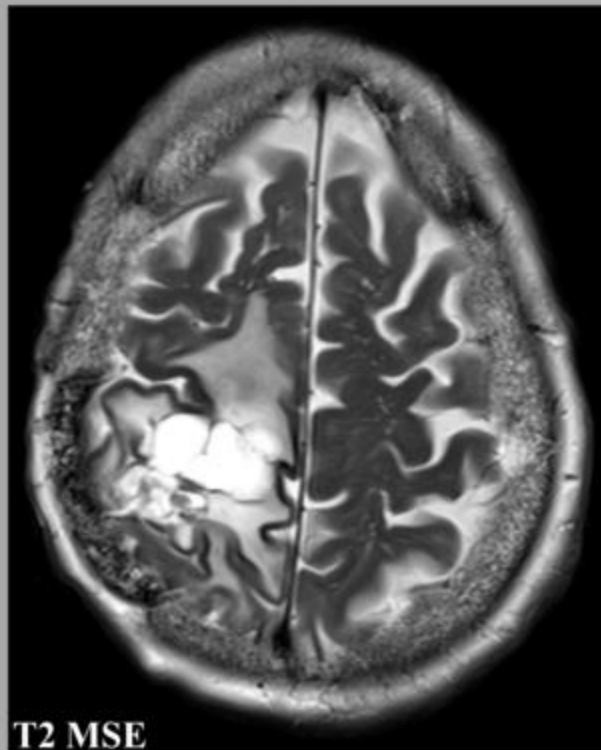
Conclusions

The imaging findings reveal the well known simple cyst characteristics: well-defined, thin walled, fluid MR characteristics (T2 hyperintense and T1 hypointense), and no enhancement. A cyst can produce mass effect and have associated edema. This picture of a new or enlarging cystic lesion causing mass effect and edema with in the setting of postoperative changes (peripheral and nodular enhancement of cavity margins, encephalomalacia and gliosis) confuses the picture and may raise the suspicion for tumor recurrence. Post-radiosurgery cyst formation may occur several years after treatment and that if a new cystic lesion occurs in the radiosurgical bed that this implied 'fluid is good' or a benign entity rather than an aggressive entity such as tumor recurrence.

AVM 6.5 years post GKRS



Atypical Meningioma 8 years post GKRS



(Filename: TCT_E-49_highresolutionbraincystimage.jpg)

E-50

11:35AM - 11:40AM

The Utility of Intraoperative Contrast-Enhanced Ultrasound in the Evaluation of Intracranial Meningiomas.

N Brauner¹, M Gulati¹, M Shiroishi¹, E Grant¹, K Chang¹, J Bakhsheshian¹, E Christian¹, G Zada¹, I Lekht¹

¹*Keck School of Medicine of the University of Southern California, Los Angeles, CA*

Purpose

Meningiomas are common intracranial neoplasms that encompass a variety of histopathologic subtypes (1). Preoperative MRI offers excellent anatomical characterization of these tumors however limitations remain. Here we highlight two separate cases of meningioma where utilization of intraoperative contrast-enhanced ultrasound (iCEUS) provided additional information, which aided in resection.

Materials and Methods

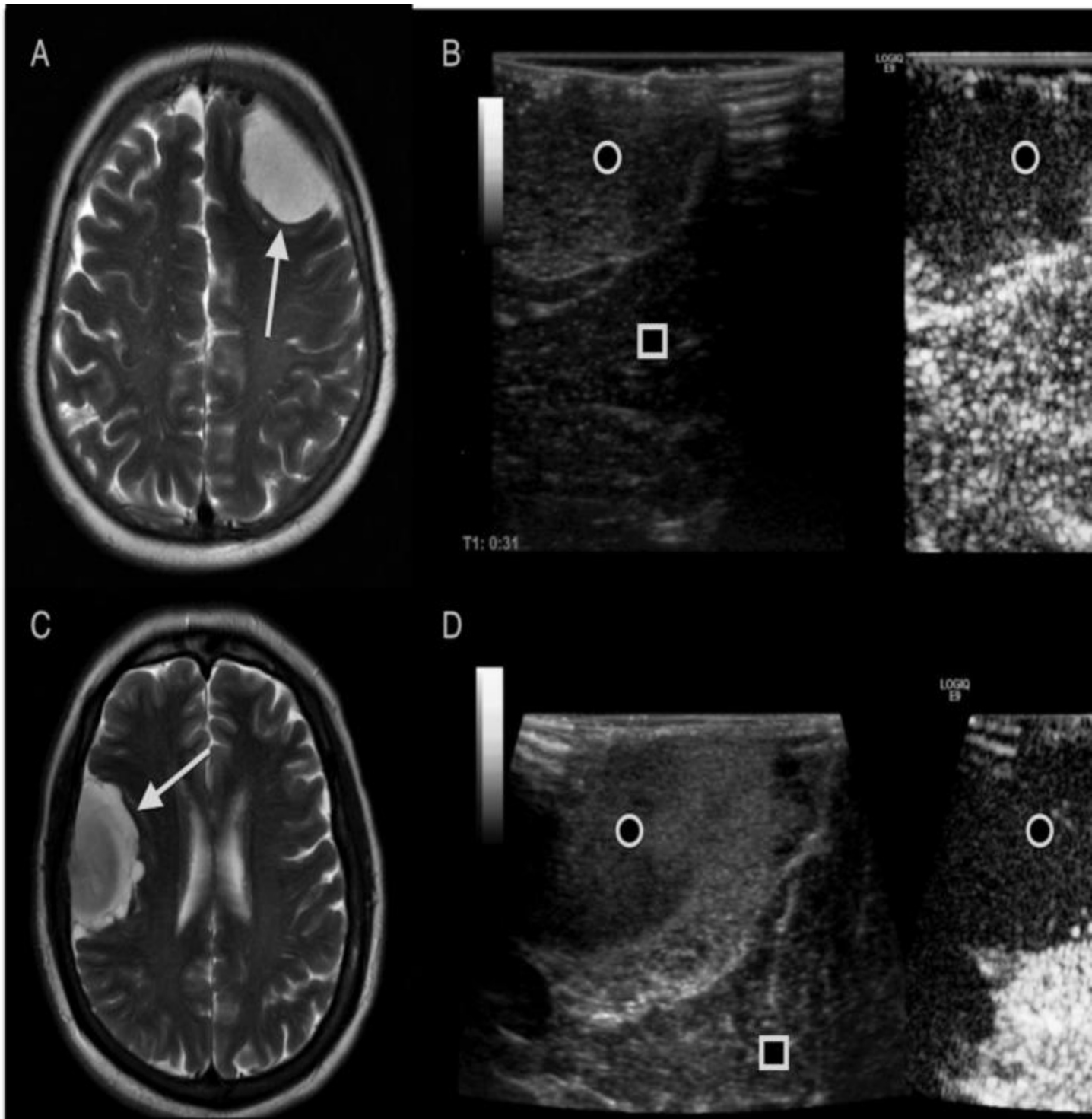
Two patients presented with headaches and were found to have intracranial masses on diagnostic imaging. The first patient, SK, reported three years of headaches and subjective facial weakness. The second patient, RG, reported 6 months of worsening headaches, blurry vision and a recent syncopal episode. Given tumor location and symptomatology, surgical resection was planned. Intraoperatively SK was found to have a well-circumscribed lesion which was easily resected, whereas RG was found to have an infiltrative tumor which was adherent to the overlying dura and underlying brain parenchyma, necessitating subtotal resection. Final histopathologic diagnosis for both lesions was WHO grade I meningioma.

Results

Preoperative MRI in RG showed a right frontotemporal, dural-based, extra axial lesion with avid enhancement and minimal adjacent vasogenic edema. Preoperative MRI of patient SK showed a similar lesion along the left frontal convexity. No significant enhancement was noted in the bulk of either tumor on iCEUS examination, likely resulting from devascularization of the meningeal blood supply during craniotomy. However, whereas patient SK showed no abnormal peritumoral contrast enhancement, patient RG had a thick rim of abnormally enhancing tissue adjacent to the devascularized tumor, suggestive of infiltrative growth.

Conclusions

iCEUS can serve as a useful adjunct in the pre-resection imaging of meningiomas. It may be especially useful in detecting and guiding resection of infiltrative components, which can be occult on MRI.



MRI and iCEUS appearance of two meningioma cases: A. T2-weighted axial MR showing left frontal, T2 hyperintense extra-axial mass (arrow) with minimal surrounding edema. B. Corresponding grayscale US (left) and iCEUS (right) shows tumor bulk (circle) with clear differentiation between the tumor edge and normal brain parenchyma (square). Absence of enhancement of the tumor is thought to result from devascularization during craniotomy. C. T2-weighted axial MR of a different patient showing a fronto-temporal, T2 hyperintense, dural based, extra-axial mass (arrow) with minimal adjacent edema. D. Corresponding grayscale US (left) and iCEUS (right) shows devascularized tumor bulk (circle), with a thick rim of enhancement adjacent to the tumor, suggesting tumor infiltration. Normal brain parenchyma (square).

(Filename: TCT_E-50_Excerpta-Meningioma.jpg)

E-51

11:40AM - 11:45AM

Brain Metastases with Pure Cystic Imaging Appearance Mimicking Neurocysticercosis

p watal¹, A Capizzano², t moritani², L Bruch², L Rachakonda³

¹*university of iowa hospital and clinics, iowa city, IA*, ²*university of iowa hospitals and clinics, iowa city, IA*, ³*University of Iowa, Iowa City, IA*

Purpose

To illustrate a pathology proven case of non-enhancing, non-edematous purely cystic brain metastases from lung adenocarcinoma with dramatically favorable response, after whole brain radiation and erlotinib, on imaging follow-up.

Materials and Methods

A 52 year male presented with headache and occasional dizziness. He had been diagnosed in the past with advanced lung adenocarcinoma which was managed with chemotherapy and radiation. No brain radiation had been administered. There was history of exposure to pigs. The patient was mildly immunosuppressed. A prior MRI brain from two years before was completely unremarkable. A biopsy of the left temporal lesion on H and E stained section shows a single layer of malignant columnar cells lining brain tissue. The immunophenotype (CK7+, TTF-1+) of these cells was consistent with metastasis from a lung primary.

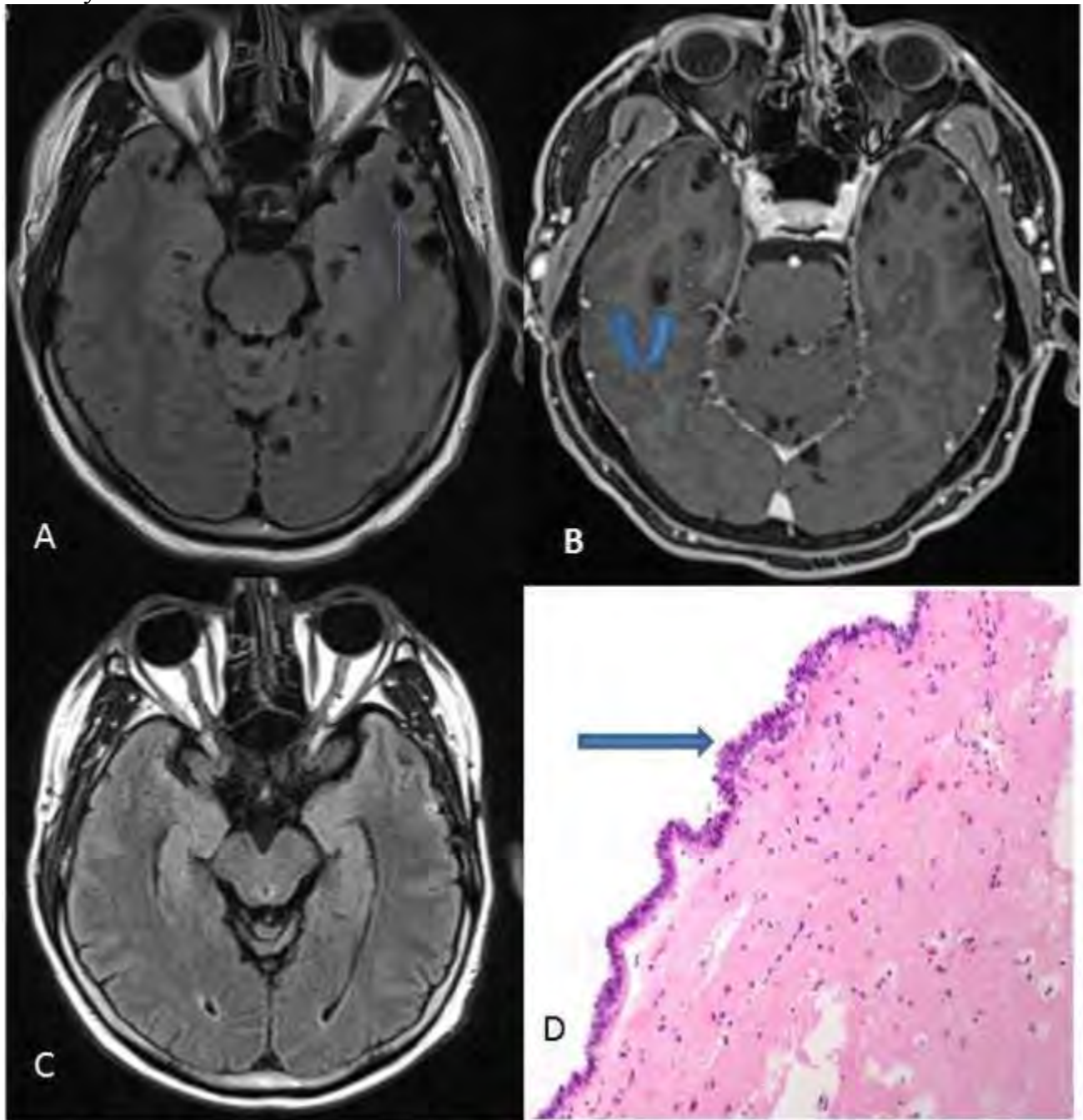
Results

Multiple intra-axial peripheral cystic lesions involving both the supra and infratentorial compartments were demonstrated on brain MRI, isointense to CSF on FLAIR sequences and without any sign of contrast enhancement or vasogenic edema. The differentials offered were cryptococosis and neurocysticercosis with metastases considered highly unlikely in view of non- enhancing appearance. Follow up sequential imaging post whole brain radiation and erlotinib treatment showed reduced number and size of the lesions. On the most recent MR imaging, 7 months after whole brain radiation, there was complete resolution of cystic lesions with no evidence of new lesions.

Conclusions

The complete lack of contrast enhancement and vasogenic edema constitute an exceptional imaging appearance of metastatic disease to the brain, which may therefore be confounded with more common cystic lesions such as parasitic diseases. A truly cystic lesion appears isointense to CSF on all imaging sequences and may display rim enhancement. Brain metastases typically show contrast enhancement and vasogenic edema from increased permeability of the blood brain barrier on imaging.

In rare instances, Brain metastases can have pure cystic imaging appearance as in the setting of adenocarcinoma, thus mimicking infective cystic lesions like neurocysticercosis.



Axial F
showe
isointe
no per
mimic
(thin b
the cor
contra
no evis
enhanc
blue ar
Follow
radiati
erlotin
images
demon
resolut
lesions
section
single
column
braint
arrow

(Filename: TCT_E-51_excerptaimage.jpg)

E-52

11:45AM - 11:50AM

Primary Leptomeningeal Gliomatosis - Radiologic and Genetic Correlation of a Rare Disease

C Li¹, S Imbesi², M McCrate², J Chen³

¹UC San Diego Health System, San Diego, CA, ²University of California, San Diego, San Diego, CA, ³San Diego VA / UCSD Med. Center, La Jolla, CA

Purpose

To provide genomic correlation with imaging of a rare case of primary leptomenigeal gliomatosis (PLG) and review proposed disease pathology in the context of the new genetic information.

Materials and Methods

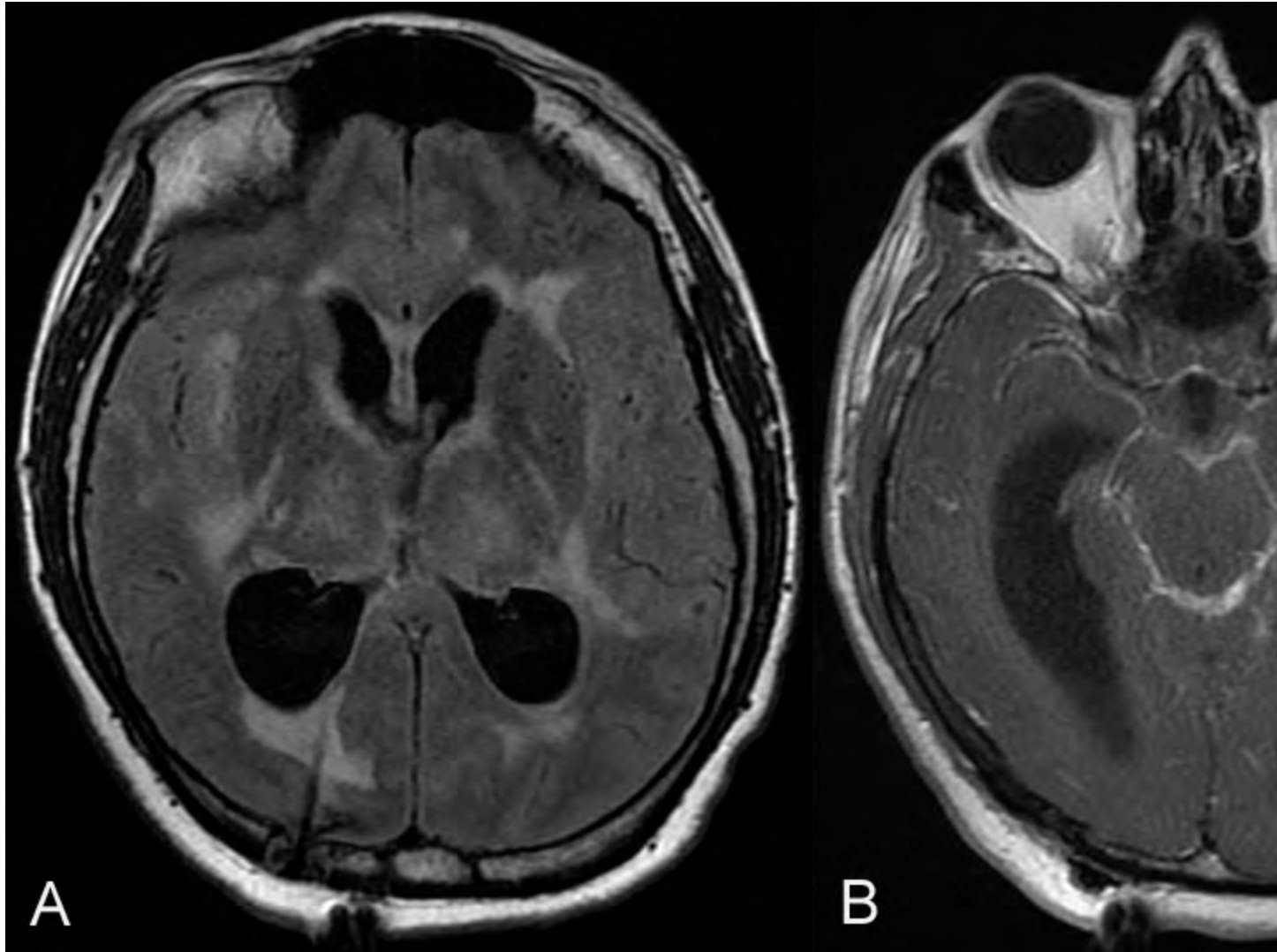
Otherwise healthy 36-year-old male presented with nausea, vomiting, headache, bilateral vision loss, hiccups, global weakness and weight loss, progressing to confusion and visual hallucination. During the work-up a brain MRI demonstrated communicating hydrocephalus and transependymal flow of CSF and extensive leptomenigeal enhancement without a focal intraparenchymal brain lesion. Cerebrospinal fluid analysis revealed elevated protein and decreased glucose without atypical cells on cytopathology or growth on cultures. Sural nerve and gastrocnemius biopsies did not reveal evidence of sarcoidosis or other granulomatous disease. A biopsy of material within the fourth ventricle revealed spindle cell proliferation in the choroid plexus, S-100 and GFAP positivity, consistent with leptomenigeal gliomatosis. Single nucleotide polymorphism (SNP) analysis revealed loss of heterozygosity at 1P, 3P and proximal 3Q, 10P and distal 10Q, distal 11q, 13 (including RB1), and 18p, with copy number gains at 1Q, and H3F3A mutation.

Results

MR images revealed communicating hydrocephalus with surrounding white matter T2 prolongation compatible with transependymal flow of CSF (Figure, A) and diffuse leptomenigeal enhancement (Figure, B) without a focal primary intraparenchymal mass.

Conclusions

Primary leptomenigeal gliomatosis is a rare and rapidly fatal disease, which may mimic infection, inflammation and other neoplastic processes. It is thought to arise from neoplastic transformation of heterotopic glial nests in the leptomeninges (1), though some have postulated drop metastases from an undetected intraparenchymal primary (2). In our case, SNP analysis revealed a genetic profile different than usually associated with the Verhaak classification subtypes (3), and raises the possibility that PLG is pathophysiologically distinct and not simply CSF-seeding of a missed intraparenchymal glioma.



(Filename: TCT_E-52_PLGFigure1.jpg)

E-53

11:50AM - 11:55AM

Mycotic Aneurysm from Cardiac Myxoma Emboli: Characterization with High Resolution Vessel Wall MR Imaging

M Fitzgibbons¹, B Yoo¹, B Salehi¹

¹*UCLA, Los Angeles, CA*

Purpose

1. To present a rare case of mycotic aneurysms from cardiac myxoma emboli 2. To illustrate the utility of high-resolution vessel wall MR imaging for mycotic aneurysm characterization

Materials and Methods

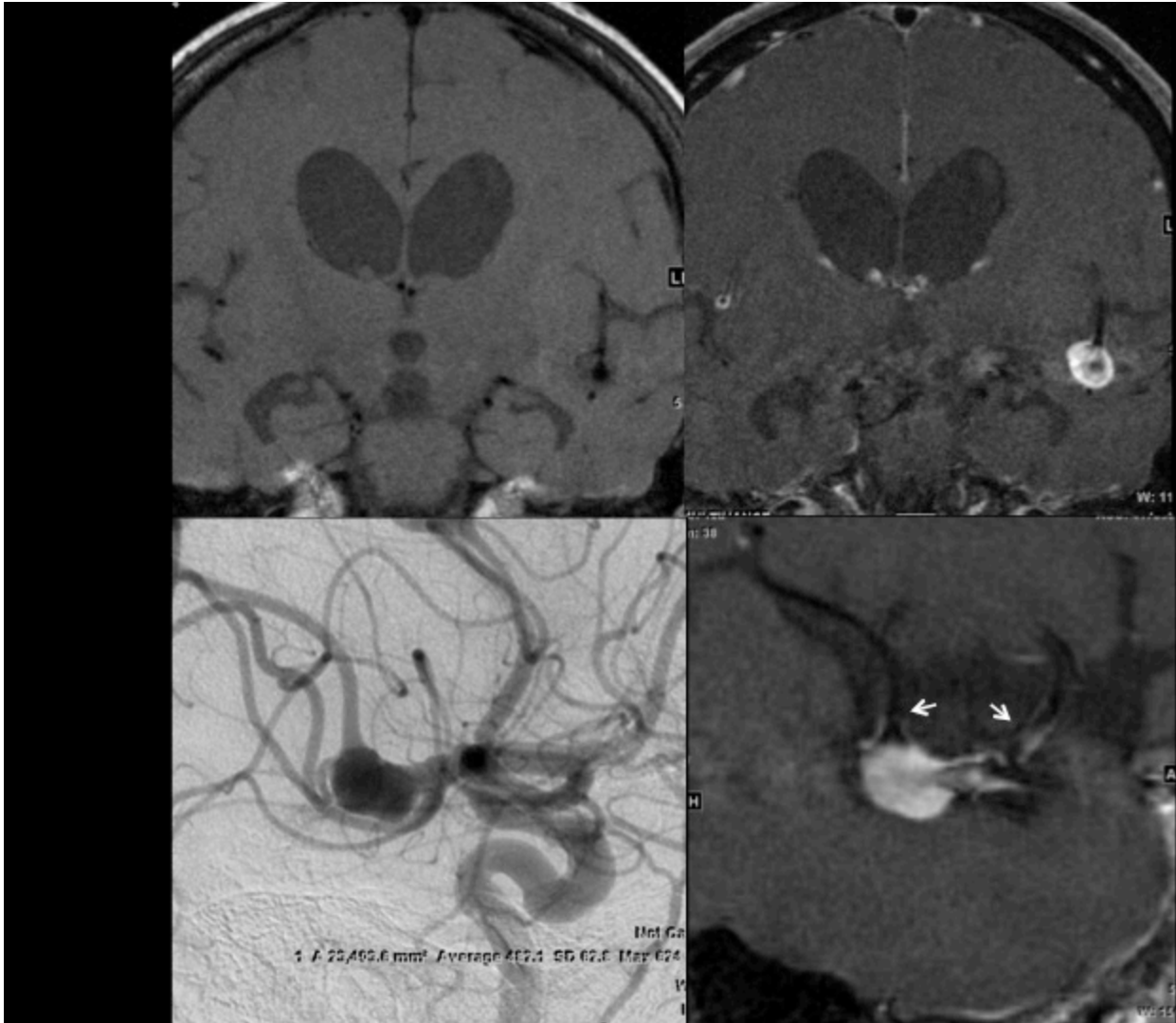
A 71-year-old woman presented to an outside hospital in 2010 with TIA symptoms. An MRI was performed at that time, which revealed scattered foci of restricted diffusion in a pattern compatible with embolic infarctions. Her stroke work-up revealed a left atrial myxoma, which was surgically resected in 2010. She subsequently developed numerous, distal fusiform aneurysms, which progressively enlarged over multiple years. The largest aneurysm was located in a left M2 branch and measured up to 10 mm in maximal dimension in 2015. A neurosurgical consultation was obtained for consideration of surgical bypass of this aneurysm. To determine the feasibility and safety of performing a vascular bypass procedure, high-resolution vessel wall MR imaging was performed to assess for adjacent vessel wall infiltration and integrity.

Results

A large, fusiform mycotic aneurysm is seen arising from a left M2 branch within the Sylvian fissure. High resolution, fat-saturated T1-weighted post-contrast images with black blood technique demonstrate marked thickening and enhancement of the aneurysm wall. Additionally, there is thin, linear enhancement extending proximally and distally to the aneurysm, suggesting vessel wall infiltration in adjacent, non-dilated segments.

Conclusions

Mycotic aneurysm from myxoma emboli is a rare, known complication of cardiac myxomas, with approximately 40 cases reported in the literature. The mechanism by which these aneurysms develop is unclear; a proposed mechanism is the direct invasion of tumor cells into the arterial wall, resulting in destruction of arterial wall architecture and aneurysm formation, as histopathologic studies have demonstrated myxoma cells within the aneurysm wall. In this case, high-resolution vessel wall imaging was performed to evaluate for potential infiltration in arterial segments adjacent to the aneurysm to assess for feasibility and safety of performing a vascular bypass procedure. Given the extension of enhancement into adjacent, non-dilated arterial segments, a surgical bypass was not pursued, and the patient will undergo radiation therapy instead. This unique case demonstrates a novel application of high-resolution vessel wall MR imaging in mycotic aneurysm characterization.



(Filename: TCT_E-53_Slide1.jpg)

E-54

11:55AM - 12:00PM

A case of secondary degeneration in the striatum subsequent to MCA territory infarction

A Tsukabe¹, Y Watanabe², M Sakai¹, K Nakanishi¹, M Sakaguchi², N Tomiyama²
¹Osaka Medical Center for Cancer and Cardiovascular Diseases, Osaka, Osaka, ²Osaka University Graduate School of Medicine, Suita, Osaka

Purpose

The secondary degeneration in the substantia nigra and the thalamus subsequent to middle cerebral artery (MCA) territory infarction has been well discussed. However the degeneration in the striatum has been little discussed. Only a few reports discussed

the degeneration in the striatum subsequent to external capsule hemorrhage and superior tentorial operation. We present a case of transneuronal degeneration in the striatum subsequent to MCA territory infarction.

Materials and Methods

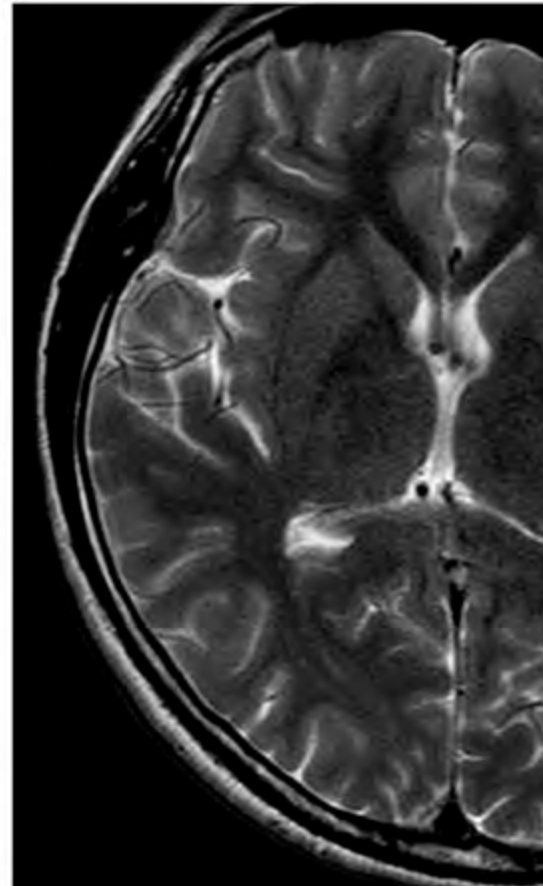
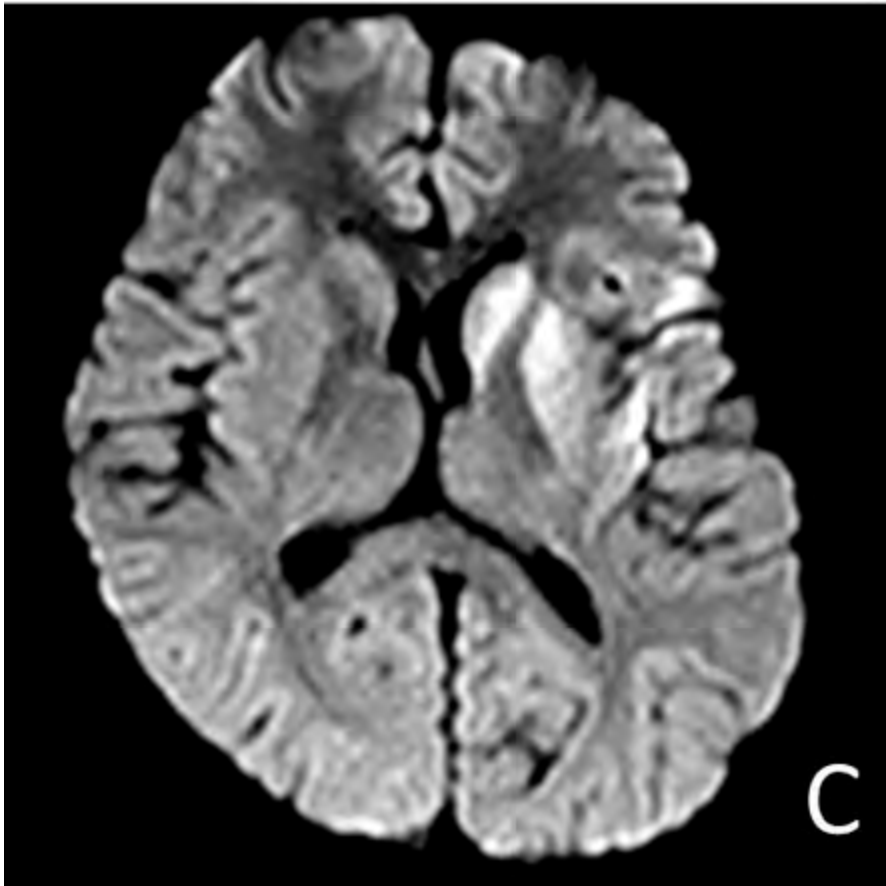
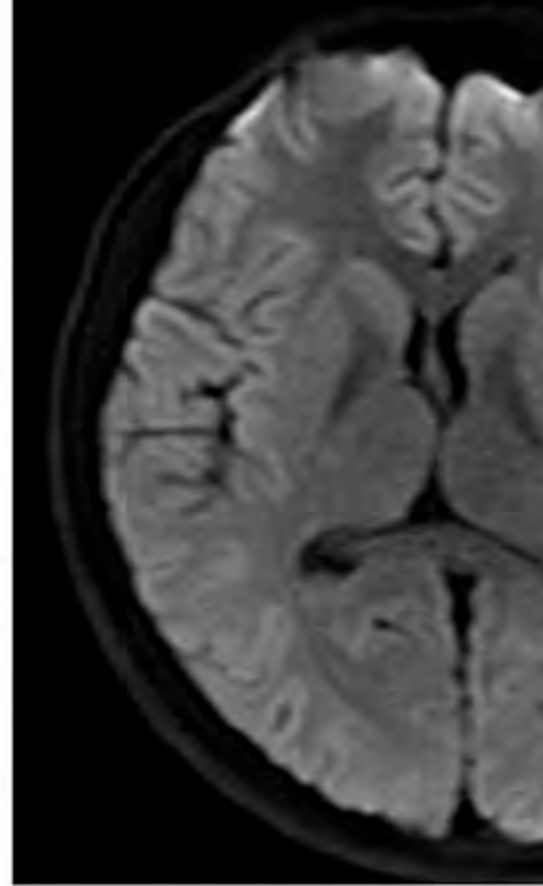
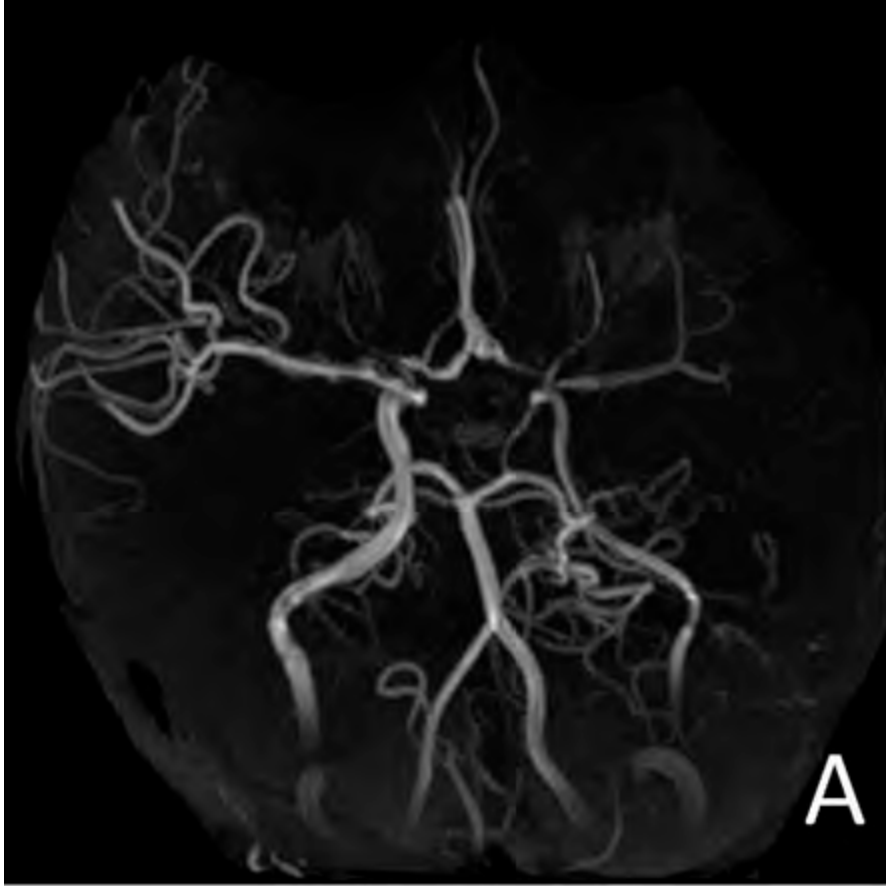
A 16 year old boy with left MCA territory infarction due to unilateral moyamoya disease was transferred to our hospital. On the MRI 8 days from ictus, the abnormal signal in the ipsilateral striatum emerged without the worsening symptoms. This finding was temporal and resolved without atrophy on the follow-up MRI. There was neither epilepsy nor worsening of symptoms. Therefore the signal change of the striatum was considered as degeneration subsequent to the infarction.

Results

At the day of ictus, MR Angiography showed signal decrease in left internal carotid artery and MCA. DWI showed high intensity in the cortex and the deep white matter in MCA territory (figure A, B). MR Angiography one week later showed the recovery of MCA signal by development of collateral flow. The signal intensity of high intensity lesion seen on MRI at the day of ictus decreased. DWI and FLAIR images showed high signal intensity involving the whole ipsilateral striatum (figure C). On follow-up MRI after three months, the abnormal signal of the striatum had resolved (figure D). There was no apparent atrophy.

Conclusions

Secondary degeneration could involve the striatum. We should be aware of the secondary degeneration in this area and avoid mistaking it for a new lesion, such as an infarction.



(Filename: TCT_E-54_Figure.jpg)

Thursday

1:15PM - 2:45PM

Washington Marriott Wardman Park, Marriott Ballroom

22A-Multiple Sclerosis (AR) (SAM)

22A-1

1:15PM - 1:40PM

MS Diagnosis and Therapy: State of the Science

Calabresi, P.

Johns Hopkins Hospital

Baltimore, MD

22A-2

1:40PM - 2:10PM

Advanced Neuroimaging in MS

Reich, D.

NIH

Bethesda, MD

22A-3

2:10PM - 2:30PM

Differential Diagnosis in MS Imaging

Field, A.

Univ. Of Wisconsin Hospital

Madison, WI

22A-4

2:30PM - 2:45PM

Questions and Answers

Thursday

1:15PM - 2:45PM

Washington Marriott Wardman Park, Washington 4/5/6

22B-SNIS Programming: Seeing Aneurysms a Whole New Way: Biophysics and Computational Fluid Dynamics of Aneurysms

22B-1

1:15PM - 1:35PM

Designing Aneurysms: A Primer on Advanced Computational Fluid Dynamics

Malek, A.

Tufts Medical Center

Boston, MA

22B-2

1:35PM - 1:55PM

Merging Biomathematics and CFD: From Equation to Patient Care

Prestigiacomo, C.

Neurological Institute Of New Jersey

Newark, NJ

22B-3

1:55PM - 2:15PM

Patient-Specific CFD: Personalized Medicine in Aneurysm Therapy?

Gounis, M.

University of Massachusetts

Worcester, MA

22B-4

2:15PM - 2:35PM

CFD and Device Assessment: Can We Predict the Optimal Treatment

Cebral, J.

George Mason University

Fairfax, VA

22B-5

2:35PM - 2:45PM

Panel Discussion

Thursday

1:15PM - 2:45PM

Washington Marriott Wardman Park, Roosevelt 1-3

**22D-PARALLEL PAPER SESSION: Advances in CNS Tumor Imaging and Treatment
O-472**

1:15PM - 1:23PM

Quantitative Imaging Analysis of Glioblastoma on Magnetic Resonance Imaging for the Demonstration of Extant Intratumoral Heterogeneity, Tumor Margins, Hypoxic Malignant Cell Populations and Identification of Subtype Habitats

J Kim¹, O Stringfield², N Raghunand², R Gatenby²

¹H. Lee Moffitt Cancer and Research Center, Royal Australian New Zealand College of Radiologists, Tampa, FL, ²H. Lee Moffitt Cancer and Research Center, Tampa, FL

Purpose

Glioblastoma (GBM) has characteristic macroscopic complexity as function of blood flow, and intratumoral molecular variations currently represented by four subtypes of genetic expression (Proneural, Classical, Neural, Mesenchymal), each with prognostic significance. This spatial heterogeneity in hypoxia and molecular properties is a potentially causal factor that limits the effectiveness of therapies for GBM. We present imaging analytic techniques to quantitatively illustrate the intratumoral heterogeneity of perfusion, edema, structural organization, enhancing tumor margins, regions of hypoxia, and zonal distribution of GBM subtypes.

Materials and Methods

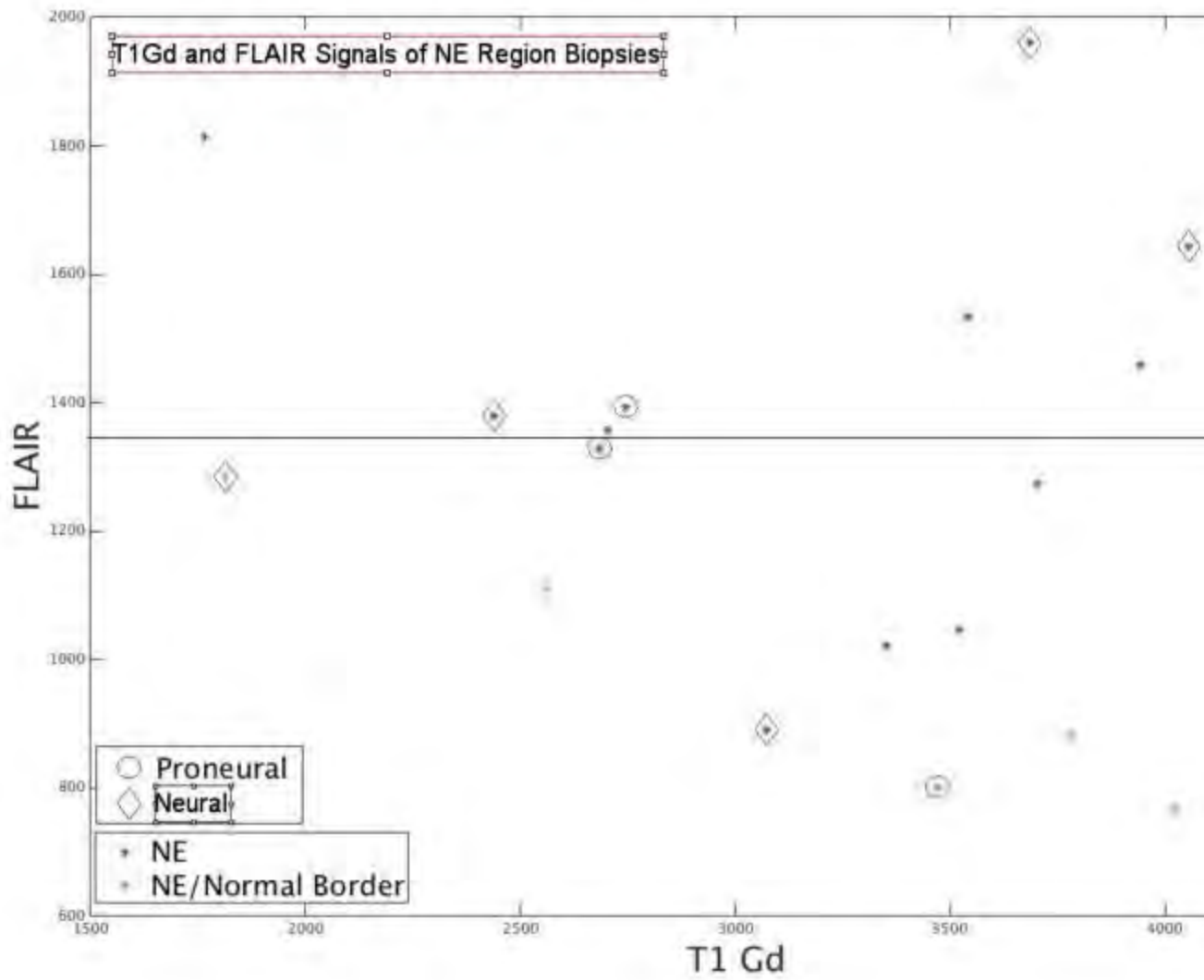
From 27 GBM patients, 80 MRI-guided biopsies were obtained. Prebiopsy diagnostic magnetic resonance (MR) sequences (T1Gd, FLAIR, ADC) were coregistered, the brain segmented, and signals standardized by two-point-normalization. Biopsy coordinates were mapped onto these images for intensity analysis of the surrounding 10x10mm square. GBM subtypes were determined using RNA sequencing on 15 primary and 11 recurrent tumor biopsies.

Results

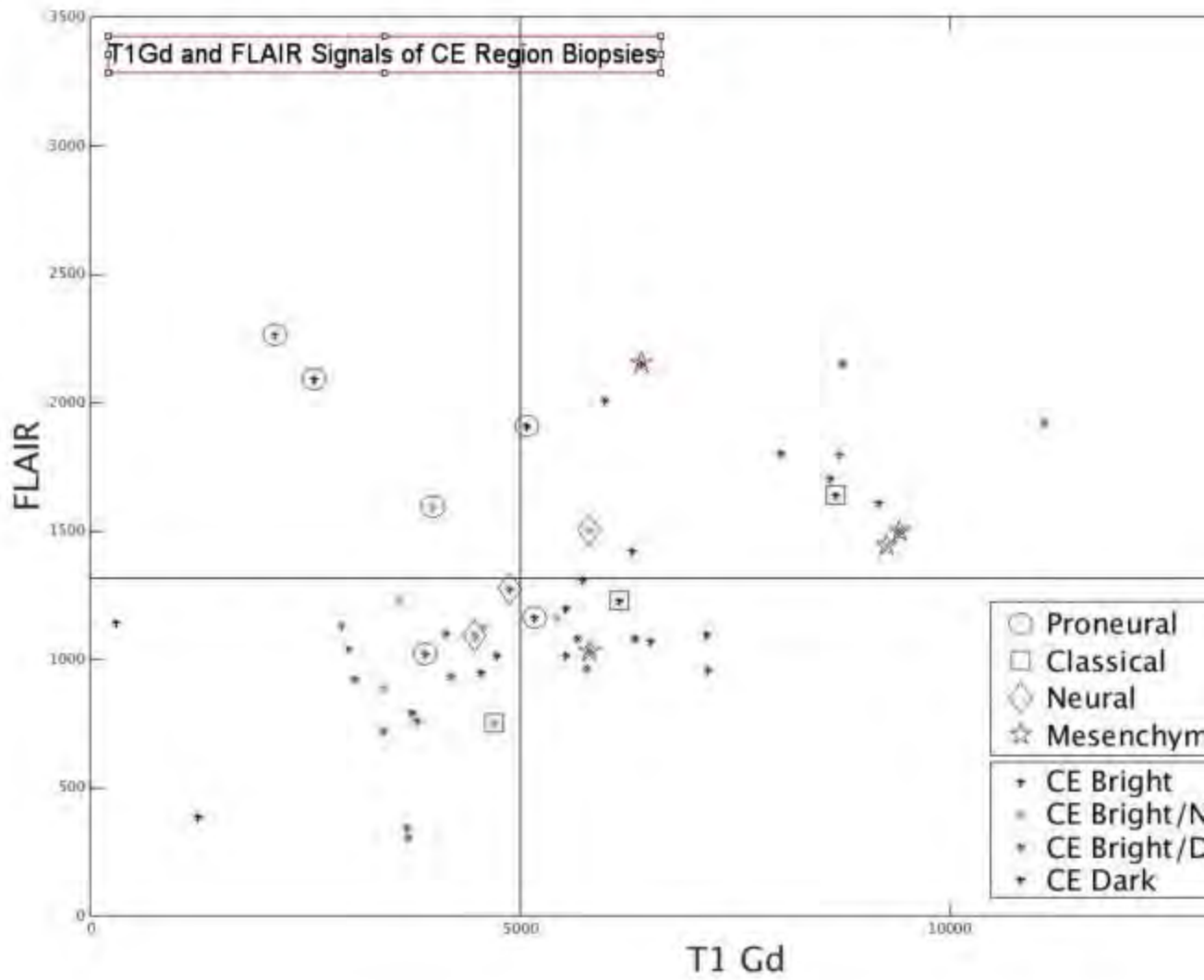
There was intraregional heterogeneity of signals within the contrast-enhancing (CE) regions (SD of T1Gd, FLAIR, ADC; 1101, 192, 1750) and the nonenhancing (NE) regions (SD 1200, 207, 1041). Mean FLAIR signal was higher in CE than NE (1312 versus 1289), with positive correlation between the degree of enhancement and FLAIR-signal within CE. A subregion of low-T1Gd, low-FLAIR is identified at the border of poorly enhancing tumor center and enhancing rim. Classical and mesenchymal subtypes were only seen in CE, while neural and proneural subtypes were seen in both CE and NE.

Conclusions

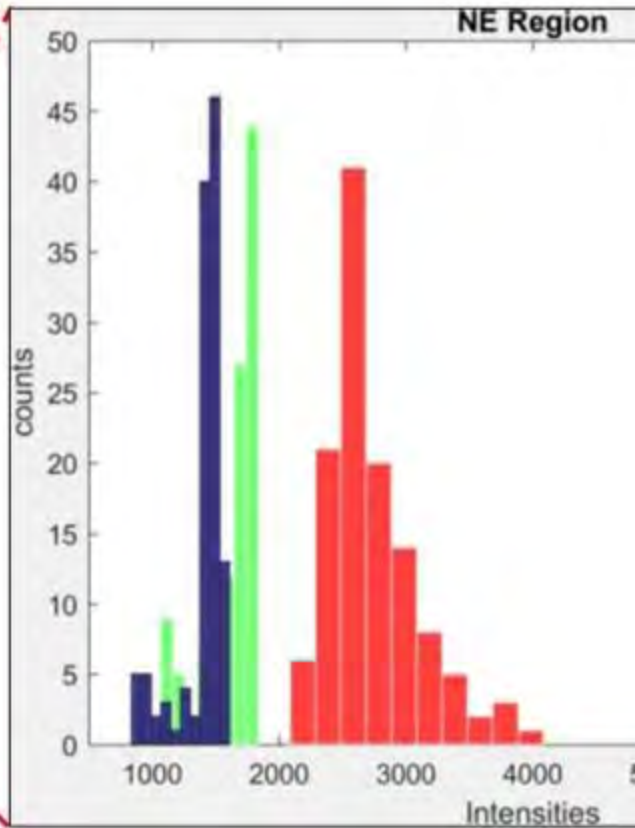
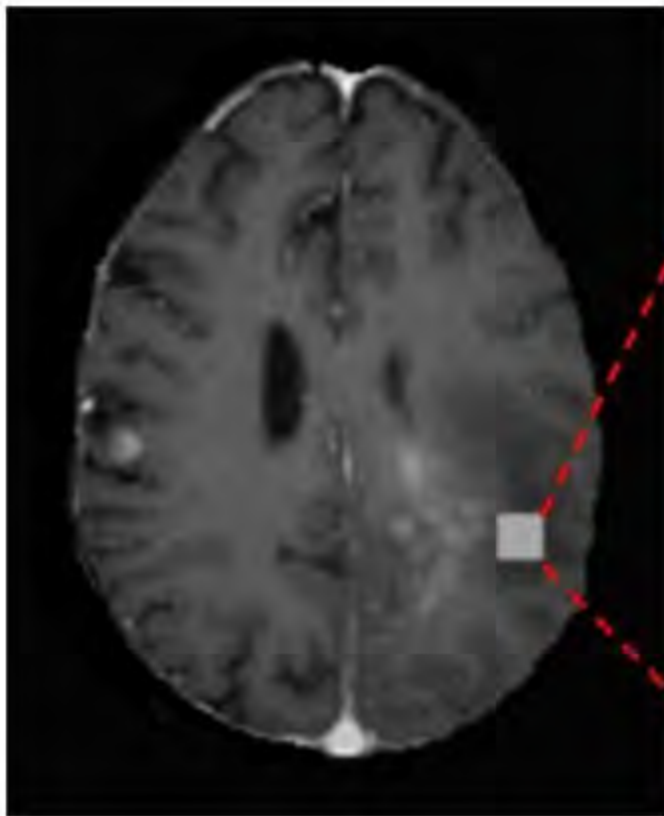
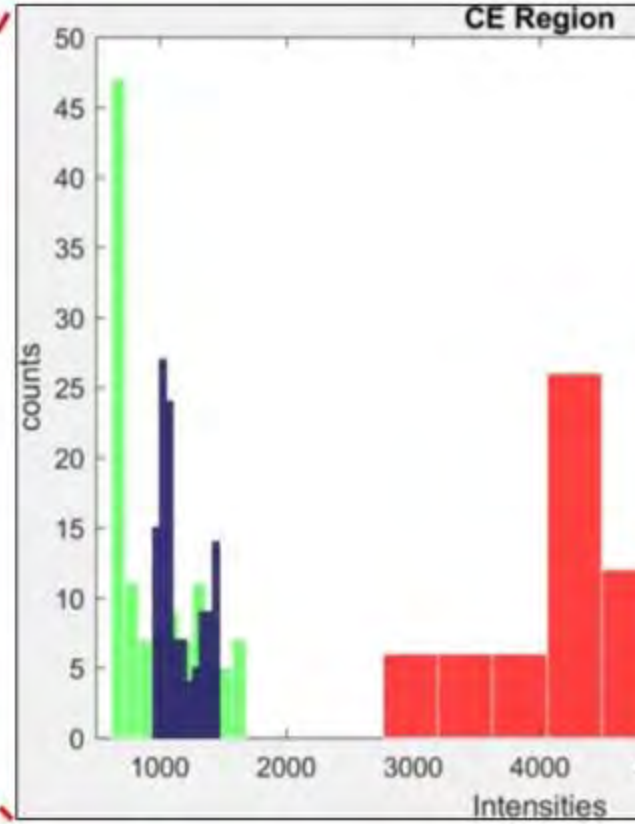
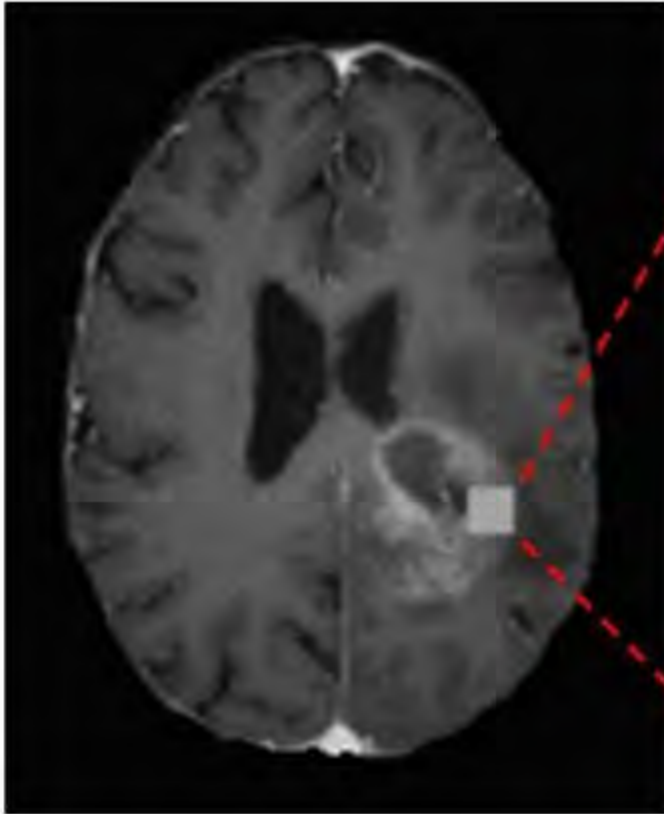
Intraregional heterogeneity of MRI signals exists within CE and NE of GBM. The transition from CE to NE is indistinct; automated delineation of enhancing margins may solve this surgical planning problem. Using quantitative analysis, a hypoxic, nonedematous core of cellular proliferation is identified as a focus of potential treatment resistance. A zonal distribution of GBM subtypes exists; classical and mesenchymal subtypes are only found in CE, while proneural and neural subtypes are found in both CE and NE.



(Filename: TCT_O-472_NEClusterssubtypes.jpg)



(Filename: TCT_O-472_CElusterssubtypes.jpg)



(Filename: TCT_O-472_Figure_CEvSNE_withADC.jpg)

O-473

1:23PM - 1:31PM

Quantification of Heterogeneity in Peritumoral Edema in Long-Term Glioblastoma Survivors: Correlation With ADC and FLAIR Histogram Metrics.

P Chang¹, Y Esterson², A Demopoulos³, B Pramanik⁴, J Lee⁵, M Schulner³, D Chow⁶, J Boockvar⁷, C Filippi⁸

¹Columbia University Medical Center, NEW YORK, NY, ²North Shore LIJ Health System, Manhasset, NY, ³Hofstra North Shore-LIJ School of Medicine, Manhasset, NY, ⁴Lenox Hill Hospital, New York, NY, ⁵North Shore-Long Island Jewish Health System, Lenox Hill Hospital, New York, NY, ⁶University of California, San Francisco, San Francisco, CA, ⁷North Shore-LIJ Health System, New York, NY, ⁸Hofstra North Shore-LIJ School of Medicine, Manhasset, NY

Purpose

Long-term survival of glioblastoma (GBM) patients is rare. We hypothesize that such patients exhibit less infiltration of nonenhancing tumor (nCET) into the peritumoral region, a known marker of poor prognosis (1-2), thus increasing the yield of gross total resection (3-4). Furthermore we hypothesize that this decreased nCET infiltration will result in higher, more homogenous FLAIR signal and apparent diffusion coefficient (ADC) value typically associated with pure edema, findings that can be quantitatively captured using histogram metrics.

Materials and Methods

After IRB approval, an institutional database was searched for GBM patients with MR imaging between 2006 and 2013. Long-term survivors (12 men, 7 women, average age 62.4 +/- 7.9 years) were defined as those with minimum survival of 2 years after resection (average survival 4.1 years, range 2.2-9.0 years). This cohort was compared to an age- and sex-matched group of GBM patients (12 men, 17 women, average age 67.1 +/- 8.2 years) with typical, poor survival (average survival 6.2 months, range from 0.5-13.8 months). Both cohorts were limited to those who had gross total resection followed by identical postresection therapy of temozolomide and radiation. Pre-operative MR images were analyzed to find predictors of long-term survival. A fully automated algorithm identified volumetric masks corresponding to enhancing tumor (CET), nonenhancing tumor (nCET), necrosis, and peritumoral edema. Histogram analysis of FLAIR and ADC was performed within the peritumoral region (nCET + edema), including mean, standard deviation (SD), skewness and kurtosis. Statistical significance was assessed with a two-tailed t-test. All segmentation masks were inspected for accuracy by a board-certified neuroradiologist blinded to results.

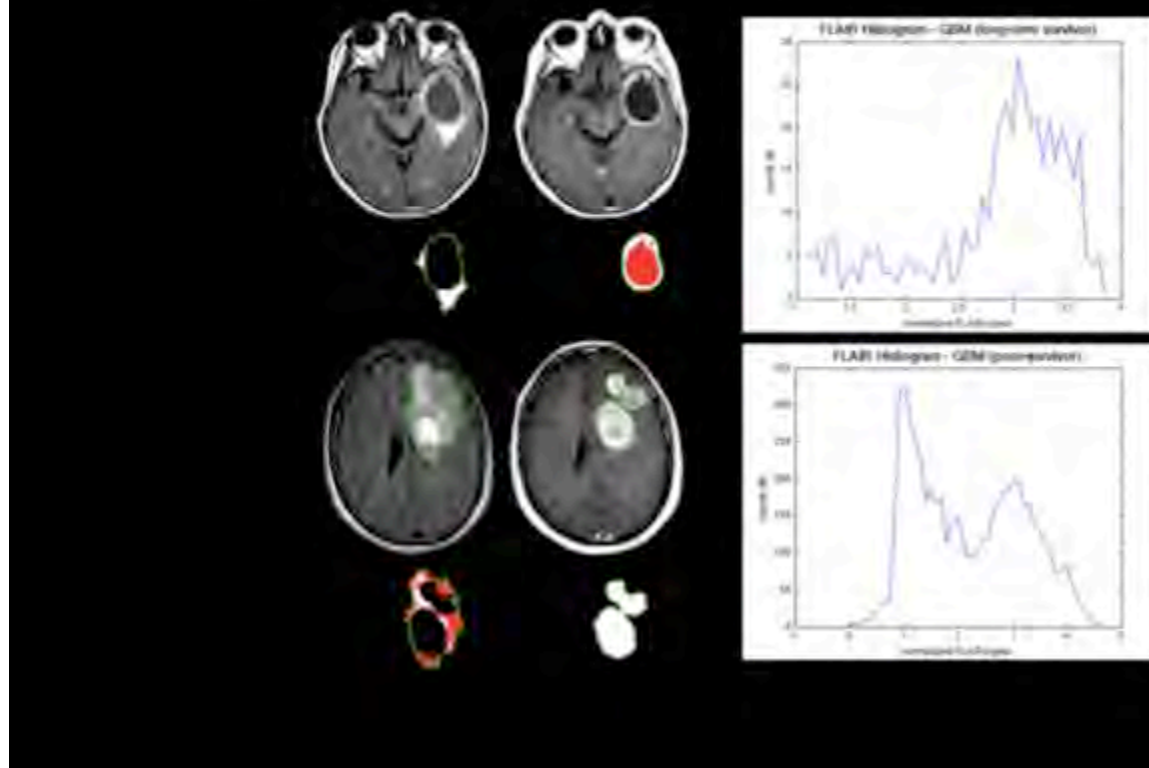
Results

Long-term survivors demonstrated significantly decreased nCET (31.7% versus 49.9%, $p = 0.006$) and increased mean normalized FLAIR intensity (2.86 versus 2.06, $p = 0.0036$) compared to controls. In addition significant differences in peritumoral heterogeneity were seen both for FLAIR (SD, $p = 0.0029$; skewness, $p = 0.0084$; kurtosis, $p = 0.019$) and ADC (SD, $p = 0.0053$; kurtosis = 0.014) histogram metrics.

Conclusions

Long-term GBM survivors demonstrate overall increased FLAIR signal and ADC value within the peritumoral region, with associated changes in histogram metrics reflecting a more homogenous distribution of signal intensity. These findings suggest that FLAIR and ADC histogram metrics can be used as quantitative biomarkers to estimate infiltrative nCET tumor burden and inform treatment decisions, management, or prognostication.

Figure: MRI and FLAIR histogram plots for long-term survivors (top) and poor outcome (below). On the left, masks corresponding to peritumoral region (green) and nCET (red) are shown. On the right, masks corresponding to contrast-enhancing margin (green) and necrosis (red). In general, long-term survivors tend to exhibit decreased nCET volume. Based on FLAIR signal intensity histograms, long-term survivors demonstrate overall higher intensity ("pure") edema signal with narrow standard deviation compared to the heterogenous broad signal distribution in the poor outcome group.



(Filename: TCT_O-473_Slide1.jpg)

O-474

1:31PM - 1:39PM

Role of MRI Texture Analysis in Differentiating Post-treatment Changes from Tumor Recurrence in Patients with High Grade Gliomas.

F Essbairheen¹, R Thornhill¹, M Kontolemos¹, J Woulfe¹, A Boivin¹, G Cron¹, B Manouchehri¹, T Nguyen¹

¹*The Ottawa Hospital University of Ottawa, Ottawa, Ontario*

Purpose

In patients with high grade gliomas who developed a newly enhancing lesion following chemoradiation, we evaluated the performance of quantitative texture features to differentiate between tumor progression and post-treatment changes (nonprogression).

Materials and Methods

This prospective study included 38 consecutive patients with a high grade glioma (grade 3- 4) treated with chemoradiation presenting with a new enhancing lesion on gadolinium-enhanced magnetic resonance imaging (MRI). Patients underwent a subsequent MR examination on a 3T MR scanner (Trio, Siemens Medical Solutions) including axial VIBE T1 postcontrast images (TR=8.48 ms, TE=3.21 ms, flip angle=12°, voxel size=1x1x1mm). These images were resampled with a 5mm thickness. Enhancing lesions were manually segmented under the supervision of a neuroradiologist and saved as volumes-of-interest (VOI) in ImageJ (National Institutes of Health, USA) for subsequent texture analysis. We extracted textural features for each 3D VOI using MaZda® version 4.6 (PM Szczypiński, Institute of Electronics, Technical University of Lodz, Poland) (1). Tumour progression was classified based on histopathological analysis obtained from surgical resection revealing predominantly viable tumor or clinical deterioration associated with progressive increase in size of the lesion(s) on follow-up MRI. Patients were classified as post-treatment changes based on histopathological analysis showing predominantly radiation necrosis or stability or decrease in size on follow-up MRI without any clinical deterioration. Differences in textural features between progression and nonprogression were assessed via Mann-Whitney U tests. Stepwise logistic regression analysis identified feature sets that would discriminate between the two groups (area under the receiver operating characteristic (ROC) curve (AUC) significantly greater than 0.5, P<0.05) and these sets subsequently were used to generate support vector machine (SVM) classifiers (The Unscrambler® X (v.10.1, CAMO Software). We evaluated classification generalizability and performance using 10-fold cross-validation.

Results

There were 29 patients with tumor progression and nine patients with post-treatment

changes (nonprogression). Length of follow up ranged from 5- 23 months. Representative volumes of interest (VOIs) for (a) nonprogression and (b) tumor progression groups are displayed in Fig. 1. The AUC and classification performance for each texture model are summarized in Table 1. Patients in the tumor progression group showed greater variance and statistically significant less skewness. The SVM classifier trained using a combination of these two features with the gray-level co-occurrence (f_{11}), run-length nonuniformity (RLNU) and gray-level nonuniformity (GLNU) resulted in a sensitivity of 93% and a postcross validation accuracy of 76% for identifying tumors with progression. Classifiers trained using variance, skewness and f_{11} alone resulted in a specificity of 89% and a similar accuracy.

Conclusions

In this prospective study, we have identified a number of quantitative textural features related to MRI gray-level variation that may assist in identifying patients with tumor progression.

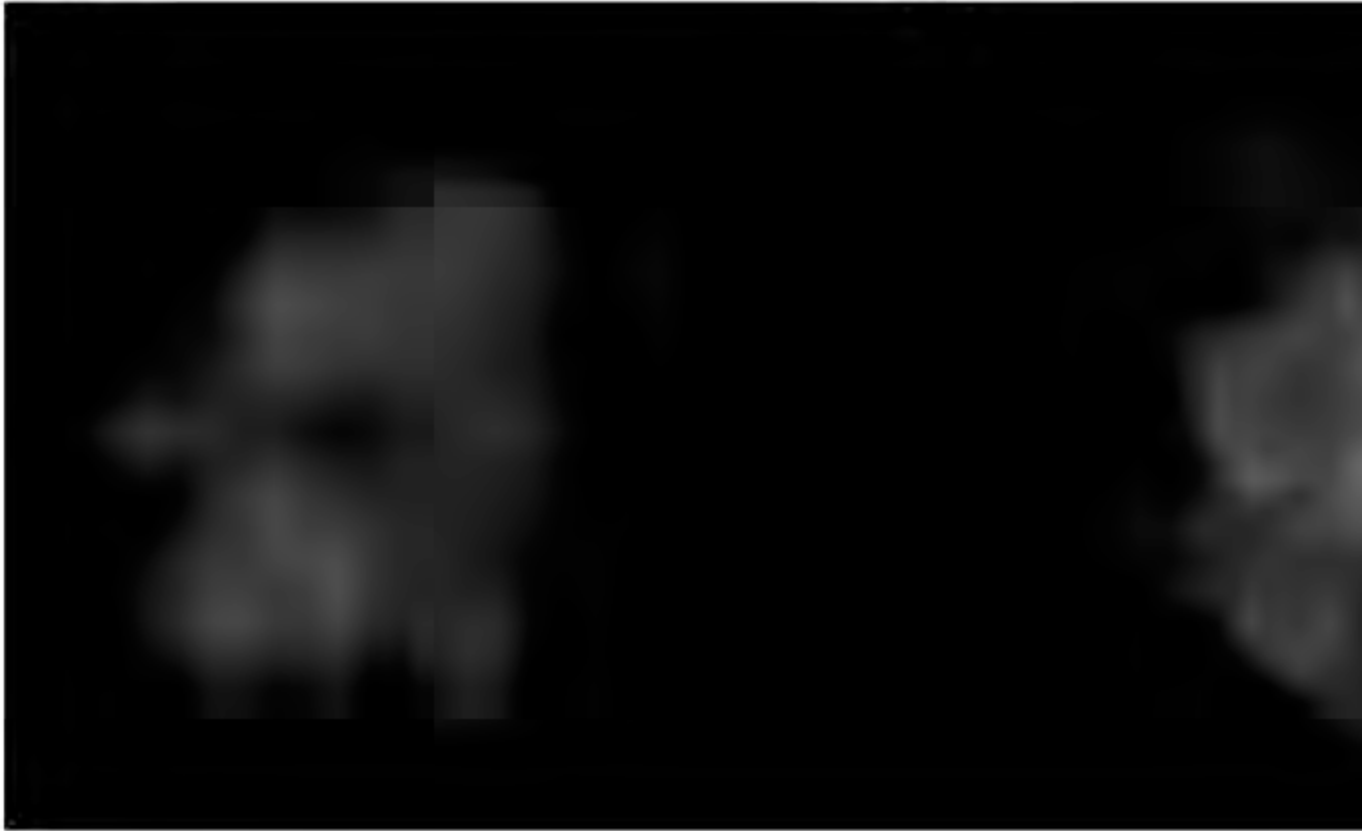
Table 1. Receiver Operator Characteristics for Combinations of Textural Features for the prediction of

| Model | AUC \pm SE ^a | P | Criterion | Se (%) | Sp (%) |
|--|---------------------------|-------|-----------|--------|--------|
| <i>Variance + Skewness + f_{11} + RLNU + GLNU</i> | 0.81 \pm 0.10 | 0.004 | >0.64 | 93 | 67 |
| <i>Variance + Skewness + f_{11}</i> | 0.76 \pm 0.10 | 0.01 | >0.80 | 62 | 89 |
| <i>Variance + Skewness + f_{11} + GLNU</i> | 0.79 \pm 0.10 | 0.004 | >0.67 | 86 | 67 |
| <i>Variance + Skewness + f_{11} + RLNU</i> | 0.79 \pm 0.10 | 0.004 | >0.67 | 86 | 67 |

^a SE = standard error of the AUC, computed by the method of DeLong; ^b accuracy of the SVM classifier following

(Filename: TCT_O-474_Table1ASNR.jpg)

FIGURE 1: (a) non-progression and (b) pro.
(a) **(b)**



(Filename: TCT_O-474_Figure1ASNR.jpg)

O-475

1:39PM - 1:47PM

Machine learning prediction of 1p19q deletion status in low grade gliomas

B Erickson¹, J Sedlar¹, Z Akkus¹, L Coufalova²

¹Mayo Clinic, Rochester, MN, ²Military University Hospital Prague, Prague, MN

Purpose

1p19q status of low grade gliomas (LGGs) is an important predictor of response to certain therapies. Some have reported on visual features that predict 1p19q status, but this is subjective. We evaluated machine learning methods to predict 1p19q status in a cohort of 85 LGGs.

Materials and Methods

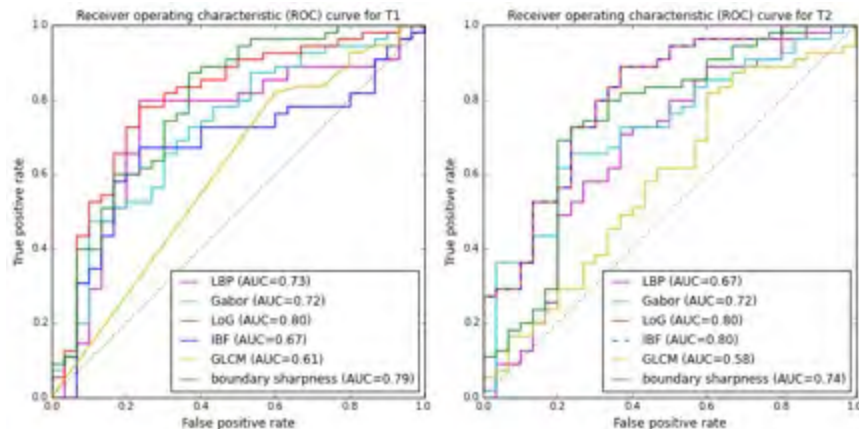
We did a database search and collected 85 consecutive cases of low grade gliomas for which 1p19q status was known. We then removed cases with mixed deletion status or supernumary copies--that is, either both 1p and 19q deleted (d/d) or both maintained (n/n). The distribution was 24 oligodendrogliomas (OD): 23 d/d, 1 n/n, 54 oligoastrocytomas (OA): 31 d/d, 23 n/n, and 7 astrocytomas (AC) 1 d/d, 6 n/n. This represents a sampling bias towards oligodendrogliomas compared to all astrocytomas, as most astrocytomas did not have 1p19q testing performed. We manually segmented the tumors on the T2-weighted image obtained for stereotactic planning purposes. The T1 postcontrast image was aligned with the T2. The brain extraction tool (BET) was used to remove nonbrain tissues, and confirmed by a human. The following standard texture features were computed within the segmented tumor shape in T1 and in T2: local binary patterns (LBP), Gabor filters, Laplacian of Gauss (LoG), intensity-based features (IBF), and gray-level co-occurrence matrix (GLCM). To analyze also the sharpness of tumor boundary, we inspected inner and outer rings along the tumor boundary (excluding parts near the brain boundary) and computed the ratio of intensity variance within and between them ("boundary sharpness"). To evaluate classification of the 1p19q status by individual features, we computed the receiver operating characteristic (ROC) curve and the area under the curve (AUC) on the dataset of 85 cases. The scores were computed by random permutations cross-validation ("shuffle and split") in 10 iterations with 80% train and 20% test split.

Results

Table 1 shows the features that were found to be most predictive of 1p19q status, and include previously described visual features (edge sharpness) as well as texture features that do not have familiar visual features (e.g., LoG). Figure 1 shows that both support vector machine (SVM) learning and Naive Bayes (NB) perform well, with the overall accuracy of SVM being 95%. This appears superior to previously published results for visual and machine learning methods, though we do not have the exact prior algorithms implemented for this data set.

Conclusions

Our research suggests that objective machine learning of readily computable features from T1- and T2-weighted images of low grade gliomas can accurately predict 1p19q codeletion. This work was supported by CA-160045 and EU project FNUSA-ICRC.



(Filename: TCT_O-475_Figure1.jpg)

O-476

1:47PM - 1:55PM

Value of Amide Proton Transfer Imaging in Correlation with Histopathological Grades of Adult Diffuse Gliomas : Comparison and Incremental Value with Dynamic Susceptibility Contrast-Enhanced MRI and Diffusion Weighted Imaging

S Ahn¹, S Lee², Y Choi³, J Kim³, H Lee³

¹Yonsei University College of Medicine, Seoul, Korea, Republic of, ²Yonsei University College of Medicine, Seoul, Seoul, ³Yonsei University College of Medicine, Seoul, AK

Purpose

To investigate the diagnostic value of amide proton transfer (APT) compared with those of apparent diffusion coefficient (ADC) and relative cerebral blood volume (rCBV), and incremental diagnostic value of APT over ADC and rCBV for predicting histopathological grade in diffuse gliomas in adults, with clinically optimized APT imaging protocols.

Materials and Methods

The study cohort consisted of 39 adult patients with histopathologically proven diffuse glioma who underwent pre-operative APT imaging, with 34 patients available for pre-operative dynamic susceptibility contrast (DSC) magnetic resonance imaging (MRI) and diffusion-weighted imaging (DWI). Regions of interest (ROIs) were obtained from circles manually placed at the area with high signal in APT and rCBV map, and low signal in ADC map. Amide proton transfer signal was compared according to WHO grade or low versus high grade of glioma. Diagnostic ability to discriminate high grade glioma from low grade glioma was compared between APT, ADC, and rCBV by using receiver operative characteristic (ROC) analysis, and incremental diagnostic value of APT over ADC and rCBV were assessed by using

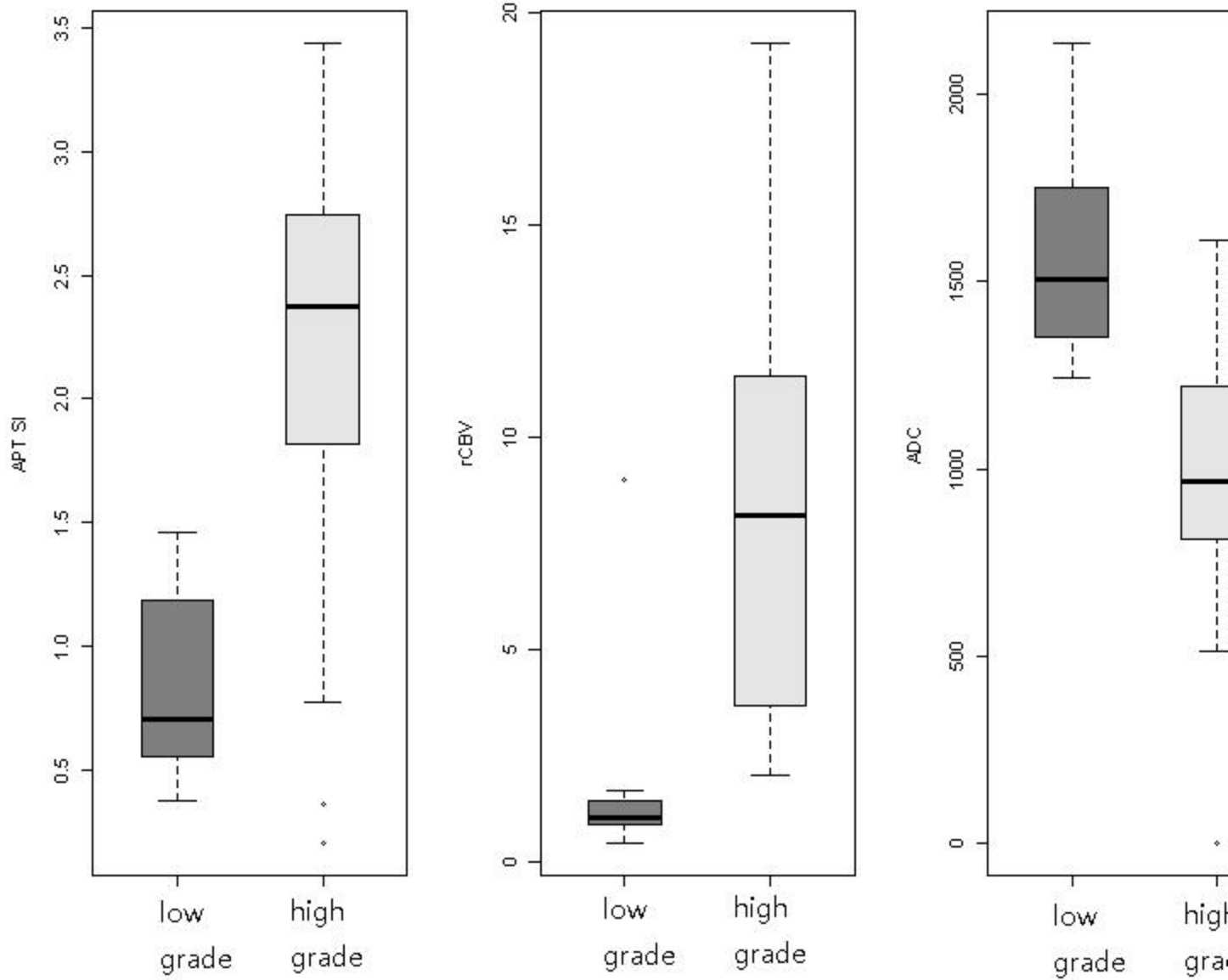
integrated discrimination index. Also, the correlation between APT values and Ki-67 labeling index (LI) was assessed by linear regression.

Results

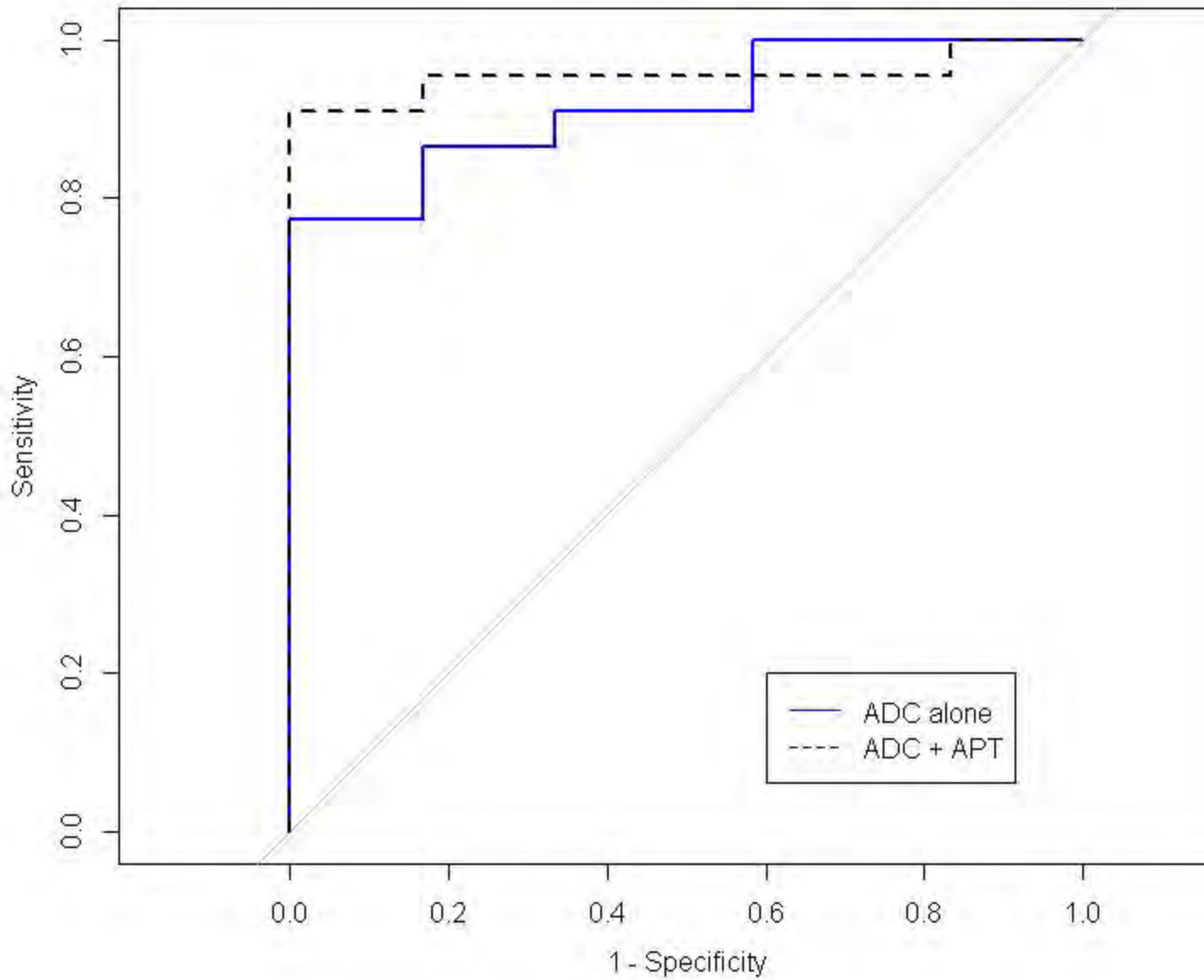
The APT SI values were $0.82 \pm 0.36\%$ in grade II gliomas, $1.73 \pm 0.86\%$ in grade III, and $2.62 \pm 0.78\%$ in grade IV gliomas, which showed significant difference between grade II and III ($p=0.018$), III and IV ($p = 0.010$), as well as II and IV ($p < 0.001$). The diagnostic value to discriminate between high and low grade glioma was not significantly different between APT, ADC and rCBV, with area under the ROC curve (AUC) of 0.890, 0.917, and 0.947, respectively ($p > 0.05$ for each comparison). Incremental diagnostic value of APT was significant over ADC ($p = 0.003$), and not significant over rCBV ($p=0.066$). Amide proton transfer signals were significantly correlated with Ki-67 LI. ($p=0.001$, R-squared = 0.26).

Conclusions

Amide proton transfer imaging can be useful, and have incremental value over ADC for predicting the histopathological grades of adult diffuse gliomas. Amide proton transfer SI can be correlated with Ki-67 LI.



(Filename: TCT_O-476_figure1.jpg)



(Filename: TCT_O-476_figure2.jpg)

| | | AUC (95%CI) | Sensitivity | Specificity | Accuracy | IDI |
|------------------|-------------------|-------------------------|--------------------|--------------------|-----------------|-------------|
| Over ADC | ADC | 0.917 (0.791 - 0.977) | 86.4% | 75.0% | 82.4% | 0.177 |
| | ADC + APT | 0.955 (0.842 - 1.000) | 90.9% | 91.7% | 91.2% | (P = 0.003) |
| Over rCBV | rCBV | 0.947 (0.798 - 1.000) | 81.8% | 91.7% | 85.3% | 0.096 |
| | rCBV + APT | 0.947 (0.833 - 0.993) | 90.9% | 91.7% | 91.2% | (P = 0.066) |

(Filename: TCT_O-476_table1.jpg)

O-477

1:55PM - 2:03PM

Noninvasive tracking the kinetic phases of distribution and tumor targeting of EGFRvIII-specific chimeric antigen receptor T cells via MRI

X Chen¹, W Zhang², T Xie²

¹Daping Hospital, Third Military Medical University, Chongqing, China, ²Daping Hospital, Third Military Medical University, Chongqing, none

Purpose

Glioblastoma (GBM) is the most common primary malignant brain tumor in adults and is uniformly lethal. T-cell-based immunotherapy offers a promising platform for treatment given its potential to specifically target tumor tissue while sparing the normal brain. However, the challenge of monitoring the therapy in real time has been continually ignored. To address this issue, we developed MR imaging approaches to evaluate a recently reported novel CAR strategy for adoptive immunotherapy against glioma xenografts expressing EGFRvIII.

Materials and Methods

T cells, isolated from the peripheral blood of healthy donors, were transduced by EGFRvIII-specific human CAR (EGFRvIII-CAR). Flow cytometry was used to detect CAR expression on transduced T cells. Elevated concentration of USPIO was labeled CAR T cells. The biological properties of these cells were detected. Cytotoxicity assay and cytokine production were analyzed in vitro. Then, USPIO-CAR T cells were transplanted into the nude mice bearing U87-EGFRvIII glioma. Magnetic resonance imaging (MRI) and immunohistochemistry were performed.

Results

We successfully labeled EGFRvIII-CAR T cells with USPIO without any influence on the biological properties and toxicity to tumor of these cells. After intravenous administration into glioma-bearing nude mice, the USPIO-EGFRvIII-CAR T cells specifically homed to gliomas and could be reliably tracked by 7.0 T MR as early as 1 day after transplantation, causing hypointensity on T2-weighted images. Prussian blue staining and CD3 immunohistochemistry staining confirmed the MRI findings. Infusion with EGFRvIII-CAR T cells led to cures in all mice with brain gliomas.

Conclusions

This therapeutic strategy offered efficient therapy effect to EGFRvIII⁺-glioma-bearing mice and implied that MR imaging is a highly useful tool in tracking the kinetic phases of CAR T cells distribution and monitor its therapeutic effect.

O-478

2:03PM - 2:11PM

Volumetric and Progression-Free Interval Analysis of post MRI-guided Laser Induced Thermal Therapy (LITT) for Intracranial Neoplasms

R Garg¹, S Sundararajan¹, A Parisi¹, M DeVita¹, I Keller¹, S Danish¹
¹*Rutgers-Robert Wood Johnson Medical School, New Brunswick, NJ*

Purpose

Laser induced thermal therapy (LITT) is a novel, minimally invasive method of treating metastatic intracranial neoplasms using thermal ablation. As this technique gains momentum as an adjunct tool in managing intracranial neoplastic burden, it is important that neuroradiologists recognize typical post-LITT imaging characteristics and size fluctuations. The purpose of this project is to assess volume changes pre- and 24 hours postablation and estimate a typical progression-free interval post-LITT. It is expected that this data will allow for better recognition of expected post-thermal ablative changes and foster better communication between neuroradiology and referring neurosurgeons.

Materials and Methods

Patients (n=20) who have undergone LITT for various intracranial metastatic neoplasia were assessed retrospectively. Lesion anatomy was reviewed on thin section, postcontrast SPGR magnetic resonance imaging (MRI) sequences pre- and 24 hours postablation. Three volume raters drew lesional regions of interest (ROIs) using the program 3D Slicer. Interrater volumes were averaged and statistically analyzed using a two-tail T test. Subsequent patient scans available in our PACS were reviewed to catalogue the number of days post-therapy a given lesion was progression-free in size. Progression was defined by the product of maximal bi-axial dimensions equating 1.5 times that of the pre-ablation dimensions.

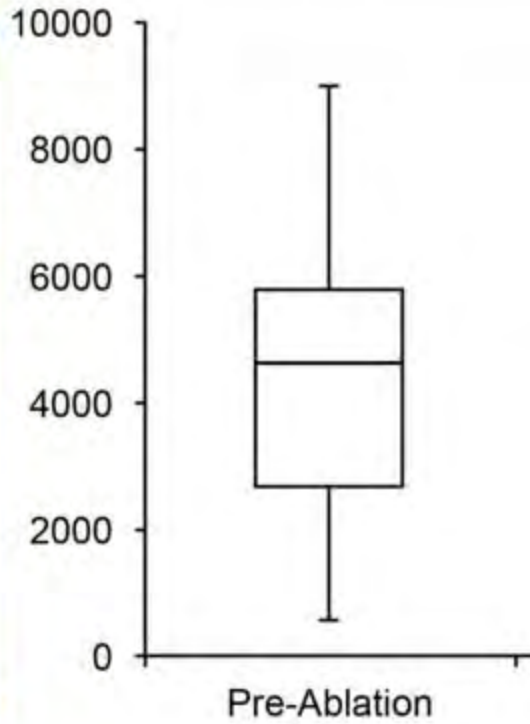
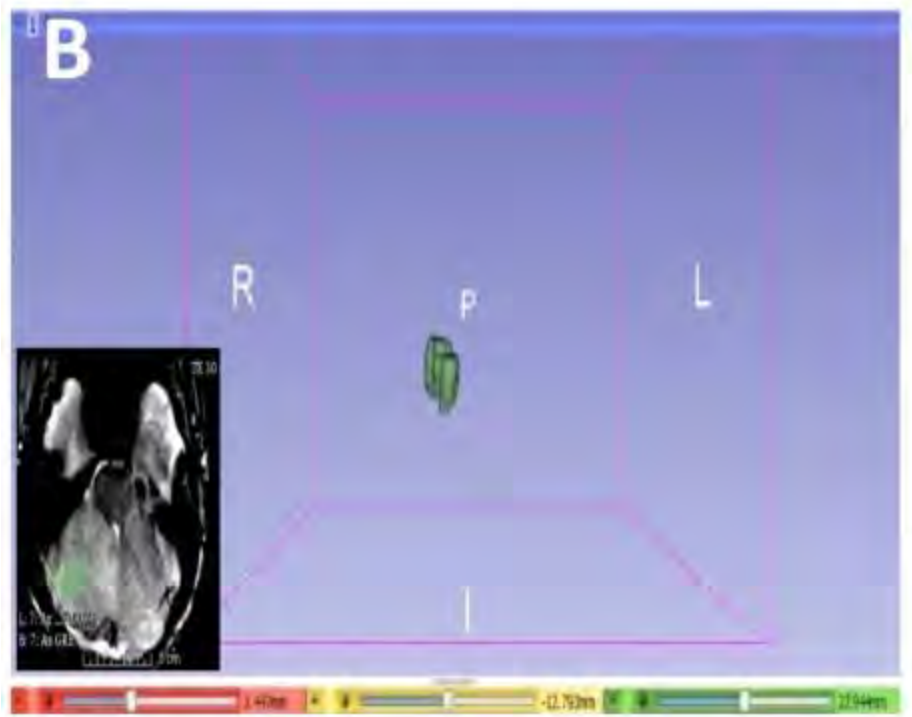
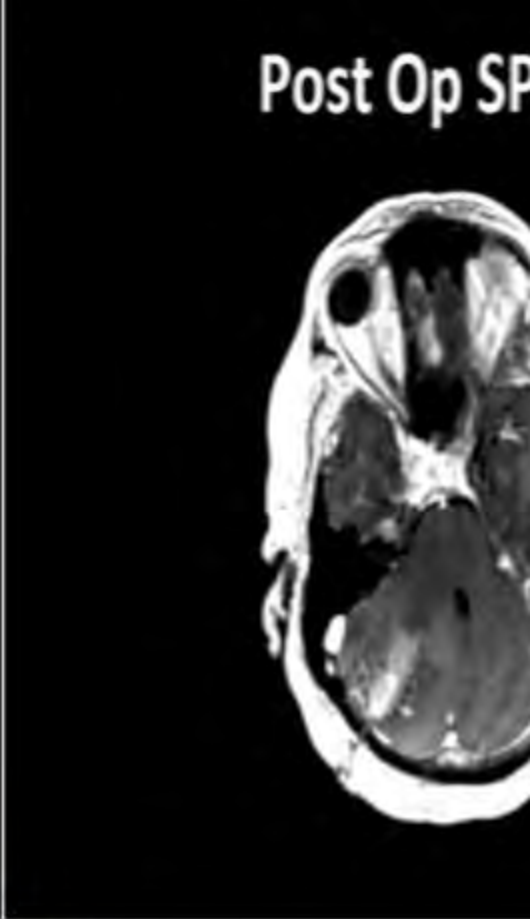
Results

Patient primary malignancy types included eight with lung, five with breast, two with colon, two with renal, one with cervical, one with testicular, and one with melanoma. All lesions demonstrated the owl's-eye target appearance postablation (Fig. A). Pre and posttherapy 3D models were subsequently reviewed (Fig. B). Each patient's lesion demonstrated statistically significant interval increase in size 24 hours following LITT ($p < 0.0007$). Average lesional size increased by approximately 500 mL on 24 hour follow-up MRI (Fig. C). Fifteen of the 20 patients showed no significant interval growth in lesion size post-therapy, with follow-up time ranging from 32 to 736 days following ablation. Five patients demonstrating progression of disease included two breast primary (65 and 272 days post-LITT), two lung primary (146 and 217 days post-LITT), and one cervical primary (85 days post-LITT).

Conclusions

Our study demonstrates statistically significant volumetric changes pre- and postablation in patients with metastatic intracranial lesions, despite primary sources. We believe immediate postablation volumes are higher mostly due to thermal-induced tissue expansion. A smaller component of this expansion may be related to edema, as

postprocedural edema resolved on follow-up scans, with LITT responders demonstrating maintained ablation zone sizes on follow-up imaging. Our data shows that survival time ranging to 2 years post-laser ablation is feasible. This study demonstrates the potential for LITT to be utilized despite varying metastatic source, given the spectrum of primary neoplasms treated and analyzed in this retrospective review. Long-term follow up and analysis of larger patient population outcomes managed with this technique will be necessary to further validate these conclusions.



(Filename: TCT_O-478_VolumeImage.jpg)

O-479

2:11PM - 2:19PM

Growth dynamics and measurement bias in pre-operative, treatment naïve human glioblastoma

B Ellingson¹, T Cloughesy¹, W Pope¹

¹*University of California Los Angeles, Los Angeles, CA*

Purpose

Little is known about the natural growth characteristics of untreated glioblastoma prior to surgical or therapeutic intervention because patients are rapidly treated after preliminary radiographic diagnosis. The purpose of the current study was to explore the growth dynamics in a cohort of untreated glioblastoma patients.

Materials and Methods

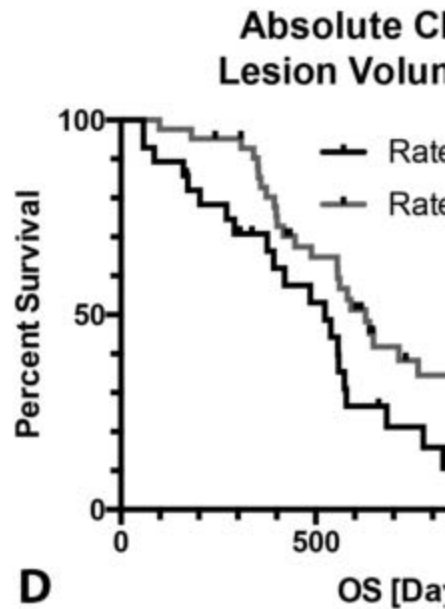
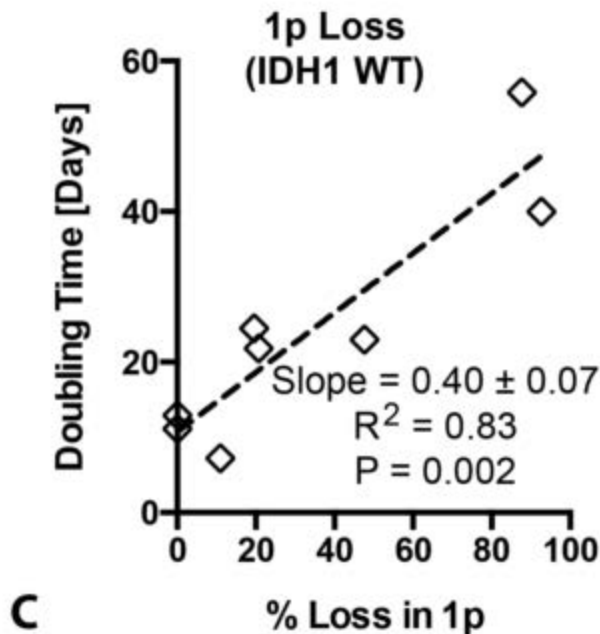
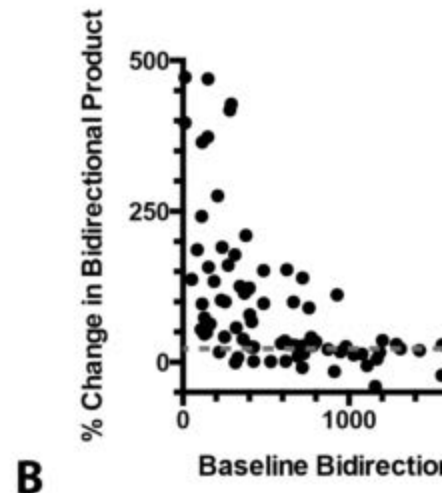
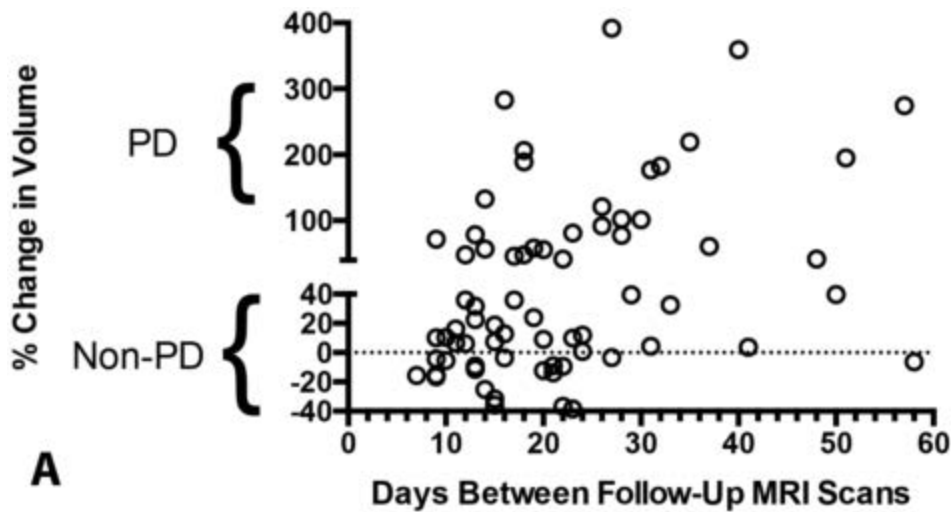
Nintey-five glioblastoma patients had measurable enhancing disease on >2 magnetic resonance imaging (MRI) scans prior to surgery. Growth rates were quantified four different ways (percentage change per day, absolute rate of change per day, estimated volumetric doubling time, and radial expansion rate) using three different approaches (bidirectional product, enhancing disease, and total lesion volume).

Results

Median volumetric doubling time was 21.1 days, percentage change in tumor volume was 2.1% per day, and rate of change in total lesion volume was 0.18 cc per day. Follow-up time between MRI examinations should be >28 days to detect progressive disease with high specificity. Small initial tumor sizes (< 3cm diameter) are biased toward large percentage change at follow up. IDH1 mutant glioblastomas had a longer doubling time compared with wild type tumors. A linear relationship was observed between degree of 1p deletion and doubling time. Age, and absolute rate of change in total tumor volume were significant predictors of OS.

Conclusions

Presurgical, treatment naïve glioblastoma growth dynamics can be estimated in a variety of ways with similar results. Growth rates are dependent on baseline tumor size, the time interval between scans, molecular features of the tumor, and are prognostic for overall survival.



(Filename: TCT_O-479_Fig.png)

O-480

2:19PM - 2:27PM

Quantitative T1 mapping for therapy monitoring of patients with glioblastoma

A Mueller¹, A Jurcoane¹, B Maedler², H Schild¹, E Hattingen¹

¹University Clinic Bonn, Bonn, Germany, ²Philips Healthcare, Best, The Netherlands

Purpose

Therapy monitoring of patients with glioblastoma (GBM) in conventional magnetic resonance imaging (MRI) is done visually and therefore reader-dependent.

Quantitative (q) MRI measures the dynamics of all tumor-associated changes and the

damage of the blood-brain barrier objectively. Peritumoral edema and infiltrating tumor lead to prolongation of the relaxation time T1. We performed qT1 mapping 1) to compare the visibility of damage of the blood-brain barrier with conventional MRI and 2) to monitor the dynamics of noncontrast qT1 during radiochemotherapy.

Materials and Methods

The study was approved by the local institutional review board and informed written consent was obtained from all patients. Twelve GBM patients were examined with standard T1-weighted spin-echo sequences and qT1 mapping using a 3D-IR-TFE sequences (TR = 4,88 ms; TE = 2,41 ms; TI = 150, 350, 750, 1200, 2300 ms) pre and postcontrast administration on a 3.0 T MR scanner (Achieva, Philips Healthcare, The Netherlands). The sequence protocol also included conventional FLAIR and T2 TSE sequences. GBM patients were examined before radiochemotherapy (timepoint 0, TP0), and in 6-week intervals (TP1,..., TPx). The median overall observation interval was TP5 [range (TP3; TP8)]. We generated co-registered differential maps of 1) T1-w and qT1 pre and postcontrast application and 2) noncontrast qT1 at TP0 and TPx. In the contrast-enhanced maps we determined the percentage shortening of qT1 (DqT1) and the percentage signal increase (DSI) in the T1-W images. Region of interests (ROI) were drawn manually in the differential maps. The differential noncontrast qT1 maps show areas with T1 increase while unchanged tumor areas are suppressed. Treatment response was assessed using the RANO criteria in the conventional MRI at each TP.

Results

1) At TP1 eight patients showed areas of qT1 shortening also outside the solid enhancing tumor area. This appeared as "cloudy" enhancement (DqT1 = 20.66 % in cloud-ROI versus DqT1 = 13.69 % in contralateral control-ROI, $p = 0.005$). In the T1-W differential maps the signal intensity of the identical ROI fluctuated around zero (DSI = -1.68% in cloud-ROI versus DSI = -3.14% in contralateral control-ROI, $p = 0.0187$). The "cloudy" enhancement appeared in patients with and without tumor progression. A persisting cloud (for more than one TP) only occurred in patients with tumor progression. 2) In GBM patients without progression the peritumoral areas with noncontrast qT1 prolongation increased at only one TP and regressed at the following TP. In contrast in GBM patients with tumor progression the areas with noncontrast qT1 prolongation increased from TP to TP.

Conclusions

qT1 mapping detects subtle ("cloudy") blood-brain barrier damage compared to conventional T1-W images. Persisting "clouds" seem to correlate with progressive disease. T1 prolongation seems to be a sensitive and objective marker of any tumor-associated change.

O-481

2:27PM - 2:35PM

UMT-CEST Imaging of Human Brain Tumors on 7.0 Tesla

G Parikh¹, D Xia¹, D Kondziolka², R Regatte¹, R Jain³

¹NYU Medical Center, New York, NY, ²NYU Medical Center, New York, NY, ³NYU School of Medicine, New York, NY

Purpose

This study assesses the feasibility to utilize uniform magnetization transfer in chemical exchange saturation transfer (uMT-CEST) contrast imaging technique measuring the myoinositol (MI), creatine (Cr), and amide proton transfer (APT) endogenous metabolites in patients with brain tumors with correlation to MR perfusion maps (rCBV) as well as FDG uptake (SUV) data obtained from hybrid MR-PET. This study hopes to determine the sensitivity and specificity of uMT-CEST to accurately grade these tumors, differentiate tumor from treatment effects as well as be useful as a surveillance tool for treatment response.

Materials and Methods

Seven treatment naive brain tumor patients were examined on a 7T whole-body scanner (Siemens, Erlangen, Germany) with a volume-transmit, 24-element receive head coil array. For the off-resonance pre-saturation, a train of ten 100 ms long Gaussian and cosine modulated Gaussian pulses ($B_{1,rms} = 1.4 \mu T$ and $1.9 \mu T$) were used to perform uMT-CEST; the frequency offsets being varied from -2500 Hz to 2500 Hz with a step size of 100 Hz. The modulation frequency of the cosine-modulated Gaussian pulse was 1.5 kHz. For imaging, a single shot GRE acquisition with centric phase encoding order was used with Flip Angle = 9° , TR = 12 ms, TE = 3.5 ms, dwell time = 15 μs , FOV = $200 \times 200 mm^2$, slice thickness = 5 mm, matrix size = 192×192 . Regions of interest (ROIs) were drawn on enhancing brain tumor as well as normal appearing white matter (control). A total of nine lesions were measured (low grade glioma = 2, radiation necrosis = 1, metastatic = 6). Positron emission tomography/magnetic resonance (PET/MR) imaging was performed on three patients, using an integrated 3T MR-PET system (Biograph mMR; Siemens Healthcare), which acquires simultaneous PET and MR data. Magnetic resonance perfusion imaging also was performed on these three patients.

Results

One patient underwent uMT-CEST prior to and following gamma knife surgery of the brain metastatic lesion from breast carcinoma. This patient had interval decrease in all metabolites MI, Cr, and APT concentrations in the metastatic lesion following gamma knife: MI=0.97+3.33 (from 8.14+3.18), Cr=-0.39+2.9 (from 0.73+2.2), and APT=-0.73+2.89 (from -0.09+2.06) (see Fig. 1). Two low grade gliomas: MI=4.05+1.45, Cr=3.34+0.64, APT=0.13+1.35. Five metastatic lesions: MI=4.78+1.78, Cr=2.37+1.76, APT=0.77+1.96. One radiation necrosis: MI=4.19+4.01, Cr=-0.93+2.70, APT=0.12+2.90 (see Table 1). Three patients underwent PET and MR

perfusion. One patient with radiation necrosis showed: MR-PWI (rCBV) of 1.94 ± 1.29 , and 18F-FDG (early SUV) of 3.4. One patient with metastasis showed: MR-PWI (rCBV) of 2.19 ± 0.98 and 18F-FDG (early SUV) of 5.1 (Max=9.2). One patient with low grade glioma showed: MR-PWI (rCBV) of 1.87 ± 0.48 (Max=3.4) and 18F-FDG (early SUV) of 4.5.

Conclusions

This study was successful in measuring MI, Cr, and APT endogenous metabolites on these brain tumor patients on a 7T magnet demonstrating the feasibility of performing uMT-CEST on humans. There is potential for uMT-CEST to be useful for grading tumors, differentiating tumor from treatment effects and used as a surveillance tool for treatment response.

Figure 1: Image A (pre-gamma knife) and Image B (post-gamma knife) displays axial T1 post contrast images of a 48 year old female with breast cancer with a parasylvian fissure inferior left parietal with interval decrease in all metabolites after gamma knife treatment.

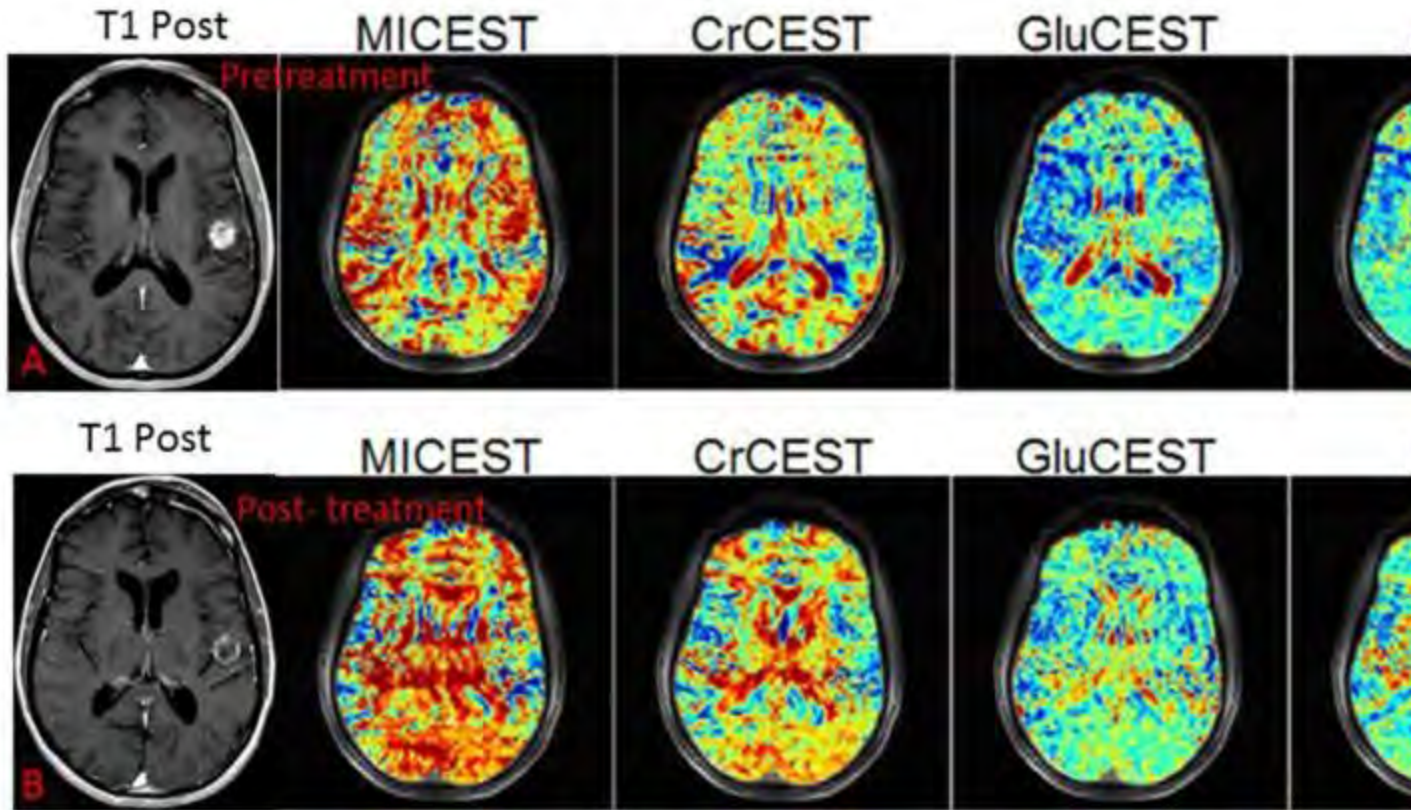


Table 1:

| | Low Grade Glioma (n=2) | Metastasis (n=5) | Radiat |
|-----------------|------------------------|------------------|--------|
| uMT-MICEST (%) | 4.05±1.45 | 4.78±1.78 | |
| uMT-CrCEST (%) | 3.34±0.64 | 2.37±1.76 | |
| uMT-APTCEST (%) | 0.13±1.35 | 0.77±1.96 | |

(Filename: TCT_O-481_highresolutionCESTFINALimage.jpg)

O-482

2:35PM - 2:43PM

Voxel-level Assessment of Cellularity in Recurrent Glioblastoma: A Multiparametric Radiologic-Histopathologic Study

P Chang¹, P Yang¹, S Bowden¹, H Malone¹, B Gill¹, J Samanamud¹, D Chow², J Grinband¹, L Schwartz¹, J Bruce¹, P Canoll¹, A Lignelli¹

¹Columbia University Medical Center, New York, NY, ²University of California, San Francisco, San Francisco, CA

Purpose

Radiographic interpretation of a newly enhancing lesion in post-treatment glioblastoma (GBM) remains an unsolved challenge (1-2). One limitation is that current approaches categorically label the entire enhancing lesion as treatment effects or recurrent tumor, while histopathologic studies show both components often coexist in varying proportions (3). We propose a novel technique to map the heterogeneous distribution of recurrent tumor cellularity by combining voxel-level signal intensity on DSC-perfusion (rCBV), ADC and FLAIR sequences.

Materials and Methods

As part of an IRB-protocol, stereotactic biopsies were obtained in GBM patients with a newly enhancing lesion suspicious for pseudoprogression or recurrence. For each biopsy site, cell count (per 40x high-power-field) and corresponding signal intensity (rCBV, ADC and FLAIR) were recorded. Image preprocessing included linear coregistration (4) and intensity normalization (5). Single ($y=\beta_0+\beta_1x$) and multiple ($y=\beta_0+\beta_1x_1+\beta_2x_2+\beta_3x_3$) linear regression models were used to estimate tumor cellularity based on signal intensity.

Results

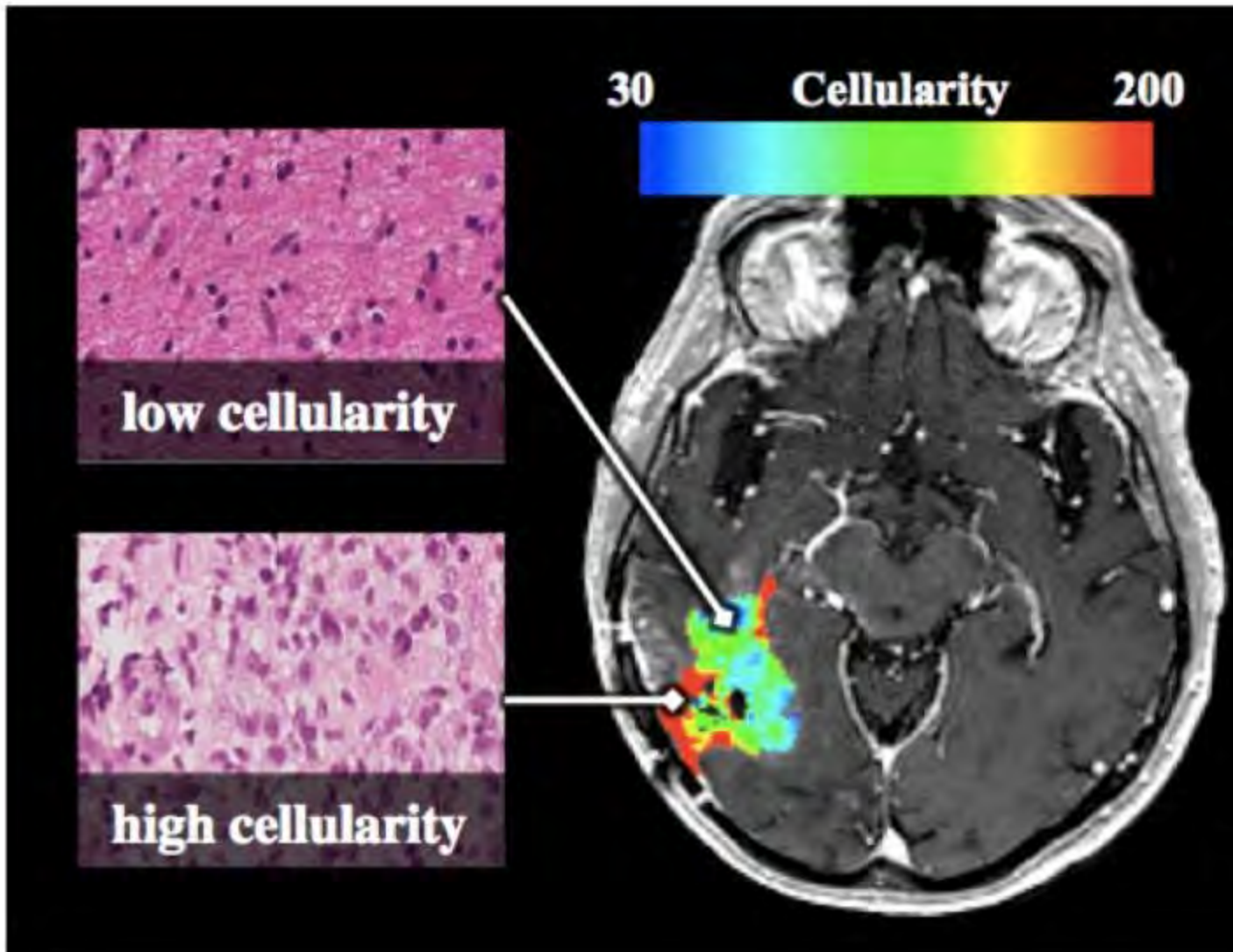
A total of 32 biopsy samples were obtained. All samples had ADC and FLAIR imaging; a subset of 16 samples had corresponding DSC-perfusion. By univariate regression, rCBV was most correlated with recurrent tumor cellularity ($r=0.827$), followed by ADC ($r=0.661$) and FLAIR ($r=0.580$). A multivariate model combining ADC and FLAIR improved overall cellularity correlation ($r=0.746$); this model weighted ADC ($\beta_1=-165.8\pm 45.7$) slightly more than FLAIR ($\beta_2=-44.5\pm 16.6$). A multivariate model combining rCBV, ADC and FLAIR yielded highest overall correlation ($r=0.869$); this model weighted rCBV ($\beta_1=110.6\pm 41.8$) more than ADC ($\beta_2=-55.8\pm 35.9$) or FLAIR ($\beta_3=8.1\pm 15.1$).

Conclusions

Voxel-level radiologic-histopathologic correlation demonstrates that changes in recurrent tumor cellularity cause corresponding signal changes in rCBV, ADC and FLAIR, a relationship that may be modeled with multiple linear regression and used to noninvasively map tumor cellularity throughout the entire lesion (Fig. 1). Further investigation is needed to translate this postprocessing technique into a robust method to differentiate pseudoprogression from tumor recurrence.

Figure 1. Multiparametric Cellularity Map For Recurrent Glioblastoma

Superimposed upon a new area of enhancement is a color map indicating relative cellularity. The estimate is based upon a multiple linear regression combining signal intensity on ADC, FLAIR and rCBV sequences calibrated to stereotactic histopathologic specimens. Within this single lesion, areas of low cellularity (blue) are seen intermixed with areas of high cellularity (red), demonstrating the heterogeneous composition of GBM lesions after chemoradiation therapy.



(Filename: TCT_O-482_Figure.jpg)

Thursday

1:15PM - 2:45PM

Washington Marriott Wardman Park, Roosevelt 4

**22F-PARALLEL PAPER SESSION: Intracranial Plaque and Vessel Wall Imaging
O-483**

1:15PM - 1:23PM

**Clot Composition and Sensitive MRI Sequences. An In Vitro Analysis with
Predetermined Clot Components**

A Narata¹, K Janot², L Barantin³, G Fromont-Hankard², J Cottier², I Filipiak⁴
¹*University Hospital of Tours, Tours, France*, ²*University Hospital of Tours, Tours, Indre et Loire*, ³*INSERM, Tours, Indre et Loire*, ⁴*Platform CIRE, Tours, Indre et Loire*

Purpose

Stroke treatment has presented an enormous evolution in the last few years. Recent studies comparing intravenous thrombolysis versus IV thrombolysis + thrombectomy, showed the superiority of the second group. As "time" is still one of the most important prognostic factors, the necessity to perform IV thrombolysis before thrombectomy should be reconsidered in some cases as recanalization rates of IV thrombolysis remain still lower than mechanical thrombectomy. In vitro studies demonstrated that high fibrin concentration could indicate lower responsiveness to IV thrombolysis and erythrocyte-rich clots should be dissolved more easily by thrombolytic. Concerning mechanical thrombectomy, clot composition could affect device performance and clinical recovery. Preselection of patients might be interesting in terms of clot composition and therapeutic decision, and take part of thrombectomy techniques developments. In this study, we used five different thrombus (one unknown composition) and magnetic resonance imaging (MRI) to evaluate erythrocyte and fibrin presences in each sample. We assessed the hypothesis that MRI used for ischemic stroke diagnosis can detect and characterize thrombus composition providing a scale that could be useful to quantify erythrocyte and fibrin compounds.

Materials and Methods

Five different experimental clots were prepared from ovine blood (Neuravi Ltd, Galway, Ireland): 100% fibrin, 80% RBC, 20% RBC, 50% RBC, one with unknown composition. All clots were submitted to histological analysis to validate MRI data. Clots were fixed in a phantom prepared with gelatin and manganese to obtain equivalent T1 and T2 human gray matter values. Measurements were performed on a 3T whole body MR scanner (Verio, Siemens, Erlangen, Germany) using a MRI protocol: 3D T1- and T2-weighted, T2EG-weighted gradient recalled echo imaging,

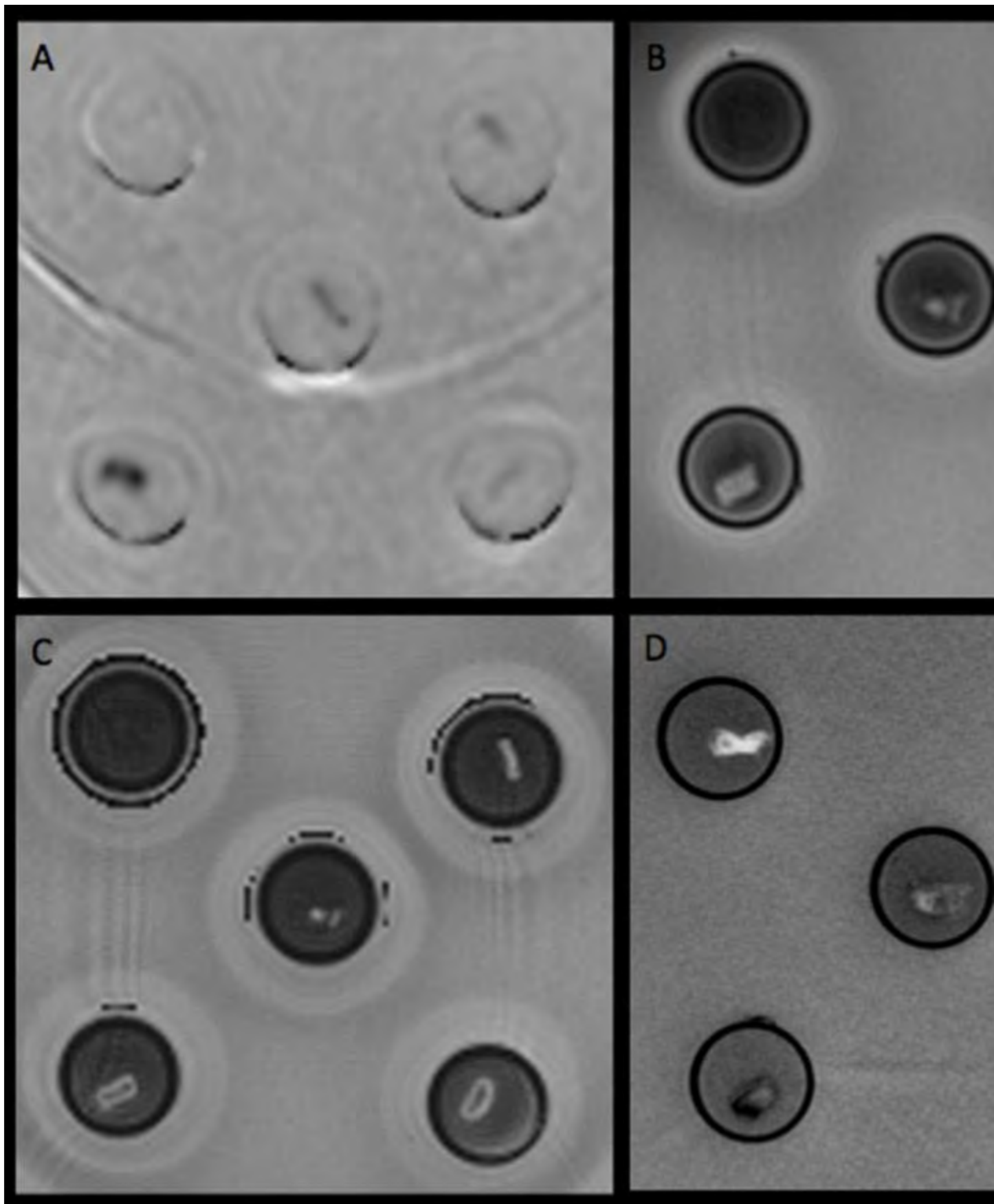
susceptibility weighted imaging (SWI), fluid-attenuated inversion recovery imaging (T2Flair) and diffusion-weighted imaging (DWI) with apparent diffusion coefficient (ADC) cartography. We have reported all clots "signal intensity" (SI) on each sequence to create an index "n". Statistical analysis were performed with R software (2.15.1 version, R Foundation, Vienna, Austria). All measures were expressed as mean +/- standard deviation (SD). We performed a t-test to compare index "n" of RBC and fibrin clots for each sequence, unpaired t-test and repeated measure analysis of variance (ANOVA) was used to examine the differences of mean of RBC index for each sequence. A p value of <0.05 was considered significant.

Results

We found a significant difference between fibrin and RBC-rich clots in ADC map (A), T2EG (B), SWI (C) and T1 (D) (Fig. 1). The mean concentration of RBC could be detected and differentiated in ADC map, SWI and T2EG. Magnetic resonance imaging and histological analysis showed that clot with unknown composition was rich in red cells.

Conclusions

Thrombus composition can be evaluated by standard MRI protocol. T1, T2EG, SWI and ADC map can differentiate fibrin from RBC-rich clots. T2EG, SWI and ADC map can quantify RBC based on a gray scale.



(Filename: TCT_O-483_figure1.jpg)

O-484

1:23PM - 1:31PM

Comparison of FLAIR hyperintense vascular sign and leptomeningeal collateral on catheter angiography in 100 patients with anterior cerebral artery stenosis or occlusion

H Liu¹, Y Lin¹, C Lee¹, Y Wang¹, Y Chen¹

¹*National Taiwan University Hospital, Taipei, Taiwan*

Purpose

To compare the appearance of FLAIR hyperintense vascular (FHV) sign and cerebral collateral circulation shown on catheter angiography.

Materials and Methods

We reviewed the magnetic resonance (MR) images of the last 100 patients diagnosed with anterior cerebral vascular stenosis or occlusion (ICA, MCA, ACA) and catheter angiography was performed in them. Patients diagnosed as moyamoya disease were excluded. The location of FLAIR hyperintense vascular (FHV) sign recorded as: intra-sylvian, temporo-occipital, high frontoparietal, and combination. The collateral score designed by ASITN/SIR were applied for the grading of cerebral collateral on catheter angiography (grade 0 to grade 4, whole grade 0= no collateral, grade 4 =rapid and complete collaterals in occluded vascular territory) and we also recorded the direction of collateral (antegrade or retrograde).

Results

FLAIR hyperintense vascular sign found in 37 patients with major cerebral vessel severe stenosis or occlusion (30 in chronic and seven in acute cases). The FHV sign was found as intra-sylvian in 25, temporo-occipital in 16, high frontoparietal in 12. All patients with FHV had anterior cerebral vascular stenosis/occlusion, and three in ICA, 26 in MCA alone, one in ACA alone, and five in ICA+MCA. Antegrade collateral associated with FHV noted in 12, retrograde collateral in 25. We also found 10 patients with leptomeningeal collateral without FHV sign, and two patients with FHV without leptomeningeal collateral on catheter angiography.

Conclusions

FLAIR hyperintense vascular sign is not definitely comparable to the leptomeningeal collateral on catheter angiography in patients with anterior cerebral artery stenosis or occlusion.

O-485

1:31PM - 1:39PM

Progression of Intracranial Atherosclerosis: a 3D High-resolution Vessel Wall MRI Study

X ZHANG¹, H Yang², l liu², y zhang², E Guallar², B Wasserman², Y Qiao²

¹*Johns Hopkins School of Medicine, Baltimore , MD*, ²*Johns Hopkins School of Medicine, Baltimore, MD*

Purpose

Recent advances in high-resolution black blood magnetic resonance imaging (BBMRI) have enabled the reliable detection and characterization of intracranial atherosclerotic disease (ICAD) (1, 2). We sought to determine the reliability of this technique to determine the progression of ICAD in an asymptomatic population.

Materials and Methods

Twenty-three asymptomatic participants (9 male; mean age, 79.2 years, ranges, 71 to 86 years) with identified ICAD were recruited from a population-based study, who underwent high resolution vessel wall MRI. All baseline MRI was performed at a 3T Siemens scanner with a standardized brain MRI protocol that consisted of a 3D time-of-flight (TOF) MRA and 3D high isotropic resolution BBMRI (2). The repeated MRI was performed on a 3T Philips scanner with mean time interval of 2.3 ± 0.49 years since baseline. Two MRI protocols were matched with acquired resolution (TOF, $0.5\text{mm} \times 0.5\text{mm} \times 0.5\text{mm}$; BBMRI, 0.5 isotropic mm) and the image coverage. Two trained readers independently analyzed MRI images and were blinded to dates and order of the exams. Plaque presence by vessel segment was recorded for both visits. Change from baseline for each identified plaque was categorized as progression, regression and no change based on the lumen (stenosis) and vessel wall assessments. Reliability was assessed by kappa statistics and intraclass correlations (ICC).

Results

A total of 134 and 149 plaques were identified at baseline and follow up, respectively (Table 1). New plaques ($n=15$) were detected in 11 participants. Among 134 plaques identified at baseline, 26 progressed, two regressed and 106 had no detectable change. Reader reliability [kappa or ICC, (95% CI)] was 0.71(0.62, 0.81) for plaque presence, 0.81 (0.70, 0.92) for plaque progression, 0.80 (0.54, 0.93) for maximum wall thickness and 0.65 (0.32, 0.88) for mean wall thickness.

Conclusions

Vessel wall MRI provides reliable MRI measurements of intracranial vessels, and enables studying the natural history of ICAD in general population.

Table 1. Characteristics of Study Population (n

| | Baseline | Follow |
|-------------------------------------|----------------|--------------|
| Age (mean \pm SD) | 75.9 \pm 5.0 | 79.1 \pm 5 |
| Male sex | -- | 9 (39% |
| Total no. of plaques | 134 | 149 |
| Plaque location | | |
| Anterior cerebral artery | 9 (7%) | 11 (7% |
| Internal carotid artery | 44 (33%) | 44 (30% |
| Middle cerebral artery | 33 (25%) | 36 (24% |
| Basilar artery | 14 (10%) | 16 (11% |
| Posterior cerebral artery | 23 (17%) | 27 (18% |
| Vertebral artery | 11 (8%) | 15 (10% |
| New plaques | -- | 11 (52% |
| Plaque progression | -- | 12 (48% |
| New plaques and plaques progression | -- | 7 (30% |

(Filename: TCT_O-485_Table1.jpg)

O-486

1:39PM - 1:47PM

Utility of Intracranial Vessel Wall Imaging to Identify Culprit Atherosclerotic Lesions: A Systematic Review and Meta-Analysis

H Baradaran¹, H Kamel¹, A Gupta¹

¹New York-Presbyterian Hosp/Weill Cornell Med Ctr, New York, NY

Purpose

Plaque inflammation within intracranial atherosclerosis is a well known cause of ischemic stroke and potentially may be characterized by a relatively simple, qualitative imaging biomarker - enhancement on high resolution magnetic resonance (MR) imaging. While this method for characterizing intracranial atherosclerotic plaque is promising, most early studies to date have been small, retrospective studies which have made it difficult to draw firm conclusions about the role of this emerging imaging technique. We therefore performed a systematic review and meta-analysis to evaluate the association between intracranial plaque enhancement on high resolution MR imaging and cerebrovascular ischemic events.

Materials and Methods

We performed a comprehensive literature search evaluating the association between intracranial plaque enhancement on in vivo, high resolution MR imaging and cerebrovascular ischemic events. The included studies were studies with patients who had undergone pre and postgadolinium based contrast-enhanced high resolution MR imaging of intracranial vessels with techniques allowing for the evaluation of the vessel wall. All studies were of patients with a prior recent history of ischemic cerebrovascular event. We extracted data on the prevalence of postcontrast vessel wall/plaque enhancement in culprit atherosclerotic lesions compared to the prevalence of enhancement in nonculprit plaques. A meta-analysis with assessment of study heterogeneity was performed. Results were presented in a forest plot and summarized using a random-effects model (Fig. 1).

Results

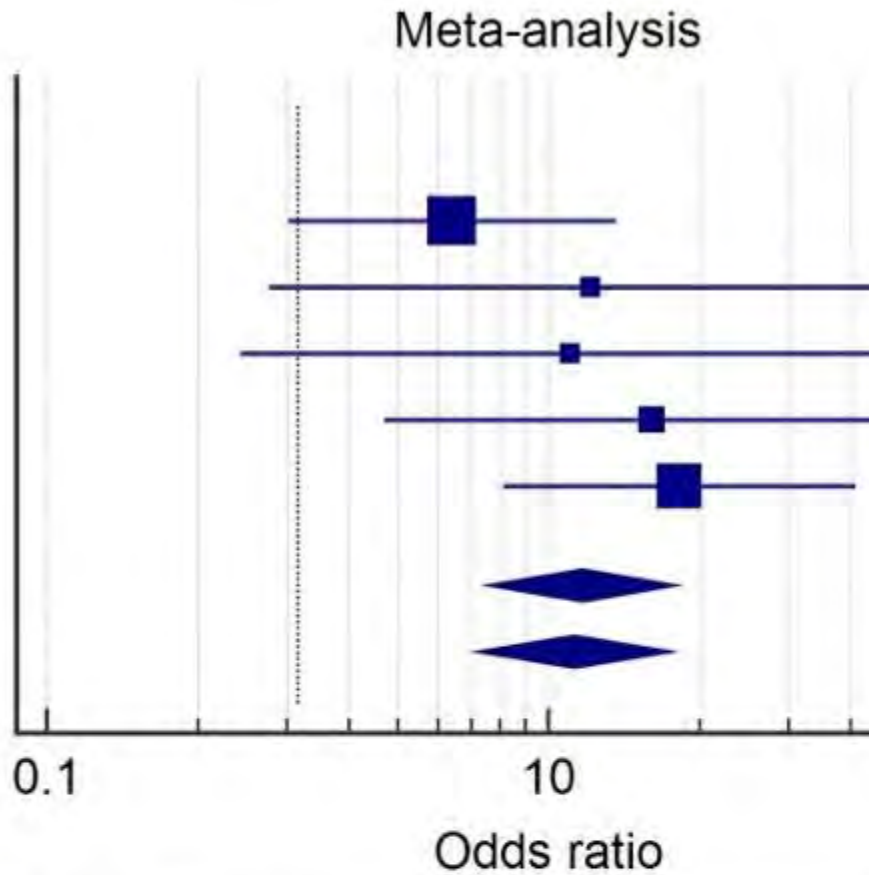
Six studies with a total of 123 patients met the inclusion criteria for systematic review and meta-analysis. Amongst the 198 plaques analyzed in these studies, 64 of 102 culprit plaques enhanced compared to 16 of 96 nonculprit plaques. We found a significant positive relationship between the presence of enhancement within intracranial atherosclerotic plaque and that plaque being the culprit plaque for a recent ischemic cerebrovascular event with a pooled random-effects odds ratio (OR) of 12.67 (95% CI, 5.12 – 31.39, $p < 0.001$). Our analysis showed no evidence of statistically significant heterogeneity (I² statistic = 0, 95% CI, 0 - 79.8; $p = 0.42$).

Conclusions

Vessel wall enhancement is strongly associated with culprit as compared to nonculprit atherosclerotic plaque in patients with recent ischemic cerebrovascular events. Accurate identification of culprit intracranial atherosclerotic lesions with vessel wall imaging could improve our ability to find an etiology for strokes currently considered cryptogenic. Future prospective studies are warranted to confirm the ability of

gadolinium enhancement to identify culprit plaques, especially in patients with nonstenosing lesions potentially causing ischemic stroke.

Klein 2006
 van der Kolk 2011
 Kim 2012
 Skarpathiotakis 2013
 Vakil 2013
 Qiao 2014
 Total (fixed effects)
 Total (random effects)



| Study | Intervention | Controls | Odds ratio | 95% CI | z | |
|------------------------|--------------|----------|------------|------------------|-------|--------|
| Klein 2006 | 5/5 | 1/1 | - | | | |
| van der Kolk 2011 | 6/14 | 4/26 | 4.125 | 0.919 to 18.521 | | |
| Kim 2012 | 12/26 | 0/8 | 14.655 | 0.766 to 280.235 | | |
| Skarpathiotakis 2013 | 15/26 | 0/4 | 12.130 | 0.592 to 248.502 | | |
| Vakil 2013 | 7/10 | 1/12 | 25.667 | 2.207 to 298.508 | | |
| Qiao 2014 | 19/21 | 10/45 | 33.250 | 6.595 to 167.627 | | |
| Total (fixed effects) | 64/102 | 16/96 | 13.581 | 5.652 to 32.632 | 5.832 | <0.001 |
| Total (random effects) | 64/102 | 16/96 | 12.674 | 5.118 to 31.385 | 5.489 | <0.001 |

(Filename: TCT_O-486_asbtractimage1.jpg)

Intracranial calcification and stenosis and their association with stroke

M Mossa-Basha¹, B Quiney², S Ying³, D Hippe¹

¹University of Washington, Seattle, WA, ²St. Paul's Hospital, University of British Columbia, Vancouver, British Columbia, ³University of Manitoba, Winnipeg, Manitoba

Purpose

Intracranial calcifications are commonly seen on CTA during the work up of acute stroke. Their significance has received increased attention recently and the cumulative effect with stenosis is not well known. This project evaluated the risk of stroke when intracranial calcifications were seen with and without stenosis.

Materials and Methods

We retrospectively reviewed the radiology database for CTA stroke exams performed from 1/2010-4/2010 and included those with ischemic stroke presumed to be secondary to intracranial atherosclerosis. Imaging studies were reviewed by two independent readers on a per vessel basis to record the presence of calcification and/or stenosis. Stenosis was identified as >30% narrowing relative to proximal or contralateral normal segment. Cerebrovascular events were confirmed by presence of infarct on magnetic resonance imaging (MRI) performed or clinical evidence of stroke. All vessels proximal to the location of stroke were considered as potential culprits. Associations between stroke, calcification and stenosis were analyzed using logistic regression based on generalized estimating equations to account for repeated measures. All models were adjusted for sex, age, prior stroke, coronary artery disease, hypertension, hyperlipidemia, smoking and diabetes.

Results

Ninety-nine patients (1287 vessels) fulfilled our criteria and were included. Nineteen percent of patients had stroke (54 proximal vessels). Fifty-eight percent of patients had intracranial calcification (172 vessels) and 43% had stenosis (99 vessels). Calcification and stenoses were most common in the cavernous (54% and 22%, respectively) and supraclinoid (24% and 6.1%) ICAs, followed by the vertebral arteries (21% and 19%). Compared to normal vessels, vessels with calcification only (OR=2.2, p=0.049), stenosis only (OR=6.7, p<0.001) and both stenosis with calcification (OR=3.9, p=0.003) were each significantly associated with stroke downstream, though noncalcified stenoses tended to imply higher risk than calcified stenoses (OR: 6.7 vs. 3.9, p=0.25).

Conclusions

The presence of intracranial stenosis alone, calcification alone or both is strongly associated with the risk of stroke.

O-488

1:55PM - 2:03PM

Cryptogenic Stroke Downstream of Nonstenosing Intracranial Atherosclerotic Lesions

H Baradaran¹, H Kamel¹, G Gialdini², A Giambone², B Navi³, M Lerario³, J Min³, C Iadecola³, A Gupta¹

¹New York-Presbyterian Hosp/Weill Cornell Med Ctr, New York, NY, ²Weill Cornell Medical College, New York, NY, ³New York Presbyterian Hospital- Weill Cornell Medical College, New York, NY

Purpose

Many strokes categorized as "cryptogenic" may result from large artery atherosclerosis that goes unrecognized because it does not cause $\geq 50\%$ luminal stenosis. To test this hypothesis, we compared the prevalence of nonstenosing atherosclerotic plaques upstream of cryptogenic cerebral infarcts versus the unaffected side.

Materials and Methods

In a prospective stroke registry, we identified patients with cerebral infarction limited to the territory of one internal carotid artery (ICA). We included patients with stroke of undetermined etiology and, as controls, patients with cardioembolic stroke. We used noncontrast computed tomography (CT) to measure calcification in both intracranial ICAs both qualitatively using the Modified Woodcock Visual scale and using a semi-automated quantitative approach by manually drawing regions of interest (ROIs) around ICA calcification and measuring Agatston-Janowitz scores. Within subjects, the Wilcoxon signed rank sum test for nonparametric paired data was used to compare the calcium burden in the ICA upstream of the infarction versus the ICA on the unaffected side.

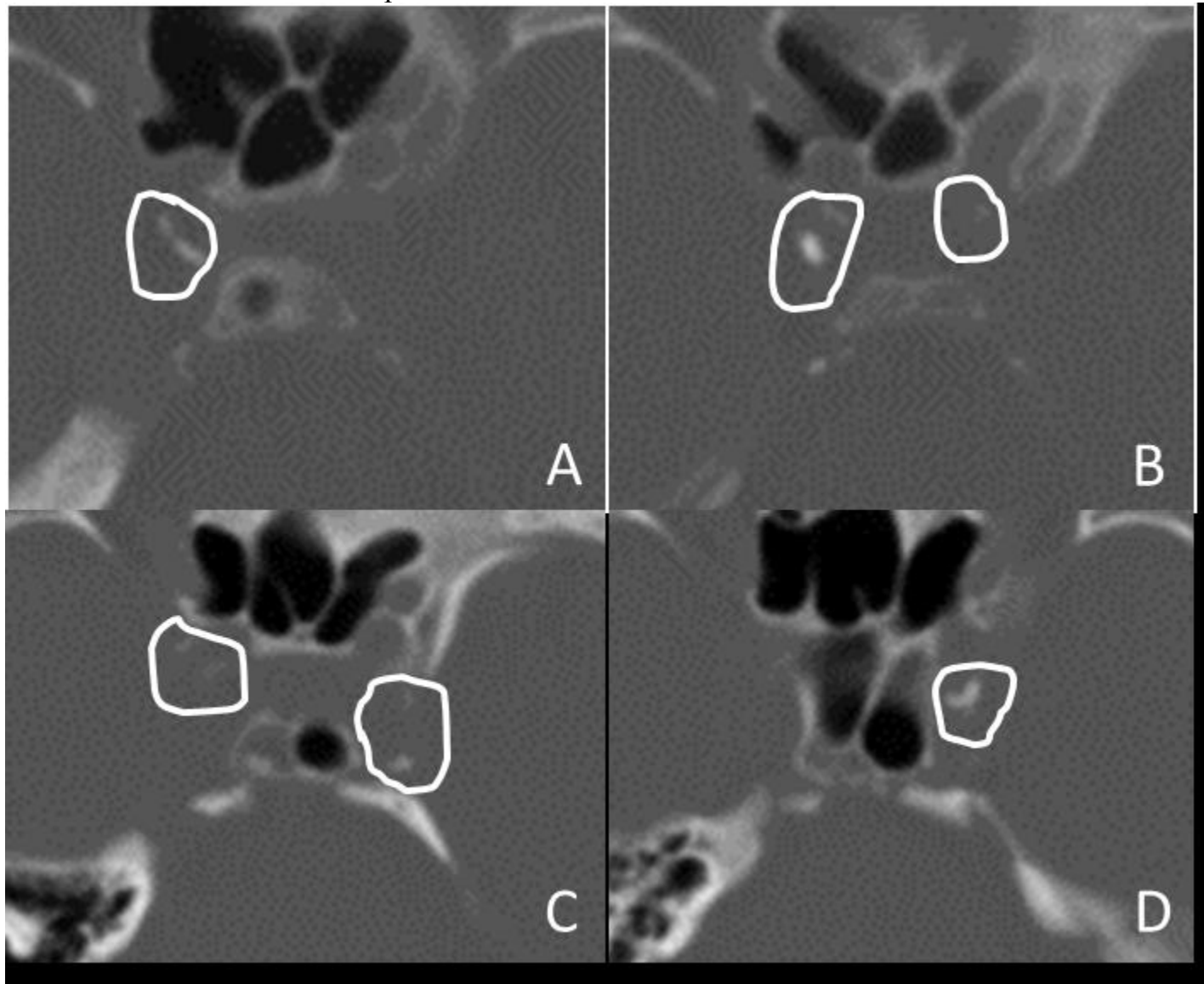
Results

We obtained 440 calcium measures from 110 ICAs in 55 patients. Among 34 patients with stroke of undetermined etiology, we found substantially greater calcium in the ICA upstream of the infarction (mean Modified Woodcock Visual Score, 6.7 ± 4.6) compared to the unaffected side (5.4 ± 4.1) ($P = 0.005$). Among 21 patients with cardioembolic stroke, we found no difference in calcium burden upstream of the infarction (6.7 ± 5.9) versus the unaffected side (7.3 ± 6.3) ($P = 0.13$). Results were similar using quantitative calcium measurements.

Conclusions

In patients with strokes of undetermined etiology, the burden of calcified intracranial large-artery plaque was associated with downstream cerebral infarction. These findings suggest that undiagnosed, nonstenosing large-artery atherosclerotic lesions

may explain some proportion of cryptogenic strokes and more aggressive therapies should be considered for these patients.



(Filename: TCT_O-488_Figure1ASNR.jpg)

O-489

2:03PM - 2:11PM

Differential Diagnosis of Dissection and Atherosclerosis of intracranial Vertebral Artery on High Resolution Vessel Wall MRI

Y Heo¹, H Jeong²

¹Busan Paik Hospital, Inje University, Busan, Korea, Republic of, ²Busan Paik Hospital, Inje University, Busan, others

Purpose

The purpose of this study was to compare the vertebral arterial dissection (VAD) and atherosclerosis involving intracranial vertebral artery.

Materials and Methods

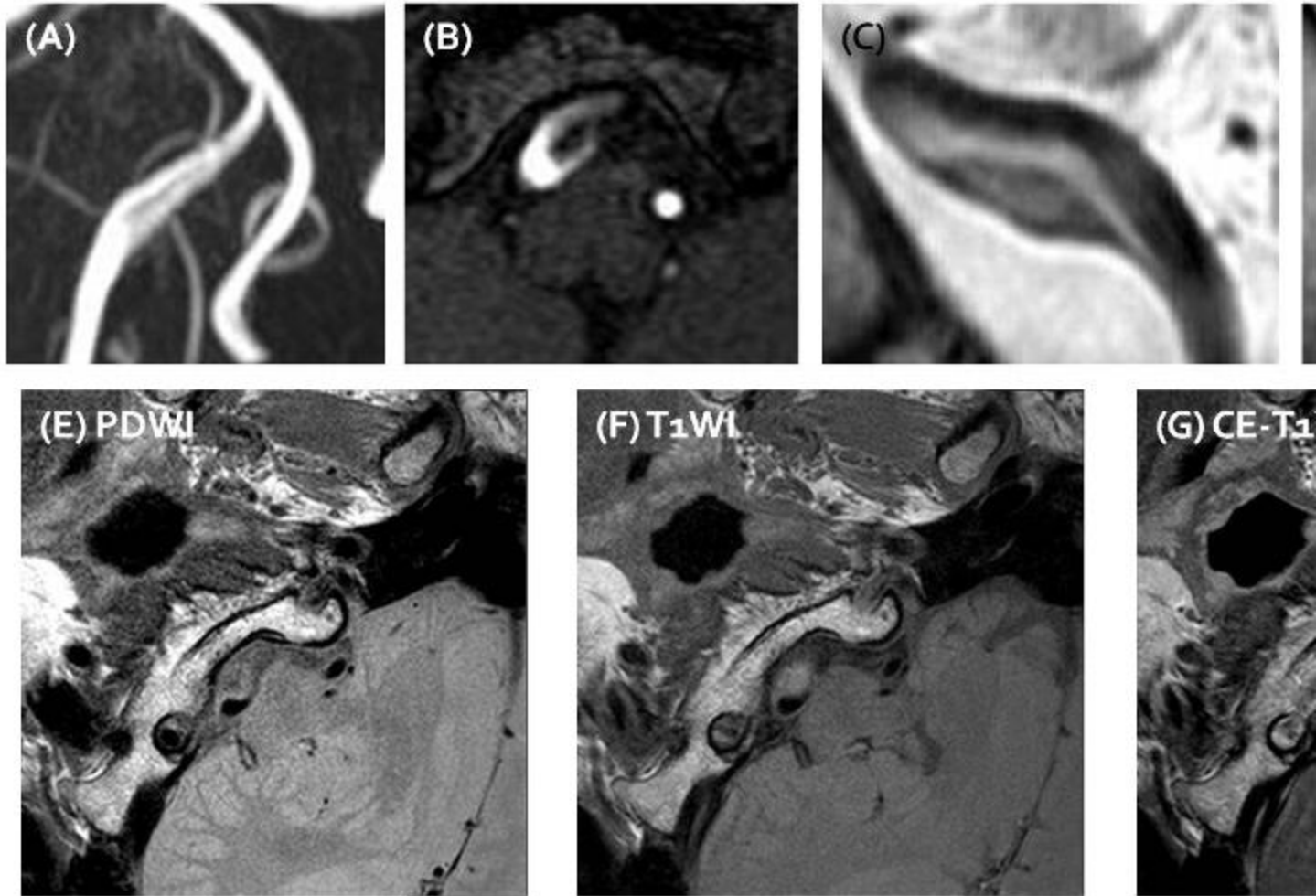
We retrospectively reviewed 24 patients suspected VAD and atherosclerosis who underwent 3.0 T high resolution vessel wall magnetic resonance imaging (MRI). Two neuroradiologists independently reviewed high resolution MR images and compared with final diagnosis based on clinicoradiologic findings. Magnetic resonance imaging findings of remodeling index, dissecting flap, contrast enhancement, accompanying cerebellar infarction and intramural T1 hyperintensity, suggesting intramural hematoma were evaluated.

Results

We finally diagnosed 18 patients as VAD and six patients as atherosclerosis. Remodeling index of dissection (1.79 ± 0.46) of VAD was significantly larger than atherosclerosis (1.17 ± 0.21). Dissection flap was observed in 10 patients and all of the patients were finally diagnosed as VAD. Accompanied cerebellar infarction was more frequently observed in VAD with clinical significance. Vessel wall enhancement and T1 high signal intensity on arterial wall were not significantly different between VAD and atherosclerosis.

Conclusions

High resolution vessel wall MR imaging is useful in differentiation of VAD and atherosclerosis.



(Filename: TCT_O-489_Figure.jpg)

O-490

2:11PM - 2:19PM

High-Resolution MRI Vessel Wall Imaging: Changes in Atherosclerosis and Moyamoya disease in Follow-up Period

Y Heo¹, H Jeong²

¹Busan Paik Hospital, Inje University, Busan, Korea, Republic of, ²Busan Paik Hospital, Inje University, Busan, others

Purpose

High resolution magnetic resonance imaging (HRMRI) has been widely used in the evaluation of intracranial artery walls. It has an advantage in defining vessel wall characteristics of intracranial vascular disease. We investigated HRMRI arterial wall characteristics of atherosclerosis and other vascular disease to determine wall pattern changes during a follow-up period.

Materials and Methods

From October 2012 to December 2015, we prospectively performed initial and follow-up HRMRI for the patients with stenosis involving anterior circulation. The HRMRI protocol included 3D proton density, oblique sagittal proton density, T1, contrast-enhanced T1-weighted black blood MRI, time-of-flight MRA of the circle of Willis. Follow-up HRMRI were performed after taking lipid lowering agents and antiplatelet medications. Vessel wall characteristics including wall enhancement, character of wall thickening, and luminal narrowing were evaluated.

Results

Twenty-four patients with atherosclerosis and five patients with moyamoya disease were included. In the atherosclerosis group, 20 patients showed eccentric wall enhancement and thickening. On follow-up HRMRI, 10 patients showed decreased extent of plaque and enhancement of vessel wall and 14 patients showed no significant interval change of the vessel wall. In the moyamoya disease group, all of the patients showed concentric wall thickening and enhancement. On follow-up HRMRI, three patients showed increased plaque volume, one patient showed no significant interval change and one patient showed decreased plaque volume.

Conclusions

Postgadolinium intracranial HRMRI appears to be a useful tool in the evaluation of vessel wall morphologic changes in atherosclerosis and moyamoya disease during a follow-up period.

O-491

2:19PM - 2:27PM

Quantifying Intracranial Plaque Permeability with Dynamic Contrast Enhanced MRI

P Vakil¹, C Cantrell², T Carroll², S Ansari³

¹University of Illinois Chicago, Chicago, IL, ²northwestern university, Chicago, IL, ³Northwestern University, Feinberg School of Medicine, Chicago, IL

Purpose

The purpose of this pilot study was to quantify contrast permeability of intracranial atherosclerotic disease (ICAD) plaques in symptomatic patients and to compare these parameters against existing markers of plaque volatility using black blood magnetic resonance imaging (BBMRI) pulse sequences.

Materials and Methods

We received IRB approval and informed consent for a prospective study of contrast uptake dynamics in the major intracranial vessels proximal and immediately distal to the circle of Willis using dynamic contrast-enhanced (DCE) MRI, specifically in patients with symptomatic ICAD. Using the standard Tofts model we extracted

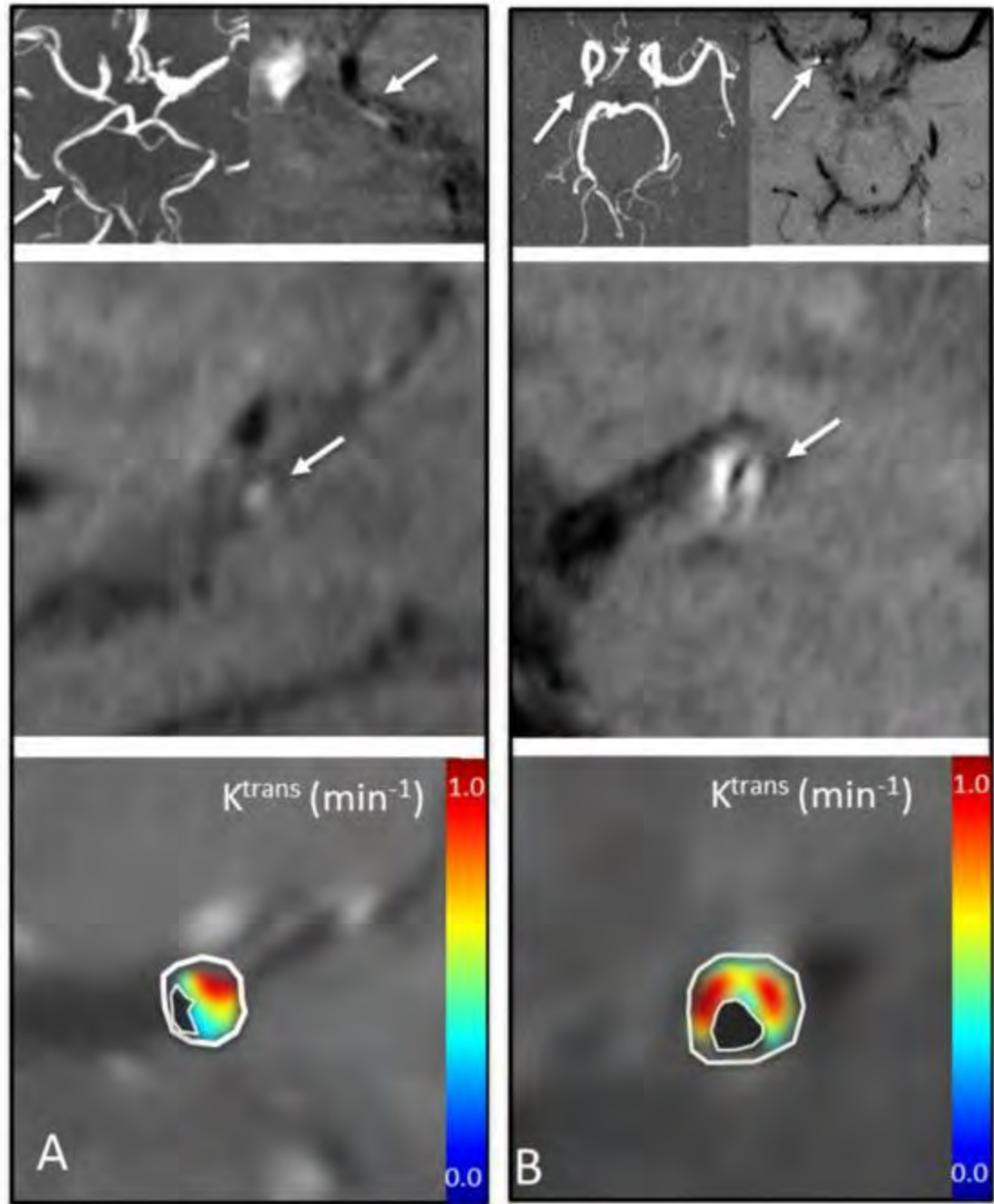
transfer constant (k_{trans}) and fractional plasma volume (v_p) parameters from plaque enhancement curves. We compared these parameters against time from symptom onset as well as intraplaque hyperintensity (IPH) and postcontrast enhancement (IPE) derived from T1 SPACE, a specific BBMRI vessel wall imaging pulse sequence, using regression analyses.

Results

We completed this analysis in 10 patients. K_{trans} and v_p measurements were higher in plaques versus healthy white matter and similar or less than values in the choroid plexus. Only k_{trans} correlated significantly with time from symptom onset (p=0.02). Dynamic contrast-enhanced MRI parameters were not found to correlate significantly with IPE or IPH (p=0.4 and p=0.17 respectively).

Conclusions

The elevated k_{trans} and v_p values found in ICAD lesions versus healthy white matter suggest that DCE-MRI is a feasible technique for studying vessel plaque characteristics in the intracranial vessels proximal and immediately distal to the circle of Willis. The significant correlations between k_{trans} and symptom onset which was not observed on T1 SPACE– derived metrics suggest that k_{trans} may be sensitive to acute and symptom-associated pathological changes in ICAD plaques.



(Filename: TCT_O-491_Figure1.jpg)

O-492

2:27PM - 2:35PM

Arterial-Spin Labeling for Non-Invasive Follow-Up of Cerebral AVMs Following Stereotactic Radiosurgery Treatment.

N Thakur¹, G Zaharchuk¹, M Iv², N Fischbein¹, J Heit¹

Purpose

Stereotactic radiosurgery (SRS) is an effective treatment for brain arteriovenous malformations (AVMs), but AVM obliteration following SRS may take 2 years or longer. Long term imaging follow-up is necessary to ensure complete AVM obliteration and to guide the need for additional treatment in the event of incomplete AVM obliteration. Digital subtraction angiography (DSA) remains the gold standard in brain AVM assessment, but DSA is invasive, carries procedural risks, involves ionizing radiation, and is relatively costly. Magnetic resonance imaging/magnetic resonance angiography (MRI/MRA) with conventional sequences has been shown to have predictive value in evaluating for obliteration of AVM post-SRS, but its sensitivity and specificity is inferior to DSA. Arterial spin labeling (ASL) is a noncontrast MRI sequence that has been shown to be sensitive in the detection of arteriovenous shunting by brain AVMs and dural arteriovenous fistulae. The purpose of this study was to determine the sensitivity and specificity of ASL in the detection of residual AVMs at least 2.5 years post-SRS, using DSA as the reference standard.

Materials and Methods

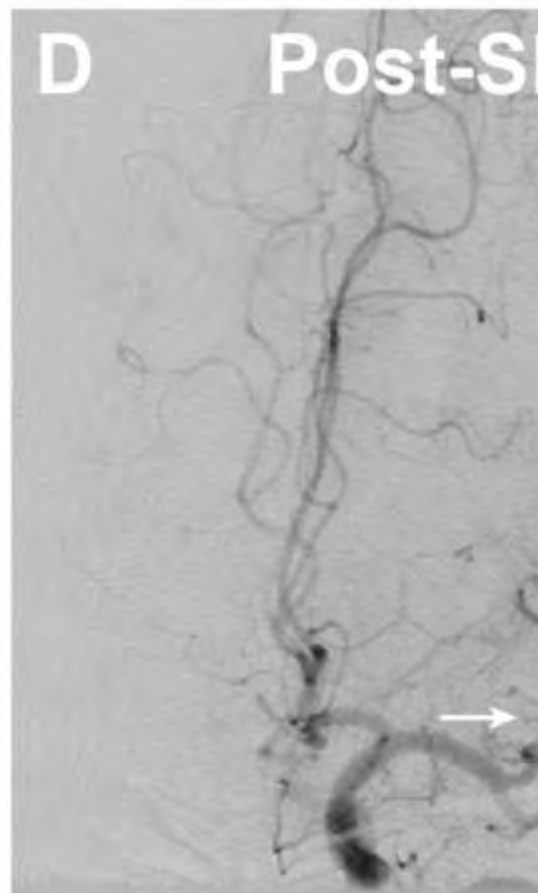
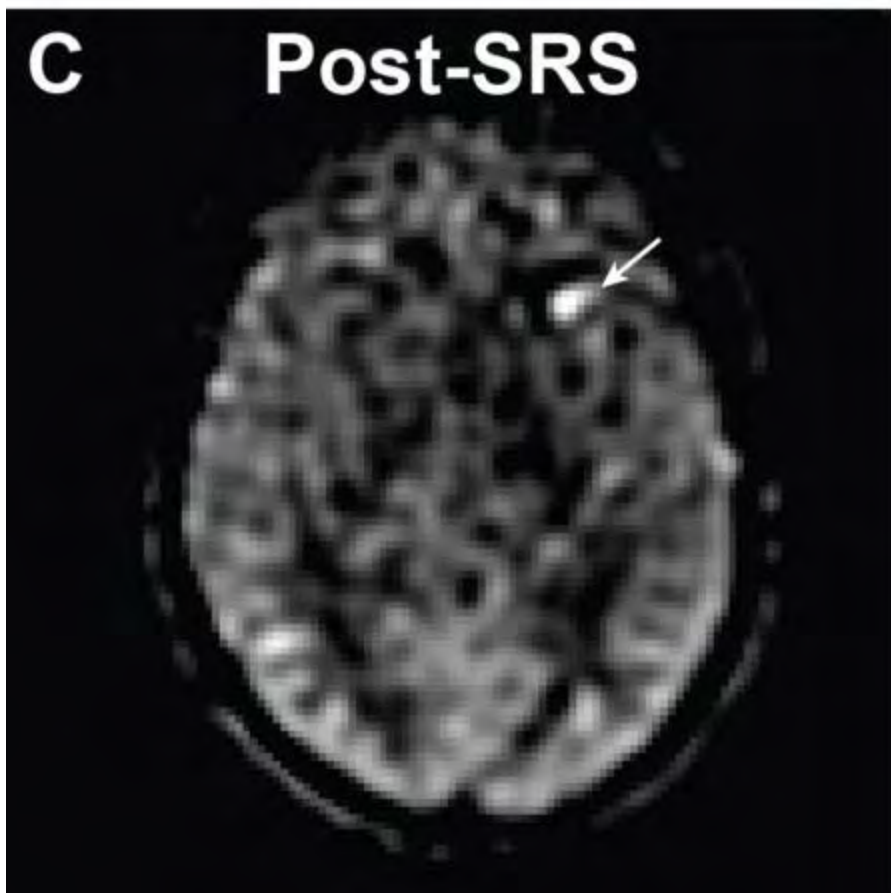
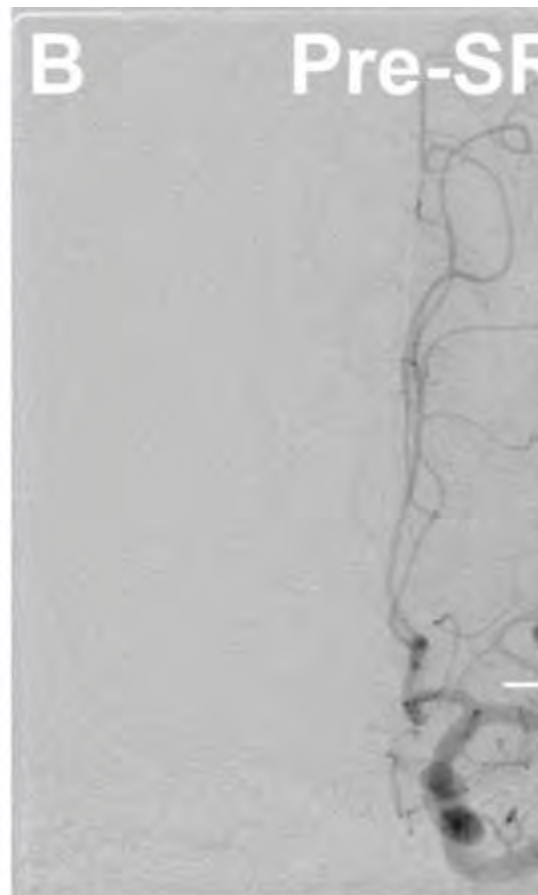
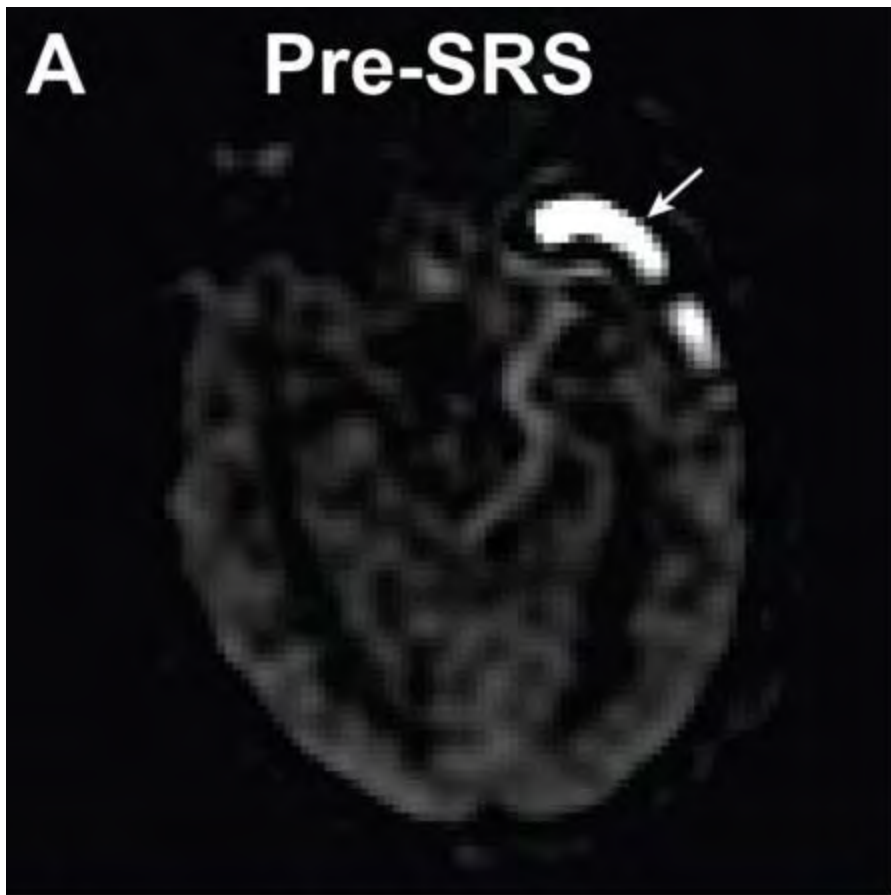
This study was approved by our institutional review board. We retrospectively reviewed our neurointerventional database and identified 241 consecutive patients who had undergone DSA for AVM evaluation from 6/2010-6/2015. Patients met inclusion criteria if they had 1) Undergone SRS for brain AVM treatment, 2) had a follow-up MRI with ASL at least 30 months after SRS, 3) had a DSA within 3 months of the follow-up MRI with ASL, and 4) had no intervening treatment between the MRI and DSA. Four neuroradiologists independently reviewed the MRIs for the presence of abnormal venous ASL signal suggestive of arteriovenous shunting. Reviewers were blinded to the results of the follow-up DSA, which was independently and blindly reviewed by an interventional neuroradiologist. Patient demographics, presentation, and imaging characteristics of the AVM were reviewed. Spetzler-Martin (SM) grading was determined from the oldest DSA before SRS. Statistical analysis was performed using XLSTAT.

Results

Fifteen patients (3 males and 12 females, mean age 29 years) met inclusion criteria. There were 12 cerebral AVMs, including SM 1 (1 patient), SM 2 (4 patients), SM 3 (2 patients), SM 4 (3 patients), and SM 5 (2 patients), and posterior fossa AVMs (3 patients). Digital subtraction angiography demonstrated complete AVM obliteration in five patients, and residual AVM in 10 patients. The sensitivity and specificity of venous ASL signal for predicting residual AVM on follow up DSA was 100% and 95%, respectively. Interobserver agreement was 0.92.

Conclusions

Arterial spin labeling with abnormal venous signal is highly accurate in identifying residual AVM following SRS treatment, with a sensitivity and specificity that approached that of DSA. Given the improved accuracy over previously reported conventional MRI sequences, ASL should be included in all MRI studies evaluating AVMs following SRS. Future studies should investigate whether MRI with ASL may be used to triage patients to DSA to guide additional AVM treatment.



(Filename: TCT_O-492_AS LAVMASNRFigurev3.jpg)

O-493

2:35PM - 2:43PM

Detailed Analysis of the Persistent Trigeminal Artery

O Narin¹, J Song², A Malhotra¹

¹*Yale New Haven Hospital, New Haven, CT*, ²*Yale University, New Haven, CT*

Purpose

Persistent trigeminal artery (PTA) is the most common of the persistent carotid-vertebrobasilar anastomoses, which was originally classified into two predominant types by Saltzman in 1959. The purpose of this study was to evaluate the incidence of the different types of PTA, the incidence of associated vascular anomalies including aortic arch anomalies and other arterial anomalies such as aneurysms, and the correlation of aortic arch anomalies with other arterial anomalies in PTA cases.

Materials and Methods

A retrospective review of the imaging database at a tertiary academic center was performed to identify all the patients with a persistent trigeminal artery identified by computed tomography angiography (CTA) imaging. Over a 5-year period (1/1/2010-12/1/2015), 42 patients were found to have a PTA on CTA examinations. Patients who did not have any diagnostic imaging studies involving the aortic arch were excluded from the study. Cases were reviewed retrospectively by two radiologists. Data collection included demographic information, classification of the Saltzman type of PTA (type 1 versus type 2), presenting symptoms, presence and type of aortic arch anomalies, and presence of aneurysms. Subsequently, data analysis was performed.

Results

Of 42 patients with PTA, 12 were excluded from the study (8 patients had no imaging of the aortic arch; 4 patients had no evidence of PTA on re-review of the cases). Among 30 patients with PTA, 18 were female and 12 male. Fifty-four percent (n=16) of the PTAs were on the left side and 46% (n=14) on the right. Type 1 was the most common Saltzman type (84%, n=25). Among 30 patients, eight had concurrent aortic arch anomalies (26.7%): six cases of common origin of the right brachiocephalic artery and the left common carotid artery and two cases of left vertebral artery arising from the aortic arch. Seven patients (23.3%) had concurrent aneurysms: three had saccular aneurysms at the origin of the PTA (42.9%) and one (14.3%) had an aneurysm of the extracranial ICA, two anterior communicating artery aneurysm (28.5%) and one contralateral middle cerebral artery aneurysm (14.3%). Eight (26.7%) cases were identified incidentally in asymptomatic patients, whereas 22 cases (73.3%) presented with neurological symptoms. There was no statistically significant

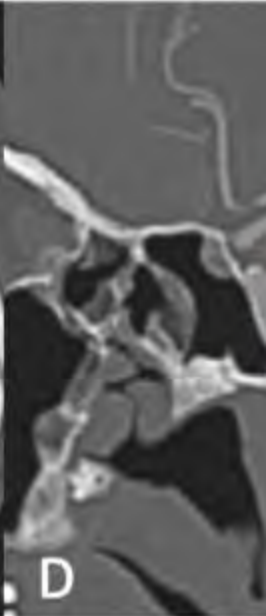
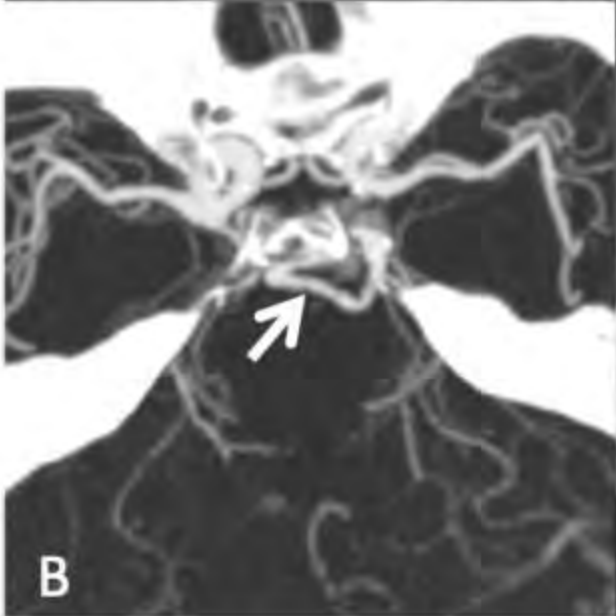
correlation between the aortic arch anomalies and concurrent arterial aneurysms in patients with PTA ($p= 0.89$).

Conclusions

This study showed a higher female predilection for persistent trigeminal artery (PTA) and overall a higher incidence of Saltzman type 1 PTA. The high incidence of associated aortic arch anomalies and arterial aneurysms suggests that there may be a common route of error during arterial vascular development. However, no statistically significant correlation was seen between aortic arch anomalies or concurrent arterial aneurysms in patients with PTA. It is important for the interpreting radiologist to understand variations and associations of cerebrovascular anatomy to understand mechanisms of disease, presenting symptoms, and to develop optimal treatment plans.



A) Coronal CTA MIP image demonstrating persistent trigeminal artery (yellow arrow) and connection between the right ICA and the trigeminal artery. The right-sided PTA joins the basilar artery below the origin of the superior cerebellar artery (blue arrow), compatible with Saltzman type 1. A fusiform aneurysm (red arrow) of the left internal carotid artery (white arrow) is seen on axial CTA MIP (B) and sagittal CTA images.



(Filename: TCT_O-493_PTAType1.jpg)